LA-UR-00-910

TRAC-M/FORTRAN 90 (VERSION 3.0)
THEORY MANUAL

by

J. W. Spore, J. S. Elson, S. J. Jolly-Woodruff, T. D. Knight,
J.-C. Lin, R. A. Nelson, K. O. Pasamehmetoglu,
R. G. Steinke, and C. Unal
Los Alamos National Laboratory
Los Alamos, New Mexico

J. H. Mahaffy and C. Murray
Pennsylvania State University
University Park, Pennsylvania

JULY 2000

TRAC-M/FORTRAN 90 (VERSION 3.0)
THEORY MANUAL

JULY 2000

Los Alamos National Laboratory
Los Alamos, NM 87545

and

Pennsylvania State University
University Park, PA 16802

EXECUTIVE SUMMARY

The United States (US) Nuclear Regulatory Commission (NRC) is developing the modernized versions of the Transient Reactor Analysis Code (TRAC-M) to provide advanced best-estimate simulations of real and postulated transients in pressurized water reactors (PWRs) and boiling water reactors (BWRs) for many related thermal-hydraulic facilities. The TRAC-M/Fortran 90 (TRAC-M/F90) program is the latest released version. This document is written for Version 3.0 of TRAC-M/F90. In addition, we indicate areas where TRAC-M/F90 differs from TRAC-M/Fortran 77 (TRAC-M/F77). The code features a one- and/or three-dimensional, two-fluid treatment for the thermal hydraulics, together with other necessary modeling capabilities to describe a PWR system. BWR capabilities will be added to future code releases of TRAC-M/F90.

This report is one of four documents describing various features of TRAC-M/F90. The remaining documents are the TRAC-M/F77 Developmental Assessment Manual and the TRAC-M/F90 User's and Programmer's Manuals. This Theory Manual provides a detailed description of the code's field equations, solution procedure, numerics, and closure correlations and models.

The Theory Manual is structured along the same lines as the code. Section 2.0. describes the field equations, finite-difference formulations, solution strategy, numerical methods, and control procedures. Also described in Section 2.0. are the heat-conduction and reactor kinetics equations and their solution.

Section 3.0. discusses TRAC's closure models and includes a "roadmap" that relates the various closure relations to the field equations. The inherent quasi-steady assumption and its implications also are discussed in Section 3.0.. Section 3.1. gives an overview of the code's closure relations. Section 3.2. describes the basic flow-regime map that is at the heart of the logic for selecting interfacial-shear and heat-transfer correlations for appropriate flow patterns. Section 3.3. summarizes the code's correlations and logic for the calculation of interfacial area. Section 3.4. describes the interfacial mass transfer. The correlations and logic describing the interfacial and wall drag are found in Sections 3.5. and 3.6., respectively, and Sections 3.7. and 3.8. cover the correlations and logic for interfacial heat transfer and wall heat transfer, respectively.

Section 4.0. provides the descriptions of special flow models, such as critical flow, offtake model, vent valves, and countercurrent flow limitation, that impact the calculation of velocities and interfacial drag. Section 4.0. also includes other special models, such as fuel-cladding gap conductance. Section 5.0. covers special function components, including pumps, boundary-condition components (fills and breaks), plenums, pressurizers, and valves. Finally, Section 6.0. provides a summary of the overall conclusions.

Much of the material in the main sections is described in greater detail in supporting appendices. Three appendices describe the water and material properties, the necessary thermodynamic and transport properties for the noncondensable-gas field, and the

solubility model for the liquid-solute field. Other appendices discuss the quasi-steady assumption and averaging operators, basic flow-regime maps, fluid closure (energy, mass, and momentum), flow process models, special component models, fuel-rod models, core power, and control procedure. We have structured the document to aid in understanding calculated results.

The audit nature of this report results in the descriptions of the individual correlation / models being relatively independent of most of the other descriptions. Because of this audit nature and the generality of TRAC, the individual results are difficult to synthesize into a global observation. Also, the process of looking closely at individual correlations makes it difficult to account for synergistic effects.

We believe that the models and correlations used in TRAC are a good representation of the state of the art in thermal-hydraulic literature. They are consistent with the literature, among themselves, and with the code numerics. The results are limited by the general assumptions, such as the quasi-steady approach, and by the time- and area-averaged field equations, which are the current state of the art in our understanding of two-phase thermal hydraulics. We believe TRAC is a viable tool for best-estimate, thermal-hydraulic analysis during various real or postulated transients in PWRs.

ACKNOWLEDGMENTS

Many people have contributed to the development of the TRAC series. The direct antecedent of TRAC-M is TRAC-PF1/MOD2 ("MOD2", otherwise known as "TRAC-P"). Most of the development of TRAC-M/F90 has involved a massive restructuring of the code's databases, data interfaces, and network solution. The database and data interface improvements are described elsewhere in the code's documentation set (mainly in the Programmer's Manual). The main impact on the Theory Manual involves the solution of the field equations, as acknowledged below. The following acknowledgments carry over mainly from a similar list compiled earlier for MOD2. However, it would be impossible to write such an acknowledgment section for TRAC-M without recognizing the enormous contributions of James F. Dearing in restructuring the code databases in Fortran 90.

Because of the long development history and because of the many people involved, we will not attempt to list everyone who worked on the code. So, with a general acknowledgment to these people, we intend to acknowledge specifically those people who developed the major new features of MOD2 and who contributed to the actual writing of the current document. Because TRAC-PF1/MOD2 is built upon TRAC-PF1/MOD1, certain parts required minor modifications only. Likewise, parts of the current document are similar to TRAC-PF1/MOD1 documents and are derived from these earlier documents with necessary modifications. We have not listed the names of the authors of these documents; however, we would like to fully acknowledge their indirect contribution to the current manual. We are especially appreciative of the effort put into the TRAC-PF1/MOD1 Correlations and Models document coordinated by Thad D. Knight, et al.

The following individuals contributed to the composing and writing of the various sections in the current manual. They are not necessarily the people who did the coding for the corresponding parts of TRAC-PF1/MOD2 or TRAC-M/F90.

Document Coordination	Ju-Chuan Lin, Jay W. Spore
Introduction	Kemal O. Pasamehmetoglu, Paul T. Giguere
Field Equations and Numerical Methods	Robert G. Steinke, Jay W. Spore, Susan J. Jolly-Woodruff, Kemal O. Pasamehmetoglu, Norman M. Schnurr, Laura A. Guffee, Ju-Chuan Lin, Stephen A. Birdsell, John H. Mahaffy, Chris Murray
Closure Relation Section	Jay S. Elson

Basic Flow-Regime Maps	Kemal O. Pasamehmetoglu
Fluid Energy Closure	Kemal O. Pasamehmetoglu, Ralph A. Nelson, Cetin Unal
Fluid Mass Closure	Kemal O. Pasamehmetoglu, Ralph A. Nelson, James R. White
Fluid Momentum Closure	Jay W. Spore, Michael W. Cappiello, Cetin Unal, Ju-Chuan Lin
Flow Process Models	Laura A. Guffee, Robert G. Steinke, Stephen A. Birdsell, James F. Lime
Special Component Models	Robert G. Steinke, Jay W. Spore, Kemal O. Pasamehmetoglu
Additional Mass-Field Closure	Robert G. Steinke, Eric Haytcher, Kemal O. Pasamehmetoglu
Summary and Conclusions	Jay W. Spore
Thermodynamic and Transport Fluid Properties	Eric Haytcher
Material Properties	Eric Haytcher, Kemal O. Pasamehmetoglu
Report Compilation	Kemal O. Pasamehmetoglu, Denise B. Pelowitz, Karyn R. Ames, Wendy M. Burditt, E. Katherine Valdez
Report Editing	Karyn R. Ames, Virginia Buchner, Lisa G. Rothrock, Lori S. Tamura

The following individuals provided the major improvements to the TRAC-PF1/MOD2 code:

Momentum Closure	Jay W. Spore, Robert G. Steinke
Capacitance Method	Robert G. Steinke, James F. Dearing

3D Two-Step Numerics	Susan B. Woodruff, John H. Mahaffy James F. Dearing
Generalized Heat Structures	John H. Mahaffy
Reflood Package	Ralph A. Nelson, Kemal O. Pasamehmetoglu, Cetin Unal
Interfacial Constitutive Package	Jay W. Spore, Michael W. Cappiello, Kemal O. Pasamehmetoglu
Improved Wall Shear	Jay W. Spore
Improved Treatment of Noncondensables	John H. Mahaffy, Ju-Chuan Lin
Special Models	
CCFL	Jay W. Spore, Paul Dotson
Decay Heat	Jay W. Spore
Offtake Model	Laura A. Guffee
Subcooled Boiling Model	Paul Dotson, Jay W. Spore
Valve Model	Jay W. Spore

In addition, we wish to acknowledge personnel at the Japan Atomic Energy Research Institute who provided the fully implicit axial-conduction solution for the TRAC-PF1/MOD2 code. These personnel are Y. Murao, H. Akimoto, Y. Abe, and A. Ohnuki. We would also like to acknowledge the United Kingdom Atomic Energy Authority for providing the external thermocouple model, and the following Los Alamos National Laboratory staff: Dennis R. Liles, for the thermal-hydraulics modeling; and Manjit S. Sahota, for the critical-flow model.

In the development of TRAC-M/F90 from MOD2, James F. Dearing restructured the code databases into Fortran 90 derived types. This has far-reaching importance for all aspects of TRAC development. John H. Mahaffy and Chris Murray significantly improved the data interfaces with two related efforts: (1) full separation of the evaluation of terms in the flow equations from the solution of the resulting system of linear equations, resulting in an improved network solution; and (2) improved inter-component communication, implemented as a system service.

CONTENTS

FIGURES

FIGURES (cont)

FIGURES (cont)

FIGURES (cont)

FIGURES (cont)

FIGURES (cont)

FIGURES (cont)

FIGURES (cont)

FIGURES (cont)

TABLES

TABLES (cont)

ACRONYMS AND ABBREVIATIONS

1D	one-dimensional
2D	two-dimensional
3D	three-dimensional
4D	four-dimensional
ANS	American Nuclear Society
ASME	American Society of Mechanical Engineers
B&W	Babcock and Wilcox
BWR	boiling water reactor
CCFL	countercurrent flow limitation
CCTF	Cylindrical-Core Test Facility
cgs	centimeter-gram-second units
CHF	critical heat flux
CPU	central processing unit
CSO	Chen, Sundaram, and Ozkaynak
CSS	constrained steady-state
CTSS	Cray Timesharing System
ECC	emergency core-coolant
ECCS	emergency core-coolant system
EPRI	Electric Power Research Institute
FSAR	final safety analysis report
GE	General Electric
GSS	generalized steady-state
HEM	homogeneous equilibrium model
HTC	heat-transfer coefficient
HTFS	heat-transfer fluid flow service
HS	heat-structure component
IAF	inverted annular flow
ICE	implicit continuous eulerian
ID	identification
IFDC	interfacial drag-coefficient selection
INEEL	Idaho National Engineering and Environmental Laboratory
JAERI	Japan Atomic Energy Research Institute
L-U	lower-upper (matrix decomposition)
LANL	Los Alamos National Laboratory
LBLOCA	large-break LOCA
LOCA	loss-of-coolant accident
LOFT	Loss-of-Fluid Test
LU	Lehigh University
LWR	light water reactor

NBS	National Bureau of Standards (now known as NIST)
NESC	National Energy Software Center
NIST	National Institute of Standards and Technology (formerly NBS)
NPP	nuclear-power-plant
NRC	United States Nuclear Regulatory Commission
OSV	onset of significant voiding
pdf	probability density function
PI	proportional plus integral
PID	proportional plus integral plus derivative
PORV	power-operated relief valve
ppm	parts per million
PWR	pressurized water reactor
RMS	root mean square
rps	revolutions per second
SBLOCA	small-break LOCA
SCTF	Slab Core Test Facility
SETS	stability-enhancing two-step
SI	International System of Units
SLOR	successive line over-relaxation
TRAC	Transient Reactor Analysis Code
UCSP	upper-core-support-plate
UPTF	Upper-Plenum Test Facility
USNRC	United States Nuclear Regulatory Commission

TRAC-M/FORTRAN 90 (VERSION 3.0)
THEORY MANUAL

by

J. W. Spore, J. S. Elson, S. J. Jolly-Woodruff, T. D. Knight,
J.-C. Lin, R. A. Nelson, K. O. Pasamehmetoglu,
R. G. Steinke, C. Unal, J. H. Mahaffy and C. Murray

ABSTRACT

The United States Nuclear Regulatory Commission (USNRC) is developing the modernized versions of the Transient Reactor Analysis Code (TRAC-M) to provide advanced best-estimate simulations of real and postulated transients in pressurized and boiling water reactors (PWRs and BWRs) and for many related thermal-hydraulic facilities. The TRAC-M/Fortran 90 (TRAC-M/F90) program, the latest released version, is written for TRAC-M/F90 Version 3.0. In addition, we indicate areas where TRAC-M/F90 differs from the TRAC-M Fortran 77 (TRAC-M/F77) code (Version 5.5.2). Both codes feature a one- and/or three-dimensional, two-fluid treatment for the thermal hydraulics, together with other necessary modeling capabilities to describe a reactor system. Currently both codes are intended for analysis of pressurized water reactors (PWRs), but future versions of TRAC-M/F90 will include a capability to model BWRs. Both codes produce graphics output that is compatible with the TRAC visualization and plotting tool XTV. In addition, TRAC-M/F90's graphics file can be used with the XMGR code. TRAC-M/F77 is written in standard Fortran 77 and includes a newly enhanced reflood model. TRAC-M/F90 is written in standard Fortran 90 and includes a derived-type database and improved data interfaces.

This report is one of four describing various features of TRAC-M/F90. Two of the other documents are the TRAC-M/F90 User's and Programmer's Manuals. The fourth document is the TRAC-M/F77 Developmental Assessment Manual. This Theory Manual provides a detailed description of the field equations, solution procedure, numerics, and closure correlations and models of the code. This report also provides the basis for each model, correlation, or solution strategy through references to original literature and/or a description of the development process. Additionally, it lists the assumptions made in the implementation, including the definitions of required parameters not normally calculated by the code, and it describes other details of the implementation. We have provided a partial assessment of some of the models and correlations against other pertinent models and correlations or separate-effects data. However, a true measure of the overall accuracy of the code must include

assessment of the code against integral experimental data because of synergistic effects. Such assessment results are provided in the TRAC-M/F77 Developmental Assessment Manual.

In the process of reviewing the details for the code and writing this report, we found that the numerics and the models and correlations used in the code are a good representation of the state of the art. However, simplified models are used in some areas where either a relevant model was not found in the literature or the literature model could not be implemented easily into the code's logic. From the assessment against integral tests, we believe that TRAC-M/F90 is a viable calculational tool for analyzing pressurized light-water reactors (LWRs) during a loss-of-coolant accident and operational transients. (Future releases of the TRAC-M/F90 documentation will address boiling water reactor (BWR) analysis.) In addition, the developmental assessment calculations for TRAC-M/F77 indicate that TRAC-M/F90 will be applicable to a wide range of test facilities.

1.0. INTRODUCTION

The Transient Reactor Analysis Code (TRAC) is an advanced, best-estimate computer program designed to calculate the transient reactor behavior of a pressurized water reactor (PWR). As such, TRAC incorporates four-component (liquid water, liquid solute, water vapor, and noncondensable gas), two-fluid (liquid and gas) modeling of thermal-hydraulic processes involved in such transients. The complexity of the thermal-hydraulic modeling requires many additional models and correlations to provide closure for the equation set. As used here, a model consists of a set of correlations with logic imposed into a coherent description of a phenomenon. This document describes for TRAC-M Fortran 90 (TRAC-M/F90) the general equation sets solved by the code, the numerical solution techniques employed, and the code's closure models and correlations. A best-estimate code continues to evolve and to incorporate new capabilities from the development process; we have written the current document for Version 3.0. In addition, we indicate areas where TRAC-M/F90 differs from TRAC-M Fortran 77 (TRAC-M/F77), Version 5.5.2.

TRAC-M/F90 and TRAC-M/F77 are the latest in a series of TRAC codes, including TRAC-PF1/MOD2 (also known as "TRAC-P"), TRAC-PF1/MOD1, TRAC-PF1, TRAC-PD2, TRAC-P1A, and TRAC-P1, the earliest publicly released version. (The main development path for TRAC now comprises the versions of TRAC-M/F90. As discussed below, TRAC-M/F77 is an important "side-branch" with an enhanced PWR reflood model.) The development history represented by these earlier code versions begins with a very fundamental and important enhancement in the analysis of the behavior of light-water reactors (LWRs). This improvement is the decision to track separately the liquid and vapor fields in the reactor-coolant system. These codes required the greatly improved computer systems that were becoming available during the 1970s and they pushed advances in numerical techniques to solve the complex equation set and to permit the large number of nodes required for the best-estimate analysis of some transients of interest.

A preliminary version of TRAC consisting of only one-dimensional (1D) components was completed in December 1976. Although this version was not released publicly nor documented formally, it was used in TRAC-P1 development and formed the basis for the 1D loop-component modules. The first publicly released version, TRAC-P1, was completed in December 1977; it is described in Ref. 1-1.

The TRAC-P1 program was designed primarily for the analysis of large-break loss-of-coolant accidents (LOCAs) in PWRs. However, because of its versatility, it could be applied directly to many analyses ranging from blowdowns in simple pipes to integral LOCA tests in multiloop facilities. A refined version, TRAC-P1A, was released to the National Energy Software Center (NESC) in March 1979. It is described in Refs. 1-1. and 1-2. Although it still treats the same class of problems, TRAC-P1A not only is more efficient than TRAC-P1 and incorporates improved hydrodynamic and heat-transfer models, but also is easier to implement on various computers. TRAC-PD2 (Ref. 1-3.) contains improvements in reflood, heat-transfer models, and numerical solution

methods. Although it is a large-break LOCA (LBLOCA) code, it has been applied successfully to small-break problems and to the Three Mile Island incident.

TRAC-PF1 (Ref. 1-4.) was designed to improve the ability of TRAC-PD2 to handle small-break LOCAs (SBLOCAs) and other transients. TRAC-PF1 has all of the major improvements of TRAC-PD2. In addition, it used a two-fluid model with stability-enhancing two-step (SETS) numerics (Ref. 1-5.) in the 1D components. The two-fluid model, in conjunction with a stratified-flow regime, models countercurrent flow better than the drift-flux model used previously. The two-step numerics allow large time steps for slow transients. A 1D core component permits calculations with reduced dimensionality although the three-dimensional (3D) VESSEL option has been retained. A noncondensable gas field has been added to the 1D and the 3D hydrodynamics. Significant improvements also have been made to the trip logic and the input. TRAC-PF1 was released publicly in July 1981.

The development of TRAC-PF1/MOD1 maintained the models necessary for applying the code to LBLOCAs and added or modified models as necessary to enhance the application of the code to SBLOCAs and operational transients (Refs. 1-6. and 1-7.). In particular, we added or enhanced many user-convenience features to promote the application of the code to transients involving more complex control of the nuclear plant. TRAC-PF1/MOD1 contains generalized reactivity-feedback models (subject to point-kinetics assumptions), generalized trip and control-system modeling, and necessary components to model the rest of the plant. The code is applicable to most transients for which large asymmetries in the power generation do not exist, the 1D fluid modeling in the pipe is valid, and thermal stratification in the liquid in the 1D components is not important. (The 3D VESSEL component can model thermal stratification in a coarse manner.) The code maintains the capability to run in either a 1D or a mixed 1D and 3D mode, with SETS numerics in the 1D components.

TRAC-PF1/MOD2 ("MOD2," otherwise known as "TRAC-P") was superior to all earlier versions of TRAC, both in its numerics and its closure relationships. Among many improvements in MOD2, the SETS numerics were extended to the 3D VESSEL component, the interfacial closure relations were completely rewritten, and a new core reflood model was introduced. The 1D and 3D SETS numerics, MOD2 closure relations, and most of MOD2's modeling capabilities have been brought directly over to TRAC-M. These still provide new and state-of-the-art features for LWR safety analysis.

MOD2 is the direct antecedent of TRAC-M/F90 (and of TRAC-M/F77, as described below in Section 1.4.). Most of the development of TRAC-M/F90, Version 3.0, has involved a massive restructuring of TRAC's databases and data interfaces. (The "M" in the code's name stands for "modernized".) Almost everything else in MOD2 that affects thermal-hydraulic modeling (including closure relations, flow process models, most special component models, fluid and material properties, reactor-power logic, heat conduction, control system, and SETS numerics) was carried over to TRAC-M/F90 (and to TRAC-M/F77). In fact, an important aspect of the development of TRAC-M/F90 (and of TRAC-M/F77) was null, or almost null, testing against an extensive set of MOD2

results. TRAC-M/F90's databases are restructured into standard, portable, Fortran 90-derived types, and almost all arrays are dynamically allocated at runtime using standard Fortran 90 calls. This had, and will continue to have, far-reaching importance for all aspects of TRAC development. Also, the code's data interfaces were significantly improved with two related efforts: (1) full separation of the evaluation of terms in the flow equations from the solution of the resulting system of linear equations, resulting in an improved network solution for the field equations; and (2) improved inter-component communication, implemented as a system service. The main impact of TRAC-M/F90 development, from its MOD2 base, on the TRAC Theory Manual involves the solution of the field equations, as described in Section 2.0. The rest of this document is based on a draft Theory Manual that was prepared earlier for MOD2. Full details on the database and data-interface improvements in the code are given in the TRAC-M/F90 Programmer's Manual (Ref. 1-4.).

In Section 1.1. a brief summary and the general features of the computer program are given. Section 1.2. lists the code's essential distinguishing characteristics. The code's modeling capabilities are summarized in Section 1.3. Section 1.4. gives the current status of TRAC development. The status includes a summary of modeling features in this newest version of TRAC that were not available in earlier versions (before MOD2), a comparison of the TRAC-M/F77 and TRAC-M/F90 codes, and an indication of future areas of TRAC development. Section 1.5. describes the value of the current code as compared to its predecessors. Section 1.6. covers the scope of this document, including subsections on its structure, its targeted interest groups, and its basic assumptions.

1.1. Computer Program Summary

The official name of the code is TRAC-M/F90 (Version 3.0). Throughout this document, the term "TRAC" will indicate both TRAC-M/F90 and TRAC-M/F77 (Version 5.5.2). Where confusion could exist with earlier versions, or where TRAC-M/F90 and TRAC-M/F77 differ, we will explicitly identify the applicable code.

The programming language of TRAC-M/F90 is standard Fortran 90; the programming language of TRAC-M/F77 is standard Fortran 77. Portability was a key goal in the development of both TRAC-M/F90 and TRAC-M/F77. Unlike MOD2, there are no conditional preprocessor directives (platform-specific "IF DEFs") embedded in the Fortran source code. Both codes use a few low-level routines written in American National Standards Institute (ANSI) standard C and use the ANSI-standard C preprocessor.

TRAC performs best-estimate analyses of LOCA and other transients in PWRs. The code also models a wide variety of thermal-hydraulic experiments in reduced-scale facilities. Models used include reflood, multidimensional two-phase flow, nonequilibrium thermodynamics, generalized heat transfer, and reactor kinetics. Automatic steady-state and dump/restart capabilities also are provided. The partial differential equations that describe the two-phase flow and the heat transfer are solved by finite differences. The heat-transfer equations are treated using a semi-implicit differencing technique.

The fluid dynamic equations in both one and three dimensions use a multistep procedure (SETS numerics) that allows the material Courant limit to be violated. The highly versatile TRAC describes most thermal-hydraulic experiments in addition to a wide variety of LWR system designs. The code modularity allows better geometric problem description, more detailed models of physical processes, and reduced maintenance cost.

The only limit on the problem size is the amount of computer memory. The number of reactor components in a problem and the manner in which they are coupled are arbitrary. Reactor components that are built into TRAC are breaks and fills (boundary conditions), generalized heat structures (rods and slabs), pipes, pressurizers, pumps, tees, valves, and vessels with associated internals. Accumulators can be modeled with a special option in the pipe component, and steam generators can be modeled with a combination of pipes, tees, and heat structures. Running time is highly problem-dependent and is a function, among other things, of the total number of mesh cells, the nature of the transient, the maximum allowable time-step size, and the selection of 1D or 3D vessel modeling. The introduction of SETS numerics to the 3D vessel component will improve runtime when the overall time step would be Courant-limited by a 3D vessel component. Some important characteristics of TRAC pertinent to LWR safety are summarized in the next section.

1.2. TRAC Characteristics

Some distinguishing characteristics of TRAC are summarized below. Within restrictions imposed by computer running times, we are incorporating state-of-the-art technology in two-phase thermal hydraulics into the code.

1.2.1. Variable-Dimensional Fluid Dynamics

A 3D (r, θ, z) flow calculation can be used within the reactor vessel to allow an accurate calculation of the complex multidimensional flow patterns inside the reactor vessel that are important in determining accident behavior. For example, phenomena such as emergency core-coolant (ECC) downcomer penetration during blowdown, multidimensional plenum and core flow effects, and upper-plenum pool formation and core penetration during reflood can be treated directly. The flow within the loop components is treated one-dimensionally.

1.2.2. Nonhomogeneous, Nonequilibrium Modeling

A full two-fluid (six-equation) hydrodynamics model describes the steam-water flow, thereby allowing important phenomena, such as a countercurrent flow, to be treated explicitly. A seventh field equation (mass balance) describes a noncondensable gas field, and an eighth field equation tracks the solutes in the liquid.

1.2.3. Flow-Regime-Dependent Constitutive Equation Package

The thermal-hydraulic equations describe the transfer of mass, energy, and momentum between the steam-water phases and the interaction of these phases with the heat flow from the system structures. Because these interactions are dependent on the flow

topology, a flow-regime-dependent constitutive equation package has been incorporated into the code. Assessment calculations performed to date with MOD2 and TRAC-M/F77 indicate that many flow conditions can be handled adequately with the current package. This continues to be an active area of research in modeling two-phase flow. Therefore, it is an area in the code that will possibly continue to improve.

1.2.4. Comprehensive Heat-Transfer Capability

TRAC incorporates detailed heat-transfer analyses of the vessel and the loop components. Included is a two-dimensional (2D) (r, z) treatment of fuel-rod heat conduction with dynamic fine-mesh rezoning to resolve both bottom-flood and falling-film quench fronts. The heat transfer from the fuel rods and other system structures is calculated using flow-regime-dependent heat-transfer coefficients (HTCs) obtained from a generalized boiling surface based on local conditions.

1.2.5. Consistent Analysis of Entire Accident Sequences

An important TRAC feature is its ability to address entire accident sequences, including computation of initial conditions, with a consistent and continuous calculation. For example, the code models the blowdown, refill, and reflood phases of a LOCA. This modeling eliminates the need to perform calculations using different codes to analyze a given accident. In addition, a steady-state solution capability provides self-consistent initial conditions for subsequent transient calculations. Both a steady-state and a transient calculation can be performed in the same run, if desired.

1.2.6. Component, Functional, and Computational Mesh Modularity

The TRAC program is completely modular by component. The components in a calculation are specified through input data. The available components allow the user to model virtually any PWR design or experimental configuration. Thus, TRAC has great versatility in its range of applications. This feature also allows component modules to be improved, modified, or added without disturbing the remainder of the code. TRAC component modules currently include breaks and fills to model pressure and flow boundary conditions, generalized heat structures (rods and slabs), pipes, pressurizers, pumps, tees, valves, and vessels with associated internals (downcomer, lower plenum, core, upper plenum, etc.).

The TRAC program also is modular by function; that is, the major aspects of the calculations are performed in separate modules. For example, the basic 1D hydrodynamics solution algorithm, the wall-temperature-field solution algorithm, HTC selection, and other functions are performed in separate sets of routines that are accessed by all component modules. This modularity allows the code to be upgraded readily as improved correlations and test information become available.

An important part of TRAC-M/F90 development, related to the functional modularity, is the strengthening of the code's existing organization by computational mesh. A new data structure, developed as part of the improved data-interface effort, views components as collections of mesh segments and contains data describing the relationships between these mesh segments. Capabilities of mesh-specific subroutines

have been made more general to meet the needs of the range of physical components. Where possible, direct references to component types have been removed from mesh-specific subroutines, and the necessary features are driven by the components in a more general way. The effect is to bring component-specific operations to a higher level of the code.

1.3. TRAC Capabilities

Most physical phenomena that are important in large- and small-break LOCA and non-LOCA analyses can be treated by TRAC. The phenomena include the following:

1. ECC downcomer penetration and bypass, including the effects of countercurrent-flow hot walls;
2. lower-plenum refill with entrainment and phase separation effects;
3. bottom-reflood and falling-film quench fronts;
4. multidimensional flow patterns in the core, downcomer, and plenum regions;
5. pool formation and countercurrent flow at the upper-core-support-plate (UCSP) region;
6. pool formation in the upper plenum;
7. steam binding;
8. average-rod and hot-rod cladding temperature histories;
9. alternate ECC-injection systems, including hot-leg and upper-head injection;
10. direct injection of subcooled ECC water, without the requirement for artificial mixing zones;
11. critical flow (choking) using the improved critical-flow model (the detailed noding technique of TRAC-PD2 can still be used, although we generally do not recommend it);
12. liquid carryover during reflood;
13. metal / water reaction;
14. water-hammer effects;
15. wall friction losses;
16. natural-circulation flows;
17. horizontally stratified flows, including horizontal countercurrent flow driven by void-fraction gradients down the pipe;
18. vertical-stratification modeling in the vessel component and in the interphase mass transfer (condensation) to better calculate pressurizer refill and the general refilling of any vertically-oriented component;

19. increased range in the water properties to permit the code to calculate fluid conditions beyond the critical point (pressures in excess of 22.12 MPa) and closer to the freezing point;

20. noncondensable-gas tracking, including the injection of the noncondensable gas from the accumulators and the effects of the noncondensable gas on the interfacial condensation;

21. liquid-solute (boron) tracking, which can be coupled to the reactivity-feedback calculation;

22. point-reactor kinetics with a generalized representation of the reactivity feedback associated with the core-average fuel temperature, the core-average coolant temperature, the core-average void fraction, and the core-average boron concentration;

23. balance-of-plant modeling capability;

24. a PLENUM component consisting of a single hydraulic cell with an essentially unlimited number of connections to simplify 1D connections;

25. mixed 1D and 3D calculations or fully 1D calculations;

26. fast computational speed for 1D and 3D problems when the transient is reasonably slow, such as SBLOCA and some non-LOCA transients;

27. very general trip, control-system, and component-action (such as feedwater-pump flow characteristics) modeling capability;

28. the ability to use trips and controls in the steady-state calculation to drive the steady-state conditions towards desired values and thus to eliminate unnecessary iterations on the steady-state calculation;

29. user-convenience features, including free-format input with capability to use comment cards or fields, forward and reverse additive-friction factors for the hydraulics, capability to choose to input Darcy K-factors for the additive friction, capability to choose to input cell-centered elevations instead of the old gravity parameters at cell interfaces, and sophisticated input checking;

30. consistent generation of steady-state conditions for initializing transients so that the same thermal-hydraulic models and numerics are used in both the steady state and the transient;

31. general orientation and magnitude of the VESSEL component for the gravitational acceleration vector; and

32. a generalized heat-structure component to allow the user to connect two hydro cells, resulting in greatly increased flexibility in heat-conduction modeling.

1.4. TRAC Significant Changes

In this section we first summarize the improvements in TRAC-PF1/MOD2 that were brought over to TRAC-M/F90 and TRAC-M/F77. We then describe the development of TRAC-M/F90 and TRAC-M/F77 from their MOD2 base (indicating the differences between the two codes), and briefly discuss planned future development of the two codes.

TRAC has the following improvements that were "inherited" from MOD2:

1. SETS numerics are applied to the 3D hydro solution. This change allows the VESSEL component to take large time-step sizes during a relatively slow transient, thus allowing faster running time. The implementation of SETS numerics is described in Section 2.1.8.
2. The development of a generalized heat-structure component allows the user to connect any hydro cell with any other hydro cell. This component allows increased flexibility for heat-conduction modeling.
3. An improved reflood model is implemented in the code. The new model is described in Appendix F, Section F.2.. (Note that, as described later in this section, this reflood model is available in both TRAC-M/F90 and TRAC-M/F77, and that TRAC-M/F77 has, in addition to this model, a newer enhanced reflood model.)
4. The wall-shear model is changed and made consistent between 1D and 3D components. The new wall-shear model is described in Appendix H, Section H.2.
5. A new valve model is developed based upon experimental data for partially closed globe valves. The new model is described in Appendix J, Section J.9.
6. The Gauss-Seidel numerical solution for the 3D VESSEL pressure matrix equation was observed to be inaccurate for small breaks and operational transients. This inaccuracy would typically be observed as a mass error in the VESSEL component. This problem is solved in TRAC by the elimination of the Gauss-Seidel method and by the development and implementation of a capacitance method for solving the VESSEL pressure matrix equations. TRAC's capacitance method is described in Section 2.0.
7. The VESSEL component is allowed general orientation with respect to the gravitational acceleration vector.
8. The ANS'79 decay-heat standard, described in Appendix M, is included in TRAC as the default model.
9. An offtake model, described in Sections 2.1.8.6.3. and 4.3. as well as Appendix I, Section I.4., is implemented in TRAC.

10. Interfacial heat-transfer and interfacial shear correlations, described in Appendix F, Section F.1., and Appendix H, Section H.1., are considerably different than those in TRAC-PF1/MOD1. The interfacial shear and heat-transfer packages are made consistent with each other. The consistency is also assured between 1D and 3D components.

11. The 60-, 120-, and 180-degree rotational symmetry in cylindrical geometry allows significantly reduced noding if loop and vessel behavior is symmetric.

12. Momentum flux terms were modified so that momentum was conserved while the stable donor-cell differencing was maintained.

13. An improved subcooled-boiling model was implemented. The new model is described in Appendix G, Section G.1. and includes a mechanistic model for partitioning the wall heat transfer between flashing water to steam and heating up the subcooled liquid. The new model also includes an empirical correlation model for determination of the liquid enthalpy at bubble departure.

14. A thermal-radiation-enclosure heat-transfer model was added to the HTSTR (heat-structure) component. (This capability currently is only available in TRAC-M/F77.)

15. An option for improved time-step-size diagnostic edits was added. (This capability currently is only available in TRAC-M/F77.)

The base code for the TRAC-M development effort was TRAC-PF1/MOD2 Version 5.4.25. (In the course of TRAC-PF1/MOD2 development, the code's name was officially shortened to TRAC-P.) TRAC-M was first developed as a series of Fortran 77 (F77) versions (TRAC-M/F77), with the main goals of increased portability and providing a good base for subsequent Fortran 90 (F90) development (TRAC-M/F90).

TRAC-M/F77 Version 1.10 is an important branch point. It is the base code for all TRAC-M/F90 versions, and it is the base code for a new reflood model in TRAC-M/F77 that analyzes simultaneous top-down and bottom-up quenching.

We summarize here the main features that distinguish the F77 and F90 versions of TRAC-M, and indicate future areas of development. (Note that essentially all future development of TRAC-M is now planned for the F90 series.)

TRAC-M/F77 is currently at Version 5.5.2. It has the following characteristics:

- Portable Fortran 77.

- Same numerics, models, and correlations as MOD2 (TRAC-P) Version 5.4.25, except for the addition of a new core-reflood model that has the capability to analyze simultaneous top-down and bottom-up quenching (Ref. 1-12. and

1-13.), and an optimization methodology for development of closure relations (Ref. 1-12.).

Note that use of the SEPD (Separator) component model, which was brought over from MOD2, is not recommended. Also, the TURB (Turbine) component model, also inherited from MOD2, had received minimal support over its years in MOD2. Both the SEPD and TURB components are to be replaced in future TRAC-M/F90 versions (post-Version 3.0).

- Removal of the graphics output file TRCGRF, which was used in older code versions for graphics post-processing. All graphics output is written to files XTVGR.T and XTVGR.B; this graphics output is compatible with the TRAC-M visualization and plotting tool XTV.

TRAC-M/F90 (Version 3.0), the base F90 code version for this document, has the following characteristics:

- Portable Fortran 90, with a complete rewrite of the databases, using F90-derived types and standard Fortran 90 dynamic memory allocation.

- Improved data interfaces, including
  - full separation of the evaluation of terms in the flow equations from the solution of the resulting system of linear equations. This provides a well-defined location for equation terms, eliminates the need for generation of this data for 1D components before evaluation of the equations in 3D components, and results in a rewrite of the network solution procedure for the fluid field equations. (The underlying SETS numerics remain unchanged.)
  - improved inter-component communication, implemented as a system service.

- Removal of the MOD2 TURB (turbine) component. The turbine capability is to be re-introduced in future TRAC-M/F90 versions (post-Version 3.0).

- Removal of the thermal-radiation-enclosure heat-transfer model from the HTSTR (heat-structure) component. The “hooks” that call the radiation model are retained in commented-out form. The associated data-access logic was also removed. (The enhanced time-step-size diagnostics, which use the same data-access logic as the radiation model, were also removed.)

- Removal of the graphics output file TRCGRF, which was used in older code versions for graphics post-processing. All graphics output is written to file TRCXTV (which combines the information in TRAC-M/F77 files XTVGR.T and XTVGR.B). Both codes produce graphics output that is compatible with

the TRAC visualization and plotting tool XTV. In addition, TRAC-M/F90's graphics file can be used with the XMGR code.

Note that Version 3.0 of TRAC-M/F90 has the same outdated SEPD (Separator) Component as MOD2 and TRAC-M/F77.

The new field-equation solution scheme in TRAC-M/F90 is described in Section 2.0.

Currently the only identified future improvement to TRAC-M/F77 is the addition of improved graphics output for the point-kinetics model (and a minor error correction for that model). The main path for future TRAC-M development is in the TRAC-M/F90 series. Major aspects of ongoing TRAC-M development include the following:

- Incorporation of boiling-water-reactor (BWR) modeling capabilities similar to those of TRAC-B. This includes addition of the following:
  - Vessel-channel (CHAN) component with leak paths,
  - Jet-pump (JETP) component,
  - Heater component,
  - Turbine (TURB) component, replacing the MOD2 TURB, and
  - Separator (SEPD) component, replacing the MOD2 SEPD.
- Separation of TRAC-M/F90 into an input engine (TracInp) and a computational engine (TracCmp). This logic is described in the TRAC-M/F90 User's Manual (Ref. 1-15.).
- Development of a new single-junction component (SJC), which will be used by the forthcoming leak-path logic for the CHAN component, and will facilitate RELAP-5-style modeling.
- Addition of improved graphics output for the point-kinetics model (and a minor error correction for that model).

1.5. TRAC Value to the United States Nuclear Regulatory Commission (USNRC)

The TRAC-M codes extend the capabilities of TRAC-PF1/MOD1 in the areas described in the previous section. We have addressed many of the areas for improvement identified in the assessment of TRAC-PF1/MOD1. Also, the TRAC-M codes continue to prove the value and applicability of the SETS numerics and provide fast-running calculational tools for many reactor transients. TRAC is a very advanced thermal-hydraulic computer code capable of predicting large-, intermediate-, and small-break LOCA transients as well as most non-LOCA transients. In most cases, TRAC-M is easier to apply than the earlier versions. Because of the added generality in the models and closure relations, the enhanced user-convenience features, and the added capabilities in

many areas, we recommend the TRAC-M code over previous versions for general use in addressing licensing problems and questions relating to PWRs.

The portability of the TRAC-M codes will assist both the user and developer communities. The database and data-interface restructuring of TRAC-M/F90 provide a very sound base for future code development and maintenance.

1.6. Scope of the TRAC -M/F90 Theory Manual

This document is one of four documents released with TRAC-M/F90. The other three documents are the Developmental Assessment Manual (to be published), the User's Manual (Ref. 1-15.), and the Programmer's Manual (Ref. 1-14.). These are equally as important as the Theory Manual to obtain a complete understanding of the TRAC-M/F90 code. In addition, there is a Developmental Assessment Manual (Ref. 1-16. and 1-17.) and a Programmer's Guide for TRAC-M/F77 (Ref. 1-18.).

In the current document, the field equations that are solved by the code and the solution strategy and numerical techniques employed are described in addition to the closure relationships. In this respect, it is more involved than the models and correlations document published for TRAC-PF1/MOD1 (Ref. 1-6.), which concentrated on the closure relationships only. We believe it is important for the reader to be exposed to the solution strategy and numerical methods employed while considering the closure relationships. Quite often, the numerical theory limits the choice and the implementation of the closure relationships. As described in Section 1.6.1., the closure relations themselves are discussed at two levels of detail. There is a complete summary in the main text that includes an explicit linkage of the closure relations to terms in the field equations, and there are appendices that provide full details on the closure relations.

In documenting the closure relationships in the appendices to this Theory Manual, we followed an identical format to the TRAC-PF1/MOD1 models and correlations document. The licensing compendium (Ref. 1-8., Section 4.4) describes a process for evaluating code scaling, applicability, and uncertainty. To support this process, the USNRC requires documentation concerning the code. Specifically, compendium Section 4.4.3.1 prescribes the objectives and requirements for the models and correlations document. The document has the following three objectives:

1. "To provide detailed information on (the quality of) closure equations, that is, on correlation models and/or criteria used in the code;"
2. "To describe how these closure relations are coded in the program and [to] assure that what is listed in the code manual is indeed what the code uses;" [and]
3. "To provide a technical rationale and justification for using these closure relations (as coded in the program) in the range of interest to NPP [nuclear-power-plant] safety evaluation."

To meet these three objectives, the licensing compendium specifies that the models and correlations document should provide the following information for each model/correlation:

1. the original model/correlation
   a. source or reference,
   b. database,
   c. accuracy, and
   d. applicability to NPP conditions;
2. assessment of effects if the model/correlation is applied outside its database;
3. implementation of the model/correlation in the code;
4. description of modifications required to overcome computational difficulties; and
5. assessment of effects of implementation and/or modification on code overall applicability and accuracy.

In terms of closure relationships, this document will attempt to address items 1-5 for the TRAC models and correlations. However, we generally limited the assessment prescribed in items 2 and 5 and concentrated the assessment in those areas we consider most important. In particular, one can interpret item 5 to require sensitivity calculations on integral plant-transient simulations. These types of sensitivity calculations are beyond the scope of this document. We performed most of the assessment of those models/correlations for which the original reference is inadequate (significant modifications have been made) or the application is far outside the database. In many cases we performed this assessment in isolation; that is, we calculated the model/correlation separately from the main code. This isolation of the model/correlation saved time and effort but may have exaggerated the importance of the assumptions used to obtain the experiment data. In particular, this procedure neglects any synergistic effects of the model/correlation coupling with the rest of the code.

The TRAC-M/F77 Developmental Assessment Manual (Ref. 1-16. and 1-17.) includes many test problems and separate-effects experiments against which TRAC is assessed (as will the Developmental Assessment document for TRAC-M/F90). These problems individually concentrate on a single or a few models, while testing the overall code performance. The contents of the TRAC-M/F77 Developmental Assessment Manual (Ref. 1-16. and 1-17.) are not repeated in this manual. Also, in describing the implementation of the model/correlation, we derive from the original reference the equation that we have incorporated into the code. We specify the location of the model/correlation by subroutine(s). We consider the documentation of specific variables and mnemonics used in the code to be a large task beyond the scope and schedule of this document. Instead, their location by subroutine and equation as coded makes the code quite readable.

We also document the transitions between related models/correlations, as appropriate. These transitions are in some cases more important than the actual models/correlations themselves and are necessary to prevent nonphysical discontinuities that can result in instabilities in the solution scheme and in unrealistic calculated results.

Finally, this document is a description of just those models and correlations used in TRAC. It is not meant to be a comprehensive survey of all available, similar models, or, for that matter, of all models that one might consider to be important to all aspects of PWR features and transients. Nor does the report survey all available data pertinent to the various models/correlations. Rather, we have used data from readily available sources to pursue the assessment activities. This document also does not fill the requirements for a textbook on thermal-hydraulic phenomena and/or modeling.

This document describes the TRAC solution strategy, numerical techniques, models, and correlations, and makes statements about them related to applicability, scaleability, adequacy, and accuracy. Through a description of the database for a model/correlation and any additional assessment for that model/correlation, we provide a basis for judging quality, although we do not provide assurance that the "best" model/correlation has been selected. While the assessment of individual correlations and models is important, we believe that one should judge the overall quality of the code based on the developmental and independent assessment results.

1.6.1. Document Structure

For much of the material in the Theory Manual we introduce a topic in an appropriate main section and provide more detail in an appendix. The main exceptions are the treatments of the hydrodynamic field equations and the heat-conduction logic, which are covered entirely in the main text. The treatment of the closure relations is "top-down" in the main text, going from the general to the specific. The appendices treat the same closure relations in more detail, and in generally a "bottom-up" fashion. This allows the reader to obtain first an overall grasp of the code's logic, and then to easily find additional detail if desired.

This document is structured along the same lines as TRAC. We have structured the document to aid in understanding the calculated results. Aside from the parts of the code that handle the details of input and output, the code basically solves a set of field equations that describe the fluid, the transport of energy in solid structures (conduction), and in certain applications, the reactor kinetics. Section 2.0. summarizes the field equations used in the code. We have not included the derivation of the field equations because that is beyond the scope of this document. However, Section 2.0. also includes the description of the solution strategy and the numerical techniques. For TRAC, the fluid field equations are by far the most complete; the solutions of the conduction equation and the reactor kinetics are more like boundary conditions applied to the fluid equations. Therefore, the document concentrates on and highlights those models and correlations required by the fluid equations while documenting the models and correlations pertaining to the conduction and kinetics at the appropriate level of detail. The heat-conduction models are described in Section 2.0., and the kinetics are introduced

in Section 2.0. and described in more detail in Appendix M. TRAC's control procedure is introduced in Section 2.0. and described in detail in Appendix N.

The document relies on the presence of the field equations in Section 2.0. to provide cohesion and structure; the terms in the field equations indicate that the closure relations are required and show how the closure relations are incorporated. To reinforce this linkage between the field equations and the closure relations, Section 3.0. provides an introduction to TRAC's closure relations that includes a "roadmap" that explicitly links the individual closure relations to the individual terms in the hydrodynamic field equations. The closure relations are described in further detail in the appendices to this document (Appendices D through H). The inherent quasi-steady assumption and its implications also are introduced in Section 3.0. and described in detail in an appendix (Appendix D). Section 3.1. gives an overview of TRAC's closure relations. Section 3.2. describes the basic flow-regime map that is at the heart of the logic for selecting interfacial shear and heat-transfer correlations for appropriate flow patterns. The description of the flow-regime map follows the field equations in Section 2.0. because the map provides the basis in the code for selecting, according to the appropriate flow pattern, many of the closure relations used to describe the two-phase fluid. The basic flow-regime map forms the basis for linking correlations into models spanning a wide variety of flow conditions. Each collection of related correlations and models, whether they describe interfacial shear or interfacial heat transfer or wall heat transfer, etc., modifies the basic map to account for the amount of knowledge available about a given phenomenon. Generally, the more detailed the knowledge is concerning a particular phenomenon, the more detailed the flow regimes must be. Additional detail on the flow regimes is given in Appendix E. Section 3.3. summarizes the code's correlations and logic for calculation of interfacial area, which is dependent on the flow regime. Section 3.4. describes the interfacial mass transfer. The correlations and logic describing the interfacial and wall drag are in Sections 3.5. and 3.6., respectively. Sections 3.7. and 3.8. cover the correlations and logic for interfacial heat transfer and wall heat transfer, respectively. Appendices F, G, and H expand the treatment of interfacial and wall heat transfer, fluid mass closure, and interfacial and wall drag, respectively. Because the logic for selecting various models and correlations is an item to be documented and because this logic tends to be localized in the code, we have grouped the models and correlations in Appendices F, G, and H by field equation. Section 3.0., and related appendices, clarify the modifications required to the basic flow-regime map for each process. The next two sections describe process and boundary models for the fluid equations. These models provide details beyond the scope of the field equations that are required to model complete reactor systems. Section 4.0. and Appendix I describe those models that are not component-oriented (in the TRAC sense of components) and that generally have an impact on the momentum equation and/or interfacial drag. Three main examples of these models are critical flow, CCFL, and form loss. Section 4.0. also includes other special models, such as fuel-cladding gap conductance. Section 5.0. and Appendix J cover special function components, including pumps, boundary condition components (fills and breaks), plenums, pressurizers, and valves. Finally, Section 6.0. provides a summary of the overall conclusions of this Theory Manual.

Appendices A and B cover the code's thermodynamic and transport fluid properties, and material properties, respectively. Appendix D discusses the quasi-steady assumption that underlies TRAC's closure logic. Appendix E gives an expanded treatment of TRAC's basic flow regime logic.

For Appendix F through K we have generally assumed that the fluid is liquid water and water vapor. We have, however, described as appropriate the effects of the noncondensable gas and the liquid solute. Appendix F describes the closure relations required by the fluid energy-field equations. These relations include both the interfacial heat transfer and the wall-to-fluid heat transfer, which includes the discussion of the heat-transfer coefficients. Appendix G provides the closure relations required by the fluid mass-conservation equations and builds on interfacial heat transfer presented in Appendix F. Appendix H provides the closure relations required by the fluid momentum equations, including both the interfacial drag and the wall drag. This appendix also describes all of those models that affect the interfacial drag, which includes the entrainment model invoked during reflood.

Appendix I describes the flow process models, including the abrupt area-change model, critical flow, countercurrent flow limitation (CCFL), and vent valves in the VESSEL component. Appendix J describes the special component models that interact specifically with the momentum equations: PUMP, steam / water separator (SEPD), FILL, BREAK, PLENUM, turbine (TURB), accumulator, pressurizer, and valve.

Appendix K provides the closure relations required by the extra mass-conservation fields: noncondensable gas and liquid solute. It provides the thermodynamic and transport properties for the noncondensable-gas field and the solubility model for the liquid-solute (boron) field. These fields are calculated by the extra fluid mass-conservation field equations. The discussion of the noncondensable-gas and liquid-solute effects on other models is provided as appropriate with each model. The code assumes that these two components move with the gas and liquid fields as appropriate and that the interactions are minimal. Other sections and appendices have described how the presence of the noncondensable gas and liquid solute have affected the interfacial and wall heat transfer, the interfacial mass transfer, and the interfacial and wall drag. For the most part, the effect of the liquid solute is limited to a feedback effect in the reactor kinetics.

Appendix L describes fuel-cladding gap conductance and the metal-water reaction model. Appendix M describes in detail the reactor-core power model. Finally, Appendix N gives details on the code's control procedure, including signal variables, control blocks, and trips.

The general structure of this document lends itself well to the writing process because it follows the code structure and does not require that descriptions of a related set of closure relations be distributed throughout the document. The localization of related models and correlations permits a more logical, clearer description of the logic linking them and minimizes the opportunities for omissions and duplications. Indeed, one of

the most important questions to be addressed concerns the transitions/couplings of various models. To the extent that the code does this, the document structure lends itself very well to describing the logic and transitions among the various models. The selected structure is also more in tune with targeted interest groups that are described in the next subsection.

The code sorts the problem of single-phase versus two-phase fluid at a very high level in determining the equation set to be solved. If the fluid is single-phase liquid or vapor, all of the interfacial processes are eliminated and the code considers only the interactions with the walls and the transport of a single-phase fluid. For the case of single-phase liquid, the code sets the vapor velocity to that of a bubble, and for the case of single-phase vapor, sets the liquid velocity to that of a droplet. The code used this prescription to prevent accelerating the appearing phase from zero velocity when the fluid first becomes two-phase. For the single-phase case, large sections of the document dealing with flow regimes, interfacial heat and mass transfer, drag, and most of the correlations for wall heat-transfer coefficients are not pertinent.

For the two-phase case, the code has to evaluate the terms dealing with the interfacial interactions plus determine two-phase effects on wall drag and wall heat transfer. The document is structured to discuss the flow-regime map in Section 3.0. because the map is important to many of the choices made in sorting the correct correlations for the interfacial phenomena. For the case of single-phase liquid or vapor, the code does not distinguish flow regimes because there is only a single velocity to describe the single-phase fluid. The only single-phase flow structures recognized by the code are laminar or turbulent flow. The code makes the choice of laminar versus turbulent at the lowest level in the correlation sets. An interesting note is that for single-phase liquid at normal PWR operating pressure and temperature in a 0.762-m-i.d. pipe (typical for a PWR), the laminar transition point occurs at ~3.5 mm/s, which is essentially loop stagnation; any significant flow results in turbulent flow conditions.

Future versions of this TRAC-M/F90 Theory Manual will address TRAC-M/F90's capabilities, which are now under development, for analysis of BWRs.

1.6.2. Targeted Interest Groups

We have structured the document to follow the code calculation. We have written this document for the code user who attempts to understand the reasons behind the qualitative and quantitative nature of the comparisons between calculated results and data; to determine the applicability of the code to particular facilities and/or transients; or to determine the appropriateness of calculated results, with or without data to support the calculations. The definition of code user includes anyone who is involved in running the code or in analyzing the calculated results.

People involved in the development of TRAC or similarly based codes should find the information contained in this document interesting. The document provides insight into the smoothness requirements of codes to maintain computational efficiency and to obtain closure and into the constraints of physical phenomena. It provides one solution

to the many problems associated with closure and demonstrates methodologies for obtaining continuity at the boundaries among correlation sets that, because of their mathematical forms and different databases, are inherently discontinuous.

A third group of individuals who may be interested in this document includes managers who are involved in funding / directing work involving TRAC or experiments producing data that could be used to develop correlations or models. While we do not wish to understate the importance of the numerical techniques incorporated in TRAC, we believe that the current schemes demonstrate exceptional stability and robustness that will serve adequately in codes like TRAC for years to come. However, the models and correlations in the code can have a significant impact on the speed of a calculation; they can and frequently do affect adversely the time-step size and the number of iterations used. Because of the impact on the speed of the calculation and because the models and correlations greatly affect the accuracy of the results, the area of model / correlation development may result in significant improvements in the overall code performance. This document provides a baseline against which to measure the adequacy of the current models and correlations and a tool to help prioritize future experiment and development activities.

As indicated before, this document is not intended to substitute for a textbook on thermal-hydraulic phenomena or modeling, but rather to provide one example of how one could select correlations and models and define logic to link them into a coherent system to describe, in conjunction with the field equations, a large variety of thermal-hydraulic conditions and transients. Even within the field of reactor safety in the United States other, similar calculational tools exist (for examples, see Ref. 1-9. through 1-11.) in which different objectives, constraints, and histories have led to different choices for solution strategies, models, and correlations.

1.6.3. Basic Assumptions Within the Document

We have attempted to state clearly that certain models do not exist in the code; however, it is difficult to be complete in listing all things not included. Because we have been thorough in writing the description of the models and correlations, one should assume that if the document does not describe a model for a given phenomenon or process, the code does not contain such a model. We have described the standard closure relationships used in the code and, where appropriate, any special cases that alter the standard prescriptions. Basically, if we have not described a special case, the code does not consider it and uses the standard relations.

In the appendices, items like interfacial areas and bubble / droplet sizes are documented in those appendix subsections that require the information. This organization of detailed information leads to some duplication but forces the documentation to be complete, both in a model / correlation description sense and in the overall sense. We have documented in a similar fashion any kind of old-time / new-time averaging, void-fraction weighting of correlation results, and any limits placed on the magnitude of the result or the rate at which the result is permitted to change. We have used a standard, detailed outline for writing the descriptions of individual correlations and models in an effort to maintain a

uniform level of detail and format in the contributions from the many authors. However, on a model-by-model basis, some variations occur because of the history of the development process. Also, as indicated in Section 1.6., the level of assessment varies based on the available references pertaining to a given model/correlation and on the need to support a given model/correlation.

The term fluid in general refers to any combination of liquid water, steam, and non-condensable gas (the liquid solute is a part of liquid water), although in specific cases the term may be restricted to a subset. For clarity, we have avoided such constructions as "fluid temperature" and refer instead to "liquid temperature" or "vapor (gas) temperature."

REFERENCES

1-1. Safety Code Development Group, "TRAC-P1: An Advanced Best Estimate Computer Program for PWR LOCA Analysis," Los Alamos Scientific Laboratory report LA-7279-MS (NUREG/CR-0063) (June 1978).

1-2. Safety Code Development Group, "TRAC-P1A: An Advanced Best Estimate Computer Program for PWR LOCA Analysis," Los Alamos Scientific Laboratory report LA-7777-MS (NUREG/CR-0665) (May 1979).

1-3. Safety Code Development Group, "TRAC-PD2: Advanced Best Estimate Computer Program for Pressurized Water Reactor Loss-of-Coolant Accident Analysis," Los Alamos Scientific Laboratory report LA-8709-MS (NUREG/CR-2054) (April 1981).

1-4. Safety Code Development Group, "TRAC-PF1: An Advanced Best Estimate Computer Program for Pressurized Water Reactor Analysis," Los Alamos National Laboratory report LA-9944-MS (NUREG/CR-3567) (February 1984).

1-5. J. H. Mahaffy, "A Stability-Enhancing Two-Step Method for Fluid Flow Calculations," *Journal of Computational Physics* **46**, 329-341 (1982).

1-6. Safety Code Development Group, "TRAC-PF1/MOD1 Correlations and Models," Los Alamos National Laboratory report LA-11208-MS (NUREG/CR-5069) (December 1988).

1-7. Safety Code Development Group, "TRAC-PF1/MOD1: An Advanced Best Estimate Computer Program for Pressurized Water Reactor Thermal-Hydraulic Analysis," Los Alamos National Laboratory report LA-10157-MS (NUREG/CR-3858) (July 1986).

1-8. "Compendium of ECCS Research for Realistic LOCA Analysis: Draft Report for Comment," US NRC report (NUREG-1230) (April 1987).

1-9. M. J. Thurgood, J. M. Kelly, T. E. Guidotti, R. J. Kohrt, and K. W. Crowell, "COBRA/TRAC—A Thermal-Hydraulics Code for Transient Analysis of Nuclear Reactor Vessels and Primary Coolant Systems," Pacific Northwest Laboratories report PNL-4385 (NUREG/CR-3046) (March 1983).

1-10. D. D. Taylor, R. W. Shumway, and G. L. Singer, "TRAC-BD1/MOD1: An Advanced Best Estimate Computer Program for Boiling Water Reactor Transient Analysis," Vols. 1-4, EG&G Idaho, Inc., report EGG-2294 (NUREG/CR-3633) (April 1984).

1-11. V. H. Ransom, R. J. Wagner, J. H. Trapp, L. R. Feinauer, G. W. Johnson, D. M. Kiser, and R. A. Riemke, "RELAP5/MOD2 Code Manual, Volume 1: Code Structure, Systems Models and Solution Methods," EG&G Idaho, Inc., report EGG-2396 (NUREG/CR-4312) (August 1985).

1-12. R. A. Nelson, Jr., D. A. Pimentel, S. J. Jolly-Woodruff, and J. W. Spore, "Reflood Completion Report, Volume I: A Phenomenological Thermal-Hydraulic Model of Hot Rod Bundles Experiencing Simultaneous Bottom and Top Quenching and an Optimization Methodology for Closure Development," Los Alamos National Laboratory report LA-UR-98-3043 (April 1998).

1-13. B. E. Boyack, J. F. Lime, D. A. Pimentel, J. W. Spore, and T. D. Knight, "Reflood Completion Report, Volume II: Developmental Assessment of a New Reflood Model for the TRAC-M/F77 Code," Los Alamos National Laboratory report LA-UR-98-3043 (April 1998).

1-14. B. T. Adams, J. F. Dearing, P. T. Giguere, R C. Johns, S. J. Jolly-Woodruff, J. Mahaffy, C. Murray, J. W. Spore, and R. G. Steinke, "TRAC-M/FORTRAN 90 (Version 3.0) Programmer's Manual," Los Alamos National Laboratory document LA-UR-00-803 (February 2000).

1-15. R. G. Steinke, V. Martinez, N. M. Schnurr, J. W. Spore, and J. V. Valdez, "TRAC-M Fortran 90 (Version 3.0) User's Manual," Los Alamos National Laboratory document LA-UR-00-835 (February 2000).

1-16. B. E. Boyack, J. F. Lime, D. A. Pimental, J. W. Spore, and J. L. Steiner, "TRAC-M/F77, Version 5.5, Developmental Assessment Manual, Volume I: Nonproprietary Assessment Sections," Los Alamos National Laboratory document LA-UR-99-6480 (December 1999).

1-17. B. E. Boyack, J. F. Lime, D. A. Pimental, J. W. Spore, and J. L. Steiner, "TRAC-M/F77, Version 5.5, Developmental Assessment Manual, Volume II: Proprietary Assessment Sections," Los Alamos National Laboratory document LA-CP-99-345 (December 1999).

1-18. R. G. Steinke, S. J. Jolly-Woodruff, and J. W. Spore, “TRAC-M: Fortran 77, Version 5.5, Programmer’s Guide, Volume III,” Los Alamos National Laboratory document LA-UR-99-2312 (NUREG / CR-6658) (October 1999).

2.0. FIELD EQUATIONS AND NUMERICAL METHODS

The following subsections briefly describe the field equations (fluid and structures). The most difficult part of the solution is to solve the thermal-hydraulic behavior of the fluid and the coupling to the fuel/structural heat transfer through the heat-transfer coefficients (HTCs). The code devotes most of the programming and most of the computer time to solving this part of the problem. This area is more complex because there are more coupled field equations associated with describing the fluid (more independent variables), more phenomena to be considered, and the HTCs are very dependent on the fluid properties and velocities. On the other hand, the field equations describing the energy field in the solid structures and the nuclear reaction are much simpler and involve fewer variables. Although less complicated, these fields are as important as the thermal-hydraulic model to the overall solution of the problem.

The TRAC code, as well as most other similar codes, invokes a quasi-steady approach to the heat-transfer coupling between the wall and the fluid as well as the closure relations for interfacial and wall-to-fluid heat transfer and drag. This quasi-steady approach assumes detailed knowledge of the local fluid parameters and ignores time dependencies so that the time rate of change in the closure relationships becomes infinite and the time constants are zero. The quasi-steady approach has the advantages of being reasonably simple and generally applicable to a wide range of problems and of not requiring previous knowledge of the given transient. Where appropriate, we will integrate the effects of the quasi-steady approach; however, the descriptions of the methodology by necessity will be somewhat limited. Appendix D discusses the quasi-steady assumption and the averaging operators used in the code.

In Section 2.1. the field equations are described, including the finite-difference methods. In the same section, the overall solution strategy and the numerical solution methods are also described. Heat-conduction calculations and the reactor kinetics are discussed in Section 2.2. and Appendix M, respectively. Brief discussions of the Reactor-Core Power Model and Control Procedures are provided in Sections 2.3. and 2.4., respectively, whereas detailed discussions on these topics appear respectively in Appendices M and N.

Section 2.0. contains many equations and symbols. As a result, we have provided separate nomenclatures for Sections 2.1. and 2.2.

2.1. Fluid Field Equations

TRAC uses a two-phase, two-fluid model for fluid flow in both the 1D and 3D components. Kocamustafaogullari (Ref. 2-1.), Ishii (Ref. 2-2.), and Bergles et al. (Ref. 2-3., pp. 40-122) have provided detailed derivations of the equations similar to those used in TRAC, and a more concise derivation related to the TRAC equations is available in a report by Addessio (Ref. 2-4.). That this model is formally ill-posed was the subject of considerable debate several years ago and is discussed by Stewart and Wendroff (Ref. 2-5., pp. 388-389). Our experience, however, has always been that this is a moot

point, since the numerical solution procedures effectively introduce minor modifications to the field equations, making them well posed. A paper by Stewart (Ref. 2-6.) confirms these observations and demonstrates clearly that with normal models for interfacial drag and reasonable finite-difference nodalizations, the problem solved numerically is well posed.

Before presenting the fluid field equations, we need to define certain terminology. In our nomenclature, the term *gas* implies a general mixture of water vapor and the noncondensable gas. The subscript *g* will denote a property or parameter applying to the gas mixture; the subscript *v* indicates a quantity applying specifically to water vapor (referred to as simply *vapor*); and the subscript *a* (for *air*) signifies a noncondensable-gas quantity. The term *liquid* implies pure liquid water, and the subscript l denotes a quantity applying specifically to liquid water. For convenience, we define the following terms that will be used in the subsequent equations and list them alphabetically with the Greek symbols at the end. In the subsections where the numerical methods are discussed, various dummy variables are used. Although the dummy variables are not listed in the following nomenclature, their significance becomes obvious to the reader by reading the text. The following notation applies to the discussion of numerical methods. A caret ($\hat{}$) above a variable denotes an explicit predictor value. A tilde ($\tilde{}$) above a variable denotes an intermediate result, and a line ($\bar{}$) above denotes an arithmetic average of values at adjacent cells. A double line underneath a symbol refers to a matrix, whereas a single line underneath means a vector (1D array).

NOMENCLATURE

A: flow area between mesh cells

A_i: interfacial area between the liquid and gas phases

c: speed of sound or shear coefficient

e: internal energy

$\dot{g}$: gravity vector

g: magnitude of the gravity vector

h: heat-transfer coefficient (HTC)

h_{sg}: gas saturation enthalpy

h_{wg}: $(1-f_\mathrm{l})\ h'_{wg}$, the effective wall HTC to gas

$h_{w\mathrm{l}}$: $f_\mathrm{l} h'_{w\mathrm{l}}$, the effective wall HTC to liquid

h'_l: liquid enthalpy of the bulk liquid if the liquid is vaporizing or the liquid saturation enthalpy if vapor is condensing

h'_v: vapor enthalpy of the bulk vapor if the vapor is condensing or the vapor saturation enthalpy if liquid is vaporizing

K: form-loss coefficient or wall friction coefficient

m: solute concentration in the liquid (mass of solute per unit mass of liquid)

P: fluid pressure or total pressure

q: heat-transfer rate per unit volume

q_d: power deposited directly (without heat-conduction process)

q_{gl}: liquid-to-gas sensible heat transfer

q': heat flux

r: radius

S: factor applied to the 1D component so that its positive flow direction becomes the positive flow direction of the vessel

S_c: plated-out solute density (mass of plated solute divided by cell volume)

SC: product of an orifice factor

S_m: source term in the solute-mass differential equation

t: time

T: temperature

T_{sv}: saturation temperature corresponding to the vapor partial pressure

$\vec{V}$: velocity vector

V: magnitude of the velocity

vol: hydrodynamic-cell volume

w: weighting factor

x: distance

Y: dummy variable

z: axial coordinate

α: gas volume fraction

β: momentum-convection temporal expansion flags

γ: weighting factor

Γ: interfacial mass-transfer rate

Γ^+: maximum of Γ and 0

Γ^-: minimum of Γ and 0

ρ: density

ΔP: pressure difference

Δr: radial ring increment for 3D components

Δt: time-step size

ΔV: velocity change

Δx: cell length for 1D components

Δz: axial level increment for 3D components

$\Delta\theta$: azimuthal segment increment for 3D components

δP: linear Taylor series expansion term for pressure

δT: linear Taylor series expansion term for temperature

$\delta\alpha$: linear Taylor series expansion term for void fraction

θ: inclination angle from vertical or the azimuthal coordinate

ϕ: angle between the main and side tubes in TEE component

Subscripts

1D: one dimensional

3D: three dimensional

donor: donor cell

T: the first cell in the side leg of the TEE or the interface between the j^{th} cell of the primary and the first cell in the side leg

a: noncondensable gas

d: generic for *r*, θ, or *z* or for *i*, *j*, or *k*

g: gas mixture

i: interfacial

l or *l*: liquid

max: maximum

min: minimum

r: radial

sat: saturation

v: water vapor

w: wall

z: axial

θ: azimuthal

Superscripts

n: current-time quantity

n + 1: new-time quantity

′: last estimate

In the discussion of the finite-difference equations, all quantities except for the velocities are centered in the hydrodynamic cell (cell-centered), and the velocities are cell-edge quantities.

2.1.1. Gas/Liquid Equations

The basic volume- and time-averaged, two-phase, two-fluid model consists of six partial differential equations.

Combined Internal Energy Equation

$$\frac{\partial\left[(1-\alpha)\,\rho_l e_l + \alpha\rho_g e_g\right]}{\partial t} + \nabla\cdot\left[(1-\alpha)\,\rho_l e_l \vec{V}_l + \alpha\,\rho_g e_g \vec{V}_g\right]$$
$$= -P\nabla\cdot\left[(1-\alpha)\vec{V}_l + \alpha\vec{V}_g\right] + q_{wl} + q_{wg} + q_{dl} + q_{dg} \quad . \tag{2-1}$$

Combined-Gas Energy Equation

$$\frac{\partial\left(\alpha\rho_g e_g\right)}{\partial t} + \nabla\cdot\left(\alpha\rho_g e_g \vec{V}_g\right) = -P\frac{\partial\alpha}{\partial t} - P\nabla\cdot\left(\alpha\vec{V}_g\right) + q_{wg} + q_{dg} + q_{ig} + q_{gl} + \Gamma\, h_v' \quad . \tag{2-2}$$

Liquid Mass Equation

$$\frac{\partial\left[(1-\alpha)\rho_l\right]}{\partial t} + \nabla\cdot\left[(1-\alpha)\rho_l\vec{V}_l\right] = -\Gamma \quad . \tag{2-3}$$

Combined-Gas Mass Equation

$$\frac{\partial\left(\alpha\rho_g\right)}{\partial t} + \nabla\cdot\left(\alpha\,\rho_g\vec{V}_g\right) = \Gamma \quad . \tag{2-4}$$

Liquid Equation of Motion

$$\frac{\partial\vec{V}_l}{\partial t} + \vec{V}_l\cdot\nabla\vec{V}_l = -\frac{1}{\rho_l}\nabla P + \frac{c_i}{(1-\alpha)\rho_l}\left(\vec{V}_g - \vec{V}_l\right)\left|\vec{V}_g - \vec{V}_l\right|$$
$$-\frac{\Gamma^-}{(1-\alpha)\rho_l}\left(\vec{V}_g - \vec{V}_l\right) - \frac{c_{wl}}{(1-\alpha)\rho_l}\vec{V}_l\left|\vec{V}_l\right| + \vec{g} \quad . \tag{2-5}$$

Combined-Gas Equation of Motion

$$\frac{\partial \vec{V}_g}{\partial t} + \vec{V}_g \cdot \nabla \vec{V}_g = -\frac{1}{\rho_g}\nabla P - \frac{c_i}{\alpha \rho_g}(\vec{V}_g - \vec{V}_l)\left|\vec{V}_g - \vec{V}_l\right|$$

$$-\frac{\Gamma^+}{\alpha \rho_g}(\vec{V}_g - \vec{V}_l) - \frac{c_{wg}}{\alpha \rho_g}\vec{V}_g\left|\vec{V}_g\right| + \vec{g} \ . \qquad (2\text{-}6)$$

An alternative to solving one of the phasic mass equations is to solve the total mass equation, which is obtained by summing Eqs. (2-3) and (2-4). This yields the following result:

Total Mass Equation

$$\frac{\partial\left[(1-\alpha)\rho_l + \alpha\rho_g\right]}{\partial t} + \nabla \cdot \left[(1-\alpha)\rho_l \vec{V}_l + \alpha\rho_g \vec{V}_g\right] = 0 \ . \qquad (2\text{-}7)$$

Solving either Eq. (2-3) or (2-4) together with Eq. (2-7) is equivalent to solving both Eqs. (2-3) and (2-4).

Closure is obtained for these equations using normal thermodynamic relations and specifications for the interfacial drag coefficients (c_i), the interfacial heat transfer (q_{ig} and q_{il}), the phase-change rate (Γ), the wall-shear coefficients (c_{wg} and c_{wl}), and the wall heat flows (q_{wg} and q_{wl}). These equations do not require directly the quasi-steady assumption as long as the correct closure relations for the given transient exist. A real difficulty arises because, depending on how the closure relations were developed, a different set of closure relations may be required for each transient, and each set must comply with the assumptions associated with the definition of the time and volume averaging used in the field equations. If a steady- or quasi-steady-state database or a relationship derived from such a database is used to represent a closure relation, the code necessarily applies the quasi-steady assumption stated in Section 2.0. This latter case applies for the closure relations within TRAC. Further discussion of this assumption is presented in Appendix D. Cross-references between TRAC'S closure relations and the field relations are provided in Section 3.0.

The phase-change rate required by the equation set is evaluated from a simple thermal-energy-jump relation

$$\Gamma = \frac{-\left(q_{ig} + q_{il}\right)}{\left(h'_v - h'_l\right)} \ , \qquad (2\text{-}8)$$

where

$$q_{ig} = \frac{P_v}{P} h_{ig} A_i \frac{(T_{sv} - T_g)}{\text{vol}} \tag{2-9}$$

and

$$q_{il} = h_{il} A_i \frac{(T_{sv} - T_l)}{\text{vol}} \quad . \tag{2-10}$$

Here A_i is the interfacial area, h_{ig} and h_{il} are HTCs, and T_{sv} is the saturation temperature corresponding to the partial steam pressure. Appendix F, Section F.1. discusses the closure relationships used to define A_i, h_{ig}, and h_{il}. The term Γ^+ is equal to Γ for positive Γ and zero for negative Γ; Γ^- is equal to Γ for negative Γ and zero for positive Γ. The quantities h'_v and h'_l are the appropriate enthalpies of the vapor and liquid, respectively. These enthalpies are the bulk fluid enthalpy for the phase moving to the interface and the saturation enthalpy for the product of the phase change.

Using Newton's law of cooling extended to a thermal nonequilibrium situation, the wall heat-transfer terms assume the form

$$q_{wg} = h_{wg} A_w \frac{\left(T_w - T_g\right)}{\text{vol}} = q'_{wg} A_w \,/\, \text{vol} \tag{2-11}$$

and

$$q_{wl} = h_{wl} A_w \frac{\left(T_w - T_l\right)}{\text{vol}} = q'_{wl} A_w \,/\, \text{vol} \quad , \tag{2-12}$$

where A_w is the actual heated surface area. The h_{wg} and h_{wl} of the cell include the information regarding the portion of the wall having gas and liquid contact. Appendix F, Section F.2. discusses the closure relationships used to define h_{wg} and h_{wl}.

The mass equations are written in fully conservative form to permit the construction of a numerical scheme that rigorously conserves some measure of the system fluid mass. The energy equations are written in a partially conservative form to make numerical solution simpler than would be possible if the fully conservative form (bulk kinetic-energy terms included) were used. The nonconservative form of the momentum equations, defined as motion equations, also permits simpler numerical solution strategies and can generally be justified because the presence of wall friction makes the fully conservative form of the momentum equation far less useful. When sharp flow-area changes exist, however, numerical solution of the nonconservative motion equations can produce significant errors. The motion equations have been modified in the MOD2 code to force momentum conservation (see Section 2.1.7.).

2.1.2. Noncondensable Gas

A single noncondensable-gas field may be modeled with TRAC. It is assumed to be in thermal equilibrium with any steam that is present and to move with the same velocity as the steam (mechanical equilibrium). Hence, only a single mass-continuity equation is needed to track the noncondensable gas.

Noncondensable-Gas Mass Equation

$$\frac{\partial(\alpha\rho_a)}{\partial t} + \nabla\cdot\left(\alpha\rho_a \vec{V}_g\right) = 0 \ . \tag{2-13}$$

With this field present, the total gas density and energy are sums of the vapor and the noncondensable components,

$$\rho_g = \rho_v + \rho_a \tag{2-14}$$

and

$$\rho_g e_g = \rho_v e_v + \rho_a e_a \ . \tag{2-15}$$

We assume Dalton's law applies; therefore,

$$P = P_v + P_a \ . \tag{2-16}$$

The subscripts v and a indicate, respectively, the steam and air properties; the code normally applies the thermodynamic properties for air to the noncondensable gas. The code user may, however, select hydrogen or helium as an alternative.

2.1.3. Liquid Solute

TRAC includes a mass-continuity equation for a solute moving with the liquid field.

Liquid-Solute Concentration Equation

$$\frac{\partial\left[(1-\alpha)m\rho_l\right]}{\partial t} + \nabla\cdot\left[(1-\alpha)m\,\rho_l \vec{V}_l\right] = S_m \ , \tag{2-17}$$

where m is the solute concentration (mass of solute / unit mass of liquid water) in the liquid phase.

The solute does not affect the hydrodynamics directly. If we assume that the solute represents orthoboric acid, the amount of the dissolved and the plated-out orthoboric acid in the core may affect the hydrodynamics indirectly through neutronic-reactivity feedback corresponding to user-specified input values obtained from a boron-mass reactivity-coefficient table (see Appendix M, Section M.2.5.). If the solute concentration exceeds the orthoboric-acid solubility at the liquid temperature in a specific

hydrodynamic cell, we assume that the excess solute in that cell plates out. Plating on structures can occur if the cell fluid flashes or boils and thus increases the concentration beyond the solubility limit. We also assume that any plated-out solute instantaneously redissolves to the maximum allowable concentration if more liquid enters the cell. Because the solute does not affect the hydrodynamics directly, the solute variable may be used as a tag to track the movement of fluid from a specific source through the system.

2.1.4. Basic Finite-Volume Approximations to the Flow Equations

Future versions of TRAC-M/F90 will contain the option to select one of two related numerical methods for solution of the two-phase-flow equations. The default Stability Enhancing Two-Step (SETS) method has the advantage of avoiding Courant stability limits on time-step size but the disadvantage of relatively high numerical diffusion. When the variable NOSETS is given a value of one in the namelist input, the default will be replaced by a semi-implicit method that usually has substantially less numerical diffusion but has time-step sizes restricted by a material Courant limit. Currently, the NOSETS option is available only for the 3D VESSEL component and all 1D components run with the SETS numerics.

Both basic finite-volume models are descendents of the Implicit Continuous Eulerian technique (ICE) (Ref. 2-7.). The key improvement introduced by Liles and Reed (Ref. 2-8.) in their semi-implicit method was a tighter coupling of the energy equation to the mass and momentum equations than that used in ICE. This coupling is crucial to stable modeling of two-phase flows with substantial boiling or condensation. The SETS method (Refs. 2-9. and 2-10.) includes the semi-implicit method at its core and increases stability with an additional evaluation of each field equation during each time step.

In the following subsections, the semi-implicit and SETS methods will be described at three levels of detail. The basic aspects of each method are illustrated for simple 1D single-phase-flow equations as follows:

$$\frac{\partial \rho}{\partial t} + \frac{\partial}{\partial x}(\rho V) = 0 \ , \tag{2-18}$$

$$\frac{\partial (\rho e)}{\partial t} + \frac{\partial}{\partial x}(\rho e V) = -P\frac{\partial V}{\partial x} + h_w A_w \frac{(T_w - T)}{\mathrm{vol}} \ , \tag{2-19}$$

and

$$\frac{\partial V}{\partial t} + V\frac{\partial V}{\partial x} = -\frac{1}{\rho}\frac{\partial P}{\partial x} - KV|V| \ , \tag{2-20}$$

where K is a wall friction coefficient that may be a function of velocity and fluid properties and T_w is a pipe wall temperature. More detail is then provided through explanation of special adaptations to improve robust simulation of single- and/or two-phase flow. Finally, the full two-phase-flow equations are presented.

Fairly standard notation is used in presenting the finite-volume equations. A superscript "*n*" indicates known values at the beginning of a step in the time integration (old-time value). A superscript "*n*+1" labels a variable value at the end of the current time step (new-time value), which must be obtained as part of the solution of the equations. Subscripts provide information on spatial location. Integer subscripts such as "*j*" or "*j*+1" label volume center information (e.g., P_j^{n+1} is the new-time pressure in volume "*j*"). A half-integer subscript indicates a value obtained at the surface separating two volumes (e.g., $V^n_{j+1/2}$ is the old-time velocity at the surface separating volume "*j*" from volume "*j*+1").

When values of cell-centered variables are needed at cell edges, an average of some form is required. The methods discussed here use values only from the volumes immediately adjacent to the given edge, so the averages are always in the following form:

$$\langle Y \rangle_{j+1/2} = w_{j+1/2} Y_j + (1 - w_{j+1/2}) Y_{j+1} \ . \tag{2-21}$$

For simple 1D flow, terms expressing mass and energy flow for the j^{th} finite volume then have the following form:

$$\frac{\partial}{\partial x_j}(YV) = \frac{[w_{j+1/2}Y_j + (1-w_{j+1/2})Y_{j+1}]V_{j+1/2} - [w_{j-1/2}Y_{j-1} + (1-w_{j-1/2})Y_j]V_{j-1/2}}{\Delta x}$$

$$= \frac{\langle Y \rangle_{j+1/2} V_{j+1/2} - \langle Y \rangle_{j-1/2} V_{j-1/2}}{\Delta x} \ . \tag{2-22}$$

The form is more complex for 1D flow with a spatially varying cross-sectional flow area. In this case the mass flux term is abbreviated as

$$\nabla_j \cdot (YV) = \tag{2-23}$$

$$\frac{[w_{j+1/2}Y_j + (1-w_{j+1/2})Y_{j+1}](A_{j+1/2}V_{j+1/2}) - [w_{j-1/2}Y_{j-1} + (1-w_{j-1/2})Y_j](A_{j-1/2}V_{j-1/2})}{vol_j} \ , \tag{2-24}$$

where $A_{j+1/2}$ is the flow area between cells *j* and *j*+1 and vol_j is the volume of the j^{th} cell.

The related derivative used in the finite-difference momentum flux involves the use of a more complicated averaging method. This is driven by a need to model Bernoulli flows when appropriate and to conserve momentum properly when a side-junction flow is present. Details of this methodology are presented in Section 2.1.7. To aid in understanding the basic numerical methods, it is worth noting that with no area changes or side junctions, the numerical form of the velocity gradient is

$$\left.\frac{\partial V}{\partial x}\right|_{j+1/2} = \frac{(1-w_{j+1/2})V_{j+3/2} + (2w_{j+1/2} - 1)V_{j+1/2} - w_{j+1/2}V_{j-1/2}}{\Delta x} \ . \tag{2-25}$$

For flows in 1D channels with variable cross-sectional area, the momentum-transfer term is abbreviated as $V_{j+1/2}\nabla_{j+1/2}V$.

Discussions of some details of the finite-volume approximations are provided in later sections of this document. Section 2.1.5. presents a generalization of the methods to 3D geometry. Special treatment of transition to single-phase flow and conditions beyond the critical point is described in Section 2.1.6. Section 2.1.7. describes details of special treatment used for momentum-flux terms. The actual solution of these equations is described in Section 2.1.8.

2.1.4.1. Basics of the Semi-Implicit Method. When fluid flow is modeled with a fully explicit method, time-step sizes are restricted by the Courant limit as

$$\Delta t \le k \cdot \frac{\Delta x}{|V| + c} \ , \tag{2-26}$$

where Δx is a characteristic mesh length, V is the flow velocity, c is the speed of sound, and parameter k varies in value depending on the details of the method, but here can be taken to be 1.0. This simple class of methods is appropriate when it is important to track the details of pressure wave propagation (e.g., shock waves). However, in most reactor transients, this level of detail is not important. At most, continuity waves (moving liquid levels or froth fronts) must be followed. Frequently the transient is simply an evolution between quasi-steady states.

Both the ICE and semi-implicit methods relax the explicit restrictions on time-step size by evaluating terms involved in pressure wave propagation at the new (n+1) time level. For a simple form of the momentum equation, this requires new-time values in the pressure gradient term as given by

$$\frac{(V^{n+1}_{j+1/2} - V^{n}_{j+1/2})}{\Delta t} + V^{n}_{j+1/2}\left.\frac{\partial V^{n}}{\partial x}\right|_{j+1/2}$$

$$+ \frac{1}{\langle\rho\rangle^{n}_{j+1/2}}\frac{(P^{n+1}_{j+1} - P^{n+1}_{j})}{\Delta x} + K^{n}_{j+1/2}V^{n+1}_{j+1/2}\left|V^{n}_{j+1/2}\right| = 0 \ . \tag{2-27}$$

Similarly, relaxation of the restrictions on time-step size also requires that velocities involved in flux of mass and energy be evaluated at the new-time level. The equations then become

$$\frac{(\rho^{n+1}_{j} - \rho^{n}_{j})}{\Delta t} + \frac{\partial}{\partial x_j}(\rho^{n}V^{n+1}) = 0 \text{ and} \tag{2-28}$$

$$\frac{(\rho_j^{n+1}e_j^{n+1}-\rho_j^n e_j^n)}{\Delta t}+\frac{\partial}{\partial x_j}(\rho^n e^n V^{n+1})+P_j^{n+1}\frac{(V_{j+1/2}^{n+1}-V_{j-1/2}^{n+1})}{\Delta x}$$

$$+\ \textit{heat sources or sinks}\ =\ 0 \qquad (2\text{-}29)$$

By using the above equation structure, information on a pressure disturbance in any cell is available to any other cell during the same time step. This eliminates the sound speed from the Courant stability limit, leaving what is commonly referred to as the "material Courant" stability limit ($\Delta t < (\Delta x)/|V|$). The absolute value of flow velocity remains in the denominator of the expression because information relevant to continuity waves is still propagated only one cell per time step by the semi-implicit method.

Completion of the problem definition requires a choice of two independent variables from the four thermodynamic variables: pressure, temperature, density, and specific internal energy. Density is not a good choice because of the need to model liquid solid regions. Given the low compressibility of liquid, a small error in a solution for density can translate to a significant error in pressure. When pressure is designated as an independent variable, a small error in the solution for pressure results in an even smaller fractional error in density. The choice of the second independent variable is driven by considerations beyond the simple equations presented above. Multiphase and multicomponent systems tend toward an equilibrium in which the phases and/or components are all at the same temperature. This behavior is reflected in constitutive relations for interphase (or wall-to-fluid) heat transfer that depend on differences of temperatures and that must be evaluated implicitly with respect to these temperature differences in the numerical equations. When the gas phase contains a mixture of species, all species are assumed to be at the same temperature. Selecting temperature as an independent variable in these situations can significantly simplify final solution of the equations.

Equations of state provide density and internal energy as functions of pressure and temperature. The relationships are generally nonlinear; therefore, the combination of discretized flow equations and state equations yields a coupled set of nonlinear equations. A key feature of this program is that an iterative method (see Section 2.1.8.) is used to obtain a solution to the nonlinear equations. The nonlinear equations are not simply replaced by a linearized approximation, as is done in RELAP5 (Ref. 2-21.).

A stability analysis of these semi-implicit equations introduces limitations on weighting factors used for cell-edge averages. The equations are unconditionally unstable unless

$$w_{j+1/2} \geq (1/2)\left(1+\frac{\Delta t|V_{j+1/2}|}{\Delta x_{j+1/2}}\right) \quad \text{for} \quad V_{j+1/2} \geq 0 \text{ and}$$

$$w_{j+1/2} \leq (1/2)\left(1-\frac{\Delta t|V_{j+1/2}|}{\Delta x_{j+1/2}}\right) \quad \text{for} \quad V_{j+1/2} < 0\ . \qquad (2\text{-}30)$$

When the inequalities are replaced with equalities in the above expression, a difference scheme with the minimal permitted numerical diffusion results. However, experience with a range of two-phase-flow problems has resulted in the final adoption of the following more robust choice of weighting factors:

$$w_{j+1/2} = 1 \quad \text{for} \quad V_{j+1/2} \geq 0 \text{ and}$$
$$w_{j+1/2} = 0 \quad \text{for} \quad V_{j+1/2} < 0 \ . \tag{2-31}$$

This is the standard donor-cell difference method.

2.1.4.2. Enhancements to the Semi-Implicit Method. The finite-volume equations given above reflect the semi-implicit method as implemented in early versions of TRAC and to some extent in RELAP5 (Ref. 2-21.). However, the discovery of instabilities in bubbly flow (Mahaffy, Ref. 2-11.) resulted in improvements to the wall friction term in Eq. (2-27) and, more importantly, to the interfacial friction term in the two-phase momentum equations. Optimal stability would be obtained by evaluating the friction terms fully implicitly. Unfortunately, this would result in serious complications for the solution procedure outlined in Section 2.1.8. The existing solution procedure relies on the finite-difference motion equations containing no more than the first power of the new-time velocity. This permits a direct solution for V^{n+1} as a linear function of adjacent new-time pressures.

More stable force terms can be obtained from linearization of a fully implicit force term. First, assume that the new-time velocity is not very different from the old-time velocity, or

$$V^{n+1}_{j+1/2} = V^{n}_{j+1/2} + \delta V_{j+1/2} \ . \tag{2-32}$$

Now, substitute this expression into the fully implicit wall friction term as follows:

$$K^{n}_{j+1/2} V^{n+1}_{j+1/2} \left| V^{n+1}_{j+1/2} \right| = K^{n}_{j+1/2} (V^{n}_{j+1/2} + \delta V_{j+1/2}) \left| V^{n}_{j+1/2} + \delta V_{j+1/2} \right|$$
$$= 2K^{n}_{j+1/2} \left| V^{n}_{j+1/2} \right| \delta V_{j+1/2} + K^{n}_{j+1/2} V^{n}_{j+1/2} \left| V^{n}_{j+1/2} \right| + 0(\delta V^2) \ . \tag{2-33}$$

Finally, drop terms containing δV^2 and replace δV with the difference between the new- and old-time velocity to give

$$K^{n}_{j+1/2} V^{n+1}_{j+1/2} \left| V^{n+1}_{j+1/2} \right| \approx 2K^{n}_{j+1/2} V^{n+1}_{j+1/2} \left| V^{n}_{j+1/2} \right| - K^{n}_{j+1/2} V^{n}_{j+1/2} \left| V^{n}_{j+1/2} \right| \ . \tag{2-34}$$

In the two-phase-flow equations, the same linearized implicit approximation is applied to the interfacial drag term.

The history of use of the semi-implicit equations within TRAC has resulted in a related approximation in the current semi-implicit method. When using the semi-implicit equations as part of the SETS method, it was found that a linearization of the implicit momentum-flux term can improve the stability of the motion equation. Details of this linearization are presented in the next subsection. The direct impact on the semi-implicit equations is reflected in the following equation:

$$V_{j+1/2}\left.\frac{\partial V}{\partial x}\right|_{j+1/2} = [\beta V^{n+1}_{j+1/2} + (1-\beta)V^{n}_{j+1/2}]\left.\frac{\partial V^n}{\partial x}\right|_{j+1/2}, \qquad (2\text{-}35)$$

where

$$\beta = \begin{bmatrix} 1 \quad for \quad \left.\dfrac{\partial V^n}{\partial x}\right|_{j+1/2} \geq 0 \\ 0 \quad for \quad \left.\dfrac{\partial V^n}{\partial x}\right|_{j+1/2} < 0 \end{bmatrix} .$$

With the special modifications to momentum-flux and friction terms, the finite-difference form of the motion equation becomes

$$\frac{(V^{n+1}_{j+1/2} - V^{n}_{j+1/2})}{\Delta t} + [\beta V^{n+1}_{j+1/2} + (1-\beta)V^{n}_{j+1/2}]\left(\frac{\partial V^n}{\partial x}\right)\Bigg|_{j+1/2} + \frac{1}{\langle\rho\rangle^{n}_{j+1/2}}\frac{(P^{n+1}_{j+1/2} - P^{n+1}_{j})}{\Delta x}$$

$$+ 2K^{n}_{j+1/2}V^{n+1}_{j+1/2}\left|V^{n}_{j+1/2}\right| - K^{n}_{j+1/2}V^{n}_{j+1/2}\left|V^{n}_{j+1/2}\right| = 0 . \qquad (2\text{-}36)$$

2.1.4.3. Semi-Implicit Method Adapted to Two-Phase Flow. Extension of the numerical method to the two-phase, two-fluid model is relatively straightforward. Special modifications to the method are necessary to treat changes from two-phase to single-phase flow and are described below. Source terms are present to model phase change and heat transfer. These are generally implicit in any driving temperature difference and explicit in any coefficient. The importance of gravitationally driven liquid flow requires an accurate model of gravitational force along the direction of motion. This uses an input angle (θ) between a vector from the center of cell j to the center of cell j+1 and a vector directed against gravity. In the application of the code, θ is more generally the inverse cosine ($\cos^{-1}$) of the change in elevation between cell centers divided by the flow length between cell centers.

To shorten notation in the following difference equations, some subscripts associated with location have been eliminated. For velocities not contained in spatial differences, the subscript denoting spatial location is assumed to be j+1/2. For cell-centered variables, the assumed subscript is j. The phrase “combined gas” refers to the mixture of noncondensable gas and steam, which is assumed to move with no interspecies diffusion.

Semi-Implicit Equations of Motion

Combined Gas

$$\frac{(V_g^{n+1}-V_g^n)}{\Delta t}+[\beta_g V_g^{n+1}+(1-\beta_g)V_g^n]\nabla_{j+1/2}V_g^n$$

$$+\frac{c_i^n\left|V_g^n-V_l^n\right|}{\langle\alpha\rho_g\rangle_{j+1/2}^n}[2(V_g^{n+1}-V_l^{n+1})-(V_g^n-V_l^n)]$$

$$+\frac{1}{\langle\rho_g\rangle_{j+1/2}^n}\frac{(P_{j+1/2}^{n+1}-P_j^{n+1})}{\Delta x_{j+1/2}}+\frac{\Gamma_{j+1/2}^{+^n}}{\langle\alpha\rho_g\rangle_{j+1/2}^n}(V_g^{n+1}-V_l^{n+1})$$

$$+\frac{c_{wg}}{\langle\alpha\rho_g\rangle_{j+1/2}^n}(2V_g^{n+1}-V_g^n)\left|V_g^n\right|+g\cos\theta\;=\;0\,. \tag{2-37}$$

Liquid

$$\frac{V_l^{n+1}-V_l^n}{\Delta t}+[\beta_l V_l^{n+1}+(1-\beta_l)V_l^n]\nabla_{j+1/2}V_l^n$$

$$+\frac{c_i^n\left|V_l^n-V_g^n\right|}{\langle(1-\alpha)\rho_l\rangle_{j+1/2}^n}[2(V_l^{n+1}-V_g^{n+1})-(V_l^n-V_g^n)]$$

$$+\frac{1}{\langle\rho_l\rangle_{j+1/2}^n}\frac{(P_{j+1}^{n+1}-P_j^{n+1})}{\Delta x_{j+1/2}}-\frac{\Gamma_{j+1/2}^{-^n}}{\langle(1-\alpha)\rho_l\rangle_{j+1/2}^n}(V_l^{n+1}-V_g^{n+1})$$

$$+\frac{c_{wl}}{\langle(1-\alpha)\rho_l\rangle_{j+1/2}^n}(2V_l^{n+1}-V_l^n)\left|V_l^n\right|+g\cos\theta\;=\;0\;. \tag{2-38}$$

Semi-Implicit Mass Equations

Combined Gas

$$\frac{\alpha_j^{n+1}\rho_{gj}^{n+1}-\alpha_j^n\rho_{gj}^n}{\Delta t}+\nabla_j\cdot[\alpha^n\rho_g^nV_g^{n+1}]\;=\;\Gamma^{n+1}\;. \tag{2-39}$$

Noncondensable Gas

$$\frac{[\alpha_j^{n+1}\rho_{aj}^{n+1}-\alpha_j^n\rho_{aj}^n]}{\Delta t}+\nabla_j\cdot[\alpha^n\rho_a^nV_g^{n+1}]\;=\;0\;. \tag{2-40}$$

Liquid

$$\frac{[(1-\alpha_j^{n+1})\rho_{lj}^{n+1} - (1-\alpha_j^n)\rho_{lj}^n]}{\Delta t} + \nabla_j \cdot [(1-\alpha^n)\rho_l^n V_l^{n+1}] = -\Gamma^{n+1} \ . \tag{2-41}$$

Liquid Solute

$$\frac{[(1-\alpha)^{n+1}\tilde{m}^{n+1}\rho_l^{n+1} - (1-\alpha)^n m^n \rho_l^n]}{\Delta t} + \nabla_j \cdot [(1-\alpha)^n m^n \rho_l^n V_l^{n+1}] = 0 \ , \tag{2-42}$$

$$m^{n+1} = \min\left[\tilde{m}^{n+1} + \frac{S_c^n}{(1-\alpha)^{n+1}\rho_l^{n+1}}, m_{\max}\right] , \tag{2-43}$$

and

$$S_c^{n+1} = (\tilde{m}^{n+1} - m^{n+1})(1-\alpha)^{n+1}\rho_l^{n+1} + S_c^n \ . \tag{2-44}$$

<u>Semi-Implicit Energy Equations</u>

Combined Gas

$$\begin{aligned} &\frac{[\alpha_j^{n+1}\rho_{gj}^{n+1}e_{gj}^{n+1} - \alpha_j^n \rho_{gj}^n e_{gj}^n]}{\Delta t} + \nabla_j \cdot [\alpha^n \rho_g^n e_g^n V_g^{n+1}] \\ &\quad + P^{n+1}\left[\frac{(\alpha^{n+1} - \alpha^n)}{\Delta t} + \nabla_j \cdot (\alpha^n V_g^{n+1})\right] \\ &\quad = q_{wg}^{n+1} + q_{dg}^n + q_{ig}^{n+1} + \Gamma^{n+1} h_{sg}^{n+1} \ . \end{aligned} \tag{2-45}$$

Total Fluid (gas and liquid)

$$\begin{aligned} &\frac{[\alpha_j^{n+1}\rho_{gj}^{n+1}e_{gj}^{n+1} + (1-\alpha_j^{n+1})\rho_{lj}^{n+1}e_{lj}^{n+1}] - \alpha_j^n \rho_{gj}^n e_{gj}^n + (1-\alpha_j^n)(\rho_{lj}^n e_{lj}^n)}{\Delta t} \\ &\quad + \nabla_j \cdot [\alpha^n \rho_g^n e_g^n V_g^{n+1} + (1-\alpha^n)\rho_l^n e_l^n V_l^{n+1}] \\ &\quad + P^{n+1}\nabla_j \cdot [(1-\alpha)^n V_l^{n+1} + \alpha^n V_g^{n+1}] \\ &\quad = q_{wg}^{n+1} + q_{wl}^{n+1} + q_{dl}^n + q_{dg}^n \, . \end{aligned} \tag{2-46}$$

The wall heat transfer to the gas and liquid, q_{wg} and q_{wl}, and the interfacial mass-transfer rate, Γ, within the difference equation also require further definition. Note the mixture of old- and new-time values in these terms. The choice of old-time heat-transfer coefficients was driven by the desire to simplify the implementation of the method, but can result in bounded instabilities during calculations. These terms are given by

$$q_{wl}^{n+1} = h_{wl}^{n} A_w (T_w^{n} - T_l^{n+1}) / \text{vol} \ , \tag{2-47}$$

$$q_{wg}^{n+1} = h_{wg}^{n} A_w (T_w^{n} - T_g^{n+1}) / \text{vol} \ , \tag{2-48}$$

and

$$\Gamma^{n+1} = \frac{-(q_{ig}^{n+1} + q_{il}^{n+1})}{(h_v^{'})^{n+1} - (h_l^{'})^{n+1}} \ , \tag{2-49}$$

where

$$q_{ig}^{n+1} = h_{ig}^{n} A_i^{n} \frac{(T_{\text{sat}}^{n+1} - T_g^{n+1})}{\text{vol}} \tag{2-50}$$

and

$$q_{il}^{n+1} = h_{il}^{n} A_i^{n} \frac{(T_{\text{sat}}^{n+1} - T_l^{n+1})}{\text{vol}} \ . \tag{2-51}$$

Further definition is also needed for a special set of density averages used in the momentum equations. Cell-edge densities used in the denominator of Eqs. (2-37) and (2-38) are defined to produce a good prediction of hydrostatic pressure heads. For example, the edge-average gas macroscopic density is defined as

$$\langle \alpha\rho \rangle_{j+1/2}^{n} = \frac{\Delta x_j (\alpha\rho)_j^{n} + \Delta x_{j+1} (\alpha\rho)_{j+1}^{n}}{\Delta x_j + \Delta x_{j+1}} \ . \tag{2-52}$$

A similar definition holds for the cell-edge liquid macroscopic density. The edge-average microscopic densities are somewhat more complex. For example,

$$\langle \rho_g \rangle_{j+1/2}^{n} = \langle \alpha\rho_g \rangle_{j+1/2}^{n} \left[\frac{\Delta x_j \alpha_j^{n} + \Delta x_{j+1} \alpha_{j+1}^{n}}{\Delta x_j + \Delta x_{j+1}} \right]^{-1} \ . \tag{2-53}$$

This particular average is necessary for consistency within the SETS equations (see Section 2.1.4.6.), where macroscopic densities have a more fundamental importance within the solution.

The above finite-volume-flow equations hold only when a two-phase mixture is present at both the old- and new-time levels. Modifications are necessary when the old- or new-time-level fluid state is single phase; these are described in Section 2.1.6.

The motion equations are evaluated in subroutine TF1DS1 for 1D flow (3D flow uses TF3DS1). This evaluation takes the solution form illustrated by Eqs. (2-37) and (2-38) for velocities as linear functions of the new-time pressure gradient (see Section 2.1.8.). Terms in the mass and energy equations are evaluated in subroutine TF1DS (TFPLN for a plenum and TF3DS for 3D). This includes terms for the Jacobian matrix needed to solve these nonlinear with a Newton iteration. The iteration is driven by subroutine HOUT.

2.1.4.4. Basics of the SETS Method. The goal of the SETS method was to eliminate the material Courant stability limit with minimal alterations to the existing semi-implicit method. Given the success of the semi-implicit method in propagating information about sound waves, a correction step was devised to perform a similar propagation of information on continuity waves. As a very simple example, consider the single-phase mass equation. For each time step, the semi-implicit method is used to establish the new-time velocity field. Next, the following correction (or "stabilizer") step is used to obtain a final value of the new-time density:

$$\frac{(\rho_j^{n+1} - \rho_j^n)}{\Delta t} + \frac{\partial}{\partial x_j}(\rho^{n+1} V^{n+1}) = 0 \ . \qquad (2\text{-}54)$$

On the surface, this appears to be a fully implicit finite-difference equation. It is not, however, because the new-time velocities (V^{n+1}) are all known numbers obtained from the semi-implicit step. New-time densities are the only unknowns in this system of equations. Information about a density change in any given computational cell is propagated to all other cells within the same time step. Formal stability analysis and direct testing confirm expectations based on information propagation. The material Courant stability limit actually is eliminated. This does not imply unconditional stability for the method. The only modifications to the semi-implicit method involve flux terms. The continued practice of evaluating heat-transfer and friction coefficients at the old time results in other poorly defined stability problems.

One unusual aspect of SETS as implemented in the code is that the pattern of evaluation of semi-implicit and stabilizer equations is not the same for the motion equations as it is for the mass and energy equations. All mass and energy equations follow the above pattern of a semi-implicit step followed by a stabilizer step. However, the analogous momentum-stabilizer equation is evaluated before the evaluation of the semi-implicit equations. This pattern was established during the original development of SETS through tests of the various combinations of equation ordering. In these tests, two-phase-flow problems ran smoothly at significantly higher time steps with the current equation ordering than with others. The physical explanation for this behavior is the importance of the pressure gradient term in problems of interest. A solution is better behaved when the velocity used for transport of mass and energy is a direct result of a pressure-balanced solution.

For our special example of 1D single-phase flow, the SETS difference equations are

Stabilizer Motion Equation

$$\frac{(\tilde{V}^{n+1}_{j+1/2} - V^{n}_{j+1/2})}{\Delta t} + V^{n}_{j+1/2}\left.\frac{\partial \tilde{V}^{n+1}}{\partial x}\right|_{j+1/2} + \frac{1}{\langle\rho\rangle^{n}_{j+1/2}}\frac{P^{n}_{j+1} - P^{n}_{j}}{\Delta x} + K^{n}_{j+1/2}(2\tilde{V}^{n+1}_{j+1/2} - V^{n}_{j+1/2})\left|V^{n}_{j+1/2}\right| = 0 \ . \tag{2-55}$$

Semi-Implicit Equation Step

$$\frac{(V^{n+1}_{j+1/2} - V^{n}_{j+1/2})}{\Delta t} + V^{n}_{j+1/2} \times \left.\frac{\partial \tilde{V}^{n+1}}{\partial x}\right|_{j+1/2} + \frac{1}{\langle\rho\rangle^{n}_{j+1/2}}\frac{(\tilde{P}^{n+1}_{j+1} - \tilde{P}^{n+1}_{j})}{\Delta x} + K^{n}_{j+1/2}V^{n+1}_{j+1/2}\left|V^{n}_{j+1/2}\right| = 0 \ , \tag{2-56}$$

$$\frac{(\tilde{\rho}^{n+1}_{j} - \rho^{n}_{j})}{\Delta t} + \frac{\partial}{\partial x_j}\rho^{n}V^{n+1} = 0 \ , \text{and} \tag{2-57}$$

$$\frac{(\tilde{\rho}^{n+1}_{j}\tilde{e}^{n+1}_{j} - (\rho e)^{n}_{j})}{\Delta t} + \frac{\partial}{\partial x_j}\rho^{n}e^{n}V^{n+1} + \tilde{P}^{n+1}_{j}\frac{V^{n+1}_{j+1/2} - V^{n+1}_{j-1/2}}{\Delta x} = 0 \ . \tag{2-58}$$

Stabilizer Mass and Energy Equations

$$\frac{(\rho^{n+1}_{j} - \rho^{n}_{j})}{\Delta t} + \frac{\partial}{\partial x_j}\rho^{n}V^{n+1} = 0 \text{ and} \tag{2-59}$$

$$\frac{(\rho e)^{n+1}_{j} - (\rho e)^{n}_{j}}{\Delta t} + \frac{\partial}{\partial x_j}(\rho e)^{n+1}V^{n+1} + \tilde{P}^{n+1}_{j}\frac{V^{n+1}_{j+1/2} - V^{n+1}_{j-1/2}}{\Delta x} = 0 \ . \tag{2-60}$$

A tilde above a variable indicates that it is a first estimate of the new-time value. Actual new-time variables have a superscript "n+1" and no tilde. Note that the only result of the above semi-implicit step appears to be just a new-time velocity field. In practice the situation is more complex. To save computational time, temperatures and pressures that are fully consistent with the densities and energies obtained from solving the stabilizer mass and energy equations are never calculated. If the correlation used to obtain an old-time wall friction coefficient requires temperature or pressure, the values used would be those obtained during the solution of the semi-implicit equation step.

As will be clear in the discussion of the solution of the SETS equations, each of the above equations is solved once per time step. During development of the method, attempts were made to make repeated evaluations of a form of the SETS equations during each time step to produce an iterative solution to the fully implicit method. This approach was found to converge poorly or not at all, particularly at time steps in excess of the material Courant limit.

2.1.4.5. Enhancements to the SETS Method. As with the semi-implicit method, linearized implicit terms are introduced in the motion equation to improve the behavior of friction and momentum transfer. The improved friction terms are identical to those derived in Section 2.1.4.2. The momentum-transfer terms are somewhat more complex. First, the new-time velocity and velocity gradient are linearized in the following forms:

$$\tilde{V}^{n+1}_{j+1/2} = V^{n}_{j+1/2} + \delta V_{j+1/2} \text{ and} \tag{2-61}$$

$$\nabla\tilde{V}^{n+1}_{j+1/2} = \nabla\tilde{V}^{n}_{j+1/2} + \delta(\nabla V_{j+1/2}) \ . \tag{2-62}$$

Substitution of these relationships into the implicit form of the momentum-transfer term gives

$$V^{n+1}_{j+1/2}\nabla\tilde{V}^{n+1}_{j+1/2} = (V^{n}_{j+1/2} + \delta V_{j+1/2})(\nabla\tilde{V}^{n}_{j+1/2} + \delta(\nabla V_{j+1/2}))$$

$$= V^{n}_{j+1/2}\nabla\tilde{V}^{n}_{j+1/2} + \delta V^{n}_{j+1/2}\nabla\tilde{V}^{n}_{j+1/2} + V^{n}_{j+1/2}\delta(\nabla V_{j+1/2}) + \delta V^{n}_{j+1/2}\delta(\nabla V_{j+1/2}) . \tag{2-63}$$

Keeping only terms with no more than the first power of a variation and back-substituting the variations in terms of differences between old- and new-time variables gives

$$\tilde{V}^{n+1}_{j+1/2}\nabla\tilde{V}^{n+1}_{j+1/2} \approx V^{n}_{j+1/2}\nabla\tilde{V}^{n+1}_{j+1/2} + (\tilde{V}^{n}_{j+1/2} - V^{n}_{j+1/2})\nabla\tilde{V}^{n}_{j+1/2} \ . \tag{2-64}$$

The difference in base points for the linearizations of Eqs. (2-61) and (2-62) is not an error in the equations. It is the result of numerical experimentation with the three possible alternatives. The situation is further complicated by instabilities resulting from negative values of the gradient or sign discrepancies between final and intermediate (tilde) velocities. Numerical experimentation resulted in the following robust form of the linearized implicit momentum-transfer term:

$$\tilde{V}^{n+1}_{j+1/2}\nabla\tilde{V}^{n+1}_{j+1/2} \approx V^{n}_{j+1/2}\nabla_{j+1/2}\tilde{V}^{n+1}_{j+1/2} + \beta(\tilde{V}^{n+1}_{j+1/2} - V^{n}_{j+1/2})\nabla_{j+1/2}\tilde{V}^{n}_{j+1/2} \ ,$$

where

$$\beta = \begin{bmatrix} 1 \quad for \quad \left.\frac{\partial V^n}{\partial x}\right|_{j+1/2} \geq 0 \ and \ V^n_{j+1/2}\tilde{V}^n_{j+1/2} > 0 \\ \\ 0 \quad for \quad \left.\frac{\partial V^n}{\partial x}\right|_{j+1/2} < 0 \ or \ V^n_{j+1/2}\tilde{V}^n_{j+1/2} \leq 0 \end{bmatrix} . \tag{2-65}$$

With these modifications, the final form of the stabilizer motion equation is

$$\frac{(\tilde{V}^{n+1}_{j+1/2} - V^n_{j+1/2})}{\Delta t} + V^n_{j+1/2}\nabla_{j+1/2}\tilde{V}^{n+1}_{j+1/2} + \beta(\tilde{V}^{n+1}_{j+1/2} - V^n_{j+1/2})\nabla_{j+1/2}\tilde{V}^n_{j+1/2}$$

$$+ \frac{1}{\langle\rho\rangle^n_{j+1/2}}\frac{(P^n_{j+1} - P^n_j)}{\Delta x} + K^n_{j+1/2}(2\tilde{V}^{n+1}_{j+1/2} - V^n_{j+1/2})\left|V^n_{j+1/2}\right| = 0 . \tag{2-66}$$

The following revised form of the motion equation in the semi-implicit step has a minor change in the flux term to increase the robustness of the method further:

$$\frac{(V^{n+1}_{j+1/2} - V^n_{j+1/2})}{\Delta t} + V^n_{j+1/2}\nabla_{j+1/2}\tilde{V}^{n+1}_{j+1/2} + \beta(V^{n+1}_{j+1/2} - V^n_{j+1/2})\nabla_{j+1/2}\tilde{V}^n_{j+1/2}$$

$$+ \frac{1}{\langle\rho\rangle^n_{j+1/2}}\frac{(P^{n+1}_{j+1} - P^{n+1}_j)}{\Delta x} + K^n_{j+1/2}(2V^{n+1}_{j+1/2} - V^n_{j+1/2})\left|V^n_{j+1/2}\right| = 0 . \tag{2-67}$$

One significant modification is introduced in the stabilizer mass and energy equations. To save computational effort and overhead associated with the communication of more variables, the stabilizer equations listed in the previous section are not directly solved. Instead, the actual equations solved are the result of subtracting the semi-implicit equations from the corresponding stabilizer equations.

Stabilizer Mass and Energy Equations as Solved

$$\frac{(\rho^{n+1}_j - \tilde{\rho}^{n+1}_j)}{\Delta t} + \frac{\partial}{\partial x_j}(\rho^{n+1}V^{n+1}) = \frac{\partial}{\partial x_j}(\rho^n V^{n+1}) \text{ and} \tag{2-68}$$

$$\frac{(\rho e)^{n+1}_j - \tilde{\rho}^{n+1}_j\tilde{e}^{n+1}_j}{\Delta t} + \frac{\partial}{\partial x_j}((\rho e)^{n+1}V^{n+1}) = \frac{\partial}{\partial x_j}((\rho e)^n V^{n+1}) . \tag{2-69}$$

The advantage of this approach is more apparent in the application of the method to the full two-phase-flow equations. In that case, all source terms (mass and energy transfer) are canceled out of the equations to be solved. The disadvantage of this approach is that the rigorous mass conservation of Eq. (2-59) is lost. Mass conservation associated with Eq. (2-68) depends on the level of convergence of the iterative solution for the semi-implicit equations.

2.1.4.6. The SETS Method Adapted to Two-Phase Flow. The two-phase forms of the SETS equations contain some significant modifications. The first, which improves code robustness, is an initial evaluation of the equations of motion that is used solely to provide an improved prediction of the interfacial force terms needed in the standard stabilizer motion equations.

Equations for Prediction of Interfacial Drag Force

Combined Gas

$$\frac{(\hat{V}_g^{n+1} - V_g^n)}{\Delta t} + V_g^n \nabla_{j+1/2} \tilde{V}_g^n + \beta(\hat{V}_g^{n+1} - V_g^n)\nabla_{j+1/2}\tilde{V}_g^n$$

$$+ \frac{c_i^n \left| V_g^n - V_l^n \right|}{\langle \alpha\rho_g \rangle_{j+1/2}^n} [2(\hat{V}_g^{n+1} - \hat{V}_l^{n+1}) - (V_g^n - V_l^n)]$$

$$+ \frac{1}{\langle \rho_g \rangle_{j+1/2}^n} \frac{(P_{j+1}^n - P_j^n)}{\Delta x_{j+1/2}} + \frac{\Gamma_{j+1/2}^{+n}}{\langle \alpha\rho_g \rangle_{j+1/2}^n} (\hat{V}_g^{n+1} - \hat{V}_l^{n+1})$$

$$+ \frac{c_{wg}}{\langle \alpha\rho_g \rangle_{j+1/2}^n} (2\hat{V}_g^{n+1} - V_g^n) \left| V_g^n \right| + g\cos\theta = 0 , \qquad (2\text{-}70)$$

where

$$\beta = 0, \quad if \ \nabla_{j+1/2} V^n < 0 \ or \ V^n \tilde{V}^n < 0 ;$$

$$= 1, \quad if \ \nabla_{j+1/2} V^n \geq 0 \ and \ V^n \tilde{V}^n \geq 0 .$$

Liquid

$$\frac{(\hat{V}_l^{n+1} - V_l^n)}{\Delta t} + V_l^n \nabla_{j+1/2} \tilde{V}_l^n + \beta(\hat{V}_l^{n+1} - V_l^n)\nabla_{j+1/2}\tilde{V}_l^n$$

$$+ \frac{c_i^n \left| V_g^n + V_l^n \right|}{\langle (1-\alpha)\rho_l \rangle_{j+1/2}^n} [2(\hat{V}_l^{n+1} - \hat{V}_g^{n+1}) - (V_l^n - V_g^n)]$$

$$+ \frac{1}{\langle \rho_l \rangle_{j+1/2}^n} \frac{(P_{j+1}^n - P_j^n)}{\Delta x_{j+1/2}} - \frac{\dot{\Gamma}_{j+1/2}^n}{\langle (1-\alpha)\rho_l \rangle_{j+1/2}^n} (\hat{V}_l^{n+1} - \hat{V}_g^{n+1})$$

$$+ \frac{c_{wl}}{\langle (1-\alpha)\rho_l \rangle_{j+1/2}^n} (2\hat{V}_l^{n+1} - V_l^n) \left| V_l^n \right| + g\cos\theta = 0 \ . \qquad (2\text{-}71)$$

Edge-average densities follow the definitions provided in the discussion of the semi-implicit method [Eqs. (2-52) and (2-53)].

The velocities obtained from the above equations are used to decouple the vapor and liquid stabilizer motion equations. The prediction of the interfacial force term is good enough that the interfacial force term in the following stabilizer equations does not need to depend on the new-time stabilizer velocities. As a result, the liquid stabilizer motion equation contains only liquid stabilizer (tilde) velocities as unknowns. The liquid and gas equations are two completely independent systems of equations, which are solved separately.

Stabilizer Equations of Motion

Combined Gas

$$\frac{(\tilde{V}_g^{n+1} - V_g^n)}{\Delta t} + V_g^n \nabla_{j+1/2} \tilde{V}_g^{n+1} + \beta(\tilde{V}_g^{n+1} - V_g^n)\nabla_{j+1/2}\tilde{V}_g^n$$

$$+ \frac{c_i^n \left| V_g^n - V_l^n \right|}{\langle \alpha\rho_g \rangle_{j+1/2}^n} [2(\hat{V}_g^{n+1} - \hat{V}_l^{n+1}) - (V_g^n - V_l^n)]$$

$$+ \frac{1}{\langle \rho_g \rangle_{j+1/2}^n} \frac{(P_{j+1}^n - P_j^n)}{\Delta x_{j+1/2}} + \frac{\dot{\Gamma}_{j+1/2}^n}{\langle \alpha\rho_g \rangle_{j+1/2}^n} (\hat{V}_g^{n+1} - \hat{V}_l^{n+1})$$

$$+ \frac{c_{wg}}{\langle \alpha\rho_g \rangle_{j+1/2}^n} (2\tilde{V}_g^{n+1} - V_g^n) \left| V_g^n \right| + g\cos\theta = 0 \ . \qquad (2\text{-}72)$$

Liquid

$$\frac{(\tilde{V}_l^{n+1} - V_l^n)}{\Delta t} + V_l^n \nabla_{j+1/2} \tilde{V}_l^{n+1} + \beta(\tilde{V}_l^{n+1} - V_l^n)\nabla_{j+1/2}\tilde{V}_l^n$$

$$+ \frac{c_i^n \left| V_g^n - V_l^n \right|}{\langle (1-\alpha)\rho_l \rangle_{j+1/2}^n} [2(\hat{V}_l^{n+1} - \hat{V}_g^{n+1}) - (V_l^n - V_g^n)]$$

$$+ \frac{1}{\langle \rho_l \rangle_{j+1/2}^n} \frac{(P_{j+1}^n - P_j^n)}{\Delta x_{j+1/2}} - \frac{\Gamma^{-n}_{j+1/2}}{\langle (1-\alpha)\rho_l \rangle_{j+1/2}^n} (\hat{V}_l^{n+1} - \hat{V}_g^{n+1})$$

$$+ \frac{c_{wl}}{\langle (1-\alpha)\rho_l \rangle_{j+1/2}^n} (2\tilde{V}_l^{n+1} - V_l^n) \left| V_l^n \right| + g\cos\theta = 0 \ . \qquad (2\text{-}73)$$

Equations of Motion for the SETS Semi-Implicit Step

The equations solved during the semi-implicit step are almost identical to those presented in Section 2.1.4.3. but are reproduced here in their entirety to avoid ambiguity in details of the implementation. The primary difference between the motion equation in a pure semi-implicit method and its corresponding form in the semi-implicit step of SETS is the use of stabilizer velocities for momentum transport.

Combined Gas

$$\frac{(V_g^{n+1} - V_g^n)}{\Delta t} + V_g^n \nabla_{j+1/2} \tilde{V}_g^{n+1} + \beta(V_g^{n+1} - V_g^n)\nabla_{j+1/2}\tilde{V}_g^n$$

$$+ \frac{c_i^n \left| V_g^n - V_l^n \right|}{\langle \alpha\rho_g \rangle_{j+1/2}^n} [2(V_g^{n+1} - V_l^{n+1}) - (V_g^n - V_l^n)]$$

$$+ \frac{1}{\langle \rho_g \rangle_{j+1/2}^n} \frac{(\tilde{P}_{j+1}^{n+1} - \tilde{P}_j^{n+1})}{\Delta x_{j+1/2}} - \frac{\tilde{\Gamma}^{+n}_{j+1/2}}{\langle \alpha\rho_g \rangle_{j+1/2}^n} (V_g^{n+1} - V_l^{n+1})$$

$$+ \frac{c_{wg}}{\langle \alpha\rho_g \rangle_{j+1/2}^n} (2V_g^{n+1} - V_g^n) \left| V_g^n \right| + g\cos\theta = 0 \ . \qquad (2\text{-}74)$$

Liquid

$$\frac{(V_l^{n+1}-V_l^n)}{\Delta t}+V_l^n\nabla_{j+1/2}\tilde{V}_l^{n+1}+\beta(V_l^{n+1}-V_l^n)\nabla_{j+1/2}\tilde{V}_l^n$$

$$+\quad\frac{c_i^n\left|V_l^n-V_g^n\right|}{\langle(1-\alpha)\rho_l\rangle_{j+1/2}^n}\,[2(V_l^{n+1}-V_g^{n+1})-(V_l^n-V_g^n)]$$

$$+\frac{1}{\langle\rho_l\rangle_{j+1/2}^n}\frac{(\tilde{P}_{j+1}^{n+1}-\tilde{P}_j^{n+1})}{\Delta x_{j+1/2}}-\frac{\tilde{\Gamma}_{j+1/2}^{n}}{\langle(1-\alpha)\rho_l\rangle_{j+1/2}^n}(V_l^{n+1}-V_g^{n+1})$$

$$+\frac{c_{wl}}{\langle(1-\alpha)\rho_l\rangle_{j+1/2}^n}(2V_l^{n+1}-V_l^n)\left|V_l^n\right|+g\cos\theta\;=\;0\;. \qquad (2\text{-}75)$$

Basic Semi-Implicit Mass Equations

These equations differ from those in a pure semi-implicit method; the resulting void fraction and new-time thermodynamic variables are intermediate results. Final new-time values for these variables are formally set by the stabilizer mass and energy equations. Individual thermodynamic variables also are carefully distinguished from products that comprise macroscopic densities and energies. These macroscopic quantities [e.g., $(\alpha\rho_g)$] are a direct result of the solution of the stabilizer mass and energy equations at the end of the previous time step. Another key difference is found in the modified form of the divergence operator, which can involve an unusual mixture of new- and old-time values [see Eq. (2-81)].

Combined Gas

$$\frac{\left|\tilde{\alpha}_j^{n+1}\tilde{\rho}_{gj}^{n+1}-(\alpha\rho_g)_j^n\right|}{\Delta t}+\nabla_j\cdot[(\alpha\rho_g)V_g^{n+1}]\;=\;\tilde{\Gamma}^{n+1}\;. \qquad (2\text{-}76)$$

Noncondensable Gas

$$\frac{\left|\tilde{\alpha}_j^{n+1}\tilde{\rho}_{aj}^{n+1}-(\alpha\rho_a)_j^n\right|}{\Delta t}+\nabla_j\cdot[(\alpha\rho_a)V_g^{n+1}]\;=\;0\;. \qquad (2\text{-}77)$$

Liquid

$$\frac{\left|(1-\tilde{\alpha}_j^{n+1})\tilde{\rho}_{lj}^{n+1} - [(1-\alpha)\rho_l]_j^n\right|}{\Delta t} + \nabla_j \cdot [(1-\alpha)\rho_l]V_l^{n+1} = -\tilde{\Gamma}^{n+1} \quad . \tag{2-78}$$

Basic Energy Equations

Combined Gas

$$\begin{aligned}
&\frac{[\tilde{\alpha}_j^{n+1}\tilde{\rho}_{gj}^{n+1}\tilde{e}_{gj}^{n+1} - (\alpha\rho_g e_g)_j^n]}{\Delta t} + \nabla_j \cdot [(\alpha\rho_g e_g)^n V_g^{n+1}] \\
&\quad + \tilde{P}^{n+1}\left[\frac{(\tilde{\alpha}^{n+1} - \alpha^n)}{\Delta t} + \nabla_j \cdot (\alpha^n V_g^{n+1})\right] \\
&\quad = \tilde{q}_{wg}^{n+1} + q_{dg}^n + \tilde{q}_{ig}^{n+1} + \tilde{\Gamma}^{n+1}\tilde{h}_{sg}^{n+1} \quad .
\end{aligned} \tag{2-79}$$

Total Fluid (gas and liquid)

$$\begin{aligned}
&\frac{\left\{\tilde{\alpha}_j^{n+1}\tilde{\rho}_j^{n+1}\tilde{e}_j^{n+1} + (1-\tilde{\alpha}_j^{n+1})\tilde{\rho}_j^{n+1}\tilde{e}_j^{n+1} - (\alpha\rho_g e_g)_j^n + [(1-\alpha)\rho_l e_l]_j^n\right\}}{\Delta t} \\
&\quad + \nabla_j \cdot \{(\alpha\rho_g e_g)^n V_g^{n+1} + [(1-\alpha)\rho_l e_l]^n V_l^{n+1}\} \\
&\quad + \tilde{P}^{n+1}\nabla_j \cdot [(1-\alpha)^n V_l^{n+1} + \alpha^n V_g^{n+1}] \\
&\quad = \tilde{q}_{wg}^{n+1} + \tilde{q}_{wl}^{n+1} + q_{dl}^n + q_{dg}^n \quad .
\end{aligned} \tag{2-80}$$

The divergence operator is revised during the semi-implicit step to improve modeling accuracy of situations in which flux can be predominately attributed to phase change in the cell for which the continuity equation is being evaluated. The idea is to use new-time information for that portion of the flux associated with the same cell as the equation (cell *j*). This makes the local solution more sensitive to variation in phase-change rates. In terms of the notation used for the basic definition of the divergence operator, the revised form is

$$\tilde{\nabla}_j \cdot (Y^n V_g^{n+1}) =$$

$$\frac{[w_{j+1/2}Y_j' + (1-w_{j+1/2})Y_{j+1}^n]A_{j+1/2}V_{j+1/2} - \langle w_{j-1/2}Y_{j-1}^n + (1-w_{j-1/2})Y_j'\rangle A_{j-1/2}V_{j-1/2}}{\mathrm{vol}_j} \quad . \tag{2-81}$$

The special feature of this operator is that all occurrences of Y_i^n in the normal finite-volume divergence operator are replaced by a mixed time average defined as

$$Y_j' = \gamma Y_j^{n+1} + (1-\gamma) Y_j^n \ . \tag{2-82}$$

The weighting factor γ is determined by several considerations. For flow that is single phase over the entire time step, γ is set to zero. When the net predicted flow out of a cell of either phase exceeds the current mass in that cell, the weight is set to one (new-time cell-centered quantities are fluxed). For less dramatic situations, three ratios are computed. The first ratio has as a numerator the sum of the change in cell vapor mass for the time step due to all mass fluxes plus twice the change due to boiling. The ratio's denominator is the cell's mass decrease due only to outwardly directed vapor mass flows (positive number). The second ratio is the analog of the first as applied to the liquid phase. For the third ratio, the numerator adds half the old-time cell liquid mass to the predicted change in cell liquid mass for the time step. The denominator is half of the mass change due to outwardly directed flows at the cell's edges (negative number). When other considerations are not in control, the maximum of the three ratios is limited to the range of zero through one and is used for γ.

The ratios used to compute the weighting factor were obtained after a long period of experimentation with two-phase-flow problems. The first two ratios force the use of a cell-centered implicit value when outflow of a phase is almost exclusively the result of phase-change terms. The factor will also force this implicit evaluation when phase change is not significant and inflow significantly exceeds the outflow. The third ratio becomes important when some liquid outflow is present and a prediction is made that over half of the existing liquid mass will flow or boil away during the time step.

The mixture of old- and new-time values of the quantity being fluxed results in a difference scheme for this step that is not rigorously conservative. However, the standard finite-volume divergence operator is applied in the stabilizer mass and energy equations, restoring conservation to the final fluxes of mass and energy.

To understand the stabilizer mass and energy equations, it is important to remember what is unknown and what quantities have fixed values. In this respect, the superscript "n+1" can be deceptive. New-time velocity values are fixed by the semi-implicit step, as are all new-time terms marked with a tilde. In the stabilizer combined-gas mass equation, the only unknown new-time variables are the macroscopic gas densities $(\alpha\rho_g)^{n+1}$. For the noncondensable mass equation, the only unknowns are the terms $(\alpha\rho_a)^{n+1}$, and for the liquid mass equation, the only unknowns are the terms $[(1-\alpha)\rho_l]^{n+1}$. In the stabilizer combined-gas energy equation, the only unknown new-time variables are the macroscopic gas energy densities $(\alpha\rho_g e_g)^{n+1}$. For the liquid energy equation, the only unknowns are the terms $[(1-\alpha)\rho_l e_l]^{n+1}$.

Stabilizer Mass Equations

Combined Gas

$$\frac{[(\alpha\rho_g)^{n+1} - (\alpha\rho_g)^n]}{\Delta t} + \nabla_j \cdot [(\alpha\rho_g)^{n+1} V_g^{n+1}] = \tilde{\Gamma}^{n+1} \ . \tag{2-83}$$

Noncondensable Gas

$$\frac{[(\alpha\rho_a)^{n+1} - (\alpha\rho_a)^n]}{\Delta t} + \nabla_j \cdot [(\alpha\rho_a)^{n+1} V_g^{n+1}] = 0 \ . \tag{2-84}$$

Liquid

$$\frac{[(1-\alpha)\rho_l]_j^{n+1} - [(1-\alpha)\rho_l]_j^n}{\Delta t} + \nabla_j \cdot \{[(1-\alpha)\rho_l]^{n+1} \cdot V_l^{n+1}\} = -\tilde{\Gamma}^{n+1} \ . \tag{2-85}$$

Liquid Solute

$$\frac{[(1-\alpha)^{n+1}\tilde{m}^{n+1}\rho_l^{n+1} - (1-\alpha)^n m^n \rho_l^n]}{\Delta t}$$

$$+ \nabla_j \cdot \left[(1-\alpha)^{n+1}\tilde{m}^{n+1}\rho_l^{n+1} V_l^{n+1}\right] = 0 \ , \tag{2-86}$$

$$m^{n+1} = \min\left[\tilde{m}^{n+1} + \frac{S_c^n}{(1-\alpha)^{n+1}\rho_l^{n+1}} \ , \ m_{\max}\right] , \tag{2-87}$$

and

$$S_c^{n+1} = (\tilde{m}^{n+1} - m^{n+1})(1-\alpha)^{n+1}\rho_l^{n+1} + S_c^n \ . \tag{2-88}$$

Stabilizer Energy Equations

Combined Gas

$$\frac{[(\alpha\rho_g e_g)^{n+1} - (\alpha\rho_g e_g)^n]}{\Delta t} + \nabla_j \cdot [(\alpha\rho_g e_g)^{n+1} V_g^{n+1}]$$

$$+ \tilde{P}^{n+1}\left[\frac{(\tilde{\alpha}^{n+1} - \alpha^n)}{\Delta t} + \nabla_j \cdot (\alpha^n V_g^{n+1})\right]$$

$$= \tilde{q}_{wg}^{n+1} + q_{dg}^n + \tilde{q}_{ig}^{n+1} + \tilde{\Gamma}^{n+1}\tilde{h}_{sg}^{n+1} \quad . \tag{2-89}$$

Liquid

$$\frac{[(1-\alpha)\rho_l e_l]_j^{n+1} - [(1-\alpha)\rho_l e_l]_j^n}{\Delta t} + \nabla_j \cdot \{[(1-\alpha)\rho_l e_l]^{n+1} V_l^{n+1}\}$$

$$+ \tilde{P}^{n+1}\left\{\frac{(\alpha^n - \tilde{\alpha}^{n+1})}{\Delta t} + \nabla_j \cdot [(1-\alpha)^n V_l^{n+1}]\right\}$$

$$= \tilde{q}_{wl}^{n+1} + q_{dl}^n - \tilde{q}_{ig}^{n+1} - \tilde{\Gamma}^{n+1}\tilde{h}_{sg}^{n+1} \quad . \tag{2-90}$$

As indicated in Section 2.1.4.5., the code does not directly solve all of the above stabilizer equations. The actual equations solved are differences between these equations and their corresponding equations from the semi-implicit step. For the case of solute transport, no corresponding equation exists in the semi-implicit step. As a result, the stabilizer solute-transport equation, Eq. (2-86), is solved exactly as listed above. The final forms of the other equations as set in subroutine STBME follow:

Stabilizer Mass Equations

Combined Gas

$$\frac{[(\alpha\rho_g)^{n+1} - \tilde{\alpha}^{n+1}\tilde{\rho}_g^{n+1}]}{\Delta t} + \nabla_j \cdot [(\alpha\rho_g)^{n+1} V_g^{n+1}] = \nabla_j \cdot [(\alpha\rho_g)^n V_g^{n+1}] \quad . \tag{2-91}$$

Noncondensable Gas

$$\frac{[(\alpha\rho_a)^{n+1} - \tilde{\alpha}^{n+1}\tilde{\rho}_g^{n+1}]}{\Delta t} + \nabla_j \cdot [(\alpha\rho_a)^{n+1} V_g^{n+1}] = \nabla_j \cdot [(\alpha\rho_a)^n V_g^{n+1}] \quad . \tag{2-92}$$

Liquid

$$\frac{[(1-\alpha)\rho_l]^{n+1} - (1-\tilde{\alpha}^{n+1})\tilde{\rho}_l^{n+1}}{\Delta t} + \nabla_j \cdot \{[(1-\alpha)\rho_l]^{n+1} V_l^{n+1}\} = \nabla_j \cdot \{[(1-\alpha)\rho_l]^n V_l^{n+1}\} . \tag{2-93}$$

Stabilizer Energy Equations

Combined Gas

$$\frac{[(\alpha\rho_g e_g)^{n+1} - \tilde{\alpha}^{n+1}\tilde{\rho}_g^{n+1}\tilde{e}_g^{n+1}]}{\Delta t} + \nabla_j \cdot [(\alpha\rho_g e_g)^{n+1} V_g^{n+1}] = \nabla_j \cdot [(\alpha\rho_g e_g)^n V_g^{n+1}] . \tag{2-94}$$

Liquid

$$\frac{\{[(1-\alpha)\rho_l e_l]^{n+1} - (1-\tilde{\alpha}^{n+1})\tilde{\rho}_l^{n+1}\tilde{e}_l^{n+1}\}}{\Delta t} + \nabla_j \cdot \{[(1-\alpha)\rho_l e_l]^{n+1} V_l^{n+1}\}$$

$$= \nabla_j \cdot \{[(1-\alpha)\rho_l e_l]^n V_l^{n+1}\} . \tag{2-95}$$

Source terms in the SETS equations follow the definitions provided during the discussion of the semi-implicit methods. They are redefined below to clarify the use of intermediate variables.

$$\tilde{q}_{wl}^{n+1} = h_{wl}^n A_w (T_w^n - \tilde{T}_l^{n+1})/\text{vol} , \tag{2-96}$$

$$\tilde{q}_{wg}^{n+1} = h_{wg}^n A_w (T_w^n - \tilde{T}_g^{n+1})/\text{vol} , \tag{2-97}$$

and

$$\tilde{\Gamma}^{n+1} = \frac{-\left(\tilde{q}_{ig}^{n+1} + \tilde{\tilde{q}}_{il}^{n+1}\right)}{(h_v')^{n+1} - (h_l')^{n+1}} , \tag{2-98}$$

where

$$\tilde{q}_{ig}^{n+1} = h_{ig}^n A_i^n \frac{(\tilde{T}_{\text{sat}}^{n+1} - \tilde{T}_g^{n+1})}{\text{vol}} \tag{2-99}$$

and

$$\tilde{q}_{il}^{n+1} = h_{il}^{n} A_i^{n} \frac{(\tilde{T}_{\text{sat}}^{n+1} - \tilde{T}_l^{n+1})}{\text{vol}} \quad . \tag{2-100}$$

As mentioned in Section 2.1.4.5., an important subtlety in the SETS application is the use of thermodynamic variables in the evaluation of specific terms. The current form of the SETS solution provides only final new-time values for void fraction (α), macroscopic densities $[\alpha\rho_g, \alpha\rho_a, (1-\alpha)\rho_l]$, and macroscopic energies $[\alpha\rho_g e_g, \alpha\rho_a e_a, (1-\alpha)\rho_l e_l]$. A final call to the thermodynamics subroutine does not occur after the solution of the stabilizer mass and energy equations. As a result, when basic thermodynamic variables are needed for evaluation properties such as viscosity or heat-transfer coefficients, values obtained from the previous semi-implicit step are used.

Equations (2-70) and (2-71) do not involve any implicit coupling between cells and can be solved directly for the gas and liquid (caret) velocities at each mesh-cell interface. Equations (2-72) and (2-73) are not coupled to each other. Each of these systems is implicitly coupled in space through the momentum-convection term, and each requires the solution of a tridiagonal linear system. Equations (2-74) through (2-80), combined with the necessary thermodynamic and constitutive equations, form a coupled system of nonlinear equations. Equations (2-74) and (2-75) are solved directly to obtain V_g^{n+1} and V_l^{n+1} as linear functions of $\tilde{P}^{n+1}$. After substituting these equations for velocity into Eqs. (2-76) through (2-80), the resulting system is solved for the independent variables $\tilde{P}^{n+1}$, $\tilde{P}_a^{n+1}$, $\tilde{T}_g^{n+1}$, $\tilde{T}_l^{n+1}$, and $\tilde{\alpha}^{n+1}$ with a standard Newton iteration, including all coupling between cells. In practice, the linearized equations solved during this Newton iteration are reduced easily to a tridiagonal system involving only total pressures. The final eight stabilizer mass and energy equations [Eqs. (2-83) through (2-90)] also are simple tridiagonal linear systems because V_g^{n+1} and V_l^{n+1} are known after solving Eqs. (2-74) through (2-80).

The drag force predictor equations are set up and solved in subroutines StbVel1D, StbVelx, StbVely, and StbVelz. The stabilizer motion equations are set up in the same subroutines and are solved with calls to subroutine Solver from subroutine PREP. The basic momentum equations associated with the semi-implicit step are set up in subroutine TF1DS1 (1D) and TF3DS1 (3D). Subroutines TF1DS (1D), TFPLN (plenum), and TF3DS (3D) set up the solution of the mass and energy equations associated with the semi-implicit step. Subroutine BlockSolver (called from subroutine OUTER) controls the solution of the full basic semi-implicit equation set within a Newton iteration driven by subroutine HOUT. The stabilizer mass and energy equations are set up in subroutines STBME (1D), STBMPL (plenum), and STBME3 (3D). These equation are solved by calls to subroutine SOLVER from subroutine POST. Finally, a value of new-time void fraction (see Section 2.1.8.2.4.) is obtained from the macroscopic densities and energy densities in subroutines BKSSTB (1D), BKSPLN (plenums), and BKSTB3.

Note: **Differences from TRAC-M/F77.** In the development of TRAC-M/F90 (Version 3.0), new subroutines were created to perform the full solution of the linear systems generated by the approximations to the flow equations. These replace statements in the following TRAC-M/F77 subroutines:

- FEMOM, FEMOMX, FEMOMY, FEMOMZ, TF1DS, STBME that begin solution of the 1D portion of the linear equations, including all local coding for solution of the local tridiagonal matrix structures, and generation of terms in the network matrices. (The names FEMOM, FEMOMX, FEMOMY, and FEMOMZ were also changed to StbVel1D, StbVelx, StbVely, and StbVelz, respectively, because forward elimination is no longer done in those routines.)

- TF1DS and TF3DS for cell block reduction;

- OUT3D, POST3D, PREP3D, and VSSL2 for vessel matrix solution;

- OUTER, POST, and PREP1D for solution of the network matrix; and

- BKSMOM, TF1DS3, TF3DS3, BKSSTB, and BKSTB3 directly related to back-substitution steps in the solution of the linear equations.

The basic and stabilizer equations involve very different numbers of equations, and generate two different matrix structures. As a result two separate subroutines were created for TRAC-M/F90 for solution of global systems of linear equations. The more basic of these, Solver, operates on equations which are dominantly tridiagonal in structure (the stabilizer equations and pressure equation). Solution of the more complex linear system associated with the basic (semi-implicit) step is driven by subroutine BlockSolver. Details on TRAC-M/F90's solution procedures are given in Section 2.1.8.

2.1.5. 3D Finite-Difference Methods

In the 3D VESSEL component, the code solves the combined-gas mass equation [Eq. (2-4)] and the total mass equation [Eq. (2-7)] as basic equations, rather than the individual basic phasic mass equations solved in the 1D components. All the other basic equations and the stabilizer equations for the 3D VESSEL component are solved in the same form as the 1D components. The vector form of the motion equation separates into three orthogonal-coordinate velocity-component motion equations. We present only the combined-gas equations with the understanding that the liquid equations are treated analogously. The 3D VESSEL component can be modeled by the TRAC user in either cylindrical or Cartesian geometry. The following equations in cylindrical geometry convert to Cartesian geometry by replacing the r divisor by unity and deleting the V^2/r term in the divergence operator that models momentum convection. The r and θ dependence is replaced by x- and y-dependence. For an orthogonal, right-handed, cylindrical coordinate system, the three velocity-component forms of the combined-gas motion differential equation are as follows:

Axial Velocity (z) Component

$$\frac{\partial V_{gz}}{\partial t} + \left(V_{gr} \frac{\partial V_{gz}}{\partial r} + \frac{V_{g\theta}}{r} \frac{\partial V_{gz}}{\partial \theta} + V_{gz} \frac{\partial V_{gz}}{\partial z} \right) = -\frac{1}{\rho_g} \frac{\partial P}{\partial z} - \frac{\Gamma^+}{\alpha \rho_g} (V_{gz} - V_{lz})$$

$$- \frac{c_{iz}}{\alpha \rho_g} \left(V_{gz} - V_{lz} \right) \left| \vec{V}_g - \vec{V}_l \right| - \frac{c_{wgz}}{\alpha \rho_g} V_{gz} \left| \vec{V}_g \right| - g g_z \quad . \tag{2-101}$$

Radial Velocity (r) Component

$$\frac{\partial V_{gr}}{\partial t} + \left(V_{gr} \frac{\partial V_{gr}}{\partial r} + \frac{V_{g\theta}}{r} \frac{\partial V_{gr}}{\partial \theta} - \frac{V_{g\theta}^2}{r} + V_{gz} \frac{\partial V_{gr}}{\partial z} \right) = -\frac{1}{\rho_g} \frac{\partial P}{\partial r} - \frac{\Gamma^+}{\alpha \rho_g} (V_{gr} - V_{lr})$$

$$- \frac{c_{ir}}{\alpha \rho_g} (V_{gr} - V_{lr}) \left| \vec{V}_g - \vec{V}_l \right| - \frac{c_{wgr}}{\alpha \rho_g} V_{gr} \left| \vec{V}_g \right| - g g_r \ . \tag{2-102}$$

Azimuthal Velocity (θ) Component

$$\frac{\partial V_{g\theta}}{\partial t} + \left(V_{gr} \frac{\partial V_{g\theta}}{\partial r} + \frac{V_{g\theta}}{r} \frac{\partial V_{g\theta}}{\partial \theta} + \frac{V_{gr} V_{g\theta}}{r} + V_{gz} \frac{\partial V_{g\theta}}{\partial z} \right) = -\frac{1}{\rho_g r} \frac{\partial P}{\partial \theta} - \frac{\Gamma^+}{\alpha \rho_g} \left(V_{g\theta} - V_{l\theta} \right)$$

$$- \frac{c_{i\theta}}{\alpha \rho_g} (V_{g\theta} - V_{l\theta}) \left| \vec{V}_g - \vec{V}_l \right| - \frac{c_{wg\theta}}{\alpha \rho_g} V_{g\theta} \left| \vec{V}_g \right| - g \ g_\theta \quad . \tag{2-103}$$

In the last term of each equation, g is the gravitational acceleration constant and g_z, g_r, and g_θ are the directional components of the gravity vector based on the orientation of the 3D VESSEL component. By setting namelist input variable NVGRAV = 1, the TRAC user may define through input a general orientation for each VESSEL component. The NVGRAV = 0 default results in TRAC internally defining $g_z = 1$, $g_r = 0$, and $g_\theta = 0$, where the *z*-axis is oriented vertically upward for all VESSEL components in the system model.

TRAC uses a staggered-mesh scheme (Ref. 2-12.) similar to that used for the 1D components in which the velocities (*V*) are defined at the mesh-cell interfaces and the pressure *(P)*, gas volume fraction (α), temperature (*T*), internal energy (*e*), and density (ρ) are defined at the mesh-cell centers. The scalar field equations (mass and energy) apply to a mesh cell, whereas the velocity-component motion equations apply to an interface between mesh cells in the three velocity-component directions. The wall heat transfer and the interfacial mass transfer required by the field equations are defined with a form similar to Eqs. (2-96) through (2-100).

The difference scheme for each motion equation is lengthy because of the cross-derivative terms. Therefore, to illustrate the procedure, we will describe only the combined-gas velocity-component, *z*-direction, finite-difference basic equation of motion for a typical mesh cell interface, together with the gas basic mass and energy equations, for a typical mesh cell. The gas velocity-component basic equations of motion in the θ and *r* directions along with all of the liquid basic equations are similar in form. The stabilizer motion, mass, and energy equations will not be illustrated; the reader is referred to the 1D component Eqs. (2-70) to (2-80) and (2-83) to (2-95) where time-level parameters with ˜, ˆ, *n*, and *n*+1 superscripts are changed in going from the basic equations to the stabilizer equations. The superscript *n* indicates a current-time quantity; the superscript *n* +1 indicates a new-time quantity. The functional dependence (r,θ,z) points to the cell center. By incrementing *r* or θ or *z* by ±1, one moves to the adjacent cell in the direction based on which coordinate is incremented and on the sign of the increment. The functional dependencies $(r-1/2,\theta,z)$ and $(r+1/2,\theta,z)$ point to the inside and outside radial faces of the cell, respectively; $(r,\theta-1/2,z)$ and $(r,\theta+1/2,z)$, the right and left azimuthal faces of the cell (based on a perspective of looking radially out of the cell), respectively; and $(r,\theta,z-1/2)$ and $(r,\theta,z+1/2)$, the bottom and top axial faces of the cell, respectively. The subscript *g* (for gas) is dropped unless it is needed for clarity.

The default for the TRAC 3D numerics is to evaluate the 3D stabilizer equations every time step. The user can override the default. (See TRAC input description for namelist variable NOSETS, which controls the status of internal flag NSTAB.) The TRAC 3D stabilizer equations and the basic step equations are solved when the flag NSTAB = 1. If NSTAB = 0, then the basic step equations are solved, which is equivalent to the TRAC-PF1/MOD1 3D numerics.

The finite-difference combined-gas basic equation of motion in the *z*-direction has the following form:

Combined-Gas Basic Equation of Motion in the *z*-Direction

$$V_z^{n+1}(r,\theta,z+1/2)=V_z^{n}(r,\theta,z+1/2)$$

$$-\Delta t\left[\frac{V_r\Delta_r V_z^{n+1}}{\Delta r}+\frac{V_\theta\Delta_\theta V_z^{n+1}}{r\Delta\theta}+\frac{1}{2}\left(\frac{A_{z+1/2}}{A_{z+1}}+\frac{A_{z+1/2}}{A_z}\right)\frac{V_z^{n+1}(r,\theta,z+1/2)}{\Delta z}\right.$$

$$\left.\left[\frac{A_{Z+1/2}}{A_{z+1}}\tilde{V}_z^{n+1}(r,\theta,Z+1/2)-\frac{A_{Z-1/2}}{A_z}\tilde{V}_z^{n+1}(r,\theta,Z-1/2)\right]\right.$$

$$
- \frac{[P(r,\theta,z+1) - P(r,\theta,z)]^{n+1}}{\rho^n(r,\theta,z+1/2)\Delta z} - \frac{c_{iz}^n(r,\theta,z+1/2)}{(\alpha,\rho)^n(r,\theta,z+1/2)}
$$

$$
\times \left\{ \left[\left| \vec{V}_g - \vec{V}_l \right|^n + \frac{((V_{gz}-V_{lz})^n(r,\theta,z+1/2))^2}{\left| \vec{V}_g - \vec{V}_l \right|^n} \right] (V_{gz}-V_{lz})^{n+1}(r,\theta,z+1/2) \right.
$$

$$
\left. - \frac{((V_{gz}-V_{lz})^n(r,\theta,z+1/2))^3}{\left| \vec{V}_g - \vec{V}_l \right|^n} \right\}
$$

$$
- \frac{\Gamma^{+n}(r,\theta,z+1/2)(V_{gz}-V_{lz})^{n+1}(r,\theta,z+1/2)}{(\alpha\rho)^n(r,\theta,z+1/2)} - gg_z
$$

$$
- \frac{c_{wz}^n(r,\theta,z+1/2)\left\{ \left[\left| \vec{V}_g \right|^n + \frac{(V_z^n(r,\theta,z+1/2))^2}{|\vec{V}_g|^n} \right] V_z^{n+1}(r,\theta,z+1/2) - \frac{(V_z^n(r,\theta,z+1/2))^3}{|\vec{V}_g|^n} \right\}}{(\alpha\rho)^n(r,\theta,z+1/2)} \Bigg],
$$

(2-104)

where $Z = z$ if $V_z^n(r,\theta,z+1/2) \geq 0$ and $Z = z+1$ if $V_z^n(r,\theta,z+1/2) < 0$.

Any finite-difference scheme requires certain quantities at locations where they are not defined formally; therefore, additional relations are needed. TRAC obtains the volume-averaged properties $\alpha\rho$ and ρ at the cell axial interface from a cell-length weighted average,

$$
(\alpha\rho)(r,\theta,z+1/2) = \frac{\Delta z(z)\alpha(r,\theta,z)\rho(r,\theta,z) + \Delta z(z+1)\alpha(r,\theta,z+1)\rho(r,\theta,z+1)}{\Delta z(z) + \Delta z(z+1)} \qquad (2\text{-}105)
$$

and

$$
\rho(r,\theta,z+1/2) = \frac{(\alpha\rho)(r,\theta,z+1/2)}{\alpha(r,\theta,z+1/2)} = \qquad (2\text{-}106)
$$

$$
\frac{\Delta z(z)\alpha(r,\theta,z)\rho(r,\theta,z) + \Delta z(z+1)\alpha(r,\theta,z+1)\rho(r,\theta,z+1)}{\Delta z(z)\alpha(r,\theta,z) + \Delta z(z+1)\alpha(r,\theta,z+1)} .
$$

This averaging is necessary to compute pressure heads accurately. The code obtains Γ at the cell interface from its phasic velocity donor cell as follows:

The cross-derivative term $V_r\Delta_r V_z^{n+1}$ reflects a donor-cell average:

$$V_r\Delta_r V_z^{n+1} = \tilde{V}_r(r+1/2,\theta,z+1/2)\left[\tilde{V}_z(r+1,\theta,z+1/2)-\tilde{V}_z(r,\theta,z+1/2)\right]$$

$$+\tilde{V}_r(r-1/2,\theta,z+1/2)\left[\tilde{V}_z(r,\theta,z+1/2)-\tilde{V}_z(r-1,\theta,z+1/2)\right], \qquad (2\text{-}107)$$

where

$$\tilde{V}_r\left(r+1/2,\theta,z+1/2\right) = \qquad (2\text{-}108)$$

$$\min\left[\frac{SC_r\left(r+1/2,\theta,z+1\right)\tilde{V}_r\left(r+1/2,\theta,z+1\right)\Delta z\left(z\right)+SC_r\left(r+1/2,\theta,z\right)\tilde{V}_r\left(r+1/2,\theta,z\right)\Delta z\left(z+1\right)}{\Delta z\left(z\right)+\Delta z\left(z+1\right)},0\right]$$

and

$$\tilde{V}_r\left(r-1/2,\theta,z+1/2\right) = \qquad (2\text{-}109)$$

$$\max\left[\frac{SC_r\left(r-1/2,\theta,z+1\right)\tilde{V}_r\left(r-1/2,\theta,z+1\right)\Delta z\left(z\right)+SC_r\left(r-1/2,\theta,z\right)\tilde{V}_r\left(r-1/2,\theta,z\right)\Delta z\left(z+1\right)}{\Delta z\left(z\right)+\Delta z\left(z+1\right)},0\right].$$

In the above equations, "min" and "max" are the mathematical functions of minimum and maximum values of the terms inside the brackets. $SC_r(r+1/2,\theta,z)$ is the product of an orifice factor that is 0 (when an orifice plate is present at the r+1/2 interface) or 1 and the ratio of the flow area through the r + 1/2 interface to the (r,θ,z) cell flow area in the radial direction, $\mathrm{vol}(r,\theta,z)/\Delta r_{cell}$. An analogous expression holds for the $V_\theta\Delta_\theta V_z^{n+1}$ term.

Note that the V_z differences in the r and θ directions do not contain the z-direction flow-area weighting form. The SC_r and SC_θ factors make this correction for z-direction momentum convection in the r and θ directions, respectively.

In the interfacial drag terms, the magnitude of the relative velocity is defined as follows:

$$\left|\vec{V}_g-\vec{V}_l\right| = \{[V_{zg}(r,\theta,z+1/2)-V_{zl}(r,\theta,z+1/2)]^2 \qquad (2\text{-}110)$$

$$+0.25[(V_{rg}(r+1/2,\theta,z)+V_{rg}(r-1/2,\theta,z)$$

$$-V_{rl}(r+1/2,\theta,z)-V_{rl}(r+-1/2,\theta,z)]^2$$

$$+0.25[V_{\theta g}(r,\theta+1/2,z)+V_{\theta g}(r,\theta-1/2,z)$$

$$-V_{\theta l}(r,\theta+1/2,z)-V_{\theta l}(r,\theta-1/2,z)]^2\}^{1/2}.$$

The convective terms in the finite-difference relations for the scalar field equations are in conservative form. The finite-difference form of the combined-gas basic mass equation is

Combined-Gas Basic Mass Equation

$$\begin{aligned}\left(\tilde{\alpha}\tilde{\rho}\right)^{n+1} = (\alpha\rho)^n - \left[\frac{\Delta t}{\text{vol}}\right]\Big\{ & A_{z+1/2}\left\langle(\alpha\rho)^n V_z^{n+1}\right\rangle_{z+1/2} - A_{z-1/2}\left\langle(\alpha\rho)^n V_z^{n+1}\right\rangle_{z-1/2} \\ & + A_{r+1/2}\left\langle(\alpha\rho)^n V_r^{n+1}\right\rangle_{r+1/2} - A_{r-1/2}\left\langle(\alpha\rho)^n V_r^{n+1}\right\rangle_{r-1/2} \\ & + A_{\theta+1/2}\left\langle(\alpha\rho)^n V_\theta^{n+1}\right\rangle_{\theta+1/2} - A_{\theta-1/2}\left\langle(\alpha\rho)^n V_\theta^{n+1}\right\rangle_{\theta-1/2}\Big\} \\ & + \Delta t\,\tilde{\Gamma}^{n+1} \quad . \end{aligned} \tag{2-111}$$

The combined-gas basic energy equation is

Combined-Gas Basic Energy Equation

$$\begin{aligned}\left(\tilde{\alpha}\tilde{\rho}\tilde{e}\right)^{n+1} = (\alpha\rho e)^n - \left[\frac{\Delta t}{\text{vol}}\right]\Big\{ & A_{z+1/2}\left\langle(\alpha\rho e)^n V_z^{n+1}\right\rangle_{z+1/2} - A_{z-1/2}\left\langle(\alpha\rho e)^n V_z^{n+1}\right\rangle_{z-1/2} \\ & + A_{r+1/2}\left\langle(\alpha\rho e)^n V_r^{n+1}\right\rangle_{r+1/2} - A_{r-1/2}\left\langle(\alpha\rho e)^n V_r^{n+1}\right\rangle_{r-1/2} \\ & + A_{\theta+1/2}\left\langle(\alpha\rho e)^n V_\theta^{n+1}\right\rangle_{\theta+1/2} - A_{\theta-1/2}\left\langle(\alpha\rho e)^n V_\theta^{n+1}\right\rangle_{\theta-1/2}\Big\} \\ & - \tilde{P}^{n+1}\left(\tilde{\alpha}^{n+1} - \alpha^n\right) \\ & - \left[\frac{\tilde{P}^{n+1}\Delta t}{\text{vol}}\right]\Big[\left\langle A\alpha^n V_z^{n+1}\right\rangle_{z+1/2} - \left\langle A\alpha^n V_z^{n+1}\right\rangle_{z-1/2} \\ & \qquad + \left\langle A\alpha^n V_r^{n+1}\right\rangle_{r+1/2} - \left\langle A\alpha^n V_r^{n+1}\right\rangle_{r-1/2} \\ & \qquad + \left\langle A\alpha^n V_\theta^{n+1}\right\rangle_{\theta+1/2} - \left\langle A\alpha^n V_\theta^{n+1}\right\rangle_{\theta-1/2}\Big] \\ & + \Delta t(\tilde{q}_{wg}^{n+1} + q_{dg}^n + \tilde{q}_{ig}^{n+1} + \tilde{\Gamma}^{n+1}\tilde{h}_{sg}^{n+1}) \end{aligned} \tag{2-112}$$

The differencing of the other scalar equations (the total mass and energy equations, the noncondensable-gas mass equation, and the liquid-solute mass equation) is similar. The time level of the convected mass $\alpha\rho$ and convected energy $\alpha\rho\varepsilon$ is the n+1 in the stabilizer equations. If the stabilizer mass and energy equations are not evaluated (NSTAB = 0), the tilde parameters in Eqs. (2-111) and (2-112) are defined without tildes.

All the field equations in the 3D VESSEL component can have additional source terms to allow one or more 1D component junctions to be connected to a mesh-cell interface anywhere in the 3D VESSEL component. The source terms in the mass and energy equations follow below. The subscripts 1D and 3D indicate that quantities are obtained from the 1D component-junction interface or junction cell and the 3D VESSEL-component mesh cell, respectively. The $\langle\ \rangle$ indicates the convected quantity has either the subscript 1D or 3D of the upstream donor cell based on the direction of the phase velocity at the source-connection 1D component-junction interface, illustrated by Eqs. (2-21) and (2-31). Each of these source terms is added to the downstream mesh cell's mass or energy equation and an equivalent sink term is subtracted from the upstream mesh cell's equation.

Total Basic Mass-Equation Source Term

$$\left[\frac{\Delta t}{\text{vol}}\right]\{\langle(\alpha\rho_g)^n V_g^{n+1}\rangle_{1D} A_{1D} + \langle[(1-\alpha)\rho_l]^n V_l^{n+1}\rangle_{1D} A_{1D}\}\ . \tag{2-113}$$

Combined-Gas Basic Mass-Equation Source Term

$$\left[\frac{\Delta t}{\text{vol}}\right]\left\{\left\langle\left(\alpha\rho_g\right)^n_{\text{Donor}} V_g^{n+1}\right\rangle_{1D} A_{1D}\right\}\ . \tag{2-114}$$

Total Basic Energy Equation Source Term

$$\left[\frac{\Delta t}{\text{vol}}\right]\left\{\left\langle\left[(1-\alpha)\rho_l e_l\right]^n V_l^{n+1}\right\rangle_{1D} A_{1D} + \left\langle\left(\alpha\rho_g e_g\right)^n V_g^{n+1}\right\rangle_{1D} A_{1D}\right.$$
$$\left. + P_{3D}\left[\left\langle\alpha^n V_g^{n+1}\right\rangle_{1D} A_{1D} + \left\langle(1-\alpha)^n V_l^{n+1}\right\rangle_{1D}\right] A_{1D}\right\}\ . \tag{2-115}$$

Combined-Gas Basic Energy Equation Source Term

$$\left[\frac{\Delta t}{\text{vol}}\right]\left\{\left\langle(\alpha\rho_g e_g)^n V_g^{n+1}\right\rangle_{1D} A_{1D} + P_{3D}\left\langle\alpha^n (V_g^{n+1})\right\rangle_{1D} A_{1D}\right\} \quad . \tag{2-116}$$

Noncondensable-Gas Basic Mass-Equation Source Term

$$\left[\frac{\Delta t}{\text{vol}}\right]\left\langle(\alpha\rho_a)^n V_g^{n+1}\right\rangle_{1D} A_{1D} \quad . \tag{2-117}$$

Liquid-Solute Basic Mass-Equation Source Term

$$\left[\frac{\Delta t}{\text{vol}}\right]\left\langle\left((1-\alpha)m\rho_l\right)^n V_l^{n+1}\right\rangle_{1D} A_{1D} \quad . \tag{2-118}$$

The momentum source term is complicated by the staggered differencing and by the fact that the actual 1D component may enter at an arbitrary angle. For TRAC, we assume that the 1D component attaches normal (perpendicular) to the vessel mesh-cell interface. The interface flow area A_{3D} and velocity V_{3D} are defined on the opposite side of the 3D mesh cell from the interface where the 1D component-junction source convection is made. It is that opposite mesh-cell interface from the source-convection interface that has in its motion equation the following momentum-convection source term for the combined-gas or liquid basic equation of motion when $V_{3D} \pm 1/2$ flows away from the 1D component source-convection interface into the 3D + 1 mesh cell. An S factor is applied to the 1D component so that its positive flow direction becomes the positive flow direction of the vessel.

Basic Equation-of-Motion Source Term

$$\frac{\Delta t}{2}\left(\frac{A_{3D}}{\text{vol}_{3D\pm1}/\Delta x_{3D\pm1}} + \frac{A_{3D}}{\text{vol}_{3D}/\Delta x_{3D}}\right)\frac{V_{3D}^{n+1}}{\Delta x_{3D}}\left[\frac{A_{1D} S \tilde{V}_{1D}^{n+1}}{\text{vol}_{3D}/\Delta x_{3D}}\right] \quad . \tag{2-119}$$

Each stabilizer equation of motion is solved with all vessels in the modeled system implicitly coupled in space through their 1D-component-loop-source connections. The spatial coupling between directions and the interfacial drag coupling between fluid phases, however, are explicit in that the motion equations for each direction and for each fluid phase are solved separately as a vessel matrix equation. When solving the stabilizer

equations, the time-step size normally exceeds the material Courant time-step limit and implicit coupling in space for a given velocity-component direction for all vessel components is necessary to assure a numerically stable solution. This means that each 1D component loop must have all its vessel-component source connections made to the same direction interfaces of the 3D vessel mesh cells. Different loops can be connected to different faces, however. For example, one loop may be connected to *r*-direction interfaces of three different vessels, another loop to *z*-direction interfaces of one vessel, and a third loop connected to θ-direction and *y*-direction interfaces of two different vessels with different geometries. The latter example is allowed because the θ- and *y*-directions are implicitly coupled between two VESSEL components in the vessel matrix equation by which their equations are evaluated. If the TRAC user defines any 1D component loop with source connections to different vessel-interface directions, TRAC edits a warning message during the input phase and limits the time-step size to not exceed the material Courant limit in the VESSEL components of the modeled system.

The number of independent parameter variables is limited to V_l, V_g, T_l, T_g, α, P, and P_a by using the thermal equations of state,

$$\rho_l = \rho_l (P, T_l) , \qquad \rho_v = \rho_v (P_v, T_g) , \text{ and} \qquad \rho_a = \rho_a (P_a, T_g) ; \tag{2-120}$$

the caloric equations of state,

$$e_l = e_l \left(P, T_l\right) , \qquad e_v = e_v \left(P_v, T_g\right) , \text{ and} \qquad e_a = e_a \left(P_a, T_g\right) ; \tag{2-121}$$

and the definitions for ρ_g, e_g, and P [Eqs. (2-14), (2-15), and (2-16)].

If hardware structure exists in the 3D mesh cells, the interface flow area (A) for fluid flow and the mesh-cell fluid volume (vol) are reduced from their geometric mesh-cell values by the user through inputting fractions of their geometric area and volume. These fractions can be input with values greater than unity, but it is recommended that the user not do so for the model to be physically valid. Thus, A should be less than or equal to the geometric mesh-cell side area and "vol" should be less than or equal to the geometric mesh-cell volume. Mesh-cell fluid volumes are constrained to be $\geq 10^{-12}$ m^3 by TRAC. When the flow area is defined to be zero, fluid flow across the mesh-cell interface is zero. This procedure allows large obstacles, such as the downcomer walls and flow channels, to be modeled within the VESSEL component.

When NSTAB = 1, the combined-gas and liquid stabilizer equations of motion are determined in subroutines StbVelx, StbVely, and StbVelz (FEMOMX, FEMOMY, and FEMOMZ in TRAC-M/F77) and solved in subroutine VSSL1 for a single vessel-component system model or in subroutine PREP3D for a multivessel-component system model. The combined-gas and liquid basic equations of motion are determined in subroutine TF3DS1 and then substituted for the velocity in determining the mass and energy basic equations in subroutine TF3DS. The reduced pressure matrix equation is solved in subroutine VSSL2 for a single vessel-component model or subroutine OUT3D

for a multivessel-component model. The pressure solution is back-substituted in subroutine TF3DS3 to determine the remainder of the basic equation solution. A Newton method iterative solution of these basic equations is performed until the pressure solution converges to within a user-defined tolerance. When NSTAB = 1, the combined-gas and liquid stabilizer mass equations are determined in subroutine STBME3 and solved in subroutine VSSL3 for a single vessel-component system model or in subroutine POST3D for a multivessel-component system model. All the different forms of the above equations are solved as vessel matrix equations by subroutine MATSOL using the capacitance matrix method described in Section 2.1.8.4.

2.1.6. Modifications to the Basic Equation Set

Because of the choice of independent parameter variables in the solution of the 1D basic equations (total pressure, air partial pressure, void fraction, combined-gas and liquid temperatures, and combined-gas and liquid velocities), the basic equation set becomes singular at void fractions of zero and one. To avoid this solution difficulty, the combined-gas mass equation is replaced with a mean mass equation at these void-fraction limits. At a void fraction of zero, the liquid mass and combined-gas energy equations are replaced with equations that set the void fraction to zero and set the combined-gas temperature equal to the saturation temperature based on the total pressure. At a void fraction of one, these same equations are replaced with equations that set the void fraction to one and the liquid temperature equal to the saturation temperature based on the partial pressure of water vapor. The same approach is used to handle this singularity in the 3D basic equations, except that here the mean mass equations are always evaluated and the combined-gas rather than the liquid mass equation is replaced when the void fraction is zero or one.

When the transition from single-phase gas or liquid to a two-phase fluid first occurs, the combined-gas and liquid mass equations are evaluated but the replacement equation for the gas energy equation is used for one more time step. This forces the second phase to initially appear at saturation conditions, which is generally a very good approximation. It drastically reduces sporadic numerical problems associated with the use of two energy equations in which the first appearance of a phase can be associated with an exceptionally bad predicted value of its temperature. Special considerations are also made during the linearization for the Newton solution of the semi-implicit equations. When an explicit mass test suggests the first appearance of a second phase, flux of the second phase is used to estimate the new-time void fraction. If air is just appearing in a cell, an initial estimate is also made of the air partial pressure. Both of these estimates are used to specify the base state for the linearization associated with the current Newton iteration.

When the pressure exceeds the critical-point pressure, the basic equations become singular. To evaluate this fluid state with minimal coding changes, the thermal properties of steam have been modified slightly. TRAC constrains the calculated steam density never to exceed 0.999 times the liquid density and thus prevents a singularity from arising. Also, at pressures above the critical point, the calculated saturation

temperature is set to a higher value than the vapor temperature to drive the fluid to be a pure liquid through phase change.

Thermodynamic properties used when evaluating the basic equations are calculated by subroutine THERMO. These properties are determined as functions of total pressure, air partial pressure, and the combined-gas and liquid temperatures. When the values of these solution parameters lie outside the database range for which the thermodynamic-property functional fits are valid, subroutine THERMO edits a warning message and constrains the parameter values to the database range limits defined in Appendix A before evaluating the thermodynamic properties. However, the solution parameter variable values are not changed.

2.1.7. Conserving Convected Momentum

The TRAC-PF1/MOD1 backward difference approach to determine the $V\nabla V$ term in the TRAC momentum equation is known to be stable numerically. For smooth area changes, however, this backward or upwind difference scheme is not accurate and does not conserve momentum. For abrupt area changes, it can be shown that the upwind difference scheme for $V\nabla V$ will result in pressure changes that include both reversible and irreversible effects. Upwind differencing is accurate for abrupt expansions and overestimates the pressure change for an abrupt contraction. (See Appendix I, Section I.1. for details.)

It has been shown that the accuracy of a central difference representation of $V\nabla V$ is quite accurate for smooth area changes and for the reversible portion of an abrupt area change. Central differencing is, in general, unconditionally unstable, however, based on linear stability analyses. An approach that was originally developed for TRAC-PF1/MOD2 to improve momentum conservation is to determine factors based on geometry that change the upwind differencing of the $V\nabla V$ so that its accuracy is consistent with central differencing. The assumption used in developing these factors is constant volumetric flow from the cell center to the cell edge. This method bas been brought over to TRAC-M.

A central difference for $V\nabla V$ for 1D flow yields

$$V\nabla V = \frac{VdV}{dx} = \frac{0.5d\left(V^2\right)}{dx} \equiv \frac{0.5\left(V_{j+1}^2 - V_j^2\right)}{\Delta x_{j+1/2}} \quad . \tag{2-122}$$

Equation (2-122) can be rewritten as

$$V\nabla V = \frac{0.5\left(V_{j+1} + V_j\right)\left(V_{j+1} - V_j\right)}{\Delta x_{j+1/2}} \quad . \tag{2-123}$$

In TRAC, velocities are calculated at cell edges, therefore cell-center velocities must be estimated from cell-edge velocities. Equation (2-123) can be written in terms of the cell-edge velocities by applying the following equations based on constant volumetric flow from cell center to the cell edge:

$$A_{j+1}V_{j+1} = A_{j+1/2}V_{j+1/2} \quad , \tag{2-124}$$

$$A_j V_j = A_{j+1/2}V_{j+1/2} \quad , \tag{2-125}$$

and

$$A_j V_j = A_{j-1/2}V_{j-1/2} \quad . \tag{2-126}$$

If Eqs. (2-124) and (2-125) are substituted into the summed portion of Eq. (2-123), and Eqs. (2-124) and (2-126) are substituted into the difference portion of Eq. (2-123), an upwind difference form that is as accurate as central differencing is obtained for $V\nabla V$.

$$V\nabla V = 0.5\,(A_{j+1/2} / A_{j+1} + A_{j+1/2} / A_j)\,V_{j+1/2}(A_{j+1/2}V_{j+1/2} / A_{j+1} - A_{j-1/2}V_{j-1/2} / A_j) / \Delta x_{j+1/2} \tag{2-127}$$

These equations assume that $V_{j+1/2} \geq 0$, but similar sets of equations can be derived for $V_{j+1/2} < 0$. In the MOD2 and TRAC-M codes, Eq. (2-127) is the approximation used in both the 1D and 3D momentum-convection terms to improve the conservation of momentum. For comparison purposes, the MOD1 representation for $V\nabla V$ is equivalent to the MOD2 and TRAC-M approximation if the cell-edge flow areas and cell-center flow areas are all equal. For the MOD1 code, $V\nabla V$ is estimated for $V_{j+1/2} \geq 0$ as

$$V\nabla V = V_{j+1/2}\left(V_{j+1/2} - V_{j-1/2}\right) / \Delta x_{j+1/2} \quad . \tag{2-128}$$

In general, TRAC, even with the corrected $V\nabla V$ term, is still solving a nonconserving momentum equation. A conserving form of the momentum equation for single-phase flow with no momentum sources or sinks can be written as

$$\frac{d(\rho V)}{dt} = \frac{d(\rho VAV)}{Adx} = 0 \tag{2-129}$$

Expanding the derivatives of Eq. (2-129) yields

$$V\left\{\frac{d(\rho)}{dt} + \frac{d(\rho V A)}{A\ dx}\right\} + \rho\left\{\frac{d(V)}{dt} + V\frac{d(V)}{dx}\right\} = 0 \quad . \tag{2-130}$$

The continuity equation for single-phase flow with no sources or sinks can be written as

$$\frac{d(\rho)}{dt} + \frac{d(\rho VA)}{Adx} = 0 \qquad (2\text{-}131)$$

Therefore, Eq. (2-130) can be written as

$$\frac{d(V)}{dt} + V\frac{d(V)}{dx} = 0 \quad . \qquad (2\text{-}132)$$

Equation (2-132) represents the type of nonconserving form of the momentum equation solved by the TRAC code. This derivation indicates that TRAC will conserve momentum with the nonconserving form of the momentum equation if mass is conserved on a point-by-point basis. TRAC conserves mass within each hydraulic cell and assumes that within that cell, the density and void fractions are constant. This assumption may lead to errors in conserving momentum, since the nonconserving momentum equation is solved from cell center to cell center and the geometry area ratio factors developed for Eq. (2-127) assume constant density and void fraction from cell center to cell edge.

If we assume constant volumetric flow from cell edge j–1/2 to cell edge j+1/2, Eq. (2-127) in the form of the Bernoulli equation is equivalent to

$$P_{j+1} - P_j + \frac{\rho}{2}\left[\left(\frac{A_{j+1/2}}{A_{j+1}}V_{j+1/2}\right)^2 - \left(\frac{A_{j-1/2}}{A_j}V_{j-1/2}\right)^2\right] + \rho g \Delta x_{j+1/2}\cos\theta = 0 \; . \qquad (2\text{-}133)$$

Substitute the constant volumetric-flow relations $A_{j+1/2}V_{j+1/2} = A_{j+1}V_{j+1}$ and $A_{j-1/2}V_{j-1/2} = A_jV_j$ into the momentum-convection term of Eq. (2-133) to obtain the Bernoulli equation

$$P_{j+1} - P_j + \tfrac{1}{2}\rho\,[V_{j+1}^2 - V_j^2] + \rho g \Delta x_{j+1/2}\cos\theta = 0 \quad . \qquad (2\text{-}134)$$

We see from the above derivation of the momentum-convection term and the assumptions made that the equation of motion for single-phase liquid (a near-incompressible fluid) to a very good approximation satisfies the conservative form of the momentum equation (and thus the Bernoulli equation). Convected momentum flux between momentum cells should be nearly conserved. Reversible form losses caused by flow-area and elevation changes should be evaluated correctly. This has been demonstrated (Ref. 2-13.) for single-phase liquid with a variable flow-area and elevation flow-channel test problem having a total of seven 1D PIPE and VESSEL components connected in series with a FILL-component velocity and BREAK-component pressure boundary condition at each end of the flow channel, respectively. Each 1D VESSEL component was evaluated in each of three Cartesian-coordinate directions in separate calculations. Wall losses in the flow channel with flow area varying from 0.1 to 0.6 m^2 were minimized by increasing the flow-channel hydraulic diameter by a factor of 100.

A plot of the MOD2-calculated Bernoulli expression $P_j / \rho_j + V_j^2 / 2 + gh_j$ versus flow-channel cell number j for four different PIPE- and VESSEL-component models is shown in Fig. 2-1., with and without flow-area ratios applied in the momentum-convection term of the liquid equation of motion. Each of the four models comprised a different combination of PIPE and/or 1D VESSEL components, yet each gave the same results. Conservation of convected momentum and an accurate evaluation of the Bernoulli equation is demonstrated by the constant value of the Bernoulli expression when flow-area ratios are applied in the momentum-convection term. Similar calculations were performed for single-phase vapor wherein MOD2 was temporarily modified to evaluate a constant vapor microscopic density (making vapor an incompressible fluid). The results determined were similar to those of liquid, which served as a check that the combined-gas equation of motion as well as the liquid equation of motion are programmed correctly for both 1D and 3D components.

For a compressible single-phase vapor, the change in its microscopic density because of fluid pressure and temperature variation over a mesh-cell distance generally is small. Approximating constant density within a fluid cell should cause only a small error in conserving convected vapor momentum flux between momentum cells.

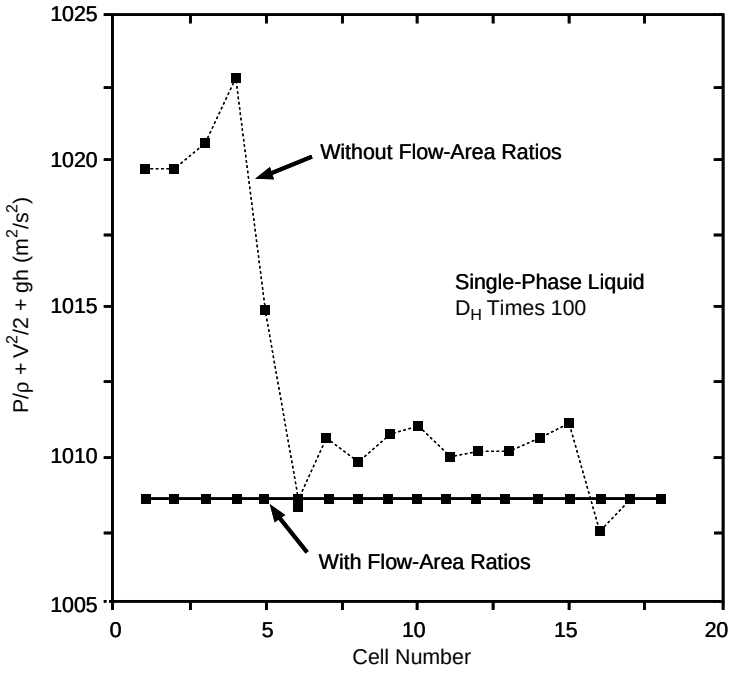

Fig. 2-1. The Bernoulli expression $P_j / \rho_j + V_j^2 / 2 + gh_j$ vs. flow-channel cell number j from a 1D flow-channel test problem having variable flow area and elevation.

A spatial variation in the fluid void fraction across a mesh cell can result in a momentum-flux conservation error because of the constant volumetric-flow assumption. The MOD2 and TRAC-M momentum equation solution has significant improvements in accuracy over the MOD1 momentum equation solution. For rapidly changing void fractions or densities within a short distance, however, MOD2 and TRAC-M still may not conserve momentum.

The ability to evaluate momentum convection with and without flow-area ratios has been provided. Each flow-area ratio is multiplied by variable ARY (Area Ratio Yes) and then summed to variable ARN (Area Ratio No) before being applied in the momentum-convection term. These two variables are initialized in module OneDDat (subroutine BLKDAT in TRAC-M/F77) to ARY=1 and ARN=0 to evaluate momentum convection with area ratios. Redefining ARY=0 and ARN=1 in module OneDDat (subroutine BLKDAT in TRAC-M/F77) sets all area ratios in the momentum-convection term to unity. This provides the TRAC user with a convenient way to compare TRAC calculations with flow-area ratios (TRAC-PF1/MOD2 and TRAC-M model) and without flow-area ratios (TRAC-PF1/MOD1 model) in the momentum-convection term.

2.1.7.1. Reversible and Irreversible Form Losses. With flow-area ratios in the momentum-convection term, TRAC approximately conserves convected momentum and evaluates only the reversible form losses of the Bernoulli equation. The TRAC user becomes responsible for input specifying all irreversible form losses due to abrupt or semi-abrupt flow-area expansions and contractions, thin-plate-orifice-type flow restrictions, and flow redirection (turning) at an elbow or tee, as discussed in Appendix I, Section I.1. Without flow-area ratios, the TRAC-PF1/MOD1-type momentum-convection term does not conserve convected momentum. That error can be shown to be the irreversible form loss of an abrupt expansion and approximately twice the irreversible form loss of an abrupt contraction. A flow-area change between mesh cells in TRAC-PF1/MOD1 calculation adds such an irreversible form loss that is appropriate for an abrupt expansion but in all other situations adds too much irreversible form loss. TRAC users who have prepared TRAC-PF1/MOD1 input-data plant models have compensated for such added irreversible form-loss error by not including other irreversible form losses at flow restrictions or at elbows and tees in order to evaluate the correct overall pressure drop through a portion or all of a flow loop. TRAC-PF1/MOD2 or TRAC-M users who inherit and convert such TRAC-PF1/MOD1 input-data files into TRAC-PF1/MOD2 (or TRAC-M) input-data files need to be aware that their plant model may have built-in compensating-error features for TRAC-PF1/MOD1 that, when evaluated by TRAC-PF1/MOD2 or TRAC-M, give wrong results. The user's response to this situation should be to never use converted TRAC-PF1/MOD1 input-data files blindly. All mesh-cell interface flow areas and mesh-cell volumes and lengths (whose ratio defines mesh-cell flow area) need to be checked against plant specifications, and all input-specified FRICs or K-factors (and those that have not been specified) need to be defined to account for their actual irreversible form losses at abrupt or semi-abrupt flow-area changes, flow restrictions, and flow turns (redirections).

TRAC assists MOD1, MOD2, and TRAC-M users by not requiring them to determine FRIC or K-factor values at abrupt expansion or contraction 1D component mesh-cell interfaces for input specification. TRAC does this internally when the user inputs the friction-factor-correlation option array NFF with a negative value at selected mesh-cell interfaces. At all such interfaces, all three versions of TRAC internally evaluate the standard K-factor formulas in Appendix I, Section I.1., for abrupt-expansion [$K = (1 - A_{min}/A_{max})^2$] and abrupt-contraction [$K = 0.5 - 0.7(A_{min}/A_{max}) + 0.2\,(A_{min}/A_{max})^2$] form losses based on mesh-cell flow areas and add them as FRICs to the input-specified FRICs or K-factors (converted to FRICs). TRAC-PF1/MOD1 also subtracts its momentum-convection term finite-difference error [$K = (1 - A_{min}/A_{max})^2$] to correctly evaluate the reversible plus irreversible form loss at interfaces where NFF < 0. Thus, all 1D mesh-cell interfaces having NFF < 0 model reversible plus irreversible abrupt-area-change form losses correctly (and in the same way) in MOD1, MOD2, and TRAC-M. This feature was extended in TRAC-PF1/MOD2 to 3D VESSEL components as well (this VESSEL extension was brought over to TRAC-M), where rather than inputting NFF < 0 (NFF is not a VESSEL-component input parameter), the MOD2 (and TRAC-M) user inputs the 3D friction-factor correlation coefficients CFZL–R < 0, CFZL–T < 0, and CFZL–Z < 0. Inputting negative values for the *X*- or *R*-, *Y*- or *θ*-, and *Z*-interface FRICs or K-factor results in MOD2 and TRAC-M internally evaluating an abrupt expansion or contraction (based on the fluid-phase flow direction) form loss and adding to it the absolute value of the input FRIC or K-factor. If the user does not want to add an additional input-specified FRIC or K-factor, a small negative value such as –1.0E-20 should be input.

2.1.7.2. Special Cases. The definition of flow-area ratios and irreversible form losses when evaluating momentum convection in BREAK, PLENUM, TEE, and VESSEL components needs further consideration. These special situations are handled in TRAC-PF1/MOD2 and TRAC-M in the following way.

2.1.7.2.1. BREAK Component. TRAC-PF1/MOD1 models a BREAK component with its mesh cell having either the same flow area as the adjacent-component mesh cell (IVDV = 0) or an infinitely large containment-room volume (IVDV = 1). Its input-specified VOLIN is not used. TRAC-PF1/MOD2 and TRAC-M specify this differently with more generality by defining the BREAK mesh-cell flow area by VOLIN / DXIN (which allows all possible flow-area changes to be modeled across the BREAK junction). The option parameter IVDV is no longer input. The BREAK-junction equation of motion is evaluated in the usual manner by the adjacent component's junction-interface equation of motion. Its momentum-convection term flow-area ratios are defined based on VOLIN and DXIN (from the BD array) defining the flow area of the BREAK mesh cell.

When the flow area changes between the BREAK mesh cell and the adjacent-component mesh cell, we recommend that at the junction interface in the adjacent component's input-data specification, the user set NFF < 0 if the area change is abrupt or input an appropriate FRIC or K-factor for the fluid-flow direction and the area change. It is important that the actual flow-area-change irreversible form loss be applied to provide a

dissipative term in the equation of motion to determine the correct and numerically stable solution. A BREAK component is a pressure boundary condition that locally removes a degree of freedom from the hydrodynamic solution. The equation set becomes locally stiffer and more sensitive to error growth when there is not a dissipative term.

For flow from the adjacent component into the BREAK component when the flow area is expanding, the donor-cell convection approximation's stabilizing effect is reduced in the momentum-convection term due to the flow-area ratios. Including the flow-area expansion irreversible form loss stabilizes the equation of motion by providing a dissipative term that compensates for the loss of the stabilizing effect from the donor-cell convection approximation with flow-area ratios. For flow from the BREAK component, TRAC assumes no momentum flux in the BREAK component. This has been found to be stable. This implies that, for flow into a BREAK component, TRAC is treating the BREAK pressure as a static pressure. For flow out of a BREAK component, the pressure is assumed to be a total pressure. For large BREAK-component volumes, both pressures are the same.

2.1.7.2.2. PLENUM Component. The PLENUM component is a single mesh cell with NPLJN junction interfaces connected to 1D components. The PLENUM component in TRAC is programmed to convect momentum across the PLENUM mesh cell in one coordinate direction only. The TRAC user specifies through input that the first JUNS1 junctions are on Side 1, the next JUNS2 junctions are on Side 2 (directly across the PLENUM mesh cell from Side 1), and the remaining $NPLJN - JUNS1 - JUNS2$ junctions are on the other sides of the plenum mesh cell. For these later junctions, we assume the PLENUM mesh cell has an infinite flow area with zero momentum flux at its center from or to each of these junctions. The PLENUM mesh-cell flow area associated with each Side 1 or Side 2 junction j is VOL/DX_j times the ratio of the junction j flow area to the sum of all junction flow areas on its side. This defines the PLENUM mesh-cell flow area which is passed through the BD array to determine the flow-area ratios for the momentum-convection term of the junction j equation of motion. Momentum is convected across the PLENUM mesh cell by assuming that junction j on Side 1 shares a common portion of the VOL/DX_j flow area with junction MIN(JUNS1+j, JUNS1+JUNS2) on Side 2 and that junction j on Side 2 shares a common portion of the VOL/DX_j flow area with junction $MIN(j - JUNS1, JUNS1)$ on Side 1. This is a rather simple model for coupling a junction on Side 1 with a junction on Side 2 in order to convect momentum between them across the PLENUM mesh cell.

Flow-area ratios should be defined by partitioning the PLENUM mesh-cell flow area with a junction-to-side volumetric-flow ratio rather than a junction-to-side flow-area ratio, but the explicit velocity feedback from the former for large time-step size can cause numerical instability. This condition is unique to the PLENUM component because momentum convection across the PLENUM component in the stabilizer equation of motion is not coupled implicitly. When the PLENUM component was implemented in TRAC-PF1/MOD1, it was programmed in this limited form to avoid the complexity of

changing the 1D component-network solution. Assuming the momentum flux goes to zero at the center of the PLENUM mesh cell eliminates the need for such coupling. Changing TRAC-PF1/MOD2 to convect momentum across the PLENUM mesh cell should have also involved convecting that momentum with implicit coupling in the stabilizer equation of motion for the JUNS1+JUNS2 junctions. That evaluation is done implicitly for components other than the PLENUM, but it is not coupled across the PLENUM mesh cell. An acceptor-cell approximation for the momentum flux convected out of the PLENUM cell is assumed. The numerical instability of that assumption is controlled by requiring that the flow area of the PLENUM mesh cell be greater that the summed junction flow areas of each side. Through flow-area ratios in the momentum-convection term, the above requirement reduces the destabilizing effect of the acceptor-cell approximation. The PLENUM mesh-cell flow area being larger than the flow area of the junctions on each of its sides is naturally satisfied for most situations where a PLENUM component is used.

2.1.7.2.3. TEE Component. The TEE component has three interface connections to mesh cell JCELL on its primary side. The momentum-convection term in the equation of motion for each of its three interfaces needs to be modified to account for the momentum flux's directional-component contribution to/from the secondary side. In addition, the volumetric-flow fraction to/from the secondary side affects the definition of the flow-area ratios. The angle ϕ between the secondary side and the low-numbered mesh-cell end of the primary side determines which of the two primary-side interfaces is coupled to the secondary-side interface through their equation-of-motion momentum-convection term. For $\cos(\phi) > 0$ the $-\cos(\phi)\, V_J$ component of the secondary-side junction J velocity V_J convects momentum to the secondary side from momentum cell JCELL+1/2 when $V_{JCELL+1/2} < 0$; the $-\cos(\phi)\, V_{JCELL+1/2}$ component of the primary-side velocity $V_{JCELL+1/2}$ convects momentum from the primary side to momentum cell J when $V_J > 0$. For $\cos(\phi) < 0$, a similar coupling applies to momentum cell JCELL–1/2. When $\cos(\phi) = 0$ (secondary side is perpendicular to the primary side), no momentum is convected between the primary and secondary sides because the $\cos(\phi)$ velocity component is zero.

The same TEE model as that in TRAC-PF1/MOD1 is used in TRAC-PF1/MOD2 and in TRAC-M. The area-ratio logic for momentum convection is not applied at the three interfaces of TEE-cell JCELL. In addition, abrupt flow-area change (and flow-turning) irreversible form losses are not evaluated for the three interfaces of JCELL when their NFF values are negative. Input for the current TEE component should observe the following:

- Define the TEE main-tube cell-averaged flow areas, VOL(j)/DX(j) for j = JCELL–1, JCELL, and JCELL+1, to be the same as the interface flow areas, FA(j) for j = JCELL and JCELL+1. For JCELLs at a network junction, this applies also to the neighboring component. Define the TEE side-tube first cell's cell-averaged flow area, VOL(1)/DX(1) (i.e., for j = 1 in the side-tube input), to be the same as the internal junction interface flow area, FA(1) in the side-tube input.

- Do not use the negative-NFF option at the three JCELL interfaces of TEE components. Abrupt flow-area change and flow-turning irreversible form losses need to be defined by the user through FRIC-array input data.

A thorough discussion of the present status of the MOD2 (and TRAC-M) TEE model is given in Ref. 2-22.

To demonstrate how the TEE momentum source is implemented in the code, we will assume a positive flow, in which case the conservative form of the liquid momentum equation can be written as

$$\mathrm{vol}_j \frac{\partial\left[(1-\alpha_j)\rho_{l_j} V_{l_{j+1/2}}\right]}{\partial t} + A_{j+1/2}(1-\alpha_j)\rho_{l_j} V_{l_{j+1/2}} V_{l_{j+1/2}} - A_{j-1/2}(1-\alpha_{j-1})\rho_{l_{j-1}} V_{l_{j-1/2}} V_{l_{j-1/2}} = \text{R.H.S.} \quad , \tag{2-135}$$

where R.H.S. stands for the terms on the right-hand side of the equation. After using the chain rule to expand the time-derivative term and substituting in the finite-difference liquid mass equation, we can write the momentum equation as

$$\frac{\partial V_{l_{j+1/2}}}{\partial t} + \frac{A_{j-1/2}(1-\alpha_{j-1})\rho_{l_{j-1}}}{\mathrm{vol}_j(1-\alpha_j)\rho_{l_j}} V_{l_{j-1/2}}\left(V_{l_{j+1/2}} - V_{l_{j-1/2}}\right) = \text{R.H.S.} \tag{2-136}$$

We do not use this form of the momentum equation directly because it requires major changes to the way that the code passes boundary information between components. Applying the finite-difference mass equation again, we can eliminate $A_{j-1/2}(1-\alpha_{j-1})\rho_{l_{j-1}} V_{l_{j-1/2}}$ to produce

$$\frac{\partial V_{l_{j+1/2}}}{\partial t} + \frac{A_{j+1/2}}{\mathrm{vol}_j} V_{l_{j+1/2}}\left(V_{l_{j+1/2}} - V_{l_{j-1/2}}\right) + \frac{V_{l_{j+1/2}} - V_{l_{j-1/2}}}{(1-\alpha_j)\rho_{l_j}} \frac{\partial\left[\left(1-\alpha_j\right)\rho_{l_j}\right]}{\partial t} = \text{R.H.S.} \tag{2-137}$$

If a TEE junction is present at a 1D cell, we add the following term to the left side of Eq. (2-135):

$$-A_T(1 - \alpha_T)\rho_{l_T} V_T V_T \cos\phi \quad , \tag{2-138}$$

where the subscript T indicates the first cell in the side leg of the TEE or the interface between the j^{th} cell of the primary (through input, this cell is labeled JCELL) and the first cell in the side leg, depending on the type of variable, and ϕ is the angle of incidence of the TEE side leg from the direction of lower-numbered cells in the primary tube. After we convert this modified momentum equation to a form similar to Eq. (2-137), we obtain a correction to the left side of the difference equation for liquid motion in the form

$$-\frac{A_T(1-\alpha_T)\rho_{l_T}}{\mathrm{vol}_j(1-\alpha_j)\rho_{l_j}} V_T\left(V_{j-1/2}+V_T\cos\phi\right) \quad . \tag{2-139}$$

As far as time levels are concerned, we evaluate this term in a linearized implicit manner that is consistent with the rest of the 1D momentum-flux term. In the standard two-step notation, it is

$$-\frac{A_T(1-\alpha_T)\rho_{l_T}}{\mathrm{vol}_j(1-\alpha_j)\rho_{l_j}} \left[\tilde{V}_T^{n+1}\left(2\tilde{V}_T^n\cos\phi+\tilde{V}_{j-1/2}^n\right) + \tilde{V}_T^n\tilde{V}_{j-1/2}^{n+1}-\tilde{V}_T^n\left(\tilde{V}_{j-1/2}^n+\tilde{V}_T^n\cos\phi\right)\right] \quad . \tag{2-140}$$

The vapor equation uses a similar term. Subroutine ETEE generates the quantities necessary for these source terms, and subroutines StbVel1D (FEMOM in TRAC-M/F77) and TF1DS1 add the source terms to the momentum equations.

2.1.7.2.4. VESSEL Component. Using flow-area ratios to correctly donor-cell the approximate momentum flux at a mesh-cell center (based on its interface-defined velocity a half mesh-cell distance away) is done only for momentum that is convected by its own component-direction velocity. This is not done in the cross-derivative terms of the divergence operator for momentum convection as shown in Eqs. (2-104), (2-108), and (2-109).

Flow-area ratios are evaluated using the mesh-cell average flow area, $\mathrm{vol}_{i,j,k}/\Delta_d$, where $d = i$, j, or k defines the component direction of the equation of motion. When the structure volume fraction within a 3D mesh cell is nonuniform in the d direction, the average flow area for the mesh cell can be incorrectly defined by $\mathrm{vol}_{i,j,k}/\Delta_d$. Nonphysical mesh-cell flow areas affect the pressure solution through the Bernoulli equation by not approximating the donor-cell-approximated velocity components at the mesh-cell centers correctly. Locating 3D mesh-cell interfaces on planes of structure volume-fraction discontinuity can minimize this modeling difficulty. A modeling example that is difficult to handle correctly is representing the internal structure curved surface of a pressure vessel that bisects mesh cells in the vessel lower plenum.

A source connection to a 3D VESSEL component by a 1D component uses the $\mathrm{vol}_{i,j,k}$ and Δ_d geometry parameters of the (i,j,k) mesh cell, whose d-direction interface it is connected to, to define the 3D mesh-cell flow area for evaluating the source-connection junction momentum-convection term flow-area ratios. The actual d-direction flow area in the VESSEL component that the 1D component flow is expanding or contracting into may be significantly different from $\mathrm{vol}_{i,j,k}/\Delta_d$. The sides of the mesh-cell volume $\mathrm{vol}_{i,j,k}$ that the source-connection flow expands or contracts into may not be physical-structure surfaces

that limit the flow area as in a 1D component pipe. Again the user needs to be aware of this when defining mesh-cell interface planes and source connections to 3D mesh cells. The effect that the resulting incorrect flow-area ratios has on evaluating a Bernoulli-equation solution needs to be recognized. These area ratios also affect the irreversible flow loss evaluated by TRAC when NFF < 0 at the 1D component source-connection junction.

2.1.8. A Synopsis of TRAC-M/F90 Solution Procedures

Solution procedures will be discussed at three levels. At the highest level, the general solution steps will be outlined for the two numerical methods approximating the flow equations (semi-implicit and SETS). At some point each of these numerical methods requires the solution of a system of nonlinear equations. A summary is provided of the Newton iteration used for both cases. Each iteration of the nonlinear solution and all stabilizer steps of the SETS method produce a sparse system of linear equations. This most basic aspect of the code's solution procedure is also described below.

Below are six subsections. The first subsection describes the overall solution strategy in terms of the computational flow. The next two subsections give the details of the basic solution strategy, as illustrated by a simple 1D problem and extensions to the solution strategy required for 3D flows, respectively. Section 2.1.8.4. describes the special capacitance matrix solution applied to any 3D blocks of a system matrix. The last two subsections describe the treatment of special numerical and physical situations, including water packing, critical flow, CCFL, and offtake of separated phases from horizontal pipes.

Note: **Differences from TRAC-M/F77** . Two TRAC-M/F90 development activities for Version 3.0 significantly improved the data interfaces within the code as compared to TRAC-M/F77. They also laid the groundwork for communication in a parallel execution of the main computational engine of the code. The first activity fully separated the evaluation of terms in the flow equations from the solution of the resulting system of linear equations. This provided a well defined location for equation terms, and eliminated the need for generation of this data for 1D components, before evaluation of the equations in 3D components. The second task dealt directly with the problem of inter-component data communication, requiring only one request at initialization to establish automatic information passing between components. This was implemented as a system service, with sufficient generality to permit later use by higher order and more implicit difference methods. Details on the data structures that were developed to implement the new equation solution procedures and inter-component communication are given in the TRAC-M/F90 Programmer's Manual (Ref. 2-23.).

2.1.8.1. Overall Solution Strategy. Solving the equations should be viewed from two perspectives. In the broadest view, we are solving an approximation to the partial differential equations modeling two-phase flow. In this context, time and spatial location are independent variables, and physical properties (pressure, temperature, etc.) are

dependent variables of the system. Initial and boundary conditions are available, and the solution is integrated forward in time over the spatial domain of the problem. Within this program, the time integration is driven by subroutine TRANS or subroutine STEADY (transient evolution to a steady-state configuration). The size of the next step forward in time is selected by a call to subroutine TIMSTP. Details of the solution within a given step in time are driven through calls to subroutines PREP, HOUT, and POST.

The second perspective on the solution ignores the original partial differential equations. Within a given time step, one or more systems of algebraic equations must be solved to obtain the state of the system at the end of the time step. In this context, time and spatial location are not independent variables. They are just contributions to constants within the algebraic equations. The independent variables for the algebraic equations are end-of-time-step state variables (e.g., velocity, temperature, pressure, and void fraction). This section takes this perspective, dealing with the solution of the algebraic equations defined in Section 2.1.4.

When using the semi-implicit approximation to the flow equations, subroutines PREP, HOUT, and POST cover three simple stages in the solution of the difference equations (Section 2.1.4.1.). First, all quantities dependent only on the state at the beginning of the time step are evaluated (PREP). This includes heat-transfer and friction coefficients and physical properties such as viscosity and conductivity. Next, the algebraic difference equations are solved (HOUT). Finally, end-of-step values are generated (POST) for various other variables needed for edits or to start the next time step.

For the SETS method, the situation is somewhat more complicated. One step involves equations basically identical to those of the semi-implicit method and is accomplished by the same coding driven from HOUT. However, this semi-implicit step is preceded by a solution of motion equations for “stabilizer” velocities. Given the existing flow of the program through system components, this solution was added to the “PREP” stage of the time step. In addition, stabilizer mass and energy equations are solved after the semi-implicit step. Again because of existing flow of the calculation, this solution was placed in the “POST” stage of the calculation. As a result, SETS involves the solution of flow equations at all three stages of a time step.

Each equation solution follows a similar flow within the program. First, a loop is made over all system components to evaluate terms in the equation and store these terms in a system-wide database. Next, the full system of equations is solved. Finally, another loop over all components copies the values of the independent variables from the system-wide database into the component data structure and, when necessary, evaluates dependent variables.

2.1.8.2. Basic Solution Strategy. Almost all aspects of the equation solution procedure can be illustrated using the 1D single-phase-flow model introduced in Section 2.1.4. For added clarity, examples will be presented based on some specific flow-path configurations. The solution of equations in the pure semi-implicit method is identical to the solution of the semi-implicit (or “basic”) step in SETS. As a result, no

specific discussion is provided for solution when the semi-implicit method is selected (namelist variable NOSETS=1).

To illustrate the 1D portion of the solution, we will describe a specific example for flow in a closed loop (Fig. 2-2.). Cells and cell faces in Fig. 2-2. have been given absolute numbers to facilitate discussion of full system-equation coupling. In terms of component numbering, cells 1–4 in this figure can be considered cells 1–4 of PIPE 1, and cells 5–8 in the figure would be cells 1–4 of PIPE 2.

2.1.8.2.1. Solution of the 1D Stabilizer Motion Equations. The stabilizer motion equations are purely linear in the unknown stabilizer velocities. If the tilde and superscript are dropped for simplicity, the general form for this linear system for the flow loop in Fig. 2-2. is

$$\begin{pmatrix} a_{1,1} & a_{1,2} & 0 & 0 & 0 & 0 & 0 & a_{1,8} \\ a_{2,1} & a_{2,2} & a_{2,3} & 0 & 0 & 0 & 0 & 0 \\ 0 & a_{3,2} & a_{3,3} & a_{3,4} & 0 & 0 & 0 & 0 \\ 0 & 0 & a_{4,3} & a_{4,4} & a_{4,5} & 0 & 0 & 0 \\ 0 & 0 & 0 & a_{5,4} & a_{5,5} & a_{5,6} & 0 & 0 \\ 0 & 0 & 0 & 0 & a_{6,5} & a_{6,6} & a_{6,7} & 0 \\ 0 & 0 & 0 & 0 & 0 & a_{7,6} & a_{7,7} & a_{7,8} \\ a_{8,1} & 0 & 0 & 0 & 0 & 0 & a_{8,7} & a_{8,8} \end{pmatrix} \begin{pmatrix} V_1 \\ V_2 \\ V_3 \\ V_4 \\ V_5 \\ V_6 \\ V_7 \\ V_8 \end{pmatrix} = \begin{pmatrix} b_1 \\ b_2 \\ b_3 \\ b_4 \\ b_5 \\ b_6 \\ b_7 \\ b_8 \end{pmatrix}. \tag{2-141}$$

One standard linear algebra trick to solve this problem is to break it into blocks that can be more easily solved. One obvious approach would be to isolate the last row and column of the matrix as follows:

$$\left(\begin{array}{ccccccc|c} a_{1,1} & a_{1,2} & 0 & 0 & 0 & 0 & 0 & a_{1,8} \\ a_{2,1} & a_{2,2} & a_{2,3} & 0 & 0 & 0 & 0 & 0 \\ 0 & a_{3,2} & a_{3,3} & a_{3,4} & 0 & 0 & 0 & 0 \\ 0 & 0 & a_{4,3} & a_{4,4} & a_{4,5} & 0 & 0 & 0 \\ 0 & 0 & 0 & a_{5,4} & a_{5,5} & a_{5,6} & 0 & 0 \\ 0 & 0 & 0 & 0 & a_{6,5} & a_{6,6} & a_{6,7} & 0 \\ 0 & 0 & 0 & 0 & 0 & a_{7,6} & a_{7,7} & a_{7,8} \\ \hline a_{8,1} & 0 & 0 & 0 & 0 & 0 & a_{8,7} & a_{8,8} \end{array}\right) \begin{pmatrix} V_1 \\ V_2 \\ V_3 \\ V_4 \\ V_5 \\ V_6 \\ V_7 \\ V_8 \end{pmatrix} = \begin{pmatrix} b_1 \\ b_2 \\ b_3 \\ b_4 \\ b_5 \\ b_6 \\ b_7 \\ b_8 \end{pmatrix}. \tag{2-142}$$

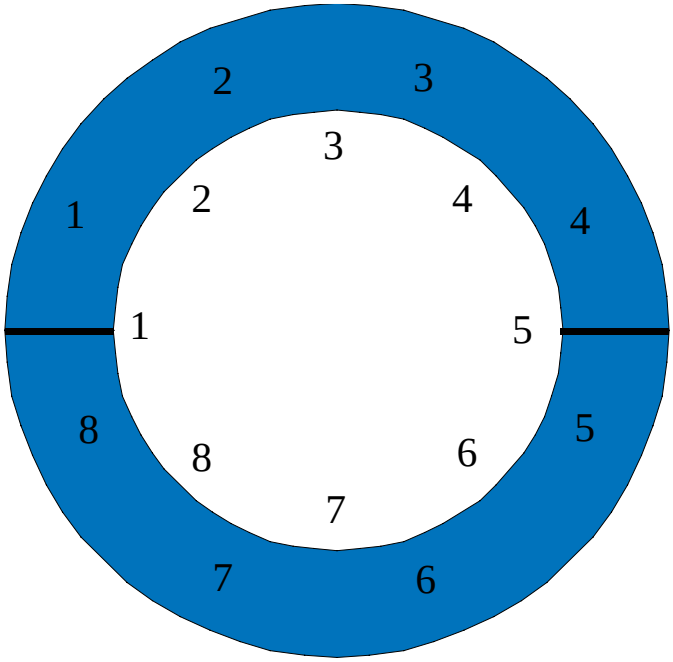

Fig. 2-2. Flow loop for an example of 1D solution.

This can then be written more clearly as the following problem:

$$\begin{pmatrix} a_{1,1} & a_{1,2} & 0 & 0 & 0 & 0 & 0 \\ a_{2,1} & a_{2,2} & a_{2,3} & 0 & 0 & 0 & 0 \\ 0 & a_{3,2} & a_{3,3} & a_{3,4} & 0 & 0 & 0 \\ 0 & 0 & a_{4,3} & a_{4,4} & a_{4,5} & 0 & 0 \\ 0 & 0 & 0 & a_{5,4} & a_{5,5} & a_{5,6} & 0 \\ 0 & 0 & 0 & 0 & a_{6,5} & a_{6,6} & a_{6,7} \\ 0 & 0 & 0 & 0 & 0 & a_{7,6} & a_{7,7} \end{pmatrix} \begin{pmatrix} V_1 \\ V_2 \\ V_3 \\ V_4 \\ V_5 \\ V_6 \\ V_7 \end{pmatrix} = \begin{pmatrix} b_1 \\ b_2 \\ b_3 \\ b_4 \\ b_5 \\ b_6 \\ b_7 \end{pmatrix} - \begin{pmatrix} a_{1,8} \\ 0 \\ 0 \\ 0 \\ 0 \\ 0 \\ a_{7,8} \end{pmatrix} V_8 \qquad (2\text{-}143)$$

and

$$a_{8,1}V_1 + a_{8,7}V_7 + a_{8,8}V_8 = b_8 \ . \qquad (2\text{-}144)$$

Equation (2-143) is solved to obtain velocities V_1 through V_7 as linear functions of V_8. The existence of two constant vectors on the right-hand side of the equation means that two solutions of a 7×7 system are required. However, use of an L-U (lower-upper) decomposition method substantially reduces the cost of the second solution. Once these solutions are available, the specific linear expressions for V_1 and V_7 as functions of V_8 are

substituted into Eq. (2-144) and a value of V_8 is obtained. Back-substitution of this value into the equations for the other velocities completes the solution.

The current version of TRAC-M is not quite as selective as the previous example in isolating submatrices for solution. When the basic matrix structure is established, all rows are scanned for the presence of those coefficients not on the main (tridiagonal) band. These rows are designated as "network equations" and variables with the same index as "network variables."

$$\left(\begin{array}{c|cccccc|c} a_{1,1} & a_{1,2} & 0 & 0 & 0 & 0 & 0 & a_{1,8} \\ \hline a_{2,1} & a_{2,2} & a_{2,3} & 0 & 0 & 0 & 0 & 0 \\ 0 & a_{3,2} & a_{3,3} & a_{3,4} & 0 & 0 & 0 & 0 \\ 0 & 0 & a_{4,3} & a_{4,4} & a_{4,5} & 0 & 0 & 0 \\ 0 & 0 & 0 & a_{5,4} & a_{5,5} & a_{5,6} & 0 & 0 \\ 0 & 0 & 0 & 0 & a_{6,5} & a_{6,6} & a_{6,7} & 0 \\ 0 & 0 & 0 & 0 & 0 & a_{7,6} & a_{7,7} & a_{7,8} \\ \hline a_{8,1} & 0 & 0 & 0 & 0 & 0 & a_{8,7} & a_{8,8} \end{array}\right)\left(\begin{array}{c} V_1 \\ V_2 \\ V_3 \\ V_4 \\ V_5 \\ V_6 \\ V_7 \\ V_8 \end{array}\right) = \left(\begin{array}{c} b_1 \\ b_2 \\ b_3 \\ b_4 \\ b_5 \\ b_6 \\ b_7 \\ b_8 \end{array}\right). \qquad (2\text{-}145)$$

Solving Eq. (2-145) is analogous to the steps outlined for Eq. (2-143). In this instance, the central tridiagonal matrix block is reduced to provide velocities V_2 through V_7 as linear functions of V_1 and V_8 (e.g., $V_j = V_{0,j} + c_{j,1}\,V_1 + c_{j,8}\,V_{8,j} = 2,7$). The resulting equations are substituted into the two isolated rows of Eq. (2-145) to obtain the following pair of network equations involving only V_1 and V_8:

$$(a_{1,1} + a_{1,2}c_{2,1})V_1 + (a_{1,2}c_{2,8} + a_{1,8})V_8 = b_1 - a_{1,2}V_{0,2} \text{ and} \qquad (2\text{-}146)$$

$$(a_{8,1} + a_{8,7}c_{7,1})V_1 + (a_{8,7}c_{7,8} + a_{8,8})V_8 = b_8 - a_{8,7}V_{0,7}\,. \qquad (2\text{-}147)$$

This closed system is solved for V_1 and V_8. Back-substitution of these values into the equations for V_2 through V_7 completes the solution of the system.

2.1.8.2.2. Solving the SETS Semi-Implicit Step. After the stabilizer motion equations are solved, the version of SETS implemented in TRAC-M proceeds to solve the semi-implicit (or "basic") equations for motion, mass, and energy. Apart from the use of stabilizer velocities in the momentum-transport term (and the special flux operator for two-phase flow), these equations are equivalent to the standard semi-implicit method used before TRAC-PF1 was developed. (Currently, the 3D VESSEL can be run in semi-implicit mode according to user option. Future versions of TRAC-M will allow both 1D and 3D components to be run in semi-implicit mode, according to user option.) Thus, solving the pure semi-implicit method and solving the semi-implicit step in SETS are identical.

The system solution begins by treating the new-time velocity as a dependent variable, reducing the motion equation at each cell edge to obtain the new-time velocity as a linear function of the pressure difference across that edge. In our single-phase example, Eq. (2-67) is rearranged to the form

$$V_{j+1/2}^{n+1} = \frac{V_{j+1/2}^{n} - \Delta t\left(V_{j+1/2}^{n}\nabla_{j+1/2}\tilde{V}_{j+1/2}^{n+1} - \beta V_{j+1/2}^{n}\nabla_{j+1/2}\tilde{V}_{j+1/2}^{n} + \dfrac{\tilde{P}_{j+1}^{n+1} - \tilde{P}_{j}^{n+1}}{\langle\rho\rangle_{j+1/2}^{n}\Delta x}\right)}{1 + \Delta t(2K_{j+1/2}^{n}\left|V_{j+1/2}^{n}\right| + \beta\nabla_{j+1/2}\tilde{V}_{j+1/2}^{n})} . \tag{2-148}$$

For the two-phase equations, the equivalent step requires simultaneous solution of the liquid and gas momentum equations at each face (2×2 linear system). This solution is accomplished in subroutine TF1DS1 for the 1D and in TF3DS1 for the 3D flow equations. At the same time, the following key variable is defined and stored for later use in updating velocities as

$$\left.\frac{dV}{dP}\right|_{j+1/2} = \frac{\Delta t}{\langle\rho\rangle_{j+1/2}^{n}\Delta x[1 + \Delta t(2K_{j+1/2}^{n}\left|V_{j+1/2}^{n}\right| + \beta\nabla_{j+1/2}\tilde{V}_{j+1/2}^{n})]} . \tag{2-149}$$

The mass and energy equations are nonlinear in the independent variables and must be solved with an iterative technique. Here a standard Newton iteration is applied. If the i^{th} approximation to the solution is given, the next level of approximation is written as

$$\tilde{T}_{j}^{n+1,i+1} = \tilde{T}_{j}^{n+1,i} + \delta T_{j} \text{ and}$$

$$\tilde{P}_{j}^{n+1,i+1} = \tilde{P}_{j}^{n+1,i} + \delta P_{j} . \tag{2-150}$$

The pressure definition can be substituted into Eq. (2-148) and simplified with the definition in Eq. (2-149) to give the following expression for the latest approximation to velocity as a linear function of the latest pressure changes:

$$V_{j+1/2}^{n+1,i+1} = V_{j+1/2}^{n+1,i} + \left.\frac{dV}{dP}\right|_{j+1/2}(\delta P_{j} - \delta P_{j+1}) . \tag{2-151}$$

These expressions are applied to the semi-implicit mass and energy equations [Eqs. (2-57) and (2-58)] through the direct substitutions

$$\tilde{P}_{j}^{n+1} \Rightarrow \tilde{P}^{n+1,i} + \delta P_{j} ,$$

$$\tilde{T}_{j}^{n+1} \Rightarrow \tilde{T}_{j}^{n+1,i} + \delta T_{j} , \text{ and}$$

$$V_{j+1/2}^{n+1} \Rightarrow V_{j+1/2}^{n+1,i} + \left.\frac{dV}{dP}\right|_{j+1/2} (\delta P_j - \delta P_{j+1}) \ .$$

Use of the state relationships $[\rho(P,T)]$ and $[e(P,T)]$ and a first-order Taylor series expansion produces the linearized mass equation

$$\left(\left.\frac{\partial\rho}{\partial T}\right|_j^{n+1,i} \delta T_j + \left.\frac{\partial\rho}{\partial P}\right|_j^{n+1,i} \delta P_j\right)/(\Delta t)$$

$$+ \frac{\left[\langle\rho\rangle_{j+\frac{1}{2}}^{n} \left.\frac{dV}{dP}\right|_{j+1/2} (\delta P_j - \delta P_{j+1}) - \langle\rho\rangle_{j-1/2}^{n} \left.\frac{dV}{dP}\right|_{j-1/2} (\delta P_{j-1} - \delta P_j)\right]}{\Delta x} \qquad (2\text{-}152)$$

$$= -\frac{\tilde{\rho}_j^{n+1,i} - \rho_j^n}{\Delta t} - \frac{\partial}{\partial x_j}(\rho^n V^{n+1,i})$$

and the linearized energy equation

$$\left(\left.\frac{\partial\rho}{\partial T}\right|_j^{n+1,i} \tilde{e}_j^{n+1,i} + \tilde{\rho}_j^{n+1,i} \left.\frac{\partial e}{\partial T}\right|_j^{n+1,i}\right)\delta T_j/\Delta t$$

$$+ \left(\left.\frac{\partial\rho}{\partial P}\right|_j^{n+1,i} \tilde{e}_j^{n+1,i} + \tilde{\rho}_j^{n+1,i} \left.\frac{\partial e}{\partial P}\right|_j^{n+1,i}\right)\delta P_j/\Delta t$$

$$+ \frac{\left[\langle\rho e\rangle_{j+1/2}^{n} \left.\frac{dV}{dP}\right|_{j+1/2} (\delta P_j - \delta P_{j+1}) - \langle\rho e\rangle_{j-1/2}^{n} \left.\frac{dV}{dP}\right|_{j-1/2} (\delta P_{j-1} - \delta P_j)\right]}{\Delta x}$$

$$+ \tilde{P}_j^{n+1,i} \frac{\left[\left.\frac{dV}{dP}\right|_{j+1/2} (\delta P_j - \delta P_{j+1}) - \left.\frac{dV}{dP}\right|_{j-1/2} (\delta P_{j-1} - \delta P_j)\right]}{\Delta x} + \delta\tilde{P}_j \frac{V_{j+1/2}^{n+1,i} - V_{j-1/2}^{n+1,i}}{\Delta x}$$

$$= -\frac{(\tilde{\rho}_j^{n+1,i}\tilde{e}_j^{n+1,i} - (\rho e)_j^n)}{\Delta t} - \frac{\partial}{\partial x^j}(\rho^n e^n V^{n+1,i}) - \tilde{P}_j^{n+1,i} \frac{V_{j+1/2}^{n+1,i} - V_{j-1/2}^{n+1,i}}{\Delta x} \ . \qquad (2\text{-}153)$$

For the particular block-reduction technique used to solve this system of linear equations, an auxiliary variable is defined as

$$\Delta P_{j+1/2} = \delta P_{j+1} - \delta P_j \ . \qquad (2\text{-}154)$$

This results in a set of linear equations for each cell in the form

$$\begin{pmatrix} a_{j,1,1} & a_{j,1,2} \\ a_{j,2,1} & a_{j,2,2} \end{pmatrix} \begin{pmatrix} \delta P_j \\ \delta T_j \end{pmatrix} = \begin{pmatrix} b_{j,1} \\ b_{j,2} \end{pmatrix} - \begin{pmatrix} c_{1j,1} \\ c_{1j,2} \end{pmatrix} \Delta P_{j-1/2} + \begin{pmatrix} c_{rj,1} \\ c_{rj,2} \end{pmatrix} \Delta P_{j+1/2} \,. \tag{2-155}$$

The first row in the above linear system can be considered to be the linearized mass conservation equation and the second to be the linearized energy equation. At each cell, this system is solved for the pressure and temperature variations in the form

$$\begin{pmatrix} \delta P_j \\ \delta T_i \end{pmatrix} = \begin{pmatrix} b'_{j,1} \\ b'_{j,2} \end{pmatrix} - \begin{pmatrix} c'_{1j,1} \\ c'_{1j,2} \end{pmatrix} \Delta P_{j-1/2} + \begin{pmatrix} c'_{rj,1} \\ c''_{rj,2} \end{pmatrix} \Delta P_{j+1/2} \,. \tag{2-156}$$

At this point, the *b*' constants represent the linearized predictions of change in pressure and temperature assuming no further velocity changes at the cell faces. The *c*' coefficients account for contributions due to velocity changes (driven by changes in the pressure gradient).

The solution of the basic equations is completed in two steps. First, for each block represented by Eq. (2-156), the pressure equation is isolated and Eq. (2-154) is substituted to provide a set of 10 equations in the form

$$-c_{1j,1}\delta P_{j-1} + (1 + c_{1j,1} + c_{rj,1})\delta P_j - c_{rj,1}\delta P_{j+1} = b_j \,. \tag{2-157}$$

This results in a system with the same form as the stabilizer velocity equations,

$$\left(\begin{array}{c|cccccc|c} a_{1,1} & a_{1,2} & 0 & 0 & 0 & 0 & 0 & a_{1,8} \\ \hline a_{2,1} & a_{2,2} & a_{2,3} & 0 & 0 & 0 & 0 & 0 \\ 0 & a_{3,2} & a_{3,3} & a_{3,4} & 0 & 0 & 0 & 0 \\ 0 & 0 & a_{4,3} & a_{4,4} & a_{4,5} & 0 & 0 & 0 \\ 0 & 0 & 0 & a_{5,4} & a_{5,5} & a_{5,6} & 0 & 0 \\ 0 & 0 & 0 & 0 & a_{6,5} & a_{6,6} & a_{6,7} & 0 \\ 0 & 0 & 0 & 0 & 0 & a_{7,6} & a_{7,7} & a_{7,8} \\ \hline a_{8,1} & 0 & 0 & 0 & 0 & 0 & a_{8,7} & a_{8,8} \end{array}\right) \left(\begin{array}{c} \delta P_1 \\ \delta P_2 \\ \delta P_3 \\ \delta P_4 \\ \delta P_5 \\ \delta P_6 \\ \delta P_7 \\ \delta P_8 \end{array}\right) = \left(\begin{array}{c} b_1 \\ b_2 \\ b_3 \\ b_4 \\ b_5 \\ b_6 \\ b_7 \\ b_8 \end{array}\right), \tag{2-158}$$

which is solved with the same procedure outlined for Eq. (2-145). The resulting values of δPs are first substituted into Eq. (2-154) to obtain a set of ΔP values, which are then substituted into the second row of Eq. (2-156) to provide values for temperature changes. The variations in pressure and temperature are substituted into Eq. (2-150) to provide an improved approximation to the new-time variables. The ΔP values are also fed to Eq. (2-151) to obtain new-time velocities, which are consistent with the updated pressure field. If variations in pressure and temperature are small enough, the iteration is

terminated. If not, the linearized equations are evaluated again to generate the next approximate solution.

The iteration usually is started by setting the initial guess at the solution to the beginning of time-step values (e.g., $P_j^{n+1,0} = P_j^n$). The only exceptions occur in the full two-phase equations. When the old-time void fraction is zero but a prediction-based flux and phase change indicates appearance of gas, an explicit evaluation of the gas mass equation is used to provide an initial estimate of the new-time void fraction. When the first appearance of noncondensable gas is predicted, information from an explicit noncondensable mass equation is added to provide an estimate of the new-time partial pressure of noncondensable gas.

Use of old-time quantities to start the iteration provides an easy cure to situations in which the initial guess is beyond the convergence radius of the method. The new-time values must approach the old-time values as the time-step size approaches zero. If an iteration fails to converge, the time-step size is reduced and the solution is retried at the new-time-step size. Preemptive action is also taken to minimize convergence problems. If more than five iterations are required to converge the solution on a given time step, the size of the next step is reduced by the ratio of five divided by the last iteration count.

2.1.8.2.3. Solution of the SETS Stabilizer Mass and Energy Equations. The final step in the SETS method is the solution of the stabilizer mass and energy equations. At this point, the new-time velocities have been determined and can be treated as constants in the solution of the equations. The equations vary from the mass and energy equations of the semi-implicit step only in that the densities and energies in flux terms are now evaluated at the new time.

The mass and energy equations are linear in ρ^{n+1} and $(\rho e)^{n+1}$ respectively, with a structure that is basically tridiagonal. For the loop flow problem, the general form of the mass equation can be written as

$$\begin{pmatrix} a_{1,1} & a_{1,2} & 0 & 0 & 0 & 0 & 0 & a_{1,8} \\ a_{2,1} & a_{2,2} & a_{2,3} & 0 & 0 & 0 & 0 & 0 \\ 0 & a_{3,2} & a_{3,3} & a_{3,4} & 0 & 0 & 0 & 0 \\ 0 & 0 & a_{4,3} & a_{4,4} & a_{4,5} & 0 & 0 & 0 \\ 0 & 0 & 0 & a_{5,4} & a_{5,5} & a_{5,6} & 0 & 0 \\ 0 & 0 & 0 & 0 & a_{6,5} & a_{6,6} & a_{6,7} & 0 \\ 0 & 0 & 0 & 0 & 0 & a_{7,6} & a_{7,7} & a_{7,8} \\ a_{8,1} & 0 & 0 & 0 & 0 & 0 & a_{8,7} & a_{8,8} \end{pmatrix} \begin{pmatrix} \rho_1 \\ \rho_2 \\ \rho_3 \\ \rho_4 \\ \rho_5 \\ \rho_6 \\ \rho_7 \\ \rho_8 \end{pmatrix} = \begin{pmatrix} b_1 \\ b_2 \\ b_3 \\ b_4 \\ b_5 \\ b_6 \\ b_7 \\ b_8 \end{pmatrix}, \tag{2-159}$$

where superscripts representing new time (n+1) have been dropped. This can be recognized as identical in form to Eq. (2-145) and is solved with the same procedure.

The linear system produced by the stabilizer energy equation has the same coefficient matrix as that of the mass equation. Time is saved by storing matrix factorization steps used in the mass equation solution and by applying the results during the solution of the energy equation.

2.1.8.2.4. Final Solution for a New-Time Void Fraction. Solving the stabilizer mass and energy equations provides new-time values only for macroscopic densities $[\alpha\rho_g, \alpha\rho_a, (1-\alpha)\rho_l]$ and macroscopic energy densities $[\alpha\rho_g e_g, (1-\alpha)\rho_l e_l]$. Experience with the method has shown that when end-of-time-step values are needed in correlations for variables such as temperature or pressure, the values obtained during the solution of the semi-implicit step are adequate. However, the method is more robust if an attempt is made to obtain a better value of the new-time void fraction.

After the stabilizer solution is completed, an approximate solution is obtained in each computational volume to the following equations:

$$\begin{aligned}
&\alpha_j^{n+1}\rho_{g,j}^{n+1} = (\alpha\rho_g)_j^{n+1}, \\
&\alpha_j^{n+1}\rho_{a,j}^{n+1} = (\alpha\rho_a)_j^{n+1}, \\
&(1-\alpha_j^{n+1})\rho_{l,j}^{n+1} = [(1-\alpha)\rho_l]_j^{n+1}, \\
&\alpha_j^{n+1}\rho_{g,j}^{n+1} e_{g,j}^{n+1} = (\alpha\rho_g e_g)_j^{n+1}, \text{ and} \\
&(1-\alpha_j^{n+1})\rho_{l,j}^{n+1} e_{l,j}^{n+1} = [(1-\alpha)\rho_l e_l]_j^{n+1}.
\end{aligned} \tag{2-160}$$

where the right-hand sides are the known results from the stabilizer equations. These equations are linearized with respect to the independent variables P^{n+1}, $T_g^{n+1}, T_l^{n+1}, P_a^{n+1}$, and α^{n+1}. The starting point of the linearization is taken to be the values of the corresponding variables obtained after the last iteration of the solution to the semi-implicit step. Thus, the values of the independent variables become

$$\begin{aligned}
T_{g,j}^{n+1} &= \tilde{T}_{g,j}^{n+1} + \delta T_{g,j}, \\
T_{l,j}^{n+1} &= \tilde{T}_{l,j}^{n+1} + \delta T_{l,j}, \\
P_j^{n+1} &= \tilde{P}_j^{n+1} + \delta P_j, \\
{}_{a,j}^{n+1} &= \tilde{P}_{a,j}^{n+1} + \delta P_{a,j}, \text{ and} \\
\alpha_j^{n+1} &= \tilde{\alpha}_j^{n+1} + \delta\alpha_j.
\end{aligned} \tag{2-161}$$

These are substituted into Eq. (2-160), and a first-order Taylor expansion is applied. As an example of the results, the linearized macroscopic gas energy density is

$$\left(\tilde{\alpha}_j^{n+1}\left.\frac{\partial\tilde{\rho}_g}{\partial T}\right|_j^{n+1}\tilde{e}_{g,j}^{n+1}+\tilde{\alpha}_j^{n+1}\tilde{\rho}_{g,j}^{n+1}\left.\frac{\partial\tilde{e}_g}{\partial T}\right|_j^{n+1}\right)\delta T_j$$

$$+\left(\alpha_j^{n+1}\left.\frac{\partial\tilde{\rho}_g}{\partial P}\right|_j^{n+1}\tilde{e}_{g,j}^{n+1}+\tilde{\alpha}_j^{n+1}\tilde{\rho}_{g,j}^{n+1}\left.\frac{\partial\tilde{e}_g}{\partial P}\right|_j^{n+1}\right)\delta P_j$$

$$+\tilde{\rho}_{g,j}^{n+1}\tilde{e}_{g,j}^{n+1}\delta\alpha_j$$

$$=(\alpha\rho_g e_g)_j^{n+1}-\tilde{\alpha}_j^{n+1}\tilde{\rho}_{g,j}^{n+1}\tilde{e}_{g,j}^{n+1}\ . \qquad (2\text{-}162)$$

This equation, combined with the other four linearized equations, produces a 5×5 linear system that is solved by direct Gauss elimination. Although linearized approximations to all new-time variables are available after this solution, only the void fraction is kept for use in the next time step. The other variables are discarded as a result of numerical experiments comparing various approaches. The consistent pressure field resulting from the solution of the semi-implicit step provides the best initial guess for velocities at the next time step. The tendency of temperatures in two-phase problems to follow the saturation temperature makes selection of temperatures consistent with that pressure field a good strategy for the most robust code behavior.

2.1.8.3. Considerations for 3D Solutions. When VESSELS are present, the above procedure is followed, with one key exception in each set of equations. When any VESSEL variable (velocity, δP, ρ, or ρe) occurs in a 1D equation, it is moved to the right-hand side with its coefficient and all 1D variables are solved as functions of the unknown VESSEL variables. These results are substituted as needed into the difference equations for the VESSEL to give a closed set of equations that can be solved for all vessel variables. Values for VESSEL variables are back-substituted into the 1D equations, and final values for all 1D unknowns are obtained.

Specific examples of this process are provided here for the system illustrated in Fig. 2-3. As in Fig. 2-2., cells are given “absolute” numbers rather than a combination of component number and component cell number. For this example, cells numbered 1–5 are in a pipe and cells 6–9 are in a 3D (collapsed to 2D here) VESSEL.

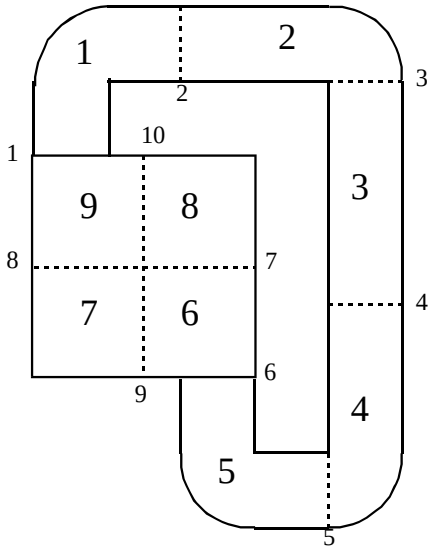

Fig. 2-3. System for 3D solution examples.

The full system of stabilizer momentum equations for the flow loop in Fig. 2-3. is represented by Eq. (2-163). The last block in the coefficient matrix is associated with the radial velocities V_9 and V_{10} and is completely isolated from equations for the axial velocities in the same "3D" region. This reflects the fundamental structure of the 3D stabilizer momentum equations. For example, the axial stabilizer momentum equations evaluate contributions from axial velocities only implicitly. Radial and azimuthal velocities appearing in momentum-transport terms are evaluated explicitly. This results in no coupling coefficients between velocity variables in the axial momentum block and those in the radial (or azimuthal) blocks. In matrix notation, we have

$$\left(\begin{array}{cccccccccc}
a_{1,1} & a_{1,2} & 0 & 0 & 0 & 0 & 0 & a_{1,8} & 0 & 0 \\
a_{2,1} & a_{2,2} & a_{2,3} & 0 & 0 & 0 & 0 & 0 & 0 & 0 \\
0 & a_{3,2} & a_{3,3} & a_{3,4} & 0 & 0 & 0 & 0 & 0 & 0 \\
0 & 0 & a_{4,3} & a_{4,4} & a_{4,5} & 0 & 0 & 0 & 0 & 0 \\
0 & 0 & 0 & a_{5,4} & a_{5,5} & a_{5,6} & 0 & 0 & 0 & 0 \\
0 & 0 & 0 & 0 & a_{6,5} & a_{6,6} & a_{6,7} & 0 & 0 & 0 \\
0 & 0 & 0 & 0 & 0 & a_{7,6} & a_{7,7} & a_{7,8} & 0 & 0 \\
a_{8,1} & 0 & 0 & 0 & 0 & 0 & a_{8,7} & a_{8,8} & 0 & 0 \\
0 & 0 & 0 & 0 & 0 & 0 & 0 & 0 & a_{9,9} & a_{9,10} \\
0 & 0 & 0 & 0 & 0 & 0 & 0 & 0 & a_{10,9} & a_{10,10}
\end{array}\right)\left(\begin{array}{c} V_1 \\ V_2 \\ V_3 \\ V_4 \\ V_5 \\ V_6 \\ V_7 \\ V_8 \\ V_9 \\ V_{10} \end{array}\right) = \left(\begin{array}{c} b_1 \\ b_2 \\ b_3 \\ b_4 \\ b_5 \\ b_6 \\ b_7 \\ b_8 \\ b_9 \\ b_{10} \end{array}\right). \qquad (2\text{-}163)$$

Solving the 1D portion of this system proceeds as before, isolating the 1D block as

$$\begin{bmatrix} a_{2,2} & a_{2,3} & 0 & 0 \\ a_{3,2} & a_{3,3} & a_{3,4} & 0 \\ 0 & a_{4,3} & a_{4,4} & a_{4,5} \\ 0 & 0 & a_{5,4} & a_{5,5} \end{bmatrix} \begin{bmatrix} V_2 \\ V_3 \\ V_4 \\ V_5 \end{bmatrix} = \begin{bmatrix} b_2 \\ b_3 \\ b_4 \\ b_5 \end{bmatrix} - \begin{bmatrix} a_{2,1} \\ 0 \\ 0 \\ 0 \end{bmatrix} V_1 - \begin{bmatrix} 0 \\ 0 \\ 0 \\ a_{5,6} \end{bmatrix} V_6 \ . \tag{2-164}$$

This is solved to obtain the equation

$$\begin{bmatrix} V_2 \\ V_3 \\ V_4 \\ V_5 \end{bmatrix} = \begin{bmatrix} b'_2 \\ b'_3 \\ b'_4 \\ b'_5 \end{bmatrix} + \begin{bmatrix} c'_{2,1} \\ c'_{3,1} \\ c'_{4,1} \\ c'_{5,1} \end{bmatrix} V_1 + \begin{bmatrix} c'_{2,6} \\ c'_{3,6} \\ c'_{4,6} \\ c'_{5,6} \end{bmatrix} V_6 \ , \tag{2-165}$$

and these results are substituted into the junction equations to obtain

$$(a_{1,1} + a_{1,2}c'_{2,1})V_1 + a_{1,2}c'_{2,6}V_6 = b_1 - a_{1,2}b'_2 - a_{1,8}V_8 \text{ and} \tag{2-166}$$

$$a_{6,5}c'_{5,1}V_1 + (a_{6,6} + a_{6,5}c'_{5,6})V_6 = b_6 - a_{6,5}b'_5 - a_{6,7}V_7 \ . \tag{2-167}$$

Solving the previous two equations gives junction velocities as a linear combination of "3D" velocities as

$$\begin{bmatrix} V_1 \\ V_6 \end{bmatrix} = \begin{bmatrix} b'_1 \\ b'_6 \end{bmatrix} + \begin{bmatrix} c'_{1,7} \\ c'_{6,7} \end{bmatrix} V_7 + \begin{bmatrix} c'_{1,8} \\ c'_{6,8} \end{bmatrix} V_8 \ . \tag{2-168}$$

These two expressions are substituted into the 3D axial flow equations to obtain a final closed set of equations for the 3D axial velocities (V_7 and V_8). The current method used to solve this final equation block is described in the next subsection. Once the 3D velocities are known, the 1D network junction velocities (V_1 and V_6) follow by back-substitution of vessel velocities V_7 and V_8 into Eq. (2-168), and the internal component velocities are obtained in a final stage of the back-substitution of V_1 and V_6 into Eq. (2-165).

A similar solution pattern follows for the pressure equation of the semi-implicit (basic) step and for the stabilizer mass and energy equations.

2.1.8.4. The Capacitance Matrix Method. The capacitance matrix method is applied in TRAC to provide an efficient numerical solution algorithm for solving the multidimensional vessel-matrix equations. Each vessel-matrix equation combines the

multidimensional mesh-cell or interface equations of all vessel components in the modeled system. The external or internal connectivity to the VESSEL component(s) of 1D hydro-component loops introduces nonzero elements into the vessel matrix, coupling the vessel mesh cells or interfaces at the loop source connections to the vessel(s). The vessel-matrix equations that are solved are the semi-implicit pressure vessel-matrix equation in the outer-stage solution and, if the stability-enhanced, two-step, 3D (SETS3D) method is applied in the VESSEL components (NSTAB = 1), the stabilizer motion x- or r-, y- or θ-, and z-direction vessel-matrix equations in the prep-stage solution and the stabilizer mass and energy vessel-matrix equations in the post-stage solution.

TRAC-PF1/MOD1 provided the user with a choice of solving the pressure vessel-matrix equation with a successive line over-relaxation (SLOR) iterative solution algorithm or a direct full-matrix L-U matrix-decomposition solution algorithm. The latter algorithm is more efficient for small vessel matrices of order <50 (<50 vessel mesh cells). For system models with a vessel or vessels having more mesh cells, SLOR is more efficient, but can result in mass and energy conservation error unless the iterative solution algorithm is tightly converged by performing more iterations, which requires more calculative effort.

TRAC-M applies the SETS3D method to the vessel hydrodynamic solution. TRAC-M cannot use the SLOR iterative solution algorithm to solve the stabilizer mass and energy vessel-matrix equations because these equations may lack matrix diagonal dominance (the magnitude of the sum of the off-diagonal elements in any row or column is equal to or greater than the magnitude of the diagonal element). The SLOR iterative solution algorithm requires that the matrix equation satisfy the matrix property of diagonal dominance for the solution algorithm to be numerically stable. The direct full-matrix L-U matrix-decomposition solution algorithm could be used to solve the stabilizer mass and energy equations but would require an excessive amount of calculative effort and computer memory for vessel matrices of order greater than a few hundred. The resolution to this dilemma was to replace both of these algorithms in TRAC-PF1/MOD2 with the capacitance matrix method (Ref. 2-14.), which provides an accurate and numerically stable direct L-U matrix-decomposition solution algorithm while being as efficient as the SLOR iterative solution algorithm for vessel matrices of large order. This method was brought over to TRAC-M. Because the capacitance matrix method is the best choice among all three methods, it is used to solve all forms of the vessel-matrix equations.

The capacitance matrix method is a direct L-U matrix-decomposition solution algorithm like the direct full-matrix L-U matrix-decomposition solution algorithm in TRAC-PF1/MOD1, but it does the L-U matrix decomposition on the banded portion of the vessel matrix with a more efficient banded-matrix solver routine. The banded portion of the vessel matrix includes the nonzero coupling elements between a vessel mesh cell or interface and its six adjacent (neighboring) mesh cells or interfaces in 3D geometry. Nonzero elements outside the bandwidth of the matrix that couple vessel mesh cells or interfaces to nonadjacent mesh cells or interfaces of the same vessel or a different vessel component (due to 1D hydro-component loop connectivity) will be referred to as

nonzero outlying elements. The effect that the nonzero outlying elements have on the matrix-equation solution is accounted for in the capacitance matrix method by a direct full-matrix L-U matrix decomposition of a lower-order capacitance matrix. That solution is used to modify the banded-matrix equation solution to give the desired solution of the vessel matrix with its nonzero outlying elements. The capacitance matrix method was found in a study to be more efficient than a direct full-matrix L-U matrix-decomposition solution of a vessel-matrix equation when fewer than 20% of the vessel-matrix rows have nonzero outlying elements. The test problem in that study had two VESSEL components coupled by PIPE, PUMP, and TEE components. Fig. 2-4. shows the matrix-equation solution CPU times on a Cray X-MP/48 computer versus the matrix order for different numbers of rows having nonzero outlying elements. For most system models (especially those with more than a hundred vessel mesh cells), only a few percent of the vessel-matrix rows have nonzero outlying elements. Thus, for a four-loop plant model with eight rows on nonzero outlying elements, Fig. 2-4. indicates that the capacitance matrix method is faster than a full-matrix method by factors of 2, 4, 8, and 12 for vessel matrices of order 100, 200, 300, and 400, respectively. Similar factors apply to computer memory storage for the vessel-matrix equation by the full-matrix method versus the capacitance matrix method.

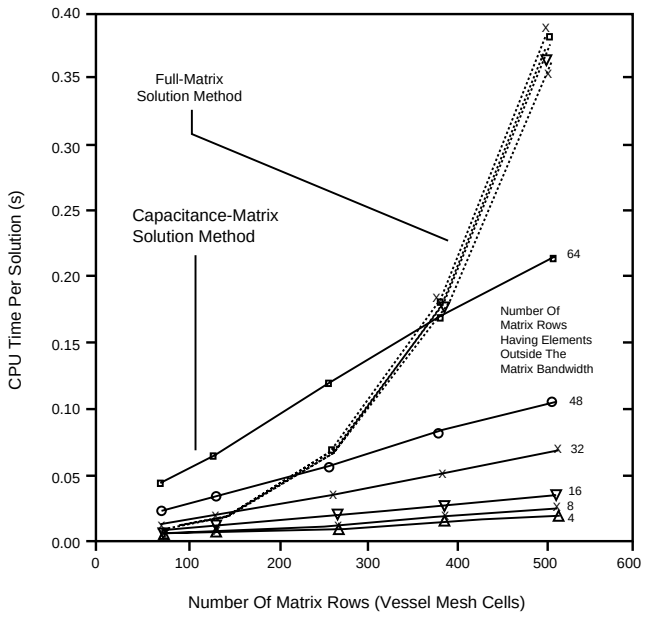

Fig. 2-4. Vessel-matrix equation solution CPU times on a Cray X-MP/48 computer vs. the order of the vessel matrix for different numbers of matrix rows having nonzero outlying elements.

We can summarize the above description of the method by noting that the capacitance matrix method is a direct two-stage procedure. In the first stage, the banded-matrix portion of the matrix equation is solved with an efficient banded-matrix solver to determine the solution for the vessel-matrix equation with zero-valued outlying elements. Then, if there are nonzero outlying elements in the vessel matrix (1D hydro-component loops that connect back to a nonadjacent vessel location generate nonzero outlying elements), the second stage evaluates a direct full-matrix L-U matrix-decomposition solution of a much lower-order capacitance-matrix equation. Doing this accounts for the effect the nonzero outlying elements have on the vessel-matrix equation solution. This results in a modification of the banded-matrix solution to determine the solution of the vessel-matrix equation with nonzero outlying elements.

The following derivation determines the working equations and presents the four-step solution procedure programmed in subroutine MATSOL of TRAC-PF1/MOD2. Given the vessel-matrix equation

$$\underline{\underline{A}} \cdot \underline{x} = \underline{b} , \tag{2-169}$$

where $\underline{\underline{A}}$ is a known (vessel) matrix, $\underline{x}$ is an unknown (mass density, velocity, energy, or pressure) vector, and $\underline{b}$ is a known vector, let us partition $\underline{\underline{A}}$ as follows into the sum of its banded matrix $\underline{\underline{B}}$ and a matrix product $\underline{\underline{E}} \cdot \underline{\underline{R}}$ that has only the nonzero elements lying outside the bandwidth:

$$\underline{\underline{A}} \cdot \underline{x} = (\underline{\underline{B}} + \underline{\underline{E}} \cdot \underline{\underline{R}}) \cdot \underline{x} = \underline{b} . \tag{2-170}$$

Consider the following example of how a simple form for $\underline{\underline{A}}$ would appear when partitioned.

$$\text{For } \underline{\underline{A}} = \begin{bmatrix} x & x & O & O & O & O \\ x & x & x & O & t & O \\ O & x & x & x & O & O \\ O & O & x & x & x & O \\ r & O & s & x & x & x \\ O & O & O & O & x & x \end{bmatrix} \text{, a matrix of order } N, \tag{2-171}$$

$$(N \times N)$$

where r, s, t, and x are nonzero elements, $N = 6$ is the total number of rows and columns in $\underline{\underline{A}}$, and $M = 2$ is the number of rows in $\underline{\underline{A}}$ having nonzero elements outside the three-diagonal bandwidth, then define

$$\underline{\underline{A}} = \underline{\underline{B}} + \underline{\underline{E}} \cdot \underline{\underline{R}} \tag{2-172}$$

where

$$\underline{\underline{B}} = \begin{bmatrix} x & x & O & O & O & O \\ x & x & x & O & O & O \\ O & x & x & x & O & O \\ O & O & x & x & x & O \\ O & O & O & x & x & x \\ O & O & O & O & x & x \end{bmatrix} \quad , \quad \underline{\underline{E}} = \begin{bmatrix} O & O \\ O & 1 \\ O & O \\ O & O \\ 1 & O \\ O & O \end{bmatrix}$$

$(N \times N)$ $(N \times M)$

$$\underline{\underline{R}} = \begin{bmatrix} r & O & s & O & O & O \\ O & O & O & O & t & O \end{bmatrix} \quad , \quad \underline{\underline{E}} \cdot \underline{\underline{R}} = \begin{bmatrix} O & O & O & O & O & O \\ O & O & O & O & t & O \\ O & O & O & O & O & O \\ O & O & O & O & O & O \\ r & O & s & O & O & O \\ O & O & O & O & O & O \end{bmatrix} . \tag{2-173}$$

$(M \times N)$ $(N \times N)$

Note that the nonzero elements in $\underline{\underline{E}}$ are unity and in $\underline{\underline{R}}$ are the actual nonzero outlying elements of $\underline{\underline{A}}$. The term $\underline{\underline{A}}$ is an $N \times N$ matrix with M rows having nonzero elements outside its bandwidth, $\underline{\underline{B}}$ is an $N \times N$ banded matrix, $\underline{\underline{E}}$ is an $N \times M$ matrix, and $\underline{\underline{R}}$ is an $M \times N$ matrix.

Multiply Eq. (2-170) by the inverse of the banded matrix, $\underline{\underline{B}}$ to get

$$(\underline{\underline{I}} + \underline{\underline{B}}^{-1} \cdot \underline{\underline{E}} \cdot \underline{\underline{R}}) \cdot \underline{x} = \underline{\underline{B}}^{-1} \cdot \underline{b} . \tag{2-174}$$

Define $\underline{\underline{R}} \cdot \underline{x} = \underline{y}$ and move its term in Eq. (2-174) to the right-hand side of the equation, giving

$$\underline{x} = \underline{\underline{B}}^{-1} \cdot \underline{b} - \underline{\underline{B}}^{-1} \underline{\underline{E}} \cdot \underline{y} . \tag{2-175}$$

Substitute Eq. (2-175) for $\underline{x}$ into Eq. (2-174) to give

$$(\underline{\underline{I}} + \underline{\underline{B}}^{-1} \cdot \underline{\underline{E}} \cdot \underline{\underline{R}}) \cdot (\underline{\underline{B}}^{-1} \cdot \underline{b} - \underline{\underline{B}}^{-1} \cdot \underline{\underline{E}} \cdot \underline{y}) = \underline{\underline{B}}^{-1} \cdot \underline{b} . \tag{2-176}$$

Expand Eq. (2-176), delete the $\underline{\underline{B}}^{-1} \cdot \underline{b}$ term from both sides of the equation, and multiply the equation by $(\underline{\underline{B}}^{-1} \cdot \underline{\underline{E}})^{-1}$ giving

$$(\underline{\underline{I}} + \underline{\underline{R}} \cdot \underline{\underline{B}}^{-1} \cdot \underline{\underline{E}}) \cdot \underline{y} = \underline{\underline{R}} \cdot \underline{\underline{B}}^{-1} \cdot \underline{b} \,. \tag{2-177}$$

Multiply Eq. (2-177) by the inverse of the matrix on its left-hand side to define $\underline{y}$ as follows:

$$\underline{y} = (\underline{\underline{I}} + \underline{\underline{R}} \cdot \underline{\underline{B}}^{-1} \cdot \underline{\underline{E}})^{-1} \cdot \underline{\underline{R}} \cdot \underline{\underline{B}}^{-1} \cdot \underline{b} \,. \tag{2-178}$$

To determine $\underline{x} = \underline{\underline{A}}^{-1} \cdot \underline{b}$, evaluate Eq. (2-178) for $\underline{y}$ and substitute $\underline{y}$ into Eq. (2-175) to evaluate $\underline{x}$.

This evaluation procedure appears lengthy until we observe that it involves the following four steps with some intermediate results used several times.

Step 1. Multiply the vector $\underline{b}$ and each of the M columns of $\underline{\underline{E}}$ by the inverse of $\underline{\underline{B}}$.

$$\underline{\hat{x}} = \underline{\underline{B}}^{-1} \cdot \underline{b} \quad \text{and} \quad \underline{\underline{\hat{E}}} = \underline{\underline{B}}^{-1} \cdot \underline{\underline{E}} \tag{2-179}$$

$$(N)(N \text{ x } N)(N)(N \text{ x } M)(N \text{ x } N)(N \text{ x } M)$$

Step 2. Multiply $\underline{\hat{x}}$ and $\underline{\underline{\hat{E}}}$ from Step 1 by $\underline{\underline{R}}$.

$$\underline{\hat{b}} = \underline{\underline{R}} \cdot \underline{\hat{x}} \quad \text{and} \quad \underline{\underline{\hat{R}}} = \underline{\underline{R}} \cdot \underline{\underline{\hat{E}}} \tag{2-180}$$

$$(M)(M \text{ x } N)(N)(M \text{ x } M)(M \text{ x } N)(N \text{ x } M)$$

Step 3. Evaluate Eq. (2-178) for $\underline{y}$ using $\underline{\hat{b}}$ and $\underline{\underline{\hat{R}}}$ from Step 2.

$$\underline{y} = (\underline{\mathrm{I}} + \underline{\underline{\hat{R}}})^{-1} \cdot \underline{\hat{b}} \tag{2-181}$$

$$(M)(M \text{ x } M)(M \text{ x } M)(M)$$

Step 4. Evaluate Eq. (2-175) for the desired solution vector $\underline{x}$ using $\underline{\hat{x}}$ and $\underline{\underline{\hat{E}}}$ from Step 1 and $\underline{y}$ from Step 3.

$$\underline{x} = \underline{\hat{x}} - \underline{\underline{\hat{E}}} \cdot \underline{\mathrm{y}} \tag{2-182}$$

$$(\mathrm{N})(\mathrm{N})(\mathrm{N \text{ x } M})(\mathrm{M})$$

Computationally, Eq. (2-178) is solved by performing a single banded-matrix L-U matrix decomposition to determine $\underline{\underline{B}}^{-1}$. Then $\underline{\underline{B}}^{-1}$ is applied to the $1+M$ column vectors of $\underline{b}$ and $\underline{\underline{E}}$ by a direct forward-elimination and backward-substitution solution procedure. Equation (2-181) requires that a L-U matrix decomposition be applied to the full (nonbanded), but much smaller, capacitance matrix $\underline{\underline{I}}+\underline{\underline{\hat{R}}}$. The method becomes rapidly less efficient as the size of the capacitance matrix $\underline{\underline{I}}+\underline{\underline{\hat{R}}}$ increases. The remainder of the computation involves matrix multiplications that are performed efficiently on a vector computer.

2.1.8.5. Water Packing. The water-packing logic in the code is triggered under certain conditions (but not all conditions) when the code attempts during a time step to overfill (pack) a liquid-full finite-difference mesh cell or to overextract (stretch) liquid from a liquid-full cell. The physical analog to water-packing is a water hammer; when cold water surges down a dead-end pipe filled with steam, a large pressure spike occurs when the last steam collapses and the water fills the pipe. Because of the low compressibility of liquid water, the spike has a very short duration.

In any Eulerian finite-difference scheme, the boundary of a mesh cell behaves like the dead end of a pipe in a water hammer. This is especially true when condensation is present. Consider a 1D mesh cell with pure liquid entering from the left and pure vapor flowing in from the right to condense on the liquid. It is not possible for a standard finite-difference momentum equation to produce a liquid-mass flow out of the right cell face that exactly balances the flow in the left cell face at the instant when the cell fills with liquid. In fact, when strong condensation is present, the momentum equation generally will predict a liquid velocity into the cell on the right face. This circumstance produces a numerical dead end for the liquid. Unlike the water hammer, the final solution is not to halt the flow, but to push the liquid on through the right cell face. As with a hammer, this is accomplished with an abrupt increase in pressure.

In TRAC, we have adopted a method for mitigating water-packing that is similar in spirit to shock-fitting techniques. Logic has been installed that detects pressure excursions caused by water-packing. When they occur, it is clear that the finite-difference momentum equation is producing invalid results. Therefore, we modify the equation at those locations and times to obtain a better solution. A standard motion equation at a cell edge can be written as

$$V_{j+1/2}^{n+1} = V_{j+1/2}^{n} + a + b(P_j^{n+1} - P_{j+1}^{n+1}) \ . \tag{2-183}$$

Additional force terms are incorporated in the term a, and b includes the time-step size and inverse of mesh length and density. If packing is detected in cell j, the equation is modified to the form

$$V_{j+1/2}^{n+1} = V_{j+1/2}^{n} + a + b(cP_j^{n+1} - P_{j+1}^{n+1}) \ . \tag{2-184}$$

The constant c multiplying P_j^{n+1} is taken to be a large number so that only small changes in the pressure of the j^{th} cell are required to obtain the appropriate velocity for the liquid outflow. To prevent excessively large vapor velocities, the value of the coefficient b in the vapor equation is set equal to the corresponding coefficient in the liquid equation.

In a given cell of a 1D component, the code does not consider the water-packing logic if the cell void fraction is greater than 0.08, if the liquid in the cell is superheated, or if the net mass flow is out of the cell. Also, the code cannot make adjustments at a cell interface or test across that interface if the associated flow area is less than or equal to $10^{-10}\,m^2$. Further, TRAC does not consider adjacent cells in which the void fraction is less than 0.1. The code predicts the change in the current cell pressure to give a new pressure; if the predicted pressure change is negative, the code transfers to logic to detect stretching. If the pressure rise is greater than or equal to 0, and if this new pressure does not exceed the maximum of its current value and the adjacent-cell pressures by at least 7%, with a minimum increase of 50 kPa (one-half bar), the water-packing logic terminates. The void-fraction tests ensure that the water-packing logic will not smooth out a true water-hammer-type phenomenon in the calculation, while the pressure checks prevent the logic from being triggered too often. If, through the tests, more than one interface of a given cell permits the water-packing correction, the code applies the correction only at the interface across which the void fraction is higher. The code does not permit the water-packing correction at the interface opposite a FILL component if the velocities at both interfaces have the same sign or at the interface at which the PUMP-component source is applied. Also, the code terminates the water-packing logic for a given cell interface if choking is detected at that interface and if the interface is either the first or last interface of a component.

The stretching logic is similar, although the code looks for a pressure drop in the current cell that reduces its pressure to less than the minimum of 95% of its current value or 95% of the neighboring cells, with the additional constraint that the projected pressure must be less than the saturation pressure corresponding to the current liquid temperature minus 20.0 K. The final constraint for stretching is that the test pressure cannot be below the lower pressure limit for the equation of state (see Appendix A). For a stretch, the code does not make an adjustment at a given interface if the void fraction on the other side of the interface is less than or equal to 0.1, if the liquid velocity at the interface is into the cell in which the stretch is detected, or if the PUMP-component source is applied at the interface.

The 3D VESSEL water-packing detection logic is very similar. The VESSEL, however, permits packing to occur if the current cell void fraction is greater than 0.1, instead of the 0.08 in the 1D components. Also, in detecting a stretch, the code requires the pressure test to be 0.8 of that in the 1D components.

Subroutine TF1DS3 contains the fairly complex logic for detecting water-packing situations in the 1D components; the logic for making the necessary corrections is in

subroutines TF1DS and TF1DS1. The corresponding coding for the 3D VESSEL is in subroutine TF3DS3.

2.1.8.6. Special Cases. In this subsection, the implementations of the special flow models [critical flow, countercurrent flow limitation (CCFL), and the offtake model] are briefly summarized. Details are provided in Section 4.0. and Appendix I.

2.1.8.6.1. Critical-Flow Model. The critical-flow model is implemented as an option that the user may turn on using the INOPTS namelist data flag ICFLOW. When ICFLOW = 0, no critical-flow calculation is performed. If ICFLOW = 1 (default), critical-flow calculations are performed only for components connected to a BREAK component using the default multipliers. This option requires no additional user input. When ICFLOW = 2, critical-flow calculations are performed with user-specified multipliers at user-specified cell edges. This option requires the user to include the critical-flow multipliers CHM12, CHM22, CHM13, CHM23, CHM14, CHM24, CHM15, and CHM25 as additional INOPTS namelist data input if values other than the default are desired. Within each 1D component's array data cards, the array ICFLG must also be included to indicate the cell edges at which the critical-flow calculations will be performed.

The only difference to the solution procedure, when the critical-flow model has been turned on, occurs in the basic step. Subroutine TF1DS1 solves for the new-time velocities as a function of the new-time pressures and the derivatives of those velocities with respect to pressure. If the critical-flow model is turned on, subroutine CHOKE is called just before subroutine TF1DS1 is exited. Based on the void fraction of the flow, subroutine CHOKE calculates a second set of new-time velocities and the derivatives with respect to pressure using a choking condition. If the new-time choking velocities calculated by subroutine CHOKE are larger in magnitude than the new-time momentum-solution velocities calculated by subroutine TF1DS1, nothing is changed and the solution proceeds as if the critical-flow model had not been turned on. If, however, the choking velocities are smaller in magnitude than the momentum-solution velocities, then the calculation proceeds with the choking velocities and the derivatives being used in place of the momentum-solution quantities.

2.1.8.6.2. Countercurrent Flow Limitation (CCFL). A special model exists in the code that allows the user to invoke characteristic CCFL correlations at specific locations in the 3D VESSEL component and in the 1D components (Appendix I, Section I.3.). The CCFL correlation for a specific geometry provides the amount of liquid delivery for a given vapor upflow. The CCFL model is applied at the top edge of the chosen VESSEL cell if the vapor velocity is greater than or equal to zero. For a given vapor upflow and an upstream void fraction, the downward liquid velocity is calculated that satisfies the correlation. The old-time vapor velocity is used as input to the CCFL correlation to calculate the new-time intermediate-step liquid velocity [subroutine StbVelz (FEMOMZ in TRAC-M/F77) for 3D components and subroutine StbVel (FEMOM in TRAC-M/F77) for 1D components]. At this point, the interfacial drag coefficient is also calculated from the Bankoff correlation (see Appendix I, Section I.3.). The new-time final-value liquid velocity and the derivative of the new-time final-value liquid velocity with respect to

pressure are calculated in subroutine TF3DS1 for 1D components and subroutine TF3DS3 for 3D components from the CCFL correlation based on the new-time final-value vapor velocity.

2.1.8.6.3. TEE-Component Offtake Model. The TEE-component offtake model is implemented as an option that the user may turn on using the INOPTS namelist data flag IOFFTK. When IOFFTK = 1 (default = 0), the user is required to insert an additional line of input for each TEE component within the TRAC input deck specifying the value of the variable IENTRN. This new Card Number 15 requires IENTRN = 1 to implement the offtake model for a particular TEE. Similarly, no offtake model is implemented for any TEE for which IENTRN = 0.

Upon initialization in subroutine ITEE, TRAC checks for the appropriate geometry for all TEEs in which the offtake model has been requested by the user. For this initial model, the side tube of the tee is required to be either top, bottom, or centrally oriented from the main tube and is required to be at a 90° angle to the main tube. In addition, the TEE main-tube junction cell is required to be horizontal. Lastly in subroutine ITEE, old-old-, old-, and new-time values of the offtake void fraction (ALPOTO, ALPOT, and ALPOTN, respectively) are initialized equal to the main-tube junction-cell void fraction input by the user. It should be noted that geometry checks traditionally are performed in subroutine RTEE. The GRAVs, however, are not computed until subroutine ITEE if a user chooses to specify cell-centered elevations in his/her input deck. Therefore, the geometry checks for this particular model are located in subroutine ITEE.

The momentum-stabilizer step for a TEE component is controlled by subroutine TEE1. At the beginning of this step, all dual-time variables are updated. If the offtake model for this particular TEE has been turned on by the user through input, all offtake void fractions are also time-updated. Next, the side-tube boundary arrays are set up. In the absence of the offtake model, the variables in the boundary array at the junction (BD4) normally reflect main-tube junction-cell conditions. If the offtake model is turned on, however, it is recognized that the void fraction that exits the offtake may be significantly different than that which exists in the main-tube junction cell. Therefore, all of the variables in this BD4 array that include a void-fraction term are reset to reflect the offtake void fraction rather than the main-tube junction-cell void fraction. Old-old-time variables are reset using the old-old-time offtake void fraction, ALPOTO, whereas old-time variables are adjusted using the old-time offtake void fraction, ALPOT. Similarly, the new-time variables are reset using the new-time offtake void fraction, ALPOTN. Except for the additional time-updating and the boundary array adjustments just described, the existing logic for the momentum-stabilizer step remains unchanged by the offtake model, and the calculation proceeds as for any other TEE component.

The mass and energy basic step for a TEE component is controlled by subroutine TEE2. As in the case of the momentum-stabilizer step, adjustments are necessary when the side-tube boundary array at the TEE junction (BD4) is set up. All elements of the boundary array containing void-fraction terms are reset again to reflect the offtake void fraction rather than the main-tube junction-cell void fraction in exactly the manner

described in the previous paragraph. In addition, a phase separator flag is activated for the main tube to accomplish two things. First, when the source-term fluxes for the main-tube junction cell are being calculated (in subroutine TF1DS), the flag signals that the offtake model is turned on. The source-term fluxes then are calculated using the offtake void fraction rather than the junction-cell void fraction. Second, the phase separator flag forces XVSET for the main-tube junction cell to be zero to ensure that only known old-time quantities (namely, void fraction) are used when calculating source-term fluxes. Except for the boundary array adjustments and the slightly different treatment of the main-tube junction-cell source-term fluxes just described, the existing logic for the mass and energy basic step remains unchanged by the offtake model, and the calculation proceeds as for any other TEE component.

The mass and energy stabilizer step for a TEE component is handled by subroutine TEE3. This final step consists of an implicit solution for the macroscopic fluid densities and energies known as the stabilizer quantities in each of the fluid cells given the flow velocities across the cell edges. Because the quantities being solved for actually include the void fraction (which the offtake model is attempting to alter), a slightly different procedure must be used within this step. To incorporate the effect of the offtake model on the fluxed quantities, the new-time TEE-junction interface velocities (which are used in subroutine STBME when setting up the stabilizer solution matrix) are scaled when offtake flow exists. This scaling factor consists of the ratio of the new-time offtake void fraction to the new-time main-tube junction-cell void fraction. The velocities are altered in both their A-array locations and in the side-tube boundary array. After the solution matrix has been set up, the new-time junction interface velocities are restored to their original values. This results in the mass and energy stabilizer equations being solved for new-time conditions that reflect the offtake void fraction rather than the main-tube junction-cell void fraction. Following the successful determination of new-time conditions, subroutine OFFTKE is called to calculate a corresponding new-time offtake void fraction, ALPOTN. If the mass and energy stabilizer step is reached with conditions indicating that a back-up is in progress, however, subroutine OFFTKE is not called to calculate a new-time offtake void fraction, and ALPOTN remains equal to ALPOT.

2.2. Heat Conduction in Solid Materials

The nuclear reaction in the core of a PWR generates energy inside the fuel. That energy is transferred to the primary fluid and crosses the steam-generator tubes to the secondary fluid. The code must calculate the heat conduction in the fuel and the steam-generator tubes to simulate correctly the heat-transfer processes involved in thermal-energy transport. Also, the passive solid structures, such as piping walls, vessel walls, and the internal vessel structures, represent significant metal masses that can store or release large amounts of thermal energy depending upon the reactor coolant temperature. Therefore, the code needs to model these additional structures.

The following nomenclature applies to Section 2.2.

NOMENCLATURE

A:	area in radial direction
A^*:	area in axial direction
$\underline{\underline{A}}$:	coefficient matrix
a:	nonzero elements of $\underline{\underline{A}}$
$\underline{B}$:	equality vector
b:	elements of $\underline{B}$
c_p:	specific heat
$\underline{\underline{C}}$, $\underline{\underline{D}}$, $\underline{\underline{E}}$:	nonzero submatrices of $\underline{\underline{A}}$
f_t, f_{ss}:	stability flags
h:	convective HTC
h_{gap}:	gap conductance
k:	thermal conductivity
NR:	number of nodes that segment the radial direction
NZ:	number of nodes that segment the axial direction
$\bar{q}$:	heat flux vector
q''':	heat generation rate per unit volume
q_{total}:	total heat flux
R:	radius
R^+, R^-:	variables defined by Eqs. (2-198) and (2-199)
r:	radial coordinate
t:	time
T:	temperature
$\underline{T}$:	temperature vector
V:	cell volume
z:	axial distance
z_b:	bottom of the fuel rod
z_u:	top of the fuel rod
Δr:	radial increment
Δt:	time increment
Δx:	slab thickness
Δz:	axial increment
ρ:	density

Subscripts

g:	gas
I:	inner surface
i, j:	finite-difference indices
l:	liquid
max:	maximum
o:	outer surface
w:	wall

Superscripts

n, *n* + 1:	current-time and new-time values
+, –:	refers to material to the right and left of the interface, respectively
‘:	new quantities when a fine mesh is added

2.2.1. Governing Equations

Because the heat flux in a solid material is a vector quantity, the following general equation describes the heat-conduction process in an arbitrary geometry:

$$\frac{\partial(\rho c_p T)}{\partial t} + \nabla \cdot \bar{q} = q''' \ . \tag{2-185}$$

In practice, the product ρc_p is assumed to be constant for purposes of taking the time derivative.

The heat flux $\bar{q}$ can be expressed in terms of the temperature gradient by Fourier’s law of conduction (Ref. 2-15.) as follows:

$$\bar{q} = -k\nabla T \ . \tag{2-186}$$

Therefore, Eq. (2-185) becomes

$$\rho c_p \frac{\partial T}{\partial t} = \nabla \cdot (k\nabla T) + q''' \ . \tag{2-187}$$

The thermal history of the reactor structure is obtained from a solution of the heat-conduction equation applied to different geometries. This section first discusses the coupling of the heat-conduction field equation in any of its many forms to the thermal-hydraulic field equations representing the fluid (see Section 2.1.2.). Following this discussion, the next two sections detail the various formulations of the heat-conduction equations to represent particular geometries typically found in reactor systems. The geometries include cylindrical walls, slabs, and core fuel rods. The first model analyzes

heat conduction within the walls of the 1D loop components, such as pipe walls. The latter two are associated with heat transfer within structural components of the vessel. They are modeled similarly in the code, differing only in the area and volume calculations used in the finite-difference equations. The calculations of slab and rod conduction are done in the same subroutines in the code. Both of these components are therefore discussed in the same section of this manual.

2.2.2. Coupling of Thermal Hydraulics with the Reactor Structure

The energy transported by convective heat transfer from any structure into the different fluid phases is modeled using Newton's law of cooling to represent the energy exchange rate between the structure and the fluid phase. These terms appear in the energy equations of the different fluid phases. Appendix F, Section F.2. discusses the logic used to determine which heat-transfer regime exists between the wall and fluid and which correlations for the wall heat-transfer coefficient (HTC) are used to represent the different regimes. The coupling algorithm (Fig. 2-5.) is semi-implicit. For each new-time step, the wall HTCs (h) of a given structure are evaluated using the surface wall temperatures (T_w) and the fluid conditions obtained for the last time step. The new-time fluid-dynamics equations are solved using these HTCs, the old-time surface temperatures, and the new-time fluid temperatures where the sum of the total energy transported into the fluid cell can be written as

$$q_{\text{total}}^{\,n+1} = h_l^n (T_w^n - T_l^{n+1}) + h_g^n (T_w^n - T_g^{n+1}) \ .$$

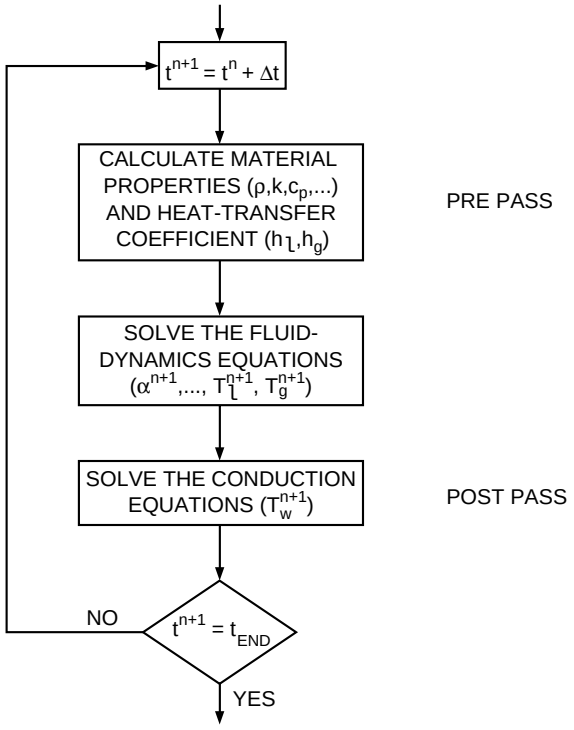

Fig. 2-5. Semi-implicit coupling between hydrodynamics and structural heat transfer.

After the fluid-dynamics equations are solved, the new-time wall temperature distributions are obtained by solution of the conduction equation for each structure modeled. This solution uses the same HTCs and the final new-time fluid temperatures.

2.2.3. Cylindrical Wall Heat Conduction

The temperature distribution within the walls of the 1D components is determined by subroutine CYLHT. A solution is obtained from a finite-difference approximation to the 1D conduction equation,

$$\rho c_p \frac{\partial T}{\partial t} = \frac{1}{r}\left[\frac{\partial}{\partial r}\left(rk\frac{\partial T}{\partial r}\right)\right] + q''' \quad . \tag{2-188}$$

The finite-difference equations are derived by applying an integral method (Ref. 2-16.) to the elemental volumes shown in Fig. 2-6. The general form of the i^{th} volume ($1 < i < N$) is

$$\begin{aligned} &\frac{r_{i-1/2}k_{i-1/2}}{\Delta r_{i-1}}T_{i-1}^{n+1} - \left\{\frac{r_{i-1/2}k_{i-1/2}}{\Delta r_{i-1}} + \frac{r_{i+1/2}k_{i+1/2}}{\Delta r_i}\right. \\ &\left. + \frac{1}{2\Delta t}\left[\left(r_i\Delta r_{i-1} - \frac{\Delta r_{i-1}^2}{4}\right)(\rho c_p)_{i-1/2} + \left(r_i\Delta r_i + \frac{\Delta r_i^2}{4}\right)(\rho c_p)_{i+1/2}\right]\right\}T_i^{n+1} \\ &+ \frac{r_{i+1/2}k_{i+1/2}}{\Delta r_i}T_{i+1}^{n+1} = -\frac{1}{2}\left\{\left(r_i\Delta r_{i-1} - \frac{\Delta r_{i-1}^2}{4}\right)\left[\frac{(\rho c_p)_{i-1/2}}{\Delta t}T_i^n + q'''\right]\right. \\ &\left. + \left(r_i\Delta r_i + \frac{\Delta r_i^2}{4}\right)\left[\frac{(\rho c_p)_{i+1/2}}{\Delta t}T_i^n + q'''\right]\right\} \end{aligned} \tag{2-189}$$

where

$$f_i^n = f(t^n, r_i) \quad .$$

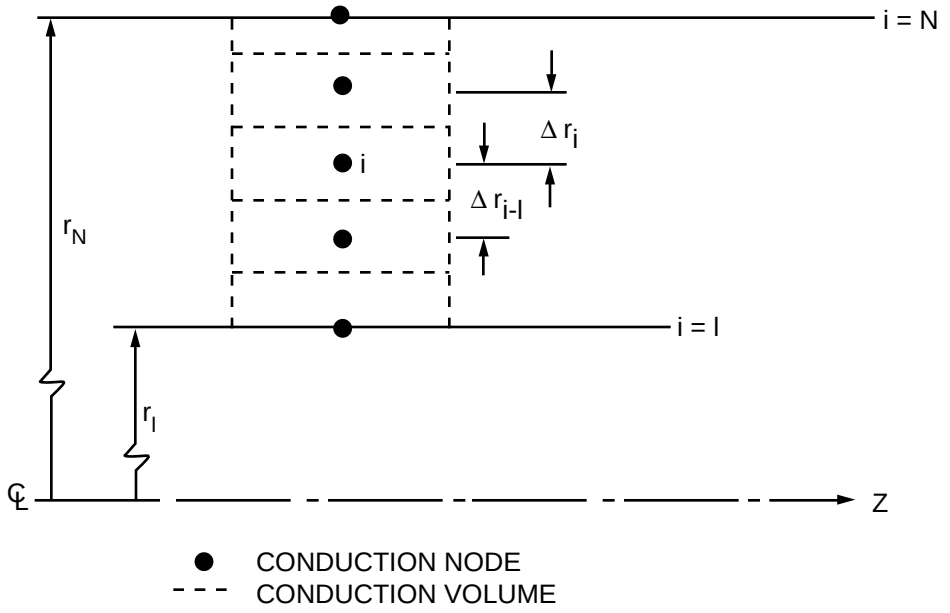

Fig. 2-6. Cylindrical wall geometry.

This formulation positions nodal points on material interfaces. Material properties are evaluated between nodes. The boundary conditions applied to the inner ($i = 1$) and outer ($i = N$) surfaces are

$$-k\frac{\partial T}{\partial r}\bigg|_{i\,=\,1,\,N} = \pm[h_l(T_l - T_i) + h_g(T_g - T_i)] \ . \tag{2-190}$$

For example, application of this boundary condition to the inner surface ($i = 1$) yields

$$-\left\{\frac{r_{3/2}k_{3/2}}{\Delta r_1} + \frac{1}{2}\left[r_1\Delta r_1 + \frac{\Delta r_1^2}{4}\right]\frac{(\rho c_p)_{3/2}}{\Delta t} + f_{ss}r_1(h_l + h_g)\right\}T_1^{n+1} + \frac{r_{3/2}k_{3/2}}{\Delta r_1}T_2^{n+1}$$

$$= -\frac{1}{2}\left(r_1\Delta r_1 + \frac{\Delta r_1^2}{4}\right)\left[\frac{(\rho c_p)_{3/2}}{\Delta t}T_1^n + q'''\right]$$

$$+ r_1[h_l(f_tT_1^n - T_l^{n+1}) + h_g(f_tT_1^n - T_g^{n+1})] \ . \tag{2-191}$$

The parameters f_t and f_{ss} are 0 and 1, respectively, to provide maximum stability.

The resulting linear equations are solved in a sequential fashion in the axial z-direction. For each axial position, a solution is achieved using Gaussian elimination.

A lumped-parameter solution is available to the user if the number of nodes is set equal to one. For this option the wall temperature is obtained from the equation,

$$T^{n+1} = \left\{\frac{1}{2}\left(2\Delta r + \frac{\Delta r^2}{R_I}\right)\left(\frac{\rho c_p}{\Delta t}T^n + q'''\right) + h_{l_I}(T_{l_I}^{n+1} - f_t T^n)\right.$$

$$\left. + h_{g_I}(T_{g_I}^{n+1} - f_t T^n) - \left(1 + \frac{\Delta r}{R_I}\right)[h_{l_o}(f_t T^n - T_{l_o}^{n+1}) + h_{g_o}(f_t T^n - T_{g_o}^{n+1})]\right\}$$

$$\left\{\frac{1}{2}\left(2\Delta r + \frac{\Delta r^2}{R_I}\right)\left(\frac{\rho c_p}{\Delta t}\right) + f_{ss}\left[h_{l_I} + h_{g_I} + \left(1 + \frac{\Delta r}{R_I}\right)(h_{l_o} + h_{g_o})\right]\right\}^{-1} . \qquad (2\text{-}192)$$

The subscripts *I* and *o* refer to the inner and outer radii, respectively.

2.2.4. Slab and Rod Heat Conduction

Structures that can exchange heat with the fluid in a reactor vessel include downcomer walls and support plates, modeled as slabs, and vessel rods. These elements are referred to as heat-structure components. Both nuclear and electrically heated rods or slabs can be analyzed. The effects of gap conduction, metal-water reaction, and variable material properties are included.

Only one rod within a cell may have hydro-cell coupling. This “average” rod is coupled to the fluid by Newton’s law of cooling. Any number of additional user-specified rods may be included in each segment. The rod power factors (that is, relative to the average rod located within each segment) are specified by the user for these supplemental rods. The supplemental rods allow the user to include hot rods in the reactor vessel. Such rods do not affect the fluid-dynamics calculation because their contributions are already represented by average rods. They are included separately only for the purpose of determining their temperature response.

More than one slab may be located within a cell. Each slab is coupled to the fluid by Newton’s law of cooling.

The user has four numerical calculation options for computing temperature distribution in slabs and rods. For thin slabs or rods of small diameter where the radial temperature profile is flat and axial conduction is negligible, the user may choose the “lumped-parameter” solution. This option gives the best calculational efficiency and should be used whenever it can be justified.

The second option is a 1D solution with implicit differencing in the radial direction and no conduction in the axial direction. This option is appropriate when steep axial profiles do not exist.

The third option is a 2D solution with implicit differencing in the radial direction and explicit differencing in the axial direction. This allows the very small radial node spacing required by the large radial power variations without severely limiting the time step. The explicit differencing in the axial direction does limit the maximum time-step size for axial spacing. In many cases, however, this maximum time-step size is much greater than that used for the fluid-dynamics calculation and is not restrictive. For those cases, the semi-implicit calculation gives good computational efficiency.

The fourth option is the fully implicit, 2D finite-difference calculation. This is the best choice for cases where the axial temperature gradient is very large, such as in the vicinity of a quench front. Then the very fine axial noding that is required would cause the time step to be severely limited if the semi-implicit calculation was used. These methods are discussed in the following sections.

2.2.4.1. The Lumped-Parameter Solution. The lumped-parameter equation for cylindrical coordinates is Eq. (2-192). If we choose $f_t = 0$ and $f_{ss} = 1$ for maximum stability, that equation reduces to

$$T^{n+1} = \left\{\frac{1}{2}\left(2\Delta r + \frac{\Delta r^2}{R_I}\right)\left(\frac{\rho c_p}{\Delta t}T^n + q'''\right) + h_{l_I}T_{l_I}^{n+1} + h_{g_I}T_{g_I}^{n+1} + \left(1 + \frac{\Delta r}{R_I}\right)[h_{l_o}T_{l_o}^{n+1} + h_{g_o}T_{g_o}^{n+1}]\right\}$$

$$\left\{\frac{1}{2}\left(2\Delta r + \frac{\Delta r^2}{R_I}\right)\left(\frac{\rho c_p}{\Delta t}\right) + \left[h_{l_I} + h_{g_I} + \left(1 + \frac{\Delta r}{R_I}\right)(h_{l_o} + h_{g_o})\right]\right\}^{-1} . \quad (2\text{-}193)$$

For a solid rod, the axial temperatures are

$$T^{n+1} = \left\{\frac{\Delta r}{2}\left[\frac{\rho c_p}{\Delta t}T^n + q'''\right] + h_{l_o}T_{l_o}^{n+1} + h_{g_o}T_{g_o}^{n+1}\right\}\left\{\frac{\Delta r \rho c_p}{2\Delta t} + h_{l_o} + h_{g_o}\right\}^{-1} . \quad (2\text{-}194)$$

The lumped-parameter equation for the temperature of a slab is

$$T^{n+1} = \left(\frac{\rho c_p \Delta x}{\Delta t}T^n + q'''\Delta x + h_{l_o}T_{l_o}^{n+1} + h_{g_o}T_{g_o}^{n+1} + h_{l_I}T_{l_I}^{n+1} + h_{g_I}T_{g_I}^{n+1}\right)$$

$$\left(\frac{\rho c_p \Delta x}{\Delta t} + h_{l_o} + h_{g_o} + h_{l_I} + h_{g_I}\right)^{-1} , \quad (2\text{-}195)$$

where Δx is the slab thickness.

2.2.4.2. The Semi-Implicit Calculation. Finite-difference equations are obtained by applying an integral method (Ref. 2-17.) to appropriate differential volumes. The noding within a rod (Fig. 2-7.) is staggered with respect to the nodes used in the fluid-dynamics calculations. This noding scheme is necessary to simplify the algorithm that generates the fine mesh required by the reflood calculations. The staggered mesh gives the further advantage of providing axial numerical smoothing.

Consider a general differential volume (that is, the volume labeled 1 in Fig. 2-7.). Using explicit differencing in the axial direction and implicit differencing in the radial direction, the finite-difference equation for this volume is

$$\left\{(\rho c_p)_{ij}\frac{T_{ij}^{n+1}-T_{ij}^{n}}{\Delta t}-q_{ij}'''\right\}\frac{1}{2}\left[\left(r_i\Delta r_i+\frac{\Delta r_i^2}{4}\right)+\left(r_i\Delta r_{i-1}-\frac{\Delta r_{i-1}^2}{4}\right)\right]\left[\frac{\Delta z_j+\Delta z_{j-1}}{2}\right]$$

$$=\left\{r_{i+1/2}k_{i+1/2,\,j}\left(\frac{T_{i+1,\,j}^{n+1}-T_{ij}^{n+1}}{\Delta r_i}\right)+r_{i-1/2}k_{i-1/2,\,j}\left(\frac{T_{i-1,\,j}^{n+1}-T_{ij}^{n+1}}{\Delta r_{i-1}}\right)\right\}$$

$$\times\left[\frac{\Delta z_j+\Delta z_{j-1}}{2}\right]+\left\{k_{i,\,j+1/2}\left(\frac{T_{i,\,j+1}^{n}-T_{ij}^{n}}{\Delta z_j}\right)+k_{i,\,j-1/2}\left(\frac{T_{i,\,j-1}^{n}-T_{ij}^{n}}{\Delta z_{j-1}}\right)\right\}$$

$$\times\frac{1}{2}\left[\left(r_i\Delta r_i+\frac{\Delta r_i^2}{4}\right)+\left(r_i\Delta r_{i-1}-\frac{\Delta r_{i-1}^2}{4}\right)\right]\ , \qquad (2\text{-}196)$$

where $f_{ij}^{n}=f(t^{n},r_i,z_j)$. In Fig. 2-7., the locations of nodes within the volumes located at the boundaries differ. This difference should be considered when values are assigned for the relative power densities at each node.

The boundary conditions applied to the vessel rods are

- the top ($z = z_u$) and bottom ($z = z_b$) of the rods are assumed to be insulated,

$$k\frac{\partial T}{\partial z}\bigg|_{z\,=\,z_b,\,z_u}=0;$$

- the rod centerline ($r = 0$) is a line of symmetry,

$$\frac{\partial T}{\partial r}\bigg|_{r\,=\,0}=0;$$

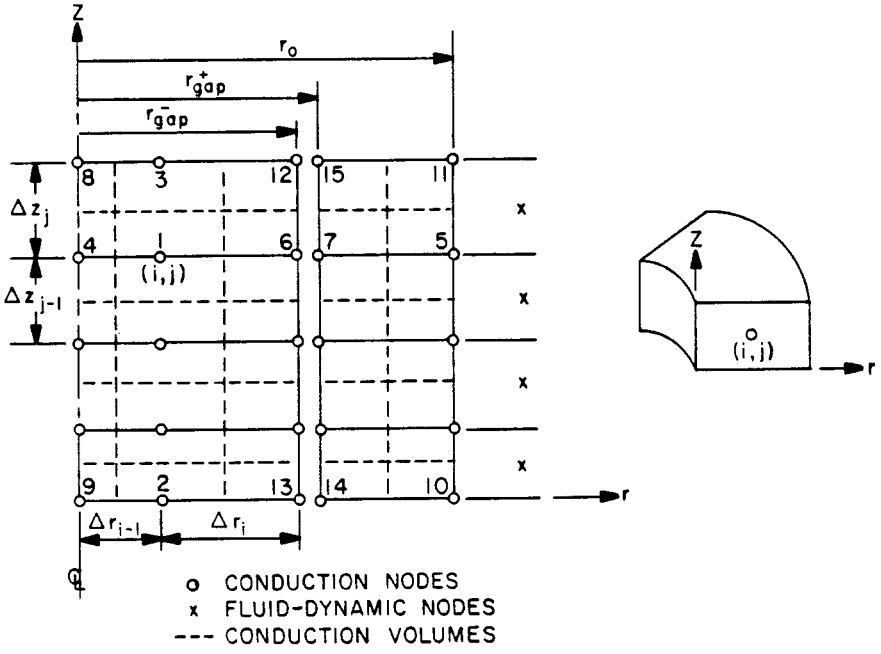

Fig. 2-7. Rod geometry.

and

- heat transfer at the inner and outer gap surfaces $(r = r^-_{gap}, r^+_{gap})$ and at the cladding surface $(r = r_o)$ is specified using Newton's law,

$$k\frac{\partial T}{\partial r}\bigg|_{r = r^{\pm}_{gap}} = -h^{\pm}_{gap}(T_{r^-_{gap}} - T_{r^+_{gap}}) \text{ , and}$$

$$k\frac{\partial T}{\partial r}\bigg|_{r = r_0} = -h_{fluid}(T_{r_0} - T_{fluid}) \text{ ,}$$

where $h^+_{gap} = h^-_{gap}(r^-_{gap}/r^+_{gap})$ to conserve energy.

All properties (that is, ρ, c_p, and k) required by the difference equations are stored at the node locations. Linear interpolation is used to obtain properties between nodes (that is, at cell surfaces). A node located at the interface between two dissimilar materials requires two sets of properties. Consider the differential volume provided in Fig. 2-8. Application of an integral technique to this volume results in the differential equation (after dividing through by the volume),

$$\overline{(\rho c_p)}_{ij}\left(\frac{T_{ij}^{n+1}-T_{ij}^{n}}{\Delta t}\right)-q_{ij}^{'''}=\left\{r_{i+1/2}k_{i+1/2,\,j}\left(\frac{T_{i+1j}^{n+1}-T_{ij}^{n+1}}{\Delta r_i}\right)+r_{i-1/2}k_{i-1/2,\,j}\right.$$

$$\left.\times\left(\frac{T_{i-1,\,j}^{n+1}-T_{ij}^{n+1}}{\Delta r_{i-1}}\right)\right\}\times\left[\frac{\left(r_i\Delta r_i+\frac{\Delta r_i^2}{4}\right)+\left(r_i\Delta r_{i-1}+\frac{\Delta r_{i-1}^2}{4}\right)}{2}\right]^{-1}$$

$$+\left\{\bar{k}_{i,\,j+1/2}\left(\frac{T_{i,\,j+1}^{n}-T_{ij}^{n}}{\Delta z_j}\right)+\bar{k}_{i,\,j-1/2}\left(\frac{T_{i,\,j+1}^{n}-T_{ij}^{n}}{\Delta z_{j-1}}\right)\right\}\left[\frac{\Delta z_j+\Delta z_{j-1}}{2}\right]^{-1}, \qquad (2\text{-}197)$$

where

$$\overline{(\rho c_p)}_{ij}\equiv\frac{\left[(\rho c_p)_{i^+,\,j}^{R^+}(\rho c_p)_{i^-,\,j}^{R^-}\right]}{R^+ + R^-}$$

and

$$\bar{k}_{i,\,j+1/2}\equiv\frac{[k_{i^+,\,j+1/2}R^+ + k_{i^-,\,j+1/2}R^-]}{[R^+ + R^-]}\ .$$

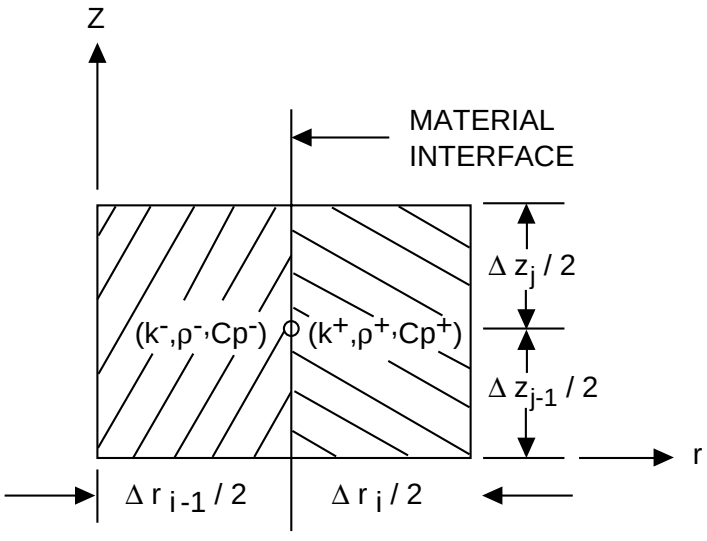

Fig. 2-8. Node located at the interface between two dissimilar materials.

In the above equations,

$$R^{+} \equiv \left(r_i + \frac{\Delta r_i}{4} \right) \frac{\Delta r_i}{2} \tag{2-198}$$

and

$$R^{-} \equiv \left(r_i - \frac{\Delta r_{i-1}}{4} \right) \frac{\Delta r_{i-1}}{2} \quad . \tag{2-199}$$

The superscripts + and – refer to the material to the right and left of the interface.

The semi-implicit finite-difference formulation for the slab is identical to that of the rod except for the obvious geometric differences.

2.2.4.3. The Fully Implicit Calculation. With the cell noding shown in Fig. 2-7., the fully implicit finite-difference equation for 2D heat conduction is (Ref. 2-18.)

$$\begin{aligned}
&(\rho c_p)_{i,j}((T_{i,j}^{n+1} - T_{i,j}^{n}) / \Delta t) V_{i,j} \\
&\quad = q_{ij}''' V_{ij} + k_{i+1/2,j}((T_{i+1,j}^{n+1} - T_{i,j}^{n+1}) / \Delta r_i) A_{i+1/2} \\
&\quad + k_{i-1/2,j}((T_{i-1,j}^{n+1} - T_{i,j}^{n+1}) / \Delta r_{i-1}) A_{i-1/2} \\
&\quad + k_{i,j+1/2}((T_{i,j+1}^{n+1} - T_{i,j}^{n+1}) / \Delta z_j) A_i^{*} \\
&\quad + k_{i,j-1/2}((T_{i,j-1}^{n+1} - T_{i,j}^{n+1}) / \Delta z_{j-1}) A_i^{*} \quad ,
\end{aligned} \tag{2-200}$$

where V = cell volume, A = area in radial direction, A^* = area in axial direction, and Δr = cell length in radial or x direction.

Note that this equation applies to both the slab and rod geometries, providing the areas and volumes of the cells are calculated correctly. Equation (2-200) can be written (Ref. 2-18.) as

$$a_{1,i,j} T_{i-1,j}^{n+1} + a_{2,i,j} T_{i,j}^{n+1} + a_{3,i,j} T_{i+1,j}^{n+1} + a_{4,i,j} T_{i,j-1}^{n+1} + a_{5,i,j} T_{i,j+1}^{n+1} = b_{i,j} \ , \tag{2-201}$$

where

$$a_{1,i,j} = -k_{i-1/2,j} A_{i-1/2} / \Delta r_{i-1} \ ,$$

$$a_{2,i,j} = \left(\rho c_p\right)_{i,j} V_{i,j} / \Delta t + k_{i+1/2,j} A_{i+1/2} / \Delta r_i + k_{i-1/2,j} A_{i-1/2} / \Delta r_{i-1} + k_{i,j+1/2,j} A_i^* / \Delta z_j + k_{i,j-1/2,j} A_i^* / \Delta z_{j-1} ,$$

$$a_{3,i,j} = -k_{i+1/2,j} A_{i+1/2} / \Delta r_i ,$$

$$a_{4,i,j} = -k_{i,j-1/2} A_i^* / \Delta z_{j-1} ,$$

$$a_{5,i,j} = -k_{i,j+1/2} A_i^* / \Delta z_j , \text{ and}$$

$$b_{i,j} = \left\{q'''_{i,j} + (\rho c_p)_{i,j} T^n_{i,j} / \Delta t\right\} V_{i,j} . \quad (2\text{-}202)$$

Equation (2-201) is rewritten in matrix notation as

$$\underline{\underline{A}} \cdot \underline{T} = \underline{B} \quad (2\text{-}203)$$

or

$$\begin{pmatrix} \underline{\underline{D}}(1) & \underline{\underline{E}}(1) & & & & \\ \underline{\underline{C}}(2) & \underline{\underline{D}}(2) & \underline{\underline{E}}(2) & & & 0 \\ & \underline{\underline{C}}(3) & \underline{\underline{D}}(3) & \underline{\underline{E}}(3) & & \\ & & \mathbf{0} & & & \\ 0 & & & & & \\ & & \underline{\underline{C}}(NZ-1) & \underline{\underline{D}}(NZ-1) & \underline{\underline{E}}(NZ-1) & \\ & & & \underline{\underline{C}}(NZ) & \underline{\underline{D}}(NZ) & \end{pmatrix} \begin{pmatrix} \underline{T}(1) \\ \underline{T}(2) \\ \underline{T}(3) \\ \mathbf{M} \\ \mathbf{M} \\ \underline{T}(NZ-1) \\ \underline{T}(NZ) \end{pmatrix} = \begin{pmatrix} \underline{B}(1) \\ \underline{B}(2) \\ \underline{B}(3) \\ \mathbf{M} \\ \mathbf{M} \\ \underline{B}(NZ-1) \\ \underline{B}(NZ) \end{pmatrix} , \quad (2\text{-}204)$$

where

$$\underline{T}^{(j)} = \begin{pmatrix} T_{1,j} \\ T_{2,j} \\ \mathbf{M} \\ T_{NR,j} \end{pmatrix} \quad (j = 1, NZ), \underline{B}^{(j)} = \begin{pmatrix} b_{1,j} \\ b_{2,j} \\ \mathbf{M} \\ b_{NR,j} \end{pmatrix} \quad (j = 1, NZ) , \quad (2\text{-}205)$$

$$\underline{\underline{C}}^{(j)} = \begin{pmatrix} a_{4,1,j} & & & 0 \\ & a_{4,2,j} & & \\ & & \mathbf{0} & \\ 0 & & & a_{4,NR,j} \end{pmatrix} \quad (j = 2, NZ) , \quad (2\text{-}206)$$

$$\underline{\underline{D}}^{(j)} = \begin{pmatrix} a_{2,1,j} & a_{3,1,j} & & & \\ a_{1,2,j} & a_{2,2,j} & a_{3,2,j} & & 0 \\ & a_{1,3,j} & a_{2,3,j} & a_{3,3,j} & \\ & & 0 & & \\ & 0 & & a_{1,NR,j} & a_{2,NR,j} \end{pmatrix} \quad (j = 1, NZ) \quad , \text{ and} \tag{2-207}$$

$$\underline{\underline{E}}^{(j)} = \begin{pmatrix} a_{5,1,j} & & & 0 \\ & a_{5,2,j} & & \\ & & 0 & \\ 0 & & & a_{5,NR,j} \end{pmatrix} \quad (j = 1, NZ-1) \quad . \tag{2-208}$$

Matrix $\underline{\underline{A}}$ is a symmetrical banded matrix. To solve for the temperatures, matrix $\underline{\underline{A}}$ is inverted by a modified Cholesky method. Then the temperatures are computed from

$$\underline{T} = \underline{\underline{A}}^{-1}\underline{B} \quad . \tag{2-209}$$

2.2.4.4. Fine-Mesh Algorithm. The reflood phase of a postulated LOCA is characterized by a sequence of heat-transfer and two-phase-flow regimes advancing rapidly through the vessel core. A correctly predicted thermal response from the fuel/heater rods during reflood requires a numerical technique that can model the quenching phenomena associated with the quench-front motion.

The leading edge of the quenching region is characterized by large variations of temperatures and heat fluxes within small axial distances ($\Delta z \sim 1$ mm) (Ref. 2-19.). The front advancement is controlled by two heat-removal mechanisms, the first being axial conduction from the post-CHF region ahead of the quenched region to the nucleate-boiling region behind the advancing film. The rod conduction model contains the necessary physics to analyze such phenomena. The second is the precursory rod cooling associated with heat transfer to the slugs and droplets entrained in the vapor field downstream of the quench front. The convective heat transfer discussed in Appendix F, Section F.2., contains the physics necessary to describe this phenomenon.

To model the inherently nonstationary, Lagrangian quench-front motion and to resolve the related thermal gradients, a fine-mesh rezoning technique (Ref. 2-20.) is used during the reflood conduction calculations. The axial gradients encountered within the quenching region are resolved by the insertion of rows of transitory nodes (Fig. 2-9.). These nodes are added whenever the temperature difference between adjacent nodes exceeds a user-specified value (T_{max}). The number of rows inserted within each fluid level is specified by the user. The rows are uniformly spaced (that is, Δz is constant) within each fluid level. The temperature values at the supplemental nodes are determined from a three-point Lagrangian interpolation technique. The nodes added in this fashion remain during the entire reflood phase. The temperatures assigned to the nodes are required to conserve energy (Fig. 2-10.),

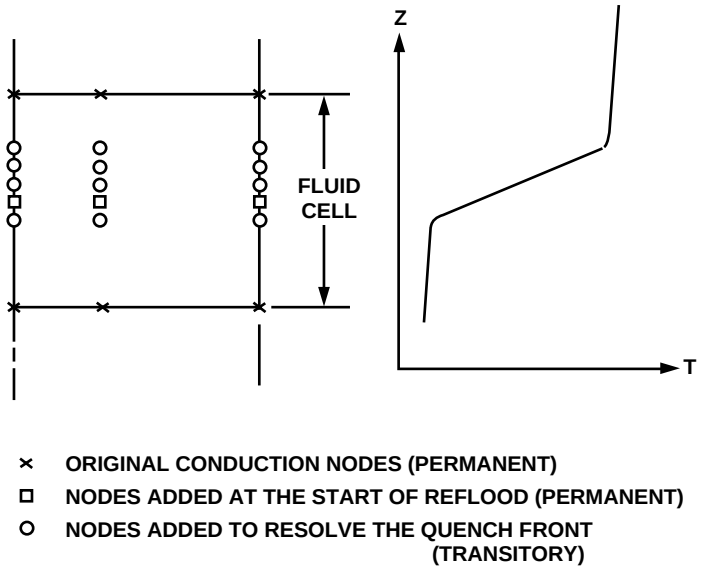

Fig. 2-9. Fine-mesh rezoning.

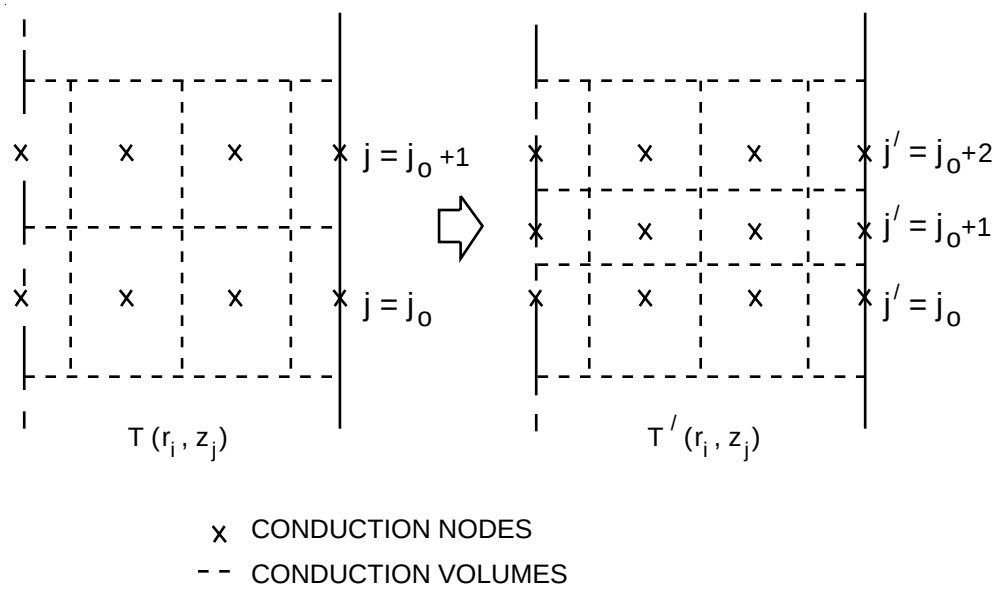

Fig. 2-10. Insertion of conduction nodes during reflood.

$$\sum_{j=j_o}^{j_o+2} \rho'_{ij} c'_{p_{ij}} T'_{ij} V'_{ij} = \sum_{j=j_o}^{j_o+1} \rho_{ij} c_{p_{ij}} T_{ij} V_{ij}, \quad \text{where } i = 1, \ldots, \text{nodes.} \tag{2-210}$$

The primed quantities denote rod properties after the nodes have been added. The values of ρ', c_p', and T' at the original node locations are set equal to their original values. After the quench front has progressed beyond the location of the inserted rows and the surface temperature difference falls below a prescribed value ($\Delta T_{\min}$), the transitory nodes are eliminated. Temperatures at nodes axially adjacent to those deleted retain their original values. For small $\Delta T_{\min}$, this results in a negligible effect on the total rod energy.

Two values for $\Delta T_{\max}$ are specified by the user. The first and smaller value is applied to the part of the quenching region that is in a nucleate- or transition-boiling regime. The largest wall heat fluxes occur in these heat-transfer regimes. The second $\Delta T_{\max}$ value is applied to all other heat-transfer regimes. The specified values for the $\Delta T_{\max}$ are the bases of the $\Delta T_{\min}$ values, which are computed internally.

The above algorithm can analyze multiple quench fronts simultaneously. Both quenching and dryout are modeled automatically.

During the reflood phase, a number of surface conduction nodes are located within each fluid cell. Therefore, it is necessary to calculate an effective wall temperature and HTC for the fluid-dynamics computations. These values are obtained by ensuring the conservation of total energy transferred to the fluid within each cell. Values applied to the liquid phase that satisfy this criterion are

$$\bar{h}_{l} \equiv \frac{\sum_j h_{l_j} A_j}{\sum_j A_j}$$

and

$$\bar{T}_{w_l} \equiv \frac{\sum_j h_{l_j} A_j T_j}{\sum_j h_{l_j} A_j},$$

where the sum is taken over all surface nodes in each fluid cell. Similar values are used in the vapor phase.

It already has been noted that, for a given time step (Δt), a minimum spacing (Δz) between rows of conduction nodes exists because of the explicit axial differencing. For reflood calculations, this axial spacing can be violated, resulting in stability problems. To avoid such problems, the time step is limited internally by a diffusion number. The user also can specify minimum spacing (Δz_{min}) beyond which supplemental rows of conduction nodes will not be added. This additional advantage can prevent excessively large computer costs.

Computing costs are reduced further by calculating material properties only at those nodes located at the edges of the fluid cells. Linear interpolation is used to obtain the properties at any additional locations required by the reflood calculations. The HTCs, however, are obtained directly from the boiling curve for all rod surface nodes.

2.2.4.5. Fuel-Cladding Gap Conductance. Two options are available in TRAC for the fuel-cladding gap conductance. If the input variable NFCI is equal to 0, a constant input value for the gap conductance is used throughout the entire calculation. If the input variable NFCI is equal to 1, the input value for the gap conductance becomes the initial value, and a thermal-expansion model is used to calculate the transient gap conductance. Section 4.5. and Appendix L, Section L.1., give additional details on TRAC's gap conductance model.

2.2.4.6. Metal-Water Reaction. TRAC calculates an additional heat source q'''_{mw} to account for zircaloy's exothermic reaction with steam. Details on this model are given in Section 4.8. and in Appendix L, Section L.2.

2.3. Reactor-Core Power Model

The primary energy source for a nuclear-reactor power plant is the reactor core. A full description of TRAC's reactor-core power model is given in Appendix M. Here we give only a brief overview. Complete input specifications for the core power model and examples of its use are given in the TRAC-M/F90 User's Manual (Ref. 2-24.).

TRAC allows the user to model the power generation in the reactor core in several ways: constant power, power specified from a table, and point-reactor kinetics with reactivity feedback. The latter cases can be run with the reactor core at a constant, user-specified trip power until a user-specified trip occurs. The core model defines the local, volumetric heat-generation rate q''' in the heat-conduction equation [Eq. (2-185)]. Subroutine RHTSTR reads the necessary input for the core description for the heat-structure components. Subroutine HTSTR1 performs the reactivity-feedback calculation in subroutine RFDBK and the point-reactor-kinetics calculation in subroutine RKIN. There is an overview of TRAC's decay-heat and sensitivity feedback models in Section 4.6.; full details are given in Appendix M.

There are several user-specified tables involved in the complete description of the reactor-core power model. In this section (or in Appendix M), we will not belabor the description of these tables and how the code obtains necessary values from them.

In particular, we will not describe signal variables, control blocks, and rate-factor tables other than briefly to define them here. Signal variables are predefined parameters, such as time, pressure, coolant levels, etc., that the code calculates and that the user can select as independent variables for tables, trips, and control blocks. Control blocks are predefined mathematical functions and logic switches, which the user can string together to model plant systems, such as control systems, or to calculate quantities not normally available from the code (and which in turn may be used to control component behavior), such as pressure drops across multiple components, liquid mass in one or more cells, etc. With the signal variables and the control blocks, the user can define the necessary independent variables for the tables. The rate-factor table is a means to vary the rate of change of the independent variable of a component-action table. That is, the rate-factor table provides a multiplier to the independent variable of a table that alters its magnitude before the code performs the table lookup. For more information, on TRAC's control procedure and component-control tables, see Section 2.4., Appendix M, and the TRAC-M/F90 User's Manual (Ref. 2-24.).

2.4. Control Procedure

A detailed description of TRAC's control procedure is given in Appendix N. Here we give a general overview. Complete input specifications for TRAC's control procedure and examples of its use are given in the TRAC-M User's Manual (Ref. 2-24.).

Simulation of PWR-plant operation involves defining its mode of operation. This requires specifying a control procedure to adjust hardware according to the state of the system and its operating plan. In that procedure one needs to model manual control by operators, automatic control by regulating hardware, and abnormal-hardware behavior. This involves specifying logic for initiating adjustable-hardware action when certain conditions occur. For example, when the coolant pressure rises above or falls below a specified level, a valve is to be opened or closed, respectively. Abnormal hardware behavior might be opening a valve to model a pipe break occurrence. The control procedure can consist of many such instructions that together direct and limit the mode of operation.

To be able to define a control procedure, one needs to understand how it fits into the TRAC model for the overall PWR-plant system. The most basic part of that model is the component description of the physical hardware (pipes, pumps, reactor core, etc.) and the mass, momentum, and energy state of the system (density, velocity, pressure, temperature, etc.). This will be referred to as the PWR physical-system model. To apply the control procedure to it, selected system parameters have their values monitored. These values are input to the control procedure along with the control procedure specifications. Evaluating the control procedure results in controllable-component hardware actions being adjusted within the PWR physical-system model. This process, diagrammed in Fig. 2-11., is evaluated at the beginning of each time step on the basis of the beginning of the time-step system state. The control procedure determines what adjustments of hardware are needed. The mode of operation of the system is thus directed as well as constrained by the control procedure.

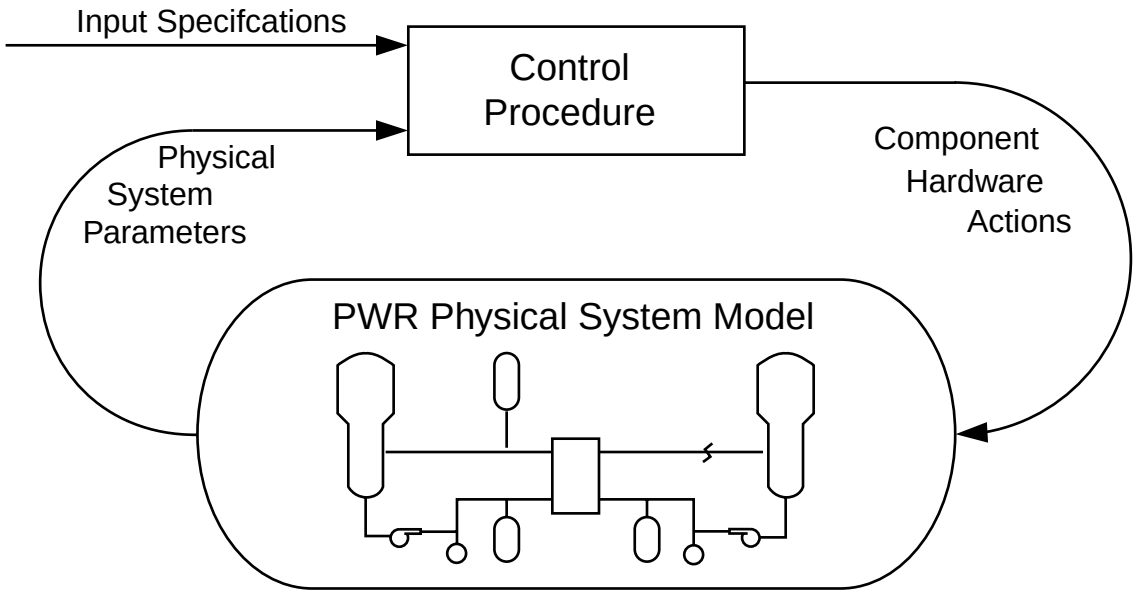

Fig. 2-11. TRAC simulation model of a PWR power plant control system.

Hardware actions that can be adjusted by the control procedure are listed in Table 2-1. The TRAC components to which they are applied are shown along with the variable-name internal letters for defining the action. In addition, the control procedure also implements the use of special time-step data, the editing of restart data dumps, and the termination of the calculation. These are the adjustable features in the TRAC model over which the user can specify control.

All information for defining the control procedure is specified in the input data for application to the general control model. Preparing the input data involves first defining the PWR physical-system model. Each hardware component is modeled by its corresponding TRAC component by specifying appropriate values for the component input parameters. For any of the components in Table 2-1., modeling one of its hardware actions is done as part of preparing the component input data. Implementing a hardware action involves specifying tabular data and associated control parameters for a component action table. Appendix N discusses the detailed form of a general component-action table, including all of its associated control parameters.

TABLE 2-1.
Adjustable Component Hardware
Actions by the Control Procedure

Actions	Components	Variable -Name Letters
Pressure boundary condition and fluid state	BREAK	B
Velocity or mass-flow boundary condition and fluid state	FILL	F
Reactor-core programmed reactivity or power	HEAT STRUCTURE	RPW
Reactor-core axial power shape	HEAT STRUCTURE	ZPW
Energy deposition in the coolant	PIPE, TEE, TURBINE	POW or PW
Energy generation in the wall	PIPE, PUMP, TEE, VALVE	QP3 or QP
Pump rotational speed	PUMP	PMP or OMG
Turbine power demand	TURBINE	TRB or POP
Valve flow-area fraction or relative stem position	VALVE	V

REFERENCES

2-1. Gunol Kocamustafaogullari, "Thermo-Fluid Dynamics of Separated Two-Phase Flow," Ph.D. thesis, Georgia Institute of Technology (December 1971).

2-2. M. Ishii, *Thermo-Fluid Dynamic Theory of Two-Phase Flow* (Collection de la Direction des Etudes et Recherches D'Electricite de France, Eyrolles, Paris, 1975).

2-3. A. E. Bergles, J. S. Collier, J. M. Delhaye, G. F. Hewitt, and F. Mayinger, *Two-Phase Flow and Heat Transfer in the Power and Process Industries* (Hemisphere Publishing Corp., New York; McGraw-Hill Book Co., New York, 1981).

2-4. F. L. Addessio, "A Review of the Development of Two-Fluid Models," Los Alamos National Laboratory report LA-8852 (NUREG/CR-2146) (August 1981).

2-5. H. Bruce Stewart and Burton Wendroff, “Two-Phase Flow: Models and Methods,” *Journal of Computational Physics* 56, 363-409 (1984).

2-6. H. Bruce Stewart, “Stability of Two-Phase Flow Calculation Using Two-Fluid Models,” *Journal of Computational Physics* 33, 259-270 (1979).

2-7. F. H. Harlow and A. A. Amsden, “A numerical fluid dynamics calculation method for all flow speeds,” J. Comput. Phys. 8 (1971) 197-213.

2-8. D. R. Liles and W. H. Reed, “A semi-implicit method for two-phase fluid dynamics,” J. Comput. Phys. 26 (1978) 390-407.

2-9. J. H. Mahaffy, “A stability enhancing two-step method for one-dimensional two-phase flow,” Los Alamos Scientific Laboratory Report LA-7951-MS, US Nuclear Regulatory Commission Report NUREG/CR-0971 (1979).

2-10. J. H. Mahaffy, “A stability-enhancing two-step method for fluid flow calculations,” J. Comput. Phys. 46 (1982) 329-341.

2-11. J. H. Mahaffy, “Numerics of Codes: Stability, Diffusion, Convergence,” Nuclear Engineering and Design, Vol. 145, pp. 131-145 (1993)

2-12. Francis H. Harlow and Anthony A. Amsden, “A Numerical Fluid Dynamics Calculation Method for All Flow Speeds,” *Journal of Computational Physics* 8, 197-213 (1971).

2-13. R. G. Steinke and J. W. Spore, “Conserving Convected Momentum in the TRAC Motion Equation,” The 18th Biennial CUBE Symposium (Albuquerque, New Mexico, November 1988), p. 116.

2-14. R. G. Steinke and J. F. Dearing, “Capacitance Matrix Method in TRAC and MEL-PROG,” American Nuclear Society Topical Meeting on Advances in Nuclear Engineering Computation & Radiation Shielding (Santa Fe, New Mexico, April 1989), Vol. 2, Paper 76.

2-15. G. B. Wallis, *One Dimensional Two-Phase Flow* (McGraw-Hill, Inc., New York, 1969).

2-16. Frank P. Incropera and David P. DeWitt, *Fundamentals of Heat Transfer* (John Wiley & Sons, New York, 1981).

2-17. P. J. Roache, *Computational Fluid Dynamics* (Hermosa Publishers, Albuquerque, New Mexico, 1972).

2-18. H. Akimoto, Y. Abe, and Y. Murao, “Implementation of an Implicit Method into Heat Conduction Calculation of TRAC-PF1/MOD2 Code,” JAERI-memo 01-008 (February 1989).

2-19. G. Yadigaroglu, “The Reflooding Phase of the LOCA in PWRs. Part I: Core Heat Transfer and Fluid Flow,” *Nuclear Safety* 19 (1978).

2-20. Reactor Safety Research Program, “Quarterly Report for the Period July 1–September 30, 1978,” Battelle Pacific Northwest Laboratories report PNL-2653-3 (NUREG/CR-0546) (1978).

2-21. K. E. Carlson, R. A. Riemke, S. Z. Rouhani, R. W. Shumway, and W. L. Weaver, “RELAP5/MOD3 Code Manual, Volume 1: Code Structure, System Models, and Solution Methods (Draft),” Idaho National Engineering Laboratory report EGG-2596 (NUREG/CR-5535) (June 1990).

2-22. R. G. Steinke, “TRAC-P and Bernoulli-Equation Momentum-Convection Terms for the TEE-Component Internal-Junction Cell Interfaces,” Los Alamos National Laboratory report LA-UR-96-3111 (August 1996).

2-23. B. T. Adams, J. F. Dearing, P. T. Giguere, R C. Johns, S. J. Jolly-Woodruff, J. Mahaffy, C. Murray, J. W. Spore, and R. G. Steinke, “TRAC-M/FORTRAN 90 (Version 3.0) Programmer’s Manual,” Los Alamos National Laboratory document LA-UR-00-803 (February 2000).

2-24. R. G. Steinke, V. Martinez, N. M. Schnurr, J. W. Spore, and J. V. Valdez, “TRAC-M Fortran 90 (Version 3.0) User’s Manual,” Los Alamos National Laboratory document LA-UR-00-835 (February 2000).

3.0. TRAC CLOSURE MODELS

Section 3.0. serves as a basic reference or road map to the thermal-hydraulic closure relations in TRAC. Additional detail on TRAC's closure models can be found in the appendices of this document. The relevant appendices are indicated in the following sections.

Before we discuss the closure relations, we will define the nomenclature to be used. In all cases, the subscript *g* (for gas) refers to a mixture of water vapor and noncondensable gas. The subscripts *v* (for vapor) and *a* (for air) denote properties or parameters specifically relating to the water vapor and noncondensable gas, respectively. Similarly, the subscript *l* (for liquid) applies specifically to properties relating to liquid water. In cases of a two-phase mixture, the subscript *m* (for mixture) is applied.

NOMENCLATURE

A:	area
a_i:	interfacial-area concentration
a_{if}:	interfacial area per unit volume
B_{cell}:	cell volume
c:	drag coefficient
C_{an}:	roughness parameter to account for waviness
C_d:	drag coefficient for spherical droplets
c_{Db}:	bubble drag coefficient
C_{eva}:	coefficient of evaporation
c_f:	coefficient of friction
c_p:	specific heat
C_r:	waviness factor
Ca:	capillary number
D, d:	diameter
D_h:	hydraulic diameter
D_o:	diffusion coefficient
e:	internal energy
E:	entrainment fraction
f:	friction factor
F:	adjustment factor
F_e:	evaporation fraction
f_{fo}:	single-phase friction factor
f_l:	liquid fraction contacting wall

F_s: sink function to account for the effect of entrained droplets

F_u: cold-wall fraction

fcdrop: numerical factor

ffd: numerical factor

ffs: numerical factor

g: gravitational acceleration

G: mass flux ($kg \cdot m^{-2} \cdot s^{-1}$)

Gr: Grashof number

h: enthalpy

H: heat-transfer factor

H_{ALV}: liquid-side heat-transfer factor during flashing

H_{ALVE}: liquid-side heat-transfer factor during condensation and evaporation

H_{CHTA}: gas-to-liquid sensible heat-transfer factor

H_{CHTI}: vapor-side heat-transfer factor ($W \cdot K^{-1}$)

h_{fg}: latent heat of vaporization

h_{fls}: liquid-side heat-transfer coefficient associated with flashing

h_{forc}: wall-to-liquid heat-transfer coefficient during single-phase forced convection

h_{gl}: gas-to-liquid sensible heat-transfer coefficient ($W \cdot m^{-2} \cdot K^{-1}$)

h_{gNC}: turbulent natural-convection heat-transfer coefficient

h_{gturb}: turbulent forced-convection heat-transfer coefficient

h_{ig}: interface-to-gas heat-transfer coefficient ($W \cdot m^{-2} \cdot K^{-1}$)

h_{il}: interface-to-liquid heat-transfer coefficient ($W \cdot m^{-2} \cdot K^{-1}$)

H_l: liquid height

h_M: mass-transfer coefficient

h_r: radiation heat-transfer coefficient

h_{wg}: wall-to-gas heat-transfer coefficient

h_{wl}: wall-to-liquid heat-transfer coefficient

h_{wllam}: Rohsenow-Choi correlation heat-transfer coefficient for laminar flow

h_{wlturb}: Dittus-Boelter correlation heat-transfer coefficient for turbulent forced convection

h_Γ: subcooled-boiling heat-transfer coefficient

h'_v: vapor enthalpy of the bulk vapor if the vapor is condensing, or the vapor saturation enthalpy if the liquid is vaporizing

j: superficial velocity

$j_{g,\ bubble}$: terminal bubble rise velocity

k: thermal conductivity, coordinate index, or phase index

L: length

L_l: stratified liquid level

L_o: Laplace coefficient

m: solute concentration in liquid phase

M_i: total interfacial drag force

$N_{\mu g}$: viscosity number

Nu: Nusselt number

P: pressure, or equivalent channel perimeter in Section 3.5.5.6.

P_s: profile slip factor

Pe: Peclet number

Pr: Prandtl number

q: heat-transfer rate per unit volume

q''': internal heat generation within heat structure

q_{CHF}: critical heat flux

q_d: power deposited directly per unit volume

q_{gl}: gas-to-liquid sensible heat transfer per unit volume

q_{ig}: interfacial heat transfer to gas phase per unit volume

q_{il}: interfacial heat transfer to liquid phase per unit volume

q_{min}: heat flux at the minimum stable film-boiling temperature

q_{total}: total wall heat flux

q_{trans}, q_{TR}: total transition-boiling heat flux

q_{wg}: wall-to-gas heat transfer per unit volume

q_{wl}: wall-to-liquid heat transfer per unit volume

r_d: drag radius

R_s: ideal gas constant for steam ($J \cdot kg^{-1} \cdot K^{-1}$)

r_{sm}: Sauter mean radius

Re: Reynolds number

S: suppression factor in Chen correlation

S_i: width of the stratified interface

S_r: slip ratio

Sc: Schmidt number

Sh: Sherwood number

St: Stanton number

t: time

T: temperature

T_{ld}: liquid temperature at the point of bubble detachment

T_{min}: minimum stable film-boiling temperature

T_{NH}: homogeneous nucleation temperature

T_{sv}: saturation temperature corresponding to the vapor partial pressure

V: velocity ($m \cdot s^{-1}$)

V_c: critical Helmholtz velocity

V^*_{max}: maximum dimensionless circulation velocity at the surface of the drop

W, WF: weighting factor

We: Weber number

We_e: effective Weber number

x: mass quality

X: static quality or dummy variable

x_e: equilibrium quality

x_f: flow quality

x_l: liquid mass fraction

X_{TT}: Martinelli factor

Y_b: bubble height

Z: axial elevation

Z_{CHF}: elevation at critical heat flux

α: gas volume fraction (i.e., void fraction)

α_{ag}: void fraction at the agitated / post-agitated IAF regime transition

α_b: bubble volume fraction

α_d: droplet area fraction

α_{dd}: volume fraction of the dispersed droplets

α_{DP}: void fraction at the dispersed (post-agitated) / highly dispersed flow regime transition

α_f: volume fraction of the liquid film

α_g: combined-gas void fraction

α_{gs}: average void fraction in the liquid slug

α_l: liquid fraction

α_{SM}: void fraction at the smooth / rough-wavy IAF regime transition

α_w: wall void fraction

Γ: interfacial mass-transfer rate per unit volume

Γ_i: mass-transfer rate per unit volume from interfacial heat transfer

Γ_{sub}: mass-transfer rate per unit volume from subcooled boiling at a heated wall

Γ^+: maximum of Γ and zero (evaporation or flashing)

Γ^-: minimum of Γ and zero (condensation)

Δx: cell length

δ: vapor-film thickness

δ_f: liquid-film thickness

λ: Taylor wavelength

ε: wall roughness or emissivity

μ: viscosity

ρ: density

σ: surface tension

σ_r: Stefan-Boltzmann constant

τ: shear stress

τ_f: interfacial shear

ξ: wet wall area fraction (transition boiling)

Subscripts

a: noncondensable gas

a: annular film

ag: agitated IAF to post-agitated (dispersed) transition

am: annular-mist flow

B: factor related to the Bromley correlation

b: bubble

bs, bubbly: bubbly slug flow

c, core: core

c, cr, crit: critical

CHF: critical heat flux

churn: churn (transition) flow

cond: condensation

D: factor related to the Denham correlation

d: droplet

dd: dispersed droplets

df: highly dispersed flow

DP: transition between dispersed (post-agitated) and highly dispersed flow regime

dr: factor related to the Dougall-Rohsenow correlation

drop: droplet field

ds:	post-agitated and dispersed flow
evap / cond:	evaporation and / or condensation
f:	film or mist flow
fBB:	factor related to the Bromley correlation
fd:	cold-wall liquid-film flow
forc:	forced convection
fr:	free-stream bubbles
g:	combined-gas mixture
hor:	horizontal
i:	interfacial
inv:	inverted annular flow
l:	liquid
lam:	laminar flow
m:	two-phase mixture
map:	basic flow-regime map
max:	maximum
min:	minimum
mod-CSO:	factor related to the momentum-transfer analogy of Chen, Sundaram, and Ozkaynak
nc:	in the presence of noncondensables
NC:	natural convection
near-wall:	near-wall liquid
nucb:	nucleate boiling
post-ag, pa:	post-agitated (or dispersed) flow
plug:	plug flow
r:	relative
rad:	radial component
rw:	rough-wavy inverted annular flow
s:	steam
sat:	saturation
sb:	subcooled boiling; bubbly and transition flow
sub:	subcooled boiling
slug:	liquid slug
SM, sm:	smooth inverted annular flow
st, strat:	stratified flow
trans, t:	transition (churn) flow

TR, tb:	transition boiling
TP:	two-phase
turb:	turbulent flow
v:	water vapor
w:	wall
W-C:	Webb-Chen correlation
θ:	azimuthal component

3.1. Overview of Closure Relations

With the eight conservation equations presented in Section 2.0., TRAC solves for eight dependent variables: the liquid and gas field velocities (V_l, V_g), the liquid and gas field temperatures (T_l, T_g), void fraction (α); pressure (P), the partial pressure of noncondensables (P_a), and the solute concentration (m). However, to achieve closure on the above equations, numerous other parameters must be specified, many of which are dependent on the specific local conditions. The key variables of interest pertain to interfacial heat transfer and drag, wall heat transfer and drag, interfacial mass transfer, thermodynamic and material properties, and geometry. This section will refine these closure needs further through definitions and brief discussion. Subsequent sections then will detail the individual flow-regime-dependent and heat-transfer-regime-dependent closure models.

Beginning with the combined-gas field, TRAC assumes that Dalton's law applies. In other words, the total pressure is equivalent to the sum of the partial pressures of the water vapor and the noncondensable gas, or

$$P = P_v + P_a \ . \tag{3-1}$$

Also within the combined-gas field, TRAC bases the total gas density and the total gas internal energy on sums of the water vapor and noncondensable components. The total gas density and internal energy thus are expressed by

$$\rho_g = \rho_v + \rho_a \tag{3-2}$$

and

$$\rho_g e_g = \rho_v e_v + \rho_a e_a \ . \tag{3-3}$$

With regard to fluid mass closure, TRAC defines Γ, the interfacial mass-transfer rate per unit volume, as the sum of the mass-transfer rates from interfacial heat transfer and subcooled boiling, or

$$\Gamma = \Gamma_i + \Gamma_{sub} \ . \tag{3-4}$$

The mass-transfer rate caused by interfacial heat transfer is evaluated from the thermal energy jump relation

$$\Gamma_i = \frac{q_{il} + q_{ig}}{(h_g - h_l)} . \tag{3-5}$$

Similarly, the mass-transfer rate from subcooled boiling is defined as

$$\Gamma_{sub} = \frac{h_\Gamma A_w (T_w - T_l)}{B_{cell} (h_g - h_l)} . \tag{3-6}$$

Additional discussion of the interfacial mass-transfer rate terms can be found in Section 3.4.

In terms of fluid energy closure, the heat-transfer rates per unit volume q_{il}, q_{ig}, and q_{gl} are required by either the interfacial mass-transfer jump relation (see previous paragraph), the conservation equations for mixture and combined-gas energy (see Section 2.1.), or both. The interface-to-liquid heat-transfer rate, the interface-to-gas heat-transfer rate, and the liquid-to-gas sensible heat-transfer rate, respectively, are given by the following equations:

$$q_{il} = \begin{cases} (h_{il})_{evaporation/condensation} \cdot A_i \dfrac{(T_l - T_{sv})}{B_{cell}} & T_l \le T_{sat} \\ \dfrac{(h_{il})_{evap/cond} \cdot A_i (T_l - T_{sv}) + (h_{il})_{flashing} \cdot A_i (T_l - T_{sat})}{B_{cell}} & T_l > T_{sat} , \end{cases} \tag{3-7}$$

$$q_{ig} = \frac{P_v}{P} h_{ig} A_i \frac{(T_g - T_{sv})}{B_{cell}} , \tag{3-8}$$

and

$$q_{gl} = \frac{P_a}{P} h_{gl} A_i \frac{(T_g - T_l)}{B_{cell}} . \tag{3-9}$$

The interface-to-liquid heat-transfer equation superimposes a flashing term when the liquid temperature exceeds the saturation temperature based on the total pressure. When the liquid temperature is below the saturation temperature based on total pressure, but is above the saturation temperature corresponding to the water vapor partial pressure, evaporation occurs. Likewise, condensation takes place when the liquid temperature is below the saturation temperature of the steam.

In addition, fluid energy closure requires a definition of the wall-to-liquid and the wall-to-gas heat-transfer rates per unit volume. The wall-to-liquid and the wall-to-gas heat-transfer rates are defined such that

$$q_{wl} = h_{wl} A_w \frac{(T_w - T_l)}{B_{cell}} \tag{3-10}$$

and

$$q_{wg} = h_{wg} A_w \frac{(T_w - T_g)}{B_{cell}} . \tag{3-11}$$

Within individual heat structures, the temperature field is calculated via the classical heat-conduction equation

$$\rho c_p \frac{\partial T}{\partial t} = \nabla \cdot (k \nabla T) + q''' .$$

Finally, coupling between the heat-structure surface and the fluid fields is dependent on the wall temperature defined such that

$$T_w = T(\text{at wall surface}).$$

Using the above definitions, we can quickly sort the remaining parameters for closure into one of four categories: input requirements, thermodynamic and transport fluid properties, material properties, and local-condition-dependent parameters. Within the input requirement category, parameters such as the wall surface area, cell volume, and hydraulic diameter are obtained either directly from or calculated from input geometry. The terms for power deposited directly in the combined-gas or liquid fields likewise are defined through input. For purposes of discussion, the internal heat-generation term for the heat structures also will be treated as input. In reality, the user may specify input data tables or exercise TRAC's point-kinetics model. For additional information on the code's reactor physics modeling, see Appendix M and Ref. 3-1.

Under the category of thermodynamic and transport fluid properties, TRAC provides parameters such as the density, viscosity, thermal conductivity, internal energy, and enthalpy for the liquid, vapor, and noncondensable components. The code also calculates saturation properties for the liquid and vapor components. These properties are obtained from polynomial fits of steam table data for the liquid and vapor and from ideal gas behavior for the noncondensables. For additional detail, see Appendix A.

To solve the heat-conduction equation within a given heat structure, the code requires material property data for density, specific heat, and thermal conductivity. TRAC contains a library of temperature-dependent properties for materials such as mixed-oxide fuel, zircaloy, stainless steel, and Inconel. For additional detail, see Appendix B.

For materials not included in the library, the temperature-dependent properties are obtained through input.

Closure of the equation solution set is approached by defining an additional 10 parameters via constitutive relationships, each of the parameters being dependent on local conditions. The parameters in question are the interfacial area (A_i), the interfacial mass-transfer rate (Γ), the interfacial drag coefficient (c_i), the wall drag coefficients for the liquid and combined-gas fields (c_{wl}, c_{wg}), the interfacial heat-transfer coefficients for the liquid and combined-gas fields (h_{il}, h_{ig}), the heat-transfer coefficient for the liquid-to-gas sensible heat transfer (h_{gl}), and the wall heat-transfer coefficients for the liquid and combined-gas fields (h_{wl}, h_{wg}). Table 3-1. identifies the field equations in which each of the 10 parameters is present. The relationship between closure parameter and field equation is illustrated further by Figs. 3-1a. through 3-1d. In general, TRAC assumes that the local-condition-dependent parameters can be treated in a quasi-steady manner, thereby eliminating time dependencies associated with the closure relationships. The implications of TRAC's quasi-steady assumption are discussed in detail in Appendix D.

Sections 3.2. to 3.8. will outline both the TRAC flow-regime map and the 10 closure parameters listed above. Summaries of the key closure models and correlations for each parameter are presented in Tables 3-2. through 3-7.

Note: TRAC-M/F90 and TRAC-M/F77 Reflood Models. TRAC-M/F90 (Version 3.0) contains a core-reflood model that was brought over from TRAC-PF1/MOD2. TRAC-M/F77, Version 5.5.2, also contains, in addition to this model, a more recent reflood model, with new closure relations, that was developed for analysis of simultaneous top-down/bottom-up quenching. An additional option for the newer model in TRAC-M/F77 allows for use of the closure relations in TRAC-PF1/MOD1 with multiple quench fronts. This document only describes the reflood model that is in TRAC-M/F90 (in this section, and in Appendices F, G, and H). A detailed discussion of the theory and use of the new TRAC-M/F77 top-down/bottom-up reflood model is given in Ref. 3-51. This includes discussion of a new optimization methodology that was developed as part of the TRAC-M/F77 reflood effort. Assessment of the new model is provided in Ref. 3-52. and in the TRAC-M/F77 Developmental Assessment Manual (Refs. 3-53. and 3-54.).

TABLE 3-1.
Requirements for Closure:
Flow/Heat-Transfer Regime-Dependent Parameters

Closure Parameter		Field Equations					
		Mass		Momentum		Energy	
	Applicable Sections	Liquid	Combined Gas	Liquid	Combined Gas	Total	Combined Gas
A_i	(3.3., F.1.)	X	X	X	X		X
Γ	(3.4., F.1., G)	X	X	X	X		X
c_i	(3.5., H.1.)			X	X		
c_{wl}	(3.6., H.2.)			X			
c_{wg}	(3.6., H.2.)				X		
h_{il}	(3.7., F.1.)	X	X	X	X		X
h_{ig}	(3.7., F.1.)	X	X	X	X		X
h_{gl}	(3.7., F.1.)						X
h_{wl}	(3.8., F.2.)	X	X	X	X	X	X
h_{wg}	(3.8., F.2.)					X	X

A_i = interfacial area.
Γ = interfacial mass-transfer rate.
c_i = interfacial drag coefficient.
c_{wl} = wall drag coefficient (liquid phase).
c_{wg} = wall drag coefficient (gas phase).
h_{il} = interface-to-liquid heat-transfer coefficient.
h_{ig} = interface-to-gas heat-transfer coefficient.
h_{gl} = gas-to-liquid sensible heat-transfer coefficient.
h_{wl} = wall-to-liquid heat-transfer coefficient.
h_{wg} = wall-to-gas heat-transfer coefficient.

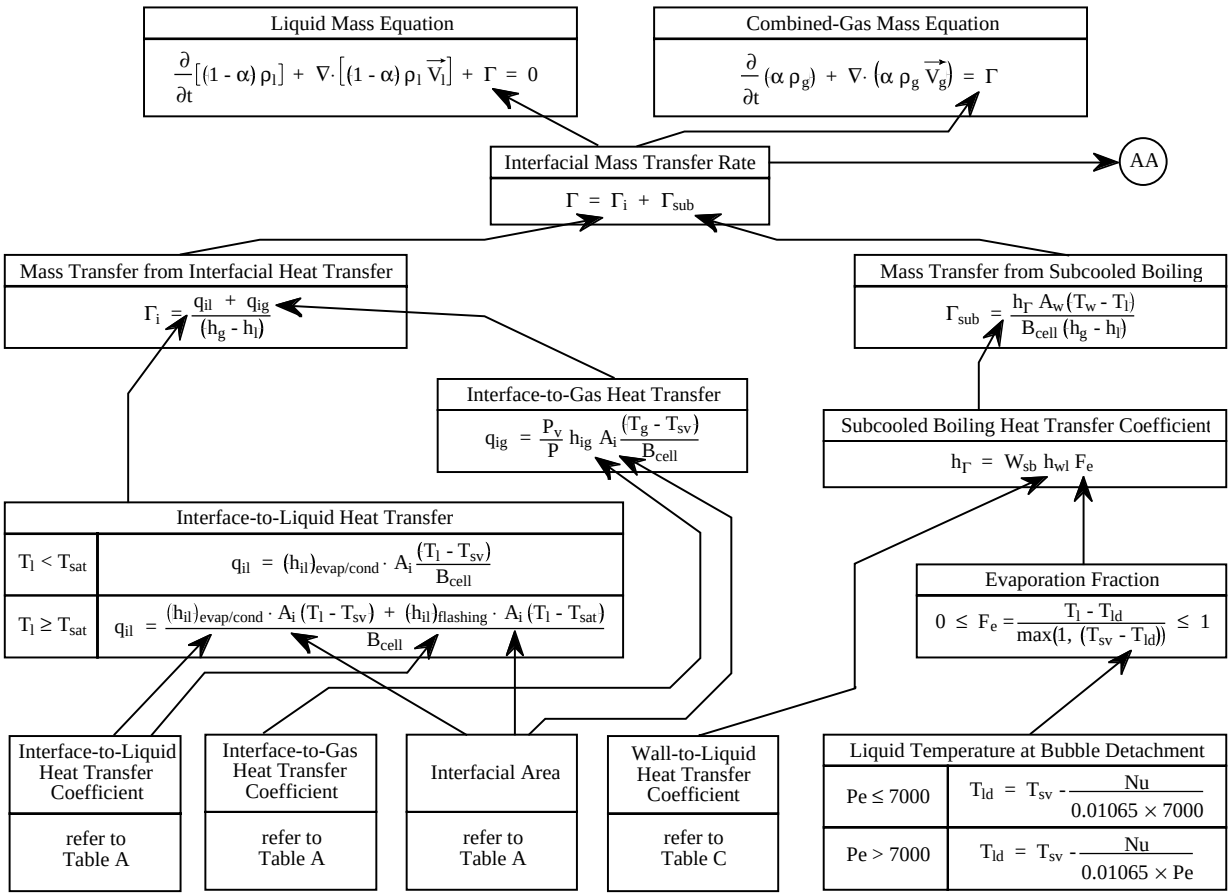

Fig. 3-1a. Mapping of regime-dependent parameters—liquid and combined-gas mass equations.

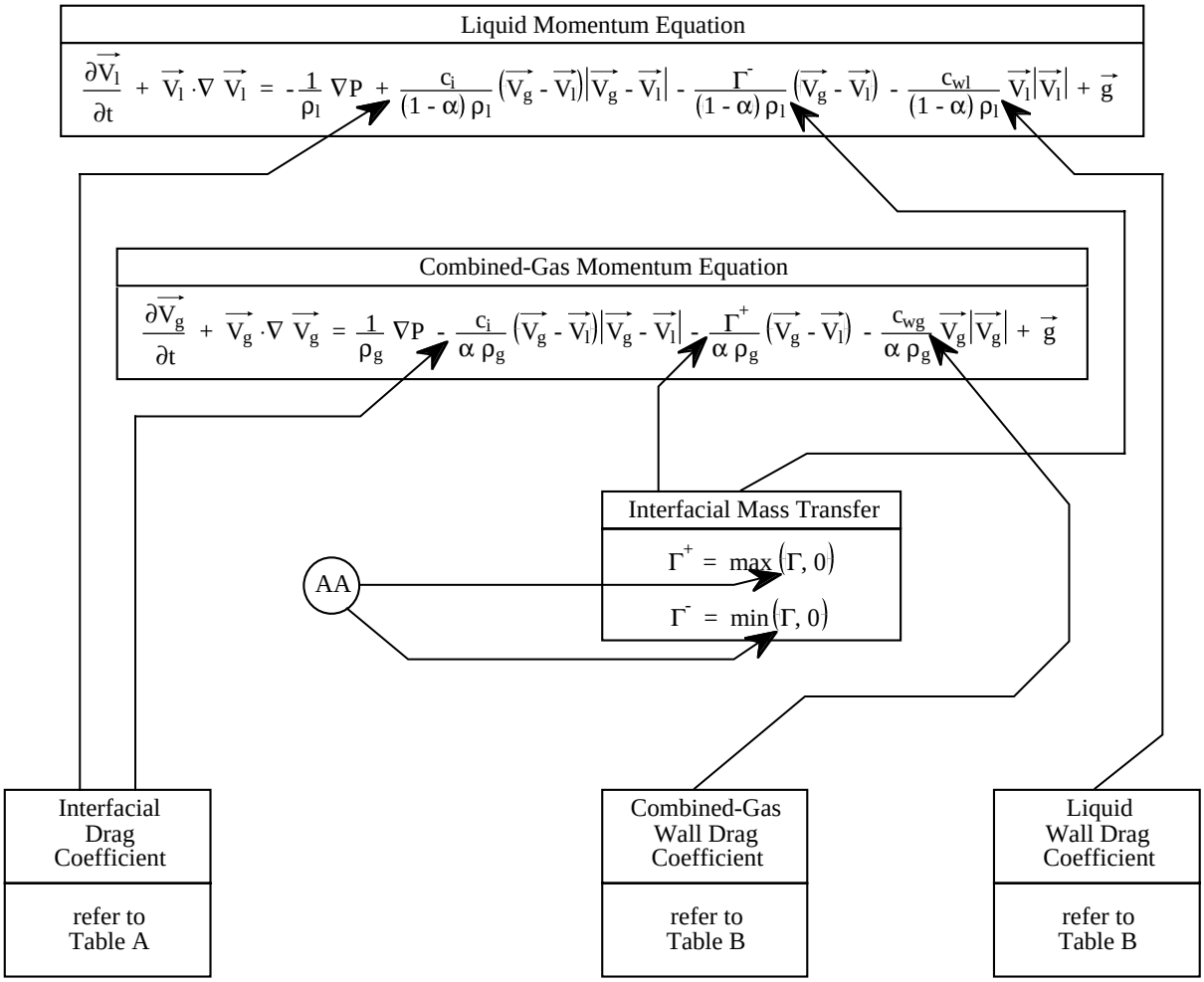

Fig. 3-1b. Mapping of regime-dependent parameters—liquid and combined-gas momentum equations.

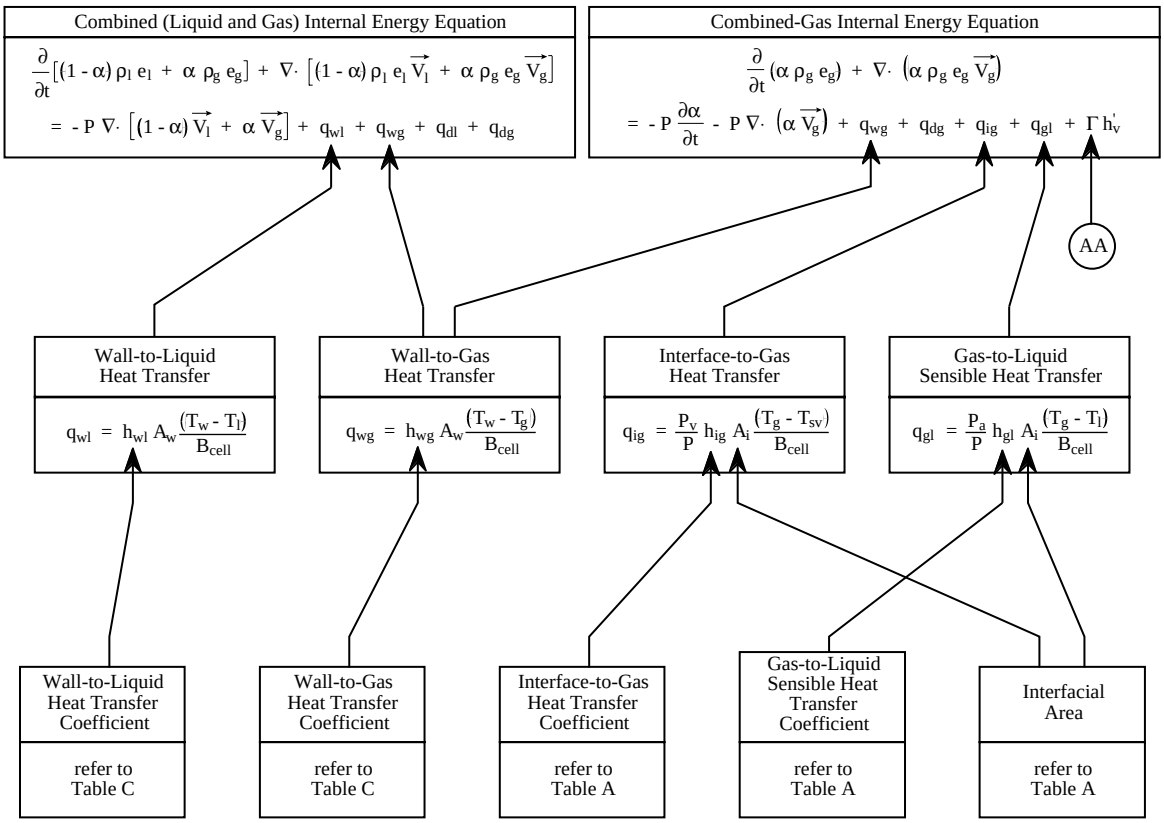

Fig. 3-1c. Mapping of regime-dependent parameters—total and combined-gas energy equations.

Table A:

Flow Regime	Section Numbers		
	A_i	c_i	h_{il}, h_{ig}, and h_{gl}
Bubbly Slug (1)[a]	3.3.1., F.1.1.1.	3.5.1., H.1.1.	3.7.1., F.1.1.
Churn (2)	3.3.2., F.1.3.	3.5.2., H.1.4.	3.7.2., F.1.3.
Annular-Mist (1)	3.3.3., F.1.2.1.	3.5.3., H.1.2.	3.7.3., F.1.2.
Stratified (3)	3.3.4., F.1.4.1.	3.5.4., H.1.3.	3.7.4., F.1.4.
Plug (3)	3.3.5., F.1.5.1.		3.7.5., F.1.5.
Reflood (4)	3.3.6., F.1.6.	3.5.5., H.1.5.	3.7.6., F.1.6.
Presence of Noncondensables (4)			3.7.7., F.1.7.

a. "Bubbly Slug" here is a collective term for the bubbly, bubbly slug, and bubbly slug transition regimes.

Table B:

Flow Regime	Section Numbers c_{wl} and c_{wg}
Single-Phase	3.6.1., H.2.
Two-Phase	3.6.2., H.2.
Horizontal Stratified	3.6.3., H.2.1.2.

Table C:

Heat-Transfer Regime	Section Numbers h_{wl} and h_{wg}
Natural Convection to Liquid	3.8.1., F.2.1.1., F.2.2.1.
Forced Convection to Liquid	3.8.2., F.2.1.1., F.2.2.1.
Nucleate Boiling (5)	3.8.3., F.2.1.2., F.2.2.2.
Transition Boiling (5)	3.8.5., F.2.1.3., F.2.2.3.
Film Boiling	3.8.7., F.2.1.4., F.2.2.4.
Single-Phase Vapor	3.8.8., F.2.1.5., F.2.2.5.
Condensation	3.8.9., F.2.1.6., F.2.2.6.
Two-Phase Forced Convection (6)	3.8.10., F.2.1.7., F.2.2.7.

Notes:
(1) Basic Flow Map
(2) Interpolation Regime
(3) Superimposed on Basic Map
(4) Specialized Regime
(5) Includes differentiated core reflood model

Fig. 3-1d. Mapping of flow / heat-transfer regime-dependent parameters—applicable document sections.

TABLE 3-2.
TRAC Closure Relation Summary:
Flow-Regime Criteria and Interfacial Area

Flow Regime	Flow-Regime Criteria	Interfacial Area (A_j)
Bubbly Flow	$\alpha \le 0.3$ or $\alpha \le 0.5$ and $G \ge 2700$ kg / m^2-s	based on Ishii and Mishima (Ref. 3-6.)
Bubbly Slug Transition	$0.3 < \alpha \le 0.5$ and $2000 < G < 2700$ kg / m^2-s	based on Ishii and Mishima (Ref. 3-6.)
Bubbly Slug Flow	$0.3 < \alpha \le 0.5$ and $G \le 2000$ kg / m^2-s	based on Ishii and Mishima (Ref. 3-6.)
Churn Flow	$0.5 < \alpha \le 0.75$	weighted average of bubbly slug and annular-mist interfacial areas
Annular-Mist Flow	$\alpha > 0.75$	superimpose film and droplet fields; droplet area based on the droplet diameter defined by Kataoka (Ref. 3-10.) or Kitscha and Kocamustafaogullari (Ref. 3-11.) and on the entrainment fraction of Ishii and Mishima (Ref. 3-9.); film area based on geometry and entrainment fraction
Transition to Stratified Flow	1D components: gas (or liquid) velocity between one and ten times the critical velocity 3D components: gas velocity between one and two times the critical velocity	weighted average of stratified-flow and basic flow-regime-map interfacial areas
Stratified Flow	1D components: critical velocity criteria 3D vessel: horizontal stratified flow uses critical relative velocity of Mishima and Ishii; (Ref. 3-2.) vertical stratified flow uses terminal bubble rise velocity criterion	interfacial area for horizontal stratified flow based on circular pipe geometry; interfacial area for vertical stratified flow based on average cross-sectional area
Plug Flow	liquid side under condensation mode; void fraction (over three contiguous cells) must satisfy plugging criterion	based on circular pipe geometry
Reflood: Bubbly Flow	transition to IAF defined by mechanistic elevation model based on critical heat flux, film-boiling heat flux, and void fraction	defined as above
IAF	flow regime defined by mechanistic elevation models based on capillary number and limited by a range of void fractions	based on liquid-core geometry

TABLE 3-2. (cont)
TRAC Closure Relation Summary:
Flow-Regime Criteria and Interfacial Area

Flow Regime	Flow-Regime Criteria	Interfacial Area (A_j)
Dispersed Flow	flow regime defined by mechanistic elevation model based on capillary number and limited by a range of void fractions	superimpose droplet and film fields (similar to annular-mist-flow regime); droplet area based on the droplet diameter defined by Kataoka or Kitscha and Kocamustafaogullari (Ref. 3-11.); film area based on geometry and the stable liquid-film thickness

TABLE 3-3.
TRAC Closure Relation Summary:
Interfacial Mass Transfer

Total Interfacial Mass-Transfer Rate (Γ)	Sum of the mass-transfer rates from interfacial heat transfer and subcooled boiling
Mass Transfer Caused by Interfacial Heat Transfer (Γ_i)	Based on the sum of the interface-to-gas and interface-to-liquid heat-transfer rates
Mass Transfer Caused by Subcooled Boiling (Γ_{sub})	Based on Lahey's mechanistic model (Ref. 3-14.) for the evaporation fraction and on the modified Saha-Zuber OSV (onset of significant voiding) correlation (Ref. 3-15.) (**Note:** This model is used only when the subcooled-boiling heat-transfer coefficient is nonzero)

TABLE 3-4.
TRAC Closure Relation Summary:
Interfacial Drag

Flow Regime	Interfacial Drag Coefficient (c_i)
Bubbly Flow, Bubbly Slug Flow, Bubbly Slug Transition	Defined as per Ishii and Chawla (Ref. 3-16.) (bubble diameter and profile slip based on Ishii; (Ref. 3-7.) bubble drag coefficient for three Reynolds number regimes based on Stokes drag law, the empirical relation proposed by Schiller and Nauman, (Ref. 3-17.) and the recommendation of Bird, Stewart, and Lightfoot (Ref. 3-18.)
Churn Flow	Weighted average of bubbly slug and annular-mist interfacial drag coefficients
Annular-Mist Flow	Based on drift velocity developed by Kataoka and Ishii (Ref. 3-12.) and total interfacial shear force defined as per Ishii and Mishima (Ref. 3-6.) (film interface friction factor obtained from Wallis (Ref. 3-20.); droplet diameter based on Kataoka, Ishii, and Mishima (Ref. 3-10.); droplet drag coefficient based on Ishii and Chawla (Ref. 3-16.); entrainment based on Kataoka and Ishii (Ref. 3-12.)
Transition to Stratified Flow	Weighted average of stratified and flow-regime map interfacial drag coefficients
Stratified Flow	Derived from the method of Taitel and Dukler (Ref. 3-21.) (interfacial friction factor based on Ohnuki et al. (Ref. 3-22.)
Plug Flow	No specific model for interfacial drag
Reflood: Subcooled Boiling	Composed of the drag coefficient from bubbles at the wall (based on the Colebrook turbulent friction factor) and by the drag coefficient from free-stream bubbles (based on Ishii (Ref. 3-7.)
Smooth IAF	Based on smooth tube friction factor correlations (laminar and turbulent flow)
Rough-Wavy IAF	Based on Colebrook friction factor for rough walls (relative roughness based on Ishii entrained droplet diameter (Ref. 3-17.)
Agitated IAF	Same as rough-wavy IAF
Post-Agitated (Dispersed) Flow	Weighted average of agitated IAF and highly dispersed interfacial drag coefficients
Highly Dispersed Flow	Composed of separate droplet and film terms; droplet interfacial drag based on form drag of Ishii and Chawla (Ref. 3-16.) and on Ishii (Ref. 3-7.) droplet size; film interfacial drag based on modified Wallis friction factor (film thickness derived by Pasamehmetoglu (Ref. 3-13.)

TABLE 3-5.
TRAC Closure Relation Summary:
Wall Drag

Model Type	Wall-to-Liquid Drag Coefficient (c_{wl})	Wall-to-Gas Drag Coefficient (c_{wg})
Single-Phase	Single-phase liquid: based on the modified friction-factor correlation (Ref. 3-25.) Single-phase vapor: zero	Single-phase liquid: zero Single-phase vapor: based on the modified Churchill friction-factor correlation (Ref. 3-25.)
Two-Phase, Homogeneous	Based on the modified Churchill friction-factor correlation (Ref. 3-25.) using the two-phase mixture Reynolds number	Based on the modified Churchill friction-factor correlation (Ref. 3-25.) using the two-phase mixture Reynolds number
Two-Phase, Horizontal Stratified	Laminar flow: based on fully developed laminar friction-factor relation Turbulent flow: based on McAdams friction-factor correlation	Laminar flow: based on fully developed laminar friction-factor relation Turbulent flow: based on McAdams friction-factor correlation

TABLE 3-6.
TRAC Closure Relation summary:
Interfacial Heat Transfer

Flow Regime	Interface-to-Liquid Heat-Transfer Coefficient (h_{il})	Interface-to-Gas Heat-Transfer Coefficient (h_{ig})	Liquid-to-Gas Sensible Heat-TransferCoefficient (h_{gl})
Bubbly Flow, Bubbly Slug Flow, Bubbly Slug Transition	Condensation or evaporation: based on the Chen and Mayinger (Ref. 3-26.) and the Whittaker (Ref. 3-27.) Nusselt number correlations Flashing: based on liquid superheat Subcooled boiling: h_{il} is weighted to include Lahey and Moody model (Ref. 3-28.)	1000 W / m^2-K	1000 W / m^2-K
Churn Flow	Cond / evap: based on weighted average of annular-mist and bubbly slug heat-transfer factors Flashing: based on maximum of weighted heat-transfer factor and liquid superheat relation	Based on weighted average of annular-mist and bubbly slug heat-transfer factors	Based on weighted average of annular-mist and bubbly slug heat-transfer factors
Annular-Mist Flow	Cond / evap: superimpose droplet and film field Droplet field: based on transient conduction solution (Ref. 3-29.) Film field: based on Bankoff correlation for Stanton number (Ref. 3-32.) Flashing: based on maximum of weighted heat-transfer factor and liquid superheat relation	Superimpose droplet and film field Droplet field: based on Ryskin correlation for Nusselt number (Ref. 3-31.) Film field: based on Bankoff correlation for Stanton number (Ref. 3-32.)	Superimpose droplet and film field Droplet field: based on Ryskin correlation for Nusselt number (Ref. 3-31.) Film field: based on Bankoff correlation for Stanton number (Ref. 3-32.)

TABLE 3-6. (cont)
TRAC Closure Relation summary:
Interfacial Heat Transfer

Flow Regime	Interface-to-Liquid Heat-Transfer Coefficient (h_{il})	Interface-to-Gas Heat-Transfer Coefficient (h_{ig})	Liquid-to-Gas Sensible Heat-TransferCoefficient (h_{gl})
Transition to Stratified Flow	Cond / evap: weighted average of stratified and flow-regime-map heat-transfer factors Flashing: based on maximum of weighted heat-transfer factor and liquid superheat relation	Heat-transfer factor equivalent to value calculated from basic flow-regime map	Heat-transfer factor equivalent to value calculated from basic flow-regime map
Stratified Flow	Cond / evap: based on Linehan Stanton number relation (Ref. 3-33.) Flashing: based on maximum of weighted heat-transfer factor and liquid superheat relation	Heat-transfer factor equivalent to value calculated from basic flow-regime map	Heat-transfer factor equivalent to value calculated from basic flow-regime map
Plug Flow	Condensation: weighted average of flow-regime-map, stratified, and plug-flow heat-transfer factors (plug-flow HTC is calculated from a constant Stanton number model)	Heat-transfer factor equivalent to value calculated from basic flow-regime map	Heat-transfer factor equivalent to value calculated from basic flow-regime map
Reflood: Bubbly Flow	Cond / evap: weighted average of bubbly, IAF, and dispersed-flow heat-transfer factors Defined as above, this table	Weighted average of bubbly, IAF, and dispersed-flow heat-transfer factors Defined as above, this table	Weighted average of bubbly, IAF, and dispersed-flow heat-transfer factors Defined as above, this table
IAF	Based on HTVSSL model for subcooled liquid Kinetic theory of evaporation for flashing (Ref. 3-34.)	$3x10^3$ W / m^2-K	10^3 W / m^2-K

TABLE 3-6. (cont)
TRAC Closure Relation summary:
Interfacial Heat Transfer

Flow Regime	Interface-to-Liquid Heat-Transfer Coefficient (h_{il})	Interface-to-Gas Heat-Transfer Coefficient (h_{ig})	Liquid-to-Gas Sensible Heat-TransferCoefficient (h_{gl})
Dispersed Flow	Heat-transfer factor equivalent to IAF value Flashing: based on maximum of above evap / cond factor and liquid superheat relation	Based on Unal (Ref. 3-34.) model	Weighted average of Ryskin (Ref. 3-31.) and Bankoff (Ref. 3-32.) models
Effect of Noncondensables	Evaporation: heat-transfer factor calculated by flow-regime-independent diffusion model Condensation: heat-transfer factor adjusted using model of Sklover and Rodivilin (Ref. 3-35.)	No modification	No modification

TABLE 3-7.
TRAC Closure Relation Summary:
Wall-to-Fluid Heat Transfer

Heat-Transfer Regime	Wall-to-Liquid Heat-Transfer Coefficient (h_{wl})	Wall-to-Gas Heat-Transfer Coefficient (h_{wg})
Natural Convection to Liquid	Laminar and turbulent natural-convection correlations (Ref. 3-36.)	zero
Forced Convection to Liquid	Dittus-Boelter correlation (Ref. 3-37.)	zero
Nucleate Boiling	Based on the total heat flux [as determined by the Chen correlation (Ref. 3-38.)} minus the wall-to-gas heat flux	Maximum of either the natural-convection (Ref. 3-40.) or Dougall-Rohsenow (Ref. 3-28.)correlations
Critical Heat Flux	Biasi correlation (Ref. 3-41.)	Biasi correlation (Ref. 3-41.)
Transition Boiling	Based on the total heat flux minus the wall-to-gas heat flux (the total heat flux is a weighted average of q_{CHF}, calculated via Biasi, and q_{min}, which is based on natural-convection (Ref. 3-40.), Dougall-Rohsenow (Ref. 3-28.), modified Bromley (Ref. 3-43.), and radiation heat-transfer coefficients) reflood model: total heat flux based on exponential decrease from q_{CHF} to q_{film}	Maximum of either the natural-convection (Ref. 3-40.) or Dougall-Rohsenow (Ref. 3-28.) correlations reflood model: Webb-Chen correlation (Ref. 3-44.)
Minimum Stable Film-Boiling Temperature	Based on the Fauske homogeneous nucleation temperature (Ref. 3-46.)	Based on the Fauske homogeneous nucleation temperature (Ref. 3-46.)
Film Boiling	Based on the modified Bromley film-boiling heat-transfer coefficient (Ref. 3-43.) and a radiation term Reflood model: based on the Denham (Ref. 3-47.) and modified Bromley (Ref. 3-43.) correlations and a radiation term	Maximum of either the natural-convection (Ref. 3-40.) or Dougall-Rohsenow (Ref. 3-28.) correlations Reflood model: based on Webb-Chen correlation (Ref. 3-44.)
Single-Phase Vapor	Zero	Maximum of the turbulent natural-convection correlation and either the Sieder-Tate (Ref. 3-18.) or Dittus-Boelter (Ref. 3-37.) correlations
Condensation	Zero or the maximum of the laminar natural-convection, turbulent natural-convection, and Chen (Ref. 3-38.) ($S = 0$) correlations	Based on Nusselt, turbulent natural-convection (Ref. 3-48.) and turbulent forced-convection (Ref. 3-36.) correlations

TABLE 3-7. (cont)
TRAC Closure Relation Summary:
Wall-to-Fluid Heat Transfer

Heat-Transfer Regime	Wall-to-Liquid Heat-Transfer Coefficient (h_{wl})	Wall-to-Gas Heat-Transfer Coefficient (h_{wg})
Two-Phase Forced Convection	Maximum of the Rohsenow-Choi (Ref. 3-49.) and Dittus-Boelter (Ref. 3-37.) correlations	Zero or the maximum of the turbulent natural-convection (Ref. 3-36.) and Dittus-Boelter (Ref. 3-37.) correlations

3.2. Flow-Regime Map

The flow-regime map in TRAC is not used directly by the field equations presented in Section 2.0. Nonetheless, each of the closure models for interfacial mass, momentum, and energy transfer are dependent on the local fluid conditions, including flow regime. The determination of flow regime thus is an important intermediate calculation for evaluating the respective interfacial parameters.

TRAC adopts a very simple flow-regime map that generally is assumed to apply for both vertical and horizontal flow geometries. The basic flow-regime map consists of bubbly flow, bubbly slug flow, bubbly slug transition, churn-flow, and annular-mist-flow regions. These regions are displayed graphically in mass-flux/void-fraction space in Fig. 3-2. In addition, the specialized flow regimes of stratified flow and plug flow may be superimposed on the basic flow-regime map, subject to certain physical and phenomenological criteria. The code also includes specialized flow-regime models to represent the post-critical-heat-flux (CHF) behavior under core reflood conditions.

The following sections will outline the various flow regimes modeled by TRAC and their respective existence criteria. A summary of the flow-regime criteria also is presented in Table 3-2. Additional details, including the basis for the flow-regime map, a description of the flow-regime models as coded, and assessment of the map, are given in Appendix E.

3.2.1. Bubbly Slug Flow

In discussing the bubbly slug flow regime, this section will collectively refer to the bubbly, bubbly slug transition, and bubbly slug flow regimes depicted in Fig. 3-2. Bubbly flow can be characterized by the combined-gas phase being distributed as individual bubbles in a continuous liquid phase. The bubbly flow regime is defined to exist when the void fraction (α) is ≤0.3 for all mass fluxes (G). Bubbly flow also exists when $\alpha \leq 0.5$ and $G \geq 2700$ kg/m^2-s. However, when the void fraction drops below 1.0×10^{-6}, the flow is assumed to be single-phase liquid.

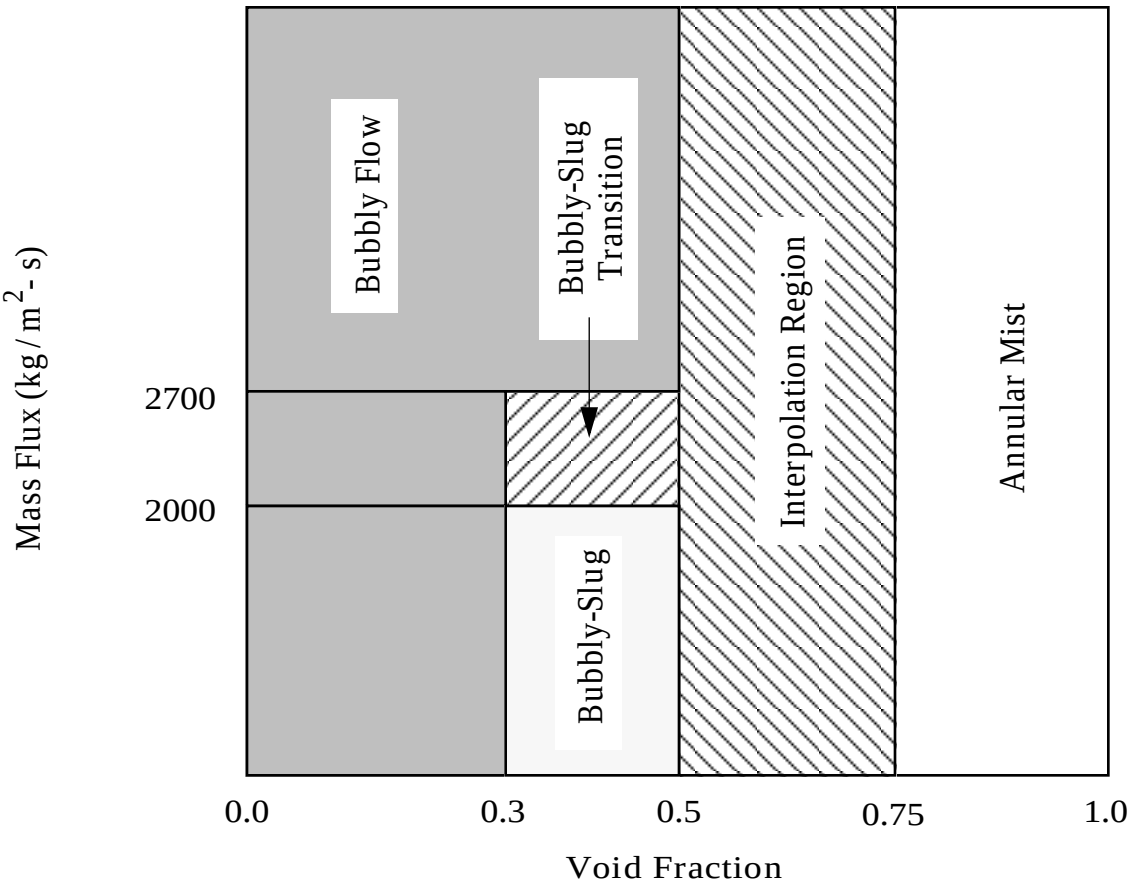

Fig. 3-2. TRAC flow-regime map.

Bubbly slug flow, or slug flow, is characterized by large combined-gas bubbles that are separated from the channel wall by a thin liquid film. The large bubbles are separated from one another by liquid slugs that may contain smaller entrained gas bubbles. In TRAC, the bubbly slug regime is defined to exist for $0.3 < \alpha \leq 0.5$ and $G \leq 2000$ kg / m^2-s.

The bubbly slug transition regime is defined to exist for $0.3 < \alpha \leq 0.5$ and $2000 < G < 2700$ kg / m^2-s. It serves as a interpolation regime between bubbly and slug flows.

3.2.2. Churn Flow

Churn flow (also referred to as transition flow) exists for void fractions in the range of $0.5 < \alpha \leq 0.75$. Physically, this flow regime is characterized by the breakup of the large vapor bubbles associated with slug flow. However, TRAC does not include any churn-flow-specific closure models. Rather, it treats churn flow as an interpolation regime between void-fraction values of 0.5 and 0.75. The interfacial-drag and heat-transfer closure parameters for churn flow are calculated as a weighted average of the appropriate bubbly slug and annular-mist values.

3.2.3. Annular-Mist Flow

For void fractions >0.75, the annular-mist-flow regime is assumed to be present. Annular-mist flow is characterized by a liquid film adjacent to the channel wall, a continuous central gas core, and entrained liquid droplets dispersed within the central gas core. However, with void fractions >0.999999, the flow is assumed to be single-phase vapor.

3.2.4. Stratified Flow

At low liquid and vapor velocities, the individual phases may separate (stratify) and form a relatively smooth interface. Thus, subject to critical velocity criteria, TRAC superimposes the stratified-flow regime on the basic flow-regime map described in Sections 3.2.1. through 3.2.3. For a given closure parameter of interest, the transition to stratified flow is accomplished by a weighted average of the parameter value from the appropriate flow-regime-map model and the stratified-flow model. This transition can be expressed by

$$X_{map,st} = (1 - W_{st})X_{map} + W_{st}X_{st} , \tag{3-12}$$

where X is the closure parameter of interest and W_{st} is the stratified-flow weighting factor.

In 1D components, the weighting factors for both vertical and horizontal stratified flow are void-fraction dependent. For transitions from bubbly slug flow to stratified flow ($\alpha \leq 0.5$), the weighting factor is calculated by

$$0 \leq W_{st,bubbly} = \frac{1}{9}\left(10 - \frac{V_l}{V_{l,cr}}\right) \leq 1 \tag{3-13}$$

for the critical velocity

$$V_{l,cr} = \frac{0.2}{(1 - \alpha)} . \tag{3-14}$$

It is evident that this weighting factor will be nonzero for liquid velocities between 1 and 10 times the critical velocity. Once the liquid velocity is less than or equal to the critical velocity, the flow becomes fully stratified. For transitions between annular-mist and stratified flow ($\alpha > 0.75$), the weighting factor is calculated by

$$0 \leq W_{st,am} = \frac{1}{9}\left(10 - \frac{V_g}{V_{g,cr}}\right) \leq 1 \tag{3-15}$$

for the critical velocity

$$V_{g,cr} = \frac{1}{\alpha} \cdot \left[\frac{0.2}{V_l (1 - \alpha)}\right]^{0.435} . \tag{3-16}$$

In this case, the flow becomes fully stratified when the gas velocity is less than or equal to the critical velocity presented in the previous equation. Additionally, for transitions from churn flow to stratified flow ($0.5 < \alpha \leq 0.75$), the weighting factor is calculated by

$$W_{st,churn} = \left(\frac{0.75 - \alpha}{0.25}\right) W_{st,bubbly} + \left(\frac{\alpha - 0.5}{0.25}\right) W_{st,am} \ . \tag{3-17}$$

For horizontal stratification to occur, 1D components also are subject to the constraint that their inclination must be within ±10 degrees of horizontal.

In a 3D vessel component, the stratification criteria are evaluated separately for the horizontal plane (horizontal stratified flow) and along the vertical axis (vertical stratified flow). In the horizontal plane, the weighting factor is calculated such that

$$0 \leq W_{st} = \left(2 - \frac{V_{g,hor}}{V_{r,cr}}\right) \leq 1 \ . \tag{3-18}$$

In this case, the horizontal gas velocity ($V_{g,hor}$) is defined as a function of the radial and azimuthal velocity components, where

$$V_{g,\,hor} = \sqrt{V_{g,\,rad}^2 + V_{g,\,\theta}^2} \ . \tag{3-19}$$

The relative critical velocity is calculated from the model of Mishima and Ishii (Ref. 3-2.), given by

$$V_{r,cr} = 0.487 \sqrt{\frac{g\,(\rho_l - \rho_g)\,(D_h - H_l)}{\rho_g}} \ , \tag{3-20}$$

where H_l is the liquid height and D_h is the hydraulic diameter. Within the 3D vessel component, the void fractions at upper and lower consecutive levels also must satisfy the criterion that the upper void fraction be >0.9 and the lower void fraction be <0.1. Otherwise, W_{st} is set to zero. Also for vessels, the term $(D_h - H_l)$ in Eq. (3-20) is replaced by the arithmetic average of the axial widths of the two levels.

Along the vertical axis of a 3D component, the stratified-flow weighting factor is calculated by

$$0 \leq W_{st} = \left(2 - \frac{|j_g|}{j_{g,bubble}}\right) \leq 1 \ . \tag{3-21}$$

In the equation above, the terminal bubble rise velocity is evaluated by

$$j_{g,bubble} = \frac{\alpha}{1 - C_0\,\alpha} \cdot \sqrt{2} \cdot \left[\frac{g\,\sigma\,(\rho_l - \rho_g)}{\rho_l^2}\right]^{1/4} \tag{3-22}$$

for

$$C_0 = 1.2 + 0.2\sqrt{\frac{\rho_g}{\rho_1}} \tag{3-23}$$

and with $\alpha = 0.3$. The void-fraction criterion for consecutive levels (discussed above) also must be satisfied for vertical stratified flow. For additional detail, see Appendix E, Section E.2.7.

3.2.5. Plug Flow

Plug flow in horizontal flow channels is roughly analogous to slug flow in a vertical channel. However, the code uses the plug-flow regime only for interfacial heat-transfer purposes. The other closure parameters are based on the basic flow-regime/stratified-flow map. For plug flow to exist, TRAC requires that the liquid side be in condensation ($T_l < T_{sv}$). The existence of plug flow further is limited by the void fraction in three consecutive cells. The code contains logic to check that at least one of the three cells has a void fraction >0.50 but <0.75. If both the condensation and void-fraction criteria are met, TRAC superimposes the plug-flow regime on the bubbly slug/churn/annular-mist/stratified-flow regimes through the use of a weighting factor. The weighting factor W_{plug} is defined in Section 3.3.5. The superposition methodology is presented in Section 3.3.5. and 3.7.5. Additional detail is available in Appendix F, Section F.1.5.

3.2.6. Reflood

The reflood flow-regime model is included in TRAC to simulate the post-CHF behavior of the fluid in a reactor core during the refill and reflood phase of a LOCA. Based on the observations of Ishii and his coworkers (Refs. 3-3. to 3-5.), the reflood model is divided into several discrete regimes. Moving downstream from the point at which the critical heat flux occurs, these regimes are identified as transition boiling, smooth inverted annular flow, rough-wavy inverted annular flow, agitated inverted annular flow, dispersed (or post-agitated) flow, and highly dispersed flow (see Fig. 3-3.). As the name suggests, smooth inverted annular flow (IAF) is characterized by a vapor film near the heated wall and a stable liquid core central to the flow channel. Rough-wavy IAF likewise is characterized by a fairly stable liquid core; however, in this case, the interface has become rough. In agitated IAF, the central liquid core begins to break up into large slugs. Both the dispersed and highly dispersed regimes are characterized by the presence of individual liquid droplets dispersed through a continuous gas phase. However, a liquid film is allowed to form in the dispersed regimes if a cold wall is adjacent to the hydraulic cell.

The transitions between flow regimes are taken from the work of Obot and Ishii (Ref. 3-5.) and are based largely on the capillary number

$$Ca = \frac{\mu_l V_l}{\sigma} . \tag{3-24}$$

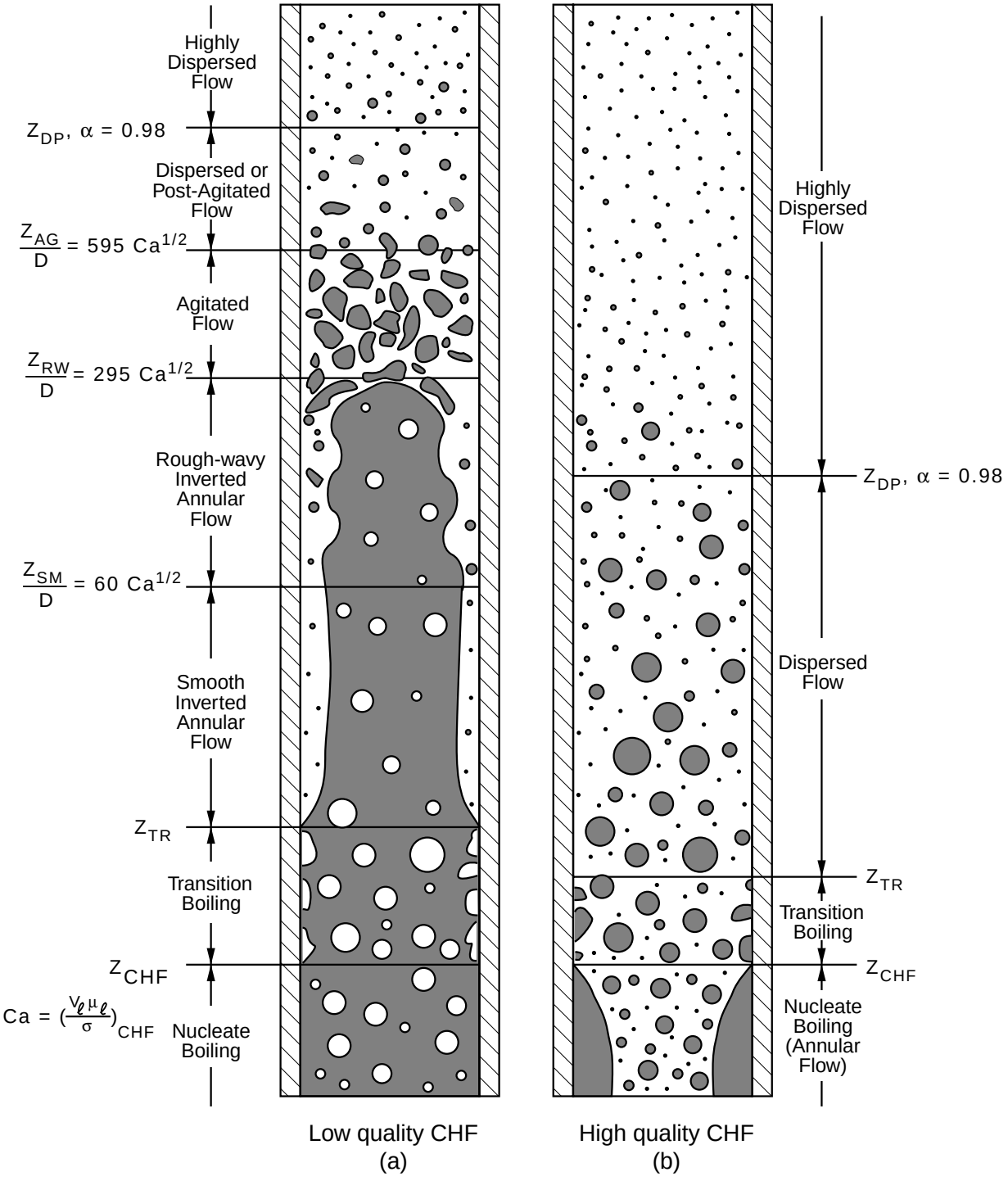

Fig. 3-3. Reflood flow regimes.

In terms of elevation above the quench front, Obot and Ishii define the transition between smooth and rough-wavy IAF as occurring at

$$\frac{L}{D} = 60 \cdot Ca^{1/2} . \quad (3\text{-}25)$$

The transition from rough-wavy to agitated IAF similarly is defined by

$$\frac{L}{D} = 295 \cdot Ca^{1/2} . \quad (3\text{-}26)$$

From agitated IAF to dispersed flow (post-agitated IAF), the transition criterion is

$$\frac{L}{D} = 595 \cdot Ca^{1/2} . \quad (3\text{-}27)$$

The TRAC implementation of the above criteria includes additional constraints based on void fraction to force the IAF regimes to occur within certain void-fraction ranges. These constraints assume that each IAF regime occurs in the following void-fraction ranges:

smooth IAF	$0.05 < \alpha < 0.3$
rough-wavy IAF	$0.3 < \alpha < 0.4$
agitated IAF	$0.4 < \alpha < 0.75$
post-agitated IAF	$0.75 < \alpha < 0.98$
highly dispersed flow	$\alpha > 0.98$.

Additionally, the transition from transition boiling to smooth inverted annular flow is defined as a function of the critical heat flux, the film-boiling heat flux, and the void fraction. The corresponding transition elevation, Z_{TR}, is discussed briefly in Section 3.8.5.1.

Finally, for interfacial heat transfer (including the interfacial area), the individual regimes described above are consolidated into the bubbly flow, inverted-annular-flow, and dispersed-flow models. In this case, the bubbly flow model is assumed to represent the subcooled nucleate-boiling, nucleate-boiling, and transition-boiling regimes. The inverted-annular-flow model incorporates the separate regimes of smooth IAF, rough-wavy IAF, and agitated IAF. The dispersed-flow model represents both dispersed and highly dispersed flows.

3.3. Interfacial Area

As seen in Section 3.1., fluid mass, momentum, and energy closure requires that the interfacial area A_i between the liquid and combined-gas phases be specified. Specifically, the interfacial area is needed to define the heat-transfer rates per unit volume for the interface-to-liquid heat transfer, the interface-to-gas heat transfer, and the liquid-to-gas sensible heat transfer. Because the interfacial-area parameter is highly dependent on

flow regime, the following sections will elaborate on the individual models as coded within TRAC. A summary of the interfacial-area models also is provided in Table 3-2.

3.3.1. Bubbly Slug Interfacial Area

In discussing the bubbly slug flow regime, this section will refer collectively to the bubbly, bubbly slug transition, and bubbly slug flow regimes depicted in Fig. 3-2. The total interfacial area for a given hydraulic cell in bubbly slug flow is defined as the product of an area concentration and the cell volume, or

$$A_i = A_{i,bs} = a_{i,bs} \cdot B_{cell} \ . \tag{3-28}$$

Based on the work of Ishii and Mishima (Ref. 3-6.), the interfacial-area concentration is calculated as a function of the average void fraction within the liquid slug, α_{gs}, such that

$$a_{i,bs} = \frac{C^*}{D^*} \cdot \frac{\alpha - \alpha_{gs}}{1 - \alpha_{gs}} + \frac{6\,\alpha_{gs}}{D_b} \cdot \frac{1 - \alpha}{1 - \alpha_{gs}} \tag{3-29}$$

for

$$\alpha_{gs} = \begin{cases} 0.3 & G < 2000 \text{ kg/m}^2\text{-s} \\ 0.3 + 0.2\,(G - 2000)/700 & 2000 \le G < 2700 \text{ kg/m}^2\text{-s} \\ 0.5 & G \ge 2700 \text{ kg/m}^2\text{-s} \ . \end{cases} \tag{3-30}$$

However, if the cell void fraction α is found to be $<\alpha_{gs}$, then α_{gs} is set equal to α.

In the area concentration equation, the Sauter mean bubble diameter D_b is defined as a function of the Laplace coefficient L_o (Ref. 3-7.), where

$$D_b = 2\,L_o \tag{3-31}$$

and

$$L_o = \sqrt{\frac{\sigma}{g\,(\rho_l - \rho_g)}} \ . \tag{3-32}$$

The bubble diameter is also subject to the constraint that $0.1 \text{ mm} \le D_b \le 0.9 D_h$.

Finally, the parameters C^* and D^* are included to account for the presence of cap bubbles or vapor slugs. The two parameters are defined as a function of hydraulic diameter such that

$$C^* = \begin{cases} 4.5 & D_h < D_{h,crit} \\ 16 & D_h \ge D_{h,crit} \end{cases} \tag{3-33}$$

$$D^* = \begin{cases} D_h & D_h < D_{h,crit} \\ D_{h,crit} & D_h \geq D_{h,crit} \end{cases} \quad (3\text{-}34)$$

where $D_{h,crit}$ is a critical hydraulic diameter for slug-to-cap-bubble transition, calculated as

$$D_{h,crit} = 50\, L_o \ . \quad (3\text{-}35)$$

The parameters C^* and D^* have been modified from the original reference to include large-diameter flow channels.

3.3.2. Churn-Flow Interfacial Area

The interfacial area for the churn- (or transition-) flow regime is calculated as a weighted average of the bubbly slug and annular-mist interfacial areas. The churn-flow interfacial area thus is defined by

$$A_i = (1 - W_t) \cdot A_{i,bs} + W_t \cdot A_{i,am} \ , \quad (3\text{-}36)$$

where

$$W_t = \frac{\alpha - 0.5}{0.25} \quad (3\text{-}37)$$

and $0 \leq W_t \leq 1$. In the above equation for interfacial area, the bubbly slug area term is evaluated using the methodology presented in Section 3.3.1. at a void fraction of 0.5. Similarly, the annular-mist area term is evaluated using the model presented in Section 3.3.3. at a void fraction of 0.75.

The churn-flow interfacial area is determined by interpolation between the bubbly slug and annular-mist interfacial-area models. The interfacial area can change by several factors of 10 between the two regimes. The interpolation method given here was developed specifically for implementation into TRAC. The interpolation algorithm itself embodies no physics; it is a mathematical operation. However, the interpolation algorithm provides a transition between two regimes, which are represented by physical models.

3.3.3. Annular-Mist Interfacial Area

For annular-mist flow, the interfacial area is based on a superposition of the film and droplet fields such that

$$A_i = A_{i,am} = (1 - W_f) \cdot (A_{i,drop} + A_{i,film}) + W_f \cdot A_{i,drop,max} \ , \quad (3\text{-}38)$$

where

$$W_f = \begin{cases} 0 & \max(V_l, V_g) < 10\ V_c \\ 0.5\ (\max(V_l, V_g) / V_c) - 5 & 10\ V_c \le \max(V_l, V_g) \le 12\ V_c \\ 1 & \max(V_l, V_g) > 12\ V_c \end{cases} \quad (3\text{-}39)$$

for the critical velocity

$$V_c = \left[\frac{g\ \sigma\ (\rho_l - \rho_g)}{\rho_g^2} \right]^{1/4} , \quad (3\text{-}40)$$

where V_c is based upon a Helmholtz disturbance wave.

The superposition method given here was developed specifically for implementation into TRAC.

The interfacial-area term for the droplets is defined by

$$A_{i,drop} = \frac{\alpha}{1 - \alpha_d} \left(\frac{6\ \alpha_d}{D_d} \right) \cdot B_{cell} , \quad (3\text{-}41)$$

where α_d represents the droplet fraction in the gas core. The droplet fraction is estimated as a function of the entrainment E, where

$$\alpha_d = E\ \frac{(1 - \alpha)\ V_l}{\alpha\ V_g} . \quad (3\text{-}42)$$

From Ishii and Mishima (Refs. 3-8. and 3-9.), the entrainment is calculated by

$$E = \tanh\left(7.25\text{e-}07\ We_e^{1.25}\ Re_l^{0.25}\right) \quad (3\text{-}43)$$

for the liquid Reynolds number

$$Re_l = \frac{\rho_l\ (1 - \alpha)\ V_l\ D_h}{\mu_l} \quad (3\text{-}44)$$

and the effective Weber number

$$We_e = \frac{\rho_g\ (\alpha\ V_g)^2\ D_h}{\sigma} \left(\frac{\rho_l - \rho_g}{\rho_g} \right)^{1/3} . \quad (3\text{-}45)$$

Additionally, the Sauter mean droplet diameter is calculated as

$$D_d = \min(D_{d1}, D_{d2}) , \quad (3\text{-}46)$$

provided that $84\,\mu m \le D_d \le 4$ mm. The first term D_{d1} is based on the correlation of Kataoka (Ref. 3-10.), where

$$D_{d1} = (7.96e\text{-}3)\cdot \frac{\sigma}{\rho_g (\alpha V_g)^2} Re_g^{2/3} \left(\frac{\rho_g}{\rho_l}\right)^{-1/3} \left(\frac{\mu_g}{\mu_l}\right)^{2/3} . \tag{3-47}$$

The second droplet diameter D_{d2} likewise is based on the work of Kataoka and of Kitscha and Kocamustafaogullari (Ref. 3-11.), such that

$$D_{d2} = 0.254\, L_o \left[-0.13\, We_m + \sqrt{16 + (0.13\, We_m)^2}\right] . \tag{3-48}$$

In the above droplet relations, the Reynolds number and Weber number are given by

$$Re_g = \frac{\rho_g \alpha V_g D_h}{\mu_g} \tag{3-49}$$

and

$$We_m = \frac{\rho_g (\alpha V_g)^2 L_o}{\sigma} . \tag{3-50}$$

Finally, if we assume that all droplets are entrained, then

$$\alpha_d = 1 - \alpha . \tag{3-51}$$

Thus, it follows that

$$A_{i,drop,max} = B_{cell}\cdot \frac{6(1-\alpha)}{D_d} . \tag{3-52}$$

From geometry, the interfacial-area term for the liquid film can be specified as

$$A_{i,film} = B_{cell}\cdot \frac{4\, C_r}{D_h} \sqrt{\frac{\alpha}{1-\alpha_d}} , \tag{3-53}$$

where the parameter C_r is included to account for waviness of the liquid interface (Ref. 3-12.). The surface waviness factor is ignored for thick films. However, as the liquid film becomes very thin (<25 mm), it is assumed that the film breaks down and rivulets form. Under these conditions, the surface wave parameter is defined by

$$C_r = \frac{D_h (1-\alpha)}{l_{min}} \le 1 \tag{3-54}$$

for $l_{min} = 0.1$ mm.

The modeling equations for the annular-mist interfacial area are coded as given in the original references cited above. The rivelt model given here is heuristic and was developed specifically for implementation into TRAC.

3.3.4. Stratified-Flow Interfacial Area

For fully stratified flow, the interfacial area can be calculated from the cell geometry. For horizontal stratified flow, the interfacial area is given by

$$A_i = A_{i,strat} = D_h \cdot \Delta x \sqrt{1 - \left(1 - \frac{2\,L_l}{D_h}\right)^2} \ , \tag{3-55}$$

where L_l and Δx represent the stratified liquid level and the cell length, respectively. For a cylindrical channel cross section, the calculation method for the liquid level is discussed in Appendix H (Section H.1.3.2.). Similarly, for vertical stratified flow, the interfacial area is specified such that

$$A_i = A_{i,strat} = \frac{B_{cell}}{\Delta x} \ . \tag{3-56}$$

These interfacial-area models are based on the idealized geometry of the interface and thus are exact.

As discussed in Section 3.2., the stratified-flow regime is superimposed on the basic flow-regime map shown in Fig. 3-2. Thus, when the flow is not fully stratified, the code interpolates between the interfacial area determined for stratified flow, calculated as above, and the value otherwise determined with respect to the basic flow-regime map. In other words,

$$A_i = A_{i,map,strat} = (1 - W_{st})\, A_{i,map} + W_{st}\, A_{i,strat} \tag{3-57}$$

for the weighting factor W_{st}, where $0 \le W_{st} \le 1$. The weighting factor is calculated as a function of both void fraction (flow regime) and critical velocity. In general, for 1D components, the weighting factor is nonzero for velocities less than 10 times the critical velocity (see Section 3.2.4.). For additional detail, see Appendix E (Section E.2.7.).

The interpolation method given here was developed specifically for implementation into TRAC. The interpolation algorithm itself embodies no physics; it is a mathematical operation. However, the interpolation algorithm provides a transition between two regimes, which are represented by physical models.

3.3.5. Plug-Flow Interfacial Area

When the bulk liquid temperature is below the saturation temperature of the vapor (condensation mode), full or partial liquid plugging may exist if there are large differences in the void fraction across three contiguous hydraulic cells. Based on a cylindrical channel geometry, the plug-flow interfacial area is calculated by

$$A_{i,plug} = M_{plug} \cdot \frac{\pi D_h^2}{4}, \tag{3-58}$$

where

$$M_{plug} = \begin{cases} 2 & \text{plug in one cell only} \\ 1 & \text{plug confined to two or more cells.} \end{cases} \tag{3-59}$$

The plug-flow-area model is based on the idealized geometry of the flow field in a cylindrical flow channel.

The above interfacial area for plug flow is superimposed on the flow-regime-map / stratified-flow value according to the following relation:

$$A_i = A_{i,map,strat,plug} = (1 - W_{plug}) A_{i,map,strat} + W_{plug} A_{i,plug} \tag{3-60}$$

for

$$W_{plug} = \frac{(\alpha_{max} - \alpha_{min})(\alpha_{max} - 0.5)(0.75 - \alpha_{min})}{(0.75 - 0.5)^3} \tag{3-61}$$

and $0 \le W_{plug} \le 1$. Finally, the maximum and minimum void fractions are defined such that

$$\alpha_{max} = \max(\alpha_{cell\ i-1}, \alpha_{cell\ i}, \alpha_{cell\ i+1})$$

and

$$\alpha_{min} = \min(\alpha_{cell\ i-1}, \alpha_{cell\ i}, \alpha_{cell\ i+1})$$

for the three contiguous cells $i - 1$, i, and $i + 1$.

The interpolation method given here was developed specifically for implementation into TRAC. The interpolation algorithm itself embodies no physics; it is a mathematical operation. However, the interpolation algorithm provides a transition between two regimes, which are represented by physical models.

3.3.6. Reflood Interfacial Area

Under core-reflood conditions, TRAC utilizes the flow-regime map of Ishii and his coworkers (Refs. 3-3. to 3-5.). Within this flow-regime map, separate interfacial-area models are provided for the three general regions of bubbly flow, inverted annular flow, and dispersed flow. The code calculates the overall interfacial area for a given hydraulic cell based on the weighted average of these individual reflood interfacial areas, or

$$A_i = A_{i,reflood} = W_{sb} \cdot A_{i,bubbly} + W_{inv} \cdot A_{i,inv} + W_{ds} \cdot A_{i,ds} \ . \quad (3\text{-}62)$$

In the above equation, the linear weighting factors W_{sb}, W_{inv}, and W_{ds} are based on the relative axial distance within each cell for which the appropriate flow regime is present. The calculation of these weighting factors is presented in Appendix F (Section F.1.6., Table F-4.). Additional detail of the interfacial-area models likewise can be found in Appendix F.

The interpolation method given here was developed specifically for implementation into TRAC. The interpolation algorithm itself embodies no physics; it is a mathematical operation. However, the interpolation algorithm provides a transition between two regimes, which are represented by physical models.

3.3.6.1. Bubbly Flow Model. The interfacial area for bubbly flow under reflood conditions is identical to that presented in Section 3.3.1., except that the void fraction is restricted to the range $0.05 \le \alpha \le 0.3$.

3.3.6.2. Inverted-Annular-Flow Model. From geometry, the hydraulic diameter of the inverted liquid core is given by

$$D_{h,core} = D_h \sqrt{1 - \alpha} \ . \quad (3\text{-}63)$$

Thus, the interfacial area can be specified such that

$$A_{i,inv} = \pi \, D_{h,core} \, \Delta x \ , \quad (3\text{-}64)$$

where Δx is the cell length.

The inverted annular interfacial-area model is based on the idealized geometry of the interface and thus is exact.

When the flashing of superheated liquid occurs ($T_l > T_{sat}$), an additional interfacial area for bubbles existing in the liquid core is added to $A_{i,inv}$. In this case,

$$A_{i,inv} = \pi \left(D_{h,core} - 2\,\delta\right) \Delta x + \frac{6\,\alpha_{fr}\,B_{cell}}{d_b} \ , \quad (3\text{-}65)$$

where α_{fr} is the void fraction in the liquid core, d_b is the bubble diameter, and δ is the vapor-film thickness.

The interfacial-area model is based on the idealized geometry of the interface and thus is exact.

3.3.6.3. Dispersed-Flow Model. In dispersed flow, the total interfacial area is based on a superposition of the droplet and film fields, where

$$A_{i,ds} = A_{i,drop} + A_{i,film} . \tag{3-66}$$

The interfacial area of the liquid film can be defined as

$$A_{i,film} = \frac{4 \alpha_f B_{cell}}{D_h} , \tag{3-67}$$

where the liquid fraction of the film, α_f, can be calculated by

$$\alpha_f = \frac{4 F_u \delta_f}{D_h} . \tag{3-68}$$

In the above equation, F_u is the cold-wall fraction adjacent to the hydro cell. The liquid-film thickness, δ_f, was derived by Pasamehmetoglu (Ref. 3-13.), such that

$$\delta_f = \frac{0.0025 \rho_l V_g^2}{g \rho_l - \frac{0.75 \rho_g V_g^2}{D_h}} , \tag{3-69}$$

subject to the constraint that $10^{-17} \le \delta_f \le 5$ mm.

The film liquid fraction also can be estimated by

$$\alpha_f = F_u (1 - \alpha) W_{fd} , \tag{3-70}$$

where W_{fd} is the cold-wall weighting factor such that

$$W_{fd} = \begin{cases} 0 & \alpha \le \min(\alpha_{ag}, 0.7) \\ 5\left[\dfrac{0.98 - \alpha^*}{0.98 - \min(\alpha_{ag}, 0.7)}\right]^{0.35} & \min(\alpha_{ag}, 0.7) < \alpha < 0.98 \\ 5 & \alpha \ge 0.98 , \end{cases} \tag{3-71}$$

where α_{ag} is the void fraction at the agitated-to-post-agitated inverted-annular-flow (IAF) regime transition and α^* is the void fraction constrained to be between 0.3 and 0.9995.[1]

The film liquid fraction, α_f, is selected as the minimum of the values obtained from the above equations.

---

1. In TRAC-M/F77, the exponent 0.35 in Eq. (3-71) is 0.5 for the reflood model that is based on MOD2.

Given the volume fraction of the liquid film, it follows that the volume fraction of the droplets must be expressed by

$$\alpha_{dd} = 1 - \alpha_f - \alpha \ . \tag{3-72}$$

Now, the droplet interfacial area is defined by

$$A_{i,drop} = B_{cell} \cdot \frac{6\ \alpha_{dd}}{D_d} \ , \tag{3-73}$$

where D_d is the Sauter mean droplet diameter. For dispersed flow, this droplet diameter is equivalent to that expressed in Section 3.3.3., based on the work of Kataoka (Ref. 3-10.) and of Kitscha and Kocamustafaogullari (Ref. 3-11.).

The interfacial area for the dispersed-flow regime accounting for liquid on the walls is based on an idealized flow field structure and thus is exact. The correlations used in the modeling are coded as given in the original references. The liquid-film-fraction weighting factor given here is original to TRAC.

3.4. Interfacial Mass Transfer

Closure for interfacial mass transfer is achieved through the term Γ, which is defined as the rate of interfacial mass transfer per unit volume. As stated in Section 3.1., the total mass-transfer rate is actually the sum of two components: mass transfer caused by interfacial heat transfer Γ_i and mass transfer caused by subcooled boiling at a heated wall Γ_{sub}:

$$\Gamma = \Gamma_i + \Gamma_{sub} \ . \tag{3-74}$$

As previously noted, the interfacial mass transfer caused by interfacial heat transfer is defined by the jump relation

$$\Gamma_i = \frac{q_{il} + q_{ig}}{(h_g - h_l)} \ . \tag{3-75}$$

The individual terms for interfacial heat transfer to the gas and to the liquid were defined in Section 3.1. To solve for the heat-transfer terms, we first must determine the flow-regime-dependent interfacial area and interfacial heat-transfer coefficients as presented in Sections 3.3. and 3.7., respectively. A positive value for Γ_i indicates vapor generation at the interface. Conversely, a negative value indicates liquid generation.

The interfacial mass transfer caused by subcooled boiling likewise is defined by the equation

$$\Gamma_{sub} = \frac{h_\Gamma A_w (T_w - T_l)}{B_{cell} (h_g - h_l)} \ . \tag{3-76}$$

The subcooled-boiling term is important for hydraulic cells coupled to a heated wall. Specifically, the term is included to improve the prediction of void fraction near the saturation point. For subcooled boiling to take place, the cell-averaged liquid temperature must be below the saturation temperature; at the same time, the wall temperature must be above T_{sat}.

When the above conditions are satisfied, the actual mass-transfer rate is in turn dependent on the subcooled-boiling liquid heat-transfer coefficient h_Γ, as defined by

$$h_\Gamma = W_{sb}\, h_{wl}\, F_e \ , \tag{3-77}$$

where h_{wl} is the wall-to-liquid heat-transfer coefficient as presented in Section 3.8. The subcooled-boiling weighting factor, W_{sb}, is empirically based and is calculated such that

$$0 \le W_{sb} = 5\,(0.7 - \alpha) \le 1 \ . \tag{3-78}$$

W_{sb} equals 1.0 for void fractions ranging from 0.0 to 0.5. Above a void fraction of 0.5, the weighting factor ramps linearly to zero. Finally, F_e is the evaporation fraction based on Lahey's mechanistic model (Ref. 3-14.), where

$$0 \le F_e = \frac{T_l - T_{ld}}{\max(1,\ (T_{sv} - T_{ld}))} \le 1 \ . \tag{3-79}$$

The liquid temperature at bubble detachment T_{ld} provides the criteria by which bubbles reside solely on the wall or bubbles may detach and move into the bulk fluid without collapsing. As demonstrated by the above equation, when T_{ld} exceeds the bulk liquid temperature, the evaporation fraction, and thus the mass-transfer rate, becomes zero. In this way, the code does not calculate any void generation associated with bubbles residing solely on the wall. However, once the bulk fluid temperature exceeds T_{ld}, the bubbles may detach and the calculated mass-transfer rate then becomes nonzero.

The value of the liquid temperature at bubble detachment is determined via the modified Saha-Zuber (Ref. 3-15.) correlation for the point of net vapor generation. Saha and Zuber (Ref. 3-15.) correlated the point of net vapor generation as a function of Nusselt, Stanton, and Peclet numbers, where

$$Nu = 455 \qquad \text{if} \quad Pe \le 70{,}000 \ , \tag{3-80}$$

and

$$St = 0.0065 \quad \text{if} \quad Pe > 70{,}000 \ . \tag{3-81}$$

A summary of the interfacial mass-transfer parameters is presented in Table 3-3.

3.5. Interfacial Drag

As shown in Section 2.1.1., the liquid- and gas-field momentum equations each include a term for the interfacial shear force. Closure of these equations thus requires that we specify the interfacial drag coefficient, c_i. However, the value of the interfacial drag coefficient is dependent on flow regime. A discussion of the individual flow-regime-dependent models can be found in the following sections. Likewise, a summary of the interfacial drag-coefficient models is presented in Table 3-4.

3.5.1. Bubbly Slug Flow Interfacial Drag Coefficient

In discussing the bubbly flow regime, this section will collectively refer to the bubbly, bubbly slug transition, and bubbly slug flow regimes depicted in Fig. 3-2. Following the methodology of Ishii and Chawla (Ref. 3-16.), TRAC defines the interfacial drag coefficient for bubbly slug flow as

$$c_i = \frac{0.75\, c_{Db}\, \alpha\, \rho_l\, P_s}{D_b} \ , \tag{3-82}$$

where c_{Db} is the bubble drag coefficient, D_b is the bubble diameter, and P_s is the profile slip. Under special circumstances, namely when bubbly slug flow is encountered in an upper plenum, the code redefines the interfacial drag coefficient according to the correlation of Wilson. Specific detail of the Wilson model is not included in this section but can be found in Appendix H, Section H.1.1.10.

For the above equation, the bubble diameter is defined as a function of the Laplace coefficient [as recommended by Ishii (Ref. 3-7.)] and the channel hydraulic diameter such that

$$D_b = 2L_o(1 - XS) + \min(40L_o, 0.9D_h) \cdot XS \tag{3-83}$$

for

$$L_o = \sqrt{\frac{\sigma}{g\,(\rho_l - \rho_g)}} \tag{3-84}$$

and

$$XS = \begin{cases} 0.0 & \text{bubbly flow} \\ \dfrac{(2700 - G)}{(2700 - 2000)} \cdot \dfrac{(\alpha - 0.3)}{(0.5 - 0.3)} & \text{bubbly slug transition} \\ \dfrac{(\alpha - 0.3)}{(0.5 - 0.3)} & \text{bubbly slug flow.} \end{cases}$$

The value of the bubble diameter further is constrained by the limitation that

$$0.0001 \text{ m} < D_b < \min(40\, L_o, 0.9\, D_h) \ . \tag{3-85}$$

The interpolation method given here, including the weighting factor, was developed specifically for implementation into TRAC. The interpolation algorithm itself embodies no physics; it is a mathematical operation. However, the interpolation algorithm provides a transition between two regimes, which are represented by physical models. The lower limit set on the bubble diameter given here is heuristic and was developed specifically for implementation into TRAC.

The profile slip factor is included to account for the migration of bubbles toward the higher-velocity region of the channel. The profile slip factor, likewise based on Ishii (Ref. 3-7.), is defined as

$$P_s = \frac{(C_1 V_g - C_0 V_l)^2}{(V_r)^2} \tag{3-86}$$

for

$$C_0 = 1.2 + 0.2 \sqrt{\frac{\rho_g}{\rho_l}} \tag{3-87}$$

and

$$C_1 = \frac{1.0 - C_0 \alpha_b}{1.0 - \alpha_b} \ , \tag{3-88}$$

where V_r is the relative velocity. For 3D components, TRAC limits the relative velocity such that $V_r \geq 0.01$ m / s.

The profile-slip factor is used in TRAC, as given in the source references for this constitutive model.

Additionally, the bubble drag coefficient is defined as a function of the Reynolds number such that

$$c_{Db} = \begin{cases} 240.0 & Re_b < 0.1031 \quad (3\text{-}89) \\ \frac{24.0}{Re_b}\left(1.0 + 0.15\, Re_b^{0.687}\right) & 0.1031 < Re_b < 989.0 \quad (3\text{-}90) \\ 0.44 & Re_b > 989.0 \quad (3\text{-}91) \end{cases}$$

for

$$Re_b = \frac{D_b V_r \rho_l}{\mu_l}. \tag{3-92}$$

The value of the bubble drag coefficient in each of the three Reynolds-number regimes corresponds to Stoke's drag law ($Re_b < 0.1031$), the empirical relation proposed by Schiller and Nauman ($0.1031 < Re_b < 989.0$, Ref. 3-17.), and the recommendation of Bird, Stewart, and Lightfoot ($Re_b > 989.0$, Ref. 3-18.).

The Reynolds numbers at the transition points have been chosen to provide continuity to the drag coefficient.

3.5.2. Churn-Flow Interfacial Drag Coefficient

In the churn-flow regime (void fractions between 0.5 and 0.75), TRAC calculates the interfacial drag coefficient as a weighted average of both the bubbly slug drag coefficient and the annular-mist drag coefficient. The churn flow (or "transition") interfacial drag coefficient thus is defined as

$$c_{itrans} = c_{iam} W_t + c_{ibs} (1-W_t) \tag{3-93}$$

for

$$W_t = 4\alpha - 2 \ , \tag{3-94}$$

where $0.0 \le W_t \le 1.0$. In the above equation, the bubbly slug interfacial drag coefficient c_{ibs} is evaluated at a void fraction of 0.5. The methodology for calculating the bubbly slug interfacial drag coefficient was discussed in Section 3.5.1. Likewise, the annular-mist interfacial drag coefficient c_{iam} is evaluated at a void fraction of 0.75. Details of the annular-mist interfacial drag coefficient are presented in Section 3.5.3.

The interpolation method for the drag coefficient in the churn flow given here was developed specifically for implementation into TRAC. The interpolation algorithm itself embodies no physics; it is a mathematical operation. However, the interpolation algorithm provides a transition between two regimes, which are represented by physical models.

3.5.3. Annular-Mist-Flow Interfacial Drag Coefficient

In the annular-mist-flow regime, the total interfacial drag force is assumed to be a superposition of the separate drag forces caused by the entrained droplets and the annular film. The annular-mist interfacial drag coefficient thus is defined by

$$c_i = \frac{M_i}{|V_r| V_r} \tag{3-95}$$

for

$$M_i = M_{id} + M_{ia} \ ,$$

where M_{id} and M_{ia} represent the drag forces caused by the droplet field and the annular film, respectively. The global model was created by Ishii and Mishima (Ref. 3-19.). In the above equation, the relative velocity V_r is based on the drift-flux formulation of Ishii (Ref. 3-30.). Details of Kataoka and Ishii's relative velocity model (Ref. 3-12.) can be found in Appendix H (Section H.1.2.1.).

The interfacial drag force caused by the annular film is calculated via the model of Ishii and Mishima (Ref. 3-19.) such that

$$M_{ia} = a_{if} \cdot \tau_f \ , \tag{3-96}$$

where τ_f is the interfacial shear. The interfacial area per unit volume a_{if} is

$$a_{if} = \frac{4\ C_{an}}{D} \sqrt{\frac{\alpha}{1 - \alpha_d}} \ , \tag{3-97}$$

where C_{an} is a roughness parameter to account for waviness in the film ($C_{an} \geq 1$). In the above equation, the area fraction of the droplets α_d is calculated as the ratio of the liquid and gas superficial velocities multiplied by the entrainment, or

$$\alpha_d = \frac{j_l}{j_g} E \ . \tag{3-98}$$

The entrainment E in turn is based on the correlation of Kataoka and Ishii (Ref. 3-12.), where

$$E = \tanh\left(7.25\text{e-}07\ We_d^{1.25}\ Re_l^{0.25}\right) \tag{3-99}$$

for the liquid Reynolds number

$$Re_l = \frac{\rho_l\ j_l\ D}{\mu_l} \tag{3-100}$$

and for the droplet Weber number

$$We_d = \frac{\rho_g\ j_g^2\ D}{\sigma} \left(\frac{\rho_l - \rho_g}{\rho_g}\right)^{1/3} = 4.0 \ . \tag{3-101}$$

Additionally, the shear force τ_f is calculated from

$$\tau_f = 0.5\ f_i\ \rho_c (V_g - V_f)^2 \ , \tag{3-102}$$

where ρ_c is the density of the gas/droplet core and V_f is the annular film velocity. The film interfacial friction factor f_i is based on the Wallis (Ref. 3-20.) correlation given by

$$f_i = 0.005\left[1 + 75(1 - \alpha)\right] . \tag{3-103}$$

The interfacial drag force caused by the entrained droplet field likewise is based on the model of Ishii and Mishima (Ref. 3-19.), where

$$M_{id} = a_i\left[\frac{c_d}{4}\left(\frac{r_{sm}}{r_d}\right)\frac{\rho_g\,(V_g - V_d)^2}{2}\right] \tag{3-104}$$

and

$$a_i = \frac{\alpha}{1 - \alpha_d}\left(\frac{3\,\alpha_d}{r_{sm}}\right) . \tag{3-105}$$

In the above equations, c_d is the droplet drag coefficient, r_{sm} is the Sauter mean radius, r_d is the drag radius, V_d is the droplet velocity, and α_d is the area fraction of the droplet (as defined above). The droplet drag coefficient is estimated using the correlation of Ishii and Chawla (Ref. 3-16.), where

$$c_d = \frac{24}{Re_d}\left(1.0 + 0.1\,Re_d^{0.75}\right) \tag{3-106}$$

for

$$Re_d = \frac{D_d\,\rho_g\,|V_g - V_d|}{\mu_m} \tag{3-107}$$

and

$$\mu_m = \frac{\mu_g}{(1 - \alpha_d)^{2.5}} . \tag{3-108}$$

The droplet diameter D_d is evaluated using the model of Kataoka, Ishii, and Mishima (Ref. 3-10.) such that

$$D_d = \frac{2.0}{\rho_g\,j_g^2}\left[0.005\,\sigma\left(\frac{\mu_g}{\mu_l}\right)^{2/3} Re_g^{2/3}\left(\frac{\rho_g}{\rho_l}\right)^{1/3}\right] \tag{3-109}$$

for $0.000042 < D_d < 0.002$ m. The Sauter mean radius likewise is dependent on the droplet diameter (Ref. 3-12.), as shown by

$$r_{sm} = 0.796\,\frac{D_d}{2} . \tag{3-110}$$

Additionally, the ratio of the Sauter mean radius over the drag radius is defined to be 1.0 for spherical particles. Finally, the relative velocity between the gas phase and the entrained droplets ($V_g - V_d$) is calculated from the model of Ishii (Ref. 3-30.). Details of Ishii's relative velocity formulation can be found in Appendix H (Section H.1.2.1.).

The correlations that make up the annular-mist interfacial drag model are used in TRAC, as given in the source references for this constitutive model.

3.5.4. Stratified-Flow Interfacial Drag Coefficient

For fully stratified flow, the interfacial drag coefficient is defined per the method of Taitel and Dukler (Ref. 3-21.). Specifically, the drag coefficient is calculated such that

$$c_i = \frac{1}{2} f_i \rho_g \frac{S_i}{A_{flow}} , \tag{3-111}$$

where f_i is the interfacial friction factor, S_i is the width of the stratified interface, and A_{flow} is the flow area. For 3D components, the above relation simplifies to

$$c_i = \frac{1}{2} f_i \rho_g \frac{1}{D_h} . \tag{3-112}$$

For 1D components, the flow area and width of the stratified interface are determined assuming a circular channel cross section. Details of the TRAC methodology can be found in Appendix H (Section H.1.3.2.).

Additionally, both 1D and 3D components use the interfacial friction-factor correlation of Ohnuki (Ref. 3-22.) such that

$$f_i = 1.84 f_{wg} , \tag{3-113}$$

where

$$f_{wg} = \begin{cases} 16.0 (Re_g)^{-1} & \text{laminar flow} \\ 0.079 (Re_g)^{-0.25} & Re_g < 10^5 \\ 0.0008 + 0.05525 (Re_g)^{-0.237} & Re_g \geq 10^5 . \end{cases} \tag{3-114}$$

The correlations are used in TRAC, as given in the source references for this constitutive model.

As mentioned in Section 3.2., the stratified-flow regime is superimposed on the basic flow-regime map shown in Fig. 3-2. Thus, when the flow is not fully stratified, the code interpolates between the drag coefficient determined for stratified flow, calculated as above, and the value otherwise determined with respect to the basic flow-regime map. In other words,

$$c_i = (1 - W_{st}) c_{imap} + W_{st} c_{ist} \tag{3-115}$$

for the weighting factor W_{st}, where $0 \le W_{st} \le 1$. The weighting factor is calculated as a function of both void fraction (flow regime) and critical velocity. In general, for 1D components, the weighting factor is nonzero for velocities less that 10 times the critical velocity (see Section 3.2.4.). For additional details, see Appendix E (Section E.2.7.).

The interpolation method given here, including the weighting factor, was developed specifically for implementation into TRAC. The interpolation algorithm itself embodies no physics; it is a mathematical operation. However, the interpolation algorithm provides a transition between two regimes, which are represented by physical models.

3.5.5. Reflood Interfacial Drag Coefficient

Under core-reflood conditions, TRAC utilizes the flow-regime map of Ishii and his coworkers (Refs. 3-3. to 3-5.). As such, the code provides separate interfacial drag models for each of the following reflood flow regimes: subcooled boiling, smooth inverted annular flow, rough-wavy inverted annular flow, agitated inverted annular flow, dispersed flow, and highly dispersed flow. A limited discussion of these flow regimes can be found in Section 3.2.6. In terms of interfacial drag, the overall interfacial drag coefficient for a given hydraulic cell is defined as the weighted average of the individual reflood flow-regime drag coefficients, or

$$c_i = WFSB \cdot c_{i,sb} + WFSM \cdot c_{i,sm} + WFRW \cdot c_{i,rw} + WFMDS \cdot c_{i,pa} + WFHDS \cdot c_{i,df}. \quad (3\text{-}116)$$

In the above equation, the individual interfacial drag coefficients correspond to subcooled boiling, smooth IAF, rough-wavy IAF, post-agitated (or dispersed) flow, and highly dispersed flow, respectively. Note the apparent omission of a separate interfacial drag coefficient for agitated IAF. In reality, it is included within the rough-wavy coefficient and weighting factor. The linear weighting factors *WFSB, WFSM, WFRW, WFMDS,* and *WFHDS* are based on the axial distance within a given hydraulic cell in which the appropriate flow regime is present. The calculation of these weighting factors is discussed in Appendix H (Section H.1.5.7.). The following paragraphs will summarize the models for each of the above drag coefficients. Additional model details likewise can be found in Appendix H.

The interpolation method given here, including the weighting factor, was developed specifically for implementation into TRAC. The interpolation algorithm itself embodies no physics; it is a mathematical operation.

3.5.5.1. Subcooled-Boiling Model. Throughout the regimes of subcooled nucleate boiling, nucleate boiling, and transition boiling, TRAC applies the subcooled-boiling interfacial drag model. This model assumes that the interfacial drag coefficient $c_{i,sb}$ comprises the drag coefficient from bubbles located at the wall $c_{i,w}$ and the drag coefficient from free-stream bubbles $c_{i,fr}$. However, the definition of the interfacial drag coefficient is dependent on whether the bulk liquid is subcooled, saturated, or superheated. Specifically, if $T_l \ge T_{sat}$,

$$c_{i,sb} = \frac{c_{i,w} \cdot V_l^2 + ffs \cdot c_{i,fr} \cdot V_r^2}{(\alpha_w + \alpha_{fr}) V_r^2} \tag{3-117}$$

for $\alpha_w > 0$, and

$$c_{i,sb} = \frac{ffs \cdot c_{i,fr}}{\alpha_{fr}} \tag{3-118}$$

for $\alpha_w \leq 0$, where $ffs = 0.00125$. The numerical factor ffs was not part of the original correlation. Otherwise, if $T_l < T_{sat}$,

$$c_{i,sb} = c_{i,w} \, . \tag{3-119}$$

In the above equations, the drag coefficient for bubbles that reside on the wall is defined using an analogous form of the Colebrook turbulent friction factor, where

$$c_{i,w} = \frac{2 \rho_g}{D_h} \left[1.14 - 2.0 \log \left(\frac{\varepsilon}{D_h} \right) \right]^{-2} \, . \tag{3-120}$$

In other words, the code assumes that the interfacial drag can be likened to that of flow through a rough pipe, where the roughness parameter ε is dependent on the bubble height from the wall Y_b such that

$$\varepsilon = 0.01 \, Y_b \, . \tag{3-121}$$

The bubble height parameter in turn is calculated based on the work of Collier (Ref. 3-23.). This parameter is given by the relation

$$Y_b = C \left[\frac{\sigma D_h}{\tau_w} \right]^{1/2} \cdot \left[1 + C' \left(\frac{g (\rho_l - \rho_g) D_h}{\tau_w} \right) \right]^{-1/2} \tag{3-122}$$

for

$$\tau_w = \frac{f_{fo} G^2}{2 \rho_l} \, , \tag{3-123}$$

where the constants C and C' are equal to 0.015 and 0.0, respectively. The above wall shear stress is dependent on the single-phase friction factor f_{fo}. This friction factor is evaluated for a relative roughness ε/D_h equal to 10^{-4}. Thus,

$$f_{fo} = \frac{1}{\left[1.14 - 2 \log \frac{\varepsilon}{D_h} \right]^2} = 0.01197037 \, . \tag{3-124}$$

The modeling of interfacial drag for subcooled boiling, including the drag caused by bubbles on the wall (as given above), is heuristic. The model is made up of correlations available from the literature, and the coefficients in these correlations are those in the source references for this constitutive model.

Alternatively, the drag coefficient for free-stream bubbles is derived from Ishii's bubbly flow drag force (Ref. 3-7.), where

$$c_{i,fr} = \frac{\alpha_{fr}}{d_b} f(\alpha) \rho_l \frac{(C_1 V_v - C_0 V_l)^2}{(V_v - V_l)^2} \tag{3-125}$$

for

$$f(\alpha) = \left[\frac{1 + 17.67 (1 - \alpha_{fr})^{1.3}}{18.67 (1 - \alpha_{fr})^{1.5}} \right]^2 \tag{3-126}$$

and

$$d_b = 2 \sqrt{\frac{\sigma}{g (\rho_l - \rho_g)}} . \tag{3-127}$$

The coefficients C_0 and C_1 were defined in Section 3.5.1.

The bubbly flow drag-force model for free-stream bubbles is used in TRAC, as given in the source references for this constitutive model.

The free-stream void is related to the combined-gas void and the wall void by

$$\alpha_{fr} = \alpha_g - \alpha_w . \tag{3-128}$$

Based on Collier (Ref. 3-23.), the wall void is defined such that

$$\alpha_w = \begin{cases} \frac{\pi}{6} \cdot \frac{Y_b}{D_h} & T_l + 5 < T_{sat} \quad (3\text{-}129) \\ \frac{\pi}{6} \cdot \frac{Y_b}{D_h} [0.2 (T_{sat} - T_l)] & T_{sat} - 5 \le T_l < T_{sat} \quad (3\text{-}130) \\ 0 & T_l \ge T_{sat} . \quad (3\text{-}131) \end{cases}$$

Finally, the above model for $c_{i,sb}$ is applied as shown for cell void fractions between 0.0 and 0.5. For cell void fractions >0.98, $c_{i,sb}$ is replaced with the annular-mist interfacial drag coefficient discussed in Section 3.5.3. Between void fractions of 0.5 and 0.98, the code uses a linear weighting of the subcooled-boiling and annular-mist drag coefficients. A discussion of this weighting factor is presented in Appendix H (Section H.1.5.1.1.). The interpolation method given here, including the weighting factor, was developed

specifically for implementation into TRAC. The interpolation algorithm itself embodies no physics; it is a mathematical operation. However, the interpolation algorithm provides a transition between two regimes, which are represented by physical models.

3.5.5.2. Smooth Inverted-Annular-Flow Model. In the smooth IAF regime, the drag coefficient $c_{i,sm}$ is defined such that

$$c_{i,sm} = 2 \rho_g f_{i,sm} \frac{(1 - \alpha_g)^{1/2}}{D_h} , \tag{3-132}$$

where $f_{i,sm}$ is calculated from the smooth-tube friction-factor relations

$$f_{i,sm} = \begin{cases} 16 \, Re_g^{-1} & Re_g < 1189.39 \quad \text{(laminar flow)} \quad (3\text{-}133) \\ 0.079 \, Re_g^{-0.25} & Re_g \geq 1189.39 \quad \text{(turbulent flow)} \quad (3\text{-}134) \end{cases}$$

for

$$Re_g = \frac{\frac{(D_h - D_c)}{2} \alpha_g \rho_v V_v}{\mu_v} . \tag{3-135}$$

In the above Reynolds number, the diameter of the inverted liquid core D_c is given by

$$D_c = (\alpha_l)^{1/2} D_h . \tag{3-136}$$

These are standard engineering correlations applied in a manner that is original to TRAC. The correlations are used in TRAC, as reported in the source references for this constitutive model.

To prevent discontinuity, if $c_{i,sm}$ is greater than one-third the value of $c_{i,sb}$, then $c_{i,sm}$ is set equal to one-third $c_{i,sb}$. Additionally, if the cell void fraction is >0.98, $c_{i,sm}$ is assumed to equal the drag coefficient for highly dispersed flow, $c_{i,df}$. Below void fractions of 0.75, the code calculates the smooth IAF drag coefficient, as presented above. Between void fractions of 0.75 and 0.98, TRAC uses a linear weighting of the smooth IAF and highly dispersed drag coefficients. The interpolation method given here, including the weighting factor, was developed specifically for implementation into TRAC. The interpolation algorithm itself embodies no physics; it is a mathematical operation. However, the interpolation algorithm provides a transition between two regimes, which are represented by physical models. Detail of the weighting factor is presented in Appendix H (Section H.1.5.2.5.).

3.5.5.3. Rough-Wavy Inverted-Annular-Flow Model. The interfacial drag coefficient for rough-wavy IAF is identical to that of the smooth IAF regime, with the exception of the friction factor $f_{i,rw}$. The drag coefficient thus is expressed as

$$c_{i,rw} = 2 \rho_g f_{i,rw} \frac{(1 - \alpha_g)^{1/2}}{D_h} . \tag{3-137}$$

Because of the presence of waves and droplets, we expect the interfacial friction to be increased over smooth IAF. The rough-wavy friction factor is evaluated from the Colebrook equation for fully turbulent flow over rough surfaces, where

$$f_{i,rw} = \begin{cases} 0.7694675 & \varepsilon / D_h > 1 \quad (3\text{-}138) \\ \left[1.14 - 2.0 \log \left(\frac{\varepsilon}{D_h}\right)\right]^{-2} & \varepsilon / D_h < 1. \quad (3\text{-}139) \end{cases}$$

These are standard engineering correlations. The correlations are used in TRAC, as reported in the source references for this constitutive model.

In the above equation, the relative roughness is evaluated as a function of the droplet diameter such that

$$\frac{\varepsilon}{D_h} = 80 \frac{d_d}{D_h} . \tag{3-140}$$

The numerical coefficient on the right-hand side of this model was determined to be 80 by comparison of TRAC predictions with Cylindrical-Core Test Facility (CCTF) pressure-drop data. The modeling approach given here is heuristic and was developed specifically for implementation into TRAC.

Additionally, the droplet diameter is calculated from the model of Ishii (Ref. 3-7.), where

$$d_d = 0.612825 \left(\frac{\sigma}{g (\rho_l - \rho_g)}\right)^{1/2} N_{\mu g} \tag{3-141}$$

for the viscosity number

$$N_{\mu g} = \frac{\mu_g}{\left[\rho_g \sigma \sqrt{\frac{\sigma}{g (\rho_l - \rho_g)}}\right]^{1/2}} . \tag{3-142}$$

Similar to the smooth IAF model, if $c_{i,rw}$ is found to be greater than twice the value of $c_{i,sm}$, then the drag coefficient is adjusted to ensure a smooth transition. Likewise, if the cell void fraction is >0.98, $c_{i,rw}$ is assumed to equal the drag coefficient for highly dispersed flow, $c_{i,df}$. Below void fractions of 0.75, the code calculates the rough-wavy IAF drag

coefficient, as presented above. Between void fractions of 0.75 and 0.98, TRAC used a linear weighting of the rough-wavy and highly dispersed drag coefficients. The interpolation method given here, including the weighting factor, was developed specifically for implementation into TRAC. The interpolation algorithm itself embodies no physics; it is a mathematical operation. However, the interpolation algorithm provides a transition between two regimes, which are represented by physical models. A discussion of the coefficient adjustment and weighting methodology is presented in Appendix H (Section H.1.5.3.5.).

3.5.5.4. Agitated Inverted-Annular-Flow Model. In the agitated IAF regime, the interfacial drag coefficient is defined by

$$c_{i,ag} = c_{i,rw} \ ,$$

where $c_{i,rw}$ is calculated as presented above.

3.5.5.5. Post-Agitated-Flow Model. In the post-agitated- (dispersed-) flow regime, the interfacial drag coefficient $c_{i,pa}$ is calculated as a weighted average of the rough-wavy and highly dispersed flow drag coefficients. The interpolation method given here, including the weighting factor, was developed specifically for implementation into TRAC. The interpolation algorithm itself embodies no physics; it is a mathematical operation. However, the interpolation algorithm provides a transition between two regimes, which are represented by physical models. Details of the weighting methodology are discussed in Appendix H (Section H.1.5.6.).

3.5.5.6. Highly Dispersed Flow Model. The highly dispersed flow regime is characterized by small liquid droplets distributed throughout the vapor and by liquid films that may form on unheated surfaces. Thus, based on the work of Cappiello (Ref. 3-24.), the total interfacial drag coefficient for the highly dispersed flow regime is calculated as a function of the drag coefficient for the dispersed droplets $c_{i,dd}$ and of the drag coefficient for the liquid film $c_{i,f}$. In other terms,

$$c_{i,df} = \frac{c_{i,dd} V_r^2 + c_{i,f} V_v^2}{\left(V_v - \frac{\alpha_{dd} V_d}{1 - \alpha_g}\right)^2} \ . \qquad (3\text{-}143)$$

The dispersed-droplet drag coefficient is given by

$$c_{i,\,dd} = fcdrop \cdot \frac{0.75 \alpha_{dd} \rho_g C_d}{d_d} \ , \qquad (3\text{-}144)$$

where $fcdrop = 0.015$. The numerical factor, *fcdrop*, was not a part of the original correlation. Similar to the rough-wavy regime, the droplet diameter d_d is calculated as per Ishii (Ref. 3-7.) such that

$$d_d = 1.838 \left(\frac{\sigma}{g(\rho_l - \rho_g)} \right)^{1/2} (N_{\mu g})^{1/3} \quad (3\text{-}145)$$

for the viscosity number

$$N_{\mu g} = \frac{\mu_g}{\left[\rho_g \sigma \sqrt{\frac{\sigma}{g(\rho_l - \rho_g)}} \right]^{1/2}} . \quad (3\text{-}146)$$

The drag coefficient for spherical droplets, C_d, is based on the work of Ishii and Chawla (Ref. 3-16.), where

$$C_d = \frac{24}{Re_d} \left(1.0 + 0.1\, Re_d^{0.75} \right) \quad (3\text{-}147)$$

for

$$Re_d = \frac{\rho_v d_d V_r}{\mu_m} , \quad (3\text{-}148)$$

$$V_r = V_v - V_d , \quad (3\text{-}149)$$

and

$$\mu_m = \frac{\mu_v}{(1 - \alpha_{dd})^{2.5}} . \quad (3\text{-}150)$$

The droplet velocity was estimated by Cappiello (Ref. 3-24.) as

$$V_d = V_v - 2.462 \left[\frac{(\rho_l - \rho_v)\, g\, d_d}{2\, \rho_v} \right]^{1/2} . \quad (3\text{-}151)$$

In addition, the droplet liquid fraction is defined as

$$\alpha_{dd} = 1 - \alpha_f - \alpha_g , \quad (3\text{-}152)$$

where α_f is the volume fraction associated with the liquid film.

The film void fraction can be obtained from geometry such that

$$\alpha_f = \frac{P\, \delta_f\, F_u}{A_{flow}} , \quad (3\text{-}153)$$

where P is the equivalent channel perimeter, δ_f is the film thickness, and F_u is the area fraction of the unheated surfaces. The film thickness was derived by Pasamehmetoglu (Ref. 3-13.) and can be expressed by

$$\delta_f = \frac{0.0025\ \rho_l\ V_g^2}{g\ \rho_l - \frac{0.75\ \rho_g\ V_g^2}{D_h}} \quad . \tag{3-154}$$

The correlations in the model are used in TRAC, as given in the source references for this constitutive model.

The film void fraction also can be limited by the total liquid void fraction available to be deposited on the unheated surface area. If the liquid and the unheated surface areas are distributed homogeneously within a control volume, the amount of liquid might be considered to be

$$\alpha_f = F_u\left(1 - \alpha_g\right) \quad .$$

However, with cross flow between subchannels and the ability of liquid to "hang" on an unheated wall, the film void fraction actually may become greater than the above expression. To account for this effect, the film void fraction is given by

$$\alpha_f = F_u\left(1 - \alpha_g\right) W \quad , \tag{3-155}$$

where W is the cold-wall liquid fraction weighting factor defined by the following:

$$W = \begin{cases} 0 & \alpha \le \min(\alpha_{ag},\ 0.7) \\ 5\left[\dfrac{0.98 - \alpha}{0.98 - \min(\alpha_{ag},\ 0.7)}\right]^{0.35} & \min(\alpha_{ag},\ 0.7) < \alpha < 0.98 \\ 5 & \alpha \ge 0.98\ , \end{cases}$$

where α_{ag} is the void fraction at the agitated-to-post-agitated IAF regime transition.

The weighting factor was developed specifically for implementation into TRAC.

Ultimately, the liquid-film fraction is based on the minimum of the above two methods, or

$$\alpha_f = \min\left(\frac{P\delta_f F_u}{A_{flow}}\ ,\ F_u(1 - \alpha_g)W\right) \quad . \tag{3-156}$$

Finally, the interfacial drag coefficient on the liquid film is estimated by

$$c_{i,f} = ffd \cdot \frac{2\ \rho_g\ f_{i,f}}{D_h} \tag{3-157}$$

(*ffd* = 0.5), using the modified Wallis friction factor (Ref. 3-20.), where

$$f_{i,f} = 0.005\,(1 + 75\ \alpha_f)\ . \tag{3-158}$$

The coefficient *ffd* was not a part of the original correlation. The numerical value was determined by comparison of TRAC predictions with CCTF Run 14 pressure-drop data.

3.6. Wall Drag

At the fluid / wall interface, closure of the liquid- and gas-field momentum equations requires two additional parameters: the wall drag coefficient for the liquid phase c_{wl} and the wall drag coefficient for the combined-gas c_{wg}. For 1D components, these two drag coefficients are defined such that

$$c_{wl} = \frac{\alpha_l\ \rho_l\ c_{fl}}{D_h} \tag{3-159}$$

and

$$c_{wg} = \frac{\alpha_g\ \rho_g\ c_{fg}}{D_h}\ , \tag{3-160}$$

where c_{fl} and c_{fg} are the coefficients of friction for the liquid and gas phases, respectively. For 3D components, the drag coefficients c_{wlk} and c_{wgk} essentially are identical to their 1D counterparts, except for the addition of the subscript *k*, which denotes the *r*, *θ*, or *z* coordinate directions.

In addition, the liquid- and gas-phase coefficients of friction are related to the Fanning friction factor such that

$$c_{fl} = c_{fg} = 2\ f\ .$$

The friction factor *f* in turn is determined by one of three model types: the single-phase model, the two-phase homogeneous model, or the horizontal stratified-flow model. As the name implies, the single-phase wall drag model is employed for single-phase liquid or single-phase vapor conditions. Likewise, the two-phase homogeneous wall drag model is called for each of the regimes included in the basic two-phase flow-regime map: bubbly slug, churn, and annular-mist flows. Under stratified-flow conditions, TRAC uses the horizontal-stratified-flow wall drag model.

A summary table of the key correlations for wall drag is provided in Table 3-5.

3.6.1. Single-Phase Wall Drag Model

For single-phase flow, TRAC uses a model in which the friction factor is obtained from the modified Churchill equation (Ref. 3-25.).

The Churchill equation (Ref. 3-25.) is a fit to the Moody diagram for laminar, transition, and turbulent flow. In the code, the Churchill friction factor is defined as

$$f_{Churchill} = 2\left[\left(\frac{8}{Re}\right)^{12} + \frac{1}{(a+b)^{3/2}}\right]^{1/12}, \tag{3-161}$$

where

$$a = \left[2.475 \ln\left(\frac{1}{\left(\frac{7}{Re}\right)^{0.9} + \frac{0.27\,\varepsilon}{D_h}}\right)\right]^{16} \tag{3-162}$$

and

$$b = \left(\frac{37530}{Re}\right)^{16} \tag{3-163}$$

for $Re \geq 100$.

The Churchill correlation is used in TRAC as given in the source reference for this constitutive model. Use of the Moody curves, and mathematical representations of the curves, for calculation of the single-phase friction factor in a variety of flow-channel geometries is a common engineering practice.

3.6.2. Two-Phase Homogeneous Wall Drag Model

The friction factor for two-phase flow likewise is obtained from the Churchill equation (see Section 3.6.1.). The single-phase Reynolds number is replaced by a two-phase mixture Reynolds number, or

$$Re_m = \frac{G_m D_h}{\mu_m} = \frac{(j_g \rho_g + j_l \rho_l) D_h}{\mu_m}.$$

In the above equation, the mixture viscosity μ_m is defined as a function of the static quality X, where

$$\mu_m = \left[\frac{X}{\mu_g} + \frac{(1-X)}{\mu_l}\right]^{-1} \tag{3-164}$$

for

$$X = \frac{1}{1 + \frac{(1 - \alpha_g)\,\rho_l}{\alpha_g\,\rho_g\,S_r}} \quad , \tag{3-165}$$

where the slip between phases is small, or

$$S_r = 1.0 \; .$$

As with the single-phase model, the mixture Reynolds number also must be ≥100 to prevent division by zero in the friction-factor equations.

The TRAC friction-factor model takes the coefficient of friction for the liquid phase to be

$$c_{fl} = 2f$$

and the coefficient of friction for the vapor phase to be

$$c_{fg} = c_{fl} \; ,$$

where the friction factor, *f*, is obtained from the Churchill equation using the two-phase Reynolds number given above.

Use of a two-phase Reynolds number in a single-phase friction-factor correlation is one method of determining the two-phase friction factor. The modeling approach needs to be validated by comparison with experimental data.

3.6.3. Two-Phase Horizontal Stratified Wall Drag Model

For fully stratified-flow conditions, the wall drag coefficients for each phase are determined using the friction-factor relation

$$f = 0.046\,Re^{-0.2} \tag{3-166}$$

for $Re \geq 1502$ (turbulent flow) and

$$f = \frac{16}{Re} \tag{3-167}$$

for $Re < 1502$ (laminar flow). In the above equations, the Reynolds number is evaluated for each phase based on

$$Re_k = \max\left(100, \frac{\rho_k\,|V_k|\,D_k}{\mu_k}\right) , \tag{3-168}$$

where $k = l$ (for liquid) or g (for gas). The hydraulic diameters, D_l and D_g, are based on the flow area and wetted perimeter for the respective phases; they replace the hydraulic diameter based on total flow area and total wetted perimeter, D_h, both in the Reynolds-number and the drag-coefficient definitions.

Application of standard engineering correlations to each phase in a two-phase mixture under separated flow conditions is a common practice for two-fluid models of two-phase flows. The modeling approach needs to be validated by comparison with experimental data.

In the transition region between stratified and nonstratified flow, TRAC interpolates between the stratified and nonstratified wall drag coefficients based on the weighting-factor methodology discussed in Section 3.2.4.

3.7. Interfacial Heat Transfer

As seen in Section 3.1., closure of the mass, momentum, and energy equations requires that we specify the interfacial heat-transfer coefficients h_{il}, h_{ig}, and h_{gl}. These coefficients are needed to define the heat-transfer rates per unit volume for the interface-to-liquid heat transfer, the interface-to-gas heat transfer, and the liquid-to-gas sensible heat transfer, respectively. Because the interfacial heat-transfer parameters are highly dependent on flow regime, the following sections will elaborate on the individual models as coded within TRAC. A summary of the interfacial heat-transfer models also is provided in Table 3-6.

In many cases, the interfacial heat-transfer coefficients are expressed in terms of a heat-transfer factor H. By definition, the heat-transfer factor for a given flow regime is expressed as the product of the interfacial heat-transfer coefficient and the interfacial area corresponding to that flow regime. The following sections will focus on four specific heat-transfer factors:

$$H_{ALV} = (h_{il})_{flashing} \cdot A_i \ , \tag{3-169}$$

$$H_{ALVE} = (h_{il})_{evap/cond} \cdot A_i \ , \tag{3-170}$$

$$H_{CHTI} = h_{ig} \cdot A_i \ , \tag{3-171}$$

and

$$H_{CHTA} = h_{gl} \cdot A_i \ . \tag{3-172}$$

As indicated above, the heat-transfer factors H_{ALV} and H_{ALVE} correspond to interface-to-liquid heat transfer via flashing for $T_l \geq T_{sat}$ and via evaporation or condensation for $T_l < T_{sat}$. Similarly, the heat-transfer factors H_{CHTI} and H_{CHTA} correspond to interface-to-

gas heat transfer and liquid-to-gas sensible heat transfer, respectively. A description of the flow-regime-dependent interfacial-area models can be found in Section 3.3.

3.7.1. Bubbly Slug Interfacial Heat Transfer

In discussing the bubbly slug flow regime, this section collectively will refer to the bubbly, bubbly slug transition, and bubbly slug flow regimes depicted in Fig. 3-2. During condensation or evaporation ($T_l < T_{sat}$), the heat-transfer coefficient h_{il} for bubbly slug flow is evaluated by the Nusselt number correlations of Chen and Mayinger (Ref. 3-26.) and of Whittaker (Ref. 3-27.). The Nusselt number correlations are given by

$$\mathrm{Nu} = \begin{cases} 116.7\,\sqrt{\mathrm{Pr_l}} & \mathrm{Re} \geq 10^4 \\ 0.185\,\mathrm{Re}^{0.7}\,\sqrt{\mathrm{Pr_l}} & \mathrm{Re} < 10^4 \quad \text{(Chen and Mayinger)} \\ 2 + \left(0.4\sqrt{\mathrm{Re}} + 0.06\,\mathrm{Re}^{2/3}\right)\mathrm{Pr_l}^{0.4} & \text{low Re} \quad \text{(Whittaker)} \end{cases} \tag{3-173}$$

where

$$\mathrm{Nu} = \frac{h_{il}\,D_b}{k_l}\,, \tag{3-174}$$

$$\mathrm{Re} = \frac{\rho_l\,D_b\,(V_g - V_l)}{\mu_l}\,, \tag{3-175}$$

and where D_b is the Sauter mean bubble diameter defined in Section 3.3.1. The Chen and Mayinger correlation is recommended for Reynolds numbers $<10^4$. However, at low Reynolds numbers, this correlation yields a smaller Nusselt number than that of the Whittaker correlation for solid spheres. Under these circumstances, the modified Whittaker correlation (expressed above) is used to calculate the Nusselt number. Additionally, at a high Reynolds number ($Re \geq 10^4$), the Nusselt number is assumed to be independent of the Reynolds number. The above correlation for high Reynolds numbers was derived from the Chen and Mayinger correlation by setting $Re = 10^4$.

The Whittaker correlation is modified from its original form by neglect of a viscosity-ratio correction.

Once the appropriate heat-transfer coefficient has been calculated, the heat-transfer factor H_{ALVE} can be defined such that

$$H_{ALVE,bubbly\text{-}slug} = h_{il} \cdot A_{i,bubbly\text{-}slug}\,. \tag{3-176}$$

Under subcooled-boiling conditions ($h_\Gamma > 0$, see Section 3.4.), the above liquid-side heat-transfer factor is modified to account for the condensation of vapor in contact with the subcooled bulk liquid. Specifically,

$$H_{ALVE,bubbly,sub} = W_{sub} \cdot H_{ALVE,sub} + (1 - W_{sub}) \cdot H_{ALVE,bubbly} \tag{3-177}$$

for the weighting factor

$$W_{sub} = 10\,(0.2 - \alpha)\,, \tag{3-178}$$

where $0 \le W_{sub} \le 1$. The subcooled-boiling heat-transfer factor is obtained from the model of Lahey and Moody (Ref. 3-28.) such that

$$H_{ALVE,sub} = H_o\, B_{cell}\, h_{fg} \frac{\rho_l\, \rho_g}{\rho_l - \rho_g}\, \alpha \tag{3-179}$$

for

$$H_o = 0.075\ (\text{s-K})^{-1}. \tag{3-180}$$

During flashing ($T_l > T_{sat}$), the liquid-side heat-transfer factor is determined by the relation

$$H_{ALV,bubbly\text{-}slug} = (2.0e{+}8)\cdot (T_l - T_{sat})\cdot B_{cell}\,, \tag{3-181}$$

where

$$1.0e{+}6 \le \frac{H_{ALV,bubbly\text{-}slug}}{B_{cell}} \le 2.0e{+}8\,. \tag{3-182}$$

Finally, the interface-to-gas and the liquid-to-gas heat-transfer coefficients are approximated by

$$h_{ig} = h_{gl} = 1000\ \text{W/m}^2\cdot\text{K}\,. \tag{3-183}$$

In terms of heat-transfer factors,

$$H_{CHTI,bubbly\text{-}slug} = H_{CHTA,bubbly\text{-}slug} = 1000\cdot A_{i,bubbly\text{-}slug}\,. \tag{3-184}$$

The weighting factors and constant heat-transfer coefficients used in this modeling are heuristic and were developed specifically for implementation into TRAC. These empirical factors are largely untested.

3.7.2. Churn-Flow Interfacial Heat Transfer

In the churn-flow or transition-flow regime, the interfacial heat-transfer factors (H_{ALVE}, H_{ALV}, H_{CHTI}, and H_{CHTA}) are defined as a weighted average of the appropriate bubbly slug and annular-mist heat-transfer factors. The generalized weighting is given by the equation

$$X_{transition} = (1 - W_t)\cdot X_{bubbly\text{-}slug} + W_t\cdot X_{annular\text{-}mist}\,,$$

where X represents the heat-transfer factors H_{ALVE}, H_{ALV}, H_{CHTI}, and H_{CHTA}. The weighting factor W_t was defined in Section 3.3.2. During flashing conditions, however, the liquid-side heat-transfer factor H_{ALV} is redefined as the maximum of the value obtained from the above weighted average and the value obtained from the expression

$$H_{ALV,transition} = (2.0e+8)\cdot(T_l - T_{sat})\cdot B_{cell} , \tag{3-185}$$

where

$$1.0e+6 \le \frac{H_{ALV,transition}}{B_{cell}} \le 2.0e+8 . \tag{3-186}$$

The constant heat-transfer coefficients given here are heuristic and were developed specifically for implementation into TRAC.

In all cases, the bubbly slug heat-transfer factors are evaluated by the expressions presented in Section 3.7.1., using a void fraction of 0.5. Similarly, the annular-mist heat-transfer factors are evaluated by the model presented in Section 3.7.3., using a void fraction of 0.75.

The interpolation method given here, including the weighting factor, was developed specifically for implementation into TRAC. The interpolation algorithm itself embodies no physics; it is a mathematical operation. However, the interpolation algorithm provides a transition between two regimes, which are represented by physical models.

3.7.3. Annular-Mist Interfacial Heat Transfer

In the annular-mist-flow regime, calculation of the interfacial heat-transfer factors is based on a superposition of the droplet and film fields. This can be generalized by the equation

$$X_{annular\text{-}mist} = (1 - W_f)\cdot(X_{drop} + X_{film}) + W_f\cdot X_{drop,max} , \tag{3-187}$$

where X represents the heat-transfer factors H_{ALVE}, H_{ALV}, H_{CHTI}, and H_{CHTA}. The weighting factor W_f was defined in Section 3.3.3. During flashing, however, the liquid-side heat-transfer factor H_{ALV} is redefined as the maximum of the value obtained from the above weighted average and the value obtained from the expression

$$H_{ALV,annular\text{-}mist} = (2.0e+8)\cdot(T_l - T_{sat})\cdot B_{cell} , \tag{3-188}$$

where

$$1.0e+6 \le \frac{H_{ALV,annular\text{-}mist}}{B_{cell}} \le 2.0e+8 . \tag{3-189}$$

The constant heat-transfer coefficients given here are heuristic and were developed specifically for implementation into TRAC.

Beginning with the droplet field, the liquid-side heat-transfer coefficient is evaluated based on a transient conduction solution (Ref. 3-29.), where

$$Nu = \frac{h_{il,drop}\, D_d}{k_l} = \frac{\pi}{3} C_c \frac{1 + T^*}{T^*} \tag{3-190}$$

for

$$T^* = \left[1 - \exp\left(-4\,\pi^2\, C_c \frac{k_l\, t_d}{2\,\rho_l\, c_{p,l}\, D_d{}^2}\right)\right]^{1/2}, \tag{3-191}$$

$$t_d = \frac{D_h}{V_r}, \tag{3-192}$$

and C_c = 1.0. In this case, the relative velocity (Ref. 3-30.) is given by

$$V_r = 2.462 \sqrt{g \frac{\rho_l - \rho_g}{\rho_g} \cdot \frac{D_d}{2}}\ . \tag{3-193}$$

The Sauter mean droplet diameter D_d is calculated as specified in Section 3.3.3.

After solving for the liquid-side heat-transfer coefficient, the relevant condensation heat-transfer factors can be defined such that

$$H_{ALVE,drop} = h_{il,drop} \cdot A_{i,drop} \tag{3-194}$$

and

$$H_{ALVE,drop,max} = h_{il,drop} \cdot A_{i,drop,max}\ , \tag{3-195}$$

and the relevant flashing heat-transfer factors can be defined such that

$$H_{ALV,drop} = h_{il,drop} \cdot A_{i,drop} \tag{3-196}$$

and

$$H_{ALV,drop,max} = h_{il,drop} \cdot A_{i,drop,max}\ . \tag{3-197}$$

The above interfacial-area terms likewise are calculated as specified in Section 3.3.3.

The vapor-side heat-transfer coefficient for the droplet field is evaluated using the method of Ryskin (Ref. 3-31.), where

$$Nu = \frac{h_{ig,drop}\, D_d}{k_g} = 2 + \sqrt{V^*_{max} \cdot P\, e} \tag{3-198}$$

for the Peclet number

$$Pe = \frac{\rho_g\, c_{p,g}\, D_d\, V_r}{k_g} . \tag{3-199}$$

The maximum dimensionless circulation velocity at the surface of the drop is defined such that

$$V^*_{max} = \frac{1.5}{1 + \dfrac{2.8\,(1 + 2\,\lambda)(2 + 3\,\kappa)}{(2 + 3\,\lambda)\sqrt{Re_g}}} , \tag{3-200}$$

where

$$Re_g = \frac{\rho_g\, D_d\, V_r}{\mu_g} ,$$

$$\lambda = \sqrt{\frac{\rho_l\, \mu_l}{\rho_g\, \mu_g}} ,$$

and

$$\kappa = \frac{\mu_l}{\mu_g} .$$

The relative velocity term V_r and the droplet diameter D_d are equivalent to the values used for the liquid-side heat transfer. The vapor-side heat-transfer factors thus can be calculated by

$$H_{CHTI,drop} = h_{ig,drop} \cdot A_{i,drop} \tag{3-201}$$

and

$$H_{CHTI,drop,max} = h_{ig,drop} \cdot A_{i,drop,max} . \tag{3-202}$$

The direct sensible heat transfer between liquid and gas in the droplet field also uses the model of Ryskin (Ref. 3-31.). For this application, however, each of the combined-gas parameters has been replaced by its counterpart for the noncondensables. The gas-to-liquid heat-transfer coefficient therefore is defined as a function of Nusselt number, where

$$Nu = \frac{h_{gl,drop}\, D_d}{k_a} = 2 + \sqrt{V^*_{max} \cdot P\, e} \qquad (3\text{-}203)$$

for

$$Pe = \frac{\rho_a\, c_{p,a}\, D_d\, V_r}{k_a}$$

and

$$V_r = 2.462 \sqrt{g \frac{\rho_l - \rho_a}{\rho_a} \cdot \frac{D_d}{2}} \ .$$

The circulation velocity term is similarly expressed by

$$V^*_{max} = \frac{1.5}{1 + \dfrac{2.8\,(1 + 2\,\lambda)(2 + 3\,\kappa)}{(2 + 3\,\lambda)\sqrt{Re_a}}}$$

for

$$Re_a = \frac{\rho_a\, D_d\, V_r}{\mu_a} \ ,$$

$$\lambda = \sqrt{\frac{\rho_l\, \mu_l}{\rho_a\, \mu_a}} \ ,$$

and

$$\kappa = \frac{\mu_l}{\mu_a} \ .$$

Based on the above heat-transfer coefficient, the appropriate heat-transfer factors are defined such that

$$H_{CHTA,drop} = h_{gl,drop} \cdot A_{i,drop}$$

and

$$H_{CHTA,drop,max} = h_{gl,drop} \cdot A_{i,drop,max} .$$

As with the liquid-side and vapor-side models, the above interfacial heat-transfer terms and the droplet diameter D_d are calculated as described in Section 3.3.3.

Alternatively, for the liquid film, all three heat-transfer coefficients (h_{il}, h_{ig}, and h_{gl}) are defined as a function of the Stanton number such that

$$St = \frac{h_{il,film}}{\rho_l \, c_{p,l} \, V_l} = \frac{h_{ig,film}}{\rho_g \, c_{p,g} \, |V_g - V_l|} = \frac{h_{gl,film}}{\rho_a \, c_{p,a} \, |V_g - V_l|} . \quad (3\text{-}204)$$

The above Stanton number criterion is based on the model of Bankoff (Ref. 3-32.), where

$$St = 0.0045 \left(\frac{\rho_g \, V_g \, \mu_l}{\rho_l \, V_l \, \mu_g} \right)^{1/3} . \quad (3\text{-}205)$$

The film-field heat-transfer factors in turn are defined by

$$H_{ALVE,film} = h_{il,film} \cdot A_{i,film} , \quad (3\text{-}206)$$

$$H_{ALV,film} = h_{il,film} \cdot A_{i,film} , \quad (3\text{-}207)$$

$$H_{CHTI,film} = h_{ig,film} \cdot A_{i,film} , \quad (3\text{-}208)$$

and

$$H_{CHTA,film} = h_{gl,film} \cdot A_{i,film} \quad (3\text{-}209)$$

for the liquid-film interfacial area defined in Section 3.3.3. All correlations used in the annular-mist interfacial heat-transfer modeling are used in TRAC, as reported in the source references for this constitutive model.

3.7.4. Stratified-Flow Interfacial Heat Transfer

Under fully stratified-flow conditions, the liquid-side heat-transfer coefficient is evaluated using the constant Stanton number criterion suggested by Linehan (Ref. 3-33.), where

$$St = \frac{h_{il,strat}}{\rho_l \, c_{p,l} \, V_l} = 0.0073 . \quad (3\text{-}210)$$

The liquid-side heat-transfer factors thus are defined by

$$H_{ALVE,strat} = h_{il,strat} \cdot A_{i,strat}$$

and

$$H_{ALV,strat} = h_{il,strat} \cdot A_{i,strat} ,$$

where the stratified-flow interfacial area is calculated as discussed in Section 3.3.4.

The Linehan criterion is used in TRAC, as given in the source reference for this constitutive model.

However, when the flow is not fully stratified, the code interpolates between the heat-transfer factors for stratified flow, as calculated above, and the values otherwise determined with respect to the basic flow-regime map. In general form, this can be expressed as

$$X_{map,strat} = (1 - W_{st}) \cdot X_{map} + W_{st} \cdot X_{strat} ,$$

where X represents the heat-transfer factors H_{ALVE} and H_{ALV} and where $0 \le W_{st} \le 1$. The weighting factor W_{st} is calculated as a function both of void fraction (flow regime) and critical velocity. In general, for 3D components, the weighting factor is nonzero for velocities less that 10 times the critical velocity (see Section 3.2.4.). For additional detail, the reader is referred to Appendix E (Section E.2.7.).

As noted for bubbly slug, annular-mist, and transition flows, the liquid-side heat-transfer factor for flashing under stratified-flow conditions ($H_{ALV,map,strat}$) likewise is redefined as the maximum of the value obtained from the above weighted average and the value obtained from the expression

$$H_{ALV,map,strat} = (2.0e+8) \cdot (T_l - T_{sat}) \cdot B_{cell} , \qquad (3\text{-}211)$$

where

$$1.0e+6 \le \frac{H_{ALV,map,strat}}{B_{cell}} \le 2.0e+8 . \qquad (3\text{-}212)$$

The constant heat-transfer coefficients given here are heuristic and were developed specifically for implementation into TRAC.

Finally, no modifications are made to the vapor-side and sensible heat-transfer factors for stratified flow. Thus,

$$H_{CHTI,map,strat} = H_{CHTI,map}$$

and

$$H_{CHTA,map,strat} = H_{CHTA,map} .$$

The interpolation method given here, including the weighting factor, was developed specifically for implementation into TRAC. The interpolation algorithm itself embodies no physics; it is a mathematical operation. However, the interpolation algorithm provides a transition between two regimes, which are represented by physical models. The constant heat-transfer coefficients were developed specifically for implementation into TRAC.

3.7.5. Plug-Flow Interfacial Heat Transfer

Under plug-flow conditions, the liquid-side heat-transfer coefficient is calculated from the constant Stanton number relation

$$St = \frac{h_{il,plug}}{\rho_l c_{p,l} V_l} = 0.02 . \qquad (3\text{-}213)$$

Thus, the heat-transfer factor $H_{ALVE,plug}$ can be defined such that

$$H_{ALVE,plug} = h_{il,plug} \cdot A_{i,plug} ,$$

where the interfacial-area term is calculated as specified in Section 3.3.5.

The above heat-transfer factor then is superimposed on the corresponding factor calculated from the bubbly slug, annular-mist, churn, and stratified-flow models, as appropriate. This can be expressed by

$$H_{ALVE,map,strat,plug} = (1 - W_{plug}) H_{ALVE,map,strat} + W_{plug} H_{ALVE,plug}$$

for the weighting factor W_{plug} defined in Section 3.3.5.

Because plug flow can occur only when the liquid side is condensing, a definition of the liquid-side heat-transfer factor for flashing (H_{ALV}) is unnecessary. Moreover, there are no modifications made to the vapor-side and sensible heat-transfer factors for plug flow. In other words,

$$H_{CHTI,map,strat,plug} = H_{CHTI,map,strat}$$

and

$$H_{CHTA,map,strat,plug} = H_{CHTA,map,strat} .$$

The constant-Stanton-number model is used in TRAC, as given in the source references for this constitutive model. The overall modeling of the plug-flow interfacial heat transfer given here is heuristic and was developed specifically for implementation into TRAC. The interpolation method presented, including the weighting factor, was developed specifically for implementation into TRAC. The interpolation algorithm itself embodies no physics; it is a mathematical operation. However, the interpolation algorithm provides a transition between two regimes, which are represented by physical models.

3.7.6. Reflood Interfacial Heat Transfer

During reflood of the core region, TRAC utilizes the flow-regime map of Ishii and his coworkers (Refs. 3-3. to 3-5.) (see Section 3.2.6.). Consistent with the interfacial areas defined in Section 3.3.6., the code calculates the overall reflood heat-transfer factors for a given hydraulic cell based on the weighted average of the individual heat-transfer factors for bubbly, inverted annular, and dispersed flow. This can be generalized by the equation

$$X_{reflood} = W_{sb} \cdot X_{bubbly} + W_{inv} \cdot X_{inv} + W_{ds} \cdot X_{ds} , \quad (3\text{-}214)$$

where X represents each of the heat-transfer factors H_{ALVE}, H_{CHTI}, and H_{CHTA}. In the above equation, the linear weighting factors W_{sb}, W_{inv}, and W_{ds} are based on the relative axial distance within each cell for which the appropriate flow regime is present. The calculation of these weighting factors is presented in Appendix F (Section F.1.6., Table F-4.).

The interpolation method given here, including the weighting factor, was developed specifically for implementation into TRAC. The interpolation algorithm itself embodies no physics; it is a mathematical operation. However, the interpolation algorithm provides a transition between two regimes, which are represented by physical models.

For flashing conditions, the liquid-side heat-transfer factor H_{ALV} is defined as the maximum of H_{ALVE} (calculated by the above relation) and the value obtained from the expression

$$H_{ALV,reflood} = (2.0e+8) \cdot (T_l - T_{sat}) \cdot B_{cell} , \quad (3\text{-}215)$$

where

$$1.0e+6 \leq \frac{H_{ALV,reflood}}{B_{cell}} \leq 2.0e+8 . \quad (3\text{-}216)$$

The constant heat-transfer coefficients given here are heuristic and were developed specifically for implementation into TRAC.

The following paragraphs summarize the calculation methodology for the bubbly, inverted-annular-, and dispersed-flow interfacial heat-transfer factors. Additional details of the reflood interfacial heat-transfer models likewise can be found in Appendix F.

3.7.6.1. Bubbly Flow. The interfacial heat-transfer coefficients (h_{il}, h_{ig}, and h_{gl}) and heat-transfer factors (H_{ALVE}, H_{CHTI}, and H_{CHTA}) for bubbly flow under reflood conditions, except for the flashing model, are identical to those defined in Section 3.7.1. The corresponding interfacial area is determined by the expressions presented in Section 3.3.1. When $T_l > T_{sat}$ (i.e., the liquid is superheated), a simple flashing model is used to determine the liquid-side heat-transfer factor. This simple model uses the kinetic theory of evaporation from liquid surfaces (Ref. 3-34., p. 56). The liquid-side heat-transfer coefficient associated with flashing is

$$h_{fls} = C_{eva}\left[0.01857\frac{\rho_v h_{fg}^2}{T_{sat}^{1.5}}\right], \tag{3-217}$$

where the coefficient of evaporation, C_{eva}, is defined for bubbly and annular-mist-flow regimes in the nucleate-boiling region, and h_{fg} is the latent heat of vaporization. The coefficient of evaporation is considered to be void-fraction-dependent in the bubbly flow regime when the cell void fraction is between 0.3 and 0.5. Currently, C_{eva} is given the value 0.0002 for all void fractions up to 0.5 in the bubbly flow.

The numerical value in the model, 0.01857, has been changed from the original value, 0.04, given by Hsu and Graham (Ref. 3-34., p. 56). In addition, the factor C_{eva} was not a part of the original correlation.

3.7.6.2. Inverted Annular Flow. The liquid-side heat-transfer factor is calculated as follows:

If $T_l < T_{sat}$, the heat-transfer coefficient is calculated using the standard subcooled heat-transfer correlations for the given flow regime.

If $T_l > T_{sat}$, i.e., the liquid is superheated, then

$$H_{ALV,inv} = h_{fls}\, A_{i,inv}, \tag{3-218}$$

where

$$h_{fls} = C_{eva}\left[0.01857\frac{\rho_v h_{fg}^2}{T_{sat}^{1.5}}\right], \tag{3-219}$$

and the coefficient of evaporation for the flashing model, C_{eva}, is set to 0.002.

The numerical value in the model, 0.01857, has been changed from the original value, 0.04, given by Hsu and Graham (Ref. 3-34., p. 56). In addition, the factor C_{eva} was not a part of the original correlation.

Additionally, the vapor-side heat-transfer factor and the liquid-to-gas sensible heat-transfer factor are defined by the simple relations

$$H_{CHTI,inv} = h_{ig,inv} \cdot A_{i,inv} \tag{3-220}$$

and

$$H_{CHTA,inv} = h_{gl,inv} \cdot A_{i,inv} , \tag{3-221}$$

where

$$h_{ig,inv} = 3 \times 10^3 \text{ W / m}^2\text{-K}$$

and

$$h_{gl,inv} = 10^3 \text{ W / m}^2\text{-K} .$$

The interfacial area for inverted annular flow is calculated as described in Section 3.3.6.

3.7.6.3. Dispersed Flow. The following are used to calculate the liquid-side heat-transfer factor:

If $T_l < T_{sat}$, the heat-transfer coefficient is calculated using the standard subcooled heat-transfer correlations for the given flow regime.

If $T_l > T_{sat}$, the liquid is superheated and

$$H_{ALV,ds} = h_{fls} A_{i,ds} , \tag{3-222}$$

where

$$h_{fls} = C_{eva}\left[0.01857 \frac{\rho_v h_{fg}^2}{T_{sat}^{1.5}}\right] \tag{3-223}$$

and the coefficient of evaporation for the flashing model, C_{eva}, is set to 0.002.

The numerical value in the model, 0.01857, has been changed from the original value, 0.04, given by Hsu and Graham (Ref. 3-34., p. 56). In addition, the factor C_{eva} was not a part of the original correlation.

The vapor-side heat-transfer factor is defined by

$$H_{CHTI,ds} = 10^{-6}\ W/K \tag{3-224}$$

for $\alpha_{hom} \geq 1$ and $(1 - \alpha_{dd}) \leq 0.95$. If the cell $\alpha < 0.98$ (post-agitated dispersed-flow regime),

$$H_{CHTI,\,pa} = H'_{CHTI}\left[\frac{\alpha - \alpha_{SM}}{\alpha_{DP} - \alpha_{SM}}\right]^{0.01}, \tag{3-225}$$

where α_{SM} and α_{DP} are the void fractions at the flow-regime transitions between smooth / rough-wavy IAF and dispersed (post-agitated) / highly dispersed flows, respectively.

If the cell $\alpha \geq 0.98$ (highly dispersed flow regime),

$$H_{CHTI,\,df} = H'_{CHTI}\ .$$

In the above equation, the factor H'_{CHTI} is calculated from a modified form of Unal's model for vapor generation (Ref. 3-34.), where

$$H'_{CHTI} = (0.05)\cdot 0.315\exp\left(-C_{u1}\frac{P}{P_{cr}}\right)\left[V_g\rho_g\frac{1-\alpha_{dd}}{\alpha_{hom}}\right]^{C_{u2}}$$

$$\cdot\frac{k_g Pr_g^{0.33}}{\mu_g^{0.55}(2L_o^2)^{0.725}}B_{cell}\left[\frac{\sqrt{\rho_g\sigma L_o}}{\mu_g}\right]^{0.4833}. \tag{3-226}$$

The constants C_{u1} and C_{u2} are equivalent to 30 and 0.33, respectively. The numerical factor, 0.05, was not a part of the original correlation.

The homogeneous void fraction α_{hom} is given by

$$\alpha_{hom} = \frac{x_l\,\rho_l}{x_l\,\rho_l + (1 - x_l)\,\rho_g} \tag{3-227}$$

for the mass fraction

$$x_l = \frac{\rho_g\,V_g\,(1 - \alpha_{dd})}{\rho_g\,V_g\,(1 - \alpha_{dd}) + \rho_l\,V_l\,\alpha_{dd}}\ . \tag{3-228}$$

The droplet fraction α_{dd} is calculated as presented in Section 3.3.6.

Finally, in the presence of noncondensables, the liquid-to-gas sensible heat-transfer factor is calculated from the linear weighting

$$H_{CHTA,ds} = W_{fd}\cdot\left(A_{i,drop}\cdot h_{gl,drop} + A_{i,film}\cdot h_{gl,film}\right) + (1 - W_{fd})\cdot A_{i,drop,max}\cdot h_{gl,drop}\ . \tag{3-229}$$

The weighting factor W_{fd} and the interfacial-area terms are defined in Section 3.3.6.3.

The interpolation method and weighting factor are heuristic and are developed specifically for TRAC.

The heat-transfer coefficient for the droplet field $h_{gl,\mathrm{drop}}$ is based on the model of Ryskin (Ref. 3-31.) for annular-mist flow. Similarly, the heat-transfer coefficient for the film field $h_{gl,\mathrm{film}}$ is calculated from Bankoff's model for annular-mist flow. Both heat-transfer coefficient models are discussed in Section 3.7.3. Both correlations are used in TRAC, as given in the source references for this constitutive model.

3.7.7. Effect of Noncondensables

In the presence of noncondensables, TRAC modifies the liquid-side heat-transfer factor H_{ALVE} during condensation and evaporation. Under evaporation conditions ($T_{sv} < T_l < T_{\mathrm{sat}}$), H_{ALVE} is calculated by a diffusion model in which

$$H_{\mathrm{ALVE,nc}} = h_M h_{fg} (\rho_s - \rho_g + \rho_a) A_i \ . \tag{3-230}$$

Here, the steam density ρ_s at the interface is estimated using the ideal gas approximation

$$\rho_s = \frac{(P_{\mathrm{sat}})_{T_{\mathrm{sat}} = T_l}}{R_s T_l} \ . \tag{3-231}$$

The mass-transfer coefficient h_M is determined, independent of flow regime, as a function of the Sherwood number

$$\mathrm{Sh} = \frac{h_M D_h}{D_o} \ , \tag{3-232}$$

where

$$\mathrm{Sh} = \begin{cases} 3.656 & \mathrm{Re} \le 2300 \quad (3\text{-}233) \\ 0.023\, \mathrm{Re}^{0.8}\, \mathrm{Sc}^{1/3} & \mathrm{Re} > 2300 \quad (3\text{-}234) \end{cases}$$

for the Schmidt number

$$\mathrm{Sc} = \frac{\mu_g}{\rho_g D_o} \tag{3-235}$$

and the Reynolds number

$$\mathrm{Re} = \frac{G_g D_h}{\mu_g} \ . \tag{3-236}$$

The mass-transfer modeling for evaporation is based on the heat- and mass-transfer analogy. The analogy has been shown to be correct for the conditions for which the heat-transfer-coefficient correlation is correct.

The diffusion coefficient D_o is evaluated from

$$D_o = \frac{10^{-3}}{P}\left(-699.2438 + 4.9249\ T_g + 0.0171\ T_g^2\right) . \tag{3-237}$$

The diffusion coefficient is a curve fit to the theoretical equation for diffusion of steam in air.

During condensation ($T_l < T_{sv}$), H_{ALVE} is modified according to the empirical correlation of Sklover and Rodivilin (Ref. 3-35.), where

$$0.1 \le \frac{H_{ALVE,nc}}{H_{ALVE}} = \frac{h_{il,nc}}{h_{il}} = 0.366\left(\frac{\rho_g - \rho_a}{\rho_a}\right)^{0.2}\left(\frac{G_v}{G_l}\right)^{0.2} \le 1.0 . \tag{3-238}$$

For the special case of fully stratified flow, the above equation is modified slightly such that

$$0.1 \le \frac{H_{ALVE,nc}}{H_{ALVE}} = \frac{h_{il,nc}}{h_{il}} = 0.366\left(\frac{\rho_g - \rho_a}{\rho_a}\right)^{0.2}\left(\frac{G_v}{G_l}\right)^{0.2} \le 0.9 .$$

However, in either equation, the liquid and vapor mass fluxes are limited by

$$3000 \le G_l \le 18{,}000\ kg/m^2\text{-}s \tag{3-239}$$

and

$$0 \le G_v \le 640\ kg/m^2\text{-}s . \tag{3-240}$$

Recall from Section 3.1. that the interface-to-gas heat transfer per unit volume is adjusted by the ratio of the vapor partial pressure to the total pressure, or

$$q_{ig} = \frac{P_v}{P} H_{CHTI} \frac{(T_g - T_{sv})}{B_{cell}} . \tag{3-241}$$

Likewise, the liquid-to-gas sensible heat transfer per unit volume is adjusted by the ratio of the noncondensable partial pressure to the total pressure such that

$$q_{gl} = \frac{P_a}{P} H_{CHTA} \frac{(T_g - T_l)}{B_{cell}} . \tag{3-242}$$

Thus, modifications to either heat-transfer factor (H_{CHTI} or H_{CHTA}) to account for the presence of noncondensables are not performed.

3.8. Wall Heat Transfer

Final closure of the fluid energy equations requires that the wall-to-liquid and wall-to-gas heat-transfer rates per unit volume be specified such that

$$q_{wl} = h_{wl} A_w \frac{(T_w - T_l)}{B_{cell}} \tag{3-243}$$

and

$$q_{wg} = h_{wg} A_w \frac{(T_w - T_g)}{B_{cell}} . \tag{3-244}$$

This likewise requires the calculation of the wall-to-liquid and wall-to-gas heat-transfer coefficients h_{wl} and h_{wg}. These heat-transfer coefficients already are assumed to include the fraction of the wall contacted by each respective phase, or

$$h_{wl} = f_l \cdot h'_{wl} \tag{3-245}$$

and

$$h_{wg} = (1 - f_l) \cdot h'_{wg} , \tag{3-246}$$

where f_l is the liquid fraction contacting the wall and h'_{wl} and h'_{wg} are the separate phasic heat-transfer coefficients.

The heat-transfer coefficients h_{wl} and h_{wg} clearly are functions of the heat-transfer regime that is present. TRAC considers eight individual heat-transfer regimes:

1. forced convection to a single-phase liquid (regime 1),
2. nucleate boiling (regime 2),
3. transition boiling (regime 3),
4. film boiling (regime 4),
5. convection to a single-phase vapor (regime 6),
6. convection to a two-phase mixture (regime 7),
7. condensation (regime 11), and
8. natural convection to a single-phase liquid (regime 12).

In addition to these eight regimes, the code includes models for the critical heat flux, which establishes the boundary between nucleate and transition boiling, and the minimum stable film-boiling temperature, which provides the boundary between transition boiling and film boiling. Under core reflood conditions, the code also provides revised models for transition boiling and film boiling that correspond to the flow-regime map of Ishii and his coworkers (Refs. 3-3. to 3-5.) (see Section 3.2.6.). In the following sections, the individual models for h_{wl} and h_{wg} will be discussed for each of the heat-transfer regimes. A summary of these correlations also is provided in Table 3-7.

3.8.1. Natural Convection to Liquid

In the heat-transfer regime for natural convection to a single-phase liquid, the wall-to-liquid heat-transfer coefficient is determined by one of two correlations. These include the correlation for laminar flow (Ref. 3-36.),

$$h_{wl} = 0.59 \frac{k_l}{D_h} (Gr \cdot Pr)^{0.25} , 10^4 < (Gr \cdot Pr) < 10^9 , \tag{3-247}$$

or the correlation for turbulent flow (Ref. 3-36.),

$$h_{wl} = 0.10 \frac{k_l}{D_h} (Gr \cdot Pr)^{0.3333} , \qquad 10^9 < (Gr \cdot Pr) < 10^{13} .$$

In the above equation, the Grashof number and Prandtl number are defined as

$$Gr = \frac{g \beta |T_w - T_l| \rho_f^2 D_h^3}{\mu_l^2} \tag{3-248}$$

and

$$Pr = \frac{\mu_l c_{p,l}}{k_l} . \tag{3-249}$$

Additionally, the parameters β and ρ_f are approximated as

$$\beta = - \frac{\partial \rho_l}{\partial T} \cdot \frac{1}{\rho_f} \tag{3-250}$$

and

$$\rho_f = \rho_l + \frac{\partial \rho_l}{\partial T} (T_f - T_l) \tag{3-251}$$

for

$$T_f = 0.5 (T_w + T_l) . \tag{3-252}$$

Under single-phase liquid conditions, the wall-to-gas heat-transfer coefficient is defined to be zero, or

$$h_{wg} = 0.$$

In the correlation for the laminar-flow natural-convection heat-transfer coefficient, the equivalent diameter is used in place of the distance over which the local value of the heat-transfer coefficient has been averaged. The same substitution has been performed in the turbulent correlation; however, the characteristic dimension cancels out of this correlation. Both of these correlations are used widely in engineering analyses of single-phase heat transfer under natural-convection conditions.

3.8.2. Forced Convection to Liquid

During single-phase forced convection to a liquid, TRAC calculates the wall-to-liquid heat-transfer coefficient via the Dittus-Boelter relation (Ref. 3-37.):

$$h_{wl} = h_{forc} = 0.023 \frac{k_l}{D_h} Re_l^{0.8} Pr_l^{0.4} , \tag{3-253}$$

where

$$Re_l = \frac{|V_l| \rho_l (1 - \alpha) D_h}{\mu_l} \tag{3-254}$$

and

$$Pr_l = \frac{\mu_l c_{p,l}}{k_l} . \tag{3-255}$$

For a single-phase liquid, the wall-to-gas heat-transfer coefficient is zero, or

$$h_{wg} = 0.$$

The Dittus-Boelter correlation is used widely in engineering analyses of single-phase forced-convection heat-transfer applications. The basic form of the correlation is based firmly on theoretical considerations, and it has been found to be applicable to a variety of fluids and flow-channel geometries. The correlation is used in TRAC as it is given in the literature.

3.8.3. Nucleate Boiling

In the nucleate-boiling heat-transfer regime, the total wall heat flux is given by Chen (Ref. 3-38.) as the summation of nucleate-boiling and convective mechanisms, where

$$q_{total} = h_{forc} (T_w - T_l) + h_{nucb} (T_w - T_{sat}) . \tag{3-256}$$

The wall-to-liquid heat flux then is calculated from the above total by subtracting the wall-to-gas heat flux. In terms of the wall-to-liquid heat-transfer coefficient, this can be expressed as

$$h_{wl} = \frac{\left[h_{forc}\,(T_w - T_l) + h_{nucb}\,(T_w - T_{sat}) - h_{wg}\,(T_w - T_g)\right]}{(T_w - T_l)} .$$

Chen (Ref. 3-38.) calculates the heat-transfer coefficient for the convective component h_{forc} from a modified form of the Dittus-Boelter correlation (Ref. 3-37.) such that

$$h_{forc} = 0.023\,\frac{k_l}{D_h}\left(\frac{|V_l|\,\rho_l\,(1-\alpha)\,D_h}{\mu_l}\right)^{0.8}\left(\frac{\mu_l\,c_{p,l}}{k_l}\right)^{0.4}\cdot F \quad . \tag{3-257}$$

The adjustment factor F in turn is based on the Martinelli factor X_{TT}, where

$$F = \begin{cases} 1.0 & (X_{TT})^{-1} \le 0.10 \quad (3\text{-}258) \\ 2.35\left(X_{TT}^{-1} + 0.213\right)^{0.736} & (X_{TT})^{-1} > 0.10 \quad (3\text{-}259) \end{cases}$$

for

$$X_{TT}^{-1} = \left(\frac{x}{1-x}\right)^{0.9}\left(\frac{\rho_l}{\rho_g}\right)^{0.5}\left(\frac{\mu_g}{\mu_l}\right)^{0.1} , \tag{3-260}$$

subject to the constraint that $(X_{TT})^{-1} \le 100$.

The nucleate-boiling term is based on the work of Forster and Zuber (Ref. 3-39.) for pool boiling. The heat-transfer coefficient h_{nucb} thus is defined by

$$h_{nucb} = 0.00122\,\frac{k_l^{0.79}\,c_{p,l}^{0.45}\,\rho_l^{0.49}}{\sigma^{0.5}\,\mu_l^{0.29}\,h_{fg}^{0.24}\,\rho_g^{0.24}}\,(T_w - T_{sat})^{0.24}\,(P_w - P)^{0.75}\cdot S \quad , \tag{3-261}$$

where P_w is the saturation pressure corresponding to the wall temperature and S is a suppression factor to account for the fact that the liquid superheat is not constant across the boundary layer. The suppression factor is evaluated from

$$S = \begin{cases} \left(1 + 0.12\,Re_{TP}^{1.14}\right)^{-1} & Re_{TP} < 32.5 \quad (3\text{-}262) \\ \left(1 + 0.42\,Re_{TP}^{0.78}\right)^{-1} & 32.5 \le Re_{TP} \le 70.0 \quad (3\text{-}263) \end{cases}$$

for

$$Re_{TP} = 10^{-4} \frac{|V_l| \rho_l (1 - \alpha) D_h}{\mu_l} \cdot F^{1.25} , \quad (3\text{-}264)$$

with the limitation that $Re_{TP} \leq 70$. At void fractions >0.7, this suppression factor is modified to produce the correct limit of 0.0 as the void fraction approaches 1.0. Further information on the interpolation scheme is available in Appendix F (Section F.2.1.2.4.).

The Chen correlation (Ref. 3-38.) has evolved over time since it was introduced. The version used in TRAC is the latest form given in the literature. The correlation is used in TRAC as it has appeared in the literature. The extensive comparisons of predictions of the correlation with experimental data are summarized in Appendix F.

Additionally, the wall-to-gas heat-transfer coefficient h_{wg} is defined as the maximum of the values obtained from the natural-convection and Dougall-Rohsenow (forced-convection) correlations, or

$$h_{wg} = \max(h_{NC}, h_{dr}) .$$

The vapor natural-convection correlation (Ref. 3-40.) was obtained from vertical planes and cylinders in the turbulent flow regime ($10^9 < Gr \cdot Pr < 10^{13}$) and is given by

$$h_{NC} = 0.13 k_g \left[\frac{\rho_g^2 g |T_w - T_g|}{\mu_g^2 T_g} \right]^{0.3333} \cdot Pr_g^{0.3333} . \quad (3\text{-}265)$$

The Dougall-Rohsenow correlation for forced convection (Ref. 3-28.) is defined by

$$h_{dr} = 0.023 \frac{k_g}{D_h} Re_{TP}^{0.8} Pr_g^{0.4} . \quad (3\text{-}266)$$

In the above equation, the two-phase Reynolds number is defined by

$$Re_{TP} = \frac{[|V_g| \alpha + |V_l| (1 - \alpha)]}{\mu_g} \rho_g D_h . \quad (3\text{-}267)$$

Likewise, in both expressions, the Prandtl number is given by

$$Pr_g = \frac{\mu_g c_{p,g}}{k_g} . \quad (3\text{-}268)$$

These correlations are used in TRAC in the same form as that given in the references. The characteristic dimension has been canceled out of the natural-convection correlation.

Final adjustments are performed on both the wall-to-liquid and the wall-to-gas heat-transfer coefficients to provide smooth transitions between heat-transfer regimes. Additional details of these adjustments are presented in Appendix F (Section F.2.1.2.4.).

3.8.4. Critical Heat Flux

The critical heat-flux model provides the transition point or boundary between the nucleate- and transition-boiling heat-transfer regimes. The code uses the empirical correlation of Biasi Ref. 3-41.). The Biasi correlation is coded as

$$q_{CHF} = \max(q_{CHF1}, q_{CHF2}) \tag{3-269}$$

for

$$q_{CHF1} = \frac{1.883e+07}{D_h^n |G|^{1/6}} \left[\frac{f_p}{|G|^{1/6}} - x_e \right] \tag{3-270}$$

and

$$q_{CHF2} = \frac{3.78e+07}{D_h^n |G|^{0.6}} h_p \left[1 - x_e \right] . \tag{3-271}$$

In the above equation, the parameters n, f_p, and h_p are defined as follows:

$$n = \begin{cases} 0.6 & D_h < 1 \text{ cm} \quad (3\text{-}272) \\ 0.4 & D_h \geq 1 \text{ cm}, \quad (3\text{-}273) \end{cases}$$

$$f_p = 0.7249 + 0.099 P \exp(-0.032 P) , \tag{3-274}$$

and

$$h_p = -1.159 + \frac{8.99 P}{10 + P^2} + 0.149 P \exp(-0.019 P) . \tag{3-275}$$

Although q_{CHF} is expressed in W/m^2, the above mass flux G is expressed in g/cm^2-s, the pressure P in bars, and the hydraulic diameter D_h in centimeters. The parameter x_e represents the equilibrium quality.

However, at low mass fluxes and at high void fractions, the code modifies the critical-heat-flux calculation. Below a mass flux of 200 kg/m^2-s, the Biasi correlation is evaluated with a constant mass flux, where $|G| = 200$ kg/m^2-s. Similarly, at void fractions >0.98, the critical heat flux is assumed to be very small. TRAC uses the value $q_{CHF} = 1.0$ W/m^2. Between void fractions of 0.97 and 0.98, TRAC linearly interpolates q_{CHF} from the value calculated by Biasi and 1.0.

The Biasi correlation is used in TRAC as given in the source references.

3.8.5. Transition Boiling

Under normal conditions, the total wall heat flux for transition boiling is defined as the sum of nucleate-boiling and film-boiling heat-transfer terms, weighted by the fraction of wall area that is wet (Ref. 3-42.). The total heat flux also is defined as the sum of the wall-to-liquid and wall-to-gas phasic heat-flux terms. The total heat flux thus can be expressed by

$$q_{trans} = \xi \cdot q_{CHF} + (1 - \xi) \cdot q_{min} = h_{wl} \cdot (T_w - T_l) + h_{wg} \cdot (T_w - T_g) \quad (3\text{-}276)$$

for the wet-wall area fraction

$$\xi = \left(\frac{T_w - T_{min}}{T_{CHF} - T_{min}} \right)^2 . \quad (3\text{-}277)$$

In the first definition of the total heat flux, the critical heat flux q_{CHF} is calculated as presented in Section 3.8.4. The heat flux (q_{min}) at the minimum stable film-boiling temperature (T_{min}) is given as

$$q_{min} = h_{wlmin} \cdot (T_{min} - T_l) + h_{wgmin} \cdot (T_{min} - T_g) + h_{fBB} \cdot (T_{min} - T_{sat}) . \quad (3\text{-}278)$$

For this expression, the heat-transfer coefficient h_{wgmin} is evaluated as the maximum of the natural-convection or the Dougall-Rohsenow correlations, or

$$h_{wgmin} = \max(h_{NC}, h_{dr}) . \quad (3\text{-}279)$$

Both the natural-convection and the Dougall-Rohsenow correlations were presented in Section 3.8.3. For purposes of computing h_{wgmin}, however, the appropriate properties in either correlation are evaluated at the minimum stable film-boiling temperature T_{min}. Similarly, the liquid heat-transfer coefficient h_{wlmin} is calculated by

$$h_{wlmin} = h_r \cdot \left(\frac{T_{min} - T_{sat}}{T_{min} - T_l} \right) \quad (3\text{-}280)$$

for the radiation heat-transfer coefficient

$$h_r = (0.9999 - \alpha) \, \sigma_r \, \varepsilon \left(\frac{T_{min}^4 - T_{sat}^4}{T_{min} - T_{sat}} \right) . \quad (3\text{-}281)$$

And finally, the heat-transfer coefficient h_{fBB} is based on the modified Bromley correlation for film boiling (Ref. 3-43.) such that

$$h_{fBB} = 0.62 \cdot \left(\frac{\rho_g \, k_g^3 \, (\rho_l - \rho_g) \, g \, h'_{fg}}{\mu_g \, (T_w - T_{sat}) \, \lambda} \right)^{0.25} \quad (3\text{-}282)$$

for the Taylor wavelength

$$\lambda = 2\pi \cdot \left(\frac{\sigma}{g\,(\rho_l - \rho_g)} \right)^{1/2} \tag{3-283}$$

and the modified latent heat

$$h'_{fg} = h_{fg} + 0.5\, c_{p,g}\,(T_g - T_{sat}) \,. \tag{3-284}$$

Now, the wall-to-gas phasic heat-transfer coefficient also is evaluated as the maximum of the natural-convection and the Dougall-Rohsenow correlations such that

$$h_{wg} = \max(h_{NC},\, h_{dr}) \,. \tag{3-285}$$

Both of the correlations in question were defined in Section 3.8.3. and will not be repeated here. Based on the value of h_{wg} and the above calculation of the total heat flux for transition boiling, the wall-to-liquid phasic heat-transfer coefficient can be determined from

$$h_{wl} = \frac{q_{trans} - h_{wg}\,(T_w - T_g)}{(T_w - T_l)} \,. \tag{3-286}$$

In those situations where the cell void fraction is >0.98, a final interpolation is performed on the total heat flux q_{trans} to provide a smooth transition between heat-transfer regimes. Details of the interpolation scheme can be found in Appendix F (Section F.2.1.3.4.).

The transition-boiling heat-transfer model given here is heuristic and was developed specifically for implementation into TRAC.

3.8.5.1. Core Reflood. Under core reflood conditions, the heat-transfer-coefficient models for the transition-boiling regime take a slightly different form. Specifically, the total transition-boiling heat flux is assumed to decrease exponentially as a function of axial distance from the critical to the film-boiling heat flux. This can be expressed as

$$q_{TR} = q_{CHF} \cdot \exp(-B\,(Z - Z_{CHF})) \tag{3-287}$$

such that

$$q_{TR} = q_{CHF} \quad \text{at} \quad Z = Z_{CHF} \,, \tag{3-288}$$

and

$$q_{TR} = q_{film} \quad \text{at} \quad Z = Z_{TR} \,. \tag{3-289}$$

The length of the transition-boiling region thus can be specified by

$$Z_{TR} - Z_{CHF} = \frac{-\ln\left(\frac{q_{film}}{q_{CHF}}\right)}{B} . \quad (3\text{-}290)$$

In the above equation, the critical heat flux q_{CHF} is calculated as defined in Section 3.8.4. However, the ratio of the film-boiling to the critical heat flux is assumed to be constant such that

$$\frac{q_{film}}{q_{CHF}} = 1.2e\text{-}10 . \quad (3\text{-}291)$$

The parameter *B* is a function of both void fraction and flow direction. The value of this parameter for different flow conditions is discussed in Appendix F (Section F.2.2.3.3.).

The wall-to-gas heat-transfer coefficient likewise is redefined for core reflood conditions. It is evaluated using the Webb-Chen correlation (Ref. 3-44.), where

$$h_{wg} = h_{mod\text{-}CSO}\,(1 + F_s)\left[1 + 0.8\left(\frac{L}{D}\right)^{-1}\right] . \quad (3\text{-}292)$$

In this equation, $h_{mod\text{-}CSO}$ is the heat-transfer coefficient based on the momentum-transfer analogy of Chen, Sundaram, and Ozkaynak (Ref. 3-45.). The parameter F_s is a sink function to account for the effect of entrained droplets. The L/D term is included to account for entrance effects. Definitions of $h_{mod\text{-}CSO}$ and F_s are provided in Appendix F (Section F.2.2.4.1.).

The Webb-Chen (Ref. 3-44.) and Chen, Sundaram, and Ozkaynak (Ref. 3-45.) correlations are used in TRAC, as given in the source references for this constitutive model.

The wall-to-liquid heat-transfer coefficient then is calculated from the total heat flux and h_{wg}, as given by

$$h_{wl} = \frac{q_{TR} - h_{wg}\,(T_w - T_g)}{(T_w - T_l)} . \quad (3\text{-}293)$$

When the cell void fraction is >0.995, a final interpolation is performed on q_{TR} and h_{wg} to provide a smooth transition between heat-transfer regimes. Details of the interpolation scheme can be found in Appendix F (Section F.2.2.3.4.).

3.8.6. Minimum Stable Film-Boiling Temperature

The minimum stable film-boiling temperature provides the transition point between the transition-boiling and film-boiling heat-transfer regimes. In the code, T_{min} is defined by

$$T_{min} = T_{NH} + (T_{NH} - T_l)\cdot R^{1/2} , \quad (3\text{-}294)$$

where

$$R = \frac{k_l \rho_l c_{p,l}}{k_w \rho_w c_{p,w}}, \tag{3-295}$$

and where T_{NH} is the homogeneous nucleation temperature (Ref. 3-46.). The homogeneous nucleation temperature in turn is evaluated from a third-order polynomial fit to the work of Fauske (Ref. 3-46.). Computation of T_{NH} is discussed in detail in Appendix F (Section F.2.1.9.). The final value of the minimum stable film-boiling temperature then is determined from the criterion

$$T_{min} = \max(T_{min}, T_{sat} + 0.0001\ K) . \tag{3-296}$$

The minimum film-boiling temperature is used in TRAC as given in the source references.

3.8.7. Film Boiling

In the film-boiling regime, the wall-to-liquid heat transfer is based on the sum of radiation heat-transfer effects and near-wall liquid effects. Specifically, the wall-to-liquid heat-transfer coefficient is defined by

$$h_{wl} = (h_r + h_{fBB}) \cdot \left(\frac{T_w - T_{sat}}{T_w - T_l} \right), \tag{3-297}$$

where the radiation term h_r is calculated as presented in Section 3.8.5. and the near-wall liquid-effects term h_{fBB} is calculated from the modified Bromley equation, also presented in Section 3.8.5.

The wall-to-gas phasic heat-transfer coefficient is evaluated as the maximum of the natural-convection and the Dougall-Rohsenow correlations, or

$$h_{wg} = \max(h_{NC}, h_{dr}) . \tag{3-298}$$

Both the natural-convection heat-transfer coefficient and the Dougall-Rohsenow coefficient are calculated as presented in Section 3.8.3. However, if the cell void fraction is >0.97, the coefficient h_{wg} is modified slightly to ensure a smooth transition between heat-transfer regimes. Details of the modification are presented in Appendix F (Section F.2.1.5.4.).

The overall modeling of the film-boiling regime is original to TRAC. The correlations that make up the model are used in TRAC as given in the source references.

3.8.7.1. Core Reflood. Under core reflood conditions, the wall-to-liquid heat-transfer coefficient still is based on the sum of radiative effects and near-wall liquid effects, or

$$h_{wl} = (h_r + h_{near\text{-}wall}) \cdot \left(\frac{T_w - T_{sat}}{T_w - T_l} \right) . \tag{3-299}$$

In this case, however, the near-wall liquid effects are based on either the modified Bromley correlation (Ref. 3-43.) or the correlation of Denham (Ref. 3-47.) such that

$$h_{near\text{-}wall} = fcn(h_{fBB}, h_{Denham}) . \quad (3\text{-}300)$$

Denham's equation is given by

$$h_{Denham} = 0.4472 \left[\frac{g(\rho_l - \rho_v)}{\mu_v V_v} \right]^{1/2} . \quad (3\text{-}301)$$

The modified Bromley (Ref. 3-43.) coefficient h_{fBB} and the radiation term h_r both were defined in Section 3.8.5.

The exact functional dependence of the near-wall term to h_{fBB} and h_{Denham} is controlled by the particular reflood flow regime. For example, if the flow regime is smooth inverted annular flow, then

$$h_{near\text{-}wall} = h_{Denham} .$$

In the rough-wavy-flow regime, $h_{near\text{-}wall}$ is a weighted average of the Denham (Ref. 3-47.) and Bromley (Ref. 3-43.) correlations such that

$$h_{near\text{-}wall} = W_D \cdot h_{Denham} + W_B \cdot h_{fBB} . \quad (3\text{-}302)$$

In the agitated inverted-annular-flow and the post-agitated (dispersed-flow) regimes, $h_{near\text{-}wall}$ is based on a weighted value from the modified Bromley correlation (Ref. 3-43.). For highly dispersed flow, $h_{near\text{-}wall}$ is zero. Details of the appropriate weighting factors can be found in Appendix F (Section F.2.2.4.1.).

The wall-to-gas heat-transfer coefficient is redefined as a function of the Webb-Chen correlation (see Section 3.8.5.). Here again, the functional dependence is controlled by the particular reflood flow regime. For smooth inverted annular flow,

$$h_{wg} = 0 .$$

In the highly dispersed flow regime,

$$h_{wg} = h_{W\text{-}C} .$$

For rough-wavy inverted annular flow through dispersed flow, h_{wg} is interpolated linearly (as a function of void fraction) between zero and the Webb-Chen correlation value $h_{W\text{-}C}$. The appropriate weighting factor is defined in Appendix F (Section F.2.2.4.1.).

At void fractions >0.995, the wall-to-liquid heat-transfer coefficient is reevaluated as a function of the above relations and the single-phase vapor value ($h_{wl} = 0$). Likewise, if the

void fraction is >0.9999, the wall-to-gas heat-transfer coefficient is interpolated from the above relations and the value for single-phase vapor. Additional details of the interpolation scheme for both h_{wl} and h_{wg} can be found in Appendix F (Section F.2.2.4.1.).

The overall modeling of the film-boiling regime for reflood conditions is heuristic and was developed specifically for implementation into TRAC. The correlations that make up the model are used in TRAC as given in the source references.

3.8.8. Single-Phase Vapor

Under single-phase vapor conditions, the wall-to-liquid heat-transfer coefficient is equal to zero:

$$h_{wl} = 0.0 .$$

Alternatively, the wall-to-gas heat-transfer coefficient is defined as the maximum of the coefficient for turbulent natural convection and the coefficient for turbulent forced convection, or

$$h_{wg} = \max(h_{gNC}, h_{gturb}) .$$

The coefficient for turbulent natural convection is given by

$$h_{gNC} = 0.13 \left(\frac{k_g}{D_h}\right) Gr_g^{0.3333} \, Pr_g^{0.3333} . \tag{3-303}$$

The coefficient for turbulent forced convection is calculated from either the Sieder-Tate or the Dittus-Boelter equations. The choice of equation is dependent on the film temperature T_f, where

$$T_f = 0.5 \, (T_w + T_g) . \tag{3-304}$$

If $T_f \geq T_{sv}$, the code uses the Sieder-Tate equation (Ref. 3-18.), given by

$$h_{gturb} = 0.027 \left(\frac{k_g}{D_h}\right) Re_g^{0.8} \, Pr_g^{0.3333} \left(\frac{\mu_g}{\mu_w}\right)^{0.14} . \tag{3-305}$$

If $T_f < T_{sv}$, the code calculates h_{gturb} from the Dittus-Boelter relation such that

$$h_{gturb} = 0.023 \frac{k_g}{D_h} Re_g^{0.8} \, Pr_g^{0.4} . \tag{3-306}$$

Under the conditions that the cell void fraction is between 0.97 and 1.0, TRAC interpolates between the single-phase heat-transfer coefficients described in this section and the appropriate two-phase heat-transfer coefficients. Details of the interpolation scheme can be found in Appendix F (Section F.2.1.5.4.).

As in the case of single-phase liquid heat transfer, these correlations are accepted widely and are used for engineering analyses of heat transfer under the stated conditions.

3.8.9. Condensation

The condensation heat-transfer regime may exist under the conditions that the wall temperature is less than both the combined-gas and the saturated-vapor temperature, the void fraction is >0.05, and the mass quality is >0.71. When these criteria are met and vapor condenses on a cold wall, the wall-to-liquid and wall-to-gas heat-transfer coefficients are described by the following:

$$h_{wl} = 0.0 \tag{3-307}$$

and

$$h_{wg} = h'''_{gcond} \tag{3-308}$$

for the mass quality *x* equal to 1.0, or

$$h_{wl} = h'_{wl} + \left(0.0 - h'_{wl}\right) \cdot \frac{x - 0.71}{1.0 - 0.71} \tag{3-309}$$

and

$$h_{wg} = h'_{wg} + \left(h'''_{gcond} - h'_{wg}\right) \cdot \frac{x - 0.71}{1.0 - 0.71} \tag{3-310}$$

for

$$0.71 < x < 1.0 .$$

In the above equation, the condensation heat-transfer coefficient originally was based on the theoretical analysis of Nusselt (Ref. 3-48.) such that

$$h_{gcond} = 0.9428 \left[\frac{\rho_l^2 \, g \, k_l^3 \, h_{fg}}{\mu_l \, L \, (T_{sv} - T_w)} \right]^{0.25} . \tag{3-311}$$

However, to account for ripples that develop on the liquid film, the Nusselt coefficient is modified by

$$h'_{gcond} = h_{gcond} \cdot (1 - WF) + \max(h_2, h_{gcond}) \cdot W F \tag{3-312}$$

for

$$WF = \min\left[1.0, \max\left(0.0, \frac{L - 0.2}{1.8}\right)\right] , \tag{3-313}$$

where L is the cell length. The heat-transfer coefficient h_2 is expressed by

$$h_2 = 0.003 \left[\frac{\rho_l^2 \, g \, k_l^3 \, L \, (T_{sv} - T_w)}{h_{fg} \, \mu_l^3} \right]^{0.5} \tag{3-314}$$

and was derived empirically for liquid-film Reynolds numbers >350 (Ref. 3-48.). The condensation heat-transfer coefficient then is modified further such that

$$h''_{gcond} = h'_{gcond} \frac{(T_{sv} - T_w)}{\max(|T_g - T_w|, \; 0.01)} \tag{3-315}$$

and

$$h'''_{gcond} = \max\left(h''_{gcond}, \; h'_{wg}\right) \tag{3-316}$$

for

$$h'_{wg} = \max(h_{gNC}, \; h_{gturb}) \; . \tag{3-317}$$

The turbulent natural-convection heat-transfer coefficient h_{gNC} and the turbulent forced-convection heat-transfer coefficient h_{gturb} are given by

$$h_{gNC} = 0.13 \left(\frac{k_g}{D_h} \right) Gr_v^{0.3333} \; Pr_g^{0.3333} \tag{3-318}$$

and

$$h_{gturb} = 0.023 \, \frac{k_g}{D_h} \, Re_g^{0.8} \; Pr_g^{0.3} \; , \tag{3-319}$$

respectively.

Finally, the wall-to-liquid heat-transfer coefficient h'_{wl} is defined by

$$h'_{wl} = \max(h_{NC1}, \; h_{NC2}, \; h_{forc}) \; , \tag{3-320}$$

where (Ref. 3-48.)

$$h_{NC1} = 0.59 \left(\frac{k_l}{D_h} \right) Gr_l^{0.25} \; Pr_l^{0.25} \; . \tag{3-321}$$

and (Ref. 3-37.)

$$h_{NC2} = 0.10 \left(\frac{k_l}{D_h}\right) Gr_l^{0.3333} \, Pr_l^{0.3333} \, . \tag{3-322}$$

The coefficient h_{forc} is calculated from the Chen correlation (Ref. 3-38.), where S equals zero. Thus,

$$h_{forc} = 0.023 \, \frac{k_l}{D_h} \left(\frac{V_l \, \rho_l \, (1 - \alpha) \, D_h}{\mu_l}\right)^{0.8} Pr_l^{0.4} \cdot F \, . \tag{3-323}$$

The overall approach to modeling condensation is heuristic and was developed specifically for implementation into TRAC. The correlations that make up the model are used in the form given in the source references for this constitutive model.

3.8.10. Two-Phase Forced Convection

At the user's option, the heat-transfer correlations for the two-phase forced-convection regime may be used in lieu of those presented for nucleate, transition, and film boiling. Within the two-phase forced-convection model, the liquid heat-transfer coefficient is evaluated as the maximum of the Rohsenow-Choi correlation (Ref. 3-49.) for laminar forced convection (h_{wllam}) and the Dittus-Boelter correlation for turbulent forced convection (h_{wlturb}). In other words,

$$h_{wl} = \max(h_{wllam}, h_{wlturb}) \, , \tag{3-324}$$

where

$$h_{wllam} = \frac{4 \, k_l}{D_h} \tag{3-325}$$

and

$$h_{wlturb} = 0.023 \, \frac{k_l}{D_h} \, Re^{0.8} \, Pr^{0.4} \, . \tag{3-326}$$

In the above equation, the Reynolds number is defined by

$$Re = \frac{G_m \, D_h}{\mu_m} \, , \tag{3-327}$$

the Prandtl number is defined by

$$Pr = \frac{\mu_l \, c_{p,l}}{k_l} \, , \tag{3-328}$$

and the mixture viscosity (Ref. 3-50.) is expressed as a function of the flow quality x_f such that

$$\mu_m = \left[\frac{x_f}{\mu_g} + \frac{(1 - x_f)}{\mu_l} \right]^{-1} . \tag{3-329}$$

Alternatively, the wall-to-gas heat-transfer coefficient is given by

$$h_{wg} = \begin{cases} 0.0 & \alpha < 0.98 \quad (3\text{-}330) \\ \max(h_{gNC}, h_{gturb}) & \alpha \geq 0.98 , \quad (3\text{-}331) \end{cases}$$

where the coefficient h_{gNC} is evaluated from the turbulent natural-convection correlation

$$h_{gNC} = 0.13 \left(\frac{k_g}{D_h} \right) \left(\frac{\rho_g^2 \, g \, |T_w - T_g|}{\mu_g^2 \, T_g} \right)^{0.3333} Pr_g^{0.4} , \tag{3-332}$$

and h_{gturb} is evaluated from the Dittus-Boelter correlation for turbulent forced convection

$$h_{gturb} = 0.023 \frac{k_g}{D_h} Re_g^{0.8} \, Pr_g^{0.4} . \tag{3-333}$$

In this case, the Reynolds and Prandtl numbers are calculated by

$$Re_g = \frac{\rho_g \, V_g \, D_h}{\mu_g} \tag{3-334}$$

and

$$Pr_g = \frac{\mu_g \, c_{p,g}}{k_g} . \tag{3-335}$$

Finally, when the cell void fraction is >0.98, the liquid and gas heat-transfer coefficients are interpolated from the values calculated for two-phase forced convection (as defined in this section) and the values calculated for single-phase vapor (see Section 3.8.8.). Details of the interpolation scheme are presented in Appendix F (Section F.2.1.7.4.).

The overall approach to modeling two-phase forced convection is heuristic and was developed specifically for implementation into TRAC. The correlations that make up the model are used in the form given in the source references.

REFERENCES

3-1. B. R. Bandini, "A Three-Dimensional Transient Neutronics Routine for the TRAC-PF1 Reactor Thermal Hydraulic Computer Code," Thesis, Pennsylvania State University (May 1990).

3-2. K. Mishima and M. Ishii, "Theoretical Prediction of Onset of Horizontal Slug Flow," *Trans. ASME, J. Fluids Engineering*, **102**, 441–445 (1980).

3-3. M. Ishii and G. DeJarlais, "Flow Visualization Study of Inverted Annular Flow of Post Dryout Heat Transfer Region," *Nuclear Engineering and Design*, **99**, 187–199 (1987).

3-4. M. Ishii and G. DeJarlais, "Flow Regime Transition and Interfacial Characteristics of Inverted Annular Flow," *Nuclear Engineering and Design*, **95**, 171–184 (1986).

3-5. N. T. Obot and M. Ishii, "Two-Phase Flow Regime Transition Criteria in Post-Dryout Region Based on Flow Visualization Experiments," *Int. J. Heat Mass Transfer*, **31**, 12, pp. 2559–2570 (1988).

3-6. M. Ishii and K. Mishima, "Study of Two-Fluid Model and Interfacial Area," Argonne National Laboratory report ANL-80-111 (NUREG / CR-1873) (1980).

3-7. M. Ishii, Argonne National Laboratory, personal communication to R. Nelson, Los Alamos National Laboratory, July 1987.

3-8. M. Ishii and K. Mishima, "Correlation for Liquid Entrainment in Annular Two-Phase Flow of Low-Viscous Fluid," Argonne National Laboratory report ANL / RAS / LWR 81-2 (1981).

3-9. M. Ishii and K. Mishima, "Droplet Entrainment Correlation in Annular Two-Phase Flow," *Int. J. Heat Mass Transfer*, **32**, 1835–1846 (1989).

3-10. I. Kataoka, M. Ishii, and K. Mishima, "Generation and Size Distribution of Droplet in Annular Two-Phase Flow," *Trans. ASME, J. Fluid Engineering*, **105**, 230–238 (1983).

3-11. J. Kitscha and G. Kocamustafaogullari, "Breakup Criteria for Fluid Particles," *Int. J. Multiphase Flow*, **15**, 573–588 (1989).

3-12. I. Kataoka and M. Ishii, "Mechanism and Correlation of Droplet Entrainment and Deposition in Annular Two-Phase Flow," Argonne National Laboratory report ANL-82-44 (NUREG / CR-2885) (1982).

3-13. K. Pasamehmetoglu, "A Formula for Limiting Film Thickness on Cold Walls," Los Alamos National Laboratory memorandum to J. W. Spore (September 1, 1989).

3-14. R. T. Lahey, "A Mechanistic Subcooled Boiling Model," *Proc. 6th Int. Heat Transfer Conf.* (Toronto, Canada, 1978), Vol. 1, pp. 293–297.

3-15. P. Saha and N. Zuber, "Point of Net Vapor Generation and Vapor Void Fraction in Subcooled Boiling," *Proc. 5th Int. Heat Transfer Conf.* (Tokyo, Japan, 1974), Paper B4.7.

3-16. M. Ishii and T. C. Chawla, "Local Drag Laws in Dispersed Two-Phase Flow," Argonne National Laboratory report ANL-79-105 (NUREG/CR-1230) (December 1979).

3-17. L. Shiller and A. Z. Nauman, *Ver. Deut. Ing.*, **77**, 318–320 (1933).

3-18. R. B. Bird, W. E. Stewart, and E. N. Lightfoot, *Transport Phenomena* (John Wiley and Sons, New York, 1960).

3-19. M. Ishii and K. Mishima, "Two Fluid Model and Hydrodynamic Constitutive Relations," *Nucl. Eng. and Design*, **82**, 107–126 (1984).

3-20. G. B. Wallis, *One Dimensional Two Phase Flow* (McGraw-Hill Book Company, New York, 1969).

3-21. Y. Taitel and A. E. Dukler, "A Model for Predicting Flow Regime Transitions in Horizontal and Near Horizontal Gas-Liquid Flow," *AIChE J.*, **22** (1), 47–55 (1976).

3-22. A. Ohnuki, H. Adachi, and Y. Murao, "Scale Effects on Countercurrent Gas-Liquid Flow in Horizontal Tube Connected to Inclined Riser," American Nuclear Society, ANS 1987 National Heat Transfer Conference (Pittsburgh, Pennsylvania, August 9-12, 1987), pp. 40-49.

3-23. J. G. Collier, *Convective Boiling and Condensation*, (McGraw-Hill Book Company, New York, 1972).

3-24. M. W. Cappiello, "A Model for the Interfacial Shear in Vertical, Adiabatic Annular-Mist Flow," Los Alamos National Laboratory document LA-CP-89-392 (October 1989).

3-25. S. W. Churchill, "Friction-Factor Equation Spans All Fluid-Flow Regimes," *Chemical Engineering*, pp. 91–92 (Nov. 7, 1977).

3-26. Y. M. Chen and F. Mayinger, "Measurement of Heat Transfer at the Phase Interface of Condensing Bubbles," *ANS Proc. 1989 National Heat Transfer Conf.* (Philadelphia, Pennsylvania, August 6-9, 1989) HTC-Vol. 4, pp. 147-152.

3-27. S. Whittaker, "Forced Convection Heat Transfer Correlations for Flows in Pipes, Past Flat Plates, Single Cylinder, Single Sphere, and Flows in Packed Beds and Tube Bundles," *AIChE J.*, **18**, 361–372 (1972).

3-28. R. T. Lahey and F. J. Moody, *The Thermal-Hydraulics of a Boiling Water Nuclear Reactor,* ANS monograph, American Nuclear Society, LaGrange Park, Illinois, (1977).

3-29. K. Pasamehmetoglu and R. Nelson, "Transient Direct-Contact Condensation on Liquid Droplets," *Nonequilibrium Transport Phenomena* (American Society of Mechanical Engineers, New York, 1987), HTD-Vol. 77, pp. 47–56.

3-30. M. Ishii, "One Dimensional Drift-Flux Model and Constitutive Equations for Relative Motion between Phases in Various Two-Phase Flow Regimes," Argonne National Laboratory report ANL-77-47 (1977).

3-31. G. Ryskin, "Heat and Mass Transfer from a Moving Drop—Some Approximate Relations for the Nusselt Number," *Int. Comm. Heat Mass Transfer,* **14**, 741–749 (1987).

3-32. S. G. Bankoff, "Some Condensation Studies Pertinent to Light Water Safety," *Int. J. Multiphase Flow,* **6**, 51–67 (1980).

3-33. J. H. Linehan, M. Petrick, and M. M. El-Wakil, "The Condensation of Saturated Vapor on a Subcooled Film During Stratified Flow," *Chem. Eng. Symp. Series,* **66** (102), 11–20 (1972).

3-34. C. Unal, K. Tuzla, C. A. Tuzla, and J. C. Chen, "Vapor Generation Model for Dispersed Drop Flow," *ANS Proc. 1989 National Heat Transfer Conf.* (August 1989), HTC-Vol. 4.

3-35. G. G. Sklover and M. D. Rodivilin, "Condensation on Water Jets with a Cross Flow of Steam," *Teploenergetika,* **23**, 48–51 (1976).

3-36. J. P. Holman, *Heat Transfer,* 5th ed. (McGraw-Hill Book Co., New York, 1981).

3-37. F. E. Incropera and D. P. DeWitt, *Fundamentals of Heat Transfer* (John Wiley & Sons, New York, 1981).

3-38. J. M Delhaye, M. Giot, and M. L. Riethmuller, *Thermohydraulics of Two-Phase Systems for Industrial Design and Nuclear Engineering* (Hemisphere Publishing Corporation, New York, 1981).

3-39. H. K. Forster and N. Zuber, "Bubble Dynamics and Boiling Heat Transfer," *AIChE J.*, **1**, 532–535 (1955).

3-40. W. M. McAdams, *Heat Transmission*, 3rd ed. (McGraw-Hill Book Co., New York, 1954).

3-41. L. Biasi, G. C. Clerici, S. Garribba, R. Sala, and A. Tozzi, "Studies on Burnout, Part 3: A New Correlation for Round Ducts and Uniform Heating and Its Comparison with World Data," *Energia Nucleare*, **14**, 530–536 (1967).

3-42. O. C. Jones, Jr. and S. G. Bankoff, editors, *Thermal and Hydraulic Aspects of Nuclear Reactor Safety, Volume 1: Light Water Reactors* (ASME, New York, 1977).

3-43. L. A. Bromley, "Heat Transfer in Stable Film Boiling," *Chem. Eng. Prog.*, **46** (5), 221–227 (May 1950).

3-44. S. Webb and J. C. Chen, "A Two-Region Vapor Generation Rate Model for Convective Film Boiling," Int. Workshop of Fundamental Aspects of Post-Dryout Heat Transfer, Salt Lake City, Utah, April 1–4, 1984.

3-45. J. C. Chen, F. T. Ozkaynak, and R. K. Sundaram, "Vapor Heat Transfer in Post-CHF Region Including the Effect of Thermodynamic Non-Equilibrium," *Nuclear Eng. and Design*, **51**, 143–155 (1979).

3-46. R. E. Henry, "A Correlation for the Minimum Film Boiling Temperature," *AIChE Symposium Series*, **138**, 81–90 (1974).

3-47. M. K. Denham, "Inverted Annular Film Boiling and the Bromley Model," AEEW-R 1590, Winfrith, Rochester (January 1983).

3-48. F. Kreith, *Principles of Heat Transfer*, 3rd. ed., (Harper and Row, New York, 1973).

3-49. W. M. Rohsenow and H. Choi, *Heat, Mass, and Momentum Transfer* (Prentice-Hall, Englewood Cliffs, New Jersey, 1961).

3-50. W. H. McAdams, "Vaporization Inside Horizontal Tubes-II-Benzene-Oil Mixtures," *Trans. ASME*, **64**, 193 (1942).

3-51. R. A. Nelson, Jr., D. A. Pimentel, S. J. Jolly-Woodruff, and J. W. Spore, "Reflood Completion Report, Volume I: A Phenomenological Thermal-Hydraulic Model of Hot Rod Bundles Experiencing Simultaneous Bottom and Top Quenching and an Optimization Methodology for Closure Development," Los Alamos National Laboratory report LA-UR-98-3043 (April, 1998).

3-52. B. E. Boyack, J. F. Lime, D. A. Pimentel, J. W. Spore, and T. D. Knight, "Reflood Completion Report, Volume II: Developmental Assessment of a New Reflood

Model for the TRAC-M/F77 Code," Los Alamos National Laboratory report LA-UR-98-3043 (April, 1998).

3-53. B. E. Boyack, J. F. Lime, D. A. Pimental, J. W. Spore, and J. L. Steiner, "TRAC-M/F77, Version 5.5, Developmental Assessment Manual, Volume I: Nonproprietary Assessment Sections," Los Alamos National Laboratory document LA-UR-99-6480 (December 1999).

3-54. B. E. Boyack, J. F. Lime, D. A. Pimental, J. W. Spore, and J. L. Steiner, "TRAC-M/F77, Version 5.5, Developmental Assessment Manual, Volume II: Proprietary Assessment Sections," Los Alamos National Laboratory document LA-CP-99-345 (December 1999).

4.0. FLOW PROCESS AND SPECIAL MODELS

Special models play an important role in the overall construction of TRAC. In the following sections, eight special models are described:

- models for critical flow,
- countercurrent flow,
- offtake flow from a large pipe in horizontal stratified flow,
- form loss,
- gap conductance,
- decay heat and void-reactivity feedback,
- reactor-vessel vent valve, and
- metal-water reaction.

The nomenclature that applies to this section follows:

NOMENCLATURE

a_{HE}: homogeneous equilibrium sound speed
A_j: flow area before the abrupt expansion
A_{j+1}: flow area after the abrupt expansion
C: virtual mass coefficient
C_B: abscissa intercept in Bankoff CCFL correlation
D: diameter
$\bar{E}$: interpolation constant used in the CCFL model
E_j: effective energy fraction of decay-heat group *j*
g: gravitational acceleration
h: critical distance from the offtake entrance plane to the liquid level
h_{gas}: heat-transfer coefficient for gap-gas conductance
H_g: dimensionless gas flux
H_j: connection of decay-heat group *j* (W · s)
H_l: dimensionless liquid delivery
j: superficial velocity
J: total number of decay-heat groups

k: phase index (liquid or gas)

k_{gas}: gap-gas thermal conductivity

K: additive loss factor

L: length

m'_{Zr}: mass per unit length of zirconium

M_B: slope in the Bankoff CCFL correlation

P: pressure or total thermal power from fission

P_c: pressure at the choking plane

P_{up}: pressure upstream of the choking plane

q'''_{mw}: heat source from the metal-water reaction

R: neutronic reactivity, including both programmed and feedback reactivity

$\bar{R}$: gas constant

R^*: nondimensional height ratio for offtake model

R_f: solid-fuel radius

R_f^*: fuel radius, including cracked fuel

R_I: cladding inner radius

$R_{I,new}$: cladding inner radius after thermal expansion

$R_{f,new}$: solid-fuel radius after thermal expansion

R_o: cladding outer radius

s: entropy

t: time

T_0: stagnation temperature

V: velocity

V_{cg}: critical velocity for single-phase vapor

V_{cl}: subcooled-liquid choking velocity

V_{up}: velocity upstream of the choking plane

W: mass flow rate in offtake model

x: distance

α: gas volume fraction

α_c: cladding fraction

α_f: fuel fraction

γ: specific heat ratio

Δr_{gap}: fuel-cladding radial gas gap

$\Delta\rho$: difference between the phasic densities

ΔT: temperature difference

Δt: time step

δ: the cracked-fuel thickness

δ_0: initial undeformed radial thickness of the cracked fuel

λ_i: decay constant for the delayed-neutron precursors in group *i*

λ_j^H: decay constant for decay-heat group *j* (s^{-1})

Λ: effective prompt-neutron lifetime

ρ: density

σ: surface tension

Subscripts

a: noncondensable gas

c: cladding

f: fuel

g: combined-gas mixture

l: liquid

m: total mixture

up: conditions upstream of the choking plane

v: vapor

4.1. Critical Flow

A detailed description of the TRAC critical flow model is provided in Appendix I, Section I.2. The critical flow model comprises three separate models:

- a subcooled-liquid choked-flow model;
- a two-phase, two-component choked-flow model; and
- a single-phase vapor choked-flow model.

Also, linear interpolation is used to treat the transition from subcooled liquid to the two-phase two-component models.

4.1.1. Subcooled-Liquid Choked Flow

During the subcooled blowdown phase, the fluid undergoes a phase change at the break because the downstream pressure is much less than the saturation pressure corresponding to the system fluid temperature. Thus, the choking velocity can be calculated following the approach of Burnell (Ref. 4-1.) until a point is reached when the system pressure is so low that the subcooled-liquid choking velocity, V_{cl}, is less than the homogeneous equilibrium sound speed, a_{HE}. Therefore, the subcooled choking criterion is given by the maximum of the homogeneous equilibrium sound speed and the Burnell

expression (a Bernoulli expansion to the point of vapor inception at the choke plane). Thus,

$$V_{cl} = \max\left\{a_{HE}, \left[V_{up,l}^2 + \frac{2(P_{up} - P_c)}{\rho_l}\right]^{1/2}\right\}, \tag{4-1}$$

where the pressure at the choking plane, P_c, is determined using the nucleation delay model of Jones (Ref. 4-2.), and the subscripts "*up*" and "*l*" denote the conditions upstream of the choking plane and liquid conditions, respectively.

4.1.2. Two-Phase, Two-Component Choked Flow

The TRAC two-phase choking model is an extension of one developed by Ransom and Trapp (Ref. 4-3.) that incorporates an additional inert gas component. Thermal equilibrium is assumed to exist between the phases. The two-fluid flow field under thermal equilibrium is described by the inert gas continuity equation, the overall continuity equation, two phasic momentum equations, and the mixture energy equation. The non-differential source terms do not enter into the characteristic analysis. Thus, the equations are

$$\frac{\partial \rho_m}{\partial t} + \frac{\partial(\rho_m V_m)}{\partial x} = 0, \tag{4-2}$$

$$\alpha\rho_g\left[\frac{\partial V_g}{\partial t} + V_g\frac{\partial V_g}{\partial x}\right] + \alpha\frac{\partial P}{\partial x} + C\alpha(1-\alpha)\rho_m\left[\frac{\partial V_g}{\partial} + V_l\frac{\partial V_g}{\partial} - \frac{\partial V_l}{\partial} - V_g\frac{\partial V_l}{\partial}\right] = 0, \tag{4-3}$$

$$(1-\alpha)\rho_l\left[\frac{\partial V_l}{\partial t} + V_l\frac{\partial V_l}{\partial x}\right] + (1-\alpha)\frac{\partial P}{\partial x} + C\alpha(1-\alpha)\rho_m\left[\frac{\partial V_l}{\partial t} + V_g\frac{\partial V_l}{\partial x} - \frac{\partial V_g}{\partial t} - V_l\frac{\partial V_g}{\partial x}\right] = 0, \tag{4-4}$$

$$\frac{\partial(\rho_m s_m)}{\partial t} + \frac{\partial\left[\alpha\rho_g V_g s_g + (1-\alpha)\rho_l V_l s_l\right]}{\partial x} = 0, \text{ and} \tag{4-5}$$

$$\frac{\partial(\alpha\rho_a)}{\partial t} + \frac{\partial(\alpha\rho_a V_g)}{\partial x} = 0, \tag{4-6}$$

where C is the virtual mass coefficient; s is the entropy; and subscripts a, g, l, and m refer to the noncondensable gas, steam/gas mixture, liquid, and total mixture, respectively. Following Ransom and Trapp's formulation (Ref. 4-3.), the energy equation is written in the form of the mixture-specific entropy that is conserved for adiabatic flow (with the irreversibilities associated with interphasic mass transfer and relative phase acceleration neglected).

In the thermal-equilibrium case, ρ_a, ρ_v, ρ_l, s_g, s_l, and s_m are known functions of P_a and P_v. If we assume that Dalton's law of partial pressures applies, the above five characteristic equations for two-phase, two-component choked flow can be written in terms of the five unknowns P_a, P_v, α, V_g, and V_l with the characteristic roots, λ_t, given by the roots of a fifth-order polynomial. Choking occurs when the signal propagating with the largest velocity relative to the fluid is stationary; that is, $\lambda_{t,re,max}$=0. An analytic solution for the characteristic roots is difficult to obtain. Thus, the characteristic roots are obtained numerically.

4.1.3. Single-Phase Vapor Choked Flow

The single-phase vapor choked-flow model is based on isentropic expansion of an ideal gas (Ref. 4-4.). The continuity equation, in conjunction with the ideal gas relations, yields the following expression for the critical velocity:

$$V_{cg} = \sqrt{\frac{2\gamma}{\gamma+1}\bar{R}T_0} \ , \tag{4-7}$$

where γ is the specific heat ratio, T_0 is the stagnation temperature, and $\bar{R}$ is the gas constant. When the downstream throat temperature is greater than the saturation temperature at the throat pressure, the fluid flow at the throat is predicted to be superheated by the ideal gas relations, and the single-phase vapor choked-flow model is applied. Appendix I discusses an iterative method that is used when the downstream throat temperature is less than or equal to the saturation temperature at the throat pressure.

4.2. Countercurrent Flow

A detailed description of the TRAC countercurrent-flow model is provided in Appendix I (Section I.3.). Characteristic countercurrent-flow-limiting (CCFL) correlations can be invoked by the user at specific locations. The basic correlation model implemented in TRAC is provided by Bankoff (Ref. 4-5.). The Bankoff correlation is given as

$$H_g^{1/2} + M_B H_l^{1/2} = C_B \ , \tag{4-8}$$

where H_g is the dimensionless gas flux, H_l is the dimensionless liquid delivery, C_B is the abscissa intercept, and M_B is the slope. The Bankoff relationship is sufficiently general that either Wallis scaling for diameter dependence (Ref. 4-6.), Kutateladze scaling for surface-tension dependence (Ref. 4-7.), or a combination of the two can be implemented. This is performed by defining a variable-length scale in the determination of the dimensionless flux as follows:

$$H_k = j_k\left(\frac{\rho_k}{gw\Delta\rho}\right)^{1/2} \ , \tag{4-9}$$

$$w = D^{1-\bar{E}} L^{\bar{E}} , \tag{4-10}$$

and

$$L = \left(\frac{\sigma}{g \Delta \rho} \right)^{1/2} , \tag{4-11}$$

where

- k = phase (liquid or gas),
- j = superficial velocity,
- D = diameter of holes,
- g = gravitational acceleration,
- σ = surface tension,
- ρ = density,
- $\Delta\rho$ = difference between the phasic densities, and
- $\bar{E}$ = interpolation constant between 0 and 1.

The Bankoff correlation reverts to Wallis scaling for $\bar{E}$ =0 and to Kutateladze scaling for $\bar{E}$ =1. For $\bar{E}$ between 0 and 1, the Bankoff scaling applies (Ref. 4-5.).

4.3. Offtake

A detailed description of the TRAC offtake model is provided in Appendix I (Section I.4.). The TEE-component offtake model is designed specifically to handle the case when a small break is made in a large pipe containing horizontal stratified flow. The model predicts the offtake flow quality that exits the break based on conditions in the main pipe, following the approach of Ardron and Bryce (Ref. 4-8.). When the entrance plane to the break is submerged, the offtake flow consists mostly of liquid and possibly an entrained gas component. When the entrance plan is above the liquid level, the offtake flow is mostly gas and possibly an entrained liquid component.

The offtake model is specific to three geometries: upward, downward, and side offtakes. Offtake flow quality has been correlated as a function of the nondimensional height ratio, R^*, where

$$R^* = \frac{h}{h_b} , \quad \text{and} \tag{4-12}$$

h is the actual or measured critical distance from the offtake entrance plane to the liquid level and the critical height at which gas or liquid entrainment begins, and h_b is determined from the expression

$$h_b = \frac{C_1 W_k^{0.4}}{(g\rho_k \Delta\rho)^{0.2}} , \tag{4-13}$$

where

C_1 = constant determined from data,
W_k = major-phase mass flow rate,
ρ_k = major-phase density, and
$\Delta\rho$ = difference between the phasic densities.

4.4. Form Loss

Detailed descriptions of the TRAC form-loss model are provided in Section 2.1.7.1. and in Appendix I, Section I.1. Irrecoverable pressure losses occur across abrupt area changes. In TRAC, only reversible losses across area changes are obtained when solving the field equations. Irreversible losses must be accounted for by using an additional form-loss term. Theoretically- and experimentally-derived form-loss terms are added to the momentum equations only if the user requests this approach via an input option at the desired cell interfaces.

For an abrupt expansion, the theoretically derived additive loss factor is

$$K = \left(1 - \frac{A_j}{A_{j+1}}\right)^2 , \tag{4-14}$$

where A_j and A_{j+1} are the flow areas before and after the abrupt expansion, respectively.

A theoretical derivation of the additive loss factor for an abrupt contraction is not possible. Thus, the data for the standard loss coefficient for an abrupt contraction cited in Massey (Ref. 4-9., p. 219) are incorporated into TRAC using a curve fit.

The user may have to account for turning losses at TEE-component internal junctions with appropriate input-specified friction factors (or K-factors). Also, there is no input option to select automatic internal calculation of losses from abrupt expansions or contractions at the three interfaces of the TEE joining cell.

The existence of a thin-plate orifice creates an abrupt flow-area change and also results in irrecoverable pressure losses. In practice, it has been found that many TRAC input-data models have cell-edge flow areas that are less than both of the bounding mesh-cell flow areas, even though in reality there is no thin-plate orifice. Therefore, if a thin-plate orifice exists, the user is advised to account for irreversible losses through the use of input-specified friction factors (or K-factors). There is no internal calculation for such a loss that can be selected via the input. A recommendation for user determination of an appropriate loss coefficient is given in Appendix I.

4.5. Fuel-Cladding Gap Conductance

A detailed description of the TRAC fuel-cladding gap-conductance model is provided in Appendix L. The user must specify the initial value of the gap conductance and appropriate geometric data. At the user's option, either the initial gap conductance is used throughout the calculation or the initial gap-conductance value is modified via a thermal-expansion model.

If we assume that the user seeks a transient evaluation, the fuel-cladding gap conductance is given by

$$h_{gas} = \frac{k_{gas}}{(\Delta r_{gap} + \delta_r)} , \tag{4-15}$$

where k_{gas} is the gap-gas thermal conductivity. A value of 4.4 x 10^{-6} m is used for δ_r, which includes the mean surface roughness of the fuel and the cladding plus the temperature jump differences (Refs. 4-11. and 4-12.). The fuel-cladding radial gas gap, Δr_{gap}, is developed following Boley and Weiner (Ref. 4-13.). The uncoupled, quasi-static approximation is applied, which eliminates the mechanical coupling term in the energy equation and the inertial term in the mechanical force balance. With these assumptions, the fuel-cladding strains minimally affect the temperature distribution; displacements are instantaneous. The fuel-cladding gap system is modeled as comprising three regions: solid fuel, cracked fuel, and cladding. Gap changes are found by calculating the radial displacement of each region caused by thermal expansion.

The gap width after a period of thermal expansion is given by

$$\text{gap width} = R_{I,new} - R_{f,new} - \delta , \tag{4-16}$$

where $R_{I,new}$ and $R_{f,new}$ are the cladding inner radius and the solid-fuel radius after thermal expansion, respectively, and δ is the cracked-fuel thickness. These are defined by the following expressions:

$$R_{I,\,new} = R_I + \frac{2\alpha_c R_I}{R_o^2 - R_I^2} \int_{R_I}^{R_o} \Delta T_c \, r \, dr , \tag{4-17}$$

$$R_{f,\,new} = R_f + \frac{2\alpha_f}{R_f} \int_{o}^{R_f} \Delta T_f \, r \, dr \text{ , and} \tag{4-18}$$

$$\delta = \delta_o \left[1 + \frac{\alpha_f}{R_f^* - R_f} \int_{R_f}^{R_f^*} \Delta T_f \, dr \right] , \tag{4-19}$$

where δ_o is the initial undeformed radial thickness of the cracked fuel, $\delta_o = R_f^* - R_f$; R_o is the initial cladding outer radius; and ΔT_c and ΔT_f are temperature differences with respect to a reference temperature (298 K) in the fuel and cladding, respectively.

4.6. Decay Heat and Reactivity Feedback

The code uses the solution of the point-reactor-kinetics model for the total fission power, *P*, in the decay-heat equations to obtain the decay heat. Detailed descriptions of the kinetics and associated models are provided in Appendix M. The decay-heat equations are

$$\frac{dH_j}{dt} = -\lambda_j^H H_j + E_j P \text{ , for } j = 1, 2, 3, \ldots, J, \tag{4-20}$$

where

H_j = energy of the decay-heat precursor concentration in group *j* (W-s),
λ_j^H = decay constant for decay-heat group *j* (s^{-1}),
E_j = effective energy fraction of decay-heat group *j*, and
J = number of decay-heat groups.

TRAC contains default data for the delayed-neutron constants λ_i, decay-heat group constants λ_j^H, and decay energy. The effective energy fraction, E_j, is obtained from the decay energy. The default values for the parameters for the decay-heat equation are taken from the 1979 American Nuclear Society (ANS) decay-heat standard (Ref. 4-14.). The code user can either use the default values or input other sets of constants.

The reactor-power and decay-heat models are fundamental standard models for the kinds of applications of interest to TRAC.

The total thermal power generated in the fuel is calculated from the sum of the nuclear fission, fission-product decay, and any external source.

The neutronic reactivity [see Appendix M, Eq. (M-6)] includes accounting for the effects of core-average fuel temperature, coolant temperature, coolant void fraction, and boron (i.e., solute) concentration. The user supplies reactivity coefficients for each of the reactivity independent-variable parameters: fuel temperature, coolant temperature, coolant void fraction, and boron concentration. The TRAC modeling again is based on widely used standard models.

It is the void reactivity-feedback coefficient that causes the shutdown of power generation for an LBLOCA. The rapid increase in void as the pressure in the core attains the saturation pressure effectively stops power production. The void increase due to flashing of the liquid in the core is so rapid that the power-generation shutdown is

almost independent of the numerical value of the user-supplied feedback coefficient. (within reasonable engineering values).

The code solves the point-reactor-kinetics equations by modifications to the Kaganove method (Ref. 4-15.), an approximate analytical method. The modifications consist of using a second-order polynomial for the power, *P*; using a first-order polynomial for the neutronic reactivity, *R*; and taking the effective prompt-neutron lifetime, Λ, as a constant.

The core-power model in TRAC, with all the options and features, has proved to be sufficiently general for describing the core assemblies in most of the reactor-safety-related experiments and in reactor plants, provided that the power shape changes only in the axial direction. The option to specify core power directly with a tabular prescription is generally sufficient for modeling most transients of interest. The decay-heat model is based on the 1979 ANS standard and is thus the best available model at this time.

The deficiencies of the core-power model are related principally to the fact that the reactor kinetics is based on the point-reactor assumption. Reactivity feedback also is based on the point-reactor assumption.

The point-reactor model has no limitations relative to applications involving LBLOCA analyses.

4.7. Reactor-Vessel Vent Valve

Reactor-vessel vent valves, such as those used in Babcock and Wilcox (B & W) plants, are modeled in the VESSEL component with user-specified values for flow-loss resistance as a function of pressure drop across the valve at user-specified locations in the VESSEL mesh. Leakage flow can be modeled. The vent-valve logic is only applicable at the outer radial (or *x*) interface of a 3D VESSEL mesh cell. Only a single vent valve may be specified at any one such interface; additional valves at the same interface would have to be lumped together. The user-supplied resistances are applied in the radial momentum equations of TRAC's 3D hydrodynamics. The inertial effects of the vent valve opening and closing are not modeled in TRAC. Additional details on TRAC's vent-valve logic are given in Appendix I, Section I.5., and complete input specifications are given in the TRAC-M/F90 User's Manual (Ref. 4-16.). Both Appendix I and the user's manual describe the form of flow-loss resistance that must be supplied by the user.

4.8. Metal-Water Reaction

When Zircaloy cladding reaches a sufficiently high temperature in a steam environment, an exothermic reaction may occur that influences the peak cladding temperature. This exothermic reaction is given by

$$Zr + 2H_2O \rightarrow ZrO_2 + 2H_2 + \text{heat} . \qquad (4\text{-}21)$$

TRAC accounts for this reaction by calculating an additional heat source q'''_{mw} that is added to the heat-conduction equation. The code assumes a single-region cladding and that there is enough steam to allow use of a standard reaction-rate equation. The term q'''_{mw} is calculated according to

$$q'''_{mw} = 6.45 \times 10^6 m'_{Zr} [\Delta t (R_o^2 - R_I^2)\pi]^{-1} , \quad (4\text{-}22)$$

where m'_{Zr} is the mass per unit length of zirconium consumed by the reaction in one time step, Δt is the time-step size, R_o and R_I are the cladding outer and inner radii, respectively, and 6.45×10^6 J/kg is the energy released per kilogram of oxidized zirconium.

The derivation of Eq. (4-22) is given in Appendix L, Section L.2.

TRAC only applies this model at nodes that are at hydrodynamic cell boundaries, and accounts for its effect at intervening fine mesh nodes by linear interpolation. This could result in a significant underprediction of clad temperature in cells with a quench front. Section L.2. of Appendix L discusses the possibility of TRAC's underprediction of peak clad temperature when the peak clad temperature is in the same hydrodynamic cell as a quench front and rod temperatures exceed 1273 K (the onset of the metal-water reaction).

REFERENCES

4-1. "RELAP5/MOD1 Code Manual, Volume 1: System Models and Numerical Methods," Idaho National Engineering Laboratory report EGG-2070 Draft, Rev. 1, also NUREG/CR1826 (March 1981).

4-2. O. C. Jones, Jr., "Flashing Inception in Flowing Liquids," Brookhaven National Laboratory report BNL-NUREG-51221 (1980).

4-3. V. H. Ransom and J. A. Trapp, "The RELAP5 Choked Flow Model and Application to a Large Scale Flow Test," in *ANS/ASME/NRC International Topical Meeting on Nuclear Reactor Thermal-Hydraulics* (Saratoga Springs, New York, 1980), pp. 799–819.

4-4. F. M. White, *Fluid Mechanics* (McGraw-Hill, Inc., New York, 1979).

4-5. S. G. Bankoff, R. S. Tankin, M. C. Yuen, and C. L. Hsieh, "Countercurrent Flow of Air/Water and Steam/Water through a Horizontal Perforated Plate," *International Journal of Heat and Mass Transfer*, **24**:8, pp. 1381–1395 (1981).

4-6. G. B. Wallis, *One Dimensional Two Phase Flow* (McGraw-Hill Book Company, New York, 1969).

4-7. S. S. Kutateladze, *Izv. Akad. Nauk SSSR, Otd. Tekhn. Nauk*, Vol. 8, p. 529 (1951).

4-8. K. H. Ardron and W. M. Bryce, "Assessment of Horizontal Stratification Entrainment Model in RELAP5/MOD2," United Kingdom Atomic Energy Authority, AEE Winfrith draft report AEEW-R 2345 (April 1988).

4-9. B. S. Massey, *Mechanics of Fluids*, D. Van Nostrand Co., New York (1968).

4-10. "Flow of Fluids through Valves, Fittings, and Pipes," Metric Edition-SI Units of the Crane Manual, Technical Paper No. 410M, Crane Co., New York (1977).

4-11. L. S. Tong and J. Weisman, *Thermal Analysis of Pressurized Water Reactors*, (American Nuclear Society, LaGrange Park, Illinois, 1979), 2nd Ed.

4-12. P. E. MacDonald and J. Weisman, "Effect of Pellet Cracking on Light Water Reactor Fuel Temperatures," *Nuclear Technology*, **31**, 357–366 (1976).

4-13. B. A. Boley and J. H. Weiner, *Theory of Thermal Stresses* (John Wiley and Sons, Inc., New York, 1960).

4-14. "American National Standard for Decay Heat in Light Water Reactors," American Nuclear Society publication ANSI/ANS-5.1 (1979).

4-15. J. J. Kaganove, "Numerical Solution of the One-Group Space-Independent Reactor Kinetics Equations for Neutron Density Given the Excess Reactivity," Argonne National Laboratory Report ANL-6132 (1960).

4-16. R. G. Steinke, V. Martinez, N. M. Schnurr, J. W. Spore, and J. V. Valdez, "TRAC-M Fortran 90 (Version 3.0) User's Manual," Los Alamos National Laboratory document LA-UR-00-835 (February 2000).

5.0. SPECIAL COMPONENT MODELS

Some 1D components in TRAC perform special functions that require modification of the solution of the 1D fluid equations. These modifications include the modeling of the behavior of pumps, valves, pressurizers, and accumulators. Also, a TRAC model of a reactor system requires appropriate boundary conditions, and it is often very useful to be able to connect several 1D components at a common point in a flow network.

The PUMP component produces a momentum source term in the form of an additional ΔP on the right-hand side of the momentum equation. The VALVE component has a variety of options to adjust the flow area at a user-specified cell face. The PRIZER component models a PWR pressurizer. PWR accumulators are modeled by special logic that is built into TRAC's PIPE component, which is triggered by one of two PIPE input options. (Note that the ACCUM component that was part of early versions of the TRAC series was removed from TRAC-PF1/MOD2, before TRAC-M development started.) The FILL and BREAK components provide boundary conditions to the normal 1D components by allowing the user to specify either flows (FILL) or pressures (BREAK) at the boundary, together with the fluid state if an inflow condition exists. The PLENUM component is a special, single-cell, 1D component that allows the user to connect as many normal 1D components as desired. To accomplish this objective, the PLENUM component interacts with the networking logic in the code and changes the form of the momentum flux terms.

Note: ACCUM (Accumulator) and STGEN (Steam Generator) Components. The ACCUM and STGEN components that were part of early versions of the TRAC series were removed from TRAC-PF1/MOD2, before TRAC-M development started. Steam generators can be modeled with a combination of PIPE, TEE, and HTSTR components. Accumulators can be modeled with special options that are built into the PIPE component. Guidelines for steam generator and accumulator modeling are given in the TRAC-M User's Manual (Ref. 5-8.). The modeling of steam generators does not involve special modification to TRAC's basic internal models. The PIPE component's special accumulator logic is described in this section and in more detail in Appendix J.

Note: Separator (SEPD) and Turbine (TURB) Components. The base code for both TRAC-M/F77 and TRAC-M/F90 had components to model steam/water separators (SEPD) and turbines (TURB). The TRAC-P SEPD component permits the user to specify the separation efficiency in such locations as the separator at the top of a normal U-tube steam generator. The TRAC-P SEPD component received minimal support over the years, and its general use was not, and is not, recommended. (It should be used with caution.) Both TRAC-M/F77, Version 5.5.2, and TRAC-M/F90 (Version 3.0), have an SEPD component that was brought over directly from TRAC-P, and the same caution applies. The separator capability will be improved in a future TRAC-M/F90 version. In the TURB component, energy is removed from the fluid as a result of work performed by the turbine. The turbine model calculates the momentum and

energy losses and the angular velocity as a function of the fluid flow rate, fluid properties, and turbine nozzle and blade geometry. These momentum and energy losses are subsequently subtracted from the TRAC momentum and energy equations, respectively. The TURB component received minimal support over its years in TRAC-P, and its general use was not, and is not, recommended. (It should be used with caution.) The TRAC-P TURB was brought over directly to TRAC-M. Currently, the TURB component is only available in TRAC-M/F77, and the same caution applies. The TRAC-P TURB has been removed entirely from TRAC-M/F90. An improved turbine modeling capability is to be included in a future TRAC-M/F90 version.

Note: Future Versions of TRAC-M/F90. Future versions of TRAC-M/F90 (post-Version 3.0) will include enhanced modeling capability, including BWR models and RELAP-5 style modeling. New components will include a vessel channel (CHAN) with leak paths, jet pump (JETP), heater, turbine (TURB, replacing the TRAC-P TURB), separator (SEPD, replacing the TRAC-P SEPD), and single-junction component (SJC, which will be used by the forthcoming leak path logic for the CHAN component and will facilitate RELAP-5-style modeling).

NOMENCLATURE

g:	gravitational acceleration
h:	normalized pump head
h_1:	normalized pump head from the single-phase performance curve
h_2:	normalized pump head from the fully degraded performance curve
H:	pump head
H_R:	rated pump head
H_1:	single-phase pump head
H_2:	fully degraded pump curve
I:	pump moment of inertia
$M(\alpha)$:	pump head degradation multiplier
$P_{dynamic}$:	dynamic pressure
P_{static}:	static pressure
q:	normalized pump volumetric flow
Q:	pump volumetric flow
Q_R:	rated pump volumetric flow
t:	time
T:	pump hydraulic torque acting on the impeller
T_f:	pump friction torque acting on the rotating parts of the motor
V_{inflow}:	inflow velocity (at BREAK boundary condition)

α: void fraction

ρ: density

ω: normalized pump speed

Ω: pump speed

Ω_R: rated pump speed

Ω_s: pump specific speed

5.1. Pump Component

The pump component in TRAC describes the momentum interaction between the coolant and the pump. The model calculates the pressure difference across the pump and the angular speed of the pump impeller and rotor as a function of the coolant flow rate and thermodynamic state. The modeling approach used in TRAC is the standard engineering method for TRAC applications and is used in the RELAP5 (Ref. 5-1.) and RETRAN (Ref. 5-2.) codes, as well as in TRAC. The model includes accounting for two-phase flow effects on pump performance. Relative to analysis of a LBLOCA in PWRs, the degradation of the pump under two-phase fluid-state conditions is the important aspect of the model. More detail on TRAC's PUMP model can be found in Appendix J, Section J.1.

5.1.1. Specific Speed

The similarity parameter that allows comparison of different pumps is the specific speed, Ω_s, given by

$$\Omega_s = \Omega Q^{1/2}/(gH)^{3/4} \quad , \tag{5-1}$$

where

Ω_s = pump specific speed,
Ω = pump speed,
Q = pump volumetric flow,
g = gravitational acceleration, and
H = pump head.

The specific speed is a constant for all similar pumps and ideally does not change as the pump speed changes. However, when comparing two pumps, the specific speed should be calculated at the point of highest operating efficiency.

The specific speed is presented to allow the user to determine that the built-in pump curves in TRAC are applicable to the system to which TRAC is to be applied. If the built-in performance curves are not appropriate for the user's system, the correct curves can be given as input to TRAC.

There are two sets of pump curves available in TRAC: the Semiscale Mod-1 system pump (Refs. 5-3. through 5-5.) and the LOFT system pump (Refs. 5-6. and 5-7.). We recommend that for full-scale pressurized-water-reactor (PWR) analyses, plant-specific pump curves be input. However, if those data are not available, the LOFT pump curves should be used.

5.1.2. Pump Head

The pump modeling in TRAC is based on the standard homologous-curves approach. These curves represent the performance of the pump in a normalized format, given the normalized pump head as a function of the normalized volumetric flow and normalized pump speed. That is, at higher pump speeds ($0 \le |q/\omega| \le 1$),

$$h / \omega^2 = f(q / \omega) \quad . \tag{5-2}$$

At low pump speed ($0 \le |\omega/q| < 1$), better results are obtained by using

$$h / q^2 = f(\omega / q) \quad . \tag{5-3}$$

In these equations, the normalized pump head is $h=H/H_R$, the normalized volumetric flow is $q=Q/Q_R$, and the normalized speed is $\omega=\Omega/\Omega_R$, where the subscript R refers to rated condition.

The normalized pump performance curves are input into TRAC as two sets of curves. One set describes the single-phase performance over the complete range of normal and off-normal operating conditions. The second set provides the same information for a reference two-phase state of the coolant. A head degradation multiplier also is used in the model. With the performance curves and head degradation factor, the pump head is obtained from

$$H = H_1 - M(\alpha)\,(H_1 - H_2) \quad , \tag{5-4}$$

where

H	=	pump head,
H_1	=	the single-phase pump head, $H_1 = h_1 H_R$,
H_2	=	the fully degraded pump curve, $H_2 = h_2 H_R$,
$M(\alpha)$	=	the head degradation multiplier,
α	=	void fraction,

and h_1 and h_2 are the normalized head values from the single-phase and fully degraded performance curves, respectively.

5.1.3. Pump Torque

Development of the homologous torque curves exactly parallels that just given for the pump head curves. The development is not repeated here, although this information can be found in Appendix J, Section J.1.

5.1.4. Pump Speed

The TRAC pump model holds the pump speed constant as long as the pump motor is energized. After a trip of the power to the pump motor, the pump speed will change according to the forces (torque) acting on the rotor. The balance of momentum applied to the motor rotor gives an equation for the rotor speed to be

$$I\,(\Omega / dt) = -\,(T + T_f) \quad , \tag{5-5}$$

where

I = moment of inertia,
T = hydraulic torque acting on the impeller, and
T_f = friction torque acting on the rotating parts of the motor.

The hydraulic torque is obtained from the pump-performance curves, the frictional torque is represented by a third-order polynomial in the pump rotational speed, and the coefficients for the polynomial are input by the user.

The pump rotational speed may be represented by a table of input values instead of the dynamic model. For this case, the pump speed is constant at the initial input value until a trip condition is met. Following the trip, the speed is taken from the table. The user may specify a variety of signal variables in addition to time as the independent variable for the pump-speed table.

5.2. Boundary-Condition Components

The BREAK and FILL components are used to impose boundary conditions at any 1D hydraulic-component junction. Consequently, these components differ from the other hydraulic components in that they do not model any physical-system component, per se, and they do not perform any hydrodynamic or heat-transfer calculations; however, they are treated as any other component with respect to ID, input, and initialization.

The BREAK- and FILL-component-specified fluid pressure, gas volume fraction, fluid temperatures, noncondensable-gas partial pressure, and solute concentration in liquid define the properties of the fluid convected into the adjacent component if an inflow condition occurs. By convention, inflow to the adjacent component corresponds to a positive velocity at the FILL component's JUN2 junction and to a negative velocity at the BREAK component's JUN1 junction. A FILL or BREAK component may not be connected directly to a VESSEL component-source connection junction or a PLENUM component junction.

5.2.1. FILLS

A FILL component imposes a coolant-velocity or mass-flow boundary condition at the junction with its adjacent component. For example, the ECC injection or secondary-side feedwater may be modeled with a FILL component.

The velocity or mass-flow boundary condition, as well as its fluid properties, are specified by user input in one of three ways, according to the FILL-type IFTY option selected. For the first type, the homogeneous fluid velocity and fluid properties are specified; for the second type, the homogeneous fluid mass flow and fluid properties are specified; and for the third type, nonhomogeneous fluid velocities and fluid properties are specified. For each type, the relevant parameters may be constant, interpolated from input FILL-component action tables, constant until a controlling trip is set ON to require their evaluation from their action tables, or defined by signal-variable or control-block signals. The independent variable of the FILL table's tabular data is a signal-variable modeled-system parameter or a control-block output signal. When the FILL's coolant velocity or mass flow varies rapidly, using this value may lead to a hydrodynamic instability in the numerical solution. This can be avoided by using a TWTOLD-weighted average of the parameter's previous value and the current specified value or by limiting the parameter's time rate of change by RFMX. (All FILL input parameters are explained in the TRAC User's Manual, Ref. 5-8.)

Additional remarks on the TRAC FILL component are given in Appendix J, including a summary of general cautions on its use.

5.2.2. BREAKs

The BREAK component imposes a pressure boundary condition one cell away from its adjacent component. This component commonly is used to model the containment system in LOCA calculations or the coolant pressure at an outflow boundary of the modeled system. The pressure boundary condition, as well as the fluid properties associated with the BREAK cell for inflow donor-cell convection, may be specified by user input as constants, defined individually by signal variables or control blocks, or defined as tabular functions of a signal variable or control block. They can also be constant until a controlling trip is set ON and then evaluated based on the tabular-function BREAK tables while the controlling trip remains ON.

Inflow momentum flux from a BREAK cell is not modeled internally by TRAC because its contribution to the momentum-convection term of the junction-interface motion equation can be numerically unstable. The inflow momentum flux must be modeled by the user through input by defining a dynamic-pressure rather than a static-pressure boundary condition as

$$P_{dynamic} = P_{static} + \rho V_{inflow}^2 / 2 \quad . \tag{5-6}$$

Averaging the BREAK component's properties with those of its adjacent cell for their junction momentum cell can be eliminated by defining in the BREAK's user input a very small BREAK-cell DXIN length (weighting factor). The user also must input a very large

BREAK-cell volume or very small BREAK-cell length (for example, VOLIN = 10^{10} or DXIN = 10^{-10}) to model a very large inflow area (VOLIN / DXIN). Use of these BREAK input parameters is explained in the TRAC User's Manual (Ref. 5-8.).

Additional remarks on TRAC's BREAK component are given in Section 2.0. and in Appendix J, where general cautions on the use of the component are summarized.

5.3. PLENUM Component

The PLENUM component models the thermal hydraulics of a volume connected to an arbitrary number of 1D hydraulic components. The PLENUM is a single-cell component that the user can set up either as a momentum sink (where all inflow momentum is converted to a coolant pressure rise) and / or for convecting momentum across the cell from one side (having user-specified junctions) to the other side (also having user-specified junctions). The effect of an elevation change between the PLENUM cell and its adjacent-component junction cells is evaluated. There are single values for the coolant pressure, noncondensable-gas pressure, gas volume fraction, liquid temperature, vapor temperature, and solute concentration in the PLENUM cell. At each of its user-specified junctions, TRAC evaluates the standard 1D, two-fluid motion equations with the PLENUM-cell momentum flux either set to zero or convected across the cell in one direction, according to user specification. There is no requirement that the liquid and gas velocities be equal at a junction. The constitutive correlations will detect stratified flow at each PLENUM-cell junction if the momentum-cell mean coolant velocity falls below a threshold velocity and the elevation change falls below a threshold slope.

The user specifies a cell length at each PLENUM junction; these lengths need not be equal. TRAC uses the PLENUM-cell length for each junction in its motion equation solution for the junction. In particular, the GRAV elevation parameter at a given junction (input by the adjacent 1D hydraulic component) is defined in terms of the cell lengths from the adjacent-component cell and the PLENUM-cell junction.

Currently, TRAC does not allow HTSTR components to be coupled by convection heat transfer to a PLENUM cell. A PLENUM-component junction cannot be connected to a BREAK, FILL, PLENUM, or VESSEL component junction. Signal variables cannot define a PLENUM-cell parameter. If needed, the signal variable should be defined in the adjacent 1D hydraulic-component cell.

Additional remarks on TRAC's PLENUM component are given in Appendix J.

5.4. Pressurizer Component (PRIZER)

A PWR pressurizer is a large fluid-volume reservoir that maintains the coolant pressure within the reactor primary-coolant system and compensates for changes in the coolant volume caused by system transients. During normal operation, this reservoir contains the highest-energy fluid in the primary-coolant system. It is usually kept 50%–60% full of saturated liquid that is pressurized by saturated steam (vapor) above it.

The pressurizer controls the primary-coolant system pressure by hydraulic coupling through a long surge line connected to one of the PWR hot legs.

TRAC's PRIZER component simulates the PWR pressurizer. Normally, the PRIZER models only the pressurizer reservoir, with the connecting surge line modeled by a PIPE or TEE component. The PRIZER component may be connected at both its junctions to other 1D hydraulic components.

For TRAC steady-state calculations, the PRIZER component is replaced automatically with the equivalent of a BREAK component at each of its junctions. User-specified thermal-hydraulic conditions in the PRIZER component during steady-state calculations remain unchanged except for the component's wall temperature, which is calculated by conduction heat transfer to obtain a steady-state, wall temperature profile.

Additional details on TRAC's PRIZER component are given in Appendix J.

5.5. VALVE Component

The VALVE component is used to model various types of valves associated with light-water reactors (LWRs). The valve action is modeled by adjustment of the flow area and form loss at a user-specified cell interface of a 1D (PIPE-like) hydraulic component.

The adjustable flow area of the VALVE component can be specified in two basic ways. The flow area can be computed directly from an adjustable flow-area fraction and a user-specified fully open flow area. In the second form, the flow area is calculated from the relative position of the valve stem, where a guillotine-like blade is assumed to cut a circular cross-section flow channel with a user-specified fully open area.

Many different types of valves can be modeled because of the flexibility to choose the independent variable of VALVE component-action tables and to perform table evaluation under trip control. These include simple valves to model pipe breaks or the opening of rupture disks, check valves, power-operated relief valves, banks of power-operated relief valves, steam-flow control valves, turbine stop valves, turbine bypass valves, main-steam isolation valves, safety relief valves, and atmospheric dump valves. Guidelines for valve modeling are given in the TRAC-M User's Manual (Ref. 5-8.).

The VALVE component's adjustable flow area may not be located at a VALVE-component junction unless that junction is connected to a BREAK component.

The VALVE closure state adjustment is made with a step change at the beginning of a hydrodynamic time step; the VALVE state is held constant during the time step.

Additional details on TRAC's VALVE component are given in Appendix J.

5.6. Accumulator Option in PIPE Component

A PWR accumulator can be modeled by use of special logic that is built into the PIPE component. This logic, when triggered by user input, evaluates a gas/liquid interface sharpener and (optionally) prevents gas outflow with a liquid separator model. To allow the accumulator-like behavior to be measured, TRAC calculates water level, volumetric flow, and liquid volume discharged from the component.

Additional details on the PIPE component accumulator model are given in Appendix J.

REFERENCES

5-1. K. E. Carlson, R. A. Riemke, S. Z. Rouhani, R. W. Shumway, and W. L. Weaver, "RELAP5/MOD3 Code Manual — Volume 1: Code Structure, System Models, and Solution Methods," Idaho National Engineering Laboratory report NUREG/CR-5535, EGG-2596 (Draft) (June 1990).

5-2. J. H. McFadden, M. P. Paulsen, G. C. Gose, C. E. Peterson, P. J. Jensen, J. A. McClure, J. L. Westacott, and J. G. Shatford, "RETRAN-3D — A Program for Transient Thermal-Hydraulic Analysis of Complex Fluid-Flow Systems, Volume 1: Theory and Numerics," Computer Simulation and Analysis, Inc. report NP-7450, Volume 1, Revision 1 (January 1996).

5-3. D. J. Olson, "Experimental Data Report for Single– and Two–Phase Steady–State Tests of the 1-1/2-Loop Mod-1 Semiscale System Pump," Aerojet Nuclear Company ANCR–1150 (May 1974).

5-4. G. G. Lomis, "Intact Loop Pump Performance During the Semiscale MOD-1 Isothermal Test Series," Aerojet Nuclear Company ANCR–1240 (October 1975).

5-5. D. J. Olson, "Single– and Two–Phase Performance Characteristics of the MOD-1 Semiscale Pump under Steady–State and Transient Fluid Conditions," Aerojet Nuclear Company ANCR–1150 (October 1974).

5-6. D. L. Reeder, "LOFT System and Test Description (5.5-Ft. Nuclear Core 1 LOCES)," EG&G Idaho, Inc. TREE–1208 (NUREG/CR–0247) (July 1978).

5-7. US Nuclear Regulatory Commission memorandum, L. E. Phillips to U. S. Standard Problem Participants, Subject: Additional Information for Prediction of LOFT L2–3 (March 1979).

5-8. R. G. Steinke, V. Martinez, N. M. Schnurr, J. W. Spore, and J. V. Valdez, "TRAC-M Fortran 90 (Version 3.0) User's Manual," Los Alamos National Laboratory document LA-UR-00-835 (February 2000).

6.0. SUMMARY

This document consists of many individual, complete descriptions that, in themselves, stand alone. The presence of the field equations, numerical methods, and the flow-regime map provides a cohesive thread linking all of the parts into a whole.

We believe that the document is structured well enough to permit the reader to find readily the discussion of any closure relation or other model contained in TRAC-M. Section 2.0. describes the numerical methods used in the code to solve all of the equations. Section 3.0. provides a basic description of TRAC-M's closure relations (including a "roadmap" that relates the closure relations to the hydrodynamic field equations), which are described in further detail in the appendices to this document (Appendices D through H).

Section 3.2. describes the basic flow-regime map that forms the basis for linking correlations into models spanning a wide variety of flow conditions. Each collection of related correlations and models, whether they describe interfacial shear or interfacial heat transfer or wall heat transfer, etc., modifies the basic map to account for the amount of knowledge available about a given phenomenon. Generally, the more detailed the knowledge is concerning a particular phenomenon, the more detailed the flow regimes must be. Section 3.3. describes TRAC-M's logic for calculation of flow-regime-dependent interfacial area.

Section 3.4. describes the code's interfacial mass transfer. Sections 3.5., 3.6., 3.7., and 3.8. cover the interfacial drag, the wall drag, the interfacial heat transfer, and the wall heat transfer, respectively. Each section (and related appendix) clarifies the modifications required to the basic flow-regime map for each process. Section 4.0. and Appendix I describe those models that are not component-oriented (in the TRAC-M sense of components) and that generally have an impact on the momentum equation and/or interfacial drag. Three main examples of these models are critical flow, CCFL, and form loss. Section 5.0. and Appendix J cover the special TRAC-M components with specific functions that are not available in other TRAC-M components (e.g., the PUMP component). Appendices A and B cover the code's thermodynamic and transport fluid properties, and material properties, respectively. Appendix K provides the thermodynamic and transport properties for the noncondensable-gas field and the solubility of the liquid solute. Discussions of the noncondensable-gas and liquid-solute effects on other models are provided as appropriate with each model. Appendix L describes fuel-cladding gap conductance and the metal-water reaction model. Appendix M describes in detail the reactor-core power model. Finally, Appendix N gives details on the code's control procedure, including signal variables, control blocks, and trips. Whereas we have tried to state explicitly when the code lacks a model or ignores an effect, the reader should assume that if an aspect or effect of something is not discussed, the code does not consider it.

The level of quality in the code is fairly uniform in that there are no big surprises lurking in the correlations, models, and logic. We expected this general level of quality because

of the long-term development program that always built on the preceding code version and because of the large variety of applications and assessments of the code over the years. This process has resulted in a mature code that is generally not susceptible to the major problems that plagued earlier versions. The development and application history of the code is summarized in the introduction in Section 1.0.

The TRAC-M code invests most of its resources in solving the thermal-hydraulic problem of the fluid. For the most part, the solution of energy generation and conduction within solid structures is straightforward. The basic problem of the thermal hydraulics is to calculate the liquid inventory and its distribution. At PWR scale, the interfacial drag has a significant impact on the calculation of the inventory distribution. Also, interfacial condensation can set up pressure gradients that can move significant amounts of liquid. The correlations that govern interfacial drag and interfacial heat and mass transfer have generally performed well even though the results in Appendices F , (Section F.1.), G, and H, (Section H.1.) show some deficiencies in the models; certain isolated analysis results relate directly to the deficiencies. In some cases for integral experiments, the biggest problem is to identify the correct flow regime on which to base the interfacial interactions. As can be seen by the application of TRAC-M/F77 to UPTF tests in that code's Developmental Assessment Manual (Refs. 6-1. and 6-2.), the interfacial models are more than adequate for full-scale geometry.

Although the TRAC-M flow-regime maps are simple, comparisons to data indicate adequate accuracy. Additional accuracy has been attempted by modifying the basic TRAC-M flow regime within components where the data indicate that modifications are necessary (i.e., lower plenum, downcomer, etc.).

Although we do not believe that we have found the best available correlations and/or model for each closure relation in all cases, we do believe that we have found a set of closure correlations and/or models that work well with the TRAC-M numerics and result in a computer code that can be used as a tool in the hands of a knowledgeable engineer or scientist to investigate and simulate many transients in PWRs. This document supports the application of the code and aids in understanding the calculated results. The code structure and numerics are sound, although some changes can be made to take better advantage of new computer architecture and new advances in numerical techniques. However, we believe that as research continues in the area of two-phase flow and heat transfer, advances in modeling flow regimes and interfacial phenomena will continue. Therefore, improvements can be obtained in TRAC-M's ability to accurately model a wide range of flows and geometries.

Future versions of this TRAC-M/F90 Theory Manual will address TRAC-M/F90's capabilities, which are now under development, for analysis of BWRs.

REFERENCES

6-1. B. E. Boyack, J. F. Lime, D. A. Pimental, J. W. Spore, and J. L. Steiner, "TRAC-M/F77, Version 5.5, Developmental Assessment Manual, Volume I: Nonproprietary Assessment Sections," Los Alamos National Laboratory document LA-UR-99-6480 (December 1999).

6-2. B. E. Boyack, J. F. Lime, D. A. Pimental, J. W. Spore, and J. L. Steiner, "TRAC-M/F77, Version 5.5, Developmental Assessment Manual, Volume II: Proprietary Assessment Sections," Los Alamos National Laboratory document LA-CP-99-345 (December 1999).

APPENDIX A

THERMODYNAMIC AND TRANSPORT FLUID PROPERTIES

The thermodynamic- and transport-properties subroutines used in TRAC are based on polynomial fits to steam-table data for water, and on ideal gas behavior for the noncondensable-gas component. Transport property fits were obtained from Ref. A-1. All TRAC component modules use the same property routines. Table A-1. through A-11., which list the values of the constants used to obtain property values, are provided throughout this appendix.

NOMENCLATURE

c_p:	constant-pressure specific heat ($J \cdot kg^{-1} \cdot K^{-1}$)
c_v:	constant-volume specific heat ($J \cdot kg^{-1} \cdot K^{-1}$)
e:	internal energy
ELP:	change in energy required to move along the isotherm at T_l between two different pressure values
h:	enthalpy
h_{lv}:	latent heat of vaporization
h_{lvs}:	enthalpy of evaporation
k:	thermal conductivity
M:	numerical constant
p:	pressure (Pa)
PSL:	saturation pressure corresponding to T_l
R:	gas constant ($J \cdot kg^{-1} \cdot K^{-1}$)
T:	temperature (K)
v:	specific volume
γ:	ratio of specific heats
μ:	viscosity
ρ:	density
σ:	surface tension

Subscripts

a:	noncondensable gas
approx:	approximate
critical:	critical
g:	gas
ideal:	ideal gas behavior

l:	liquid
m:	steam-gas mixture
sat, *s*:	saturation
v:	steam

A.1. Thermodynamic Properties

Subroutine THERMO supplies thermodynamic properties for TRAC. The input variables are the total pressure; the partial pressure of the noncondensable gas, if any is present; and the liquid- and gas-phase temperatures, where the gas phase is either steam, a noncondensable gas, or a steam-gas mixture. The output variables include the saturation temperature corresponding to the total pressure and its derivative with respect to the total pressure; the saturation temperature corresponding to the partial pressure of steam and its derivative with respect to the steam partial pressure; the internal energies and densities of the liquid and gas phases, and their partial derivatives with respect to pressure (at constant temperature) and with respect to temperature (at constant pressure); and, finally, the saturated liquid and saturated steam enthalpies and their derivatives with respect to pressure.

THERMO supplies thermodynamic properties valid for temperatures and pressures within the following ranges:

$$273.15 \text{ K} \leq T_l \leq 713.94025779311 \text{ K} \quad ,$$

$$273.15 \text{ K} \leq T_g \leq 3000.0 \text{ K} \quad ,$$

and

$$1.0 \text{ Pa} \leq p \leq 45.0 \times 10^6 \text{ Pa}.$$

If THERMO is provided with data outside this range, it adjusts the data to the corresponding limit and issues a warning message.

Equations for the various properties used in THERMO are given below. Tables A-1. through A-6. list the values of the constants.

A.1.1. Saturation Properties

A.1.1.1. Relationship Between Saturation Temperature and Pressure. Subroutine SATPRS calculates the saturation pressure for a given temperature, while subroutine SATTMP calculates the saturation temperature for a given pressure. Subroutine SATDER evaluates the derivative of saturation temperature with respect to saturation pressure when given the values of the saturation temperature and pressure. Four temperature and pressure regions are used to evaluate the saturation pressure, saturation

temperature, and derivative of saturation temperature with respect to saturation pressure.

A.1.1.1.1. 610.8 Pa $\le p_s <$ 90.56466 $\times 10^3$ Pa and 273.15 K $\le T_s <$ 370.4251 K.
In subroutine HEV, a linear function of temperature accurately represents the enthalpy of evaporation h_{lvs}, such that

$$h_{lvs} = 3180619.59 - 2470.2120\ T_s$$

for all $T_s \le 425.01$ K (corresponding to all $p_s \le 0.5 \times 10^6$ Pa). The Clausius-Clapeyron equation, which assumes that steam is an ideal gas and neglects liquid volume compared to steam volume, can be written as

$$\frac{dp_s}{dT_s} = \frac{h_{lvs} p_s}{R_v T_s^2} \quad ,$$

where R_v is the gas constant for steam (Table A-1.). Substituting for h_{lvs} and integrating using the boundary condition p_s = 24821 Pa at T_s = 338 K, gives

$$p_s = 24821.0(T_s / 338.0)^{-5.3512} \exp\,[20.387(T_s - 338.0) / T_s] \quad .$$

TRAC calculations also require determination of T_s from a given p_s, which can only be calculated by trial and error from the above equation. A simplified logic for calculating T_s is used that guarantees solution in two iterations with an error of only a fraction of a percent. First, an approximate value of T_s is calculated from

$$T_{s,\,approx} = \frac{-2263.0}{0.434 ln(p_s / 100000.0) - 6.064} \quad ,$$

which gives $T_{s,approx}$ within a few degrees of the actual value. Integration of the Clausius-Clapeyron equation, assuming constant h_{lvs} between $T_{s,approx}$ and T_s, calculates the first iteration value of T_s to be

$$T_s = \frac{T_{s,approx}}{1 - \frac{R_v T_{s,approx}}{h_{lvs,approx}} ln\left(\frac{p_s}{p_{s,approx}}\right)} \quad .$$

The resulting T_s value is then input into this equation again as the new $T_{s,approx}$ value. Both $h_{lvs,approx}$ and $p_{s,approx}$ are calculated corresponding to $T_{s,approx}$ using the equations given above.

TABLE A-1.
Ideal Gas Constants

R_v	=	461.4975 [J/(kg·K)]	R_a	=	287.0516 [J/(kg·K)] for air 4124.2988 [J/(kg·K)] for hydrogen
g_{ideal}	=	1.3			2077.2345 [J/(kg·K)] for helium
$c_{pv,\text{ideal}}$	=	$\frac{\gamma_{\text{ideal}} R_v}{\gamma_{\text{ideal}} - 1}$	c_{pa}	=	1004.832 [J/(kg·K)] for air 14533.2 [J/(kg·K)] for hydrogen 5193.086 [J/(kg·K)] for helium
$c_{vv,\text{ideal}}$	=	$\frac{R_v}{\gamma_{\text{ideal}} - 1}$	c_{va}	=	$c_{pa} - R_a$

Inverting the Clausius-Clapeyron equation allows the derivative of the saturation temperature with respect to the saturation pressure to be evaluated, such that

$$\frac{\mathrm{d}T_s}{\mathrm{d}p_s} = \frac{R_v T_s^2}{h_{lvs} p_s} \quad .$$

Note: For values of p_s such that

$$1.0 \text{ Pa} \le p_s < 610.8 \text{ Pa} \quad ,$$

subroutines SATTMP and SATDER reset the value of p_s to 610.8 Pa, and proceed with the calculation of T_s and $\mathrm{d}T_s/\mathrm{d}p_s$.

A.1.1.1.2. 90.56466 $\times 10^3$ Pa $\le p_s <$ 13.969971285053 $\times 10^6$ Pa and 370.4251 $\le T_s <$ 609.62462615967 K. Ref. A-2. recommends using the following relationships between saturation temperature and pressure within this range:

$$p_s = 1.0 \times 10^5 \left(\frac{T_s - 255.2}{117.8} \right)^{\frac{1}{0.223}} \quad ,$$

$$T_s = 117.8 \left(1.0 \times 10^{-5} p_s \right)^{0.223} + 255.2 \quad ,$$

and

$$\frac{dT_s}{dp_s} = \frac{0.223(T_s - 255.2)}{p_s} \quad .$$

A.1.1.1.3. 13.969971285053 $\times 10^6$ Pa $\le p_s <$ 22.12 $\times 10^6$ Pa and 609.62462615967 K $\le T_s <$647.3 K. The relationships given below are based on an equation-of-state of the form

$$\ln(p_r) = a + \frac{b}{T_r} + \frac{c}{T_r^2} \quad .$$

In the above relation,

$$p_r = \frac{p_s}{p_{\text{critical}}}$$

and

$$T_r = \frac{T_s}{T_{\text{critical}}} \quad ,$$

where p_s and T_s are the saturation pressure and temperature and p_{critical} and T_{critical} are the critical pressure and temperature (Ref. A-3.). These relationships were formulated to provide a good fit to the data and to provide a smooth transition between the preceding and the following temperature and pressure ranges:

$$p_s = 7.2166948490268 \times 10^{11} \exp\left(\frac{-8529.6481905883 + \frac{1166669.3278328}{T_s}}{T_s}\right) \quad ,$$

$$T_s = \frac{4264.8240952941 + \sqrt{-13666986.708428 + 1166669.3278328 \ln p_s}}{27.304833093884 - \ln p_s} \quad ,$$

and

$$\frac{dT_s}{dp_s} = \frac{-T_s^2}{p_s\left(-8529.6481905883 + \frac{2333338.6556656}{T_s}\right)} \quad .$$

A.1.1.1.4. 22.12×10^6 Pa $\le p_s \le$ 45.0×10^6 Pa and 647.3 K $\le T_s \le$ 713.94025779311 K. The relationships given below are based on an equation-of-state of the form

$$\frac{\mathrm{d}[\ln(p_r)]}{\mathrm{d}\left[\ln\left(\frac{1}{T_r}\right)\right]} = M \quad ,$$

where p_r and T_r are defined as in the previous pressure and temperature range and M is a constant (Ref. A-3.):

$$p_s = 22.12 \times 10^6 \exp\left(7.6084087 - \frac{4924.9229}{T_s}\right) ,$$

$$T_s = \frac{4924.9229}{24.520401 - \ln(p_s)}$$

and

$$\frac{\mathrm{d}T_s}{\mathrm{d}p_s} = \frac{2.0304886238506 \times 10^{-4}\ T_s^2}{p_s} \quad .$$

A.1.1.2. Saturated Steam Internal Energy. Two main pressure regions exist when calculating the internal energy of steam at saturation, e_{vs}, and the derivative of e_{vs}, with respect to the partial pressure of steam, p_v. In this section, T_{sv} denotes the saturation temperature corresponding to p_v.

A.1.1.2.1. 1.0 Pa < p_v < 0.5×10^6 Pa.

$$e_{vs} = h_{vs} - \frac{p_v}{\rho_{vs}} = h_{vs} - R_v T_{sv}$$

and

$$\frac{\mathrm{d}e_{vs}}{\mathrm{d}p_v} = \frac{\mathrm{d}h_{vs}}{\mathrm{d}p_v} - R_v \frac{\mathrm{d}T_{sv}}{\mathrm{d}p_v} \quad ,$$

where h_{vs} and $\frac{\mathrm{d}h_{vs}}{\mathrm{d}p_v}$ are calculated as described in Section A.1.1.4. for the same pressure range, 1.0 Pa $\le p_v \le 0.5 \times 10^6$ Pa.

A.1.1.2.2. 0.5×10^6 Pa< $p_v \le 45.0 \times 10^6$ Pa. A sequence of polynomials in the partial pressure of steam, p_v, is used to calculate e_{vs} and de_{vs}/dp_v as

$$e_{vs} = AVE(i) + BVE(i)\, p_v + CVE(i)\, p_v^2 + DVE(i)\, p_v^3$$

and

$$\frac{\mathrm{d}e_{vs}}{\mathrm{d}p_v} = BVE(i) + 2\, CVE(i)\, p_v + 3\, DVE(i)\, p_v^2 \quad ,$$

where

$i = 1$ for $0.5\times10^6 < p_v \le 2.0\times10^6$ Pa ,
$i = 2$ for $2.0\times10^6 < p_v < 5.0\times10^6$ Pa ,
$i = 3$ for $5.0\times10^6 \le p_v < 10.0\times10^6$ Pa ,
$i = 4$ for $10.0\times10^6 \le p_v < 15.0\times10^6$ Pa ,
$i = 5$ for $15.0\times10^6 \le p_v < 20.0\times10^6$ Pa ,
$i = 6$ for $20.0\times10^6 \le p_v \le 22.0\times10^6$ Pa ,
$i = 7$ for $22.0\times10^6 < p_v < 25.0\times10^6$ Pa ,
$i = 8$ for $25.0\times10^6 \le p_v < 30.0\times10^6$ Pa ,
$i = 9$ for $30.0\times10^6 \le p_v < 35.0\times10^6$ Pa ,
$i = 10$ for $35.0\times10^6 \le p_v < 40.0\times10^6$ Pa , and
$i = 11$ for $40.0\times10^6 \le p_v \le 45.0\times10^6$ Pa .

Table A-2. lists the constants *AVE(i)*, *BVE(i)*, *CVE(i)*, and *DVE(i)* for the given pressure ranges.

Function $\mathrm{d}e_{vs}/\mathrm{d}p_v$ is discontinuous near the critical point at junction point $p_v = 22.0 \times 10^6$ Pa. At this point the left-side value of the function is 4.37931×10^{-3} while the right-side value is 0.0, giving a fractional change across the junction point of 1.00.

A.1.1.3. Saturated Liquid Internal Energy. A sequence of polynomials in the saturated liquid temperature, T_{sat}, is used to calculate the internal energy of saturated liquid, e_{ls}, and its derivatives with respect to T_{sat}. We use

$$e_{ls} = ALE(i) + BLE(i)\, T_{sat} + CLE(i)\, T_{sat}^2 + DLE(i)\, T_{sat}^3$$

TABLE A-2.
Saturated Steam Internal Energy Constants

i	*AVE*(*i*)	*BVE*(*i*)	*CVE*(*i*)	*DVE*(*i*)
1	2.4949771766385E+06	2.0855856331827E–01	– 1.3553894579716E–07	2.8522684989198E–14
2	2.5600870370371E+06	3.1086111111026E–02	–6.8988888888580E–09	4.3203703703379E–16
3	2.5915500000006E+06	8.7749999997567E–03	–1.7499999999663E–09	4.2999999998503E–17
4	2.6606000000024E+06	–1.3545000000581E–02	6.4250000004682E–10	–4.2100000001248E–17
5	3.8201600000097E+06	–2.3019900000170E–01	1.4068900000098E–08	–3.1786000000187E–16
6	–1.2103411633350E+08	1.8018803375785E+01	–8.7442426507726E–07	1.4091076856088E–14
7	2.2000000000000E+06	0.	0.	0.
8	2.2000000000000E+06	0.	0.	0.
9	2.2000000000000E+06	0.	0.	0.
10	2.2000000000000E+06	0.	0.	0.
11	2.2000000000000E+06	0.	0.	0.

and

$$\frac{\mathrm{d}e_{\mathrm{ls}}}{\mathrm{d}T_{\mathrm{sat}}} = BLE(i) + 2\,CLE(i)\,T_{\mathrm{sat}} + 3\,DLE(i)\,T_{\mathrm{sat}}^{2} \quad ,$$

where

$i = 1$ for $273.15 \leq T_{\mathrm{sat}} < 423.15$ K ,
$i = 2$ for $423.15 \leq T_{\mathrm{sat}} < 473.15$ K ,
$i = 3$ for $473.15 \leq T_{\mathrm{sat}} < 523.15$ K ,
$i = 4$ for $523.15 \leq T_{\mathrm{sat}} < 573.15$ K ,
$i = 5$ for $573.15 \leq T_{\mathrm{sat}} < 623.15$ K ,
$i = 6$ for $623.15 \leq T_{\mathrm{sat}} \leq 645.15$ K ,
$i = 7$ for $645.15 < T_{\mathrm{sat}} < 673.15$ K , and
$i = 8$ for $673.15 \leq T_{\mathrm{sat}} \leq 713.94025779311$ K .

Table A-3. lists the constants *ALE(i)*, *BLE(i)*, *CLE(i)*, and *DLE(i)* for the given temperature ranges.

TABLE A-3.
Saturated Liquid Internal Energy Constants

i	*ALE*(*i*)	*BLE*(*i*)	*CLE*(*i*)	*DLE*(*i*)
1	–1.1436668993222E+06	4.1868000000000E+03	0.	0.
2	8.0957542810383E+06	–5.7008855264640E+04	1.3443632119671E+02	–9.7879669155946E–02
3	–1.9373932457007E+06	9.7492797103351E+03	–1.3299615999876E+0l	1.0879999999922E–02
4	–5.3245827703670E+06	2.9179372045334E+04	–5.0452192000967E+0l	3.4560000000583E–02
5	–6.3583523639930E+07	3.2873715263424E+05	–5.6371182000208E+02	3.2760000000116E–01
6	–6.6239163195929E+09	3.1605562257270E+07	–5.0263730855532E+04	2.6650075114186E+01
7	–5.4759091078157E+09	2.4635618770681E+07	–3.6931079506707E+04	1.8454719393083E+01
8	–7.1536399439453E+07	3.0560801674842E+05	–4.2424553999630E+02	1.9719999999823E–01

A.1.1.4. Saturated Steam Enthalpy. Two main pressure regions exist when the enthalpy of steam at saturation is calculated. T_{sv} in this section denotes the saturation temperature corresponding to the partial pressure of steam, p_v.

A.1.1.4.1. 1.0 Pa $\le p_v \le 0.5 \times 10^6$ Pa. Within this pressure region, the enthalpy of saturated steam at temperature T_{sv} is approximated as the sum of the enthalpy of saturated liquid water at the reference temperature of 273.15 K, plus the enthalpy necessary to raise the saturated liquid water temperature from 273.15 K to T_{sv}, plus the latent heat of vaporization needed to convert saturated liquid water at T_{sv} to saturated steam at T_{sv}. If we define the enthalpy of saturated water at 273.16 K to be exactly zero, this gives

$$h_{vs} = 4186.8(273.15 - 273.16) + 4186.8\,(T_{sv} - 273.15) + h_{lvs} \quad ,$$

where h_{lvs} is evaluated at T_{sv} in subroutine HEV as described earlier in Section A.1.1.1. The derivative with respect to the partial pressure of the vapor, p_v, becomes

$$\frac{\mathrm{d}h_{vs}}{\mathrm{d}p_v} = 4186.8\,\frac{\mathrm{d}T_{sv}}{\mathrm{d}p_v} + \frac{\mathrm{d}h_{lvs}}{\mathrm{d}p_v} = (4186.8 - 2470.2120)\,\frac{\mathrm{d}T_{sv}}{\mathrm{d}p_v} \quad .$$

A.1.1.4.2. 0.5 $\times 10^6$ Pa < $p_v \le 45.0 \times 10^6$ Pa.

$$h_{vs} = e_{vs}\gamma_s$$

and

$$\frac{dh_{vs}}{dp_v} = \gamma_s \frac{de_{vs}}{dp_v} + e_{vs} \frac{d\gamma_s}{dp_v} \quad ,$$

where

$$\gamma_s = AVG(i) + BVG(i)\, p_v + CVG(i)\, p_v^2 + DVG(i)\, p_v^3 \ ,$$

$$\frac{d\gamma_s}{dp_v} = BVG(i) + 2\, CVG(i)\, p_v + 3\, DVG(i)\, p_v^2 \quad ,$$

and

$i = 1$ for $0.5 \times 10^6 < p_v \leq 2.0 \times 10^6$ Pa ,
$i = 2$ for $2.0 \times 10^6 < p_v < 5.0 \times 10^6$ Pa ,
$i = 3$ for $5.0 \times 10^6 \leq p_v < 10.0 \times 10^6$ Pa ,
$i = 4$ for $10.0 \times 10^6 \leq p_v < 15.0 \times 10^6$ Pa ,
$i = 5$ for $15.0 \times 10^6 \leq p_v < 20.0 \times 10^6$ Pa ,
$i = 6$ for $20.0 \times 10^6 \leq p_v \leq 22.0 \times 10^6$ Pa ,
$i = 7$ for $22.0 \times 10^6 < p_v < 25.0 \times 10^6$ Pa ,
$i = 8$ for $25.0 \times 10^6 \leq p_v < 30.0 \times 10^6$ Pa ,
$i = 9$ for $30.0 \times 10^6 \leq p_v < 35.0 \times 10^6$ Pa ,
$i = 10$ for $35.0 \times 10^6 \leq p_v < 40.0 \times 10^6$ Pa , and
$i = 11$ for $40.0 \times 10^6 \leq p_v \leq 45.0 \times 10^6$ Pa .

Table A-4. lists the constants *AVG(i)*, *BVG(i)*, *CVG(i)*, and *DVG(i)* for the given pressure ranges.

Functions h_{vs}/dp_v and $d\gamma_s/dp_v$ are both discontinuous near the critical point at junction point $p_v = 22.0 \times 10^6$ Pa. At this point, the left-side value of h_{vs}/dp_v is 4.6073×10^{-3} and the right-side value is -5.1790×10^{-6} for a fractional change here of 1.0011. The left-side value of $d\gamma_s/dp_v$ is 6.6694×10^{-12} and the right-side value is -2.3541×10^{-2} giving a fractional change at this junction point of 1.3530.

TABLE A-4.
Saturated Steam Enthalpy Constants

i	*AVG*(*i*)	*BVG*(*i*)	*CVG*(*i*)	*DVG*(*i*)
1	1.0666845123419E+00	2.8310838172462E–08	–2.1151097428905E–14	4.7404001285964E–21
2	1.0735412407407E+00	2.6518055555551E–09	–6.3461111111128E–16	3.9824074074117E–23
3	1.0777730000000E+00	–2.4300000008021E–11	–7.1979999998378E–17	4.8799999990422E–25
4	1.0851130000007E+00	–1.9307000001824E–09	8.9100000014826E–17	–3.8960000003946E–24
5	1.1639800000015E+00	–1.6338350000254E–08	9.5856000001448E–16	–2.1194000000274E–23
6	3.8898867259868E+00	–3.8595945559811E–07	1.7476370114910E–14	–2.6377008249858E–22
7	2.7168710524682E+00	–2.2832718294604E–07	1.0417331983836E–14	–1.5842822199773E–22
8	3.9749829999964E+00	–3.0657099999960E–07	1.0637899999985E–14	–1.2257999999981E–22
9	1.2946929999997E+00	–2.4834999999979E–08	7.8979999999944E–16	–8.0799999999948E–24
10	1.0590519999963E+00	–2.4615999996941E–09	8.8399999991573E–17	–8.0799999992269E–25
11	1.1430199999838E+00	–7.7095999988588E–09	1.9335999997331E–16	–1.4639999997924E–24

A.1.1.5. Saturated Liquid Enthalpy. From the definition of enthalpy,

$$h_{ls} = e_{ls} + \frac{p}{\rho_{ls}}$$

and

$$\frac{dh_{ls}}{dp} = \frac{de_{ls}}{dT_{sat}} \frac{dT_{sat}}{dp} + \frac{1}{\rho_{ls}} - \frac{p}{\rho_{ls}^2} \left[\left(\frac{\partial \rho_{ls}}{\partial p} \right)_{T_{sat}} + \left(\frac{\partial \rho_{ls}}{\partial T_{sat}} \right)_{p} \frac{dT_{sat}}{dp} \right] ,$$

where e_{ls} and its derivative are evaluated as shown in Section A.1.1.3., and where ρ_{ls} and its derivatives are evaluated using the equations in Section A.1.2.2. with T_l equal to T_{sat}.

A.1.1.6. Heat Capacity of Saturated Steam at Constant Pressure. Although the heat capacity of saturated steam is not an output variable of THERMO, subsequent steam property calculations require its definition. In this section, T_{sv} denotes the saturation temperature corresponding to the partial pressure of steam, p_v. The heat capacity of saturated steam is

$$c_{pvs} = ACP(i) + BCP(i)\, T_{sv} + CCP(i)\, T_{sv}^2 + DCP(i)\, T_{sv}^3$$

and

$$\frac{dc_{pvs}}{dp_v} = \left[BCP(i) + 2\,CCP(i)\,T_{sv} + 3\,DCP(i)\,T_{sv}^2\right]\frac{dT_{sv}}{dp_v} \quad ,$$

where

$i = 1$ for $273.15 \le T_{sv} < 323.15$ K ,
$i = 2$ for $323.15 \le T_{sv} < 373.15$ K ,
$i = 3$ for $373.15 \le T_{sv} < 423.15$ K ,
$i = 4$ for $423.15 \le T_{sv} < 473.15$ K ,
$i = 5$ for $473.15 \le T_{sv} < 523.15$ K ,
$i = 6$ for $523.15 \le T_{sv} < 573.15$ K ,
$i = 7$ for $573.15 \le T_{sv} < 623.15$ K ,
$i = 8$ for $623.15 \le T_{sv} < 647.3$ K ,
$i = 9$ for $647.3 < T_{sv} < 673.15$ K , and
$i = 10$ for $673.15 \le T_{sv} < 713.94025779311$ K .

Table A-5. lists the constants *ACP(i), BCP(i), CCP(i), and DCP*(*i*) for the given temperature ranges.

TABLE A-5.
Saturated Steam Heat Capacity Constants

i	***ACP*(*i*)**	***BCP*(*i*)**	***CCP*(*i*)**	***DCP*(*i*)**
1	–7.9678485852270E+02	2.8187658437259E+01	–1.0180624999920E–01	1.2499999999912E–04
2	–9.7082632232795E+02	2.8324981030402E+01	–9.7656200001157E–02	1.1600000000110E–04
3	–1.6649701690752E+03	3.3159363169596E+01	–1.0861179999898E–01	1.2399999999915E–04
4	–6.1420486441088E+03	6.3630987079837E+01	–1.7762319999965E–01	1.7599999999975E–04
5	–8.2289951961933E+04	5.3773958896061E+02	–1.1612491999609E+00	8.5599999997375E–04
6	–6.5842104212475E+05	3.7934294783212E+03	–7.2924928000022E+00	4.7040000000014E–03
7	3.4561620732510E+05	–2.2129380791446E+02	–2.4524285999925E+00	3.1479999999958E–03
8	1.9798369474597E+06	–1.4782551342826E+04	3.1656481897637E+01	–2.0843356864237E–02
9	–9.6249385211359E+07	4.3633668884423E+05	–6.5887615106930E+02	3.3146147264269E–01
10	–1.1074934463333E+07	4.8073794630970E+04	–6.9212173247881E+0l	3.3091693999800E–02

A.1.2. Liquid Properties

A.1.2.1. Internal Energy. Given a liquid at some temperature, T_l, and some pressure, p, the liquid internal energy associated with that state is calculated by beginning with the internal energy of the saturated liquid state described by T_l and PSL, where PSL is the saturation pressure corresponding to T_l, and adding an additional term that represents the change in internal energy from the state (T_l, PSL) to the state T_l, p. That is,

$$e_l(T_l, p) = e_{ls}(T_l, \text{PSL}) + \text{ELP} \quad .$$

The additional term, ELP, which represents the change in energy required to move along the isotherm at T_l between two different pressure values, namely PSL and p, is represented as

$$\text{ELP} = (p - \text{PSL}) \left(\frac{\partial e_l}{\partial p} \right)_{T_l} \quad ,$$

where

$$\left(\frac{\partial e_l}{\partial p} \right)_{T_l} = -8.329595 \times 10^{-4} \left[1 - \exp\left(1.450382 \times 10^{-6} \cdot \text{PSL}\right) \right] - 2.245825 \times 10^{-17} \cdot \text{PSL}^2 \quad .$$

Therefore, the partial derivative with respect to T_l of the internal energy is calculated as

$$\left(\frac{\partial e_l}{\partial T_l} \right)_p = \frac{\mathrm{d}e_{ls}}{\mathrm{d}T_{sat}} + \text{ERT} \quad ,$$

where

$$\text{ERT} = \left[\frac{\partial}{\partial T_l} (\text{ELP}) \right]_p = \left\{ -8.329595 \times 10^{-4} \left[-1 + \exp\left(-1.450382 \times 10^{-6} \cdot \text{PSL} \right) \times \left[1 + 1.450382 \times 10^{-6} \, (p - \text{PSL}) \right] \right] - 2.245825 \times 10^{-17} \left(2p \cdot \text{PSL} - 3 \, \text{PSL}^2 \right) \right\} \frac{\mathrm{d}}{\mathrm{d}T_l} (\text{PSL}) \quad ,$$

and $\mathrm{d}e_{ls} / \mathrm{d}T_{sat}$ is calculated as in Section A.1.1.3.

A.1.2.2. Density.

A.1.2.2.1. Initial Calculation. Given the pressure p and temperature T_l of liquid water, Tait's equation-of-state in the form

$$\frac{v(0,T_l) - v(p,T_l)}{v(0,T_l)} = \frac{1}{n} \ln\left[1 + \frac{p}{B(T_l)}\right]$$

is used to determine the liquid density and its partial derivatives, where v is the specific volume of the liquid. The constant n is quoted in work by Richardson, Arens, and Haverson (Ref. A-4.) to be 7.146. The terms $v(0, T_l)$ and $B(T_l)$ are third-order polynomials of liquid temperature fitted to steam-table data, such that

$$v(0,T_l) = AVO(i) + BVO(i)\,T_l + CVO(i)\,T_l^2 + DVO(i)\,T_l^3$$

and

$$B(T_l) = AFN(i) + BFN(i)\,T_l + CFN(i)\,T_l^2 + DFN(i)\,T_l^3 ,$$

where

$i = 1$ for $273.15 \le T_l < 373.15$ K ,
$i = 2$ for $373.15 \le T_l < 473.15$ K ,
$i = 3$ for $473.15 \le T_l < 573.15$ K ,
$i = 4$ for $573.15 \le T_l < 603.15$ K ,
$i = 5$ for $603.15 \le T_l < 613.15$ K ,
$i = 6$ for $613.15 \le T_l < 623.15$ K ,
$i = 7$ for $623.15 \le T_l < 633.15$ K ,
$i = 8$ for $633.15 \le T_l < 643.15$ K ,
$i = 9$ for $643.15 \le T_l < 653.15$ K ,
$i = 10$ for $653.15 \le T_l < 663.15$ K ,
$i = 11$ for $663.15 \le T_l < 673.15$ K , and
$i = 12$ for $673.15 \le T_l \le 713.94025779311$ K .

Table A-6. lists the constants $AVO(i)$, $BVO(i)$, $CVO(i)$, $DVO(i)$, $AFN(i)$, $BFN(i)$, $CFN(i)$, and $DFN(i)$ for the given temperature ranges.

TABLE A-6.
Liquid Density Constants

i	*AVO*(*i*)	*BVO*(*i*)	*CVO*(*i*)	*DVO*(*i*)
1	1.7057666777468E–03	–6.0320895569365E–06	1.5944423965594E–08	–1.2149418561177E–11
2	5.2145931517155E–04	3.5189228252915E–06	–9.7304881862624E–09	1.0856688130631E–11
3	–1.4931865836934E–02	9.7931556400429E–05	–2.0172817692512E–07	1.4080475270259E–10
4	–4.9334201381918E–01	2.5928571576499E–03	–4.5387107397840E–06	2.6537936475365E–09
5	–3.4558955902321E+00	1.7351793841884E–02	–2.9047483637289E–05	1.6220227777320E–08
6	–1. 1952528427292E+01	5.8904962031842E–02	–9.6786687447220E–05	5.3029284583415E–08
7	–3.7446629978341E+0l	1.8173474403006E–01	–2.9404991620713E–04	1.5863005350824E–07
8	–3.9713284923576E+02	1.8801824705202E+00	–2.9673900150051E–03	1.5612171739106E–06
9	–2.3142714272157E+03	1.0710216457395E+01	–1.6521763202064E–02	8.4955209566212E–06
10	2.0481569977849E+03	–9.3452783115489E+00	1.4212077056589E–02	–7.2037202704367E–06
11	–7.3864713248117E+01	3.3144939132191E–01	–4.9608715522591E–04	2.4771793009809E–07
12	–2.1891320674084E+01	9.6758467414310E–02	–1.4289074953436E–04	7.0567217785700E–08

i	*AFN*(*i*)	*BFN*(*i*)	*CFN*(*i*)	*DFN*(*i*)
1	–4.2486354144244E+09	3.7516769853867E+07	–1.0064945851796E+05	8.7507285129715E+01
2	–2.7936308563236E+08	5.5663179995300E+06	–1.4921749894688E+04	1.0834095198280E+01
3	–1.1761210016041E+08	4.3832221802974E+06	–1.2088373365747E+04	8.6034520917150E+00
4	–4.5415129389018E+09	2.7368608704680E+07	–5.1 894794477625E+04	3.1581281016141E+01
5	–4.0104325667716E+10	2.0292575433752E+08	–3.4075971373732E+05	1.9000660267975E+02
6	–6.0173879922257E+10	2.9984925450490E+08	–4.9675963282729E+05	2.7368658401451E+02
7	2.0678826351719E+10	–8.9503807129603E+07	1.2822787819385E+05	–6.0722291833340E+01
8	8.3793557728900E+10	–3.8997180562867E+08	6.0502628698976E+05	–3.1291965911464E+02
9	9.2402374347985E+10	–4.2674923965292E+08	6.5695613829284E+05	–3.3711122197289E+02
10	–2.7547713637194E+10	1.2580004134443E+08	–1.9147491048695E+05	9.7136148925404E+01
11	6.8608195287374E+08	–3.0636028439513E+06	4.5613625244005E+03	–2.2642074876391E+00
12	4.3458430609231E+07	–1.8379937116289E+05	2.5971646178490E+02	–1.2244044950391E–01

This allows the density, ρ_l, to be calculated as

$$\rho_l = \frac{1}{v(0,T_l)\left\{1.0 - \frac{1}{7.146}\ln\left[1.0+\frac{p}{B(T_l)}\right]\right\}} \quad .$$

Therefore,

$$\left(\frac{\partial\rho_l}{\partial p}\right)_{T_l} = \frac{\rho_l^2\, v(0,T_l)}{7.146\ [p\ + B(T_l)]}$$

and

$$\left(\frac{\partial\rho_l}{\partial T_l}\right)_p = -\rho_l \frac{v'(0,T_l)}{v(0,T_l)} - B'(T_l)\ \frac{p}{B(T_l)}\left(\frac{\partial\rho_l}{\partial p}\right)_{T_l} \quad ,$$

where

$$v'(0,T_l) = BVO(i) + 2\ CVO(i)\ T_l + 3\ DVO(i)\ T_l^2$$

and

$$B'(T_l) = BFN(i) + 2\ CFN(i)\ T_l + 3\ DFN(i)\ T_l^2 \quad .$$

The polynomial constants for $v'(0,T_l)$ and $B'(T_l)$ are the same as for $v(0,T_l)$ and $B(T_l)$ and are given in Table A-6.

A.1.2.2.2. Residual Void Correction.[1] After evaluation in the above section, ρ_l and its derivatives are corrected to reflect a residual void fraction. In the following, the values calculated above are denoted by a tilde (˜).

A.1.2.2.2.1. $p \geq 4.0 \times 10^5$ Pa.

$$\left(\frac{\partial\rho_l}{\partial T_l}\right)_p = \left(1-\frac{1000}{p}\right)\left(\frac{\partial\tilde{\rho}_l}{\partial T_l}\right)_p \quad ,$$

$$\left(\frac{\partial\rho_l}{\partial p}\right)_{T_l} = \left(1-\frac{1000}{p}\right)\left(\frac{\partial\tilde{\rho}_l}{\partial p}\right)_{T_l} + \frac{1000\tilde{\rho}_l}{p^2} \quad ,$$

1. This artificial compressibility of liquid is presently turned off in the code. It can be turned on by setting the flag NOAC to 0 in subroutine RHOLIQ if it is needed.

and

$$\rho_l = \left(1 - \frac{1000}{p}\right)\tilde{\rho}_l \ .$$

A.1.2.2.2.2. $p < 4.0 \times 10^5$ Pa.

$$\left(\frac{\partial \rho_l}{\partial T_l}\right)_p = (0.995 + 6.25 \times 10^{-9} p)\left(\frac{\partial \tilde{\rho}_l}{\partial T_l}\right)_p \quad ,$$

$$\left(\frac{\partial \rho_l}{\partial p}\right)_{T_l} = (0.995 + 6.25 \times 10^{-9} p)\left(\frac{\partial \tilde{\rho}_l}{\partial p}\right)_{T_l} + 6.25 \times 10^{-9}\ \tilde{\rho}_l \quad ,$$

and

$$\rho_l = (0.995 + 6.25 \times 10^{-9} p)\ \tilde{\rho}_l \quad .$$

A.1.3. Steam Properties

A.1.3.1. Superheated Vapor. $(T_g - T_{sv}) > 0$, where T_{sv} is the saturation temperature corresponding to the partial pressure of the vapor, p_v, throughout this section. The constant-pressure specific heat of steam at temperature T_g is approximated as

$$c_{pv} = \left(\frac{\partial h_v}{\partial T_v}\right)_{p_v} = \frac{c_{pv,\text{ideal}}}{2}\left[1 + \frac{T_g}{\left(T_g^2 - \beta\right)^{\frac{1}{2}}}\right] \quad ,$$

where

$$\beta = T_{sv}^2\left[1 - \frac{1}{\left(\frac{2\, c_{pvs}}{c_{pv,\text{ideal}}} - 1\right)^2}\right] \quad .$$

The term c_{pvs} is calculated as defined in Section A.1.1.6., and $c_{pv,\text{ideal}}$ is defined by ideal gas behavior, such that

$$c_{pv,\text{ideal}} = \frac{R_v \gamma_{\text{ideal}}}{\gamma_{\text{ideal}} - 1} \quad ,$$

where R_v is the gas constant for steam (Table A-1.) and γ_{ideal} is the ratio of ideal specific heats for steam (Table A-1.).

Integrating the equation for c_{pv} along a constant p_v line gives

$$h_v = h_{vs} + \frac{c_{pv,\text{ideal}}}{2}\left[\left(T_g - T_{sv}\right) + \left(T_g^2 - \beta\right)^{\frac{1}{2}} - \frac{T_{sv}}{\left(\frac{2c_{pvs}}{c_{pv,\text{ideal}}} - 1\right)}\right] .$$

The internal energy of vapor is therefore calculated as

$$e_v = e_{vs} + \frac{c_{pv,\text{ideal}}}{2}\left[\left(T_g - T_{sv}\right) + \left(T_g^2 - \beta\right)^{\frac{1}{2}} - \frac{T_{sv}}{\left(\frac{2c_{pvs}}{c_{pv,\text{ideal}}} - 1\right)}\right] - p_v\left(\frac{1}{\rho_v} - \frac{1}{\rho_{vs}}\right) .$$

The definitions of enthalpy and internal energy allow the density of the water vapor to be written, such that

$$\rho_v = \frac{p_v}{h_v - e_v} = \frac{p_v}{\left[h_{vs} + c_{pv,\text{ideal}}\left(T_g - T_{sv}\right)\right] - \left[e_{vs} + c_{vv,\text{ideal}}\left(T_g - T_{sv}\right)\right]}$$

$$= \frac{p_v}{(h_{vs} - e_{vs}) + (\gamma_{\text{ideal}} - 1)(e_v - e_{vs})} ,$$

where $c_{vv,\text{ideal}}$ is defined in Table A-1.

A.1.3.1.1. Internal Energy. Substitution of ρ_v and ρ_{vs}, as defined by the preceding equation, into the equation for the internal energy of the vapor gives the following equations.

For $p_v \leq 1.9 \times 10^7$ Pa,

$$e_v = e_{vs} + \frac{c_{vv,\text{ideal}}}{2}\left[(T_g - T_{sv}) + (T_g^2 - \beta)^{\frac{1}{2}} - \frac{T_{sv}}{\left(\frac{2c_{pvs}}{c_{pv,\text{ideal}}} - 1\right)}\right] ,$$

where again $c_{vv,\text{ideal}}$ is the constant-volume specific heat for steam, as defined by ideal gas behavior (Table A-1.). Therefore,

$$\left(\frac{\partial e_v}{\partial T_g}\right)_{p_v} = \frac{c_{vv,\text{ideal}}}{\left(1 - \frac{\beta}{\kappa^2}\right)}$$

and

$$\left(\frac{\partial e_v}{\partial p_v}\right)_{T_g} = -\frac{1}{2}\left(\frac{\partial e_v}{\partial T_g}\right)_{p_v}\left[\left(1-\frac{\beta}{\kappa^2}\right)\kappa'_p + \frac{1}{\kappa}\frac{\mathrm{d}\beta}{\mathrm{d}p_v}\right] \quad ,$$

where

$$\kappa = \frac{2}{c_{vv,\mathrm{ideal}}}(e_v - e_{vs}) + T_{sv}\left[1 + \frac{1}{\frac{2c_{pvs}}{c_{pv,\mathrm{ideal}}} - 1}\right] \quad ,$$

and

$$\kappa'_p = \left(\frac{\partial \kappa}{\partial p_v}\right)_{T_g} = -\frac{2}{c_{vv,\mathrm{ideal}}}\frac{\mathrm{d}e_{vs}}{\mathrm{d}p_v} + \left[1 + \frac{1}{\left(\frac{2c_{pvs}}{c_{pv,\mathrm{ideal}}} - 1\right)}\right]\frac{\mathrm{d}T_{sv}}{\mathrm{d}p_v}$$
$$- \frac{2}{c_{pv,\mathrm{ideal}}}\left[\frac{T_{sv}}{\left(\frac{2c_{pvs}}{c_{pv,\mathrm{ideal}}} - 1\right)^2}\right]\frac{\mathrm{d}c_{pvs}}{\mathrm{d}p_v} \quad ,$$

and

$$\frac{\mathrm{d}\beta}{\mathrm{d}p_v} = \frac{2}{T_{sv}}\left\{\beta\frac{\mathrm{d}T_{sv}}{\mathrm{d}p_v} + \frac{2}{c_{pv,\mathrm{ideal}}}\left[\frac{T_{sv}}{\left(\frac{2c_{pvs}}{c_{pv,\mathrm{ideal}}} - 1\right)}\right]^3\frac{\mathrm{d}c_{pvs}}{\mathrm{d}p_v}\right\} \quad .$$

For $p_v \geq 2.0 \times 10^7$ Pa,

$$e_v = e_{vs} + \frac{c_{pv,\,\mathrm{ideal}}}{2\gamma_s}\left[\frac{(T_g - T_{sv}) + (T_g^2 - \beta)^{1/2} - T_{sv}}{\left(\frac{2c_{pvs}}{c_{pv,\,\mathrm{ideal}}} - 1\right)}\right],$$

$$\left(\frac{\partial e_v}{\partial T_g}\right)_{p_v} = \frac{c_{pv,\mathrm{ideal}}}{2\gamma_s}\left(1 + \frac{T_g}{\left(T_g^2 - \beta\right)^{\frac{1}{2}}}\right),$$

and

$$\left(\frac{\partial e_v}{\partial p_v}\right)_{T_g} = \frac{\mathrm{d}e_{vs}}{\mathrm{d}p_v} - \frac{e_v - e_{vs}}{\gamma_s}\frac{\mathrm{d}\gamma_s}{\mathrm{d}p_v} + \frac{c_{pv,\mathrm{ideal}}}{2\gamma_s} \cdot \left[\left(-\frac{\mathrm{d}T_{sv}}{\mathrm{d}p_v}\right) - \frac{1}{2}\frac{\mathrm{d}\beta}{\mathrm{d}p_v}\frac{1}{\left(T_g^2 - \beta\right)^{\frac{1}{2}}}\right.$$

$$\left. - \frac{\mathrm{d}T_{sv}}{\mathrm{d}p_v} \cdot \left(\frac{1}{\frac{2c_{pvs}}{c_{pv,\mathrm{ideal}}} - 1}\right) + \frac{2}{c_{pv,\mathrm{ideal}}}\left[\frac{T_{sv}}{\left(\frac{2c_{pvs}}{c_{pv,\mathrm{ideal}}} - 1\right)^2}\right]\frac{\mathrm{d}c_{pvs}}{\mathrm{d}p_v}\right] \quad ,$$

where

$$\frac{\partial \beta}{\partial p_v} = \frac{2}{T_{sv}}\left\{\beta\frac{\mathrm{d}T_{sv}}{\mathrm{d}p_v} + \frac{2}{c_{pv,\mathrm{ideal}}}\left[\frac{T_{sv}}{\left(\frac{2c_{pvs}}{c_{pv,\mathrm{ideal}}} - 1\right)}\right]^3\frac{\mathrm{d}c_{pvs}}{\mathrm{d}p_v}\right\} \quad .$$

For 1.9×10^7 Pa $< p_v <$ 2.0×10^7 Pa, the values of e_v and its derivatives are calculated by interpolating between the values of the two curve fits.

A.1.3.1.2. Density. If $p_v \leq 1.9 \times 10^7$ Pa, the vapor density is calculated as

$$\rho_v = \frac{p_v}{(\gamma_s - 1)e_{vs} + (\gamma_{\mathrm{ideal}} - 1)(e_v - e_{vs})} \quad .$$

Therefore,

$$\left(\frac{\partial \rho_v}{\partial T_g}\right)_{p_v} = -\left(\frac{\partial e_v}{\partial T_g}\right)_{p_v}\left[\frac{(\gamma_{\mathrm{ideal}} - 1)\rho_v}{(\gamma_s - 1)e_{vs} + (\gamma_{\mathrm{ideal}} - 1)(e_v - e_{vs})}\right] \quad ,$$

and

$$\left(\frac{\partial \rho_v}{\partial p_v}\right)_{T_g} = \left\{(1 - \rho_v)\left[e_{vs}\frac{\mathrm{d}\gamma_s}{\mathrm{d}p_v} + (\gamma_s - \gamma_{\mathrm{ideal}})\frac{\mathrm{d}e_{vs}}{\mathrm{d}p_v}\right]\right.$$

$$\left. \times \left[\frac{1}{(\gamma_s - 1)e_{vs} + (\gamma_{\mathrm{ideal}} - 1)(e_v - e_{vs})}\right]\right\} + \left(\frac{\partial \rho_v}{\partial e_v}\right)_{p_v}\left(\frac{\partial e_v}{\partial p_v}\right)_{T_g} \quad ,$$

where

$$\left(\frac{\partial \rho_v}{\partial e_v}\right)_{p_v} = -\frac{(\gamma_{\text{ideal}} - 1)\rho_v}{\left[(\gamma_s - 1)e_{vs} + (\gamma_{\text{ideal}} - 1)(e_v - e_{vs})\right]} \quad .$$

If $p_v \geq 2.0 \times 10^7$ Pa, the vapor density is calculated as

$$\rho_v = \frac{p_v}{(\gamma_s - 1)e_v} \quad .$$

Therefore,

$$\left(\frac{\partial \rho_v}{\partial T_g}\right)_{p_v} = \left(\frac{\partial \rho_v}{\partial e_v}\right)_{p_v} \left(\frac{\partial e_v}{\partial T_g}\right)_{p_v} \quad ,$$

and

$$\left(\frac{\partial \rho_v}{\partial p_v}\right)_{T_g} = \left(1 - \rho_v e_v \frac{d\gamma_s}{dp_v}\right)\frac{1}{(\gamma_s - 1)e_v} + \left(\frac{\partial \rho_v}{\partial e_v}\right)_{p_v} \left(\frac{\partial e_v}{\partial p_v}\right)_{T_g} \quad ,$$

where

$$\left(\frac{\partial \rho_v}{\partial e_v}\right)_{p_v} = -\frac{\rho_v}{e_v} \quad .$$

If $1.9 \times 10^7 < p_v < 2.0 \times 10^7$ Pa, the vapor density and its derivatives are calculated by linearly interpolating between the values of the two curve fits.

Minimum and maximum limits are placed on the calculated values of the density, and its partial derivatives. In low-pressure regions where the above equations may predict a negative density, the density and its derivatives are recalculated based on ideal gas behavior. If ρ_v is less than zero, the vapor density and its derivatives are superseded by

$$\rho_v = \frac{p_v}{R_v T_g} \quad ,$$

$$\left(\frac{\partial \rho_v}{\partial T_v}\right)_{p_v} = -\frac{\rho_v}{T_g} \quad ,$$

and

$$\left(\frac{\partial \rho_v}{\partial p_v}\right)_{T_g} = \frac{\rho_v}{p_g} \quad .$$

Near the critical point, it is necessary to impose the following limit on the density ratio

$$\frac{\rho_v}{\rho_l} \leq 0.999 \quad ,$$

to avoid singularities when calculating certain parameters. If the calculated value of ρ_v exceeds 0.999 ρ_l, the vapor density and its derivatives are superseded by

$$\rho_v = 0.999\rho_l \ ,$$

$$\left(\frac{\partial \rho_v}{\partial T_g}\right)_{p_v} = 0.999\left(\frac{\partial \rho_l}{\partial T_l}\right)_p \ ,$$

and

$$\left(\frac{\partial \rho_v}{\partial p_v}\right)_{T_g} = 0.999 \left(\frac{\partial \rho_l}{\partial p}\right)_{T_l} \quad .$$

A.1.3.1.3. Enthalpy. Subroutine FPROP calculates the enthalpy of the superheated vapor using the definition of enthalpy, such that

$$h_v = e_v + \frac{p_v}{\rho_v} \quad ,$$

where e_v and ρ_v are calculated according to Sections A.1.3.1.1. and A.1.3.1.2., respectively.

A.1.3.2. Subcooled Vapor. $(T_g - T_{sv}) \leq 0$, where T_{sv} refers to the saturation temperature corresponding to the partial pressure of the vapor, p_v, throughout this section.

A.1.3.2.1. Internal Energy.

$$e_v = e_{vs} + (T_g - T_{sv}) \frac{c_{pvs}}{\gamma_{\text{ideal}}} \quad ,$$

$$\left(\frac{\partial e_v}{\partial T_g}\right)_{p_v} = \frac{c_{pvs}}{\gamma_{\text{ideal}}} \quad ,$$

and

$$\left(\frac{\partial e_v}{\partial p_v}\right)_{T_g} = \frac{de_{vs}}{\mathrm{d}p_v} + \left(\frac{e_v - e_{vs}}{c_{pvs}}\right)\frac{\mathrm{d}c_{pvs}}{\mathrm{d}p_v} - \frac{\partial e_v}{\partial T_g}\frac{\mathrm{d}T_{sv}}{\mathrm{d}p_v} \quad .$$

A.1.3.2.2. Density. The method used to determine the subcooled vapor density, and its derivatives for all pressure ranges is identical to the one outlined in the case of superheated vapor for $p_v \leq 1.9 \times 10^7$ Pa in Section A.1.3.1.2.

A.1.3.2.3. Enthalpy. Subroutine FPROP calculates the enthalpy of the subcooled vapor using the definition of enthalpy, such that

$$h_v = e_v + \frac{p_v}{\rho_v} \quad ,$$

where e_v and ρ_v are calculated according to Sections A.1.3.2.1. and A.1.3.2.2., respectively.

A.1.4. Noncondensable Gas (Air, Hydrogen, or Helium) Properties

Additional information on the noncondensable-gas thermodynamic properties is provided in Appendix K.

A.1.4.1. Internal Energy.

$$e_a = c_{va}T_g \quad ,$$

$$\left(\frac{\partial e_a}{\partial T_g}\right)_{p_a} = c_{va} \quad ,$$

and

$$\left(\frac{\partial e_a}{\partial p_a}\right)_{T_g} = 0.0 \quad .$$

The constant-volume specific heat, c_{va}, is calculated from

$$c_{va} = c_{pa} - R_a \quad ,$$

where c_{pa} is determined as described in Section A.2.2.3. for noncondensable gases and where R_a is the gas constant for the noncondensable gas (Table A-1.).

A.1.4.2. Density.

$$\rho_a = \frac{p_a}{R_a T_g} \ ,$$

$$\left(\frac{\partial \rho_a}{\partial p_a}\right)_{T_g} = \frac{1}{R_a T_g} \quad ,$$

and

$$\left(\frac{\partial \rho_a}{\partial T_g}\right)_{p_a} = -R_a \rho_a \left(\frac{\partial \rho_a}{\partial p_a}\right)_{T_g} \quad .$$

A.1.4.3. Enthalpy. Subroutine FPROP calculates the enthalpy of the noncondensable gas, such that

$$h_a = e_a + \frac{p_a}{\rho_a} \quad ,$$

where e_a and ρ_a are calculated as described in the two previous Sections, A.1.4.1. and A.1.4.2., respectively.

A.1.5. Steam-Gas Mixture Properties

A.1.5.1. Internal Energy. Subroutine THERMO calculates the steam-air, steam-hydrogen, or steam-helium mixture internal energy, such that

$$e_m = \frac{e_v \rho_v + e_a \rho_a}{\rho_v + \rho_a} \quad ,$$

where e_v is calculated according to Sections A.1.3.1.1. or A.1.3.2.1., depending on whether the vapor is superheated or subcooled, e_a is calculated as described in Section A.1.4.1., ρ_v is the water vapor density as calculated in Section A.1.3.1.2., and ρ_a is the noncondensable-gas density as calculated in Section A.1.4.2.

A.1.5.2. Density. Subroutine THERMO calculates the steam-air, steam-hydrogen, or steam-helium mixture density, such that

$$\rho_m = \rho_v + \rho_a \quad ,$$

where ρ_v is the water vapor density as calculated in Section A.1.3.1.2. and ρ_a is the noncondensable-gas density as calculated in Section A.1.4.2.

A.1.5.3. Enthalpy. Subroutine FPROP calculates the steam-air, steam-hydrogen, or steam-helium mixture enthalpy, such that

$$\begin{aligned} h_m &= \frac{h_v\rho_v + h_a\rho_a}{\rho_v + \rho_a} \\ &= e_m + \frac{p}{\rho_m} \quad , \end{aligned}$$

where e_m is calculated according to Section A.1.5.1., ρ_m is calculated as described in Section A.1.5.2., and p is the total pressure.

A.2. Transport Properties

Subroutine FPROP is used to obtain transport properties for liquid- and vapor-phase water, noncondensable gases, and steam-gas mixtures. The input variables for this subroutine are the saturation temperature corresponding to the total pressure; the internal energies, densities, and temperatures of the liquid and gas phases where the gas is either steam, a noncondensable gas, or a steam-gas mixture; the total pressure; and the partial pressure of the noncondensable gas, if any is present. The output transport variables include the latent heat of vaporization, the constant-pressure specific heats, viscosities, and thermal conductivities of the liquid and gas phases, and the surface tension of the liquid.

The transport property calls are function calls within the FPROP subroutine. Function CPLL calculates the constant-pressure specific heat of the liquid, while function CPVV1 determines the value of the constant-pressure specific heat of the steam, noncondensable gas, or steam-gas mixture. Function THCL evaluates the liquid thermal conductivity, and function THCV calculates the steam, noncondensable-gas, or steam-gas mixture thermal conductivity. Similarly, functions VISCL and VISCV determine viscosity values. Finally, function SIGMA calculates the surface tension of the liquid water.

The polynomial equation fits for the transport properties used in FPROP are described in the remainder of this section. Values of the constants are given in Tables A-7. through A-11. Additional information on the noncondensable-gas transport properties is provided in Appendix K.

A.2.1. Latent Heat of Vaporization

Subroutine FPROP calculates the latent heat of vaporization as

$$h_{lv} = h_{vs} - h_{ls} \quad ,$$

where h_{lv} and h_{ls} are calculated according to Sections A.1.1.4. and A.1.1.5., respectively.

A.2.2. Constant-Pressure Specific Heat

Functions CPLL and CPVV1 calculate the constant-pressure specific heats for the liquid and the steam, gas, or steam-gas mixture, respectively. Constants used in this section are given in Table A-7.

A.2.2.1. Liquid. Function CPLL calculates the liquid constant-pressure specific heat, such that

$$c_{pl} = \left\{ h_l [h_l (D_{0l} + D_{1l} p) + (C_{0l} + C_{1l} p)] + B_{0l} + B_{1l} p \right\}^{-1} \quad .$$

The maximum permitted value for c_{pl} is 4.0×10^4, and if the above calculation of c_{pl} yields a value greater than this, it is reset to be 4.0×10^4.

A.2.2.2. Steam. Function CPVV1 calculates the steam constant-pressure specific heat, such that

$$c_{pv} = C_{1v} + C_{2v} T_g + \frac{C_{3v} p}{\left(C_{5v} T_g - C_{6v} \right)^{2.4}} + \frac{C_{4v} p^3}{\left(C_{5v} T_g - C_{6v} \right)^9} \quad .$$

TABLE A-7.
Constant-Pressure Specific Heat Constants

B_{0l} =	2.394907×10^{-4}	B_{1l} =	$-5.196250 \times 10^{-13}$
C_{0l} =	1.193203×10^{-11}	C_{1l} =	2.412704×10^{-18}
D_{0l} =	$-3.944067 \times 10^{-17}$	D_{1l} =	$-1.680771 \times 10^{-24}$

$C_{1v} = 1.68835968 \times 10^3$
$C_{2v} = 0.6029856$
$C_{3v} = 4.820979623 \times 10^2$
$C_{4v} = 2.95317905 \times 10^7$
$C_{5v} = 1.8$
$C_{6v} = 4.60 \times 10^2$

A.2.2.3. Noncondensable Gas. Function CPVV1 assumes the constant-pressure specific heat of the noncondensable gas to be constant, such that

c_{pa} = 1004.832 [J/(kg·K)] for air,

c_{pa} = 14533.2 [J/(kg·K)] for hydrogen,

and

c_{pa} = 5193.086 [J/(kg·K)] for helium.

A.2.2.4. Steam-Gas Mixtures. Function CPVV1 uses an averaging technique to calculate the specific heat of a steam-air, steam-hydrogen, or steam-helium mixture, such that

$$c_{pg} = \frac{(p - p_a)\, c_{pv} + p_a\, c_{pa}}{p} \quad ,$$

where c_{pv} and c_{pa} are calculated as in Sections A.2.2.2. and A.2.2.3.

Note: Because these values of specific heats are used only for calculating heat-transfer coefficients, these fits were chosen for simplicity and smoothness and are not necessarily consistent with those derivable from the thermodynamic routines.

A.2.3. Fluid Viscosity

Functions VISCL and VISCV calculate the fluid viscosities for the liquid and the steam, for the gas, or for the steam-gas mixture, respectively. Constants used in this section are given in Tables A-8., A-9., and A-10.

A.2.3.1. Liquid. Function VISCL divides the evaluation of liquid viscosity into three different enthalpy ranges. Table A-8. gives the constants used in this section.

A.2.3.1.1. $h_l \le 0.276 \times 10^6$ J/kg.

$$\mu_l = \left[A_{0l} + A_{1l}x + A_{2l}x^2 + A_{3l}x^3 + A_{4l}x^4\right] - \left[B_{0l} + B_{1l}\eta + B_{2l}\eta^2 + B_{3l}\eta^3\right](p - p_i) \quad ,$$

where

$$x = (h_l - c_{0n})h_0$$

and

$$\eta = (h_l - e_{c0n})e_{h0} \quad .$$

TABLE A-8.
Liquid Viscosity Constants

A_{0l}	=	1.298	102	340	$\times 10^{-3}$		B_{0l}	=	–6.595	9	$\times 10^{-12}$			
A_{1l}	=	–9.264	032	108	$\times 10^{-4}$		B_{1l}	=	6.763		$\times 10^{-12}$			
A_{2l}	=	3.810	470	61	$\times 10^{-4}$		B_{2l}	=	–2.888	25	$\times 10^{-12}$			
A_{3l}	=	–8.219	444	458	$\times 10^{-5}$		B_{3l}	=	4.452	5	$\times 10^{-13}$			
A_{4l}	=	7.022	437	984	$\times 10^{-6}$									
D_{0l}	=	3.026	032	306	$\times 10^{-4}$		E_{0l}	=	1.452	605	261	2	$\times 10^{-3}$	
D_{1l}	=	–1.836	606	896	$\times 10^{-4}$		E_{1l}	=	–6.988	008	498	5	$\times 10^{-9}$	
D_{2l}	=	7.567	075	775	$\times 10^{-5}$		E_{2l}	=	1.521	023	033	4	$\times 10^{-14}$	
D_{3l}	=	–1.647	878	879	$\times 10^{-5}$		E_{3l}	=	–1.230	319	494	6	$\times 10^{-20}$	
D_{4l}	=	1.416	457	633	$\times 10^{-6}$									
F_{0l}	=	–3.806	350	753	3	$\times 10^{-11}$	h_0	=	8.581	289	699		$\times 10^{-6}$	
F_{1l}	=	3.928	520	767	7	$\times 10^{-16}$	c_{0n}	=	4.265	884			$\times 10^{4}$	
F_{2l}	=	–1.258	579	929	2	$\times 10^{-21}$	p_i	=	6.894	575	293		$\times 10^{5}$	
F_{3l}	=	1.286	018	078	8	$\times 10^{-27}$								
h_{00}	=	3.892	077	365		$\times 10^{-6}$	e_{h0}	=	6.484	503	981		$\times 10^{-6}$	
e_{con}	=	5.535	88			$\times 10^{4}$	c_n	=	4.014	676			$\times 10^{5}$	

A.2.3.1.2. 0.276×10^6 J/kg < $h_l \leq 0.394 \times 10^6$ J/kg.

$$\mu_l = \left[E_{0l} + E_{1l}h_l + E_{2l}h_l^2 + E_{3l}h_l^3\right] + \left[F_{0l} + F_{1l}h_l + F_{2l}h_l^2 + F_{3l}h_l^3\right](p - p_i) \quad .$$

A.2.3.1.3. $h_l > 0.394 \times 10^6$ J/kg.

$$\mu_l = \left[D_{0l} + D_{1l}z + D_{2l}z^2 + D_{3l}z^3 + D_{4l}z^4\right] \quad ,$$

where

$$z = \left(h_1 - c_n\right)h_{00} \quad .$$

A.2.3.2. Steam. Function VISCV uses three gas temperature ranges to evaluate the steam viscosity. Constants used in this section are given in Table A-9.

A.2.3.2.1. $T_g \leq$ 573.15 K.

$$\mu_v = \left[B_{1v}\left(T_g - 273.15\right) + C_{1v}\right] - \rho_v\left[D_{1v} - E_{1v}\left(T_g - 273.15\right)\right] \quad .$$

If $\mu_v < 10^{-7}$, it is set to that value.

A.2.3.2.2. 573.15 K < T_g < 648.15 K.

$$\begin{aligned}\mu_v &= B_{1v}(T_g - 273.15) + C_{1v} + \rho_v\left[F_{0v} + F_{1v}(T_g - 273.15)\right. \\ &+ \left. F_{2v}(T_g - 273.15)^2 + F_{3v}(T_g - 273.15)^3\right] \\ &+ \rho_v\left[G_{0v} + G_{1v}(T_g - 273.15) + G_{2v}(T_g - 273.15)^2\right. \\ &+ \left. G_{3v}(T_g - 273.15)^3\right]\left(A_{0v} + A_{1v}\rho_v + A_{2v}\rho_v^2\right) \quad .\end{aligned}$$

A.2.3.2.3. $T_g \geq$ 648.15 K.

$$\mu_v = B_{1v}(T_g - 273.15) + C_{1v} + \rho_v\left(A_{0v} + A_{1v}\rho_v + A_{2v}\rho_v^2\right) \quad .$$

TABLE A-9.
Noncondensable-Gas Viscosity Constants

H_{a0}	=	1.707623×10^{-5}	H_{b0}	=	1.735×10^{-5}
H_{a1}	=	5.927×10^{-8}	H_{b1}	=	4.193×10^{-8}
H_{a2}	=	-8.14×10^{-11}	H_{b2}	=	-1.09×10^{-11}
H_{c0}	=	4.175×10^{-6}	H_{d1}	=	5.9642×10^{-6}
H_{c1}	=	1.588×10^{-8}	H_{d2}	=	5.2047×10^{-8}
H_{c2}	=	7.6705×10^{-13}	H_{d3}	=	-1.5345×10^{-11}

A.2.3.3. Noncondensable Gas. Constants used in this section are given in Table A-10.

A.2.3.3.1. Air. If the noncondensable gas is air, function VISCV uses two ranges of T_g to determine the gas viscosity.

A.2.3.3.1.1. $T_g \leq 502.15$ K. $\mu_a = H_{a0} + H_{a1}(T_g - 273.15) + H_{a2}(T_g - 273.15)^2$.

A.2.3.3.1.2. $T_g > 502.15$ K. $\mu_a = H_{b0} + H_{b1}(T_g - 273.15) + H_{b2}(T_g - 273.15)^2$.

A.2.3.3.2. Hydrogen. If the noncondensable gas is hydrogen, function VISCV calculates the gas viscosity as

$$\mu_a = H_{c0} + H_{c1}T_g + H_{c2}T_g^2 \quad .$$

A.2.3.3.3. Helium. If the noncondensable gas is helium, function VISCV calculates the gas viscosity as

$$\mu_a = H_{d0} + H_{d1}T_g + H_{d2}T_g^2 \quad .$$

TABLE A-10.
Thermal Conductivity Constants

h_0	=	5.815×10^5
A_{l0}	=	0.573738622
A_{l1}	=	0.2536103551
A_{l2}	=	–0.145468269
A_{l3}	=	–0.01387472485
C	=	2.1482×10^5
A_{v0}	=	1.76×10^{-2}
A_{v1}	=	3.87×10^{-5}
A_{v2}	=	1.04×10^{-7}
A_{v3}	=	-4.51×10^{-11}
B_{v0}	=	1.0351×10^{-4}
B_{v2}	=	0.4198×10^{-6}
B_{v3}	=	-2.771×10^{-11}

A.2.3.4. Steam-Gas Mixture. Function VISCV uses an averaging technique to calculate the viscosity of a steam-air, steam-hydrogen, or steam-helium mixture, such that

$$\mu_g = \frac{(p - p_a)\,\mu_v + p_a \mu_a}{p} ,$$

where μ_v and μ_a are calculated as in Sections A.2.3.2. and A.2.3.3.

A.2.4. Fluid Thermal Conductivity

Functions THCL and THCV calculate the fluid thermal conductivities for the liquid and the steam, gas, or steam-gas mixture, respectively. Constants used in this section are given in Table A-11.

A.2.4.1. Liquid. Function THCL calculates the liquid-water thermal conductivity, such that

$$k_l = A_{l0} + A_{l1} x_k + A_{l2} x_k^2 + A_{l3} x_k^3 ,$$

TABLE A-11.
Thermal Conductivity Constants

h_0	=	5.815×10^{5}
A_{l0}	=	0.573738622
A_{l1}	=	0.2536103551
A_{l2}	=	–0.145468269
A_{l3}	=	–0.01387472485
C	=	2.1482×10^{5}
A_{v0}	=	1.76×10^{-2}
A_{v1}	=	3.87×10^{-5}
A_{v2}	=	1.04×10^{-7}
A_{v3}	=	-4.51×10^{-11}
B_{v0}	=	1.0351×10^{-4}
B_{v2}	=	0.4198×10^{-6}
B_{v3}	=	-2.771×10^{-11}

where

$$x_k = \frac{h_l}{h_0} \quad .$$

If $k_l < 0.09$, it is set to that value.

A.2.4.2. Steam. Function THCV uses two gas temperature ranges to calculate the steam thermal conductivity.

A.2.4.2.1. 273.15 K $\leq T_g \leq$ 273.25 K.

$$k_v = x_1 + \rho_v \left[x_2 + \frac{C\ \rho_v}{(0.1)^{4.2}} \right] \quad ,$$

where

$$x_1 = A_{v0} + A_{v1}(0.1) + A_{v2}(0.1)^2 + A_{v3}(0.1)^3$$

and

$$x_2 = B_{v0} + B_{v1}(0.1) + B_{v2}(0.1)^2 \quad .$$

A.2.4.2.2. 273.25 K < $T_g \leq$ 713.94025779311 K.

$$k_v = x_1 + \rho_v \left[x_2 + \frac{C\ \rho_v}{\left(T_g - 273.15\right)^{4.2}} \right] \quad ,$$

where

$$x_1 = A_{v0} + A_{v1}\left(T_g - 273.15\right) + A_{v2}\left(T_g - 273.15\right)^2 + A_{v3}\left(T_g - 273.15\right)^3$$

and

$$x_2 = B_{v0} + B_{v1}\left(T_g - 273.15\right) + B_{v2}\left(T_g - 273.15\right)^2 \quad .$$

If $k_v < 1.0 \times 10^{-4}$, it is set equal to that value.

A.2.4.3. Noncondensable Gas. Function THCV assumes the thermal conductivity of the noncondensable gas to be an exponential function of temperature, such that

$$k_a = 2.091\ x\ 10^{-4} T_g^{0.846}\ \left[\mathrm{W / m \cdot K}\right] \text{ for air} \quad ,$$

$$k_a = 1.6355\ x\ 10^{-3} T_g^{0.8213}\ \left[\mathrm{W / m \cdot K}\right] \text{ for hydrogen} \quad ,$$

and

$$k_a = 3.366\ x\ 10^{-3} T_g^{0.668}\ \left[\mathrm{W / m \cdot K}\right] \text{ for helium} \quad .$$

A.2.4.4. Steam-Gas Mixtures. Function THCV uses an averaging technique to calculate the thermal conductivity of a steam-air, steam-hydrogen, or steam-helium mixture, such that

$$k_g = \frac{\left(p - p_a\right) k_v + p_a\, k_a}{p} \quad ,$$

where k_v and k_a are calculated as in Sections A.2.4.2. and A.2.4.3.

A.2.5. Surface Tension

Function SIGMA uses two ranges of the saturation temperature corresponding to the total pressure to determine the surface tension of liquid water.

A.2.5.1. 273.15 K $\le T_{sat} \le$ 582.435 K. Within this range, the surface tension of liquid water is calculated using the following ASME Steam Tables Recommended Interpolation Equation (Ref. A-5.):

$$\sigma = 0.2358 \left(1 - 0.625 \frac{647.15 - T_{\mathrm{sat}}}{647.15}\right) \left(\frac{647.15 - T_{\mathrm{sat}}}{647.15}\right)^{1.256} \quad .$$

The ASME Steam Tables state that this equation is valid for temperatures between the triple point (273.16 K) and the critical point, which the reference assumes to be 647.15 K. It is necessary in TRAC, however, to place a lower limit on the calculated value of the surface tension to avoid singularities when evaluating such things as the Chen nucleate-boiling relation. For this reason, the surface tension is set equal to a constant value for the remaining TRAC temperature range, 582.435 K to 713.94025779311 K.

A.2.5.2. 582.435 K < $T_{sat} \le$ 713.94025779311 K. A constant value of surface tension is calculated in this range to keep the surface tension from becoming too low. Constraining the temperature difference ratio to be no less than 0.1 gives

$$\sigma = 0.2358\ [1 - 0.625\ (0.1)]\ (0.1)^{1.256} \quad .$$

A.3. Verification

The thermodynamic and transport property fits used in TRAC have been compared with steam-table data over a wide range of parameters. The agreement is satisfactory in the saturation region and in the superheated steam region for $p < p_{\text{critical}}$ and $T_g < 823.0$ K. For example, the saturation temperature corresponding to a given pressure is always calculated within a maximum error of ± 1 K. However, in most situations, the error is significantly smaller. The agreement also is good in the subcooled-water region for $T_l < T_{\text{critical}}$.

Further verification was performed by comparing the TRAC polynomial fits with the WATER package (Ref. A-1.) over a wider range of nonequilibrium [99 K of both superheat and subcooling (liquid superheat or vapor subcooling exceeding 99 K are highly unlikely in reactor applications)] for pressures up to 20 MPa. The comparisons showed good agreement for both the thermodynamic and transport properties throughout the saturation and nonequilibrium regions, except for very extreme cases. However, at high degrees of subcooling or superheat, some minor inconsistencies were noticed. Because there are no data in these extreme cases, it is impossible to compare TRAC and the WATER package adequately.

In addition, the output of subroutine THERMO variables p_v, e_v, ρ_v, and e_l was checked against values generated from the Sesame database. Sesame is a database, developed by members of the Theoretical Division at LANL, that includes various equation-of-state data (Ref. A-6.). For all of the results below, we used the EOSPAC program (Ref. A-7.) to read the Sesame data. Sesame material 7152 (water) was used in these data comparisons. This particular data fit for water was originally developed by the National Bureau of Standards [NBS, now known as the National Institute for Standards and Technology (NIST)]. A 64-term fit was used by the NBS to closely model equation-of-state data (Ref. A-8.). Sesame data for material 7152 can be assumed to be accurate to within 1% for materials on the saturation line and within 5% for metastable regions off the saturation line (Ref. A-9.). Because the NBS data were based on a fit to experimental data for equilibrium states, no attempt has been made to compare the data with our values for the metastable states corresponding to subcooled steam or superheated liquid.

The ρ_v values from THERMO agreed very well with Sesame data. On the saturation line at pressures below the critical pressure ($p_{\text{crit}} = 2.232 \times 10^7$ Pa), the agreement is excellent. Here the fractional error is less than 1%. Above p_{crit} (Fig. A-1.), the THERMO ρ_v values also agree with the Sesame data (dashed lines in graphs), often to better than 1% accuracy. However, there is a slight departure between the two curves in the pressure range $p_{\text{crit}} < p_v < 2.8 \times 10^7$ Pa. Here the fractional error is about 5%. For superheating, the plots near the saturation line also appear good. For superheats of 8 K and less, the THERMO ρ_v plot follows the Sesame data fairly well. Larger than 10 K superheat yields fractional errors larger than 10% (Fig. A-2.).

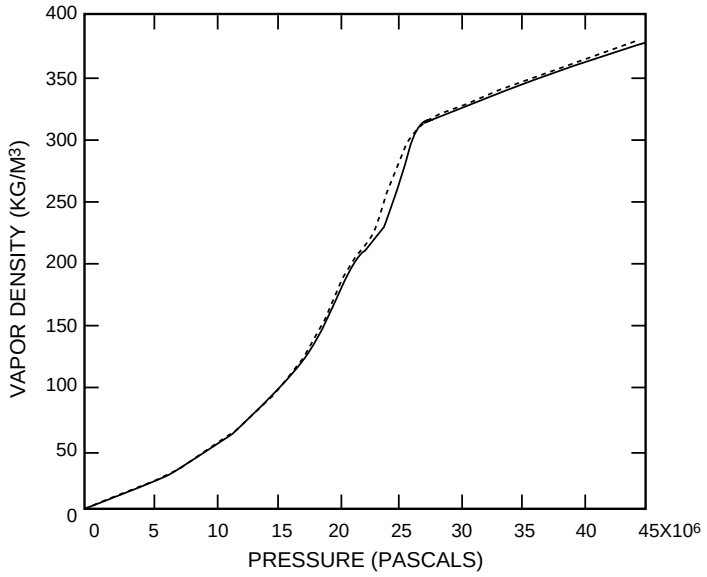

Fig. A-1. Vapor density vs. pressure along the saturation line. Solid: TRAC; Dashed: Sesame.

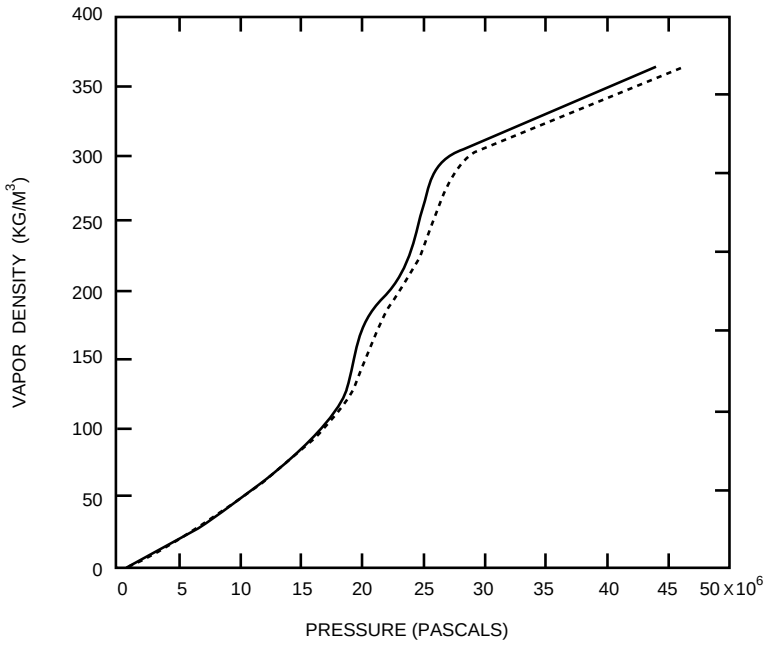

Fig. A-2. Vapor density vs. pressure at a superheat of 8 K. Solid: TRAC; Dashed: Sesame.

For the e_v plot on the saturation line, Sesame and THERMO seem to agree well up to p_{crit} (Fig. A-3.). However, one significant departure is noted in the pressure range $1.0 \times 10^5 < p_v < 2.0 \times 10^6$ Pa. Here, although the fractional error is only 0.5%, the slope of the THERMO plot goes slightly negative in the pressure range $1.3 \times 10^6 < p_v < 2.0 \times 10^6$ Pa, while the Sesame slope remains positive. It should be noted that the THERMO e_v slope is only slightly negative, and then only for a short pressure range. At pressures above p_{crit} along the saturation line (Fig. A-3.), the difference between the THERMO curve and the Sesame data becomes more significant. At approximately $p_v = 2.75 \times 10^7$ Pa, the fractional error between the two curves is almost 4%. The fractional error decreases as pressure increases until, at $p_v = 4.5 \times 10^7$ Pa, the fractional error between the two curves is about 1.5%. For superheating, the Sesame data follow the THERMO e_v plot well up to p_{crit}, and departures between the Sesame and THERMO curves are more significant above p_{crit} (Fig. A-4.). Superheated conditions yield small departures of the THERMO e_v curve from the Sesame data above p_{crit}. Superheats as great at 100 K have fractional errors less than 6% across the pressure range $2.5 \times 10^7 < p_v < 3.0 \times 10^7$ Pa. Here also, the fractional error is only about 3% at $p_v = 4.5 \times 10^7$ Pa.

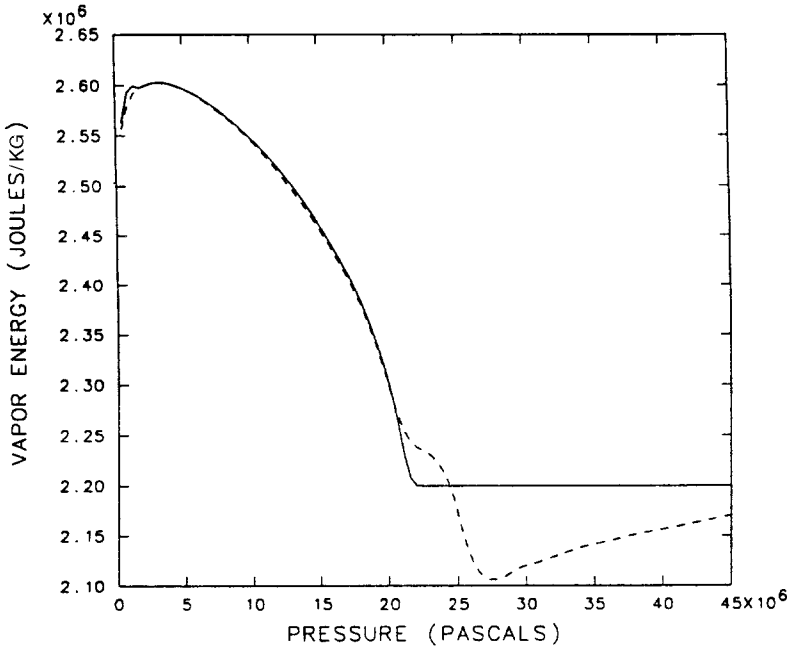

Fig. A-3. Vapor energy vs. pressure along the saturation line.
Solid: TRAC; Dashed: Sesame.

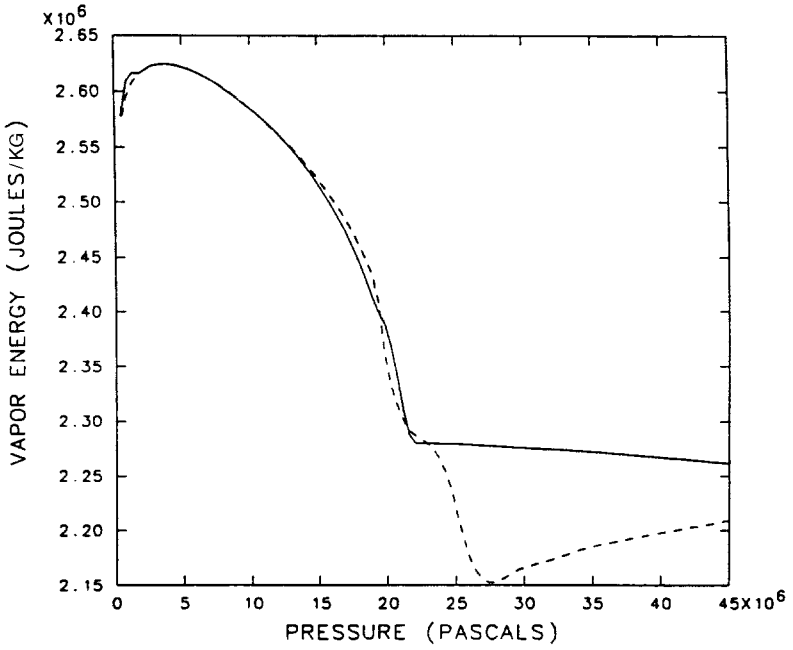

Fig. A-4. Vapor energy vs. pressure at a superheat of 8 K.
Solid: TRAC; Dashed: Sesame.

The ρ_l plot of THERMO seems to agree well with the Sesame liquid density data on the saturation line over the full range of pressures ($1.0 < p_v < 4.5 \times 10^7$ Pa) (Fig. A-5.). However, significant "scalloping" in the Sesame plot is evident. This is due to errors in the EOSPAC interpolation between different data sets to generate a pressure-vs.-liquid density plot. For greater than 100 K subcooling values, the THERMO plots show general agreement with the Sesame subroutine. Here also, however, there is scalloping present. Because of the presence of this scalloping, it is difficult to establish whether there are any departures between the THERMO ρ_l curve and true data points.

The THERMO plot of e_l on the saturation line agrees very well with the Sesame data for liquid internal energy, at pressures below p_{crit}. In this range, accuracy appears to be far better than 1%. At pressures above p_{crit}, a departure between the two curves is noted (Fig. A-6.). In the pressure range $2.1 \times 10^7 < p_v < 3.0 \times 10^7$ Pa, fractional errors as great as 8% between the curves for the e_l data are observed. These departures, however, occur when the curves of the Sesame and THERMO e_l plots are rising steeply. For this reason, the size of the fractional errors is not as significant. Also, because the THERMO output variable ρ_l must be input into the Sesame routine to generate the Sesame data for liquid energy and because of the aforementioned difficulty in determining the accuracy of the

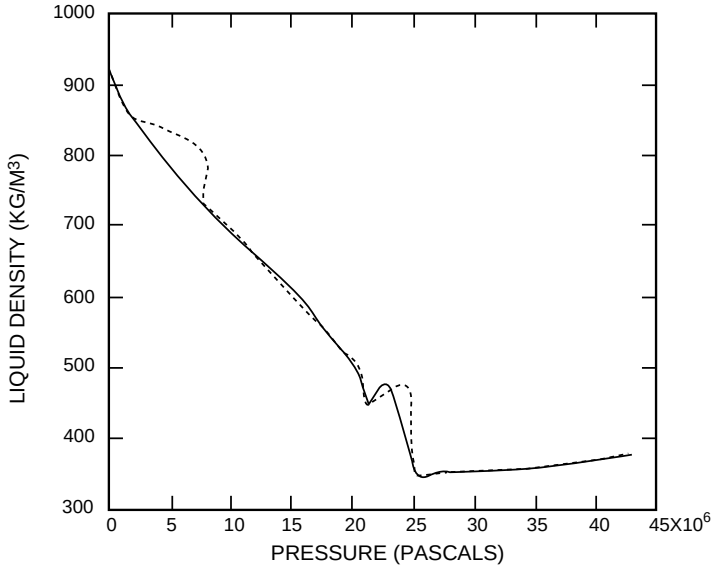

Fig. A-5. Liquid density vs. pressure along the saturation line.
Solid: TRAC; Dashed: Sesame.

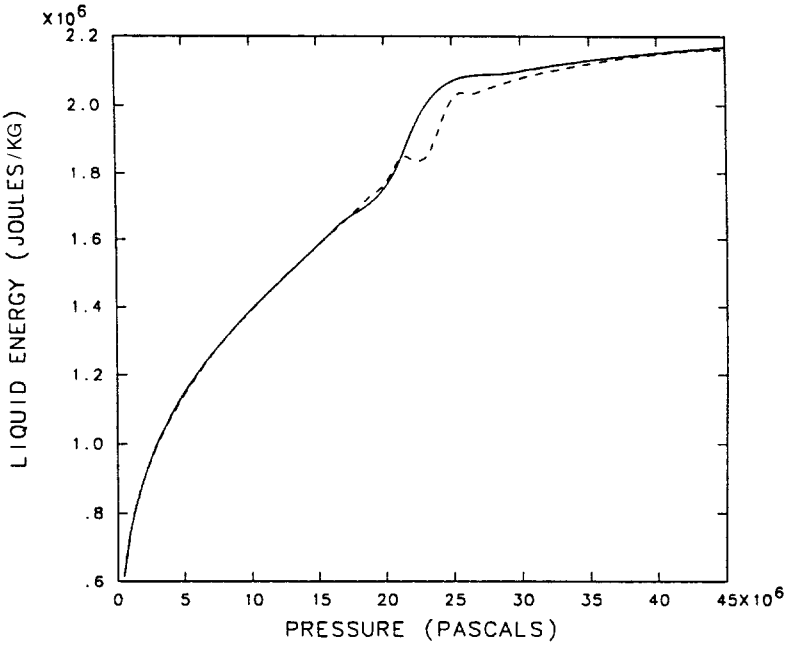

Fig. A-6. Liquid energy vs. pressure along the saturation line.
Solid: TRAC; Dashed: Sesame.

THERMO ρ_l data, it follows that the validity of departures in the e_l plots is also questionable. THERMO plots of subcooled liquid also follow Sesame e_l data closely (Fig. A-7.). For subcooling as great as 100 K for pressures below p_{crit}, the THERMO and the Sesame plots are quite close, with fractional errors in e_l between the two curves of less than 1%. The Sesame and THERMO curves, however, begin to depart in the region $p_{crit} < p_v < 3.3 \times 10^7$ Pa. Here the fractional errors in e_l between the two curves reach as high as 8%, although the errors are not as significant, as they again occur where both the Sesame and the THERMO curves are rising steeply. At pressures above 3.3×10^7 Pa, the curves begin to depart again, although here reaching only a 3% fractional error.

In conclusion, for most TRAC applications, the thermodynamic and transport property routines provide realistic values up to the critical point. The simplified polynomial fits provide an efficient and low-cost method compared to such other approaches as steam-table interpolation.

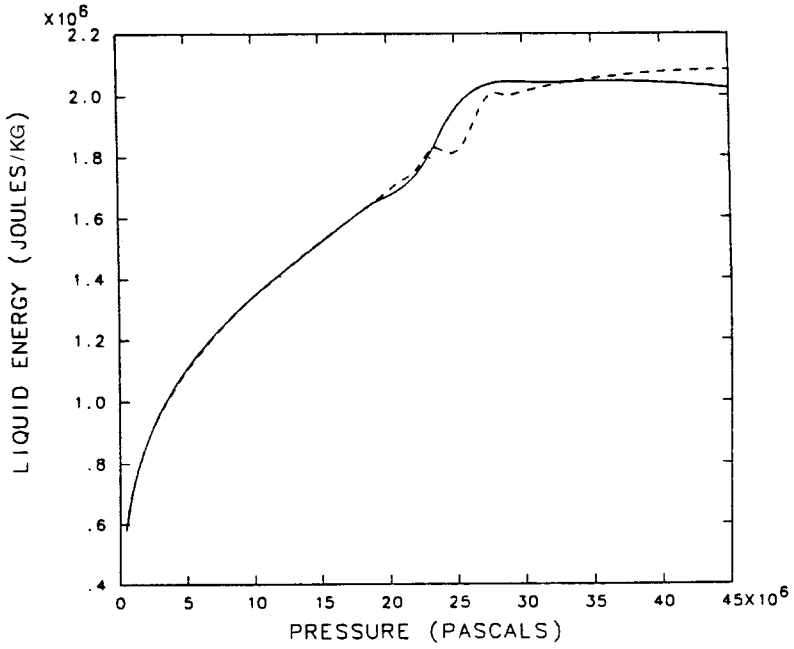

Fig. A-7. Liquid energy vs. pressure for 8 K subcooling.
Solid: TRAC; Dashed: Sesame.

REFERENCES

A-1. W. A. Coffman and L. L. Lynn, "WATER: A Large Range Thermodynamic and Transport Water Property FORTRAN-IV Computer Program," Bettis Atomic Power Laboratory report WAPD-TM-568 (December 1966).

A-2. W. C. Rivard and M. D. Torrey, "Numerical Calculation of Flashing from Long Pipes Using a Two-Field Model," Los Alamos Scientific Laboratory report LA-6104-MS (November 1975).

A-3. J. J. Martin and Y. Hou, "Development of an Equation of State for Gases," *AIChE Jour.* **1**(2), 142–151 (1955).

A-4. J. M. Richardson, A. B. Arons, and R. R. Halverson, "Hydrodynamic Properties of Sea Water at the Front of a Shock Wave," *The Journal of Chemical Physics* **15**(11), 785–794 (1947).

A-5. *ASME Steam Tables: Thermodynamic and Transport Properties of Steam,* 5th ed. (The American Society of Mechanical Engineers, New York, 1983).

A-6. K. S. Holian, "T-4 Handbook of Material Data Bases Volume 1C: Equations of State," Los Alamos National Laboratory, report LA-10160-MS (November 1984).

A-7. C. Cranfill, "EOSPAC: A Subroutine Package for Accessing the Los Alamos Sesame EOS Data Library," Los Alamos National Laboratory report LA-9728-M (August 1983).

A-8. L. Haar, J. Gallagher, and G. Kell, "A Thermodynamic Surface for Water: The Formulation and Computer Program," National Bureau of Standards report NBSIR 81-2253 (May 1981).

A-9. J. D. Johnson of Los Alamos National Laboratory Group T-4, private communication (June 1989).

APPENDIX B

MATERIAL PROPERTIES

The following nomenclature is used in this appendix:

NOMENCLATURE

c_p:	specific heat capacity at constant pressure ($J \cdot kg^{-1} \cdot K^{-1}$)
f:	weight fraction
k:	Boltzmann's constant ($J \cdot K^{-1}$) in Section B.2.1. or thermal conductivity ($W \cdot m^{-1} \cdot K^{-1}$) in Sections B.2.3. and B.4.
k_{gap}:	gap-mixture thermal conductivity
$\frac{\Delta L}{L_0}$:	linear strain caused by thermal expansion
M:	molecular weight
p:	pressure (Pa)
T:	temperature (K)
x:	mole fraction
ε:	emissivity
λ:	characteristic fuel RMS roughness (m)
ρ:	density ($kg \cdot m^{-3}$)

Subscripts

c:	Celsius (°C)
f:	Fahrenheit (°F)
g:	gas gap
i:	constituent gas
PuO_2:	plutonium oxide
r:	radial direction
steam:	steam
TD:	theoretical fuel density
UO_2:	uranium oxide
z:	axial direction

Superscripts

n:	time step
n+1:	time-step increment

B.1. Introduction

An extensive library of temperature-dependent material properties is incorporated in the TRAC code. The entire library is accessible by the ROD and SLAB (heat-structure) components; however, the remaining components have access to structural material-property sets only. There are 12 sets of material properties that make up the library. Each set supplies values for thermal conductivity, specific heat, density, and spectral emissivity for use in the heat-transfer calculations. The first 5 sets and set 11 contain properties for nuclear-heated or electrically heated fuel-rod simulation. Included are nuclear fuels, Zircaloy cladding, fuel-cladding gap gases, electrical heater-rod filaments, electrical heater-rod insulating material, and Zircaloy dioxide. Sets 6 through 10 and set 12 are for structural materials, including stainless steels, carbon steel, and Inconels. In addition, fuel and cladding coefficients of thermal expansion obtained from MATPRO (Refs. B-1. through B-3.) subroutines FTHEX and CDTHEX are available when the gap-conductance thermal-expansion model is used.

Figure B-1. illustrates the calling tree for obtaining the property values. The subroutines MFROD and MPROP are simple processors for calculating the average temperature and calling the appropriate subroutine based on the user-specified material index. Subroutine FROD controls the fuel-cladding gap conductance and fuel-rod thermal conduction calculations.

The figure further indicates that the material properties are evaluated at the beginning of the time step, the prepass at time level n, while the gap conductance and fuel-rod thermal expansion and conduction are evaluated at the end of the time-step advancement, the postpass at time level $n+1$.

The subroutines called out in Fig. B-1. perform the following functions (we have listed the subroutines alphabetically for convenience):

CDTHEX – calculates the thermal expansion of Zircaloy cladding;

CORE1 – controls the thermal analysis for the heat-structure component including fuel and electrically heated rods, in the prepass;

CORE3 – controls the heat-structure component in the postpass;

DELTAR – calculates the fuel-cladding gap dimension in the fuel rod based on thermal expansion;

FROD – calculates the rod temperature distribution, including fuel-cladding conductance and metal-water reaction models;

FTHEX – calculates the thermal expansion of the fuel;

GAPHT – calculates the fuel-cladding gap conductance;

MBN – calculates the properties of boron nitride;

MFROD – controls the calculation of heat-structure and rod properties;

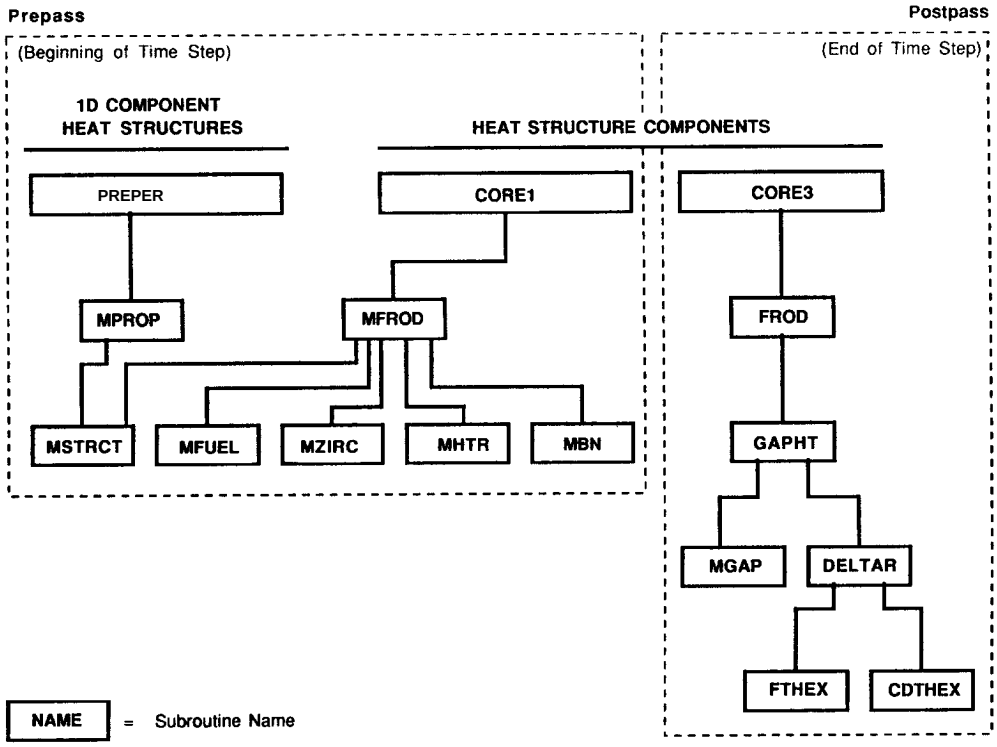

Fig. B-1. Material-properties code organization.

MFUEL – calculates the properties of UO_2 and mixed-oxide fuel;
MGAP – calculates the thermal conductivity of the gap-gas mixture;
MHTR – calculates the properties for the electrical heater element;
MPROP – controls the calculation of heat-structure properties;
MSTRC – calculates the properties of the various steels and Inconels;
MZIRC – calculates the Zircaloy and oxidized-Zircaloy properties; and
PREPER – controls the prepass calculations for all 1D components.

The material indexes in the library are

1 – mixed-oxide fuel;
2 – Zircaloy;
3 – fuel-clad gap gases;
4 – boron-nitride insulation;
5 – Constantan / Nichrome heater coil;
6 – stainless steel, type 304;
7 – stainless steel, type 316;

8 – stainless steel, type 347;
9 – carbon steel, type A508;
10 – Inconel, type 718;
11 – Zircaloy dioxide; and
12 – Inconel, type 600.

Gap-gas properties are calculated only when the dynamic fuel-cladding-gap HTC option is used (NFC = 1). Also, while all properties include an emissivity for doing a radiative-heat-transfer calculation, the calculation is only done in connection with the gap-conductivity calculation. The film-boiling heat-transfer model also includes a radiative-heat-transfer calculation, but the emissivity is specified in connection with that model (see Appendix F).

B.2. Nuclear Fuel Mixed-Oxide Properties

Subroutine MFUEL calculates the properties for mixed-oxide (UO_2 and PuO_2) nuclear fuels. Values obtained are influenced by three user-specified input variables: the fraction of theoretical density, the fraction of plutonium dioxide in the fuel, and the fuel burnup. Property changes upon melting are not included in this code version.

B.2.1. Density

The mixed-oxide fuel density is calculated with a correction factor to account for thermal expansion, which is assumed to be axisymmetric, as

$$\rho = \frac{d}{\left(1+3\frac{\Delta L}{L_0}\right)} \quad ,$$

where

ρ = density $(\mathrm{kg}\cdot\mathrm{m}^{-3})$,

d = $f_{TD}\left[\left(1-f_{PuO_2}\right)\rho_{UO_2}+f_{PuO_2}\rho_{PuO_2}\right]$,

f_{TD} = fraction of theoretical fuel density,

f_{PuO_2} = weight fraction of PuO_2 in the fuel,

ρ_{UO_2} = 1.097×10^4 $(\mathrm{kg}\cdot\mathrm{m}^{-3})$,

ρ_{PuO_2} = 1.146×10^4 $(\mathrm{kg}\cdot\mathrm{m}^{-3})$, and

$\frac{\Delta L}{L_0}$ = linear thermal expansion.

The value calculated for the linear thermal expansion is based on the following MATPRO formulation [Ref. B-1., Eq. (A-4.1)]

$$\frac{\Delta L}{L_0} = K_1 T - K_2 + K_3 \exp\left(-E_D / kT\right) \quad ,$$

where

$\frac{\Delta L}{L_0}$ = inner strain caused by thermal expansion (equal to 0 at 300 K, unitless),
T = temperature (K), and
k = Boltzmann's constant $(1.38 \times 10^{-23}\ \mathrm{J \cdot K^{-1}})$.

The constants K_1, K_2, K_3, and E_D are listed below.

Constants	Uranium Dioxide	Mixed Oxides	Units
K_1	1.0×10^{-5}	9.0×10^{-6}	$\mathrm{K^{-1}}$
K_2	3.0×10^{-3}	2.7×10^{-3}	Unitless
K_3	4.0×10^{-4}	7.0×10^{-2}	Unitless
E_D	6.9×10^{-20}	7.0×10^{-20}	J

B.2.2. Specific Heat

The following mixed-oxide fuel-specific heat correlations are taken from the MATPRO reports [Ref. B-1.; Ref. B-2., Eq. (A-1.1)]:

$$c_p = 15.496 \left\{ \frac{b_1 b_4^2 \exp(b_4 / T)}{T^2 \left[\exp\left(b_4 / T\right) - 1\right]^2} + 2 b_2 T + \frac{b_3 b_5}{b_6 T^2} \exp\left(-b_5 / b_6 T\right) \right\} \quad ,$$

where c_p = specific heat capacity $(\mathrm{J \cdot kg^{-1} \cdot K^{-1}})$ and T = fuel temperature (K). The constants b_1 through b_6 are listed below.

Constants	Uranium Dioxide (Ref. B-1.)	Mixed Oxides (Ref. B-2.)
b_1	19.145	19.53
b_2	7.8473×10^{-4}	9.25×10^{-4}
b_3	5.6437×10^{6}	6.02×10^{6}
b_4	535.285	539.0
b_5	37694.6	40100.0
b_6	1.987	1.987

The resulting correlation for c_p for uranium dioxide is essentially that given in the latest revision of the MATPRO document [Ref. B-3., Eq. (A-1.8)].

B.2.3. Thermal Conductivity

The mixed-oxide fuel thermal conductivity correlations are taken from the MATPRO report [Ref. B-2., Eqs. (A-2.1a) and (A-2.1b)] and include porosity and density correction factors. For $T_c \le T_1$,

$$k = c\left[\frac{c_1}{c_2 + T_c} + c_3 \exp(c_4 T_c)\right] \quad ,$$

and for $T_c > T_1$,

$$k = c\left[c_5 + c_3 \exp\left(c_4 T_c\right)\right] \quad ,$$

where

T_c = temperature (°C) ,

$$c = 100.0\left[\frac{f_{TD}}{1-\beta(1-f_{TD})}\left(\frac{1+0.04\beta}{0.96}\right)\right] \qquad \text{if using mixed-oxide fuel,}$$

$$c = 100.0\left[\frac{1-\beta(1-f_{TD})}{1-0.05\beta}\right] \qquad \text{if using uranium dioxide fuel,}$$

$\beta = c_6 + c_7 T_c$, and

f_{TD} = fraction of theoretical fuel density.

The constants c_1 through c_7 and T_1 are listed below.

Constants	Uranium Dioxide (Ref. B-1.)	Mixed Oxides (Ref. B-2.)
c_1	40.4	33.0
c_2	464.0	375.0
c_3	1.216×10^{-4}	1.54×10^{-4}
c_4	1.867×10^{-3}	1.71×10^{-3}
c_5	0.0191	0.0171
c_6	2.58	1.43
c_7	-5.8×10^{-4}	0.0
T_1 (°C)	1650.0	1550.0

The mixed-oxide values for the constants c_6 and c_7 above are from the coding shown in Ref. B-2. (Table A-2. III).

B.2.4. Spectral Emissivity

The uranium-dioxide spectral emissivity is calculated as a function of temperature based on the MATPRO correlations (Ref. B-2., Appendix A, Section 3.1, p. 29).

The following values for uranium dioxide and mixed oxide fuels are assumed equivalent:

$$\varepsilon = 0.8707 \qquad \text{for} \quad T \le 1000 \text{ K},$$

$$\varepsilon = 1.311 - 4.404 \times 10^{-4} T \qquad \text{for} \quad 1000 < T \le 2050 \text{ K},$$

and

$$\varepsilon = 0.4083 \qquad \text{for} \quad T > 2050 \text{ K}.$$

B.3. Zircaloy Cladding Properties

Subroutine MZIRC calculates the properties for Zircaloy and oxidized Zircaloy cladding. The values obtained are for Zircaloy-4. Zircaloy-2 properties are assumed to be identical. The equations used are based on the correlations in the MATPRO report (Ref. B-2.). The only difference in properties between Zircaloy and oxidized Zircaloy is in the thermal conductivity.

B.3.1. Density

Zircaloy cladding exhibits an asymmetric thermal-expansion behavior. Thermal expansion is calculated in the radial and axial directions, and these effects are included in the density calculation as follows:

$$\rho = \frac{6551.4}{1 + \left[2\left(\frac{\Delta L}{L}\right)_r + \left(\frac{\Delta L}{L}\right)_z\right]} \quad ,$$

where

$$\left(\frac{\Delta L}{L}\right)_r = -2.373 \times 10^{-4} + 6.721 \times 10^{-6} T_c$$

and

$$\left(\frac{\Delta L}{L}\right)_z = -2.506 \times 10^{-5} + 4.441 \times 10^{-6} T_c \quad ,$$

for T ≤ 1073.15 K;

$$\left(\frac{\Delta L}{L}\right)_r = 5.1395 \times 10^{-3} - 1.12 \times 10^{-5} (T - 1073.15)$$

and

$$\left(\frac{\Delta L}{L}\right)_z = 3.5277 \times 10^{-3} - 1.06385 \times 10^{-5}(T - 1073.15)$$

for $1073.15 < T \leq 1273.15$ K; and

$$\left(\frac{\Delta L}{L}\right)_r = -6.8 \times 10^{-3} + 9.7 \times 10^{-6} T_c$$

and

$$\left(\frac{\Delta L}{L}\right)_z = -8.3 \times 10^{-3} + 9.7 \times 10^{-6} T_c \quad ,$$

for $T > 1273.15$ K; where T = temperature (K) and T_c = temperature (°C).

B.3.2. Specific Heat

Because Zircaloy undergoes a phase change (alpha to beta) from 1090 to 1248 K, with a resultant sharp spike in the specific-heat value during the transition, the specific heat is calculated by linear interpolation. Table B-1. is used for $T \leq 1248$ K. For $T > 248$ K, $c_p = 356\ \mathrm{J \cdot kg^{-1} \cdot K^{-1}}$.

TABLE B-1.
Zircaloy Specific Heat vs. Temperature for the α Phase and the Transition to the β Phase

T (K)	c_p (J · kg $^{-1}$ · K^{-1})
300	281
400	302
640	381
1090	375
1093	502
1113	590
1133	615
1153	719
1173	816
1193	770
1213	619
1233	469
1248	356

B.3.3. Thermal Conductivity

Four-term polynomials are used to calculate the Zircaloy and oxidized Zircaloy thermal conductivities. The Kelvin temperature is the independent variable; the polynomial constants are listed below.

Constants	Zirconium	Zirconium Dioxide
a_0	7.51	1.96
a_1	2.09×10^{-2}	-2.41×10^{-4}
a_2	-1.45×10^{-5}	6.43×10^{-7}
a_3	7.67×10^{-9}	-1.95×10^{-10}

The form of the polynomial used in this section and in the subsequent material-properties sections is

$$y = a_0 + a_1 x + a_2 x^2 + \ldots + a_m x^m \quad .$$

B.3.4. Spectral Emissivity

The emissivity of Zircaloy and the emissivity of Zircaloy oxide are temperature-dependent. For simplicity, a constant value of $\varepsilon = 0.75$ is used.

B.4. Fuel-Cladding Gap-Gas Properties

Subroutine MGAP calculates values for the gap-gas-mixture thermal conductivity that are used in predicting gap HTCs. The method is taken from the MATPRO report (Ref. B-1.) and is based on calculating mixture values for seven possible constituent gases as follows:

$$k_{\text{gap}} = \sum_{i=1}^{n} \left(\frac{k_i x_i}{x_i + \sum_{\substack{j=1 \\ j \neq 1}}^{n} \Psi_{ij} x_j} \right) ,$$

where

k_{gap} = gap mixture thermal conductivity $(\text{W} \cdot \text{m}^{-1} \cdot \text{K}^{-1})$,

$$\psi_{ij} = \phi_{ij}\left[1 + 2.41\frac{\left(M_i - M_j\right)\left(M_i - 0.142\,M_j\right)}{M_j\left(M_i + M_j\right)^2}\right] \quad ,$$

$$\phi_{ij} = \frac{\left[1 + \left(\frac{k_i}{k_j}\right)^{1/2}\left(\frac{M_i}{M_j}\right)^{1/4}\right]^2}{2^{3/2}\left(1 + \frac{M_i}{M_j}\right)^{1/2}} \quad ,$$

k_i = constituent gas thermal conductivity $(\mathrm{W \cdot m^{-1} \cdot K^{-1}})$, M_i = constituent gas molecular weight, and x_i = constituent gas mole fraction. In the code $2^{3/2}$ is approximated as 2.8284.

The seven constituent gases considered are helium, argon, xenon, krypton, hydrogen, air / nitrogen, and water vapor. Except for water vapor, their thermal conductivities are defined as

$$k = aT^b \quad ,$$

where T is the gap-gas temperature (K). The constants in the above thermal conductivity equation for the various gases are listed below.

Gas	a	b
helium	3.366×10^{-3}	0.668
argon	3.421×10^{-4}	0.701
xenon	4.0288×10^{-5}	0.872
krypton	4.726×10^{-5}	0.923
hydrogen	1.6355×10^{-3}	0.823
air / nitrogen	2.091×10^{-4}	0.846

For water vapor the following correlation is used:

$$k_{\mathrm{steam}} = (-2.8516 \times 10^{-8} + 9.424 \times 10^{-10}T - 6.004 \times 10^{-14}T^2)\frac{p}{T}$$
$$+ \frac{1.009\,p^2}{T^2(T - 273)^{4.2}} + 8.4083 \times 10^{-3} + 1.19998 \times 10^{-5}T$$
$$+ 6.706 \times 10^{-8}T^2 + 4.51 \times 10^{-11}T^3 \quad ,$$

where p is the gap-gas pressure (Pa).

When the gap dimension shrinks to the order of the gas mean-free path, a correction factor is applied to the light-gas thermal conductivities to account for the change in energy exchange between the gas and the surface. Again, using the MATPRO recommendations (Ref. B-1.), the correction factor for hydrogen and helium is

$$k = \frac{k_i}{1 + f\,k_i} \quad ,$$

where

$$f = \frac{0.210\ \ 3\ \sqrt{T_g}}{p_g \lambda} \quad ,$$

T_g is the average gap-gas temperature (K), p_g is the gap-gas pressure, and λ is the characteristic fuel RMS roughness equal to $4.389\ \times 10^{-6}$ m. The correction is only made for hydrogen and helium; no correction is applied to the other component gases.

B.5. Electrical Fuel-Rod Insulator (BN) Properties

Subroutine MBN calculates values for boron nitride insulators that are used in electrically heated nuclear fuel-rod simulators. Magnesium oxide insulators are assumed to have roughly equivalent values.

B.5.1. Density

A constant value of 2002 kg · m^{-3} from Ref. B-4. is used.

B.5.2. Specific Heat

A four-term polynomial is used to calculate the specific heat. The independent variable is temperature in degrees Fahrenheit, and the constants, which are modifications of those reported in an EPRI report (Ref. B-5.), are listed below.

a_0	a_1	a_2	a_3
760.59	1.7955	-8.6704×10^{-4}	1.5896×10^{-7}

B.5.3. Thermal Conductivity

The boron-nitride thermal-conductivity calculation, based on a conversion to SI units of a curve fit reported in Ref. B-6., is

$$k\ =\ 25.27\ -\ 1.365\ \times\ 10^{-3}\ T_f \quad ,$$

where k is the thermal conductivity $(\mathrm{W \cdot m^{-1} \cdot K^{-1}})$ and T_f is the temperature (°F).

B.5.4. Spectral Emissivity

A constant value of unity is used for the boron nitride spectral emissivity.

B.6. Electrical Fuel-Rod Heater-Coil (Constantan) Properties

Subroutine MHTR calculates property values for Constantan heater coils as used in electrically heated nuclear fuel-rod simulators. We assume that Nichrome coils, used in some installations in place of Constantan, have similar properties. The correlations used are from Ref. B-6.

B.6.1. Density

A constant value of 8393.4 $\mathrm{kg \cdot m^{-3}}$ is used.

B.6.2. Specific Heat

The specific heat is

$$c_p = 110\ T_f^{0.207\ 5} \quad ,$$

where c_p is the specific heat $(\mathrm{J \cdot kg^{-1} \cdot K^{-1}})$ and T_f is the temperature (°F).

B.6.3. Thermal Conductivity

The thermal conductivity is

$$k = 29.18 + 2.683 \times 10^{-3}\ (T_f - 100) \quad ,$$

where k is the thermal conductivity $(\mathrm{W \cdot m^{-1} \cdot K^{-1}})$ and T_f is the temperature (°F).

B.6.4. Spectral Emissivity

A constant value of unity is used.

B.7. Structural Material Properties

Subroutine MSTRCT supplies property values for six types of structural materials normally used in LWRs: stainless steel, type 304; stainless steel, type 316; stainless steel, type 347; carbon steel, type A508; and Inconel, types 718 and 600. These properties were obtained from Refs. B-6. through B-8. A tabulation of the correlations used is given in Tables B-2. through B-7.

TABLE B-2.
Structural Material Properties
Stainless Steel, Type 304

Property	Independent Variable	Polynomial Constants	Reference Number
ρ	T	$a_0 = 7984.0$ $a_1 = -2.651 \times 10^{-1}$ $a_2 = -1.158 \times 10^{-4}$	B-7.
c_p	T_f	$a_0 = 426.17$ $a_1 = 0.43816$ $a_2 = -6.3759 \times 10^{-4}$ $a_3 = 4.4803 \times 10^{-7}$ $a_4 = -1.0729 \times 10^{-10}$	B-7.
k	T	$a_0 = 8.116$ $a_1 = 1.618 \times 10^{-2}$	B-7.
ε	—	$a_0 = 0.84$	B-7.

ρ = density ($kg \cdot m^{-3}$)

c_p = specific heat ($J \cdot kg^{-1} \cdot K^{-1}$)

k = thermal conductivity ($W \cdot m^{-1} \cdot K^{-1}$)

T = temperature (K)

T_f = temperature (°F)

$y = a_0 + a_1 x = a_2 x^2 + \ldots + a_m x^m$

TABLE B-3.
Structural Material Properties
Stainless Steel, Type 316

Property	Independent Variable	Polynomial Constants	Reference Number
ρ	T	$a_0 = 8084.0$ $a_1 = -4.209 \times 10^{-1}$ $a_2 = -3.894 \times 10^{-5}$	B-8.
c_p	T_f	$a_0 = 426.17$ $a_1 = 0.43816$ $a_2 = -6.3759 \times 10^{-4}$ $a_3 = 4.4803 \times 10^{-7}$ $a_4 = -1.7029 \times 10^{-10}$	B-8.
k	T	$a_0 = 9.248$ $a_1 = 1.571 \times 10^{-2}$	B-8.
ε	—	$a_0 = 0.84$	B-8.

ρ = density ($kg \cdot m^{-3}$)

c_p = specific heat ($J \cdot kg^{-1} \cdot K^{-1}$)

k = thermal conductivity ($W \cdot m^{-1} \cdot K^{-1}$)

T = temperature (K)

T_f = temperature (°F)

$y = a_0 + a_1 x = a_2 x^2 + \ldots + a_m x^m$

TABLE B-4.
Structural Material Properties
Stainless Steel, Type 347

Property	Independent Variable	Polynomial Constants	Reference Number
ρ	T	$a_0 = 7913.0$	B-6.
c_p	$(T_f - 240)$	$a_0 = 502.416$ $a_1 = 0.0984$	B-6.
k	T_f	$a_0 = 14.1926$ $a_1 = 7.269 \times 10^{-3}$	B-6.
ε	—	$a_0 = 0.84$	B-6.

ρ = density ($kg \cdot m^{-3}$)

c_p = specific heat ($J \cdot kg^{-1} \cdot K^{-1}$)

k = thermal conductivity ($W \cdot m^{-1} \cdot K^{-1}$)

T = temperature (K)

T_f = temperature (°F)

$y = a_0 + a_1 x = a_2 x^2 + \ldots + a_m x^m$

TABLE B-5.
Structural Material properties
Carbon Steel, Type A508

Property	Independent Variable	Polynomial Constants	Reference Number
ρ	T_f	$a_0 = 7859.82$ $a_1 = -2.6428 \times 10^{-2}$ $a_2 = -4.5471 \times 10^{-4}$ $a_3 = 3.3111 \times 10^{-7}$	B-7.
c_p	T_f	$a_0 = 66.155$ $a_1 = 0.4582$ $a_2 = -6.5532 \times 10^{-4}$ $a_3 = 5.3706 \times 10^{-7}$	B-7.
k	T_f	$a_0 = 66.1558$ $a_1 = 1.4386 \times 10^{-2}$ $a_2 = -2.6987 \times 10^{-4}$ $a_3 = 1.8306 \times 10^{-6}$ $a_4 = -6.0673 \times 10^{-9}$ $a_5 = 1.0524 \times 10^{-11}$ $a_6 = -9.1603 \times 10^{-15}$ $a_7 = 3.1597 \times 10^{-18}$	B-7.
ε	—	$a_0 = 0.84$	B-7.

ρ = density ($kg \cdot m^{-3}$)
c_p = specific heat ($J \cdot kg^{-1} \cdot K^{-1}$)
k = thermal conductivity ($W \cdot m^{-1} \cdot K^{-1}$)
T = temperature (K)
T_f = temperature (°F)
$y = a_0 + a_1 x = a_2 x^2 + \ldots + a_m x^m$

TABLE B-6.
Structural Material properties
Inconel, Type 718

Property	Independent Variable	Polynomial Constants	Reference Number
ρ	T_f	$a_0 = 8233.4$ $a_1 = -1.8351 \times 10^{-1}$ $a_2 = -9.8415 \times 10^{-6}$ $a_3 = -6.5343 \times 10^{-9}$	B-7.
c_p	T_f	$a_0 = 418.18$ $a_1 = 0.1204$	B-7.
k	T_f	$a_0 = 10.8046$ $a_1 = 8.8293 \times 10^{-3}$	B-7.
ε	—	$a_0 = 0.84$	B-7.

ρ = density ($kg \cdot m^{-3}$)

c_p = specific heat ($J \cdot kg^{-1} \cdot K^{-1}$)

k = thermal conductivity ($W \cdot m^{-1} \cdot K^{-1}$)

T = temperature (K)

T_f = temperature (°F)

$y = a_0 + a_1 x = a_2 x^2 + \ldots + a_m x^m$

TABLE B-7.
Structural Material properties
Inconel, Type 600 [a]

Property	Independent Variable	Polynomial Constants	Reference Number
ρ	T_f	$a_0 = 5.261008 \times 10^{2}$	B-7.
		$a_1 = -1.345453 \times 10^{-2}$	
		$a_2 = -1.194357 \times 10^{-7}$	
c_p	T_f	$a_0 = 0.1014$	B-7.
		$a_1 = 4.378952 \times 10^{-5}$	
		$a_2 = -2.046138 \times 10^{-8}$	
		$a_3 = 3.418111 \times 10^{-11}$	
		$a_4 = -2.060318 \times 10^{-13}$	
		$a_5 = 3.682836 \times 10^{-16}$	
		$a_6 = -2.458648 \times 10^{-19}$	
		$a_7 = 5.597571 \times 10^{-23}$	
k	T_f	$a_0 = 8.011\ 332$	B-7.
		$a_1 = 4.643\ 719 \times 10^{-3}$	
		$a_2 = 1.872\ 857 \times 10^{-6}$	
		$a_3 = -3.914\ 512 \times 10^{-9}$	
		$a_4 = 3.475\ 513 \times 10^{-12}$	
		$a_5 = -9.936\ 696 \times 10^{-16}$	
ε	—	$a_0 = 0.84$	B-7.

ρ = density ($kg \cdot m^{-3}$)
c_p = specific heat ($J \cdot kg^{-1} \cdot K^{-1}$)
k = thermal conductivity ($W \cdot m^{-1} \cdot K^{-1}$)
T = temperature (K)
T_f = temperature (°F)
$y = a_0 + a_1 x = a_2 x^2 + \ldots + a_m x^m$

a. Inconel type 600 coefficients are in British units; ρ is multiplied by 16.01846 $(kg \cdot m^{-3}) / (lb_m \cdot ft^{-3})$, c_p by 4.1868×10^3 $(J \cdot kg^{-1} \cdot K) / (Btu \cdot lb_m^{-1} \cdot °F^{-1})$, and k by 1.729577 $(W \cdot m^{-1} \cdot K^{-1}) / (Btu \cdot h^{-1} \cdot ft^{-1} \cdot °F^{-1})$. The conversion factor for the thermal conductivity k assumes the thermochemical Btu instead of the international Btu.

REFERENCES

B-1. D. L. Hagerman, G. A. Reymann, and R. E. Mason, "MATPRO–Version 11 (Revision 1): A Handbook of Material Properties for Use in the Analysis of Light Water Reactor Fuel Rod Behavior," EG&G Idaho, Inc. report TREE-280, Rev. 1 (NUREG / CR-0479) (February 1980).

B-2. Philip E. MacDonald and Loren B. Thompson, compilers and editors, "MATPRO–Version 09: A Handbook of Materials Properties for Use in the Analysis of Light Water Reactor Fuel Rod Behavior," EG&G Idaho, Inc. report (TREE-NUREG-1005) (December 1976).

B-3. Donald L. Hagerman, Gregory A. Reymann, and Richard E. Mason, "MATPRO-Version 11 (Revision 2): A Handbook of Material Properties for Use in the Analysis of Light Water Reactor Fuel Rod Behavior," EG&G Idaho, Inc. report TREE-1280, Rev. 2 (NUREG / CR-0479) (August 1981).

B-4. Y. S. Touloukian, editor, Thermophysical Properties of High Temperature Solid Materials (MacMillan Co., New York, 1967).

B-5. "A Prediction of the SEMISCALE Blowdown Heat Transfer Test S-02-8 (NRC Standard Problem Five)," Electric Power Research Institute report EPRI / NP-212 (October 1976).

B-6. W. L. Kirchner, "Reflood Heat Transfer in a Light Water Reactor," US Nuclear Regulatory Commission report (NUREG-0106) Vols. I and II (August 1976).

B-7. J. C. Spanner, editor, "Nuclear Systems Materials Handbook—Vol. 1 Design Data," Hanford Engineering Development Laboratory report TID-26666 (1976).

B-8. "Properties for LMFBR Safety Analysis," Argonne National Laboratory report ANL-CEN-RSD-76-1 (1976).

APPENDIX C

This appendix is intentionally left blank.

APPENDIX D

IMPLICATIONS OF THE QUASI-STEADY ASSUMPTION AND THE AVERAGING OPERATORS

The coupled-equation set that combines the single-phase, multidimensional, fluid field equations for mass, momentum, and energy with the equation for heat diffusion within a bounding wall is called the conjugate problem. The transient two-phase flow problem becomes even more difficult because an additional set of field equations for the second fluid phase must be solved simultaneously together with the necessary closure relations to couple the two fluid phases. The TRAC code, as well as most other similar codes, invokes a quasi-steady approach to the heat-transfer coupling between the wall and the fluid as well as the closure relations for interfacial heat transfer and drag and wall-to-fluid drag. This quasi-steady approach assumes detailed knowledge of the local fluid parameters and ignores time dependencies such that the time rate of change in the closure relationships becomes infinite and the time constants are zero. The quasi-steady approach has the advantages of being reasonably simple and generally applicable to a wide range of problems and of not requiring previous knowledge of the given transient.

In this appendix, the quasi-steady approach and the averaging operators used in TRAC are discussed. The following nomenclature is valid for Appendix D.

NOMENCLATURE

A:	area
A_{wg}:	fraction of wall contacted by gas
A_{wl}:	fraction of wall contacted by liquid
f_l:	area fraction contacted by liquid
q:	local phasic heat flux
q_{total}:	total heat flux
q':	area-averaged effective phasic heat flux
q'':	area-averaged phasic heat flux
S:	dimensionless number defined by Eq. (D-15)
t:	time
X:	generic for independent variable
Y:	generic for dependent variable
Δt *or* δt:	time-step size
θ:	ratio of transient and phenomenological time constants
τ:	transient time constraint
τ_c:	phenomenological time constant
ψ:	weighting factor between old- and new-time values

Subscripts

g:	gas
i:	independent-variable indices
l:	liquid
max:	maximum
min:	minimum
qs:	quasi-steady
ss:	steady state
tr:	transient
used:	old-time weighted new-time value
w:	wall
wg:	wall-to-gas
*w*l:	wall to-liquid

Superscripts

n:	new-time value
n –1:	old-time value

An alternative to the quasi-steady approach does exist on a case-by-case basis. If the necessary initial and boundary conditions are known, the solution of the conjugate problem requires no a priori knowledge of the wall-to-fluid convective heat transfer. Studies such as those of Sucec (Refs. D-1. and D-2.) have used this latter approach to obtain both analytical and numerical solutions for many single-phase transients. The results, when compared to those using the quasi-steady approach, have led to an understanding of the conditions under which the quasi-steady approach produces valid results.

For the heat-transfer coupling between the wall and the fluid, the quasi-steady approach works well provided that the fluid responds more rapidly than the wall. For example, the fluid boundary layer responds so quickly that the surface temperature of a thick, high-conductivity wall does not have time to change. When the wall changes faster than the fluid, however, one must use transient closure relations to solve the problem accurately.

Despite the difficulties and limitations of the quasi-steady solution approach to the conjugate problem for two-phase flow, this approach is the only method available to simulate transient conditions in large, complex, two-phase systems such as a nuclear power plant. Often, in order to obtain an answer to a difficult problem, engineers apply codes like TRAC even when the quasi-steady assumption is not valid. The literature does contain many papers in which the closure relationships have been modified to

obtain agreement with what is, in fact, transient data. Although this process can provide valuable insight, the resulting relationships may be misleading and may produce inaccurate results when applied either to other transient experiments or to truly quasi-steady transients. Unfortunately, within the English literature, there are very few systematic studies of the problems inherent to the quasi-steady assumptions. The initial study by Nelson (Ref. D-3.) and the more recent work of Pasamehmetoglu and Nelson (Ref. D-4.) do address the problem. As Kuznetsov (Ref. D-5.) presented in his overview, the Soviets at least may have defined more clearly the existence of these limitations.

Section 2.1.1. indicated the importance of the quasi-steady assumption and the averaging operators (volume and temporal) on the closure relationships. While these considerations are of equal importance to all the closure relationships, it is not possible to discuss each set individually. This section will investigate those considerations relative to the wall-to-fluid heat-transfer process. Extension to the other relationships follows similar logic.

The wall-to-fluid heat transfer appears in the two-phase-fluid equation set within the total-energy equation [Eq. (2-1)] as $q_{w\ell} + q_{wg}$ and the combined-gas-energy equation [Eq. (2-2)] as q_{wg}. These terms, $q_{w\ell}$ and q_{wg}, represent the rate of sensible energy per unit volume being transferred into the phasic components of the fluid [see Eqs. (2-11) and (2-12)]. Mass transfer resulting from the superheating of a liquid and its subsequent evaporation, for example, must take place through the phasic-change equation represented by Eqs. (2-8) through (2-10). The total wall-to-fluid heat flux, $q'_{w\ell} + q'_{wg}$ is also required in order to provide the boundary condition necessary for the solution of all structures exposed to the fluid.

Perhaps the easiest way to envision these phasic terms arising is to realize that, within the volume-averaged equations, the total surface area over which one integrates can be decomposed into two parts [see term number 5 of Ref. D-6., Eq. (2-125), p. 70]. One part has liquid contacting it while the other has gas contacting it, so that

$$A_w = A_{w\ell} + A_{wg} \ . \tag{D-1}$$

Thus,

$$\int_{A_w} q dA = \int_{A_{w\ell}} q dA + \int_{A_{wg}} q dA \ . \tag{D-2}$$

By defining the following terms,

$$\int_{A_{w\ell}} q dA \equiv q''_{w\ell} A_{w\ell} \ , \tag{D-3}$$

$$\int_{A_{wg}} qdA \equiv q''_{wg} A_{wg} \ , \tag{D-4}$$

and

$$\int_{A_w} qdA \equiv q_{\text{total}} A_w \ , \tag{D-5}$$

Eq. (D-2) becomes

$$q_{\text{total}} = q'_{wg} + q'_{w\text{l}} = q''_{w\text{l}} f_{\text{l}} + q''_{wg}(1 - f_{\text{l}}) \ , \tag{D-6}$$

where

$$f_{\text{l}} = A_{w\text{l}} / A_w \ .$$

Integration of Eqs. (D-2) through (D-6) with respect to time is an obvious step not shown here and produces "volume-time" averaged quantities required by the two-phase conservation equations [Eqs. (2-1) through (2-6)]. The time interval δt over which the integration is performed must meet those requirements described by Bergles et al. (Ref. D-6., pp. 70–71). The right-hand sides of Eqs. (D-3) through (D-5) and Eq. (D-6) are assumed to reflect the temporal averaging without any further notation change.

The influence of the spatial-averaging operator is realized principally through its influence in data reduction and is therefore inherent within the closure relationships. The code makes no checks to investigate the influence of the spatial averaging, and we delay further discussion of this effect until Appendix F, Section F.2.

A temporal effect is present in both the quasi-steady assumption and the temporal-averaging operator. To further differentiate between the problems that may arise from these two sources, we will first assume that the transient under consideration is slow enough that the quasi-steady assumption is valid. The question becomes what is the relationship among the time-step size desired by the code, Δt, the time constant of the physical phenomena, τ_c (the minimum time of integration for the temporal averager), and the time constant of the transient, τ (some fraction of this time will be the maximum time of integration for the temporal averager). This relationship is the point raised by Bergles et al. (Ref. D-6., pp. 70-71), which was noted earlier. Nelson (Ref. D-3., p. 1133) further refined the question concerning the minimum time of integration, denoted as δt_{min}, by pointing out that δt_{min} must include a sufficient number of events of the governing phenomena, reflected by τ_c, to make the integral "independent" of time. Therefore, the question becomes what should happen when $\Delta t < \delta t_{\text{min}}$ or $\Delta t > \tau$.

Generally, the second part of the above question, $\Delta t > \tau$ is not important in TRAC because calculations are controlled frequently by the rate of change of the quantities. In the future, however, as time-step sizes continue to increase as a result of improved numerics, this portion of the question may become more important. For TRAC, the first part of the question is important and is a condition that frequently arises in the code. Again, Nelson (Ref. D-3., pp. 1127–1129) has pointed out that in addressing this question, we must decide which of two questions we wish to answer. If we wish to model the instantaneous response inside the time interval represented by $\delta t_{\min}$, a transient closure model is required even for "steady-state" conditions. In general, this representation is beyond the state of the art. Thus, only the average response during these "small" time steps, $\Delta t < \delta t_{\min}$, can be defined and the quasi-steady closure relationship should be constant over the time interval corresponding to $\delta t_{\min}$. Early in the TRAC development, we observed the effect of $\delta t_{\min}$ and developed crude averagers to minimize the observed problems. (It is not clear that early code developers had interpreted these problems as arising from this cause.) Only recently have calculations again identified these temporal-averaging problems as significant; the new observations center on noding and time-step sensitivities in the calculated results. Sections D.1. and D.2. will discuss the models currently in TRAC to address this problem of $\Delta t < \delta t_{\min}$.

In the preceding discussion, we assumed the quasi-steady assumption was valid. The question remains as to when the assumption breaks down. As pointed out by Nelson (Ref. D-3., pp. 1132-1133), one way of perceiving this breakdown arises from temporal-averaging considerations. The observed characteristic is that when Δt is decreased to the $\delta t_{\min}$, the resulting quantity will still show a sensitivity to Δt. Once this happens, the transient is a true transient. Section D.3. will discuss more recent techniques for determining when the quasi-steady assumption is valid. Because the code at this time only implements the quasi-steady assumption, we offer no alternative procedures for dealing with a true transient.

D.1. Averagers and Limiters Arising from Temporal-Averager Considerations

A potential problem that one sees in transient analysis using the quasi-steady approach is that the closure relations are free to respond instantaneously (within a single time step) to any changes occurring within the flow field. Thus, unless some type of averager and/or limiter is used, flow regimes may change instantly. While the averagers/limiters used in TRAC-PF1/MOD1 vary among closure packages, they are typically represented by the following relations. Averagers from one time step to the next generally appear as

$$Y^n_{\text{used}} = \psi Y^{n-1} + (1-\psi) Y^n \ , \tag{D-7}$$

where Y represents some closure quantity, ψ is a fraction between zero and one, and the superscripts $n-1$ and n indicate old- and new-time values of Y, respectively. The Y^n_{used} is the closure-relationship value used in the current time step and becomes Y^{n-1} for the next

time step. Thus, as ψ approaches one, Y_{used} would change very slowly, and for ψ equal to zero, Y_{used} would change instantly. Typical limiters are given as

$$Y_{min} < Y^n < Y_{max} ,$$

where Y_{min} and Y_{max} are reasonable bounds for Y and depend on the phenomenon addressed by the closure relationship.

An alternative method to these averagers and/or limiters is the use of additional transport equations within the code to convect such quantities as interfacial area or drop/bubble diameter. While these transport equations do "stabilize" the potential "instantaneous-response" problem, however, they do not directly address the problem that still exists—that the closure relationships are quasi-steady at best.

D.2. Variations in the Application of Temporal Averagers and Limiters

The problem with the above averager [given by Eq. (D-7)] is that it produces a time-averaging scheme which is time-step-size dependent. For example, if we were to run a transient calculation with a fixed time-step size of 100 ms and then repeat the calculation with a time-step size of 10 ms, we would obtain a change in the answer because of this type averager. Fortunately, this sensitivity has been found to be limited to those flow regimes where either large interfacial heat-transfer or interfacial area changes may take place. Appendix F, Section F.1.8. discusses an averager/limiter that minimizes the time-step size sensitivity and is based upon the concept that below δt_{min}, the closure property should remain constant.

Another potential problem with Eq. (D-7) can occur when Δt is very small. For example, assume that due to a rapid transient, the time-step size, Δt, is reduced by the time-step controller to 10^{-6} s. This might occur as the code limits Δt as a result of the allowable changes in the void fraction, pressure, temperature, etc. This Δt is typically much smaller than any δt that an experimentalist might use in time averaging his data. This example is another case where the code should hold this closure quantity constant. But, due to the time averaging currently used, Eq. (D-7) this quantity would be allowed to change over short time spans (remember 10 time steps would still be only 10^{-5} s) and could further aggravate the problem. In effect, the numerics of the code are being forced to track unreal physical phenomena within the time interval δt_{min} and the time-step controls may continue to prevent the time-step size from increasing.

Consequently, during transient calculations, we chose to use relaxation-type relations as limiters during transient calculations. These relaxation relationships can be cast into the following general format:

$$Y^{n-1} C_1^{-C_2 \Delta t} \le Y^n_{used} \le Y^{n-1} C_1^{C_2 \Delta t} . \qquad \text{(D-8)}$$

While this kind of approach reduces the time-step dependency of a transient solution, it does not eliminate it completely. Furthermore, C_1 and C_2 and are currently based upon engineering judgment. As our understanding of transient problems and phenomenological time constants continues to evolve, the relaxation relationships will possibly receive further improvements.

D.3. Validity of the Quasi-Steady Assumption

This section contains information on how the quasi-steady assumption should enter into the consideration of whether the use of quasi-steady closure relations is valid. The information is principally of recent origin and was unavailable to earlier code developers. It is included within this document, however, to provide a basis for understanding some problems that exist within the current code and the need for future work.

A generic and systematic discussion of the quasi-steady versus transient heat-transfer problems was provided by Nelson (Refs. D-3. and D-7.). This discussion is based upon the total rate of change of the dependent variable when the independent variable(s) is (are) under transient. For example, let us assume a simple steady-state constitutive relationship in the form

$$Y_{ss} = F(X_i) \ , \tag{D-9}$$

where i is the index denoting the different independent variables. If the independent variable, X_i, changes with time, then the time, t, must enter into the closure relationship as another independent variable as follows:

$$Y_{tr} = F(t, X_i) \ . \tag{D-10}$$

As a result, the total rate of change of the dependent variable, Y_{tr}, becomes

$$\frac{dY_{tr}}{dt} = \frac{\partial Y_{tr}}{\partial t} + \sum_{i=1}^{N} \frac{\partial Y_{tr}}{\partial X_i} \frac{dX_i}{dt} \ , \tag{D-11}$$

where N is the total number of time-dependent independent variables. In Eq. (D-11), if

$$\left| \frac{\partial Y_{tr}}{\partial t} \right| \quad << \quad \left| \frac{\partial Y_{tr}}{\partial X_i} \frac{dX_i}{dt} \right| \ ,$$

and

$$\left| \frac{\partial Y_{tr}}{\partial t} \right| \quad << \quad \left| \sum_{i=1}^{N} \left| \frac{\partial Y_{tr}}{\partial X_i} \frac{dX_i}{dt} \right| \right. \ ,$$

then the problem becomes quasi-steady for both separate-effects and combined-effects transients. Consequently, a steady-state closure relationship may be used to quantify the transient-dependent parameter, Y_{tr}, such that

$$Y_{tr} \cong Y_{qs} = F\{X_i(t)\} \quad . \tag{D-12}$$

Further discussion of Eqs. (D-10), (D-11), and (D-12) may be found in the studies of Nelson and Pasamehmetoglu (Refs. D-3. and D-4.). This discussion includes consideration of the time constant of the physical phenomena and the influence of the averaging operator (Ref. D-3., pp. 1132-1133). Equation (D-11) has its merits in the original discussion of the quasi-steady versus transient problems, and provides a sound mathematical basis for differentiating them. The practical use, however, of Eq. (D-11) is difficult. The different terms on the right-hand side of Eq. (D-11) cannot be readily quantified. Because the decision on whether a problem is quasi-steady is based upon the relative magnitude of these terms, Eq. (D-11) does not directly lead to a firm criterion.

A more practical equivalent to Eq. (D-11) may be developed (see Ref. D-4.) by considering Eq. (D-11) relative to a simple generic transient model. The physical model with a single independent variable (N =1) consists of a signal source that emits signals with a time-dependent property, a filter or amplifier that processes this signal in a prescribed form, and a receiver that receives the altered signals delayed by τ_c. In this simple example, τ_c may be regarded as the time required for a signal to travel from the source to the receiver. In a more general case, τ_c represents the time constant of the phenomena and may vary in time. The τ_c may be a function of the characteristic properties of the signal or the signal processor or both. This model may symbolize a more concrete example, such as the transient heat-transfer problem, in which the signal emitted may represent a time-dependent wall temperature, the processor may represent the convective heat-transfer phenomena, and the received signal may represent the fluid temperature.

From this simple model, the signal received at time t is equal to the delayed signal emitted at time t - τ_c and processed through the filter. Thus if we assume Y_{ss} to be the filter (we will determine the requirement for this assumption to be valid),

$$Y_{tr}(t, X) = Y_{ss}[X(t - \tau_c)] \ . \tag{D-13}$$

Using the Taylor series expansion for small τ_c, the right-hand side of Eq. (D-13) can be rewritten to yield

$$Y_{tr}(t, X) = Y_{ss}(X) - \tau_c \frac{dY_{ss}}{dX}\frac{dX}{dt} \ , \tag{D-14}$$

where higher-order terms are neglected. Defining a parameter S to be

$$S = \frac{X}{Y_{ss}} \frac{dY_{ss}}{dX} \ , \tag{D-15}$$

Eq. (D-14) may be written as

$$Y_{tr}(t, X) = Y_{ss}[X(t)] \left[1 - S \frac{\tau_c}{X} \frac{dX}{dt} \right] . \tag{D-16}$$

Equation (D-16) suggests that, for the quasi-steady approach to be valid as assumed by Eq. (D-13) the following condition must be satisfied:

$$\left| \frac{dX}{dt} \frac{\tau_c}{X} \right| \quad << \quad \left| \frac{1}{S} \right| \ , \tag{D-17}$$

where S can be calculated by using the definition given by Eq. (D-15) once the steady-state closure relationship Y_{ss} is known. When the inequality in Eq. (D-17) is satisfied, the problem is quasi-steady and

$$Y_{qs}(t, X) \cong Y_{ss}[X(t)] \quad . \tag{D-18}$$

Otherwise, the problem is a true transient. In this case, Eq. (D-18) is no longer valid, and a transient closure relationship is required.

It is important to note that Eq. (D-16) is merely an approximation for a transient closure relationship obtained by simply translating the steady-state closure relationship along the time axis by an amount τ_c. It is derived for the purpose of obtaining a criterion for limiting the quasi-steady approach. In reality, τ_c is not constant but is a function of time and of the magnitudes and time rates of changes of the dependent and independent variables. This functionality is why each transient yields a unique closure relationship. If τ_c can be appropriately correlated as a function of these variables, however, Eq. (D-16) may be used as a generic form for transient closure relationships. Equation (D-16) is a practical alternative to Eq. (D-11) because it can be used more easily to identify and quantify the time constants of the different phenomena.

Another commonly used qualitative criterion for the quasi-steady approach is in terms of the time-constants ratio. If the time constant of the transient is much greater than the time constant of the representative phenomenon, then the problem is quasi-steady. Notice that, when applied to an exponential transient in the form,

$$X = X_o \exp(\pm t / \tau) \ , \tag{D-19}$$

Eq. (D-17) reduces to

$$\left|\frac{1}{\theta}\right| \quad << \quad \left|\frac{1}{S}\right| \ , \tag{D-20}$$

where $\theta = \tau / \tau_c$. This example readily illustrates the concepts of time-constants ratio mentioned above, although Eq. (D-17) is not restricted to exponential transients. For an exponential decay, then, we can classify the transient problem as follows:

θ	>>	$\lvert S \rvert$	(quasi-steady)
θ	<<	$\lvert S \rvert$	(truly transient)
θ	~	$\lvert S \rvert$	(transition) .

Figure D-1. shows a tentative map for the quasi-steady criterion from Ref. D-4. In Fig. D-1., the boundaries between the different transients are tentatively assigned, assuming that << or >> means at least an order of magnitude difference. Especially, the difference between the transition and truly transient problems is not very clear but the problem is, at some point, within the transition region when the quasi-steady approach becomes invalid.

The dimensionless group on the left-hand side of Eq. (D-17) was previously discussed by Pasamehmetoglu and Gunnerson (Refs. D-8. and D-9.) in the context of transient critical heat flux (CHF). The final transient CHF correlation explicitly includes the time-constants ratio in Ref. D-10., Eq. (12). From the overview of Kuznetsov (Ref. D-5.), the Soviets appear to use a similar dimensionless group in conjunction with *unsteady problems*.[1] However, to the best of our knowledge, the English literature does not contain anything regarding the origin or the quantitative application of this dimensionless group.

D.4. Summary and Conclusions

This appendix has discussed the influence of the quasi-steady assumption and the temporal-averaging operator upon the closure relations. It has been pointed out in Sections D.1. and D.2. that most of the code's current time averagers are time-step-size insensitive. Work needs to continue in this area on either development of improved averagers or use of additional transport equations within the code to minimize the use of averagers and limiters. No estimate of how much inaccuracy is introduced into the code due to current averagers is available, but it is a function that will increase as the speed of the transient increases. The discussion of the influence of spatial averaging has been delayed until Appendix F, Section F.2., because its effects are typically included within data-reduction techniques used in correlation development.

---

1. In Soviet literature, the term *unsteady problem* is equivalent to what we refer to as a truly transient problem.

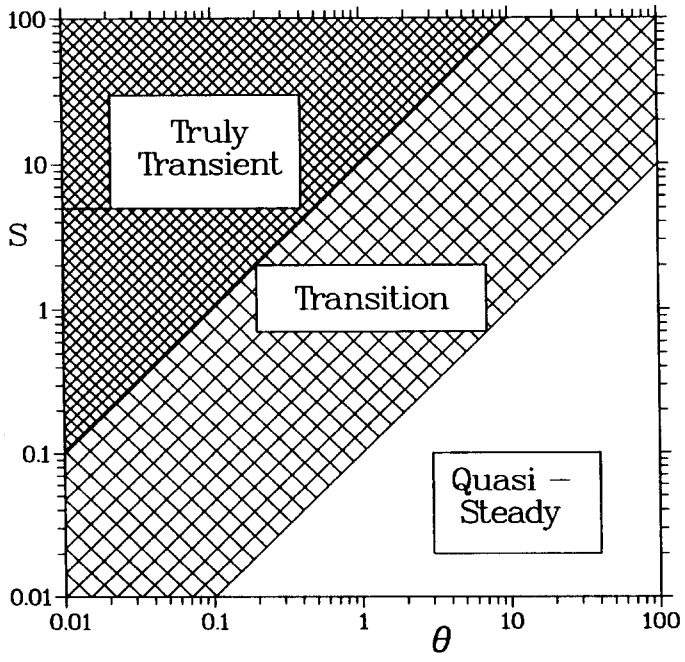

Fig. D-1. Tentative map for transient problems.

REFERENCES

D-1. J. Sucec, "Unsteady Heat Transfer Between a Fluid, With a Time Varying Temperature, and a Plate: An Exact Solution," *International Journal of Heat Mass Transfer* 18, 25–36 (1975).

D-2. J. Sucec, "Analytical Solution for Unsteady Heat Transfer in a Pipe," presented at the ASME Winter Annual Meeting (Anaheim, California, December 7-12, 1986) ASME paper 86-WA / HT-75.

D-3. R. A. Nelson, "Mechanisms of Quenching Surfaces," in *Handbook of Heat and Mass Transfer*, N. P. Cheremisinoff, Ed., Vol. 1: Heat Transfer Operations (Gulf Publishing Company, Houston, Texas, 1986), pp. 1103–1153.

D-4. K. O. Pasamehmetoglu and R. A. Nelson, "Investigation of The Quasi-Steady Approach Used In Transient Two-Phase Flow Analysis," ANS Proceedings of 1988 National Heat Transfer Conf. (Houston, Texas), HTC-Vol. 3, pp. 279-290.

D-5. Y. Kuznetsov, “Overview of Mathematical Models for Nuclear Reactor Safety Heat Transfer Codes and Experiments,” in *Heat Transfer in Nuclear Reactor Safety,* S. G. Bankoff and N. H. Afgan, Eds. (Hemisphere Publishing Corporation, New York, 1982), pp. 111–132.

D-6. A. E. Bergles, J. S. Collier, J. M. Delhaye, G. F. Hewitt, and F. Mayinger, *Two-Phase Flow and Heat Transfer in the Power and Process Industries* (Hemisphere Publishing Corp., New York; McGraw-Hill Book Co., New York, 1981).

D-7. R. A. Nelson, “Forced Convective Post-CHF Heat Transfer and Quenching,” *Trans. ASME, Journal of Heat Transfer* 104, 48-54 (1982).

D-8. K. O. Pasamehmetoglu, “Transient Critical Heat Flux,” Ph. D. Dissertation, University of Central Florida (August 1986) (also EIES report number 86-87-1).

D-9. K. O. Pasamehmetoglu and F. S. Gunnerson, “Theoretical Considerations of Transient Critical Heat Flux,” *Proceedings of the 3rd International Topical Meeting on Reactor-Thermal Hydraulics* (Newport, Rhode Island, October 15–18, 1985), Vol. 2, paper 18-F.

D-10. K. O. Pasamehmetoglu, R. A. Nelson, and F. S. Gunnerson, “A Theoretical Prediction of Critical Heat Flux in Saturated Pool Boiling During Power Transients,” in *Nonequilibrium Transport Phenomena* (ASME, New York, 1987), HTD-Vol. 77, pp. 57–64.

APPENDIX E

BASIC FLOW-REGIME MAPS

To get estimates for the interfacial heat and momentum transfer needed by the fluid field equations, first we have chosen to define a flow regime. We felt that this would be more accurate than trying to arrive at these interfacial quantities directly by "full range" models, as has been done with the normal wall-shear package. The flow-regime specification described here does not, in general, affect the wall shear or wall heat transfer. Exceptions are noted in the appropriate sections of this manual.

Because the flow map is an intermediate calculation needed by the interfacial heat and momentum transfer, some comments on the correlations used in those packages will be made in this appendix to improve the reader's understanding.

In this appendix, we provide a brief description of the basic flow-regime map defined on a mass-flux void-fraction plane and employed at various parts of the code. Special flow regimes implemented for specific closure relationships are not included here. For such special flow regimes, the readers are referred to Appendix F, Section F.2., and Appendix H, Section H.1., where interfacial-shear and heat-transfer closure relationships are described.We first discuss the basis for the vertical flow map followed by that for the horizontal map. Comparisons with some other maps will be made and conclusions drawn for full-size systems.

The entire matter of flow regimes is somewhat subjective. For example, larger capped bubbles can coexist with smaller spherical or oblate bubbles. Churn flow, which is a chaotic oscillating mixture of gas and liquid with relatively indistinct entities, is considered by some to be a precursor to bubbly slug flow or more generally a transition region between bubbly/bubbly slug and annular-mist flow. Entrance effects as well as both the imagination and measurement techniques of the experimentalists can affect the flow-regime descriptions.

This is primarily an audit document for TRAC. The emphasis is on describing what is in the code rather than on reviewing the literature extensively. Excellent reviews of two-phase flow-regime maps and flow-pattern transitions are provided by Rouhani and Sohal (Ref. E-1.) and Dukler and Taitel (Ref. E-2.). We give a brief description of the flow regimes considered. Correlation comparisons are limited to relatively recent analyses of steady-state "fully developed" data. In this appendix, the following nomenclature is used.

NOMENCLATURE

A: flow area

C_o: bubble distribution parameter

D_b: bubble diameter

D_e: equivalent bubble diameter in bubbly slug flow

D_H: hydraulic diameter

D_s: maximum bubble diameter for bubbly slug interfacial-drag model

g: gravitational acceleration

G: mass flux ($kg \cdot m^{-1} \cdot s^{-1}$)

H_l: liquid height

j: superficial velocity ($m \cdot s^{-1}$)

$j_{g,\,bubble}$: terminal bubble rise velocity

N_μ: viscosity number

V: velocity

W: weighting factor

X: dummy variable representing a given closure quantity

α: void fraction

α_{gs}: average void fraction in liquid slug

Δz: elevation difference

μ: dynamic viscosity ($kg \cdot m^{-2} \cdot s^{-1}$)

ρ: density ($kg \cdot m^{-3}$)

σ: surface tension (N / m)

Subscripts

annular: annular-mist flow

bubbly: bubbly and bubbly slug flow

cr: critical

g: gas

hor: horizontal

l: liquid

map: flow-regime map

r: radial or relative

s: bubbly slug flow

st: stratified flow

t: transition (churn) flow

θ: azimuthal

E.1. Basis for the Flow-Regime Map

This section discusses the original foundation (references) for the flow map used in TRAC. Since the vertical map was basically invented to fulfill a need, no original reference for this map exists.

E.1.1. Vertical Flow

We decided to develop a very simple flow-regime map for the P1 version of TRAC. It was sufficiently successful and, with the primary addition of a stratified-flow regime, the map has remained basically unchanged through all subsequent versions of the code.

We assumed that it was sufficient to consider bubbly, bubbly slug, churn (or transition), and annular-mist flows. The bubbly flow regime occurs for $\alpha \leq 0.3$, the bubbly slug regime for $0.3 < \alpha \leq 0.5$, the churn regime for $0.5 < \alpha \leq 0.75$, and the annular-mist regime for $\alpha > 0.75$. These limits were initially based on physical intuition. In addition, bubbly slug flow could not occur if the total mass flux exceeded 2700 $kg \cdot m^{-2} \cdot s^{-1}$. This limit was obtained from an article by Choe et al. for horizontal pipe flow (Ref. E-3., p. 1368, Eq. 2, where the English value $G = 2 \times 10^6\ lb_m \cdot ft^{-2} \cdot h^{-1}$ was rounded to 2700 $kg \cdot m^{-2} \cdot s^{-1}$). We assumed that at these higher mass fluxes, the angle of inclination was irrelevant. The authors showed good agreement with the transition line for air / water flows in 1 / 2-, 1- and 2-in. pipes, and reasonable agreement with other experimental data with other working fluids for small-diameter pipes.

Figure E-1. shows this basic map. The crosshatched region $0.5 < \alpha \leq 0.75$ is referred to in this discussion as a churn (transition) region. The values for interfacial drag and heat transfer in TRAC are interpolated between the values at $\alpha = 0.5$ and $\alpha = 0.75$ as described in Appendices H and F, respectively, rather than determined using separate correlations specifically derived from churn flows. In a similar fashion, we do not switch from bubbly slug to dispersed bubbly flow at a total mass flux of 2700, but rather interpolate the results smoothly over the arbitrary range $2000 < G < 2700\ kg \cdot m^{-2}s^{-1}$.

Although this map was based originally more on physical intuition than on data, it has served TRAC reasonably well for a wide variety of transients. We felt that the then-existing j_g and j_l maps, which are more complex and difficult to code and use, were not in general physically based and might give more numerical problems than this simpler map.

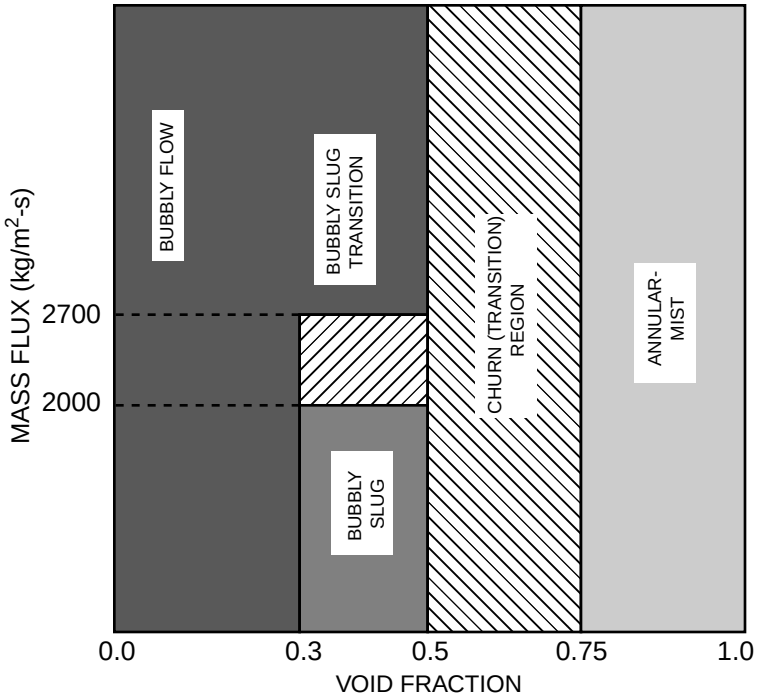

Fig. E-1. Basic flow-regime map of TRAC.

E.1.2. Horizontal Flow

The horizontal flow-regime map is identical to the vertical flow-regime map with the exception of horizontal stratification. The horizontal stratification model, used in the 3D VESSEL component of TRAC, is based upon the study of Mishima and Ishii (Ref. E-4.). Using potential flow analysis with waves of finite amplitude, Mishima and Ishii developed a relative velocity criterion above which horizontal stratification is impossible. The critical relative velocity is obtained as (Ref. E-4., Eq. 38)

$$V_{r,cr} = V_g - V_l = 0.487\sqrt{\frac{g(\rho_l - \rho_g)(D_H - H_l)}{\rho_g}} \ . \qquad \text{(E-1)}$$

The authors reported that this model agrees very well with a large number of experimental data and other empirical correlations (see, for instance, Fig. 4 in Ref. E-4.).

For 1D components, a simplified version of the existing flow-regime map is implemented for critical velocity. The basis is the horizontal flow-regime map that was developed by Mandhane et al. (Ref. E-5.). The authors developed their map using 5935 flow-pattern observations contained in the University of Calgary Multiphase Pipe Flow Data Bank. The parametric range of the database is reported as follows (Ref. E-5., p. 541):

Pipe i.d.:	1.27 — 16.51 cm
Liquid Density:	706 — 1010 kg / m^3
Gas Density:	0.8 — 50.6 kg / m^3
Liquid Viscosity:	3×10^{-4} — 9×10^{-2} kg / m-s
Gas Velocity:	1×10^{-5} — 2.2×10^{-5} kg / m-s
Surface Tension	0.024 — 0.103 N / m
Liquid Superficial Velocity:	0.001 — 7 m / s
Gas Superficial Velocity:	0.04 — 171 m / s

The basic flow-regime map was developed from flow-pattern observations in 1-in.-i.d. pipes with air-water flow at atmospheric pressure. The results were mapped on a phasic superficial-velocity plane, as shown in Fig. E-2. The authors also proposed fluid properties correction factors normalized with respect to the standard problem (air-water at atmospheric pressure). These factors are multiplied by either the j_l or j_g superficial-velocity coordinate of a given point on the map. However, within the database examined, the authors concluded that property correction was negligible and the standard map could be used for practical purposes. Dukler and Taitel (Ref. E-2., p. 28) state that high viscosity has a strong effect on transition in or out of stratified flow. However, the viscosities quoted in the Dukler and Taitel study are a few orders of magnitude greater than water viscosities at various temperatures. As a result, we concluded that the fluid properties have little influence on transition to stratified flow.

Mandhane et al. (Ref. E-5.) also reported that the basic flow regime performed reasonably for larger-diameter pipes and no correction for pipe diameter was deemed necessary. Subsequently, Dukler and Taitel (Ref. E-2.) developed theoretical models for flow-pattern transitions in horizontal flow. The transition from stratified to elongated bubble (called intermittent flow by Dukler and Taitel) and from wave to annular-mist flow is given by (Ref. E-2., Eqs. 26 and 28)

$$V_g = \left(1-\frac{H_l}{D_H}\right)\sqrt{\frac{(\rho_l-\rho_g)gA_g}{\rho_g(dA_l/dH_l)}} \quad . \tag{E-2}$$

Note that for a rectangular channel Eq. (E-2) is almost identical to Eq. (E-1), except for the coefficient in front of the square root sign. Dukler and Taitel converted Eq. (E-2) into a liquid superficial-velocity criterion using the appropriate relationships between the liquid flow rate and liquid height. The resulting equation yielded a transition to intermittent flow criterion which is independent of gas flow rate and in perfect agreement with the constant liquid volumetric-flux criterion of Mandhane et al.

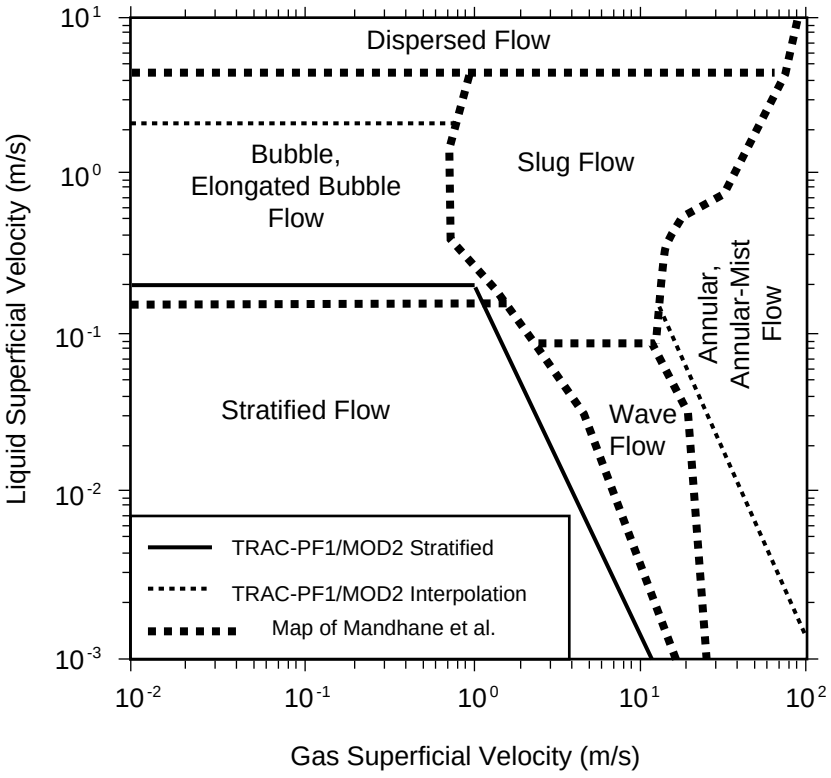

Fig. E-2. Flow-regime map of Mandhane et al., and TRAC criteria for horizontal stratified flow.

At higher void fractions, the transition between stratified flow and wave flow is formulated by Dukler and Taitel (Ref. E-2., Eq. 32) as

$$V_g = 20\sqrt{\frac{\mu_l(\rho_l - \rho_g)g}{\rho_g V_l}} \ . \qquad \text{(E-3)}$$

Figures 14 and 15 in Ref. E-2. show that these theoretically based equations are in good agreement with the empirical map of Mandhane et al. (Ref. E-5.) and the more recent data of Barnea et al. (Ref. E-6.).

In the code, we used simple expressions, which are in reasonable agreement with the above cited references. For transition from bubbly slug to stratified flow, we formulated the liquid critical velocity as

$$V_{l,cr}(1-\alpha) = 0.2 \ . \qquad \text{(E-4)}$$

The transition from annular-mist to stratified flow is formulated as

$$\alpha V_{g,cr} = \left[\frac{0.2}{V_l (1-\alpha)} \right]^{0.435} . \qquad \text{(E-5)}$$

The TRAC horizontal flow-regime map is illustrated in Fig. E-3. The transition between churn and stratified flows is treated as an interpolation region as described in Section E.2.7.

In TRAC, we do not have specific interfacial-shear and heat-transfer models for elongated bubbles, wave flow, or other intermittent flows. Thus, the transitions are treated as interpolation between the basic flow-map closure relationships and stratified-flow relationships. These interpolation regimes also are illustrated in Fig. E-2.

E.2. Flow-Regime Models as Coded

The basic flow map implementation is discussed in the following subsections. Note that, for the 3D VESSEL component, the flow-regime map is implemented separately in each direction, except for stratified flow, as discussed in Section E.2.7.

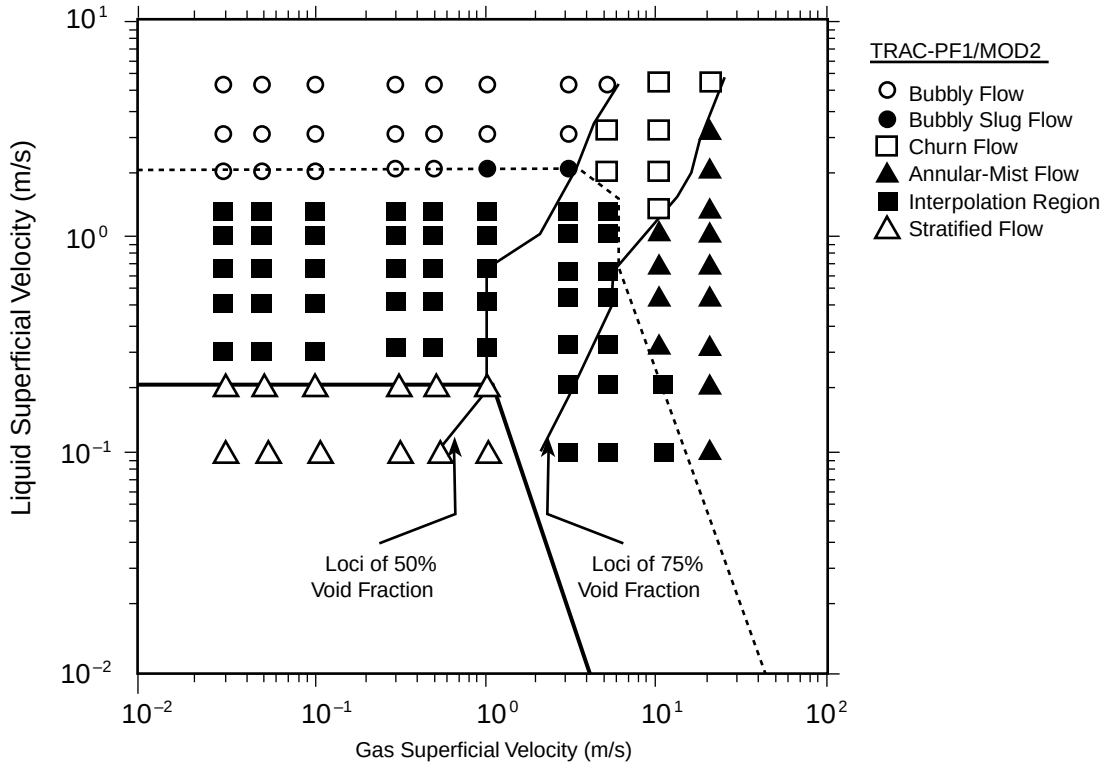

Fig. E-3. TRAC flow-pattern prediction for horizontal flow.

E.2.1. Single-Phase Flow

Single-phase gas or liquid flow occurs according to the following limits on void fraction: $\alpha < 1.0 \times 1\ 0^{-6}$ or $\alpha > 0.999999$. The limits help to provide the necessary drag calculation in the code to couple the velocity of the non-existing phase to that of the other phase and to prevent having to accelerate either the incipient bubble or droplet from zero velocity when it appears.

E.2.2. Bubbly Flow

For interfacial-shear and heat-transfer calculations, bubbly flow occurs in the following ranges of void fraction and mass flux: $1.0 \times 10^{-6} \le \alpha < 0.30$ for all values of the mass flux and $1.0 \times 10^{-6} \le \alpha \le 0.50$ for $G \ge 2700\ \mathrm{kg/m^2\text{-}s}$.

E.2.3. Bubbly Slug Flow

For interfacial-shear and heat-transfer calculations, if $G<2700\ \mathrm{kg/m^2\text{-}s}$ then slugs can form in the void-fraction range of $0.30<\alpha\le0.50$. If $G>2700\ \mathrm{kg/m^2\text{-}s}$, slugs are not allowed to form. The region between void-fraction values of 0.3 and 0.5 and mass flux values of 2000 and $2700\ \mathrm{kg/m^2\text{-}s}$ is treated by interpolation between the bubbly flow and bubbly slug flow regimes. Note that, if the hydraulic diameter is greater than a critical diameter, slugs are replaced by cap bubbles. This transition is further discussed in Section F.1.1.1.2. In bubbly slug flow, vapor slugs and bubbles coexist.

For the interfacial drag, an equivalent bubble diameter is calculated through a linear weighting as follows:

$$D_e = (1 - W_s)D_b + W_s D_s \ , \tag{E-6}$$

where the weighting factor is defined as

$$W_s = \begin{cases} 0 & \text{if } G \ge 2700\mathrm{kg\ /\ m^2\ -\ s} \\ (5\alpha - 1.5)\ \left(\dfrac{2700 - G}{700}\right) & \text{if } 2000 < G < 2700\mathrm{kg\ /\ m^2\ -\ s} \\ (5\alpha - 1.5) & \text{if } G \le 2000\mathrm{kg\ /\ m^2\ -\ s} \end{cases} \tag{E-7}$$

and $0.0 \ \le \ W_s \le \ 1.0$.

For the interfacial heat-transfer calculations, the average void fraction in the liquid slug is used as the weighting factor and formulated as

$$\alpha_{gs} \ = \ \begin{cases} 0.5 & \text{if } G \ge 2700\ \mathrm{kg/m^2\text{-}s} \\ 0.3 + 0.2\left(\dfrac{G - 2000}{700}\right) & \text{if } 2000 \le G < 2700\ \mathrm{kg/m^2\text{-}s} \\ 0.3 & \text{if } G < 2000\ \mathrm{kg/m^2\text{-}s}\ . \end{cases} \tag{E-8}$$

Further discussion of these models can be found in Sections F.1.1. and H.1.1.

E.2.4. Annular-Mist Flow

For interfacial-drag and heat-transfer calculations, annular-mist flow occurs if $0.75 < \alpha \leq 0.999999$. The models for partitioning the liquid phase into liquid film and droplets are discussed in Sections F.1.2. and H.1.2.

E.2.5. Mist Flow

In annular-mist flow, if one of the phasic velocities is very large, then all the liquid is entrained in terms of liquid droplets. The criterion for complete entrainment is formulated as

$$\max(V_l, V_g) \geq 12\left[\frac{g\sigma(\rho_l - \rho_g)}{\rho_g^2}\right]^{1/4} . \tag{E-9}$$

This model is further discussed in Sections F.1.2. and H.1.2.

E.2.6. Churn (Transition) Flow

Churn flow occurs if the void fraction is in the following range: $0.50 < \alpha \leq 0.75$ TRAC does not have a churn region per se but rather interpolates between the bubbly / bubbly slug values and the annular-mist values for both interfacial drag and heat transfer. The linear interpolation is done as follows:

$$X_{\text{churn}} = (1 - W_t)X_{\text{bubbly/bubbly slug}(\alpha\,=\,0.50)} + W_t X_{\text{annular-mist}(\alpha\,=\,0.75)} \tag{E-10}$$

where X represents the desired closure relationship for interfacial shear or heat transfer. The weighting factor is defined as

$$0 \leq W_t = \frac{\alpha - 0.5}{0.25} \leq 1 . \tag{E-11}$$

E.2.7. Horizontal Stratified Flow

For 1D components, the component inclination from horizontal must be within ±10 degrees for stratification to occur. The stratified flow is superimposed on the basic map as follows:

$$X_{\text{map / stratified}} = (1 - W_{st})X_{\text{map}} + W_{st}X_{\text{stratified}} , \tag{E-12}$$

where X represents the desired closure relationship.

For the 3D VESSEL component, the stratification in the vertical direction is allowed if there is a steep void profile in the axial direction. For this, the void fractions in two consecutive levels are checked. If α in the lower level is less than 0.1 and α in the upper level is greater than 0.9, stratification is allowed. Furthermore, the horizontal gas velocity must be less than the critical velocity defined by Eq. (E-1). The horizontal gas velocity is defined as the average vector velocity as follows:

$$V_{g,\mathrm{hor}} = \sqrt{V_{g,r}^2 + V_{g,\theta}^2} \ , \tag{E-13}$$

where $V_{g,r}$ and $V_{g,\theta}$ are the radial and azimuthal velocity components. The stratified flow is superimposed on the basic map also through Eq. (E-12). However, the weighting factor is defined differently as

$$0 \le W_{st} = 2 - \frac{V_{g,\mathrm{hor}}}{V_{r,cr}} \le 1 \ , \tag{E-14}$$

where $V_{r,cr}$ is obtained from Eq. (E-1) by replacing $(D_H - H_l)$ by the arithmetic average of Δz_S for the two levels.

For 1D components, the weighting factor is modeled as void-fraction dependent. For bubbly and bubbly slug flow ($\alpha \le 0.5$), the weighting factor is formulated as

$$0 \le W_{st,\mathrm{bubbly}} = \frac{1}{9}\left(10 - \frac{V_l}{V_{l,cr}}\right) \le 1 \ , \tag{E-15}$$

where $V_{l,cr}$ is given by Eq. (E-4). For annular-mist flow ($\alpha > 0.75$), the weighting factor is calculated as

$$0 \le W_{st,\mathrm{annular}} = \frac{1}{9}\left(10 - \frac{V_g}{V_{g,cr}}\right) \le 1 \ , \tag{E-16}$$

where $V_{g,cr}$ is given by Eq. (E-5). For churn flow ($0.5 < \alpha \le 0.75$), a linear weighting based upon void fraction is used to calculate the weighting factor, which yields

$$W_{st,\mathrm{churn}} = \left(\frac{0.75 - \alpha}{0.25}\right) W_{st,\mathrm{bubbly}} + \left(\frac{\alpha - 0.5}{0.25}\right) W_{st,\mathrm{annular}} \ . \tag{E-17}$$

The resulting flow-regime map of TRAC for the standard problem is shown in Fig. E-3.

E.2.8. Vertical Stratified Flow

In case of liquid downflow, 1D components are allowed to stratify regardless of orientation. The critical velocities for this kind of stratification also are given by Eqs. (E-4) and (E-5). Likewise, the weighting factors are obtained from Eqs. (E-15), (E-16), and (E-17).

For 3D components, the vertical stratification criterion is obtained through comparison with a terminal bubble rise velocity, which is computed as

$$j_{g,\text{bubble}} = \frac{\alpha}{1 - C_o \alpha} \sqrt{2} \left[\frac{g\sigma(\rho - \rho_g)}{\rho^2} \right]^{1/4} , \tag{E-18}$$

where

$$C_o = 1.2 - 0.2 \sqrt{\frac{\rho_g}{\rho}} . \tag{E-19}$$

In this formulation α is set to 0.3. A stratified-flow weighting factor is calculated as

$$0 \le W_{st} = 2 - \frac{|j_g|}{j_{g,\text{bubble}}} \le 1 . \tag{E-20}$$

This weighting factor is computed if (*i*) there is no subcooled boiling, and (*ii*) the cell void fraction is less than 0.1, or (*iii*) void fractions at two consecutive levels are less than 0.1 and greater than 0.9, respectively. Otherwise, W_{st} is set to zero. For the stratified-flow weighting factor in the axial direction, the maximum obtained from Eq. (E-20) or (E-14) is used.

E.3. Assessment and Closing Remarks

In the literature, many flow-regime maps exist that could be used for assessment. Many are not mechanistic and simply are correlations of the data, often in terms of phasic volumetric fluxes. Assumptions about the interfacial drag or relative velocity are required to convert this type of map to the *G-vs.-*α map used in TRAC. We decided not to do an extensive assessment against the *G-vs.-*α map. It is important for us to note that the flow regime per se is not used by the field equations; instead these equations use the values of the interfacial parameters. In this context, the important assessment must reside with comparisons involving interfacial drag and interfacial heat transfer. In general also, we expect the flows in a reactor system to be somewhat more homogeneous than otherwise predicted in pipes with long length-to-diameter ratios, since the primary piping of nuclear plants generally has many bends.

One of the important flow-regime transitions in two-phase flow is the slug formation. In TRAC, we restricted this formation to void fractions greater than 0.3 and mass fluxes less than 2700 kg / m^2-s The upper bound of the mass flux is obtained from the study of Choe et al. (Ref. E-3.). Their data showed reasonable agreement with this fixed mass flux value for slug formation. However, there is no reason to believe that this observation is independent of pressure and pipe diameter for the entire range of steam / water cases of interest.

For slug formation the limiting void fraction is reported to be around 0.30 by various investigators. Taitel et al. (Ref. E-7.) reported this value as 0.25. Ishii and Mishima (Ref. E-8.) employed the argument regarding the effect of agglomeration of smaller bubbles as the main mechanism in bubbly slug flow transition. They postulated that 0.3 is the maximum possible void fraction for sustaining isolated bubbles. This criterion is identical to that used in TRAC for small mass fluxes. Ishii and Mishima do not consider the inability of bubbles to coalesce at high mass fluxes even though some data that are used (Ref. E-9.) to compare with the model occasionally show this trend.

Inserting $\alpha = 0.3$ into the drift velocity equation given by Mishima and Ishii (Ref. E-9., Eq. 3) obtained the following transition criterion on the superficial-velocity plane between bubbly and slug flows (Ref. E-9., Eq. 7):

$$j_l = \left(\frac{3.33}{C_o} - 1\right) j_g - \frac{0.76}{C_o}\left[\frac{\rho g(\sigma_l - \rho_g)}{\rho_g^2}\right]^{1/4} , \tag{E-21}$$

where C_o is defined earlier by Eq. (E-19).

For slug-to-churn-flow transition, the following relationship is developed by Mishima and Ishii (Ref. E-9., Eq. 29):

$$\alpha = j_g\left[C_o(j_l + j_g) + 0.35\frac{gD_H(\rho_l - \rho_g)}{\rho_l}\right]^{-1} , \tag{E-22}$$

where a complicated expression for the void fraction as a function of diameter, fluid properties, and volumetric fluxes is provided in the same reference (Ref. E-9., Eq. 28). However, for all practical purposes and for a wide range of fluid properties, tube diameters, and volumetric fluxes, the critical void fraction expression can be replaced by $\alpha = 0.765$. Then, Eq. (E-22) yields the following transition criterion on the superficial-velocity plane:

$$j_l = \frac{1 - 0.765C_o}{0.765C_o} j_g - 0.268\frac{gD_H(\rho_l - \rho_g)}{\rho_l} . \tag{E-23}$$

For churn-to-annular-mist flow transition in small-diameter tubes, Mishima and Ishii obtained (Ref. E-9., Eq. 32)

$$j_g = (1 - \alpha)\sqrt{\frac{gD_H(\rho_l - \rho_g)}{\rho_g}} , \tag{E-24}$$

where α can be approximated by 0.765. However, for large-diameter tubes satisfying

$$D_H > \left(\frac{C_o}{1 - 0.11 C_o} \right)^2 \sqrt{\frac{\sigma}{g(\rho_l - \rho_g)}} N_\mu^{-0.4} \ , \tag{E-25}$$

where the viscosity number is defined as

$$N_\mu = \mu_l \left[\rho_l \sigma \sqrt{\frac{\sigma}{g(\rho_l - \rho_g)}} \right]^{-1/2} \ , \tag{E-26}$$

the criterion becomes (Ref. E-9., Eq. 35)

$$j_g = \left[\frac{g\sigma(\rho_l - \rho_g)}{\rho_g^2} \right]^{1/4} N_\mu^{-0.2} \ . \tag{E-27}$$

Mishima and Ishii (Ref. E-9.) compared these theoretically based transition criteria with other maps and data in the literature. The criteria agreed reasonably well in most comparisons. TRAC predictions for fully developed adiabatic air-water flow in a 2.54-cm-i.d. pipe are shown in comparison with these criteria in Fig. E-4. Water and air properties are evaluated at atmospheric pressure and at 300 K. Curves A, B, C, and D in this figure correspond to the respective Eqs. (E-21), (E-23), (E-24), and (E-27). As shown, the agreement is quite good except for slug-to-churn-flow transition. However, as mentioned earlier, TRAC does not have a churn flow per se and treats this flow regime as an interpolation region. We do not have specific closure relationships for churn flow and, rather, we interpolate between bubbly/bubbly slug and annular-mist-flow closure relationships. Consequently, the transition in or out of churn flow is immaterial to the field equations.

As a closing remark on assessment, we must note that TRAC's simple flow-regime map agrees well with the observations of Jones and Zuber (Ref. E-10.).

In closing, we must note that the majority of the flow-pattern transition studies available in the open literature deal with steady-state, adiabatic, fully developed flow in pipes with large length-to-diameter ratios. The applicability of such models to real reactor flow situations, especially under transient conditions, is highly questionable. As outlined by Rouhani and Sohal (Ref. E-1.), there are very few studies dealing with the effect of the following parameters on flow-regime transition:

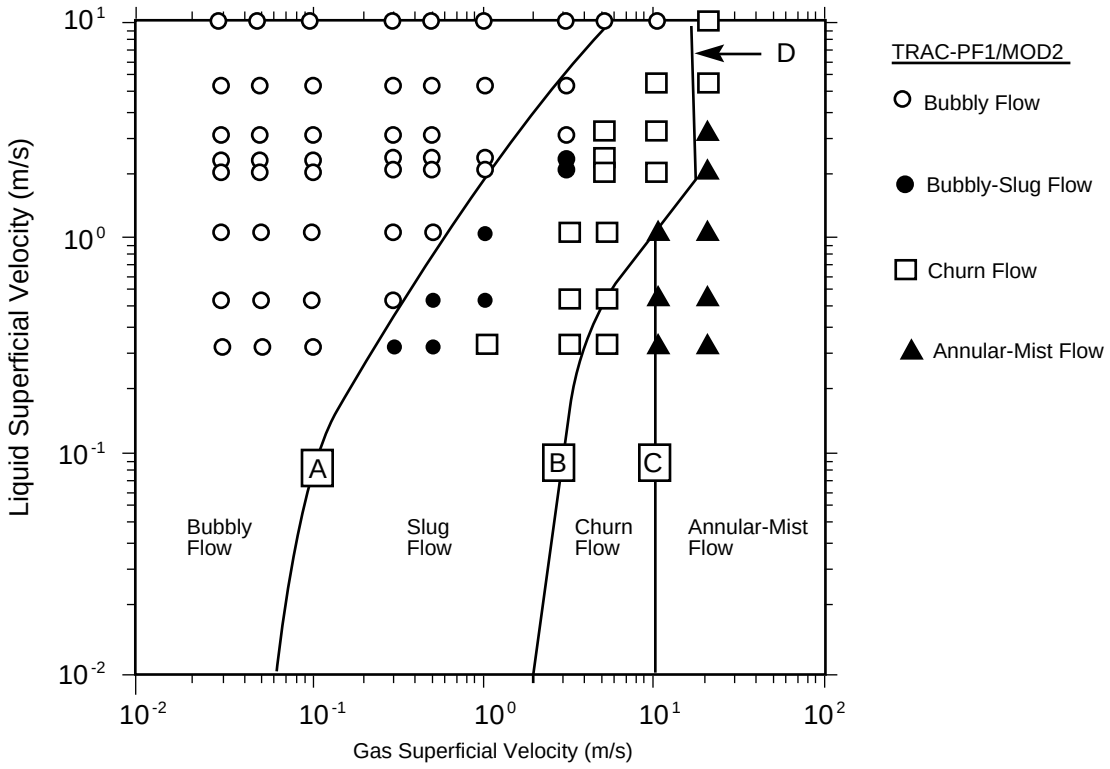

Fig. E-4. Comparison of TRAC results with the flow-pattern transition criteria of Mishima and Ishii for vertical upflow.

1. wall roughness,
2. boiling on the heater wall,
3. flow acceleration or deceleration due to local changes in volumetric fluxes or pressure resulting from condensation or boiling,
4. relaxation time constants during transient flow,
5. effect of large hydraulic diameters, and
6. entry-length effects for short pipes or channels.

All these parameters are involved in two-phase flow situations during nuclear reactor operations and cannot be neglected. Unfortunately, they are shown to have appreciable effects on the flow-regime transitions. An accurate quantification of these effects requires further studies. This is an actively evolving area of research in two-phase flow. Naturally, the models of TRAC are expected to improve along with our understanding of two-phase flow.

REFERENCES

E-1. S. Z. Rouhani and M. S. Sohal, "Two-Phase Flow Patterns: A Review of Research Results," Progress in Nuclear Energy 11, 219-259 (1983).

E-2. A. E. Dukler and Y. Taitel, "Flow Pattern Transitions in Gas-Liquid Systems: Measurements and Modeling," Chapter 1 in *Multiphase Science and Technology*, G. F. Hewitt, J. M. Delhaye, and N. Zuber, editors (Hemisphere Publishing Company, New York, 1986), Vol. 2, 1-94.

E-3. W. G. Choe, L. Weinberg, and J. Weisman, "Observation and Correlation of Flow Pattern Transitions in Horizontal Cocurrent Gas-Liquid Flow," in *Two-Phase Transport and Reactor Safety*, T. N. Veziroglu and S. Kakac, editors (Fort Lauderdale, Florida, 1976), Vol. IV, 1357-1393.

E-4. K. Mishima and M. Ishii, "Theoretical Prediction of Onset of Horizontal Slug Flow," *Trans. ASME, J. Fluids Engineering* 102, 441-445 (1980).

E-5. J. M. Mandhane, G. A. Gregory, and K. Aziz, "A Flow Pattern Map for Gas Liquid Flow in Horizontal Pipes," *Int. J. Multiphase Flow* 1, 537-553 (1974).

E-6. D. Barnea, O. Shoham, and Y. Taitel, "Flow Pattern Transition for Downward Inclined Two-Phase Flow; Horizontal to Vertical," *Chem. Eng. Sci.* 37, 741 (1982).

E-7. Y. Taitel, D. Barnea, A. E. Dukler, "Modeling Flow Pattern Transitions for Steady Upward Gas-Liquid Flow in Vertical Tubes," *AIChE J.* 26, 345-354 (1980).

E-8. M. Ishii and K. Mishima, "Study of Two-Fluid Model and Interfacial Area," Argonne National Laboratory report ANL-80-111 (NUREG / CR-1873) (1980).

E-9. K. Mishima and M. Ishii, "Flow Regime Transition Criteria for Upward Two-Phase Flow in Vertical Tubes," Int. J. Heat Mass Transfer 27, 723-737 (1984).

E-10. O. C. Jones and N. Zuber, "The Interaction between Void Fraction Fluctuations and Two-Phase Flow Patterns in Two-Phase Flow," Int. J. Multiphase Flow 2, 273-306 (1975).

APPENDIX F

FLUID ENERGY CLOSURE

This section describes the closure relationships for the energy equations given in Section 2.1.1. The quantities required are the phase-change rate, Γ, phasic interfacial heat flows, q_{ig} and q_{il}, sensible heat flow between liquid and gas, q_{gl}, and phasic wall heat flows, q_{wl} and q_{wg}. Section F.1. below will discuss the interfacial heat transfer between phases, and Section F.2. will discuss wall-to-fluid heat transfer. Before the reader begins this section, a review of the following sections is recommended: Section 2.1., and Appendices D and E. The following nomenclature applies to the models discussed in this section.

NOMENCLATURE

a_i: interfacial-area concentration
$a_1 - a_4$: empirical constants [see Eq. (F-97)]
A: area
$\bar{A}$: average area
A_f: cell-edge flow area
A_{fr}: interfacial surface area for bubbles traveling in the liquid core
B: volume
$\bar{B}$: average volume
B_{cell}: cell volume
c_p: specific heat at constant pressure ($J \cdot kg^{-1} \cdot K^{-1}$)
C^*: dummy constant [see Eq. (F-21)]
C_1, C_2: relaxation constants
C_c: correction factor for droplet internal circulation
C_{eva}: coefficient of evaporation
C_i: steam concentration at the interface
C_r: correction factor for liquid-film interfacial area
C_{u1}, C_{u2}: empirical constants in Eq. (F-118).
Ca: capillary number
D: diameter (m)
D^*: dummy diameter [see Eq. (F-20)]
D_o: diffusion coefficient (m / s)
D_b: bubble Sauter mean diameter
$D_{b,A}$: bubble area-equivalent diameter
$D_{b,V}$: bubble volume-equivalent diameter

D_c: cap-bubble base diameter

D_d: droplet Sauter mean diameter

D_H: hydraulic diameter (m)

D_{vm}: droplet volume median diameter

E: entrainment fraction

f: new-time fraction in Eq. (F-160) or friction factor in Section F.2.2.4.

f_{cp}: two-phase friction factor

f_l: liquid fraction contacting wall

F: correction factor to Dittus-Boelter equation

F_s: sink function

F_u: cold-wall fraction

g: gravitational constant

G: mass flux (kg/m^2-s)

h: heat-transfer coefficient ($W \cdot m^{-2} \cdot K^{-1}$)

h': separate phasic heat-transfer coefficient ($W \cdot m^{-2} \cdot K^{-1}$)

h^*: phasic enthalpy

h_{fg}: latent heat of vaporization

h_{fls}: liquid-side HTC due to flashing

h_{gl}: gas-to-liquid sensible heat-transfer coefficient

h_{gsav}: single-phase wall-to-vapor heat-transfer coefficient

h'_{lg}: modified latent heat to account for the superheated vapor ($J \cdot kg^{-1}$)

h_M: mass-transfer coefficient

h_r: radiation heat-transfer coefficient ($W \cdot m^{-2} \cdot K^{-1}$)

h_Γ: subcooled-boiling heat-transfer coefficient ($W \cdot m^{-2} \cdot K^{-1}$)

H_{ALV}: liquid-side heat-transfer factor during flashing

H_{ALVE}: liquid-side heat-transfer factor during condensation and evaporation

H_{CHTA}: gas-to-liquid sensible heat-transfer factor

H_{CHTI}: vapor-side heat-transfer factor

H_o: empirical constant [see Eqs. (F-30), (F-32)]

J: superficial velocity ($m \cdot s^{-1}$) or volumetric flux

k: thermal conductivity ($W \cdot m^{-2} \cdot K^{-1}$)

l_{min}: thickness related to minimum film thickness

L: length (m)

L_b: length over which saturated boiling takes place (m)

L_c: characteristic length

L_l: stratified liquid level

L_o: Laplace coefficient

M: molecular weight ($kg \cdot mol^{-1}$)

M_{plug}: multiplication factor for plug flow interfacial area

$\dot{m}_e$: evaporative mass flux

$\dot{m}_v$: film vapor mass flux

N: number of bubbles in Section F.1. or number of fields in Section F.2.

P: total pressure (Pa)

q: phasic sensible energy rate of change (heat-transfer rate)

q': heat flux ($W \cdot m^{-2}$)

q_{gl}: sensible heat flow between liquid and gas

q_{total}: total wall heat-transfer rate

q_{wi}: wall-to-water interface heat-transfer rate

r: radius of radial ring

R: gas constant

s: slip ratio

S: suppression factor in Chen correlation

t: time (s)

t_d: droplet thermal boundary layer lifetime

T: temperature (K)

T^*: dimensionless droplet mixing-cup temperature

T_{NH}: homogenous nucleation temperature

T_{sv}: saturation temperature corresponding to steam partial pressure (K)

V: velocity ($m \cdot s^{-1}$)

V_{bubble}: bubble terminal velocity

V_c: Helmholtz velocity

V^*_{max}: dimensionless droplet maximum circulation velocity

WF, W: weighting factor

W_f: annular-mist-flow weighting factor

W_{fd}: cold-wall liquid-film-flow weighting factor

W_t: transition-flow weighting factor

x: mass quality

x_e: equilibrium quality

x_f: flow quality

X: dummy variable

X_{TT}: Martinelli parameter

z: axial elevation

z_b: bottom elevation of the hydro cell

z_c: entry length for equilibrium entrainment fraction

z_t: top elevation of the hydro cell

Z: transition elevation between flow regimes

α: void fraction

α_d: droplet fraction in gas core

α_{dd}: droplet fraction in channel cross section

α_f: cold-wall liquid-film fraction

α_{fr}: void fraction for bubbles traveling in the liquid-core region

α_{gs}: average void fraction within the liquid slug

α_{hom}: homogeneous void fraction

β: coefficient of thermal expansion (K^{-1})

δ_f: film thickness

Δq: change in heat flux

ΔT_e: effective superheat

Δt: time-step size or time increment (s)

ΔT_{min}: wall superheat at minimum film boiling point (K)

ΔT_{HN}: wall superheat at homogenous nucleation temperature (K)

ΔT_{sat}: wall superheat

ΔT_{sub}: liquid subcooling (°C)

Δr: radial ring increment for 3D component

Δx: cell length for 1D component (m)

Δz: axial level increment for 3D component

$\Delta\theta$: azimuthal segment increment for 3D component

ε: emissivity or surface roughness

Γ: phase change rate per unit volume ($kg / m^3\text{-}s^1$)

λ: square root of phasic density-viscosity product ratio or Taylor instability wavelength defined by Eq. (F-250)

κ: phasic viscosity ratio

μ: dynamic viscosity (Pa·s)

θ: angle of inclination from horizontal (rad)

ρ: density ($kg \cdot m^{-3}$)

σ: surface tension ($N \cdot m^{-1}$)

σ_r: Stefan-Boltzmann constant ($W \cdot m^{-2} \cdot K^{-4}$)

ϕ: cap-bubble wake angle

Ψ: sphericity

χ: dummy integration variable

τ: time (s)

ξ: transition-boiling weighting factor in Section F.2.1.3.1. or coefficient dependent upon the velocity profile in the vapor film in Section F.2.2.4.1.

Subscripts

a: noncondensable gas or air [in Eq. (F-150)]

AG: agitated IAF regime

Brom: related to the Bromley correlation

bub: bubbly flow

CHF: critical heat flux

cond: condensation

core: liquid core

crit, *cr*: critical

D: drag

d: droplet

Den: related to the Denham correlation

dr: related to Dougall-Rohsenow correlation

drop: droplet

DP, *ds*: dispersed (or post-agitated) flow

f: film properties

fBB: related to Bromley correlation

forc: forced convection

film: film boiling

g: gas-vapor mixture

grid: grid spacer

i: interfacial or radial ring counter for 3D component

inv: inverted annular flow

j: azimuthal segment or cell counter for 3D or 1D component

k: axial level counter for 3D component

l: liquid

lam: laminar flow

m: two-phase mixture properties

map: quantities calculated using the basic flow-regime map

max: maximum

min: minimum film boiling or minimum
mist: annular-mist flow
Mod: modified
mod-CSO: modified Chen-Sundaram-Ozkaynak
n: arbitrary index of a single bubble
NC: natural convection
nc: in the presence of noncondensables
nucb: nucleate boiling
plug: plug flow
post-ag: post-agitated flow
RW, *rw*: rough-wavy inverted annular flow
s: steam
sat: saturation
sb: bubbly and transition flow
SM, *sm*: smooth inverted annular flow
st: stratified flow
sub: subcooled boiling
teo: theoretical
TR,trans: transition boiling
TP: two phase
turb: turbulent flow
v: vapor
vf: vapor at film temperature
w: wall
wl: wall-to-liquid
wg: wall-to-gas
∞: infinity

Dimensionless Numbers

Eo: Eötvös number
Gr: Grashof number
Ja: Jakob number
Mo: Morton number
Nu: Nusselt number
N_{μ}: viscosity number
Pe: Peclet number

Pr: Prandtl number
Re: Reynolds number
Sc: Schmidt number
Sh: Sherwood number
St: Stanton number
We_b: bubble Weber number
We_e: effective Weber number
We_m: modified Weber number

F.1. Interfacial Heat Transfer

As discussed before, TRAC solves nonequilibrium, two-phase-flow equations where the liquid and the gas phases are not in thermodynamic equilibrium. As a result, the different phasic temperatures lead to a heat and mass exchange between the phases through the interface. The interfacial transport is calculated in subroutines TF1DS and TF3DS for 1D and 3D components, respectively.

The gas phase is assumed to be a homogeneous mixture of vapor and noncondensable gas in thermodynamic equilibrium. Further, the mixture obeys Dalton's law. The rate of change of the gas-phase sensible energy is given by

$$q_g = \underbrace{\frac{P_s}{P} H_{\mathrm{CHTI}}(T_g - T_{sv})}_{\text{gas to interface}} + \underbrace{\frac{P_a}{P} H_{\mathrm{CHTA}}(T_g - T_l)}_{\text{gas to liquid}} , \tag{F-1}$$

where H is the heat-transfer factor, defined as the product of the convective heat-transfer coefficient and the interfacial area. The first term in Eq. (F-1) corresponds to heat transfer to or from the interface (q_{ig}) and is converted to or released as latent heat through phase change. The second term is the direct sensible heat exchange between the liquid and the gas.

Similarly, the rate of change of the liquid-phase sensible energy is given by

$$q_l = \underbrace{\{H_{\mathrm{ALVE}}(T_l - T_{sv}) + H_{\mathrm{ALV}}\langle T_l - T_{\mathrm{sat}}\rangle'\}}_{\text{liquid to interface}} + \underbrace{\frac{P_a}{P} H_{\mathrm{CHTA}}(T_l - T_g)}_{\text{liquid to gas}} . \tag{F-2}$$

Likewise, the first term (q_{il}) accounts for the sensible heat transferred to or from the interface where it is converted to or released as latent heat, and the second term is the direct sensible heat exchange between the liquid and the gas. In TRAC, evaporation and flashing are accounted for separately. Consequently, we have two liquid-side interfacial heat-transfer factors, H_{ALV} and H_{ALVE}. For condensation and evaporation, H_{ALVE} is used. As shown in Fig. F-1., evaporation occurs if $T_{sv} < T_l < T_{\mathrm{sat}}$ and flashing occurs if $T_l > T_{\mathrm{sat}}$.

H_{ALV} is used during flashing. Note that the flashing term is incorporated into Eq. (F-2) through a singularity function, which is defined as follows:

$$\langle T_l - T_{sat} \rangle' = \begin{cases} 0 & \text{if } T_l \le T_{sat} \\ T_l - T_{sat} & \text{if } T_l > T_{sat} \end{cases} .$$

When Eqs. (F-1) and (F-2) are added, the direct sensible heat-transfer terms cancel out, and we can calculate the mass-transfer rate per unit volume as a result of interfacial heat transfer between the phases as

$$\Gamma_i = \frac{q_{ig} + q_{il}}{B_{cell}(h_v^* - h_l^*)} , \tag{F-3}$$

where

$$q_{il} = \underbrace{H_{ALVE}(T_l - T_{sv})}_{\text{evaporation or condensation}} + \underbrace{H_{ALV}\langle T_l - T_{sat}\rangle'}_{\text{flashing}} \tag{F-4}$$

and

$$q_{ig} = \frac{P_s}{P} H_{CHTI}(T_g - T_{sv}) . \tag{F-5}$$

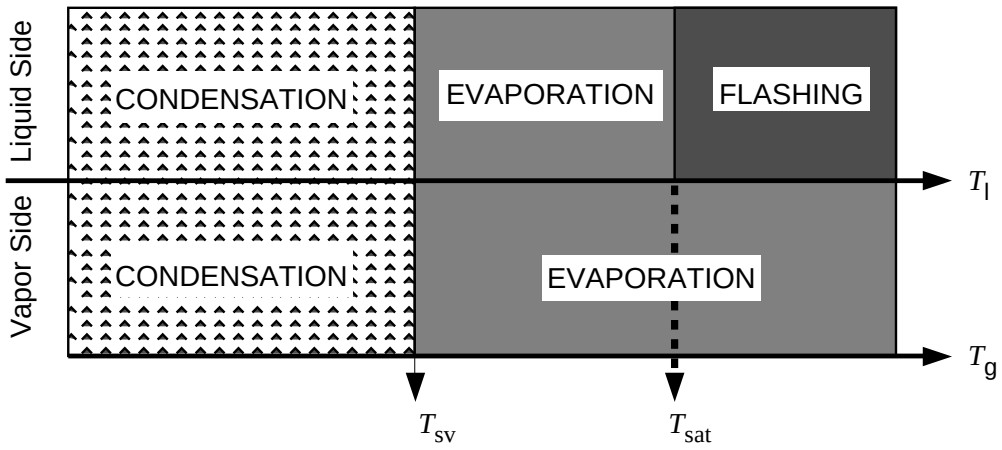

Fig. F-1. Illustration of the selection logic for condensation, evaporation, and flashing.

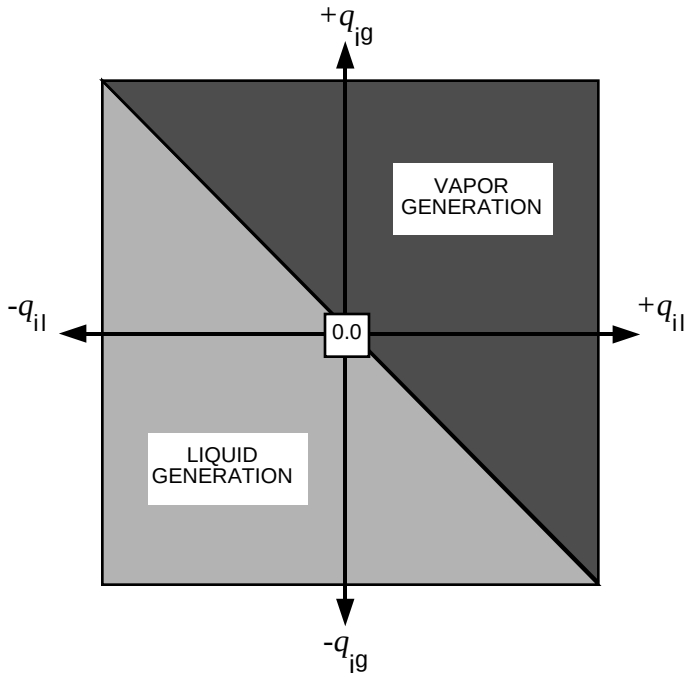

Fig. F-2. Interfacial mass-transfer map.

A positive Γ_i indicates vapor generation and a negative Γ_i indicates liquid generation. Notice that while q_{ig} is negative, q_{il} may be positive, and vice versa. The net vapor or liquid generation is determined by the relative magnitude of these quantities and is illustrated in Fig. F-2. The total rate of phase change also includes the effect of subcooled boiling and is given by

$$\Gamma = \Gamma_i + \Gamma_{sub} \ , \tag{F-6}$$

where Γ_{sub} is determined through wall heat transfer and is treated in Section G.1.

To calculate q_g, q_l, and Γ_i, we need closure relationships for the interfacial area and liquid- and vapor-side heat-transfer coefficients, which provide H_{ALVE}, H_{ALV}, H_{CHTI}, and H_{CHTA}. These closure relationships are provided in subroutine HTIF for 1D and 3D components and are described in the following sections for various flow regimes. In general, the interfacial area and convective heat-transfer coefficients depend on the flow pattern and are calculated in conjunction with a flow-regime map. The flow-regime map of TRAC is discussed in Appendix E and the details are not repeated here. For the sake of completeness, the basic flow-regime map is redrawn in Fig. F-3.

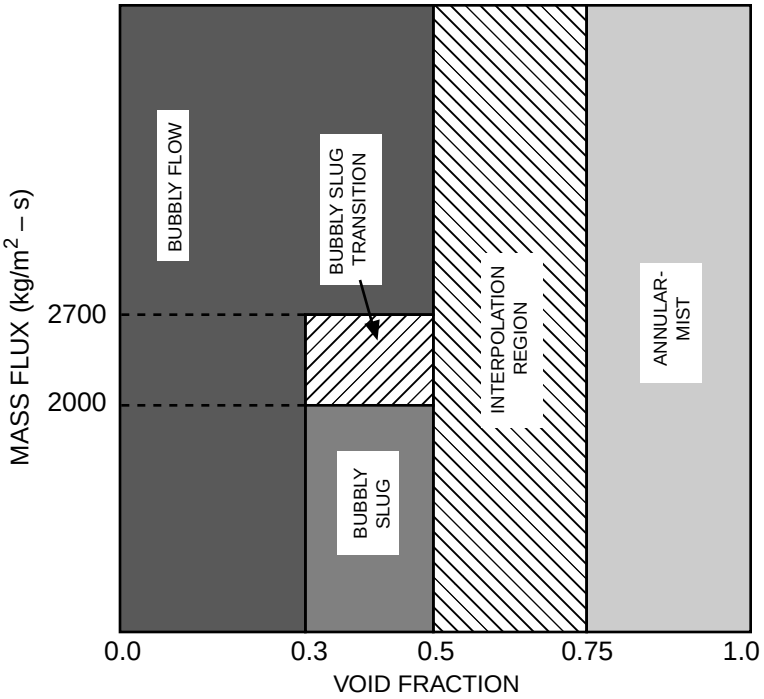

Fig. F-3. TRAC basic flow-regime map.

F.1.1. Models and Correlations in Bubbly Slug Flow

In this section and its subsections, we collectively refer to the three regions in Fig. F-3. labeled "bubbly flow," "bubbly slug transition," and "bubbly slug" as bubbly slug flow. The logic used in determining pure bubbly and transition flows is explained below in Section F.1.1.1. Older versions of TRAC documentation called the "bubbly slug" region in Fig. F-3. simply "slug" flow. Physically, the current names in Fig. F-3. are more accurate (although strictly, "bubbly slug transition" should be called bubbly / bubbly slug transition), but it is more convenient to combine the three names in the figure under the single term "bubbly slug" when describing the interfacial area logic.

For void fractions less than 30%, slugs do not form, irrespective of the mass flux. For void fractions between 30% and 50%, slugs and bubbles coexist for $G < 2000$ kg / m^2-s and slug formation is prohibited for $G > 2700$ kg / m^2-s. The intermediate mass-flux range is treated as a transition region. The models for interfacial area and convective heat-transfer coefficients in bubbly slug flow are described in the following section. The convective-heat-transfer coefficients during condensation and flashing are described in this section. Evaporation is included in Section F.1.7. because it can occur only in the presence of noncondensables. The direct sensible heat transfer between gas and liquid also is possible only in the presence of noncondensables. However, these models are flow-regime dependent and very similar to vapor-to-interface heat-transfer models.

Consequently, the calculation of H_{CHTA} is included in this section, even though it is meaningless unless noncondensables are present.

F.1.1.1. Description of Interfacial-Area Model. An idealized flow pattern for bubbly slug flow (in the sense of Fig. F-3.) is shown in Fig. F-4. Starting from the geometrically idealized shapes in this figure, Ishii and Mishima obtained (Ref. F-1., p. 32, Eq. 54)

$$a_{i,\,\text{bubbly slug}} = \frac{1}{D_{\text{slug}}}\frac{\alpha-\alpha_{gs}}{1-\alpha_{gs}}\frac{4+\dfrac{D_{\text{slug}}}{L_{\text{slug}}}}{1-\dfrac{D_{\text{slug}}}{6L_{\text{slug}}}} + \frac{6\alpha_{gs}}{D_b}\frac{1-\alpha}{1-\alpha_{gs}}\ , \tag{F-7}$$

where a_i is the interfacial-area concentration, α_{gs} is the average void fraction within the liquid slug, and D_b is the Sauter mean diameter of a spherical bubble population. Assuming that $D_{\text{slug}}/L_{\text{slug}} << 4$ and $D_{\text{slug}} \approx 0.88 D_H$, Ishii and Mishima obtained (Ref. F-1., p. 32, Eq. 55)

$$a_{i,\,\text{bubbly slug}} = \frac{4.5}{D_H}\frac{\alpha-\alpha_{gs}}{1-\alpha_{gs}} + \frac{6\alpha_{gs}}{D_b}\frac{1-\alpha}{1-\alpha_{gs}}\ . \tag{F-8}$$

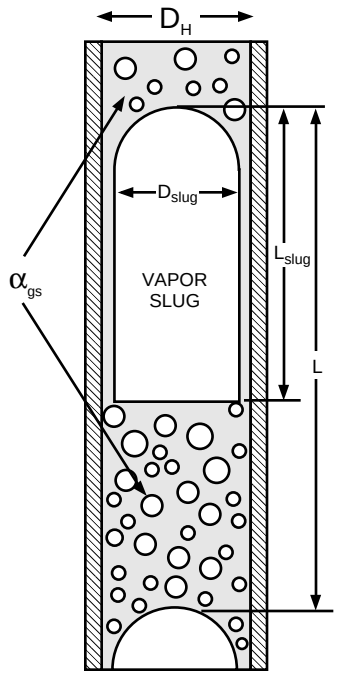

Fig. F-4. Schematic of flow pattern in bubbly slug flow.

In the code this equation appears as

$$a_{i,\text{ bubbly slug}} = \frac{C^*}{D^*}\frac{\alpha-\alpha_{gs}}{1-\alpha_{gs}} + \frac{6\alpha_{gs}}{D_b}\frac{1-\alpha}{1-\alpha_{gs}} \tag{F-9}$$

to include the cap-bubble regime for channels with large hydraulic diameters. The parameters C^* and D^* depend upon whether we have vapor slugs or cap bubbles and are a function of the channel hydraulic diameter. They will be described in Section F.1.1.1.2. Once the interfacial-area concentration is calculated using Eq. (F-9), it is converted to total interfacial area within a given cell through

$$A_{i,\text{ bubbly slug}} = a_{i,\text{ bubbly slug}} B_{\text{cell}} \ , \tag{F-10}$$

where B_{cell} is the cell volume.

In the code, we calculate the average void fraction in the liquid slug, α_{gs}, as follows:

$$\alpha_{gs} = \begin{cases} 0.3 & \text{if } G < 2000 \text{ kg / m}^2\text{-s} \\ 0.3 + 0.2\left(\frac{G-2000}{700}\right) & \text{if } 2000 \le G < 2700 \text{ kg / m}^2\text{-s} \\ 0.5 & \text{if } G \ge 2700 \text{ kg / m}^2\text{-s} \end{cases} . \tag{F-11}$$

Fernandes (cited in Ref. F-2.) measured α_{gs} in a 5-cm-diameter vertical pipe. In bubbly slug flow, the average α_{gs} is reported as ~27.5%. Barnea and Shemer (Ref. F-2.) also measured α_{gs} in a 5-cm-diameter vertical pipe. They obtained an average value of ~25%. This void fraction also corresponds to the transition from bubbly to bubbly slug flow (in the sense of Fig. F-3.) in their experiment where $G \approx 10$ kg / m^2-s. They concluded that, in the liquid slug between the vapor slugs, the flow behaves as bubbly flow. Based upon this observation, we set $\alpha_{gs} = 0.3$ at mass fluxes less than 2000 kg / m^2-s. This void fraction also corresponds to the case where the probability of collision between spherical bubbles becomes very high, as discussed by Ishii and Mishima (Ref. F-1., p. 37). For $G \approx 2700$ kg / m^2-s, we set $\alpha_{gs} = 0.5$ to be consistent with our flow-regime map. In the intermediate mass flux range, α_{gs} is obtained through linear interpolation as given by Eq. (F-11).

If the actual void fraction, α, is less than α_{gs}, then α_{gs} is set equal to α, i.e., the flow is pure bubbly. The first term in Eq. (F-9) becomes zero and only bubbles contribute to the interfacial-area concentration.

F.1.1.1.1. Bubbly Flow Interfacial Area. In order to compute the bubbly flow interfacial area, we need the Sauter mean diameter of the bubble population. Depending upon the flow conditions and bubble-generation techniques, a wide range of bubble diameters are observed in the literature. We used a simple expression suggested by Ishii (Ref. F-3.), as follows:

$$D_b = 2L_o \ , \tag{F-12}$$

where L_o is the Laplace coefficient defined as

$$L_o = \sqrt{\frac{\sigma}{g(\rho_l - \rho_g)}} \ . \tag{F-13}$$

Ishii suggested this expression as an approximate arithmetic average of minimum and maximum bubble diameters observed experimentally. Figure F-5. shows the bubble diameter given by Eq. (F-12) in saturated water as a function of pressure. As shown, bubble diameter is a weak function of pressure and decreases with increasing pressure. As the pressure increases from atmospheric to 10 MPa, the bubble diameter decreases from 5 to 2.8 mm. In the code, the upper and lower limits for bubble diameter are as follows:

$$0.1 \text{ mm} \le D_b \le 0.9 D_H \ .$$

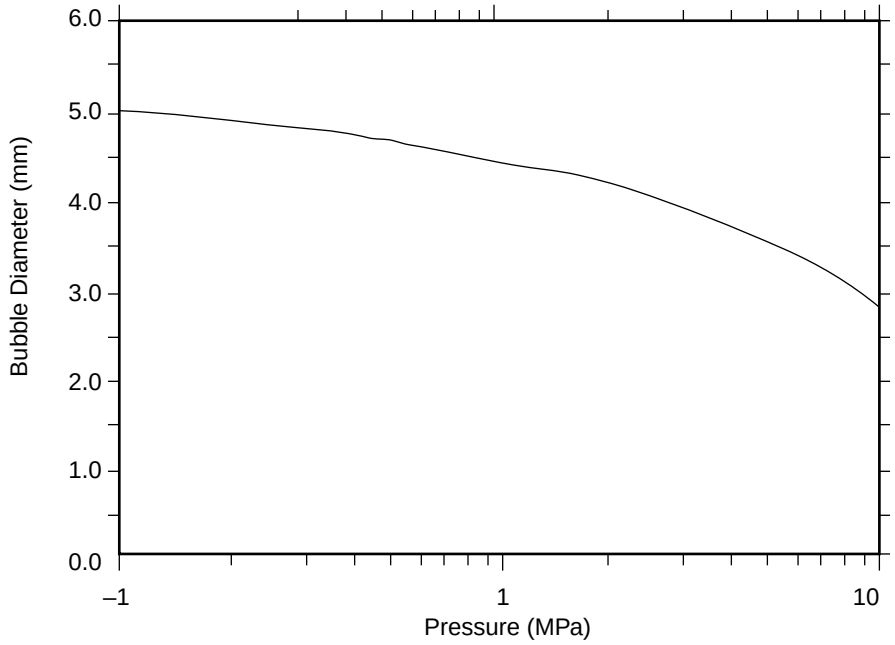

Fig. F-5. Calculated bubble diameters for saturated water as a function of pressure.

F.1.1.1.2. Bubbly Slug Flow Interfacial Area. If $\alpha > \alpha_{gs}$, then slugs or cap bubbles form, depending upon the diameter of the flow channel, and the first term in Eq. (F-9) contributes to the interfacial-area concentration. If the hydraulic diameter is less than a critical diameter, slugs can form and we use $C^* = 4.5$ and $D^* = D_H$ as given by Eq. (F-8). Otherwise, cap bubbles can form and appropriate magnitudes for C^* and D^* must be used.

Kataoka and Ishii (Ref. F-4., p. 1933) state that the slug bubbles cannot be sustained in channels with a diameter much larger than $40L_o$. Because of interfacial instability, the slug bubbles disintegrate into cap bubbles. This argument is also consistent with the data of Grace et al. (Ref. F-5.) and the analysis of Kitscha and Kocamustafaogullari (Ref. F-6.). The analysis shows that the maximum stable bubble diameter in an infinite liquid is given by (Ref. F-6., Eq. 44)

$$D_{b,V} = 27.07(1 + N_\mu)^{0.83} L_o \ , \tag{F-14}$$

where $D_{b,V}$ is the volume-equivalent bubble diameter and N_μ is the viscosity number defined as

$$N_\mu = \frac{\mu_l}{\sqrt{\rho_l \sigma L_o}} \ . \tag{F-15}$$

Equation (F-14) agrees well with the data of Grace et al. (Ref. F-5., Fig. 8). For water, $N_\mu << 1$, thus

$$D_{b,V} = 27.07 L_o \ . \tag{F-16}$$

To compare this expression with the criterion of Kataoka and Ishii and the critical channel diameter, we need to convert the volume-equivalent diameter to cap-base diameter.

An idealized cap bubble is shown in Fig. F-6. Ishii and Mishima (Ref. F-1., p. 31) state that the observed wake angle ϕ ranges from 46° to 65°. From pure geometry and using $\phi \approx 55°$, it can be shown that

$$D_{b,V} = 0.6 D_c \ , \tag{F-17}$$

where D_c is the cap-base diameter. Thus, Eq. (F-16) becomes

$$D_c = 45 L_o \ , \tag{F-18}$$

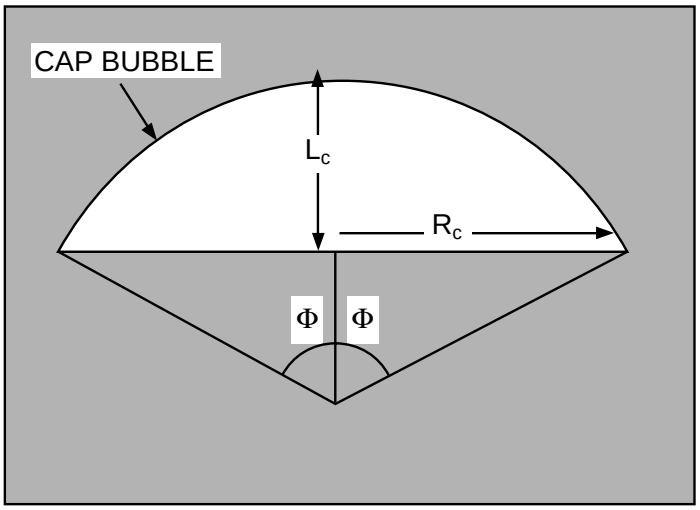

Fig. F-6. Schematic of idealized cap bubble.

which agrees with the criterion cited by Kataoka and Ishii. In the code we assumed that $D_c = 0.9D_{\mathrm{H,crit}}$, which yields

$$D_{H,\mathrm{crit}} = 50L_o \quad . \tag{F-19}$$

For saturated water, the critical hydraulic diameter is plotted as a function of pressure in Fig. F-7. As shown, the transition from vapor slugs to cap bubbles occurs at smaller hydraulic diameters with increasing pressure. Using Fig. F-6., it can also be shown that C^*=16 for cap bubbles. Consequently, Eq. (F-9) is coded as follows:

$$D^* = \begin{cases} D_H & \text{if } D_H < D_{H,\mathrm{crit}} \\ D_{H,\mathrm{crit}} & \text{if } D_H \geq D_{H,\mathrm{crit}} \end{cases} \tag{F-20}$$

and

$$C^* = \begin{cases} 4.5 & \text{if } D_H < D_{H,\mathrm{crit}} \\ 16 & \text{if } D_H \geq D_{H,\mathrm{crit}} \end{cases} \quad . \tag{F-21}$$

Figure F-8. illustrates the interfacial-area concentration calculated by TRAC as a function of void fraction and mass flux in the bubbly slug flow regime.

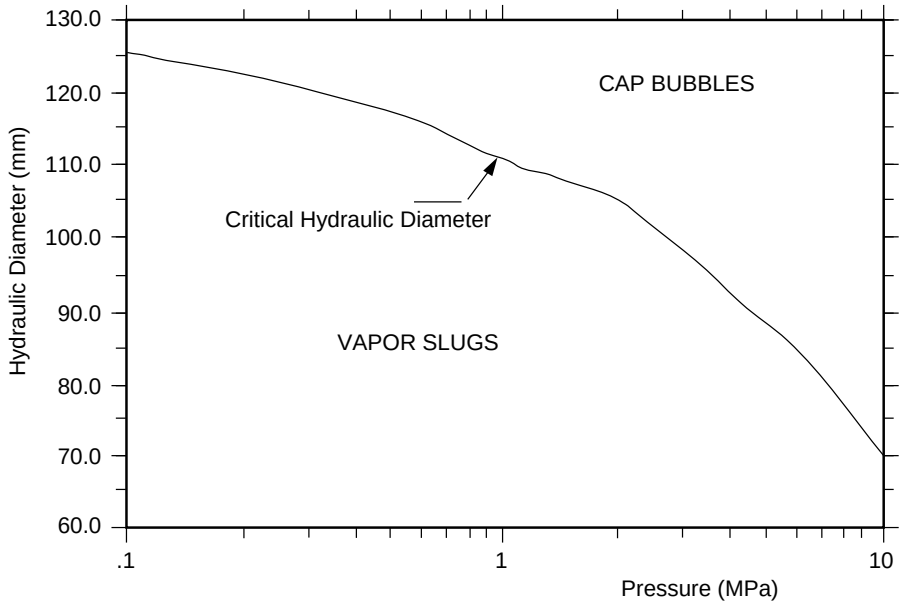

Fig. F-7. Vapor-slug-to-cap-bubbles transition map for saturated water.

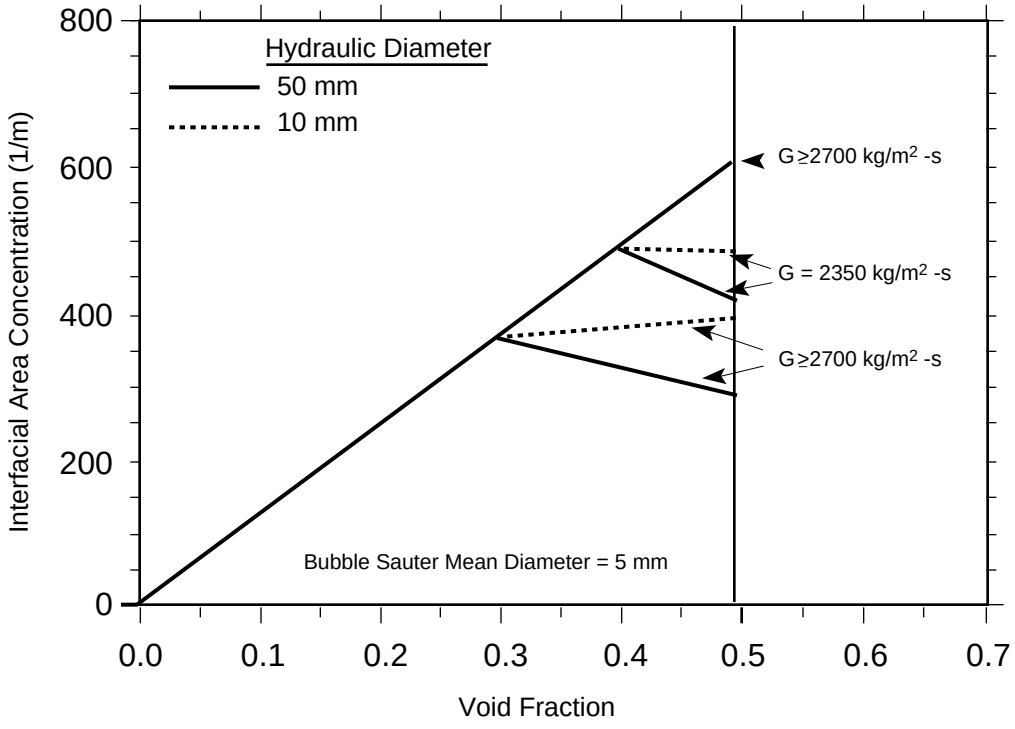

Fig. F-8. Interfacial-area concentration calculated by TRAC in bubbly slug flow.

F.1.1.2. Description of Heat-Transfer Coefficients Models. If the liquid temperature is smaller than the saturation temperature, the liquid side is in condensation mode. To calculate the heat-transfer coefficient during condensation, the correlation developed by Chen and Mayinger is used (Ref. F-7., p. 151, Eq. 24). The correlation is given by

$$Nu = 0.185\ Re^{0.7}\sqrt{Pr_l} \quad , \tag{F-22}$$

where

$$Nu = \frac{h_{il} D_b}{k_l}$$

and

$$Re = \frac{\rho_l D_b (V_g - V_l)}{\mu_l} \quad .$$

In these experiments, bubbles were produced by blowing saturated vapor into subcooled liquid slowly moving downward. Heat-transfer data are obtained at the interface of condensing bubbles using holographic interferometry and high-speed photography. Ethanol, propanol, refrigerant-113, and water were used as working fluids. These fluids provided Prandtl numbers ranging from 1.96 to 14.4. The experimental Reynolds number ranged from ~350 to ~7000. However, the Reynolds number for only water data had a shorter range from ~4000 to ~7000. In deriving the correlation given by Eq. (F-22), Chen and Mayinger used the experimentally observed bubble detachment diameter in defining *Re* and *Nu*. In the code, we used the Sauter mean diameter given by Eq. (F-12). Chen and Mayinger recommend the use of their correlation for $Re < 10^4$ and $Ja < 80$. The Jakob number, *Ja*, is a measure of liquid subcooling and is defined as

$$Ja = \frac{\rho_l c_{p,l} \Delta T_{sub}}{\rho_g h_{fg}} \quad .$$

For $Ja < 80$, the condensation is controlled by heat transfer at the phase interface. If $Ja > 100$, the collapse of the vapor bubble is controlled by the inertia of the liquid mass when entering into the space set free by the condensing bubble. The Chen and Mayinger correlation is valid for heat-transfer-controlled condensation. However, in the code, it is also used in the inertia-controlled regime, independently of the Jakob number.

At high Reynolds numbers, we assumed that the Nusselt number is independent of the Reynolds number. This upper limit is calculated through the Chen and Mayinger correlation by setting $Re = 10^4$, which yields

$$Nu_{max} = 116.7\sqrt{Pr_l} \quad . \tag{F-23}$$

For water, $Re = 10^4$ corresponds to 0.5–0.6 m/s bubble-relative velocities, which are higher than observed terminal bubble-rise velocities. Thus, for quasi-steady conditions, the Reynolds numbers are usually smaller than 10^4. At low Reynolds numbers, the Chen and Mayinger correlation yields Nusselt numbers smaller than solid-sphere correlations, which is not realistic. Thus, we used the solid-sphere heat-transfer correlation of Whittaker (Ref. F-8.) as the lower limit of the Nusselt number. The original correlation is given by

$$Nu = 2 + (0.4\sqrt{Re} + 0.06Re^{2/3})Pr_l^{0.4}\left(\frac{\mu_w}{\mu_\infty}\right) , \tag{F-24}$$

where the Reynolds and Nusselt numbers are defined based upon the sphere diameter, and μ_w and μ_∞ are the fluid viscosities at the sphere wall and far field, respectively. In the code, we neglected the viscosity correction and used the bubble diameter instead of sphere diameter to obtain

$$Nu = 2 + (0.4\sqrt{Re} + 0.06Re^{2/3})Pr_l^{0.4} . \tag{F-25}$$

Figure F-9. shows the code-calculated Nu as a function of Re for two values of Pr that are representative of high and low limits for water. Once the liquid-side heat-transfer coefficient is obtained, the heat-transfer factor for condensation is calculated as

$$H_{\text{ALVE, bubbly slug}} = h_{il} A_{i,\text{ bubbly slug}} . \tag{F-26}$$

where $A_{i,\text{bubbly slug}}$ is the total interfacial area given by Eq. (F-10).

During flashing, where $T_l > T_{\text{sat}}$, the liquid-side heat-transfer factor is calculated using the following approximate model:

$$10^6 \le \frac{H_{\text{ALV, bubbly slug}}}{B_{\text{cell}}} = [20 \times 10^7 (T_l - T_{\text{sat}})] \le 20 \times 10^7 . \tag{F-27}$$

The basis for this model is its high magnitude, which quickly decreases the liquid temperature to saturation temperature. This model is flow-regime independent and is used for all flow patterns. It will be used in the other flow regimes as well.

For both condensation and flashing, the vapor-to-interface and gas-to-liquid heat-transfer coefficients are given by

$$h_{gl} = h_{ig} = 1000 \text{ W/m}^2\text{ K} . \tag{F-28}$$

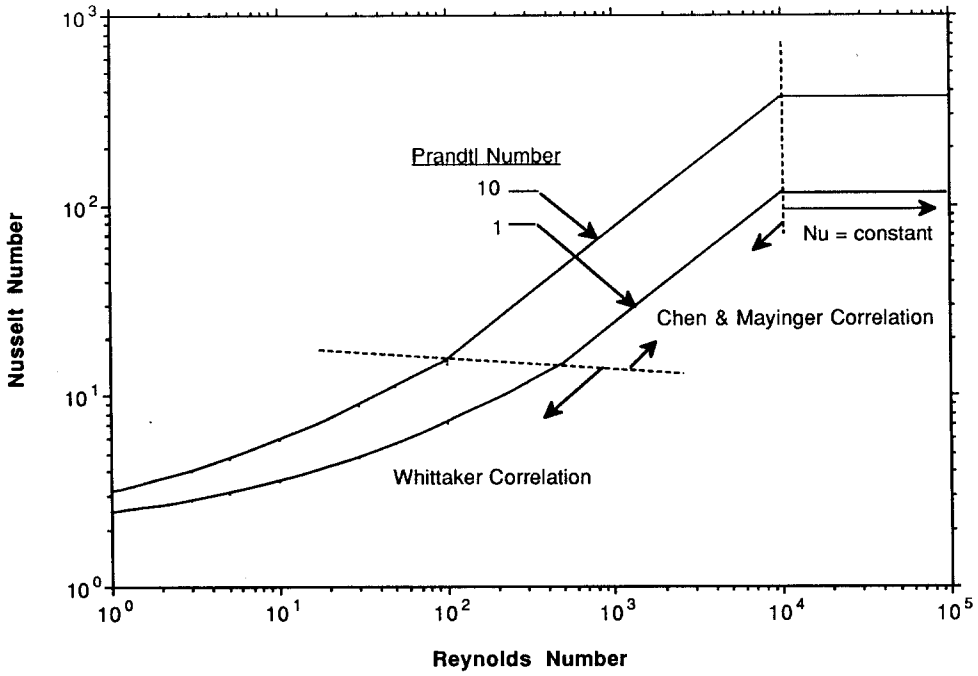

Fig. F-9. TRAC liquid-side heat-transfer-coefficient model during condensation in bubbly slug flow.

Thus,

$$H_{\text{CHTA, bubbly slug}} = H_{\text{CHTI, bubbly slug}} = 1000 A_{i,\text{ bubbly slug}} \ . \tag{F-29}$$

This is also an engineering approximation. This model is motivated by the fact that during quasi-steady conditions, the vapor-side heat-transfer coefficient is commonly about an order of magnitude smaller than the liquid-side heat-transfer coefficients.

F.1.1.3. Effect of Subcooled Boiling. The subcooled-boiling model is documented in Section G.1. and is not repeated here. In subcooled boiling, vapor is generated near the heater wall even though the bulk liquid is subcooled. However, part of this vapor condenses when in contact with the subcooled bulk liquid. Thus, during subcooled boiling, a mechanistic model is required to account for this interfacial condensation. We used the model suggested by Lahey and Moody (Ref. F-9., Eq. 5.174), which is given by

$$q_{\text{cond}} = H_o \frac{D_H}{4} h_{fg} \frac{\rho_l \rho_g}{\rho_l - \rho_g} \alpha (T_{sv} - T_l) \ , \tag{F-30}$$

where H_o is an empirical constant and q_{cond} is the interfacial condensation heat flux. Setting

$$\pi D_H q_{cond} \Delta x = H_{ALVE,sub}(T_{sv} - T_l) \ , \tag{F-31}$$

we obtain

$$H_{ALVE,sub} = H_o B_{cell} h_{fg} \frac{\rho_l \rho_g}{\rho_l - \rho_g} \alpha \ . \tag{F-32}$$

Lahey and Moody (Ref. F-9., p. 221) suggest $H_o = 0.075$ (s-K)$^{-1}$ and we used this value in the code.

We assumed that subcooled boiling can occur only in bubbly flow. Thus, the subcooled-boiling heat-transfer factor is superimposed on the bubbly flow liquid-side heat-transfer factor through a weighting factor as

$$H_{ALVE,bubbly/sub} = W_{sub} H_{ALVE,sub} + (1 - W_{sub}) H_{ALVE,bubbly} \ , \tag{F-33}$$

where the weighting factor is given by

$$0 \le W_{sub} = 10(0.2 - \alpha) \le 1 \ . \tag{F-34}$$

As shown by this equation, if the void fraction is greater than 0.2, the weighting factor becomes zero. Thus, for the subcooled-boiling effect to be present in the interfacial heat transfer, the following conditions must be satisfied:

7. The liquid temperature must be less than saturation temperature.
8. Subcooled boiling must be occurring ($h_\Gamma > 0$).
9. The void fraction must be less than 20%.

F.1.1.4. Assessment. As cited by Ishii and Mishima (Ref. F-1.), there are a number of studies where interfacial areas are measured by chemical-absorption techniques. In these studies, the measured interfacial-area concentrations are reported as a function of liquid and vapor volumetric fluxes. To compare the data with the TRAC prediction, we need the interfacial-area concentration as a function of void fraction. A limited number of studies report void-fraction measurements along with interfacial-area concentration data. The majority of the data correspond to high void fractions. These studies are discussed in Section F.1.10.

Figure 10 in Ref. F-7. shows the comparison of the Chen and Mayinger correlation with their own data. As shown, ±25% discrepancy is typical between the water data and the correlation. The discrepancy increases with an increasing Prandtl number (see the refrigerant-113 data). To assess the Chen-Mayinger bubble-condensation correlation, first we compared it with some of the solid-sphere correlations. The correlations used for this comparison are the ones given by McAdams (Ref. F-10.) as

$$Nu = 0.37 Re^{0.6} \quad , \tag{F-35}$$

by Vliet and Leppert (Ref. F-11.) as

$$Nu \times Pr^{0.3} \left(\frac{\mu_w}{\mu_\infty} \right) = 1.2 + Re^{0.54} \quad , \tag{F-36}$$

and by Whittaker (Ref. F-8.) in Eq. (F-25). Figure F-10. shows these correlations for a Prandtl number of unity. In plotting Eq. (F-36), the viscosity correction is neglected. As shown, within its range of applicability, the Chen and Mayinger correlation overpredicts all the solid-sphere data, as expected. At lower Reynolds numbers, all the solid-sphere correlations predict a higher Nusselt number than the Chen-Mayinger correlation. As a result, the Whittaker correlation is used in the code as the lower limit for the Chen-Mayinger correlation. Similar trends are observed at higher Prandtl numbers.

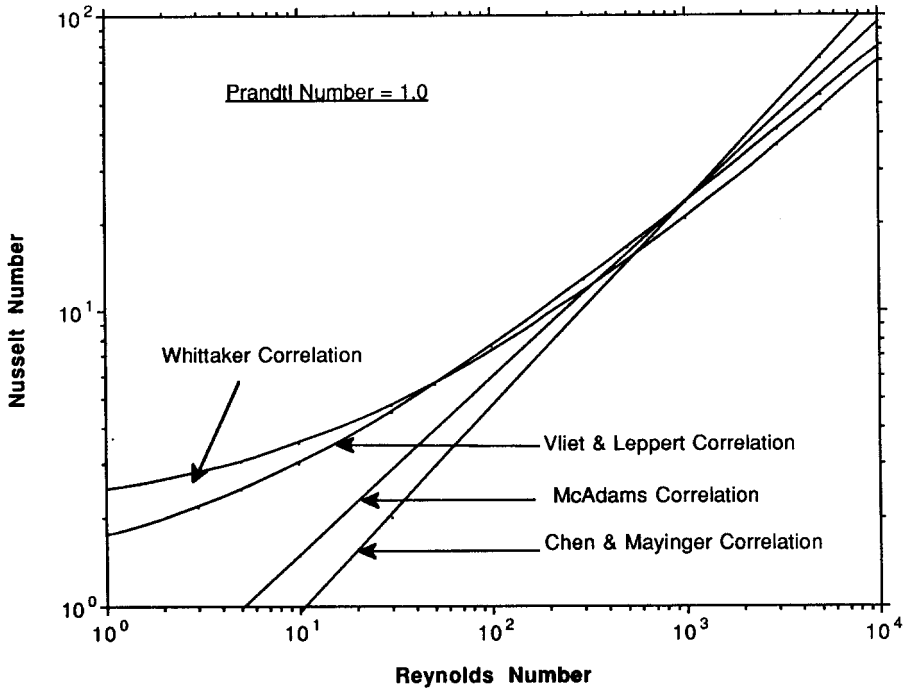

Fig. F-10. Comparison of the Chen and Mayinger with solid sphere heat-transfer correlations.

Brucker and Sparrow (Ref. F-12.) obtained data similar to the data of Chen and Mayinger by introducing steam bubbles into a quiescent subcooled water pool. The pressure in these experiments ranged from 10 to 62 bars. The subcooling of the water ranged from 15˚C to 100˚C and the initial bubble diameter was approximately 3 mm.

Data were obtained by high-speed motion-picture and frame-by-frame analysis. The bubble-rise velocity ranged from 15 to 25 cm/s, which roughly yields Reynolds numbers ranging from 3000 to 5000. Brucker and Sparrow reported an average heat-transfer coefficient of $h_{i\,l}$~10000 W/m^2-s. They further reported that all data fell within ±50% of this value as well as of the value predicted by the McAdams solid-sphere correlation given by Eq. (F-35). This range is in good agreement with the correlation of Chen and Mayinger, which suggests that their correlation can be extrapolated to higher pressures.

F.1.1.5. Conclusions and Final Remarks. In bubbly flow, vapor and noncondensable-gas mixture is the discontinuous phase and is distributed within the continuous liquid phase as discrete bubbles of different sizes and shapes. To compute the interfacial area within a given volume, the interfacial areas of the individual bubbles must be known, such that

$$A_{i,\text{bubbly}} = \overline{A}_{i,\text{bubble}} = N\left\{\frac{1}{N}\sum_{n=1}^{N} A_{i,n}\right\}, \tag{F-37}$$

where $A_{i,\text{bubbly}}$ is the total interfacial area within a fixed volume of bubbly flow, N is the number of bubbles in that volume, and $A_{i,n}$ is the surface area of an individual bubble, and $\overline{A}_{i,\text{bubble}}$ is the average surface area of the bubble population. If the probability density function, pdf, for bubble surface area is known for a given set of thermal-hydraulic conditions, then the average bubble surface area becomes

$$\overline{A}_{i,\text{bubble}} = \int_0^\infty A_i(\chi_a)\,\text{pdf}(\chi_a)\,d\chi_a\,, \tag{F-38}$$

where χ_a is the size parameter and represents an equivalent radius (or diameter). The total volume of the vapor phase within a fixed material volume is equal to B_{cell} and is related to the volume of individual bubbles through

$$\alpha B_{\text{cell}} = N\overline{B}_{\text{bubble}} = N\left\{\frac{1}{N}\sum_{n=1}^{N} B_n\right\}, \tag{F-39}$$

where B_n is the volume of an individual bubble. An equation similar to Eq. (F-38) can be written if a continuous pdf is known as a function of an equivalent diameter χ_b as follows:

$$\bar{B}_{\text{bubble}} = \int_0^\infty B(\chi_b)\,\text{pdf}(\chi_b)\,d\chi_b \ . \tag{F-40}$$

Equivalent bubble diameters can be defined in a number of ways depending upon the applications. For Eq. (F-38) the appropriate equivalent diameter would be the surface-area-based diameter, where the surface areas of the actual bubble and an equivalent spherical bubble are set equal, to yield

$$D_{b,\,A} = \sqrt{\frac{\bar{A}_{i,\,\text{bubble}}}{\pi}} \ . \tag{F-41}$$

Similarly, a volume-based equivalent diameter can be defined for use in Eq. (F-40) as follows:

$$D_{b,\,V} = \left(\frac{6\bar{B}_{\text{bubble}}}{\pi}\right)^{1/3} \ . \tag{F-42}$$

For a sphere, Eqs. (F-41) and (F-42) yield identical diameters. However, for a nonspherical particle, the two diameters are not equal and the definition of the equivalent diameter must be given in reporting the data. Using the proper equivalent diameter also becomes important in averaging the diameter over a certain population of particles, even if they are spherical, in case the population has a nonuniform pdf. In general, the equivalent diameter for a nonuniform distribution can be defined as

$$D_{b,\text{pq}}^{\text{p}-\text{q}} = \frac{\int_0^\infty D_{b,\text{p}}^{\text{p}}\,\text{pdf}(\text{D}_{b,\text{p}})\,d\text{D}_{b,\text{p}}}{\int_0^\infty D_{b,\text{q}}^{\text{q}}\,\text{pdf}(\text{D}_{b,\text{q}})\,d\text{D}_{b,\text{q}}} = \frac{\bar{D}_{b,\text{p}}^{\text{p}}}{\bar{D}_{b,\text{q}}^{\text{q}}} \ , \tag{F-43}$$

where (p = 3, q = 0) is the volume-based average diameter of the bubble population, (p = 2, q = 0) is the area-based average diameter of the bubble population, etc. The Sauter mean diameter, which is another important equivalent diameter, corresponds to the case where (p = 3, q = 2). For p = 3 and q = 2, for instance, $D_{b,\text{p}}$ and $D_{b,\text{q}}$ are defined by Eqs. (F-41) and (F-42), respectively, for individual bubbles. If the bubbles can be assumed to be spherical in shape, the definition in Eq. (F-43) simplifies because $D_{b,\text{p}}$ becomes equal to $D_{b,\text{q}}$. For nonspherical particles, however, they are not equal, and a larger amount of statistical data is required for the proper definition of equivalent diameters. For instance, let us look at the Sauter mean diameter for a nonspherical bubble population. For a nonspherical object, the sphericity is defined as follows (Ref. F-13.):

$$\Psi = \frac{\text{surface area of volume – equivalent sphere}}{\text{surface area of particle}} \ .$$

Note that if the particle is a perfect sphere, Ψ becomes 1. Thus, by substituting all the diameters on the right-hand side of Eq. (F-43) with the equivalent diameter defined by Eq. (F-42), the Sauter mean diameter becomes

$$D_b = \frac{\int_0^\infty D_{b,V}^3 \mathrm{pdf}(D_{b,V}) dD_{b,V}}{\int_0^\infty \left(D_{b,V}^2 / \Psi\right) \mathrm{pdf}\left(D_{b,V}\right) dD_{b,V}} \quad , \tag{F-44}$$

which assumes that sphericity is a deterministic function of the bubble equivalent diameter. Now, to define the Sauter mean diameter, deterministic data for Ψ as a function of $D_{b,V}$ are needed, in addition to the pdf for $D_{b,V}$. If the sphericity becomes a statistical function, the definition becomes even more complicated. The Sauter mean diameter is important for our particular application because, when the interfacial area in bubbly flow is calculated from a given void fraction, we obtain

$$A_{i,\mathrm{bubbly}} = \frac{6\alpha B_{\mathrm{cell}} \int_0^\infty (D_{b,V}^2 / \Psi) \mathrm{pdf}(D_{b,V}) dD_{b,V}}{\int_0^\infty D_{b,V}^3 \mathrm{pdf}(D_{b,V}) dD_{b,V}} = \frac{6\alpha B_{\mathrm{cell}}}{D_b} \quad . \tag{F-45}$$

Because we are not aware of extensive statistical data that would enable an accurate quantification of Eq. (F-45), we are forced to assume that the bubbles are nearly spherical. This practice is rather common in many other applications of two-phase flow. On the other hand, there are studies indicating that under commonly encountered situations, bubbles are nonspherical. For instance, Fig. F-11. obtained from Ref. F-13., Fig. 2.5, illustrates a typical map for bubble shapes. The map is plotted as a function of Reynolds, Eötvös, and Morton numbers that are defined as follows:

$$Re = \frac{\rho_l D_{b,V} V_{\mathrm{bubble}}}{\mu_l} \quad ,$$

$$Eo = \frac{g(\rho_l - \rho_g) D_{b,V}^2}{\sigma} \quad ,$$

and

$$Mo = \frac{g\mu_l^4(\rho_l - \rho_g)}{\rho_l^2 \sigma^3} \quad .$$

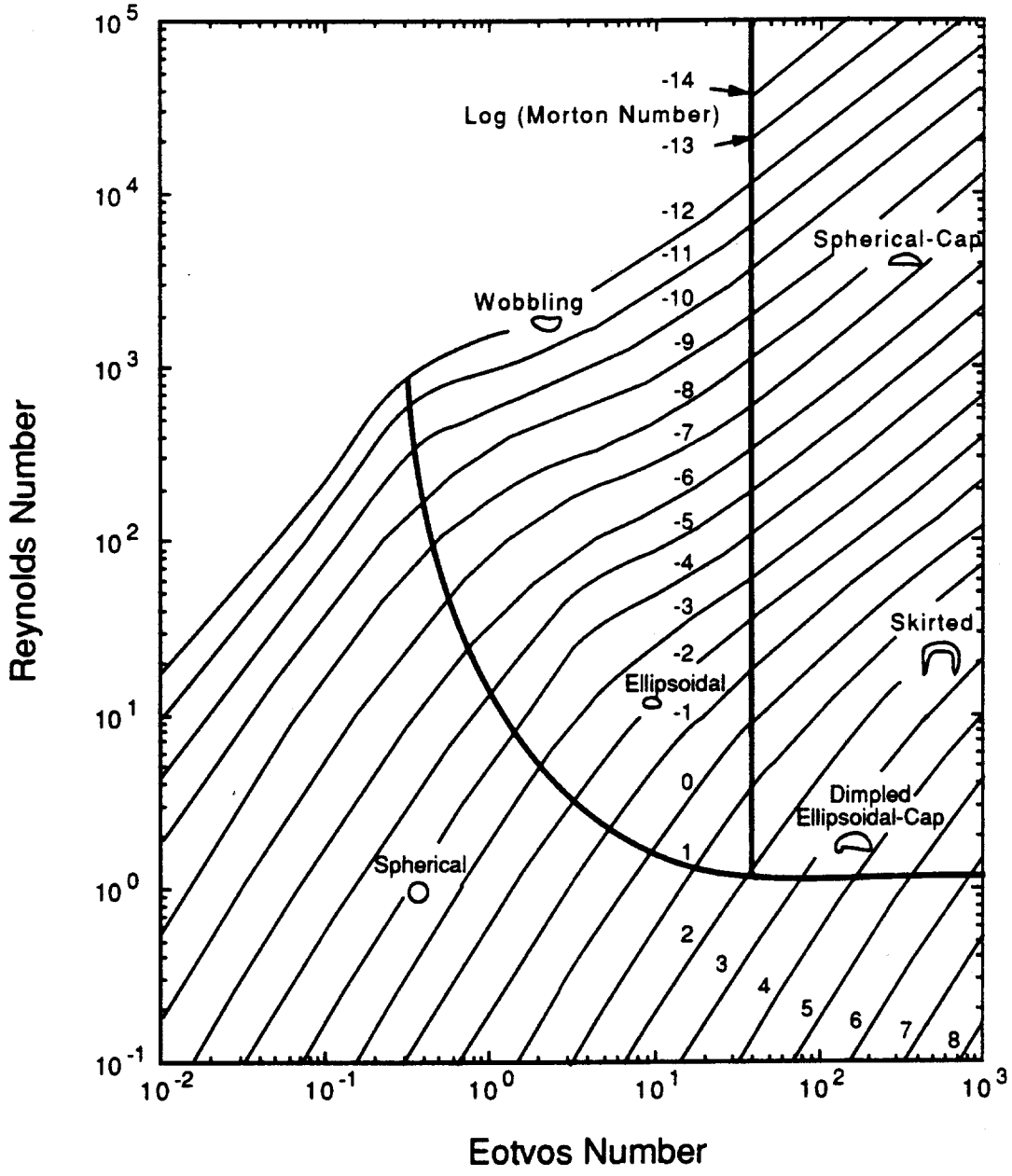

Fig. F-11. A typical map for bubble shapes (Ref. F-13., p. 27, Fig. 2.5).

Note that the Morton number is directly related to the viscosity number defined earlier. Here it is referred to as the Morton number merely for consistency with the original reference (Ref. F-13.). This map is given for bubbles freely rising in liquids. Thus, the Reynolds number is based upon bubble terminal velocity. A similar map, however, can be used as a first estimate of bubble shapes in two-phase-flow situations by replacing the bubble terminal velocity with bubble relative velocity (Ref. F-1.). The Morton number for saturated water at various pressures is on the order of 10^{-12}. Thus, the bubble shape is

spherical if the Eötvös number is less than 0.3. For an Eötvös number between 0.3 and 40, the bubble shape is shown to be wobbling and, for an Eötvös number greater than 40, the bubbles will have a spherical cap shape.

In TRAC, the bubble diameter is calculated using Eq. (F-12), which corresponds to a constant-Eötvös-number criterion given by $Eo = 4$, where the constant 4 is suggested as an average value by Ishii (Ref. F-3.). Ishii reported that the bubble diameter range is given by

$$4\sqrt{2}\,Mo^{1/12} < \sqrt{Eo} < 4 \quad ,$$

where the Morton number is on the order of 10^{-12}. Thus,

$$0.57 < \sqrt{Eo} < 4 \quad .$$

Ishii recommends $Eo = 4$ as a rough estimate for practical use. This simply reflects an approximate arithmetic average between maximum and minimum bubble diameters and does not take into account the bubble size and shape probability distributions. Consequently, it is difficult to determine whether it corresponds to the volume mean, to the area mean, or to the Sauter mean diameter. Ishii recommends its use as drag diameter, which is defined as

$$D_{b,D} = \frac{3 \times \text{Bubble Volume}}{\text{Projected Bubble Area}} \quad .$$

For a population of spherical bubbles, the drag diameter is equivalent to the Sauter mean diameter. For nonspherical bubbles, however, the two quantities are different. Note that the map provided by Clift et al. in Fig. F-11. suggests wobbling bubbles for $Eo = 4$. Presently, not enough data exist to quantify how well the $Eo = 4$ criterion approximates the Sauter mean diameter needed to estimate the interfacial area. Furthermore, this formulation is independent of local-instantaneous phasic velocities (inertia forces) that are known to influence the bubble diameter in steady-state situations. However, the quasi-steady assumption inherent in the code makes it difficult to incorporate such dependence through Weber-number correlations, for instance, during transient analysis. Because the quasi-steady assumption allows an instantaneous change in bubble size due to a sudden change in velocity, a constant-Weber-number criterion results in sudden and unrealistic changes in the bubble sizes, which occasionally may lead to numerical oscillations.

Our final remarks about the heat-transfer correlations used in bubbly slug flow are that some of our simple models could have been replaced by better-founded correlations. For instance, the flashing model could have been replaced by either the Chen-Mayinger correlation, or by a solid-sphere heat-transfer correlation along with bubble-growth equations, such as the one by Mikic et al. (Ref. F-14.). Further discussion of why these

approximate models are used and what their implications are can be found in Section F.1.10.

F.1.2. Models and Correlations in Annular-Mist Flow

As shown in Fig. F-3., annular-mist flow occurs if the void fraction is greater than or equal to 75%, independent of mass flux. A schematic of flow pattern in annular-mist flow is shown in Fig. F-12. As shown, the liquid flows as droplets in the gas core and also forms a liquid film on a solid wall. Therefore, a more rigorous treatment requires at least two fields for the liquid phase. In TRAC, the liquid phase is represented as a single field. Thus, the characteristics of liquid droplets and film must be properly superimposed within a single field. The following generic equation shows the way the various closure parameters are calculated in annular-mist flow:

$$X = (1 - W_f)(X_{\text{drop}} + X_{\text{film}}) + W_f X_{\text{drop,max}} \ , \tag{F-46}$$

where X represents either A_i, H_{ALVE}, or H_{CHTI}. The weighting factor, W_f, is introduced to account for the fact that beyond a certain limit in phasic velocities, all the liquid will be entrained in the form of droplets, thus no liquid film will exist. The phasic velocities are compared to a critical velocity defined based upon Helmholtz disturbance wave and given by

$$V_c = \left[\frac{g\sigma(\rho_l - \rho_g)}{\rho_g^2} \right]^{1/4} \ . \tag{F-47}$$

Then the weighting factor is coded as follows:

$$W_f = \begin{cases} 0 & \text{if } \max(V_l, V_g) < 10V_c \\ 0.5\dfrac{\max(V_l, V_g)}{V_c} - 5 & \text{if } 10V_c \le \max(V_l, V_g) \le 12V_c \\ 1 & \text{if } \max(V_l, V_g) > 12V_c \end{cases} \ . \tag{F-48}$$

Figure F-13. illustrates the transition from annular-mist to mist flow as a function of pressure for saturated water. As shown in this figure, the critical velocity is a strong function of pressure and decreases rapidly with increasing pressure.

F.1.2.1. Description of Interfacial-Area Models. The interfacial area (A_i) Eq. (F-46) becomes

$$A_{i,\text{annular-mist}} = (1 - W_f)(A_{i,\text{drop}} + A_{i,\text{film}}) + W_f A_{i,\text{drop,max}} \ . \tag{F-49}$$

The individual contributions of the droplet and film flow on the interfacial area are described in the following sections.

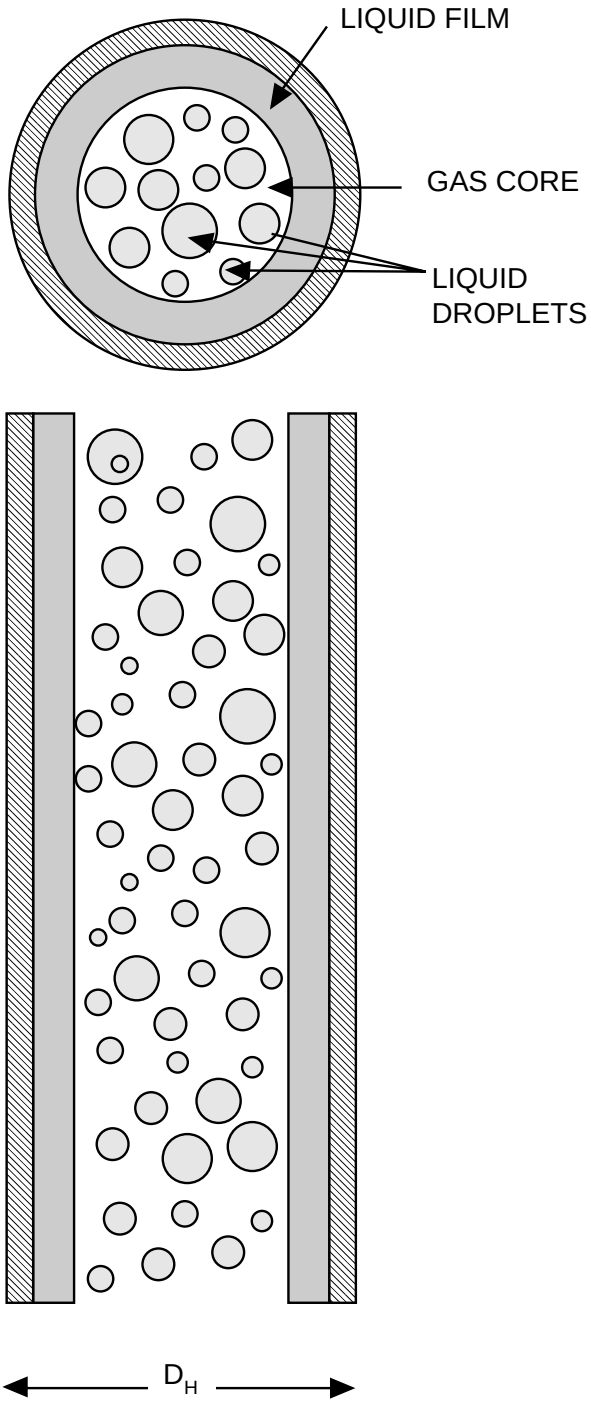

Fig. F-12. Schematic of flow pattern in annular-mist flow.

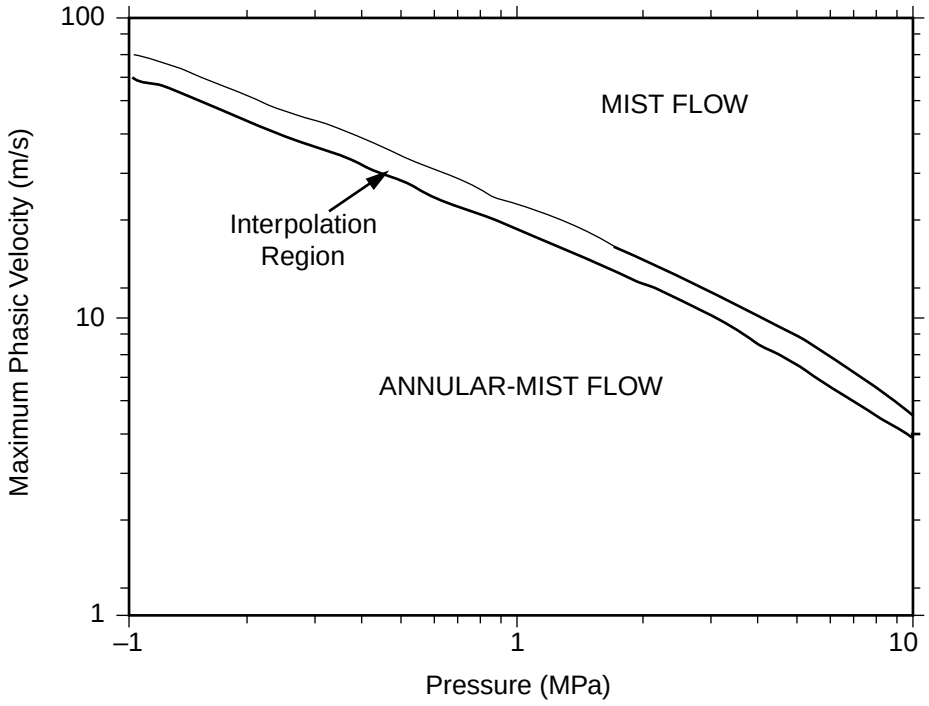

Fig. F-13. Transition from annular-mist to mist flow as a function of pressure for saturated water.

F.1.2.1.1. Mist-Flow Interfacial Area. The interfacial-area concentration in the mist-flow portion is given by (Ref. F-15., p. 55, Eq. 89) as

$$a_{i,\,\mathrm{drop}} = \frac{\alpha}{1-\alpha_d}\left(\frac{6\alpha_d}{D_d}\right), \tag{F-50}$$

where D_d is the Sauter mean diameter of the droplet population and α_d is the droplet fraction in the gas core. If all the liquid is entrained as liquid droplets, then $\alpha_d = 1-\alpha$ and

$$a_{i,\mathrm{drop,max}} = B_{\mathrm{cell}}\,\frac{6(1-\alpha)}{D_d} \quad . \tag{F-51}$$

The droplet Sauter mean diameter is calculated using the correlations of Kataoka et al. (Ref. F-16.) and Kitscha and Kocamustafaogullari (Ref. F-6.). Kataoka et al. proposed a droplet diameter model that assumes that the majority of droplets are generated at the time of entrainment and that the size distribution is a direct reflection of the entrainment mechanism. The final correlation is obtained by combining with a large amount of data as follows (Ref. F-16., Eq. 28):

$$D_{vm} = 0.028 \frac{\sigma}{\rho_g (\alpha V_g)^2} Re_l^{-1/6} Re_g^{-2/3} \left(\frac{\rho_g}{\rho_l}\right)^{-1/3} \left(\frac{\mu_g}{\mu_l}\right)^{2/3} \quad , \tag{F-52}$$

where D_{vm} is the droplet volume median diameter,

$$Re_l = \frac{\rho_l D_H (1-\alpha) V_l}{\mu_l} \quad ,$$

and

$$Re_g = \frac{\rho_g D_H \alpha V_g}{\mu_g} \quad .$$

The database of this correlation is summarized in Table F-1. (obtained from Ref. F-16., Table 1). Data were obtained using an air-water mixture. Kataoka et al. argued that, within the range investigated, the droplet diameter shows little sensitivity to liquid Reynolds number as

$$0.24 \leq Re_l^{-1/6} \leq 0.46 \quad .$$

Using an average value of $Re_l^{-1/6} \approx 0.35$, they obtained (Ref. F-16., Eq. 42)

$$D_{vm} = 0.01 \frac{\sigma}{\rho_g (\alpha V_g)^2} Re_g^{2/3} \left(\frac{\rho_g}{\rho_l}\right)^{-1/3} \left(\frac{\mu_g}{\mu_l}\right)^{2/3} \quad . \tag{F-53}$$

TABLE F-1.
Database of Droplet Diameter Correlation
Kataoka et al. (Ref. F-15., Table 1)

Reference	Geometry	Flow Direction	Measurement	Operational Conditions
Wicks & Dukler (1966) Wicks (1967)	1.9 × 15-cm channel	Vertical down	Electrical conductance	P = 1 atm R_{ef} = 930 – 9700 R_{eg} = 6.6 – 17 × 10^4
Cousins & Hewitt (1968)	0.95-cm tube	Vertical up	Photography	P = 2 atm R_{ef} = 640 – 4200 R_{eg} = .6 – 6.2 × 10^4
Lindsted et al. (1978)	3.2-cm tube	Vertical up	Photography	P = 1 atm R_{ef} = 100 – 3500 R_{eg} = 2.5 – 4.4 × 10^4

To calculate the interfacial-area concentration, we need the Sauter mean diameter. Kataoka et al. report that (Ref. F-16., Table 2)

$$\frac{D_d}{D_{vm}} = 0.796 \quad .$$

Therefore, the droplet Sauter mean diameter is calculated using

$$D_d = 7.96 \times 10^{-3} \frac{\sigma}{\rho_g (\alpha V_g)^2} \; Re_g^{2/3} \left(\frac{\rho_g}{\rho_l} \right)^{-1/3} \left(\frac{\mu_g}{\mu_l} \right)^{2/3} \quad . \tag{F-54}$$

This correlation, however, shows that $D_d \sim (D_H)^{2/3}$ which can result in unrealistically large droplet diameters in flow channels with large hydraulic diameter. We believe that this feature results from the limited database of the correlation. As shown in Table F-1., the maximum hydraulic diameter in the database is 3.37 cm (corresponding to the channel used by Wicks). It is expected that beyond a certain limiting value, the effect of hydraulic diameter on droplet size will vanish. Kitscha and Kocamustafaogullari (Ref. F-6.) formulated this problem and proposed a correlation for maximum droplet diameter in a high-velocity gas-field free of wall effects. The correlation is given by (Ref. F-6., Eq. 38)

$$\left(\frac{D_{\max}}{L_o} \right)^2 + 0.26 We_m \left(\frac{D_{\max}}{L_o} \right) - 16 = 0 \quad , \tag{F-55}$$

where the modified Weber number is defined as

$$We_m = \frac{\rho_g (\alpha V_g)^2 L_o}{\sigma} \quad .$$

Kitscha and Kocamustafaogullari compared Eq. (F-55) with the maximum droplet diameter correlation of Kataoka et al. (Ref. F-16., Eq. 43) and showed that Eq. (F-55) is over-predicted by Kataoka et al. for hydraulic diameters larger than ~5 cm. The value of this critical diameter changes with gas velocity and pressure. In the code, we used the correlation of Kitscha and Kocamustafaogullari as the upper limit of the correlation of Kataoka et al. given by Eq. (F-54). However, we modified Eq. (F-55) to yield the Sauter mean diameter rather than the maximum diameter. The conversion between these two quantities is also obtained from the relation reported by Kataoka et al. (Ref. F-16., Table 2) as follows:

$$\frac{D_d}{D_{\max}} = 0.254 \quad .$$

Consequently, Eq. (F-55) yields

$$D_d = 0.254 L_o \left[-0.13 We_m + \sqrt{16 + (0.13 We_m)^2} \right] \quad . \tag{F-56}$$

Note that for small values of modified Weber number, the droplet diameter is given by

$$D_d \approx L_o \quad ,$$

which is a criterion that is commonly used to determine the size of the dispersed phase [see the bubble diameter correlation given by Eq. (F-11)]. In the code, the droplet diameter is given by the minimum of either Eq. (F-54) or Eq. (F-56). We further imposed the following limits on the droplet diameter:

$$84\ \mu\text{m} \le D_d \le 4\ \text{mm} \ .$$

Figure F-14. shows the droplet diameters predicted by the TRAC model for air-water mixture at atmospheric pressure and 20°C. The hydraulic diameter is also varied in this figure. As shown, the correlation of Kataoka et al. is effective for small hydraulic diameters. As the hydraulic diameters increase, the effective range of the correlation by Kitscha and Kocamustafaogullari also increases. Beyond a certain hydraulic diameter (~55 mm for this case), the correlation of Kitscha and Kocamustafaogullari always dominates. Note that this limiting hydraulic diameter decreases with increasing temperature. For saturated water at or above atmospheric pressure, the correlation of Kitscha and Kocamustafaogullari dominates beyond ~20-mm hydraulic diameter. In Fig. F-15., the effect of pressure on the droplet diameter is illustrated using saturated water properties at 1 and 20 atm for a hydraulic diameter of 10 mm. This figure shows that the droplet diameter is not strongly affected by the pressure at low gas-flow rates, whereas it decreases rapidly with increasing pressure at higher gas-flow rates.

The knowledge of the void fraction and the droplet Sauter mean diameter is sufficient to obtain the interfacial-area concentration in mist flow ($a_{i,\text{drop,max}}$). However, in annular-mist flow we further need to know the fraction of liquid in the form of entrained droplets (α_d). This quantity is based upon the entrainment fraction, E, defined by Ishii and Mishima (Ref. F-17.) as

$$E = \frac{J_d}{J_l} \ , \tag{F-57}$$

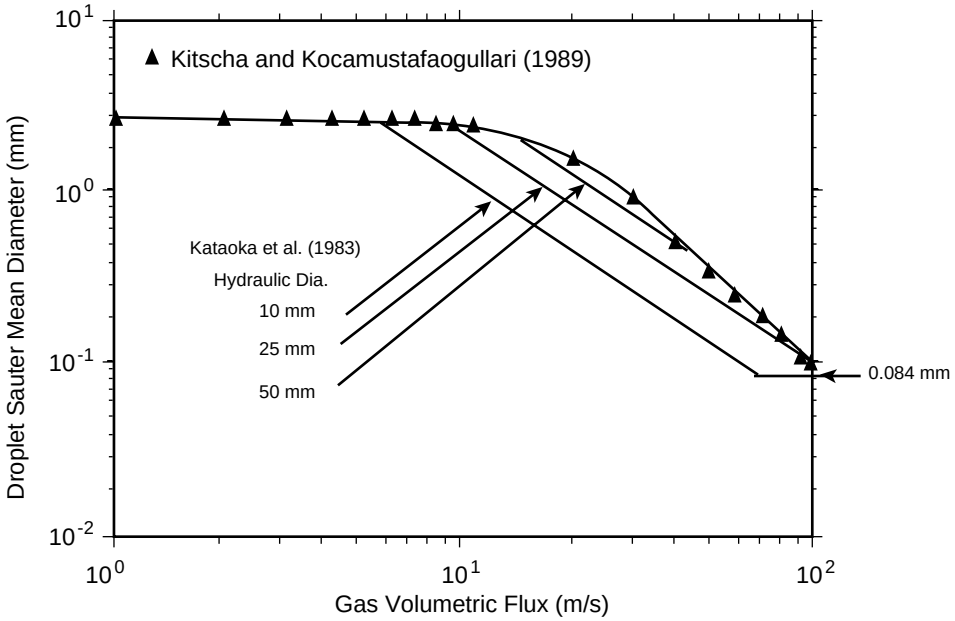

Fig. F-14. Droplet diameter calculated by TRAC for air-water mixture at atmospheric pressure and 20°C temperature in tubes with various hydraulic diameters.

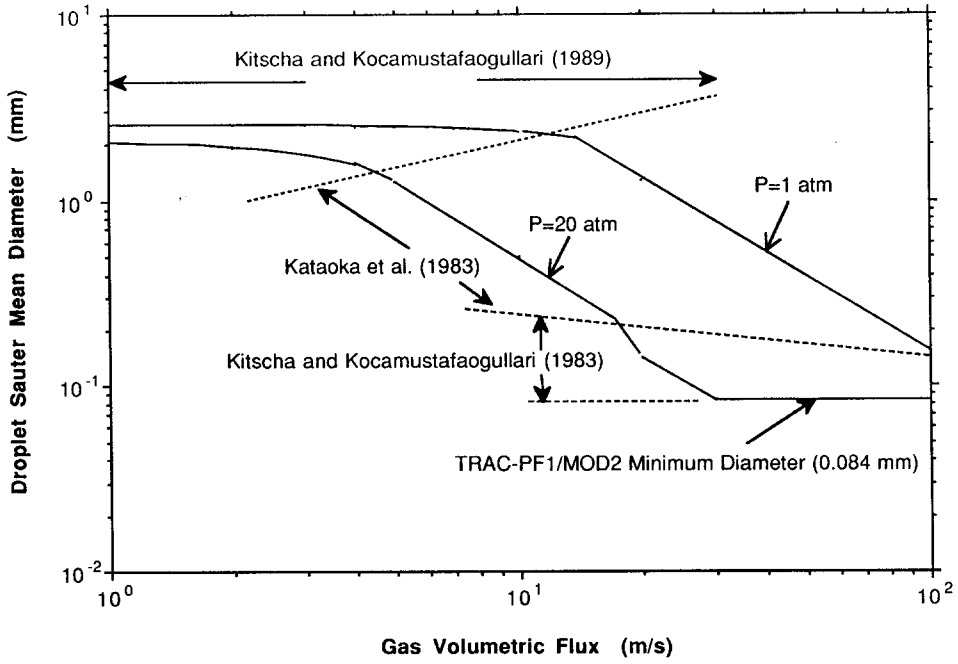

Fig. F-15. Droplet diameter calculated by TRAC for saturated water at 1 and 20 atm and for a 10-mm hydraulic diameter.

where J_d is the droplet volumetric flux and J_l is the total liquid volumetric flux (or superficial velocity). The entrainment fraction is calculated using the correlation developed by Ishii and Mishima, which is given as (Ref. F-17., p. 10, Eq. 23, and Ref. F-18., Eq. 28)

$$E = \tanh\left(7.25\times10^{-7} We_e^{1.25} Re_l^{0.25}\right) \quad , \tag{F-58}$$

where the effective Weber number is defined as

$$We_e = \frac{\rho_g(\alpha V_g)^2 D_H}{\sigma}\left(\frac{\rho_l-\rho_g}{\rho_g}\right)^{1/3} \quad ,$$

and

$$Re_l = \frac{\rho_l(1-\alpha)V_l D_H}{\mu_l} \quad .$$

Figure F-16. shows the calculated entrainment fraction for saturated water at atmospheric pressure as a function of gas volumetric flux and the parameter $s\alpha/(1-\alpha)$, where s is the slip ratio. As shown, the entrainment fraction is a strong function of the former, whereas it is weakly affected by the latter. Figure F-17. illustrates the effect of pressure using saturated water properties. As shown, the entrainment fraction increases with increasing pressure. As discussed before, the entrainment fraction correlation is limited by the transition to fully mist flow described by Eqs. (F-46), (F-47), and (F-48). These limits are also superimposed on Figs. F-16. and F-17. Ishii and Mishima compared Eq. (F-58) to various data within the following parametric range:

$$\begin{aligned} 1 &\le P \le 4 \text{ atm} , \\ 0.95 &\le D_H \le 3.2 \text{ cm} , \\ 370 &\le Re_l \le 6400 , \text{ and} \\ & J_g < 100 \text{ m/s} . \end{aligned}$$

Equation (F-58) is proposed as a fully developed entrainment correlation for adiabatic flow. It is valid beyond a certain distance, z_c, away from the entrance. This entry length is correlated by Mishima and Ishii as (Ref. F-17., p. 13, Eq. 35, and Ref. F-18., Eq. 36)

$$z_c \approx 600 D_H \frac{1}{\sqrt{Re_l}}\sqrt{\alpha V_g}\left[\frac{\sigma g(\rho_l-\rho_g)}{\sigma_g^2}\left(\frac{\rho_g}{\rho_l-\rho_g}\right)^{2/3}\right]^{-1/8} \quad . \tag{F-59}$$

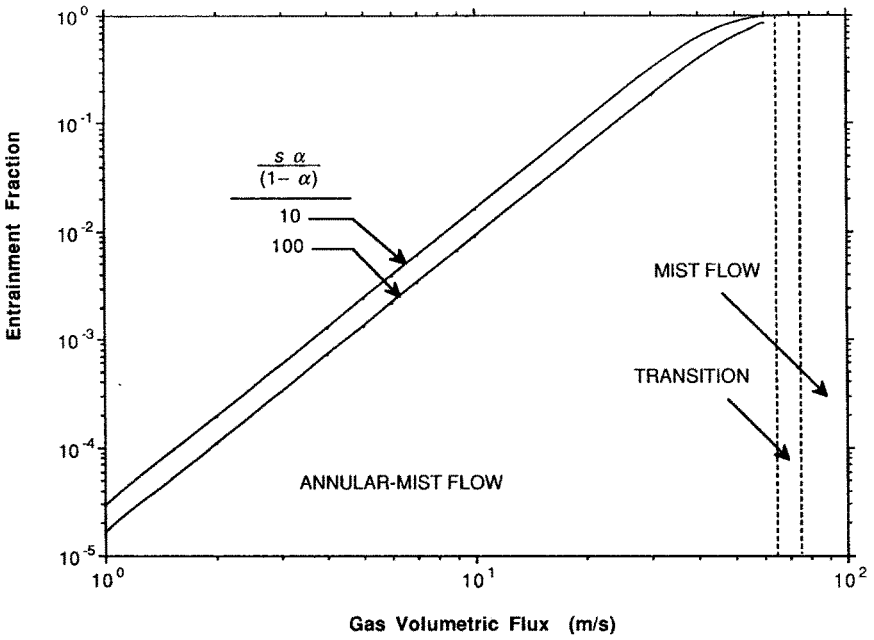

Fig. F-16. TRAC-calculated entrainment fraction for saturated water at atmospheric pressure.

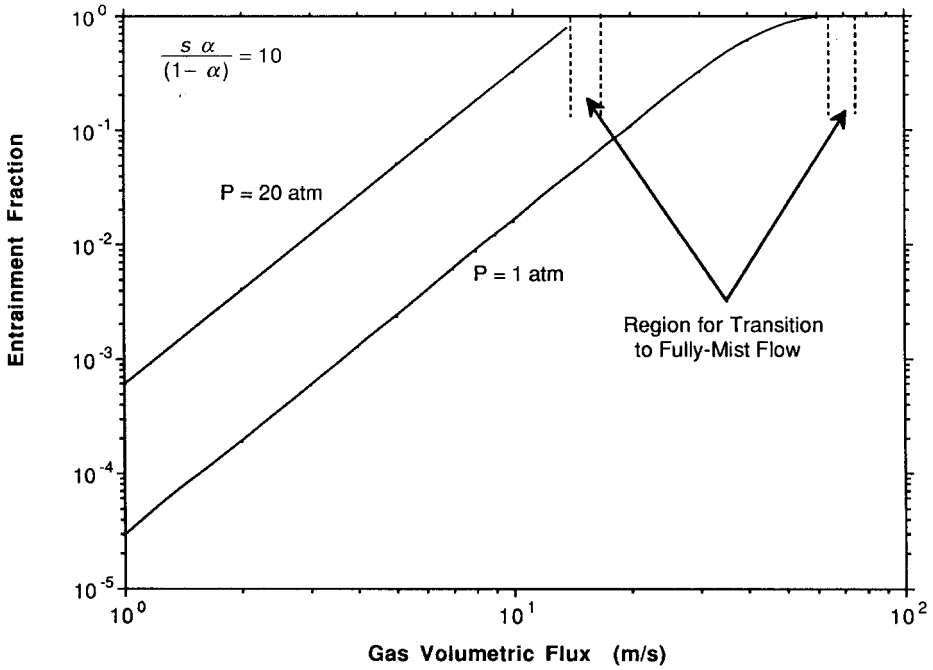

Fig. F-17. Effect of pressure on the entrainment fraction for saturated water.

Within the entry length, the entrainment rate is formulated as an exponential relaxation that approaches Eq. (F-58) as the distance approaches z_c. In the code, we neglected the entry length and used Eq. (F-58) within a given cell, assuming local-instantaneous equilibrium.

Assuming that the velocity of the droplets is approximately equal to the gas velocity and using the definition of the entrainment fraction given by Eq. (F-57), the following relationship between E and α_d can be obtained:

$$\frac{\alpha_d \alpha V_g}{1-\alpha_d} = E(1-\alpha)V_l \quad . \tag{F-60}$$

Setting $1-\alpha_d \approx 1$, Eq. (F-60) yields

$$\alpha_d \approx E\frac{(1-\alpha)V_l}{\alpha V_g} \quad , \tag{F-61}$$

which can be replaced into Eq. (F-50) to obtain the mist portion of the interfacial-area concentration in annular-mist flow. Then, the interfacial area in a given cell is calculated as

$$A_{i,\text{drop}} = B_{\text{cell}} a_{i,\text{drop}} \quad . \tag{F-62}$$

F.1.2.1.2. Annular-Mist-Flow Interfacial Area. From purely geometric considerations, the interfacial-area concentration for the liquid film can be calculated as (Ref. F-15., p. 55, Eq. 89)

$$A_{i,\text{film}} = \frac{4C_r}{D_H}\sqrt{\frac{\alpha}{1-\alpha_d}} \quad , \tag{F-63}$$

where α_d is given by Eq. (F-61) and C_r is a correlation factor that accounts for interfacial waviness. In the code, the surface waves are ignored for thick films. However, if the film becomes very thin, rivulet formation is acknowledged and its effect is incorporated into C_r. This effect is calculated using the following simple model:

$$C_r = \frac{D_H(1-\alpha)}{l_{\text{min}}} \le 1 \quad , \tag{F-64}$$

where l_{min} is set to 0.1 mm. Physically, this model neglects α_d and assumes that a liquid film thinner than 25 μm cannot be stable and breaks into rivulets. Having obtained α_d and C_r, the film flow contribution to the total interfacial area can be calculated as

$$A_{i,\text{film}} = B_{\text{cell}} a_{i,\text{film}} \quad . \tag{F-65}$$

F.1.2.2. Description of Heat-Transfer Coefficient Models. During condensation and flashing, the heat-transfer factors are calculated as

$$H_{\mathrm{ALVE}} = (1 - W_f)(H_{\mathrm{ALVE,drop}} + H_{\mathrm{ALVE,film}}) + W_f H_{\mathrm{ALVE,drop,max}} \ , \tag{F-66}$$

$$H_{\mathrm{ALV}} = (1 - W_f)(H_{\mathrm{ALV,drop}} + H_{\mathrm{ALV,film}}) + W_f H_{\mathrm{ALV,drop,max}} \ , \tag{F-67}$$

$$H_{\mathrm{CHTI}} = (1 - W_f)(H_{\mathrm{CHTI,drop}} + H_{\mathrm{CHTI,film}}) + W_f H_{\mathrm{CHTI,drop,max}} \ , \tag{F-68}$$

and

$$H_{\mathrm{CHTA}} = (1 - W_f)(H_{\mathrm{CHTA,drop}} + H_{\mathrm{CHTA,film}}) + W_f H_{\mathrm{CHTA,drop,max}} \ . \tag{F-69}$$

During flashing, the maximum H_{ALV} predicted by either Eq. (F-67) or Eq. (F-27) is used. Liquid- and vapor-side heat-transfer coefficients for the droplets and liquid film are described in the following sections.

F.1.2.2.1. Mist-Flow Heat-Transfer Coefficients. The liquid-side interfacial heat-transfer coefficient, $h_{i\mathrm{l}}$, is calculated using the transient conduction solution in liquid droplets. The conduction solution is approximated as follows (Ref. F-19., Eqs. 4 and 6):

$$Nu = \frac{\pi}{3} C_c \frac{1 + T^*}{T^*} \ , \tag{F-70}$$

where

$$Nu = \frac{h_{i\mathrm{l}} D_d}{k_{\mathrm{l}}}$$

and T^* is the dimensionless instantaneous mixing cup temperature given by

$$T^* \approx \left[1 - \exp\left(-4\pi^2 C_c \frac{k_{\mathrm{l}} t}{\rho_{\mathrm{l}} c_{p,\,\mathrm{l}} D_d^2} \right) \right]^{1/2} \ . \tag{F-71}$$

The conduction solution was used in the code because Ford and Lekic (Ref. F-20.) were able to correlate their single-component (steam / water) droplet-condensation data with reasonable accuracy. Also, Iciek et al. (Ref. F-21., p. 175) suggest that for small droplets with low relative velocity and for fluids with a high ratio of liquid viscosity to vapor viscosity, the condensation solution is satisfactory.

In Eqs. (F-70) and (F-71), C_c is a correction factor to account for circulation effects within the droplet. In the code, we assumed that such effects are negligible and C_c is set equal to 1. To use this transient solution in a quasi-steady, single-liquid-field code, we need to estimate a mean free path for the droplet population. Knowing the mean free path and the droplet velocity, we can estimate the droplet thermal-boundary-layer lifetime, defined as the time elapsed between the initiation of thermal-boundary-layer growth and destruction. We can assume that the thermal boundary layer is destroyed through droplet coalescence, breakup, deposition, and entrainment. In the code, it is arbitrarily assumed that the mean free path is equal to channel hydraulic diameter. The droplet velocity is calculated as

$$V_d = V_g - V_r \ ,$$

where the relative velocity, V_r, is obtained from a force balance between gravity and drag using an interfacial-drag coefficient of 0.44, which yields (Ref. F-22., p. 14, Eq. 18)

$$V_r = 2.462\sqrt{g\frac{\rho_l - \rho_g}{\rho_g}\ \frac{D_d}{2}} \quad . \tag{F-72}$$

At each cell, we assumed that the average droplet is in the middle of its thermal lifetime, t_d. Thus, t in Eq. (F-71) is replaced by $t_d/2$ where

$$t_d \approx \frac{D_H}{V_r} \ . \tag{F-73}$$

Therefore, knowing the liquid-side heat-transfer coefficient, the heat-transfer factors become

$$H_{\mathrm{ALVE,drop}} = h_{il} A_{i,\mathrm{drop}} \ \text{and} \tag{F-74}$$

$$H_{\mathrm{ALVE,drop,max}} = h_{il} A_{i,\mathrm{drop,max}} \tag{F-75}$$

during condensation, and

$$H_{\mathrm{ALV,drop}} = h_{il} A_{i,\mathrm{drop}} \ \text{and} \tag{F-76}$$

$$H_{\mathrm{ALV,drop,max}} = h_{il} A_{i,\mathrm{drop,max}} \tag{F-77}$$

during flashing. Note that further correction is made on the combined H_{ALV} for annular-mist flow, as described in Section F.1.2.2.

During both condensation and evaporation, the vapor-side heat-transfer coefficient is calculated using the correlation developed by Ryskin, given by (Ref. F-23., Eq. 3)

$$Nu = 2 + \sqrt{V^*_{\max} Pe} \ . \tag{F-78}$$

In Eq. (F-78), the Nusselt and Peclet numbers are defined as

$$Nu = \frac{h_{ig} D_d}{k_g}$$

and

$$Pe = \frac{\rho_g c_{p,g} D_d V_r}{k_g} \ ,$$

respectively, where V_r is obtained from Eq. (F-72). The maximum dimensionless circulation velocity at the surface of the drop is defined as

$$V^*_{\max} = \frac{1.5}{1 + \dfrac{2.8(1+2\lambda)(2+3\kappa)}{(2+3\lambda)\sqrt{Re_g}}} \ ,$$

where

$$Re_g = \frac{\rho_g D_d V_r}{\mu_g} \ ,$$

$$\lambda = \sqrt{\frac{\rho_l \mu_l}{\rho_g \mu_g}} \ ,$$

and

$$\kappa = \frac{\mu_l}{\mu_g} \ .$$

Thus, the vapor-side heat-transfer factors can be calculated as

$$H_{\text{CHTI,drop}} = h_{i,g} A_{i,\text{drop}} \tag{F-79}$$

and

$$H_{\mathrm{CHTI,drop,max}} = h_{i,g} A_{i,\mathrm{drop,max}} \ . \tag{F-80}$$

The same model given by Eq. (F-78) is used to calculate the direct sensible heat factor, H_{CHTA}, between the gas and liquid phases. In order to calculate H_{CHTA}, the mixture properties are replaced by noncondensable-gas properties in the model.

F.1.2.2.2. Annular-Mist-Flow Heat-Transfer Coefficients. For the liquid film, both the liquid- and vapor-side heat-transfer coefficients are calculated using a Stanton-number correlation given by

$$St = 0.0045 \left(\frac{\rho_g V_g \mu_l}{\rho_l V_l \mu_g} \right)^{1/3} \ . \tag{F-81}$$

This correlation was originally developed by Bankoff (Ref. F-24., Eq. 21) for the liquid-side heat-transfer coefficient during stratified cocurrent steam-water flow. The advantage of this correlation is its independence from the position vector, which makes its use convenient in an Eulerian quasi-steady code, such as TRAC. For saturated water, the effect of slip ratio and pressure on the calculated Stanton number is illustrated in Fig. F-18. For the original correlation, the Stanton number is defined based upon the liquid properties and liquid velocity. In the code, the Stanton number is defined as

$$St \equiv \frac{h_{i,l}}{\rho_l c_{p,l} V_l} \ ,$$

$$St \equiv \frac{h_{i,g}}{\rho_g c_{p,g} \left| V_g - V_l \right|} \ ,$$

or

$$St \equiv \frac{h_{gl}}{\rho_a c_{p,a} \left| V_g - V_l \right|}$$

to calculate the liquid-side, the vapor-to-interface, or the gas-to-liquid heat-transfer coefficient.

Thus, the heat-transfer factors can be obtained as

$$H_{\mathrm{ALVE,film}} = h_{il} A_{i,\mathrm{film}} \ , \tag{F-82}$$

$$H_{\mathrm{ALV,film}} = h_{il} A_{i,\mathrm{film}} \ , \tag{F-83}$$

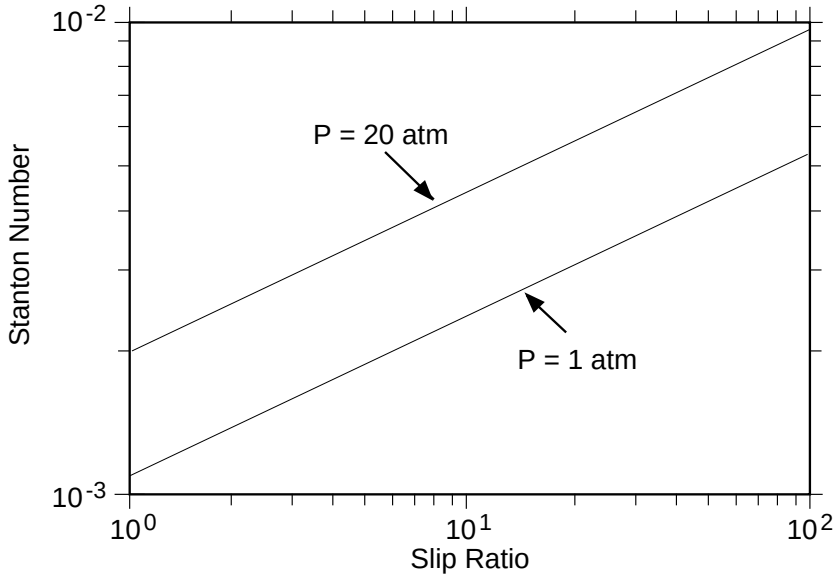

Fig. F-18. Calculated Stanton numbers for liquid-film flow using saturated water properties.

$$H_{\mathrm{CHTI,film}} = h_{i\ell} A_{i,\mathrm{film}} \ , \tag{F-84}$$

and

$$H_{\mathrm{CHTA,film}} = h_{g\ell} A_{i,\mathrm{film}} \ . \tag{F-85}$$

F.1.2.3. Assessment. The droplet diameter model of TRAC is compared with more recent data of Lopes and Dukler (Ref. F-25.). In this study, air-water mixture is used in a 10-m-long vertical pipe with an internal diameter of 50.74 mm. Lopes and Dukler used a novel laser optical technique to measure simultaneously the droplet size and axial and radial velocities. The technique allows these measurements for droplets passing through a fixed point in the flow channel; thus, it provides statistical data on temporal variations. From these data, various mean droplet diameters are computed and reported (Ref. F-25., Table 3.2). In the experiments, the liquid volumetric flux ranged between 3.4 and 12.1 cm/s and the gas volumetric flux ranged between 14 and 25 m/s. As shown in Fig. F-14., within this range of J_g and for $D_H \approx 50$ mm the droplet diameters are predicted by the correlation of Kataoka et al. (Ref. F-16.). Consequently, the data of Lopes and Dukler are compared with this correlation and the results are shown in Fig. F-19. As shown, the correlation agrees well with the data obtained near the wall (15–20 mm from the centerline). The data obtained at the centerline is overpredicted by the code by about 40%. Apparently, the droplet Sauter mean diameter is larger near the wall. We have to note that the correlation of Kataoka et al. represents the area-averaged data. Unfortunately, Lopes and Dukler did not compute their area-averaged data. However,

because the area of radial rings is larger near the wall than around the centerline, the area-averaged data are expected to be much closer to the data near the wall than to the data at the centerline. The database of the Kataoka et al. correlation mostly contains data from photographic observations (see Table F-1.). As discussed by Lopes and Dukler, these data seem to be biased towards larger droplets because very small droplets (less than ~100 μm) cannot be detected, which may be another reason for the slight overprediction by the correlation. Finally, as reported by Kataoka et al. (Ref. F-16., Fig. 3), the accuracy of their correlation is within ±40% when compared to its own database. All data of Lopes and Dukler fall within this range.

For the droplet-field liquid-side heat-transfer coefficient, the transient conduction solution is used based upon the observations of Ford and Lekic (Ref. F-20.) and the suggestion by Iciek et al. (Ref. F-21.). Recently, Celata et al. (Ref. F-26.) compared Eq. (F-71) with their own data and suggested a correlation for the correction factor C_c as

$$C_c = 0.153\left[\left(\frac{\mu_g}{\mu_g + \mu_l}\right)\frac{\rho_l c_{p,l} V_d D_d}{k_l}\right]^{0.454} , \qquad \text{(F-86)}$$

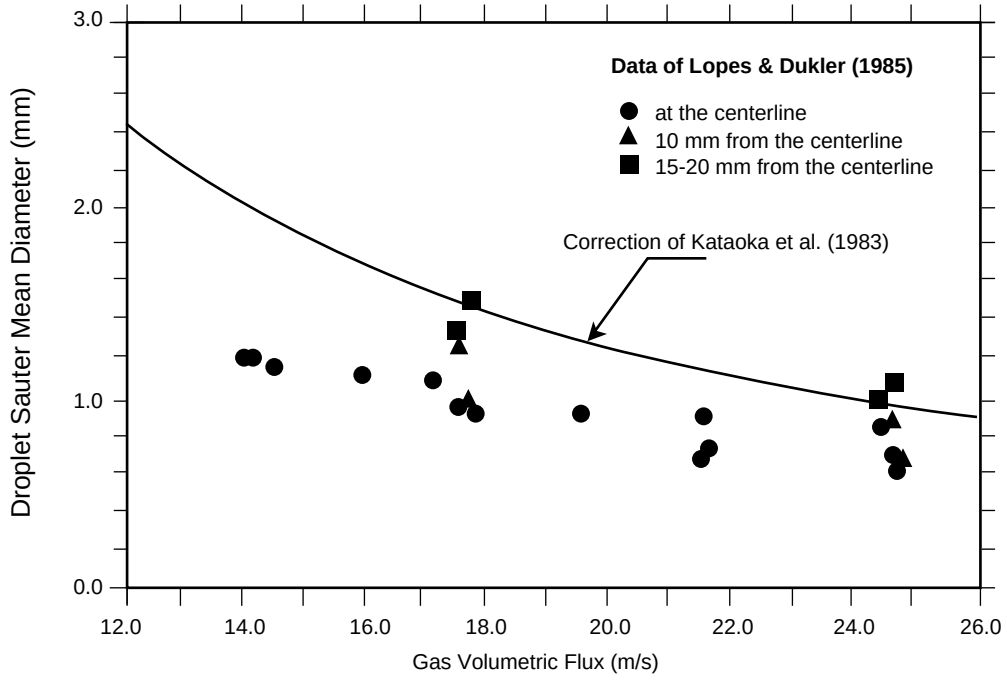

Fig. F-19. Comparison of Kataoka et al. correlation (Ref. F-6.) with the data of Lopes and Dukler (Ref. F-25.).

where V_d is the droplet velocity traveling through a stationary steam volume. In a mist-flow scenario, it must be replaced by the relative velocity. The relative velocity in mist flow is usually very small, however. Thus the correction factor tends towards 1 with decreasing relative velocity. Consequently, it is concluded that the transient conduction solution is a fairly reasonable representation of liquid-side heat transfer within droplets. The major source of error is the time-averaging of this transient process over an assumed droplet lifetime. This will be further discussed in Section F.1.2.4. Furthermore, the correlation for entrainment fractions also has limited accuracy: (*i*) it assumes a local-instantaneous equilibrium for entrainment phenomena and introduces considerable error if these conditions are not satisfied, and (*ii*) its accuracy is limited from ±50% to ±75%, especially for 1% to 10% entrainment fractions (Ref. F-17., Fig. 13, and Ref. F-18., Fig. 13). In the TRAC-M/F77 Developmental Assessment Manual (Refs. F-100. and F-101.), we showed that the new droplet-condensation model agrees fairly well with the data of Aoki et al. (Ref. F-27.) and Akimoto et al. (Ref. F-28.).

The correlation proposed by Ryskin (Ref. F-23.) to calculate the vapor-side heat-transfer coefficient for droplets is a theoretically based correlation and no data comparison was provided. For water, it commonly yields Nusselt numbers on the order of unity, comparable to the conduction solution. Actually, as the relative velocity tends towards zero, as expected in mist flow, the Ryskin correlation yields $Nu = 2$, which is the steady-state conduction limit. This would also be obtained by using Whittaker's solid sphere correlation (Ref. F-8.) given by Eq. (F-24).

The Bankoff correlation used to calculate the liquid- and vapor-side heat-transfer correlations for the liquid film was originally developed for horizontal, stratified, condensing-flow conditions. As shown by Bankoff (Ref. F-24., Fig. 7), the correlation is accurate only within 100% when compared to its own database. The liquid layer thickness is much larger under these conditions as compared to the liquid-film thickness in annular-mist flow. The heat-transfer mechanism may change considerably with this thickness. In stratified condensing flow, the heat-transfer is commonly dominated by highly turbulent mixing. For thin liquid films, conduction or laminar convection may be the dominant mechanisms. Finally, the application of the Bankoff correlation to calculate the vapor-side heat-transfer coefficient is an engineering approximation.

F.1.2.4. Conclusion and Final Remarks. The lengthy discussion of the averaging of the statistical data of the dispersed-phase sizes, provided in Section F.1.1.5., also applies to droplet flow. However, the droplets are smaller in size and tend to be more spherical than bubbles. Consequently, the sphericity considerations are expected to be less important. Furthermore, the data used by Kataoka et al. (Ref. F-16.) and the recent data of Lopes and Dukler (Ref. F-25.) are examined and the effect of statistical variations on the various averages are incorporated. Consequently, droplet diameters are better documented than bubble diameters. However, the parametric range of the data and the resulting correlations are limited. Both the diameter and the entrainment fraction correlations are based upon low-pressure air-water data. In the code, these relations are used at high pressures and use steam-water properties. As illustrated before, pressure and steam properties considerably change the quantitative predictions. The trends

follow our physical expectations. However, the quantitative error committed by extrapolating these correlations beyond their parametric range cannot be quantified. Further data are needed for this purpose.

A discrete phase, such as drops in annular-mist flow, usually exhibits a transient heat-transfer characteristic with a small time constant. For proper averaging of this transient behavior, further model development efforts are needed, for instance for the average droplet lifetime. Such a model for a mean free path can be obtained from carefully obtained data, as in the study of Lopes and Dukler. More similar data are needed, however, where sizes and velocities are measured simultaneously over a wider parametric range to obtain a widely applicable model.

F.1.3. Models and Correlations in Churn (Transition) Flow

Transition flow exists if the void fraction is between 50% and 75%. This regime is commonly called churn flow in two-phase-flow literature. In TRAC, we treat this regime as an interpolation regime between bubbly slug (in the sense of the three regimes up to a void fraction of 0.5) and annular-mist-flow regimes (see Fig. F-3.). The closure parameters are obtained from the following relationship:

$$X_{\text{transition}} = (1 - W_t)X_{\text{bubbly slug}_{(\alpha = 0.5)}} + W_t X_{\text{annular mist}_{(\alpha = 0.75)}} , \tag{F-87}$$

where X corresponds to either A_i, H_{ALVE}, H_{ALV}, H_{CHTI}, or H_{CHTA}. The linear weighting factor, W_t, is defined based upon the void fraction as follows:

$$0 \le W_t = \frac{\alpha - 0.5}{0.25} \le 1 \ . \tag{F-88}$$

Note that for flashing, the calculated value of H_{ALV} is compared with Eq. (F-27) and the maximum is chosen.

We are not aware of any interfacial-area or heat-transfer models that are specifically developed for churn flow. This may be due to the chaotic nature of the flow pattern, which does not lend itself to a simple geometric idealization. Consequently, we could not make any separate-effect assessments.

F.1.4. Models and Correlations in Stratified Flow

Stratified flow is super-imposed on the general flow-regime map if certain criteria—in terms of phasic velocities and channel orientation—are met to yield phase stratification. The criteria are described in the flow-regime map description (Appendix E). The weighting factor that superimposes stratified flow on the flow-regime map, W_{st}, is different for 1D and 3D components. It is calculated in the interfacial shear packages [subroutine StbVel1D (FEMOM in TRAC-M/F77) for 1D and subroutine CIF3 for 3D] and carried over to interfacial heat-transfer calculations. In interfacial drag routines, the weighting factors are computed as cell-edge quantities. An arithmetic average is calculated in subroutine HTIF to obtain a cell-centered weighting factor. A weighting

factor of unity implies full stratification whereas a weighting factor of zero means the stratification conditions are not met. In the accumulator and during condensation in the pressurizer, W_{st} is set equal to 1 to represent vertically stratified flow.

With the known weighting factor, the various closure parameters are calculated based upon

$$X_{\text{map-stratified}} = (1 - W_{st}) X_{\text{map}} + W_{st} X_{\text{stratified}} \ , \tag{F-89}$$

where X corresponds to either A_i, H_{ALVE}, or H_{ALV}. The subscript *map* refers to quantities calculated using the basic flow-regime map as described in Sections F.1.1., F.1.2., and F.1.3. Note that for flashing, the calculated value of H_{ALV} is compared with Eq. (F-27) and the maximum is chosen. For vapor-side heat-transfer factors, no modification is made due to stratified flow; consequently,

$$H_{\text{CHTI,map-stratified}} = H_{\text{CHTI,map}} \tag{F-90}$$

and

$$H_{\text{CHTA,map-stratified}} = H_{\text{CHTA,map}} \ . \tag{F-91}$$

F.1.4.1. Interfacial-Area Model. Figure F-20. shows a schematic of horizontal stratified flow in a circular pipe. From purely geometric considerations and neglecting the surface waves, the interfacial area is calculated as

$$A_i = D_H \times \Delta x \sqrt{1 - \left(1 - \frac{2L_l}{D_H}\right)^2} \ . \tag{F-92}$$

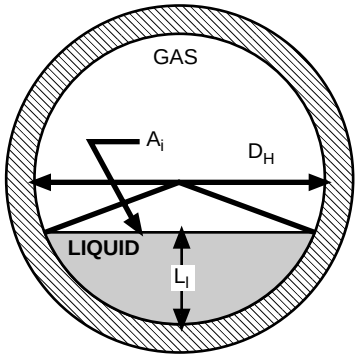

Fig. F-20. Schematic of stratified flow.

For vertically stratified flow, such as in the accumulator and pressurizer, the interfacial area is equal to the average cross-sectional area within the cell given by

$$A_i = \frac{B_{\text{cell}}}{\Delta x} \ . \tag{F-93}$$

F.1.4.2. Interfacial Heat-Transfer Models. For the liquid-side heat-transfer coefficient, a constant-Stanton-number criterion is used. The value of the Stanton number is fixed as suggested by Linehan et al. (Ref. F-29., p. 17) at

$$St \equiv \frac{h_{i,\,l}}{\rho_l c_{p,\,l} V_l} = 0.0073 \ . \tag{F-94}$$

Linehan et al. obtained the magnitude of the Stanton number using their experimental data where steam condenses on subcooled water. They used a horizontal rectangular channel that was 46-cm long, 15-cm wide, and 1.7-cm high. Steam and subcooled water were injected separately, satisfying stratified-flow conditions. The steam Reynolds number ranged from 14000 to 17500. The liquid Reynolds number corresponding to injection flow rate ranged between 250 to 1800. The inlet liquid subcooling ranged between 7°C and 80°C. The value of the liquid-side interfacial heat-transfer coefficient obtained from Eq. (F-91) is used to compute the stratified-flow heat-transfer factors during condensation and flashing.

As mentioned above, no modification is made to the vapor-side heat-transfer coefficient due to stratification, except in the accumulator where

$$h_{gl} = h_{ig} = 10000 \ \frac{\text{W}}{\text{m}^2\text{-K}} \ . \tag{F-95}$$

F.1.4.3. Assessment. As discussed in Section F.1.2.2.2., the Bankoff correlation (Ref. F-24.), which we are using to estimate the heat-transfer coefficient in liquid films, was originally developed for stratified-condensing-cocurrent flow. Thus, we compared the constant-Stanton-number criterion proposed by Linehan et al. with the Bankoff correlation. The comparison is shown in Fig. F-21. As shown, if the slip ratio is on the order of unity, the two correlations are in order of magnitude agreement.

Increasing the pressure increases the Stanton number predicted by the Bankoff correlation. If we consider that the Bankoff and the Linehan et al. correlations are accurate within ±100%, the agreement in Fig. F-21. must be considered to be satisfactory.

Kim (Ref. F-30.) measured condensation rates in countercurrent stratified steam-water flow. In these experiments, Kim used rectangular channels with different inclination angles from horizontal, θ. Table F-2., obtained from Ref. F-30., Table 2-2, shows the parametric range for various tests. Kim obtained an empirical power-law correlation in the form

$$Nu_l = a_1 Re_v^{a_2} Re_l^{a_3} Pr_l^{a_4} \ . \tag{F-96}$$

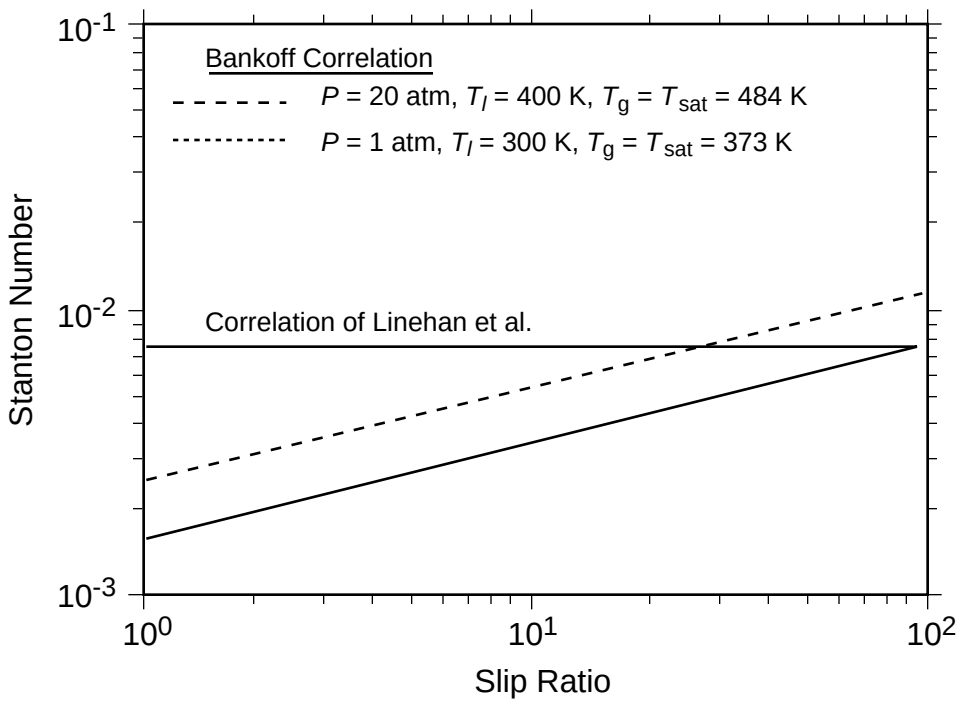

Fig. F-21. Comparison of Bankoff (Ref. F-24.) and Linehan et al. correlations. (Ref. F-29.).

TABLE F-2.
Parametric Range of Kim's Experiments
(Ref. F-30., Table 2 -2)

Data Set	Aspect Ratio [a]	q	Re_g	Re_j
A	5	4°	2500 ~ 30000	800 ~ 15000
B	5	30°	5000 ~ 30000	1000 ~ 8000
C	5	87°	3000 ~ 20000	800 ~ 7000
D, E	5	33°	3000 ~ 18000	800 ~ 5000

a. This is width-to-height ratio for rectangular channels.

Equation (F-96) can be written in Stanton-number form as follows:

$$St_l = a_1 Re_v^{a_2} Re_l^{a_3 - 1} Pr_l^{a_4 - 1} \quad . \tag{F-97}$$

Table F-3., obtained from Ref. F-30., Table 3-1, shows the empirical constants a_1 through a_4 for different experiments. Figure F-22. shows the comparison of the Linehan et al. correlation—used in the code—with the Kim correlations. Only tests denoted by A, B, and E are plotted in this figure. As shown in Fig. F-22. and in Table F-3., the inclination angle, the appearance of the interface, the liquid Reynolds number, and the vapor Reynolds number strongly affect the results. Our constant-Stanton-number correlation is the same order of magnitude with the majority of Kim's data.

TABLE F-3.
Empirical Constants of Kim's Correlations
(Ref. F-30., Table 3 -1)

Data Set	a_1	a_2	a_3	a_4	
A	6.30×10^{-6}	0.900	0.75	0.81	
B	1.35×10^{-4}	0.350	1.00	0.56	
C	8.45×10^{-10}	1.230	1.47	0.50	
D	1.73×10^{-1}	0.027	0.49	0.42	smooth interface
E	3.43×10^{-10}	2.100	0.56	1.16	rough interface

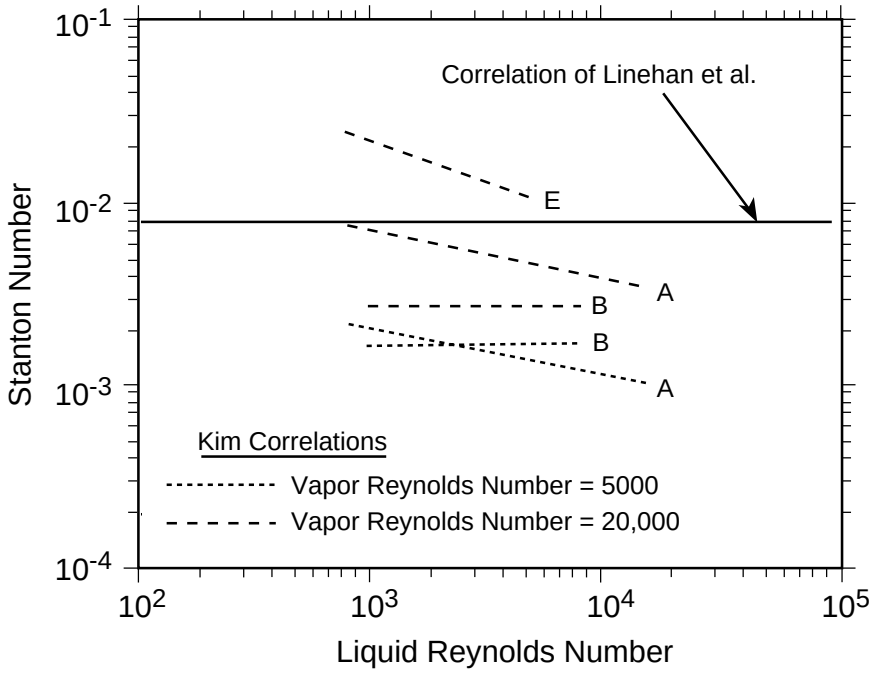

Fig. F-22. Comparison of Kim (Ref. F-30.) and Linehan et al. (Ref. F-29.) correlations.

F.1.4.4. Conclusion and Final Remarks. Stratified flow with phase change is not very easy to analyze using an Eulerian quasi-steady code. The averaging of various models is typically done over the stratified-flow length, which is commonly much greater than a typical cell length. Even for the experiments where the stratified-flow conditions are carefully controlled, the resulting correlations in the literature have a low degree of accuracy. In an integral analysis, the detection of the onset of stratified flow is difficult because it depends on history and upstream effects. Consequently, the total length of the stratified-flow region cannot be accurately predicted for proper averaging. This situation becomes more complicated during a hydrodynamic transient. Within this perspective, a very accurate stratified-flow heat-transfer package is not possible. The current package must be judged on its overall performance in an integral analysis. We must note that, in stratified flow, especially with high gas velocities, one would expect the interface to be wavy. Consequently, our geometric model to estimate the interfacial area is not accurate. However, the constant-Stanton-number criterion developed by Linehan et al. already accounts for this waviness in the correlation. The heat-transfer coefficients are obtained directly from the local rate of change of the liquid flow rate. The measured change in liquid flow rates is converted to an interfacial heat-transfer coefficient assuming the incremental time-averaged interfacial area to be smooth. As a result, any error committed by assuming a smooth interface is already absorbed by the $St = 0.0073$ correlation.

F.1.5. Models and Correlations in Plug Flow

The existence of the liquid plug is superimposed upon bubbly slug / transition / annular-mist / stratified flows if the liquid side is under condensation mode. A schematic of plug flow is shown in Fig. F-23. The weighting factor, W_{plug}, incorporates the effect of plugging on the liquid-side condensation heat-transfer factor as follows:

$$H_{ALVE,map-stratified\text{-}plug} = (1 - W_{plug}) H_{ALVE,map-stratified} + W_{plug} H_{ALVE,plug} \quad . \tag{F-98}$$

The purpose of W_{plug} is to recognize when the void fractions in three contiguous cells are significantly different from each other and at least one cell has a void fraction above 50% but below 75%, warranting the assumption that plugs may exist. The weighting factor W_{plug} is given by

$$0 \le W_{plug} \equiv \frac{(\alpha_{max} - \alpha_{min})(\alpha_{max} - 0.5)(0.75 - \alpha_{min})}{(0.75 - 0.5)^3} \le 1 \ , \tag{F-99}$$

where α_{min} and α_{max} are the minimum and maximum of the void fractions in the group of three contiguous cells. Figure F-24. is a contour plot showing W_{plug} in terms of α_{min} and α_{max}. Notice that when $\alpha_{min} = \alpha_{max}$, $\alpha_{max} \le 0.5$, or $\alpha_{min} \ge 0.75$, W_{plug} is equal to zero, which means that there is no plugging.

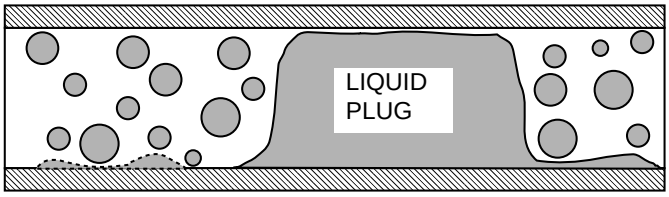

Fig. F-23. Schematic of plug flow.

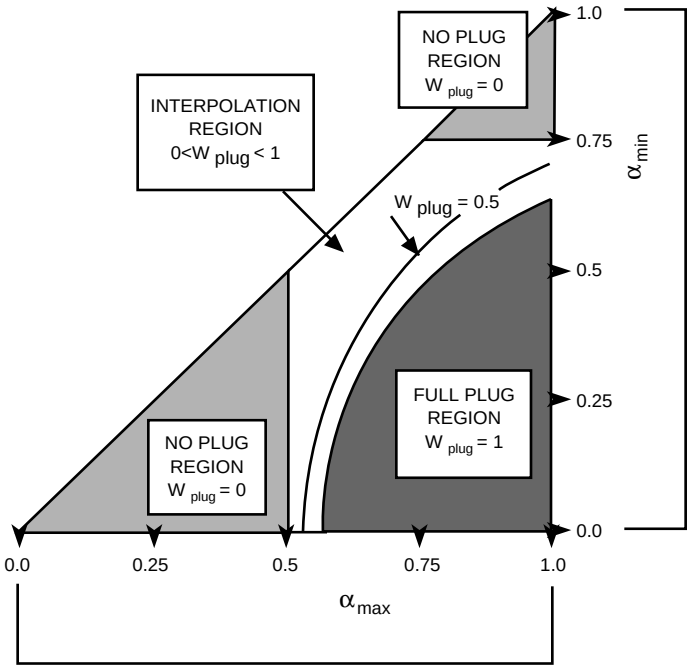

Fig. F-24. Liquid plug formation map.

F.1.5.1. Interfacial-Area Model. The interfacial area of a plug is calculated assuming a cylindrical geometry, which yields

$$A_{i,\text{plug}} = M_{\text{plug}} \times \frac{\pi}{4} D_H^2 \ , \tag{F-100}$$

where M_{plug} is either 1 or 2, depending upon whether the plug is confined within one or more cells.

F.1.5.2. Heat-Transfer Coefficient Models. The liquid-side heat-transfer coefficient is calculated through a simple constant-Stanton-number model given by

$$St \equiv \frac{h_{i,\,l}}{\rho_l c_{p,\,l} V_l} = 0.02 \ . \qquad \text{(F-101)}$$

Vapor-side heat-transfer is not affected by plug formation.

F.1.5.3. Assessment. To the best of our knowledge, no interfacial heat-transfer model specifically has been developed for liquid plugs. Liquid-plug behaviors were experimentally observed by Akimoto et al. (Ref. F-31.). The plug behavior predicted by TRAC is in good agreement with these data. This comparison is further documented in the TRAC-M/F77 Developmental Assessment Manual (Refs. F-100. and F-101.).

F.1.5.4. Conclusions and Final Remarks. Currently, the TRAC model for condensation during plugging is a simple model. Unfortunately, we are not aware of a mechanistic model to replace the $St = 0.02$ criterion. However, the existing model seems to predict well the plug behavior in the experiments of Akimoto et al. (Ref. F-31.).

F.1.6. Reflood Models and Correlations

During reflood of the core region, a special flow-regime map is activated. The flow-regime map during reflood shown in Fig. F-25. is based upon the observations of DeJarlais and Ishii (Ref. F-32.). Figure F-25. illustrates that, along the flow channel, various flow configurations occur beyond the CHF point. Because of considerable differences in flow patterns, these various regimes require different closure relationships. Such relationships are incorporated into the code in accordance with the flow patterns shown in Fig. F-25. Naturally, in order to make transitions from one flow pattern to the next, the various elevations for such transitions must be known. The code calculates these elevations through mechanistic models mostly scaled through capillary number. These models are discussed in Section F.2.2. and are not repeated here.

This document only describes the core reflood model that is in TRAC-M/F90 (Version 3.0), which was bought over from MOD2. References F-102. and F-103. describe the additional reflood model that was developed for TRAC-M/F77.

The reflood model is applicable only for the VESSEL component and is used only in a core region that is specified in the VESSEL's input. The model is activated by the user via the NAMELIST input variable NEWRFD (which cannot be changed in a restart calculation). In addition to setting NEWRFD, the user must also specify a reflood trip and identify that trip via HTSTR input variable IRFTR2. If the reflood model is activated at the start of a LOCA transient, it will be used also during the blowdown and refill phases of the transient.

Note that the work of DeJarlais and Ishii, on which the reflood model is based, is directly applicable to high reflood rates.

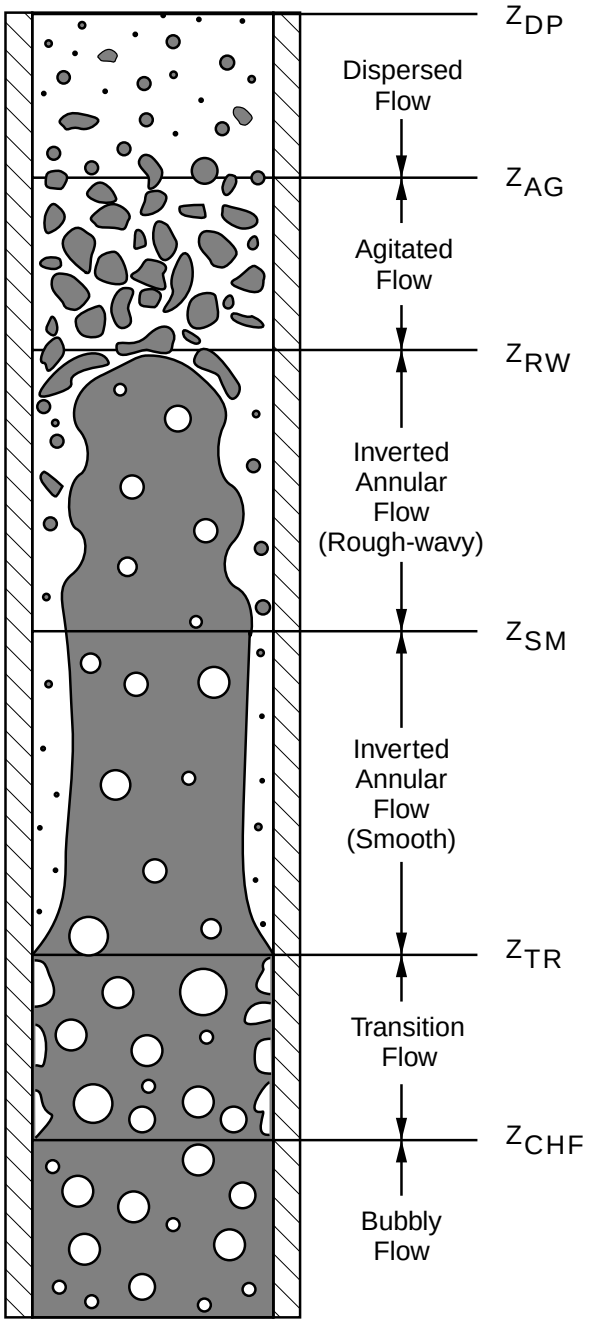

Fig. F-25. Flow-regime map during reflood.

The discussion in this section presumes that the elevations Z_{CHF}, Z_{TR}, Z_{SM}, Z_{RW}, Z_{AG}, and Z_{DP} are known. (Z_{DP} is the transition to highly dispersed flow. See Sections F.1.6.2., F.2.2., and Appendix H, Section H.1.5.) Depending upon the location of a given cell with reference to these elevations, the appropriate closure relationships are computed using weighting factors based upon the cell length. The weighting factors are determined

using the top and bottom cell-edge elevation of a given cell, denoted by z_t and z_b, respectively. Table F-4. reports the way the following weighting factors are calculated:

$$0 \le W_{sb} = \frac{Z_{\mathrm{TR}} - z_t}{\Delta x} \le 1 \tag{F-102}$$

$$0 \le W_{sm} = \frac{\min(Z_{\mathrm{SM}}, z_t) - \max(Z_{\mathrm{TR}}, z_b)}{\Delta x} \le 1 \tag{F-103}$$

$$0 \le W_{rw} = \frac{\min(Z_{\mathrm{AG}}, z_t) - \max(Z_{\mathrm{SM}}, z_b)}{\Delta x} \le 1 \tag{F-104}$$

$$W_{inv} = W_{rw} + W_{sm} \tag{F-105}$$

$$W_{ds} = 1 - W_{sb} - W_{rw} - W_{sm} \tag{F-106}$$

Once the weighting factors are obtained from Table F-4., they are used to calculate the various closure relationships through

$$X_{\mathrm{reflood}} = W_{sb} \times X_{\mathrm{bubbly}} + W_{ds} \times X_{\mathrm{dispersed}} + W_{inv} \times X_{\mathrm{inverted}} \ , \tag{F-107}$$

where X represents either A_i, H_{ALVE}, H_{CHTI}, or H_{CHTA}. For flashing, the maximum between H_{ALVE} and the model discussed in the next section is used. If noncondensables are present, H_{ALVE} for evaporation and condensation is modified as described in Section F.1.7. The individual models used for bubbly, dispersed, and inverted annular flows are described in the following subsections.

TABLE F-4.
Weighting Factors of Reflood Interfacial Heat-Transfer Models

z	W_{sb}	W_{sm}	W_{rw}	W_{ds}	W_{inv}
$z_t \le Z_{\mathrm{TR}}$	1	0	0	0	0
$Z_{\mathrm{TR}} < z_t < Z_{\mathrm{SM}}$	Eq. (F-102)	Eq. (F-103)	0	0	Eq. (F-105)
$Z_{\mathrm{SM}} < z_t < Z_{\mathrm{AG}}$	Eq. (F-102)	Eq. (F-103)	Eq. (F-104)	0	Eq. (F-105)
$Z_{\mathrm{AG}} < z_t$	Eq. (F-102)	Eq. (F-103)	Eq. (F-104)	Eq. (F-106)	Eq. (F-105)
$z_b \ge Z_{\mathrm{AG}}$	0	0	0	1	0

F.1.6.1. Bubbly Flow Models. In bubbly CHF upstream of the quench front, the void fraction is restricted to the following range: $0.05 \le \alpha \le 0.30$. Slugs are not allowed to form. The interfacial area and heat-transfer coefficients, except for the flashing model, are identical to those described in Sections F.1.1.1.1., F.1.1.2., and F.1.1.3. When the reflood model is used and $T_l > T_{sat}$, the liquid-side heat-transfer factor is not calculated by Eq. (F-27). The reflood model uses a simple flashing model to determine the liquid-side heat-transfer factor. This simple model uses the kinetic theory of evaporation from liquid surfaces (see Ref. F-33., p. 56). The theoretical maximum evaporation rate was converted to an equivalent HTC. The coefficient of evaporation of 0.04 (suggested by Hsu and Graham, Ref. F-34.) to predict the evaporation rate in experimental studies was modified for each of the individual flow regimes in nucleate and film boiling. The liquid-side HTC due to flashing is given by the following equation:

$$h_{\text{fls}} = C_{\text{eva}} h_{\text{fls,teo}} = C_{\text{eva}} \times 0.01857 \frac{\rho_v h_{fg}^2}{T_{\text{sat}}^{1.5}} \quad . \tag{F-108}$$

The coefficient of evaporation, C_{eva}, is defined for bubbly and annular-mist-flow regimes in the nucleate-boiling region. The selection of C_{eva} is considered to be void-fraction dependent in the bubbly flow when the cell void fraction is between 0.3 and 0.5. The evaluation logic of C_{eva} for the bubbly flow is

$$C_{\text{eva}} = 0.002 \times \left[C_1 + (C_2 - C_1) \times \left(\frac{\alpha - 0.3}{0.5 - 0.3} \right)^{0.5} \right] \text{ if } 0.3 < \alpha < 0.5 , \tag{F-109}$$

$$C_{\text{eva}} = 0.002 C_2 \text{ if } \alpha = 0.5 , \text{ and} \tag{F-110}$$

$$C_{\text{eva}} = 0.002 C_1 \text{ if } \alpha < 0.3 . \tag{F-111}$$

The current values for C_1 and C_2 are 0.1 so that C_{eva} becomes 0.0002 for all void fractions up to 0.5 in bubbly flow. The interfacial surface area in bubbly flow is identical to that described in Section F.1.1.1.1. The liquid-side heat-transfer factor during the flashing in the bubbly flow is given by

$$H_{\text{ALV,bub}} = h_{\text{fls}} A_{i,\text{bubble}} \quad . \tag{F-112}$$

C_{eva} is selected as 0.0002 in the annular-mist-flow regime. The liquid-side heat-transfer factor during flashing in annular-mist flow is given by

$$H_{\text{ALV,mist}} = h_{\text{fls}} A_{i,\text{mist}} \quad . \tag{F-113}$$

The interfacial surface area, $A_{i,\text{mist}}$, is identical to that described in Section F.1.2.

If the flow regime is determined as the transition between bubbly and annular-mist flows ($0.5 < \alpha < 0.75$), an interpolation is used to determine $H_{\mathrm{ALV,trans}}$ in the nucleate-boiling region as

$$H_{\mathrm{ALV,trans}} = W \times H_{\mathrm{ALV,mist}} + (1-W) \times H_{\mathrm{ALV,bubbly}} \ , \tag{F-114}$$

where

$$W = \frac{\alpha}{0.75-0.5} - \frac{0.5}{0.75-0.5} = 4\alpha - 2 \ . \tag{F-115}$$

F.1.6.2. Dispersed (Post-Agitated) and Highly Dispersed Inverted Annular Flows. This flow regime is furthest from the quench front, as shown in Eq. (F-25). The region immediately above elevation Z_{AG} is considered to be the post-agitated region of dispersed flow. As shown in Section F.2.2. and in Appendix H (Section H.1.5.), at higher elevations we distinguish a highly dispersed flow regime. The void fraction is restricted to being between 0.3 and 0.9995. If there is a cold wall adjacent to the hydro cell, however, liquid film is allowed to form. Thus, the models are very similar to those used in annular-mist flow.

F.1.6.2.1. Interfacial-Area Models. Using a simple force balance, the thickness of a stable film on a cold wall is calculated as

$$10^{-17} \le \delta_{lf} = \frac{0.0025 D_H \rho_l V_g^2}{g\rho_l D_H - 0.75\rho_g V_g^2} \le 5 \text{ mm} \ , \tag{F-116}$$

where the minimum limit on the denominator is 0.01. With a known film thickness, the liquid fraction corresponding to the film can be computed as

$$\alpha_f = \frac{4F_u \delta_{lf}}{D_H} \ , \tag{F-117}$$

where F_u is the cold-wall fraction adjacent to the hydro cell. The liquid-film fraction also is estimated with the following equations:

$$\alpha_f = F_u W_{fd} (1-\alpha) \ , \tag{F-118}$$

where W_{fd} is the cold-wall liquid-fraction weighting factor defined as

$$W_{fd} = 0 \qquad \text{if} \quad \alpha \le \min(\alpha_{AG}, 0.7)$$

$$W_{fd} = 5\left[\frac{0.98 - \alpha^*}{0.98 - \min(\alpha_{AG}, 0.7)}\right]^{0.35} \qquad \text{if} \quad \min(\alpha_{AG}, 0.7) < \alpha < 0.98 \qquad \text{(F-119)}$$

$$W_{fd} = 5 \qquad \text{if} \quad \alpha \ge 0.98 \ ,$$

where α^* is the void fraction that has been constrained to be between 0.3 and 0.9995. (The tests are made with the actual void fraction.) In TRAC-M/F77, the exponent 0.35 in Eq. (F-119) is 0.5 for the reflood model in that code based on MOD2.

The liquid-film fraction, α_f, is selected as the minimum of values obtained from Eqs. (F-117) and (F-118).

The liquid droplet fraction is obtained by

$$\alpha_{dd} = 1 - \alpha_f - \alpha \ . \qquad \text{(F-120)}$$

Then, the interfacial areas corresponding to liquid film and droplets are obtained as

$$A_{i,\text{film}} = \frac{4\alpha_f B_{\text{cell}}}{D_H} \qquad \text{(F-121)}$$

and

$$A_{i,\text{drop}} = B_{\text{cell}} \frac{6\alpha_{dd}}{D_d} \ . \qquad \text{(F-122)}$$

The final interfacial area in the dispersed (or post-agitated) IAF is

$$A_{i,\text{dispersed (or post-agitated)}} = A_{i,\text{film}} + A_{i,\text{drop}} \ . \qquad \text{(F-123)}$$

The droplet Sauter mean diameter in Eq. (F-119) is calculated using the same models as the annular-mist-flow models, given by Eqs. (F-54) and (F-56).

F.1.6.2.2. Vapor-Side Heat-Transfer Models. Before the vapor-to-interface heat-transfer factor is calculated in the dispersed-flow regime, a mass fraction is calculated as

$$x_l = \frac{\rho_g V_g (1 - \alpha_{dd})}{\rho_g V_g (1 - \alpha_{dd}) + \rho_l V_l \alpha_{dd}} \ . \qquad \text{(F-124)}$$

Based upon this mass fraction, we calculate a homogeneous void fraction defined as

$$\alpha_{\text{hom}} = \frac{x_{\text{l}}\rho_{\text{l}}}{x_{\text{l}}\rho_{\text{l}} + (1 - x_{\text{l}})\rho_g} \ . \tag{F-125}$$

Then, if $\alpha_{\text{hom}} \geq 1$ and $1 - \alpha_{dd} \leq 0.95$, $H_{\text{CHTI,dispersed}}$ is set to 10^{-6} W/K. Otherwise, the correlation proposed by Unal et al. (Ref. F-33.) is used to calculate H_{CHTI}. The correlation was originally developed for the vapor-generation rate (see Ref. F-34., Eq. 21). In the code, we converted it to a heat-transfer factor as follows:

$$H_{\text{CHTI},\,ds} = 0.05 \times 0.315 \exp\left(-C_{u1}\frac{P}{P_{cr}}\right)\left[V_g \rho_g \left(\frac{1 - \alpha_{dd}}{\alpha_{\text{hom}}}\right)\right]^{C_{u2}} \tag{F-126}$$

$$\times \frac{k_g Pr_g^{0.33}\left[g\left(\rho_{\text{l}} - \rho_g\right)\right]^{0.725}}{\mu_g^{0.55}(2\sigma)^{0.725}} B_{\text{cell}} \left[\frac{\sqrt{\rho_g \sigma \sqrt{\dfrac{\sigma}{g\left(\rho_{\text{l}} - \rho_g\right)}}}}{\mu_g}\right]^{0.4833} ,$$

where the constants C_{u1} and C_{u2} are given as 10.894 and 0.55 in the original reference. During code assessment, they are modified to be 30 and 0.33, respectively.

If the cell void fraction is less than 0.98, then the flow regime is post-agitated IAF. The H_{CHTI} in post-agitated IAF is calculated also by Eq. (F-126) with a void-fraction weighting applied between smooth and dispersed IAFs, as indicated by

$$H_{\text{CHTI, post-ag}} = H_{\text{CHTI},\,ds}\left[\frac{\alpha - \alpha_{\text{SM}}}{\alpha_{\text{DP}} - \alpha_{\text{SM}}}\right] . \tag{F-127}$$

Using an exponent of 0.01 results in $H_{\text{CHTI,post-ag}}$ being equal to $H_{\text{CHTI},ds}$ in post-agitated IAF.

In the presence of noncondensables, the gas-to-liquid sensible heat-transfer factor, H_{CHTA}, is calculated using previously described models. For the droplets, the Ryskin correlation described in and given by Eq. (F-78) is used to calculate $h_{g\text{l,drop}}$ using noncondensable-gas properties. For the liquid film, the Bankoff correlation given by Eq. (F-81) is used, also using noncondensable-gas properties. Then, the final quantity is obtained as

$$H_{\text{CHTI,dispersed}} = W_{fd}\left(A_{\text{i,drop}} h_{g\text{l,drop}} + A_{\text{i,film}} A_{g\text{l,film}}\right) + (1 - W_{fd}) A_{\text{i,drop,max}} h_{g\text{l,drop}} \ , \tag{F-128}$$

where W_{fd} is the weighting factor as described before.

F.1.6.2.3. Liquid-Side Heat-Transfer Models. In the reflood model, the liquid-side heat-transfer factor, H_{ALVE}, is not calculated in subroutine HTIF for the inverted-annular-flow regimes when $T_l < T_{\text{sat}}$. Rather, the sensible heat that goes to the subcooled liquid is calculated in subroutine HTVSSL in the wall-to-liquid HTC. If the liquid is superheated, the coefficient of evaporation for the flashing model, C_{eva}, is set to 0.002. The H_{ALV} for the dispersed (or post-agitated IAF) is calculated as

$$H_{\text{ALV, dispersed (or post-agitated)}} = h_{\text{fls}} A_{i,\text{ dispersed (or post-agitated)}} \ , \tag{F-129}$$

where h_{fls} is calculated by Eq. (F-108).

F.1.6.3. Inverted Annular Flow. In inverted annular flow, the void fraction is limited between 0.05 and 0.95. The following models are used to calculate the interfacial area and heat-transfer factors.

F.1.6.3.1. Interfacial-Area Model. First, we calculated the hydraulic diameter of the liquid core from purely geometric considerations as

$$D_{H,\text{core}} = D_H \sqrt{1-\alpha} \ . \tag{F-130}$$

Then, the interfacial area is computed as

$$A_{i,\text{inverted}} = \pi D_H \Delta x \ . \tag{F-131}$$

In the case of flashing, the interfacial area is recalculated considering possible bubbles in the liquid core. Using an expression suggested by Denham (Ref. F-35.), the vapor film thickness is calculated as

$$\delta_{vf} = \sqrt{\frac{V_l \mu_v}{g(\rho_l - \rho_v)}} \tag{F-132}$$

The wall void fraction can be calculated by

$$\alpha_w = 4\frac{\delta_{vf}}{D_H}\left(1 - \frac{\delta_{vf}}{D_H}\right) \ . \tag{F-133}$$

The interfacial surface area near the wall then becomes

$$A_w = \pi\left(D_H - 2\delta_{vf}\right)\Delta z \ . \tag{F-134}$$

The void fraction for bubbles traveling in the liquid-core region is

$$\alpha_{fr} = \alpha - \alpha_w \ . \tag{F-135}$$

The bubble diameter is calculated as it was calculated for the bubbly flow in Section F.1.1.1. The interfacial surface area for bubbles traveling in the liquid core is

$$A_{fr} = \frac{6\alpha_{fr} B_{\text{cell}}}{D_b} \ . \tag{F-136}$$

The total interfacial area becomes

$$A_{i,\text{ inverted}} = A_w + A_{fr} \ . \tag{F-137}$$

F.1.6.3.2. Vapor-Side Heat-Transfer Models. For the vapor-side heat-transfer, the following simple models are used

$$H_{\text{CHTI, inverted}} = 3 \times 10^3 \times A_{i,\text{ inverted}} \tag{F-138}$$

and

$$H_{\text{CHTA,inverted}} = 10^3 \times A_{i,\text{ inverted}} \ . \tag{F-139}$$

F.1.6.3.3. Liquid-Side Heat-Transfer Model. In the reflood model, the liquid-side heat-transfer factor, H_{ALVE}, is not calculated in subroutine HTIF for the inverted-annular-flow regimes when $T_l < T_{\text{sat}}$. Rather, the sensible heat that goes to the subcooled liquid is calculated in subroutine HTVSSL in the wall-to-liquid HTC. If the liquid is superheated, the coefficient of evaporation for the flashing model, C_{eva}, is set to 0.002. The H_{ALV} for the IAFs (smooth, rough-wavy, and agitated IAFs) is calculated as

$$H_{\text{ALV,inverted}} = h_{\text{fls}} A_{i,\text{inverted}} \ , \tag{F-140}$$

where h_{fls} is calculated by Eq. (F-108).

F.1.6.4. Effect of Grid Spacers. If there is a grid spacer in the hydro cell and the hydro cell is fully above the quench front, then the calculated vapor-to-liquid heat-transfer factor is modified as

$$H_{\text{CHTI, grid}} = H_{\text{CHTI}} + \frac{D_H}{B_{\text{cell}}} \times \frac{10^6}{T_g - T_{sv}} \ . \tag{F-141}$$

No modifications are made to the liquid-side heat-transfer factor.

F.1.6.5. Assessment. Extensive assessment results for the reflood model are provided in Section F.2. and also in the TRAC-M/F77 Developmental Assessment Manual (Refs. F-100. and F-101.). These results are not repeated here.

F.1.7. The Effect of Noncondensables

The noncondensables affect the interfacial heat- and mass-transfer rates by lowering the partial pressure and thus, the saturation temperature of steam. In addition, the existence of noncondensables triggers a new set of models in the code. These models are described below.

F.1.7.1. Effects on Liquid-Side Heat-Transfer. On the liquid side, the presence of noncondensables affects both the evaporation and condensation.

F.1.7.1.1. Evaporation. If noncondensable gases are present, T_{sat} is greater than T_{sv}. Consequently, evaporation mode is possible when $T_{sv} < T_l < T_{sat}$. In the code, we assumed that the interfacial mass transfer is diffusion controlled, regardless of the amount of noncondensables. A simple diffusion model, independent of the flow-regime map, is used. The mass-transfer coefficient is obtained from the following equation:

$$Sh = 3.656 \quad \text{if} \quad Re \le 2300 \text{ and}$$

$$Sh = 0.023 Re^{0.8} Sc^{1/3} \quad \text{if} \quad Re > 2300 , \tag{F-142}$$

where *Sh*, *Sc*, and *Re* are Sherwood, Schmidt, and Reynolds numbers defined as

$$Sh = \frac{h_M D_H}{D_o} ,$$

$$Sc = \frac{\mu_g}{\rho_g D_o} ,$$

and

$$Re = \frac{G_g D_H}{\mu_g} .$$

These equations are reported in Ref. F-36. for mass-transfer coefficient h_M in fully developed pipe flow with constant concentration on the pipe wall. Note that Eq. (F-142) is identical to the analytical solution for laminar flow and the well-known Dittus-Boelter equation for turbulent flow if the Sherwood number is replaced by the Nusselt number and the Schmidt number is replaced by the Prandtl number. The diffusion coefficient is obtained from a curve fit to a theoretical equation for the diffusion of steam in air. The curve fit is given by

$$D_o = \frac{1 \times 10^{-3}}{P}(-699.2438 + 4.9249 T_g + 0.0171 T_g^2) \ , \tag{F-143}$$

where the diffusion coefficient D_o is in m/s, gas temperature T_g is in K, and total pressure P is in Pa. The curve fit is obtained for T_g between 273 and 600 K. Once the mass-transfer coefficient, h_M, is obtained from Eq. (F-142), the evaporative mass flux can be computed as

$$\dot{m}_e = h_M (C_i - C_\infty) \ , \tag{F-144}$$

where C_i and C_∞ are the steam concentration at the interface and away from the interface, respectively. We assumed that at the interface, the steam concentration is equal to the density of pure steam with $T = T_l$ and $P = P_{\text{sat}}$ when $T_{\text{sat}} = T_l$. Using an ideal-gas approximation, the density is calculated as

$$C_i = \rho_s = \frac{(P_{\text{sat}})_{T_{\text{sat}} = T_l}}{R_s T_l} \ , \tag{F-145}$$

where R_s is the ideal-gas constant for steam and is set equal to 462 J/kg-K. Far from the interface, the concentration is given by

$$C_\infty = \rho_g - \rho_a \ , \tag{F-146}$$

where ρ_g and ρ_a are the mixture and noncondensable-gas densities, respectively. This formulation assumes that the densities are additive in the gas mixture. Using Eqs. (F-3) through (F-5) and (F-144) through (F-146), we obtain

$$\frac{1}{h_{fg}}\left[H_{\text{ALVE}}(T_l - T_{sv}) + \frac{P_s}{P} H_{\text{CHTI}}(T_g - T_{sv})\right] = h_M A_i (\rho_s - \rho_g + \rho_a) \ . \tag{F-147}$$

Solving for H_{ALVE}, Eq. (F-147) yields

$$H_{\text{ALVE}} = \frac{1}{(T_l - T_{sv})}\left[h_M h_{fg} A_i (\rho_s - \rho_g + \rho_a) - \frac{P_s}{P} H_{\text{CHTI}}(T_g - T_{sv})\right] . \tag{F-148}$$

In the code, the vapor-side heat-transfer coefficient is neglected (the second term is set to zero). Thus, H_{ALVE} is coded as

$$H_{\text{ALVE}} = h_M h_{fg} A_i (\rho_s - \rho_g + \rho_a) \frac{1}{(T_l - T_{sv})} \ , \tag{F-149}$$

where $T_l - T_{sv}$ is set to 1.

These models represent an approximate formulation of interfacial evaporation in the presence of noncondensables. The model can be improved through the following considerations.

1. Even in the presence of noncondensables, the evaporation process may be heat-transfer controlled. This depends on how the noncondensable gas is distributed within the gas phase and also on the amount of noncondensable gas.
2. By replacing the Sherwood number by the Nusselt number and the Schmidt number by the Prandtl number, various heat-transfer correlations can be converted to mass-transfer correlations. This way, the package can be made flow-regime-dependent instead of using Eq. (F-142) for all the flow regimes.
3. Equation (F-144) can be used directly to compute the evaporation rate. However, this approach requires a model to partition the supply of sensible heat between the phases. The lack of such a model forced us to assume that all the sensible heat is supplied by the liquid side, thus yielding the approximation in Eq. (F-149).

F.1.7.1.2. Condensation. During condensation in the presence of noncondensables, the liquid-side heat-transfer factor, H_{ALVE}, is reduced. The reduction is based upon the empirical correlation developed by Sklover and Rodivilin (Ref. F-37.). The original correlation is given by (Ref. F-37., Eq. 5) as

$$\frac{h_{\mathrm{l},nc}}{h_{\mathrm{l}}} = 0.366 \left(\frac{G_a G_{\mathrm{l}}}{G_s^2} \right)^{-0.2} , \tag{F-150}$$

where $h_{\mathrm{l},nc}$ is the liquid-side heat-transfer coefficient in the presence of noncondensables, and G_a, G_l, and G_s are the air, water, and steam mass fluxes, respectively. This is an empirical correlation obtained by measuring the condensation rates on multiple subcooled-water jets. Steam and air are injected perpendicular to the water jets. In the experiments, the liquid mass flux ranged between 3000 and 15000 $\mathrm{kg/m^2\text{-}s}$. The steam mass flux ranged between 100 and 710 $\mathrm{kg/m^2\text{-}s}$. The range for air mass flux was not reported.

In TRAC, condensable and noncondensable gases in the mixture flow with the same velocity. Thus, Eq. (F-150) reduces to

$$\frac{h_{\mathrm{l},nc}}{h_{\mathrm{l}}} = 0.366 \left(\frac{\rho_s}{\rho_a} \right)^{0.2} \left(\frac{G_s}{G_{\mathrm{l}}} \right)^{0.2} . \tag{F-151}$$

In the code, we further assumed that the densities are additive in the gas mixture. As a result of this assumption, the steam density is calculated as

$$\rho_s = \rho_g - \rho_a \ . \tag{F-152}$$

Thus, the final correction is coded as follows:

$$0.1 \le \frac{H_{\mathrm{ALVE},\,nc}}{H_{\mathrm{ALVE}}} = \frac{h_{l,\,nc}}{h_l} = 0.366\left(\frac{\rho_g - \rho_a}{\rho_a}\right)^{0.2}\left(\frac{G_s}{G_l}\right)^{0.2} \le 0.1 \ , \tag{F-153}$$

where H_{ALVE} is the flow-regime-dependent heat-transfer factor as described in the previous sections. For fully stratified flow, $H_{\mathrm{ALVE},nc}/H_{\mathrm{ALVE}}$ is limited to be less than 90%. In the code, we limited the mass fluxes as

$$3000 \le G_l \le 18\ 000 \ \mathrm{kg/m^2\text{-}s}$$

and

$$0 \le G_s \le 640 \ \mathrm{kg/m^2\text{-}s}$$

to make the model consistent with the experimental database of Sklover and Rodivilin. A contour map for correction in the presence of noncondensables is shown in Fig. F-26.

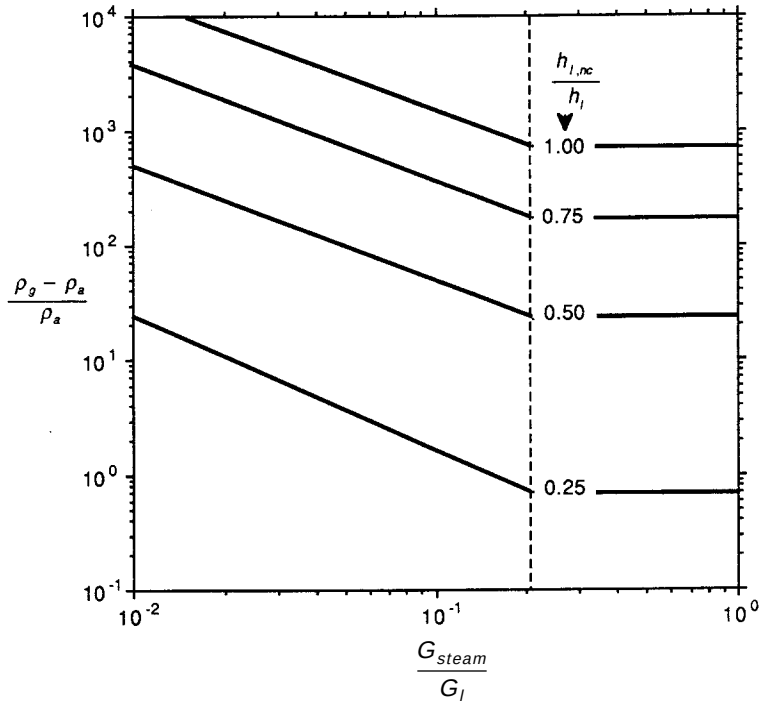

Fig. F-26. Contour map for liquid-side heat-transfer correction in the presence of noncondensables.

A major drawback of this model is that it is flow-regime-independent. Different flow situations and mixing conditions in different flow regimes may yield different models. However, the basic characteristics of the models are expected to be the same. The current model also is highly empirical. Extrapolation beyond its database will lead to questionable results.

F.1.7.2. Vapor-Side Heat Transfer. During evaporation or condensation in the presence of noncondensables, no modifications are made to the gas-to-interface heat-transfer factor, H_{CHTI}. As given by Eq. (F-1), however, the heat-transfer factor is multiplied by the relative partial pressure of steam in the energy equation. Thus, the presence of noncondensables decreases the effective vapor-side heat-transfer factor through the ratio of steam partial pressure and total partial pressure.

The sensible heat transfer between the phases becomes effective only if the partial pressure of noncondensables is non-zero. Thus, the heat-transfer factor, H_{CHTA}, is only effective in the presence of noncondensables. The models for calculating H_{CHTA} are flow-regime dependent and were described in the previous sections.

F.1.8. Magnitude Limits and New-Time/Old-Time Averaging

At the end of subroutine HTIF, the calculated closure quantities are limited due to physical and numerical computations. In the following subsections, the various limiters are described.

F.1.8.1. Limits for Subcooled Vapor. If the vapor temperature is less than the saturation temperature, the vapor-side heat-transfer factor is limited by

$$H_{\text{CHTI, map/stratified/plug/}nc} \le 10^6 \times B_{\text{cell}} \ . \tag{F-154}$$

Then, the final value of H_{CHTI} is further modified based upon the degree of subcooling as follows:

$$H_{\text{CHTI, map/stratified/plug/}nc} = H_{\text{CHTI, map/stratified/plug/}nc} \times \exp(T_{sv} - T_g) \ , \tag{F-155}$$

where

$$0 \le T_{sv} - T_g \le 7 \ .$$

Note that in the code, this magnitude limit is applied before the effects of liquid plugging and noncondensable gases. In these two cases, no modification is made to H_{CHTI}; thus, the calculated magnitude is final except for old-time weighting.

If the gas temperature is less than the liquid temperature, the magnitude of H_{CHTA} is similarly modified as

$$H_{\text{CHTA, map/stratified/plug/}nc} \le 10^6 \times B_{\text{cell}} \ . \tag{F-156}$$

Then, the final value of H_{CHTA} is further modified based upon the temperature difference as follows:

$$H_{\mathrm{CHTA,\,map/stratified/plug/}nc} = H_{\mathrm{CHTA,\,map/stratified/plug/}nc} \times \exp(T_{\mathrm{l}} - T_g) \ , \qquad \text{(F-157)}$$

where

$$0 \le T_{\mathrm{l}} - T_g \le 7 \ .$$

F.1.8.2. Kinetic Theory Limits on Liquid-Side Heat Transfer. In TRAC, we limited the liquid-side heat-transfer coefficient by kinetic theory. We assumed that the condensation or evaporation rate cannot exceed the molecular flux towards the interface. Using the linearized approximation of kinetic theory, the maximum limit of $h_{i\mathrm{l}}$ is coded as

$$h_{i\mathrm{l},\max} = \sqrt{\frac{M_s}{2\pi R_s}} \times \frac{\rho_g h_{fg}^2}{T_g^2} \quad \text{if } \mathrm{T_l} < \mathrm{T_{sv}} \ , \qquad \text{(F-158)}$$

where M_s is the molecular weight of water. The liquid-side heat-transfer factor during condensation or evaporation is limited as

$$0.1 B_{\mathrm{cell}} \le H_{\mathrm{ALVE,\,map/stratified/plug/}nc\mathrm{/vertical}} \le A_i h_{i\mathrm{l},\max} \ . \qquad \text{(F-159)}$$

F.1.8.3. Old-Time/New-Time Averaging. No old-time/new-time averaging is applied if the phasic temperature crosses the saturation line, the cell was single phase at the previous time step, or the magnitudes of H_{ALV}, H_{ALVE}, H_{CHTI}, and H_{CHTA} were less than 10^{-10} at the previous time step. Otherwise different averaging techniques are applied, depending upon whether the code is run in steady-state or in transient mode.

F.1.8.3.1. Steady-State Averagers. During a steady-state run, the following simple old-time/new-time averaging technique is used

$$x^n = f \times X^n + (1 - f) \times X^{n-1} \ , \qquad \text{(F-160)}$$

where the superscript n represents the new-time value and n–1 is the old-time value. In Eq. (F-160), X corresponds to either H_{ALV}, H_{ALVE}, H_{CHTI}, or H_{CHTA}. In the code, f is currently set equal to 0.1. Thus, the weighting heavily favors the old-time value. This means that many time-step sizes are required before reaching the steady-state value from a given initial condition. The time-wise variation of the quantity X is time-step-size dependent. For this reason, time averaging is more suitable for steady-state calculations where the time-wise variation is not as important as the final equilibrium result. By allowing slower changes of X, this kind of weighting enhances the stability of the numerical scheme.

F.1.8.3.2. Transient Limiters. During a transient run, new-time/old-time averaging given by Eq. (F-160) is not done. Instead, upper and lower bounds for the new-time value are determined based upon an old-time value through a relaxation relationship.

For the vapor-side and liquid-side heat-transfer factors, the following relaxation relationships are used during condensation and evaporation:

$$X^n_{\max} = X^{n-1} \times C_1^{C_2 \times \Delta t} \tag{F-161}$$

and

$$X^n_{\min} = X^{n-1} \times C_1^{-C_2 \times \Delta t} \ , \tag{F-162}$$

where C_1 and C_2 are relaxation constants. Equations (F-161) and (F-162) are applied to H_{CHTI}, H_{CHTA}, H_{ALVE}, and H_{ALV}. Table F-5. gives the various values of C_1 and C_2 used in subroutine HTIF. Figures F-27. and F-28. illustrate the allowable changes for liquid- and vapor-side heat-transfer factors, respectively.

F.1.9. Notes on the Model Implementation

In this section, some important features of the model implementation are summarized. The interfacial heat-transfer closure relationships are calculated at the cell centers. The fluid properties, pressure, temperature, and void fractions are cell-centered quantities. However, in TRAC, velocities are calculated at the cell edges. In subroutine HTIF, cell-edge velocities are occasionally used. More commonly, cell-centered velocities are used in various correlations. Here, we describe how these cell-centered quantities are obtained.

TABLE F-5.
Relaxation Constants In TRAC

Temperature	X	C_1	C_2
$T_l < T_{sv}$	H_{ALVE}	2	8
$T_l > T_{sv}$	H_{ALVE}	2	10
$T_l > T_{sat}$	H_{ALVE}	2	10
$T_g < T_{sv}$	H_{CHTI}	2	10
$T_g < T_{sv}$	H_{CHTA}	2	10
$T_g \geq T_{sv}$	H_{CHTI}	2	10
$T_g \geq T_{sv}$	H_{CHTA}	2	10

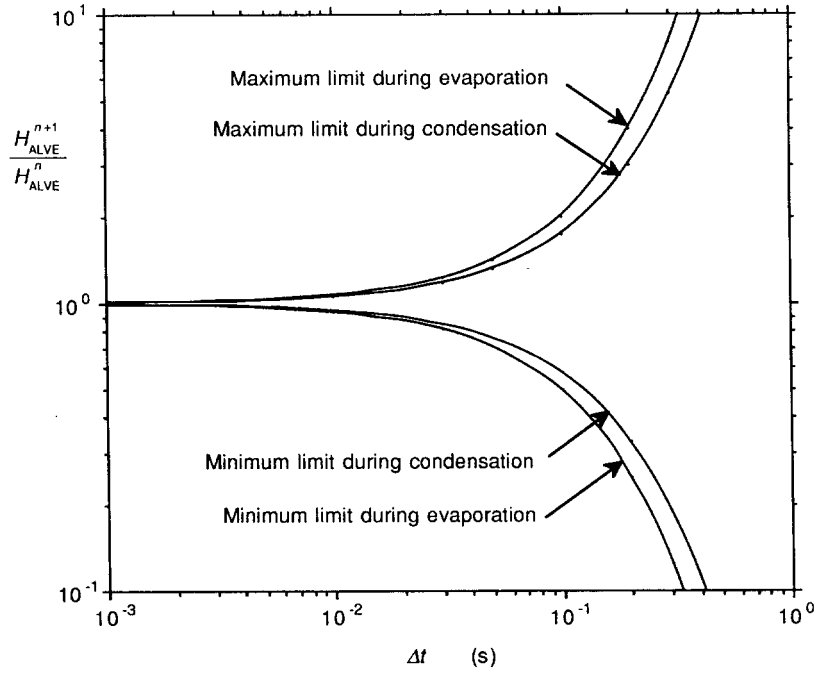

Fig. F-27. Allowable changes on H_{ALVE} within a time step during transient solution.

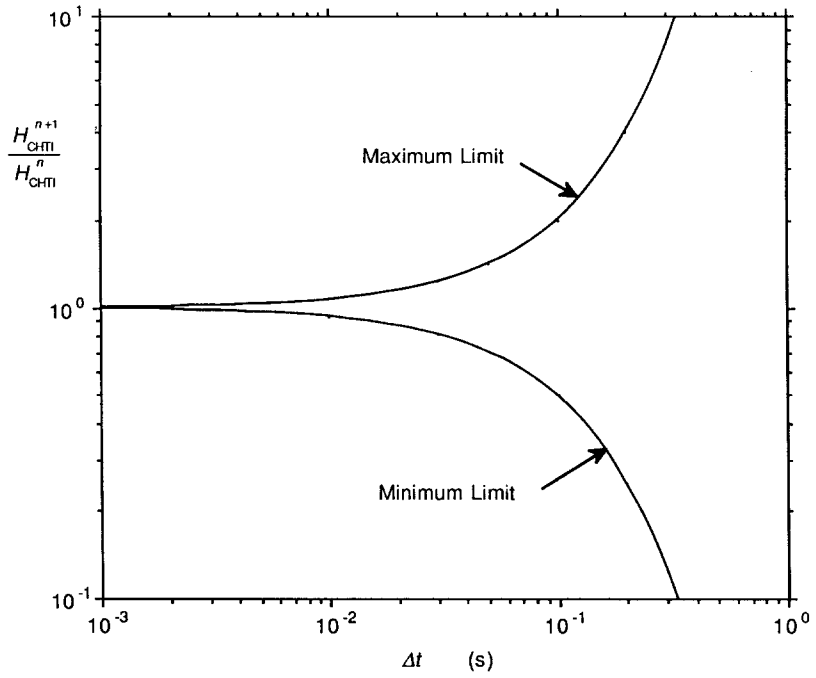

Fig. F-28. Allowable changes on H_{CHTI} within a time step during transient solution.

F.1.9.1. Hydraulic Diameter. For 1D components, the cell-averaged hydraulic diameter is obtained as

$$H_D = 2\sqrt{\frac{B_{\text{cell}}}{\pi \Delta x}} \ . \tag{F-163}$$

For 3D components, the average hydraulic diameter is set equal to the hydraulic diameter in the axial direction. However, if the hydraulic diameter in the axial direction is less than 0.01 mm, then the maximum of the hydraulic diameters in the radial and azimuthal directions is used as the average hydraulic diameter. If the result is still less than 0.01 mm, a volume-averaged diameter is defined as

$$H_D = \frac{2B_{\text{cell}}}{\Delta z(\Delta r + r\Delta\theta)} \ . \tag{F-164}$$

The average hydraulic diameter for a 3D VESSEL cell is computed in subroutine CELLA3. In subroutine HTIF, the average hydraulic diameter in a cell of the 3D VESSEL component is not allowed to be greater than 10 cm.

In all models that require a hydraulic diameter, these average hydraulic diameters are used.

F.1.9.2. Velocities and Mass Fluxes. For 1D components, cell-centered velocities are calculated in subroutine VOLV as

$$\left(V_\ell\right)_j = \frac{\left[\rho_\ell(1-\alpha)V_\ell A_f\right]_{j-1/2} + \left[\rho_\ell(1-\alpha)V_\ell A_f\right]_{j+1/2}}{\left[2\rho_\ell(1-\alpha)B_{\text{cell}} \ / \ \Delta x\right]_j} \tag{F-165}$$

and

$$\left(V_g\right)_j = \frac{\left[\rho_g \alpha V_g A_f\right]_{j-1/2} + \left[\rho_g \alpha V_g A_f\right]_{j+1/2}}{\left[2\rho_g \alpha B_{\text{cell}} \ / \ \Delta x\right]_j} \ , \tag{F-166}$$

where the counters $j+1/2$ and $j-1/2$ represent cell-edge quantities, while j represents the cell-centered vector velocity. In subroutine HTIF, the lower limit for the liquid and vapor cell-centered velocities are set to 0.001 and 0.01 m/s, respectively. In the same subroutine, however, the relative velocity is computed as an arithmetic average of the cell-edge relative velocities as

$$(V_r)_j = \frac{1}{2}\left[\ \left|\left(V_g - V_\ell\right)_{j-1/2}\right| \ + \ \left|\left(V_g - V_\ell\right)_{j+1/2}\right| \ \right] \ . \tag{F-167}$$

In subroutine HTIF, this cell-centered relative velocity is not allowed to be less than 0.01 m/s.

The average mass flux for a 1D cell is calculated in subroutine HTIF as

$$G = (1-\alpha)\rho_l (V_l)_j + \alpha \rho_g (V_g)_j \ . \tag{F-168}$$

For 3D components, the definition of cell-centered velocities is slightly more complicated. They are computed in subroutine CELLA3. For the gas phase, the axial average velocity is calculated as

$$(V_g)_k = \left[\frac{1}{2} \left(\frac{B_{\text{cell},i,j,k}}{\Delta z_{i,j,k}} + \frac{B_{\text{cell},i,j,k+1}}{\Delta z_{i,j,k+1}} \right) \right] V_{g,k+1/2} \ . \tag{F-169}$$

The term in brackets is set to 1 if it is less than 10^{-5}. The azimuthal and radial velocities are computed as

$$\left(V_g\right)_i = \frac{1}{2} \left(V_{g,i+1/2} + V_{g,i-1/2} \right) \tag{F-170}$$

and

$$\left(V_g\right)_j = \frac{1}{2} \left(V_{g,j+1/2} + V_{g,j-1/2} \right) \ . \tag{F-171}$$

Then, the cell-averaged vector velocity is calculated as

$$\left(V_g\right)_{i,j,k} = \sqrt{\left(V_g\right)_i^2 + \left(V_g\right)_j^2 + \left(V_g\right)_k^2} \ . \tag{F-172}$$

In subroutine HTIF, this velocity is limited to be greater than or equal to 0.01 m/s.

For the liquid cell-averaged vector velocity, the same procedure is applied. Subroutine HTIF limits the liquid cell-averaged velocity to be greater than or equal to 0.001 m/s. The cell-centered relative velocity is also calculated in subroutine CELLA3 as

$$\left(V_r\right)_{i,j,k} = \sqrt{\left[\left(V_g\right)_i - \left(V_l\right)_i\right]^2 + \left[\left(V_g\right)_j - (V_l)_j\right]^2 + \left[\left(V_g\right)_k - \left(V_l\right)_k\right]^2} \ , \tag{F-173}$$

and it is limited at the lower end by 0.01 m/s in subroutine HTIF.

Finally, the cell-averaged mass flux is computed in subroutine CELLA3 as

$$G = (1-\alpha)\rho_l\left(V_l\right)_{i,j,k} + \alpha\rho_l\left(V_g\right)_{i,j,k} \quad . \tag{F-174}$$

In subroutine HTIF, everywhere an average mass flux is needed, the quantities described above are used for 1D and 3D components. The cell-centered velocities are used in most correlations. However, cell-edge velocities are also used occasionally. Cell-edge velocities are used in the entrainment fraction correlation Eq. (F-58)] and in defining the stratified- and plug-flow Stanton numbers [Eqs. (F-94) and (F-101)].

F.1.10. Summary, Conclusions, and Discussion

Section F.1. outlines the constitutive relationships used within TRAC to calculate the interfacial heat-transfer rates. These constitutive relationships are strongly influenced by the flow-regime map and by the phase velocities, and, in turn, predicting these quantities is strongly influenced by the heat-transfer rates. Therefore, success in predicting the interfacial heat-transfer rates is dependent upon how well the flow-regime and the phase velocities are predicted and vice versa. TRAC's interfacial heat-transfer package contains many models. The rest of this section provides a critical general discussion of the interfacial heat-transfer models used in TRAC.

The estimation of the direct-contact condensation rates is an integral part of reactor safety analysis and is a difficult task for the following reasons.

1. In almost all situations, direct-contact condensation in LWR analysis arises during transient accident scenarios. The sources of these transients may differ, but they can be catalogued into the following four basic groups.
    a. In the simplest possible case, the transient remains independent of the condensation process. For instance, during a blowdown-dominated LOCA, direct-contact condensation generally occurs where the pressure, and therefore the saturation temperature, is decreasing as a function of time. This situation arises because the depressurization caused by very localized condensation, if it occurs, is small when compared with the global depressurization.
    b. In certain cases, direct-contact condensation is purely a transient relaxation problem, in which the ambient or global parameters remain constant. These are problems in which one of the phases exists in a limited quantity, such as vapor bubbles in subcooled liquids and subcooled-liquid droplets in saturated vapor. In these types of problems, the steady state is defined by the thermal equilibrium, and heat-transfer and condensation rates converge to zero as the bubble or drop approaches the steady state.

c. Often, the ambient or global parameters are affected by the condensation process itself and a condensation-induced transient may result. Typically, these are the problems in which the condensation causes a rapid change in the specific volume of the vapor. For instance, if the vapor supply is not large enough to replace the condensed vapor, then the condensation is accompanied by a sudden depressurization that decreases the saturation temperature and subsequently causes the condensation to cease. An added level of complexity can occur if the system can resupply the vapor phase and repressurize the region, allowing the cycle to repeat. Such problems are of an oscillatory nature and can be characterized as steam chugging and liquid plugging.
d. Many practical problems require an analysis based on the combination of the above elementary cases.

2. Another difficulty in estimating the direct-contact heat-transfer in reactor safety analysis arises from the fact that condensation or evaporation may occur under a variety of steam/liquid contact configurations. Each configuration may promote different heat-transfer mechanisms: conduction limited, laminar/turbulent-convection limited, mass-transport limited, or combinations of these. Condensation on very thin liquid films or on small droplets, for instance, is likely to be conduction-driven because the liquid motion is too small to enhance convection. On the other hand, condensation on liquid jets and on thick liquid films during cocurrent or countercurrent flow must be modeled using an appropriate convective mechanism. In the early stages of direct-contact condensation, before thermal-boundary-layer development, the heat-diffusion equation yields high condensation rates, which may exceed steam-supply rates. In these cases, the condensation process becomes steam-supply-limited and must be modeled accordingly. Steam-supply-limited condensation becomes particularly important in the presence of noncondensables in the steam environment. These mechanisms result in different condensation rates. Furthermore, each configuration may have different transient response times (relaxation times) and the severity of the induced transients will vary. The steam/liquid contact configurations of principal interest here and the physical situations in which they may occur are as follows:

   a. subcooled-liquid droplets in saturated (or superheated) steam environment (hot- or cold-leg ECC injection, pressurizer spray, upper-head spray);
   b. saturated (or superheated) steam bubble in subcooled liquid (subcooled boiling, CCFL with low vapor-generation rate in core);
   c. saturated (or superheated) steam jet into subcooled-liquid pool (CCFL with high vapor-generation rate in the core);

d. subcooled-liquid jet injected into saturated (or superheated) steam flow (hot- or cold-leg ECC injection);
e. stratified or plugged steam/liquid flows in direct contact (ECC injection), which may include (*i*) slowly moving cocurrent or countercurrent liquid and vapor flow (insufficient drag to cause wave breakup) and (*ii*) cocurrent or countercurrent liquid-vapor flow with sufficient phasic motion to cause interfacial wave instability resulting periodically in extremely high condensation rates; and
f. slowly moving liquid pool in contact with slowly moving steam atmosphere (pressurizer, upper plenum with CCFL).

These configurations are not always independent of each other. In many cases, a few of them coexist and/or one is followed by another. An example is the injection of an ECC liquid into steam flowing in the hot or cold legs. The liquid jet may result in droplets and either countercurrent or cocurrent steam/liquid flow. The prediction of the condensation rates under all these various transients and the various contact configurations requires a wide variety of correlations.

Interfacial heat and mass transfer is an active area of research in two-phase flow and heat transfer. Our understanding of these phenomena continues to grow as we answer more of the above questions. Therefore, it is only natural that the constitutive relationships of TRAC and other similar codes will continue to be improved along with the evolvement of the pertinent literature. Currently, we believe that our interfacial heat-transfer constitutive packages represent a good cross section of the state-of-the-art in this area. Of course, this comment only applies to those studies that can be directly used within a best-estimate code, such as TRAC. We would like to acknowledge that there are various detailed studies of interfacial heat-transfer phenomena that we could not implement into the code. The overwhelming numbers of studies dealing with single droplets or single bubbles are examples of such. Even though these analytical and empirical studies are very useful in understanding the phenomena involved, their results can not be directly implemented into an integral code, such as TRAC. We have to remember that even today's computers are not powerful enough to track down every single bubble or droplet in the flow field. Thus, we need more research in terms of obtaining statistical data that represent an averaged behavior of droplet and bubble fields, etc.

After reading Section F.1., the reader must be aware that we still have a number of simple models in the code. These are commonly constant-Stanton-number or constant-heat-transfer-coefficient models. The following are two reasons for having these in the code: (1) Sometimes it is not possible to find an appropriate model for a specific closure relationship in the open literature. One such example is the heat transfer during the liquid plugging phenomenon. In these cases, we produced our own model based upon our engineering judgment; and (2) Occasionally, we preferred using a simple model instead of a more complicated, literature-based model because we thought that the simpler relation was appropriate for the purpose of a best-estimate code. In doing that, we were motivated by the fact that the computation time is somewhat related to the complexity of the closure relationships, and one purpose of a best-estimate code is to

provide a faster running time. Also, the quasi-steady nature of the solution scheme forces us to make sure that the closure relationship does not show a strong dependence on local instantaneous changes. Because most models available in the literature are steady-state models, they can result in unrealistically rapid changes in the phenomenon when applied to transient analysis. Consequently, this can have a destabilizing effect on the code's numerics. We tried to rectify this problem by using averagers and limiters as discussed in Appendix D. We must note that our current approximate models can easily be replaced by others if the phenomenon under analysis requires more elaborate models. The modular nature of the code makes such replacements easy.

Our models and correlations have shortcomings similar to those of other models and correlations in the literature. Limitations exist on available information in the following areas:

1. Almost all available separate-effects data are obtained from small-scale experiments. Quite often, it is uncertain whether the results of such experiments can be extrapolated to full-plant analysis.
2. Most interfacial heat-transfer data are obtained at or near atmospheric pressure. The extension of the results to the higher pressures that are of interest to PWRs must be done with caution.
3. Almost all the available data in the literature come from steady-state or quasi-steady experiments. We do not have transient models and we lack the necessary information on relaxation time constants. The applicability of such data to transient conditions using a quasi-steady approach is currently an active area of research in the two-phase-flow community.
4. Additional flow regimes and flow-pattern-transition studies directly applicable to nuclear reactor steady-state and transient operating conditions are needed. Further discussion of the limitations of the state of the art in this area is provided in Appendix E, Section E.3.

Despite all these limitations, the interfacial heat-transfer package in TRAC-PF1/MOD2 (and TRAC-M) is considerably improved over that of MOD1. The MOD2 and TRAC-M codes have been able to accurately analyze both the small-scale Akimoto condensation tests and the full-scale UPTF tests. [See the TRAC-M/F77 Developmental Assessment Manual (Refs. F-100. and F-101.).] In addition to adding many new models and correlations, we made conceptual improvements in the following important areas:

1. 1D and 3D constitutive models and correlations are made identical. Differences in these models between 1D and 3D algorithms were an area of criticism in the MOD1 code.
2. Interfacial-shear and heat-transfer packages are made consistent and compatible.

3. In the presence of noncondensables, flashing and evaporation phenomena are recognized as qualitatively and quantitatively different and are implemented separately. Currently we are using simple but separate models for these phenomena. Evaporation is modeled as being mass-transfer controlled through a basic correlation. This is one area where the code will possibly continue to improve as the effect of noncondensables in various flow patterns becomes better understood.

So far we have discussed the heat-transfer aspects of the interfacial heat-transfer phenomenon. Equally important, not only for heat transfer but also for interfacial-shear computation, is the modeling of the interfacial area. We have made improvements in these models as well, but we are again limited by the information available in the open literature.

Predicting interfacial area during reactor safety analysis is a major thrust of research in two-phase flow. As pointed out by Ishii and Mishima (Ref. F-1.), the prediction of this quantity for transients or not fully developed flow situations is beyond the current state of the art. We fully agree with Ishii and Mishima that the most general prediction method for this problem would be to introduce transport equations into the two-fluid formulation for interfacial-area concentration. Currently, we do not have these transport equations in TRAC-M. As a reason for not having this viable mechanistic tool, we would like to cite the following paragraph from Ishii and Mishima (Ref. F-1., p. 5):

> *So far, almost no analyses have been made in this direction. Furthermore, basic experimental data needed to develop this surface-area transport equation are grossly inadequate. In view of fundamental difficulties encountered in modeling entrance and transient flow regimes under reactor-accident conditions, considerable efforts should be made to develop an acceptable data base in this area.*

Currently, in TRAC-PF1/MOD2 and TRAC-M, we have interfacial-area models that are based mostly upon steady-state and fully developed flow data. These models are obviously only valid if the quasi-steady and local equilibrium assumptions are not violated. Even these data are very limited, not only in their parametric range but also in the flow patterns that are studied. Almost all pertinent data are aimed at dispersed-phase flow, such as droplet flow or bubbly flow. Again, almost all the data are obtained from adiabatic air-water experiments, at or near atmospheric pressure, in flow channels long enough to satisfy the fully developed and quasi-steady assumptions.

Studies abound, however, where interfacial-area concentrations are measured for a variety of flow patterns for vertical upflow using chemical-absorption techniques. An extensive list of such studies is provided by Ishii and Mishima (Ref. F-1., Table 2). We tried to analyze these data using TRAC constitutive packages. We could only do independent assessments of the interfacial-area data if the void fraction in the channel was reported along with interfacial-area data. The studies of Shilimkan and Stepanek

(Ref. F-38.), Kasturi and Stepanek (Ref. F-39.), and DeJesus and Kawaji (Ref. F-40.) met this requirement.

In all three studies, the authors used a chemical-absorption technique where carbon dioxide from air was absorbed into sodium-hydroxide solutions with different concentrations. The experiments were very similar as they all dealt with upflow in a long vertical tube. The tube diameters were different in different experiments. DeJesus and Kawaji used a 2.54-cm-i.d. tube whereas Kasturi and Stepanek used a 0.6-cm-i.d. tube. Shilimkan and Stepanek used three different 1-, 1.5-, and 2-cm-i.d. tubes. The interfacial-area concentration and void-fraction data were reported as a function of liquid and gas volumetric fluxes. The ranges of these parameters were similar in all the experiments. DeJesus and Kawaji were able to extend their experiments to higher liquid flow rates and lower void fractions. Unfortunately, a clear trend applicable to all the data could not be observed. We would like to report some examples from this assessment analysis. Figure F-29. shows the results of our assessment with all the data of DeJesus and Kawaji. As shown, there is considerable discrepancy. In Fig. F-30., we report the assessment for a given liquid flow rate and for various void fractions. As shown, the code overpredicts the data at low void fractions (bubbly slug flow), whereas the data are underpredicted at high void fractions (annular-mist flow). This figure also shows the maximum interfacial-area concentration predicted by the code (by assuming all the liquid to be entrained in the annular-mist flow). The data are still overpredicted by this curve. This means that the code is underpredicting the entrainment fraction, provided the droplet diameters are predicted accurately. Our droplet-diameter model and the entrainment fraction model, however, agree fairly well with air-water data, as discussed in Section F.1.2.3.

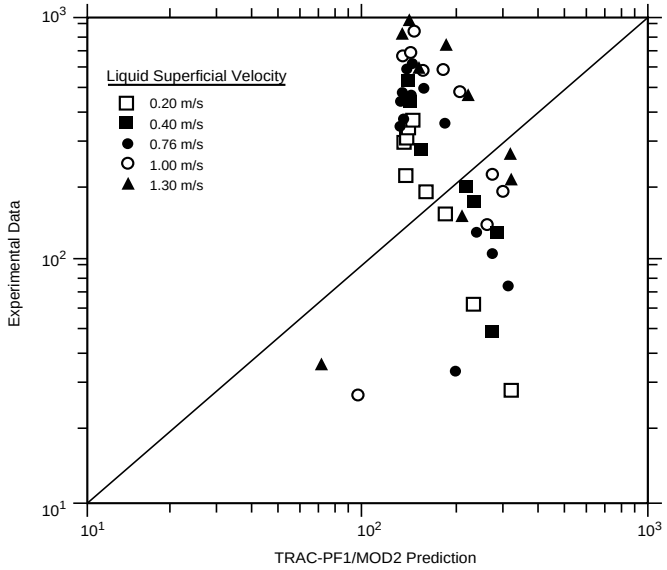

Fig. F-29. TRAC-calculated interfacial-area concentration in comparison with the data of DeJesus and Kawaji (Ref. F-40.).

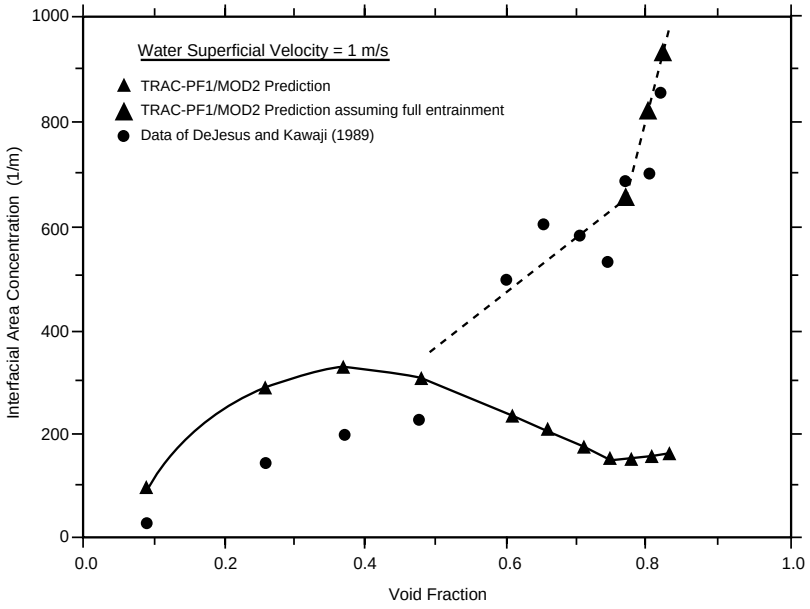

Fig. F-30. Comparison of TRAC results with the data of DeJesus and Kawaji (Ref. F-40.) for J_l = 1 m/s.

Similarly, we were surprised that the code overpredicted by so much the bubbly slug interfacial-area data. We decided to back-calculate a Sauter mean diameter from the low-void-fraction data of DeJesus and Kawaji. The calculated results are shown in Fig. F-31. In this figure, the bubbly flow, the slug-flow, or the churn-flow classification is made according to the authors' flow-regime map. All data are for void fractions less than 50% and are treated as bubbly slug flow in the code. As shown, the Sauter mean diameters for their bubbly flow data are quite large and comparable to the pipe size.

This seems to suggest that their experimental setup does not allow a breakup mechanism into dispersed bubbles at these flow rates. The comparison with the data of Kasturi and Stepanek and Shilimkan and Stepanek is not repeated here but exhibited similar patterns during assessment.

Apparently, the available interfacial-area data are not directly applicable for reactor safety analysis, which is the aim of our models. Besides the fact that the chemical-absorption technique has its inherent uncertainties, there may be various reasons why these data exhibit this unexpected behavior.

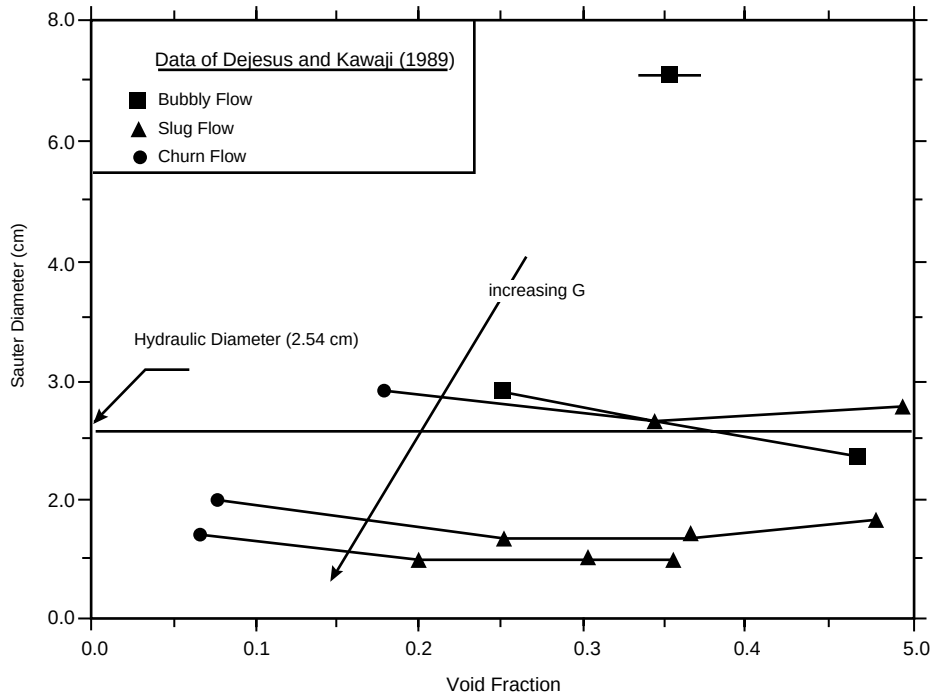

Fig. F-31. Sauter mean diameters for the low-void data of DeJesus and Kawaji (Ref. F-40.).

1. We used air-water properties for this assessment. The properties of CO_2-air and NaOH-water mixtures, however, can be considerably different depending upon concentrations. Thus, there may be a property effect on our existing models. However, if such property effects are indeed this strong, then the experiments do not meet the condition of local equilibrium because the concentration and the properties change along the flow channel as the CO_2 is continuously being absorbed by NaOH.
2. As discussed by Hewitt (Ref. F-41.), the presence of surface-active contaminants can considerably affect the flow patterns. The presence of CO_2 and NaOH may well result in a totally different flow-pattern behavior, such as froth instead of bubbles and slugs, etc.

As a closure, we would like to point out that for developing more accurate models for reactor-safety analysis, interfacial-area data under a variety of conditions are most needed. Currently, the data obtained from chemical-absorption techniques do not seem to fill this gap. Alternatives, such as three-point probe data, must be investigated.

F.2. Wall-to-Fluid Heat Transfer

The wall-to-fluid HTCs are obtained from a heat-transfer-surface model constructed within subroutines HTCOR and HTVSSL. [The terms heat-transfer surface (Ref. F-42.) and boiling surface are used interchangeably in this discussion.] The HTCs in HTCOR are used by all TRAC components under all conditions except for HTSTR components when the core reflood model is active. Subroutine HTVSSL incorporates a model to determine HTCs in the post-CHF region for a HTSTR component that undergoes reflood. (To use HTVSSL, the core reflood model must be activated by the user through an input option.) This section, therefore, is divided into two separate subsections after the introduction. The first section describes HTCs used in subroutine HTCOR, while the second one discusses HTCs used in subroutine HTVSSL.

The boiling surface requires clarification because its use in the past has led to some confusion. The local-conditions hypothesis and the history effect in correlation development are discussed first, independent of the heat-transfer-surface approach. The heat-transfer-surface approach is then reviewed. This approach is independent of the method chosen by the correlation developer.

The Local-Conditions Hypothesis and History Effects in Correlation Development. A principal problem in understanding the boiling surface is that frequently it is confused with the local-conditions hypothesis. In fact, the boiling surface is independent of the local-conditions assumption. The local-conditions assumption implies that the wall heat flux, or HTC, at a given location can be written as a function of the conditions at the same location. This can be expressed in a functional relationship,

$$q_{\text{total}} = f(T_w, D_H, \alpha, P, T_g, T_l, V_g, V_l) \ , \tag{F-175}$$

which represents any heat-transfer correlation or family of correlations in a two-fluid code, such as TRAC-PF1/MOD1 (Ref. F-43.). This heat flux represents a surface-area-time-averaged quantity resulting from the volume-time-averaged energy equation given in Appendix D by Eq. (D-6). This expression becomes simpler for the case of a homogeneous equilibrium code such as RELAP4 (Ref. F-44.) and is given by

$$q_{\text{total}} = f(T_w, D_H, x_e, P, G) \ . \tag{F-176}$$

Note that the equilibrium quality is defined on an energy basis and, therefore, includes the fluid temperatures for subcooled liquid or superheated vapor. For either of these two cases, the hydraulic parameters, such as α, P, T_g, T_l, V_g, and V_l, for the nonhomogeneous-nonequilibrium case, or x_e, P, and G for the homogeneous-equilibrium case, are values taken at the location at which the heat flux is to be evaluated, i.e., local conditions.

Within the strict definition of the local-conditions assumption, additional fields introduced into the hydraulic model introduce the additional local quantities required to describe the influence of the new fields upon the heat flux. For a code with N fields,

[3×(N−1)+5] independent variables (the same pressure is assumed in all fields) could be used in an expression similar to that given by Eq. (F-175). The above representations have been written as functions of only the local instantaneous hydraulic parameters. However, nothing precludes the inclusion of local rate-of-change terms with respect to either temporal or spatial quantities in the formulation. These terms still fit within the local-conditions hypothesis. For example, the post-CHF dispersed-flow film-boiling regime might include the term dT_g/dz for the nonhomogeneous-nonequilibrium model, so that Eq. (F-175) would be written

$$q_{\text{total}} = f(T_w, D_H, \alpha, P, T_g, dT_g/dz, T_l, V_g, V_l) \ .$$

The problem with the local-condition hypothesis is that regimes have been found in which its application yields questionable results. The post-CHF and high-void, nonuniform axial-power-profile CHF cases are two such regimes. Thus, history effects sometimes are included to model these regimes more accurately. For the post-CHF regime, the axial position downstream of the CHF point, z_{CHF}, sometimes is included in Eq. (F-175) and produces

$$q_{\text{total}} = f(T_w, D_H, \alpha, P, T_g, T_l, V_g, V_l, z_{\text{CHF}}) \ . \tag{F-177}$$

The high-void nonuniform axial-power-profile CHF case frequently is modeled using a boiling-length correlation. This type of correlation predicts the quality at which CHF occurs, and can be written in functional form as

$$x_{e,\text{CHF}} = f(D_H, P, G, L_b) \ , \tag{F-178}$$

where L_b is the length over which saturated boiling takes place.

Computer codes such as TRAC-PF1/MOD1 (Ref. F-43.) historically have avoided the use of the history effect because it requires knowledge of the spatial position at which some event occurs (either the CHF location or the beginning of boiling, respectively, for the two examples mentioned here) to evaluate the heat flux or CHF downstream of the event. The determination and tracking of these locations are difficult and, for PWR applications, frequently poorly defined. One example is the situation in which fluid is flowing into the core through the entrance and the exit simultaneously and, therefore, is producing two different CHF locations in the core. The question becomes, which CHF location is used to calculate the post-CHF heat flux? Similarly, the history-effect correlations for CHF cannot model flow reversals. These correlations assume increasing quality or void fraction along the flow direction. The opposite is seen to be the case in many situations. Although it is possible to address these types of problems in some fashion, the difficulties encountered in addressing them in a general manner have led to an almost exclusive use of local-condition correlations within the codes.

The Heat-Transfer-Surface or Boiling-Surface Approach. To this point nothing has been said about the boiling-surface approach. The discussion has involved only the local-conditions hypothesis, the inclusion of the history effect within the formulation of the heat flux or CHF phenomenon, and comments concerning their potential implementation into the codes.

The term heat-transfer surface or boiling surface arose from some simple observations and in no way influences nor limits any of the previous considerations. To investigate these observations, we will step through a series of thought experiments. Consider first pool boiling for a fixed geometry (a thin horizontal wire within a large pool), pressure, and subcooling where a unique boiling curve exists. Pool-boiling curves for a number of fluid conditions can be collected and can be expressed functionally as

$$q_{\text{total}} = f(T_w, D_H, P, T_l)\,. \tag{F-179}$$

Note that the boiling curve (Ref. F-45.) was first defined as a plot of heat flux versus either wall temperature or wall superheat (wall superheat is obtained by subtracting the saturation temperature from the wall temperature). Typically, the boiling curve is assumed to have single-phase-convection, nucleate-boiling, transition-boiling, and film-boiling regimes. The curves are found either by starting from low power and increasing power to generate the boiling curve or by feedback control of power based upon a desired wall temperature. For the power-controlled experiment, the transition-boiling regime is unstable and historically gave rise to the temperature-control-feedback experiments. The boiling curve is generated by varying only one variable, the power, and assumes the fluid-reservoir size is large enough to maintain a constant fluid temperature during the experiment. Each experimental run varies one of the fluid parameters and yields a single unique boiling curve. Thus, the experiment itself provides proper separation of variables.

Using the family of boiling curves represented by Eq. (F-179), the wall response for any given quasi-steady transient can be analyzed. Considering a pressure-power transient, and plotting heat flux as a function of wall superheat and pressure (a 3D plot), the path across this 3D surface could be traced during the transient. Each constant pressure plane in the 3D surface is the boiling curve obtained experimentally at that pressure.

As an example, consider an experiment with decaying pressure, increasing surface temperature, and fixed fluid temperature for a horizontal wire. The initial conditions for the pressure and wall temperature are 6.9 MPa and the saturation temperature, respectively. This experiment produces an apparent boiling curve across the above 3D plot. This boiling curve is called *apparent* because two of the independent parameters (power and pressure) in Eq. (F-179) are changing as a function of time. This apparent boiling curve has single-phase-convection, nucleate-boiling, transition-boiling, and film-boiling regimes caused by the fact that CHF will be exceeded as the pressure decreases and the power is increased. (Note that CHF becomes a decreasing function of pressure below approximately 6.9 MPa.)

The heat flux in this experiment is affected by two factors that can be represented more clearly by denoting the heat-flux rate of change as obtained from Eq. (F-179) as

$$\frac{dq}{dt} = \frac{\partial q}{\partial T_w}\frac{dT_w}{dt} + \frac{\partial q}{\partial P}\frac{dP}{dt} \ , \tag{F-180}$$

where the "total" subscript is dropped for convenience. Thus, the change in heat flux at any time t during the transient can be found from

$$\Delta q(\tau) = q(\tau) - q(\tau - \Delta t) = \int_{\tau-\frac{\Delta t}{2}}^{\tau+\frac{\Delta t}{2}} (dq \,/\, dt)dt \ , \tag{F-181}$$

where Δt is some small time period larger than the time constant of the boiling process, but smaller than the time required for the quasi-steady transient to have changed its state. (See the discussion of the time-averaging operator in Appendix D.) Substitution of Eq. (F-180) into Eq. (F-181) yields

$$\Delta q(\tau) \ = \int_{\tau-\frac{\Delta t}{2}}^{\tau+\frac{\Delta t}{2}} (\partial q/\partial T_w)(dT_w/dt)dt + \int_{\tau-\frac{\Delta t}{2}}^{\tau+\frac{\Delta t}{2}} (\partial q/\partial P)(dP/dt)dt \ . \tag{F-182}$$

The change in heat flux at any time comprises two parts. One is caused by the wall temperature change over the time period Δt, and the other is caused by the pressure change over the same period. The apparent boiling curve obtained by plotting $q(\tau)$ versus $T_w(\tau)$ for different times τ over the transient includes not only the effect of changing wall temperature but also the effect of changing pressure. Equation (F-182) can be generalized further to include a change in the fluid temperature because of a finite liquid volume (for this consideration, $T_l < T_{sat}$ is required) by including the term

$$\int_{\tau-\frac{\Delta t}{2}}^{\tau+\frac{\Delta t}{2}} (\partial q \,/\, \partial T_l)(dt_l \,/\, dt)dt \ .$$

Two rather obvious results are now clear. One is that the boiling curves inherent within Eq. (F-179) are not the same as the apparent boiling curves that arise from a quasi-steady transient. This difference can be amplified further by noting that the slope of the boiling curve, as it has been defined correctly for a simple pool-boiling experiment, is $\partial q/\partial T_w$. The slope of an apparent boiling curve, however, can be obtained from Eq. (F-180) by dividing by dT_w/dt so that

$$\frac{dq}{dT_w} = \frac{\partial q}{\partial T_w} + \frac{\frac{\partial q}{\partial P}\frac{dP}{dt}}{\frac{dT_w}{dt}} \ . \tag{F-183}$$

The slope of this apparent boiling curve is a combination of the original boiling curve plus an effect introduced by the transient itself.

These observations can be extended in steps to consider forced convection. First, extend the preceding thought-experiment to allow flow across the wire. Again, a unique boiling curve is obtained as the wall temperature is increased while all the other parameters are held constant. In this case, Eq. (F-179) now has the velocity of the subcooled fluid as one of the independent variables, and is given by

$$q_{\text{total}} = f(T_w, D_H, P, T_l, V_l) \ . \tag{F-184}$$

Arguments similar to those made for the pool-boiling case now can be made for this experiment and for the analysis of any quasi-steady transient. Again, proper separation of the variables is inherent within the experiment.

Next, the flow conditions can be changed to include two-phase flow. Again, boiling curves can be generated by increasing the power or wall temperature. In this case, however, the single-phase-convection portion of the boiling curve will be missing. For this case, Eq. (F-175) would represent the boiling curves obtained and, again, the same arguments may be repeated.

In all the experiments considered so far, the fluid volumes have been large enough so that the fluid properties do not change because of any heat addition. Thus, the fluid variables represent volume-averaged quantities. For example, the liquid temperature, either in Eq. (F-175)for the pool-boiling experiment or in Eq. (F-184) for the single-phase forced-convection experiment, represents the volume-averaged fluid temperature. For the forced-convection experiment, the inlet-flow temperature is equal to the volume-averaged fluid temperature because the fluid volume is large. Each experiment yields a true boiling curve, that is, one with a slope of $\partial q/\partial T_w$.

There are experiments, however, that will not yield true boiling curves and from which the experimentalist and/or correlation developer must extract the functional relationship by proper separation of the variables to obtain such expressions as Eq. (F-175). Consider the case of single-phase subcooled liquid flowing into a heated vertical tube and try to generate a boiling curve for this experiment by varying the power, as was done in the preceding experiments. For this case, the fluid variables in Eq. (F-175) are the local fluid properties at a fixed axial level of the tube (local-conditions hypothesis). Along the tube, the void fraction as well as phasic velocities and temperatures change at each level as the power is increased. No point exists on the tube from which one can plot directly a true boiling curve because the wall temperature and the fluid variables are changing as the power is increased. Therefore the plotting of heat flux versus wall temperature produces an apparent boiling curve that has a slope represented by dq/dT_w, not $\partial q/\partial T_w$.

From these thought experiments, it is obvious that cases exist in which the true boiling curve becomes a mathematical abstraction rather than a curve with physical significance, as in pool boiling, for which the boiling-curve concept was defined originally. The approach used to reach this conclusion has been called the heat-transfer-surface approach or boiling-surface approach because it uses the simple mathematics of functions with N dimensions.

The heat-transfer-surface approach in no way changes work done in the past to develop correlations, as long as the correlation developer used proper techniques to ensure valid separation of variables. It is important to realize that proper separation has not been done in all correlations in the literature. Possibly the most painful example of this problem arises within the definition of the minimum film-boiling temperature, $T_{\min}$. This point is discussed below.

Correlations may be based upon the local-conditions approach or may include the history effect. The heat-transfer-surface approach requires only the addition of as many parameters as the correlation developer feels necessary to represent accurately the history effect. Thus, the trivial point can be made that the true boiling curve obtained from the above experiment with flow up the tube, using z_{CHF} to model the history effect, would be denoted by

$$\left.\frac{\partial q}{\partial T_w}\right|_{D_H,\ \alpha,\ P,\ T_g,\ T_l,\ V_l,\ V_g,\ z_{\mathrm{CHF}}\ =\ \text{constant}} .$$

The boiling-surface approach does place a strict mathematical definition upon the boiling curve; that is, it is the relationship whose characteristic slope with respect to wall temperature is given by $\partial q/\partial T_w$. For this reason, the adjectives *true* and *apparent* have been used to describe the types of boiling curves possible. The true boiling curve has been differentiated from the apparent boiling curve that is dependent upon the experiment or transient under consideration. This strict definition of the true boiling curve must be applied to ensure a unique mathematical definition of the boiling curve. Failure to satisfy this requirement is the same as saying that proper separation of different effects (variables) is unimportant, and makes application of any correlation developed with this lack of understanding highly questionable for different transients. There is no question but that this point is the most important of all the results from the heat-transfer-surface approach.

One other point is worthy of note. Frequently, 3D plots have been used to represent a boiling surface. Again, it appears that this use has created confusion. As with the boiling curve, there are situations in which the 3D surface has physical meaning and others in which its representation is totally abstract. In the first, simple, pool-boiling experiment, the surface had physical meaning, and movement across the surface could be used to represent what happened in the quasi-steady transient and to obtain the corresponding apparent boiling curve. In the case of forced flow up the tube, the 3D surface would be abstract.

One problem inherent in our 4D world (three spatial coordinates and time) is how to represent something that is dependent upon four or more independent variables. A quantity dependent upon three independent variables can be represented by plotting the quantity itself on the *z*-axis and using the *x*-axis, *y*-axis, and time to represent the three independent variables, that is, make a movie using time to represent one of the independent variables. The appearance, however, of a fourth independent variable creates a problem. One of the variables must remain constant and its effect studied parametrically, or two of the independent variables must vary together in some prescribed manner.

What has been done most frequently in the boiling-surface approach is to designate wall superheat as the *y*-axis independent variable with heat flux, the dependent quantity, represented on the *z*-axis. This designation is a natural choice because, historically, everyone thinks in terms of boiling curves. It must be remembered that some of these boiling curves are mathematical, not physical. The variable that frequently has been chosen as the *x*-axis is either void fraction or quality, depending upon the particular formulation in use, for example Eqs. (F-175) and (F-176). This choice of independent variables yields a right-hand coordinate system that shows the boiling curves progressing from near-single-phase liquid for x-axis $= 0^+$ to near single-phase vapor at x-axis $= 1^-$. [The term *near single phase* is used because once single-phase conditions exist, boiling curves that are defined as having several boiling regimes no longer exist, at least for Eq. (F-175)]. The effects of the remaining independent variables on the surface are then studied parametrically.

Obviously, instead of wall superheat and void fraction, any two independent variables can be chosen if someone desires to study the effects of other variables. The boiling-surface approach is independent of the choice of how to plot the influence of any two of its variables.

Total Wall Heat Flux and Phasic Wall Heat Fluxes. In determining the total wall heat flux for a two-phase mixture in a nonhomogeneous-nonequilibrium code, such as TRAC, the energy from the wall must be partitioned into the components going into the respective phases [see Eqs. (2-1) and (2-2)]. This division is required by the hydraulic model to determine the sensible heat present in each phase. For the solution of the conduction problem associated with each structure present in the fluid, the sum of the energy transferred into the phasic components is required [see Ref. F-99., Eq. (2-93)]. The simple relationship that defines this total wall heat flux with respect to the phasic components is given by

$$q_{\text{total}} = q'_{w\ell} + q'_{wg} \ , \tag{F-185}$$

where

$$q'_{w\ell} = h_{w\ell}\,(T_w - T_\ell) \tag{F-186}$$

and

$$q'_{wg} = h_{wg}(T_w - T_g) \ . \qquad \text{(F-187)}$$

It should be remembered that these phasic HTCs include the fraction of the wall being contacted by the phase according to the definitions used in Section 2.0.

At this point, it is appropriate to consider how we should go about the process of defining the quantities needed in Eqs. (F-185) through (F-187). The basic problem is that the theoretical two-phase two-fluid model requires definition of quantities that the experiments are not yet able to measure. This almost as true today as it was when the development of TRAC began in the early 1970s.

Basically, we have two choices. First, the majority of the closure relations within the literature for the total wall heat flux, q_{total}, are based upon data that cannot be separated into their phasic components. Thus, one choice available to us is to define correlations based upon this ability to calculate the total heat flux removed from the wall by the convective process. Then, we must define one of the phasic components based upon some model that we feel is appropriate. Subtracting this component from the total will then yield the remaining phasic contribution. The advantage to this approach, at least in concept, is that it should preserve the correct total amount of energy removed from the wall. The second choice available to us is the modification of homogeneous thermodynamic-equilibrium models to try to encompass the general characteristics within a particular flow regime. Then we combine various models representing different phenomena to develop the required phasic contributions. The only apparent justification for this choice, at least at this point, is that it provides the desired framework to include improved phasic models easily in the future.

We have chosen to use both methods in TRAC. The factor that influences the selection of the second approach the most is the interdependence of the closure relations. In some regimes, such as fully developed nucleate boiling, for example, departures from mechanical and thermodynamic equilibrium are not as significant, and the first method works reasonably well. For other regimes, such as the post-CHF regime, however, wide departures from equilibrium are encountered. This departure strongly couples the models chosen for the interfacial-drag, the interfacial heat-transfer, and the wall heat-transfer closure relations. Because most of the correlations for the total wall heat transfer are referenced to the saturation temperature of the mixture as the sink temperature, their application to this highly thermodynamic nonequilibrium situation is just as much in question as having chosen the second approach to start. This observation has lead to the choice of the second method for these regimes. In either case, the code developers then use comparison calculations with many experiments, including some of the older experiments that reduced their data using the equilibrium assumption, to ensure that the correct amount of energy is being extracted from the wall. Further definition of how these comparisons can be made and how they are made within this document is contained in Section F.2.2.

Finally, as noted, the phasic HTCs include the fraction of the wall being contacted by the phase according to the definitions used in Section 2.0., given by

$$h_{w\mathrm{l}} = f_{\mathrm{l}} h'_{w\mathrm{l}}$$

and

$$h_{wg} = (1 - f_{\mathrm{l}}) h'_{wg} \ ,$$

where $h'_{w\mathrm{l}}$ and h'_{wg} are the separate phasic HTCs. The measurements (Refs. F-46. and F-47.) and modeling (Refs. F-48. and F-49.) of the quantity f_{l} for the most part have been limited to the case of pool boiling on a horizontal surface. Thus, for forced convection, little is known. With this in mind, the effect of the phasic wall contact area is assumed to be encompassed within the phasic models developed under the second method and the weighting factors used to combine the separate correlations.

The Minimum Film-Boiling Temperature and Transition Boiling. The current literature on the minimum film-boiling temperature, $T_{\min}$, and transition boiling for forced convection provides, at best, a very confusing picture. The primary contributing factors in the confusion are believed to be the following:

- that the data-reduction procedure may produce results dependent upon the quenching transient,
- that different types of experiments have been used, and
- the effect of axial conduction upon $T_{\min}$.

The effect of axial conduction has undergone much discussion in the literature, whereas the effect of the other two factors has received little notice.

To understand how the data-reduction procedure and the quenching transient influenced the results obtained for different experiments, two general types of experiments are discussed. Axial conduction is then factored into the discussion conceptually after the effects of these two factors are understood. The first type of experiment considered is forced-convective-quenching experiments with flow inside long tubes and/or outside along bundles of tubes. The second is forced-convective-quenching experiments using short test sections with flow inside tubes having high thermal inertia.

We will first consider the quenching of a point by convection alone. The quenching of this point will be slow enough and generally broad enough that the quasi-steady approach is valid. Thus, the heat flux can be thought of as being represented by Eq. (F-175). To simplify this consideration, the liquid will be assumed to be saturated, $T_l = T_{\mathrm{sat}}$, so that the wall superheat will be used as a variable instead of the wall

temperature alone. This variable change represents only a rigid body translation of the origin on the temperature axis but is more consistent with standard practices. Also, the velocities will be combined through the mass flux term, G, for the moment, so that either one velocity or the slip ratio remains undefined. Thus, Eq. (F-175) can be rewritten as

$$q_{\text{total}} = q(\Delta T_{\text{sat}}, P, G, \alpha, \ldots) \ . \tag{F-188}$$

Within the data-reduction procedure, the heat flux is assumed to be obtained from a 1D (radial) inverse-conduction calculation using thermocouple measurements at the elevation of interest. If the thermocouple is located on the heated surface, its measurement yields T_w directly, neglecting fin effects; otherwise the inverse calculation must also yield this quantity.

In considering the apparent boiling curve determined from the quenching of the point, the rate of change of heat flux is given by

$$\frac{dq}{dt} = \frac{\partial q}{\partial(\Delta T_{\text{sat}})}\frac{d(\Delta T_{\text{sat}})}{dt} + \frac{\partial q}{\partial P}\frac{dP}{dt} + \frac{\partial q}{\partial G}\frac{dG}{dt} + \ldots \ , \tag{F-189}$$

which is similar to Eq. (F-180). Again, for convenience, the total subscript is dropped. Multiplying both sides of Eq. (F-189) by $dt/d(\Delta T_{\text{sat}})$ then yields

$$\frac{dq}{d(\Delta T_{\text{sat}})} = \frac{\partial q}{\partial(\Delta T_{\text{sat}})} + \frac{\frac{\partial q}{\partial P}\frac{dP}{dt} + \frac{\partial q}{\partial G}\frac{dG}{dt} + \frac{\partial q}{\partial \alpha}\frac{d\alpha}{dt} + \ldots}{\frac{d(\Delta T_{\text{sat}})}{dt}} \ , \tag{F-190}$$

so that the slope of the apparent boiling curve is given by the total derivative of heat flux with respect to wall superheat, $dq/(d\Delta T_{\text{sat}})$. Equation (F-190) indicates how different factors will affect the apparent boiling curve when q is plotted against ΔT_{sat} for given times in the quenching transient. Thus, the apparent boiling curve for quenching experiments with tubes and bundles is a complex relationship of the convective heat transfer [$\partial q/\partial(\Delta T_{\text{sat}})$, $\partial q/\partial \alpha$ . . .], the hydraulic transient ($d\alpha/dt$, dP/dt, . . .), and the conduction-convection transient of the wall [$(d(\Delta T_{\text{sat}})/dt$].

A special case of the general quenching experiments on tubes and bundles exists in those experiments that are run at constant pressure and inlet mass flux. For this case,

$$\frac{dP}{dt} = \frac{dG}{dt} = 0 \ , \tag{F-191}$$

so that Eq. (F-190) reduces to

$$\frac{dq}{d(\Delta T_{\text{sat}})} = \frac{\partial q}{\partial(\Delta T_{\text{sat}})} + \frac{\frac{\partial q}{\partial \alpha}\frac{d\alpha}{dt}}{\frac{d(\Delta T_{\text{sat}})}{dt}} \ . \tag{F-192}$$

This data-reduction procedure is frequently used to obtain a minimum wall superheat, found from $dq/(d\Delta T_{sat}) = 0$, and a transition-boiling region, where $dq/(d\Delta T_{sat}) < 0$. From Eq. (F-192), it is observed that both the ΔT_{min} and transition boiling are dependent on the experimental transient. Transition boiling will thus appear to occur when, for example,

$$\frac{d\alpha}{dt} < -\left[\frac{\frac{\partial q}{\partial(\Delta T_{sat})}}{\frac{\partial q}{\partial \alpha}}\right]\frac{d(\Delta T_{sat})}{dt} \quad . \tag{F-193}$$

Equation (F-193) can now be interpreted in terms of a typical quench. Void fraction is decreasing as the conduction-convection quench front progresses toward the point being considered, and the following relationships are assumed to exist in the film-boiling regime:

$$\frac{\partial q}{\partial(\Delta T_{sat})} > 0 \ , \qquad \frac{\partial q}{\partial \alpha} < 0 \ , \quad \text{and} \quad \frac{d(\Delta T_{sat})}{dt} < 0 \ ,$$

so that transition boiling appears to occur when $d\alpha/dt$ is decreasing at a sufficient rate. The apparent ΔT_{min} resulting from this interpretation, when Eq. (F-193) is satisfied, is greater than the homogeneous nucleation point, and, as just shown, will depend upon the experimental transient.

Another interesting result from this analysis is that the ΔT_{min} obtained from a quenching experiment, where Eq. (F-193) is satisfied, will be hydraulically controlled by the transient. When the transient does not satisfy Eq. (F-193), however—that is, does not decrease the void fraction fast enough—the resulting ΔT_{min} will be limited by the true minimum, $\partial q / \partial(\Delta T_{sat}) = 0$. This true minimum temperature was hypothesized by Nelson (Ref. F-42., Eq. 4, p. 51) to be approximated by the expression denoted as ΔT_{HN}. This denotes the wall superheat corresponding to a minimum temperature defined by the instantaneous interfacial-contact temperature of two semi-infinite media brought together, with the wall having a temperature corresponding to that of the homogeneous nucleation temperature in the liquid. This approximation is discussed further in Section F.2.1.9. This true minimum will be thermodynamically controlled. Similar results are obtained for the more general quenching experiment, indicated by Eq. (F-190); however, the relationships are more complex.

As discussed earlier under the boiling-surface concept, it is the improper separation of variables resulting from the apparent boiling curve–particularly void fraction, flow rates, and wall temperature–that has led to the confusion associated with ΔT_{min} and transition boiling for forced-convective heat transfer. Comparison of recent ΔT_{min} data to ΔT_{HN}, which TRAC uses, further supports this point (see Section F.2.1.9.).

Until recently, the short test session with high thermal inertia provided the only other source of ΔT_{min} data. The advantage this test section held over a long thin tube was that it

quenches, due to its shortness, with “constant” hydraulic conditions defined by the inlet conditions. Thus, the change in the hydraulic conditions over the short test section can be ignored, i.e.,

$$\frac{dP}{dt} = \frac{dG}{dt} = \frac{d\alpha}{dt} = 0 \ ,$$

and Eq. (F-190) reduces to

$$\frac{dq}{d(\Delta T_{sat})} = \frac{\partial q}{\partial(\Delta T_{sat})} \ . \tag{F-194}$$

The high thermal inertia prolongs the quenching period so that sufficient data can be acquired during the true transition-boiling period, $\partial q / \partial T_w < 0$. Equation (F-194) indicates that the results obtained from this type of experiment will provide boiling curves that immediately separate the variables properly. The problem—if it can be termed that—created by this type of experiment has been that its results, $\Delta T_{min} \approx \Delta T_{HN}$ often disagree with tube results that are analyzed according to Eqs. (F-190) or (F-192), and confusion has arisen.

Now it should be apparent what the characteristics of the post-CHF regime must be and how quenches result. This has been heavily implied by Eq. (F-192). True minimum temperatures and true transition boiling have strict definitions relative to the boiling surface. These are denoted by

$$\frac{\partial q}{\partial(\Delta T_{sat})} = 0$$

and

$$\frac{\partial q}{\partial(\Delta T_{sat})} < 0 \ ,$$

respectively. Similarly, film boiling can be denoted as that region where

$$\frac{\partial q}{\partial(\Delta T_{sat})} > 0 \ ,$$

and $T_w > T_{CHF}$. Quenches must be modeled by having the proper characteristics of the film-boiling regime with respect to void fraction and phasic flows, i.e., $\partial q/\partial \alpha$ and $\partial q/\partial G$ (mass flux is used here for simplicity). As noted earlier, strong coupling exists between the closure relations within this regime. This coupling is reflected further by the importance of these quantities.

With this understanding of how the data-reduction procedures influence the convective heat-flux correlations obtained from the quenching of tubes, bundles, or short test sections, the effect of axial conduction can be integrated into our thinking. Originally, the term $d(\Delta T_{sat})/dt$ in Eq. (F-190) was discussed in terms of 1D conduction solution. This limitation to one dimension, however, was not required by Eq. (F-190). The limitation arises because of the problem caused by multi-dimensional considerations involving the inverse-conduction solution when the heat flux must be found from the wall thermocouples. Without correct accounting of multi-dimensional conduction, erroneous convective heat fluxes are found and result in ΔT_{min} appearing higher than it really is.

This integration of multi-dimensional conduction into the situation yields a picture that better represents the real quenching process. Usually when quenching of a tube or bundle is studied, a point located immediately downstream of the quenching front is the location that provides the majority of the data with respect to transition boiling or the ΔT_{min}. Unfortunately, this is also the point where axial conduction and the rate of change of the hydraulic transient are at their maximum, making analysis of this type of experiment very difficult.

Having dissected the concepts used within the modeling of the convective heat transfer within the post-CHF regime in the code, one must note how the code models the axial conduction present in the quenching process. This is done by a renodalization of the typical coarse-mesh conduction-solution nodes into much smaller nodes capable of accurately representing the sharp temperature gradients present near the quench front. This renodalization is discussed in Section 2.2.4.4. It is important to realize that this renodalization does present a potential problem with respect to the spatial-averaging operation and the local-condition assumption that is inherent within the closure relations for the wall-to-fluid heat transfer. As noted in Appendix D, no checks are made with respect to the spatial averagers.

Spatial-Averaging Operator. Spatial averaging enters our consideration through the definitions in Eqs. (D-3) through (D-5). Nelson (Ref. F-50., pp. 1129-1132) discusses the requirements and influence of those spatial-averaging operations upon the wall-to-fluid heat transfer. An area average often enters the data-reduction procedure when steady-state experiments are analyzed. For upflow in a tube or rod bundle, thermocouples at different axial levels often define the midpoint of the area. Flowing experiments in a tube or rod bundle with a progressing quench front may contain either an area average or a line average (around the circumference of the tube/rod). Line-average data may be reported/obtained, provided the experimenter sampled the data at a sufficient rate to determine dT_w/dt accurately, that can be transformed to dT_w/dz, based on a constant quench front velocity assumption applied between thermocouples. Therefore, the reduced area-averaged data frequently include the effect of the area averaging arising from the thermocouple spacing. If analyzed in sufficient detail, the reduced line-averaged data may provide either heat flux as a function of distance from the quench front or heat flux with the accompanying dT_w/dz. It can be noted that the area-averaged data contain the same information but it is present on an average basis, i.e., it has been averaged over some axial length. When a quench front is present on either a thin tube or

rod bundle, area averaging frequently presents a problem because it will typically average over a length greater than the length of the quench front.

When the local-conditions hypothesis is used to develop correlations from the reduced data, the averaging operators also pose a potential problem if precautions are not taken. This problem is analogous to the $\delta t_{\min}$ problem discussed in Appendix D but arises from spatial considerations. The problem is described best by considering the example of quenching. Near the quench front, steep gradients of the wall temperature are encountered frequently. If a closure relation is developed using a history effect such as z_{CHF}, the correct amount of energy may be obtained based upon code renodalization (as described above). This assumes that the correlation is being applied to a situation similar to the data upon which it was based, i.e., dT_w/dz must have the same type of distribution. If a closure relation is developed using the local-conditions hypothesis with the wall temperature alone, additional precautions must be taken to ensure that the correct amount of energy is taken out when renodalization of the conduction solution to include axial-conduction effects occurs. These precautions must check that if the renodalization is becoming smaller than some minimum length (which must be determined from the data and its dT_w/dz), then the total heat flux over this $\Delta z_{\min}$ is preserved. Without this check, codes using a fine-mesh renodalization scheme will continue to increase the steepness of the quench front until axial conduction limits the process.

HTC Selection Logic. Discussion of the selection of the heat-transfer correlations to be used in the calculation of the wall-to-fluid-transfer rate will be done using the void-fraction wall-superheat plane shown in Fig. F-32. As just discussed, this plane has some advantages when considered from the heat-transfer-surface approach. This discussion will concentrate on where the different boiling regimes exist and, where necessary, the steps taken to assure continuity across boundaries where discontinuities otherwise would exist when changing from one correlation to another. The definitions of the correlations will be given in the next section because their definition is independent of the selection logic itself. Table F-6. lists the TRAC heat-transfer-regime numbers. Where appropriate, these heat-transfer-regime numbers are noted on Fig. F-32. Figure F-32. is used to discuss the selection of the HTCs (h_{wl} and h_{wg}). Note that heat-transfer surfaces could be plotted for h_{wl}, h_{wg}, q'_{wl}, q'_{wg}, and/or q_{total}.

Because Fig. F-32. considers only the effects of wall superheat and void fraction, the influence of the pressure and the phasic temperatures and velocities must be mentioned separately. The pressure enters the correlations through their physical property evaluation. No correlation switching is done based upon a pressure criterion so that the same correlations are used for all pressures. Although the physical properties may reflect a consideration of whether the pressure is greater than the critical pressure, the correlations have not been changed to reflect this effect. For the phasic temperatures, their effect generally enters the heat fluxes through the thermal potential and physical property evaluation required in the HTCs. In some cases, these sink temperatures directly enter the correlations themselves, but not frequently. No switching, to any extent, is done on phasic temperature. Finally, the phasic velocities do not give rise to

switching logic. Because, however, both natural-circulation and forced-flow conditions may exist during many of the transients considered, the natural-convection correlations are used to provide a lower boundary to the forced-convection correlations. Early versions of the code sometimes used the Grashof number or flow rate to switch between the correlations. These switches almost always produced discontinuities in the heat flux. Current versions of the code evaluate both conditions and use the maximum HTC. This can be expressed as

$$h = \max(h_{\mathrm{NC,\,lam}}, h_{\mathrm{NC,\,turb}}, h_{\mathrm{forc}}) \tag{F-195}$$

and eliminates any discontinuities with respect to flow-change logic encountered in earlier versions.

Radiation heat-transfer effects are considered in the transition-boiling and film-boiling regimes only. The radiation heat-transfer from the wall to the vapor is calculated using the Stefan-Boltzmann law of thermal radiation. The wall emissivity and geometric view factor are assumed to be unity.

The wall-to-fluid heat-transfer coefficients, h_{wl} and h_{wg}, are determined by subroutines HTCOR and HTVSSL. Subroutine HTCOR computes heat-transfer coefficients (h_{wl} and h_{wg}) based on local surface and fluid conditions for HTSTR components for which the core reflood model is not active and for 1D-component walls. For HTSTR components with the core reflood model active, wall-to-fluid heat transfer is estimated by subroutine HTVSSL. Most of correlations to model the boiling curve in these two subroutines, HTCOR and HTVSSL, are the same, except the post-CHF heat-transfer regime (film- and transition-boiling regimes). Subroutine HTVSSL considers a position-dependent post-CHF heat-transfer model for transition- and film-boiling regimes, as explained in Section F.2.2.

Figures F-33a. to F-33d. provide an overview of subroutine HTCOR, which contains the logic for the wall-to-fluid heat-transfer correlations. These four figures show the logic interconnected at the circles with letters to indicate the correct connection points. Whereas a detailed discussion of Figs. F-33a. to F-33d. relative to the regions noted in Fig. F-32. is not presented within this document, it is useful to note several points. Figure F-33a. generally denotes how those single-phase and two-phase regimes not normally considered to be part of the boiling curve (such as condensation) are selected. The “if-test” on RIDREG (corresponding to IDREG in Table F-6.) at the bottom of Fig. F-33a. decides whether we will work from right to left on the two-phase-boiling curve (Fig. F-33b.) or left to right Fig. F-33c. While this if-test adds a significant amount of Fortran coding to subroutine HTCOR, it saves a significant amount of central processing unit (CPU) time by eliminating a large number of calculations that might result if one always worked in one direction along the boiling curve. Figure F-33d. then denotes those operations performed upon the HTCs after they have been determined.

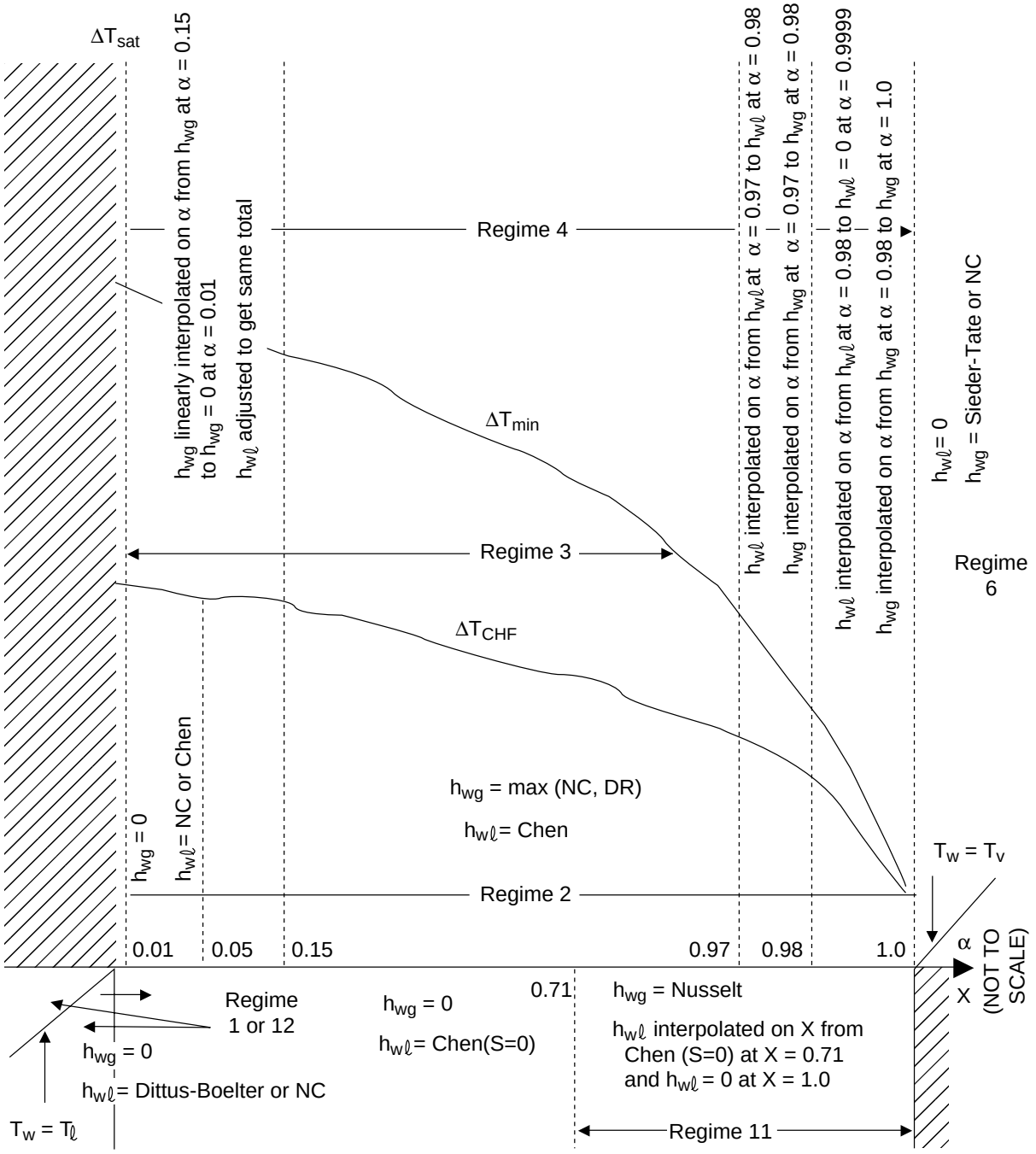

Fig. F-32. Void-fraction superheat plane.

TABLE F-6.
TRAC Heat-transfer Regimes

IDREG (IHTF)	Wall-to-Fluid Heat-Transfer Regime
1	Forced convection to single-phase liquid
2	Nucleate boiling
3	Transition boiling
4	Film boiling
6	Convection to single-phase vapor
7	Convection to two-phase mixture
11	Condensation
12	Liquid natural convection

The wall-to-fluid heat-transfer correlation selection logic used in subroutine HTVSSL for the reflood model is slightly different than that used in subroutine HTCOR. The difference is in the selection logic of transition- and film-boiling regimes (post-CHF heat-transfer regimes). Subroutines HTCOR and HTVSSL use the same HTC selection logic until points D and B shown in Figs. F-33b. and F-33c. The new HTC selection logic for the reflood model, performed after points D and B, is presented in Figs. F-33e. and F-33f.

F.2.1. Correlations Used in Subroutine HTCOR

This section discusses the HTC correlations used in subroutine HTCOR. Correlations for the wall-to-fluid heat transfer are discussed relative to the regimes denoted in Table F-6. After a discussion of each of these regimes, the critical-heat-flux and minimum wall superheat correlations are discussed.

F.2.1.1. Single-Phase Liquid (Heat-Transfer Regimes 1 and 12). Either forced convection (regime 1) or natural convection (regime 12) can occur when single-phase liquid is present. Laminar and turbulent HTCs are available. To avoid discontinuities with respect to flow-change logic encountered in earlier versions of TRAC, both laminar and turbulent conditions are evaluated and the maximum HTC is used. Because only single-phase liquid is assumed to be present, the vapor HTC, h_{wg}, is set equal to zero.

F.2.1.1.1. Forced Convection (Regime 1). Heat-transfer regime 1 is forced convection to single-phase liquid.

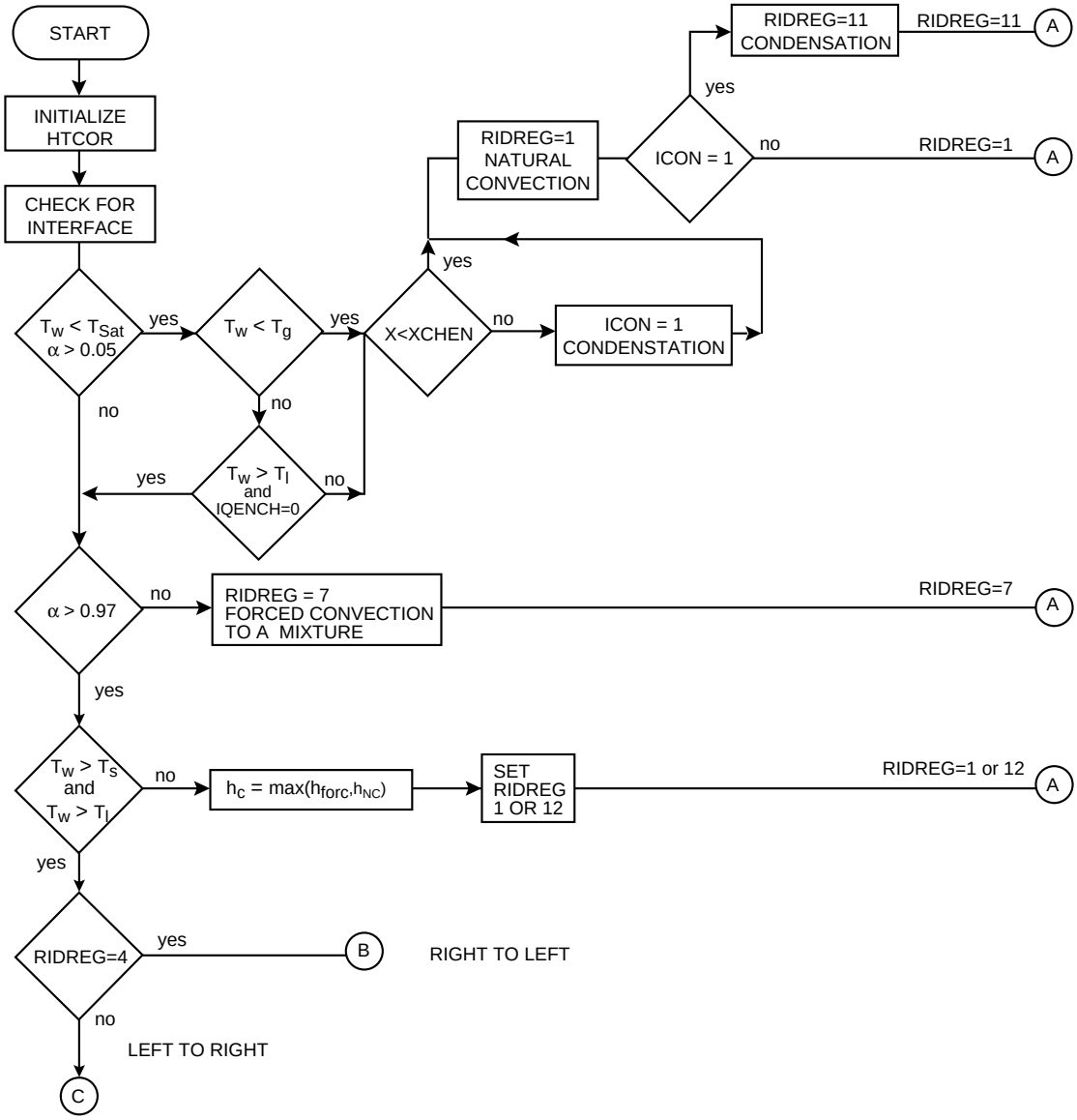

Fig. F-33a. HTC correlation selection logic.

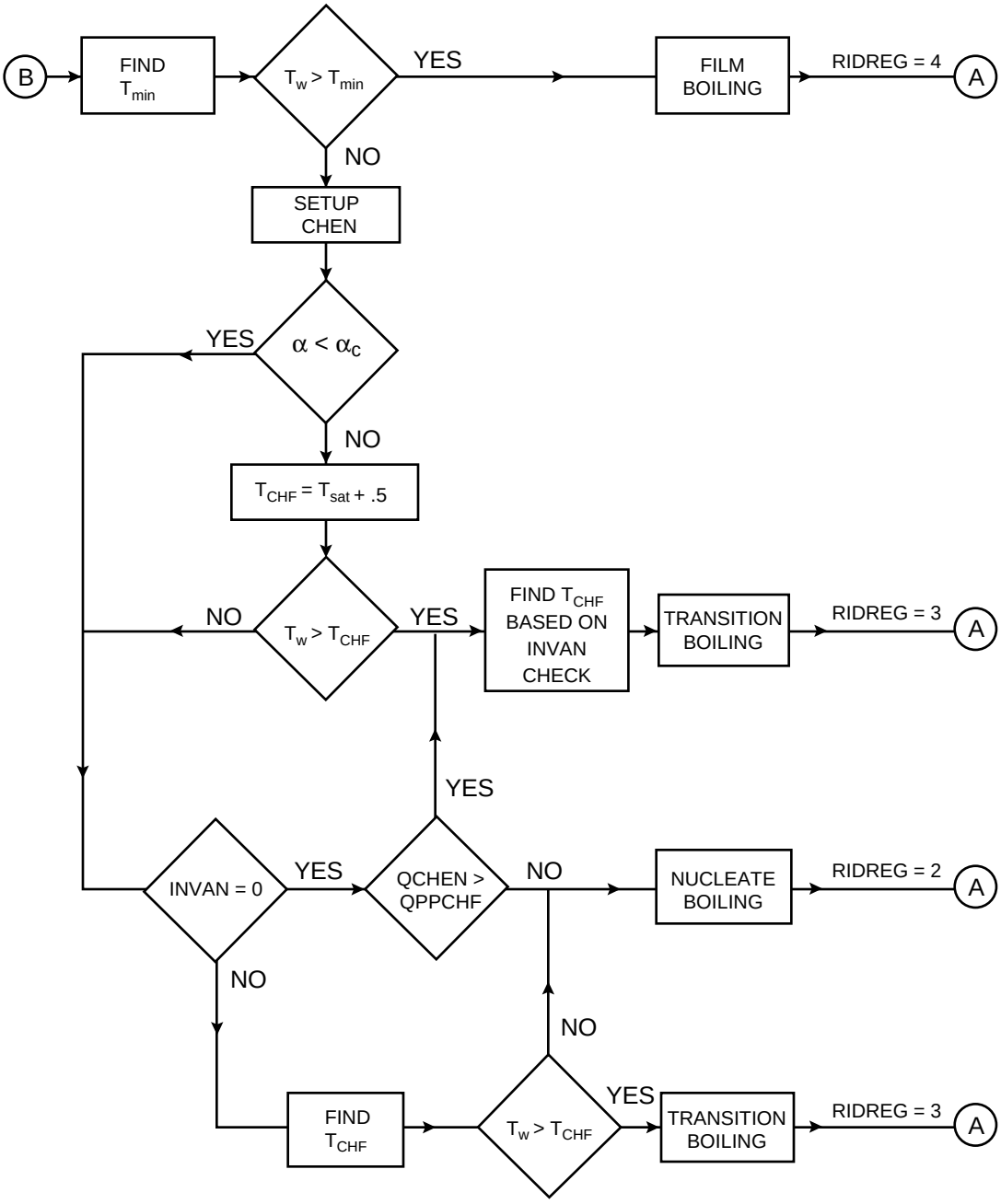

RIGHT TO LEFT ON BOILING CURVE

Fig. F-33b. HTC correlation selection logic.

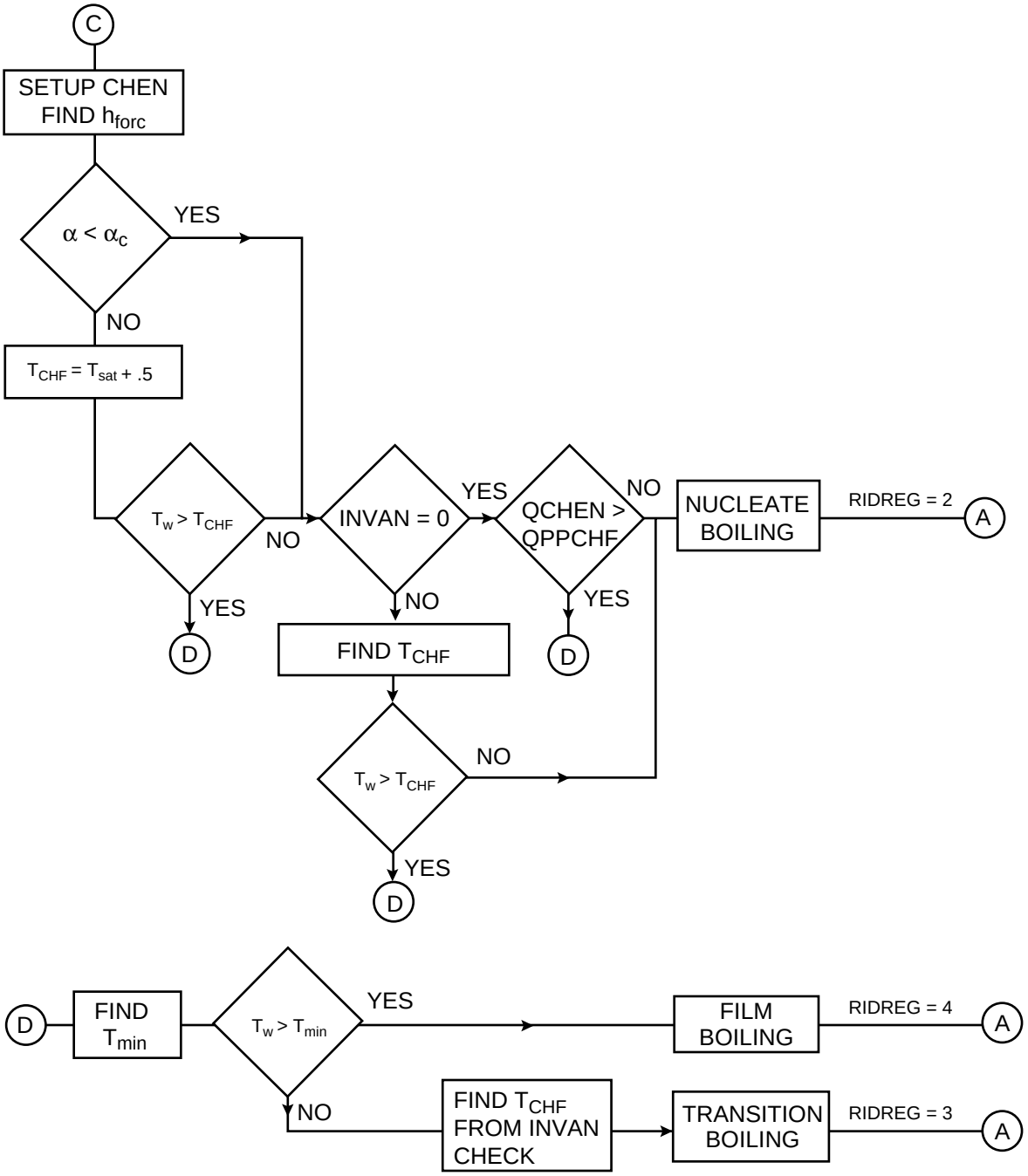

LEFT TO RIGHT ON BOILING CURVE

Fig. F-33c. HTC correlation selection logic.

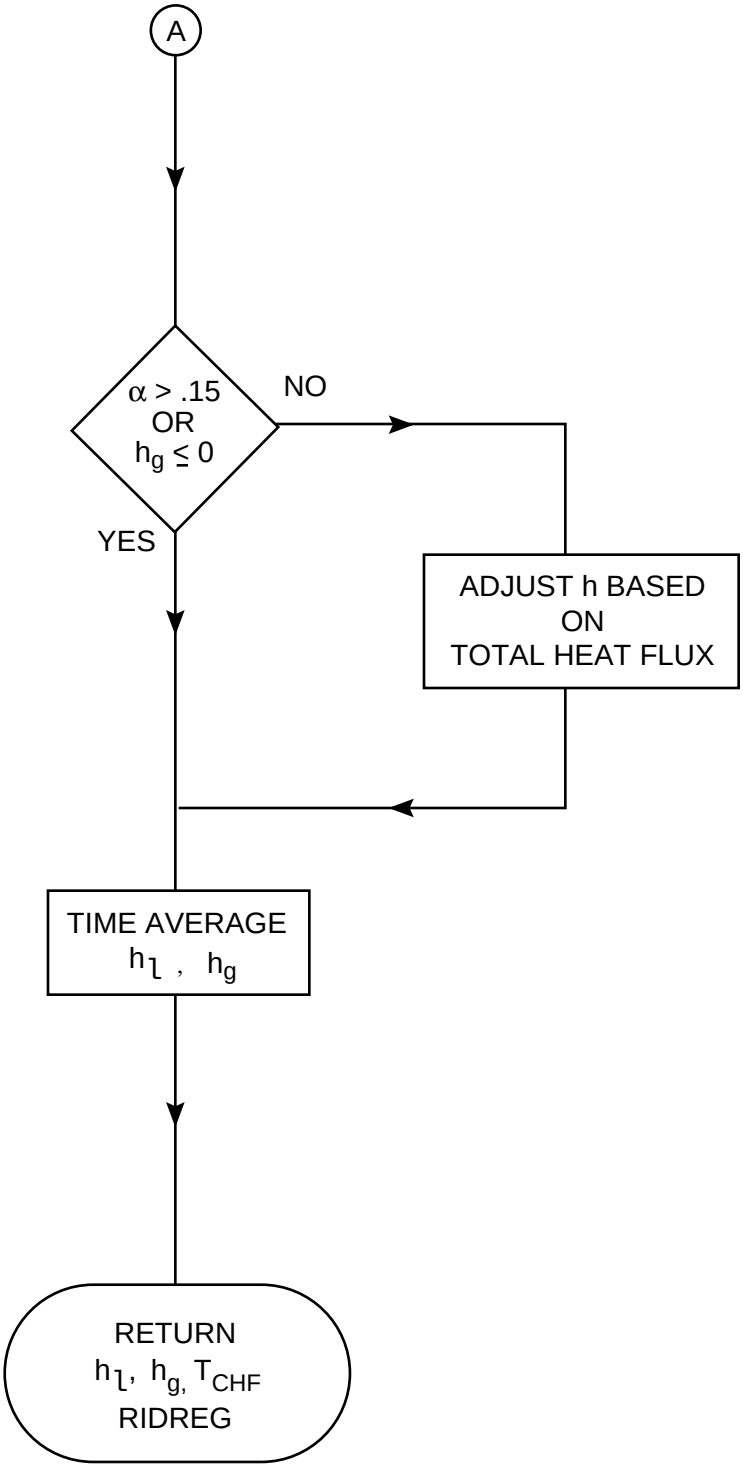

Fig. F-33d. HTC correlation section logic.

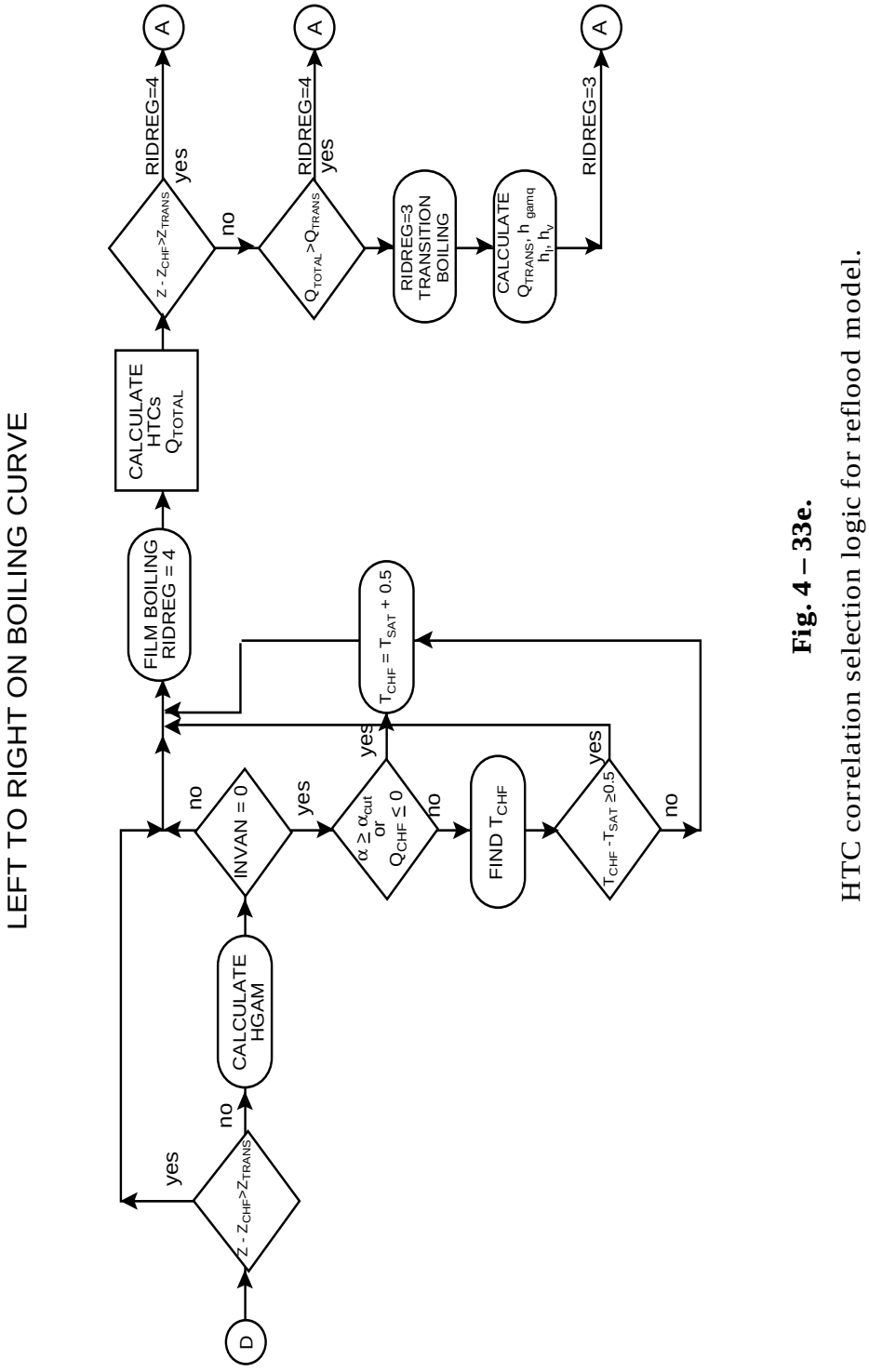

Fig. 4 – 33e.

HTC correlation selection logic for reflood model.

Fig. F-33e. HTC correlation selection logic for reflood model.

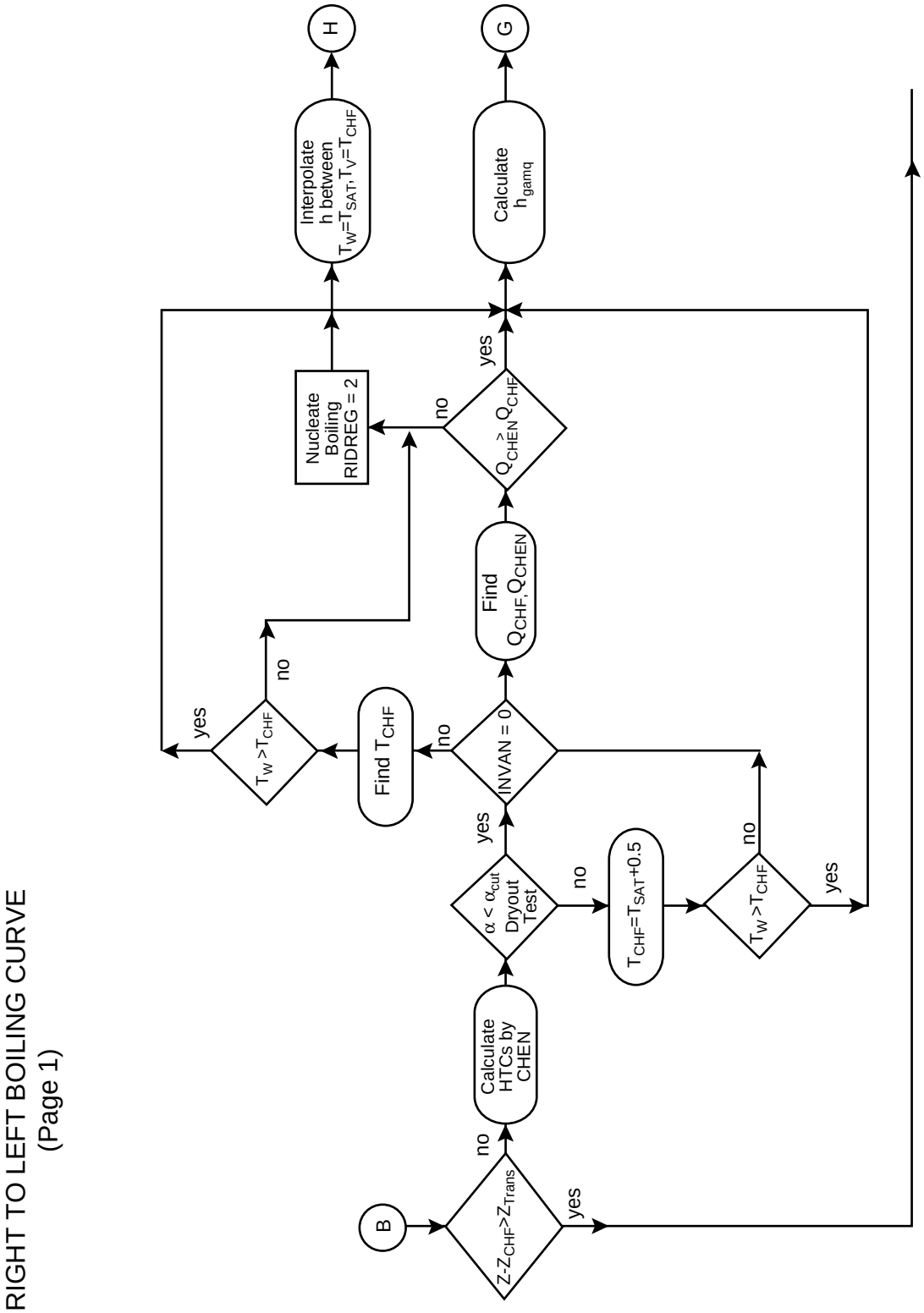

Fig. F-33f. HTC correlation selection logic for reflood model.

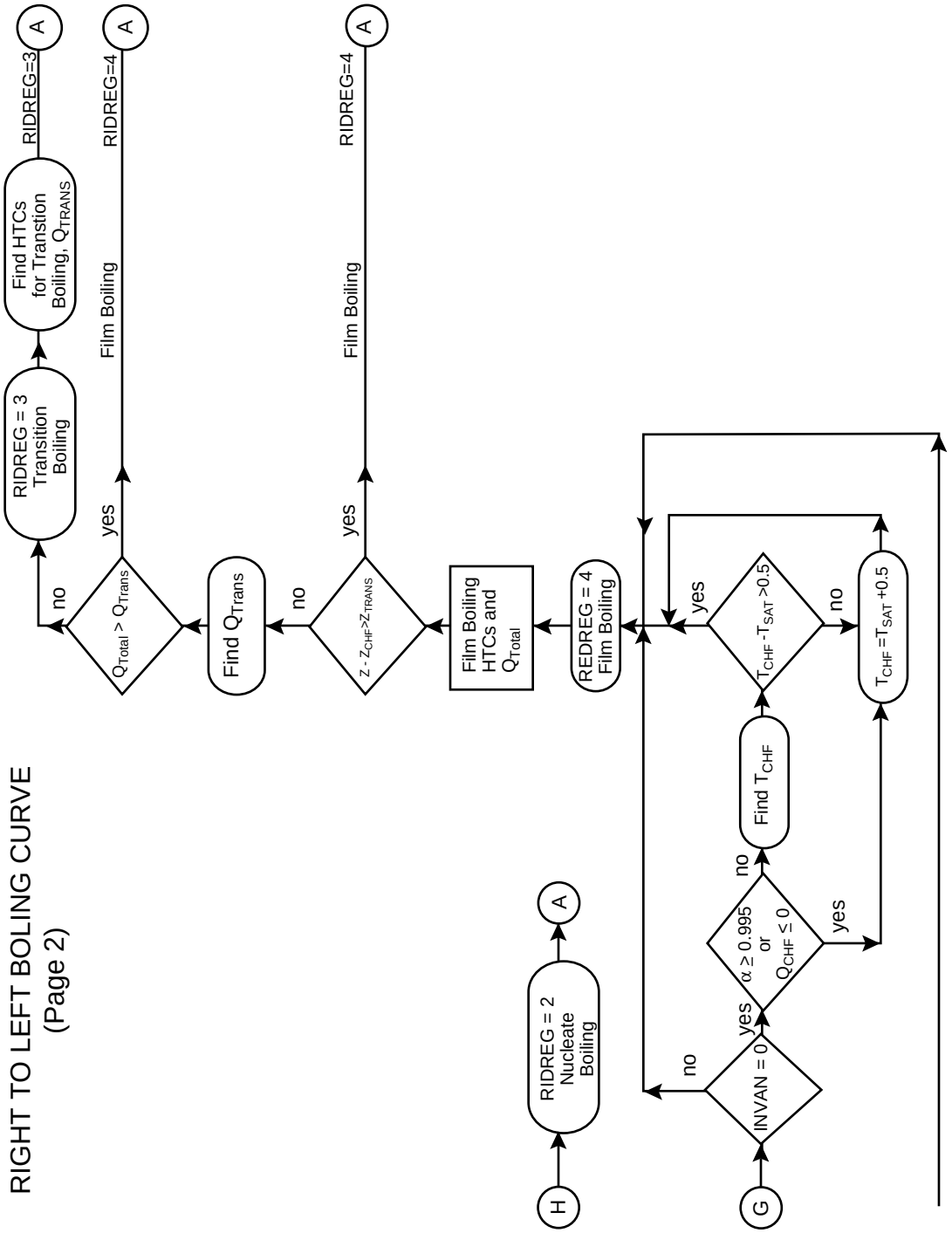

Fig. F-33f. (cont). HTC correlation selection logic for reflood model.

F.2.1.1.1.1. Basis for the Model. Wall-to-liquid heat-transfer coefficients are calculated by the Chen correlation (Ref. F-51., p. 262). The Chen correlation was developed for nucleate-boiling heat transfer and considered two separate heat-transfer mechanisms: heat transfer by nucleate boiling and heat transfer by forced convection. A Dittus-Boelter-type equation was used to represent the convective contribution. To account for the enhancement in heat transfer due to the formation of vapor bubbles, the Dittus-Boelter equation [Ref. F-52., Eq. (8-58)] was multiplied by a factor, *F*. The equation for the forced convection contribution is

$$h_{\text{forc}} = 0.023\frac{k_{\text{l}}}{D_H}Re_{\text{l}}^{0.8}Pr_{\text{l}}^{0.4}\cdot F \text{ , where} \tag{F-196}$$

$$F = 1.0 \text{ for } X_{TT}^{-1} \le 0.10 \text{ ,} \tag{F-197}$$

$$F = 2.35(X_{TT}^{-1} + 0.213)^{0.736} \text{ for } X_{TT}^{-1} > 0.01 \text{ ,} \tag{F-198}$$

$$Re_{\text{l}} = \frac{|V_{\text{l}}|\rho_{\text{l}}(1-\alpha)D_H}{\mu_{\text{l}}} \text{ , and } Pr_{\text{l}} = \left(\frac{\mu c_p}{k}\right)_{\text{l}} . \tag{F-199}$$

The convective part of the Chen correlation, Eq. (F-196), can be used for single-phase liquid heat transfer by taking *F* to be unity. In this case, the equation for h_{forc} is exactly the same as the Dittus-Boelter equation [Ref. F-52., Eq. (8-58)].

F.2.1.1.1.2. Input Quantities to the Model. The fluid properties are evaluated at the liquid temperature and pressure. The velocity used in determining the Reynolds number is the absolute value of the axial velocity of the liquid. This is the average of the velocities at the upper and lower cell edges for the VESSEL component and the average of the velocities at the left and right cell edges for 1D components. The hydraulic diameter is the hydraulic diameter of the flow passage.

F.2.1.1.1.3. Constants. None of the constants in the correlations was changed from that given in the reference cited. The dimensions used for the fluid properties, velocity, and hydraulic diameter result in HTCs with the units of $W\cdot m^{-2}\cdot K^{-1}$.

F.2.1.1.1.4. Model as Coded. The single-phase liquid HTC, h_{wl}, is calculated in subroutine CHEN (see Section F.2.1.2.). The enhancement factor, *F*, is set to unity if the inverse of the Martinelli factor, $(X_{TT})^{-1}$, is less than 0.10. The single-phase liquid HTC, h_{wl}, finally, is selected to be the maximum of those calculated by the Dittus-Boelter and the natural circulation equations [see Eq. (F-195)]. Subroutine CHEN returns the liquid HTC to subroutine HTCOR for regime 1. The final selection for the liquid HTC is the maximum of forced-convection and of laminar and turbulent natural-convection HTCs.

F.2.1.1.1.5. Assessment of the Correlations. When single-phase liquid forced convection is considered, the liquid HTC becomes the Dittus-Boelter equation in subroutine CHEN.

The Dittus-Boelter equation has been widely used for many years and has been verified by single-phase, turbulent, forced-convection data for many fluids. It is well supported by a broad database with an error of approximately 20%. Figure F-34. is a typical data correlation for forced-convection, turbulent flow in smooth tubes. The correlation is limited to forced-convection flows in which the Reynolds number, *Re*, is greater than 10^4 and with Prandtl numbers ranging from 0.7 to 160. If wide temperature differences are present in the flow such that appreciable changes in the fluid properties exist between the wall and the central flow, a correction is required to account for the property variations.

Both natural-circulation and forced-flow conditions may exist during many of the transients considered. Earlier versions of the code sometimes used the Grashof number or flow rate to switch between correlations. This method usually produced numerical instabilities and discontinuities. It was found that evaluating both the natural-convection and forced-convection correlations for laminar and turbulent flow and using the maximum HTC calculated eliminated the discontinuities caused by flow-change logic. In this heat-transfer regime, the Dittus-Boelter correlation is evaluated and maximum HTC is used; no switching between correlation is made on the basis of the Reynold's number.

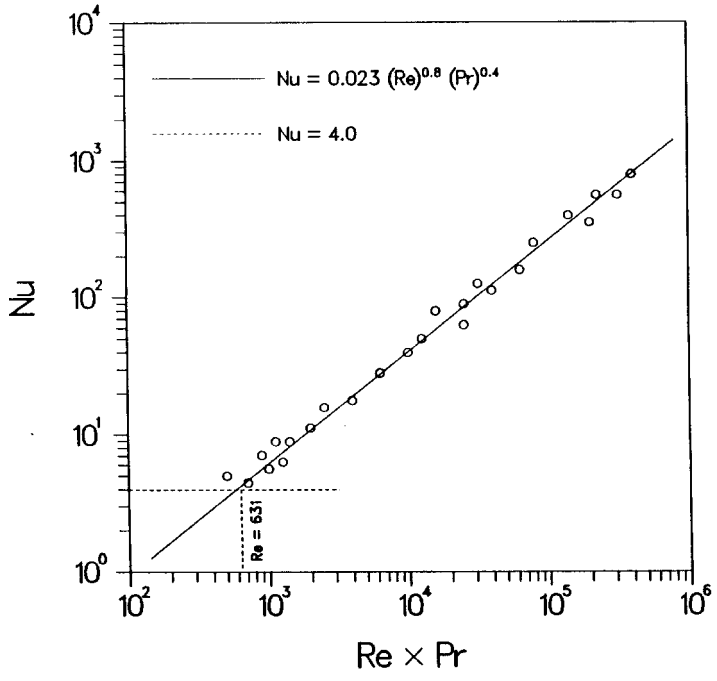

Fig. F-34. Typical data correlation for forced convection in smooth tubes, turbulent flow.

The Dittus-Boelter equation is used for external water flow parallel to tube banks. Available data indicate that the numerical coefficient varies with the pitch-to-diameter ratio. The HTCs obtained from Eq. (F-196) with $F = 1$ for the pitch-to-diameter ratios of typical PWR fuel assemblies can underpredict the HTCs by 30 to 40% (Ref. F-53., Eqs. 3 and 4).

F.2.1.1.1.6. Scaling Considerations. The Dittus-Boelter correlation has been found to predict the HTC for a wide range of flow geometries and fluids at moderate temperature differences (wall-to-fluid). At high flow rates, the form of the equation should account for geometry and flow rate (Reynolds number) and fluid properties (Prandtl number). At low flows (laminar range), natural-convection flow patterns may become significant.

F.2.1.1.1.7. Summary and Conclusions. The convective contribution of the Chen correlation, with the *F* factor being unity, is used for single-phase liquid heat transfer. With the *F* factor being unity, the convective part of the Chen correlation becomes exactly the same as the Dittus-Boelter equation. If the correlations are used within their ranges of applicability, they predict HTCs within approximately 20%. The Dittus-Boelter equation has been found applicable to a wide range of geometries, flow rates, and fluids.

F.2.1.1.2. Natural Convection (Regime 12). Heat-transfer regime 12 is natural convection to a single-phase liquid.

F.2.1.1.2.1. Basis for the Model. For the laminar-flow regime, the following correlation (Ref. F-54., Table 7.1) is used:

$$h_{wl} = 0.59 \frac{k_l}{L_c} (Gr \cdot Pr)^{0.25} \ , \tag{F-200}$$

where the Grashof number, *Gr*, is defined as

$$Gr = \frac{g\beta |T_w - T_l| \rho_f^2 L_c^3}{\mu_l^2} \tag{F-201}$$

and the Prandtl number, *Pr*, is defined as

$$Pr = \left(\frac{\mu c_p}{k} \right)_l \ . \tag{F-202}$$

To avoid extra calls to the thermodynamic properties subroutine, THERMO, all properties except β and ρ are evaluated at the liquid temperature. The properties β and ρ are approximated as

$$\rho_f = \rho_l + \frac{\partial \rho_l}{\partial T} (T_f - T_l) \tag{F-203}$$

and

$$\beta = -\frac{\partial \rho_l}{\partial T}\frac{1}{\rho_f} \ , \tag{F-204}$$

where

$$T_f = 0.5 \cdot (T_w + T_l) \ . \tag{F-205}$$

This correlation is valid in the range $10^4 < Gr \cdot Pr < 10^9$.

For the turbulent flow regime, the following correlation (Ref. F-54., Table 7.1) is used:

$$h_{wl} = 0.10\frac{k_l}{D_H}(Gr \cdot Pr)^{0.3333} \ . \tag{F-206}$$

The associated parameters are defined as in Eq. (F-200). This correlation is valid in the range $10^9 < Gr \cdot Pr < 10^{13}$.

F.2.1.1.2.2. Input Quantities to the Model. In Eqs. (F-200) and (F-206), the vertical height is normally chosen as the characteristic length in the Grashof number. To avoid nodalization dependence, the hydraulic diameter of the flow channel, D_H, is used as the characteristic length. Because the length term drops out of Eq. (F-206) and appears to the –0.25 power in Eq. (F-200), the choice of the characteristic dimension has a small effect on the value of the HTC.

All fluid properties except the density (ρ) and the coefficient of volumetric expansion (β) are evaluated at the liquid temperature T_l. The properties ρ and β are approximated using Eqs. (F-203) through (F-205).

By using the maximum of the HTCs calculated from Eqs. (F-200) and (F-206), the laminar model is actually applied up to a value of $Gr \cdot Pr = 1.794 \times 10^9$; this assures continuity in the HTC.

F.2.1.1.2.3. Constants. None of the constants in the correlations was changed from that given in the reference cited. The dimensions used for the fluid properties, velocity, hydraulic diameter, temperature, and gravitational constant result in HTCs with dimensions of $W \cdot m^{-2} \cdot K^{-1}$.

F.2.1.1.2.4. Model as Coded. These correlations are evaluated in subroutine HTCOR. They are compared with the value of h_{wl} obtained from subroutine CHEN (see Section F.2.1.2.) for regime 1 and the maximum value is chosen. If the forced-convection HTC from subroutine CHEN is the largest, heat-transfer regime 1 is assigned; otherwise heat-transfer regime 12 (natural circulation to a single-phase liquid) exists.

F.2.1.1.2.5. Assessment of the Correlations. The form of Eq. (F-200) results from an analysis of a vertical surface at a uniform temperature in an extensive fluid at rest. It was assumed that the flow in the convective layer is primarily parallel to the surface. A force balance, which included the effects of buoyancy and fluid shear, resulted in an expression for the thickness of the convection layer. By considering this layer to be a thin slab across which heat is conducted, an expression for the HTC was found. For $Gr \cdot Pr < 10^4$, the boundary layer solution is no longer valid; for $Gr \cdot Pr > 10^9$, the transition to turbulent flow occurs and Eq. (F-206) should be used. As noted previously, by choosing the larger value of HTC from Eqs. (F-200) and (F-206), the transition to turbulent flow is assumed to occur when $Gr \cdot Pr = 1.794 \times 10^9$.

If the boundary layer thickness is very small compared with the diameter, *D*, the effect of transverse curvature is small and the results for vertical flat plates may be applied to flow over vertical cylinders. For large-diameter cylinders and Prandtl numbers near 1.0, it has been shown (Ref. F-55., Eq. 8-55) that a vertical cylinder may be treated as a vertical flat plate if

$$\frac{D}{L} \geq 35 \cdot (Gr)^{-0.25} \ , \qquad \text{(F-207)}$$

where *D* is the diameter of the cylinder, *L* is the vertical height, and *Gr* is the Grashof number based upon *L*. It is estimated that the flat-surface solution does not differ from the heat-transfer rate for vertical cylinders by more than 5% when Eq. (F-207) is satisfied. At small Grashof numbers, the cylinder must be short with a large diameter to satisfy Eq. (F-207).

F.2.1.1.2.6. Scaling Considerations. Both the laminar and turbulent correlations, Eqs. (F-200) and (F-206), were developed for isothermal plates in an extensive fluid at rest. The laminar-flow correlation is a weak function of geometry $L_c^{-0.25}$; in the turbulent-flow correlation, the length dependence drops out. The correlations are relatively insensitive to the choice and magnitude of the characteristic dimension.

F.2.1.1.2.7. Summary and Conclusions. If the correlations are used within their ranges of applicability, the predicted HTCs are in good agreement with data (see Fig. F-35. and Ref. F-10., Fig. 7-7). In TRAC, the correlations are applied to geometries other than those for which they were developed. Equation (F-207) provides a possible criterion to determine the applicability of the correlations to vertical cylinders.

Both correlations are evaluated and the maximum HTC is chosen; switching between correlations is not based upon the value of the parameter $Gr \cdot Pr$. This method avoids discontinuities in the HTCs and numerical instabilities. As $Gr \cdot Pr$ decreases below $\sim 1 \times 10^4$ and increases above $\sim 1 \times 10^{11}$, the correlations underestimate the experimental data.

F.2.1.2. Nucleate Boiling (Heat-Transfer Regime 2). Heat-transfer regime 2 is nucleate boiling and includes subcooled nucleate boiling.

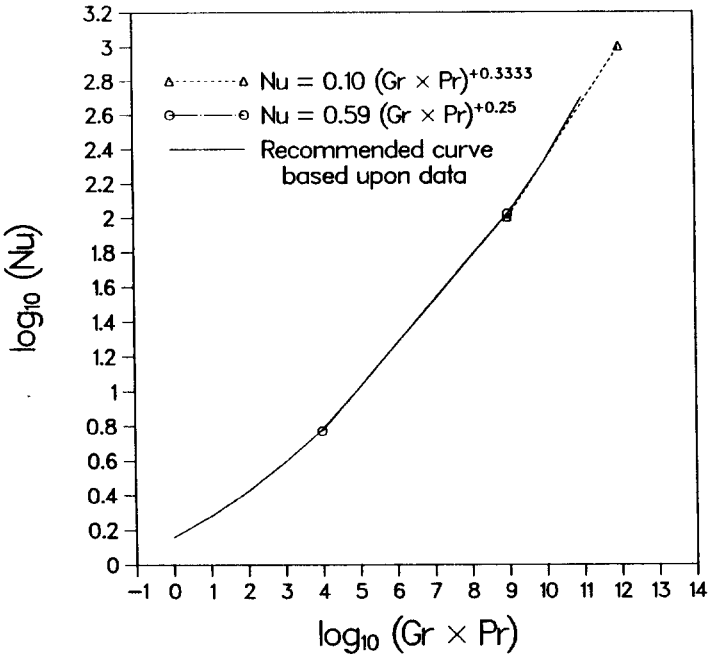

Fig. F-35. Natural convection for short vertical plates to air.

F.2.1.2.1. Basis for the Model. The Chen correlation (Ref. F-51., p. 262) is used in the nucleate-boiling heat-transfer regime. The correlation assumes that both nucleation and convective mechanisms occur and that the contributions made by the two mechanisms are additive. The convective component is assumed to be represented by a Dittus-Boelter-type equation where the thermal conductivity, Reynolds number, and Prandtl number are effective values associated with the two-phase flow. Heat is transferred to a liquid film in annular-mist and dispersed flow and it is reasonable to use the liquid conductivity. The values of the Prandtl number for liquid and vapor are normally of the same order of magnitude and it is reasonable to expect the two-phase Prandtl number to have a similar value. A parameter, F >1.0, which is a function of the Reynolds number, is used to modify the convective part of the correlation, h_{forc} (called the macroterm), to account for increased agitation caused by the formation of vapor bubbles.

The basis for the nucleate-boiling component of the correlation is the analysis of Forster and Zuber (Ref. F-56.) for pool boiling. Their analysis relates a bubble Nusselt number to a bubble Reynolds number and a liquid Prandtl number. It can be shown that the product of growth rate and bubble radius is constant for a given superheat. In pool boiling and convective boiling, the superheat is not constant across the boundary layer. In pool boiling, this effect can be neglected. In forced-convective boiling, the boundary layer is thinner and temperature gradients are steeper. The difference between the wall superheat and the mean superheat to which the bubble is exposed must be considered. A suppression factor, S, modifies the nucleate-boiling part of the correlation, h_{nucb} (called the microterm), to account for this effect.

The equations for the Chen correlation are as follows:

$$q_{\text{total}} = h_{\text{forc}}(T_w - T_l) + h_{\text{nucb}}(T_w - T_{\text{sat}}) \ , \tag{F-208}$$

where

$$h_{\text{forc}} = 0.023 \frac{k_l}{D_H} \left(\frac{|V_l| \rho_l (1-\alpha) D_H}{\mu_l} \right)^{0.8} \left(\frac{\mu c_p}{k} \right)_l^{0.4} \cdot F \ , \tag{F-209}$$

$$h_{\text{nucb}} = 0.00122 \frac{k_l^{0.79} c_{pl}^{0.45} \rho_l^{0.49}}{\sigma^{0.5} \mu_l^{0.29} h_{lg}^{0.24} \rho_g^{0.24}} (T_w - T_s)^{0.24} (P_w - P)^{0.75} \cdot S \ , \tag{F-210}$$

$$F = 1.0 \text{ for } X_{TT}^{-1} \le 0.10 \ , \tag{F-211}$$

$$F = 2.35(X_{TT}^{-1} + 0.213)^{0.736} \text{ for } X_{TT}^{-1} > 0.01 \text{ (see also Eq. (F-217)}, \tag{F-212}$$

$$X_{TT}^{-1} = (\text{Martinelli factor})^{-1} = \left(\frac{x}{1-x} \right)^{0.9} \left(\frac{\rho_l}{\rho_g} \right)^{0.5} \left(\frac{\mu_g}{\mu_l} \right)^{0.1} \ , \tag{F-213}$$

$$S = (1 + 0.12\ Re_{TP}^{1.14})^{-1} \text{ for } Re_{TP} < 32.5 \ , \tag{F-214}$$

$$S = (1 + 0.42\ Re_{TP}^{0.78})^{-1} \text{ for } 32.5 \le Re_{TP} \le 70.0 \ , \text{ and} \tag{F-215}$$

$$Re_{TP} = 10^{-4} \frac{|V_l| \rho_l (1-\alpha) D_H}{\mu_l} \cdot F^{1.25} \ . \tag{F-216}$$

The maximum value of X_{TT}^{-1} is limited to 100. The maximum value of Re_{TP} is limited to 70. The parameter F is defined as

$$F = \left(\frac{Re_{TP}}{Re_l} \right)^{0.8} = \left(\frac{Re_{TP}}{G(1-x) D_H / \mu_l} \right)^{0.8} \ . \tag{F-217}$$

Because this ratio is a flow parameter only, it may be expected that it could be expressed as a function of the Martinelli factor X_{TT}.

The suppression factor, S, is defined as

$$S = \left(\frac{\Delta T_e}{\Delta T_{\text{sat}}} \right)^{0.99} \ , \tag{F-218}$$

where ΔT_e is the effective superheat seen by a bubble. The functions F and S were determined from experimental data.

The vapor HTC is defined using the natural-convection and forced-convection correlations given by

$$h_{\mathrm{NC}} = 0.13 k_g \left[\frac{\rho_g^2 g |T_w - T_g|}{\mu_g^2 T_g} \right]^{0.333} \cdot Pr_g^{\,0.333} \tag{F-219}$$

and

$$h_{dr} = 0.023\, Re_{TP}^{0.8} Pr_g^{0.4} \left(\frac{k_g}{D_H} \right), \tag{F-220}$$

where

$$Re_{TP} = \frac{\left[|V_g| \alpha + |V_l| (1-\alpha) \right]}{\mu_g} \cdot \left(\rho_g D_H \right) \tag{F-221}$$

and

$$Pr_g = \left(\frac{c_p \mu}{k} \right)_g . \tag{F-222}$$

Equation (F-219) is a correlation for natural convection for vertical planes and cylinders in the turbulent-flow regime where $10^9 < Gr \cdot Pr < 10^{13}$ (Ref. F-10., Eq. 7-4a). It should be noted that in Eq. (F-219), the characteristic length has dropped out and β has been approximated by $1/T_g$. Equation (F-220) is the Dougall-Rohsenow correlation (Ref. F-9., Eq. F-153).

F.2.1.2.2. Input Quantities to the Model. All liquid properties are evaluated at the liquid temperature. All vapor properties are evaluated at the film temperature $T_f = 0.5(T_w + T_g)$. The velocity in the Reynolds number of Eq. (F-216) is the absolute value of the axial velocity of the liquid. The velocities in the two-phase Reynolds number [Eq. (F-221)] are the absolute values of the axial velocities of the vapor and liquid. Axial velocities are calculated as described in Section F.2.1.1.1. The characteristic length in the correlations is the hydraulic diameter of the flow passage.

F.2.1.2.3. Constants. None of the constants in the correlation was changed from that given in the references cited. The dimensions used for the fluid properties, velocity, temperature, and characteristic length result in HTCs with units of $W \cdot m^{-2} \cdot K^{-1}$. The functions F and S were determined from experimental data (see Figs. F-36. and F-37.).

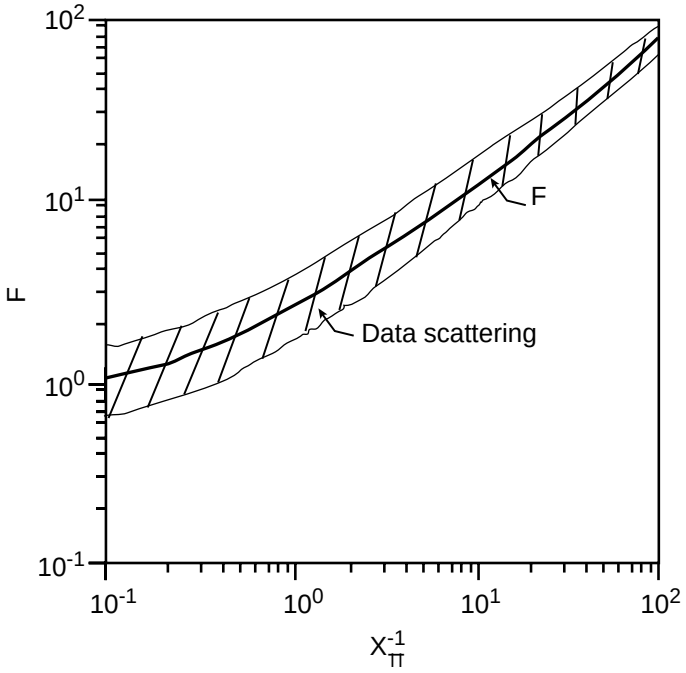

Fig. F-36. Dimensionless function *F* for forced convection in Chen's correlation.

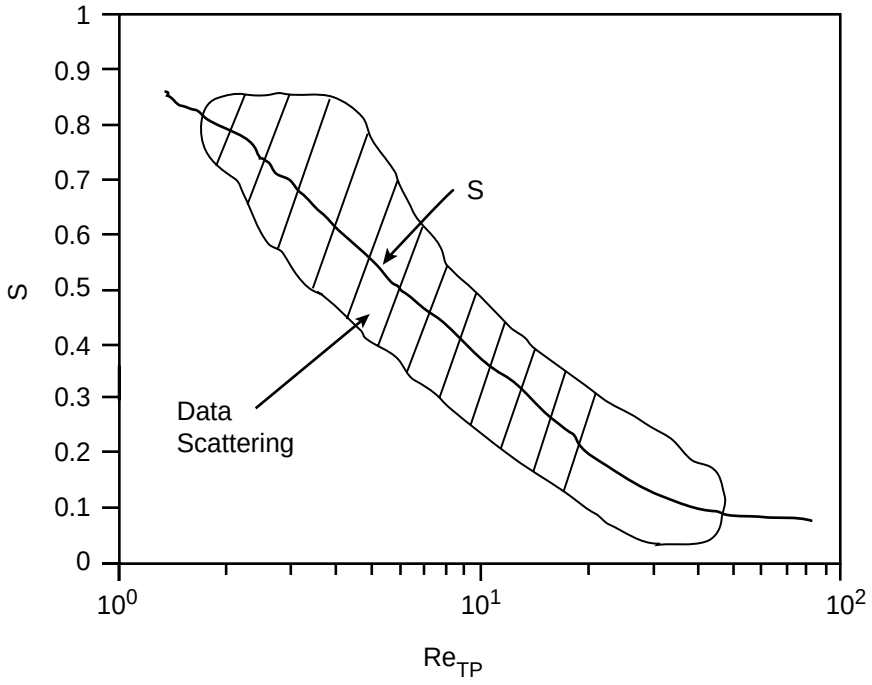

Fig. F-37. Dimensionless function *S* for nucleate boiling in Chen's correlation.

F.2.1.2.4. Model as Coded. The quantities h_{forc} and h_{nucb} are calculated in subroutine CHEN and the vapor HTC is calculated in subroutine HVNB. Because the Chen correlation was developed to represent the total heat flux and a vapor HTC is used for the phasic heat transfer, the liquid HTC is given by

$$h_{wl} = [h_{\text{forc}}(T_w - T_l) + h_{\text{nucb}}(T_w - T_{\text{sat}}) - h_{wg}\,(T_w - T_g)] / (T_w - T_l)\ . \tag{F-223}$$

The vapor heat transfer is always limited to be 50% or less.

In subroutine HVNB, if the void fraction is ≤ 0.5, the vapor HTC, h_{wg}, is set to 0.0. If the void fraction is ≥ 0.75, h_{wg} is the maximum of the values given by Eqs. (F-219) and (F-220). Linear interpolation is done between 0.0 and max(h_{NC}, h_{dr}) for void fractions between 0.5 and 0.75.

The suppression factor, S, should approach zero as $\alpha \rightarrow 1.0$. From the definition of S, Eqs. (F-214) and (F-215), it is clear that $S \rightarrow 1.0$ as $\alpha \rightarrow 1.0$. To ensure that S approaches the correct value for $\alpha = 1.0$, the following procedure is used. When $\alpha > 0.70$, S is evaluated at $\alpha_s = 0.70$ and the current value of α; the minimum of the two values, S_{min}, is saved. Linear interpolation is then used between the two values, S_{min} and $S = 0.0$ at $\alpha_c = 0.98$. That is,

$$S = S_{\text{min}} \frac{(\alpha_c - \alpha)}{(\alpha_c - \alpha_s)} \text{ for } \alpha > \alpha_s\ (\alpha_s = 0.70)\text{, and} \tag{F-224}$$

$$S = 0.0 \text{ for } \qquad \alpha > \alpha_c\ (\alpha_c = 0.98)\ . \tag{F-225}$$

At high void fractions ($\alpha > \alpha_c = 0.98$), the HTCs are revised by linear interpolation between the current values of h_{wl} and h_{wg} and those for single-phase vapor ($h_{wl} = 0.0$ and $h_{wg} = h_{gsav}$) so that

$$h_{g\text{sav}} = \max(h_{g\text{NC}}, h_{g\text{turb}})\ , \tag{F-226}$$

where $h_{g\text{NC}}$ and $h_{g\text{turb}}$ are calculated as described in Section F.2.1.5.:

$$h_{g\text{NC}} = 0.13 k_g \left(\frac{\rho_g^2 g (T_w - T_g)}{\mu_g{}^2 T_g} \right)^{0.333} \cdot (Pr_g)^{0.333}\ , \tag{F-227}$$

and

$$h_{g\text{turb}} = 0.023 \frac{k_g}{D_H} (Re_g)^{0.8} \cdot (Pr_g)^{0.4}\ . \tag{F-228}$$

Note also in Section F.2.1.5. that Eq. (F-255) replaces Eq. (F-228) when $T_f = 0.5(T_w + T_g) \geq T_{sv}$. At high void fractions,

$$\bar{h}_{wl} = h_{wl} + (0 - h_{wl})\frac{(\alpha - \alpha_c)}{(\alpha_3 - \alpha_c)} \text{ for } \quad \alpha_c < \alpha < \alpha_3 , \tag{F-229}$$

$$\bar{h}_{wl} = 0 \text{ for } \quad \alpha \geq \alpha_3 , \tag{F-230}$$

$$\bar{h}_{wg} = h_{wg} + (h_{gsav} - h_{wg})\frac{(\alpha - \alpha_c)}{(\alpha_2 - \alpha_c)} \text{ for } \alpha_c < \alpha < \alpha_2 , \text{ and} \tag{F-231}$$

$$\bar{h}_{wg} = h_{gsav} \text{ for } \quad \alpha \geq \alpha_2 , \tag{F-232}$$

where

$\alpha_c = 0.98$, $\alpha_2 = 1.0$, and $\alpha_3 = 0.9999$.

F.2.1.2.5. Weighting, Limits, and Averaging. The vapor HTC is multiplied by the square of the temperature ratio $(T_w - T_{sat})/(T_{CHF} - T_{sat})$ so that h_{wg} is zero when $T_w = T_{sat}$ and goes to its transition-boiling value at $T_w = T_{CHF}$. Limits are placed on the range of values of the Chen F and S factors, the two-phase Reynolds number, and the inverse of the Martinelli factor [see Eqs. (F-211) through (F-216)]. The Chen S factor is also modified for void fractions greater than 0.70 so that it approaches its correct limit of 0.0 as the void fraction approaches 1.0. Subroutine CHEN constrains the h_{forc} term to be $\geq 4.0 \cdot (k_l / D_H)$.

At high void fractions, the liquid and vapor HTCs are linearly interpolated between the current values and the values for single-phase vapor to ensure that the boiling curve is smooth between heat-transfer regimes. No rate limits are used for the nucleate-boiling heat-transfer correlations.

F.2.1.2.6. Assessment of the Correlation. The Chen correlation works well for a wide variety of fluids and covers both the low- and high-quality flow regions. It approaches the Forster-Zuber pool-boiling relation at low flows. When quality is high and the flow pattern is in the form of annular-mist flow with a thin evaporating film on the wall, the correlation approaches that for forced convection of steam. The original database for the Chen correlation covered the following ranges:

Pressure:	0.09 to 3.45 MPa
Mass Flow:	54 to 4070 kg / m^2-s
Quality:	0.0 to 0.7

The pressure range has been extended to 6.9 MPa. Tables F-7. and F-8. (Ref. F-57.) show the range of conditions for data used in testing various correlations and a comparison of the correlations. The modified correlation used for subcooled boiling underpredicts the highly subcooled experimental data.

TABLE F-7.
Range of Conditions for Data Used
In testing Correlations (Ref. F-57.)

Fluid	Geometry	Flow	Pressure Bar	Liquid Inlet Velocity	Quality (wt%)	Heat Flux
Water	Tube	Up	0.55–2.76	0.06–1.45	15–71	88–630
Water	Tube	Up	2.9–34.8	0.24–4.50	3–50	205–2400
Water	Tube	Down	1.1–2.1	0.24–0.82	2–14	44–158
Water	Annulus	Up	1–2.4	0.06–0.27	1–59	100–500
Methanol	Tube	Up	1	0.3–0.76	1–4	22–54
Cyclohexane	Tube	Up	1	0.4–0.85	2–10	9.5–41
Pentane	Tube	Up	1	0.27–0.67	2–12	9.5–38
Heptane	Tube	Up	1	0.3–0.73	2–10	6.2–28
Benzene	Tube	Up	1	0.3–0.73	2–9	12.5–41

TABLE F-8.
Comparison of Correlations (Ref. F-57.)

Data	Average Percentage Deviations for Correlations				
	Dengler and Addoms	Guerrieri and Talty	Bennett et al.	Schrock and Grossman	Chen
Dengler and Addoms (water)	30.5	62.3	20.0	20.3	14.7
Schrock and Grossman (water)	89.5	16.4	24.9	20.0	15.1
Sani (water)	26.9	70.3	26.5	48.6	8.5
Bennett et al. (water)	17.9	61.8	11.9	14.6	10.8
Guerrieri and Talty (methanol)	42.5	9.5	64.8	62.5	11.3
Guerrieri and Talty (cyclohexane)	39.8	11.1	65.9	50.7	13.6
Guerrieri and Talty (benzene)	65.1	8.6	56.4	40.1	6.3
Guerrieri and Talty (heptane)	61.2	12.3	58.0	31.8	11.0
Guerrieri and Talty (pentane)	66.6	9.4	59.2	35.8	11.9
Combined average for all data	38.1	42.6	32.6	31.7	11.0

Equation (F-220) is the Dougall-Rohsenow correlation and can be recognized as a simple modification to the Dittus-Boelter correlation. The Dougall-Rohsenow correlation was developed for the film-boiling flow regime. It was postulated that the thermal resistance existed at the liquid / vapor interface and was the result of a laminar zone, a buffer zone, and a turbulent zone. As the film Reynolds number was increased, the various zones of resistance were gradually removed. None remained in dispersed flow.

Pre-CHF boiling heat transfer can occur in either a saturated two-phase mixture or in a subcooled, two-phase liquid. For the saturated two-phase mixture, the heat-transfer mechanisms are saturated nucleate boiling in the low-quality region and forced-convective evaporation (normally associated with annular-mist flow) in the high-quality, high-flow region. It is assumed that there is little difference between upflow and downflow nucleate-boiling heat transfer.

If the wall temperature exceeds the minimum temperature required for nucleation, subcooled boiling can occur. It is assumed that a simple temperature ratio correlation is sufficient to modify the nucleate-boiling part of the Chen correlation for subcooled boiling. It is assumed that both the nucleation and convection mechanisms occur and that their effects are additive.

F.2.1.2.7. Scaling Considerations. Most of the data from which the correlations were developed were for boiling inside vertical tubes. The accuracy of the HTCs predicted by the correlations when applied to PWR rod-bundle geometry has not been determined. The Chen correlation, although semi-empirical, does have a physical basis. It works well for a variety of fluids (including water), covers both the low- and high-quality regions, and transforms into the Forster-Zuber correlation for pool boiling at low flows.

The Dougall-Rohsenow correlation is used to make the vapor HTC continuous as a function of wall temperature. Based upon limited tube-bundle data, it seems to predict bundle data better than tube data (Ref. F-51., p. 277, and Fig. F-38.).

F.2.1.2.8. Summary and Conclusions. The Chen correlation has been widely used for water in the saturated, forced-convective boiling region in vertical ducts. It is valid for situations in which all surfaces are wet. Evaporation within inclined and horizontal tubes is encountered frequently (U-tubes in steam generators). Stratification of the flow results, with the majority of the fluid in the bottom of the tube, and dryout of the upper surfaces may occur. The correlation of Shah (Ref. F-58., p. 572, and Ref. F-59.) is valid for saturated, forced-convection boiling in horizontal ducts, but for water it is best suited to situations in which heating is from a fluid.

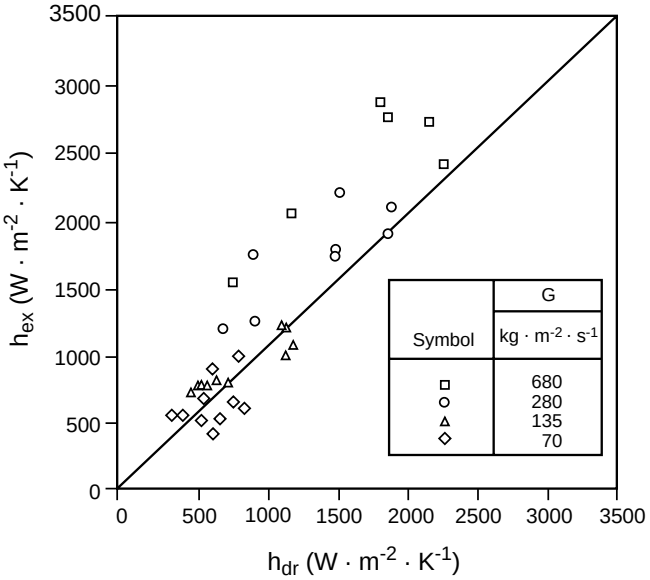

Fig. F-38. Comparison of measured HTCs during stable film boiling in rod bundles with the predictions of the Dougall-Rohsenow correlation.

Newer correlations (Refs. F-60. and F-61.) for forced-convection boiling heat-transfer data have extended the method of superposition to cover subcooled to high quality ranges. Reference F-61. uses single-phase and two-phase forced-convection equations, a pool-boiling equation, and an incipient-boiling criterion. A single, empirically determined coefficient is required. The agreement with water data is better than that provided by the Chen correlation. Reference F-61. used a large data bank (7 fluids and 28 authors) for saturated boiling in vertical and horizontal tubes, subcooled boiling, and boiling in annuli to develop a correlation giving a closer fit to the data than existing correlations. Future code development efforts should consider possible improvements to the correlations used in the nucleate boiling regime.

F.2.1.3. Transition Boiling (Heat-Transfer Regime 3). The transition-boiling regime spans the boiling surface between CHF and minimum film boiling.

F.2.1.3.1. Basis for the Model. It is assumed that transition-boiling heat transfer is composed of both nucleate-boiling (wet-wall) and film-boiling (dry-wall) heat transfer. Each component is weighted by a factor ξ, the fraction of wall area that is wet. The equations used in the transition-boiling regime are (Ref. F-62., p. 27)

$$q_{\text{trans}} = \xi q_{\text{CHF}} + (1-\xi) q_{\text{min}} \tag{F-233}$$

$$= h_{w\text{l}}(T_w - T_{\text{l}}) + h_{wg}(T_w - T_g)\ , \tag{F-234}$$

where

$$\xi = \left(\frac{T_w - T_{\min}}{T_{\mathrm{CHF}} - T_{\min}} \right)^2 , \tag{F-235}$$

$$q_{\min} = h_{w\mathrm{l}\min}(T_{\min} - T_{\mathrm{l}}) + h_{wg\min}(T_{\min} - T_g) + h_{fBB}(T_{\min} - T_{\mathrm{sat}}) , \tag{F-236}$$

$$h_{wg\min} = \max(h_{\mathrm{NC}}, h_{dr}) \text{ at } T_{\min}, \tag{F-237}$$

$$h_{\mathrm{NC}} = 0.13 k_g \left(\frac{\rho_g^2 g_c |T_w - T_g|}{\mu_g^2 T_g} \right)^{0.3333} \cdot (Pr_g)^{0.3333} , \tag{F-238}$$

$$h_{dr} = 0.023 \, Re_{TP}^{0.8} \, Pr_g^{0.4} \frac{k_g}{D_H} , \tag{F-239}$$

$$Pr_g = \left(\frac{c_p \mu}{k} \right)_g , \tag{F-240}$$

$$Re_{TP} = \frac{\rho_g \left[|V_g| \alpha + |V_{\mathrm{l}}| (1-\alpha) \right] D_H}{\mu_g} , \tag{F-241}$$

$$h_{w\mathrm{l}\min} = h_r \cdot \frac{(T_{\min} - T_{\mathrm{sat}})}{(T_{\min} - T_{\mathrm{l}})} , \tag{F-242}$$

and

$$h_r = (\alpha_3 - \alpha) \cdot \sigma_r \cdot \varepsilon \cdot \frac{(T_{\min}^4 - T_{\mathrm{sat}}^4)}{(T_{\min} - T_{\mathrm{sat}})} , \tag{F-243}$$

where α_3= 0.9999.

The gas phasic HTC is evaluated from

$$h_{wg} = \max(h_{\mathrm{NC}}, h_{dr}) . \tag{F-244}$$

Then, Eq. (F-234) can be used to solve for $h_{w\mathrm{l}}$ as follows:

$$h_{w\mathrm{l}} = \frac{q_{\mathrm{trans}} - h_{wg}(T_w - T_g)}{(T_w - T_{\mathrm{l}})} . \tag{F-245}$$

The critical heat flux, q_{CHF}, is calculated in subroutine CHF1 using the Biasi correlation (Section F.2.1.8.); q_{min} is the heat flux at the minimum stable film-boiling temperature. This temperature is calculated in subroutine TMSFB and is discussed in Section F.2.1.9. The Bromley HTC for film boiling, h_{fBB}, is calculated in subroutine HLFILM and discussed in Section F.2.1.4. The radiation from the wall to the liquid is included by the coefficient h_r. Equations (F-238) and (F-239) are discussed in Section F.2.1.2.

F.2.1.3.2. Input Quantities to the Model. The liquid and vapor properties are evaluated at the liquid and vapor temperatures. The velocities in the two-phase Reynolds number are the absolute values of the liquid and vapor axial velocities (see Section F.2.1.1.1.). The emissivity, ε, in the radiation HTC is assumed to be 1.0. The characteristic length is the hydraulic diameter of the flow passage.

F.2.1.3.3. Constants. The simple form of the weighting factor, ξ, defined in Eq. (F-235), was found to fit the experimental data best if an exponent of 2 was used. The constants in the correlations used in the transition-boiling regime are those given in the references cited. The dimensions used for the variables yield HTCs in units of $W \cdot m^{-2} \cdot K^{-1}$ and heat fluxes in units of $W \cdot m^{-2}$.

F.2.1.3.4. Model as Coded. Most of the calculations are carried out in subroutine HTCOR. Subroutines CHEN, CHF, CHF1, HLFILM, HVFILM, and TMSFB are called as needed to evaluate the nucleate-boiling HTC, critical heat flux (CHF), the CHF temperature T_{CHF}, the film-boiling liquid HTC, the film-boiling vapor HTC, and the minimum stable film-boiling temperature, T_{min}, respectively. A number of tests are made in subroutine HTCOR to determine if the transition-boiling regime exists. Transition boiling is assumed to exist if $T_{CHF} < T_w < T_{min}$. (See Section F.2.1.3. concerning transition boiling and Section F.2.1.9. concerning T_{min}.)

The critical heat flux, q_{CHF}, and the heat flux at T_{min}, q_{min}, are evaluated and Eq. (F-233) is used to calculate the transition-boiling heat flux, q_{trans}. If $\alpha > 0.98$, q_{trans} is reevaluated as

$$q'_{trans} = q_{trans}\frac{(\alpha_3 - \alpha)}{(\alpha_3 - \alpha_c)} + h_{gsav}(T_w - T_g)\frac{(\alpha - \alpha_c)}{(\alpha_3 - \alpha_c)}\ , \qquad \text{(F-246)}$$

where $\alpha_c = 0.98$ and $\alpha_3 = 0.9999$. This interpolation ensures a smooth transition to convective heat transfer to a vapor at high void fractions.

F.2.1.3.5. Weighting, Limits, and Averaging. In Eq. (F-233), a weighting factor is used to estimate the fraction of the wall area that is wet. In Eq. (F-246), interpolation is used to ensure a smooth transition to the single-phase vapor HTC at high void fractions. No rate limits are used. Limits are imposed on mass flow in the Biasi correlation for CHF and are discussed in Section F.2.1.8.

F.2.1.3.6. Assessment of the Correlation. The major assumption made in implementing the equations for the heat flux in the transition-boiling regime is that this

regime can be modeled as a combination of steady-state nucleate boiling and film boiling. As its name implies, transition boiling is a combination of unstable film boiling and unstable nucleate boiling alternately existing at any given location on a heating surface. The variation in heat-transfer rate with temperature is primarily a result of a change in the fraction of time each boiling regime exists at a given location.

The transition-boiling section of the boiling curve is bounded by the CHF and the minimum film-boiling heat flux. The CHF has been studied extensively and can be predicted by a number of correlations. The minimum heat flux has been studied less; it is known to be affected by flow, pressure, surface properties, fluid properties, and heated-surface parameters.

Data on transition boiling are relatively scarce and have a common shortcoming in that they cover only narrow ranges of conditions. The data are not considered accurate enough or plentiful enough to serve as the basis for deriving a correlation. Also, much of the data include apparent transition-boiling effects, as discussed in Section F.2., and make the amount of usable data even more limited. Some parametric trends have been deduced, however. In general, an increase in mass flux increases the transition-boiling heat flux and shifts the wall superheat at the minimum heat flux to higher temperatures. Increasing subcooling has a similar effect but the effect of quality is less obvious. Disagreement exists about whether the vapor film, which is in violent motion, will be maintained at wall superheats less than ΔT_{min} or if liquid will contact the wall.

Despite scarcity of data and disagreements on the appropriate physical model, correlations have been proposed that are of three types: those that contain boiling and convective components, those based on a physical model of heat transfer (phenomenological), and empirical correlations.

Transition boiling is inherently an unstable process and is difficult to incorporate into a code such as TRAC. In light of this fact, the choice of the simple forms of Eqs. (F-233) and (F-246) to calculate the transition heat flux was motivated by their simplicity.

F.2.1.3.7. Scaling Considerations. Application of this transition-boiling formulation to quenching problems, such as those normally encountered in a reflooding core, is not recommended. (See discussion in Section F.2. of spatial-averager problems, that is, problems where the influence of quench front progression become important.)

F.2.1.3.8. Summary and Conclusions. The major assumption of the transition-boiling model is that it can be considered a combination of steady-state nucleate boiling and film boiling. Because the data are not considered accurate or plentiful enough to provide a basis for deriving a correlation, this simple and physically based model is justified for those situations where spontaneous, convection-controlled quenches occur.

F.2.1.4. Film Boiling (Heat-Transfer Regime 4). To fully describe film boiling, the film-boiling heat-transfer regime incorporates several different correlations.

F.2.1.4.1. Basis for the Model. The film-boiling regime in subroutine HTCOR is assumed to occur when the wall temperature exceeds the minimum stable film-boiling temperature ($T_w > T_{\min}$). The wall-to-vapor and wall-to-liquid heat transfer are treated separately. The wall-to-liquid HTC is assumed to be the sum of two components: radiation and near-wall liquid effects. The liquid HTC is given by

$$h_{w\ell} = (h_\Gamma + h_{fBB}) \cdot \left[\frac{(T_w - T_{\text{sat}})}{(T_w - T_\ell)}\right], \tag{F-247}$$

where the radiative component is

$$h_r = \alpha_1 \cdot \sigma_r \cdot \varepsilon \cdot \frac{(T_w^4 - T_{\text{sat}}^4)}{(T_w - T_{\text{sat}})} . \tag{F-248}$$

The film-boiling component is given by the modified Bromley correlation (Ref. F-51., p. 273, and Ref. F-63.) as

$$h_{fBB} = 0.62 \cdot \left(\frac{\rho_g k_g^3 (\rho_\ell - \rho_g) g h'_{\ell g}}{\mu_g (T_w - T_{\text{sat}}) \lambda}\right)^{0.25} . \tag{F-249}$$

In these correlations $\alpha_1 = (\alpha_3 - \alpha) = 0.9999 - \alpha$, σ_r is the Stefan-Boltzmann constant, ε is the wall emissivity (assumed to be 1.0), and λ is the characteristic length (Taylor wavelength) given by

$$\lambda = 2\pi \left(\frac{\sigma}{g(\rho_\ell - \rho_g)}\right)^{1/2} , \tag{F-250}$$

where $h'_{\ell g}$ is a modified latent heat to account for the superheated vapor such that

$$h'_{\ell g} = h_{\ell g} + 0.5 \cdot c_{pg} \cdot (T_g - T_{\text{sat}}) . \tag{F-251}$$

The temperature ratio in Eq. (F-247) changes the sink temperature of the HTC using T_{sat} to T_ℓ as used by the code.

The wall-to-vapor HTC used in this heat-transfer regime is the greater of the Dougall-Rohsenow (h_{dr}) or the turbulent, natural-convection (h_{NC}) correlations. That is,

$$h_{wg} = \max(h_{dr}, h_{\text{NC}}) , \tag{F-252}$$

where h_{dr} and h_{NC} are defined by Eqs. (F-238) through (F-241).

F.2.1.4.2. Input Quantities to the Model. The liquid and vapor properties are evaluated at the liquid and vapor temperatures. The velocities are the liquid and vapor axial velocities (see Section F.2.1.1.1.); the wall emissivity is assumed to be 1.0.

F.2.1.4.3. Constants. All other constants used in the correlations for the film-boiling regime are those given in the references cited. The dimensions used for the variables yield HTCs in units of $W \cdot m^{-2} K^{-1}$.

F.2.1.4.4. Model as Coded. The film-boiling regime, $\partial q / \partial (T_{sat}) > 0$, is assumed to occur when the wall temperature exceeds the minimum stable film-boiling temperature, that is, $T_w > T_{min}$. The wall-to-vapor HTC, evaluated in subroutine HVFILM, is the greater of the Dougall-Rohsenow or natural-convection correlations [Eqs. (F-238) and (F-239)]. The radiation HTC is evaluated in subroutine HTCOR. The Bromley correlation is evaluated in subroutine HLFILM.

If $\alpha > \alpha_c = 0.98$, the wall-to-vapor HTC is modified as follows:

$$h_{wg} = h_{wg} + (h_{gsav} - h_{wg}) \frac{\alpha - \alpha_c}{1 - \alpha_c} \ . \qquad \text{(F-253)}$$

This ensures that the vapor HTC approaches that for convective heat transfer to a single-phase vapor, h_{gsav}, at high void fractions.

F.2.1.4.5. Weighting, Limits, and Averaging. To ensure a smooth transition to convection to a single-phase vapor, h_{gsav}, at high void fractions, an interpolation is also used for the vapor HTC when $\alpha > 0.999$ in HTCOR. There are no rate limits used in the film-boiling heat-transfer regime.

F.2.1.4.6. Assessment of the Correlation. It was assumed that the wall heat transfer can be adequately described by the two components of radiation and pool boiling. Using a pool-boiling type of correlation, such as Bromley, to describe inverted annular-flow film boiling implicitly ignores the effect of mass flow rate on the magnitude of the HTC.

In film boiling, the liquid can be thought of as being in one of three forms. At high void fractions, the liquid is in the form of a dispersed spray of drops in a vapor and is referred to as the liquid-deficient region. At low void fractions, there is a continuous liquid core surrounded by a vapor annulus in which there may be entrained droplets; this regime is referred to as inverted annular flow (IAF). In the transition between these two regimes, the liquid is in the form of slugs and drops. It is assumed that the wall-to-liquid heat-transfer model can account for the effect of these different flow regimes by weighting factors. The Bromley correlation dominates at low void fractions.

The Bromley correlation is one of the most widely used for inverted annular-flow film boiling and was developed from data for boiling in a horizontal tube. The database for this correlation covered the following ranges:

Pressure	0.1 to 0.7 MPa
Heat Flux	30.0 to 130.0 kW · m^{-2}
Wall Superheat	278.0 to 778.0 K
Subcooling	< 77.9 K
Velocity	< 0.3 m · s^{-1}
Void	< 0.4

Recent film-boiling experiments indicate that several additional interacting factors influence heat-transfer rates during film boiling. The main ones are liquid subcooling, liquid velocity, vapor superheat, turbulence in the liquid, and instability of the vapor/liquid interface. The most important effects seem to be liquid subcooling and increased flow rate, both of which increase the heat-transfer rate. Neither of these effects is accounted for in the Bromley correlation. Figures F-39. to F-41. show some comparisons of the Bromley correlation with recent data (Ref. F-64.): in these figures T_c is the liquid subcooling and T_w is the wall superheat.

The Dougall-Rohsenow correlation was discussed in Section F.2.1.2.

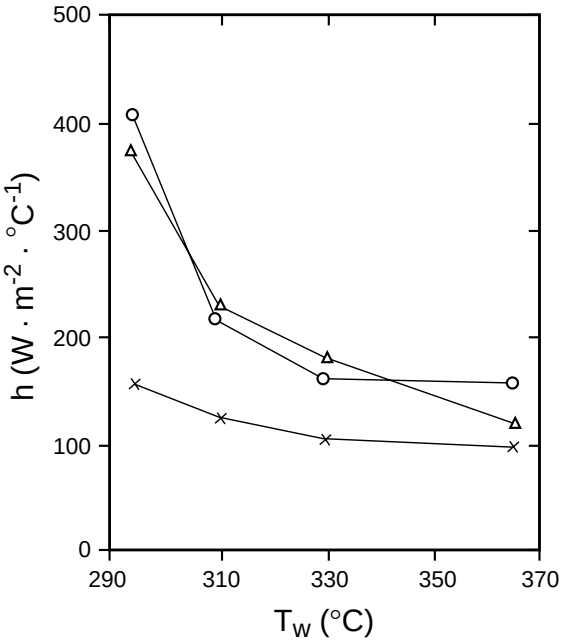

Fig. F-39. Effect of initial wall temperature. G=200 kg / m^2-s, T_c = 60°C.
Q, Experimental; Δ (Ref. F-64.); ×, Bromley-type equation.

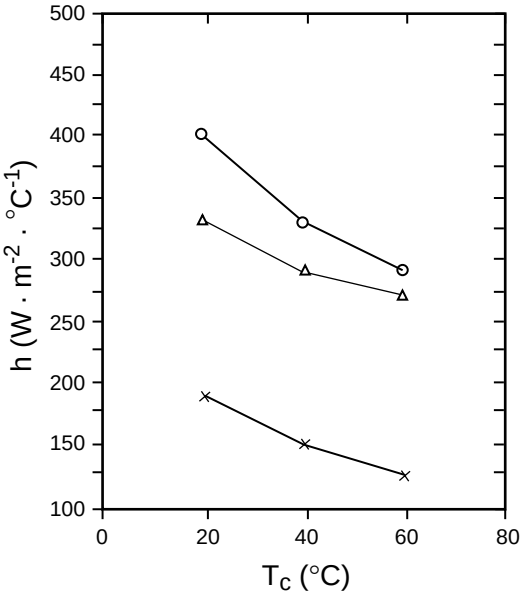

Fig. F-40. Effect of coolant inlet subcooling on the heat-transfer coefficient.
G = 200 kg / m^2-s, T_w = 550°C.
Q, Experimental; Δ (Ref. F-64.); ×, Bromley-type equation.

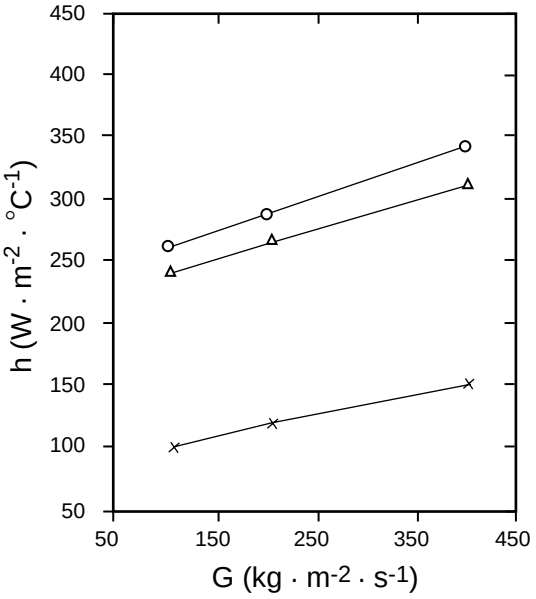

Fig. F-41. Effect of coolant inlet subcooling on the HTC. T_w = 550°C, T_c = 60°C.
Q, experimental; Δ (Ref. F-64.); ×, Bromley-type equation.

A study was carried out with the TRAC-PF1/MOD1 code to calculate dispersed-flow heat transfer using different heat-transfer correlations, and the results were compared with experimental data from the heat-transfer test facility at Karlstein, FRG (Ref. F-65.). None of the film-boiling HTCs could be used with sufficient confidence over the entire post-CHF portion of the blowdown phase of a LOCA. Analysis of experimental and calculated results showed that in the post-CHF portion of the transient experiments, two significantly different HTCs could be calculated from the same thermal-hydraulic parameters. This effect of flow regime on the wall-to-liquid heat transfer cannot be reproduced by the HTCs that were developed and assessed using the data from steady-state conditions. The film-boiling model in TRAC attempts to account for the flow-regime effect by weighting the various HTCs by factors that are a function of void fraction except the Bromley correlation.

F.2.1.4.7. Scaling Considerations. Most of the experimental data on post-CHF heat transfer was obtained for tube geometry, and the validity of scaling to rod-bundle geometry has not been verified. The Bromley correlation, a pool-boiling correlation, was developed from data for a horizontal, heated cylinder. Applying it to vertical geometry in two-phase-flow film boiling is questionable.

F.2.1.4.8. Summary and Conclusions. A substantial amount of data for film-boiling heat transfer, obtained for simple geometries, is available and has been used to develop and evaluate film-boiling HTCs. Results of an evaluation of different heat-transfer correlations (Ref. F-65.) have shown that none of the correlations predicted HTCs of sufficient accuracy in the entire post-CHF region. This further emphasizes the discussion earlier in Section F.2. about how the closure relationships for Eqs. (F-185) through (F-186) should be determined.

The film-boiling model in TRAC is based upon correlations that were developed principally from post-CHF heat-transfer data for tube geometry and assuming thermodynamic equilibrium; the validity of scaling to rod-bundle geometry or thermodynamic nonequilibrium has not been verified. Significant discrepancies still exist among different correlations and between correlations and experimental data. Future code development work should examine new experimental data and correlations for possible improvements in the film-boiling model.

The discussions contained in Section F.2. concerning the minimum film-boiling temperature and Sections F.2.1.3. and F.2.1.9. should be reviewed in connection with this section.

F.2.1.5. Single-Phase Vapor (Heat-Transfer Regime 6). The case of convective heat transfer to a single-phase vapor is described by heat-transfer regime 6.

F.2.1.5.1. Basis for the Model. In this heat-transfer regime, when $T_f = 0.5\,(T_w + T_g) \geq T_{sv}$, the vapor HTC is the larger of either the turbulent natural-convection HTC, $h_{g\mathrm{NC}}$, or the forced-convection HTC, $h_{g\mathrm{turb}}$, obtained from the empirical correlation of Sieder and Tate (Ref. F-66., Eq. 8.59). These HTCs are expressed as

$$h_{g\mathrm{NC}} = 0.13(k_g/D_H)Gr_g^{0.333}Pr_g^{0.333} \ , \tag{F-254}$$

and

$$h_{g\mathrm{turb}} = 0.023(k_g/D_H)Re_g^{0.8}Pr_g^{0.333}(\mu_g/\mu_w)^{0.14} \ . \tag{F-255}$$

The viscosity ratio in Eq. (F-255) accounts for the effect of the radial viscosity gradient on the axial velocity distribution. The Sieder-Tate correlation is recommended for the following conditions:

$$\begin{array}{rlll} & \text{Reynolds number} & > & 1.0\times10^4 \\ 0.7 < & \text{Prandtl number} & < & 16\ 700 \\ & \text{L / D} & > & 60 \end{array} \ .$$

When $T_f < T_{sv}$ the Dittus-Boelter correlation

$$h_{g\mathrm{turb}} = 0.023\ (k_g\ /\ D_H)\ Re_g^{0.8}\ Pr_g^{0.4} \tag{F-256}$$

replaces the Sieder-Tate correlation. T_{sv} is the saturation temperature of steam at its partial pressure.

F.2.1.5.2. Input Quantities to the Model. All properties are evaluated at temperature T_g in Eqs. (F-254) and (F-256) and at the film temperature, $T_f = 0.5\,(T_w + T_g)$, in Eq. (F-255), except μ_w, which is evaluated at the wall temperature, T_w. The velocity in the Reynolds number is the absolute value of the axial vapor velocity (see Section F.2.1.1.1.). The hydraulic diameter of the flow passage is used as the characteristic length. Viscosity, thermal conductivity, and specific heat are obtained from the functions VISCV, TMCV, and CPVV1. In order to avoid extra calls to the thermodynamics properties subroutine, THERMO, densities evaluated at either the film or wall temperatures are approximated by the first-order Taylor series terms as follows:

$$\rho_f = \rho_g + \frac{\partial \rho_g}{\partial T}(T_f - T_g) \tag{F-257}$$

and

$$\rho_w = \rho_g + \frac{\partial \rho_g}{\partial T}(T_w - T_g) \ . \tag{F-258}$$

In the correlation for the turbulent natural-convection HTC, Eq. (F-254), the coefficient of volumetric expansion, β, is approximated by $1/T_g$.

F.2.1.5.3. Constants. The correlations used in heat-transfer regime 6 are the same as in the cited references; no changes were made to any of the constants.

F.2.1.5.4. Model as Coded. The HTCs for heat-transfer regime 6 are evaluated in subroutine HTCOR. Equation (F-254) is used to calculate the turbulent, natural-convection HTC. For the turbulent, forced-convection HTC, Eq. (F-255) is evaluated if $T_f \geq T_{sv}$ and Eq. (F-256) is evaluated if $T_f < T_{sv}$. The Reynolds number is limited to minimum value of 1.0×10^{-20}.

The vapor HTC is found as follows:

$$h_{wg} = \max(h_{g\mathrm{NC}}, h_{g\mathrm{turb}}) \ . \tag{F-259}$$

A test is made on the void fraction. If $\alpha < 1$, two-phase liquid and vapor HTCs are calculated. For void fractions between $\alpha_c = 0.98$ and 1.0, the vapor HTC is found by interpolating between the single-phase and two-phase results and the liquid HTC is found by interpolating between a value of zero and the two-phase results. The resulting coefficients are therefore

$$\bar{h}_{w\mathrm{l}} = h_{w\mathrm{l}} + (0.0 - h_{w\mathrm{l}}) \frac{\alpha - \alpha_c}{\alpha_3 + -\alpha_c} \tag{F-260}$$

and

$$\bar{h}_{wg} = h_{wg} + (h_{g\mathrm{sav}} - h_{wg}) \frac{\alpha - \alpha_c}{\alpha_2 - \alpha_c} \ , \tag{F-261}$$

where $h_{w\mathrm{l}}$ and h_{wg} are the liquid and vapor two-phase HTCs and $h_{g\mathrm{sav}}$ is the HTC for single-phase vapor. If $0.97 < \alpha < 0.98$ (and $T_w \geq T_{sv}$ and $T_w \geq T_{\mathrm{l}}$), two passes are made, first with $\alpha = 0.97$, and then with $\alpha = 0.98$. Finally, linear interpolation is done for both $h_{w\mathrm{l}}$ and h_{wg} using their values computed at $\alpha = 0.97$ and $\alpha = 0.98$. The values of α_c, α_2, and α_3 are 0.98, 1.0, and 0.9999, respectively.

F.2.1.5.5. Assessment of the Correlation. When forced or natural convection to a two-phase mixture is not present and if the void fraction is $\geq \alpha_{\mathrm{CHF}} = 0.97$, heat transfer to a single-phase fluid exists and Eqs. (F-254) to (F-256) are used together with the interpolation logic described in Section F.2.1.5.4. Equation (F-254) for the natural-convection HTC was discussed in Section F.2.1.2. Equation (F-256), the Dittus-Boelter correlation, was discussed in Section F.2.1.1. These correlations are well known and have been applied to a wide variety of fluids and geometries. If used within the recommended range of their parameters, the predicted HTCs are in good agreement with the data.

The Sieder-Tate correlation, Eq. (F-255), was developed to account for the effect of radial temperature gradients on the axial velocity distribution. For fluids with a large

temperature-dependent coefficient of viscosity or where there is a large temperature difference between the wall and the bulk fluid, a large radial gradient in the viscosity can result, which produces a velocity distribution that is considerably different from that occurring in isothermal flow. The viscosity gradient has opposite signs for heating and cooling. In channels having an axial power distribution, it is possible to have regions of $T_f \geq T_{sv}$ at the midplane yet $T_f \leq T_{sv}$ at the exit. This causes numerical problems in Eq. (F-257) in addition to the fact that high radial temperature differences have decreased so that the Dittus-Boelter equation is used for this situation.

F.2.1.5.6. Scaling Considerations. The Sieder-Tate correlation is a straightforward modification of the Dittus-Boelter equation. The Dittus-Boelter equation has been applied to a wide variety of fluids and geometries and is in good agreement with experimental data. The Sieder-Tate correlation should, therefore, also be applicable to the same fluids and geometries. Equation (F-256) for natural convection may be applied to flow past vertical cylinders if the criterion of Eq. (F-207) is met. In the turbulent regime, this implies $0.02 < D/L < 0.20$.

F.2.1.5.7. Summary and Conclusions. All of the correlations used in heat-transfer regime 6 are well known and have been applied to a wide variety of fluids and geometries. If used within the specified range of parameters, they predict HTCs that are in good agreement with experimental data.

F.2.1.6. Condensation (Heat-Transfer Regime 11). Heat-transfer regime 11 describes condensation of vapor on a cold wall.

F.2.1.6.1. Basis for the Model. The vapor HTC is determined from the following correlations:

$$h_{g\text{cond}} = 0.9428 \left[\frac{\rho_l^2 g k_l^3 h_{fg}}{\mu_l L (T_{sv} - T_w)} \right]^{0.25} \tag{F-262}$$

is the result of a theoretical analysis by Nusselt for the average HTC for a vapor condensing on a liquid film in laminar flow on a vertical wall (Ref. F-67., Eq. 13.6-5);

$$h_2 = 0.003 \left[\frac{\rho_l^2 g k_l^3 L (T_{sv} - T_w)}{h_{fg} \mu_l^3} \right]^{0.5} \tag{F-263}$$

is an empirical correlation used when the film Reynolds number is greater than 350 (Ref. F-67., Eq. 13.6-6);

$$h_{g\text{NC}} = 0.13 \frac{k_g}{D_H} Gr_g^{0.333} Pr_g^{0.333} \tag{F-264}$$

evaluates the turbulent, natural-convection vapor HTC on a vertical plate for $1.0\times10^{9} < \mathrm{Gr}\cdot\mathrm{Pr} < 1.0\times10^{13}$; and

$$h_{g\mathrm{turb}} = 0.023\frac{k_g}{D_h} Re_g^{0.8}\, Pr_g^{0.3} \ . \tag{F-265}$$

The liquid HTC is evaluated from

$$h_{\mathrm{forc}} = 0.023\frac{k_l}{D_H}\left[\frac{\rho_l V(1.0-\alpha)D_H}{\mu_l}\right]^{0.8} (Pr_l)^{0.4} F \ , \tag{F-266}$$

where F is the Chen F factor defined by Eqs. (F-211) to (F-213). Equation (F-266) is the macroterm of the Chen correlation. In addition,

$$h_{wl} = \max(h_{\mathrm{NC1}}, h_{\mathrm{NC2}}, h_{g\mathrm{forc}}) \ , \tag{F-267}$$

where

$$h_{\mathrm{NC1}} = 0.59\frac{k_l}{D_H} Gr_l^{0.25} Pr_l^{0.25} \tag{F-268}$$

is recommended for vertical plates and cylinders when $1.0\times10^{4} < \mathrm{Gr}\cdot\mathrm{Pr} < 1.0\times10^{9}$ (Ref. F-10., Eq. 7-4b), and

$$h_{\mathrm{NC2}} = 0.10\frac{k_l}{D_H} Gr_l^{0.3333} Pr_l^{0.3333} \tag{F-269}$$

is recommended for vertical plates and cylinders when $1.0\times10^{9} < \mathrm{Gr}\cdot\mathrm{Pr} < 1.0\times10^{13}$ (Ref. F-54., Table 7-1).

F.2.1.6.2. Input Quantities to the Model. In Eqs. (F-262) and (F-263), fluid properties are evaluated at the liquid temperature (T_l), L is the cell length, and h_{fg} is the latent heat. In Eq. (F-264), vapor properties are evaluated at the vapor temperature T_g. In Eq. (F-265), if the film temperature $T_f = 0.5(T_w + T_g)$ is less than T_{sv}, the vapor properties are evaluated at temperature T_g. If $T_f \geq T_{sv}$ the fluid properties are evaluated at temperature T_f. The characteristic length is the hydraulic diameter of the flow channel and the velocity is the absolute value of the axial vapor velocity (see Section F.2.1.1.1.).

In Eq. (F-266), the fluid properties are evaluated at the liquid temperature T_l, the characteristic length is the hydraulic diameter of the flow channel, and the velocity is the absolute value of the axial liquid velocity defined previously.

In Eqs. (F-268) and (F-269), all fluid properties except density are evaluated at the liquid temperature T_l. The density is evaluated at a temperature $T_f = 0.5(T_w + T_l)$ by a first-order Taylor-series approximation as

$$\rho_f = \rho_l + \frac{\partial \rho_l}{\partial T}(T_f - T_l) \ . \tag{F-270}$$

The coefficient of volumetric expansion is given by

$$\beta = -\frac{\partial \rho_l}{\partial T} / \rho_f \ . \tag{F-271}$$

F.2.1.6.3. Constants. The correlations used in heat-transfer regime 11 are the same as given in the references cited; no changes were made to the constants.

F.2.1.6.4. Model as Coded. This heat-transfer regime is assumed to exist when the following conditions are met:

a. $T_w < T_{sv}$ and $\alpha > 0.05$,

b. $T_w < T_g$ (or $T_w < T_l$ and IQUENCH not zero), and

c. $x \geq XCHEN = 0.71$,

where x is quality and IQUENCH is a flag indicating whether an interface exists (0 indicates no interface and 1 indicates an interface is present). When conditions *a*, *b*, and *c* are satisfied, Eqs. (F-262) to (F-265) are evaluated in subroutine HTCOR to calculate a value for the vapor HTC, $h_{g\text{cond}}$. For long tubes, Eq. (F-262) underestimates the HTC caused by ripples that develop on the liquid film. To account for this effect, a weighting factor WF ($0.0 \leq WF \leq 1.0$) based upon the length L is calculated. This factor is used to combine the laminar and turbulent HTCs $h_{g\text{cond}}$ and h_2 to determine a weighted average vapor HTC. For short lengths where $WF \rightarrow 0.0$, the laminar HTC, $h_{g\text{cond}}$, is used; for large values of L where $WF \rightarrow 1.0$, the larger of the turbulent and laminar HTCs is used. The sink temperature for $h_{g\text{cond}}$ is then converted from T_{sv} to T_g. These equations are as follows:

$$\bar{h}_{g\text{cond}} = h_{g\text{cond}}(1.0 - WF) + \max(h_{g\text{cond}}, h_2)WF \ , \tag{F-272}$$

$$WF = \min\left[1.0, \max\left(0.0, \frac{L - 0.2}{1.8}\right)\right] \ , \tag{F-273}$$

and

$$\bar{h}_{g\text{cond}} = h_{g\text{cond}} \frac{(T_{sv} - T_w)}{\max(|T_g - T_w|, 0.01)} \ . \tag{F-274}$$

The bar over $h_{g\text{cond}}$ on the left-hand side of the equation indicates that it has been modified (as in a Fortran statement). For simplicity, the bar notation is dropped in the subsequent discussion.

The vapor HTC for single-phase vapor (called h'_{wg} here to avoid confusion with the final result) and the HTC for a condensing vapor are then found as follows:

$$h'_{wg} = \max(h_{g\text{NC}}, h_{g\text{turb}}) \tag{F-275}$$

and

$$\bar{h}_{g\text{cond}} = \max(h'_{wg}, h_{g\text{cond}}) \ . \tag{F-276}$$

For the liquid HTC, Equation (F-266) is evaluated in subroutine CHEN and the macroterm of the Chen correlation, h_{forc}, is returned to subroutine HTCOR (see Section F.2.1.2.). The microterm of the Chen correlation, h_{nucb}, is not evaluated in subroutine CHEN because in heat-transfer regime 11, $T_w < T_{\text{sat}}$. An if-test in the subroutine will cause the calculation of h_{nucb} to be bypassed when $(T_w - T_{\text{sat}}) < 0.0$. The following equation, evaluated in subroutine CHEN, determines the macroterm, h_{forc}, which is returned to subroutine HTCOR:

$$\bar{h}_{\text{forc}} = \max\left(h_{\text{forc}}, \frac{4.0k_l}{D_H}\right) . \tag{F-277}$$

Equation (F-268) and (F-269) are evaluated in subroutine HTCOR and the liquid HTC is determined as follows:

$$h_{wl} = \max(h_{\text{NC1}}, h_{\text{NC2}}, h_{\text{forc}}) \ . \tag{F-278}$$

The final values for the liquid and vapor HTCs are then determined by the following method:

If $x > 1.0$,

$$h_{wl} = 0.0 \quad \text{and} \tag{F-279}$$

$$h_{wg} = h_{g\text{cond}} \ . \tag{F-280}$$

If $0.71 \le x \le 1.0$,

$$\bar{h}_{wl} = h_{wl} + (0.0 - h_{wl})\frac{x - XCHEN}{1.0 - XCHEN} \tag{F-281}$$

and

$$\bar{h}_{wg} = h_{g\text{cond}} \cdot \frac{x - XCHEN}{1.0 - XCHEN} \ . \qquad \text{(F-282)}$$

F.2.1.6.5. Weighting, Limits, and Averaging. The term $L(T_{sv} - T_w)$ in Eq. (F-262) is constrained to be ≥0.01. Equation (F-273) is used to weight the laminar and turbulent vapor HTCs calculated from Eqs. (F-262) and (F-263). The weighting function, *WF*, is limited to values between 0.0 and 1.0. The limits on the parameters in Eq. (F-266) are discussed in Section F.2.1.2. There are no rate limits.

F.2.1.6.6. Assessment of the Correlations. Equation (F-262) has been found to underestimate most experimental results for laminar film condensation by approximately 20%; a coefficient of 1.13 is recommended in place of 0.9428 (Ref. F-32., p. 488). Equation (F-263) is an empirical equation proposed for turbulent flow and fits the data for turbulent flow on vertical plates quite well (Ref. F-52., Fig. 13.6-2). Equations (F-264), (F-265), and (F-266) are discussed in Section F.2.1.2. and Eqs. (F-268) and (F-269) are discussed in Section F.2.1.1.

Equation (F-262) underestimates the HTC by about 20% in the laminar regime. If used at values of the Reynolds number >350, the error increases as the Reynolds number increases. Equation (F-263) will underestimate the HTC below a film Reynolds number of 350. The Dittus-Boelter correlation will underestimate the HTC below the recommended Reynolds number and L / D ratio. Equation (F-269) underestimates HTCs by approximately 10% for the range $1.0 \times 10^9 < Gr \cdot Pr < 1.0 \times 10^{13}$ as $Gr \cdot Pr$ decreases below 1.0×10^9, the correlation underestimates the HTC by an increasingly larger percentage.

F.2.1.6.7. Scaling Considerations. Although the Nusselt analysis for film-condensation heat transfer was developed for vertical flat plates, it may be applied to the internal or external surfaces of vertical tubes if the tube diameter is large compared to the film thickness (Ref. F-67., p. 527). The other correlations used in heat-transfer regime 11 are discussed in Sections F.2.1.1. and F.2.1.2.

F.2.1.6.8. Summary and Conclusions. The correlations used in heat-transfer regime 11 are all well known and, if used within the specified ranges of their parameters, predict HTCs that agree within 20% of the experimental data. Some minor adjustments of the constants [e.g., Eq. (F-262)] may improve the agreement.

The Chen correlation is based upon data for qualities, *x*, up to 0.71, and wall-to-fluid heat transfer. This quality limit is extrapolated in an ad hoc manner to apply to mixture-to-wall heat transfer. There is no basis for this extrapolation, however, it is assumed that when $x > 0.71$, the wall heat-transfer mechanism is convection to vapor or condensation. When $x \leq 0.71$, the wall heat-transfer mechanism is convection from a two-phase mixture.

The presence of small amounts of noncondensable gases will degrade the condensation heat transfer. This effect is not considered in the model. Future code development efforts should consider improving the wall condensation model.

F.2.1.7. Two-Phase Forced Convection (Heat-Transfer Regime 7). This heat-transfer regime is unique in that it is not part of the boiling curve discussed previously. The regime is used only when the input flag ICHF = 0. The liquid and vapor HTCs, h_{wl} and h_{wg}, are calculated from regime 7 only.

F.2.1.7.1. Basis for the Model. The liquid HTC uses the Rohsenow-Choi equation (Ref. F-68.) for laminar forced convection, h_{wllam}, and the Dittus-Boelter correlation for turbulent forced convection, h_{wlturb}, as follows:

$$h_{wllam} = \frac{4.0 k_l}{D_H} \tag{F-283}$$

and

$$h_{wlturb} = \frac{0.023 k_l (Re)^{0.8} (Pr)^{0.4}}{D_H} \ , \tag{F-284}$$

where

$$Pr = \frac{c_{pl} \mu_l}{k_l} \ , \tag{F-285}$$

$$Re = \frac{G_m D_H}{\mu_m} , \tag{F-286}$$

and

$$\mu_m = \frac{1}{\frac{X_f}{\mu_g} + \frac{1 - X_f}{\mu_l}} \ . \tag{F-287}$$

The term μ_m is the two-phase viscosity proposed by McAdams (Ref. F-69.), x_f is the flow quality, and G_m is the product of mixture velocity, V_m, and mixture density, ρ_m. Equation (F-283) is not recommended for Reynolds numbers greater than 2000. Equation (F-284) is recommended for the following conditions:

		Reynolds number	>	1.0×10^4
0.7	<	Prandtl number	<	160
		L / D	>	60

The vapor HTC is either the turbulent natural-convection HTC, $h_{g\mathrm{NC}}$, or the Dittus-Boelter correlation for turbulent forced convection, $h_{g\mathrm{turb}}$. These HTCs are given as

$$h_{g\mathrm{NC}} = 0.13 k_g \left(\frac{\rho_g^2 g |T_w - T_g|}{\mu_g^2 T_g} \right)^{0.3333} \cdot (Pr)^{0.4} \tag{F-288}$$

and

$$h_{g\mathrm{turb}} = 0.023 k_g (Re)^{0.8} (Pr)^{0.4} \; / \; D_H \; , \tag{F-289}$$

where

$$Re = \frac{\rho_g V_g D_H}{\mu_g} \tag{F-290}$$

and

$$Pr = \frac{c_{pg} \mu_g}{k_g} \; . \tag{F-291}$$

Equation (F-288) is recommended when the product of the Grashof and Prandtl numbers is in the range 1.0×10^9 to 1.0×10^{12}. Equation (F-289) is recommended for the same conditions as Eq. (F-284).

F.2.1.7.2. Input Quantities to the Model. In Eqs. (F-283) and (F-284), the liquid properties are evaluated at the liquid temperature T_l. In Eq. (F-288), the vapor properties are evaluated at temperature T_g, the bulk temperature of the vapor. If the film temperature, $T_f = 0.5 (T_w + T_g)$, is greater than T_{sv}, the saturation temperature of steam at its partial pressure, the vapor properties in Eq. (F-289) are evaluated at the film temperature. If $T_f < T_{sv}$, the vapor properties in Eq. (F-289) are evaluated at the bulk temperature, T_g. The velocity in the Reynolds number in Eq. (F-290) is the axial vapor velocity (see Section F.2.1.1.1.). The hydraulic diameter of the flow channel is used as the characteristic length in Eqs. (F-286) and (F-290). Viscosity, thermal conductivity, and specific heat are obtained from the functions VISCV, THCV, and CPVV1. In order to avoid extra calls to the thermodynamic properties subroutine, THERMO, the density is approximated by a first-order Taylor-series expansion as follows:

$$\rho_f = \rho_g + \frac{\partial \rho_g}{\partial T} (T_f - T_g) \; . \tag{F-292}$$

In the correlation for turbulent natural convection, Eq. (F-288), the coefficient of volumetric expansion β has been approximated by $1/T_g$.

F.2.1.7.3. Constants. The correlations used in heat-transfer regime 7, Eqs. (F-283), (F-284), (F-288), and (F-289), are the same as in the references cited. No changes were made to any of the numerical constants.

F.2.1.7.4. Model as Coded. The HTCs for heat-transfer regime 7 are evaluated in subroutine HTCOR. If tests determine that heat-transfer regimes 1, 12, 11, and 6 (forced convection or natural convection to single-phase liquid, and condensation or forced convection to single-phase vapor) are not present and if $\alpha < \alpha_{CHF} = 0.97$ and ICHF = 0, it is assumed that heat-transfer regime 7 exists. The liquid HTC, h_{wl}, is evaluated from Eqs. (F-283) through (F-287). The liquid HTC is then determined as follows:

$$h_{wl} = \max(h_{wllam}, h_{wlturb}) \ . \tag{F-293}$$

If $\alpha < \alpha_c = 0.98$, $h_{wg} = 0.0$; otherwise Eqs. (F-288) through (F-291) are used to evaluate h_{gNC} and h_{gturb}. The value of h_{wg} is determined from the equation

$$h_{wg} = \max(h_{gNC}, h_{gturb}) \ . \tag{F-294}$$

When the void fraction is greater than 0.98, the liquid and vapor HTCs are found by interpolating between the present values and the values for single-phase vapor ($h_{wl} = 0.0$ and $h_{wg} = h_{gsav}$). That is,

$$\bar{h}_{wl} = h_{wl} + (0.0 - h_{wl})\left(\frac{\alpha - \alpha_c}{\alpha_3 - \alpha_c}\right) \tag{F-295}$$

and

$$\bar{h}_{wg} = h_{wg} + (h_{gsav} - h_{wg})\left(\frac{\alpha - \alpha_c}{\alpha_2 - \alpha_c}\right) , \tag{F-296}$$

where

$\alpha_2 = 1.0$, $\alpha_3 = 0.9999$, and $\alpha_c = 0.98$.

F.2.1.7.5. Weighting, Limits, and Averaging. For void fractions between 0.98 and 1.0, Eqs. (F-295) and (F-296) are used to weight the current two-phase HTCs, h_{wl} and h_{wg}, with the single-phase vapor HTCs, h_{gsav} and $h_{wl} = 0$. The Reynolds number and temperature difference $|T_w - T_g|$ are limited to minimum values of 1.0×10^{-20}. There are no rate limits.

F.2.1.7.6. Assessment of the Correlations. The correlations for heat-transfer regime 7 are discussed in Sections F.2.1.1. and F.2.1.2.

F.2.1.7.7. Scaling Considerations. Refer to Sections F.2.1.1. and F.2.1.2.

F.2.1.7.8. Summary and Conclusions. Refer to Sections F.2.1.1. and F.2.1.2. This regime was placed in the code in its early days to minimize the execution time associated with wall heat transfer. It is recommended that the user not use the model, i.e., set ICHF = 0.

F.2.1.8. Critical Heat Flux. The code requires the CHF correlation to provide a boundary between nucleate boiling and transition boiling.

F.2.1.8.1. Basis for the Model. The CHF prediction package in TRAC consists of the Biasi correlation (Ref. F-70.) with modifications at low mass velocities and high void fractions. The Biasi correlation is chosen because it is (*i*) an empirical correlation with a wide database, (*ii*) based upon the local-condition approach, and (*iii*) valid for the high-void-fraction, dryout type of CHF. The alternatives to empirical correlations are theoretical correlations and CHF tables. Theoretical correlations have a limited applicability because of their various simplifying assumptions. Their use is difficult because, in general, they do not yield a closed-form correlation. Similarly, CHF tables are expensive to use in large, multipurpose codes such as TRAC because they require multiple interpolations or extrapolations during each iteration.

The more successful CHF correlations developed in recent years are based upon the boiling-length concept, in which the inlet quality or enthalpy explicitly appears in the correlation. During transient analysis, however, the use of boiling-length correlations is often not appropriate. (See the discussion in Section F.2.) For example, during certain reactor accidents, such as cold-leg-break LOCAs, the core experiences a flow reversal, in which case the inlet becomes ambiguous.

Consequently, the CHF-prediction package of TRAC is restricted to correlations based upon the local-condition approach. A complete CHF package should include a number of these correlations to cover the entire spectrum of thermal-hydraulic conditions. As mentioned earlier, the Biasi correlation (Ref. F-70.) is only valid for the low- and high-quality, dryout type of CHF. A very low-quality, departure-from-nucleate-boiling type of CHF correlation is not included in the TRAC package because most transients (such as LOCA) yield a high void fraction in the core before reaching the CHF.

The Biasi correlation (Ref. F-70., p. 531. Eq. 2) consists of the following two equations from which the maximum CHF value calculated by these equation is assigned:

$$q_{\mathrm{CHF}} = \frac{1.883 \times 10^3}{D^n G^{1/6}} \left[\frac{f_p}{G^{1/6}} - x_e \right] \tag{F-297}$$

and

$$q_{\mathrm{CHF}} = \frac{3.78 \times 10^3}{D^n G^{0.6}} h_p (1 - x_e) \ , \tag{F-298}$$

where

$n = 0.4$ for $D \geq 1$ cm,

$n = 0.6$ for $D < 1$ cm,

$f_p = 0.7246 + 0.099P \exp(-0.032P)$,

$h_p = -1.159 + \frac{8.99P}{10+P^2} + 0.149P \exp(-0.019P)$,

D = diameter (cm),

G = mass flux ($g \cdot cm^{-2} \cdot s^{-1}$),

P = pressure (bar), and

x_e = equilibrium quality.

Typically, Eq. (F-297) is for low quality and Eq. (F-298) is for high quality. For a given mass flux and tube diameter, the switch-over quality between the two equations is shown as a function of pressure in Fig. F-42. As seen in this figure, the switch-over quality is not constant and varies between 0.3 and 0.68 within the pressure range of the Biasi correlation. It exhibits a peak between 2 and 3 MPa.

The Biasi correlation was originally correlated over a database containing 4551 CHF data points. The ranges of the CHF parameters within this database are as follows:

0.3 cm	<	D	<	3.75 cm
20 cm	<	L	<	600 cm
0.27 MPa	<	P	<	14.0 MPa
10 $g \cdot cm^{-2} \cdot s^{-1}$	<	G	<	600 $g \cdot cm^{-2} \cdot s^{-1}$
x_{inlet}	<	0		
$\frac{1}{1+\rho_l/\rho_g}$	<	x	<	1

Figures F-43., F-44., F-45., and F-46. show the typical behavior of the Biasi correlation on the $q_{CHF}-|G|$, $q_{CHF}-x_e$, $q_{CHF}-P$, and $q_{CHF}-D$ planes, respectively. These figures also show the parametric range of the Biasi correlation. Figure F-43. illustrates the inverse mass flux effect, where the CHF decreases with increasing mass flux. The behavior of CHF with respect to the equilibrium quality is shown in Fig. F-44. The point at which the slope is discontinuous is the intersection between Eqs. (F-297) and (F-298). As shown in Fig. F-45., CHF exhibits a maximum between 2 and 3 MPa when plotted with respect to the system pressure. Finally, Fig. F-46. shows that CHF decreases with increasing diameter. The effect for small diameters ($D \leq 1$ cm) is important, possibly because of the enhanced droplet deposition in small-diameter with increasing diameter.

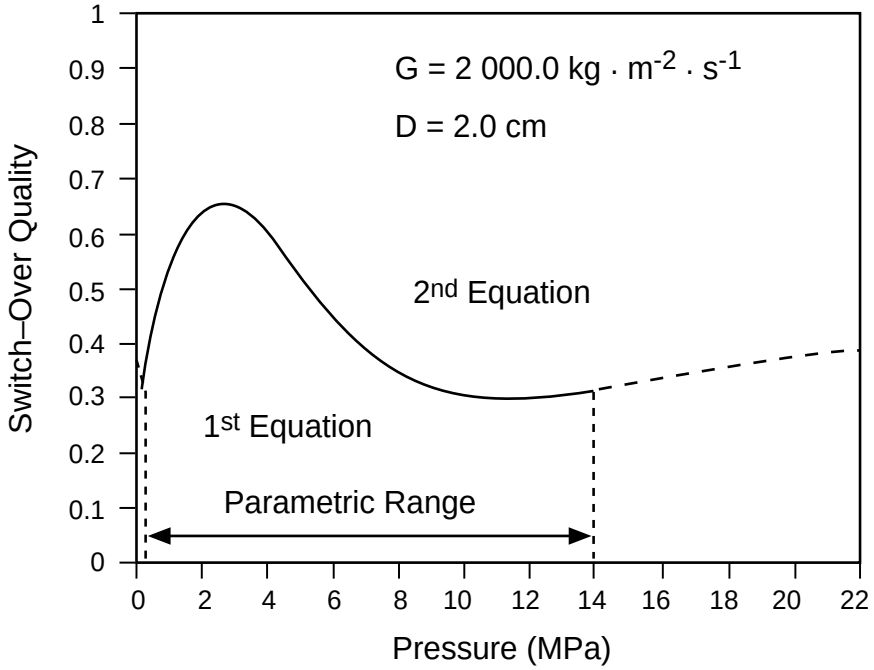

Fig. F-42. The switch-over quality between the two equations of the Biasi correlation as a function of the system pressure.

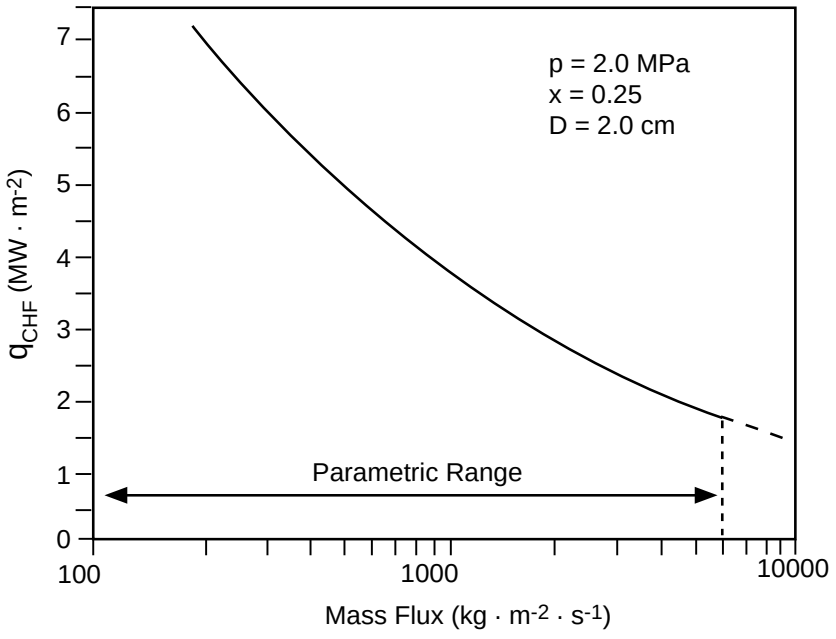

Fig. F-43. CHF vs. mass flux predicted by the Biasi correlation.

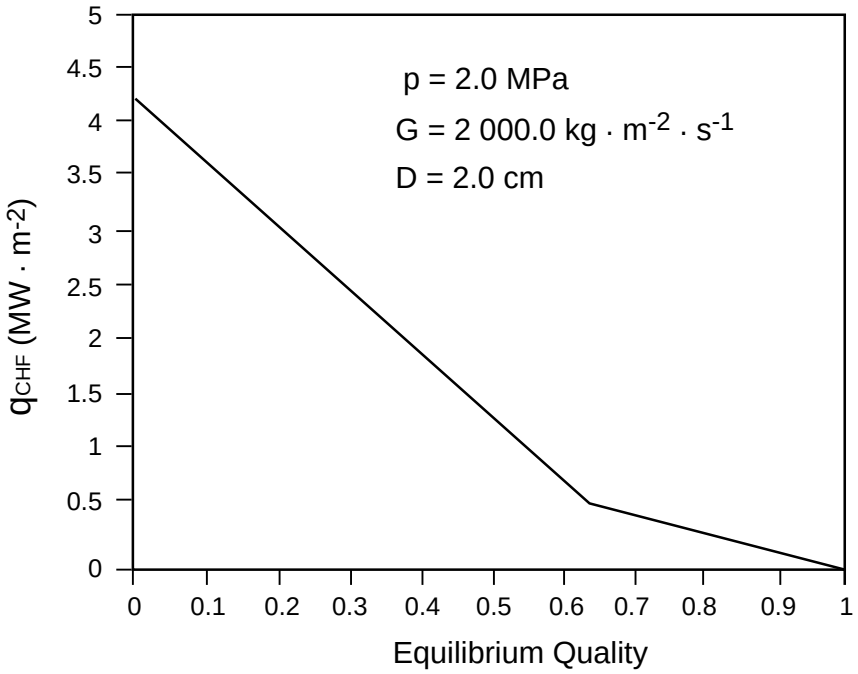

Fig. F-44. CHF vs. equilibrium quality predicted by the Biasi correlation.

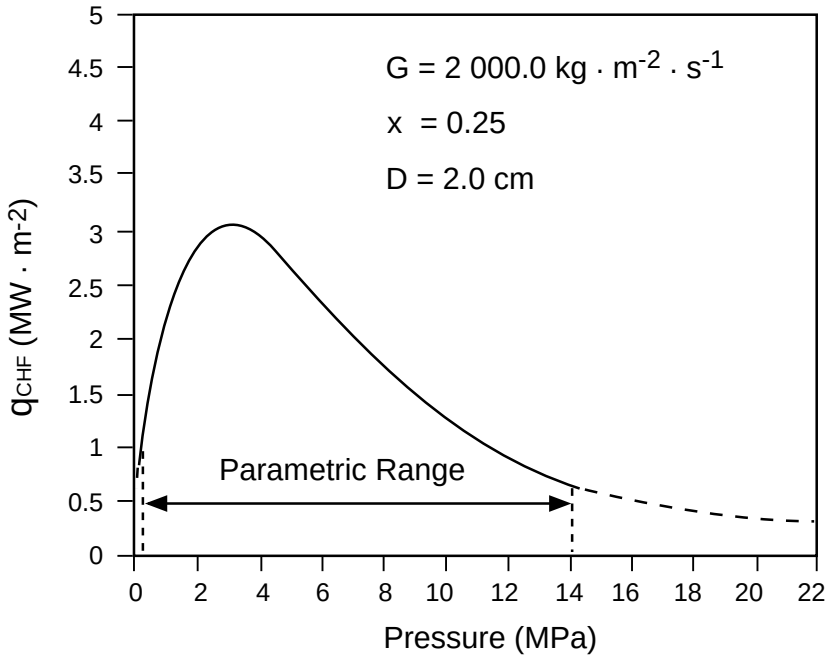

Fig. F-45. CHF vs. system pressure predicted by the Biasi correlation.

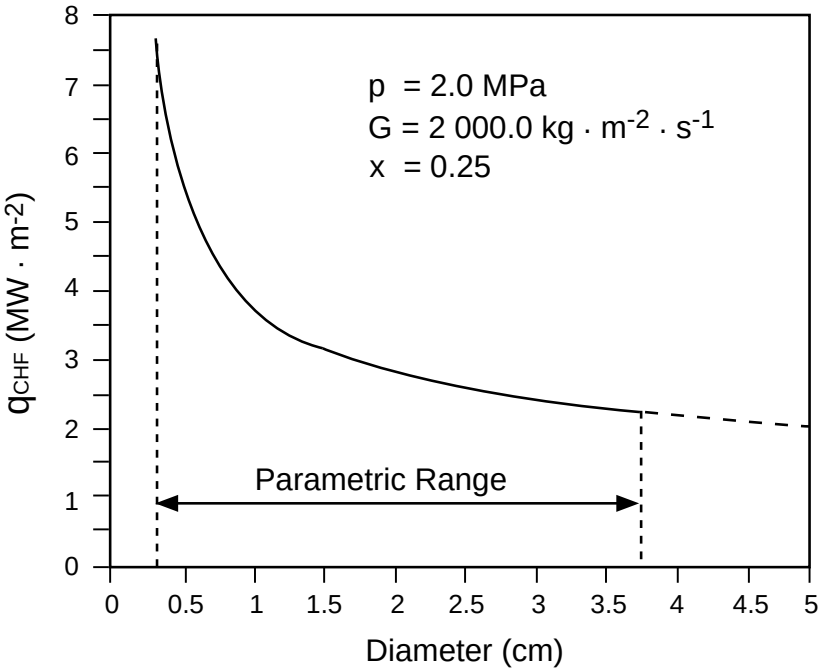

Fig. F-46. CHF vs. tube diameter predicted by the Biasi correlation.

F.2.1.8.2. Assumptions Made in Implementing the Correlations in the Code. CHF prediction in TRAC using the Biasi correlation is based upon the following assumptions:

i. CHF is only a function of the local thermal-hydraulic parameters, and the history effects are negligible.

ii. CHF is not affected by the flow direction. Using this assumption, the mass flux G in the original correlation is replaced by $|G|$ in the code.

iii. The Biasi correlation is originally written for round tubes. In the code it is assumed that the tube diameter may be replaced by the subchannel hydraulic diameter in rod-bundle geometry.

F.2.1.8.3. Constants. The Biasi correlation is written in cgs units. Thus, Eqs. (F-297) and (F-298) yield the CHF in $W \cdot cm^{-2}$. To obtain the CHF directly in $W \cdot m^{-2}$, Eqs. (F-297) and (F-298) are multiplied by 10^4 in the code. All the other constants remain unchanged.

F.2.1.8.4. Model as Coded. In TRAC, the CHF calculations are done in subroutines CHF and CHF1. The CHF temperature is needed in HTCOR to differentiate between the nucleate-boiling and transition-boiling regimes. The CHF temperature is also needed for computing the HTC in the transition-boiling regime. For this information, subroutine CHF is called from within subroutine HTCOR when the value of INVAN≠0. INVAN is a flag used to determine the wall temperature that is used in the flow regime. When

INVAN = 0, T_{sat} is used as the temperature at which transition boiling begins. When INVAN ≠ 0, T_{CHF} is used to define the start of transition boiling. In subroutine CHF, the value of the CHF calculated in subroutine CHF1 is used with the Chen nucleate-boiling heat-transfer correlation to obtain the corresponding CHF temperature. This requires an iterative solution that is done by using both the Newton-Raphson and bisection procedures as described in Ref. F-75., Chapter 2. The iteration is started by using $T_{CHF} = T_{sat} + 0.5\,K$ as the initial guess. The latest calculated value of T_{CHF} is used in subsequent iterations. A maximum of 35 iterations are allowed during the solution of a single value of T_{CHF}. The magnitude of the CHF temperature is bound at the lower and upper ends as follows:

$$T_{sat} + 0.5K \le T_{CHF} \le T_{sat} + 100K \ .$$

The CHF prediction package of TRAC subroutine CHF1 consists of the Biasi correlation with one change in the constants, as described above. Therefore, the correlation is coded as follows:

$$q_{CHF1} = \frac{1.883 \times 10^7}{D_H^n |G|^{1/6}} \left[\frac{f_p}{|G|^{1/6}} - x_e \right] , \tag{F-299}$$

$$q_{CHF2} = \frac{3.78 \times 10^7}{D_H^n |G|^{0.6}} h_p (1 - x_e) , \tag{F-300}$$

and

$$q_{CHF} = \max(q_{CHF1}, q_{CHF2}) \ . \tag{F-301}$$

For low mass fluxes and high void fractions, subroutine CHF1 also contains additional considerations. At mass fluxes lower than 200 kg / m^2-s, the Biasi correlation overpredicts the data due to an inverse mass-flux effect (see Fig. F-43.). Currently, for such low mass fluxes, the CHF is evaluated by using the Biasi correlation with $|G| = 200$ kg / m^2-s. Figure F-47. shows this low mass flux model for a given pressure, hydraulic diameter, and equilibrium quality.

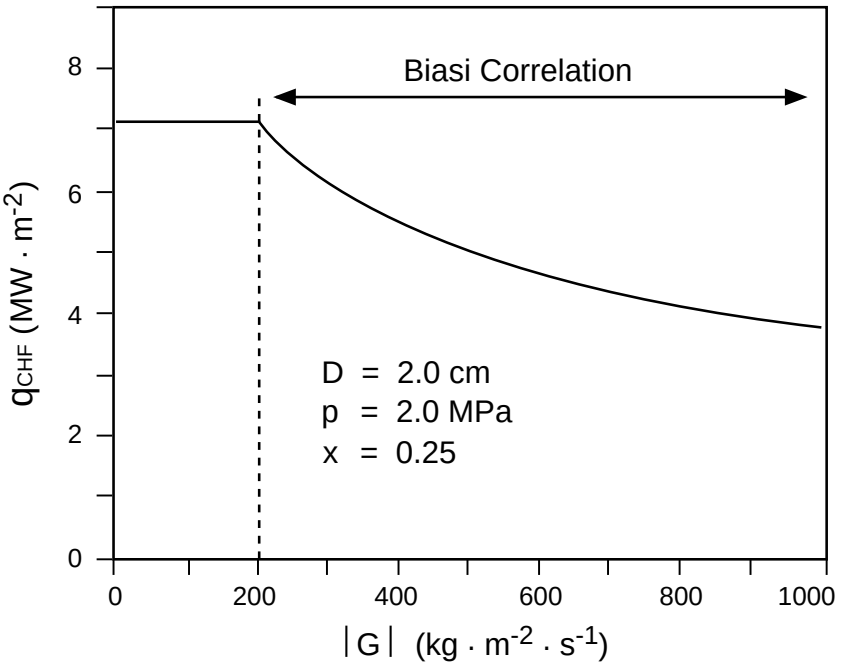

Fig. F-47. CHF model for $|G| \leq 200$ kg / m^2-s.

At high void fractions, the Biasi correlation is restricted by a limiting void fraction. In TRAC, the limiting void fraction is taken as 0.98. Above this value, CHF is assumed to be very small (1 W· m^{-2} is the value used in TRAC). Void fractions between 0.97 and 0.98 fall in the transition region where the CHF is linearly interpolated between the Biasi prediction at $\alpha = 0.97$ and 1 W· m^{-2}. Figure F-48. shows a qualitative description of this limiting-void-fraction concept. Because the Biasi correlation is written in terms of the equilibrium quality, it is hard to translate this limiting void fraction into a limiting quality. The relation between these two quantities is strongly affected by the slip ratio between the phase velocities. Figure F-49. shows the equilibrium quality corresponding to the limiting void fraction of 0.97 for a cocurrent flow, as a function of the slip ratio and system pressure. As seen in this figure, the limiting void fraction is less than or equal to 1; for some transient upflow or cocurrent downflow situations this may not be true. For this reason, slip ratios of less than 1 are shown in Fig. F-49.

F.2.1.8.5. Assessment of the Correlation. The Biasi correlation is one of the more frequently referenced correlations in the literature. The results of a major assessment of this correlation were recently reported by Groeneveld et al. (Ref. F-71., Figs. 3 and 4, Table 4), in which the Biasi correlation was compared to approximately 15000 steady-state water data points that are stored in the Chalk River Nuclear Laboratories' CHF data bank. The results of this assessment are shown in Table F-9. As shown in this table, the Biasi correlation is fairly successful in predicting the data with constant inlet subcooling, where the local equilibrium quality is calculated through an energy balance.

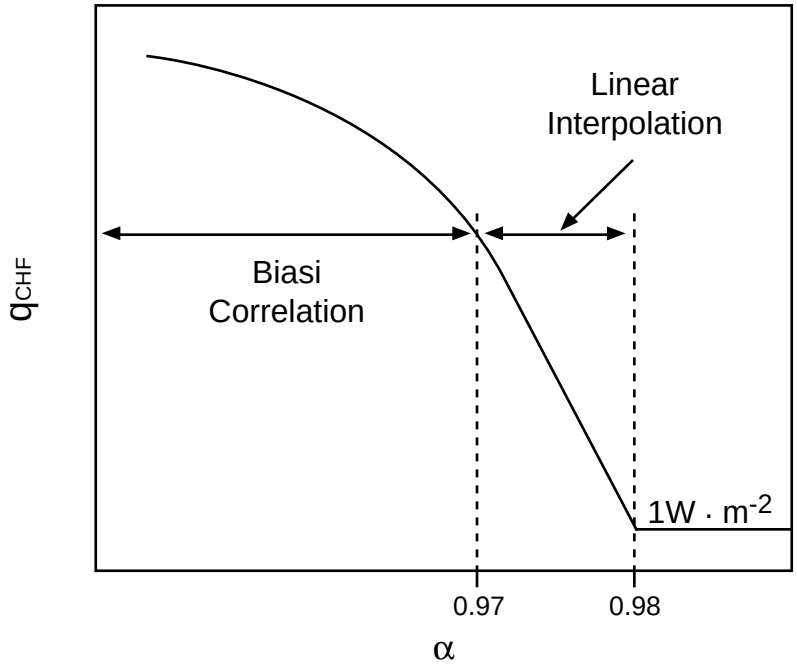

Fig. F-48. CHF model at high void fraction.

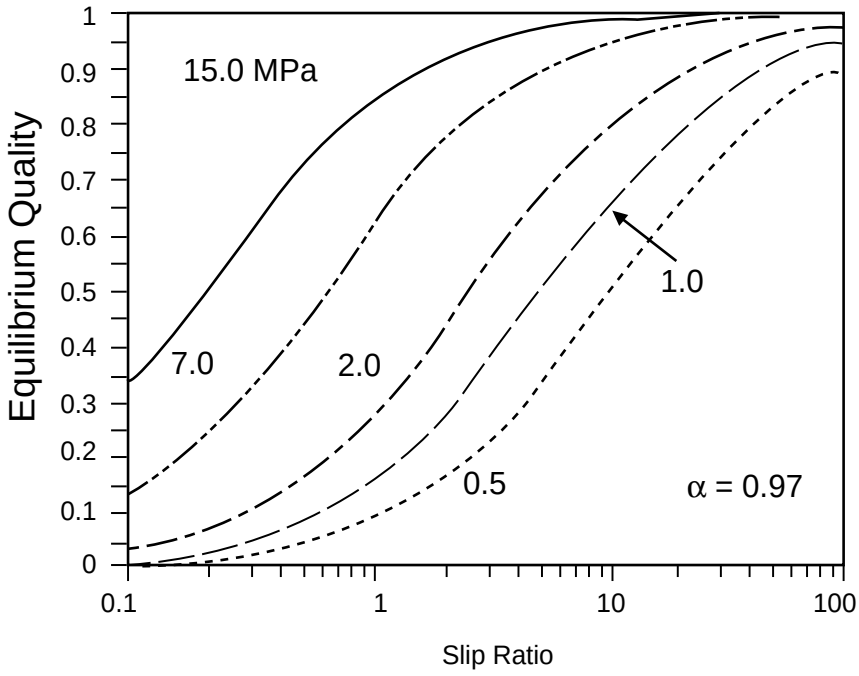

Fig. F-49. Equilibrium quality vs. slip ratio at different pressures for $\alpha = 0.97$.

TABLE F-9.
Performance of the BIASI Correlation as Compared to the Chalk River Nuclear Laboratories' CHF Data Bank (Ref. F-71., Table 4)

	DATA WITHIN THE ERROR BOUND (%)						No. of Data
	Constant Dryout Quality Data			ConstantInletSubcooling			
	±10%	±20%	±50%	±10%	±20%	±50%	Points
All Data	19.30	36.64	67.04	71.23	92.38	99.39	14401
Range of Validity Only	21.32	41.12	73.04	77.60	96.60	99.91	9936

The Biasi correlation is also compared to transient CHF data by Leung (Ref. F-72.). Table F-10. contains the blowdown and flow transient experiments analyzed by Leung. Most of these experiments were very well-instrumented for CHF where the CHF was measured at various locations. Figure F-50. shows the results of the data comparison for the experiments with high mass fluxes. For each test, at locations at which CHF occurs more than once, only the earliest CHF is plotted in this figure. The data corresponding to low mass fluxes ($|G| < 200\ kg/m^2\text{-s}$) are not included in Figure F-50. Leung's analysis (Ref. F-72.) shows that these low-mass-flux data are best predicted by using the Griffith-Zuber correlation (Ref. F-73.). However, because of various uncertainties associated with this assessment, the Griffith-Zuber correlation is not included in TRAC. CHF modeling at low mass fluxes suffers from the following limitations:

i. As reported by Groeneveld et al. (Ref. F-71., p. 47), the number of steady-state CHF data for low mass fluxes is very limited. This makes the development of a reliable correlation very difficult.

ii. At such low magnitudes, an accurate measurement of two-phase mass fluxes is very difficult, as discussed by Leung (Ref. F-72.).

iii. At low mass fluxes, the CHF with upward flow may be considerably different from the CHF with downward flow.

iv. At low mass fluxes, the slip ratios may be very high. Therefore, a homogeneous flow analysis, as done by Leung (Ref. F-72.), may be erroneous.

v. In homogeneous flow, there is a big discontinuity between the Griffith-Zuber and Biasi correlations at their suggested boundary.

TABLE F-10.
Blowdown and Flow Transient CHF Experiments
Analyzed by Leung (Ref. F-72.)

Blowdown (high mass flux)	Blowdown (low mass flux)	Flow Transients
LOFT Columbia Loop THTF-Test 105 - Test 104 - Test 178 - Test 181 - Test 177	PBF LOC-IIC Semiscale Mod-1, S-02-1 S-06-6	Moxon-Edwards Roumy
Semiscale Mod-1-S-02-9 -S-29-2 -S-28-1		
Semiscale Mod-3-S-07-3 -S-07-9		

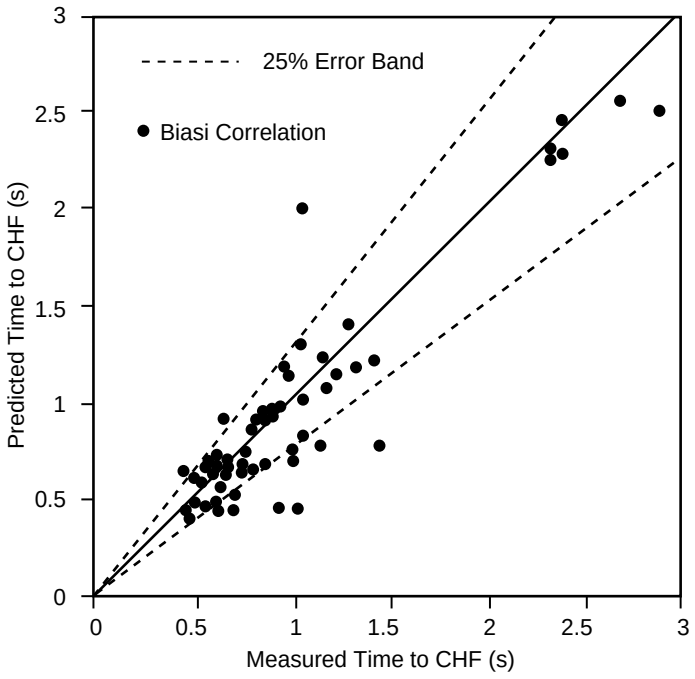

Fig. F-50. Comparison of the Biasi correlation with the blowdown CHF data.

A more detailed analysis and discussion of blowdown CHF experiments may be found within Ref. F-74., Chap. 6.

The assessment of the Biasi correlation as compared to the flow transients is shown in Fig. F-51. As shown in this figure, the earlier CHFs measured in Moxon-Edwards' tests (Ref. F-72.) are overpredicted by the Biasi correlation, whereas the later CHFs are better predicted. The only CHF measure in Roumy's experiment (Ref. F-72.) is predicted with exceptional accuracy by the Biasi correlation.

F.2.1.8.6. Scaling Considerations. The Biasi correlation is developed for round tubes; its success in predicting the blowdown data in various tests (as shown in Fig. F-50.) suggests that it can be scaled to rod-bundle geometry using a hydraulic diameter.

F.2.1.8.7. Summary and Conclusions. When compared to steady-state (Ref. F-75.) and transient (Ref. F-71.) annular-flow dryout type of CHF data, the Biasi correlation yields reasonable results, as shown in Table F-9. and Figs. F-50. and F-51. Most of the blowdown and flow transients result in an annular-flow regime prior to reaching the CHF. Consequently, the CHF package of TRAC gives reasonably accurate CHF predictions in many cases. However, the package has deficiencies in the three areas described below.

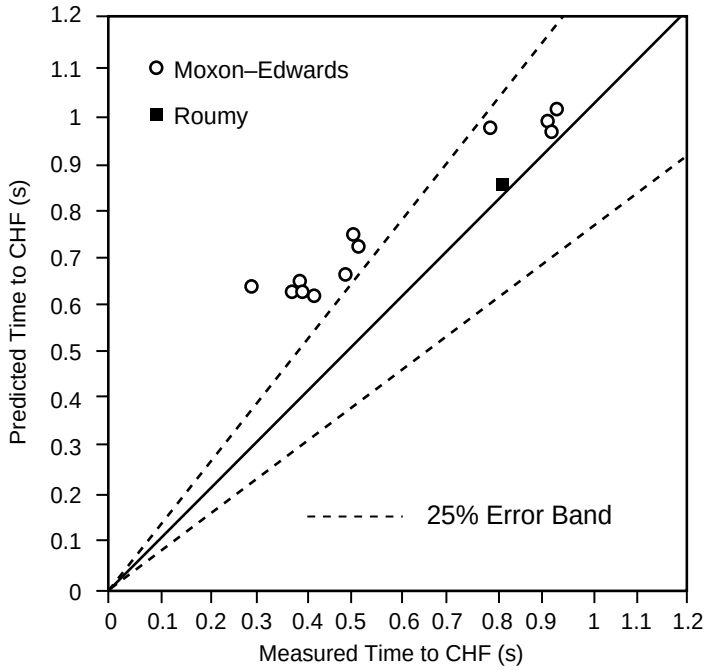

Fig. F-51. Comparison of the Biasi correlation with the flow-transient CHF data.

First, the code cannot accurately model subcooled or very low-quality departure from nucleate boiling. Future code development efforts must consider implementing a departure from the nucleate-boiling-correlation model into the code. Second, at low mass fluxes ($|G| \leq 2200\ \mathrm{kg/m^2\text{-}s}$), one must use the code prediction with extreme caution. Very little information is available in this area, and further experimental CHF studies are required. Third, the high-void-fraction model must be further assessed even though it gives favorable results for rapid depressurization transients in which a sudden core voiding occurs.

One must also be aware of the limitations imposed by the quasi-steady approach used by TRAC. One example in which this might prove to be a problem is applying the present model to rapid transients such as quenching, where the CHF prediction is needed to calculate the return to nucleate boiling while going from right to left on a typical boiling curve. A second example would be the application of the code to reactivity-initiated accident transients.

Finally, one should be aware of the question of whether the quenching CHF is the same as the heat-up CHF. TRAC models assume this to be true, but most data show it not to be the case.

F.2.1.9. Minimum Stable Film-Boiling Temperature Correlation. The minimum stable film-boiling temperature, $T_{\min}$, is the intersection point between the transition- and film-boiling heat-transfer regimes. It is also used in the interpolation scheme for determining the transition-boiling heat flux. It has been discussed in detail as a subtopic in Section F.2. relative to the interpretation of a true minimum temperature and an apparent minimum temperature. The quantity defined in TRAC is meant to represent the true minimum temperature.

F.2.1.9.1. Basis for the Model. The homogeneous-nucleation minimum stable film-boiling-temperature correlation (Ref. F-76., Eq. 7) used is

$$T_{\min} = T_{\mathrm{NH}} + (T_{\mathrm{NH}} - T_{\mathrm{l}})R^{1/2}\ , \tag{F-302}$$

where

$$R = \frac{\left(k\rho c_p\right)_{\mathrm{l}}}{\left(k\rho c_p\right)_{w}} \tag{F-303}$$

and T_{NH} is the homogenous-nucleation temperature. In Eq. (F-303), the subscript l indicates liquid properties and the subscript w refers to wall properties. The homogenous-nucleation temperature, given by Fauske, is fitted by a third-order polynomial taken from the COBRA-TF code[1] and is given as

$$T_{\mathrm{NH}} = 705.44 - (4.722 \times 10^{-2})DP + (2.3907 \times 10^{-5})DP^2 - (5.8193 \times 10^{-9})DP^3\ , \tag{F-304}$$

where

$$DP = 3203.6 - P \ . \qquad \text{(F-305)}$$

The pressure is in units of pounds per square inch and the temperature is in Fahrenheit units.

F.2.1.9.2. Input Quantities to the Model. The thermal conductivity, specific heat, and density of the wall material are evaluated in subroutine MSTRCT; the corresponding fluid properties are evaluated in functions THCV, CPVV1, and subroutine THERMO. The fluid pressure is temporarily converted from Pascals to pounds per square inch in subroutine TMSFB. Equation (F-304) is evaluated and T_{NH} is converted from Fahrenheit units to Kelvin.

F.2.1.9.3. Constants. The homogeneous-nucleation temperature given by Fauske was fitted by a third-order polynomial for the pressure difference, *DP*. No changes were made to any of the numerical constants in the model.

F.2.1.9.4. Model as Coded. The minimum stable film-boiling temperature, T_{min}, is calculated in subroutine TMSFB. This subroutine is called from subroutine HTCOR when a value for T_{min} is required. All required data needed in subroutine TMSFB are in the call statement. In subroutine TMSFB, pressure is converted from units of Pascals to units of pounds per square inch and Eqs. (F-304) and (F-305) are evaluated. The homogeneous-nucleation temperature, T_{NH} is then converted from °F to K and Eq. (F-302) evaluated for T_{min}. The final value for T_{min} is determined by the following relation:

$$T_{min} = \max\,(T_{min},\, T_{sat} + 0.0001\ \text{K}) \ . \qquad \text{(F-306)}$$

This value of T_{min} is returned to subroutine HTCOR.

F.2.1.9.5. Weighting, Limits, and Averaging. Equation (F-306) limits the minimum value of T_{min} to T_{sat} + 0.0001 K. There are no weighting factors or rate limits applied to the correlation.

F.2.1.9.6. Assessment of the Correlation. Cheng et al. (Ref. F-77.) have recently presented a measurement of true minimum film-boiling temperatures to which a comparison of Eq. (F-302) can be made. Cheng's experiment extends earlier work by Groeneveld and Stewart (Ref. F-78.) to separate the effects of axial conduction and hydraulic transients and is run over a short-enough test section in a steady-state manner such that these data, along with those of Groeneveld, represent the only known forced-convective true T_{min} data.

---

1. This information was provided by M. J. Thurgood and J. M. Kelly, Batelle Pacific Northwest Laboratories, December 1979.

Both Cheng and Groeneveld developed empirical correlations to represent their data. We note these correlations because they will be used in the data comparison instead of the data itself. Cheng's correlation is given by

$$T_{\min} = 169.66 + 0.1050 \times 10^3 P + 0.1444 G + 3.0347 \Delta T_{\text{sub}} , \quad \text{(F-307)}$$

where temperature is in °C, P in MPa, G in kg/m^2-s, and ΔT_{sub} is the subcooling in °C. His database included subcoolings of 2° to 300°C, mass fluxes of 50 to 682 kg/m^2-s, and pressures of 0.101 to 1.03 MPa. Groeneveld's correlation had two parts given by

$$T_{\min} = 284.7 + 44.11P - 3.72P^2 \quad \text{(F-308)}$$

for the saturated inlet flow case (quality ≥ 0), and

$$T_{\min} = 284.7 + 44.11P - 3.72P^2 - \frac{x(10)^4}{2.819 + 1.22P} \quad \text{(F-309)}$$

for the subcooled case ($x < 0$), where x is the quality corresponding to the subcooling on an energy basis. His database included saturated two-phase conditions and qualities down to –0.0215 at 0.1 MPa and –0.1212 at 9.064 MPa, mass fluxes of 110 to 2750 kg/m^2-s, and pressures of 3.1 to 9.087 MPa.

Figures F-52. and F-53. plot Eq. (F-302) against Cheng's correlation, Eq. (F-307), as a function of pressure over his pressure range. Figure F-52. shows the effect of mass flux at a fixed subcooling of 10 K. Figure F-53. shows the effect of subcooling at a fixed mass flux of 200 kg/m^2-s. The TRAC correlation shows little sensitivity to the subcooling variation. It typically overpredicts the minimum temperature over the range of flows studied, but, as seen, this is a function of pressure and subcooling. For the higher pressures, higher mass fluxes, and higher subcoolings, the TRAC prediction is better. It should be noted that the range of temperatures represented by Cheng's results are much lower than those typically quoted in many reflood experiments. This is because these are true $T_{\min}$s as opposed to apparent $T_{\min}$s arising from transient hydraulic and axial conduction effects. Figure F-54. plots Eq. (F-302) evaluated at saturated conditions against Groeneveld's correlation, Eqs. (F-308) and (F-309). The effect of subcooling on Groeneveld's correlation is also noted. The prediction of saturated conditions is reasonable but subcooling increases the difference. Figure F-55. further investigates the subcooling effect relative to Groeneveld's correlation at 2 MPa. As observed in Figs. F-52. and F-53., Eq. (F-302) does not correctly include the effects of any significant subcoolings. It should be noted that at this pressure, Groeneveld's data had qualities of -0.0534 or greater so that the left-hand portion of his curve as plotted is an extrapolation. Nelson noted this breakdown in the model with respect to subcooling (Ref. F-42., p. 51), but these comparisons to data show the breakdown to be earlier than he indicated. (Note that there was a misprint within the reference in that the subcooling limit should be 28.7 K instead of the 287 K as shown.)

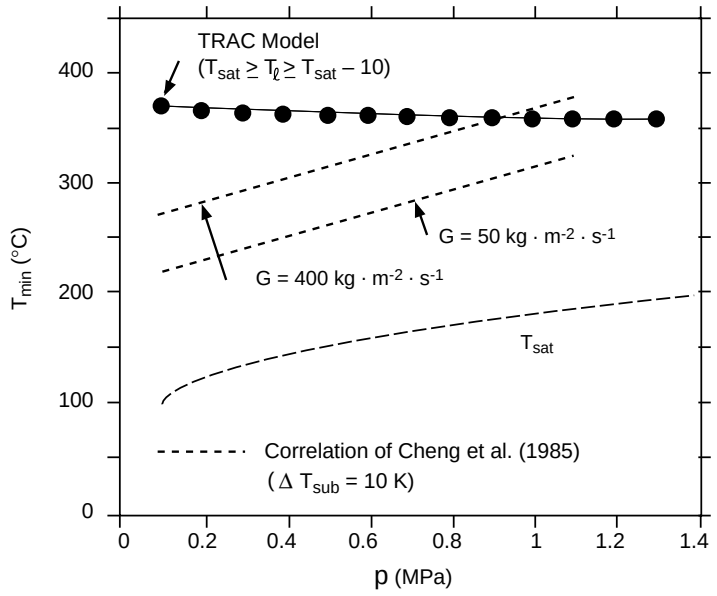

Fig. F-52. Comparison with Cheng's results of true T_{min} vs. pressure with fixed subcooling (10 K) and parametric effect of mass flux.

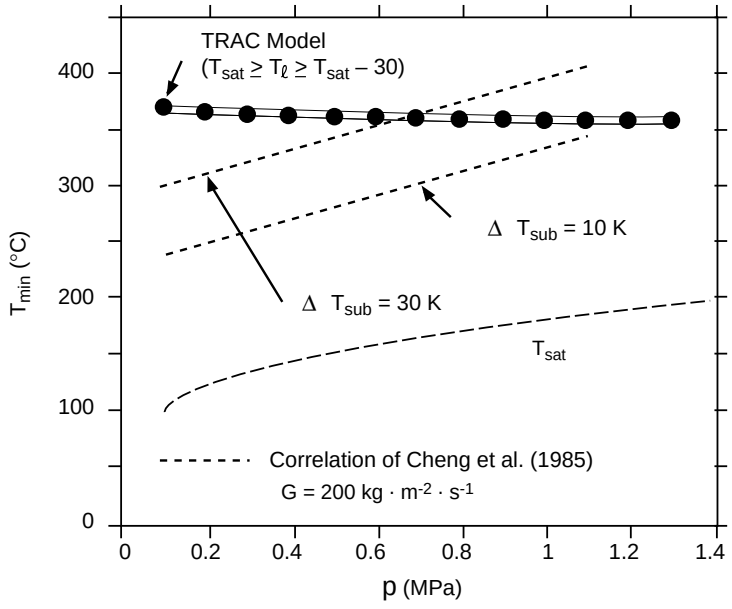

Fig. F-53. Comparison with Cheng's results of true T_{min} vs. pressure with fixed mass flux (200 kg / m^2-s) and parametric effect of subcooling.

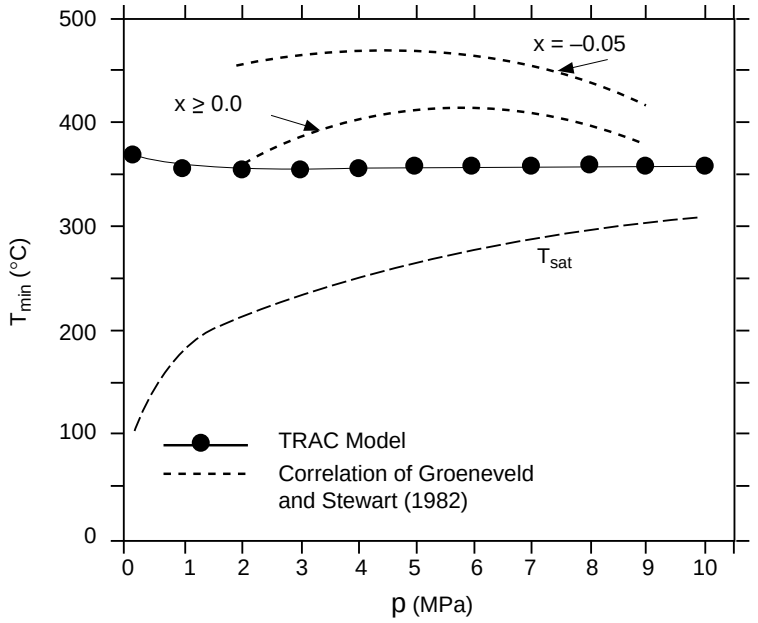

Fig. F-54. Comparison with Groeneveld's results of true T_{min} vs. pressure with parametric effect of subcooling.

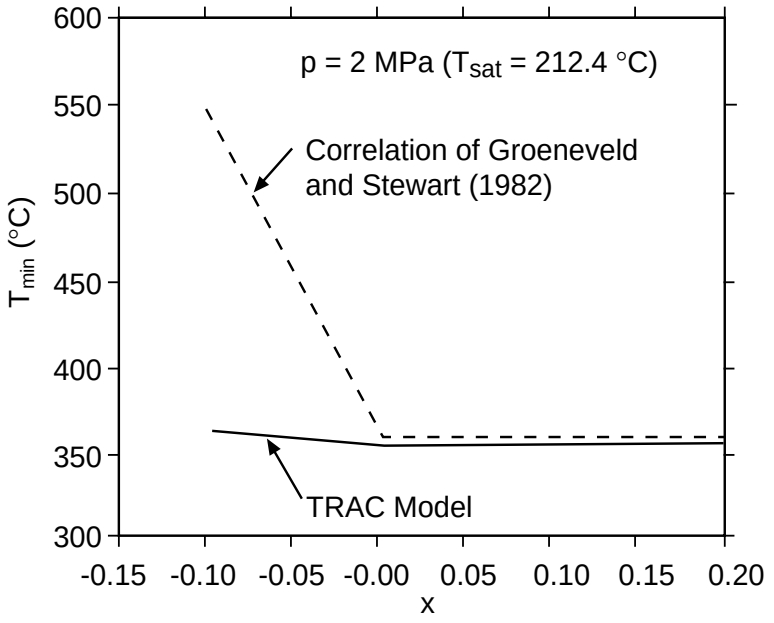

Fig. F-55. Comparison with Groeneveld's results of true T_{min} vs. subcooling at 2 MPa.

F.2.1.9.7. Scaling Considerations. There are no parameters in the correlation to account for scaling geometry or mass flux. Fluid pressure, temperature, and thermal properties and wall thermal properties are the only parameters in the correlation; no limits are specified for these parameters.

F.2.1.9.8. Summary and Conclusions. The comparison of the TRAC T_{min} model to true T_{min} data shows that the prediction is reasonable but could stand improvement in light of the more recent data. The prediction is called reasonable because the prediction is much closer to the data than are the apparent T_{min}s often developed from reflood and blowdown experiments (see the earlier discussion in Section F.2.). To predict the quenches from these experiments, the proper characteristics of the boiling surface with respect to mass flux and void fraction are required. From the comparisons presented, we can say that the current TRAC T_{min} model overpredicts the data at typical reflood conditions (0.1 to 0.4 MPa) by 100 to 150 K and underpredicts the data at typical blowdown conditions (7 MPa) by about 60 to 100 K.

F.2.2. Correlations Used in Subroutine HTVSSL (Core Reflood Model)

Subroutine HTVSSL was developed with an emphasis on the post-CHF region (transition- and film-boiling regimes). The routine, like HTCOR, is self-contained to provide HTCs for all the potential convective regimes using many of the same correlations used by HTCOR for the other boiling regimes. For completeness, all the structure of HTVSSL will be discussed in detail even though it is very similar to that of HTCOR. The correlations that are the same as those in HTCOR will be noted with the appropriate sections so that the reader may revisit them if so desired. Those correlations that are different obviously will be discussed here. We note here that the two-pass logic of HTCOR for void fractions between 0.97 and 0.98 is not in HTVSSL, and that the high-void interpolation threshold has been increased to 0.995 from 0.98.

Post-CHF heat transfer occurs in a reactor core principally during the refill and reflood phase of a LOCA. The flow regimes after CHF of quenching hot fuel rods are very important in determining the heat transfer as well as the mass and momentum transfer. If CHF occurs at low or negative (subcooling) flow qualities, the flow pattern can be expected to be an inverted annular flow where a liquid core is surrounded by an annular vapor film as shown in Fig. F-56. Further downstream, the liquid core may break up into an agitated region of slugs or large droplets and liquid filaments, and later be followed by a small droplet dispersed flow region. At moderate to high qualities, the flow pattern may be thought of as a dryout of liquid film at the wall, which creates a small droplet dispersed-flow regime downstream of the dryout.

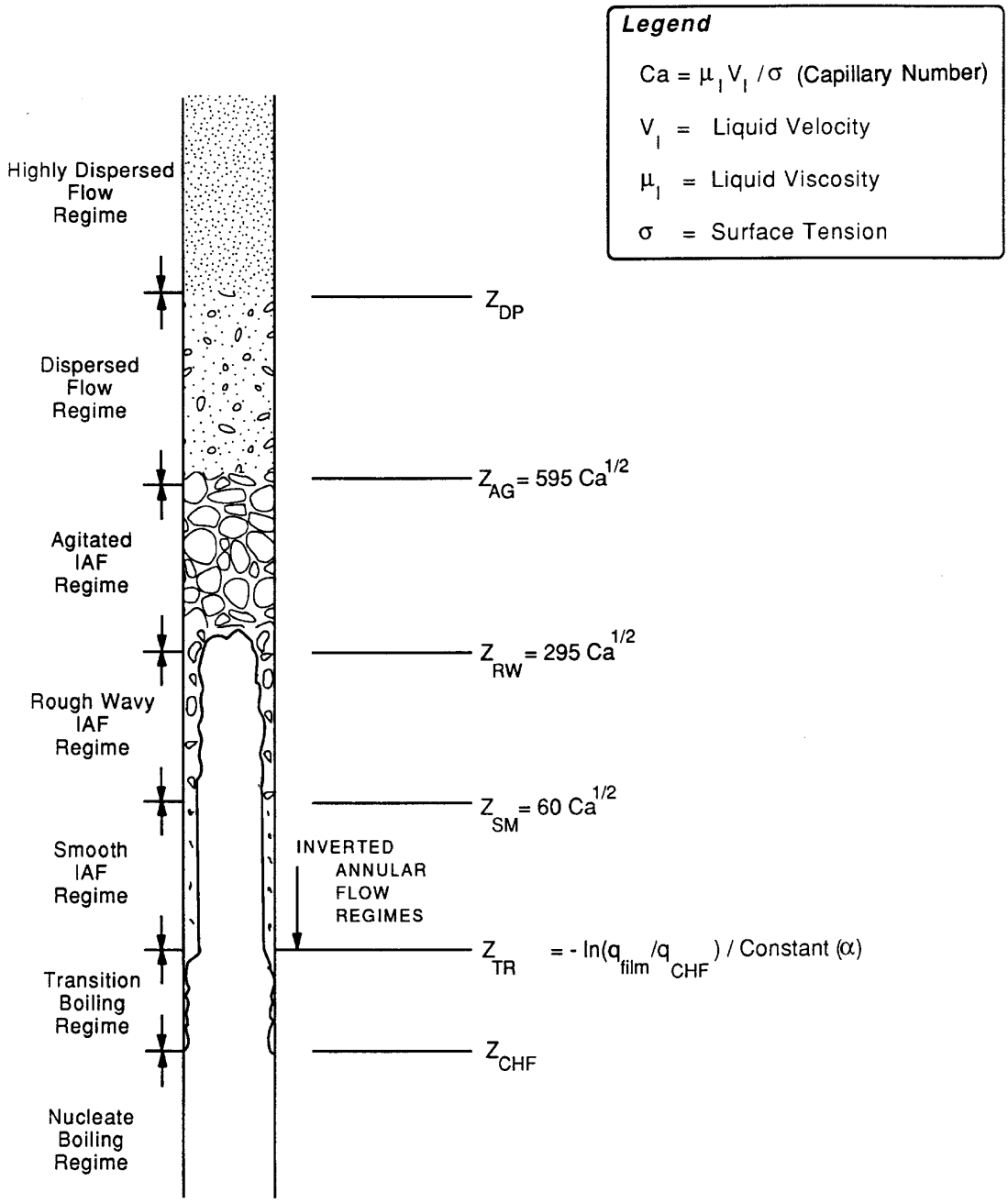

Fig. F-56. Inverted-annular-flow regimes.

Recently Ishii and his co-workers (Ref. F-32.) reported a detailed study of inverted annular flow (characterization of the post-CHF flow regimes and transitions between them). They observed that there are basically four flow regimes downstream of the transition-boiling region located next to the CHF point. It is important to note that their

test setup was constructed in such a way that the transition-boiling region could not be simulated. Inverted annular flow was simulated by two coaxial tubes with the inner tube being a thin-walled tubular nozzle. Right after the nozzle exit to as many as 20 nozzle diameters downstream, the flow was a smooth inverted annular flow with a stable liquid core. Following this smooth regime was the rough-wavy section with its dominant feature being the presence of a fairly stable, intact liquid core, along with a very rough annular gas/core-liquid interface. The agitated region was located immediately downstream of the rough-wavy region. In this regime, significant interfacial deformation was observed. The presence of a highly agitated liquid annulus in the vicinity of the heated wall and large liquid slugs in the central portion of the test section were also observed. The last flow regime observed downstream of the agitated region was a dispersed-ligaments/droplets-flow regime. A generalized transition criterion between these flow regimes was given.

The TRAC core reflood model is based upon the above-mentioned flow-regime map of inverted annular flow, as illustrated in Fig. F-56. The criterion to determine the flow-regime transitions is based upon a capillary number, except for the transition-boiling-to-smooth-inverted-annular-flow and the dispersed-flow to highly dispersed flow transitions. The highly dispersed flow is defined when the void fraction at a particular elevation is higher than 98%. The transition-boiling region is assumed to end at a location where the transition wall heat flux coincides with the heat flux typical of those encountered in the film-boiling regime. The following section describes the HTC correlations used in TRAC (subroutine HTVSSL) for wall-to-fluid heat transfer for inverted-annular-flow regimes.

F.2.2.1. Single-Phase Liquid (Heat-Transfer Regimes 1 and 12). Either forced convection (regime 1) or natural circulation (regime 12) can occur when single-phase liquid is present. Laminar and turbulent HTCs are available. Because only single-phase liquid is assumed to be present, the vapor HTC, h_{wg}, is set equal to zero. HTC correlations for forced convection and natural convection, input quantities and constants for these correlations, and the method of coding are identical to those used in subroutine HTCOR as explained in Section F.2.1.1.

F.2.2.2. Nucleate Boiling (Heat-Transfer Regime 2). Heat-transfer regime 2 is nucleate boiling and includes subcooled nucleate boiling. The Chen correlation is used in the nucleate-boiling heat-transfer regime as in subroutine HTCOR. None of the constants in the correlations was changed from that given in subroutine HTCOR. The coding for the Chen correlation, input quantities, and constants are the same as those given in Section F.2.1.2.

F.2.2.3. Transition Boiling (Heat-Transfer Regime 3). The transition-boiling regime spans the boiling surface between CHF and minimum film boiling.

F.2.2.3.1. Basis for the Model. Previously in subroutine HTCOR, transition boiling is represented as a combination of both nucleate-boiling (wet-wall) and film-boiling (dry-wall) heat transfer with a weighting factor applied to both parts. Transition boiling is assumed to occur if the wall temperature is between T_{CHF} and T_{min}. This modeling approach by definition does not depend upon the axial position but rather on the local wall temperature for a given control volume at a given axial distance from the CHF point. It has been observed that very different results in predicting wall-temperature history and the precursory cooling can be obtained if the axial node size is changed from small to large or vice versa. This difference arises because the only limiting factor within the code in such an analysis is that imposed by the numerics associated with axial conduction. Until the node size has been decreased to a size smaller than that required to properly model the axial-conduction effect, the axial temperature distribution will change as the node size is changed, and a sensitivity to node size will be reflected in the HTCs because they are being evaluated based upon the local wall temperatures. Nothing is present within the local wall-temperature formulation of transition boiling to prevent the "collapse in the axial direction" of convective boiling as the node size is decreased to that thermal distribution limit imposed by axial conduction. Thus, the determination of wall-to-fluid HTCs, used in the conduction solution for the transition-boiling regime, becomes axial-nodalization dependent. Whereas some flow states exist where this is the correct representation of convection, in general, this collapse of transition boiling in the axial direction to the axial-conduction limit is not correct. (See previous discussion in the spatial-averaging operator portion of Section F.2.)

As seen in many experimental studies (Refs. F-79., F-80., and F-81.), the extension of transition boiling downstream of a CHF point in forced-convective flow depends upon the thermal-hydraulic conditions at the CHF point. Thus, there is a need to develop an axial-history-dependent transition-boiling model in order to eliminate difficulties associated with the nodalization in the transition-boiling model used in subroutine HTCOR. The following paragraphs explain the axial-history-dependent transition-boiling model used in subroutine HTVSSL to determine wall-to-fluid HTCs.

The typical conditions in a post-CHF convective flow are illustrated in Figs. F-57a. and F-57b., which show Ishii's inverted annular-flow-regime maps with the postulated axial wall heat-flux profiles. The wall heat flux at the CHF point is significantly high relative to the heat flux of the film-boiling regime. The transition-boiling heat flux is limited by a maximum of q_{CHF} and a minimum of q_{film}. It is assumed in the current model that the transition-boiling heat flux exponentially decreases with the axial distance from q_{CHF} to q_{film}. The transition-boiling heat flux is given by

$$q_{TR} = q_{CHF} e^{-B(Z - Z_{CHF})}, \text{ so that at} \tag{F-310}$$

$$z = Z_{CHF}\ ,\ q_{TR} = q_{CHF}\ , \text{ and at} \tag{F-311}$$

$$z = Z_{TR}\ ,\ q_{TR} = q_{film}\ .$$

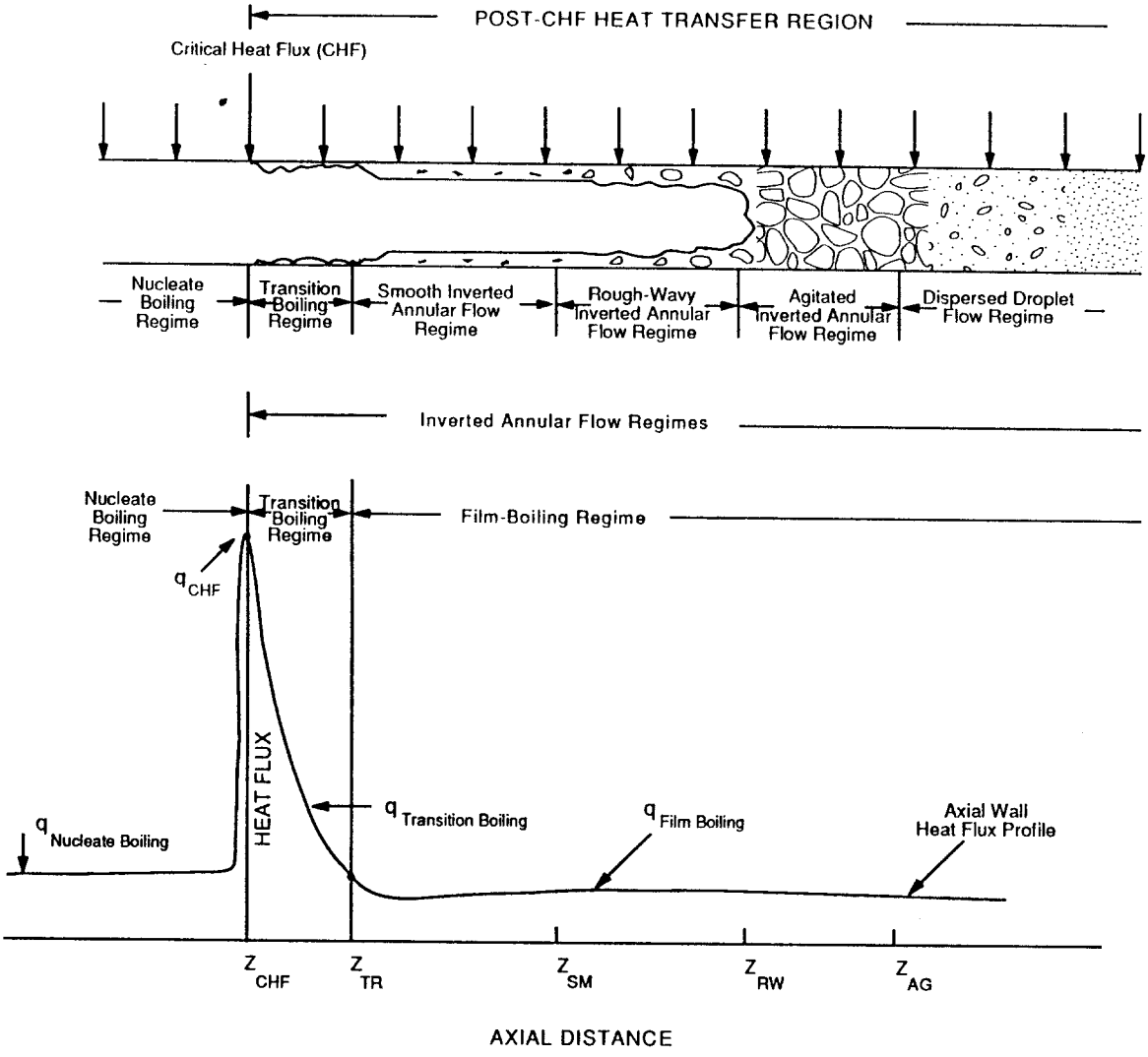

Fig. F-57a. Typical axial wall heat-flux profile for an inverted annular flow with low inlet qualities at the CHF point.

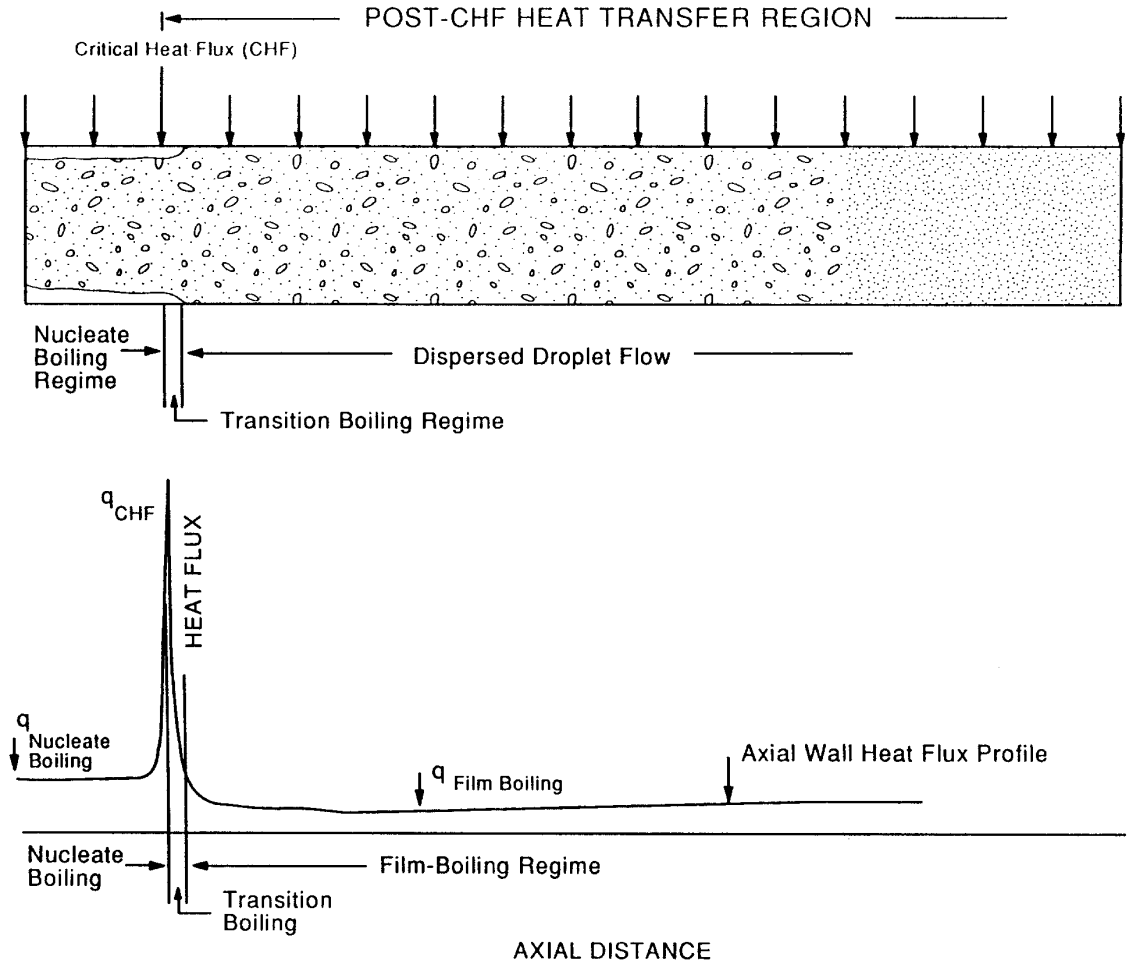

Fig. F-57b. Typical axial wall heat-flux profile for an inverted annular flow with high inlet qualities at the CHF point.

The length of the transition-boiling region then can be determined by

$$Z_{TR} - Z_{CHF} = \frac{-\ln(q_{film} / q_{CHF})}{B} \qquad \text{(F-312)}$$

if the constant B is specified. Although the ratio of the film-boiling heat flux to the peak, CHF heat flux is a function of thermal-hydraulic conditions at the quench front, the ratio is considered to be constant in the current reflood model. The CCTF Run-14 test was used to determine the constant. Determining the coefficient B is not straightforward and ideally, all possible combinations of post-CHF flow conditions, wall materials, and thicknesses that are of interest should be considered.

To partition the total transition-boiling heat flux into its phasic components, the gas-phase HTC, h_{wg}, is evaluated by the Webb-Chen correlation. This correlation and its limitations and weightings are explained in Section F.2.2.4. Once h_{wg} is evaluated, the wall-to-liquid HTC can be found by the following equation at a given axial position:

$$h_{w\ell} = (q_{\mathrm{TR}} - h_{wg}(T_w - T_g)) / (T_w - T_\ell) \ . \tag{F-313}$$

The CHF in Eq. (F-312), q_{CHF}, is calculated in subroutine CHF1 using the Biasi correlations (see Section F.2.1.8.).

If the liquid is subcooled ($T_\ell < T_{\mathrm{sat}}$), the heat-transfer coefficient due to the subcooled conditions is determined by

$$h_\Gamma = h_{\Gamma,\,\mathrm{CHF}} e^{-B(z - Z_{\mathrm{CHF}})} \ . \tag{F-314}$$

The final selection of h_Γ is made by

$$h_\Gamma = \min(h_{w\ell}, \max(h_\Gamma, h_{\Gamma,\,\mathrm{CHF}})) \ , \tag{F-315}$$

where $h_{\Gamma,\mathrm{CHF}}$ is the subcooled-boiling heat-transfer coefficient defined at the CHF point.

F.2.2.3.2. Input Quantities to the Model. The liquid and vapor properties are evaluated at the film temperature for h_{wg}. The velocities in the Reynolds number (Webb-Chen correlation) are the absolute values of the liquid and vapor axial velocities (see Section F.2.1.1.1.). The characteristic length is the hydraulic diameter of the unit subchannel or channel.

F.2.2.3.3. Constants. The constant B is considered to be vapor-Reynolds-number, capillary-number, and void-fraction dependent. The reasons for selecting these dimensionless numbers are discussed below.

Ishii's flow-regime map indicates that the length of each IAF regime is proportional to the square root of the capillary number defined at the CHF point. Thus, for a given pressure, the IAF regimes extend farther when the liquid velocity increases at the CHF point. We assume that the length of the transition-boiling regime should exhibit the same trend—higher liquid velocities at the CHF point should extend the transition-boiling region further downstream. Therefore, the first dimensionless parameter in determining B is the capillary number at CHF. B is assumed to be proportional to the inverse square root of the capillary number (B=Constant $\times Ca^{-1/2}$). The proportionality constant was found to vary with the vapor Reynolds number (defined at the CHF point).

For higher void fractions, the flow regimes downstream of the CHF point are expected to be annular-mist transition and dispersed flow. We believe that the transition-boiling regime should occur in a relatively short region for these high-void flow conditions and

should diminish when the void fraction goes to unity. Thus, the transition-boiling regime is forced to decrease with increasing void fraction if the void fraction at CHF is between 0.8 and 0.995.

The coefficient B is found by the following:

for $\alpha < 0.8$,

$$B = \text{Cons.} Ca_l^{-0.5} \; ; \tag{F-316}$$

for $0.80 < \alpha < 0.995$,

$$B = e^{\left(ln(\text{Cons. } Ca_l^{-0.5}) + \left(\frac{\alpha - 0.80}{0.995 - 0.8}\right)^{1.5} (7.601 - ln(\text{Cons.}) \, Ca_l^{-0.5}) \right)} \; ; \tag{F-317}$$

for $0.995 < \alpha$,

$$B = 2000 \; ; \tag{F-318}$$

where

$$\text{Cons.} = 18.75 + 1 \times 10^{-4} Re_v - 3 \times 10^{-6} Re_v^2 \qquad \text{if } Re_v < 2000 \; ; \tag{F-319}$$

$$\text{Cons.} = 10.425 - 1.93 \times 10^{-3} Re_v + 1.25 \times 10^{-7} Re_v^2 \qquad \text{if } Re_v > 2000 \; ; \tag{F-320}$$

$$Ca_l = \left(\frac{V_l \mu_l}{\sigma} \right)_{\text{CHF}} \; ; \text{and} \tag{F-321}$$

$$Re_v = \left(\frac{\alpha \rho_v D_h V_v}{\mu_v} \right)_{\text{CHF}} \; . \tag{F-322}$$

To better understand this formulation, we can first note that the length of the transition-boiling region can be determined from Eq. (F-312) to be

$$Z_{\text{TR}} - Z_{\text{CHF}} = \frac{-\ln\left(\frac{q_{\text{film}}}{q_{\text{CHF}}}\right)}{\text{Constant}(Ca_l^{-0.5})} \tag{F-323}$$

for the case where α<0.8. Dividing Eq. (F-313) by the diameter yields

$$\frac{Z_{\text{TR}} - Z_{\text{CHF}}}{D} = \text{Constant} Ca^{0.5} \; , \tag{F-324}$$

which is the same type of formulation developed by Obot and Ishii (Ref. F-85.) for their flow-regime map.

So far, we have discussed the transition-boiling region for upflow conditions. In computer code calculations, as well as in integral experiments, the vapor and/or liquid can flow downward. In such situations, the capillary and Reynolds numbers become negative. As with Ishii's flow map, the transition-boiling model discussed above is not valid under downflow conditions. Until data are available for the flow regime, as well as for other thermal hydraulic behavior in downflows, the coefficient B is assumed either to be a constant or to be void-fraction dependent.

In steady-state post-CHF tests using hot patches (Ref. F-81.), the CHF point and transition boiling are downstream of the hot patch. We believe that the transition-boiling regime for such tests should be limited to a very short region. Therefore, in calculations that include hot patches, the coefficient B is multiplied by a constant to ensure that the length of the transition region is very small.

For downward flows where the capillary number becomes negative, Cons. is assumed to be a linear function of the void fraction with a proportionality constant being 250 for void fractions less than 60%. If the void fraction is higher than 0.60, Cons. is assumed to be constant, 150. The ratio of q_{film}/q_{CHF} is taken to be 1.2×10^{-10}. These values are obtained to best fit the CCTF Run-14 data. The constants used in other correlations (Webb-Chen) are those given in the reference cited. The dimensions used for the variables yield HTCs in units of $W\cdot m^{-2}\cdot K^{-1}$ and heat fluxes in units of $W\cdot m^{-2}$.

F.2.2.3.4. Model as Coded. For the transition-boiling regime, most of the calculations are carried out in subroutine HTVSSL. Subroutines CHEN, CHF, CHF1, HLFLMR, and HVWEBB are called as needed to evaluate the nucleate-boiling HTC, CHF, the CHF temperature (T_{CHF}), the film-boiling liquid HTC, and the film-boiling vapor HTC, respectively. A number of tests are made in subroutine HTVSSL to determine if the transition-boiling regime exists. The tests involve three basic considerations: (1) occurrence of CHF, (2) axial distance, and (3) void fraction. The first consideration is relatively simple and determines that CHF has been exceeded if $T_w > T_{CHF}$ (based on temperature) or $q_{nucb} > q_{CHF}$ (based on heat flux).

The second consideration involves several steps. The first step is to use a criterion of maximum possible distance past the CHF point in an effort to save computational time. For transition boiling to be possible, this criterion requires that $z - Z_{CHF} < Z_{TR,max}$. If transition boiling is thus possible, the next step is to check whether $q_{TR} > q_{film}$. If so, transition boiling occurred at that particular z.

The third consideration involves a test on the void fraction to ensure continuity in the high-void region as the flow turns into single-phase vapor. If $\alpha > \alpha_{cut}$ (with α_{cut} =0.995, defining single-phase vapor flow), q_{TR} is reevaluated as follows to ensure a smooth transition between flow regimes:

$$q'_{TR} = q_{TR}\frac{(\alpha_3 - \alpha)}{(\alpha_3 - \alpha_{cut})} + h_{gsav}(T_w - T_g)\frac{(\alpha - \alpha_{cut})}{(\alpha_3 - \alpha_{cut})} , \quad \text{(F-325)}$$

where $\alpha_3 = 0.9999$.

Also, if $\alpha > \alpha_3$, the wall-to-vapor HTC, h_{wg}, is interpolated to ensure a smooth transition between flow regimes using the following relationship:

$$h_{wg} = h_{wg} + (h_{gsav} - h_{wg})\frac{(\alpha - \alpha_3)}{(\alpha_2 - \alpha_3)} , \quad \text{(F-326)}$$

where

$$\alpha_2 = 1.0 .$$

This ensures that the vapor HTC approaches that for the convective heat transfer to single-phase vapor, h_{gsav}, at high void fractions.

F.2.2.3.5. Weighting, Limits, and Averaging. The maximum transition-boiling heat flux is limited by the q_{CHF} while the minimum transition-boiling length is 1×10^{-6} m. The coefficient Cons. is limited by a minimum of 50 and a maximum of 2000. Interpolation is used to ensure a smooth transition to the single-phase vapor HTC at high void fractions. No rate limits are used. Limits are imposed on mass flow in the Biasi correlation for CHF and are discussed in Section F.2.1.8.

F.2.2.3.6. Assessment of the Correlation. The major assumption made in implementing the equations for the heat flux in the transition-boiling regime is that the heat flux can be modeled as an exponentially decreasing function. The heat flux is forced to decrease over the axial elevation from q_{CHF} to q_{film}. The wall-temperature history of a quenching hot rod (Ref. F-81.) indicates that the wall temperature also increases sharply with the axial distance downstream of the quench front. If the quench-front velocities are constant when a particular small region experiences transition boiling, a temperature-time plot (at a particular elevation) can be converted to a temperature-axial distance plot by multiplying the time by the quench-front velocity (chain rule). Thus, the wall temperature increase downstream of the quench front can be represented by a function logarithmic in nature (except within a few millimeters of the quench front). The transient heat balance calculation then gives an axial-heat-flux profile indicating that it decreases sharply from q_{CHF} to q_{film}, as shown by Unal in Ref. F-81.. The comparisons of the calculated and measured axial wall heat-flux profiles obtained from a developmental assessment run for Lehigh rod-bundle data (Ref. F-83.) are shown in Fig. F-58., which shows reasonable agreement. (See also Ref. F-82. for additional discussion of the Lehigh rod-bundle work.)

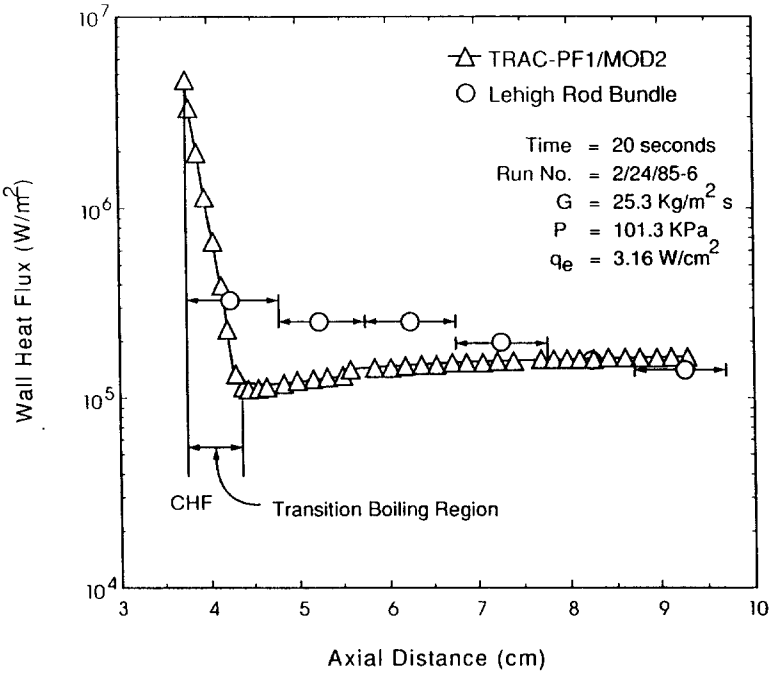

Fig. F-58. The calculated and measured axial wall heat-flux profiles for a Lehigh rod bundle test.

F.2.2.3.7. Scaling Considerations. The equation for calculating h_{wg} was based mostly on data from tubes (Ref. F-84.). The validity of using these data to calculate rod-bundle transition-boiling heat transfer has not been demonstrated. The variation of the transition-boiling heat flux with the axial distance is controlled by thermal-hydraulic conditions at the quench-front location (Ref. F-81.). Thus, coefficients defining the heat-flux profile should be functions of local thermal-hydraulic conditions at the quench front. Currently, these coefficients are assumed to be constant. In the future, code improvement efforts should consider more phenomenological modeling of the position-dependent transition boiling, for upflow and downflow conditions, and for rod bundles as well as single-tube geometries.

F.2.2.3.8. Summary and Conclusions. The major assumption used in the transition-boiling model is that the transition-boiling heat flux decreases exponentially with the axial distance downstream of the quench front. This approach eliminates problems associated with the axial nodalization. A sensitivity study on nodalization indicates that the prediction of the quench-front velocities as well as the peak wall temperatures at a particular axial elevation are not sensitive to the selection of the axial hydro and conduction cell sizes. Significant discrepancies still exist between the predicted and measured data. Future code development should emphasize more phenomenological modeling of the transition boiling, following the concepts discussed here and in

Section F.2. This would allow the prediction of transition-boiling heat transfer in all situations, such as bottom, top quenching, and reversal flows.

F.2.2.4. Film Boiling (Regime 4). The film-boiling heat-transfer regime incorporates several different correlations to describe the HTCs in the inverted annular-flow regime as observed by Ishii and his coworkers (Refs. F-32. and F-85.). The flow-regime boundaries are determined by a capillary number based upon liquid flow rate, liquid viscosity, and surface tension at the CHF point. Additional tests in determining the flow-regime boundaries are also implemented in the model. These are based upon the predetermined maximum and minimum void fractions at flow-regime transition boundaries.

F.2.2.4.1. Basis for the Model. The film-boiling regime is assumed to occur when $T_w > T_{\mathrm{CHF}}$ and $z - Z_{\mathrm{CHF}} > Z_{\mathrm{TR}}$. The wall-to-liquid and wall-to-vapor HTCs are treated separately. The wall-to-liquid HTC, h_{wl}, is assumed to be the sum of two components: radiation and near-wall liquid effects. The near-wall effects are calculated by either the Denham (Ref. F-35.) or the modified Bromley correlations (Ref. F-63.) or a combination of these two, depending upon the type of flow regime at a particular location under consideration. The liquid HTC is given by

$$h_{wl} = (h_r + (h_{\mathrm{Denham}} \text{ or } h_{\mathrm{Bromley}})) \left(\frac{T_w - T_{\mathrm{sat}}}{T_w - T_l} \right). \tag{F-327}$$

The radiation component, h_r, is the same as Eq. (F-248) given in Section F.2.1.4.1. The film-boiling component is calculated using either the Denham or modified Bromley correlations. The modified Bromley correlation is discussed in Section F.2.1.4.1. The heat-transfer model for the inverted annular flow proposed by Denham is summarized below.

The heat conducted across the vapor film from the wall to the vapor-water interface in an inverted annular flow is given by

$$q_{wi} = k_v \frac{(T_w - T_{\mathrm{sat}})}{\delta_{vf}} , \tag{F-328}$$

where δ_{vf} is the vapor film thickness that is obtained from a force balance on the vapor film and given by Denham (Ref. F-35.) as

$$\delta_{vf} = \left[\frac{\xi \dot{m}_v \mu_v}{g(\rho_l - \rho_v)\rho_v} \right]^{1/2} . \tag{F-329}$$

The coefficient ξ depends on the velocity profile in the vapor film and is assumed to be 5. The vapor-film flow rate can be expressed in terms of vapor velocity

$$\dot{m}_v = \rho_v V_v \ . \tag{F-330}$$

Then Eq. (F-329) becomes

$$\delta_{vf} = 2.2361\left[\frac{\mu_v V_v}{g(\rho_l - \rho_v)}\right]^{1/2} \ . \tag{F-331}$$

It is assumed that the heat conducted through the vapor film, q_{wi}, goes to the liquid phase. Thus, the wall-to-liquid HTC can be obtained with the use of Denham's film thickness equation, Eq. (F-331), as

$$h_{\text{Denham}} = \frac{k_v}{\delta_{vf}} = 0.4472\left[\frac{g(\rho_l - \rho_v)}{\mu_v V_v}\right]^{1/2} k_v . \tag{F-332}$$

Subroutine HTVSSL calls subroutine HLFLMR to determine the near-wall liquid effects in Eq. (F-327). Subroutine HLFLMR returns either h_{Denham} or h_{Bromley} or a weighted combination of these two correlations depending upon the IAF regime. The selection logic of liquid HTC is explained below following the description of h_{wg}.

The wall-to-vapor HTC is obtained from the Webb-Chen correlation (Ref. F-84.). The Webb-Chen correlation is developed from a nonequilibrium database for single tubes. It is based upon the momentum-transfer analogy (as used by Chen-Sundaram-Ozkaynak, Ref. F-86.) and also considers the possible entrance-region effects and the effect of entrained liquid droplets. The wall-to-vapor HTC, h_{wg}, for the film-boiling component is given by

$$h_{wg} = h_{\text{mod-CSO}}(1 + F_s)\left(1 + 0.8\left(\frac{z}{D}\right)^{-1}\right) \tag{F-333}$$

and

$$h_{\text{mod}-\text{CSO}} = \frac{f}{2} c_{p,\,vf} G X_a Pr_{vf}^{-2/3} \ , \tag{F-334}$$

where the friction factor, *f*, is weighted by the ratio of wall to vapor temperatures and is given by

$$f = f_{cp}\left(\frac{T_w}{T_v}\right)^{-0.1} \ . \tag{F-335}$$

In Eq. (F-335), f_{cp} is the two-phase friction factor given by

$$\frac{1}{f_{cp}^{1/2}} = 3.48 - \log_{10}\left(\frac{2\varepsilon}{D_H} + \frac{9.35}{Re_v f_{cp}^{1/2}}\right), \tag{F-336}$$

where

Re_v = vapor Reynolds number = $\frac{V_v \rho_v D_H}{\mu_v}$,

ε = surface roughness, and

D_H = hydraulic diameter.

The term of $[1 + 0.8\,(z/D)^{-1}]$ in Eq. (F-333) represents the entrance-region effect on h_{wg}.

The sink function, which accounts for the effect of the entrained droplets, is given by

$$F_s = 250\left(\frac{P}{P_{cr}}\right)^{0.69}\left(\frac{1-x}{x}\right)^{0.49} Re_v^{-0.55} . \tag{F-337}$$

The wall-to-vapor HTC is weighted based upon the flow regime, as explained below. The HTC selection logic based upon the IAF flow regimes is illustrated in Fig. F-59. The locations of flow-regime boundaries and the void fractions at these locations are input to subroutine HTVSSL. Therefore, before calling HTVSSL, subroutine CORE1 calls subroutine ZCORE to determine the location of the quench-front and IAF-regime transition boundaries with corresponding void fractions. Subroutine ZCORE first determines the location of the quench front (CHF). Then, in the first pass, using old-time variables, it calculates elevations corresponding to each IAF-regime transition boundary, using Ishii and coworkers' flow-regime criteria based upon the capillary number (Ref. F-32.). These calculated elevations are shown in Fig. F-59. by Z_{SM}, Z_{RW}, Z_{AG}, and Z_{DP} for the smooth, rough-wavy, agitated, and dispersed IAF regimes, respectively. The void fractions at these elevations are obtained by linear interpolation using the derivative of the void fraction with respect to axial distance (determined by the hydro solution before subroutine CORE1 calls subroutine ZCORE). To assure that these calculated void fractions describing the flow-regime transitions are consistent with those expected to exist in IAF regimes, the following checks and corrections are done in the second pass. Using predefined void fractions (possible maximum and minimum void fractions defined as input to this model) at flow-regime transition boundaries, α_{SM}, α_{RW}, α_{AG}, and α_{DP}, and updated void fractions and the derivative of void fractions with respect to axial distance, subroutine ZCORE reevaluates the elevations at flow-regime transition boundaries and the corresponding void fractions at these elevations by linear interpolation. The linear interpolation using the fine-mesh nodes is applied from hydraulic cell center to cell center. At the end, subroutine ZCORE returns the elevations and void fractions at IAF regime transition boundaries to subroutine CORE1. Subroutine CORE1, then calls subroutine HTVSSL to determine HTCs at each particular axial elevation. The selection is described below.

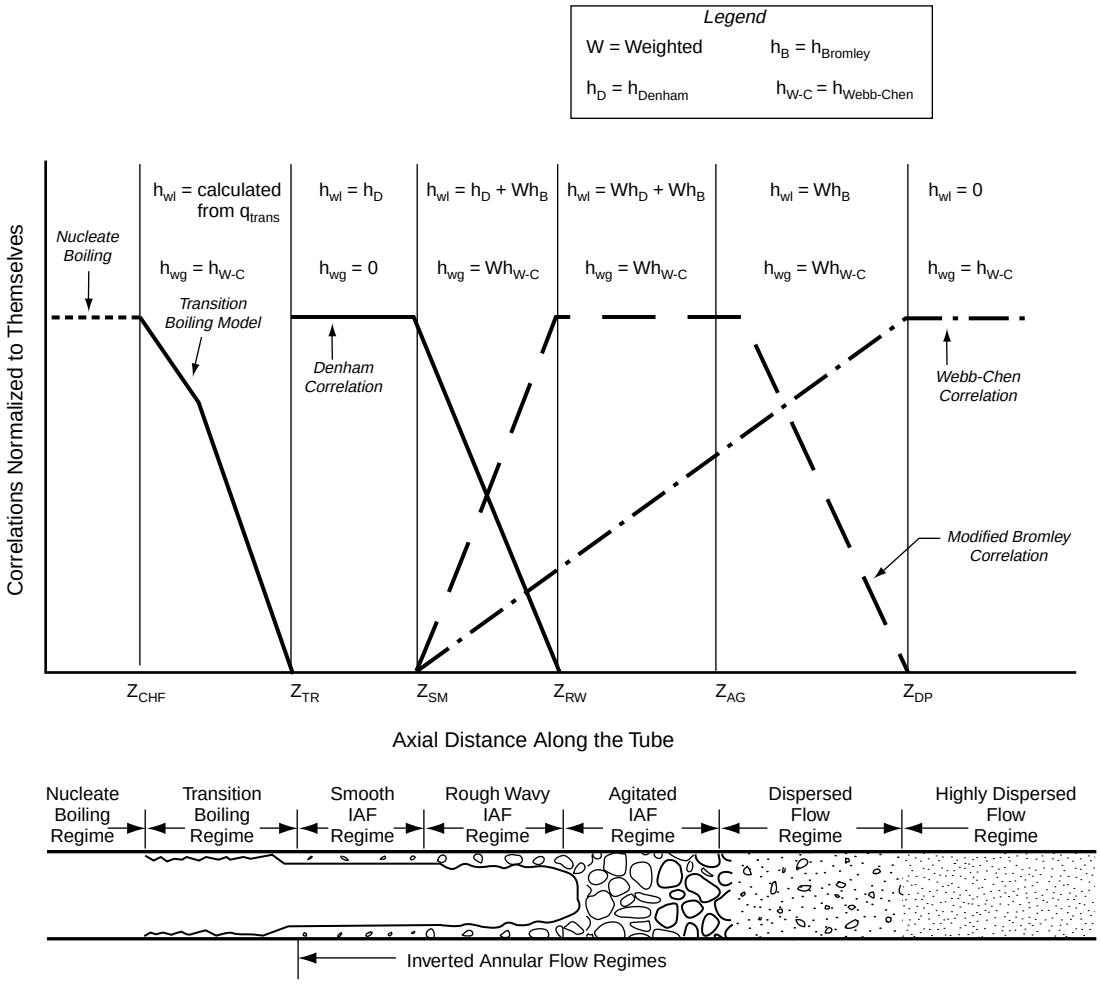

Fig. F-59. Illustration of HTCs selection logic used in the reflood model.

In the smooth IAF regime, the total heat generated by the wall is assumed to be transferred directly to the liquid interface across the vapor film surrounding the liquid core. The Denham correlation, Eq. (F-332), is used to determine the wall-to-liquid HTC. Because the total heat generated by the wall is assumed to be transferred directly to the liquid, no heat transfer to the vapor phase is assumed to occur.

In the flow regimes downstream of smooth IAF, the wall is assumed to be cooled by a combination of vapor and liquid. The Webb-Chen correlation (Ref. F-84.) is used to obtain the wall-to-vapor HTC in the remainder of the flow regimes downstream of smooth IAF.

The Webb-Chen correlation alone cannot result in the correct prediction of the heat transfer in the IAF regimes downstream of smooth IAF. Ishii (Ref. F-85.) observed the existence of a fine sheet of liquid drops/ligaments between the liquid core of the IAF

regime and the wall. From Ishii's study, it is clear that the hydrodynamic behavior in the rough-wavy and agitated IAF regimes shows a unique characteristic. Interfacial surface area is increased significantly and liquid exists near the wall, possibly in momentary contact with the wall. Hence, the heat-transfer mechanism in these flow regimes is significantly enhanced. Whereas the heat-transfer aspects of the flows were not measured by Ishii and coworkers, the existence of a post-transition-boiling region (near region) immediately downstream of the CHF point was found by Unal et al. (Ref. F-81.). The authors indicated that the evaporation of liquid is very efficient in the post-transition-boiling region, so the measured vapor temperature is close to the saturation temperature of the fluid. They hypothesized that the heat-transfer enhancement could be due to liquid / wall direct-contact heat transfer. Another mechanism that might explain this efficient process is the increase in local turbulence near the wall because of the existence of liquid droplets (Ref. F-91., F-92.).

Although either of these theories can predict heat-transfer enhancement in the IAF regimes downstream of smooth IAF, whether only one mechanism is responsible for the overall heat-transfer enhancement is not clear. Rather, it is likely that both heat-transfer mechanisms can coexist. In our model, we name this heat-transfer mechanism the "near-wall liquid" effect. We assumed that it starts at the beginning of rough-wavy IAF and gradually increases with increasing axial distance up to the agitated IAF region. In agitated flow, we postulate that the near-wall liquid effect is at a maximum due to high turbulence and some liquid-wall contact. Downstream of the agitated region, this effect gradually decreases, finally becoming negligible in highly dispersed flow (Ref. F-93.).

We consider this near-wall liquid effect through the wall-to-liquid HTC, h_{wl}. One can argue that this effect is due either to liquid / wall contact or to turbulence enhancement, where—much like Denham's model—the transport of wall energy into the vapor and then into the liquid is short-circuited because of the extremely fast and efficient transport process. Because no mechanistic model exists to predict this contribution, we selected the modified Bromley correlation (Ref. F-93.) as the "kernel" for the model. Our initial assessment attempts indicated that the magnitude of the near-wall effect for different mass and heat fluxes could not be predicted correctly by the Bromley correlation alone because this correlation depends only on the pressure and the wall temperature, a point raised several years ago by Denham. The results indicated that the near-wall effects tend to increase with increasing mass flux at a given heat flux and inlet subcooling, which is consistent with the experimental findings reported by Unal et al. (Ref. F-93., Fig. 9). They indicated that their transition region extended further downstream with an increase in vapor flux.

Therefore, for the Bromley correlation, we introduce a multiplier that depends on the vapor Reynolds number. The functional form of the multiplier was found by matching the measured wall and vapor temperatures to five of the Winfrith steady-state post-CHF tests. It was found to be a linear function of the vapor Reynolds number defined at the agitated IAF. The functional form given below gives a multiplication factor varying between 0.2 and 1.0 for a Reynolds number varying between 900 and 2300. With this

modification, low-pressure data were predicted reasonably well, whereas higher-pressure data showed an underprediction of the measured wall temperatures. This underprediction arises because the Reynolds number becomes much greater than 2300 due to the increase in vapor density with pressure. The multiplication factor always becomes 1, resulting in high wall-to-liquid HTCs at higher pressures. Therefore, a pressure-dependent exponent was introduced and applied to the Reynolds number, as summarized below. Obviously, this is an area in which phenomenological modeling is needed.

The wall-to-liquid HTC for the rough-wavy IAF regime, $Z_{SM} < z < Z_{RW}$, is given by the combination of weighted Denham and modified Bromley HTCs as

$$h_{wl} = h_{Den}\left(\frac{z - Z_{SM}}{Z_{RW} - Z_{SM}}\right)^{0.5} + h_{Brom,\,Mod}\left(\frac{z - Z_{SM}}{Z_{RW} - Z_{SM}}\right)^{0.9} , \tag{F-338}$$

where

$$h_{Brom,Mod} = F(Re_{v,AG})h_{Brom} . \tag{F-339}$$

The wall-to-vapor HTC was obtained from the Webb-Chen correlation (Ref. F-84.) as

$$h_{wg} = 1.2\left(\frac{\alpha - \alpha_{SM}}{\alpha_{DP} - \alpha_{SM}}\right)^{0.01} h_{Webb-Chen} . \tag{F-340}$$

In the agitated and post-agitated IAF regimes, $Z_{RW} < z < Z_{DP}$, the wall-to-liquid HTC is calculated by

$$h_{wl} = h_{Brom,Mod}\left(\frac{0.75 - \alpha}{0.75 - \alpha_2}\right)^{F_1(Re_{v,AG})} , \tag{F-341}$$

where

$$\alpha_2 = \min(\max(\alpha_{off1}, \alpha_{AG}), \alpha_{off3}) \tag{F-342}$$

$$F\left(Re_{v,AG}\right) = -0.51498 + 6.4895\ 10^{-4} Re_{v,AG} , \tag{F-343}$$

$$F_1\left(Re_{v,AG}\right) = 14.61 - 2.442\ 10^{-2} Re_{v,AG} + 1.4313\ 10^{-5} Re_{v,AG}^2 - 2.7787\ 10^{-9} Re_{v,AG}^3 , \tag{F-344}$$

and

$$Re_v = \left(\frac{\alpha\rho_v D_H V_v}{\mu_v}\right)_{\mathrm{AG}}^{\left(1+(1-0.95)\left(\frac{P-2\times10^5}{10\times10^5-2\times10^5}\right)\right)} \quad . \tag{F-345}$$

The weighting used in Eq. (F-341) allows h_{wl} to decrease gradually after the point where the void fraction equals α_2. This point could be in either the post-agitated region or at the end of the agitated region, depending upon the values of the predicted α_{AG}, and specified α_{off1} and α_{off2}. The respective α_{off1}, α_{off2}, and α_{off3} values were set to 0.45, 0.75, and 0.98. If ($\alpha_{\mathrm{AG}} < 0.45$), the turning point is extended to the point where the void fraction becomes 0.45. If $\alpha_{\mathrm{AG}} > \alpha_{\mathrm{off1}}$, then the turning point could be extended to a location where α equals 0.75. In the region in which ($\alpha < 0.75$), h_{wl} gradually decreases according to Eq. (F-341) and becomes zero in highly dispersed flow ($\alpha > 0.98$),

The wall-to-vapor HTC in the agitated, post-agitated, and highly dispersed IAF regions is calculated by Eq. (F-340).

If the liquid is subcooled in the film-boiling regime, an additional HTC, h_Γ, is calculated and used to separate the latent heat of evaporation effect from the sensible heat effect. The h_Γ is calculated in the following fashion.

As Denham (Ref. F-35.) indicated, the interface of the subcooled liquid becomes saturated due to condensation. Thus, the heat transfer from the saturated interface to the subcooled liquid core, q_{il}, was expressed as the conduction solution of a cylinder with a change in surface temperature. The time required by Denham's expression can be calculated as the ratio of node size to liquid velocity. The q_{il} becomes

$$q_{il} = k_l\sqrt{\frac{V_l}{\pi\alpha_l(z_t - Z_{\mathrm{TR}})}}\frac{V_l D_H^2}{V_l D_H^2 + 15\alpha_l(z_t - Z_{\mathrm{TR}})}(T_{\mathrm{sat}} - T_l) \quad . \tag{F-346}$$

The subcooled-boiling heat-transfer coefficient, h_Γ, is calculated by

$$h_\Gamma = \frac{h_{wl}(T_w - T_l) - q_{il}}{T_w - T_l} \quad . \tag{F-347}$$

This h_Γ is calculated in all IAF regimes except in highly dispersed flow. In the highly dispersed flow ($\alpha > 0.98$), h_Γ is assumed as zero.

Figure F-59. shows the selection logic for HTCs h_{wl} and h_{wg}. In this figure, the trend of each correlation in each IAF regime is shown.

F.2.2.4.2. Weighting, Limits, and Averaging. Subroutine HLFLMR limits the minimum Denham and Bromley HTCs to be 1×10^{-20}. All weightings used in Eqs. (F-338), (F-339), (F-340), and (F-341) are limited with a minimum of zero and maximum of one. If $\alpha > \alpha_3$ ($\alpha_3 = 0.9999$), the wall-to-vapor HTC, h_{wg}, is reevaluated as

$$h_{wg} = h_{wg} + (h_{g\text{sav}} - h_{wg})\frac{(\alpha - \alpha_3)}{(\alpha_2 - \alpha_3)} \ , \tag{F-348}$$

where

$$\alpha_2 = 1.0 \quad .$$

If $\alpha > \alpha_{\text{cut}}$ ($\alpha_{\text{cut}} = 0.995$) and $h_{wl} > 0$, the wall-to-liquid HTC is reevaluated as

$$h_{wl} = h_{wl} + (0 - h_{wl})\ \frac{(\alpha - \alpha_{\text{cut}})}{(\alpha_3 - \alpha_{\text{cut}})} \ . \tag{F-349}$$

The above weightings are performed to ensure that the HTCs do not show discontinuities between the single-phase and two-phase results.

No limits or weighting other than those mentioned above are applied to wall-to-vapor and wall-to-liquid HTCs in the film-boiling regime. There are also no rate limits used in the film-boiling region.

F.2.2.4.3. Assessment of the Correlations. A study was carried out with the TRAC code to select the best HTC correlations to predict post-CHF heat-transfer data. The following correlations were tried before the current reflood model was finalized:

Denham (Ref. F-35.),
Analytis and Yadigaroglu (Ref. F-87.),
Forslund and Rohsenow (Ref. F-88.),
Anderson (Ref. F-89.),
Sudo (Ref. F-90.),
Bromley (Ref. F-63.), and
Webb-Chen (Ref. F-84.).

The assessment of the Webb-Chen correlation with the nonequilibrium INEEL (Ref. F-80.) and Lehigh (Ref. F-79.) single-tube post-CHF data has been discussed in Ref. F-84. The INEEL and Lehigh post-CHF data cover the following range of parameters:

Pressure	250–7000 kPa
Mass Flux	14–100 kg / m^2-s
Heat Flux	1.3–22.5 W$\cdot$ cm^{-2}
Quality	0–0.99

The correlation does not consider subcooled inlet conditions (qualities should be higher than zero). The calculated and measured wall-to-vapor heat-transfer coefficients are shown in Fig. F-60. (from Ref. F-84.). Although there is a considerable scatter in predicted HTCs, the overall results relative to the original modified CSO correlation were significantly improved. Applicability of the Webb-Chen correlation to rod bundles has not been verified. Future code improvement efforts should address this problem.

Denham's inverted annular-flow model is developed from the Bromley model. The thickness of the vapor film is formulated as a function of the vapor mass flow rate by a force balance as in Bromley's derivation. Assessment of this model with the experimental data obtained from the REFLEX Rig at Winfrith (Ref. F-35.) is given in Figs. F-61., F-62., and F-63. (from Ref. F-35.). Figure F-61. shows the effect of the quench-front quality on the heat-transfer coefficient. The model accounts well for the effect of subcooling, as well as positive qualities. The effect of mass flux as shown in Fig. F-62. is also well accounted for in the region approximately 40 cm downstream of the quench front. The overall assessment of the model with Winfrith data is given in Fig. F-63. Ninety-five percent of the results, for which the Weber number was less than the suggested critical value of 20 for the breakdown of the inverted annular flow, agreed to within 20 $W \cdot m^{-2} \cdot K^{-1}$ plus 5%. The parametric range of the Winfrith data is as follows:

Pressure	1–4 bar
Mass Flux	2–16 g/cm^2-s
Heat Flux	1–12 $W \cdot cm^{-2}$
Inlet Subcooling	0–80˚C
Initial Temperature	600˚C

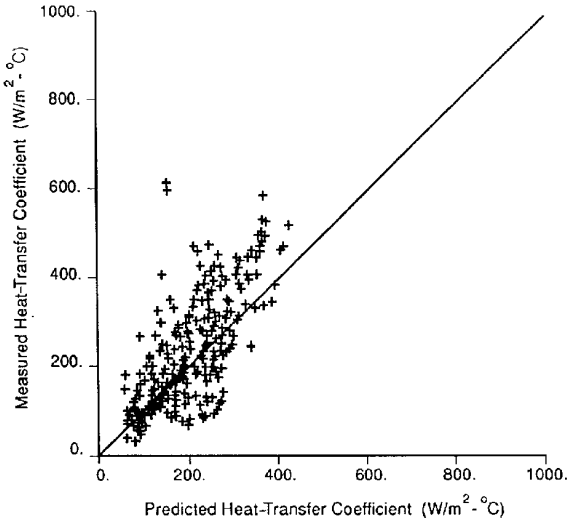

Fig. F-60. Modified heat-transfer coefficient data-model comparison for Lehigh and INEEL data (Ref. F-83.).

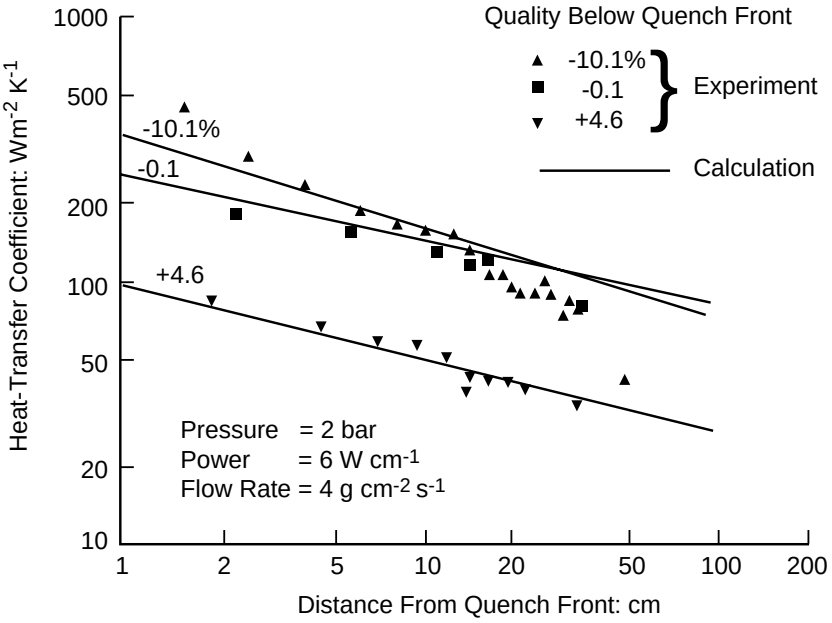

Fig. F-61. Effect of quality (Ref. F-35.).

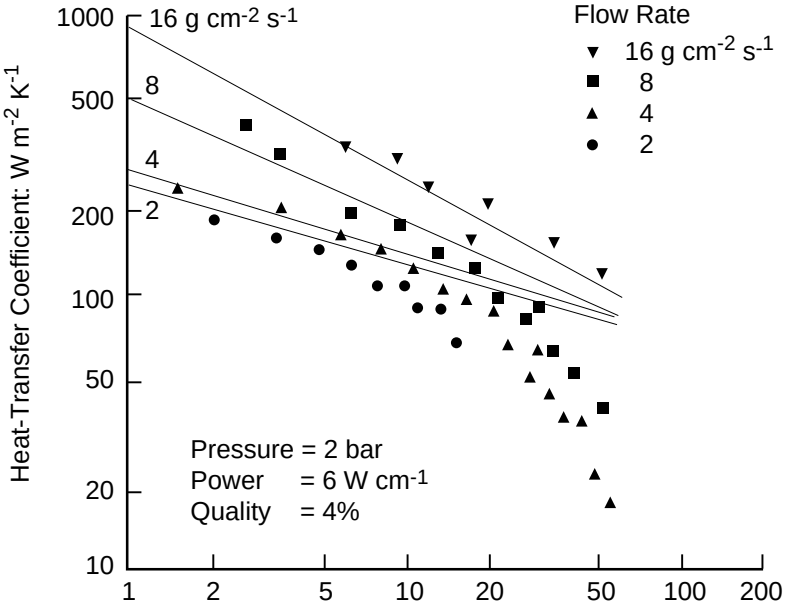

Fig. F-62. Effect of flow rate (Ref. F-35.).

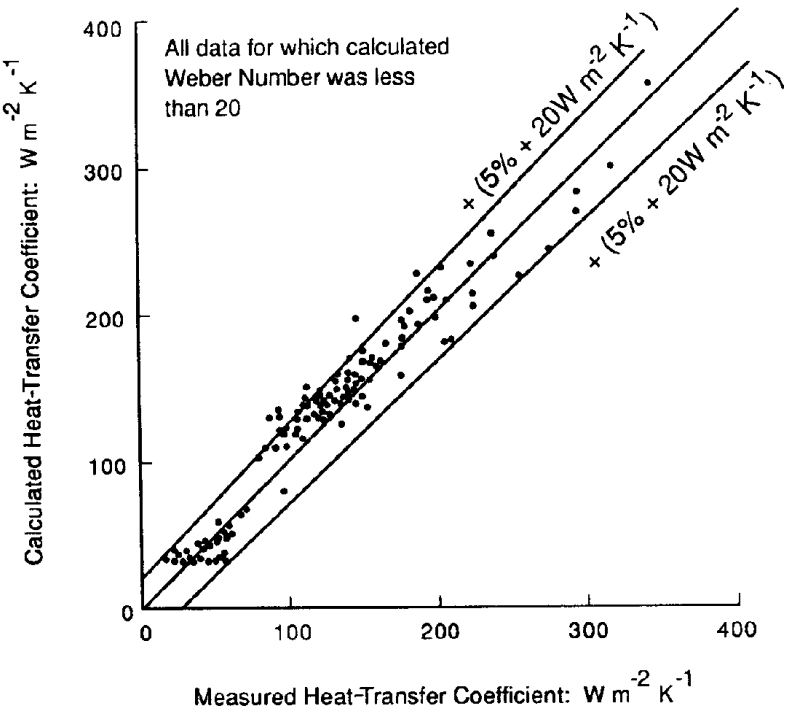

Fig. F-63. Comparison of measured and calculated heat-transfer coefficients (Ref. F-35.).

The assessment of the Denham correlation to rod-bundle data and single-tube data other than those obtained at Winfrith is not available and future code development efforts should address this problem.

F.2.2.4.4. Scaling Considerations. The Bromley correlation, a pool-boiling correlation, was developed from data for a horizontal heated cylinder. Applying it to vertical geometry in two-phase-flow film boiling is questionable, but is based upon numerous early developmental assessments. It was thought to be the best base upon which to build. The Denham correlation is developed from single-tube data, although the applicability of this correlation to rod bundles needs to be justified. The Webb-Chen correlation is developed from a nonequilibrium database for tube geometry. The validity of scaling to rod-bundle geometry has not yet been verified.

F.2.2.4.5. Summary and Conclusions. A substantial amount of data for film-boiling heat transfer, obtained mainly for simple geometries except for a few for rod bundles, is available and has been used to develop and evaluate film-boiling HTCs. Results of an evaluation of different heat-transfer correlations (Refs. F-34. and F-65.) have shown that none of the correlations predicted HTCs with sufficient accuracy over the entire post-CHF region. This further emphasizes the earlier discussion in Section F.2. concerning how the closure relationships for film-boiling equations should be determined.

The film-boiling model in TRAC was based upon correlations developed primarily from post-CHF heat-transfer data for tube geometry and assumed thermodynamic equilibrium (except the Webb-Chen correlation). The validity of scaling to rod-bundle geometry or thermodynamic nonequilibrium has not been verified. The Webb-Chen correlation for the wall-to-vapor HTC is developed from a nonequilibrium post-CHF database for single tubes. The validity of scaling to rod-bundle geometry has not been verified. Significant discrepancies still exist among different correlations and between correlations and experimental data. Future code development work should examine new experimental data and correlations for possible improvements in the film-boiling model.

The discussions contained in Section F.2. concerning the minimum film-boiling temperature and in Sections F.2.1.3. and F.2.1.9. should be reviewed in connection with this section.

F.2.2.5. Single-Phase Vapor (Heat-Transfer Regime 6). The case of convective heat transfer to a single-phase vapor is described by heat-transfer regime 6. Correlations, constants, weighting, and coding used in subroutine HTVSSL are exactly the same as those used in subroutine HTCOR and given in Section F.2.1.5. Subroutine HTVSSL will evaluate this regime when the void fraction is ≥0.995.

F.2.2.6. Condensation (Heat-Transfer Regime 11). All correlations used in heat-transfer regime 11 are well known and have been applied to a wide variety of fluids and geometries. Correlations, constants, weighting, and coding in subroutine HTVSSL are exactly the same as those used in subroutine HTCOR and given in Section F.2.1.6.

F.2.2.7. Two-Phase Forced Convection (Heat-Transfer Regime 7). This heat-transfer regime is unique in that it is not part of the boiling curve discussed. The regime is used only when the input flag ICHF=0. The liquid and vapor HTCs, h_{wl} and h_{wg}, are calculated from regime 7 only. Correlations, constants, weighting, and coding are exactly the same as those used in subroutine HTCOR and given in Section F.2.1.7.

F.2.2.8. Critical Heat Flux. The CHF is required to define the boundary between nucleate and transition boiling. Subroutine HTVSSL calls the same subroutines that are called by subroutine HTCOR to determine CHF, as explained in Section F.2.1.8.

F.2.3. TRAC-Data Comparisons

In the total- and phasic-wall-heat-flux portion of Section F.2., we indicated that comparison calculations are used with numerous experiments (including some of the older separate-effects experiments where data were reduced using the equilibrium assumption) to ensure that the correct amount of energy was being extracted from the wall. This is done because many modifications have been made to what were basically equilibrium mixture heat-transfer correlations to use them in a two-phase two-fluid model. The phasic heat fluxes and their relationship to the total heat flux were given by Eqs. (F-185) through (F-187). Many of these comparisons (typically called assessments) have been made to large-scale systems, such as LOFT (Loss-of-Fluid Test), SCTF

(Slab Core Test Facility), CCTF (Cylindrical-Core Test Facility), and UPTF (Upper-Plenum Test Facility). Whereas these comparisons give an assessment of the code's overall ability, it is frequently difficult, if not impossible, to separate the coupling that exists among all the closure relations. Even the nonequilibrium, separate-effects experiments performed to date do not provide the detailed information necessary. Thus, whereas we know how well a given wall temperature (and, therefore, heat flux) may be predicted, we do not know the corresponding hydraulic conditions well enough to ensure that this prediction is being obtained from the right conditions. Therefore, whereas this assessment is useful, it does not provide direct evidence as to the capability of the wall heat-transfer models discussed in Section F.2.

Whereas the nonequilibrium separate-effects experiments noted above do have the problem indicated, they can be used to provide an assessment of the models because of the greater confidence in the boundary conditions being applied to the test apparatus. This section will not look at any flow regimes other than the post-CHF regime because it is the only one that has had experimental work done to investigate the thermal nonequilibrium effects. Thermal nonequilibrium effects are very significant in terms of correct modeling of the heat transported by convection into the fluid. Two other regimes where thermal nonequilibrium is of importance are condensation and subcooled boiling. These regimes are investigated in Section F.1. in terms of the interfacial heat transfer. Mechanical nonequilibrium has not been studied in terms of its relationship to wall heat transfer, and whereas parametric studies can be done, no direct comparisons can be made.

TRAC calculations have been compared to the results of four post-CHF experiments. One of the databases was generated at the Idaho National Engineering and Environmental Laboratory (INEEL) and three other databases were generated at Lehigh University (LU). These data were chosen because they represent the only thermal nonequilibrium data available having a high degree of confidence in the measured superheated vapor temperature. The four databases represent a total of 1719 data points. A brief description of each of the four experiments follows.

F.2.3.1. LU: Evans, Webb, and Chen. Forced-convection, nonequilibrium post-CHF experiments were conducted at LU for water flowing upwards within a vertical Inconel tube of 15.4-mm i.d. with a heated length of 135.0 cm. The tests utilized a slow reflood process during which wall temperature and nonequilibrium vapor temperature were obtained as functions of distance from the quench front. In all the runs, the quench-front velocity was sufficiently slow to satisfy the criterion for quasi-steady-state thermal conditions downstream of the quench front. The test pressure varied from 0.24 to 0.57 MPa, mass flux ranged from 13.0 to 85.0 kg/m^2-s, inlet vapor quality varied from 0% to 70%, and the range of wall heat fluxes was 18.0 to 58.0 $kW \cdot m^{-2}$. The tests are described in Ref. F-79.

F.2.3.2. INEEL. Forced-convection, nonequilibrium, post-CHF heat-transfer experiments were conducted at INEEL for water flowing upwards within a vertical tube. Steady-state (fixed-quench-front) tests similar to those run at LU were conducted at

pressures of 0.2 to 0.7 MPa, mass fluxes of 12.0 to 24.0 kg/m^2-s, test section inlet qualities of 38% to 64%, and heat fluxes of 7.7 to 27.5 $kW \cdot m^{-2}$. Quasi-steady-state (slow-moving quench front) experiments also were run with test section inlet qualities of 7% to 47% and heat fluxes of 8.0 to 225.0 $kW \cdot m^{-2}$. Eighty-three steady-state and 683 quasi-steady-state heat-transfer data points were reported. The test section was an Inconel-625 seamless tube (19.14-mm o.d., 15.70-mm i.d.) with a heated length of 213.4 cm. High-pressure test results are given in Ref. F-80.

F.2.3.3. LU: Rod Bundle. Forced-convection, nonequilibrium, post-CHF experiments were conducted at LU for water flowing upwards within a rod bundle consisting of a square array of nine Inconel-600 rods of 9.5-mm o.d. surrounded by a square shroud. The pitch of the rods was 12.6 mm, which provided a rod-to-rod gap of 3.1 mm. The distance between the shroud surface and the nearest row of rods was chosen to obtain thermal-hydraulic conditions similar to those of a PWR. The heated section was 122.0-cm long.

Two separate databases were generated from these LU rod-bundle experiments. Moving-quench-front (276 data points) and fixed-quench-front (98 data points) experiments were run and reported as two sets of data. For the advancing-quench-front data, the pressure range was 0.1 to 0.12 MPa, the mass flow range was 7.08 to 26.15 $kg \cdot m^{-2} \cdot s^{-1}$, wall heat fluxes ranged from 11.47 to 45.15 $kW \cdot m^{-2}$, and equilibrium inlet qualities varied from –1.6% to 69%. For the fixed-quench-front data the pressure range was 0.1 to 0.127 MPa, mass flows varied from 8.44 to 29.51 kg/m^2-s, heat fluxes varied from 14.45 to 43.31 $kW \cdot m^{-2}$, and equilibrium inlet qualities varied from 0.6% to 40%. Detailed descriptions of both the fixed and advancing quench-front experiments for the rod bundles are given in Ref. F-81.

F.2.3.4. Method of Comparison. In making a code comparison to data such as these four data sets, we have the following three choices:

1. We can model the test section and apply the proper hydraulic boundary conditions (inlet flow conditions and pressure) and the power to the test rod(s). For the bundle, the test rods must be modeled separately. The measured wall temperatures would be compared to the predicted ones.
2. Here we can do the same as (1) but specify the wall temperature history for the measured levels. (This requires internal modification to the code.) The measured heat fluxes would be compared to the predicted ones. This eliminates the conduction solution in the code and removes the problem caused by slight energy imbalances. These energy imbalances may cause the quench of some steady-state experiments when only an insignificant but excess amount of energy is being calculated as being convected into the fluid. When this happens, a quench will result at some time in the calculation and a problem that is not really serious will appear to be serious.

3. Local-conditions-type calculations can be made (see Section F.2.). These calculations remove the coupling between the different closure relations that will still be part of choices (1) and (2). This, however, requires either the definition of a slip relationship or a parametric study of the effects of slip between the phases.

Because we wish to study only the wall heat-transfer closure relations themselves, we have chosen the third method.

TRAC-calculated results and the data were compared in the following manner. The experimental data provided the thermal-hydraulic conditions at the location of the vapor probe. These conditions were supplied to TRAC subroutine HTCOR, which determined values for the vapor and liquid HTCs. It should be emphasized that the experimental apparatus was not modeled with the TRAC code to simulate the conditions in the test section, i.e., neither method (1) nor method (2) was used. Only local test conditions were supplied to subroutine HTCOR. The call statement to subroutine HTCOR requires that a number of thermodynamic parameters be supplied in addition to the data available from the database. It was necessary to write a driver program to read the thermal-hydraulic information from the databases and to calculate the additional information required by subroutine HTCOR. A number of other subroutines and functions from TRAC were also incorporated into the driver program to compute the additional input required by HTCOR.

To calculate the void fraction from the known experimental quality, it is necessary to know the slip ratio. Because this parameter is not known, a set of parametric calculations was made for slip ratios of 1.0, 5.0, 10.0, and 20.0. Subroutine HTCOR returns values for the liquid HTC, h_{wl}, and the vapor HTC, h_{wg}. The heat transfer from the wall to the liquid, q'_{wl}, and the heat transfer from the wall to the vapor, q'_{wg}, are then calculated from the following equations:

$$q'_{wl} = h_{wl}(T_w - T_{sat}) \tag{F-350}$$

and

$$q'_{wg} = h_{wg}(T_w - T_g) \ . \tag{F-351}$$

The total TRAC HTC, which is compared to the experimental HTC, is then calculated as

$$h_{total} = (q'_{wl} + q'_{wg}) / (T_w - T_g) \ . \tag{F-352}$$

F.2.3.5. Results of Comparisons. Figures F-64. to F-78. show the TRAC data-comparison plots for the four databases. Figures F-64. to F-66. are plots of the experimental HTC and the calculated HTC for each of the databases for a slip ratio of 1.0. For the INEEL database (Fig. F-64.), it can be seen that several calculated HTCs are much greater than the experimental values. These points generally represent data points

where the fractions were lowest. The databases for the Evans-Webb experiment and the rod-bundle experiment with the advancing quench front (Figs. F-65., F-66.) cover a relatively narrow void-fraction range ($\alpha > 0.99$) and the comparisons with the TRAC predictions are much better than for the INEEL data. The comparison with the rod-bundle data with a fixed quench front indicates that TRAC underpredicts the HTC for a slip ratio of 1.0 (Fig. F-67.). For a slip ratio of 5.0, the comparison is much better (Fig. F-68.). Results from the Evans-Webb experiment indicate that there is a zone near the quench front where the vapor generation is quite high (Ref. F-79.). When the vapor probe location is close to the quench front, the high vapor-generation rate can result in slip ratios larger than unity. In this case, the TRAC results would correlate better with the data if a larger slip ratio were assumed.

Figures F-69. to F-71. are plots of the ratio of the TRAC HTC to the experimental HTC as a function of void fraction at the vapor-probe location assuming a slip ratio of 1.0. It can be seen that at high void fractions, the HTC ratio is approximately unity and the points are grouped quite closely. For the INEEL data (Fig. F-69.), the scatter becomes greater as the void fraction decreases; TRAC overpredicts the experimental HTC by as much as a factor of 10 for void fractions less than 0.95. For the other databases, the range of the experimental parameters is much smaller and most of the void fractions are greater than 0.99. TRAC predictions in these cases are close to the experimental values. At the lower void fractions, the contribution from the wall to the liquid heat transfer dominates, and the HTC is overpredicted.

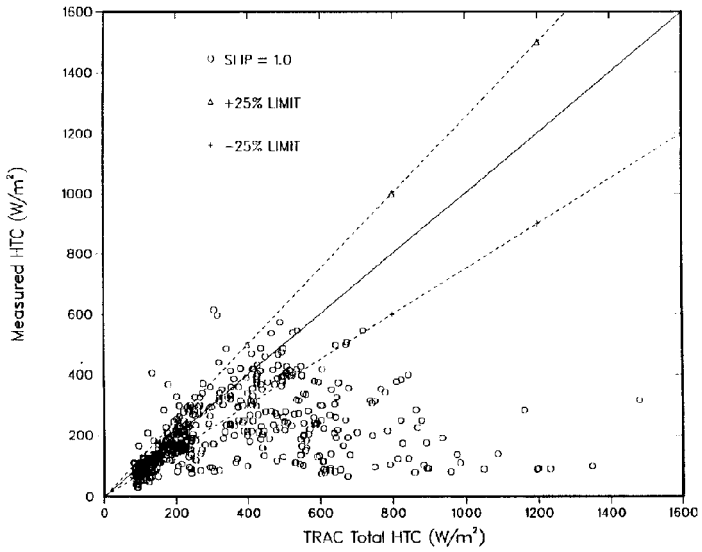

Fig. F-64. INEEL data comparison: experimental HTC vs. TRAC total HTC, slip ratio = 1.0.

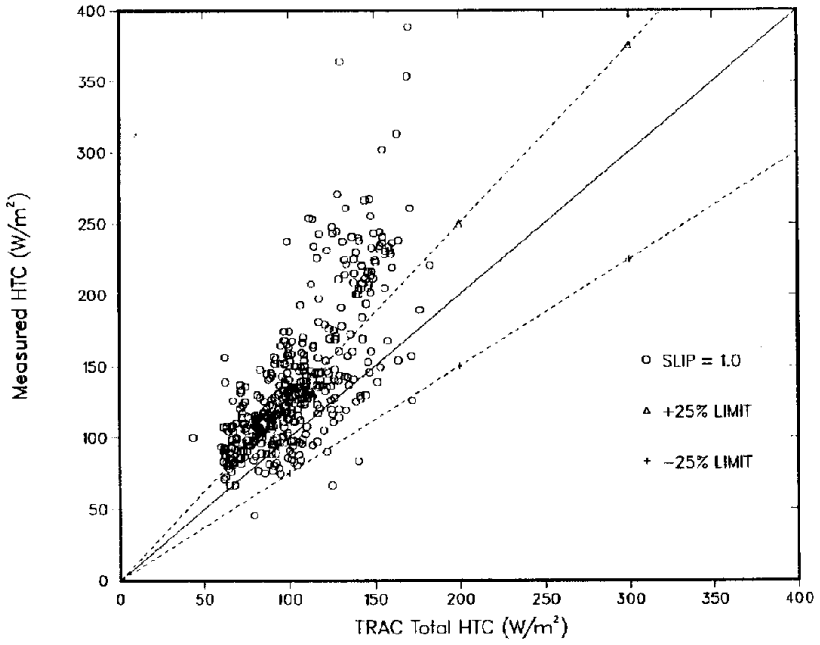

Fig. F-65. Evans-Webb data comparison: experimental HTC vs. TRAC vs. total HTC, slip ratio = 1.0.

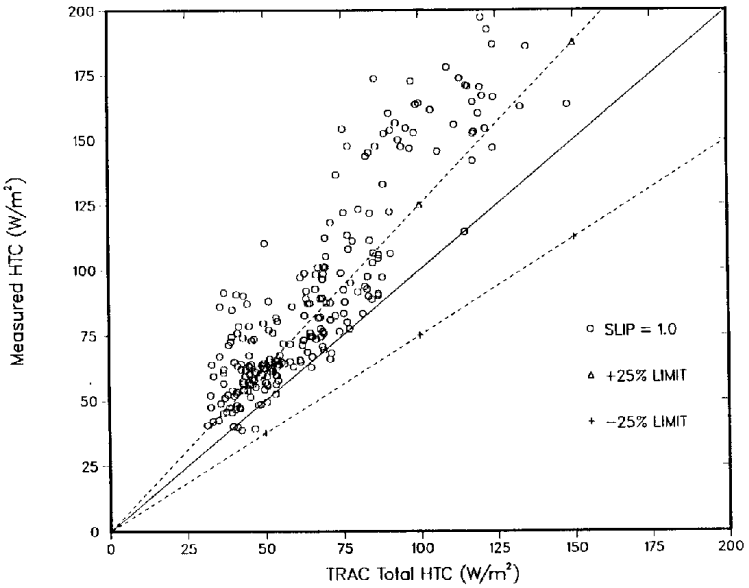

Fig. F-66. LU rod-bundle data comparison: experimental HTC vs. TRAC total HTC, advancing quench front, slip ratio = 1.0.

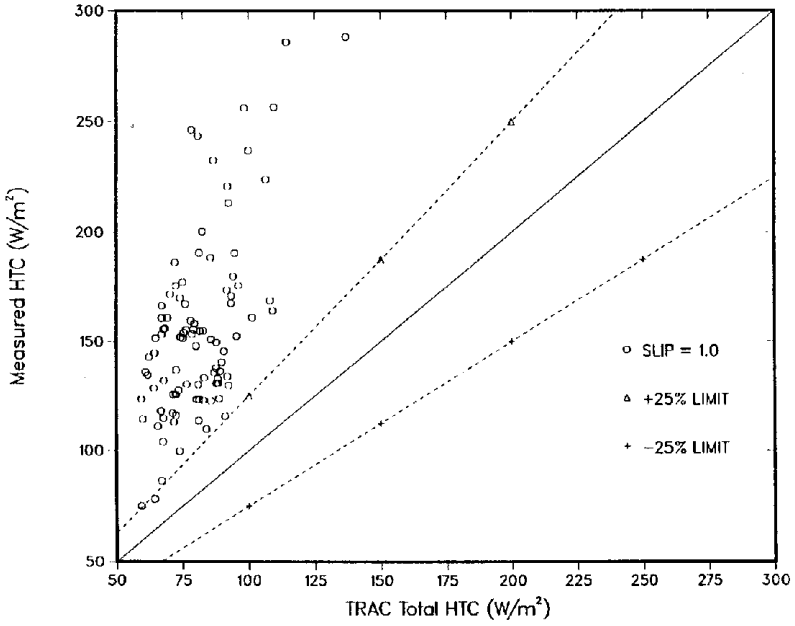

Fig. F-67. LU rod-bundle data comparison: experimental HTC vs. TRAC total HTC, fixed quench front, slip ratio = 1.0.

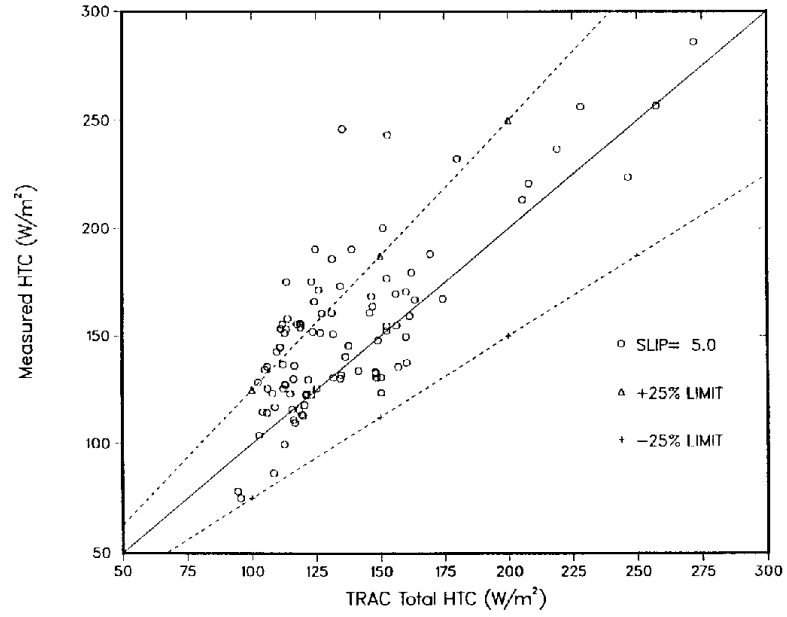

Fig. F-68. LU rod-bundle data comparison: experimental HTC vs. TRAC total HTC, fixed quench front, slip ratio = 5.0.

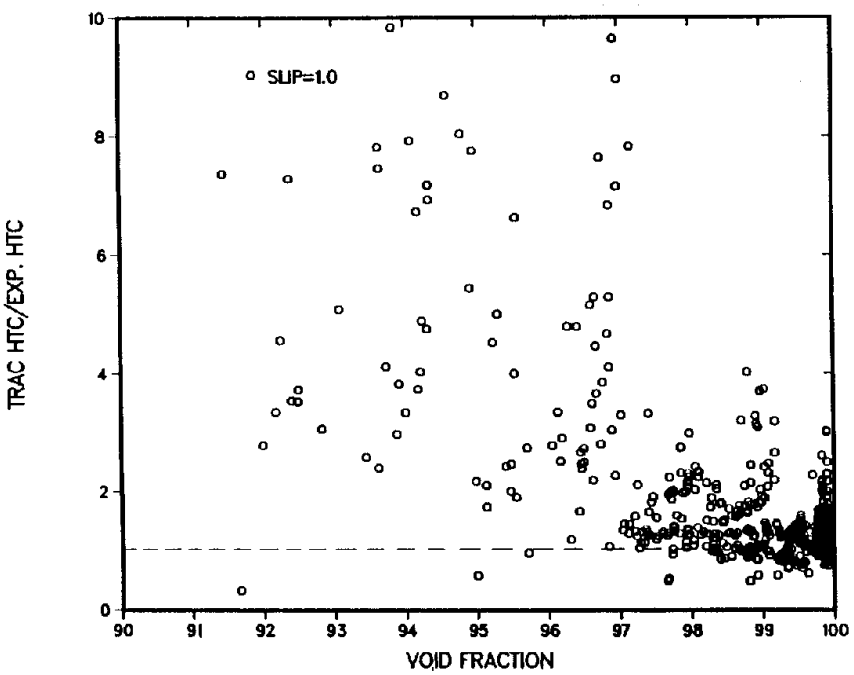

Fig. F-69. INEEL data comparison: ratio of TRAC total HTC to experimental HTC vs. void fraction, slip ratio = 1.0.

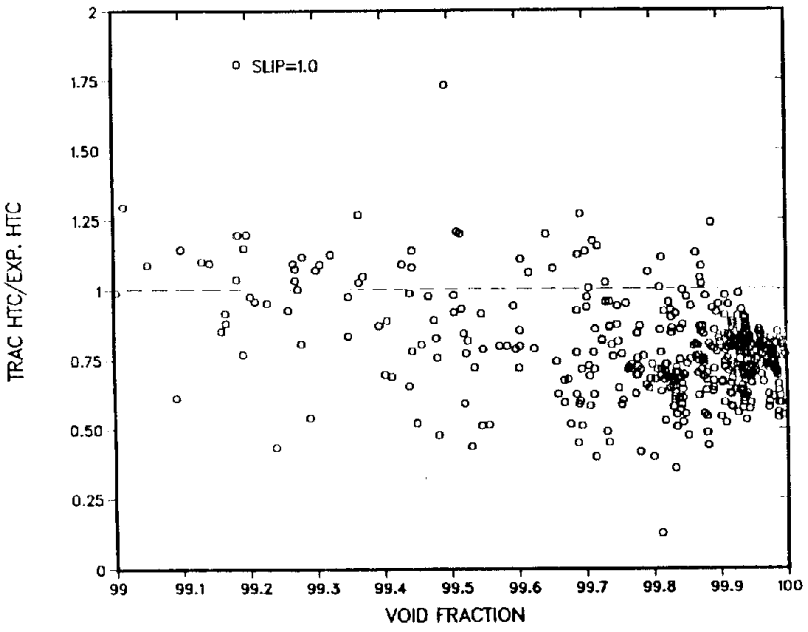

Fig. F-70. Evans-Webb data comparison: ratio of TRAC total HTC to experimental HTC vs. void fraction, slip ratio = 1.0.

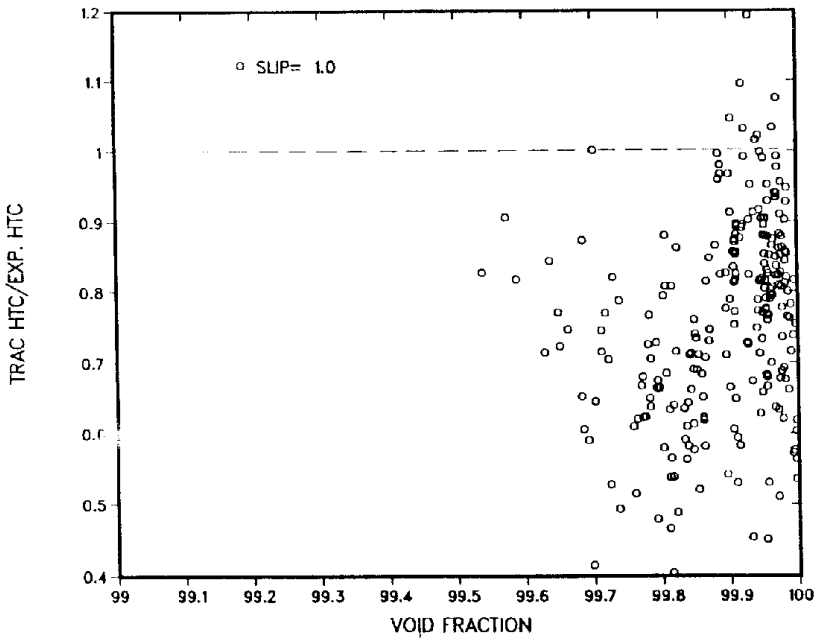

Fig. F-71. LU rod-bundle data comparison: ratio of TRAC total HTC to experimental HTC vs. void fraction, advancing quench front, slip ratio = 1.0.

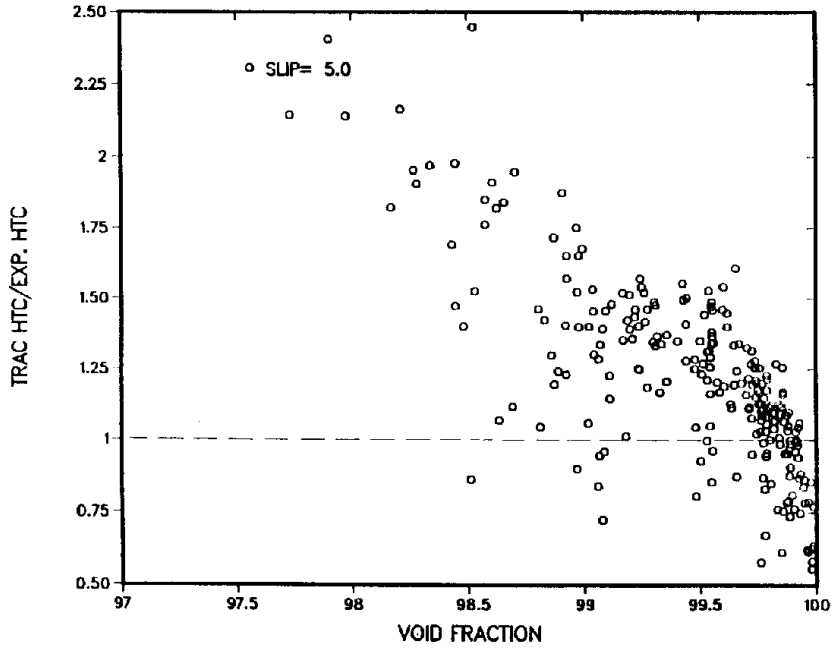

Fig. F-72. LU rod-bundle data comparison: ratio of TRAC total HTC to experimental HTC vs. void fraction, advancing quench front, slip ratio = 5.0.

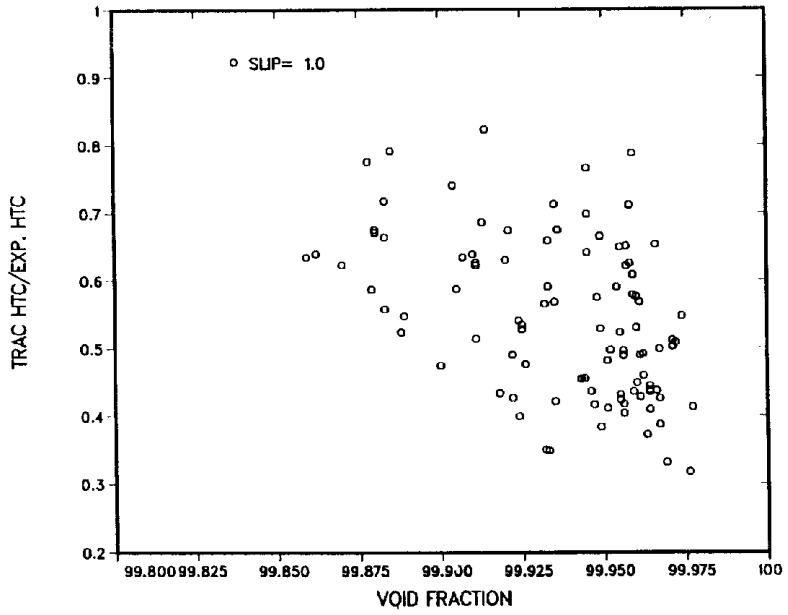

Fig. F-73. LU rod-bundle data comparison: ratio of TRAC total HTC to experimental HTC vs. void fraction, fixed quench front, slip ratio = 1.0.

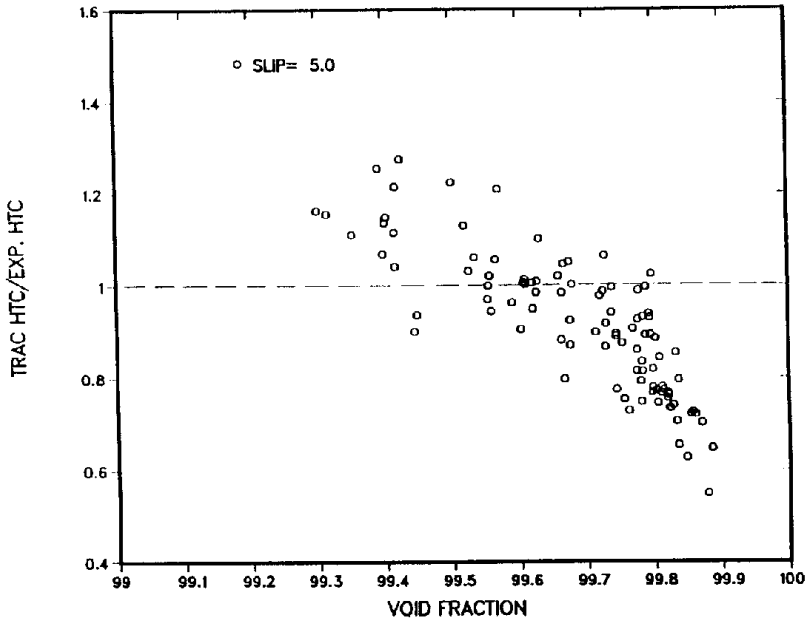

Fig. F-74. LU rod-bundle data comparison: ratio of TRAC total HTC to experimental HTC vs. void fraction, fixed quench front, slip ratio = 5.0.

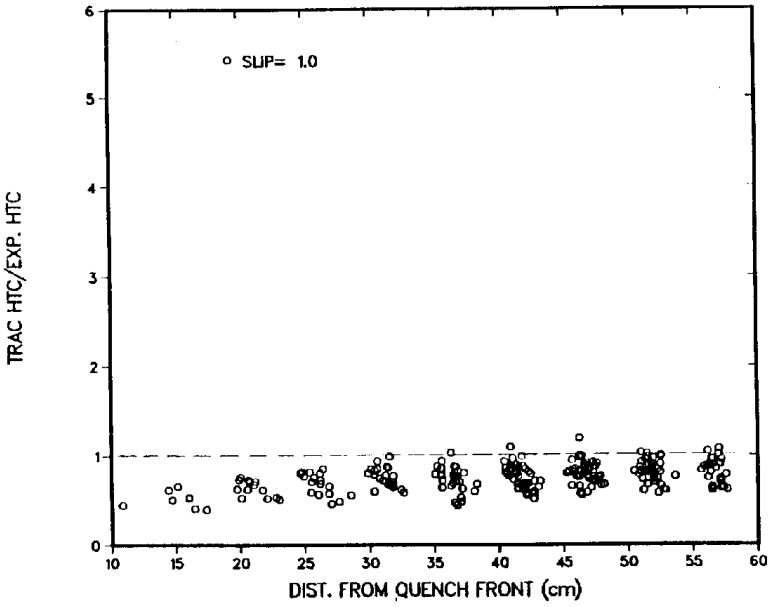

Fig. F-75. LU rod-bundle data comparison: ratio of TRAC total HTC to experimental HTC vs. distance from quench front, advancing quench front, slip ratio = 1.0.

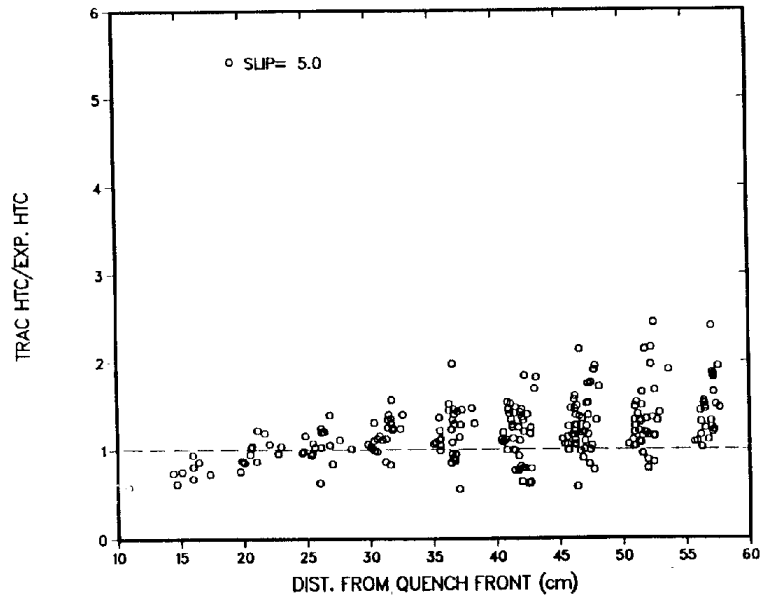

Fig. F-76. LU rod-bundle data comparison: ratio of TRAC total HTC to experimental HTC vs. distance from quench front, advancing quench front, slip ratio = 5.0.

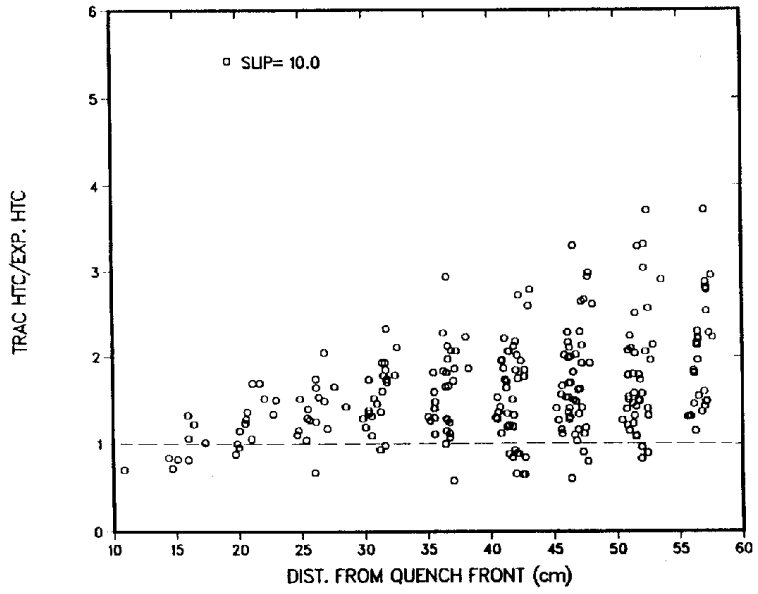

Fig. F-77. LU rod-bundle data comparison: ratio of TRAC total HTC to experimental HTC vs. distance from quench front, advancing quench front, slip ratio = 10.0.

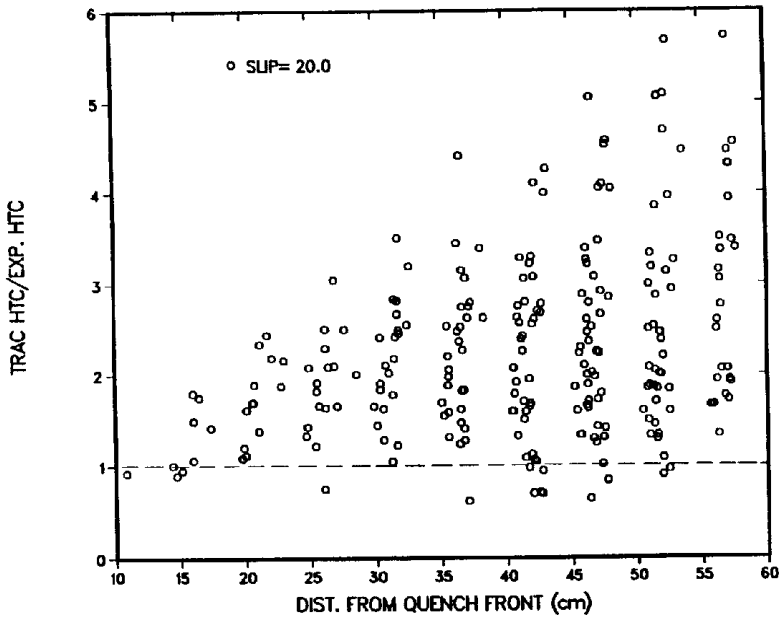

Fig. F-78. LU rod-bundle data comparison: ratio of TRAC total HTC to experimental HTC vs. distance from quench front, advancing quench front, slip ratio = 20.0.

Figures F-72. to F-74. show the sensitivity of the TRAC HTC to the void fraction. It can be seen that for a slip ratio of 1.0, the TRAC HTC is less than the experimental HTC for almost all of the LU rod-bundle data points. When the slip ratio is assumed to be 5.0 (void fraction decreases), the TRAC HTC is greater than the experimental HTC for most data points for the advancing quench front and for approximately one-third of the data points for the fixed quench front.

Figures F-75. to F-78. show the ratio of the TRAC HTC to the experimental HTC as a function of the distance between the vapor probe and the quench front for the LU rod-bundle data with an advancing quench front. The slip ratios are 1.0, 5.0, 10.0, and 20.0. Close to the quench front, the comparison between the calculations and the experimental data improves as the slip ratio increases, which is a consequence of the high vapor-generation rate close to the quench front resulting in a slip ratio greater than 1.0. For a slip ratio of 1.0, the TRAC predictions are grouped quite closely and are in reasonable agreement with the data when the vapor probe is far from the quench front. As the slip ratio increases, the HTCs predicted by TRAC become very scattered and reach values that are as much as six times as large as the experimental values. However, as the slip is increased, the data groups near the quench front are shifted from below 1.0 up through 1.0, indicating again an apparent increasing slip closer to the quench front. Similar trends can be seen in the other data sets. There is nothing in the TRAC correlations to correlate this distance effect and the trend is to overpredict the HTCs. *The distance effect must* be represented by the correct slip being allowed by the interfacial-drag correlation, as discussed in Appendix H. Again, this reflects the tight coupling that can exist between the different closure relationships.

Most experimental data points reported in the four databases examined were taken at very high void fractions–higher than are present during the reflood portion of large-break LOCAs. The CCTF and SCTF tests analyzed using TRAC indicated that even though the void fractions predicted in the upper half of the core were too high, the predicted cladding temperatures were reasonably good. This implies that the heat transfer predicted by the TRAC code exhibits too much sensitivity to void fraction.

F.2.4. TRAC-Data Comparison of the Reflood Model

The TRAC-data comparison of the reflood model coded in subroutine HTVSSL is discussed in Refs. F-94., F-95., and F-96. It uses method 1 as discussed in Section F.2.3.4. The independent data comparison available in these references considered steady-state Winfrith (Ref. F-97.) tests as well as transient Berkeley reflood tests (Ref. F-98.). The results presented were obtained with the earlier version of 5.3.

The results presented in Refs. F-94., F-95., and F-96. indicated that the thermal-hydraulic model gave reasonable predictions of Winfrith post-CHF void fractions (Ref. F-97.) and their variation with axial distance. The relative error between predicted and measured void fractions was 10% at locations far downstream of the post-agitated IAF for a pressure range of 2–10 bar and a heat flux range of 3.6–8.03 $W \cdot cm^{-2}$. Just downstream of the post-agitated IAF, the predictions deviated by about 40% from the measured values. The predictions improved for lower pressures and higher heat fluxes. The effects of

pressure and power on the void fraction and its variation with axial distance were predicted correctly. The effect of pressure is more apparent than the effect of heat flux.

The effects of pressure and test section power on axial wall temperature for Winfrith post-CHF data are predicted reasonably well for steady-state data. A comparison of the predicted and measured wall temperatures at the beginning, middle, and end of the test tube for 20 Winfrith steady-state post-CHF tests (Ref. F-97.) indicated that the maximum average deviation in the predictions was 15.15%.

The vapor temperature for Winfrith steady-state data (Ref. F-97.) was underpredicted and the average deviation was 37.63% for 14 data points. The predicted wall temperature histories show very reasonable agreement for all the Berkeley transient reflood tests (Ref. F-98.) used in this work, indicating reasonable prediction of overall wall and interfacial heat transfer. The agreement was very good for relatively low heat fluxes. At high heat fluxes, the wall temperature trace showed some oscillations that were not seen in the experiments. Further improvements are needed for high-heat-flux conditions in which the vapor generation rate could be high or the interfacial drag model could not consider the correct void fraction effect so that the void fraction could change drastically causing large frequency oscillations in calculations.

The predicted rewetting velocity and its variation along the test tube was in reasonable agreement with measured data for all Berkeley runs (Ref. F-98.). The overall comparison of predicted and measured data indicated an average deviation of 26% and a standard deviation of 40%. These values are considered reasonable.

It was concluded that the thermal-hydraulic reflood model used in TRAC gives very reasonable results in predicting void fraction, wall temperature, and their variations with tube axial distance for Winfrith steady-state, post-CHF databases (Ref. F-97.). It is expected that assessment results will also be very reasonable for any other steady-state, post-CHF database or any other Winfrith steady-state, post-CHF test. The model also gave very satisfactory results in predicting the Berkeley reflood test data (Ref. F-98.), except for the conditions included in high heat fluxes where some disagreement between predicted and measured data existed.

REFERENCES

F-1. M. Ishii and K. Mishima, "Study of Two-Fluid Model and Interfacial Area," Argonne National Laboratory report ANL-80-111 (NUREG/CR-1873) (1980).

F-2. D. Barnea and L. Shemer, "Void Fraction Measurements in Vertical Slug Flow: Applications to Slug Characteristics and Transition," *Int. J. Multiphase Flow* **15,** 495-504 (1989).

F-3. M. Ishii, Argonne National Laboratory, Private Communication, Letter to R. Nelson, Los Alamos National Laboratory (July 1987).

F-4. I. Kataoka and M. Ishii, "Drift Flux Model for Large Diameter Pipe and New Correlation for Pool Void Fraction," *Int. J. Heat Mass Transfer* **30**, 1927-1939 (1987).

F-5. J. R. Grace, T. Wairegi, and J. Brophy, "Breakup of Drops and Bubbles in Stagnant Media," *Can. J. Chem. Eng.* **56**, 3-8 (1978).

F-6. J. Kitscha and G. Kocamustafaogullari, "Breakup Criteria for Fluid Particles," *Int. J. Multiphase Flow* **15**, 573-588 (1989).

F-7. Y. M. Chen and F. Mayinger, "Measurement of Heat Transfer at the Phase Interface of Condensing Bubbles," in *ANS Proc. 1989 National Heat Transfer Conf.* (Philadelphia, Pennsylvania, August 6-9, 1989) HTC-Vol. 4, pp. 147-152.

F-8. S. Whittaker, "Forced Convection Heat Transfer Correlations for Flows in Pipes, Past Flat Plates, Single Cylinder, Single Sphere, and Flows in Packed Bids and Tube Bundles," *AIChE J.* **18**, 361-372 (1972).

F-9. R. T. Lahey, Jr. and F. J. Moody, *The Thermal-Hydraulics of a Boiling Water Nuclear Reactor,* ANS monograph (1977).

F-10. W. M. McAdams, *Heat Transmission*, 3rd Ed. (McGraw-Hill Book Co., Inc., New York, 1954).

F-11. G. C. Vliet and G. Leppert, "Forced Convection Heat Transfer from an Isothermal Sphere to Water," *Trans. ASME, J. Heat Transfer* **83**, 163-171 (1961).

F-12. G. G. Brucker and E. M. Sparrow, "Direct Contact Condensation of Steam Bubbles in Water at High Pressure," *Int. J. Heat Mass Transfer* **20**, 371-381 (1977).

F-13. R. Clift, J. R. Grace, and M. E. Weber, *Bubbles, Drops, and Particles,* (Academic Press, New York, 1978).

F-14. B. B. Mikic, W. M. Rohsenow, and P. Griffith, "On Bubble Growth Rates," *Int. J. Heat Mass Transfer* **13**, 657-665 (1970).

F-15. I. Kataoka and M. Ishii, "Mechanism and Correlation of Droplet Entrainment and Deposition in Annular Two-Phase Flow," Argonne National Laboratory report ANL-82-44 (NUREG/CR-2885) (1982).

F-16. I. Kataoka, M. Ishii, and K. Mishima, "Generation and Size Distribution of Droplet in Annular Two-Phase Flow," *Trans. ASME, J. Fluid Engineering* **105**, pp. 230-238 (1983).

F-17. M. Ishii and K. Mishima, "Correlation for Liquid Entrainment in Annular Two-Phase Flow of Low-Viscous Fluid," Argonne National Laboratory report ANL/RAS/LWR 81-2 (1981).

F-18. M. Ishii and K. Mishima, "Droplet Entrainment Correlation in Annular Two-Phase Flow," *Int. J. Heat Mass Transfer* **32**, 1835-1846 (1989).

F-19. K. O. Pasamehmetoglu and R. A. Nelson, "Transient Direct-Contact Condensation on Liquid Droplets," *Nonequilibrium Transport Phenomena,* ASME: New York, HTD-Vol. 77, pp. 47-56 (1987).

F-20. J. D. Ford and A. Lekic, "Rate of Growth of Drops During Condensation," *Int. J. Heat Mass Transfer* **16**, 61-64 (1973).

F-21. J. Iciek, U. Cyvinska, and R. Blaszcyck, "Hydrodynamics of Free Liquid Jets and Their Influence on Heat Transfer," in *Handbook of Heat and Mass Transfer*, "Vol. 1: Heat Transfer Operations," N. P. Cheremisinoff, editor (Gulf Publishing Co., Houston, Texas, 1986) pp. 151-181.

F-22. M. Ishii, "One Dimensional Drift-Flux Model and Constitutive Equations for Relative Motion Between Phases in Various Two-Phase Flow Regimes," Argonne National Laboratory report ANL-77-47 (1977).

F-23. G. Ryskin, "Heat and Mass Transfer from a Moving Drop–Some Approximate Relations for the Nusselt Number," *Int. Comm. Heat Mass Transfer* **14**, pp. 741-749 (1987).

F-24. S. G. Bankoff, "Some Condensation Studies Pertinent to Light Water Safety," *Int. J. Multiphase Flow* **6**, 51-67 (1980).

F-25. J. C. B. Lopes and A. E. Dukler, "Droplet Size, Dynamics and Deposition in Vertical Annular Flow," (NUREG / CR-4424) (1985).

F-26. G. P. Celata, ENEA, Thermal Reactors Department, Private Communication to K. Pasamehmetoglu, Los Alamos National Laboratory (July 1989).

F-27. S. Aoki, A. Inoue, Y. Kozawa, and H. Akimoto, "Direct-Contact Condensation of Flowing Steam onto Injected Water," *Proc. 6th Int. Heat Transfer Conf.* (Toronto, Canada, 1982) Vol. 6, pp. 107-112.

F-28. H. Akimoto, Y. Kozawa, A. Inoue, and S. Aoki, "Analysis of Direct-Contact Condensation of Flowing Steam onto Injected Water with Multifluid Model of Two-Phase Flow," *J. Nucl. Sci. Tech.* **20**, 1006-1022 (1983).

F-29. J. H. Linehan, M. Petrick, and M. M. El-Wakil, "The Condensation of Saturated Vapor on a Subcooled Film During Stratified Flow," *Chem. Eng. Symp. Series* **66** (102), 11-20 (1972).

F-30. H. J. Kim, "Local Properties of Countercurrent Stratified Steam-Water Flow," US Nuclear Regulatory Commission contractor report (NUREG / CR-4417) (1985).

F-31. H. Akimoto, Y. Tanaka, Y. Kozawa, A. Inoue, and S. Aoki, "Oscillatory Flows Induced by Direct-Contact Condensation of Flowing Steam with Injected Water," *J. Nucl. Sci. Tech.* **22**, 269-283 (1985).

F-32. G. DeJarlais and M. Ishii, "Inverted Annular Flow Experimental Study," Argonne National Laboratory report ANL-85-31 (NUREG/CR-4277) (1985).

F-33. C. Unal, K. Tuzla, C. A. Tuzla, and J. C. Chen, "Vapor Generation Model for Dispersed Drop Flow," in *ANS Proc. 1989 National Heat Transfer Conf.* (August 1989), HTC-Vol. 4.

F-34. Y. Y. Hsu and R. W. Graham, "*Transport Processes in Boiling and Two-Phase Systems* (Hemisphere Publishing Corporation, Washington, 1976).

F-35. M. K. Denham, "Inverted Annular Film Boiling and the Bromley Model," AEEW-R 1590, Winfrith, Rochester (January 1983).

F-36. A. H. P. Skelland, *Diffusional Mass Transfer* (Robert E. Kreiger Publishing Co, Malabar, Florida, 1985).

F-37. G. G. Sklover and M. D. Rodivilin, "Condensation on Water Jets with a Cross Flow of Steam," *Teploenergetika* **23**, 48-51 (1976).

F-38. R. V. Shilimkan and J. B. Stepanek, "Interfacial Area in Cocurrent Gas-Liquid Upflow in Tubes of Various Sizes," *Chem. Eng. Sci.* **32**, 149-154 (1977).

F-39. G. Kasturi and J. B. Stepanek, "Two-Phase Flow-III. Interfacial Area in Co-Current Gas-Liquid Flow," *Chem. Eng. Sci.* **29**, 713-719 (1974).

F-40. J. M. DeJesus and M. Kawaji, "Measurement of Interfacial Area and Void Fraction in Upward, Cocurrent Gas-Liquid Flow," *ANS Proc. 1989 National Heat Transfer Conf.* (Philadelphia, Pennsylvania, August 6-9, 1989) HTC-Vol. 4, pp. 137-145.

F-41. G. F. Hewitt, "Liquid-Gas Systems," Chapter 2 in *Handbook of Multiphase Flow,* G. Hestroni, editor (Hemisphere Publishing Corporation, Washington, 1981).

F-42. R. A. Nelson, "Forced Convective Post-CHF Heat Transfer and Quenching," *J. Heat Trans.* **104**, 48-54 (1982).

F-43. Safety Code Development Group, "TRAC-PF1/MOD1: An Advanced Best-Estimate Computer Program for Pressurized Water Reactor Thermal-Hydraulic Analysis," Los Alamos National Laboratory report LA-10157-MS (NUREG/CR-3858) (July 1986).

F-44. "RELAP4/MOD6–A Computer Program for Transient Thermal-Hydraulic Analysis of Nuclear Reactors and Related Systems, User's Manual," Idaho National Engineering Laboratory report CDAP-TR-003 (January 1978).

F-45. I. Nukiyama, "Maximum and Minimum Values of Heat Transmitted from a Metal to Boiling Water Under Atmospheric Pressure," *J. Soc. Mech. Eng. Japan* **37** (1934).

F-46. S. C Yao and R. E. Henry, "An Investigation of the Minimum Film Boiling Temperature on Horizontal Surfaces," *J. Heat Trans.*, **100**, 260-267 (1987).

F-47. L. Y. Lee, J. C. Chen, and R. A. Nelson, "Liquid-Solid Contact Measurement Using a Surface Thermocouple Temperature Probe in Atmospheric Pool Boiling Water," *Int. J. Heat Mass Transf.*, **28**, 1415-1423 (1985).

F-48. M. T. Farmer, B. G. Jones, and R. W. Spencer, "Analysis of Transient Contacting in the Low Temperature Film Boiling Regime. Part I: Modeling of the Process," *Nonequilibrium Transport Phenomena,* ASME HTD-Vol. 77, pp. 23-29 (1987).

F-49. M. T. Farmer, B. G. Jones, and R. W. Spencer, "Analysis of Transient Contacting in the Low Temperature Film Boiling Regime. Part II: Comparison With Experiment," *Nonequilibrium Transport Phenomena*, ASME HTD-Vol. 77, pp. 39-45 (1987).

F-50. R. A. Nelson, "Mechanisms of Quenching Surfaces," in *Handbook of Heat and Mass Transfer*, "Vol. 1: Heat Transfer Operations," N. P. Cheremisinoff, editor (Gulf Publishing Company, Houston, Texas 1986), pp. 1103-1153.

F-51. J. M. Delhaye, M. Giot, and M. L. Riethmuller, *Thermohydraulics of Two-Phase Systems for Industrial Design and Nuclear Engineering* (Hemisphere Publishing Corporation, New York, 1981).

F-52. F. E. Incropera and D. P. DeWitt, *Fundamentals of Heat Transfer* (John Wiley & Sons, Inc., New York, 1981).

F-53. J. Weisman, "Heat Transfer to Water Flowing Parallel to Tubes, " *Nucl. Sci. Eng.* **6**, 79 (1959).

F-54. J. P. Holman, *Heat Transfer,* 5th ed. (McGraw-Hill Book Co., Inc., New York, 1981).

F-55. B. Gebhart, *Heat Transfer,* 2nd ed. (McGraw-Hill Book Co., Inc., New York, 1971).

F-56. H. K. Forster and N. Zuber, "Bubble Dynamics and Boiling Heat Transfer," *AIChE J.* **1**, 532-535 (1955).

F-57. J. G. Collier, *Convective Boiling and Condensation*, 2nd ed. (McGraw-Hill Book Co., Inc., New York, 1981).

F-58. A. E. Bergles, J. G. Collier, J. M. Delhaye, G. F. Hewitt, and F. Mayinger, *Two-Phase Flow and Heat Transfer in the Power and Process Industries* (Hemisphere Publishing Corporation, New York, 1981).

F-59. M. Shah, "A New Correlation for Heat Transfer During Boiling Flow Through Tubes," *ASHRAE Trans.* **82** (2), 66-86 (1976).

F-60. R. W. Bjorge, G. R. Hall, and W. M. Rohsenow, "Correlation of Forced Convection Boiling Heat Transfer Data," *Int. J. Heat Mass Transfer* **25** (6), 753-757 (1982).

F-61. K. E. Gungor and R. H. S. Winterton, "A General Correlation for Flow Boiling in Tubes and Annuli," *Int. J. Heat Mass Transfer* **29** (3), 351-358 (1986).

F-62. O. C. Jones, Jr. and S. G. Bankoff, editors, *Thermal and Hydraulic Aspects of Nuclear Reactor Safety, Volume 1: Light Water Reactor*s (ASME, New York, 1977).

F-63. L. A. Bromley, "Heat Transfer in Stable Film Boiling," *Chem. Eng. Prog.* **46** (5), 221-227 (May 1950).

F-64. Y. Lee and K. H. Kim, "Inverted Annular Flow Boiling," *Int. J. Multiphase Flow* **13** (3), 345-355 (1987).

F-65. I. Vojtek, "Investigation of Dispersed Flow Heat Transfer Using Different Computer Codes and Heat Transfer Correlations," The First International Workshop on Fundamental Aspects of Post-Dryout Heat Transfer, report (NUREG/CP-0060) (April 2-4, 1984).

F-66. R. B. Bird, W. E. Stewart, and E. N. Lightfoot, *Transport Phenomena* (John Wiley & Sons, Inc., New York, 1960).

F-67. F. Kreith, *Principles of Heat Transfer*, 3rd ed. (Harper and Row, Inc., New York, 1973).

F-68. W. M. Rohsenow and H. Choi, *Heat, Mass, and Momentum Transfer* (Prentice-Hall, Englewood Cliffs, New Jersey, 1961).

F-69. W. H. McAdams, "Vaporization Inside Horizontal Tubes-II-Benzene-Oil Mixtures," *Trans. ASME* **64**, 193 (1942).

F-70. L. Biasi, G. C. Clerici, S. Garribba, R. Sala, and A. Tozzi, "Studies on Burnout, Part 3: A New Correlation for Round Ducts and Uniform Heating and Its Comparison with World Data," *Energia Nucleare* **14**, 530-536 (1967).

F-71. D. C. Groeneveld, S. C. Cheng, and T. Doan, "1986 AECL-UO Critical Heat Flux Lookup Table," *Heat Transfer Engineering* **7**, 46-62 (1986).

F-72. J. C. M. Leung, "Transient Critical Heat Flux and Blowdown Heat Transfer Studies," Ph.D. dissertation, Northwestern University (June 1980).

F-73. P. Griffith, J. F. Pearson, and R. J. Lepkowski, "Critical Heat Flux During a Loss-of-Coolant Accident," *Nuclear Safety* **18**, 298-309 (1977).

F-74. K. O. Pasamehmetoglu, "Transient Critical Heat Flux," Ph.D. dissertation, University of Central Florida (also EIES report 86-87-1) (August 1986).

F-75. M. L. James, G. M. Smith, and J. C. Wolford, *Applied Numerical Methods for Digital Computation with FORTRAN and CSMP*, 2nd ed. (Harper and Row, Inc., New York, 1977).

F-76. R. E. Henry, "A Correlation for the Minimum Film Boiling Temperature," *AIChE Symposium Series* **138**, 81-90 (1974).

F-77. S. C. Cheng, P. W. K. Law, and K. T. Poon, "Measurements of True Quench Temperature of Subcooled Water Under Forced Convection Conditions," *Int. J. Heat Mass Transfer*, **20** (1), 235-243 (1985).

F-78. D. C. Groeneveld and J. C. Stewart, "The Minimum Film Boiling Temperature for Water During Film Boiling Collapse," in *Proc. 7th Int. Heat Transfer Conf.* (Munich, FRG, 1982), Vol. 4, pp. 393-398.

F-79. D. G. Evans, S. W. Webb, and J. C. Chen, "Measurement of Axially Varying Non-equilibrium in Post-Critical-Heat-Flux Boiling in a Vertical Tube," Lehigh University report (NUREG / CR-3363) (June 1983).

F-80. R. C. Gottula, R. G. Condie, R. K. Sundaram, S. Neti, J. C. Chen, and R. A. Nelson, "Forced Convective, Nonequilibrium, Post-CHF Heat Transfer Experiment Data and Correlation Comparison Report," Idaho National Engineering Laboratory report EGG-2245 (NUREG / CR-3193) (March 1985).

F-81. C. Unal, "An Experimental Study of Thermal Nonequilibrium Convective Boiling in Post-Critical-Heat-Flux Region in Rod Bundles," Ph.D. dissertation, Lehigh University (1985).

F-82. C. Unal, K. Tuzla, O. Badr, S. Neti, and J. C. Chen, "Convective Film Boiling in a Rod Bundle: Transverse Variation of Vapor Superheat Temperature Under Stabilized Post-CHF Conditions," *Heat Mass Transfer* **34** (7), 1695-1706 (1991).

F-83. K. Tuzla, C. Unal, O. Badr, S. Neti, and J. C. Chen, "Thermodynamic Nonequilibrium in Post-Critical-Heat-Flux Boiling in a Rod Bundle," US Nuclear Regulatory Comission report (NUREG / CR-5095, Volumes I-IV) (July 1987).

F-84. S. Webb and J. C. Chen, "A Two-Region Vapor Generation Rate Model for Convective Film Boiling," Int. Workshop of Fundamental Aspects of Post-Dryout Heat Transfer, Salt Lake City, Utah, April 1-4, 1984.

F-85. N. T. Obot and M. Ishii, "Two-Phase Flow Regime Transition Criteria in Post-Dryout Region Based on Flow Visualization Experiments," Argonne National Laboratory report ANL-87-27 (NUREG / CR-4972) (June 1987).

F-86. J. C. Chen, F. T. Ozkaynak, and R. K. Sundaram, "Vapor Heat Transfer in Post-CHF Region Including the Effect of Thermodynamic Non-Equilibrium," *Nuclear Eng. and Design* **51**, 143-155 (1979).

F-87. Th. Analytis and G. Yadigaroglu, "Analytical Modeling of Inverted Annular Film Boiling," *Nuclear Eng. and Design* **99** (1987).

F-88. R. P. Forslund and W. M. Rohsenow, "Dispersed Flow Film Boiling," *J. Heat Trans.* **90** (6), 399-407 (1968).

F-89. G. M. Anderson, "Low Flow Film Boiling Heat Transfer on Vertical Surfaces; Part 1: Theoretical Model," *AIChE Symposium Series* **73** (164), 2-6 (1977).

F-90. Y. Sudo, "Film Boiling Heat Transfer During Reflood Phase in Postulated PWR Loss-of-Coolant Accident," *J. Nuclear Science and Tech.* **17** (7), 516-530 (July 1980).

F-91. A. F. Varone, Jr. and W. M. Rohsenow, "Post-dryout Heat-Transfer Predictions," *Nuclear Eng. and Design* **95**, 315-327 (1986).

F-92. K. Kiangah and D. K. Dhir, "An Experimental and Analytical Study of Disposed Flow Heat Transfer," *Int. J. Thermal and Fluid Science*, **2**, 410-424 (1989).

F-93. R. A. Nelson and C. Unal, "A Phenomenological model of the Thermal hydraulics of convective boiling during the quenching of hot rod bundles. Part I: Thermal hydraulic model," Nuclear *Eng. and Design* **136**, 277-298 (1992).

F-94. R. A. Nelson and C. Unal, "A Phenomenological Model of the Thermal-Hydraulics of Convective Boiling During the Quenching of Hot Rod Bundles Part I: Thermal Hydraulic Model," *Nuclear Engineering and Design*, Vol. 136 pp. 277-298, 1992.

F-95. C. Unal and R. A. Nelson, "A Phenomenological Model of the Thermal-Hydraulics of Convective Boiling During the Quenching of Hot Rod Bundles Part II: Assessment of the Model with Steady-State and Transient Post-CHF Data," *Nuclear Engineering and Design*, Vol. 136, pp. 298-319, 1992.

F-96. C. Unal, E. Haytcher, and R. A. Nelson, "Thermal-Hydraulics of Convective Boiling During the Quenching of Hot Rod Bundles Part III: Model Assessment Using Winfrith Steady-State Post-CHF Void Fraction and Heat Transfer Measurements and Berkeley Transient Reflood Test Data," *Nuclear Engineering and Design*, Vol. 19, 1993.

F-97. D. Swinnerton, R. A. Savage, and K. G. Pearson, "Heat Transfer Measurements in Steady-State Post-Dryout at Low Quality and Medium Pressure," AEA Thermal Reactor Services, Physics and Thermal Hydraulic Division report AEA-TRS-1045, Winfrith United Kingdom Atomic Energy report AEEW-R 2503 (April 1990).

F-98. R. Seban., et al., "UC-B Reflood Program: Experimental Data Report," NP-743, Research Project 248-1, April 1978.

F-99. Safety Code Development Group, "TRAC-PF1/MOD1 Correlations and Models," Los Alamos National Laboratory report LA-11208-MS (NUREG/CR-5069) (December 1988).

F-100. B. E. Boyack, J. F. Lime, D. A. Pimental, J. W. Spore, and J. L. Steiner, "TRAC-M/F77, Version 5.5, Developmental Assessment Manual, Volume I: Nonproprietary Assessment Sections," Los Alamos National Laboratory document LA-UR-99-6480 (December 1999).

F-101. B. E. Boyack, J. F. Lime, D. A. Pimental, J. W. Spore, and J. L. Steiner, "TRAC-M/F77, Version 5.5, Developmental Assessment Manual, Volume II: Proprietary Assessment Sections," Los Alamos National Laboratory document LA-CP-99-345 (December 1999).

F-102. R. A. Nelson, Jr., D. A. Pimentel, S. J. Jolly-Woodruff, and J. W. Spore, "Reflood Completion Report, Volume I: A Phenomenological Thermal-Hydraulic Model of Hot Rod Bundles Experiencing Simultaneous Bottom and Top Quenching and an Optimization Methodology for Closure Development," Los Alamos National Laboratory report LA-UR-98-3043 (April, 1998).

F-103. B. E. Boyack, J. F. Lime, D. A. Pimentel, J. W. Spore, and T. D. Knight, "Reflood Completion Report, Volume II: Developmental Assessment of a New Reflood Model for the TRAC-M/F77 Code," Los Alamos National Laboratory report LA-UR-98-3043 (April, 1998).

APPENDIX G

FLUID MASS CLOSURE

Closure of the fluid mass-conservation equations involves the net vapor (or liquid) generation between the phases. This mass transfer includes the following considerations: (1) the subcooled-boiling model, (2) the interfacial heat-transfer models, and (3) the effect of noncondensables. The effect of noncondensables might be divided further into two parts: (1) Dalton's law applied to the two-component mixture of steam and noncondensable gas and (2) the influence of noncondensables upon the condensation and evaporation of water.

Section 2.1. discussed the field equations and identified the mass-transfer terms present in the two-fluid formulation. Appendix F, Section F.1. further defined in detail how the mass transfer is determined as it results from the interfacial heat transfer. This appendix will further consider the mass transfer present in two-fluid formulation by investigating those portions of the models used in the mass-conservation equation.

To begin this section, it is instructive to note the code input variables that control the inclusion of a noncondensable. There are two input variables, IEOS and NOAIR, that affect how noncondensables are included within the equation set by the code. There are also two input variables, IGAS and IH2SRC, that specify which noncondensable is present. IEOS is the main data card number 2. NOAIR, IGAS, and IH2SRC are NAMELIST variables.

IEOS was the first attempt within the code to allow for noncondensables and represented an on / off switch to allow for purely noncondensable / liquid-water mixtures by setting IEOS = 1, i.e., no steam vapor present. The setting of this switch turns off the interfacial mass transfer caused by evaporation and condensation.

NOAIR is an option that was added to improve the calculational efficiency by specifying that the noncondensables will be present during the calculation so that additional equations may be eliminated. Setting NOAIR = 1 results in the partial pressure of noncondensables being set to zero and only the two-fluid equation set for steam water being considered. Setting NOAIR = 0 results in the solution of a system of equations, which includes a nonzero partial pressure of the noncondensable.

The NAMELIST variable IGAS specifies which noncondensable is present. If IGAS = 1, the noncondensable is air. If IGAS = 2, the noncondensable is hydrogen. Finally, if IGAS = 3, the noncondensable is helium. IGAS = 1 is the default value. An additional NAMELIST variable IH2SRC allows a hydrogen source to be present. If the hydrogen source flag is on (that is, IH2SRC is nonzero), NOAIR is reset to zero, and IGAS is reset to 2. The basis for the models used for closure of the fluid mass-conservation equations involves the net vapor (or liquid) generation arising between the phases. The introduction of Appendix F, Section F.1. discussed the vapor generation rate per unit volume. The final expression for total vapor generation rate per unit volume is given by

$$\Gamma = \Gamma_i + \Gamma_{sub} \ , \qquad \text{(G-1)}$$

where Γ_i and Γ_{sub} are the vapor generation rates per unit cell volume resulting from interfacial heat transfer and subcooled boiling, respectively. The following nomenclature is used within Appendix G.

NOMENCLATURE

A: area
B_{cell}: cell volume
$C_{p,l}$: liquid specific heat
D_H: hydraulic diameter
F_e: evaporation fraction
G: mass flux
h: specific enthalpy
h_{ig}: gas-to-interface heat-transfer correlation
h_{il}: liquid-to-interface heat-transfer correlation
h_{ld}: liquid specific enthalpy at the point of bubble departure
$h_{l,sat}$: saturated liquid specific enthalpy
h_Γ: subcooled-boiling heat-transfer coefficient
H_{ALV}: liquid-side heat-transfer factor during flashing
H_{ALVE}: liquid-side heat-transfer factor during evaporation and condensation
H_{CHTI}: vapor-side heat-transfer factor
k: thermal conductivity
m: mass
N: number of moles
P: total pressure (Pa)
q: heat-transfer rate
q_{ig}: gas-to-interface heat-transfer rate
q_{il}: liquid-to-interface heat-transfer rate
q_{sub}: subcooled-boiling heat-transfer rate
q_{wl}: wall-to-liquid heat-transfer rate
R: universal gas constant
T: temperature
T_{ld}: liquid temperature at the point of bubble detachment
T_{sv}: saturation temperature corresponding to steam partial pressure
v: specific volume
v'_r: pseudo-reduced specific volume

V: volume

W_{sb}: subcooled-boiling weighting factor

y_i: mole fraction of component i

Z: compressibility factor

α: void fraction

Γ: total phase change rate per unit volume

Subscripts

c: critical

g: gas phase

i: interfacial

l: liquid phase

r: reduced

s: steam

sat: saturation

sub, sb: subcooled boiling

w: wall

Dimensionless Groups

Nu: Nusselt number

Nu^*: modified Nusselt number

Pe: Peclet number

St: Stanton number

G.1. Subcooled-Boiling Model

To properly predict the void fraction in heated cells near the saturation point, the effect of subcooled boiling must be accounted for. Normally one thinks that boiling will start when the local liquid temperature exceeds the local saturation temperature. In a computer simulation code such as TRAC, however, microscopic local temperatures are not available. Instead, the liquid temperature over a region as defined by a computational cell are in effect averaged to yield a liquid temperature that represents the conditions in that cell. In reality, the true liquid temperature near the hot wall will be greater than the cell-averaged liquid temperature, and could be greater than the saturation temperature. If this were the case, vapor could be formed at the wall even though the cell-averaged liquid temperature is subcooled. This is referred to as subcooled boiling. The vapor generation resulting from subcooled boiling is formulated as

$$\Gamma_{sub} = \frac{q_{sub}}{B_{cell}(h_g - h_l)} \ , \tag{G-2}$$

where

$$q_{sub} = h_\Gamma A_w (T_w - T_l) \ . \tag{G-3}$$

In previous TRAC-PF1/MOD1 versions (Ref. G-1.), subcooled boiling was accounted for only in cells containing ROD or SLAB components. It was done by adjusting the evaporation rate when both the wall temperature was greater than the saturation temperature, and the convective heat-transfer coefficient was higher than that predicted by the Dittus-Boelter equation. For TRAC-PF1/MOD2 (and TRAC-M), we use a different approach that applies to all cells containing heat structures.

G.1.1. Basis for the Correlation

The approach suggested by the Saha-Zuber correlation (Ref. G-2.) is used in TRAC-PF1/MOD2 (and TRAC-M). In Ref. G-2., Saha and Zuber pointed out that subcooled boiling occurs in two regimes—thermally controlled and hydrodynamically controlled. At low mass fluxes, it has been found that the point of net vapor generation is dependent only on local thermal conditions, which determine the rates of vapor condensation and evaporation at the wall. To make an estimate of these two rates it was assumed that the rate of evaporation at the wall will be proportional to heat flux, whereas the rate of condensation will be proportional to the local subcooling. Thus, the similarity parameter was taken to be the local Nusselt number

$$Nu = \frac{q_{wl} D_H}{k_l (T_{sat} - T_l)} \ . \tag{G-4}$$

For the high mass fluxes, the phenomenon is hydrodynamically controlled, and the appropriate similarity parameter is the local Stanton number defined as

$$St = \frac{q_{wl}}{G C_{\rho,l} (T_{sat} - T_l)} \ . \tag{G-5}$$

The Peclet number, which by definition is the ratio of the Nusselt number and the Stanton number,

$$Pe = \frac{Nu}{St} = \frac{G D_H C_{\rho,l}}{k_l} \ , \tag{G-6}$$

was selected to be the correlation-independent parameter with the Stanton number as the dependent parameter. Data from 10 different sources were plotted as shown in the Fig. G-1.

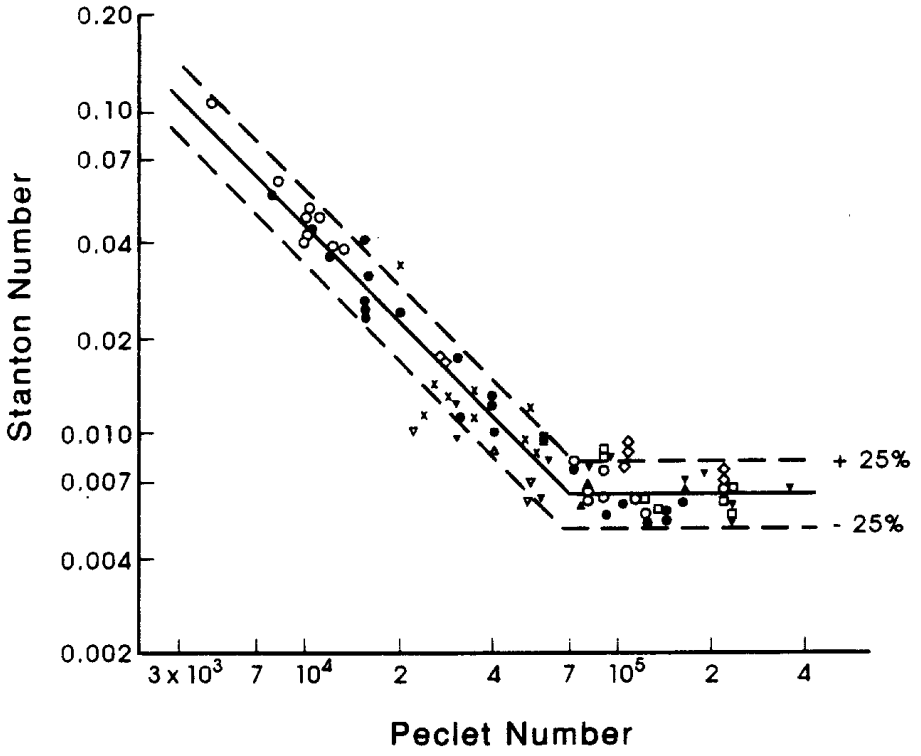

Fig. G-1. Original database of Saha-Zuber correlation.

The two distinct regions can easily be identified. Up to a Peclet number of 70000, the data fall in a straight line having the slope of minus one, which implies a constant value for the local Nusselt number. This is the thermally controlled region. Beyond a Peclet number of 70000, the data fall on a constant Stanton number, which is referred to as the hydrodynamically controlled region. The entire correlation for the point of net vapor generation is expressed as

$Nu = 455$, if $Pe \leq 70000$

and

$St = 0.0065$, if $Pe > 70000$.

This correlation is interpreted by the authors as follows. In the thermally controlled region, the bubbles stay attached to the walls until a characteristic roughness parameter is reached, at which point they detach from the surface (as soon as the local Stanton number becomes 0.0065). Since the local subcooling is still high, the bubbles are forced to stay near the heated wall and flow downstream until the local Nusselt number becomes 455. At this point, the local subcooling is low enough to initiate a rapid increase in void fraction. For the hydrodynamically controlled region, the Stanton number reaches the

value of 0.0065 at a point where the Nusselt number is already higher than 455. Thus, as soon as the bubbles are detached from the wall they can move to the liquid core without being rapidly condensed. This results in a rapid increase in vapor void fraction at the point of bubble detachment.

Once it has been determined that subcooled boiling is taking place, the energy must be partitioned between the energy going into raising the temperature of the liquid and the energy going into vaporization. The Lahey mechanistic model (Ref. G-3.) is used for this purpose. This model takes the form

$$q_{\text{sub}} = q_{w\text{l}} \times \left(\frac{h_{\text{l}} - h_{\text{l}d}}{h_{\text{l,sat}} - h_{\text{l}d}} \right) \quad , \tag{G-7}$$

where q_{sub} is the subcooled-boiling heat flux, $q_{w\text{l}}$ is the total heat flux, h_{l} is the liquid specific enthalpy, $h_{\text{l}d}$ is the liquid specific enthalpy at the point of bubble departure, and $h_{\text{l,sat}}$ is the saturated liquid enthalpy.

Part of the vapor generated near the wall condenses because of contact with subcooled liquid. This effect of subcooled boiling on interfacial condensation is described in Appendix F, Section F.1.1.3.

G.1.2. Database of the Original Correlation

The data shown plotted in Fig. G-1. include data for water, freon-22, and freon-114, and cover a wide range of pressure, mass flow rate, heat flux, and channel geometries in either horizontal or upflow conditions.

G.1.3. Changes to Original Correlation

Developmental-assessment-calculation comparisons were made using preliminary versions of TRAC-PF1/MOD2 against flow-rate and pressure-drop data taken at Columbia University in support of the Savannah River Production Facility (Ref. G-4.). Developmental assessment calculations were also made against the Savannah River Laboratory Subcooling Boiling Tests (Ref. G-5.). The objective of this analysis was to assess the adequacy of TRAC to adequately model the flow instability phenomenon in downflow situations. It was found that early versions of TRAC-PF1/MOD2 tended to predict the onset of the flow instability at too low a mass flux. It was reasoned that the transition between the thermally controlled region and the hydrodynamically controlled region could be altered when the flow went from horizontal to vertical downflow. Using the Savannah River Heat Transfer Laboratory tube test data for downflow geometries, the correlation was altered as follows:

$Nu = 74.55$ if $Pe \leq 7000$

and

$St = 0.01065$ if $Pe > 7000$.

The value of 0.01065 was determined by performing a weighted fit of the Savannah River Heat Transfer Laboratory downflow tube test data. These values are only used as part of the core reflood model (Section F.1.6.).

G.1.4. Correlation as Coded

For the core reflood model, the subcooled-boiling heat-transfer coefficient is calculated in subroutine HTVSSL using the modified Saha-Zuber correlation described in Section G.1.3. Once it has been determined that subcooled-boiling conditions may exist (the wall temperature is greater than the fluid saturation temperature with the liquid temperature less than saturation temperature), then the liquid heat-transfer coefficient is adjusted for subcooled boiling as follows:

$$h_{\Gamma} = W_{sb} h_{w\mathrm{l}} F_e \ , \tag{G-8}$$

where W_s is the subcooled-boiling weighting factor and is coded as

$$0 \le 5(0.7 - \alpha) \le 1 \ , \tag{G-9}$$

using Fortran min and max functions.

The evaporation fraction, F_e, in Eq. (G-8) is computed from Lahey's mechanistic model as

$$0 \ \le \ F_e \ = \ \frac{T_{\mathrm{l}} - T_{\mathrm{l}d}}{\max[1,(T_{sv} - T_{\mathrm{l}d})]} \ \le \ 1 \quad , \tag{G-10}$$

where the liquid temperature at bubble detachment, $T_{\mathrm{l}d}$, is computed from the modified Saha-Zuber model (as described in Section G.1.3.) as follows:

$$T_{\mathrm{l}d} \ = \ T_{sv} - \frac{Nu^*}{0.01065 \times 7000} \ \text{if } Pe \le 7000,$$

and (G-11)

$$T_{\mathrm{l}d} \ = \ T_{sv} - \frac{Nu^*}{0.01065 \times Pe} \ \text{if } Pe > 7000,$$

where Nu^* is a modified Nusselt number that does not include a $(T_{\mathrm{sat}} - T_{\mathrm{l}})$ term.

For HTSTR components that are not participating in the reflood logic, the subcooled-boiling heat transfer is calculated in subroutine HTCOR. The same equations [Eqs. (G-8) through (G-11)] are used, except that the Stanton number 0.0065 and the Peclet number 70000 are used in Eq. (G-11).

G.1.5. Scaling Considerations on Correlation

The original Saha-Zuber correlation covered a wide range of channel sizes and geometries, including 7-mm-i.d. and 13-mm-o.d. annular geometries through 63-mm channels. The correlation is expected to be independent of scale.

G.1.6. Input and Constants of Correlation

The constants of the Saha-Zuber correlation have been changed for the core reflood model, as described above. The original Saha-Zuber correlation is used in all other cases.

G.1.7. Parametric Range of the Coded Correlation

The original Saha-Zuber correlation covered a wide range of pressures (1.01 to 138 bar) and three different fluids (water, freon-22, and freon-114). The correlation is expected to cover the range of fluid conditions encountered in reactor safety analysis.

G.2. Interfacial Heat-Transfer Models

As discussed in the introduction of Appendix F, Section F.1., the vapor generation resulting from interfacial heat transfer is calculated through

$$\Gamma_i = \frac{q_{ig} + q_{i\ell}}{B_{\text{cell}}(h_g - h_\ell)} \ , \tag{G-12}$$

where

$$q_{i\ell} = \underbrace{H_{\text{ALVE}}(T_\ell - T_{sv})}_{\text{evaporation or condensation}} + \underbrace{H_{\text{ALV}}\langle T_\ell - T_{\text{sat}}\rangle'}_{\text{flashing}} \tag{G-13}$$

and

$$q_{ig} = \frac{P_s}{P} H_{\text{CHTI}}(T_g - T_{sv}) \ . \tag{G-14}$$

The interfacial heat-transfer factors, H_{ALV}, H_{ALVE}, and H_{CHTI}, are defined as

$$H_{\text{ALV}} = H_{\text{ALVE}} = h_{i\ell} A_i \tag{G-15}$$

and

$$H_{\text{CHTI}} = h_{ig} A_i \quad , \tag{G-16}$$

where the closure relationships for the convective heat-transfer coefficients and interfacial area are described in Appendix F, Section F.1.

Also note that, in TRAC-PF1/MOD1 (Ref. G-1.), evaporation and flashing were treated the same way. In TRAC-PF1/MOD2 and TRAC-M, flashing is superimposed on the energy equation through a singularity function $\langle T_l - T_{sat} \rangle'$, as shown in Eq. (G-13). As shown in Fig. G-2., evaporation occurs if $T_{sv} < T_l < T_{sat}$ and flashing occurs if $T_l > T_{sat}$. A positive Γ_i indicates vapor generation and a negative Γ_i indicates liquid generation. Notice that, whereas q_{ig} is negative, q_{il} may be positive and vice versa. The net vapor or liquid generation is determined by the relative magnitude of these quantities and is illustrated in Fig. G-3.

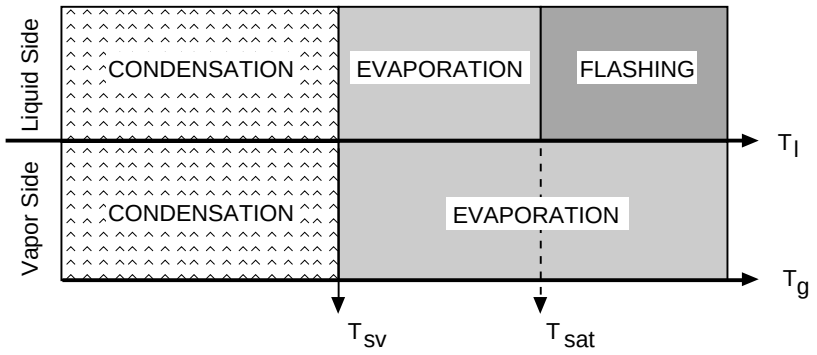

Fig. G-2. Graphical illustration of the selection logic for condensation, evaporation, and flashing.

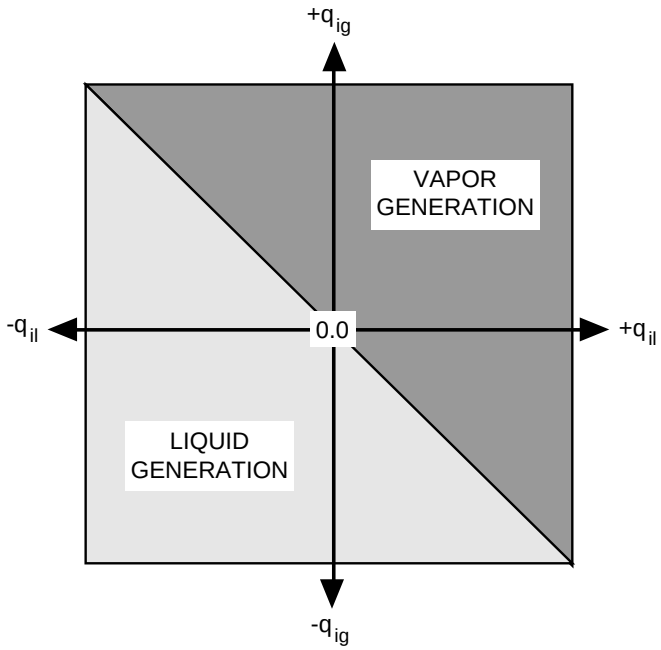

Fig. G-3. Interfacial mass-transfer map.

G.3. The Effect of Noncondensables

The effect of noncondensables will be divided further into two parts. The first includes Dalton's law applied to the mixture of steam and a noncondensable gas. The second includes the influence of the noncondensable upon the condensation or evaporation of water.

G.3.1. Dalton's Law

The partial pressure of a given component in a gas mixture is defined as (Ref. G-6., Eq. 3-20)

$$P_i \equiv y_i \times P \ , \tag{G-17}$$

where y_i is the mole fraction of component i and P is the total pressure. This choice of the definition of partial pressure makes the sum of partial pressures equal to the total pressure, even if the mixture is not ideal (see Ref. G-6., p. 115). Thus,

$$P = \sum P_i \quad . \tag{G-18}$$

The term *partial pressure*, however, has a physical relevance only for ideal gases (Ref. G-7., p. 428). The "law of partial pressures" is obtained by applying the definition of partial pressure to the ideal gas equation given by

$$P_i V = NRT \quad , \tag{G-19}$$

assuming that the mixture is at uniform temperature and each component occupies the entire volume by itself. The resulting relationship is also known as Dalton's law, which basically states that, "in a mixture, every gas is a vacuum to every other gas" (Ref. G-6., p. 116). This is consistent with the definition of an ideal gas.

The behavior of ideal gases can be explained by making two assumptions: (1) the molecules are so far apart that there are no molecular attractions, and (2) the size of the molecules is so small relative to the volume they occupy that the presence of the molecules can be neglected. When the pressure is increased with the temperature fixed, the molecules are forced closer together so that molecular attractions and molecular size become progressively more important and the gas departs from its ideal gas characteristics. If the temperature is raised with the pressure held constant, two effects result. First, the volume (and hence the distance between the molecules) will increase. Second, there is an increase in the kinetic energy of the molecules, thus helping overcome molecular attractions. Therefore, as the temperature of a gas is increased, it tends to behave more nearly as an ideal gas.

The pressure exerted by an ideal gas occupying a given volume is directly proportional to the product of the number of molecules of the gas and the mean molecular kinetic energy (temperature). This observation leads to the ideal gas law, or equation of state,

given by Eq. (G-19), where P = pressure, V = volume, N = number of moles of gas, T = temperature, and R = a proportionality constant known as the universal gas constant. If a second gas occupies the same volume at the same temperature as the first gas, no intermolecular attractions can exist so that each will exist independently. Gas A will exert the same pressure on the system as it did prior to the introduction of gas B. Likewise, gas B will exert a pressure equal to the pressure it would have had if it existed alone in the system. This observation resulted in Dalton's law of partial pressures for ideal gases, as given by Eq. (G-18).

In general, there is no sharp distinction between a vapor and a noncondensable gas. A noncondensable gas is frequently considered as being far removed from its liquid state, whereas the vapor is thought of as being readily liquefiable. A vapor also may be thought of as an actual gas requiring either a unique P-V-T relationship or the definition of its compressibility factors, where the compressibility factor is defined by

$$Z = \frac{PV}{NRT} \ . \tag{G-20}$$

If Z = 1, the vapor can be represented as an ideal gas.

While the properties of steam have been measured over a wide range of the pressures and temperatures, those of many substances have not. If an accurate P-V-T formulation (that is, equation of state) has been found for a substance, it is possible through the Gibbs relationships to determine the changes of other properties such as internal energy, enthalpy, and entropy. For those substances, however, in which a P-V-T formulation is not available and the state conditions have thus most likely not been measured, the concept of corresponding states may be used to obtain an approximate value of the desired properties. Here, the concept of corresponding states will be used to look at the validity of the assumption of ideal gases within the steam / noncondensable mixtures.

To consider the concept of corresponding states, reduced properties must be defined. A reduced property is the ratio of the property in a given state to the value of the property at the substance's critical state. Using the subscripts r to represent the reduced property and c for the critical property, the reduced pressure, reduced temperature, and reduced specific volume can be written as

$$P_r = P/P_c \ , \tag{G-21}$$

$$T_r = T/T_c \ . \tag{G-22}$$

and

$$v_r = v/v_c \ , \tag{G-23}$$

where $v = V/m$ = specific volume and m is the mass of the gas contained in volume V. Table G-1. gives the critical properties of the fluids currently modeled in TRAC.

TABLE G-1.
Critical Properties of TRAC Fluids

Substance	Critical Pressure (MPa)	Critical Temperature (K)	Critical Volume ($cm^3 \cdot g^{-1}$)
Air	3.772	133.0	2.86
Hydrogen	1.298	33.3	33.03
Helium	0.230	5.3	14.45
Water Vapor	22.089	647.3	3.16

When two gases are at the same reduced pressure and reduced temperature, they are said to be at corresponding states. An examination of various properties of various gases shows that gases at the same corresponding states have approximately the same reduced properties in addition to pressure and temperature. Nelson and Obert (Ref. G-8.) applied the concept of corresponding states to the determination of compressibility factors. They found that over an extensive region of temperatures and pressures, the compressibility factors for various substances did not deviate by more than a small percentage. They used a pseudo-reduced specific volume defined as

$$v'_r = Z\, T_r \,/\, P_r \tag{G-24}$$

so that

$$v'_r = f'(P_r \,/\, T_r)\ . \tag{G-25}$$

Figures G-4. and G-5. give the compressibility factor as a function of these reduced properties. From Fig. G-4., it can be seen that at very low pressures a so-called vapor may be treated as an ideal gas for most engineering purposes. On the other hand, from Fig. G-5., when a vapor exists at very high pressures it deviates from an ideal gas, even when its temperature is much higher than the boiling point.

Using the critical properties of substances of interest to TRAC given in Table G-1. and Figs. G-4. and G-5., we can determine how near to an ideal gas the vapors of interest are for some potential PWR pressure conditions. Table G-2. shows typical results for air and water vapor. In Table G-2., the air temperature is taken as that corresponding to saturated steam. The plus sign indicates that the volume is approximate. We can see that air can reasonably be approximated by an ideal gas. One potential region for this ideal gas approximation to become invalid for the noncondensables is at pressures above operational pressures for a PWR, 17.0 MPa, when a mixture has significant superheating. For this case, the error will increase above 10%. On the other hand, water vapor cannot be accurately approximated as an ideal gas once the pressure exceeds 1.0 MPa unless there is excessive superheating. Below 1.0 MPa, the ideal gas assumption for steam is acceptable.

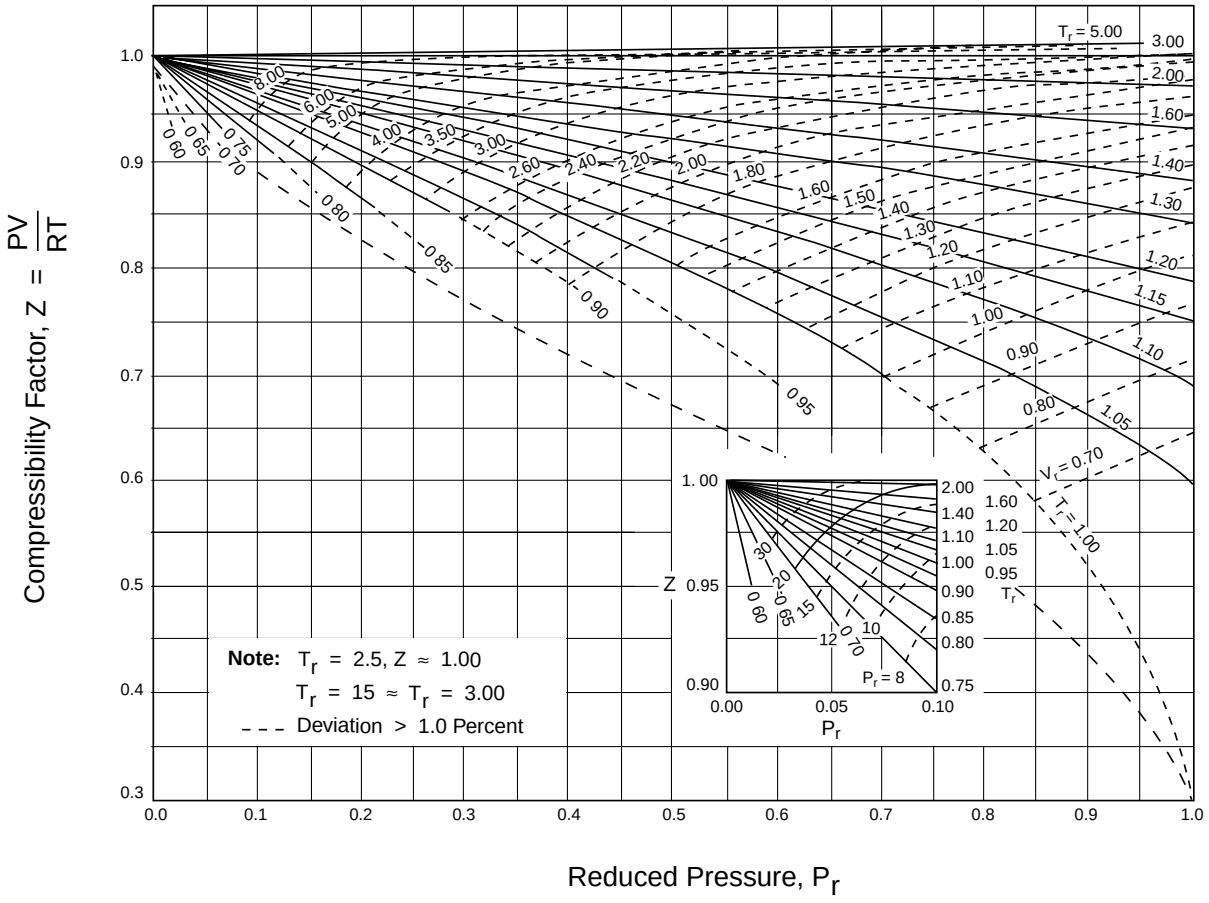

Fig. G-4. Compressibility factors for reduced pressures 0 to 1.0. (Reprinted from Ref. G-8. with permission.)

Using the critical properties of substances of interest to TRAC given in Table G-1. and Figs. G-4. and G-5., we can determine how near to an ideal gas the vapors of interest are for some potential PWR pressure conditions. Table G-2. shows typical results for air and water vapor. In Table G-2., the air temperature is taken as that corresponding to saturated steam. The plus sign indicates that the volume is approximate. We can see that air can reasonably be approximated by an ideal gas. One potential region for this ideal gas approximation to become invalid for the noncondensables is at pressures above operational pressures for a PWR, 17.0 MPa, when a mixture has significant superheating. For this case, the error will increase above 10%. On the other hand, water vapor cannot be accurately approximated as an ideal gas once the pressure exceeds 1.0 MPa unless there is excessive superheating. Below 1.0 MPa, the ideal gas assumption for steam is acceptable.

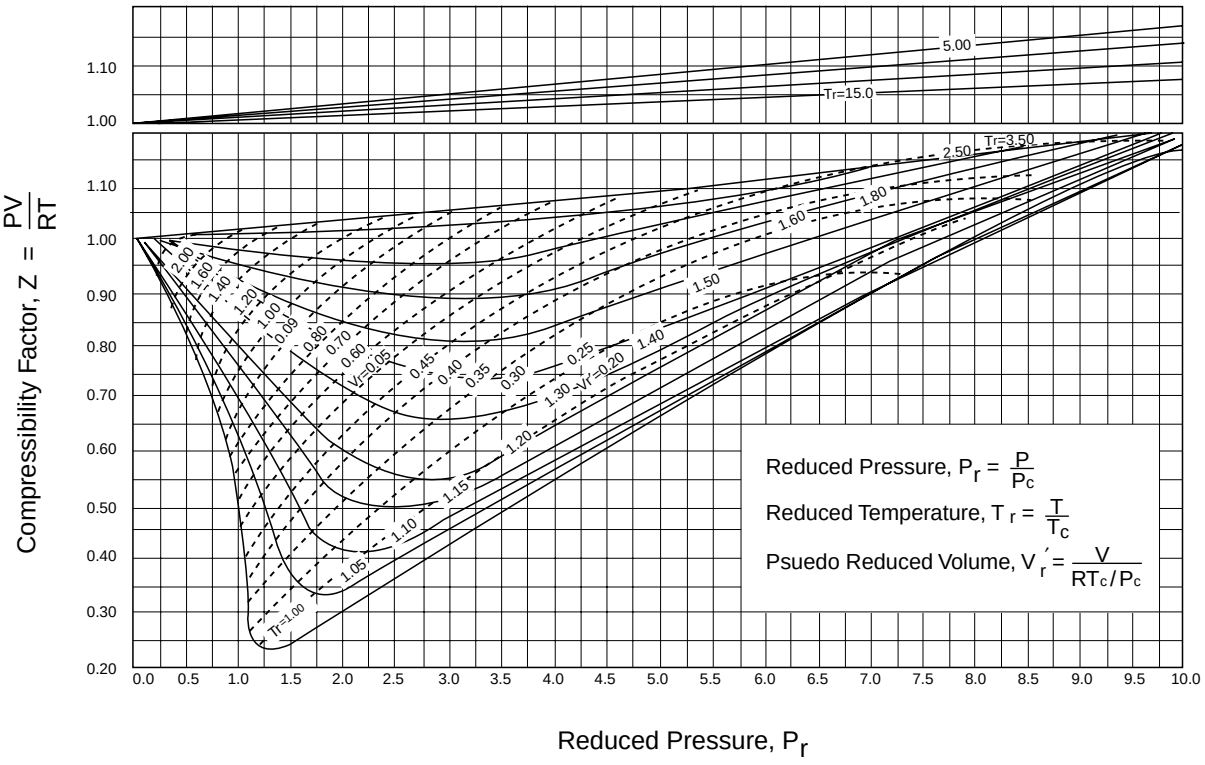

Fig. G-5. Compressibility factors for reduced pressures 0 to 10.0.
(Reprinted from Ref. G-8. with permission.)

From Fig. G-5., we can further observe that the worst case for a vapor is in the vicinity of its critical point. Assuming the pressure corresponds to the critical points of air and hydrogen and the temperature is that corresponding to saturation for steam, we can determine the nature of the two noncondensables at these states. This is shown in Table G-3. Because of the high reduced temperatures that result for both air and hydrogen, they can easily be approximated as ideal gases.

Thus, we have shown that the noncondensables can be treated typically as ideal gases, but that in general, the steam is a nonideal gas. The exception to this nonideal behavior occurs when steam is at lower pressures, i.e., less than 1 MPa. To apply Dalton's law, we must assume that the mixture of one nonideal gas with ideal gases still allows the use of Dalton's law provided the proper equation of state is used for the actual vapor. Such is the case in TRAC.

G.3.2. Influence of Noncondensables Upon Evaporation and Condensation

The noncondensables influence the phase change by lowering the saturation temperature, and thus, the interface temperature. On the vapor side, no special models are used to account for the presence of the noncondensables. As given by Eq. (G-14), however, the vapor side interfacial heat-transfer factor is reduced by P_s / P. On the liquid

side, the existence of noncondensables triggers model changes. During evaporation, a simple diffusion-controlled model is used to calculate H_{ALVE}, as discussed in Appendix F, Section F.1.7.1.1.

TABLE G-2.
Typical Compressibility Factors of Air and Water

(Sat. Temp.)	Pressure (MPa)		Air	Water
(373 K)	0.1	P_r T_r Z	0.026 2.8 1.00+	0.005 0.58 0.98
(453 K)	1.0	P_r T_r Z	0.27 3.4 1.00+	0.045 0.70 0.93
(559 K)	7.0	P_r T_r Z	1.86 4.2 1.02+	0.31 0.86 0.78
(625 K)	17.0	P_r T_r Z	4.5 4.7 1.07	0.77 0.97 0.64
(647.3 K)	22.089	P_r T_r Z	5.9 4.9 1.09	1.0 1.0 0.3

TABLE G-3.
Compressibility Factors of Air and Hydrogen at $P_r = 1.0$

	Air	Hydrogen
Pressure (MPa)	3.772	1.298
Sat. Temp. (K)	520.0	464.7
Reference Temp.	3.9	13.95
Compressibility	1.01+	1.00+

During condensation, H_{CHTI} is modified via the empirical correlation developed by Sklover and Rodivilin (Ref. G-9.). This correlation is further discussed in Appendix F, Section F.1.7.1.2.

G.4. Summary and Conclusions

Considerable improvements over TRAC-PF1/MOD1 have been made in terms of mass closure models. In subcooled boiling, the mechanistic model of Lahey (Ref. G-3.) is coupled with a model similar to the one suggested by Saha and Zuber (Ref. G-2.). The effect of noncondensables is made consistent between one- and three-dimensional components. Evaporation and flashing are accounted for using separate models. Evaporation is modeled as being diffusion controlled.

REFERENCES

G-1. Safety Code Development Group, "TRAC-PF1/MOD1 Correlations and Models," Los Alamos National Laboratory document LA-11208-MS (NUREG/CR-5069) (December 1988).

G-2. P. Saha and N. Zuber, "Point of Net Vapor Generation and Vapor Void Fraction in Subcooled Boiling," *Proc. 5th Int. Heat Transfer Conf.* (Tokyo, Japan, 1974), Paper B4.7.

G-3. R. T. Lahey, "A Mechanistic Subcooled Boiling Model," *Proc. 6th Int. Heat Transfer Conf.* (Toronto, Canada, 1978), Vol. 1, pp. 293-297.

G-4. D. M. Lee, "Additional Pressure-Drop-Flow Curves for Simulated Mark VII-AL Fuel Assembly," Supplement to Technical Note TN-XIV-1-63, Savannah River Laboratory report DPW2-883-XIV-3-63 (April 1963).

G-5. B. S. Johnston, "Subcooled Boiling of Downward Flow in a Vertical Annulus," ASME Proc. 1989 National Heat Transfer Conf. (Philadelphia, 1989), *Multiphase Flow Heat and Mass Transfer,* HTD. Vol. 109, pp. 149-156.

G-6. K. Denbigh, *The Principles of Chemical Equilibrium*, 3rd ed. (Cambridge University Press, Boston, 1971).

G-7. G. J. Van Wylen and R. E. Sonntag, *Fundamentals of Classical Thermodynamics,* SI version, 2nd ed. (John Wiley & Sons, Inc. New York, 1976).

G-8. L. C. Nelson and E. F. Obert, "Generalized P-V-T Properties of Gases," *Trans.* ASME, pp. 1057-1066 (1954).

G-9. G. G. Sklover and M. D. Rodivilin, "Condensation of Water Jets with a Cross Flow of Steam," *Teploenergetika* **23**, 48-51 (1976).

APPENDIX H

FLUID MOMENTUM CLOSURE

The TRAC field equations include the phasic momentum equations as described in Section 2.1. The code uses separate equations for the gas and liquid phases. These equations relate the total pressure drop between cell centers to the following:

1. temporal acceleration,
2. spatial acceleration,
3. gravitational acceleration,
4. interphasic momentum transfer caused by phase change,
5. interphasic momentum transfer caused by interfacial drag, and
6. wall drag.

The first three components of the momentum equations listed above are calculated as described in Section 2.1. The phase-change component, also incorporated as described in Section 2.1., requires the details of the calculation of the interphase mass-transfer rate provided in Appendix G. This section describes the calculation of the interfacial-drag term and the wall drag in Appendix H, Sections H.1. and H.2., respectively. The following nomenclature is used in Appendix H.

NOMENCLATURE

A: flow area of the channel
A_t: total surface area of rods
A_{Pb}: projected area of the bubble (m^2)
A_u: unheated surface area of rods
c_{Db}: bubble-drag coefficient
c_f: coefficient of friction
c_{flo}: single-phase liquid friction-factor correlation
c_{hwg}: horizontal 1D wall-shear coefficient
c_{hwl}: horizontal 1D wall-shear coefficient
c_i, C_i: interfacial-drag coefficient ($kg \cdot m^{-4}$)
c_{vwg}: nonstratified 1D wall-shear coefficient
c_{vwl}: nonstratified 1D wall-shear coefficient
c_{wg}: gas-phase wall drag
c_{wl}: liquid-phase wall drag
C_0, C_1: bubble distribution parameters
$C_1 - C_5$: correlation parameters in Eq. (H-32)

C, C': constants in bubble-height calculation [Eq. (H-89)]

C_{an}: roughness parameter

C_d: form drag coefficient for droplets

C_{wg}: wall-gas drag coefficient

Ca: capillary number

d, D, diam: diameter

D_g: hydraulic diameter for the gas phase

D_h: hydraulic diameter (m)

D_l: hydraulic diameter for the liquid phase

DX: cell lengths

E: relative entrainment

f: friction factor

f_{fo}: single-phase friction factor

f_{wg}: wall-gas friction factor

fc4: proportionality constant for pipe roughness

fcdrop: constant

fdis: constant

ffd: constant

ffs: constant

fmdis: constant

frw: constant

fsb: constant

fsm: constant

F_b: force on the gas bubbles

F_d: force on the droplets

F_u: fraction of unheated surface area

FA: cell-edge flow area

g, g_c: magnitude of the gravity vector

G: mass flux ($kg \cdot m^{-2} \cdot s^{-1}$)

h_l: height of the stratified layer of liquid

HD: hydraulic diameter (m) or average of the level height in Eq. (H-74)

j: cell designator

j: superficial velocity ($m \cdot s^{-1}$)

j^*: dimensionless superficial velocity

k: cell level index or dummy directional index

L: length

L_0: Laplace coefficient

M: drag force per unit volume ($N \cdot m^{-3}$)

$NTSX$: number of azimuthal sectors

$N_{\mu g}$: viscosity number

p: pressure (Pa)

P: equivalent perimeter

P_s: profile slip factor

r: radial position or bubble radius

r_d: drag radius

r_{sm}: Sauter mean radius

Re: Reynolds number

s: distance between bubbles

S_i: width of the stratified interface (m)

S_r: slip ratio

T: temperature (K)

u: liquid velocity parallel to the wall

vol: cell volume

vol_b: bubble volume

Vol_d: droplet volume

V: velocity ($m \cdot s^{-1}$)

V_{fd}: liquid velocity combining the effects of both annular film and entrained droplets [Eqs. (H-57) and (H-58)]

$\vec{V}_r$: vector-average velocity in the axial and radial directions

$\vec{V}_{g\theta}$: vector-average velocity in the azimuthal direction

$\langle V_r \rangle$: vector-average velocity at the r face for the ijk cell

$\langle V_z \rangle$: vector-average velocity at the z face for the ijk cell

$\langle V_\theta \rangle$: vector-average velocity at the θ face for the ijk cell

V_{gj}: drift-flux velocity ($m \cdot s^{-1}$)

V_{gr}: magnitude of gas velocity in the radial direction ($m \cdot s^{-1}$)

V_{gz}: magnitude of gas velocity in the axial direction ($m \cdot s^{-1}$)

$V_{g\theta}$: magnitude of gas velocity in the azimuthal direction ($m \cdot s^{-1}$)

V_{lr}: magnitude of liquid velocity in the radial direction ($m \cdot s^{-1}$)

V_{lz}: magnitude of liquid velocity in the axial direction ($m \cdot s^{-1}$)

$V_{l\theta}$: magnitude of liquid velocity in the azimuthal direction ($m \cdot s^{-1}$)

V_{rr}: magnitude of the relative velocity in the radial direction ($m \cdot s^{-1}$)

V_{rz}: magnitude of the relative velocity in the axial direction ($m \cdot s^{-1}$)

$V_{r\theta}$: magnitude of the relative velocity in the azimuthal direction ($m \cdot s^{-1}$)

W: weighting factor

We: Weber number

WF: weighting factor

$WFHDS$: weighting factor

$WFHF$: weighting factor

$WFMDS$: weighting factor

$WFRW$: weighting factor

$WFSB$: weighting factor

$WFSM$: weighting factor

WX: weighting factor

$xmdis$: constant

X: quality or polynomial curve-fit parameter defined in Eq. (H-80)

X_f: flow quality

X_s: static quality

XS: weighting factor

y: coordinate perpendicular to wall

Y: polynomial curve-fit parameter defined in Eq. (H-80)

Y_b: bubble height from the wall

z: axial elevation

α: volume fraction or void fraction

α_{AG}: void fraction at the agitated / post-agitated IAF-regime transition

α_b: bubble fraction

α_c: gas-droplet-core area fraction

α_d: droplet area fraction

$\alpha_{d\,d}$: liquid dispersed droplet fraction

α_f: liquid film area fraction

α_{fr}: void fraction of bubbles traveling in the free stream

α_g: void fraction associated with the gas phase

α_k: area fraction of the k^{th} phase

α_l: liquid fraction

α_w: void fraction of bubbles attached to the wall

α_1, α_2: void-fraction parameters used to calculate the weighting factor for the total interfacial-drag coefficient in the transition regime

Δp: pressure difference

Δt: time step (s)

Δx: cell length

Δz: elevation difference or length

$\Delta\alpha$: fractional difference

$\Delta\rho$: liquid density minus gas density

δ_f: liquid film thickness (mm)

γ: ratio of densities

ε: roughness parameter

μ: viscosity ($N \cdot s \cdot m^{-2}$)

ρ: density ($kg \cdot m^{-3}$)

ρ_c: gas core density

ρ_m: density of two-phase mixture

ξ: cell-centered fluid property

θ: azimuthal angle

$(\Phi^2)_{lo}$: TRAC effective two-phase multiplier

$(\Phi)^2_H$: homogeneous two-phase multiplier

σ: surface tension

τ: shear stress

τ_f: shear stress at the film-to-core interface

dp/dx: pressure drop per unit length

Ω: cell lengths adjoining the cell edge

Subscripts

a: annular film

ag: agitated flow

am: annular mist

b: bubble

bot: bottom

bs: bubbly slug flow

c: core

CHF: critical heat flux

d: droplet

dd: dispersed droplet

df: highly dispersed flow

f: film

fr: free stream

g: gas phase

i: interfacial
k: phase dummy index
l: liquid phase
m: modified or two-phase mixture
min: minimum
max: maximum
old: old-time value
pa: post-agitated IAF flow
r: relative
r: radial direction
rw: rough-wavy IAF
sat: saturation
sb: subcooled nucleate boiling
sm: smooth IAF
st: stratified flow
top: top
tr: transition boiling
trans: transition flow
v: vapor
w: wall
z: axial direction
θ: azimuthal direction

H.1. Interfacial Drag

The interfacial-drag term in the TRAC field equations accounts for the interfacial force that can occur as a result of the momentum interchange between the phases. The code assumes that this term is proportional to the square of the relative velocity. It calculates an interfacial-drag coefficient as the constant of proportionality. The interfacial-drag coefficient is dependent on the flow regime that is determined by the local total mass flux and the void fraction. (See Appendix E for a description of the flow-regime map.) The following discussion describes how the interfacial-drag coefficient is determined for bubbly slug flow, annular-mist flow, stratified flow, and the transitions among them. The special core-reflood model and other process models are described in detail. The CCFL model that modifies the interfacial shear in the VESSEL component at user-prescribed positions is described separately in Appendix I, Section I.3.

During development of TRAC-PF1/MOD2, a major goal was to improve the interfacial-drag and heat-transfer relations that were being used in the MOD1 code. A detailed review of the MOD1 models and correlations produced a number of errors and

shortcomings and areas that needed improvement. This criticism is tempered with the fact that at the time of MOD1 development, many mechanistic models for interfacial drag as well as pertinent data were not available. The developers at that time sought to provide a robust efficient version of the code that would accommodate a wide range of two-phase flow processes. With this in mind, the developers adopted the use of simple, quasi-steady correlations that could be applied to a variety of geometric configurations and scales.

This approach has proved to be very attractive with regard to applicability and computation time, but has not been without its problems. Several cases occurred in which the code predicted incorrect phenomena and therefore, estimated the interfacial drag incorrectly. In the MOD2 version, we attempted to correct these problems. We have tried to reduce the number of engineering models and to use recent correlations from the literature wherever possible.

In essence, we have striven to provide a more realistic and accurate prediction of the actual phenomena, and therefore, make the code more justifiable. The major changes that were implemented into TRAC-PF1/MOD2 include the following:

- determination of the flow regime using a void fraction that is donor-celled on the vapor velocity,
- definition of the bubble diameter based on the Laplace coefficient rather than on the Weber number,
- definition of the droplet diameter based on a wave-crest-shear correlation rather than on the Weber number,
- addition of the profile slip effect to the bubble drag,
- momentum weighting of the droplet and film components in the annular-mist regime,
- addition of a stratified-flow regime in the VESSEL component,
- a complete rewrite of the core-reflood interfacial drag to model the physical phenomena as described in the recent literature, and
- the allowable change in the interfacial drag from one time step to the next, based on real time rather than on an average of new- and old-time values.

H.1.1. Bubbly Slug Flow Correlations

This section describes the calculation of interfacial drag for the bubbly slug regime. [As in Appendix F, here we will refer to bubbly flow, bubbly slug transition, and bubbly slug flow, as shown in Fig. F-3., collectively as the bubbly slug regime.] For mass fluxes less than 2000 $kg \cdot s^{-1} \cdot m^{-2}$, bubbly flow is assumed for void fractions up to 0.3, and slug

flow for void fractions between 0.3 and 0.5. (Physically, slug flow is more accurately described as bubbly slug flow as shown in Fig. F-3. To avoid confusion, we will use "slug flow" here.) For mass fluxes greater than 2700 $kg \cdot s^{-1} \cdot m^{-2}$, bubbly flow is assumed for void fractions up to 0.5. For mass fluxes between 2000 and 2700, bubbly flow is assumed up to a void fraction of 0.3, and an interpolation is made between bubbly and slug flows for void fractions between 0.3 and 0.5. (See Appendix E for a full description of the flow-regime map, and refer to Fig. E-1. in Appendix E to visualize the limits of this regime.)

The basic relations described here for this regime are used throughout the code in all 1D components and in the 3D VESSEL component. In some special cases, the interfacial drag is overridden or altered. These cases are

1. core reflood in the VESSEL component,
2. stratified flow in the VESSEL component,
3. flow in an upper plenum,
4. accumulator logic in the PIPE component,
5. stratified flow in 1D components,
6. user-defined CCFL in the VESSEL, and
7. complete phase-separation option in 1D components.

These special cases are described separately in subsequent sections. Except for these cases, and except for mass fluxes and void fractions outside the range of the bubbly slug regime, the model described below is used for the interfacial drag in each direction in the VESSEL component and in all 1D components.

H.1.1.1. Basis for the Model. We base the interfacial-drag prediction for bubbly slug flow in TRAC upon the following assumptions:

1. The interfacial drag on bubbles can be represented with the correlations commonly used for solid spherical particles. Therefore, no bubble distortion is assumed.
2. The transient is sufficiently slow that interfacial-drag phenomena are quasi-steady. Therefore, the transient forces during the acceleration of bubbles (apparent mass and Basset force) can be neglected.
3. The bubble diameter used for bubbly flow can be determined using the Laplace coefficient.
4. The increased slip due to the bubble distribution in a channel is accounted for.
5. The interfacial drag in the slug-flow regime can be represented with the correlations used for solid spherical particles, with the diameter increased up to the hydraulic diameter of the channel.

The method for determining the interfacial-drag force in the bubbly slug flow regime follows that of Ishii and Chawla (Ref. H-1., p. 12). Here, the interfacial force for the dispersed phase (in this case, gas bubbles) is given by

$$M_i = \frac{\alpha F_b}{\mathrm{vol}_b} \quad . \tag{H-1}$$

This relation assumes steady-state conditions; therefore, the force on the bubble is caused by skin friction and form drag only. We neglect the transient forces that occur during bubble or slug acceleration (apparent mass and the Basset force), but include the increased slip caused by the nonuniform distribution of bubbles in a channel (also known as profile slip because bubbles redistribute due to the velocity profile). Thus, the force on the bubble can be represented as

$$F_b = \frac{1}{2} c_{Db} \rho_l V_r |V_r| A_{Pb} \, P_s \quad . \tag{H-2}$$

Combining Eqs. (H-1) and (H-2) with the relations for the projected area and the volume of a sphere, we have

$$M_i = \frac{\frac{3}{4} c_{Db} \alpha \rho_l V_r |V_r| P_s}{D_b} \quad . \tag{H-3}$$

Defining the interfacial-drag coefficient as

$$c_i = \frac{\frac{3}{4} c_{Db} \alpha \rho_l P_s}{D_b} \quad , \tag{H-4}$$

the interfacial force becomes

$$M_i = c_i |V_r| V_r \quad . \tag{H-5}$$

Equation (H-5) represents how the interfacial force appears in the TRAC momentum equations. Because it is calculated with the assumption of steady-state skin friction and form drag only, it is also called the interfacial-drag force, and the coefficient c_i, the interfacial-drag coefficient. The interfacial-drag force appears in the liquid and in the gas momentum equations, so that a drag force on one phase causes a pulling force of equal magnitude on the other phase. As shown in Eq. (H-5), the sign of the force (and therefore the direction) is determined by the relative velocity, which is defined as the gas velocity minus the liquid velocity.

To determine the interfacial-drag coefficient from Eq. (H-4), constitutive relations are required for the bubble diameter, the bubble-drag coefficient, and the profile slip factor.

A wide range of bubble diameters is observed in the literature. We used a simple expression suggested by Ishii (Ref. H-2.), as follows:

$$D_b = 2L_o \ , \tag{H-6}$$

where L_o is the Laplace coefficient defined as

$$L_o = \sqrt{\frac{\sigma}{g(\rho_l - \rho_g)}} \ . \tag{H-7}$$

Ishii suggested this expression as an approximate arithmetic average of minimum and maximum bubble diameters observed experimentally.

From Eq. (H-4), the interfacial-drag coefficient is inversely proportional to the bubble diameter, which therefore has a direct effect on the interfacial drag.

H.1.1.1.1. Bubbly Flow Interfacial-Drag Coefficient. To determine the bubble-drag coefficient (c_{Db}) we first calculate the bubble Reynolds number. This is defined as

$$Re_b = \frac{D_b \, V_r \, \rho_l}{\mu_l} \ . \tag{H-8}$$

The dependence of the bubble-drag coefficient on the bubble Reynolds number is calculated for three separate regimes: Stokes regime, viscous regime, and Newton's regime. The relations used are very similar to those proposed by Ishii and Chawla (Ref. H-1., pp. 13 and 14) for solid particles. Thus, this development assumes no bubble deformation and greatly simplifies the equations.

The three ranges of Reynolds numbers and their respective bubble-drag coefficients are as follows:

Stokes regime $(Re_b \le 0.1031)$,

$$c_{Db} = 240.0 \ ; \tag{H-9}$$

Viscous regime $(0.1031 < Re_b < 989.0)$,

$$c_{Db} = \frac{24.0}{Re_b}(1.0 + 0.15 Re_b^{0.687}) \ ; \tag{H-10}$$

and

Newton's regime $(989.0 \le Re_b)$,

$$c_{Db} = 0.44 \ . \tag{H-11}$$

The constant-Stokes-regime drag coefficient is equivalent to $24.0 / Re_b$, for $Re_b = 0.1$. Thus, at the very low bubble Reynolds numbers, this constant drag coefficient provides an upper limit on the drag equivalent to the well-known Stokes' drag law at $Re_b = 0.1$. Setting the drag coefficient equal to the constant value of 240.0 also prevents dividing by zero for the case in which the relative velocity (and therefore the Reynolds number) is zero. Bird, Stewart, and Lightfoot (Ref. H-3., p. 193) propose that Stokes flow can be assumed up to a Reynolds number of 0.1. Ishii and Chawla (Ref. H-1., p. 14) recommend a value of 1.0. In TRAC, a value of 0.1031 is used. This limit was adjusted from the 0.1 value so that the drag coefficient is essentially continuous with the viscous regime. [That is, using a value of 0.1031 for the bubble Reynolds number in Eq. (H-10) results in a drag coefficient of 240.1.]

The viscous-regime drag coefficient is an empirical relation proposed by Shiller and Nauman (Ref. H-4.). The upper range of this regime is chosen to be a bubble Reynolds number of 989.0. This is greater than the value of 800.0 suggested by Shiller and Nauman (Ref. H-4.), but less than the value of 1000.0 proposed by Ishii and Chawla (Ref. H-1., p. 14). The upper limit of 989.0 was chosen so that the drag coefficient was continuous with the Reynolds number at the transition to Newton's regime.

In Newton's regime, the drag force is approximately proportional to the square of the velocity of the fluid moving past the bubble, and the drag coefficient reaches an asymptotic value. We use a value of 0.44 as recommended by Bird, Stewart, and Lightfoot (Ref. H-3., p. 192). For comparison, a value of 0.45 is proposed by Ishii and Chawla (Ref. H-1.). The Newton's-regime bubble-drag coefficient is assumed to exist for all Reynolds numbers greater than 989.0. Comparisons with data (Ref. H-1., p. 14, and Ref. H-3., p. 193) suggest that this is true for solid particles up to a Reynolds number of 2×10^5.

H.1.1.1.2. Profile Slip in Bubbly Flow. In TRAC, we have added a factor to the interfacial-drag coefficient to account for the increased slip in channel flow that occurs as the bubbles redistribute in the velocity profile. Physically, the lighter phase (in this case bubbles) tends to migrate to a higher-velocity region of the channel, resulting in a higher void concentration in the central regime. In the two-fluid formulation, the additional slip between the phases can be accounted for by the introduction of a profile slip factor that appears in Eq. (H-4). Following Ishii (Ref. H-2.), this is defined as

$$P_s = \frac{\left(C_1 V_g - C_0 V_l\right)^2}{\left(V_r\right)^2} \quad , \tag{H-12}$$

where the distribution parameters are given by

$$C_0 = 1.2 + 0.2 \sqrt{\frac{\rho_g}{\rho_l}} \tag{H-13}$$

and

$$C_1 = \frac{1.0 - C_0 \alpha_b}{1.0 - \alpha_b}. \qquad \text{(H-14)}$$

This expression for the distribution parameter assumes fully developed turbulent flow in a circular channel (Ref. H-5.).

H.1.1.1.3. Slug-Flow Interfacial-Drag Coefficient. In TRAC, the interfacial-drag coefficient for slug flow is calculated in the same manner as for bubbly flow, but with a different bubble diameter. Referring to the flow-regime map (Fig. E-1. in Appendix E), the slug-flow regime is assumed to exist for local void fractions between 0.3 and 0.5, when the mass flux is less than 2000 $kg \cdot s^{-1} \cdot m^{-2}$. In this regime, the bubble diameter is calculated by linear interpolation between the bubble diameter from the Laplace coefficient [Eq. (H-6)] and the minimum of $40L_o$ or $0.9HD$. Kataoka and Ishii (Ref. H-6., p. 1933) cite that the slug bubbles cannot be sustained for channels with a diameter much larger than $40L_o$ because of interfacial instability. At this point, they form cap bubbles. This argument is also consistent with the data of Grace et al. (Ref. H-7.) and the analysis of Kitscha and Kocamustafaogullari (Ref. H-8.). Also, Ishii and Chawla (Ref. H-1., p. 25) limit the bubble size to 90% of the hydraulic diameter.

The interpolation uses the void fraction as the independent variable. Thus, the interfacial-drag coefficient used in the code for the slug-flow regime uses a solid spherical particle drag correlation, modified by increasing the diameter up to that of the channel hydraulic diameter. This has a significant effect on the interfacial drag because the calculated value is inversely proportional to the bubble diameter [Eq. (H-3)].

H.1.1.2. Input Required to Implement the Correlations. To calculate the interfacial drag, the relative velocity, void fraction, liquid density, vapor density, surface tension, and liquid viscosity are used as input [see Eqs. (H-4), (H-6), (H-7), (H-8), (H-12), (H-13), and (H-14)].

Because the interfacial drag is calculated at cell edges, these quantities must be calculated accordingly. The definitions are given below.

The relative velocity V_r used in Eqs. (H-8) and (H-12) is required in the 3D VESSEL for all three directions. In this case, the code uses the magnitude of a vector-average relative velocity rather than the absolute value of the actual relative velocity at the interface. In this way, spatial averaging is achieved, and the potential for radical changes in the relative velocity is reduced. To present the definitions of the relative velocities, the same nomenclature for the 3D mesh-cell velocities given in Section 2.0. is used.

Referring to Section 2.1.5., the magnitude of the vector relative velocity that is used for the calculation of the interfacial drag in the axial direction is given by

$$V_{rz} = \left\{ \left[V_{gz}(r,\theta,z+\tfrac{1}{2}) - V_{lz}(r,\theta,z+\tfrac{1}{2}) \right]^2 \right.$$
$$+ \left[\left\{ V_{gr}(r+\tfrac{1}{2},\theta,z) + V_{gr}(r-\tfrac{1}{2},\theta,z) \right\} / 2 \right.$$
$$\left. - \left\{ V_{lr}(r+\tfrac{1}{2},\theta,z) + V_{lr}(r-\tfrac{1}{2},\theta,z) \right\} / 2 \right]^2$$
$$+ \left[\left\{ V_{g\theta}(r,\theta+\tfrac{1}{2},z) + V_{g\theta}(r,\theta-\tfrac{1}{2},z) \right\} / 2 \right.$$
$$\left. \left. - \left\{ V_{l\theta}(r,\theta+\tfrac{1}{2},z) + V_{l\theta}(r,\theta-\tfrac{1}{2},z) \right\} / 2 \right]^2 \right\}^{0.5} . \qquad \text{(H-15)}$$

Thus, this relative velocity contains an arithmetic average of the surrounding relative velocities in the three directions. Recall from Section 2.0. that the *g* and *l* subscripts refer to the gas and liquid phases, respectively; the *z*, *r*, and θ subscripts refer to the axial, radial, and azimuthal directions, respectively; and the $+1/2$ or $-1/2$ positions refer to the cell-edge locations. To avoid divisions by small numbers and to prevent the calculation of nonphysical, interfacial-drag coefficients at the start of transients (the relative velocity may be identically 0.0), the relative velocity given in Eq. (H-15) is not allowed to be less than 0.01.

In the radial direction, the magnitude of the vector relative velocity is given by

$$V_{rr} = \left\{ \left[V_{gr}(r+\tfrac{1}{2},\theta,z) - V_{lr}(r+\tfrac{1}{2},\theta,z) \right]^2 \right.$$
$$+ \left[\left\{ V_{gz}(r,\theta,z+\tfrac{1}{2}) + V_{gz}(r,\theta,z-\tfrac{1}{2}) \right\} / 2 \right.$$
$$\left. - \left\{ V_{lz}(r,\theta,z+\tfrac{1}{2}) + V_{lz}(r,\theta,z-\tfrac{1}{2}) \right\} / 2 \right]^2$$
$$+ \left[\left\{ V_{g\theta}(r,\theta+\tfrac{1}{2},z) + V_{g\theta}(r,\theta-\tfrac{1}{2},z) \right\} / 2 \right.$$
$$\left. \left. - \left\{ V_{l\theta}(r,\theta+\tfrac{1}{2},z) + V_{l\theta}(r,\theta-\tfrac{1}{2},z) \right\} / 2 \right]^2 \right\}^{0.5} . \qquad \text{(H-16)}$$

The magnitude of the vector relative velocity that is used for the calculation of the interfacial drag in the azimuthal direction is defined differently because the interface is adjacent to locations in sectors θ and $\theta + 1$. The code calculates this velocity as

$$V_{r\theta} = \left\{ \left[\frac{V_{gz}(r,\theta,z+\frac{1}{2}) + V_{gz}(r,\theta,z-\frac{1}{2}) + V_{gz}(r,\theta+1,z+\frac{1}{2}) + V_{gz}(r,\theta+1,z-\frac{1}{2})}{4.0} \right.\right.$$

$$\left.\left. - \frac{V_{lz}(r,\theta,z+\frac{1}{2}) + V_{lz}(r,\theta,z-\frac{1}{2}) + V_{lz}(r,\theta+1,z+\frac{1}{2}) + V_{lz}(r,\theta+1,z-\frac{1}{2})}{4.0} \right]^2 \right.$$

$$+ \left[\frac{VVR13 / 2.0 + [V_{gr}(r+\frac{1}{2},\theta,z) + V_{gr}(r+\frac{1}{2},\theta+1,z)]}{4.0} \right.$$

$$\left. - \frac{VLR13 / 2.0 + [V_{lr}(r+\frac{1}{2},\theta,z) + V_{lr}(r+\frac{1}{2},\theta+1,z)]}{4.0} \right]^2$$

$$\left. + \left[V_{g\theta}(r,\theta+\frac{1}{2},z) - V_{l\theta}(r,\theta+\frac{1}{2},z) \right]^2 \right\}^{0.5} . \qquad \text{(H-17)}$$

In the above equation, the terms *VVR13* and *VLR13* have special meaning, depending on the ring number and the number of azimuthal sectors. For convenience, the chosen variable names, *VVR13* and *VLR13*, are identical to the actual coding. For the innermost ring, *VVR13* and *VLR13* have the same definition except that *VVR13* refers to the gas phase and *VLR13* refers to the liquid phase. Thus, the definition given below for *VVR13* is identical for the liquid phase, with the liquid subscript used in place of the gas subscript. In the innermost ring, the code averages in the velocities in the radial direction on the opposite side of the apex of the cylindrical geometry 3D mesh cell. Thus,

$$VVR13 = \left[V_{gr}(r+\tfrac{1}{2},\theta,z) + V_{gr}(r+\tfrac{1}{2},\theta+\tfrac{1}{2},z) \right] / 4.0$$
$$- \left[V_{gr}(r+\tfrac{1}{2},\theta+\frac{NTSX}{2},z) + V_{gr}(r+\tfrac{1}{2},\theta+1+\frac{NTSX}{2},z) \right] RS / 2.0 \ , \qquad \text{(H-18)}$$

where

NTSX	=		number of azimuthal sectors,
RS	=	0.0	if *NTSX* = 1, and
RS	=	0.5	if *NTSX* > 1.

The above equation holds for the case in which *NTSX* is an even number (which is typical for most input decks). In the case in which *NTSX* is odd, the following relation for *VVR13* is used:

$$VVR13 = \left[V_{gr}(r+\tfrac{1}{2},\theta,z) + V_{gr}(r+\tfrac{1}{2},\theta+\tfrac{1}{2},z)\right] / 4.0 - \left[V_{gr}(r+\tfrac{1}{2},\theta+1+\frac{NTSX}{2},z)\right]RS \quad , \tag{H-19}$$

where *RS* and *NTSX* have the same meanings as above. As noted above, Eqs. (H-13) and (H-14) are identical for *VLR13* except for the change in subscript from *g* to l.

For rings outside of the innermost ring (i.e., rings 2, 3, 4, . . .), the variables *VVR13* and *VLR13* take on different definitions. In this case, *VVR13* is defined as

$$VVR13 = \left[V_{gr}(r-\tfrac{1}{2},\theta,z) + V_{gr}(r-\tfrac{1}{2},\theta+1,z)\right] / 2.0 \quad . \tag{H-20}$$

Thus, combining Eq. (H-15) with Eq. (H-12), we see that the radial gas velocity contribution is simply the arithmetic average of the four components near the azimuthal interface. The code calculates *VLR13* in this case with special weighting factors on the liquid velocities to take into account the momentum of the liquid. Thus,

$$VLR13 = (FWTK)(FV1)V_{lr}(r-\tfrac{1}{2},\theta,z) + (FWTE)(FV2)V_{lr}(r-\tfrac{1}{2},\theta+1,z) \quad , \tag{H-21}$$

where

$$FWTK = \left[1.00001-\alpha(r,\theta,z)\right]\mathrm{vol}(r,\theta,z) / \left\{\left[1.00001-\alpha(r,\theta,z)\right]\mathrm{vol}(r,\theta,z) + \left[1.00001-\alpha(r,\theta+1,z)\right]\mathrm{vol}(r,\theta+1,z)\right\} \quad ,$$

$$FWTE = \left[1.00001-\alpha(r,\theta+1,z)\right]\mathrm{vol}(r,\theta+1,z) / \left\{\left[1.00001-\alpha(r,\theta,z)\right]\mathrm{vol}(r,\theta,z) + \left[1.00001-\alpha(r,\theta+1,z)\right]\mathrm{vol}(r,\theta+1,z)\right\} \quad ,$$

$$FV1 = \left[VOLG(r,\theta,z)FA_r(r-\tfrac{1}{2},\theta,z)(1.0-\alpha(r-1,\theta,z))\right] / \left[\mathrm{vol}(r,\theta,z)FAG_r(r-\tfrac{1}{2},\theta,z)(1.00001-\alpha(r,\theta,z))\right] \quad ,$$

and

$$FV2 = \left[VOLG(r,\theta+1,z)FA_r(r-\tfrac{1}{2},\theta+1,z)(1.0-\alpha(r-1,\theta+1,z))\right] / \left[\mathrm{vol}(r,\theta+1,z)FAG_r(r-\tfrac{1}{2},\theta+1,z)(1.00001-\alpha(r,\theta+1,z))\right] \quad .$$

The code restricts *FV*1 and *FV*2 to be less than or equal to 1.0. As in the case of the axial and radial directions, the magnitude of the vector-average relative velocity used for the interfacial drag in the azimuthal direction is not allowed to drop below a value of 0.01.

In the 1D components, the definition of the relative velocity for use in the interfacial-drag calculations is much simpler because only one direction is considered. Thus,

$$V_r = V_g(j+\tfrac{1}{2}) - V_l(j+\tfrac{1}{2}) \quad . \tag{H-22}$$

The void fraction that is used for Eq. (H-4) is averaged spatially. This is required because the void fraction is a cell-centered quantity, whereas the interfacial drag is calculated at the cell edges. The averaging technique is the same regardless of the flow direction and is the same for the 3D VESSEL component as well as for the 1D components. The spatially averaged void fraction is defined as

$$\langle \alpha \rangle = \frac{\Omega(j)\alpha(j) + \Omega(j+1)\alpha(j+1)}{\Omega(j) + \Omega(j+1)} \quad . \tag{H-23}$$

The Ωs used in the equation above are the input cell lengths adjoining the cell edge. For instance, in the axial direction in the vessel, the Ωs represent the heights of the cells. In the radial direction, this is the thickness of the rings and in the azimuthal direction, this is the average azimuthal thickness of the adjacent cells. In the 1D components, this is the input cell lengths. The void fraction is restricted to the range 0.00001 to 0.9999 in all components to avoid division by zero.

The other variables that are required to compute the bubbly slug interfacial drag are the following properties: liquid density, vapor density, surface tension, and liquid viscosity. In all directions in the 3D VESSEL, the code uses an arithmetic average of the adjacent cell-center values. For instance, in the azimuthal direction the average surface tension is given by

$$\sigma = \left[\sigma(r,\theta,z) + \sigma(r,\theta+1,z)\right] / \, 2.0 \quad . \tag{H-24}$$

In the 1D components, the code uses a weighted average of the liquid and vapor density with the adjacent cell lengths. Thus, for example, the liquid density is given by

$$\langle \rho_l \rangle = \frac{\rho_l(j)DX(j) + \rho_l(j+1)DX(j+1)}{DX(j) + DX(j+1)} \quad . \tag{H-25}$$

The surface tension, liquid viscosity, and vapor viscosity are donor-celled. For surface tension and liquid viscosity, the upstream values are used, depending on the sign of the liquid velocity. Therefore,

$$\sigma = \sigma(j) \text{ if } V_l\left(j+\tfrac{1}{2}\right) \geq 0 \quad ,$$

$$\sigma = \sigma(j+1) \text{ if } V_l\left(j+\tfrac{1}{2}\right) < 0 \quad ,$$

$$\mu_l = \mu_l(j) \text{ if } V_l\left(j+\tfrac{1}{2}\right) \geq 0 \quad ,$$

and

$$\mu_l = \mu_l(j+1) \text{ if } V_l\left(j+\tfrac{1}{2}\right) < 0 \quad . \tag{H-26}$$

In the above definitions, a special case occurs in the 3D VESSEL at the boundaries of the component. For instance, at the top level it is sufficient to say that the void fraction in a cell in level $k + 1$ must be set to the value for a corresponding cell in level k, because level $k + 1$ does not exist. Similar situations occur at the bottom level and in the outermost ring. Thus, the required properties and void fraction are revised when the adjacent cell of interest lies outside the boundary of the vessel.

H.1.1.3. Model as Coded. For the 1D components, the interfacial-drag coefficients are determined in subroutine StbVel1D (FEMOM in TRAC-M/F77). In the 3D VESSEL component, they are calculated in subroutine CIF3. The interfacial-drag force is calculated at the cell edges rather than the cell centers because the velocities and the momentum equations are defined here. The models are identical in all three directions in the 3D VESSEL and in the 1D components. Thus, Eqs. (H-4) through (H-14) are used in all cases, and their implementation varies only in the definition of the local relative velocities, void fractions, and properties. These differences are described in Section H.1.1.2. above.

The code calculates the interfacial-drag coefficient explicitly. That is, for the input velocities and properties, the values from the previous time step are used. No iterations are performed.

In the coding, the 3/4 factor appearing in Eq. (H-4) is combined with the constants that appear in Eqs. (H-9), (H-10), and (H-11). Therefore, if one inspects the actual coding, one will find that Eqs. (H-9), (H-10), and (H-11) are written with the constants 180.0, 18.0, and 0.33, respectively.

The interfacial drag is a flow-regime-dependent quantity. Thus, the bubbly slug correlations described in this section are only used when the total mass flux and void fraction are in a certain range. The limits are given at the beginning of Section H.1.1. but are repeated here for completeness.

For mass fluxes less than 2000 $kg \cdot s^{-1} \cdot m^{-2}$, bubbly flow is assumed for void fractions up to 0.3, and slug flow between a void fraction of 0.3 and 0.5. For mass fluxes greater than 2700 $kg \cdot s^{-1} \cdot m^{-2}$, bubbly flow is assumed for void fractions up to 0.5. For mass fluxes

between 2000 and 2700, bubbly flow is assumed up to a void fraction of 0.3, and an interpolation is made between bubbly and slug for void fractions between 0.3 and 0.5. (See Appendix E for a full description of the flow-regime map, and refer to Fig. E-1. in Appendix E to visualize the limits of this regime.)

A change between TRAC-PF1/MOD2 and MOD1 in the flow-regime determination is that in MOD2, the void fraction that is used to determine the flow regime is donor-celled with the vapor velocity. Physically this makes sense because the cell-edge interfacial drag should represent the fluid that is passing through it.

H.1.1.4. Weighting, Magnitude Limits, and Rate Limits. Several limits are imposed to prevent unreasonably large or small numbers from occurring and thus, to prevent numerical difficulties. These are applied to the bubble diameter, D_b, to the interfacial-drag coefficient, c_i, to the relative velocity, and to the void fraction. We chose the limits based on the range of data provided in the literature and on experience obtained during the course of code development.

H.1.1.4.1. Bubble-Diameter Weighting and Limits. In the bubbly flow regime, the bubble diameter is not allowed to be less than 0.0001 m and is not allowed to be greater than the minimum of $40L_o$ or $0.9HD$ [where, because of Eq. (H-6), $0.9HD$ will be the controlling limit]. In the slug regime, the diameter is interpolated with a weighting factor between the bubble diameter determined from the Laplace coefficient and the minimum of $40L_o$ or $0.9HD$. As described in Appendix E, the slug regime is allowed for void fractions between 0.3 and 0.5 and mass fluxes less than 2000 $kg\cdot s^{-1}\cdot m^{-2}$. The weighting factor is 0.0 at void fraction 0.3 and below, 1.0 at void fractions 0.5 and above, and is increasing between the extremes.

For mass fluxes between 2000 and 2700 $kg\cdot s^{-1}\cdot m^{-2}$ and void fractions between 0.3 and 0.5, the code alters the weighting factor with a linear interpolation in mass flux between the 2000 and 2700 $kg\cdot s^{-1}\cdot m^{-2}$ values. After the weighting factor is limited between the values of 0.0 and 1.0, the code calculates a bubbly slug equivalent bubble diameter that is used to find the interfacial drag as

$$D_b = D_b(1.0 - XS) + \min(40L_o, 0.9HD)(XS) \ , \qquad \text{(H-27)}$$

where XS is the weighting factor. A plot of this weighting factor for the 3D VESSEL is presented in Fig. H-1. for mass fluxes below the 2000 $kg\cdot s^{-1}\cdot m^{-2}$ limit, above the 2700 $kg\cdot s^{-1}\cdot m^{-2}$ limit, and at an intermediate value of 2350 $kg\cdot s^{-1}\cdot m^{-2}$

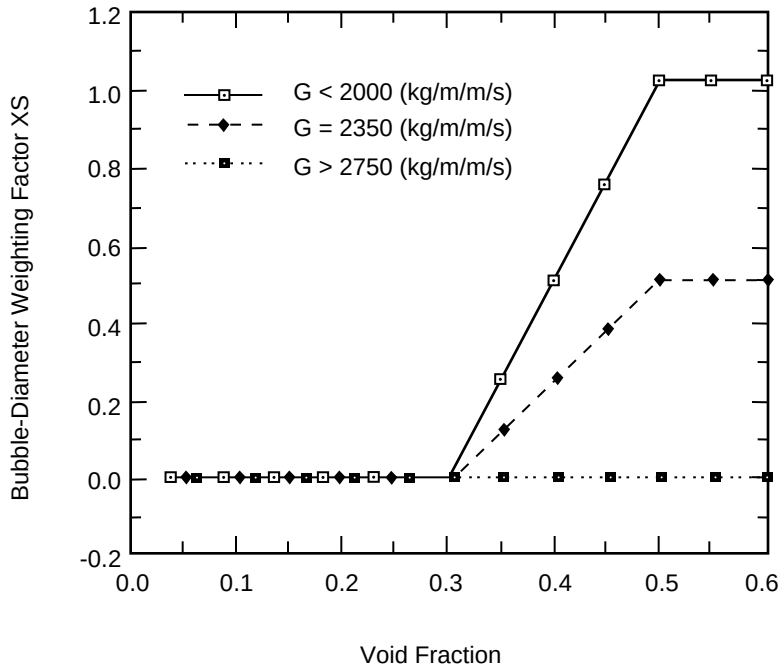

Fig. H-1. Bubble-diameter weighting factor in the bubbly slug regime for the 3D VESSEL.

H.1.1.4.2. Relative Velocity Limits. For calculations of the bubble Reynolds number in a 3D VESSEL, the relative velocity is limited to be greater than 0.01 $m \cdot s^{-1}$. As shown in Section H.1.1.2., the relative velocity used in calculating the interfacial drag is always positive. The limit ensures that, for instance, at the start of transients or when a flow reversal occurs and the relative velocity is near zero, a very large drag coefficient is not calculated. This limit is imposed with the rate limit in mind because some iterations may be required to allow the interfacial drag to reach a reasonable number, if a very large number was calculated initially.

H.1.1.4.3. Rate Limit on the Interfacial Drag. The allowable change in the interfacial drag from one time step to the next is identical for both the 3D VESSEL and the 1D components. In a departure from the method used in MOD1 where a new-time and old-time average was taken, the allowable change in MOD2 is based on real time to eliminate the sensitivity to the time-step size. The maximum and minimum allowable changes in the interfacial drag are given by

$$c_{i,\max} = c_{i,old} 2^{20.0\Delta t} \tag{H-28}$$

and

$$c_{i,\min} = c_{i,old} 0.5^{20.0\Delta t} \quad . \tag{H-29}$$

Thus, the amount of transient time required for the interfacial drag to double or halve is 0.05 s. The maximum allowable change is limited to be less than 2.0, and the minimum allowable change is limited to be greater than 0.4. For the special case of steady-state calculations, the new-time interfacial drag is a weighted average of 90% old time and 10% new time to provide stable convergence.

H.1.1.4.4. Interfacial Drag for Zero Flow Area and Zero Volume. If the flow area of the cell edge of interest is less than 1.0×10^{-10} m^2 or the cell volume is less than 1.0×10^{-12} m^3, the interfacial drag is set to zero to avoid extra computation.

H.1.1.4.5. Limits on the Void Fraction. The void fraction used to calculate the interfacial drag is restricted to the range 0.00001 to 0.9999 in all components.

H.1.1.5. Variations in the Application of the Correlations. The basic relations described here for the bubbly slug regime are used throughout the code in all 1D components and in the 3D VESSEL component. In some special cases, the interfacial drag is overridden or altered. These cases are

1. core reflood in the vessel (Section H.1.5.),
2. accumulator logic in the PIPE component (Sections H.1. and H.2.),
3. stratified flow in 1D components (Section H.1.3.),
4. user-defined CCFL in the vessel (Appendix J, Section J.4.),
5. complete phase-separation option in 1D components (Section H.1.6.1.),
6. stratified flow in the vessel (Section H.1.3.), and
7. two-phase flow in the upper plenum of the vessel (Section H.1.1.10.).

H.1.1.6. Consistency with the Interfacial Heat Transfer. In the development of Eq. (H-4), it is noted that instead of the actual interfacial area, the projected bubble area is used. For spherical geometry, the projected area is one-quarter times the surface area. In the calculation of the interfacial heat transfer, the code calculates the bubble diameter using Eq. (H-6), and the bubble surface area is used to calculate the interfacial heat-transfer area. Thus, in all cases (each direction in the 3D VESSEL and in the 1D components), the method is consistent in the calculation of both the interfacial drag and heat transfer in the bubbly regime because the same method is used in the calculation of the bubble diameter. However, differences do occur in the definition of the transport properties and in the calculation of the slug-regime interfacial area.

In general, the flow regime used in the interfacial heat transfer is determined using the local cell-center quantities. The case of stratified flow is one exception: the cell-edge, stratified-flow weighting factors that are calculated for the interfacial drag at the cell edges are averaged and used in the interfacial heat-transfer calculation.

With respect to the surface tension and densities used in the calculation of the bubble diameter, the cell-centered quantities are used in the interfacial heat-transfer calculation because this is also a cell-centered quantity. The differences that arise between it and the interfacial-drag calculation bubble diameter are expected to be small.

In the determination of the slug-regime interfacial heat transfer, a correlation from the literature is used for the interfacial area that takes into account the range in possible bubble diameters trailing the slug. In our determination of the interfacial drag, the trailing bubbles are neglected because of the domination of the slug on the drag.

H.1.1.7. Assessment of the Correlations. For this report, most of the individual bubbly slug, interfacial-drag correlations are not directly assessed against data, but rather the code as a whole is assessed. An effort was made to find previous assessments of the correlations if available, to perform some new data assessments, and to show comparisons with other interfacial-drag methods. The primary contributions to the calculation of the interfacial-drag coefficient are from the bubble diameter and the drag coefficient. In the discussion below, we try to separate the effects by first providing assessment of the drag coefficient.

H.1.1.7.1. Previous Assessment. In the Stokes regime for bubbly flow, a constant drag coefficient is used [Eq. (H-8)]. This gives a coefficient equivalent to Stokes' drag law for a bubble Reynolds number of 0.1, but underpredicts the drag for Reynolds numbers less than this value. Stokes' drag law gives excellent agreement with data as shown by many in the literature (Refs. H-1., H-3., and H-9.). Except for rare conditions (such as at the start of transients when the relative velocity is near zero), this regime is not encountered in normal two-phase flow experiments, or in typical reactor-safety accidents. Thus, the constant value chosen gives a reasonable maximum value of the drag coefficient at such low velocities and prevents very large numbers from being calculated.

The viscous-regime drag coefficient is an empirical relation proposed by Shiller and Nauman (Ref. H-4.). It was determined by Clift et al. (Ref. H-10., p. 111) that this relation is in agreement with the drag data for spheres within +5% to –4%. The Shiller and Nauman correlation is very similar to a relation proposed by Ishii and Chawla (Ref. H-1., p. 14),

$$c_{Db} = \frac{24.0}{Re_b}\left(1.0 + 0.1 Re_b^{0.75}\right) \quad , \tag{H-30}$$

which they show to provide excellent agreement with solid particle data (Ref. H-1., p. 27). A comparison between the two relations is given in Fig. H-2. Because both correlations provide nearly identical bubble-drag coefficients, the viscous-regime drag coefficient used in TRAC should give good agreement with the data shown in Ishii and Chawla.

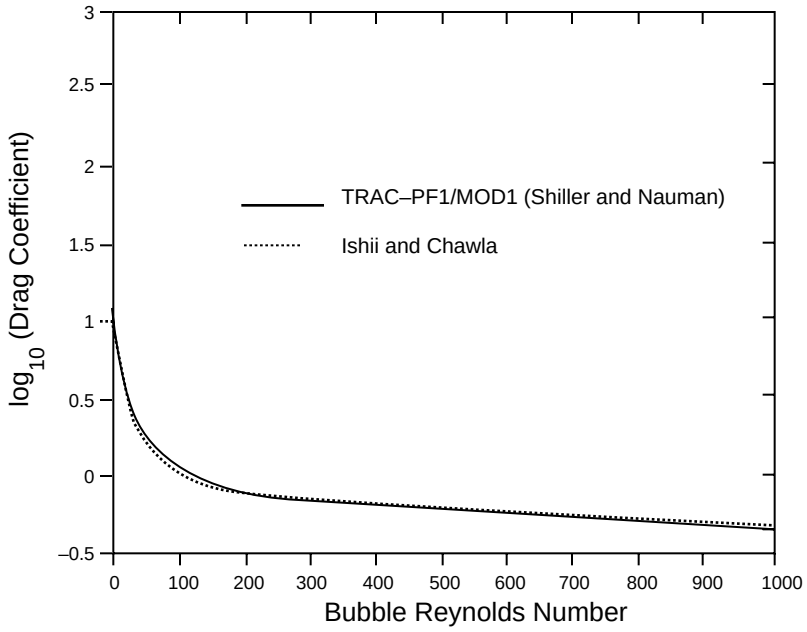

Fig. H-2. Comparison of the viscous-regime drag coefficient from Shiller and Nauman with the correlation proposed by Ishii and Chawla.

As mentioned above in Section H.1.1.1., in Newton's regime the code assumes a drag coefficient of 0.44. Bird et al. (Ref. H-3., p. 193) have shown this value to provide excellent agreement with solid particle data.

From the discussion above, it is apparent that the correlations used in TRAC for the bubble drag have a solid foundation of data to support them, if the particles are spherical. Since these correlations are used in dispersed bubbly flow, the conditions of bubble distortion and distribution are not accounted for. For this reason, some new assessment against other two-phase flow correlations was performed and is described in the following subsection.

H.1.1.7.2. Comparison to Other Correlations. The TRAC bubbly slug interfacial-drag coefficient [as defined by Eq. (H-4)] is compared to those given by Ishii and Chawla (Ref. H-1., Eq. 40, p. 22) and Chexal and Lellouche [Ref. H-11., Eqs. (2-1) through (2-5), pp. 2-3]. For this discussion, the three models are referred to as TRAC, Ishii, and Chexal, respectively. The comparison to Ishii is direct, since this is a two-fluid model. However, the Chexal correlation was developed using the drift-flux momentum equation, and some manipulation is required to make a direct comparison. Following the development of Anderson and Chu (Ref. H-12.), the following equation is used to calculate the interfacial-drag coefficient using a drift flux and a void fraction predicted from the Chexal model:

$$c_i = \frac{g(\rho_l - \rho_g)(1-\alpha)^3 \alpha}{|V_{gj}| V_{gj}} \quad . \tag{H-31}$$

The Chexal model has been assessed against a wide range of data (Ref. H-13.). Because of the database supporting the correlation, it was chosen for this comparison. The range in the data used to develop and assess the Chexal model is given in Table H-1.

The comparison among the Ishii, TRAC, and Chexal interfacial-drag predictions for a superficial liquid velocity (j_l) of 0.1 m·s^{-1}, a pressure of 0.4 MPa, and a hydraulic diameter of 0.011 m is given in Fig. H-3. The values presented in the figures were calculated with a small driver code (approximately 700 Fortran statements). To avoid forcing the correlations used in TRAC and in Ishii into nonphysical situations, the following method was used. Using the fixed j_l and the physical properties, the superficial gas velocity (j_g) was varied between 0.0 and 25.0 m·s^{-1}. For each j_g and j_l, the void fraction was determined by iteration using the Chexal correlation. Using the computed void fraction, the TRAC and Ishii drag coefficients were determined explicitly. The Chexal drag coefficient was then determined using Eq. (H-31), for the void fraction and the drift flux predicted by the correlation. The drag coefficient is presented as a logarithm for easier comparison. Note also that the interfacial-drag coefficient has the units kg·m^{-4} [Eq. (H-4)].

The comparison in Fig. H-3. shows that in the bubbly slug regime, the TRAC-calculated interfacial-drag coefficient lies between the Chexal and Ishii values. This result is a significant improvement over the MOD1 prediction that predicted values above that of Ishii's value for bubbly flow. The use of a more realistic bubble-diameter correlation (rather than the Weber number criterion) and the addition of the profile slip are the reasons for the improvement. For a hydraulic diameter of 0.01968 m, the comparison is very similar (Fig. H-4.). This diameter was chosen because it is typical of the steam-generator tubes in a full-size plant. For a hydraulic diameter of 0.738 m (Fig. H-5.), the TRAC prediction in the bubbly regime is in excellent agreement with Chexal. In the slug

TABLE H-1.
Range of Data Supporting the EPRI Correlation (Ref. H-11.)

Parameter	Range
Pressure	0.1–16.0 MPa
Pipe Diameter	0.16–0.457 m
Bundle Geometry:	
Rods / Bundle	6–161
Hydraulic Diameter	0.0097–0.047 m

regime, however, the code underpredicts the drag as the bubble diameter is allowed to increase up to about 0.1 m. This diameter is typical of hot-leg and cold-leg piping in full-size plants. Thus, for a variety of diameters, and at conditions similar to large-break LOCAs, the code is in very good agreement with the Chexal model and is an improvement over the MOD1 code.

H.1.1.8. Use of TRAC Bubbly Slug Correlations Outside the Database. The TRAC bubbly slug interfacial-drag-coefficient correlations are based on the assumptions that the bubbles (and slugs) are spherical (see Section H.1.1.1. for a full description). The database for the spherical geometry correlations is in general for single, solid particles in open channels with no effect on the drag from the distortion of the spheres. Thus, the database does not include the effect of bubble distortion. Also for very large channels, the TRAC correlations are being used outside the database. In Fig. H-6., the comparison of TRAC with Ishii and Chexal for large diameter (0.738 m) and higher pressure (1.0 MPa) shows that TRAC and Chexal are in reasonable agreement for the bubbly regime. A similar comparison is evident at 7.0 MPa (Fig. H-7.). This large diameter is typical of PWR primary-system piping and is outside the range of the Chexal correlation (Table H-1.). However, the comparison indicates that the TRAC-calculated drag coefficient is reasonable at these large diameters.

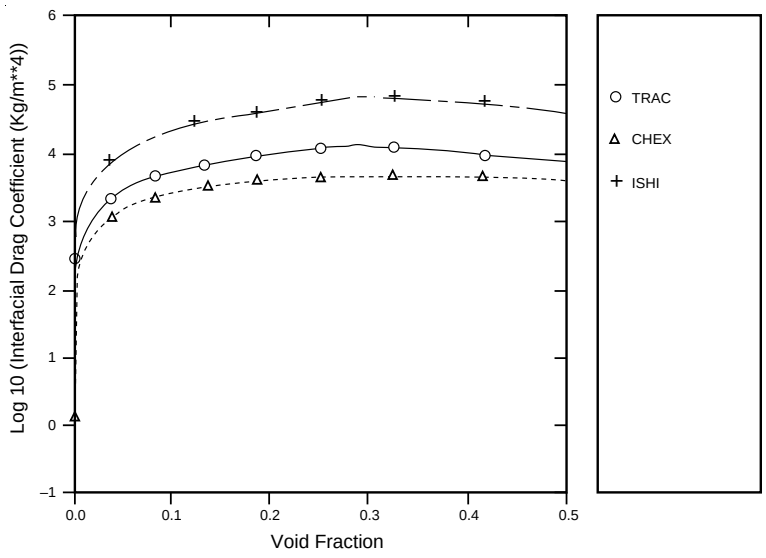

Fig. H-3. Comparison of the TRAC-calculated interfacial-drag coefficient (solid line) to the prediction by Ishii and Chawla (long dash) and the prediction by Chexal and Lellouche (dashed line) for a superficial liquid velocity of 0.1 $m \cdot s^{-1}$, a pressure of 0.4 MPa, and a hydraulic diameter of 0.011 m.

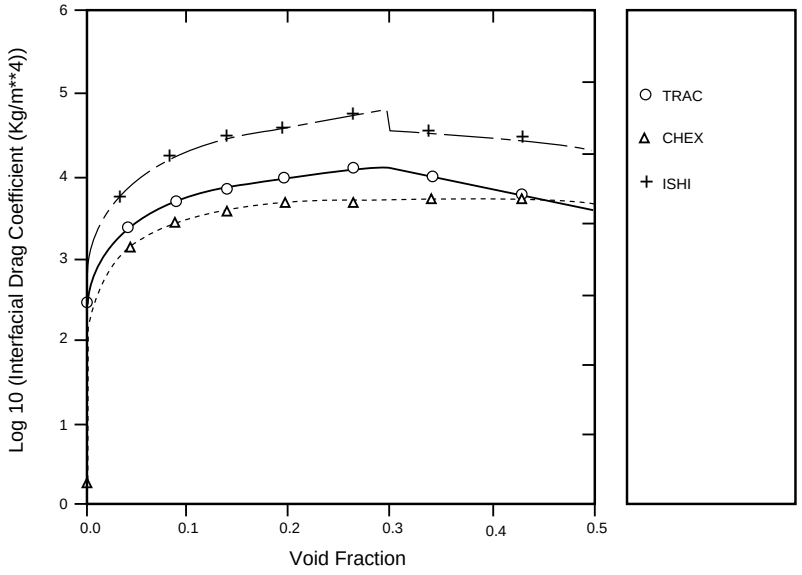

Fig. H-4. Comparison of the TRAC-calculated interfacial-drag coefficient (solid line) to the prediction by Ishii and Chawla (long dash) and the prediction by Chexal and Lellouche (dashed line) for a superficial liquid velocity of 0.1 $m \cdot s^{-1}$, a pressure of 0.4 MPa, and a hydraulic diameter of 0.0197 m.

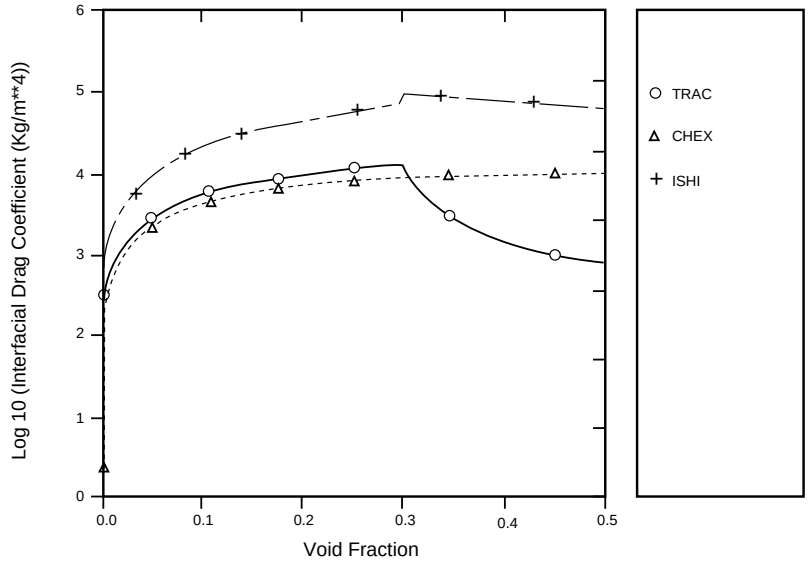

Fig. H-5. Comparison of the TRAC-calculated interfacial-drag coefficient (solid line) to the prediction by Ishii and Chawla (long dash) and the prediction by Chexal and Lellouche (dashed line) for a superficial liquid velocity of 0.1 $m \cdot s^{-1}$, a pressure of 0.4 MPa, and a hydraulic diameter of 0.0738 m.

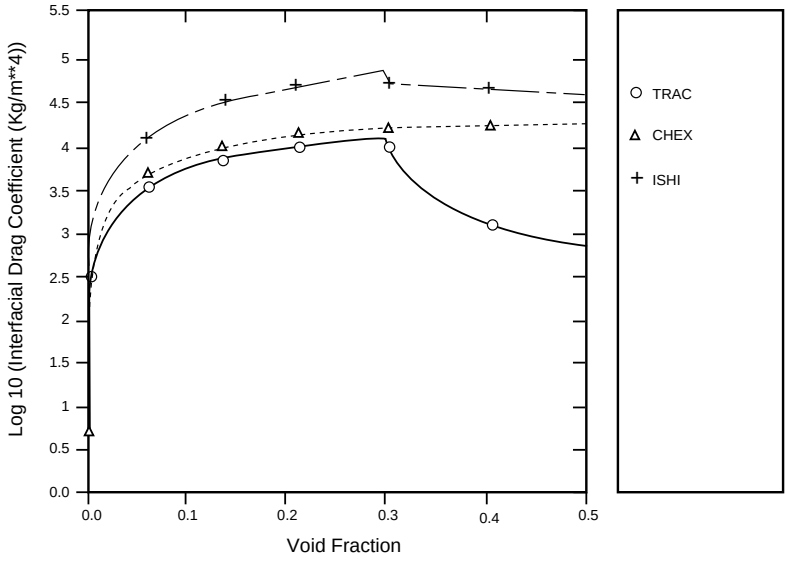

Fig. H-6. Comparison of the TRAC-calculated interfacial-drag coefficient (solid line) to the prediction by Ishii and Chawla (long dash) and the prediction by Chexal and Lellouche (dashed line) for a superficial liquid velocity of 0.1 $m \cdot s^{-1}$, a pressure of 1.0 MPa, and a hydraulic diameter of 0.0738 m.

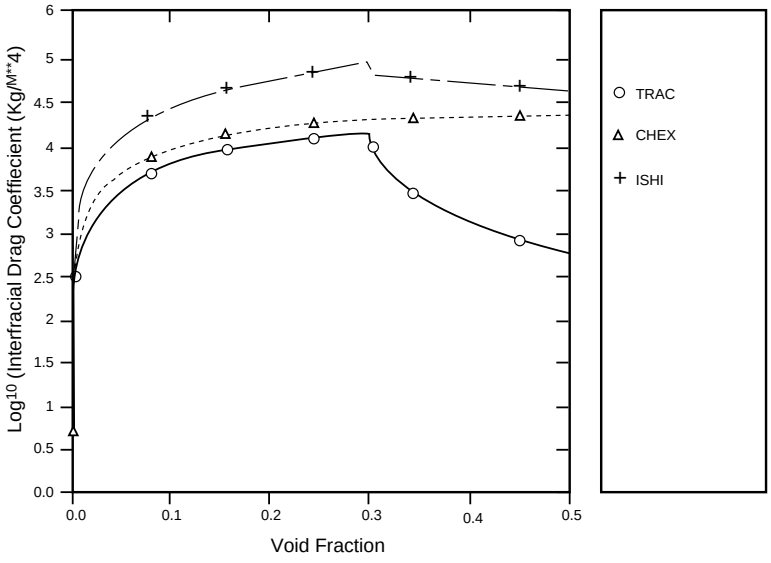

Fig. H-7. Comparison of the TRAC-calculated interfacial-drag coefficient (solid line) to the prediction by Ishii and Chawla (long dash) and the prediction by Chexal and Lellouche (dashed line) for a superficial liquid velocity of 0.1 $m \cdot s^{-1}$, a pressure of 7.0 MPa, and a hydraulic diameter of 0.0738 m.

H.1.1.9. Scaling Considerations. The correlations for the interfacial-drag coefficient for bubbly flow used in TRAC were developed based on the data for single spherical particles. Assessment results given in Section H.1.1.7. show that, depending on the bubble diameter calculated by the Laplace coefficient criterion, TRAC can provide a reasonable estimate for the interfacial drag and therefore, can predict the relative velocity between the phases. For most applications, the bubble Reynolds number is greater than 1000.0. Thus, the drag coefficient is a constant value of 0.44, independent of hydraulic diameter and pressure. A significant part of the prediction, therefore, is the Laplace coefficient criterion that is used to predict the bubble diameter. The form of this relation includes the effect of increased pressure on the change in surface tension and liquid density [see Eq. (H-6)]. We have shown previously that for large hydraulic diameters at high pressure, the bubbly regime interfacial drag predicted by TRAC is in reasonable agreement with Ishii and Chexal (Figs. H-6. and H-7.). At small diameters and low pressure, the comparison is also very good and shows that the bubble concentration is taken into account accurately with the new profile slip factor. A comparison of TRAC with the other correlations for a small diameter and high pressure again shows a reasonable comparison (Fig. H-8.). Thus, as the pressure increases, TRAC provides a reasonable prediction for the bubbly interfacial drag. This pressure effect at a single hydraulic diameter of 0.01968 m is shown in Fig. H-9. for the pressure range 0.1 to 7.0 MPa (1.0 to 70.0 bar).

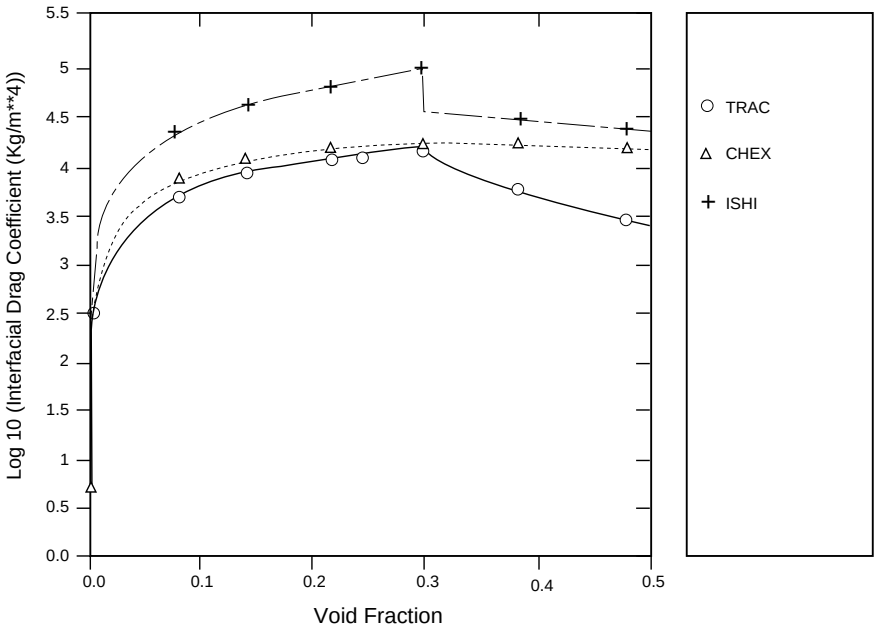

Fig. H-8. Comparison of the TRAC-calculated interfacial-drag coefficient (solid line) to the prediction by Ishii and Chawla (long dash) and the prediction by Chexal and Lellouche (dashed line) for a superficial liquid velocity of 0.1 $m \cdot s^{-1}$, a pressure of 7.0 MPa, and a hydraulic diameter of 0.01968 m.

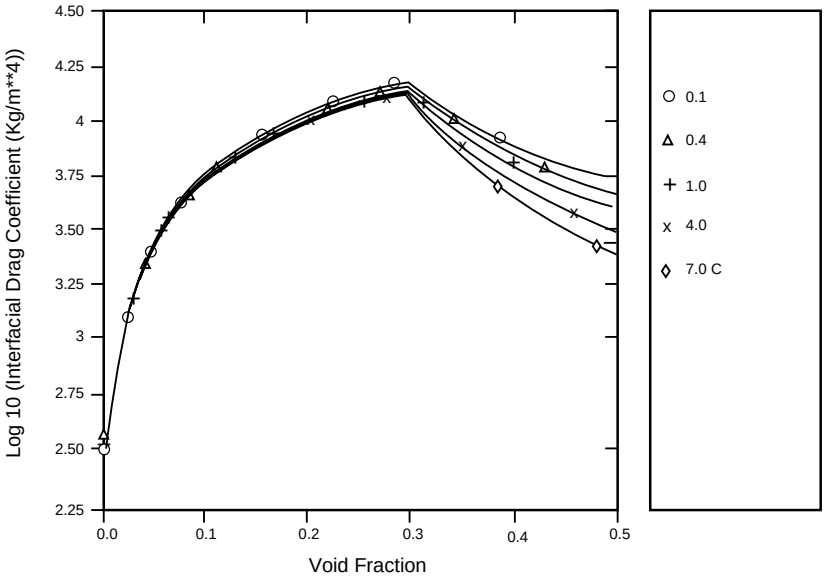

Fig. H-9. Comparison of the TRAC-calculated interfacial-drag coefficient for a superficial liquid velocity of 0.1 $m \cdot s^{-1}$, a hydraulic diameter of 0.01968 m, and a range in pressure of 0.1–7.0 MPa.

The effect of increased scale is discussed in the previous section. It is shown there that as the hydraulic diameter is increased, the TRAC prediction for the bubbly drag is reasonable in comparison with Ishii and Chexal.

H.1.1.10. Special Model for Bubbly Flow in the Upper Plenum. Through the input, the user can describe which regions of the VESSEL component are in the core, lower plenum, downcomer, and upper plenum. If there is bubbly slug flow in the upper plenum, a special void-fraction correlation is used to determine the interfacial-drag coefficient. The model of choice is the Wilson correlation (Ref. H-14.). This correlation is based on steam-water data in pipes of 0.1- and 0.48-m diameter at pressures between 2.0 and 5.5 MPa, and additional data obtained in 0.46- and 0.914-m-diameter pipes between pressures of 4.1 and 13.8 MPa. The tests were done with either zero liquid-flow rate (stagnant pool-type conditions) or at small liquid-flow rates established by natural circulation. The correlation has the following form:

$$\alpha_w = C_1 \left(\frac{\rho_g}{\rho} \right)^{C_2} k u_g^{C_3} \left(\frac{\sqrt{\sigma / g_c \Delta\rho}}{HD} \right)^{C_4} \left(\frac{j_g}{j} \right)^{C_5} \quad , \tag{H-32}$$

where

$$ku_g = \frac{j_g}{\left(\frac{\sigma g_c}{\Delta\rho}\right)^{0.25}} \quad ,$$

$$C_2 = 0.12,\ C_4 = 0.1,\ C_5 = 0.6 \quad ,$$

and

$$\left.\begin{matrix} C_1 = 0.564 \\ C_3 = 0.67 \end{matrix}\right\} ku_g \le 1.5$$

$$\left.\begin{matrix} C_1 = 0.619 \\ C_3 = 0.47 \end{matrix}\right\} ku_g > 1.5.$$

This model is implemented into TRAC using the relation

$$C_i = g_c \Delta\rho\ \alpha_w (1-\alpha) / (j_g\ /\ \alpha_w)^2 \quad , \tag{H-33}$$

which is developed by solving for the interfacial drag from the steady-state two-fluid momentum equations.

To perform an assessment of the correlation, we used the same method as before (i.e., comparisons to the Chexal and Ishii correlations). Assuming prototypical upper-plenum conditions (3.5-m diameter, low liquid flow), the comparisons are shown in Figs. H-10. and H-11. for 0.1 and 0.4 MPa, respectively. The results show very good agreement with the Chexal correlation, but this agreement is much lower than the prediction of the Ishii model. This is to be expected because the Chexal model was developed against larger-diameter data, whereas the Ishii model was developed against smaller-diameter data.

H.1.1.11. Summary and Conclusions. The correlations used to predict the interfacial-drag force in the calculation of the bubbly slug flow regime in TRAC have been fully described. Many changes have been made since MOD1 was released. These changes represent a significant improvement and were recommended through the detailed assessment efforts that occurred in the 2D/3D, MIST, and ICAP programs associated with USNRC research. The assessments have been very beneficial because of the many recommendations that have been incorporated. The primary improvements were in the calculation of the bubble diameter (elimination of the Weber number criterion) and the implementation of the profile-slip effect. Both changes tended, in most cases, to reduce the drag.

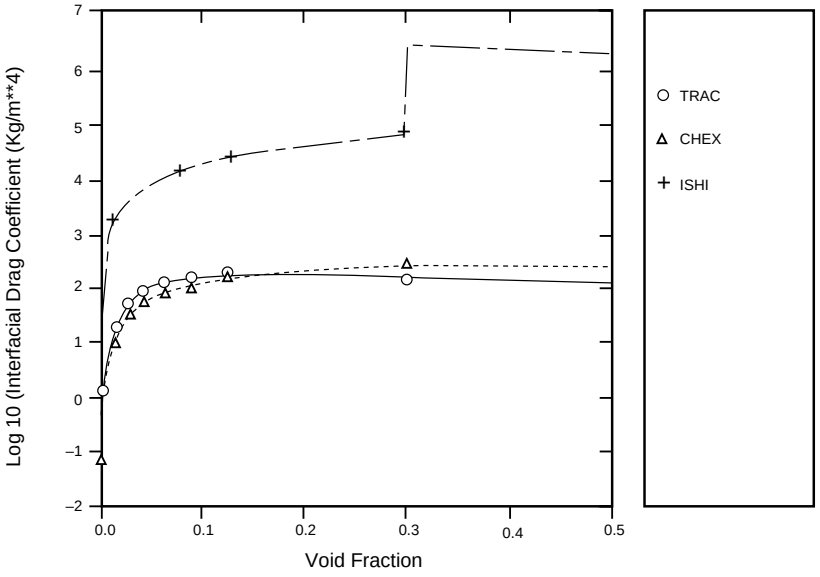

Fig. H-10. Comparison of the TRAC-calculated interfacial-drag coefficient (solid line) to the prediction by Ishii and Chawla (long dash) and the prediction by Chexal and Lellouche (dashed line) for a superficial liquid velocity of 0.1 $m \cdot s^{-1}$, a pressure of 0.1 MPa, and a hydraulic diameter of 3.5 m.

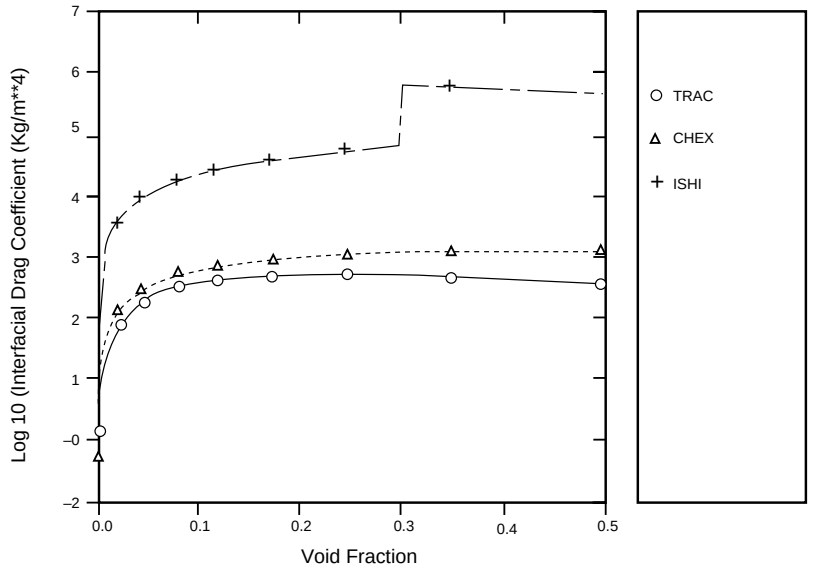

Fig. H-11. Comparison of the TRAC-calculated interfacial-drag coefficient (solid line) to the prediction by Ishii and Chawla (long dash) and the prediction by Chexal and Lellouche (dashed line) for a superficial liquid velocity of 0.1 $m \cdot s^{-1}$, a pressure of 0.1 MPa, and a hydraulic diameter of 3.5 m.

We believe that the current models are up to date, consistent, and as realistic as possible. However, we fully expect that there will continue to be discrepancies in future assessments because of the complex nature of two-phase flow and the dependence on the local geometry.

H.1.2. Annular-Mist Correlations

Annular-mist flow is assumed to exist if the void fraction is greater than 0.75. Exceptions to this are stratified flow, flow in the upper plenum of the vessel, core reflood, flow in the accumulator, and CCFL. Major improvements were made to the calculation of the annular-mist interfacial drag in the development of the MOD2 code. The most significant changes were the replacement of the static combination of the droplet and film contributions with an area-weighted average and the use of a recent droplet-diameter correlation from the literature. This provides for a more realistic estimate of the drag and for better comparisons with the data than was possible with the MOD1 code. The calculation of the interfacial drag is identical for the three directions in the 3D VESSEL and for all the 1D components. The description below applies to all components unless specified otherwise.

H.1.2.1. Basis for the Model. The interfacial-drag prediction for annular mist flow in TRAC was based upon the following assumptions:

1. The transient is sufficiently slow so that the interfacial-drag phenomenon is quasi-steady. Therefore, transient forces, such as the apparent mass and the Basset force, are neglected.
2. The effective interfacial-drag coefficient for annular mist can be determined by the addition of the contributions due to the annular film and the entrained drops weighted by their respective area fractions.
3. For the droplet contribution, the interfacial drag can be represented with correlations developed for a solid spherical particle. Therefore, no droplet distortion is assumed. The average droplet diameter can be determined from a correlation as a function of the Weber number based on a roll-wave shearing mechanism.
4. For annular film, the interfacial drag can be represented with a friction-factor correction developed from annular-flow data. In addition, the film thickness is limited by a minimum value so that a transition to rivulet flow will occur.

The annular-mist regime implies the existence of the liquid phase as a combination of annular film and entrained droplets. The code calculates the amount of entrainment based on correlations from Kataoka and Ishii (Ref. H-6.). It calculates the amount of liquid existing as a film by subtracting the entrained liquid from the total amount of liquid. An interfacial-drag coefficient is calculated for the droplets in a manner similar to bubbly flow by assuming there is no droplet distortion. Thus, it follows the theory developed by Ishii and Chawla (Ref. H-1.), Bird, Steward, and Lightfoot (Ref. H-3.), and Shiller and Nauman (Ref. H-4.). A separate interfacial-drag coefficient is calculated for

the liquid film using a correlation proposed by Wallis (Ref. H-15.). The two coefficients are combined with an area-weighted average and divided by a drift velocity developed by Kataoka and Ishii (Ref. H-16.) to determine the interfacial-drag coefficient for annular-mist flow. Since only one liquid field exists in the current version of TRAC, this interfacial-drag coefficient must represent the combined effect of the annular film and the entrained droplets.

As in the case of bubbly slug flow (Section H.1.1.), the pressure drop for the k^{th} phase is proportional to interfacial force per unit volume. Following the theory developed by Ishii and Chawla (Ref. H-1., pp. 13 and 14),

$$\alpha_k \frac{dp}{dz} \sim M_{ik} \ , \tag{H-34}$$

where α_k is the area fraction of the k^{th} phase and is equal to A_k / A. The force is assumed to be proportional to the square of the relative velocities

$$M_i = C_i |V_r| V_r \quad , \tag{H-35}$$

where C_i is the total interfacial-drag coefficient and has units of kg$\cdot$ m^{-4}. The total interfacial drag force for the annular-mist-flow regime consists of two components. One component is the contribution from droplets and the other is the contribution from the annular film, i.e., $M_i = M_{id} + M_{ia}$. Before we proceed to calculate the total interfacial-drag coefficient, we need to obtain the individual interfacial-drag coefficients for the components.

The basis for the interfacial-drag coefficient for the droplets follows that of Ishii and Chawla (Ref. H-1.). The drag force on the droplets balances with the total pressure drop as

$$M_{id} \sim \alpha_d \frac{dp}{dz} \ , \tag{H-36}$$

where

$$M_{id} = \frac{\alpha_d F_d}{Vol_d} \quad . \tag{H-37}$$

For the dispersed flow, we use the drag-force equation given by Ishii and Mishima (Ref. H-17.) as

$$M_{id} = a_i \left[\frac{C_d}{4} \left(\frac{r_{sm}}{r_d} \right) \frac{\rho_g (V_g - V_d)^2}{2} \right] \ , \tag{H-38}$$

where

$$a_i = \frac{\alpha}{1-\alpha_d}\frac{3\alpha_d}{r_{sm}} \quad , \tag{H-39}$$

α_d is the droplet area fraction, r_{sm} is the Sauter mean radius, and r_d is the drag radius. The ratio of the Sauter mean radius to the drag radius is defined as a shape factor. For a spherical particle, the shape factor is one. The Sauter mean radius is related to the droplet diameter (Ref. H-16.) by

$$r_{sm} = 0.796\frac{D_d}{2} \quad . \tag{H-40}$$

Then to determine the drag force, estimates are required for the droplet diameter, for the area fraction of droplets, and for the droplet-drag coefficient. To estimate the droplet diameter, we use a correlation for the volume mean diameter of droplets developed by Kataoka, Ishii, and Mishima (Ref. H-18.). The mechanism assumed for the generation of the droplets is that of shearing from wave crests, such as those produced in annular-mist flow. The droplet diameter is given by

$$D_d = \frac{2.0}{\rho_g j_g^2}\left[0.005\sigma\left(\frac{\mu_g}{\mu_l}\right)^{2/3} Re_g^{2/3}\left(\frac{\rho_g}{\rho_l}\right)^{1/3}\right] . \tag{H-41}$$

To estimate the droplet-drag coefficient, we use a correlation recommended by Ishii and Chawla (Ref. H-1.). The correlation is given by

$$C_d = \frac{24}{Re_d}\left(1.0 + 0.1Re_d^{0.75}\right) \quad , \tag{H-42}$$

where the droplet Reynolds number is given by

$$Re_d = \frac{D_d\rho_g\left|V_g - V_d\right|}{\mu_m} \tag{H-43}$$

and the modified viscosity is

$$\mu_m = \frac{\mu_g}{(1-\alpha_d)^{2.5}} \quad . \tag{H-44}$$

In annular-dispersed flow, most droplets are in the wake regime because of their relatively small size. We use a relative velocity by Ishii (Ref. H-5.) given by

$$V_g - V_d = D_d \left[\frac{(g\Delta\rho)^2}{\mu_g \rho_g} \right]^{1/3} \alpha_d (1-\alpha_d)^{1.5} \text{ for}$$
$$j > 1.456 \left(\frac{\sigma g \Delta\rho}{\rho_g^2} \right)^{1/4} \left[\frac{\mu_g^2}{\rho_g \sigma (\sigma / g\Delta\rho)^{1/2}} \right]^{-1/12} \quad \text{(H-45)}$$

or

$$V_g - V_d = \sqrt{2} \left(\frac{\sigma g \Delta\rho}{\rho_g^2} \right)^{1/4} \alpha_d (1-\alpha_d)^{1.5} \quad . \quad \text{(H-46)}$$

To estimate the droplet area fraction, we use an entrainment correlation developed by Kataoka and Ishii (Ref. H-16.). The correlation is given by

$$E = \tanh(7.25 \times 10^{-7} We_d^{1.25} Re_l^{0.25}) \quad , \quad \text{(H-47)}$$

where the liquid Reynolds number is given by

$$Re_l = \frac{\rho_l j_l D}{\mu_l} \quad , \quad \text{(H-48)}$$

and the droplet Weber number is

$$We_d = \frac{\rho_g j_g^2 D}{\sigma} \left(\frac{\Delta\rho}{\rho_g} \right)^{1/3} \quad , \quad \text{(H-49)}$$

where

$$\Delta\rho = \rho_l - \rho_g \quad .$$

For a small droplet, the area fraction of droplets is related to the entrainment by [see Ref. H-16., Eq. (90)]

$$\alpha_d = \frac{j_l E}{j_g} \quad . \quad \text{(H-50)}$$

The basis for the interfacial-drag coefficient for the annular film follows a force balance for a segment of liquid film as shown in Fig. H-12. By integrating the shear stress at the core-to-film interface over a length Δz, we obtain

$$\pi D_c \Delta z \tau_f = \frac{\pi}{4} D^2 \alpha_f \Delta p \ . \tag{H-51}$$

Here, D_c is the diameter of the core that, from geometric considerations, is given as

$$D_c = \alpha_c^{1/2} D \ , \tag{H-52}$$

where α_c is the core area fraction [$\alpha_c = \alpha/(1 - \alpha_d)$], α_f is the film area fraction ($\alpha_f 1 - \alpha_c$), and τ_f is the shear stress at the film-to-core interface.

Similar to the wall-shear stress in single-phase channel flow, the shear stress at the film-to-core interface is given by

$$\tau_f = \frac{1}{2} f_i \rho_c (V_g - V_f)^2 \quad , \tag{H-53}$$

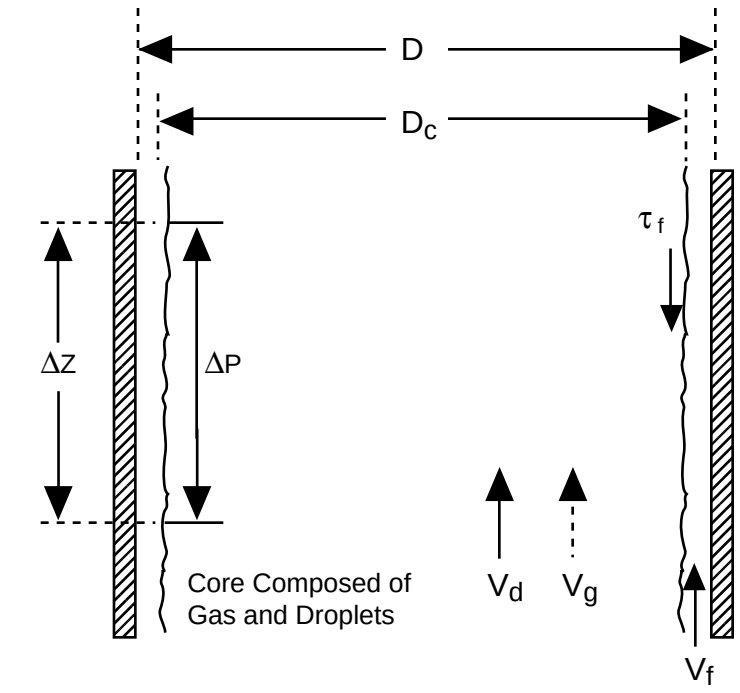

Fig. H-12. Core-to-film momentum balance.

where the density term refers to the gas core and f_i is the film-interface friction factor obtained from correlations. Wallis (Ref. H-15.) provided an empirical relationship for the friction factor in Eq. (11.19) of the reference,

$$f_i = 0.005[1 + 75(1 - \alpha_f)] \ , \tag{H-54}$$

where, as previously noted, α_f is the film area fraction.

For annular-mist flow, we use the model developed by Ishii and Mishima (Ref. H-17.). The total interfacial shear force denoted by M_i has two sources, namely, the generalized drag M_{id} and the interfacial shear and void gradient M_{ia}. The M_{id} for droplets is given by Eq. (H-38). Ishii and Mishima showed that the interfacial shear and void gradient for annular flow in a tube is

$$M_{ia} = \left(\Delta\alpha_k \cdot \tau_i\right) = \alpha_{if} \cdot \tau_f \quad , \tag{H-55}$$

where

$$\alpha_{if} = \frac{4C_{an}}{D}\sqrt{\frac{\alpha}{1-\alpha_d}} \quad . \tag{H-56}$$

The term τ_f is given by Eq. (H-53) and C_{an} is the roughness parameter due to waves in the film ($C_{an} \geq 1$). By definition, we have

$$M_i = C_{i\mathrm{am}} \cdot \left(V_g - V_{fd}\right)\left|V_g - V_{fd}\right| \quad , \tag{H-57}$$

where $C_{i\mathrm{am}}$ is the overall interfacial-drag coefficient for annular-mist flow. In the above equation, we need a formulation for the relative velocity $(V_g - V_{fd})$ to calculate the interfacial-drag coefficient $C_{i\mathrm{am}}$. Kataoka and Ishii (Ref. H-16.) developed a correlation for the relative velocity $(V_g - V_{fd})$ based on the drift-flux model (Ref. H-5.). The correlation is given as

$$\begin{aligned} V_g - V_{fd} = {} & \frac{1}{\alpha_c + \left[\frac{1+75(1-\alpha_c)}{\sqrt{\alpha_c}}\frac{\rho_g}{\rho_l}\right]} \left\{ j + \sqrt{\frac{\Delta\rho g_c D(1-\alpha_c)}{0.015\rho_l}} \right\} \cdot (1-\alpha_c) \\ & + \frac{r_d}{2}\left[\frac{(g_c\Delta\rho)^2}{\mu_g\rho_g}\right]^{1/3} \alpha_d(1-\alpha_d)^{1.5} \quad , \end{aligned} \tag{H-58}$$

where, as before,

$$\alpha_c = \frac{\alpha}{1-\alpha_d} \quad . \tag{H-59}$$

H.1.2.2. Input Required for Implementation. To calculate the interfacial drag using Eqs. (H-38) through (H-58), the void fraction, hydraulic diameter, gas density, liquid density, surface tension, gas viscosity, liquid and vapor viscosity, and relative velocity need to be input.

The definitions are first given for the 1D components. Here, the void fraction is spatially averaged as

$$\langle \alpha \rangle = \frac{\Omega(j)\alpha(j) + \Omega(j+1)\alpha(j+1)}{\Omega(j) + \Omega(j+1)} , \tag{H-60}$$

where the Ω_s used in the equation above represent the cell lengths adjoining the cell edge.

The gas density and gas viscosity are donor-celled based on the direction of the gas velocity. The liquid density, surface tension, and liquid viscosity are donor-celled based on the direction of the liquid velocity. [See Eq. (H-24) in Section H.1.1.2. for an example.] The gas velocity used to calculate entrainment is the absolute value of the velocity at the cell edge. The relative velocity used is the absolute value of the difference of the gas and liquid velocities as given in Eq. (H-22).

In the 3D VESSEL, the definitions for the variables are similar to those given for the bubbly slug flow. The void fraction is spatially averaged as given in Eq. (H-60) with cell lengths taking on the values for the three respective directions. For instance, in the axial direction, the Ω_s represent the heights of the cells; in the radial direction, the thickness of the rings; and in the azimuthal direction, the average azimuthal thickness of the adjacent cells.

The hydraulic diameter used for the axial and radial direction is the input value given for the axial direction. If the input hydraulic diameter is less than 1.0×10^{-5}, a calculation is made based on the slab heat-transfer area, rod heat-transfer area, and the flow area in the axial direction to provide an effective hydraulic diameter. In the azimuthal direction, the input value at the azimuthal cell edge is used. The azimuthal hydraulic diameter is not allowed to be less than 1.0×10^{-5}.

In the radial and axial directions, the phasic densities, surface tension, and phasic viscosities are the cell-centered values. In the azimuthal direction, the arithmetic average of the adjacent cell-centered values is calculated. [See Eqs. (H-19) and (H-20), for example.]

The relative velocity is required to calculate the Reynolds number for evaluating the droplet diameter [Eq. (H-41)]. In the VESSEL, the relative velocity is defined in the same way as in bubbly slug flow. Therefore, in the axial and radial directions, the V_r is given as described in Eqs. (H-15) and (H-16), respectively. In the azimuthal direction, the V_r is given as described in Eqs. (H-17) through (H-20).

The gas velocity used to calculate the entrainment in Eqs. (H-39) and (H-42) is defined as a vector-average velocity. In the axial and radial directions, this is given as

$$\check{V}_r = (VVZAV^2 + VVTAV^2 + VVRAV^2)^{0.5} \quad , \tag{H-61}$$

where

$$VVZAV = V_{gz}\left(r, \theta, z + \frac{1}{2}\right) \quad , \tag{H-62}$$

$$VVRAV = \left[V_{gr}\left(r + \frac{1}{2}, \theta, z\right) + V_{gr}\left(r - \frac{1}{2}, \theta, z\right)\right] / 2 \quad , \tag{H-63}$$

and

$$VVTAV = \left[V_{g_\theta}\left(r, \theta + \frac{1}{2}, z\right) + V_{g_\theta}\left(r, \theta - \frac{1}{2}, z\right)\right] / 2 \quad . \tag{H-64}$$

In the azimuthal direction, a different definition is required because the cell edge adjoins the two cells at θ and $\theta + 1$:

$$\check{V}_{g_\theta} = (VVZAVT^2 + VVTAVT^2 + VVRAVT^2)^{0.5} \quad , \tag{H-65}$$

where

$$VVZAVT = \left[V_{gz}\left(r, \theta, z + \frac{1}{2}\right) + V_{gz}\left(r, \theta, z - \frac{1}{2}\right) + V_{gz}\left(r, \theta, +1, z + \frac{1}{2}\right) + V_{gz}\left(r, \theta + 1, z - \frac{1}{2}\right)\right] \quad , \tag{H-66}$$

$$VVRAVT = \left[VVR13 + 0.5\left(V_{gr}\left(r + \frac{1}{2}, \theta, z\right) + V_{gr}\left(r + \frac{1}{2}, \theta + 1, z\right)\right)\right] / 2 \quad , \tag{H-67}$$

and

$$VVTAVT = \left[V_{g_\theta}\left(r, \theta + \frac{1}{2}, z\right)\right] \quad . \tag{H-68}$$

As in the case of bubbly flow, the variable *VVR13* is used to account for the special cases that occur in the innermost ring. This variable is defined in Eqs. (H-19) and (H-20).

H.1.2.3. Constants. In the case of the annular film, the constants are coded as they appear in Eq. (H-54). In determination of the entrainment, the Weber number is chosen to be a constant 4.0. This value was chosen based on acceptable developmental assessment results. Sensitivity tests on the effect of the droplet Weber number have shown that variations between 2 and 12 did not strongly influence the results. The work of Hinze (Ref. H-15.) suggests a value of 3.46.

H.1.2.4. Model as Coded. All the coding for the 3D VESSEL is in subroutine CIF3. The interfacial drag in the 1D components is calculated in subroutine StbVel1D (FEMOM in TRAC-M/F77). The model is coded as shown in Eqs. (H-38) through (H-59).

H.1.2.5. Weighting, Averaging, and Limits. Limits are imposed on the allowable droplet size to prevent the calculation of excessively large drag coefficients. In the 3D and 1D models, the droplet diameter is limited to the range 0.000042 to 0.002 m. Other limits imposed on the void fractions are identical to those used in bubbly slug flow. The void fraction used to calculate the interfacial drag is restricted to the range 0.00001 to 0.9999 in all the components.

The rate limits (i.e., allowable changes from one time step to the next) are imposed after the interfacial-drag coefficient computation is complete. Thus, this restriction is the same for all regimes and is fully described in Section H.1.1.4.3.

H.1.2.6. Variations in the Application of the Correlations. The basic relations described here for the annular-mist regime are used throughout the code in all 1D components and in the 3D VESSEL component. In some special cases the interfacial drag is overridden or altered. These cases are

1. core reflood in the vessel (Section H.1.5.),
2. accumulator logic in the PIPE component (Section H.1.6.2.),
3. inverted annular flow (Sections 3.5.5. and H.1.5.),
4. stratified flow in 1D components (Section H.1.3.),
5. user-defined CCFL in the vessel (Appendix I, Section I.3.), and
6. complete phase-separation option in 1D components (Section H.1.6.1.).

These special cases are described separately in the sections listed. Except for these cases and for mass fluxes and void fractions outside the range of the annular-mist regime, the models described here are used for the interfacial drag in each direction in the VESSEL component and in all 1D components.

H.1.2.7. Consistency with the Interfacial Heat Transfer. The interfacial heat-transfer calculation depends directly on the value of the interfacial area. In this respect, the code is consistent, since the same method is used to calculate the entrainment fraction and the droplet diameter. In fact, the same low-level subroutine DEEQ is used in this regard. Differences may occur because the interfacial heat transfer is computed at

the cell centers, and cell-average quantities (such as densities and velocities) are used. Cell-edge quantities are used in the calculation of the interfacial drag.

H.1.2.8. Assessment. The data of Hossfeld and Barathan (Ref. H-19.) were chosen for the assessment calculations because pipe diameters of 0.051 and 0.152 m were both tested. A detailed description of the test facility and test conditions was given in the reference. A comparison of TRAC-calculated liquid fraction versus the dimensionless superficial gas velocity with the data is shown in Fig. H-13., where the dimensionless superficial gas velocity is given as

$$j_g^* = j_g \left(\frac{\rho_g}{g_c D \Delta\rho} \right)^{1/2} \tag{H-69}$$

and

$$j_l^* = j_l \left(\frac{\rho_l}{g_c D \Delta\rho} \right)^{1/2} . \tag{H-70}$$

The TRAC results are in good agreement with the data in the middle and high ranges of the gas velocities but show a poor comparison at the low values.

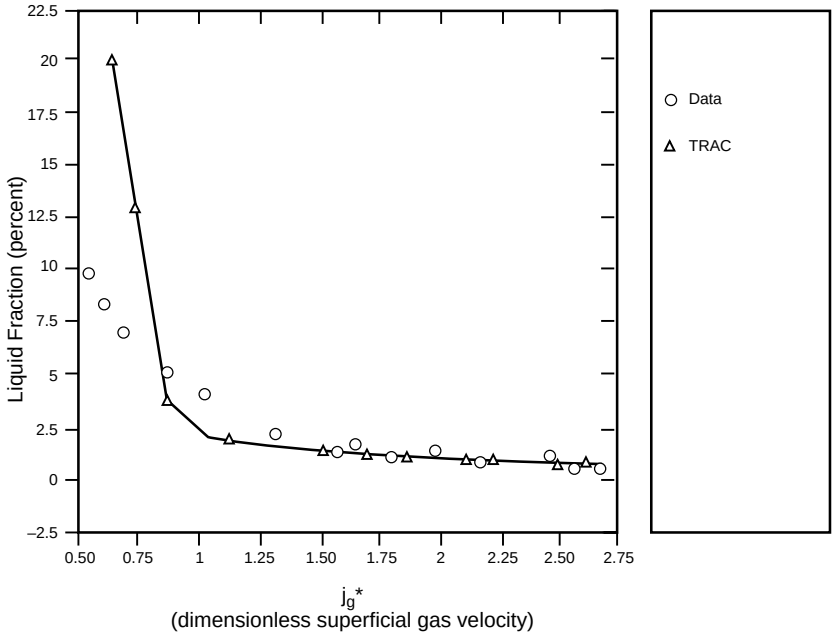

Fig. H-13. Liquid fraction comparison using the modified Wallis correlation.

H.1.2.9. Effects of Using the Correlations Outside the Database. As discussed in Section H.1.2.8., the database for the film-drag coefficient was small-scale pipe data. When applied to the case of downcomer geometry, the calculated interfacial drag appeared to be too small, thus allowing the excessive downflow of liquid at low gas velocities. At the higher gas velocities near the CCFL point, the prediction was in reasonable agreement with the data.

H.1.2.10. Scaling Considerations. The film-drag component of the annular-mist-flow regime is based on the Wallis correlation. Since this correlation was developed based on small-scale data, it may prove to be unacceptable at larger diameters associated with actual PWR hardware.

The droplet-drag component of the annular-mist-flow regime should scale appropriately if we assume that the droplet diameter and entrainment rate are accurately predicted.

H.1.2.11. Summary and Conclusions. As indicated in Section H.1.2.8., TRAC overpredicted the liquid fraction in the low dimensionless superficial gas velocities. In the future, we need to improve the model in the low dimensionless superficial gas velocity range. The interfacial-drag coefficient in the annular-mist-flow regime is calculated using a film-drag coefficient combined with a droplet-drag coefficient. The contributions of each are weighted with their respective liquid fractions based on the computed entrainment. An alternative method for combining the drag coefficients should be investigated to better represent the total movement of liquid.

H.1.3. Stratified-Flow Correlation

In the 1D components, the code calculates a stratified-flow interfacial-drag coefficient if the cell-edge velocities are less than critical values and if the angle that the cell edge makes with the horizontal is within certain limits. In the 3D VESSEL, stratified flow is allowed if there is a certain gradient in the void fraction and if the vapor flow from the bottom is below a certain limit. The limits for both the 1D and 3D models are described in Appendix E, Section E.2.7. This section describes the interfacial-drag coefficient in stratified flow.

H.1.3.1. Basis for the Model. The calculation of the stratified-flow interfacial-drag coefficient is based on Taitel and Dukler (Ref. H-20.) and Ohnuki et al. (Ref. H-21.).

As in the case of bubbly slug and annular-mist flows, we assume that the stratified flow is quasi-steady and that the transient forces can be neglected. In the code we assume that the stratified-flow regime can occur in the 1D components and the 3D VESSEL. Temporal changes in the stratified-flow interfacial-drag coefficient are limited in the same manner as the bubbly slug and annular-mist coefficients.

The stratified-flow interfacial-drag coefficient is derived from the method given in Taitel and Dukler (Ref. H-20.). In the reference, the momentum equations for the liquid and gas phases are combined through the elimination of the pressure drop. In TRAC the momentum equations are solved separately. Therefore, to demonstrate the derivation of

the interfacial-drag coefficient, we consider the gas-phase momentum equation only. From Taitel and Dukler (Ref. H-20., Eq. 2), the pressure drop in the gas caused by interfacial drag with the liquid is given by

$$\frac{dp}{dx} = \frac{1}{2} f_i \rho_g V_r^2 \frac{S_i}{A_g} \quad , \tag{H-71}$$

where

$\frac{dp}{dx}$ is the pressure drop,
f_i is the interfacial friction factor,
ρ_g is the density of the gas,
V_r is the relative velocity,
S_i is the width of the stratified interface, and
A_g is the gas phase flow area.

In the reference, Taitel and Dukler assume that the liquid velocity is small, so that the relative velocity is approximated by the gas velocity. In the code, however, we use the relative velocity.

The TRAC gas momentum equation [Section 2.1.1., Eq. (2-6)] gives the same pressure drop as

$$\frac{dp}{dx} = \frac{c_i V_r^2}{\alpha} \quad , \tag{H-72}$$

where

c_i is the interfacial-drag coefficient (kg· m^{-4}) and
α is the gas fraction.

Note that the term $c_i V_r^2$ is the volumetric interfacial force (N· m^{-3}) described in Section H.1.1.1. Combining Eqs. (H-71) and (H-72) and solving for c_i yields

$$c_i = \frac{1}{2} f_i \rho_g \frac{S_i}{FA} \quad , \tag{H-73}$$

where A_g has been replaced with the product of the total flow area of the channel (FA) and the void fraction (α).

This is the equation used in the 1D components and is consistent with the assumption of circular pipe geometry. In the 3D VESSEL, however, the ratio of the width of the stratified interface to the available flow area is equivalent to a hydraulic diameter, or in this case, the height of the flow channel that exists in the radial and azimuthal directions. Therefore, in this situation we use

$$C_i = \frac{1}{2}\frac{f_i \rho_g}{HD} \quad , \tag{H-74}$$

where *HD* is the average of the level height in the level of interest and the level above. If there is a zero flow in the radial or azimuthal direction or in the level above, *HD* is calculated by multiplying the current level height by the local void fraction. A situation like this may occur in the region between the lower plenum and the downcomer skirt. In this situation, a stratified-flow interfacial-drag coefficient is significantly lower than that of bubbly flow and would allow far less sweep-out during blowdown.

In the code, f_i is determined using the Ohnuki correlation as

$$f_i = 1.84 f_{wg} \quad , \tag{H-75}$$

where

$$\begin{aligned} f_{wg} &= \frac{16.0}{Re_g} && \text{if laminar,} \\ f_{wg} &= \frac{0.079}{Re_g^{0.25}} && \text{if } Re_g < 10^5, \\ f_{wg} &= 0.0008 + \frac{0.05525}{Re_g^{0.237}} && \text{if } Re_g \geq 10^5, \text{ and} \\ Re_g &= \text{the liquid Reynolds number.} \end{aligned} \tag{H-76}$$

This correlation provides the best assessment results of the available correlations found in the literature.

H.1.3.2. Input Required to Implement the Correlation. To calculate the interfacial-drag coefficient as given in Eq. (H-74), it is necessary to define the gas density, the void fraction, the flow area of the channel, and the width of the stratified interface. In the 1D model, the gas density used is distance-weighted with the lengths of the cells on either side of the interface as follows:

$$\left\langle \rho_g \right\rangle = \frac{\rho_g(j)DX(j) + \rho_g(j+1)DX(j+1)}{DX(j) + DX(j+1)} \quad , \tag{H-77}$$

where

DX = cell lengths

and the j and $j + 1$ indexes refer to the cell locations adjacent to the cell edge or interface.

The void fraction used is calculated in the same manner as in Eq. (H-77), with the additional constraint that it is not allowed to be greater than 0.9999 or less than 1.0×10^{-5} to avoid divisions by zero.

The channel cross section in the 1D model is assumed to be circular. The flow area is calculated from

$$FA = \frac{\pi}{4}\text{diam}^2 \quad , \tag{H-78}$$

where

$$\text{diam} = \max[\text{diam}(j+1), \text{diam}(j)] \ ,$$

$$\text{diam}(j) = \left(\frac{4\text{vol}(j)}{\pi DX(j)}\right)^{0.5} \ ,$$

$$\text{diam}(j+1) = \left(\frac{4\text{vol}(j+1)}{\pi DX(j+1)}\right)^{0.5} \ ,$$

$\text{vol}(j)$ = volume of cell j , and

$\text{vol}(j+1)$ = volume of cell $j+1$.

Thus, the flow area used is the maximum of the cells on each side of the interface (as designated by the j and $j+1$ indexes). The width of the stratified interface is calculated from

$$S_i = \text{diam}\left[1.0 - \left(\frac{2h_l}{\text{diam}} - 1.0\right)^2\right]^{0.5} \ , \tag{H-79}$$

where h_l is the height of the stratified layer of liquid lying in the bottom of the pipe. In the code, h_l is calculated from the void fraction using a polynomial curve fit as follows:

if $\alpha \le 0.5$ then $X = \alpha$ and

$h_l = Y$, or

if $\alpha > 0.5$ then $X = 1.0 - \alpha$ and

$h_l = \text{diam} - Y$,

where

if $X \leq 0.001$ then

$$Y = (1.0 - 7.612668 \cdot X) \cdot \text{diam}, \quad \text{or} \tag{H-80}$$

if $0.001 < X \leq 0.5$ then

$$Y = (1.0 - 0.70269591 \cdot X^{0.6666666667} - 0.034146667 \cdot X - 0.161023911 \cdot X^{2.0}) \cdot \text{diam}.$$

The void fraction used above is the distance-weighted value described above, and the diameter is as given in Eq. (H-78). The value of h_l is not allowed to be less than 0.001 times the diameter (diameter). As noted above, in the 3D model the horizontal direction hydraulic diameter is used rather than the S_i and *FA* used in the 1D model.

H.1.3.3. Constants. The value of π used in Eq. (H-78) is a constant 3.14159.

H.1.3.4. Model as Coded. The model is coded as shown in Eq. (H-74) in subroutine StbVel1D (FEMOM in TRAC-M/F77) for the 1D component, and in subroutine CIF3 for the 3D component. The calculation of the stratified liquid level is determined as shown in Eq. (H-80) in subroutine LEVEL.

H.1.3.5. Weighting, Averaging, and Limits. The gas density and void fraction are averaged over distance as shown in Eq. (H-77). The height of the liquid level [Eq. (H-80)] is limited to 0.001 times the diameter [diameter given in Eq. (H-78)]. The void fraction is limited to a range less than or equal to 0.9999, and greater than or equal to 1.0×10^{-5}. These limits avoid divisions by zero. The final interfacial-drag coefficient used in the momentum equation is as shown in Eq. (H-74) if the gas and liquid velocities are below the critical values (described in Appendix E). If the critical values are exceeded, then the transition from stratified flow is calculated with weighting factors using the phasic velocities as the independent variable. The weighting factor is calculated in Appendix E.

The weighting factors are applied to calculate the final interfacial-drag coefficient and are combined with the bubbly slug or annular-mist interfacial-drag coefficients if the transition is occurring. The application of the weighting factors and the limits on the final interfacial-drag coefficient are described in the section on transitions (Section H.1.4.).

H.1.3.6. Consistency with Interfacial Heat Transfer. The calculation of the interfacial heat transfer in stratified flow is determined using an interfacial area, a heat-transfer coefficient, and the temperature difference between the steam and the liquid. To be consistent with the interfacial-drag calculation, the interfacial area calculation must be similar, but because the interfacial drag is calculated at the cell edges and the heat transfer is calculated at the cell centers, small inconsistencies may exist. The interfacial area is calculated from the definition of the width of the stratified interface and the length of the cell. The width of the stratified interface is calculated in the same manner as given in Eq. (H-79). The value for the height of the liquid level used in Eq. (H-79) may be

slightly different since the cell-centered quantities for the void fraction and the diameter may in some cases be different from the cell-edge average quantities used in the calculation of the interfacial drag.

In addition, for the calculation of the interfacial heat transfer, the determination of the critical velocities is based on the cell-average quantities rather than the cell-edge quantities. To make the models more consistent, the weighting factor *WFHF* is saved during the interfacial-drag calculation and used in the calculation of the interfacial heat transfer.

H.1.3.7. Assessment of the Correlation. In this section we present the assessment of the code against full-scale countercurrent flow data recently obtained in the Upper Plenum Test Facility (UPTF). Therefore, although the interfacial friction factor is not assessed directly, this work is a verification of the two-fluid model with the calculation of the interfacial shear as a dominant term in the momentum equations.

The test setup for the countercurrent flow test in the UPTF hot leg is shown in Fig. H-14. Saturated water is injected into the inlet plenum of the steam-generator simulator and flows through the hot leg towards the vessel (not shown). Steam is injected through the core simulator in the vessel, and because of the configuration of the facility, is forced to flow countercurrent to the liquid in the hot leg. This situation is similar to what is hypothesized to occur in the event of a small-break LOCA in a PWR, in which steam produced in the core flows into the steam generator, is condensed on the tubes, and then flows back towards the vessel as condensate. This phenomenon is referred to as “reflux condensation.” It is important to determine whether TRAC can predict the countercurrent flow of liquid in such a situation.

The test procedure is depicted in Fig. H-15. First the water flow in the hot leg was established, and then the steam flow. Both were held constant for the duration of the test. Each test run lasted about 100 to 150 s. The TRAC calculations were run in the same manner. In addition to testing the constant friction factor used in TRAC, we also tested other correlations for the purpose of comparison, using an experimental version of the code. The other correlations tested were Lee and Bankoff, Ohnuki et al. (Ref. H-21.), Kim (Ref. H-22.), and Linehan (Ref. H-23.).

The following Kim and Linehan correlations are similar in that they are dependent on the liquid Reynolds number:

$$f_i = a\, Re_l + b \quad , \tag{H-81}$$

where

$a = 0.14 \times 10^{-5}$, $b = 0.021$, Kim ,
$a = 0.23 \times 10^{-5}$, $b = 0.013$, Linehan .

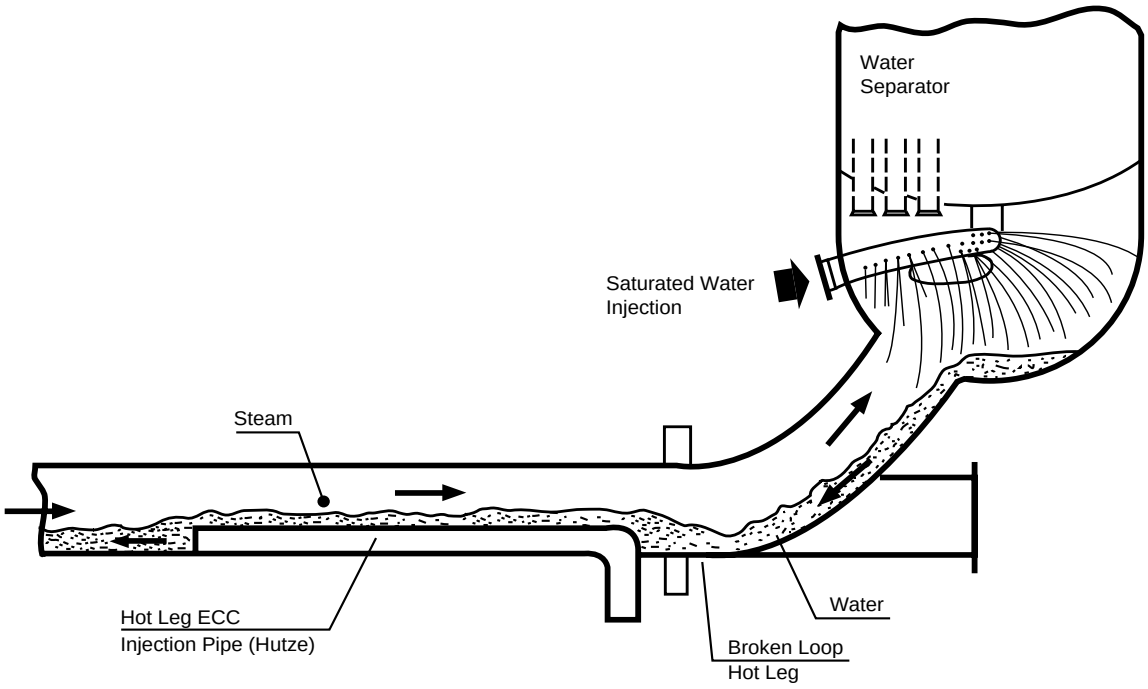

Fig. H-14. Test setup for the UPTF hot-leg countercurrent flow test.

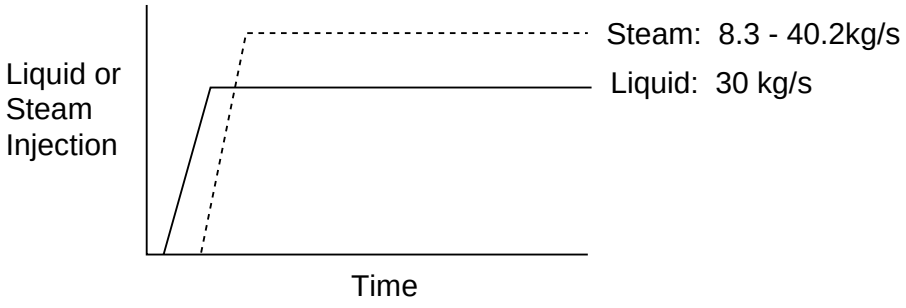

Fig. H-15. Procedure used for the injection of steam and water for the hot-leg countercurrent flow test.

The results for the assessment against the data at 1.5 MPa are shown in Table H-2. Here, the liquid downflow rate is presented at the various steam flows. In all test runs (except Run 037), the liquid-injection rate was 30 kg/s. In test Run 037 a liquid-injection rate of 9.8 kg/s was used to model the actual PWR conditions during reflux condensation. As shown in the table, the liquid downflow rate in the experiment decreased as the steam flow was increased. For TRAC-PF1/MOD1, the complete liquid delivery at the reflux condensation conditions was predicted. However, the liquid delivery at the low

steam flows was overpredicted, and the CCFL point was underpredicted. The MOD2 code using the Ohnuki correlation predicts the CCFL point, but still overpredicts the downflow of liquid at the low steam-flow rates. The Lee and Bankoff and the Kim and Linehan correlations overpredicted the interfacial friction factor, and prevented the downflow of liquid except at the very low steam-injection rate of 8.3 kg/s. This is caused by the fact that at full-scale, high-pressure conditions, the gas Reynolds number for this test is on the order of 1.0×10^6, and the liquid Reynolds number is on the order of 1.0×10^5**.** Thus, all three correlations produce very high friction factors and cause the early turnaround as shown in the table.

TABLE H-2.
Comparison to Data

—UPTF Test no. 11, Phase A
—Pressure = 1.5 MPa
—Saturated Steam and Water Injection
—Water Injection 30 kg/s (except Run 037, 9.8 kg/s)

		Water Downflow Rate (kg/s)				
–UPTF Test No.	**Steam Injection Rate (kg/s)**	**UPTF Test Result**	**MOD1 f_i=0.02**	**MOD2 f_i based on Ohnuki**	**MOD2 f_i based on Lee, Bankoff**	**MOD2 f_i based on Kim, Linehan**
037[a]	8.3	9.8	9.8	9.8	9.8	9.8
038	18.1	30.0	30.0	30.0	0.0	0.0
039	24.0	25.2	30.0	30.0	0.0	0.0
045	28.0	14.2	22.2	22.2	0.0	0.0
040	31.0	5.4	21.8	22.0	0.0	0.0
043	33.5	2.0	0.0	20.0	0.0	0.0
042	36.0	0.6	0.0	15.0	0.0	0.0
041	40.2	0.0	0.0	0.0	0.0	0.0

a. Typical PWR reflux condensation conditions.

The use of the Ohnuki correlation shows a better prediction of the CCFL point and does not produce the large friction factors associated with the other correlations tested. When we compare this correlation to the constant value used in MOD1 at typical gas Reynolds numbers (Fig. H-16.), we observe that at the higher values of gas flow, the MOD1 friction factor is too large. This is consistent with the assessment result in Table H-2., where the CCFL point is calculated at a lower steam flow than occurred in the data. Based on this assessment, we conclude that at full-scale conditions, the constant value of the friction factor provides an overall reasonable estimate of the interfacial drag. However, the prediction of the CCFL point is improved with the use of the Ohnuki correlation. This correlation was therefore chosen for use in MOD2.

H.1.3.8. Effects of Applying the Model Outside the Database. The Ohnuki correlation is applicable to a very large Reynolds number range and, therefore, should be applicable in most situations.

H.1.3.9. Scaling Considerations. Although the Ohnuki correlation was developed from small-scale data, assessment against full-scale UPTF data is favorable. Therefore, the scaling of the correlation appears promising.

H.1.3.10. Summary and Conclusions. The method used for the calculation of the interfacial drag in stratified flow follows that of Taitel and Dukler and Ohnuki. Assessment shows that the correlation proposed by Ohnuki for the friction factor better predicts the CCFL point. Based on our assessment, the MOD2 and TRAC-M codes should provide a reasonable simulation of full-scale PWR stratified flow.

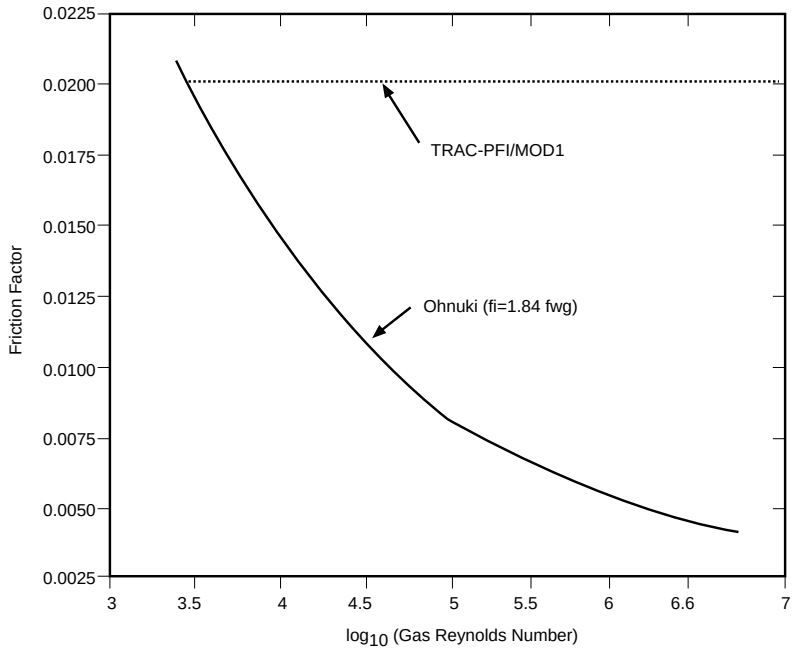

Fig. H-16. Comparison of the Ohnuki correlation with TRAC.

H.1.4. Transitions Between Bubbly Slug, Annular-Mist, and Stratified Flows

In the void-fraction range 0.5 to 0.75, the transition is made between the bubbly slug and annular-mist-flow regimes. This is sometimes referred to as churn-turbulent flow. In the code, a separate correlation for the interfacial drag is not used; rather, we average the bubbly slug interfacial-drag coefficient with the annular-mist interfacial-drag coefficient.

H.1.4.1. Transition Between Bubbly Slug and Annular-Mist Flows. The code calculates an interfacial-drag coefficient assuming the bubbly slug flow regime if the void fraction is ≤0.5. If the void fraction is ≥0.75, the annular-mist-flow regime is assumed. If the void fraction is between 0.5 and 0.75, the interfacial drag is calculated from the following average:

$$c_{i\text{trans}} = c_{i\text{am}}(WX) + c_{i\text{bs}}(1 - WX) \quad , \tag{H-82}$$

where

$c_{i\text{trans}}$ = transition interfacial-drag coefficient,
$c_{i\text{am}}$ = annular-mist interfacial-drag coefficient,
$c_{i\text{bs}}$ = bubbly slug interfacial-drag coefficient,
WX = $4\alpha - 2$, and
α = the distance-weighted void fraction.

The weighting factor WX is limited to be between 0.0 and 1.0. From the above equations we note that at a void fraction of 0.5, WX is 0.0. At a void fraction of 0.75, WX is 1.0. The method of calculating the transition interfacial-drag coefficient is identical in each of the three directions in the 3D. The differences occur in the distance weighting of the void fraction, which is directionally dependent, as described in Section H.1.1.2. The annular-mist drag coefficient ($c_{i\text{am}}$) is calculated in the method as described in Section H.1.2.1. The bubbly slug drag coefficient ($c_{i\text{bs}}$) is calculated using the method described in Section H.1.1.1.

H.1.4.2. Transition to Stratified Flow. Transition to stratified flow is also linear, depending on the critical velocity. Stratified flow may occur in any 1D component or in the 3D VESSEL in the radial or azimuthal direction. As described above in Section H.1.3.5., the weighting factor *(WFHF)* is calculated as the velocity drops below the critical velocity required for stratified flow to exist. For transition to stratified flow, the total interfacial drag is calculated by

$$c_i = (1 - WFHF)(c_{i\text{bs}} + c_{i\text{am}} + c_{i\text{trans}}) + WFHF(c_{i\text{st}}) \quad , \tag{H-83}$$

where $c_{i\text{bs}}$, $c_{i\text{am}}$, and $c_{i\text{trans}}$ are set to 0.0 unless the void fraction dictates their respective regimes.

H.1.5. The Core-Reflood Interfacial-Drag-Coefficient Model

During postulated severe accidents in PWRs, the core can become uncovered, lose its cooling, and eventually heat up due to the decay heat of the fission process. Emergency core-cooling systems are designed to replenish the water that was lost from the system, and in the case of core uncovery, reflood it. The reflooding rates are typically large (greater than 2.54 cm/s), and the water usually contains a large amount of subcooling (liquid temperature of 300 K, with the saturation temperature near 400 K). Experiments have shown that for typical conditions, one can expect inverted annular flow to exist in the core region as it refloods (see Appendix F, Section F.1., Fig. F-25.). A quench front is established that eventually moves up the core as the rods cool. The heat-transfer regimes from bottom to the top are listed as forced convection to liquid, subcooled nucleate boiling, transition boiling near the quench front, inverted annular-flow film boiling, and dispersed-flow film boiling as shown in Fig. F-25. in Appendix F, Section F.1. The location of the critical heat flux is at the top of the transition boiling region.

Ishii and DeJarlais (Ref. H-24.) performed visualization experiments of inverted annular flow (IAF) in the central channel of a heated double-quartz tube. A summary of their qualitative results is depicted in Fig. F-25. (see Appendix F, Section F.1.). The inverted annular region was initiated using a concentric injection nozzle. Motion pictures, as well as still photographs, were taken to identify the flow-regime characteristics. In a region directly downstream of the nozzle, a smooth liquid core was observed. This was followed by an inverted annular region with wave development on the liquid surface. The wavelengths were of the order 10 mm, with droplets being sheared from the wave crests. Also observed (although not shown in the figure) was a thin, highly agitated annulus of liquid near the heated wall. Above this region, an agitated slug/churn region was observed. Droplets (0.003-m diameter) swept past the slugs. The slugs were deformed into multiple ligaments and eventually broke up. In the dispersed region, the droplets evaporated and acted to de-superheat the steam. Several droplet sizes were observed originating from the agitated liquid annulus (0.00005 m), from the wave crests (0.0002 m), and from the slug break-up (0.0006 to 0.003 m).

Ishii and DeJarlais (Ref. H-25.) derived flow-regime transition models for their double-quartz tube experiment. Also, it was observed that the interfacial waves in the agitated region moved at a velocity 5 to 10 times the liquid injection velocity.

Obot and Ishii (Ref. H-26.) derive the transition criteria based on the visualization experiments. The final results are put in terms of the capillary number and the length above the quench front as follows:

Smooth Section: $L / D \leq 60\ Ca^{1/2}$, (H-84)

Rough Wavy: $60\ Ca^{1/2} < L / D \leq 295\ Ca^{1/2}$, (H-85)

Agitated: $295\ Ca^{1/2} < L / D \leq 595\ Ca^{1/2}$, and (H-86)

Dispersed: $595\ Ca^{1/2} < L / D$, (H-87)

where

$$\text{Ca} = \text{ Capillary Number } = \frac{\mu_l V_l}{\sigma}. \qquad \text{(H-88)}$$

Obot and Ishii observed large droplets in the dispersed flow. These large droplets get smaller and smaller when the void fraction increases further downstream of the agitated region. Thus, the dispersed flow in the TRAC core-reflood model is considered to consist of a dispersed-flow regime with large droplets (post-agitated region) and of a highly dispersed flow regime with fine droplets. The highly dispersed flow regime is assumed to occur when the cell void fraction is greater than 98%.

Models for the interfacial drag in a reflooding core are developed based on the inverted-annular-flow map, as shown in Fig. F-25. of Appendix F, Section F.1., proposed by Ishii and his coworkers (Refs. H-24., H-25., and H-26.). For each flow regime shown in Fig. F-25., a separate interfacial-drag model is developed. Furthermore, models for each flow regime are redefined in the flow-regime void-fraction plane based upon the cell void fraction, as in Fig. H-17a. Three void-fraction regions are identified: (1) the low-void-fraction region characterized by void fractions less than 75%; (2) the high-void-fraction region characterized by void fractions higher than 98%; and (3) the intermediate void-fraction region between high- and low-void-fraction regions. Fig. H-17b. shows the interfacial-drag coefficient (IFDC) selection logic used in the TRAC core-reflood model. The core-reflood IFDC model is coded in subroutine CIF3, which is called by VSSL1 for each level in the VESSEL component. In the following section, the interfacial-drag models for each IAF regime are presented from the bottom to the top of the channel in the following order: subcooled boiling, smooth inverted annular, rough-wavy inverted annular, agitated, dispersed (or post-agitated region), and highly dispersed flow. The assessment of individual models is not discussed in each section. The last section discusses the assessment of overall core-reflood drag models with CCTF Run-14 data.

H.1.5.1. Subcooled-Boiling Interfacial-Drag Model.

H.1.5.1.1. Basis for the Model. The subcooled-boiling models are characterized by two regions: (1) the partial boiling region, in which the bubbles remain attached to the wall, and (2) the fully developed boiling region, where bubbles enter the free stream and eventually collapse due to condensation (Ref. H-27.). In the partial boiling region, the wall is sufficiently hot to cause a layer of superheated liquid to exist in the vicinity of the surface and cause bubble formation. The bulk fluid remains subcooled, hence the term “subcooled boiling”. As shown in Fig. H-18., the dominant forces on a bubble are buoyancy, drag, and surface tension.

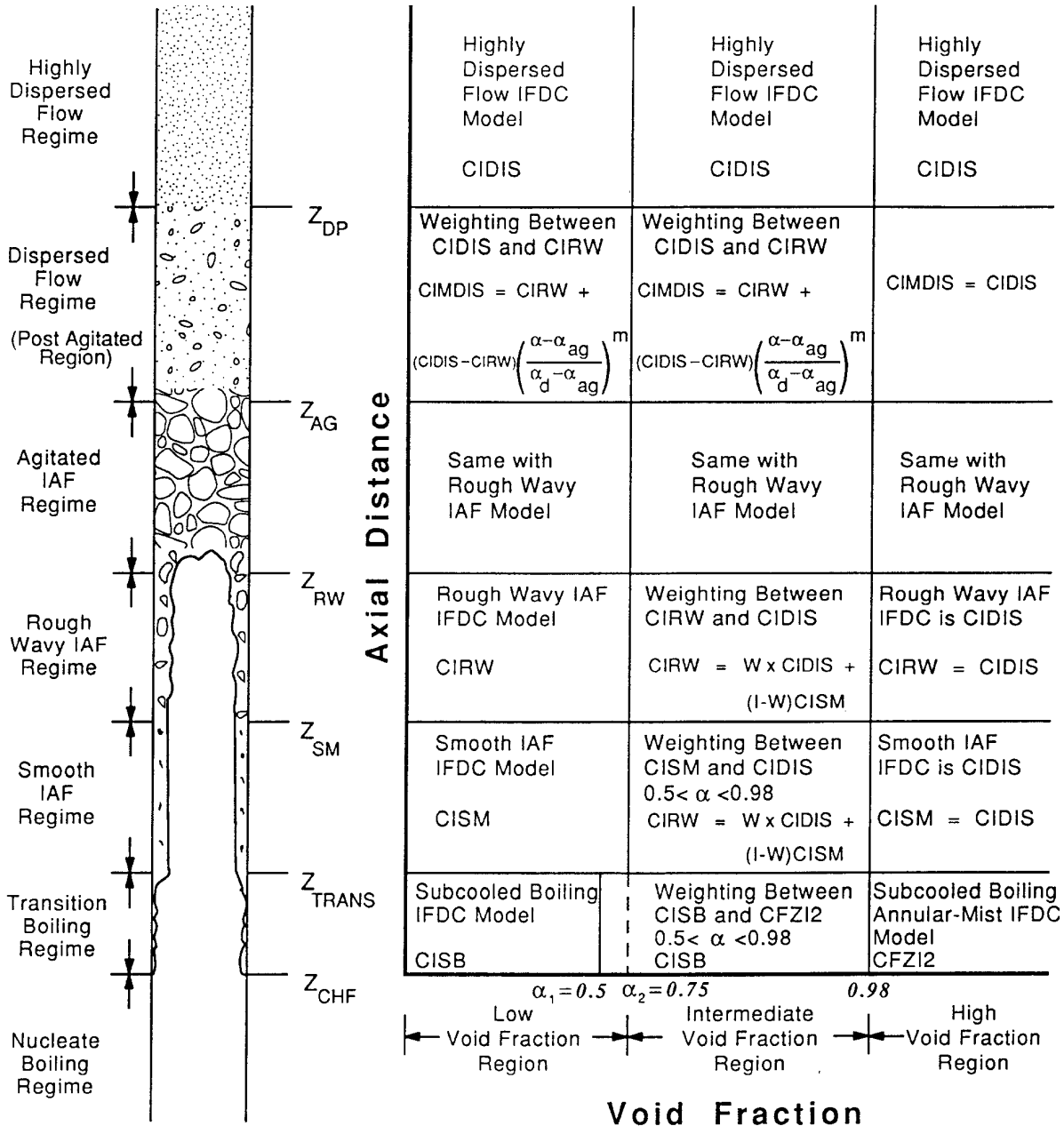

Fig. H-17a. The interfacial-drag coefficient model selection logic in the IAF regimes—void-fraction plane.

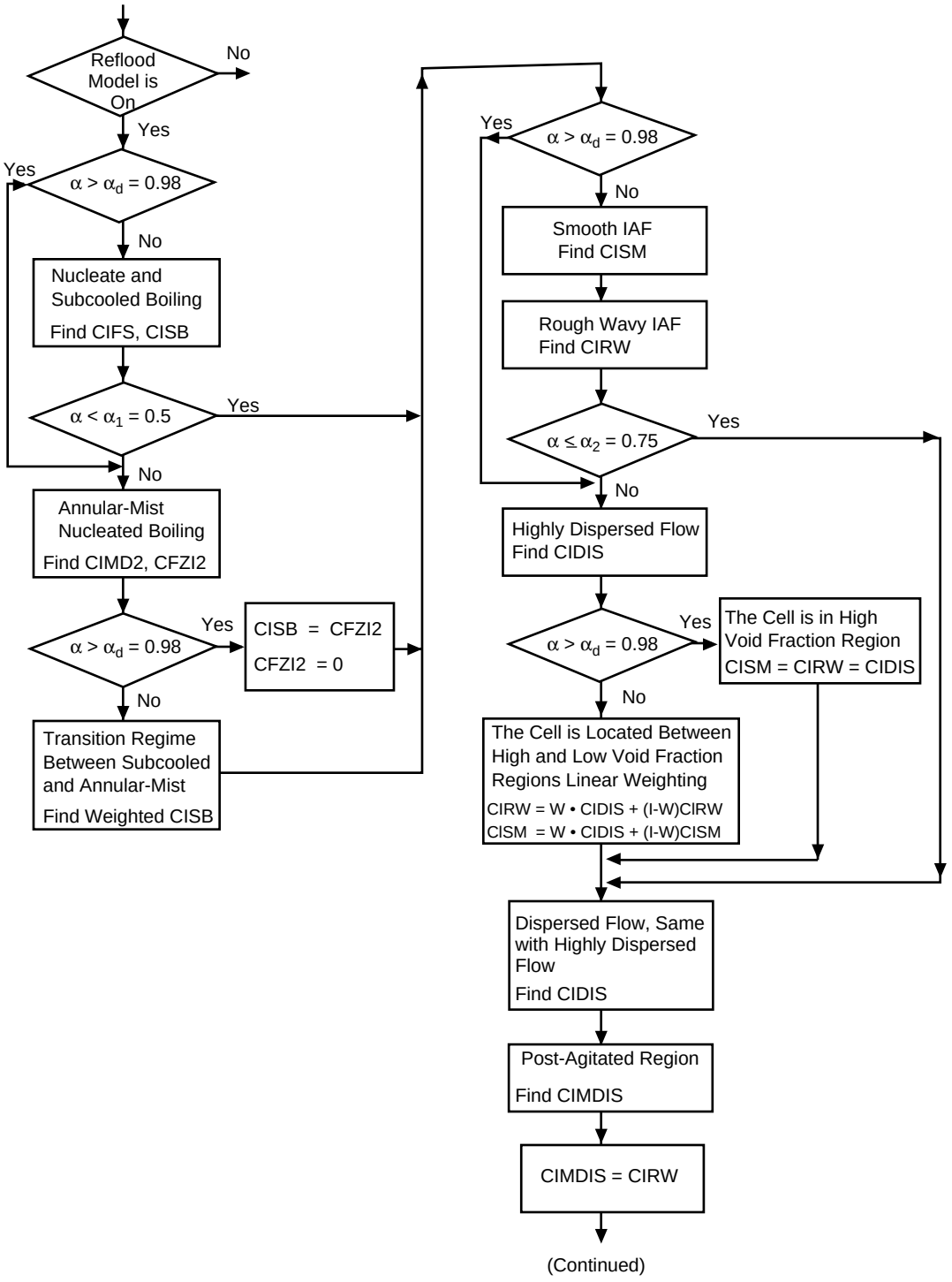

Fig. H-17b. The interfacial-drag coefficient model selection logic used in the core-reflood model.

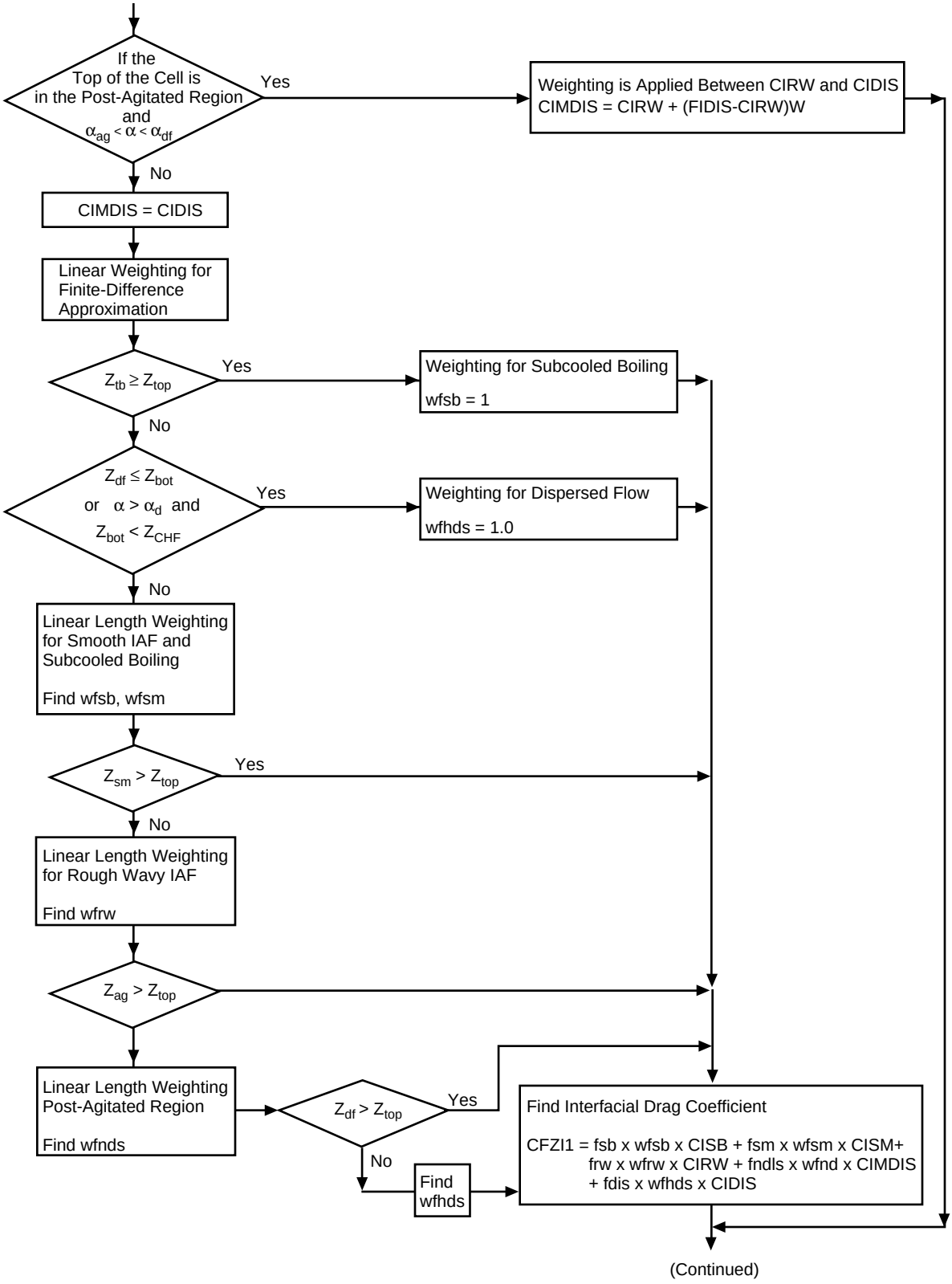

Fig. H-17b (cont). The interfacial-drag coefficient model selection logic used in the core-reflood model.

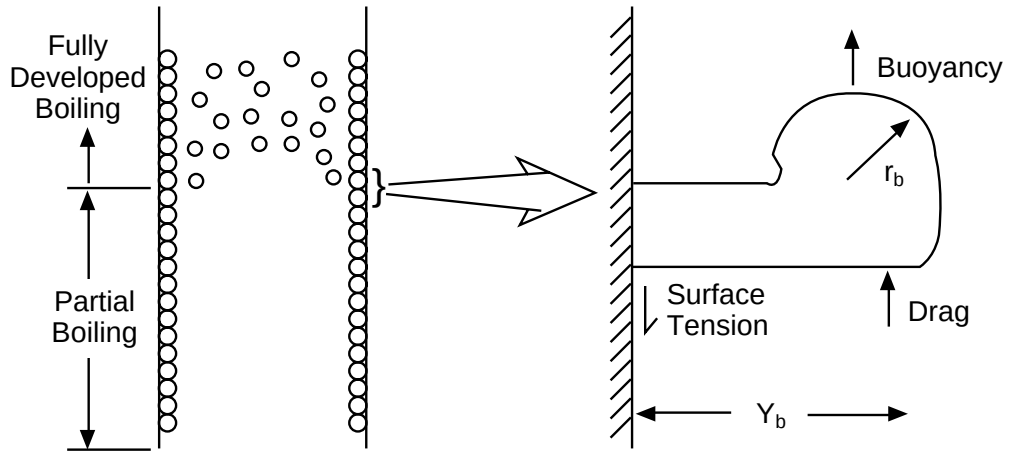

Fig. H-18. Bubble attached to wall in subcooled boiling (Ref. H-27.).

For a bubble of diameter 1 mm, near atmospheric pressure, the surface-tension force is of the order 60×10^{-6} N, and the buoyancy force about 10×10^{-6} N. The drag force depends on the liquid flow, bubble distortion, and other parameters, but it can be seen by this simple order-of-magnitude calculation that the surface-tension force can be significant, keeping the bubbles close to the wall. In addition, if many bubbles are closely packed, then the drag force should decrease due to the "shielding" effect of the surrounding bubbles. Collier (Ref. H-27.) indicates that the bubble height from the wall can be estimated by

$$Y_b = C\left[\frac{\sigma D_h}{\tau_w}\right]^{1/2}\left[1 + C'\left(\frac{g(\rho_l - \rho_g)D_h}{\tau_w}\right)\right]^{-1/2} \tag{H-89}$$

for the case of closely packed bubbles.

Collier indicated that Levy evaluated the constants C and *C'* in Eq. (H-89) from experimental data and gave 0.015 and 0.0 for C and *C'*, respectively. The wall shear stress, τ_w, in Eq. (H-89) is obtained from the relationship

$$\tau_w = \left[\frac{f_{fo} G^2}{2\rho_l}\right], \tag{H-90}$$

where f_{fo} is the single-phase friction factor corresponding to a relative roughness of $\varepsilon/D_h = 10^{-4}$. Thus, based on the Colebrook correlation for fully turbulent flow over rough surfaces, the friction factor can be found as

$$f_{fo} = \frac{1}{(1.14 - 2\log_{10}\frac{\varepsilon}{D_h})^2} = 0.01197037\ . \tag{H-91}$$

To develop an interfacial-drag model for the subcooled-boiling region, one could attempt to analyze the partial boiling and fully developed boiling regions separately. In the fully developed region, the bubbles entering the free stream quickly collapse due to condensation, and the majority of the bubbles remain in the vicinity of the wall. Therefore, the bubbles for both regions are assumed to exist in a layer close to the wall, and models developed for the partial boiling region are assumed to apply to the fully developed region as well. However, if the liquid core becomes saturated or superheated, a model for IFDC is also developed to account for the interfacial drag resulting from bubbles flowing in the free stream.

In the partial boiling region, the surface-tension force that firmly attaches the bubbles to the wall is not taken into account for the two-fluid approximation. A modification to the interfacial-drag coefficient to account for this restoring force would require a negative value. This is clearly unacceptable due to the potential for destabilization of the solution. Sensitivity calculations show that a small positive value on the order of $1 - 10\ \mathrm{kg/m^4}$ for C_i will allow for a reasonable prediction of the void fraction below the quench front.

If one assumes a bubble-drag model similar to the case of adiabatic flow in a channel, where the bubbles are dispersed, the calculated interfacial drag is very large (for a bubble size of 0.001 m, $C_i = 300\ 000\ \mathrm{kg/m^4}$). When applied to the two-fluid model, this would cause the bubbles to flow at or near the liquid velocity. A C_i of this magnitude is obviously inappropriate for the flow situation at hand.

If one assumes that the flow of the liquid in the subcooled-boiling region is very similar to the flow through a roughened pipe, a much smaller value of C_i is obtained. Using the Colebrook friction factor for turbulent flow and a completely rough zone, the shear stress is

$$\tau_i = \frac{1}{2}\rho_l V_l^2 \left[1.14 - 2.0 \log_{10}\left(\frac{\varepsilon}{D_h}\right) \right]^{-2} . \tag{H-92}$$

The roughness parameter is estimated to be a percentage of the time-averaged height of the growing bubbles (Ref. H-27.). We use the following relation for the roughness parameter:

$$\varepsilon = 0.01 Y_b \quad . \tag{H-93}$$

To develop the interfacial-drag coefficient, we perform the following steady-state force balance on the channel:

$$\pi D_h \Delta z \tau_i = \frac{\pi}{4} D_h^2 \Delta p \alpha_l \tag{H-94}$$

and

$$\alpha_l \frac{\Delta p}{\Delta z} = \frac{4\tau_i}{D_h} , \tag{H-95}$$

where it is assumed that the hydraulic diameter is equivalent to the hydraulic diameter of the channel. From the liquid momentum equation,

$$\alpha_l \frac{dp}{dz} \sim C_{i,sb} V_r^2 , \tag{H-96}$$

so that $C_{i,sb}$ is found to be

$$C_{i,sb} = \frac{2\rho_l}{D_h}\left[1.14 - 2.0 \log_{10}\left(\frac{\varepsilon}{D_h}\right)\right]^{-2} . \tag{H-97}$$

For a hydraulic diameter of 0.00129 m (typical of PWR cores), and a bubble diameter of 1 mm, equation Eq. (H-97) overestimates the drag coefficient. This is basically due to the liquid density used in the equation.

To determine an appropriate interfacial-drag coefficient, the following argument is proposed. The film of bubbles attached to the wall in subcooled boiling can be considered to be a film of vapor instead of individual bubbles. At the interface, the surface is rough or dimpled. The vapor is moving relative to the liquid and is now considered to be in the continuous phase. Thus, the vapor is seen to be flowing around a roughened liquid core with a diameter very similar to the diameter of the channel. Equation (H-97) then applies as before except that the liquid density is replaced with the vapor density:

$$C_{i,sb} = \frac{2\rho_g}{D_h}\left[1.14 - 2.0 \log_{10}\left(\frac{\varepsilon}{D_h}\right)\right]^{-2} . \tag{H-98}$$

In the case where the liquid is saturated or superheated, the bubbles can exist in the free stream. Thus, the interfacial-drag-coefficient model should consist of two components: (1) the interfacial drag due to bubbles attached to the wall and (2) the interfacial drag due to bubbles traveling in the free stream. The contribution due to bubbles attached to the wall is calculated by Eq. (H-98), as discussed above. The contribution due to bubbles in the free stream is determined in the same fashion as for bubbly flow (see Section H.1.). For completeness, it is summarized below.

Collier (Ref. H-27.) indicated that if the bubbles attached to the wall are assumed to be packed in a square array and to interfere with each other when $r/s \approx 0.25$ (s is the distance between bubbles), then the void fraction at the wall can be given by

$$\alpha_w = \frac{\pi}{6}\frac{Y_b}{D_h} \quad . \tag{H-99}$$

If the liquid temperature becomes saturated or greater than the saturation temperature, α_w becomes zero. For subcooled liquid conditions, α_w obtained from Eq. (H-99) is recorrected based upon the liquid temperature in order to make a smooth transition to the saturated conditions. This correction is done when the liquid temperature plus 5°C(T_l+5°C) is greater than or equal to the saturation temperature of the fluid and is given by

$$\alpha_w = \frac{\pi}{6}\frac{Y_b}{D_h}[0.2(T_{\text{sat}} - T_l)] \text{ for } T_{\text{sat}} - 5K \le T_l < T_{\text{sat}} \text{ and} \tag{H-100}$$

$$\alpha_w = 0 \qquad \text{for} \qquad T_l \ge T_{\text{sat}} \ .$$

Then, the void fraction of bubbles traveling in the free stream is expressed by

$$\alpha_{fr} = \alpha_g - \alpha_w \quad . \tag{H-101}$$

Ishii (Ref. H-2.) gave the bubbly flow drag force by

$$M = -\frac{\alpha}{2}\left[\sqrt{\frac{g\Delta\rho}{\sigma}f(\alpha)}\right]\rho_l(C_1V_v - C_0V_l)^2 \ . \tag{H-102}$$

Thus, the free-stream drag coefficient can be obtained by equating Eq. (H-102) to $C_{i,fr}V_r^2$, and is given by

$$C_{i,fr} = \frac{\alpha_{fr}}{d_b}f(\alpha)\rho_l\frac{(C_1V_v - C_0V_l)^2}{(V_v - V_l)^2} \tag{H-103}$$

where

$$f(\alpha) = \left[\frac{1 + 17.67(1-\alpha_{fr})^{1.3}}{18.67(1-\alpha_{fr})^{1.5}}\right]^2 \tag{H-104}$$

and

$$d_b = 2\sqrt{\frac{\sigma}{g\Delta\rho}} \quad . \tag{H-105}$$

Finally, the total interfacial-drag coefficient for subcooled nucleate boiling is obtained as follows by a momentum-weighted equation as

If $T_l \geq T_{sat}$,

$$C_{i,sb} = \frac{C_{i,sb} V_l^2 + ffs \cdot C_{i,fr} V_r^2}{(\alpha_w + \alpha_{fr}) V_r^2}, \text{ if } \alpha_w > 0 \qquad \text{(H-106)}$$

$$C_{i,sb} = \frac{ffs\, C_{i,fr}}{\alpha_{fr}} \quad , \text{ if } \alpha_w \leq 0 \ , \qquad \text{(H-107)}$$

where the constant *ffs*, which multiplies the free-stream bubble IFDC, is assigned a value of 0.00175 to fit CCTF Run-14 pressure-drop data.

If $T_l < T_{sat}$, then (H-108)

$C_{i,fr} = 0$ and

$C_{i,sb} = C_{i,sb}$ [Eq. (H-98)] .

The interfacial-drag model summarized above is used when the cell void fraction is between 0 and 0.5. For void fractions greater than 0.98, the interfacial-drag coefficient is calculated by the interfacial-drag model for the annular-mist-flow regime that is given in the previous section. For void fractions between 0.5 and 0.98, a linear weighting is used to obtain $C_{i,sb}$. The linear weighting is given by

$$C_{i,sb} = C_{i,sb} + (C_{i,\text{am}} - C_{i,sb})(WX)^{0.4} \ , \qquad \text{(H-109)}$$

where $C_{i,\text{am}}$ is the interfacial-drag coefficient for annular-mist flow in nucleate boiling and

$$WX = \frac{1}{\alpha_{df} - \alpha_1}\alpha - \frac{\alpha_1}{\alpha_d - \alpha_1} \quad , \quad \alpha_1 = 0.5 \ . \qquad \text{(H-110)}$$

H.1.5.1.2. Input Required for Implementation. Implementation of the subcooled interfacial-drag model requires the definition of fluid properties and the hydraulic diameter of the channel.

H.1.5.1.3. Constants. No changes were made to any of the numerical constants, and they are the same as in the references cited. The free-stream bubble IFDC is multiplied by a constant, *ffs*, of 0.00175 to fit CCTF Run-14 pressure-drop data.

H.1.5.1.4. Model as Coded. The core-reflood model is coded in subroutine CIF3. This subroutine is called by VSSL1 for each level in the VESSEL component. Several tests exist to determine whether the cell of interest resides in the core region. The subcooled

interfacial-drag model is used when the cell resides in the core region and the core-reflood model is turned on.

H.1.5.1.5. Weightings, Averaging, and Limits. The void fraction of bubbles attached to the wall is restricted, with a minimum value of 0.05 and maximum value of 0.3. The free-stream void fraction is also limited, with a minimum of 0.005 and a maximum of 0.5. The height of the bubble from the wall cannot be higher than 0.00001 m. If the liquid becomes saturated or superheated, the diameter of the bubbles calculated from Eq. (H-105) is limited by a maximum value of 0.9 times the hydraulic diameter, and the free-stream void fraction is limited by a minimum value of 0.001. No other weightings or limits are applied.

H.1.5.1.6. Scaling Consideration. The Colebrook friction-factor relation and the equation for the bubble height are given internal tube flows. Although the hydraulic diameter of the open channel used is similar to the tube diameter, the applicability of these equations to rod bundles is not verified and subject to further investigation.

H.1.5.1.7. Summary and Conclusions. The interfacial-drag coefficient for subcooled boiling is obtained by using the Colebrook friction factor for flows through roughened pipes. The bubbles attached to the wall in subcooled boiling are considered to be a film of vapor instead of individual bubbles. The vapor is thought to flow around a roughened liquid core with a diameter similar to the diameter of the channel. Therefore, the density of liquid is replaced by the density of vapor in Eq. (H-97). In the case where the liquid is superheated or saturated, the IFDC is considered to consist of two components: (1) the interfacial drag due to bubbles attached to the wall, and (2) the interfacial drag due to bubbles in the free stream. The free-stream contribution is obtained using Ishii's drag coefficient formulation for bubbly flows.

H.1.5.2. Smooth Inverted-Annular-Flow Model.

H.1.5.2.1. Basis for the Model. In this region, the interface is assumed to be smooth. Therefore, the following simple smooth-tube correlation for the interfacial friction factor is used (Ref. H-28.):

$$f_{i,sm} = \frac{16}{Re_g} \qquad \text{for laminar flow, and} \qquad \text{(H-111)}$$

$$f_{i,sm} = 0.079 Re_g^{-0.25} \qquad \text{for turbulent flow,} \qquad \text{(H-112)}$$

where

$$Re_g = \frac{\frac{(D_h - D_c)}{2} \alpha_g \rho_v V_v}{\mu_v} \quad .$$

To develop $C_{i,sm}$, a force balance is performed as before, using Fig. H-19. as follows:

$$\alpha_g \Delta p \frac{\pi}{4} D_h^2 = -\tau_i \pi D_c \Delta z - \tau_w \pi D_h \Delta z \ . \tag{H-113}$$

From the vapor momentum equation, we have

$$\alpha_g \left(\frac{dp}{dz}\right) \sim C_i V_r^2 - C_{wg} V_g^2 \ . \tag{H-114}$$

The core diameter can be determined from the geometric consideration as

$$D_c = \alpha_l^{1/2} D_h \quad , \tag{H-115}$$

and, from the definition of the friction factor, we have

$$\tau = \frac{1}{2} \rho V^2 f \quad . \tag{H-116}$$

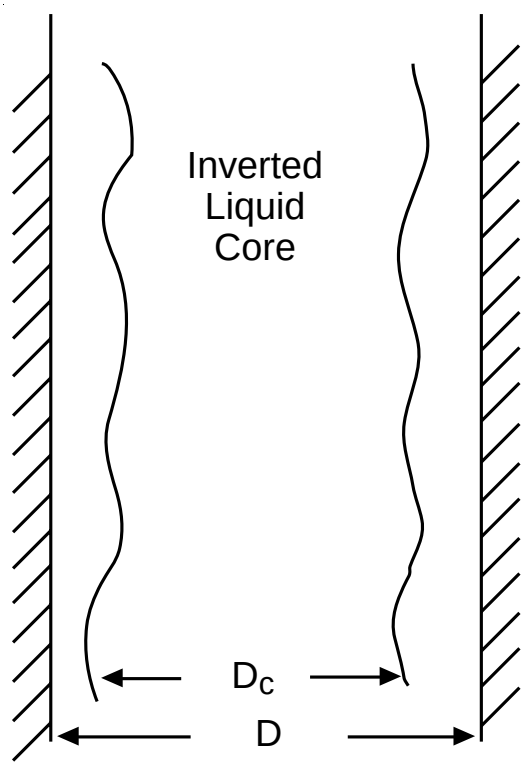

Fig. H-19. Representation of the smooth inverted annular regime.

The interfacial-drag coefficient then becomes

$$C_{i,sm} = 2\rho_g f_{i,sm} \frac{(1-\alpha_g)^{1/2}}{D_h} \quad . \tag{H-117}$$

The hydraulic diameter of the channel is used instead of the tube diameter in Eq. (H-117).

H.1.5.2.2. Input Required for Implementation. The fluid properties, channel hydraulic diameter, and the cell void fraction are the required input for the smooth IAF interfacial-drag model.

H.1.5.2.3. Constants. No changes were made to any of the numerical constants for friction-factor correlations, and they are the same as in the references cited.

H.1.5.2.4. Model as Coded. The interfacial-drag model for the smooth IAF is determined in subroutine CIF3 as a part of the core-reflood interfacial-drag model. This subroutine is called by VSSL1 for each level in the VESSEL component. Several tests exist to determine whether the cell of interest resides in the core region. The smooth IAF interfacial-drag model is used when the cell resides in the core region and the core-reflood model is turned on, and the cell void fraction is less than 98%.

H.1.5.2.5. Weightings, Averaging, and Limits. The void fraction at the smooth/rough-wavy IAF boundary is limited by a maximum value of 30% and a minimum value of 0.05%. The Reynolds number used in Eqs. (H-111) and (H-112) has a minimum value of 1.0. If $C_{i,sb} \times fsb$ is less than $C_{i,sm} \times fsm$ then, to prevent discontinuity, $C_{i,sm}$ is assumed to be

$$C_{i,sm} = C_{i,sb} \frac{fsb}{fsm} \ , \ fsb = 1 \text{ and } fsm = 3.0 \quad . \tag{H-118}$$

The interfacial-drag coefficient is further redefined based upon the cell void fraction, as illustrated in Fig. H-17a. If the cell resides in the low-void-fraction region, $\alpha < 0.75$ (see Fig. H-17a.), no adjustment is done, and the model mentioned above is used to estimate the interfacial-drag coefficient. If the cell is located in the high-void-fraction region, $\alpha > 0.98$, the interfacial-drag coefficient for the smooth IAF, $C_{i,sm}$, is assumed to be equal to that of the highly dispersed flow $C_{i,df}$. In the transition between the high- and low-void-fraction regions ($0.75 < \alpha < 0.98$), the following linear weighting based upon the void fraction is applied to avoid discontinuities between low- and high-void-fraction regions:

$$C_{i,sm} = C_{i,sm} + (C_{i,df} - C_{i,sm}) W^{0.5} \ , \tag{H-119}$$

where

$$W = \frac{1}{(\alpha_{df} - \alpha_2)}\alpha_g - \left(\frac{\alpha_2}{(\alpha_{df} - \alpha_2)}\right) \quad .$$

The weighting, W, is limited by a maximum value of 1.0 and minimum value of 0.0, and $\alpha_{df} = 0.98$ and $\alpha_2 = 0.75$.

In summary, the interfacial-drag coefficient for the smooth IAF is determined by the following equations:

$$\begin{aligned} C_{i,sm} &= C_{i,df} && \text{if } \alpha_g > 0.98 \text{ or } C_{i,sm} < C_{i,df} \\ C_{i,sm} &= C_{i,sm} + (C_{i,df} - C_{i,sm})W && \text{if } 0.75 < \alpha_g < 0.98 \\ C_{i,sm} &= C_{i,sm} && \text{if } 0.75 > \alpha_g . \end{aligned} \qquad \text{(H-120)}$$

From sensitivity calculations and comparisons to reflood data, an appropriate value of $C_{i,sm}$ for this regime is of the order 1.0 to 5.0 kg / m^4. If we apply Eqs. (H-111), (H-112), and (H-117), with typical PWR conditions (D = 0.0129 m, p = 2.5 bar, V_g = 20 m / s, and a void fraction of 10%), we obtain a value for $C_{i,sm}$ of 1.25 kg / m^4. In this case, the vapor film is calculated to be turbulent. If we use the gap between the wall and liquid core as the characteristic diameter, we obtain a laminar vapor film and a $C_{i,sm}$ value of 4.5 kg / m^4. Thus, the use of a smooth-tube-friction correlation in this regime appears to be valid, and it is expected that Eqs. (H-111), (H-112), and (H-117) will give an appropriate estimate of the interfacial drag. The interfacial drag is observed to be dependent on the definition of the hydraulic diameter. The use of the gap width is appropriate for the case of a small gap-to-diameter ratio as we have here.

H.1.5.2.6. Scaling Consideration. The smooth-tube friction factors for laminar and turbulent flows are given for internal flows. In the case of rod bundles, in which the flow is an external flow, the use of these equations is an engineering approximation. However, the hydraulic diameter of the open channel used in the model is similar to the rod diameter.

H.1.5.2.7. Summary and Conclusions. In the smooth IAF region, the smooth-tube-friction-factor correlations are used for the smooth IAF. The interfacial-drag coefficient is obtained from the force balance equation. The interfacial-drag coefficient depends on the definition of the hydraulic diameter. The sensitivity study indicated that for small gap-to-diameter ratios, the use of the gap width is appropriate. The IFDC for this flow regime is readjusted according to IFDC selection logic illustrated in Fig. H-17b. For the high void fractions ($\alpha_g > 0.98$), IFDC is identical to that of the highly dispersed flow. In the transition region ($0.75 < \alpha_g < 0.98$), IFDC for this flow regime is obtained by a linear weighting between IFDCs for the smooth and highly dispersed flow regimes. For low void fractions ($\alpha_g < 0.75$), the smooth IFDC model is used.

H.1.5.3. Rough-Wavy Inverted-Annular-Flow Model.

H.1.5.3.1. Basis for the Model. This regime is similar to the smooth IAF case. However, the interfacial friction is now increased due to the presence of waves and the shearing of droplets from the wave crests (Fig. H-20.).

The interfacial-drag coefficient for the rough-wavy inverted annular flow is formulated in the same way as the smooth inverted-annular-flow model. The interfacial-drag coefficient can be expressed with Eq. (H-117) as

$$C_{i,rw} = \frac{2\rho_v f_{i,rw}(1-\alpha_g)^{1/2}}{D_h} \quad . \tag{H-121}$$

In order to express the friction factor, $f_{i,rw}$, in Eq. (H-121), the turbulent, rough-pipe correlation suggested by Colebrook, given by Eq. (H-91), is used. The wavy vapor-liquid interface is considered to represent the pipe roughness in Eq. (H-91). The roughness is assumed to be proportional to the diameter of liquid droplets entrained from the wavy interface. Thus, the relative roughness in Eq. (H-121) becomes

$$\frac{\varepsilon}{D_h} = fc4 \times \frac{d_d}{D_h} \ , \tag{H-122}$$

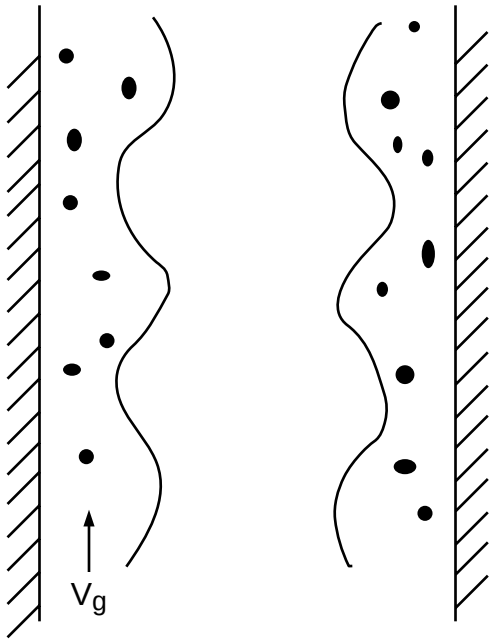

Fig. H-20. Representation of the rough-wavy IAF region.

where d_d is the droplet diameter. Ishii (Ref. H-2.) calculated droplet diameter for small droplets observed in inverted annular flow using

$$d_d = 0.613 \left(\frac{\sigma}{g\Delta\rho} \right)^{1/2} N_{\mu g} \quad , \tag{H-123}$$

where

$$N_{\mu g} = \frac{\mu_g}{\left[\rho_g \sigma \sqrt{\frac{\sigma}{g\Delta\rho}} \right]^{1/2}} \, . \tag{H-124}$$

If $\varepsilon / D_h > 1$, then a constant of 0.77 is used for $f_{i,rw}$. If $\varepsilon / D_h < 1$, then $f_{i,rw}$ is calculated from Colebrook's equation, Eq. (H-91).

H.1.5.3.2. Input Required for Implementation. The fluid properties, hydraulic diameter, and the void fraction of the cell that is in the rough-wavy IAF are input into the model.

H.1.5.3.3. Constants. The proportionality constant for the pipe roughness was found to be 80 to fit best the CCTF pressure drop.

H.1.5.3.4. Model as Coded. The interfacial-drag model for the rough-wavy IAF is determined in subroutine CIF3 as a part of the reflood interfacial-drag model. If the cell void fraction is less than 98%, the interfacial-drag coefficient for the rough-wavy IAF is calculated as indicated in Fig. H-17b.

H.1.5.3.5. Weightings, Averaging, and Limits. The void fraction at the boundary between the rough-wavy and agitated IAF regimes is limited by a maximum value of 40% and minimum value of 30%. The interfacial-drag coefficient in the rough-wavy IAF regime is expected to be higher than that of the smooth IAF regime. If $C_{i,sm} \times fsm$ is found to be less than $C_{i,sm} \times frw$, then, to ensure smooth transition, $C_{i,sm}$ is multiplied by the ratio of frw / fsm. The constants frw and fsm are 1.25 and 3.0, respectively.

The interfacial-drag coefficient is further weighted based upon the cell void fraction as done before for the smooth IAF regime. If the cell is located in the low-void-fraction region, no adjustment is done, and the above-mentioned model, Eq. (H-121), is used to estimate the drag coefficient. If the cell is located in the high-void-fraction region, the interfacial-drag coefficient for the smooth IAF is assumed to equal that of the dispersed flow. In the transition between the high- and low-void-fraction regions, the following linear weighting is applied to accurately predict CCTF Run-14 pressure-drop data:

$$C_{i,rw} = C_{i,rw} + (C_{i,df} - C_{i,rw}) W^{0.5} \quad , \tag{H-125}$$

where

$$W = \frac{1}{\alpha_{df} - \alpha_2}\alpha_g - \frac{\alpha_2}{\alpha_{df} - \alpha_2} \quad .$$

The weighting, *W*, is limited by a maximum value of 1.0 and minimum value of 0.0, and $\alpha_{df} = 0.98$ and $\alpha_2 = 0.75$.

The interfacial-drag coefficient for the rough-wavy IAF regime is

$$\begin{aligned} C_{i,rw} &= C_{i,df} && \text{if } \alpha_g > 0.98,\ C_{i,rw} < C_{i,df} \\ C_{i,rw} &= C_{i,rw} + (C_{i,df} - C_{i,rw})W && \text{if } 0.75 < \alpha_g < 0.98 \\ C_{i,rw} &= C_{i,rw} && \text{if } 0.75 > \alpha_g \quad . \end{aligned} \tag{H-126}$$

H.1.5.3.6. Scaling Consideration. The Wallis correlation is given for internal tube flows. In the case of rod bundles in which the flow is an external flow, the use of these equations is an engineering approximation. However, the hydraulic diameter of the core channel is similar to the rod diameter.

H.1.5.3.7. Summary and Conclusions. The interfacial-drag model for the rough-wavy IAF is similar to Wallis' (Ref. H-15.) interfacial-drag model for annular-mist flow. The TRAC core-reflood model includes the gas void fraction instead of liquid fraction. The interfacial-drag coefficient obtained from the model is used in low-void-fraction regions. For the high-void-fraction region, the dispersed flow interfacial-drag coefficient is used, whereas between these low- and high-void-fraction regions, a linear weighting is applied.

H.1.5.4. Agitated Inverted Annular Region Model. This region is characterized by large liquid slugs of similar diameter to the tongue diameter in the rough-wavy region. Breakup of the slugs into smaller pieces and droplets eventually occurs. The region is quite chaotic. It may be similar to the churn-turbulent regime in adiabatic flow that is used to characterize the transition region between slug flow and annular mist. The interfacial drag should again be dominated by the mechanism of droplet entrainment and breakup of the inverted tongue. For this region, it is proposed to use the same correlation as the rough-wavy region, with possibly a constant multiplier to be determined from comparisons with data.

H.1.5.5. Highly Dispersed Flow Model. This region of IAF is characterized by liquid droplets, small in size, suspended in the vapor stream.

H.1.5.5.1. Basis for the Model. The dispersed region is comprised of droplets flowing up the channel. The liquid droplet size is determined by a correlation suggested by Ishii (Ref. H-2.). This correlation gives droplet sizes on the order of millimeters at reasonable reflood pressures, as given by

$$d_d = 1.838 \left(\frac{\sigma}{g(\rho_l - \rho_v)} \right)^{1/2} N_{\mu g}^{1/3}, \tag{H-127}$$

where $N_{\mu g}$ is the viscosity number,

$$N_{\mu g} = \frac{\mu_g}{\left[\rho_g \sigma \sqrt{\frac{\sigma}{g(\rho_l - \rho_g)}} \right]^{1/2}} \tag{H-128}$$

An interfacial-drag coefficient for the droplet in this fully dispersed flow is found by a separate force balance on the droplet as

$$C_{i,dd} = \frac{\frac{3}{4} \alpha_{dd} \rho_g C_d}{d_d} \quad , \tag{H-129}$$

where C_d is the form drag coefficient and α_{dd} is the liquid droplet fraction that is given below. The following equation, suggested by Ishii and Chawla (Ref. H-1.), is used for the spherical-drop form drag coefficient:

$$C_d = \frac{24(1 + 0.1 Re_d^{0.75})}{Re_d} \quad , \tag{H-130}$$

where

Re_d = Reynolds number = $\frac{\rho_v d_d V_r}{\mu_m}$,

V_r = relative velocity = $V_v - V_d$, and

μ_m = viscosity of two-phase mixture = $\frac{\mu_v}{(1 - \alpha_{dd})^{2.5}}$.

An estimate of the droplet velocity can be obtained from a separate momentum balance, assuming the droplet-drag coefficient is 0.44 (Ref. H-29.), as

$$V_d = V_v - 2.462 \left[\frac{(\rho_l - \rho_v) g d_d}{2 \rho_v} \right]^{1/2}. \tag{H-131}$$

In actual reactor hardware, not all the surfaces are heated because control rods and structures are present at the periphery of the core. Thus, a liquid film may establish itself on the cold surfaces, adding significantly to the overall liquid fraction at the top of the core. A typical PWR core contains 45548 heated rods at 0.01073 m diameter and 3860 control rods of 0.0138 m diameter. Thus, the unheated surface for the control rods alone

accounts for 9.83% of the total heat-transfer surface area. From geometric considerations, one can calculate the local volumetric liquid fraction for a given film thickness. For the typical reactor hardware, Table H-3. presents such a calculation. This table shows that a liquid film thickness of 1 mm on the cold surface alone provides a total liquid fraction of about 3%. Thus the contribution of this film cannot be neglected since it can represent a significant portion of the total liquid fraction.

Williams (Ref. H-30.) has shown that the vapor velocities generated in the core during reflood are at about the correct value to cause countercurrent flow limitation. Thus, the drag and gravity forces balance, creating a "hanging" film condition. Figure H-21. depicts this condition from a top view.

In tests with only heated surfaces, exit-droplet liquid fractions are typically less than 1%. Thus the film on the unheated surfaces represents a significant component of the total volumetric liquid fraction. The overall drag coefficient must take into account both droplet and film. It is not possible to do this directly with the two-fluid approximation because only one liquid field is assumed, and the droplets flow at a much different velocity than the film.

The thickness of liquid film on a cold wall was derived by Pasamehmetoglu (Ref. H-31.). The following assumptions were made in deriving the formula:

1. the liquid flow is assumed laminar and incompressible,
2. the force balance includes gravity and interfacial shear only (i.e., wall shear and liquid momentum are negligible),
3. surface forces are negligible, and
4. the flow is fully developed and quasi-steady.

TABLE H-3.
Liquid Volume Fraction at Various Film Thicknesses

Film Thickness (m)	Liquid Volume Fraction (%)
0.0002	0.6
0.0005	1.5
0.001	3.2
0.002	6.9
0.003	11.0

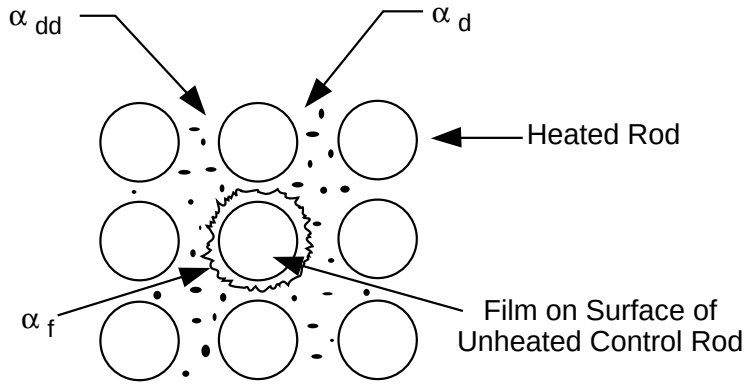

Fig. H-21. Proposed scheme for the dispersed region in reactor geometry.

The force balance on a differential liquid element gives

$$\mu_l \frac{\partial^2 u}{\partial y^2} = g\rho_l \quad , \tag{H-132}$$

where u is the liquid velocity parallel to the wall and y is the coordinate perpendicular to the wall. Thus, the velocity profile can be obtained as

$$u = \frac{1}{2}\frac{\rho_l g}{\mu_l} y^2 + \left[\frac{\tau_i}{\mu_l} - \frac{\rho_l g \delta_f}{\mu_l}\right] y \tag{H-133}$$

using the following boundary conditions:

$$\begin{aligned} &\text{at} \quad y = 0 \ , \quad u = 0 \\ &\text{at} \quad y = \delta_{f,} \quad \tau = \tau_i \quad . \end{aligned} \tag{H-134}$$

The liquid film thickness can be expressed by

$$\delta_f = C\frac{\tau_i}{\rho_l g} \quad . \tag{H-135}$$

To determine C, the following criteria are proposed:

1. the velocity, u, is positive for all y, and
2. the volume flow rate in the axial direction is zero.

Using criterion 1, C is obtained as 1. The second criterion gives a value of 1.5 for C.

Substituting the Wallis interfacial shear correlation (Ref. H-15.) given by

$$\tau_i = \frac{1}{2} f_i \rho_g V_g^2 \quad , \tag{H-136}$$

where the interfacial friction factor is

$$f_i = 0.005 \left(1 - 300 \frac{\delta_f}{D_h} \right) , \tag{H-137}$$

into Eq. (H-135), the liquid film thickness is obtained as

$$\delta_f = \frac{0.0025 C \rho_g V_g^2}{g \rho_l + \dfrac{0.75 C \rho_g V_g^2}{D_h}} \tag{H-138}$$

Equation (H-138) is valid for

$$V_g < \sqrt{\frac{1.333}{C} \frac{\rho_l}{\rho_g} g D_h} \quad . \tag{H-139}$$

This equation gives the maximum liquid thickness that can be sustained by the flowing vapor. If the thickness is larger, liquid will flow downwards due to gravity and if it is smaller, liquid will be carried with vapor. For unheated flow, under fully developed conditions, the deposition and entrainment will reach an equilibrium such that the deposition rate will be equal to the entrainment and yield a constant entrainment fraction. Thus, the film thickness will not be affected by entrainment and deposition. However, changes in vapor velocity in the flow direction will change the film thickness. the above equation is valid only if these changes are gradual because of fully developed flow assumptions.

For the typical reflooding conditions, V_g = 10 m / s, p = 2 bar, D_h = 2 cm, and Eq. (H-139) with C = 1.5 yields δ_f = 1.46 mm. Because this thickness is small, the turbulence effects can be neglected. Equation (H-139) is also independent of viscosity; therefore, for homogeneous turbulence (where the eddies are uniform), the result would be the same. The result would be altered by turbulence only if the eddy viscosity is a function of y. The turbulence at the interface is accounted for by using Wallis' equation for the interfacial shear.

Then, the liquid film fraction is obtained from the geometrical consideration

$$\alpha_f = \frac{P\delta_f F_u}{A} \quad , \tag{H-140}$$

where

$P = 4\frac{A}{D_h}$ = equivalent perimeter of the channel,

δ_f = film thickness,

F_u = fraction of the unheated surface area in the core $= \frac{A_u}{A_t}$,

A = flow area of the channel,

A_u = unheated surface area, and

A_t = total surface area.

The liquid film fraction, α_f, can also be limited by the total liquid fraction, α_l, available to be deposited on the unheated surface area. If the liquid and the unheated surface area are homogeneously distributed within a control volume, the amount of liquid might be considered to be $F_u(1-\alpha_g)$. With cross flow between subchannels, however, and the ability of unheated surfaces to collect liquid and hold it, the amount of liquid "hanging" on an unheated wall may become greater than $F_u(1-\alpha_g)$. This effect is included in the following relationship, which has been developed using results from CCTF Run 14:

$$\alpha_f = F_u W(1-\alpha_g) \ , \tag{H-141}$$

where W is the cold-wall liquid fraction weighting that is defined as

$$W = 5\left[\frac{0.98-\alpha}{0.98-\min(\alpha_{AG}, 0.7)}\right]^{0.35} \quad \text{if} \quad \min(\alpha_{AG}, 0.7) < \alpha < 0.98 \ ,$$

$$W = 5 \quad \text{if} \quad \alpha \geq 0.98 \ , \text{and}$$

$$W = 0 \quad \text{if} \quad \alpha \leq \min(\alpha_{AG}, 0.7) \ .$$

The weighting factor allows the limiting amount of liquid deposited on the cold wall to be an amount greater than the homogeneous fraction of the unheated surface area. We assumed that the weighting becomes unimportant when the void fraction is less than α_{AG}. The weighting also allows the maximum fraction of the liquid to be accumulated in the dispersed-flow regime. The liquid film fraction is selected to be the minimum of values obtained by Eqs. (H-140) and (H-141),

$$\alpha_f = \min\left(\frac{P\delta_f F_u}{A}, F_u W(1-\alpha)\right) \tag{H-142}$$

The liquid droplet fraction then becomes

$$\alpha_{dd} = 1 - \alpha_f - \alpha_g \quad . \tag{H-143}$$

Using the modified Wallis relation (Ref. H-15.), the interfacial friction factor between the liquid film and the vapor is

$$f_{i,f} = 0.005(1 + 75\alpha_f) \quad . \tag{H-144}$$

The interfacial drag on the film can be estimated using a relation similar to Eq. (H-117), except that the hydraulic diameter is replaced with the diameter of the cold rod and the weighting factor is applied as the fraction of the unheated surface area when the total heat-transfer area approaches zero. Then we have

$$C_{i,f} = \frac{2\rho_g f_{i,f}}{D_h} \quad . \tag{H-145}$$

The linear relationship given in Eq. (H-140) assumes that the factor F_u has a value of 1.0 when the unheated surface area is 100% of the total. As discussed above, a value of 10% is typical of PWR geometry.

We can now calculate the total averaged interfacial drag for this regime by using an average momentum balance equation between the liquid and the gas (Ref. H-29.). Simplifying the relation by assuming that the film velocity is small compared to the vapor velocity, and that the total liquid velocity is similar to the film velocity, we have

$$C_{i,df} = \frac{C_{i,dd}V_r^2 + C_{i,f}V_v^2}{\left(V_v - \frac{\alpha_{dd}V_d}{(1-\alpha_g)}\right)^2} \quad . \tag{H-146}$$

H.1.5.5.2. Input Required for Implementation. The fluid properties, hydraulic diameter, the fraction of unheated surface area in the core, and the void fraction of the cell that is in the rough-wavy IAF are input into the model.

H.1.5.5.3. Constants. The $C_{i,dd}$ obtained by Eq. (H-129) is multiplied by a constant, *fcdrop*, currently set to 0.015. The $C_{i,f}$, Eq. (H-145), is also multiplied by a constant, *ffd*, currently 0.5. This is done to fit best the CCTF Run-14 pressure-drop data . The constant, *C*, in Eq. (H-138) is set to 1.0. No other changes were made to any of the numerical constants for friction-factor correlations and they are the same as in the references cited.

H.1.5.5.4. Model as Coded. The highly dispersed flow interfacial-drag model is coded in subroutine CIF3, which is called by VSSL1. In the highly dispersed flow regime, evaluation of IFDC is performed in the following order. First, the droplet diameter is calculated. The velocity of the droplet is obtained from a momentum balance, assuming the droplet-drag coefficient is 0.44 [Eq. (H-131)]. The film thickness is evaluated from a force balance on the liquid film by Eq. (H-138). After calculating the droplet-drag coefficient and the friction factor for the film, the interfacial-drag coefficients for the film, droplet, and dispersed flow are obtained. Finally, the overall interfacial-drag coefficient for highly dispersed flow is obtained by Eq. (H-146).

H.1.5.5.5. Weightings, Averaging and Limits. There are several limits on various parameters to prevent numerical difficulties associated with Fortran coding and to prevent unacceptable conditions. The cell void fraction is limited by a minimum value of 30% for the dispersed flow. The droplet diameter estimated from Ishii's equation cannot be greater than 0.005 m or smaller than 0.0001 m. The diameter of the liquid slug is limited by a minimum value of 0.000001 m. The calculated droplet velocity and the relative velocity are restricted with a minimum value of 0.01 m/s. The calculated film thickness is also limited to a minimum value of 1×10^{-20} m and maximum value of 0.040 m. The droplet fraction cannot be smaller than zero. The droplet velocity calculated from Eq. (H-130) is limited by minimum value of 0.1. The relative droplet velocity is limited by a minimum of 0.05. No other weighting, averaging, or limits are applied to the model.

H.1.5.5.6. Scaling Consideration. The application of this model to rod bundles needs further investigation for various operating conditions different from those used in the development of this model.

H.1.5.5.7. Summary and Conclusions. The interfacial-drag model for the highly dispersed flow includes the IFDCs between the interface to droplet and interface to film, given by Eq. (H-146). The droplet IFDC is obtained from a force balance on the droplet. To determine the droplet-drag coefficient, the equation suggested by Ishii [Eq. (H-129)] is used. The friction factor for the film is calculated by the modified Wallis correlation [Eq. (H-144)].

H.1.5.6. Dispersed Flow with Large Droplets (Post-Agitated Region). This region is located downstream of the agitated IAF and extends until highly dispersed flow occurs and the droplets become smaller in size. In this region, the IFDC is obtained by performing a weighting based upon the void fractions and IFDCs between the rough-wavy and highly dispersed flow regimes. As shown in the flow-pattern/void-fraction map in Fig. H-17b., the IFDC is calculated by the following weightings for this region of IAF:

If $\alpha_{df} > \min(\alpha_{ag}, 0.7)$, $\alpha > \min(\alpha_{ag}, 0.7)$, and $z_{top} > z_{ag}$, then the interfacial-drag coefficient is given by

$$C_{i,pa} = C_{i,rw}\frac{frw}{fmdis} + \left(C_{i,df}\frac{fdis}{fmdis} - C_{i,rw}\frac{frw}{fmdis} \right) \left(\frac{\alpha - \min(\alpha_{ag}, 0.7)}{\alpha_{df} - \min(\alpha_{ag}, 0.7)} \right)^{xmdis} \qquad \text{(H-147)}$$

if $C_{i,\,df} \times fdis < C_{i,\,rw} \times frw$ or by

$$C_{i,pa} = C_{i,rw}\frac{frw}{fmdis} \qquad \text{if} \qquad C_{i,\,df} \times fdis \geq C_{i,\,rw} \times frw \text{ .} \qquad \text{(H-148)}$$

If $z_{df} < z_{bot}$, then a simple correction is made as

$$C_{i,pa} = C_{i,df}\frac{fdis}{fmdis} \quad . \qquad \text{(H-149)}$$

If $\alpha < \min(\alpha_{ag}, 0.7)$ and $z_{ag} < z_{top}$, the correction is given by Eq. (H-148).

The coefficients used in above weightings are

frw = 1.25 ,
fmdis = 1.0 ,
fdis = 1.0 , and
xmdis = 0.5 .

H.1.5.7. Combinations of the Individual Drag Models.

H.1.5.7.1. Basis for the Model. The models developed for each region of the core during reflood must be brought together in to apply them to a finite-difference two-fluid approximation. In this situation the finite-difference mesh (typically 4 to 10 levels in the core region) is stationary, and the core-reflood quench front moves through it. The levels of each regime are calculated by subroutine ZCORE (see Appendix F, Section F.2., for more information). It is proposed to apply the models for the individual regions with the following method: (1) superimpose the level correlations above the quench for each of the regions and determine the amount of axial distance that each region occupies in a given hydrodynamic mesh, and then (2) average the lengths of the interfacial-drag coefficients in each mesh and apply the result at the top of the mesh cell (assuming positive vertical flow).

H.1.5.7.2. Constants. No constants are used.

H.1.5.7.3. Model as Coded. For each IAF regime, a linear weighting is defined based upon the axial distance. If the top of the cell, z_{top} is less than the elevation where transition boiling ends, z_{tr}, then the weighting for subcooled boiling *WFSB* is set to 1. In this case, the cell resides completely in the transition boiling regime and the weightings for other flow regimes are zero.

If the cell resides in the dispersed-flow regime, $z_{bot} > z_{df}$ or $z_{bot} < z_{\mathrm{CHF}}$, the weighting for the highly dispersed flow regime, *WFHDS*, is set to 1 while the rest of the weightings for other regimes is zero.

If the cell is located in-between the transition boiling and the dispersed-flow regimes (inverted annular flow), $z_{tr} < z_{top}$ and $z_{df} > z_{bot}$, the following weightings are used for the subcooled boiling and smooth IAF regions:

$$WFSB = \frac{[\min(z_{tr}, z_{top}) - z_{bot}]}{dz} \tag{H-150}$$

and

$$WFSM = \frac{[\min(z_{sm}, z_{top}) - \max(z_{tr}, z_{bot})]}{dz} \; . \tag{H-151}$$

In the case where the top of the cell is in the agitated region, $z_{top} > z_{sm}$, the weighting for the agitated region is

$$WFRW = \frac{[\min(z_{ag}, z_{top}) - max(z_{sm}, z_{bot})]}{dz} \; ; \tag{H-152}$$

otherwise *WFRW* is zero.

If z_{top} is higher than z_{ag}, indicating that the cell has some parts located in the post-agitated region, the weighting for the post-agitated region is

$$WFMDS = \frac{[\min(z_{df}, z_{top}) - \max(z_{ag}, z_{bot})]}{dz} \; ; \tag{H-153}$$

otherwise *WFMDS* is zero.

The values of *WFSB*, *WFSM*, *WFRW*, and *WFMDS* are constrained to be ≥ 0.0 and ≤ 1.0.

Finally if $z_{top} > z_{df}$ and some part of the cell is in the highly dispersed flow, the weighting for the dispersed flow is

$$WFHDS = 1 - WFMDS - WFRW - WFSM - WFSB \; ; \tag{H-154}$$

otherwise *WFHDS* is zero.

The overall interfacial-drag coefficient for a cell is given by

$$C_i = WFSB \cdot fsb \cdot C_{i,\,sb} + WFSM \cdot fsm \cdot C_{i,\,sm} + WFRW \cdot frw \cdot C_{i,\,rw} + WFMDS \cdot fmdis \cdot C_{i,\,pa} + WFHDS \cdot fdis \cdot C_{i,\,df} \; . \tag{H-155}$$

The coefficients *fsb, fsm, frw, fmdis,* and *fdis* are currently set to 1.0, 3.0, 1.25, 1.0, and 1.0, respectively. These values are obtained to fit the CCTF Run-14 data.

H.1.5.8. Assessment. As mentioned in the introduction, the assessment of each individual model is not considered, since there is no available data for the reactor-core geometry. Therefore, the models developed for each inverted-annular-flow regime are used as an integral part of the core-reflood interfacial-drag package. To evaluate proper coefficients for weightings and drag coefficients, the CCTF Run-14 pressure-drop data are used.

In this section, therefore, we discuss only the overall results obtained when the overall core-reflood interfacial-drag model is used to predict CCTF Run-14 reflood data. Results presented in this section were obtained with MOD2, Version 5.3. The detailed assessment of the overall model that went into MOD2, Version 5.4, and subsequently into TRAC-M, is discussed in the TRAC-M/F77 Developmental Assessment Manual (Refs. H-40. and H-41.).

The CCTF facility (Ref. H-32.) is an experimental test facility designed to provide information on the thermal-hydraulic behavior of ECCS during the refill and reflood phases of a LOCA. It is an integrated test loop containing several features of a PWR such as core, downcomer, upper plenum, simulated steam generator, and pump. The CCTF Run-14 test procedure started with the preheating of the pressure vessel for initial conditions. After establishing initial conditions, the preheating was shut down and the lower plenum was filled to 0.87 m with near-saturated water before test initiation. The ECCS water was directly injected into the lower plenum after the heater rod surface temperature reached 502°C to prevent the possibility of rapid condensation. Later, the location of injection was changed to three intact cold legs. Typical operating conditions for this particular test were as follows:

Pressure	2.02 kg / cm^2 ,
Power	9.36 kW ,
Cold - leg injection rate	30.2 m^3 / s , and
Cold - leg injection temperature	39°C .

The TRAC model of CCTF considers only the pressure vessel. A schematic of the model is shown in Fig. H-22. The TRAC model of CCTF consists of six components: fill, inlet-injection pipe, vessel, outlet pipe, break, and heat structures. The 1D vessel model includes a lower plenum cell located at the beginning of the vessel, 18 cells in the core region, and 6 cells in the upper plenum.

The calculated flooding rates were 0.0094 and 0.0044 m/s at the lower section and the mid-section of the core, respectively, which showed good agreement with the experimental data. The predicted wall temperature and quench times were in good agreement with the data, except at upper elevations where the wall heat flux was decreasing with the axial distance (chopped cosine power profile).

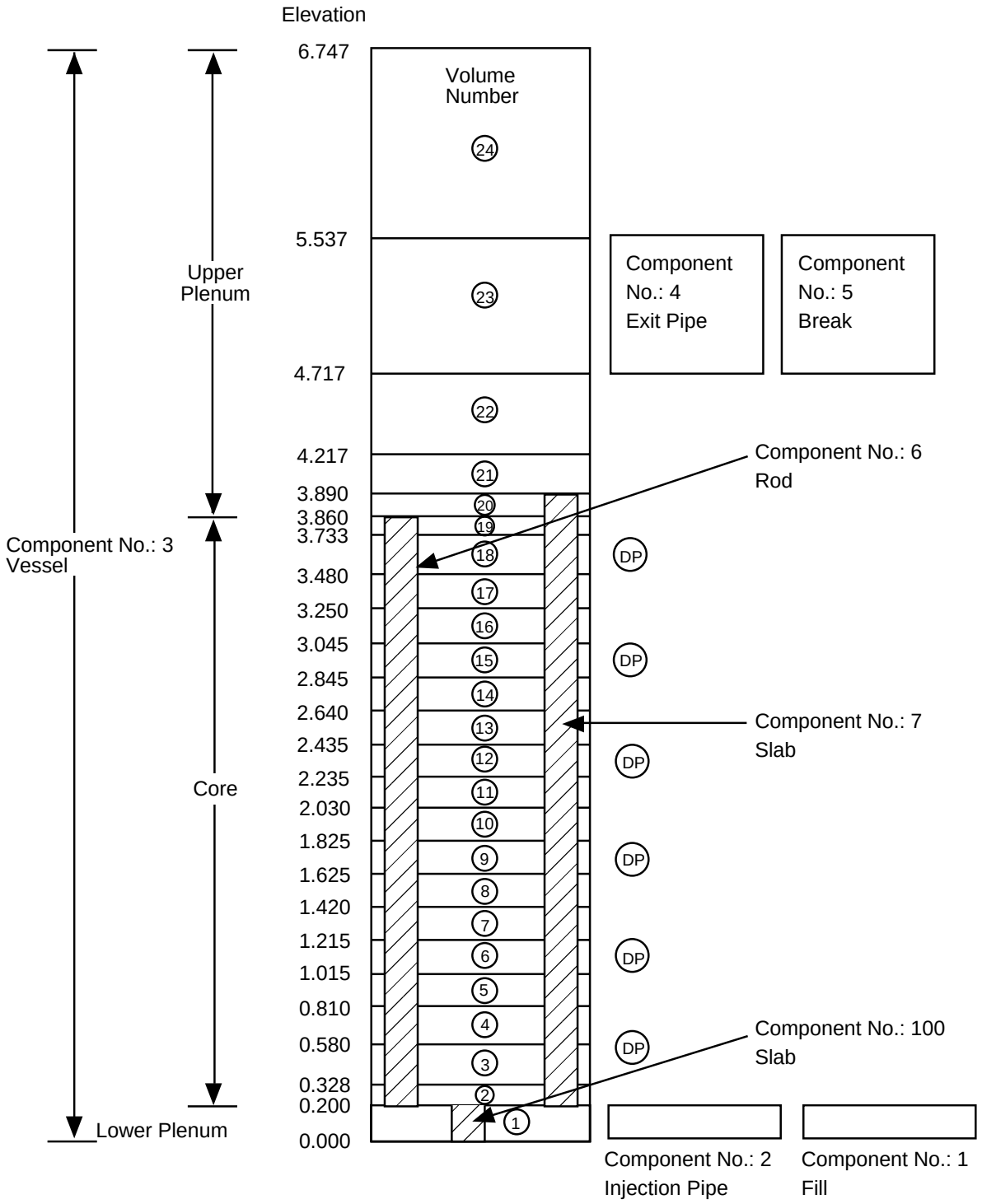

Fig. H-22. TRAC model for CCTF Run-14 test.

Comparisons of the calculated differential pressures at various elevations with the data are shown in Figs. H-23. to H-26. Figure H-23. shows the calculated and measured differential pressures between axial elevations of 0 and 0.61 m from the core inlet as a function of time. The calculated and measured differential pressure drops are in good agreement during the transient, with the exception of transient times between 10–80 s. At about 80 s in the transient, the quench front reaches the axial elevation of 0.38 m away from the inlet (corresponds to an axial location of 0.18 m from the beginning of the heated section). In this initial period of the transient, the interfacial-drag coefficient is slightly overestimated, which causes the liquid to be carried out to upper elevations, as seen in Figs. H-24. to H-26. These figures show pressure-drop peaks at higher elevations. However, this has a negligible effect on the prediction of pressure drop in the later times of the transient. In summary, the core-reflood interfacial-drag model provides a reasonable estimate of the pressure drop.

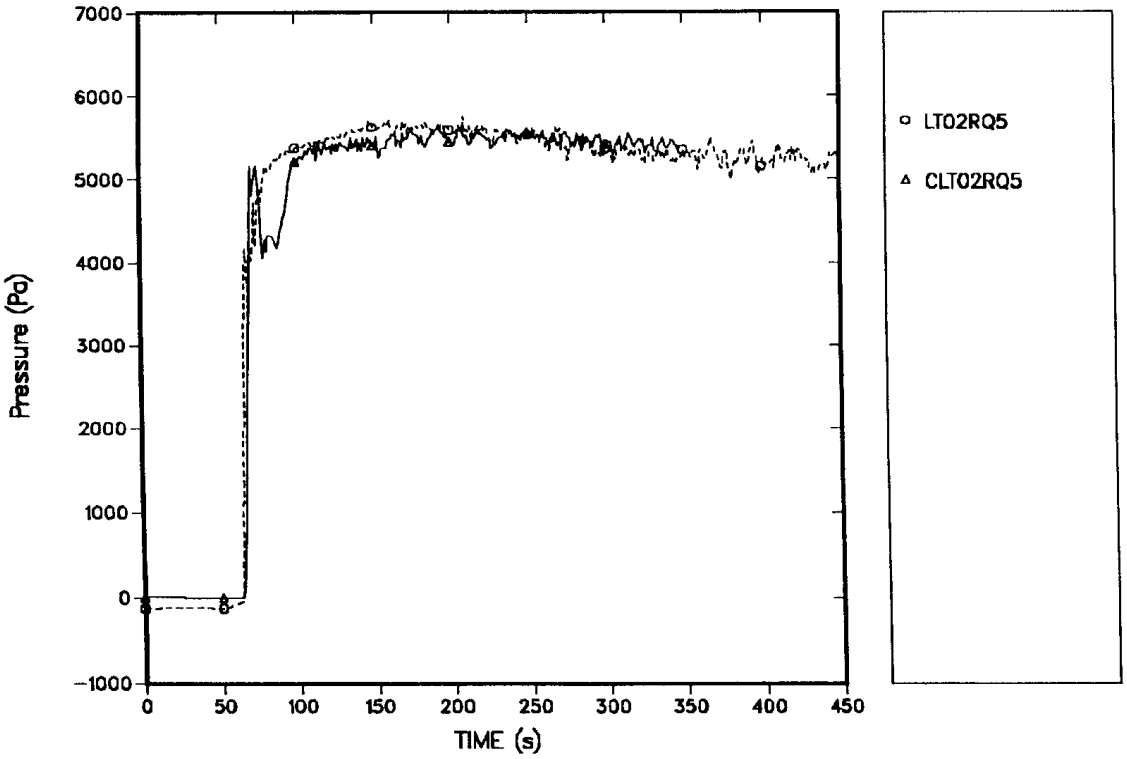

Fig. H-23. The predicted (solid) and measured (dashed) pressure-drop traces between axial elevations of 0–0.61 m.

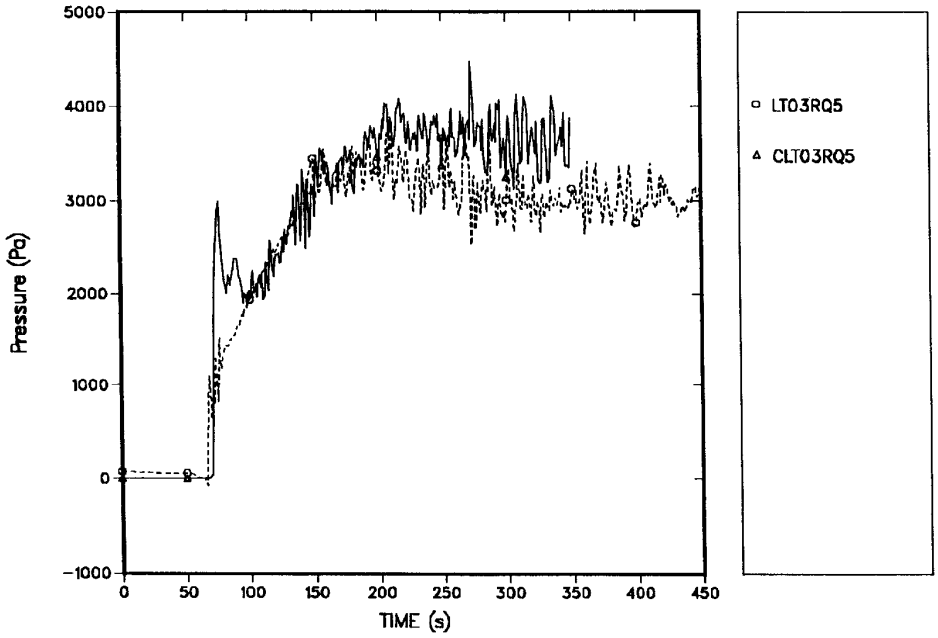

Fig. H-24. The predicted (solid) and measured (dashed) pressure-drop traces between axial elevations of 0.61–1.22 m.

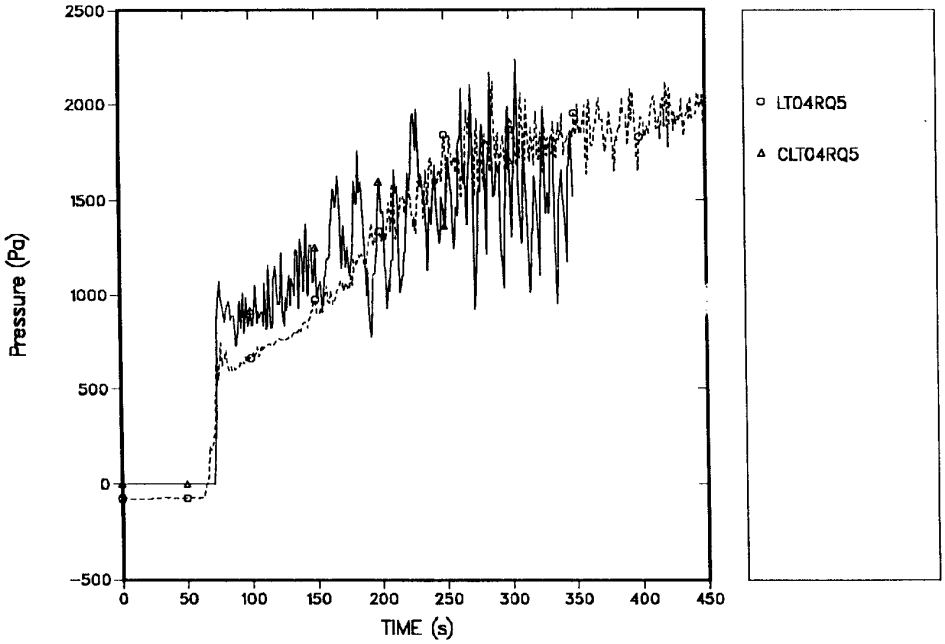

Fig. H-25. The predicted (solid) and measured (dashed) pressure-drop traces between axial elevations of 1.22–1.83 m.

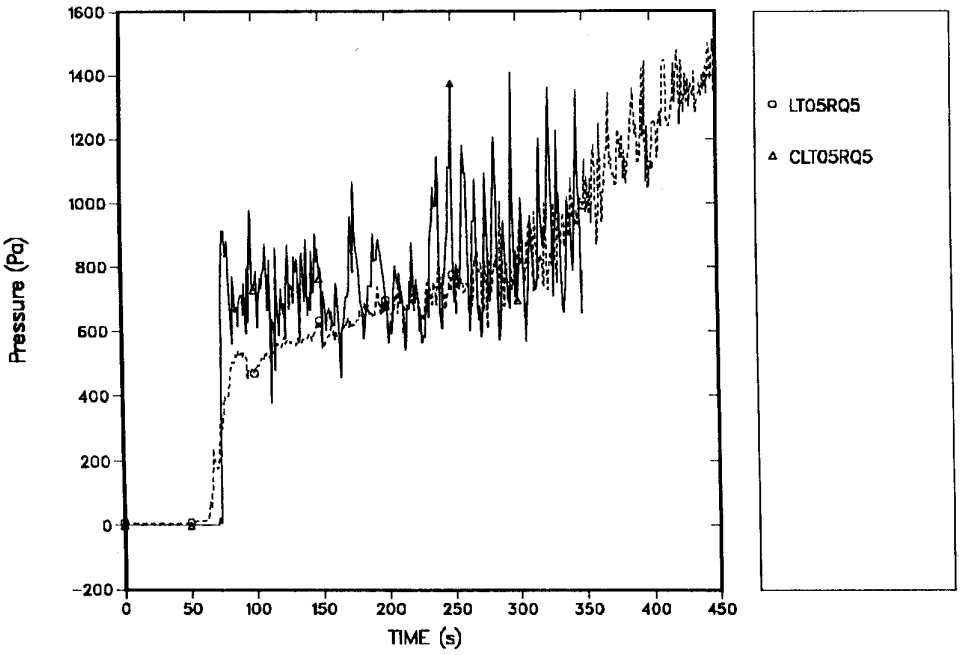

Fig. H-26. The predicted (solid) and measured (dashed) pressure-drop traces between axial elevations of 1.83–2.44 m.

H.1.5.9. Conclusion. The reflooding of a hot reactor core produces a quench front that passes through the core as the rods cool. Below the quench, subcooled boiling exists, and above the quench, regions of smooth inverted annular flow, rough-wavy flow, agitated flow, and dispersed flow exist. Transition correlations and visual images for each region above the quench are taken from the literature. Models are developed for the interfacial drag in each region for application to the two-fluid approximation. Order-of-magnitude analyses show that the various models provide values for the interfacial drag that are in the correct range.

In the subcooled-boiling region, a roughened pipe approach is recommended. Arguments are put forth to use the vapor as the continuous phase in this regime. In the smooth inverted annular region, smooth-tube correlations are used. In the rough-wavy region, the modified Wallis correlation is used. In the agitated region, for lack of correlations from the literature and details on the characteristics, it is recommended to use the models developed for the rough-wavy region. In the dispersed region, there is the possibility for a significant amount of liquid to exist as liquid film on the unheated surfaces. Thus, a method similar to that developed for annular-mist flow is recommended. To combine all the regions into a finite-difference scheme, we propose to use a length-weighted average of the components that exist within a given mesh. The coefficients used in the model for the drag coefficients and their weightings were obtained by fitting the CCTF Run-14 pressure-drop data. The comparison of the

calculated and predicted overall pressure drops at various elevations shows reasonable agreement when the overall model is used.

H.1.6. Process Models

In TRAC the interfacial-drag calculation is overridden for the case in which the user invokes the phase-separation logic or the accumulator logic. These two cases are described below.

H.1.6.1. Phase-Separation Option in 1D Components. The user invokes this option at any 1D component cell edge by setting the variable FRIC to a number greater than 10×10^{20} or less than -10×10^{20}. In the case where directional loss coefficients are input (variable NFRC1 is set to 2 in the NAMELIST input), then both values of FRIC must pass this test. If this test is passed, then the interfacial-drag coefficient is set to 0.0 to allow phase separation. Additionally, the code sets the liquid velocity at the interface to 0.

H.1.6.2. Accumulator Option. The user invokes this option by using a PIPE component in conjunction with the variable IACC = 1 or 2. IACC = 1 invokes an interface sharpener, which sets the interfacial drag to zero at user-selected cell internal interfaces. IACC = 2 invokes both a liquid separator model at the bottom of the PIPE and the interface sharpener. The separator model operates by manipulation of the FRIC array (i.e., the additive friction factor, which affects the phasic momentum solutions, but is not part of the interfacial logic per se), as described in Appendix J, Section J.7.

H.1.7. Conclusions Regarding Interfacial Drag

The correlations used to predict the interfacial-drag force in TRAC have been fully described. Many changes have been made since MOD1 has been released. These changes represent a significant improvement and are the result of the detailed assessment efforts that occurred in the 2D/3D, MIST, and ICAP programs associated with USNRC research. The assessments have been very beneficial because of the many recommendations that have been incorporated. The primary improvements were in the calculation of the bubble diameter (elimination of the Weber number criterion), the implementation of the profile slip effect, the addition of a realistic model for annular-mist flow, the addition of an inverted-flow regime for core reflood, the addition of stratified flow to the vessel, consistency with the interfacial heat transfer, and general code clean-up.

We believe that the current models are up to date, consistent, and as realistic as possible. However, we fully expect that there will continue to be discrepancies in future assessments because of the complex nature of the two-phase approach and the dependence on the local geometry. Nevertheless, the current models represent the best available data at this time and should provide a firm basis for any future improvements or additions.

H.2. Wall Drag.

The TRAC computer code models the pressure gradient caused by wall drag as the sum of the wall drag acting on the gas and liquid phases. TRAC models the wall drag acting

on the gas phase as a constant of proportionality times the momentum flux in the gas phase and the wall drag acting on the liquid phase as a constant of proportionality times the momentum flux in the liquid phase. This section will describe the TRAC wall-drag models for single-phase laminar and turbulent 1D flow, for two-phase vertical and horizontal-nonstratified 1D flow, for two-phase horizontal-stratified 1D flow, for single-phase laminar and turbulent 3D flow, and for two-phase 3D flow.

H.2.1. 1D Models

The TRAC-calculated pressure gradient caused by wall drag for two-phase 1D flow is given by the sum of the gas- and liquid-phase wall-drag terms

$$\left(\frac{dp}{dz}\right)_f = -c_{wg}\left|V_g\right|V_g - c_{w\ell}\left|V_\ell\right|V_\ell \quad , \tag{H-156}$$

where

$$c_{wg} = \frac{\alpha_g \rho_g c_{fg}}{D_h} \quad , \tag{H-157}$$

$$c_{w\ell} = \frac{\alpha_\ell \rho_\ell c_{f\ell}}{D_h} \quad , \tag{H-158}$$

c_{fg} and $c_{f\ell}$ are the gas and liquid friction factors, α_g is the void fraction associated with the gas phase, and α_ℓ is the liquid fraction ($\alpha_\ell = 1 - \alpha_g$). From these equations, it can be seen that the constant of proportionality is c_{fg}/D_h for the gas phase and that the momentum flux for the gas phase is $\alpha_g \rho_g \mid V_g \mid V_g$. For the liquid phase, the constant of proportionality is $c_{f\ell}/D_h$ and the momentum flux is $\alpha_\ell \rho_\ell \mid V_\ell \mid V_\ell$.

As the void fraction goes to zero, Eq. (H-156) will result in the correct single-phase liquid pressure gradient caused by wall drag consistent with $c_{f\ell}$, the liquid-phase friction factor. As the void fraction goes to one, Eq. (H-156) will result in the correct single-phase gas pressure gradient caused by wall drag consistent with c_{fg}, the gas-phase friction factor. Therefore, the single-phase correlations for $c_{f\ell}$ and c_{fg} for laminar and turbulent flow will determine the single pressure gradient caused by wall shear.

For the purposes of comparison with correlations of known accuracy, the TRAC wall-drag model will be rewritten in terms of a two-phase multiplier (Ref. H-15., pp. 27-32, 49-68; Ref. H-27., Chapter-2). Division of Eq. (H-156) by the single-phase liquid wall drag flowing at the total mass flux yields the following effective two-phase multiplier for TRAC (Ref. H-15., Eq. 2.64, p. 28):

$$(\Phi^2)_{lo} = \left(\frac{\left.\frac{dp}{dz}\right|_f}{\left.\frac{dp}{dz}\right|_{flo}} \right) = \frac{\left(\alpha_g \rho_g c_{fg} \left|V_g\right| V_g + \alpha_l \rho_l c_{fl} |V_l| V_l\right)}{c_{flo} |G| G} \rho_l \quad , \tag{H-159}$$

where c_{flo} is the single-phase liquid friction-factor correlation based on a liquid mass flux of $G = \rho_m V_m$. The gas and liquid friction factors in the above equation are based on different correlations depending upon the type of flow. The different correlations for each regime will be discussed in the following sections.

NFF is the user-input parameter for selecting 1D wall-drag options. Setting NFF equal to ±1 selects the homogeneous wall-drag option. Setting NFF to zero results in constant wall friction with only the user-input values (FRIC array in input). A negative NFF results in the automatic calculation of an appropriate form loss coefficient (see Appendix I, Section I.1.) in addition to the selected two-phase-flow friction factor.

H.2.1.1. Homogeneous Model. If the user selects NFF equal to ±1, the homogeneous wall-drag model is used. This model is described below.

H.2.1.1.1. Basis for the Model. The friction-factor model for single-phase turbulent flow was chosen based on Churchill's model (Ref. H-33.),

$$f = 2 \left[\left(\frac{8}{Re} \right)^{12} + \frac{1}{(a+b)^{3/2}} \right]^{1/12} \quad , \tag{H-160}$$

where

$$a = \left[2.457 \times \ln \left(\frac{1}{\left(\frac{7}{Re} \right)^{0.9} + \frac{0.27\varepsilon}{D_h}} \right) \right]^{16} \tag{H-161}$$

and

$$b = (37530/Re)^{16} \quad .$$

Churchill's equation represents a fit to the Moody curves, which include the laminar, transition, turbulent, smooth, and rough regimes in a single equation. The Reynolds number in the Churchill correlation is not allowed to go below 100 to prevent division by zero.

The TRAC two-fluid momentum equations result in a two-phase multiplier that includes the effect of slip without the modification for the single-phase friction factor.

The homogeneous wall-drag model alters the single-phase friction factor by using a two-phase viscosity (μ) defined in terms of the flow quality (X_f) [Ref. H-27., p. 33, Eq. (2-38)],

$$\mu = \left[\frac{X_f}{\mu_g} + \frac{(1 - X_f)}{\mu_l} \right]^{-1} \quad . \tag{H-162}$$

According to Ref. H-34., of the different methods for defining the two-phase viscosity, this method is more accurate than the methods of Owens (Ref. H-35.) or Cicchitti (Ref. H-36.), but is not as accurate as Dukler's method (Ref. H-37.). Whalley (Ref. H-38.) indicates that the standard deviation for the homogeneous wall-drag model with a two-phase viscosity based on Eq. (H-162) is ~38% for steam / water systems.

The coefficient of friction for the liquid phase is related to the Fanning friction factor by Eq. (H-163) and that for the gas phase by Eq. (H-164), such that

$$c_{fl} = 2f \text{ and} \tag{H-163}$$

$$c_{fg} = c_{fl} \, . \tag{H-164}$$

Substitution of Eqs. (H-162), (H-163), and (H-164) into Eq. (H-159) yields

$$(\Phi)^2_{lo} = \left[\frac{(1 - X_f)^2}{\alpha_l} + \frac{X_f^2 \rho_l}{\alpha_g \rho_g} \right] \left(\frac{c_f}{c_{flo}} \right) \quad . \tag{H-165}$$

From Eq. (H-165), it can be seen that the TRAC effective two-phase multiplier is not equivalent to the homogeneous two-phase multiplier as defined in Wallis [Ref. H-15., p. 29, Eq. (2-70)],

$$(\Phi)^2_H = \left[1 + X_f \left(\frac{\rho_l}{\rho_g} - 1 \right) \right] \left[1 + X_f \left(\frac{\mu_l}{\mu_g} - 1 \right) \right]^{-0.25} \quad . \tag{H-166}$$

It can be shown that if the flow is homogeneous, and if c_{fl}=c_{fg}=0.158$Re^{-0.25}$, then the TRAC homogeneous two-phase wall-drag model is equivalent to Eq. (H-166). Therefore, for slip ratios close to unity, the TRAC model will result in homogeneous two-phase multipliers consistent with Eq. (H-166).

H.2.1.1.2. Assumptions. In TRAC, the flow qualities in Eq. (H-162) are replaced with static quality to avoid discontinuities as $G \rightarrow 0$. More specifically,

$$X_f = \frac{\alpha_g \rho_g V_g}{(\alpha_g \rho_g V_g + \alpha_l \rho_l V_l)} = \frac{G_g}{G} = \frac{\alpha_g}{\alpha_g + \frac{\alpha_l}{\gamma S_r}} \tag{H-167}$$

and

$$X_s = \frac{\alpha_g \rho_g}{(\alpha_g \rho_g + \alpha_l \rho_l)} \quad , \tag{H-168}$$

where $S_r = V_g / V_l$ and $\gamma = \rho_g / \rho_l$. For slip ratios close to unity, this approximation is accurate. As the slip ratio increases, the difference between flow quality and static quality also increases.

The TRAC 1D homogeneous wall-drag model assumes that the wall drag acts on both phases, independent of whether both phases are in contact with the wall. When the liquid phase is in contact with the wall, it is assumed that some portion of the wall drag is transmitted to the gas phase. The total wall drag is apportioned between the liquid and the gas phases, based on the momentum flux in each phase.

H.2.1.1.3. Model as Coded. The homogeneous 1D wall-drag model is coded in subroutine FWALL, as described by Eqs. (H-160) through (H-164), except that the flow quality in Eq. (H-162) is replaced by the static quality, defined by Eq. (H-168). The quality is calculated in FWALL using

$$X = \frac{1}{1 + \frac{(1-\alpha_g)\rho_l}{\alpha_g \rho_g S_r}} \quad , \tag{H-169}$$

with $S_r = 1$.

H.2.1.1.4. Weighting, Magnitude Limits, Rate Limits, and Averaging. The void fractions, densities, and viscosities used in the wall-drag correlations are volume-averaged. The momentum cell in TRAC is from cell center to cell center. The TRAC-calculated velocities are defined to be cell-edge quantities and the user-input hydraulic diameter is a cell-edge quantity. However, the TRAC-calculated fluid properties such as density, void fraction, and viscosity are cell-center quantities. The approach used in FWALL to obtain cell-edge quantities for the void fraction, density, and viscosity is to calculate a volume-average quantity using

$$\xi_{j+1/2} = \frac{\xi_j \mathrm{vol}_j + \xi_{j+1} \mathrm{vol}_{j+1}}{\mathrm{vol}_j + \mathrm{vol}_{j+1}} \quad , \tag{H-170}$$

where ξ can be any cell-center fluid property. This process yields an averaged fluid property for the TRAC momentum cell.

FWALL also sets the calculated quality to zero when the volume-averaged void fraction is less than 0.001. This eliminates any divisions by zero in Eq. (H-169).

FWALL calculates the mass flux to be used in the calculation of the Reynolds number as the product of the volume-averaged mixture density and the absolute value of the two-phase mixture velocity. The absolute value of the mixture velocity is used to ensure that the Reynolds number is always positive. The mixture velocity is calculated in the PREPER routine with the following equation:

$$V_{mj+1/2} = \frac{\langle \alpha_g \rho_g V_g \rangle_{j+1/2} + \langle \alpha_l \rho_l V_l \rangle_{j+1/2}}{\rho_{mj+1/2}} \quad . \tag{H-171}$$

In this expression, $\rho_{mj+1/2}$ is the donor-cell two-phase mixture density and $\langle \xi V \rangle_{j+1/2}$ is the donor-cell operator given by

$$\begin{aligned} \langle \xi V \rangle_{j+1/2} &= \xi_j V_{j+1/2} \quad \text{if} \quad V_{j+1/2} \geq 0 \\ &= \xi_{j+1} V_{j+1/2} \quad \text{if} \quad V_{j+1/2} < 0 \quad . \end{aligned} \tag{H-172}$$

H.2.1.1.5. Assessment. The Churchill equation fits the Moody curves over the full range of the Moody curves. The Churchill equation includes the roughness effect and the laminar-flow regime.

To evaluate the TRAC effective homogeneous two-phase multiplier at a given pressure, mass flux, and void fraction, the relative velocity or slip ratio must be known. For all the comparisons to be made in this section of the report, the relative velocity at a given pressure, mass flux, and void fraction was determined by solving simultaneously the steady-state TRAC momentum equations and interfacial-shear model. Typical results for the calculated relative velocity based on the TRAC models are given in Figs. H-27. and H-28. These figures show two extreme hydrodynamic conditions: one at high pressure, high mass flux, and small hydraulic diameter, which all tend to reduce the TRAC-based relative velocity; the other at low pressure, low mass flux, and large hydraulic diameter, which all tend to increase the TRAC-based relative velocity. The hydraulic-diameter range spans the expected hydraulic diameters in a full-size four-loop Westinghouse plant. The pressure range spans the expected range of pressures for two-phase flow during a large-break LOCA in a Westinghouse four-loop plant. The high mass flux is approximately equal to the cold-leg and hot-leg steady-state mass flux for a Westinghouse four-loop plant, and the low mass flux was chosen so that the resulting phase velocities remained co-current.

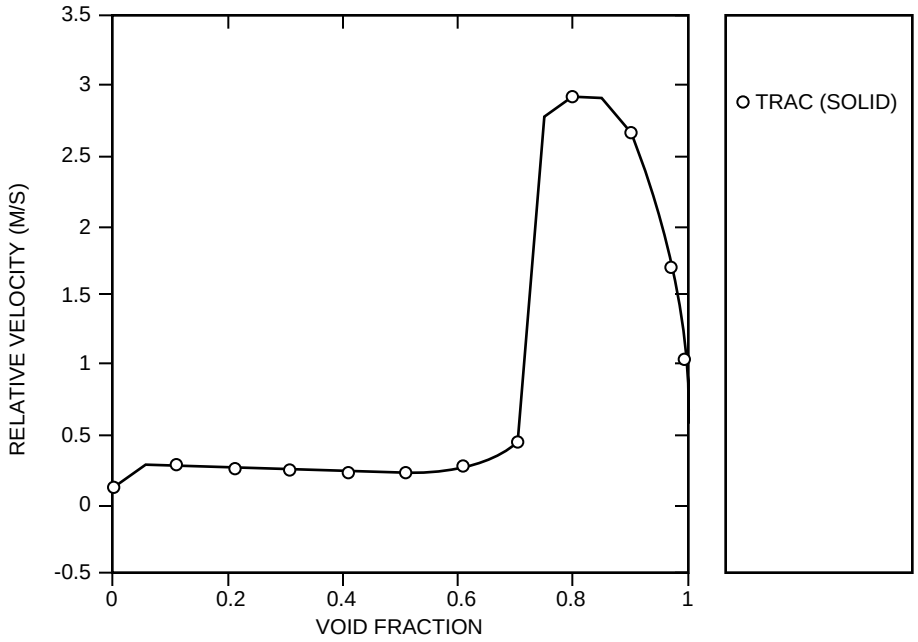

Fig. H-27. TRAC-calculated relative velocity for p = 7.0 MPa, D_h = 0.011 m, and G = 10000 kg· m^{-2}· s^{-1}.

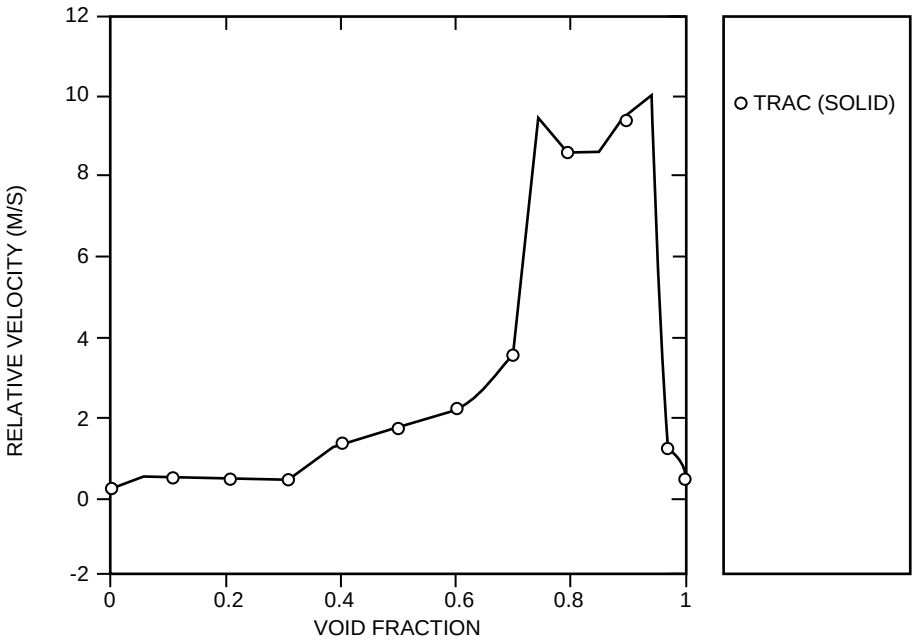

Fig. H-28. TRAC-calculated relative velocity for p = 0.10 MPa, D_h = 0.7 m, and G = 1000 kg· m^{-2}· s^{-1}.

Figure H-29. is a comparison of the TRAC homogeneous two-phase multiplier [Eq. (H-165)] evaluated with the two-phase viscosity static quality and flow quality. As can be seen from this figure, the approximation of using the static quality in place of the flow quality to determine the two-phase viscosity has no significant impact. Figures H-30. and H-31. compare the TRAC homogeneous two-phase multiplier with the Heat-Transfer Fluid Flow Service (HTFS) (Ref. H-38.) two-phase multiplier. As can be seen from these comparisons at low void fraction and high void fraction, both models tend to the same limits. For high slip ratios, the HTFS model tends to yield higher two-phase multipliers than does the TRAC homogeneous two-phase multiplier. The HTFS correlation (Ref. H-38.) is reported to have an uncertainty of ±19% for vertical flows and ±51% for horizontal flows. Also, according to Whatley, the homogeneous multiplier (using a two-phase viscosity) as defined by Eq. (H-166) has an uncertainty of ±40% for vertical steam / water flow and an uncertainty of ±55% for horizontal steam / water flow. These uncertainties are based on a 95% confidence level. As compared to the HTFS model, the root mean square (RMS) error of the TRAC homogeneous two-phase multiplier model is 0.21, based on 4992 points over the range of hydrodynamic conditions given in Table H-4.

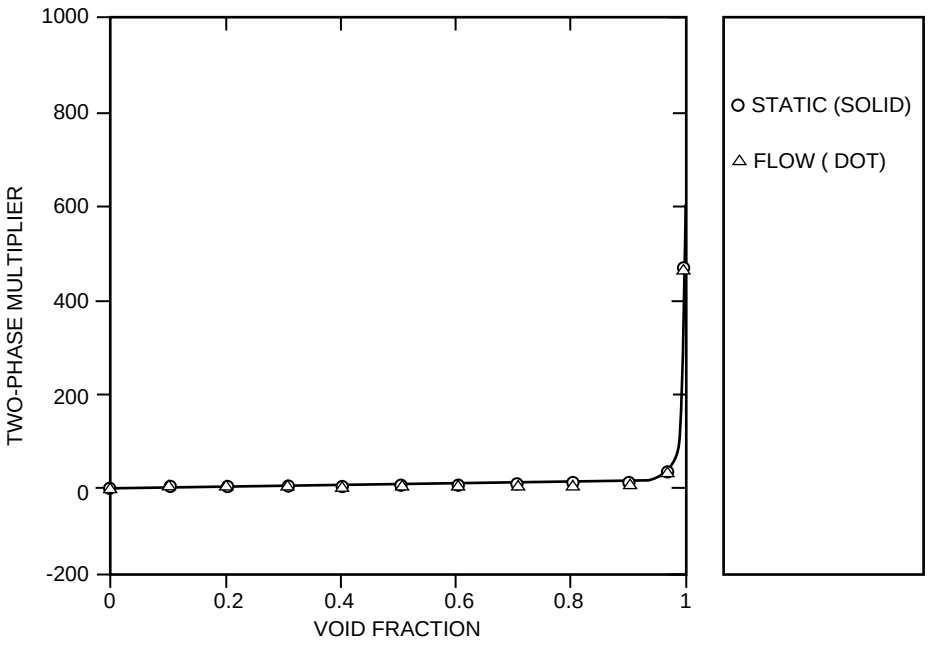

Fig. H-29. Comparison of two-phase multipliers, static vs. flow quality, for p = 0.10 MPa, D_h = 0.7 m, and G = 1000 kg· m^{-2}· s^{-1}.

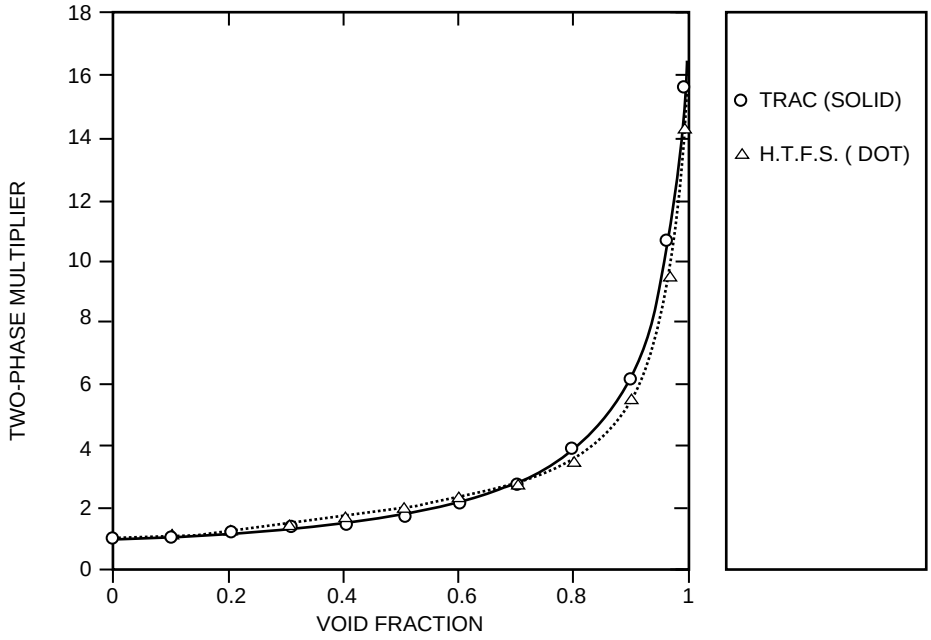

Fig. H-30. Comparison of two-phase multipliers, static vs. flow quality, for p = 7.0 MPa, D_h = 0.011 m, and G = 10 000 kg· m^{-2}· s^{-1}.

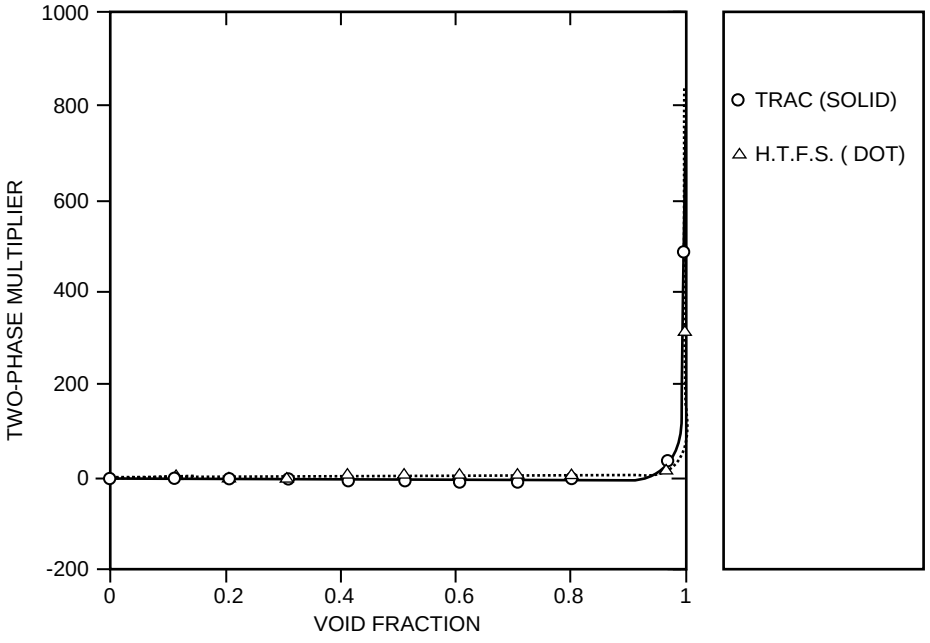

Fig. H-31. Comparison of two-phase multipliers for p = 0.10 MPa, D_h = 0.7 m, and G = 1000 kg· m^{-2}· s^{-1}.

TABLE H-4.
Range of Comparison Between TRAC Homogeneous Model and HTFS Correlation

Parameter	Maximum	Minimum
Mass Flux ($kg \cdot m^{-2} \cdot s^{-1}$)	10000.0	1000.0
Flow Quality	1.0	0.0
Tube Diameter (m)	0.7	0.011
Pressure (MPa)	7.0	0.10

H.2.1.1.6. Application Outside the Original Database. The TRAC homogeneous wall-drag model has no original database; however, comparisons to the HTFS correlation and the homogeneous model defined by Eq. (H-159) indicate that the model has an uncertainty of ±40% to ±50% over the range of the experimental data that formed the basis for the HTFS correlation, which is given in Table H-5. All the normal operating conditions and most of the abnormal conditions that would occur during a LOCA are covered in the database, with the exception of countercurrent flow. For countercurrent flow, it is not obvious which approach would be more accurate; however, the dominant phenomenon during countercurrent flow tends to be interfacial shear, not wall shear.

TABLE H-5.
Range of HTFS Data

Parameter	Maximum	Minimum
Mass Flux ($kg \cdot m^{-2} \cdot s^{-1}$)	24990.0	1.7
Flow Quality	1.0	0.0
Tube Diameter (m)	0.305	0.001
Pressure (MPa)	197.6	0.088
Roughness (ε / D)	0.068	0.0
~19000 total data points 28% of the data points were steam / water 43% of the data points were air / water 29% of the data points were fluids systems 44% of the data points were horizontal flow 31% of the data points were vertical flow 25% of the data points were inclined flow		

Eq. (H-160) is an accurate fit of the Moody Curves over a wide range of conditions. This equation includes laminar, turbulent, and rough wall effects. It is anticipated that no significant error will be introduced by using Eq. (H-160) for light-water-reactor applications. It has been observed, however, that the Churchill model is inaccurate for narrow annuli.

H.2.1.1.7. Scaling. The TRAC 1D wall-shear model is a function of Re, X_f, and S_f, all of which are nondimensional parameters that generally are accepted as independent of scale. It is also important to note that the wall shear is less important for a full-size plant (volume/surface area effect) than for the assessed experiments in which satisfactory overall answers have been obtained. As the scale increases, the importance of wall shear decreases. Inspection of the wall-shear term in the momentum equations reveals that it has a $D^{-1.2}$ dependence. The effect of this dependence on D can be illustrated by comparing the wall-shear pressure gradient for a full-size plant cold leg, for a LOFT cold leg, and for a semiscale cold leg. From Table H-6. it can be seen that the LOFT wall-shear pressure gradient in the cold leg is about three times larger than the full-size plant wall-shear pressure gradient for the same hydrodynamic conditions. The semiscale wall-shear pressure gradient in the cold leg is ~17 times larger than the full-size plant wall-shear pressure gradient for the same hydrodynamic conditions. No other term in the fluid momentum equations contains this inverse diameter effect (except for the interfacial drag during pure annular flow); therefore, as scale increases, the relative magnitude of the wall-shear term decreases. TRAC has successfully simulated both large and small breaks in both the LOFT and semiscale facilities. These subscale simulations with TRAC indicate that the wall shear is adequate for full-size plants if the flow-regime assumptions scale.

TABLE H-6.
Wall Shear Dependence Upon Pipe Diameter
for $g = 10^4$ kg · m^{-2} · s^{-1}, p = 15.8 MPa, T = 551.4 K)

Facility	Cold-leg D (m)	Wall Shear Pressure Gradient (Pa · m^{-1})
Full-Size Plant	0.698	446.0
LOFT	0.284	1353.0
Semiscale	0.067	7635.0

H.2.1.1.8. Summary and Conclusions. For the simulation of a typical four-loop Westinghouse plant, the total steady-state pressure loss against which the pump has to work (which is the total irrecoverable loss around a single loop and through the vessel) is ~0.6 MPa. Approximately 35% of the total loss is due to wall-friction effects. Of the pressure drop that is due to wall-friction effects, ~80% of the wall-friction pressure drop in a full-scale plant is a result of the steam-generator tubes. For plant calculations, most of the pressure drop around a loop is due to irrecoverable pressure losses at bends, flow-area changes, flow-direction changes, orifice plates, and spacers. Therefore, when modeling a plant, code users typically will simulate these irrecoverable losses by inputting additive pressure-loss factors or allowing the code to calculate the irrecoverable loss. These factors are adjusted until the user obtains the correct steady-state pressure loss around the loop at the correct loop flow rate with the correct pump speed. In addition, the user verifies that the flow splits are correct, which indicates that the flow resistances along parallel flow paths are modeled correctly. For large-break and small-break LOCAs, the transient response of the system is determined primarily by the break-flow rate (which is not dependent upon wall shear), the core and steam-generator heat-transfer rates, the gravitational heads, and the actions of all the boundary-condition systems (e.g., ECCS, secondary-side systems, etc.). The flows through the loops tend to be determined by the user-input additive losses, abrupt area-change losses, and changes in momentum fluxes. The wall-shear losses tend to be of minor importance once the transient starts. This is especially true as the flow rates drop off. The TRAC wall-drag model is accurate over a wide range of Reynolds flow. Therefore, the TRAC wall-drag model is adequate for full-scale plant calculations.

H.2.1.2. Horizontal Wall-Drag Model. A horizontal 1D interface is defined to be a 1D interface for which the angle of inclination above or below the horizon is less than 10 degrees for liquid upflow and up to 90 degrees for liquid downflow. Stratified horizontal flow occurs when the phase velocities fall below twice the critical velocity, V_c. The critical velocity for transition between stratified and dispersed or plug flow is given in Appendix E of this manual. The calculation of the wall drag for this model is described below.

H.2.1.2.1. Basis for the Model. The horizontal stratified-flow wall-shear model is based on the assumption that the wall shear for each phase can be determined by assuming smooth-pipe wall-shear models for each phase. The local-phase velocity and the hydraulic diameter based on the local-phase flow area and wetted perimeter are used to determine the phase-dependent Reynolds number. This approach for the wall shear for horizontal stratified two-phase flow is based on Ref. H-39.

The horizontal 1D wall-shear coefficients are calculated from a Blasius-like relation using Reynolds numbers based on the velocities for each phase as given below:

$$Re_g = \max\left(100, \frac{\rho_g |V_g| D_g}{\mu_g}\right) \tag{H-173}$$

and

$$Re_l = \max\left(100, \frac{\rho_l |V_l| D_l}{\mu_l}\right) \quad , \tag{H-174}$$

where D_l and D_g are the hydraulic diameters based on the flow area and wetted perimeter for each phase, which are based on the height of the collapsed liquid level in the horizontal pipe. The stratified-flow wall-shear coefficients to be used in Eq. (H-156) are

$$c_{hwg} = \frac{2\alpha_g \rho_g 0.046 (Re_g)^{-0.2}}{D_g} \tag{H-175}$$

and

$$c_{hwl} = \frac{2\alpha_l \rho_l 0.046 (Re_l)^{-0.2}}{D_l} \quad . \tag{H-176}$$

This model is equivalent to the model recommended by Dukler in Ref. H-39. for the turbulent-flow regime. For laminar flow in either or both of the phases, Dukler recommends using the laminar-flow friction model given by

$$f = \frac{16}{Re} \quad . \tag{H-177}$$

H.2.1.2.2. Assumptions. For Re_p (where p may be g or l) below 1502, the Blasius-like friction-factor correlations in Eqs. (H-175) and (H-176) are replaced by the laminar-flow correlation given by Eq. (H-177). The total two-phase wall drag is assumed to be the sum of wall drag for both phases based on single-phase correlations evaluated with the appropriate phase velocities and hydraulic diameters. This model assumes a circular pipe geometry.

H.2.1.2.3. Constants. This model uses a Reynolds number of 1502 for laminar-to-turbulent-flow transitions.

H.2.1.2.4. Model as Coded. Interpolation between the nonstratified 1D wall-shear model defined in Sections H.2.1.1. and H.2.1.2. and the horizontal stratified wall-shear model is based on the stratified-flow-model transition logic described in Appendix E.

The interpolation function is used in the following manner:

$$c_{wg} = (WF) c_{hwg} + (1 - WF) c_{vwg} \tag{H-178}$$

and

$$c_{wl} = (WF)c_{hwl} + (1 - WF)c_{vwl} \quad , \tag{H-179}$$

where c_{wl} and c_{wg} are the coefficients to be used in Eq. (H-156), c_{hwl} and c_{hwg} are the horizontal 1D wall-shear coefficients, and c_{vwl} and c_{vwg} are the nonstratified 1D wall-shear coefficients.

H.2.1.2.5. Weighting, Magnitude Limits, Rate Limits, and Averaging. The densities and void fractions used in the horizontal stratified-flow wall-drag correlation are based on a length-weighted average, as described by

$$\xi_{j+1/2} = \frac{\xi_j \Delta x_j + \xi_{j+1} \Delta x_{j+1}}{\Delta x_j + \Delta x_{j+1}}, \tag{H-180}$$

where ξ can be any cell-center fluid property. This process yields an averaged fluid property for the TRAC momentum cell. This averaging equation will yield the same result as Eq. (H-170) if the volume-averaged flow area is not changing from cell j to $j + 1$. The length-weighted averaging process is appropriate for properties that appear in the wall-drag terms, since the wall drag is proportional to the cell length, not to the cell volume. The diameter used in the horizontal stratified-flow model is based on the volume-averaged flow area of the upstream and downstream hydrodynamic cells. The maximum pipe diameter between the two adjacent hydrodynamic cells is used in the wall-drag model for horizontal-stratified flow. The viscosity and surface tension are donor-cell properties, with the surface tension and the liquid-phase viscosity based on the liquid-phase flow direction and the gas-phase viscosity based on the gas-phase flow direction.

H.2.1.2.6. Assessment. The TRAC horizontal flow wall-shear model is compared to the homogeneous and HTFS models in Fig. H-32. For the conditions shown, TRAC calculated that the flow was stratified for void fractions between 10% and 90%. The comparison to the homogeneous and HTFS models is good except for void fractions between 0.8 and 0.9. In this region, TRAC predicts a larger two-phase multiplier than the other two correlations; however, the slip ratio chosen for this comparison is not appropriate for high-void stratified flow and may be the cause of the differences. At a more realistic slip ratio, the TRAC two-phase multiplier will be reduced for the high-void region.

According to Ref. H-38., the HTFS correlation has an uncertainty of ±19% for vertical two-phase flow and an uncertainty of ±51% for horizontal two-phase flow. The horizontal pipe two-phase flow pressure-drop data used to develop the HTFS correlation may have been stratified for some of the data points. Perhaps because the HTFS correlation attempts to include both stratified and nonstratified pressure-drop data in one correlation, it is much less accurate for horizontal pipes than for vertical pipes. Therefore, for horizontal stratified two-phase flow, the Dukler model (Ref. H-39.) used by TRAC may be more accurate than the HTFS model.

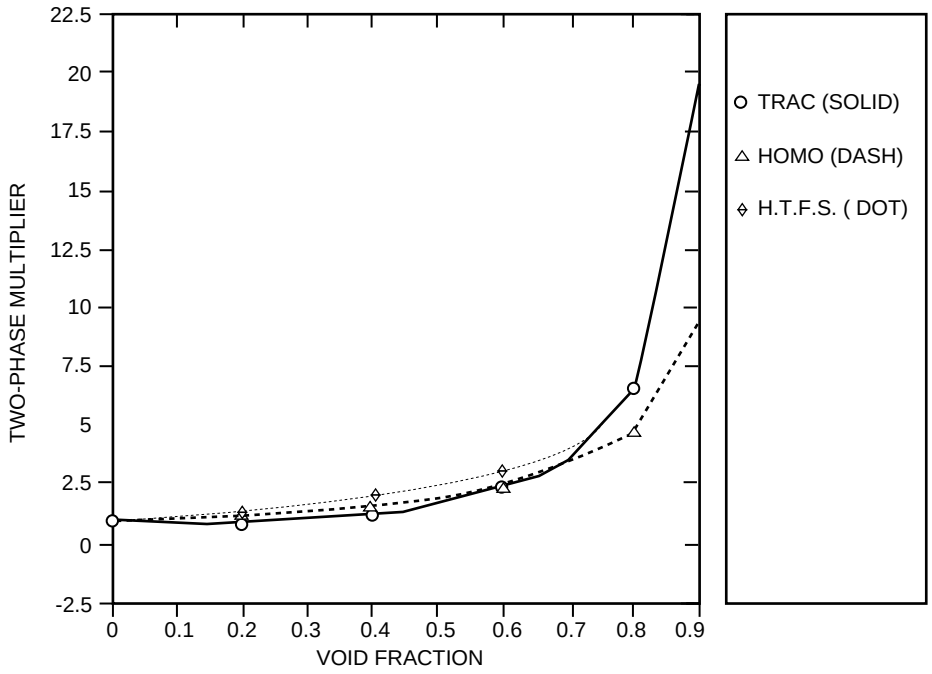

Fig. H-32. Comparison of wall drag in a horizontal pipe at p = 1.0 bar, S_r = 1.012, and G = 500 kg· m^{-2}· s^{-1}.

H.2.1.2.7. Scaling. It is anticipated that the wall-drag correlations are independent of scale. However, there is some experimental evidence that indicates that the stratified-flow transition criteria will not scale to large-diameter pipes.

H.2.1.2.8. Summary and Conclusions. If the flow regime is predicted accurately, then the stratified-flow wall-drag model will predict accurately the wall drag on each phase.

H.2.2. 3D Models

The pressure gradient caused by wall shear for the TRAC 3D hydrodynamic equations is

$$\frac{dp}{dk} = c_{wgk}\left\langle V_{gk}\right\rangle V_{gk} + c_{w\ell k}\left\langle V_{\ell k}\right\rangle V_{\ell k} \quad , \tag{H-181}$$

where k can be r, θ, or z, corresponding to the three orthogonal directions in the TRAC 3D VESSEL, and $\langle V_k \rangle$ is defined as a vector-average velocity for the k^{th} face of cell ijk. The wall-shear coefficients c_{wgk} and $c_{w\ell k}$ are defined the same way as in Eqs. (H-157) and (H-158),

$$c_{wgk} = \frac{\alpha_g \rho_g c_{fgk}}{D_{hk}} \tag{H-182}$$

and

$$c_{w\ell k} = \frac{\alpha_\ell \rho_\ell c_{f\ell k}}{D_{hk}} \quad . \tag{H-183}$$

As the void fraction goes to zero, Eq. (H-183) will result in the appropriate equations for the single-phase liquid wall drag based upon the $c_{f\ell k}$ coefficient. As the void fraction goes to one, Eq. (H-182) will result in the appropriate equations for the single-phase gas wall drag based upon the c_{fgk} coefficient. The following sections will address the correlations and models used to calculate α_ℓ, $c_{f\ell k}$, α_g, c_{fgk}, $\langle V_{gk} \rangle$, and $\langle V_{\ell k} \rangle$.

H.2.2.1. Basis for the Models. The laminar- and turbulent-flow friction-factor correlations for the 3D wall-drag model are based on the same references and databases as Eqs. (H-160) and (H-161) in the 1D homogeneous model.

The 3D model used the same mixture viscosity equation as defined in the 1D wall-shear-model description [Eq. (H-162)]. The flow quality used in the mixture viscosity equation is replaced with the static quality as in the 1D wall-shear model.

The Reynolds number in Eqs. (H-160) and (H-161) can be written as

$$Re_k = \frac{G_k D_{hk}}{\mu} \quad , \tag{H-184}$$

where μ is the two-phase viscosity [see Eq. (H-162)], which goes to the appropriate single-phase viscosity when the void fraction is zero or one.

H.2.2.2. Assumptions. The static quality, rather than the flow quality, is used to calculate the two-phase viscosity. The flow-regime assumptions are the same as in the 1D homogeneous model.

H.2.2.3. Model as Coded. The 3D wall drag is evaluated in the WDRAG routine and the equations given above and below are evaluated as described.

H.2.2.4. Weighting, Magnitude Limits, Rate Limits, and Averaging. The vector-average velocity used in the above equations can be written as

$$\langle V_z \rangle = 0.5 \left\{ \left[2V_{zijk} \right]^2 + \left[V_{rijk} + V_{r(i-1)jk} \right]^2 + \left[V_{\theta ijk} + V_{\theta i(j-1)k} \right]^2 \right\}^{0.5} \quad , \tag{H-185}$$

where V_{zijk} is the velocity in the axial direction at the z face of the ijk cell, V_{rijk} is the velocity in the radial direction at the radial face of the ijk cell, etc. The velocities used in Eq. (H-185) can be either the gas- or liquid-phase velocities.

The mass flux used in Eq. (H-184) can be written as

$$G_k = \alpha_g \rho_g \left\langle V_{gk} \right\rangle^* + \alpha_l \rho_l \left\langle V_{lk} \right\rangle^* \quad . \tag{H-186}$$

The vector-average velocities used in Eq. (H-186) are given by

$$\left\langle V_z \right\rangle^* = 0.5 \left\{ \left[2A_{zijk} V_{zijk} \,/\, A_{ijk} \right]^2 + \left[V_{rijk} + V_{r(i-1)jk} \right]^2 + \left[V_{\theta ijk} + V_{\theta i(j-1)k} \right]^2 \right\}^{0.5} \quad . \tag{H-187}$$

The vector-average velocity defined in Eq. (H-187) and used in Eq. (H-186) is the same as the vector-average velocity defined in Eq. (H-185), except for the ratio of *z*-face flow area A_{zijk} to volume-averaged flow area A_{ijk} that is applied to the axial-direction component of the velocity. This ratio is an attempt to relate the cell-edge velocity to the volume-average velocity. In situations in which a local flow-area restriction occurs at the *z* face of the *ijk* cell (e.g., an orifice), the wall shear should be based on the volume-average velocity rather than on the cell-edge velocity. The θ-face average vector velocity is defined by equations similar to Eqs. (H-185) and (H-187). However, the radial-face average vector velocity is set equal to the axial-face average vector velocity for the wall-shear calculation to save computational time.

H.2.2.5. Assessment. For 3D flow, the approximations for the vector-average velocities at each of the three faces for cell *ijk* are reasonable. However, a more accurate approximation to the averaged vector velocity at face *z* of cell *ijk* is

$$\begin{aligned} \left\langle V_{ijk} \right\rangle = \Bigg[& \left\{ \left[V_{zijk} A_{zijk} + V_{zij(k-1)} A_{zij(k-1)} \right]^2 + \left[V_{rijk} A_{rijk} + V_{r(i-1)jk} A_{r(i-1)jk} \right]^2 \right. \\ & \left. + \left[V_{\theta ijk} A_{\theta ijk} + V_{\theta i(j-1)k} A_{\theta i(j-1)k} \right]^2 \right\}^{0.5} \Bigg] \Big/ \left[2A_{ijk} \right] \quad , \end{aligned} \tag{H-188}$$

and

$$\left\langle V_z \right\rangle = \frac{\left\langle V_{ijk} \right\rangle A_{ijk} + \left\langle V_{ij(k+1)} \right\rangle A_{ij(k+1)}}{A_{ijk} + A_{ij(k+1)}} \quad . \tag{H-189}$$

Equation (H-188) results in an accurate estimation of the volume-averaged vector velocity for cell *ijk*, while Eq. (H-189) averages the cell *ijk* volume-averaged vector velocity with the cell *ij(k* + 1) volume-averaged vector velocity to obtain the average vector velocity with the *z* face of the *ijk* cell. The average vector velocity at the *r* and θ faces for the *ijk* cell can be written as

$$\langle V_r \rangle = \frac{\langle V_{ijk} \rangle A_{ijk} + \langle V_{(i+1)jk} \rangle A_{(i+1)jk}}{A_{ijk} + A_{(i+1)jk}} \tag{H-190}$$

and

$$\langle V_\theta \rangle = \frac{\langle V_{ijk} \rangle A_{ijk} + \langle V_{i(j+1)k} \rangle A_{i(j+1)k}}{A_{ijk} + A_{i(j+1)k}} \quad . \tag{H-191}$$

The additional accuracy obtained by using Eqs. (H-188) through (H-191) in the 3D wall-shear model is dependent upon the local geometry.

The approximations for the vector-average velocity have a negligible effect on the overall results. This is demonstrated by the following example that used typical geometry for a full-size plant with representative velocities that would occur at steady-state full-power operating conditions. The location in the VESSEL at which the largest difference in cell-average flow areas and cell-face flow areas occurs is at the core inlet location between the lower plenum and the first cell in the core region. At this location with the assumed operating conditions, Eq. (H-185) predicts a vector-average velocity of 3.51 $m \cdot s^{-1}$, while Eq. (H-189) predicts a vector-average velocity of 3.97 $m \cdot s^{-1}$. For this typical Westinghouse four-loop plant, the wall shear is ~18% of the total core pressure drop; therefore this represents ~2% error in the total core pressure-drop calculation. The user will typically adjust the user-input loss factors to account for this error.

According to Ref. H-38., the homogeneous multiplier using the mixture viscosity as defined in the 1D wall-shear model description and used in the 3D wall-shear model has an uncertainty of ±40% for vertical steam / water flow and an uncertainty of ±55% for horizontal steam / water flow. These uncertainties are based on a 95% confidence level.

REFERENCES

H-1. M. Ishii and T. C. Chawla, “Local Drag Laws in Dispersed Two-Phase Flow,” Argonne National Laboratory report ANL-79-105 (NUREG / CR-1230) (December 1979).

H-2. M. Ishii, Letter to R. Nelson, Los Alamos National Laboratory (July 1987).

H-3. R. B. Bird, W. E. Stewart, and E. N. Lightfoot, *Transport Phenomena* (John Wiley and Sons, New York, 1960), pp. 190-195.

H-4. L. Shiller and A. Z. Nauman, *Ver. Deut. Ing.* **77,** 318-320 (1933).

H-5. M. Ishii, “One-Dimensional Drift-Flux Model and Constitutive Equations for Relative Motion Between Phases in Various Two-Phase Flow Regimes,” Argonne National Laboratory Report ANL-77-47 (1977).

H-6. I. Kataoka and M. Ishii, “Drift Flux Model for Large Diameter Pipe and New Correlation for Pool Void Reaction,” *Int. J. Heat Mass Transfer* **30,** 1927-1939 (1987).

H-7. J. R. Grace, T. Wairegi, and J. Brophy, “Break-up of Drops and Bubbles in Stagnant Media,” *Can. J. Chem. Eng* **56,** 3-8 (1978).

H-8. J. Kitscha and G. Kocamustafaogullari, “Break-up Criteria for Fluid Particles,” *Int. J. Multiphase Flow* **15,** 573-588 (1989).

H-9. G. W. Govier and K. Aziz, *The Flow of Complex Mixtures in Pipes* (Von Nostrand Reinhold, New York, 1972).

H-10. R. Clift, J. R. Grace, and M. E. Weber, *Bubbles, Drops and Particles* (Academic Press, New York, 1978), pp. 110-111.

H-11. B. Chexal and G. Lellouche, “A Full-Range Drift-Flux Correlation for Vertical Flows (Rev. 1),” EPRI report NP-3939-SR, Rev. 1 (September 1986).

H-12. J. Anderson and C. Chu, “BWR Refill-Reflood Program Constitutive Correlations for Shear and Heat Transfer for the BWR Version of TRAC,” EPRI report NP-1582 (NUREG/CR-2134) (January 1983).

H-13. B. Chexal, J. Horowitz, and G. Lellouche, “An Assessment of Eight Void-Fraction Models for Vertical Flows,” EPRI report NSAC-107 (December 1986).

H-14. Wilson, J. F. Grenda, R. J., and Patterson, J. F., “Steam Volume Fraction in a Bubbling Two Phase Mixture,” Trans ANS, Nov. 1961.

H-15. G. B. Wallis, *One Dimensional Two Phase Flow* (McGraw-Hill Book Company, New York, 1969).

H-16. I. Kataoka and M. Ishii, “Mechanism-1 and Correlation of Droplet Entrainment and Deposition in Annular Two-phase Flow,” Argonne National Laboratory report ANL82-44 (NUREG/CR-2885) (1982).

H-17. M. Ishii and K. Mishima, “Two Fluid Model and Hydrodynamic Constitutive Relations,” *Nucl. Eng. and Design*, **82,** 107-126 (1984).

H-18. I. Kataoka, M. Ishii, and K. Mishima, “Generation and Size Distribution of Droplet in Annular Two-Phase Flow,” Transactions of the ASME, Vol. 105, pp. 230-238 (June 1983).

H-19. L. M. Hossfeld and D. Barathan, “Interfacial Friction in Co-current Upward Annular Flow,” Electric Power Research Institute report EPRI NP-2326, Research Project 443-2 (March 1982).

H-20. Y. Taitel and A. E. Dukler, “A Model for Predicting Flow Regime Transitions in Horizontal and Near Horizontal Gas-Liquid Flow,” *AlChE J.* **22**(1), 47-55 (1976).

H-21. A. Ohnuki, H. Adachi, and Y. Murao, “Scale Effects on Countercurrent Gas-Liquid Flow in Horizontal Tube Connected to Inclined Riser,” in the ANS 1987 National Heat Transfer Conference (Pittsburgh, Pennsylvania, August 9-12, 1987), pp. 40-49.

H-22. H. J Kim, “Heat Transfer and Interfacial Drag in Countercurrent Steam-Water Stratified Flow,” *Int. J. Multiphase Flow,* **11**(5), 593-606 (1985).

H-23. J. H. Linehan, “The Interaction of Two-Dimensional Stratified, Turbulent Air-Water and Steam-Water Flows,” Ph.D. dissertation, Department of Mechanical Engineering, University of Wisconsin (1968).

H-24. M. Ishii and G. DeJarlais, “Flow Visualization Study of Inverted Annular Flow of Post Dryout Heat Transfer Region,” *Nuclear Engineering and Design*, **99,** 187-199 (1987).

H-25. M. Ishii and G. DeJarlais, “Flow Regime Transition and Interfacial Characteristics of Inverted Annular Flow,” *Nuclear Engineering and Design*, **95,** 171-184 (1986).

H-26. N. T. Obot and M. Ishii, “Two-Phase Flow Regime Transition Criteria in Post-Dryout Region Based on Flow Visualization Experiments,” *Int. J. Heat Mass Transfer*, **31**, 12, pp. 2559-2570, (1988).

H-27. J. G. Collier, Convective Boiling and Condensation, (McGraw-Hill Book Company, New York, 1972).

H-28. H. Schlichting, *Boundary-layer Theory*, (McGraw-Hill Book Company, New York, 1979).

H-29. M. W. Cappiello, “A Model for the Interfacial Shear in Vertical, Adiabatic Annular-Mist Flow,” Los Alamos National Laboratory document LA-CP-89-392 (October 1989).

H-30. K. A. Williams, “On the Explanation and Calculation of Anomalous Reflood Hydrodynamics in Large PWR Cores,” presented at the Winter ASME meeting, Miami, Florida, 85-MTA / HT-30 (November 1985).

H-31. K. Pasamehmetoglu, "A Formula for Limiting Film Thickness on Cold Walls," Los Alamos National Laboratory memo from Pasamehmetoglu to Spore (September 1, 1989).

H-32. "Data Report on Large Scale Reflood Test-14, CCTF Test C1-C5 (Run 14)," JAERI memo, 57-214 (August 1982).

H-33. S. W. Churchill, "Friction-Factor Equation Spans All Fluid-Flow Regimes," *Chemical Engineering*, Nov. 7, 1977, pp. 91-92.

H-34. P. B. Whalley, "Two-Phase Pressure Drop Design Report Part 5: The Calculation of Frictional Pressure Gradients in Two-Phase Flow," Atomic Energy Research Establishment report AERE-R9793, HTFS DR28, Rev. (February 1981).

H-35. W. L. Owens, "Two-Phase Pressure Gradient," International Heat Transfer Conference, Boulder, Colorado, 1981.

H-36. A. Cicchitti, C. Lombardi, M. Silvestri, G. Soldaini, and R. Zavatarelli, "Two-Phase Cooling Experiments: Pressure Drop, Heat Transfer and Burnout Measurements," *Energia Nucleare* **7,** 407-425 (1960).

H-37. A. E. Dukler, M. Wicks, and K. T. Cleveland, "Frictional Pressure Drops in Two-Phase Flow," *AIChE J.* **10**, 44 (1964).

H-38. P. B. Whalley, "Two-Phase Pressure Drop Design Report Part 6: The Calculation of Total Pressure Drop in Adiabatic Two-Phase Flow," Atomic Energy Research Establishment report AERE-R9794, HTFS DR28 (February 1981).

H-39. Y. Taitel and A. E. Dukler, "A Model for Predicting Flow Regime Transitions in Horizontal and Near-Horizontal Gas Liquid Flows," *AIChE J.* **22** (1)**,** 47-55 (1976).

H-40. B. E. Boyack, J. F. Lime, D. A. Pimental, J. W. Spore, and J. L. Steiner, "TRAC-M/F77, Version 5.5, Developmental Assessment Manual, Volume I: Nonproprietary Assessment Sections," Los Alamos National Laboratory document LA-UR-99-6480 (December 1999).

H-41. B. E. Boyack, J. F. Lime, D. A. Pimental, J. W. Spore, and J. L. Steiner, "TRAC-M/F77, Version 5.5, Developmental Assessment Manual, Volume II: Proprietary Assessment Sections," Los Alamos National Laboratory document LA-CP-99-345 (December 1999).

APPENDIX I

FLOW PROCESS MODELS

This section describes how the following flow processes are treated within TRAC: 1D abrupt area changes, 1D and 3D critical flow, countercurrent flow, TEE-component offtake flow, and vent valves. The following nomenclature applies to Appendix I.

NOMENCLATURE

a_{HE}: homogeneous equilibrium sound speed
A: area
$\underline{\underline{A}}$, $\underline{\underline{B}}$: matrices
c_p: specific heat at constant pressure
c_v: specific heat at constant volume
C: virtual mass coefficient
C_1, C_2: constants
C_B, M_B: empirical parameters of Bankoff correlation
CFZ: default additive loss coefficient
D: diameter
e: internal energy
E: interpolation constant used in CCFL model
f: Darcy friction factor
g: gravitational constant
G: mass flux
h: enthalpy in Section I.2. and characteristic height in Section I.4.
h_{fg}: latent heat of vaporization
h_b: critical height
H: dimensionless flux
H_L: head losses
HD_r: hydraulic diameter in the r-direction
j: superficial velocity
k: Boltzmann constant
k_c: critical wave number
K: form-loss coefficient
K_{TRAC}: loss coefficient
L: length
L^*: Bond number

M: Mach number

n: number of holes

p: pressure

Q: volumetric flow rate

R: ideal-gas constant in Section I.2. and nondimensional height ratio in Section I.4.

s: entropy

s^*: thermodynamic function defined by Eq. (I-42)

S: slip ratio

t: time

t_p: tie-plate thickness

T: temperature

T_{sv}: saturation temperature corresponding to steam partial pressure

$\overline{U}$: solution vector to the conservation equations

vol: cell volume

V: velocity

V_s: cell-edge (throat) velocity at location of area change

V_{gc}: cell-center (upstream) gas velocity

V_{ge}: fluid choking velocity

V_{le}: cell-edge (throat) liquid velocity

V_{lc}: cell-center (upstream) liquid velocity

w: parameter defined by Eq. (I-187)

W: mass-flow rate

WFHF: horizontal-flow weighting factor

x: quality or axial coordinate

x_0: quality defined by Eqs. (I-196), (I-213), and (I-234)

α: void fraction

Δp: pressure drop

Δr: radial length of the fluid cell that connects to the vent valve

Δx: cell length

$\Delta\rho$: density difference between liquid and gas

γ: specific heat ratio

η: ratio of the hole area to tie-plate area

λ_i: characteristic root

ρ: density

ρ^*: function of the main-tube-junction cell density derivatives defined by Eq. (I-39)

σ: surface tension

Subscripts

1: main-tube-junction cell

2nd: second pass

a: noncondensable gas

actual: actual

c: cell-center condition (upstream of throat) or critical

dn: downward offtake

donored: donor-cell value

e: cell-edge condition (at throat)

equil: equilibrium

g: gas mixture

JCELL: mesh-cell designation

j,*j*+1, etc.: cell-center quantity

$j + 1/2$, etc.: cell-edge quantity

k: major phase

l: liquid

m: two-phase mixture or model-predicted result

max: maximum

min: minimum

nuc: nucleation

o: stagnation property

ot: offtake

re: real root

sat: saturation

sc: subcooled

sd: side-oriented offtake

tp: two-phase

up: upward offtake

v: vapor

Superscripts

+:	downstream
–:	upstream
1, 2, 3:	first, second, and third predictions
n,n + 1:	current- and new-time values
p:	predicted

I.1. 1D and 3D Abrupt Flow-Area Change Model

Here we describe the coding invoked when a user inputs a negative value for a 1D component's friction-factor variable NFF. When NFF is negative at a cell edge, TRAC calculates an additional flow loss caused by an abrupt area change encountered at a sudden expansion or contraction between mesh cells. This loss is based on user-input data for the volume-averaged mesh-cell flow area ($A_j = \mathrm{vol}_j / \Delta x_j$) and the fluid-velocity direction. TRAC adds the additional losses into the basic momentum equations to calculate correctly the pressure drop at the location of the abrupt area change.

The flow loss of a thin-plate orifice that is modeled at a mesh-cell interface is associated with an abrupt flow-area change. This flow loss is discussed here, but it is not added as an additional loss by TRAC when NFF is negative. Such losses that are modeled at interfaces need to be defined by the user through FRIC additive friction-loss-coefficient input data.

Similarly, the user may have to account for turning losses and abrupt area changes (including expansions and contractions) at the TEE-component joining cell with the FRIC input array.

TRAC is programmed also to add abrupt flow-area change losses to the 3D VESSEL component. Because NFF is not a VESSEL-component input parameter, the negative values for the liquid additive friction-loss coefficients CFZL-T, CFZL-Z, and CFZL-R are used as a user-defined input flag that turns on the 3D abrupt area change model. TRAC evaluates the same abrupt flow-area change loss and adds it to the absolute value of the input-specified additive friction-loss coefficient. This is done for both liquid and vapor and forward and reverse flow. The volume-averaged flow area in the radial direction for cylindrical geometry is divided by $R_{\mathrm{mean}_i} = (1/2)(R_{\mathrm{in}_i} + R_{\mathrm{out}_i})$ [that is, $A_i = \mathrm{vol}_i/(R_{\mathrm{mean}_i}\Delta r_i)$] to remove the smooth flow-area change effect from cylindrical geometry.

I.1.1. Basis for the Model

In addition to ordinary friction losses in a uniform straight pipe, other losses can occur because of sudden velocity changes resulting from abrupt area changes. In long pipes, these additional losses may be neglected in comparison to the normal friction loss of the pipe. In short pipes, however, these additional losses may actually be much larger than the ordinary friction loss.

In the case of abrupt area changes, the source of the loss is confined to a very short length of pipe, although the turbulence produced may persist for a considerable distance downstream. The flow after the change may be exceedingly complex. For the purposes of analysis, however, we assume that the effects of ordinary friction and of the additional large-scale turbulence may be separated, and that the abrupt area change loss is concentrated at the location of the area change. The total head loss in a pipe may then be considered to be the sum of the ordinary friction for the length of pipe considered and the extra loss due to the abrupt area change.

For an abrupt expansion, a theoretical determination of the loss is possible. For an abrupt contraction, however, this is not true, and experimental results must be used to determine the flow loss. Because the losses have been found to vary as the square of the mean velocity, they are frequently expressed in the form

$$\text{Head Loss} = K\frac{V^2}{2g} \quad , \tag{I-1}$$

where K is the loss coefficient, V is the mean velocity, and g is the gravitational acceleration constant.

We determine corrective terms added to the TRAC momentum equations by first considering the momentum equation for single-phase flow and by neglecting the gravity head and wall shear,

$$\frac{1}{\rho}\frac{\partial p}{\partial x} + V\frac{\partial V}{\partial x} = 0 \quad . \tag{I-2}$$

For a pipe noded as in Fig. I-1., integration of Eq. (I-2) with the assumptions of steady state and of constant density from point j to point $j + 1$ yields a Bernoulli-type equation for the pressure change from point j to point $j + 1$ as follows:

$$p_{j+1} - p_j = 0.5\rho(V_j^2 - V_{j+1}^2) \quad . \tag{I-3}$$

If Eq. (I-3) is rewritten in terms of a pressure drop, then

$$\Delta p_{j\rightarrow(j+1)} = -(p_{j+1} - p_j) = 0.5\rho(V_{j+1}^2 - V_j^2) \quad . \tag{I-4}$$

The pressure drop given by Eq. (I-4) typically is referred to as the reversible pressure drop. We use the term reversible because the pressure loss associated with a contraction can be regained by a pressure rise at an expansion of the same magnitude. Consider the following three situations. If no area change occurs between points j and $j + 1$, the velocity of the flow does not change, and Eq. (I-4) predicts

$$\Delta p_{j\rightarrow(j+1)} = 0 \tag{I-5}$$

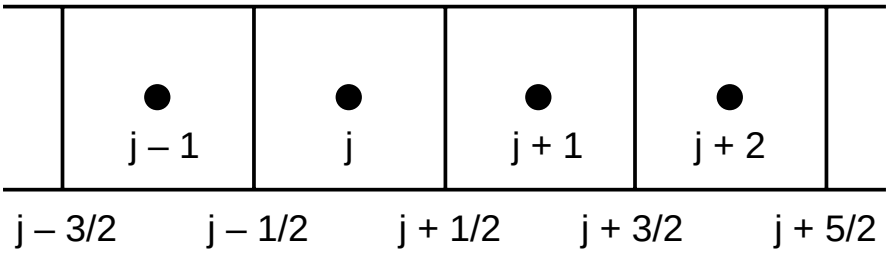

Fig. I-1. 1D TRAC noding.

as expected. If a smooth area change occurs between sections j and $j + 1$, then the irreversible losses may be small, and Eq. (I-4) yields an approximation to the pressure drop from point j to $j + 1$. If the area change between sections j and $j + 1$ is abrupt, however, the irreversible losses cannot be ignored, and it is standard practice to add a form-loss factor to Eq. (I-4) to account for the additional irrecoverable pressure loss caused by the area change in question. This yields a general equation for the pressure drop between sections j and $j + 1$ when an abrupt area change is present, such that

$$\Delta p_{j\to(j+1)} = -(p_{j+1} - p_j) = 0.5\rho(V_{j+1}^2 - V_j^2) + 0.5K\rho V_s^2 \quad , \tag{I-6}$$

where V_s is the velocity at the cross section where the area change occurs. Once the loss coefficient K for the specific area change in question has been determined, either theoretically or experimentally, the pressure drop at the abrupt area change can be calculated using Eq. (I-6) above.

I.1.1.1. Abrupt Expansion. To determine the loss coefficient for an abrupt expansion, consider the expansion of Fig. I-2. If the pipes run full and the flow is assumed steady, two simplifying assumptions may be made that allow the pressure change across the expansion to be calculated. First, assume that the pressure and velocity at section j are uniform across the cross section. This assumption is valid for the high Reynolds-number flow found in most practical applications. Second, assume that the pressure and velocity at section $j + 1$ are also uniform. This assumption is valid if section $j + 1$ is sufficiently downstream of the expansion where the mixing caused by the turbulence has had a chance to even out the velocity profile again. A control-volume analysis using steady-flow equations may now be made on the fluid contained between sections j and $j + 1$.

Application of the momentum equation for steady, incompressible flow neglecting wall friction to the fluid between sections j and $j + 1$ yields the following force balance:

$$(p_j - p_{j+1})A_{j+1} = \rho Q(V_{j+1} - V_j) = \rho A_{j+1}V_{j+1}(V_{j+1} - V_j) \quad , \tag{I-7}$$

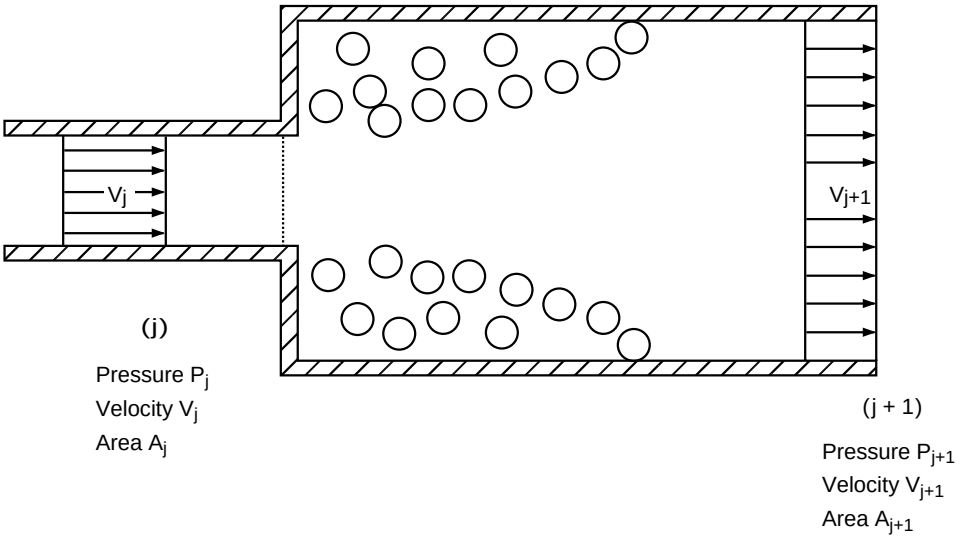

Fig. I-2. Abrupt expansion.

where Q is the volumetric flow rate and $V_j > V_{j+1}$ because of the change in the cross section at $j + 1/2$. Therefore,

$$(p_j - p_{j+1}) = \rho V_{j+1}(V_{j+1} - V_j) \quad . \tag{I-8}$$

Application of the Bernoulli equation for an incompressible fluid yields

$$\frac{p_j}{\rho g} + \frac{V_j^2}{2g} - H_L = \frac{p_{j+1}}{\rho g} + \frac{V_{j+1}^2}{2g} \quad , \tag{I-9}$$

where H_L is the total head loss across the expansion. Solving Eq. (I-9) for this head loss gives

$$H_L = \frac{p_j - p_{j+1}}{\rho g} + \frac{V_j^2 - V_{j+1}^2}{2g} \quad . \tag{I-10}$$

Substitution for the term $(p_j - p_{j+1})$ using Eq. (I-8) yields

$$H_L = \frac{(V_j - V_{j+1})^2}{2g} \quad . \tag{I-11}$$

From continuity, $A_j V_j = A_{j+1} V_{j+1}$ so that we may rewrite Eq. (I-11) as

$$H_L = \frac{V_j^2}{2g}\left(1 - \frac{A_j}{A_{j+1}}\right)^2 \quad . \tag{I-12}$$

Comparison of this result with Eq. (I-1) shows that the loss coefficient K for an abrupt expansion at the $j + 1/2$ interface is

$$K = \left(1 - \frac{A_j}{A_{j+1}}\right)^2 \tag{I-13}$$

when the mean velocity V of Eq. (I-1) is taken as V_j. Equation (I-13) is also known as the Borda-Carnot loss coefficient.

Now that the theoretical loss coefficient K has been determined, the pressure change between points j and $j + 1$ may be calculated using Eq. (I-6). Substitution of the result for K into Eq. (I-6) yields

$$\Delta p_{j\to(j+1)} = -(p_{j+1} - p_j) = \rho V_{j+1}(V_{j+1} - V_j) \quad , \tag{I-14}$$

which is exactly the result expressed in Eq. (I-8).

I.1.1.2. Abrupt Contraction. Consider the abrupt contraction of Fig. I-3. Although an abrupt contraction is geometrically the reverse of an abrupt expansion, it is not possible to solve exactly for the loss coefficient for an abrupt contraction using a control-volume analysis on the fluid between sections j and $j + 1$ as was done for the abrupt expansion of Fig. I-2. This is because the pressure at section j just upstream of the contraction varies in an unknown way as a result of the curvature of the streamlines and the acceleration of the fluid. Thus, application of the steady-flow momentum equation to the fluid at section j is not valid. Without the relationship between pressure and velocity provided by the momentum equation [as in Eq. (I-7) for the case of the abrupt expansion], it is not possible to solve explicitly for the total head loss across the contraction. Loss coefficients have been determined experimentally for circular coaxial pipes and fairly high Reynolds numbers, and Massey (Ref. I-1., p. 219) recommends the use of Table I-1. when determining values for K.

Once K has been determined using Table I-1., the pressure drop across the abrupt contraction may be calculated as follows. The flow at section j has a velocity V_j, while the flow upon reaching section $j + 1$ has a velocity V_{j+1} that is higher than V_j because of the abrupt cross-section change. Using Eq. (I-6) to calculate the change in pressure from points j to $j + 1$ caused by the abrupt area change yields

$$\Delta p_{j\to(j+1)} = -(p_{j+1} - p_j) = 0.5\rho\left(V_{j+1}^2 - V_j^2\right) + 0.5K\rho V_{j+1}^2 \quad , \tag{I-15}$$

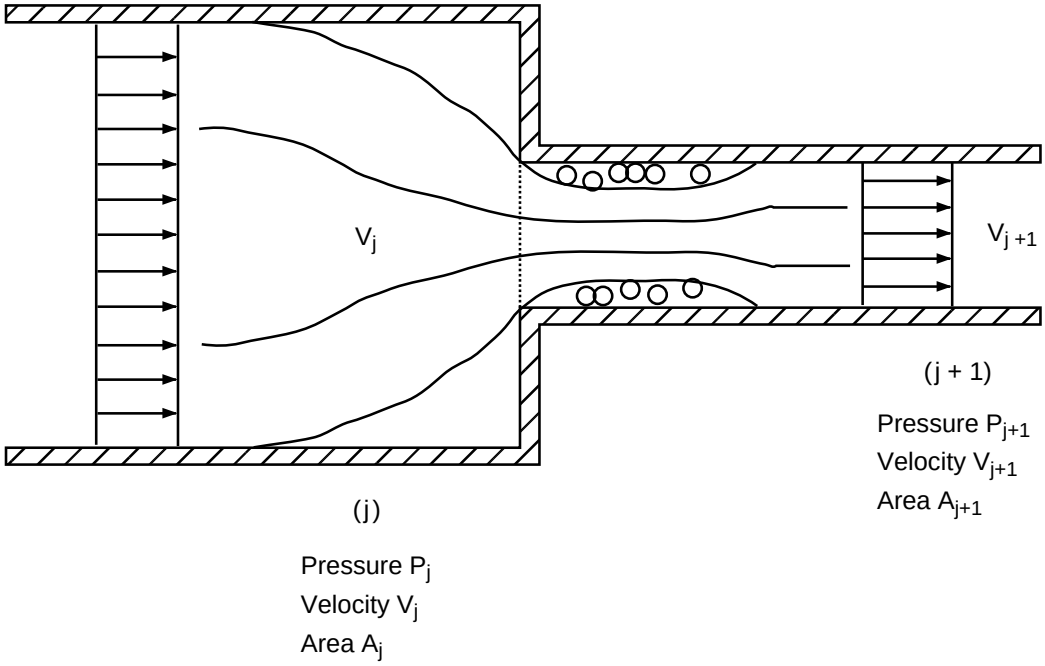

Fig. I-3. Abrupt contraction.

where K is taken from Table I-1.

I.1.1.3. Thin-Plate Orifice. As in the case of the abrupt contraction, it is not possible to determine theoretically the loss coefficient across a thin-plate orifice, and experimental data must be used. For a sharp-edged, thin-plate orifice in a straight conduit (Fig. I-4.), Idel'Chik (Ref. I-3., p. 139) suggests that the following expression be used for the loss coefficient K in the presence of high Reynolds numbers ($\geq 10^5$):

$$K = \left(1 + 0.707 \sqrt{1 - \frac{A_{j+\frac{1}{2}}}{A_j}} - \frac{A_{j+\frac{1}{2}}}{A_j} \right)^2 \quad . \tag{I-16}$$

This curve fit also agrees well with the data plotted in White (Ref. I-4., p. 384) for the irrecoverable head loss across a thin-plate orifice.

TABLE I-1.
Abrupt Contraction Standard Loss-Coefficient Data

A_{j+1}/A_j	0.0	0.04	0.16	0.36	0.64	1.0
K	0.5	0.45	0.38	0.28	0.14	0.0

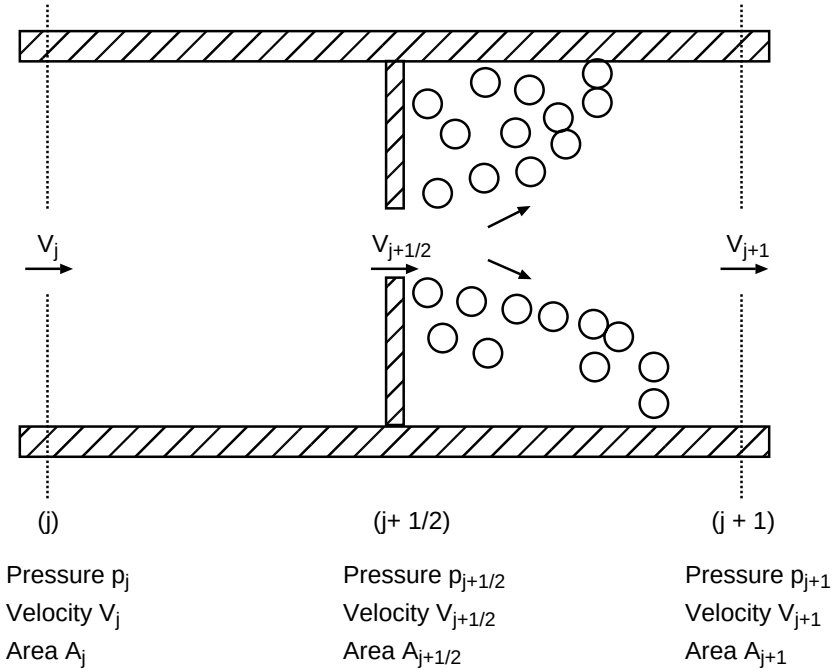

Fig. I-4. Sharp-edged, thin-plate orifice.

Once the loss coefficient K for a sharp-edged, thin-plate orifice has been determined using Eq. (I-16), the pressure drop across the orifice may be calculated as follows. The flow at section j has a velocity V_j, while the flow upon reaching section $j + 1/2$ has a velocity $V_{j+1/2}$, which is higher than V_j because of the abrupt cross-section change. Using Eq. (I-6) to calculate the change in pressure from points j to $j + 1/2$ caused by the abrupt area change yields

$$\Delta p_{j\to(j+\frac{1}{2})} = -(p_{j+\frac{1}{2}} - p_j) = 0.5\rho(V^2_{j+\frac{1}{2}} - V^2_j) + 0.5K\rho V_{j+\frac{1}{2}} \quad , \tag{I-17}$$

where K is calculated using Eq. (I-16). Another abrupt area change occurs between points $j + 1/2$ and $j + 1$. The flow at section $j + 1/2$ has a velocity $V_{j+1/2}$, while the flow at section $V_{j+1/2}$ has a velocity $V_{j+1/2}$, which is less than $V_{j+1/2}$ because of the expansion in cross section. Because the irreversible losses caused by the presence of the orifice have already been accounted for in the pressure drop between j and $j + 1/2$ and should not be accounted for twice, the pressure change between $j + 1/2$ and $j + 1$ is simply

$$\Delta p_{(j+\frac{1}{2})\to(j+1)} = -(p_{j+1} - p_{j+\frac{1}{2}}) = 0.5\rho(V^2_{j+1} - V^2_{j+\frac{1}{2}}) \quad . \tag{I-18}$$

Adding Eqs. (I-17) and (I-18) (noticing that $V_j = V_{j+1}$) shows that the total pressure drop from points j to $j + 1$ for the orifice of Fig. I-4. is

$$\Delta p_{j\rightarrow(j+1)} = -(p_{j+1} - p_j) = 0.5\rho K V^2_{j+\frac{1}{2}} \quad , \tag{I-19}$$

where K is calculated according to Eq. (I-16).

I.1.1.4. Turning-Flow Loss. The current TEE-component momentum-source-term logic is discussed in Section 2.0. We note here that while this model exhibits numerical stability, it does not give perfect predictions of losses at TEE internal junctions. Usually, the current model will underpredict TEE losses, although in some situations the losses will be overpredicted. The user must account for any additional losses with appropriate use of the FRIC input array that specifies friction factors (or, optionally, K-factors) at 1D mesh-cell interfaces. Reference I-2. is a source of such data. Note that the correlations in Ref. I-2. for TEE losses include velocities based on experiments that have equal flow areas in all three TEE flow channels. Also note that, as stated in Section 2.0., TRAC's flow-area logic for reversible losses is not activated at the three interfaces of the TEE joining cell and that there is no internal calculation available for abrupt expansion or contraction at those faces.

I.1.2. Assumptions and Preliminary Calculations

We make several assumptions when deriving the loss coefficients for each of the abrupt area changes discussed.

To perform a control-volume analysis on the abrupt expansion, we must assume that the pressures and velocities are uniform over the cross sections at sections j and $j + 1$ (Fig. I-2.). As discussed in Section I.1.1.1., this is largely true for section j at high Reynolds-number values and at section $j + 1$ when it is taken sufficiently far downstream of the enlargement [about 8 times the larger diameter according to Massey (Ref. I-1., p. 217)].

For the case of the abrupt contraction, the data reported in Massey (Ref. I-1., p. 219) represent loss coefficients for coaxial circular pipes and fairly high Reynolds numbers. It is assumed that the data also apply to any abrupt contraction modeled using TRAC, and that the data give a good estimate of the loss coefficient.

For the thin-plate orifice, the loss-coefficient expression [Eq. (I-16)] recommended by Idel'Chik (Ref. I-3., p. 139) represents a curve fit to data for a sharp-edged, thin-plate orifice in a conduit for high Reynolds-number flow. As is the case for the abrupt contraction, it is assumed that this curve fit is applicable to any general sharp-edged, thin-plate orifice modeled by the user, and that the curve fit provides a good estimate of the loss coefficient.

If the correlations of Ref. I-2. are used for TEE turning losses through the FRIC array, the user still must account for any flow-area changes at the three TEE joining-cell interfaces (again, using FRIC).

I.1.3. Model as Coded

Again consider the momentum equation for single-phase flow, neglecting the gravity-head and wall-shear terms,

$$\frac{1}{\rho}\frac{\partial p}{\partial x} + \frac{1}{2}\frac{\partial V^2}{\partial x} = 0 \quad . \tag{I-20}$$

Whereas MOD1 differences the $V\partial V/\partial x$ form of the momentum-convection term, MOD2 and TRAC-M difference the momentum-convection term form in Eq. (I-20) (for the pipe noded as in Fig. I-1.) as

$$\frac{1}{\rho}(p_{j+1} - p_j) + 0.5\,(V_{j+1}^2 - V_j^2) = 0 \quad . \tag{I-21}$$

Written in terms of a pressure drop between points j and $j + 1$,

$$\Delta p_{j\rightarrow(j+1)} = -(p_{j+1} - p_j) = 0.5\rho\,(V_{j+1}^2 - V_j^2) \quad . \tag{I-22}$$

This finite-difference result is identical to the integral result of Eq. (I-4).

As before, if no area change occurs between points j and $j + 1$, the velocity of the flow does not change, and Eq. (I-22) predicts

$$\Delta p_{j\rightarrow(j+1)} = 0 \tag{I-23}$$

as expected. If an abrupt area change between sections j and $j + 1$ does occur, however, then a form-loss factor is again added to the pressure-drop equation to account for irreversible losses. This yields the general equation for a pressure drop between point j and $j + 1$ when an abrupt area change is present, such that,

$$\Delta p_{j\rightarrow(j+1)} = -(p_{j+1} - p_j) = 0.5\rho\,(V_{j+1}^2 - V_j^2) + 0.5K_{\mathrm{TRAC}}\,\rho V_s^2 \quad , \tag{I-24}$$

where V_s is the cell-edge velocity at the location of the area change.

In TRAC, pressures are cell-centered quantities whereas velocities are cell-edge quantities. Therefore, approximating the cell-centered velocities in Eq. (I-24) by donoring the interface velocities and assuming continuity of volumetric flow gives for a positive-direction flow velocity,

$$\begin{aligned}\Delta p_{j\rightarrow(j+1)} &= -(p_{j+1} - p_j) \\ &= 0.5\rho\left[\frac{A_{j+\frac{1}{2}}}{A_{j+1}} + \frac{A_{j+\frac{1}{2}}}{A_j}\right] V_{j+\frac{1}{2}} \left[\frac{A_{j+\frac{1}{2}}}{A_{j+1}} V_{j+\frac{1}{2}} - \frac{A_{j-\frac{1}{2}}}{A_j} V_{j-\frac{1}{2}}\right] \quad .\end{aligned} \tag{I-25}$$

Because the pressure-drop equation in MOD2 and TRAC-M is identical in form to Eq. (I-6), the loss coefficient K_{TRAC} calculated in subroutine FWKF is exactly that developed in the previous pages for the cases of abrupt expansion and contraction.

Namely, for an abrupt expansion noded as in Fig. I-5., subroutine FWKF calculates the loss coefficient as

$$K_{TRAC} = \left(1 - \frac{A_j}{A_{j+1}}\right)^2 \left(\frac{A_{j+\frac{1}{2}}}{A_j}\right)^2 \quad . \tag{I-26}$$

The factor $(1-A_j/A_{j+1})^2$ is the K-factor to be applied to the minimum flow-area-velocity squared, v_j^2, as presented in Eq. (I-13). The other factor $(A_{j+1/2}/A_j)^2$ converts that K-factor to K_{TRAC}, which is applied to the mesh-cell interface-velocity squared, $v_{j+1/2}^2$. This conversion is based on assuming continuity of volumetric flow; i.e., $A_j V_j = A_{j+1/2} V_{j+1/2}$. Similarly, the loss coefficient for an abrupt contraction noded as in Fig. I-6. is calculated by subroutine FWKF as a curve fit to the data of Table I-1., such that

$$K_{TRAC} = \left\{0.5 - 0.7\left(\frac{A_{j+1}}{A_j}\right) + 0.2\left(\frac{A_{j+1}}{A_j}\right)^2\right\}\left(\frac{A_{j+\frac{1}{2}}}{A_{j+1}}\right)^2 \quad . \tag{I-27}$$

The bracketed factor is the K-factor to be applied to the minimum flow-area-velocity v_{j+1}^2 Multiplying by the following factor $(A_{j+1/2}/A_{j+1})^2$ defines K_{TRAC} to be applied to the mesh-cell interface-velocity squared, $v_{j+1/2}^2$.

For the case of a thin-plate orifice noded as in Fig. I-7., the loss coefficient recommended by Idel'Chik is not evaluated by subroutine FWKF. This is because many TRAC input-data models have cell-edge flow areas that are less than both of its mesh-cell flow areas without being a model for a thin-plate orifice. The user needs to input a FRIC to account for the irreversible loss across this type of abrupt area change.

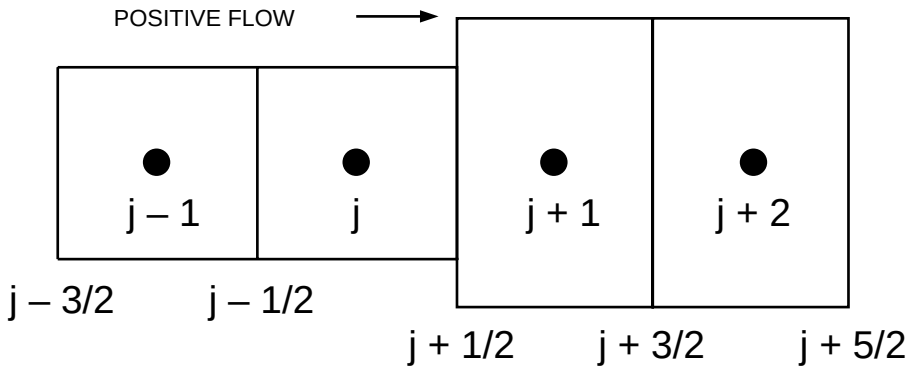

Fig. I-5. TRAC noding for abrupt expansion if $V_{j+1/2} > 0$ and for abrupt contraction if $V_{j+1/2} < 0$.

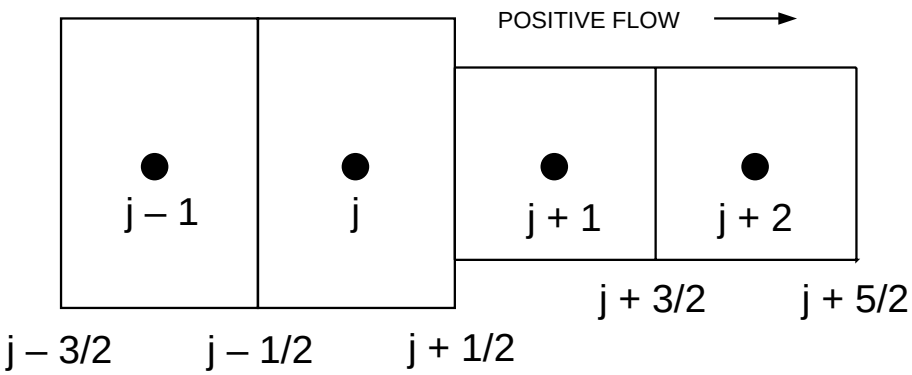

Fig. I-6. TRAC noding for abrupt contraction if $V_{j+1/2} > 0$ and for abrupt expansion if $V_{j+1/2} < 0$.

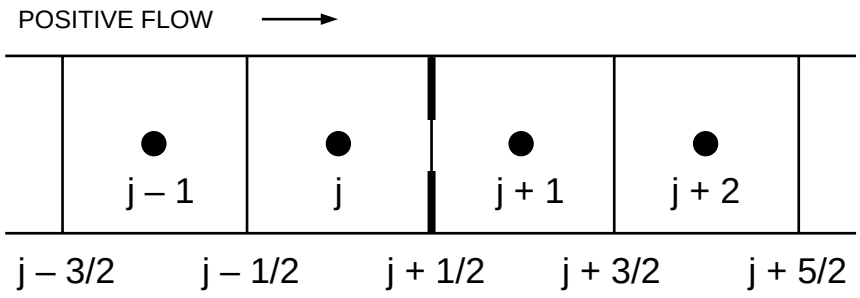

Fig. I-7. TRAC noding for sharp-edged, thin-plate orifice.

I.1.4. Assessment

The flow-area-ratio defining form of Eq. (I-25) used by MOD2 and TRAC-M predicts reversible losses across area changes, and any irreversible losses need to be accounted for by using an additional form-loss term. When the variable NFF or CFZL is set equal to a negative value at a cell edge containing an abrupt expansion, TRAC adds the theoretically derived form loss for such an area change into the momentum equations. This results in the proper pressure change being calculated and no error being introduced at cell edges containing abrupt expansions.

The data for the standard loss coefficient for an abrupt contraction cited in Massey (Ref. I-1., p. 219) (see Table I-1.) are incorporated into TRAC using a curve fit. Table I-2. compares the original data and the *K*-value predicted using the curve fit of Eq. (I-27). For this analysis, it is assumed that $A_{j+1/2} = A_{j+1}$. Inspection of Table I-2. shows that Eq. (I-27) very closely predicts the standard loss coefficients measured experimentally. As a result, when NFF or CFZL is set to a negative value, TRAC calculates an additional loss term that is added into the momentum equations to accurately predict the pressure drop

across an abrupt contraction. Hence, Table I-2. shows a few percent error at cell edges containing abrupt contractions when the variable NFF or CFZL is negative.

Idel'Chik (Ref. I-3., p. 139) recommends that the standard loss coefficient for a sharp-edged, thin-plate orifice be calculated using Eq. (I-16). This correlation, however, is not evaluated by subroutine FWKF. Hence, TRAC will underpredict the pressure drop across an orifice unless an appropriate FRIC, such as defined by Eq. (I-16), is input by the user.

I.1.5. Geometry Effects

A major improvement in the calculation of pressure drops was realized in the MOD2 code (and now in TRAC-M) with the incorporation of flow-area ratios in the momentum-convection term to accurately evaluate reversible Bernoulli flow losses. In the MOD1 version, finite-differencing error occurs in the momentum-convection term because variation in flow area is not modeled and momentum convection is not conserved. The pressure drop does not occur until the second cell downstream of the area change for abrupt expansions and orifices. With the introduction of the flow-area ratios in MOD2, pressure drops are now calculated to occur across the area change itself, rather than in cells downstream of the area change. Therefore, it is no longer necessary that at least two cells separate each abrupt area change to prevent unexpected results as is suggested for MOD1.

TABLE I-2.
Abrubt Contraction Standard Loss-Coefficient
Data Comparison

$\frac{A_j}{A_{j-1}}$	K_{DATA} (Table I-1.)	$K_{\text{Eq. (I-27)}}$	$\%\ \text{error} = \frac{(K_{\text{DATA}} - K_{\text{Eq. (I-27)}})}{K_{\text{DATA}}} \times 100\%$
0.0	0.5	0.5	0.0
0.04	0.45	0.47	–4.4
0.16	0.38	0.39	–2.6
0.36	0.28	0.27	3.6
0.64	0.14	0.13	7.1
1.0	0.0	0.0	0.0

It is possible to retrieve the MOD1 form of the momentum equation using TRAC-M by setting the variable flags ARY to 0.0 and ARN to 1.0 in module OneDDat (subroutine BLKDAT in TRAC-M/F77). This causes all area ratios in Eq. (I-25) to be unity because each flow-area ratio is evaluated as (A/A)*ARY+ARN by TRAC-M. A thorough discussion of the pressure drops calculated for each of the abrupt area changes is given in the MOD1 correlations and models document (Ref. I-5.), and the reader is referred to this for more information regarding this particular option.

I.1.6. Summary and Conclusions

Irrecoverable pressure losses occur across abrupt area changes. In standard practice, these losses are accounted for in the momentum equation using an additional form-loss term. If the user sets the 1D-component variable NFF or the 3D VESSEL-component additive friction-loss coefficients CFZL to a negative value at the cell edge where the abrupt area change (an expansion or a contraction) is located, TRAC will calculate a form-loss coefficient based on the user-input cell-edge flow area, the volume-averaged mesh-flow flow areas, and the velocity direction. TRAC then adds this additional form-loss term to the momentum equation to account for the irrecoverable losses caused by the abrupt area change.

The abrupt flow-area change coding invoked when NFF or CFZL is negative is contained in subroutine FWKF. For an abrupt expansion or contraction, TRAC accurately calculates the pressure drop across the area change by adding an additional form-loss term into the momentum equations to account for the irrecoverable head loss. Although an additional loss coefficient should also be calculated for the case of an orifice, the recommended correlation is not evaluated by subroutine FWKF. The user is currently advised to account for irreversible losses through the use of input-specified FRICs.

The user may have to account for irrecoverable turning pressure loss through a TEE internal junction with appropriate FRICs. The current TEE model does not implement the area-ratio logic for reversible losses at the three joining-cell interfaces, nor is there evaluation of abrupt area changes at those faces when NFF is negative.

Modeling the momentum-convection term with area ratios conserves momentum flux convection between momentum cells and provides an accurate evaluation of reversible Bernoulli flow losses. The TRAC user has the responsibility then to account for all irreversible flow losses either by setting NFF or CFZL negative, so that TRAC internally evaluates and adds in abrupt flow-area-change losses for abrupt expansions and contractions, or by providing appropriate irreversible form-loss FRIC values at selected mesh-cell edges.

I.2. 1D Critical-Flow Model

The TRAC 1D critical-flow model comprises three separate models: a subcooled-liquid choked-flow model; a two-phase, two-component, choked-flow model; and a single-phase vapor choked-flow model.

I.2.1. Basis for the Models

The subcooled-liquid choked-flow model is a modified form of the Burnell model. The two-phase, two-component, choked-flow model is based on first principles and a characteristic analysis approach. The single-phase vapor choked-flow model uses an ideal-gas isentropic expansion assumption. Each model basis is now described in more detail.

I.2.1.1. Subcooled Liquid. The subcooled choked-flow model is a modified form of the Burnell model (Ref. I-6.). During the subcooled blowdown phase, the fluid changes phase at the break because the downstream pressure is much lower than the saturation pressure corresponding to the system fluid temperature. The transition from single- to two-phase flow, which is accompanied by discontinuous change in the fluid bulk modulus, leads to a large discontinuity in the sound speed at the break. The physical process that occurs during the subcooled blowdown phase is described briefly in the following paragraphs. Reference I-6. discusses this phenomenon in greater detail.

Figure I-8. shows a converging-diverging nozzle. The pressure downstream is such that the fluid just begins to flash at the throat. The flow upstream of the throat is subsonic. Because the sound speed is discontinuous when the fluid becomes saturated, however, and because mass conservation dictates that the velocity just upstream of the throat must be equal to the velocity just downstream of the throat (where the fluid has only a minuscule void fraction), the flow is supersonic throughout the diverging section. Thus, the nozzle does not contain any point in which the Mach number, *M*, equals one. Figure I-8. also shows the velocity profile and the sound speeds for this situation.

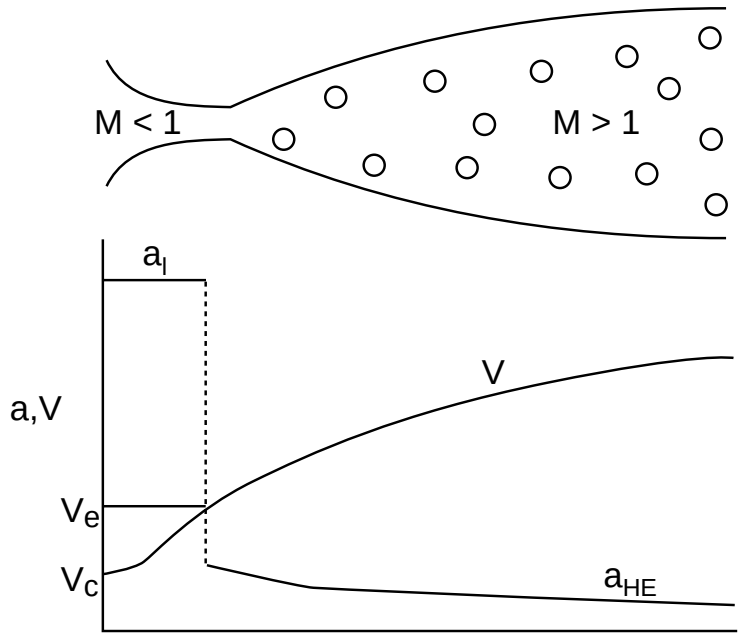

Fig. I-8. Subcooled choking process when nucleation begins at the throat.

The liquid velocity at the throat is calculated from Bernoulli's equation, assuming steady frictionless incompressible flow, such that

$$V_{le} = \left[V_{lc}^2 + \frac{2(p_c - p_e)}{\rho_l} \right]^{\frac{1}{2}} \quad , \tag{I-28}$$

where subscripts c and e refer to the cell-center (upstream) and the cell-edge (throat) conditions, respectively. The throat pressure, p_e, is equal to the nucleation pressure, p_{nuc}, and can be considerably lower than the local saturation pressure, p_{sat}, because thermal nonequilibrium causes nucleation delay.

Any further reduction in the downstream pressure does not affect the flow because the disturbance cannot move upstream where the flow is supersonic in the diverging section. Thus, Eq. (I-28) gives the liquid throat velocity for any downstream pressure lower than the pressure necessary to cause the subcooled liquid to begin flashing at the throat (which is the case for most problems of interest in LWR applications).

Next we consider the situation in which the subcooled choked flow, as described above, exists initially, and the upstream pressure is lowered. As the upstream pressure decreases, the pressure at the throat remains equal to p_{nuc}, and again Eq. (I-28) can be used to calculate the liquid throat velocity. The liquid throat velocity decreases, however, because the upstream pressure decreases. If the upstream pressure is lowered further, a point is reached at which the liquid exit velocity is just equal to the homogeneous equilibrium sound speed, that is,

$$V_{le} = a_{HE} \quad . \tag{I-29}$$

Any further reduction in the upstream pressure moves the point where $p = p_{nuc}$ upstream. In this case, the flow in the subcooled zone and two-phase zone upstream of the throat is subsonic. The flow at the throat is sonic with $V_{le} = a_{HE}$; the flow in the diverging section is supersonic. If the upstream pressure is reduced further, the p_{nuc} point moves upstream until complete two-phase flow exists. Therefore, the maximum of the Burnell expression and the homogeneous equilibrium sound speed give the subcooled choking criterion. Thus,

$$V_{le} = \max \left\{ a_{HE}, \left[V_{lc}^2 + \frac{2(p_c - p_e)}{\rho_l} \right]^{\frac{1}{2}} \right\} \quad . \tag{I-30}$$

In TRAC, a nucleation delay model, developed by Jones (Ref. I-7.), determines the cell-edge pressure, p_e, from the saturation pressure, p_{sat} (corresponding to the donor-cell liquid temperature, T_l), such that

$$p_e = p_{\text{sat}} - \max\left\{0.0, 0.258 \frac{\sigma^{1.5}\left(\frac{T_l}{T_c}\right)^{13.76}\left[1+13.25\left(-\frac{1}{1.01325\times10^{11}}\frac{Dp}{Dt}\right)^{0.8}\right]^{0.5}}{(kT_c)^{0.5}\left(1-\frac{\rho_g}{\rho_l}\right)}\right.$$

$$\left. -27(0.072)^2\left(\frac{A_e}{A_c}\right)^2\frac{\rho_l V_l^2}{2}\right\} \qquad \text{(I-31)}$$

where σ is the surface tension, T_l is the donor-cell liquid temperature, T_c is the critical temperature, *Dp/Dt* is the substantial derivative of the pressure, k is the Boltzmann constant, ρ_l and ρ_g are cell-edge phasic densities, V_l is the cell-edge liquid velocity as calculated by the standard momentum solution, and A_e and A_c are cell-edge and cell-center flow areas. The calculational sequence for the TRAC subcooled-liquid choking model is described in Section I.2.4.

I.2.1.2. Two-Phase, Two-Component Fluid. We developed the two-phase, two-component, choked-flow model from first principles using the characteristic analysis approach. The TRAC model is an extension of a model developed by Ransom and Trapp (Ref. I-8.) that incorporates an additional inert-gas component and nonequilibrium effects. As suggested by Ransom and Trapp, we assume that thermal equilibrium exists between the phases. The validity of this assumption has not been investigated in the presence of an inert gas. This assumption, however, is not an inherent feature of the TRAC model and can be changed easily, if necessary.

The two-fluid field under thermal equilibrium is described by the overall continuity equation, two-phasic momentum equations, the mixture energy equation, and the inert-gas continuity equation. When the nondifferential source terms are omitted (because they do not enter into characteristic analysis), the equations are

$$\frac{\partial \rho_m}{\partial t} + \frac{\partial}{\partial x}(\rho_m V_m) = 0 \ , \qquad \text{(I-32)}$$

$$\alpha\rho_g\left[\frac{\partial V_g}{\partial t} + V_g\frac{\partial V_g}{\partial x}\right] + \alpha\frac{\partial p}{\partial x}$$

$$+ C\alpha(1-\alpha)\rho_m\left[\frac{\partial V_g}{\partial t} + V_l\frac{\partial V_g}{\partial x} - \frac{\partial V_l}{\partial t} - V_g\frac{\partial V_l}{\partial x}\right] = 0 \quad , \qquad \text{(I-33)}$$

$$(1-\alpha)\rho_l\left[\frac{\partial V_l}{\partial t} + V_l\frac{\partial V_l}{\partial x}\right] + (1-\alpha)\frac{\partial p}{\partial x}$$

$$+ C\alpha(1-\alpha)\rho_m\left[\frac{\partial V_l}{\partial t} + V_g\frac{\partial V_l}{\partial x} - \frac{\partial V_g}{\partial t} - V_l\frac{\partial V_g}{\partial x}\right] = 0 \quad , \tag{I-34}$$

$$\frac{\partial}{\partial t}(\rho_m s_m) + \frac{\partial}{\partial x}[\alpha\rho_g V_g s_g + (1-\alpha)\rho_l V_l s_l] = 0 \quad , \tag{I-35}$$

and

$$\frac{\partial}{\partial t}(\alpha\rho_a) + \frac{\partial}{\partial x}(\alpha\rho_a V_g) = 0 \quad , \tag{I-36}$$

where C is the virtual mass coefficient; s is the entropy; and subscripts a, g, l, and m refer to the noncondensable gas, steam/gas mixture, liquid, and total mixture, respectively. The last terms in Eqs. (I-33) and (I-34) represent interphasic force terms caused by relative acceleration. These terms are discussed in detail in Refs. I-6. and I-8. Following Ransom and Trapp's formulation, the energy equation is written in the form of the mixture-specific entropy that is conserved for adiabatic flow (with the irreversibilities associated with interphasic mass transfer and relative phase acceleration neglected). No basic difficulty in the analysis is experienced, however, if the mixture energy equation is written in terms of the internal energy or enthalpy.

In the thermal-equilibrium case, ρ_v, ρ_l, s_g, s_l, and ρ_a are known functions of p_a and p_v. If we assume that Dalton's law of partial pressures applies, Eqs. (I-32) through (I-36) can be written in terms of the five unknowns p_v, α, V_g, V_l, and p_a. The matrix representation of these equations is

$$A(\bar{U})\frac{\partial \bar{U}}{\partial t} + B(\bar{U})\frac{\partial \bar{U}}{\partial x} = 0 \quad , \tag{I-37}$$

where the $\bar{U}$ consists of $p_v, \alpha, V_g, V_l,$ and p_a.

An example of one of the equations in the system given by Eq. (I-37) is the mixture or overall continuity equation, Eq. (I-32). We will provide here the details of the derivation of that equation, then merely list the other equations. Under equilibrium, we know that

$$\begin{aligned} T_l &= T_g = T \quad , \\ \rho_a &= \rho_a(p_a, T) \quad , \\ \rho_v &= \rho_v(p_v \text{ only}) \quad , \text{ and} \\ \rho_l &= \rho_l(p, T) \quad , \end{aligned} \tag{I-38}$$

which results in

$$
\begin{aligned}
d\rho_a &= \left(\frac{\partial \rho_a}{\partial p_a}\right)_T dp_a + \left(\frac{\partial \rho_a}{\partial T}\right)_{p_a} dT \\
&= \left(\frac{\partial \rho_a}{\partial p_a}\right)_T dp_a + \left(\frac{\partial \rho_a}{\partial T}\right)_{p_a} \frac{dT}{dp_v} dp_v , \\
d\rho_l &= \left(\frac{\partial \rho_l}{\partial p}\right)_T dp + \left(\frac{\partial \rho_l}{\partial T}\right)_p dT \\
&= \left(\frac{\partial \rho_l}{\partial p}\right)_T (dp_a + dp_v) + \left(\frac{\partial \rho_l}{\partial T}\right)_p \frac{dT}{dp_v} dp_v \\
&= \left(\frac{\partial \rho_l}{\partial p}\right)_T dp_a + \left[\left(\frac{\partial \rho_l}{\partial p}\right)_T + \left(\frac{\partial \rho_l}{\partial T}\right)_p \frac{dT}{dp_v}\right] dp_v \qquad \text{(I-39)} \\
&\doteq \left(\frac{\partial \rho_l}{\partial p}\right)_T dp_a + \rho_l^* dp_v \quad , \quad \text{and} \\
d\rho_v &= \left(\frac{\partial \rho_v}{\partial p_v}\right)_T dp_v + \left(\frac{\partial \rho_v}{\partial T}\right)_{p_v} dT \\
&= \left(\frac{\partial \rho_v}{\partial p_v}\right)_T dp_v + \left(\frac{\partial \rho_v}{\partial T}\right)_{p_v} \frac{dT}{dp_v} dp_v \\
&\doteq \rho_v^* dp_v \quad .
\end{aligned}
$$

Expanding the differential terms of Eq. (I-32),

$$d\rho_m = \alpha d\rho_a + \alpha d\rho_v + \rho_g d\alpha + (1-\alpha) d\rho_l - \rho_l d\alpha$$

and

$$
\begin{aligned}
d(\rho_m V_m) = {} & \alpha \rho_g dV_g + \alpha V_g (d\rho_a + d\rho_v) + \rho_g V_g d\alpha \\
& + (1-\alpha)\rho_l dV_l + (1-\alpha) V_l d\rho_l - \rho_l V_l d\alpha \quad .
\end{aligned}
\qquad \text{(I-40)}
$$

Using the relationships derived above and rearranging, Eq. (I-32) can be written as

$$\left\{\alpha\left[\left(\frac{\partial\rho_a}{\partial T}\right)_{p_a}\frac{dT}{dp_v}+\rho_v^*\right]+(1-\alpha)\rho_l^*\right\}\frac{\partial p_v}{\partial t}+(\rho_g-\rho_l)\frac{\partial\alpha}{\partial t}$$
$$+\ 0\cdot\frac{\partial V_g}{\partial t}+0\cdot\frac{\partial V_l}{\partial t}+\left[\alpha\left(\frac{\partial\rho_a}{\partial p}\right)_T+(1-\alpha)\left(\frac{\partial\rho_l}{\partial p}\right)_T\right]\frac{\partial p_a}{\partial t}$$
$$+\left\{V_g\alpha\left[\left(\frac{\partial\rho_a}{\partial T}\right)_{p_a}\frac{dT}{dp_v}+\rho_v^*\right]+V_l(1-\alpha)\rho_l^*\right\}\frac{\partial p_v}{\partial x}+(\rho_g V_g-\rho_l V_l)\frac{\partial\alpha}{\partial t} \qquad \text{(I-41)}$$
$$+\ \alpha\rho_g\frac{\partial V_g}{\partial x}+(1-\alpha)\rho_l\frac{\partial V_l}{\partial x}+\left[V_g\alpha\left(\frac{\partial\rho_a}{\partial p}\right)_T+V_l(1-\alpha)\left(\frac{\partial\rho_l}{\partial_p}\right)_T\right]\frac{\partial p_a}{\partial t}$$
$$=0\quad .$$

The complete matrices for the system are given in Figs. I-9.a and I-9.b, where

$$s_v^*=\frac{1}{T}\left[\left(\frac{\partial e_v}{\partial p_v}\right)_T+\left(\frac{\partial e_v}{\partial T}\right)_{p_v}\frac{dT}{dp_v}\right]-\frac{p_v}{\rho_v^2 T}\left[\left(\frac{\partial\rho_v}{\partial p_v}\right)_T+\left(\frac{\partial\rho_v}{\partial T}\right)_{p_v}\frac{dt}{dp_v}\right]$$

and

$$s_l^*=\frac{1}{T}\left[\left(\frac{\partial e_l}{\partial p}\right)_T+\left(\frac{\partial e_l}{\partial T}\right)_p\frac{dT}{dp_v}\right]-\frac{p}{\rho_l^2 T}\left[\left(\frac{\partial\rho_l}{\partial p}\right)_T+\left(\frac{\partial\rho_l}{\partial T}\right)_p\frac{dT}{dp_v}\right]\quad . \qquad \text{(I-42)}$$

With p, p_a, and T known, all of the thermodynamic partial derivatives used in the above equations are obtained by a call to subroutine THERMO.

The characteristic roots, λ_i, of the above system of equations are defined as the roots of the fifth-order polynomial,

$$\text{determinant}\ (\underline{\underline{A}}\lambda - \underline{\underline{B}}) = 0\ . \qquad \text{(I-43)}$$

Choking occurs when the signal propagating with the largest velocity relative to the fluid is stationary; that is, the maximum value of the real part of a characteristic root, $\lambda_{i,\,re,max}$, is zero. Equation (I-43) is extremely difficult to solve analytically. Thus, TRAC obtains the characteristic roots of Eq. (I-43) numerically. This method advantageously maintains generality and facilitates computations under different assumptions. The calculational sequence for the TRAC two-phase choking model is described in Section I.2.4.

$$\underline{\underline{A}} = \begin{bmatrix} \alpha\left[\left(\frac{\partial \rho_a}{\partial T}\right)_{p_a}\frac{\mathrm{d}T}{\mathrm{d}p_v}+\rho_v^*\right] & \rho_g-\rho_l & 0 & 0 & \alpha\left(\frac{\partial \rho_a}{\partial p}\right)_T \\ +(1-\alpha)\rho_l^* & & & & +(1-\alpha)\left(\frac{\partial \rho_l}{\partial p}\right)_T \\ 0 & 0 & \alpha\rho_g & -C\alpha(1-\alpha)\rho_m & 0 \\ & & +C\alpha(1-\alpha)\rho_m & & \\ 0 & 0 & -C\alpha(1-\alpha)\rho_m & (1-\alpha)\rho_l & 0 \\ & & & +C\alpha(1-\alpha)\rho_m & \\ \alpha\left[-\rho_v s_v^*+s_v\rho_v^*+\frac{\mathrm{d}T}{\mathrm{d}p_v}\right. & \left(\rho_g s_g-\rho_l s_l\right) & 0 & 0 & \alpha\left[\rho_a\left(\frac{\partial s_a}{\partial p_a}\right)_T\right. \\ \left.\left(\rho_a\left(\frac{\partial s_a}{\partial T}\right)_{p_a}+s_a\left(\frac{\rho_a}{\partial T}\right)_{p_a}\right)\right] & & & & \left.+s_a\left(\frac{\partial \rho_a}{\partial p_a}\right)_T\right] \\ +(1-\alpha)\left[\rho_l s_l+\rho_l s_l^*\right] & & & & +(1-\alpha)\left[\rho_l\left(\frac{\partial s_l}{\partial p}\right)_T\right. \\ & & & & \left.+s_l\left(\frac{\partial \rho_l}{\partial p_l}\right)_T\right] \\ \alpha\left(\frac{\partial \rho_a}{\partial T}\right)_{p_a}\frac{\mathrm{d}T}{\mathrm{d}p_v} & \rho_a & 0 & 0 & \alpha\left(\frac{\partial \rho_a}{\partial p_a}\right)_T \end{bmatrix} \begin{bmatrix} \frac{\partial p_v}{\partial t} \\ \\ \frac{\partial \alpha}{\partial t} \\ \frac{\partial V_g}{\partial t} \\ \\ \frac{\partial V_l}{\partial t} \\ \\ \\ \\ \frac{\partial p_a}{\partial t} \end{bmatrix}$$

Fig. I-9.a Matrix $\underline{\underline{A}}$.

$$\underline{\underline{B}} = \begin{bmatrix} V_g\alpha\left[\left(\frac{\partial \rho_a}{\partial T}\right)_{p_a}\frac{\mathrm{d}T}{\mathrm{d}p_v}+\rho_v^*\right] & \rho_g V_g-\rho_l V_l & \alpha\rho_g & (1-\alpha)\rho_l & V_g\alpha\left(\frac{\partial \rho_a}{\partial p_\delta}\right)_T \\ +V_l(1-\alpha)\rho_l^* & & & & +V_l(1-\alpha)\left(\frac{\partial \rho_l}{\partial p}\right)_T \\ \alpha & 0 & V_g\alpha\rho_g & -V_g C\alpha(1-\alpha)\rho_m & \alpha \\ & & +V_l C\alpha(1-\alpha)\rho_m & & \\ (1-\alpha) & 0 & -V_l C\alpha(1-\alpha)\rho_m & V_g C\alpha(1-\alpha)\rho_m & (1-\alpha) \\ & & & +V_l(1-\alpha)\rho_l & \\ V_g\alpha\left[-\rho_v s_v^*+s_v\rho_v^*\right. & V_g\rho_g s_g-V_l\rho_l s_l & \alpha\rho_g s_g & (1-\alpha)\rho_l s_l & V_g\alpha\left[\rho_a\left(\frac{\partial s_a}{\partial p_a}\right)_T\right. \\ +\frac{\mathrm{d}T}{\mathrm{d}p_v}\left(\rho_a\left(\frac{\partial s_a}{\partial T}\right)_{p_a}\right. & & & & \left.+s_a\left(\frac{\partial \rho_a}{\partial p_a}\right)_T\right] \\ \left.\left.+s_a\left(\frac{\partial \rho_a}{\partial T}\right)_{p_a}\right)\right] & & & & +V_l(1-\alpha)\left[\rho_l\left(\frac{\partial s_l}{\partial p}\right)_T\right. \\ +V_l(1-\alpha)\left[\rho_l s_l^*+s_l\rho_l^*\right] & & & & \left.+s_l\left(\frac{\partial \rho_l}{\partial p}\right)_T\right] \\ V_g\alpha\left(\frac{\partial \rho_a}{\partial T}\right)_{p_a}\frac{\mathrm{d}T}{\mathrm{d}p_v} & V_g\rho_a & \alpha\rho_a & 0 & V_g\alpha\left(\frac{\partial \rho_a}{\partial p_a}\right)_T \end{bmatrix} \begin{bmatrix} \frac{\partial p_v}{\partial x} \\ \\ \frac{\partial \alpha}{\partial x} \\ \frac{\partial V_g}{\partial x} \\ \\ \frac{\partial V_l}{\partial x} \\ \\ \\ \\ \frac{\partial p_a}{\partial x} \end{bmatrix}$$

Fig. I-9.b Matrix $\underline{\underline{B}}$.

I.2.1.3. Single-Phase Vapor. The single-phase vapor choked-flow model is based on isentropic expansion of an ideal gas (Ref. I-4., p. 515). A throat pressure, p_e, is calculated from the stagnation pressure, p_o, such that

$$p_e = p_o \left(\frac{2}{\gamma + 1} \right)^{\gamma / \gamma - 1} \quad , \tag{I-44}$$

where γ is the specific-heat ratio. A downstream throat temperature, T_e, is calculated from the stagnation temperature, T_o, using the ideal-gas relation

$$T_e = T_o \left(\frac{2}{\gamma + 1} \right) \quad . \tag{I-45}$$

When T_e is greater than the saturation temperature at p_e, the fluid flow at the throat is predicted to be superheated by the ideal-gas relations. The continuity equation, in conjunction with the ideal-gas relations, yields a fluid choking velocity,

$$V_{ge} = \sqrt{\frac{2\gamma}{\gamma + 1} R T_o} \quad , \tag{I-46}$$

where R is the gas constant.

If T_e is less than or equal to the saturation temperature at p_e, then the fluid flow at the throat is not predicted to be superheated by the ideal-gas relations, and the choking velocity is calculated using iterations to maximize mass flux along the isentrope that extends from the superheated conditions upstream of the throat to the two-phase conditions at the throat. This method assumes that no delay in condensation occurs as the steam expands to the saturated two-phase state at the throat.

The calculational sequence for the TRAC single-phase vapor choking model is described in Section I.2.4.

I.2.1.4. Transition Regions. Because there is a discontinuity in the sound speed during the transition from liquid to two-phase flow, the flow during this transition regime must be analyzed carefully. In TRAC, this transition is handled by linear interpolation between the subcooled ($\alpha \leq 0.01$) and the two-phase ($\alpha \geq 0.1$) regimes. The calculational sequence for the TRAC transition region is described in Section I.2.4.

The transition from the two-phase to the vapor-phase regime is smooth because the two-phase characteristic solution approaches the homogeneous equilibrium limit as $\alpha \rightarrow 1$. Thus, this transition is made by switching the calculational logic at $\alpha = 0.999$.

I.2.2. Assumptions and Preliminary Calculations

I.2.2.1. Cell-Center Momentum-Solution Velocities. The velocities obtained from the momentum solution are cell-edge values. However, in order to evaluate stagnation conditions (in subroutine SOUND), it is necessary to know the phasic velocities at cell center. This transition between cell edge and cell center is accomplished in subroutine VOLV by averaging the mass flux between cell edges, such that

$$V_{gc} = \frac{\frac{1}{2}\left[(\rho_g\alpha)_{e^-} V_{g,e^-} A_{e^-} + (\rho_g\alpha)_{e^+} V_{g,e^+} A_{e^+}\right]}{\rho_{gc}\alpha_c A_c} \tag{I-47}$$

and

$$V_{lc} = \frac{\frac{1}{2}\left[(\rho_l(1-\alpha))_{e^-} V_{l,e^-} A_{e^-} + (\rho_l(1-\alpha))_{e^+} V_{l,e^+} A_{e^+}\right]}{\rho_{lc}(1-\alpha)_c A_c} \quad , \tag{I-48}$$

where V_{gc} and V_{lc} are the transformed cell-center velocities, ρ_g and ρ_l are the steam/gas-mixture and liquid densities, α is the void fraction, V_l and V_g are the liquid and steam/gas-mixture velocities, and A is the cross-sectional flow area. The subscripts e^- and e^+ refer to upstream cell-edge and downstream cell-edge quantities, while the subscript c refers to cell-center quantities for the particular cell in question. It is assumed that $\rho\alpha$ at the upstream face is equal to the upstream cell product value, whereas $\rho\alpha$ at the downstream face is taken to be equal to the current cell value because densities and void fractions are normally associated with cell-center rather than with cell-edge positions.

I.2.2.2. Subroutine SOUND. The evaluation of Eqs. (I-30) and (I-31) in the subcooled-liquid choking model and the solution of Eq. (I-43) in the two-phase, two-component choking model require that conditions at the cell-edge where the choking criterion is applied be known. Subroutine CHOKE calls subroutine SOUND to calculate a homogeneous equilibrium sound speed and to estimate the corresponding cell-edge conditions, given the conditions at cell center. Three basic calculational sequences exist in subroutine SOUND:

1. If the cell contains pure noncondensable gas, the homogeneous equilibrium sound speed and corresponding cell-edge conditions are computed by assuming an isentropic expansion of an ideal gas.
2. If the cell length-to-hydraulic-diameter ratio, L/D, is greater than or equal to 1.5, or if some noncondensable gas is present in the vapor phase of a two-phase flow at cell center (regardless of the value of L/D), then the conditions at cell center are required to come to equilibrium by means of an isenthalpic process before stagnation conditions are calculated. Once the stagnation conditions have been determined, a homogeneous equilibrium sound speed and the corresponding cell-edge conditions are calculated by first assuming thermal equilibrium and no slip at the cell

edge and an isentropic expansion from stagnation to cell edge. We then iterate for the cell-edge pressure, which results in the maximum or critical mass flux at the cell edge (a classical technique used in generating the HEM tables).

3. If the cell length-to-hydraulic-diameter ratio, L/D, is less than 1.5, or if only the superheated vapor phase or the subcooled-liquid phase exists at the cell center, then the stagnation conditions are calculated from the actual cell-center properties, rather than from the effective equilibrium properties as in (2). Once stagnation conditions have been determined, a homogeneous equilibrium sound speed and the corresponding cell-edge conditions are determined either by assuming an isentropic expansion of an ideal gas (for the case of superheated vapor phase at the cell edge) or by iterating for the cell-edge pressure, which gives the maximum mass flux as in (2) above. The details of each procedure follow.

I.2.2.2.1. Isentropic Expansion of Ideal Gas. When the cell-center conditions represent a pure noncondensable-gas field, the sound speed and cell-edge conditions are calculated using ideal-gas theory. First, a cell-edge temperature and a cell-edge pressure are computed, such that

$$T_e = \frac{2T_g}{\gamma_a + 1}\left(1 + \frac{V_{gc}^2}{2c_{pa}T_g}\right) \tag{I-49}$$

and

$$p_e = p\left[\frac{2}{\gamma_a + 1}\left(1 + \frac{V_{gc}^2}{2c_{pa}T_g}\right)\right]^{\gamma_a/(\gamma_a - 1)} , \tag{I-50}$$

where T_g is the cell-center gas temperature, γ_a is the specific heat ratio for the noncondensable gas (as defined in subroutine SETEOS), V_{gc} is the cell-center gas velocity [as computed in Eq. (I-47)], c_{pa} is the constant-pressure specific heat for the noncondensable gas (as defined in subroutine SETEOS), and p is the cell-center total pressure.

Next, a cell-edge noncondensable-gas density is calculated according to

$$\rho_{ae} = \frac{p_e}{R_a T_e} , \tag{I-51}$$

where R_a is the noncondensable-gas constant (as defined in subroutine SETEOS), and p_e and T_e, are the cell-edge pressure and temperature calculated above.

The gas sound speed now becomes

$$a_{\mathrm{HE}} = \sqrt{\gamma_a R_a T_e} \quad , \tag{I-52}$$

where γ_a is the specific heat ratio for the noncondensable gas (as defined in subroutine SETEOS), R_a is the noncondensable-gas constant (also defined in subroutine SETEOS), and T_e is the cell-edge temperature calculated in Eq. (I-49) above.

This concludes the calculation of the gas sound speed and cell-edge conditions for the case of pure noncondensable gas at cell center. At this point, the logic returns to subroutine CHOKE.

I.2.2.2.2. L/D $\leq$ 1.5 or Noncondensable Gas Present in Two-Phase Flow at Cell Center. Subroutine SOUND calculates the stagnation conditions using the effective equilibrium void fraction, rather than the actual void fraction, if the cell center is not in equilibrium. The calculational sequence to arrive at the cell-edge conditions and the homogeneous equilibrium sound speed is as follows.

Initially, subroutine THERMO is called with the actual cell-center total pressure, p; the partial pressure of any noncondensable gas that may be present, p_a; and the steam/gas-mixture and liquid temperatures, T_g and T_l. With these variables, THERMO calculates the actual mixture density, actual quality, and liquid, steam, noncondensable-gas, steam/gas-mixture, and steam/liquid-water-mixture enthalpies:

$$\rho_m = \alpha_{\mathrm{actual}} \rho_g + (1 - \alpha_{\mathrm{actual}}) \rho_l \quad , \tag{I-53}$$

$$x_{\mathrm{actual}} = \alpha_{\mathrm{actual}} \left(\frac{\rho_g}{\rho_m} \right) \quad , \tag{I-54}$$

$$h_l = e_l + \frac{p}{\rho_l} \quad , \tag{I-55}$$

$$h_v = e_v + \frac{p - p_a}{\rho_g - \rho_a} \quad , \tag{I-56}$$

$$h_a = e_a + \frac{p_a}{\rho_a + 1.0 \times 10^{-20}} \quad , \tag{I-57}$$

$$h_g = e_g + \frac{p}{\rho_g} \quad , \tag{I-58}$$

and

$$h_m = x_{\text{actual}} h_v + (1 - x_{\text{actual}}) h_l \quad , \tag{I-59}$$

where α_{actual} is the actual cell-center void fraction, x_{actual} is the actual cell-center quality, and all fluid properties are actual cell-center values.

If the cell-center conditions do not represent an equilibrium state, an effective equilibrium void fraction at the cell center is determined assuming an isenthalpic process from the actual cell-center state. A call to subroutine THERMO with the saturation temperature corresponding to the cell-center partial pressure of steam allows cell-center liquid, steam, noncondensable-gas, and steam/gas-mixture saturated enthalpies to be determined. From this the equilibrium quality at cell center and equilibrium void fraction at cell center may be calculated, such that

$$x_{\text{equil}} = \frac{h_m - h_{l,\text{equil}}}{h_{v,\text{equil}} - h_{l,\text{equil}} + \frac{\rho_{a,\text{equil}}}{\rho_{g,\text{equil}}}(h_{a,\text{equil}} - h_a - h_{v,\text{equil}} + h_v)} \tag{I-60}$$

and

$$\alpha_{\text{equil}} = \frac{x_{\text{equil}}\, \rho_{l,\text{equil}}}{\rho_{g,\text{equil}} + x_{\text{equil}}(\rho_{l,\text{equil}} - \rho_{g,\text{equil}})} \quad , \tag{I-61}$$

where h_m is the cell-center steam/liquid-water-mixture actual enthalpy from Eq. (I-59); $h_{l,\text{equil}}$, $h_{v,\text{equil}}$, and $h_{a,\text{equil}}$ are the cell-center liquid, steam, and noncondensable-gas equilibrium enthalpies for the saturation temperature corresponding to the cell-center partial pressure of steam; h_v and h_a are the cell-center steam and noncondensable-gas actual enthalpies [Eqs. (I-56) and (I-57)]; and $\rho_{l,\text{equil}}$, $\rho_{a,\text{equil}}$, and $\rho_{g,\text{equil}}$ are the cell-center liquid, noncondensable-gas, and steam/gas-mixture equilibrium densities for the saturation temperature corresponding to the cell-center partial pressure of steam.

Such quantities as constant-pressure specific heats, constant-volume specific heats, and specific-heat ratios are now defined for the fluid. If the fluid at cell center is a single-phase saturated vapor, the steam specific-heat ratio is defined as

$$\gamma_v = 1.3 \quad . \tag{I-62}$$

However, if the fluid at cell center is two-phase or subcooled, the steam ratio of specific heats is defined as

$$\gamma_v = 1.035 + 0.1\alpha_{\text{equil}} \left(\frac{\rho_{g,\text{equil}} - \rho_{a,\text{equil}}}{\alpha_{\text{equil}} \rho_{g,\text{equil}} + (1 - \alpha_{\text{equil}}) \rho_{l,\text{equil}}} \right) \quad , \tag{I-63}$$

where α_{equil} is the cell-center equilibrium void fraction and $\rho_{g,\text{equil}}$, $\rho_{a,\text{equil}}$, and $\rho_{\text{l,equil}}$ are cell-center steam/gas-mixture, noncondensable-gas, and liquid equilibrium densities at the saturation temperature corresponding to the cell-center partial pressure of steam.

The steam and steam/gas-mixture specific heats are then defined, such that

$$c_{pv} = \frac{\gamma_v R_v}{\gamma_v - 1} \quad , \tag{I-64}$$

$$c_{vv} = c_{pv} - R_v \quad , \tag{I-65}$$

$$c_{pg} = c_{pa}\left(\frac{\rho_{a,\text{equil}}}{\rho_{g,\text{equil}}}\right) + c_{pv}\left(1 - \frac{\rho_{a,\text{equil}}}{\rho_{g,\text{equil}}}\right) \quad , \tag{I-66}$$

and

$$c_{vg} = c_{va}\left(\frac{\rho_{a,\text{equil}}}{\rho_{g,\text{equil}}}\right) + c_{vv}\left(1 - \frac{\rho_{a,\text{equil}}}{\rho_{g,\text{equil}}}\right) \quad , \tag{I-67}$$

where γ_v is the steam specific-heat ratio [as defined by Eqs. (I-62) or (I-63)], R_v is the steam gas constant (defined by subroutine SETEOS), and $\rho_{a,\text{equil}}$ and $\rho_{g,\text{equil}}$ are the cell-center noncondensable-gas and steam/gas-mixture equilibrium densities at the saturation temperature corresponding to the cell-center partial pressure of steam.

The steam/gas-mixture ratio of specific heats becomes

$$\gamma_g = \frac{c_{pg}}{c_{vg}} \quad . \tag{I-68}$$

Cell-center liquid, steam, noncondensable-gas, steam/gas-mixture, and steam/liquid-water-mixture equilibrium entropies for the saturation temperature corresponding to the cell-center partial pressure of steam are calculated, such that

$$s_{\text{l,equil}} = c_{v\text{l}} \ln\left(\frac{T_{sv}}{273.15}\right) \quad , \tag{I-69}$$

$$s_{v,\text{equil}} = c_{v\text{l}} \ln\left(\frac{T_{sv}}{273.15}\right) + \frac{h_{fg,\text{equil}}}{T_{sv}} \quad , \tag{I-70}$$

$$s_{a,\text{equil}} = c_{pa} \ln\left(\frac{T_{sv}}{273.15}\right) - R_a \ln\left(\frac{\max\left\{p_a,\ 1.0\times10^{-5}\right\}}{1.0\times10^{5}}\right) \quad , \tag{I-71}$$

$$s_{g,\text{equil}} = s_{a,\text{equil}}\left(\frac{\rho_{a,\text{equil}}}{\rho_{g,\text{equil}}}\right) + s_{v,\text{equil}}\left(1-\frac{\rho_{a,\text{equil}}}{\rho_{g,\text{equil}}}\right) \quad , \tag{I-72}$$

and

$$s_{m,\text{equil}} = x_{\text{equil}} s_{v,\text{equil}} + (1-x_{\text{equil}}) s_{\text{l},\text{equil}} \quad , \tag{I-73}$$

where T_{sv} is the saturation temperature corresponding to the cell-center partial pressure of steam, $c_{v\text{l}}$ is the liquid constant-volume specific heat (defined in subroutine SETEOS), $h_{fg,\text{equil}}$ is the latent heat of vaporization at T_{sv}, c_{pa} is the noncondensable-gas constant-pressure specific heat (defined by subroutine SETEOS), R_a is the noncondensable-gas constant (defined in subroutine SETEOS), p_a is the cell-center partial pressure of the noncondensable gas, $\rho_{a,\text{equil}}$ and $\rho_{g,\text{equil}}$ are the cell-center noncondensable-gas and steam / gas-mixture equilibrium densities at the saturation temperature corresponding to the cell-center partial pressure of steam, and x_{equil} is the cell-center effective equilibrium quality as computed in Eq. (I-60).

Finally, stagnation conditions are computed according to the following:

$$h_o = x_{\text{equil}}\left(h_{g,\text{equil}} + \frac{1}{2}V_{gc}^2\right) + (1-x_{\text{equil}})\left(h_{\text{l},\text{equil}} + \frac{1}{2}V_{\text{l}c}^2\right) \quad , \tag{I-74}$$

$$p_o = x_{\text{equil}} p\left(1+\frac{1}{2}\frac{V_{gc}^2}{c_{pg}T_{sv}}\right)^{\frac{\gamma_g}{\gamma_g - 1}} + (1-x_{\text{equil}})\left(p + \frac{1}{2}\rho_{\text{l}}V_{\text{l}c}^2\right) \quad , \tag{I-75}$$

and

$$s_o = x_{\text{equil}} s_{g,\text{equil}} + (1-x_{\text{equil}}) s_{\text{l},\text{equil}} \quad , \tag{I-76}$$

where x_{equil} is the cell-center effective equilibrium quality as computed in Eq. (I-60), $h_{\text{l,equil}}$ and $h_{g,\text{equil}}$ are the cell-center liquid and steam / gas-mixture equilibrium enthalpies evaluated at the saturation temperature corresponding to the cell-center partial pressure of steam, $V_{\text{l}c}$ and V_{gc} are the cell-center liquid and steam / gas-mixture velocities [as computed in Eqs. (I-47) and (I-48)], p is the cell-center total pressure, γ_g is the ratio of specific heats [as defined in Eq. (I-68)], c_{pg} is the steam / gas-mixture specific heat at constant pressure [as defined in Eq. (I-66)], T_{sv} is the saturation temperature corresponding to the cell-center partial pressure of steam, ρ_{l} is the cell-center liquid actual density, and $s_{\text{l,equil}}$ and $s_{g,\text{equil}}$ are the cell-center liquid and steam / gas-mixture

equilibrium entropies evaluated at the saturation temperature corresponding to the cell-center partial pressure of steam [as in Eqs. (I-69) and (I-72)].

Iterations can now be performed to determine the maximum mass flux and the corresponding cell-edge conditions.

An initial cell-edge pressure equal to that predicted by ideal-gas expansion theory is guessed by using the relationship

$$p_e = p_o \left(\frac{2}{\gamma_g + 1} \right)^{\gamma_g / (\gamma_g - 1)} \quad , \tag{I-77}$$

where p_o is the stagnation pressure [as in Eq. (I-75)] and γ_g is the steam/gas-mixture specific-heat ratio [as in Eq. (I-68)].

Subroutine THERMO is then called to determine the saturation properties at the cell edge corresponding to the cell-edge pressure, p_e.

Saturated cell-edge values for liquid, steam, and steam/gas-mixture enthalpies and for liquid, steam, and noncondensable-gas entropies are computed, such that

$$h_{le} = e_{le} + \frac{p_e}{\rho_{le}} \quad , \tag{I-78}$$

$$h_{ve} = e_{ve} + \frac{p_e - p_{ae}}{\rho_{ge} - \rho_{ae}} \quad , \tag{I-79}$$

$$h_{ge} = e_{ge} + \frac{p_e}{\rho_{ge}} \quad , \tag{I-80}$$

$$s_{le} = c_{vl} \ln \left(\frac{T_e}{273.15} \right) \quad , \tag{I-81}$$

$$s_{ve} = s_{le} + \frac{h_{ve} - h_{le}}{T_e} \quad , \tag{I-82}$$

and

$$s_{ae} = c_{pa} \ln \left(\frac{T_e}{273.15} \right) - R_a \ln \left(\frac{\min\{p_{ae},\ 1.0 \times 10^{-5}\}}{1.0 \times 10^5} \right) \quad , \tag{I-83}$$

where e_{le}, e_{ve}, and e_{ge} are the cell-edge liquid, steam, and steam/gas-mixture saturated internal energies for the pressure p_e; p_e is the cell-edge pressure; p_{ae} is the cell-edge partial pressure of the noncondensable gas given by $p_{ae} = p_a(p_e)/p$; ρ_{le}, ρ_{ae}, and ρ_{ge} are the cell-edge liquid, noncondensable-gas, and steam/gas-mixture saturated densities for the pressure p_e; c_{vl} is the liquid constant-volume specific heat (as defined in subroutine SETEOS); T_e is the cell-edge temperature equal to the saturation temperature at p_e; c_{pa} is the noncondensable-gas constant-pressure specific heat (as defined in subroutine SETEOS); and R_a is the noncondensable-gas constant (as defined in subroutine SETEOS).

Then, assuming a constant entropy expansion from the stagnation condition, a cell-edge quality may be calculated from

$$x_e = \frac{s_{m,\text{equil}} - s_{le}}{s_{ve,} - s_{le} + \left(\frac{\rho_{ae}}{\rho_{ge}}\right)\left(s_{ae} - s_{a,\text{equil}} - s_{ve} - s_{v,\text{equil}}\right)} \quad , \tag{I-84}$$

where $s_{m,\text{equil}}$, $s_{v,\text{equil}}$, and $s_{a,\text{equil}}$ are the cell-center steam/liquid-water-mixture, steam, and noncondensable-gas equilibrium entropies for the saturation temperature corresponding to the cell-center partial pressure of steam [as in Eqs. (I-73), (I-70), and (I-71)]; s_{le}, s_{ve}, and s_{ae} are the cell-edge liquid, steam, and noncondensable-gas saturated entropies for the pressure p_e [as computed above in Eqs. (I-81), (I-82), and (I-83)]; and ρ_{ae} and ρ_{ge} are the cell-edge noncondensable-gas and steam/gas-mixture saturated densities for the pressure p_e.

Once the cell-edge quality has been determined, a cell-edge total mixture enthalpy and cell-edge total mixture density are calculated as follows:

$$h_{me} = x_e h_{ge} + (1 - x_e) h_{le} \tag{I-85}$$

and

$$\rho_{me} = \frac{\rho_{le}\rho_{ge}}{x_e(\rho_{le} - \rho_{ge}) + \rho_{ge}} \quad , \tag{I-86}$$

where x_e is the cell-edge quality [as in Eq. (I-84)]; h_{le} and h_{ge} are the cell-edge liquid and steam/gas-mixture saturated enthalpies for the pressure p_e [as in Eqs. (I-78) and (I-80)]; and ρ_{le} and ρ_{ge} are the cell-edge liquid and steam/gas-mixture saturated densities for the pressure p_e.

The mass flux, then, for a cell-edge pressure of p_e becomes

$$G = \rho_{me}\sqrt{2(h_o - h_{me})}, \tag{I-87}$$

where ρ_{me} is the cell-edge total mixture density [as in Eq. (I-86)], h_o is the stagnation enthalpy [as in Eq. (I-74)], and h_{me} is the cell-edge total mixture enthalpy [as in Eq. (I-85)].

The pressure is varied slightly and the iteration is repeated until the pressure that gives the maximum or critical mass flux as predicted by Eq. (I-87) is determined. Once the cell-edge pressure corresponding to the critical flux has been found, the saturated cell-edge conditions become known, and a homogeneous equilibrium sound speed, a_{HE}, is computed as follows:

$$a_{\mathrm{HE}} = \frac{G_{\max}}{\rho_{me}} \quad . \tag{I-88}$$

This concludes the calculation of the homogeneous equilibrium sound speed and the corresponding cell-edge conditions for the case of nonsuperheated vapor phase at cell center when $\mathrm{L/D} \geq 1.5$ or when noncondensable gas is present in two-phase cell-center flow. At this point, the logic returns to subroutine CHOKE.

I.2.2.2.3. L/D < 1.5 or Only Superheated Vapor Phase, or Only Subcooled-Liquid Phase Present at Cell Center. In this case, instead of allowing the cell-center conditions to come to equilibrium along an isenthalpic process (if the cell center is not originally in equilibrium), the stagnation conditions are derived from the cell-center actual properties. The method of arriving at these stagnation conditions follows that of the $\mathrm{L/D} \geq 1.5$ case, except that actual properties are used instead of equilibrium properties. Then, as in the case for $\mathrm{L/D} \geq 1.5$, SOUND determines a homogeneous equilibrium sound speed and the corresponding cell-edge conditions by again assuming thermal equilibrium, no slip at the cell edge, and a constant entropy expansion between stagnation and cell edge, and by again iterating for the cell-edge pressure that gives the maximum mass flux at the cell edge if two-phase flow is predicted at the cell edge. Otherwise, the homogeneous equilibrium sound speed and corresponding cell-edge conditions are found by assuming an isentropic expansion of the superheated vapor phase existing at cell center according to ideal-gas behavior. The following gives the exact coding in detail.

As before, subroutine THERMO is called with the actual cell-center total pressure, p; the partial pressure of any noncondensable gas that may be present, p_a; and the steam/gas-mixture and liquid-phase temperatures, T_g and T_l. With these variables, THERMO calculates such properties as actual mixture density, actual quality, and liquid, steam, noncondensable-gas, steam/gas-mixture, and steam/liquid-water-mixture enthalpies, such that,

$$\rho_m = \alpha_{\mathrm{actual}}\,\rho_g + (1-\alpha_{\mathrm{actual}})\rho_l \quad , \tag{I-89}$$

$$x_{\mathrm{actual}} = \alpha_{\mathrm{actual}}\left(\frac{\rho_g}{\rho_m}\right) \quad , \tag{I-90}$$

$$h_l = e_l + \frac{p}{\rho_l} \quad , \tag{I-91}$$

$$h_v = e_v + \frac{p - p_a}{\rho_g - \rho_a} \quad , \tag{I-92}$$

$$h_a = e_a + \frac{p_a}{\rho_a + 1.0 \times 10^{-20}} \quad , \tag{I-93}$$

$$h_g = e_g + \frac{p}{\rho_g} \quad , \tag{I-94}$$

and

$$h_m = x_{\text{actual}} h_v + (1 - x_{\text{actual}}) h_l \quad , \tag{I-95}$$

where α_{actual} is the actual cell-center void fraction, x_{actual} is the actual cell-center quality, and all fluid properties are actual cell-center values.

Such quantities as constant-pressure specific heats, constant-volume specific heats, and specific-heat ratios are now defined for the fluid. If the fluid at cell center is a superheated vapor, the steam specific-heat ratio is defined as

$$\gamma_v = 1.3 \quad . \tag{I-96}$$

However, if the fluid at cell center is two-phase or subcooled, the steam ratio of specific heats is defined as

$$\gamma_v = 1.035 + 0.1 \alpha_{\text{actual}} \left(\frac{\rho_g - \rho_a}{\rho_m} \right) \quad , \tag{I-97}$$

where α_{actual} is the cell-center actual void fraction and ρ_g, ρ_a, and ρ_m are cell-center steam / gas-mixture, noncondensable-gas, and total mixture actual densities.

Next the steam and steam / gas-mixture specific heats are defined, such that

$$c_{pv} = \frac{\gamma_v R_v}{\gamma_v - 1} \quad , \tag{I-98}$$

$$c_{vv} = c_{pv} - R_v \quad , \tag{I-99}$$

$$c_{pg} = c_{pa}\left(\frac{\rho_a}{\rho_g}\right) + c_{pv}\left(1 - \frac{\rho_a}{\rho_g}\right) \quad , \tag{I-100}$$

and

$$c_{vg} = c_{va}\left(\frac{\rho_a}{\rho_g}\right) + c_{vv}\left(1 - \frac{\rho_a}{\rho_g}\right) \quad , \tag{I-101}$$

where γ_v is the steam specific-heat ratio [as defined by Eqs. (I-96) or (I-97)], R_v is the steam gas constant (defined by subroutine SETEOS), and ρ_a and ρ_g are the cell-center noncondensable-gas and steam / gas-mixture actual densities.

The steam / gas-mixture ratio of specific heats becomes

$$\gamma_g = \frac{c_{pg}}{c_{vg}} \quad . \tag{I-102}$$

Cell-center liquid, steam, noncondensable-gas, steam / gas-mixture, and steam / liquid-water-mixture actual entropies are calculated, such that

$$s_l = c_{vl} \ln\left(\frac{T_l}{273.15}\right) \quad , \tag{I-103}$$

$$s_v = c_{vl} \ln\left(\frac{T_{sv}}{273.15}\right) + \frac{h_{fg,\text{equil}}}{T_{sv}} + c_{pv} \ln\left(\frac{T_g}{T_{sv}}\right) \quad , \tag{I-104}$$

$$s_a = c_{pa} \ln\left(\frac{T_g}{273.15}\right) - R_a \ln\left(\frac{\max\left\{p_a,\ 1.0\times10^{-5}\right\}}{1.0\times10^{5}}\right) \quad , \tag{I-105}$$

$$s_g = s_a\left(\frac{\rho_a}{\rho_g}\right) + s_v\left(1 - \frac{\rho_a}{\rho_g}\right) \quad , \tag{I-106}$$

and

$$s_m = x_{\text{actual}} s_v + (1 - x_{\text{actual}}) s_l, \tag{I-107}$$

where T_l is the cell-center liquid temperature, T_{sv} is the saturation temperature corresponding to the cell-center partial pressure of steam, c_{vl} is the liquid constant-volume specific heat (defined in subroutine SETEOS), $h_{fg,\text{equil}}$ is the latent heat of vaporization at T_{sv}, c_{pv} and c_{pa} are the steam and noncondensable-gas constant-pressure specific heats [defined by Eq. (I-98) and subroutine SETEOS, respectively], T_g is the cell-center steam / gas-mixture temperature, R_a is the noncondensable-gas constant (defined in subroutine SETEOS), p_a is the cell-center partial pressure of the noncondensable gas, ρ_a and ρ_g are the cell-center noncondensable-gas and steam / gas-mixture actual densities, and x_{actual} is the cell-center actual quality as computed in Eq. (I-1).

Finally, stagnation conditions are computed according to the following:

$$h_o = x_{\text{actual}} \left(h_g + \frac{1}{2} V_{gc}^2 \right) + (1 - x_{\text{actual}}) \left(h_l + \frac{1}{2} V_{lc}^2 \right) \quad , \tag{I-108}$$

$$p_o = x_{\text{actual}}\, p \left(1 + \frac{1}{2} \frac{V_{gc}^2}{c_{pg} T_g} \right)^{\frac{\gamma_g}{\gamma_g - 1}} + (1 - x_{\text{actual}}) \left(p + \frac{1}{2} \rho_l V_{lc}^2 \right) \quad , \tag{I-109}$$

and

$$s_o = x_{\text{actual}} s_g + (1 - x_{\text{actual}}) s_l \quad , \tag{I-110}$$

where x_{actual} is the cell-center actual quality as computed in Eq. (I-90), h_l and h_g are the cell-center liquid and steam / gas-mixture actual enthalpies, V_{gc} and V_{lc} are the cell-center steam / gas-mixture and liquid velocities [as computed in Eqs. (I-47) and (I-48)], p is the cell-center total pressure, γ_g is the ratio of specific heats [as defined in Eq. (I-102)], c_{pg} is the steam / gas-mixture specific heat at constant pressure [as defined in Eq. (I-100)], T_g is the cell-center steam / gas-mixture temperature, ρ_l is the cell-center liquid actual density, and s_l and s_g are the cell-center liquid and steam / gas-mixture actual entropies [as in Eqs. (I-103) and (I-106)]. At this point, the logic splits to handle either superheated vapor phase at cell center or nonsuperheated vapor phase at cell center based on a check of the cell-center steam / gas-mixture temperature and the cell-center actual quality [Eq. (I-90)].

I.2.2.2.3.1. Superheated Vapor Phase at Cell Center. If the cell-center steam / gas-mixture temperature, T_g, is greater than the saturation temperature corresponding to the cell-center partial pressure of steam or if the cell-center actual quality [Eq. (I-90)] is equal to 1, then TRAC determines the cell-center fluid to be a superheated vapor phase, and the homogeneous equilibrium sound speed and corresponding cell-edge conditions are computed as follows.

A cell-edge pressure, p_e, is calculated from the stagnation pressure, p_o, using the ideal-gas expansion theory, such that

$$p_e = p_o \left(\frac{2}{\gamma_g + 1} \right)^{\gamma_g / (\gamma_g - 1)} \quad , \tag{I-111}$$

where γ_g is the steam / gas-mixture specific-heat ratio [as in Eq. (I-102)]. A downstream cell-edge temperature, T_e, is estimated from the cell-center steam / gas-mixture temperature, T_g, again using the ideal-gas expansion theory,

$$T_e = T_g \left(\frac{2}{\gamma_g + 1} \right) \quad , \tag{I-112}$$

where T_g is assumed to be close to the stagnation temperature.

When T_e is greater than the saturation temperature at p_e, the fluid flow at cell-edge is predicted to be superheated by the ideal-gas relations, and the following logic occurs. Subroutine THERMO is called to determine the cell-edge properties for the superheated steam / gas mixture at pressure p_e and temperature T_e. The continuity equation, in conjunction with the ideal-gas relations, then yields a cell-edge steam / gas-mixture choking velocity,

$$V_{ge} = \frac{p_o}{\rho_{ge} \sqrt{T_g}} \sqrt{\frac{\gamma_g}{R_g} \left(\frac{2}{\gamma_g + 1} \right)^{(\gamma_g + 1)/(\gamma_g - 1)}} \quad , \tag{I-113}$$

where p_o is the stagnation pressure [as in Eq. (I-109)]; ρ_{ge} is the cell-edge steam / gas-mixture density; T_g is the cell-center steam / gas-mixture temperature, which is assumed to be approximately equal to the stagnation temperature; and γ_g is the steam / gas-mixture specific-heat ratio [as in Eq. (I-102)]. R_g is the steam / gas-mixture gas constant and is defined by

$$R_g = R_a \left(\frac{\rho_a}{\rho_g} \right) + R_v \left(1 - \frac{\rho_a}{\rho_g} \right) \quad , \tag{I-114}$$

where R_v and R_a are the steam and noncondensable-gas constants (defined by subroutine SETEOS), ρ_a and ρ_g are the cell-center noncondensable-gas and steam / gas-mixture actual densities.

If, in addition, the enthalpy at cell edge is greater than the stagnation enthalpy, the first law of thermodynamics also is used to calculate a cell-edge steam / gas-mixture choking velocity,

$$V_{ge} = \sqrt{2(h_o - h_{ge})} \quad , \tag{I-115}$$

where h_o is the stagnation enthalpy [as in Eq. (I-107)] and h_{ge} is the steam/gas-mixture cell-edge enthalpy calculated from the cell-edge properties as

$$h_{ge} = e_{ge} + \frac{p_e}{\rho_{ge}} \quad . \tag{I-116}$$

When both Eqs. (I-113) and (I-115) are used to compute a velocity, the actual steam/gas-mixture choking velocity is chosen to be the larger of the two calculated values. This concludes the calculation of the homogeneous equilibrium sound speed and the corresponding cell-edge conditions for the case of a superheated vapor phase at cell edge. At this point, the logic returns to subroutine CHOKE.

When T_e is less than or equal to the saturation temperature at p_e, one additional check is made to determine whether the fluid at cell edge is a superheated vapor phase. A steam/gas-mixture sound speed at cell edge is calculated from

$$V_{ge} = \sqrt{2\left[h_o - \left(e_{ge} + \frac{p_e}{\rho_{ge}}\right)\right]} \quad , \tag{I-117}$$

where h_o is the stagnation enthalpy [as in Eq. (I-108)], p_e is the cell-edge pressure [as in Eq. (I-111)], and e_{ge} and ρ_{ge} are the cell-edge steam/gas-mixture internal energy and density as determined in the call to THERMO for the pressure p_e and the temperature T_e.

In addition, a sound speed for an ideal gas at the same temperature is calculated from

$$a_{\mathrm{HE}} = \sqrt{\gamma_g R_g T_e} \quad , \tag{I-118}$$

where γ_g is the steam/gas-mixture specific-heat ratio [Eq. (I-102)], R_g is the steam/gas-mixture gas constant [Eq. (I-114)], and T_e is the cell-edge temperature [Eq. (I-112)].

If the steam/gas-mixture velocity at the cell edge computed in Eq. (I-117) is greater than (or equal to) the ideal-gas sound speed of Eq. (I-118), then a superheated vapor phase is assumed to occur at the cell edge, and the choking velocity is calculated by maximizing the mass flux through pressure iterations in the following way.

Initially, the code chooses the cell-edge pressure and temperature to be equal to those values predicted by ideal-gas theory as in Eqs. (I-111) and (I-112). After calling THERMO to determine the cell-edge steam/gas-mixture properties corresponding to p_e and T_e, a steam/gas-mixture sound speed at cell edge is calculated using Eq. (I-117). A mass flux may then be computed from

$$G = V_{ge}\,\rho_{ge} \quad , \tag{I-119}$$

where ρ_{ge} is the steam/gas-mixture cell-edge density and V_{ge} is the steam/gas-mixture cell-edge sound speed [Eq. (I-117)].

The cell-edge pressure guess is varied slightly, and the calculation of cell-edge mass flux is repeated until the pressure that gives the maximum mass flux is located. Once the maximum mass flux and the cell-edge properties for that particular cell-edge pressure have been found, a homogeneous equilibrium sound-speed velocity is calculated according to

$$a_{\mathrm{HE}} = \frac{G_{\max}}{\rho_{ge}} \quad . \tag{I-120}$$

This concludes the calculation of the homogeneous equilibrium sound speed and the corresponding cell-edge conditions for the case of a slightly superheated vapor phase at cell edge. At this point, the logic returns to subroutine CHOKE.

If neither T_e is greater than the saturation temperature corresponding to the partial pressure of steam at cell edge, nor is the steam/gas-mixture sound speed greater than the ideal-gas sound speed [Eqs. (I-117) and (I-118)], then two-phase saturated fluid is assumed to be present at the cell edge. In this case, the pressure iteration necessary to determine the maximum mass flux and corresponding cell-edge conditions is exactly that described in the $L/D \geq 1.5$ section. This method assumes that no delay in condensation occurs as the steam/gas mixture expands to the saturation temperature corresponding to the cell-edge partial pressure of steam. The equations are repeated here for completeness.

An initial cell-edge pressure equal to that predicted by ideal-gas expansion theory is guessed as

$$p_e = p_o \left(\frac{2}{\gamma_g + 1} \right)^{\gamma_g/(\gamma_g - 1)} \quad , \tag{I-121}$$

where p_o is the stagnation pressure [as in Eq. (I-109)] and γ_g is the steam/gas-mixture specific-heat ratio [as in Eq. (I-102)].

Subroutine THERMO is then called to determine the saturation properties at the cell edge corresponding to the cell-edge pressure, p_e.

Saturated cell-edge values for liquid, steam, and steam/gas-mixture enthalpies and for liquid, steam, and noncondensable-gas entropies are computed, such that

$$h_{le} = e_{le} + \frac{p_e}{\rho_{le}} \quad , \tag{I-122}$$

$$h_{ve} = e_{ve} + \frac{p_e - p_{ae}}{\rho_{ge} - \rho_{ae}} \quad , \tag{I-123}$$

$$h_{ge} = e_{ge} + \frac{p_e}{\rho_{ge}} \quad , \tag{I-124}$$

$$s_{le} = c_{vl} \ln\left(\frac{T_e}{273.15}\right) \quad , \tag{I-125}$$

$$s_{ve} = s_{le} + \frac{h_{ve} - h_{le}}{T_e} \quad , \tag{I-126}$$

and

$$s_{ae} = c_{pa} \ln\left(\frac{T_e}{273.15}\right) - R_a \ln\left(\frac{\min\left\{p_{ae},\ 1.0\times10^{-5}\right\}}{1.0\times10^{5}}\right) \quad , \tag{I-127}$$

where e_{le}, e_{ve}, and e_{ge} are the cell-edge liquid, steam, and steam/gas-mixture saturated internal energies for the pressure p_e; p_e is the cell-edge pressure; p_{ae} is the cell-edge partial pressure of the noncondensable gas given by $p_{ae} = p_a(p_e/p)$; ρ_{le}, ρ_{ae}, and ρ_{ge} are the cell-edge liquid, noncondensable-gas, and steam/gas-mixture saturated densities for the pressure p_e; c_{vl} is the liquid constant-volume specific heat (as defined in subroutine SETEOS); T_e is the cell-edge temperature equal to the saturation temperature at p_e; c_{pa} is the noncondensable-gas constant-pressure specific heat (as defined in subroutine SETEOS); and R_a is the noncondensable-gas constant (as defined in subroutine SETEOS).

Then, assuming a constant entropy expansion from the stagnation condition, a cell-edge quality may be calculated from

$$x_e = \frac{s_m - s_{le}}{s_{ve} - s_{le} + \left(\frac{\rho_{ae}}{\rho_{ge}}\right)(s_{ae} - s_a - s_{ve} - s_v)} \quad , \tag{I-128}$$

where s_m, s_v, and s_a are the cell-center steam/liquid-water-mixture, steam, and noncondensable-gas actual entropies for the saturation temperature corresponding to the cell-center partial pressure of steam [as in Eqs. (I-107), (I-104), and (I-105)]; s_{le}, s_{ve}, and s_{ae} are the cell-edge liquid, steam, and noncondensable-gas saturated entropies for the pressure p_e [as computed above in Eqs. (I-125), (I-126), and (I-127)]; and ρ_{ae} and ρ_{ge} are the cell-edge noncondensable-gas and steam/gas-mixture saturated densities for the pressure p_e.

Once the cell-edge quality has been determined, a cell-edge total mixture enthalpy and cell-edge total mixture density are calculated as

$$h_{me} = x_e h_{ge} + (1 - x_e) h_{le} \tag{I-129}$$

and

$$\rho_{me} = \frac{\rho_{le}\rho_{ge}}{x_e\,(\rho_{le} - \rho_{ge}) + \rho_{ge}} \quad , \tag{I-130}$$

where x_e is the cell-edge quality [as in Eq. (I-128)]; h_{le} and h_{ge} are the cell-edge liquid and steam/gas-mixture saturated enthalpies for the pressure p_e [as in Eqs. (I-122) and (I-124)]; and ρ_{le} and ρ_{ge} are the cell-edge liquid and steam/gas-mixture saturated densities for the pressure p_e.

The mass flux, then, for a cell-edge pressure of p_e, becomes

$$G = \rho_{me}\sqrt{2\,(h_o - h_{me})} \quad , \tag{I-131}$$

where ρ_{me} is the cell-edge total mixture density [as in Eq. (I-130)], h_o is the stagnation enthalpy [as in Eq. (I-108)], and h_{me} is the cell-edge total mixture enthalpy [as in Eq. (I-129)].

The pressure is varied slightly and the iteration is repeated until the pressure that gives the maximum or critical mass flux as predicted by Eq. (I-131) is determined. Once the cell-edge pressure corresponding to the critical flux has been found, the saturated cell-edge conditions become known, and a homogeneous equilibrium sound speed, a_{HE}, is computed as follows:

$$a_{\mathrm{HE}} = \frac{G_{\max}}{\rho_{me}} \quad . \tag{I-132}$$

This concludes the calculation of the homogeneous equilibrium sound speed and the corresponding cell-edge conditions for the case of a nonsuperheated vapor phase at the cell edge when a superheated vapor phase existed at cell center. At this point, the logic returns to subroutine CHOKE.

I.2.2.2.3.2. Nonsuperheated Vapor Phase at Cell Center. If the cell-center steam/gas-mixture temperature, T_g, is less than or equal to the saturation temperature corresponding to the cell-center partial pressure of steam, or if the cell-center actual quality [Eq. (I-90)] is less than 1, the cell-center fluid is determined to be a nonsuperheated vapor phase, and the homogeneous equilibrium sound speed and corresponding cell-edge conditions are computed using the same iterative process

outlined in Section I.2.2.2.2., once the stagnation properties have been identified. The equations are repeated here for completeness.

An initial cell-edge pressure equal to that predicted by ideal-gas expansion theory is guessed as

$$p_e = p_o \left(\frac{2}{\gamma_g + 1} \right)^{\gamma_g / (\gamma_g - 1)} \quad , \tag{I-133}$$

where p_o is the stagnation pressure [as in Eq. (I-109)] and γ_g is the steam/gas-mixture specific-heat ratio [as in Eq. (I-102)].

Subroutine THERMO is then called to determine the saturation properties at the cell edge corresponding to the cell-edge pressure, p_e.

Saturated cell-edge values for liquid, steam, and steam/gas-mixture enthalpies and for liquid, steam, and noncondensable-gas entropies are computed, such that

$$h_{le} = e_{le} + \frac{p_e}{\rho_{le}} \quad , \tag{I-134}$$

$$h_{ve} = e_{ve} + \frac{p_e - p_{ae}}{\rho_{ge} - \rho_{ae}} \quad , \tag{I-135}$$

$$h_{ge} = e_{ge} + \frac{p_e}{\rho_{ge}} \quad , \tag{I-136}$$

$$s_{le} = c_{vl} \ln \left(\frac{T_e}{273.15} \right) \quad , \tag{I-137}$$

$$s_{ve} = s_{le} + \frac{h_{ve} - h_{le}}{T_e} \quad , \tag{I-138}$$

and

$$s_{ae} = c_{pa} \ln \left(\frac{T_e}{273.15} \right) - R_a \ln \left(\frac{\min \left\{ p_{ae}, \, 1.0 \times 10^{-5} \right\}}{1.0 \times 10^5} \right) \quad , \tag{I-139}$$

where e_{le}, e_{ve}, and e_{ge} are the cell-edge liquid, steam, and steam/gas-mixture saturated internal energies for the pressure p_e; p_e is the cell-edge pressure; p_{ae} is the cell-edge partial

pressure of the noncondensable gas given by $p_{ae} = p_a(p_e / p)$; ρ_{le}, ρ_{ae}, and ρ_{ge} are the cell-edge liquid, noncondensable-gas, and steam/gas-mixture saturated densities for the pressure p_e; c_{vl} is the liquid constant-volume specific heat (as defined in subroutine SETEOS); T_e is the cell-edge temperature equal to the saturation temperature at p_e; c_{pa} is the noncondensable-gas constant-pressure specific heat (as defined in subroutine SETEOS); and R_a is the noncondensable-gas constant (as defined in subroutine SETEOS).

Then, assuming a constant entropy expansion from the stagnation condition, the code calculates a cell-edge quality from

$$x_e = \frac{s_m - s_{le}}{s_{ve} - s_{le} + \left(\frac{\rho_{ae}}{\rho_{ge}}\right)(s_{ae} - s_a - s_{ve} - s_v)} \quad , \tag{I-140}$$

where s_m, s_v, and s_a are the cell-center steam/liquid-water-mixture, steam, and noncondensable-gas actual entropies for the saturation temperature corresponding to the cell-center partial pressure of steam [as in Eqs. (I-107), (I-104), and (I-105)]; s_{le}, s_{ve}, and s_{ae} are the cell-edge liquid, steam, and noncondensable-gas saturated entropies for the pressure p_e [as computed above in Eqs. (I-137), (I-138), and (I-139)]; and ρ_{ae} and ρ_{ge} are the cell-edge noncondensable-gas and steam/gas-mixture saturated densities for the pressure p_e.

Once the cell-edge quality has been determined, a cell-edge total mixture enthalpy and cell-edge total mixture density are calculated as

$$h_{me} = x_e h_{ge} + (1 - x_e) h_{le} \tag{I-141}$$

and

$$\rho_{me} = \frac{\rho_{le}\rho_{ge}}{x_e(\rho_{le} - \rho_{ge}) + \rho_{ge}} \quad , \tag{I-142}$$

where x_e is the cell-edge quality [as in Eq. (I-140)]; h_{le} and h_{ge} are the cell-edge liquid and steam/gas-mixture saturated enthalpies for the pressure p_e [as in Eqs. (I-134) and (I-136)]; and ρ_{le} and ρ_{ge} are the cell-edge liquid and steam/gas-mixture saturated densities for the pressure p_e.

The mass flux, then, for a cell-edge pressure of p_e becomes

$$G = \rho_{me}\sqrt{2\,(h_o - h_{me})} \quad , \tag{I-143}$$

where ρ_{me} is the cell-edge total mixture density [as in Eq. (I-142)], h_o is the stagnation enthalpy [as in Eq. (I-108)], and h_{me} is the cell-edge total mixture enthalpy [as in Eq. (I-141)].

The pressure is varied slightly and the iteration is repeated until the pressure that gives the maximum or critical mass flux as predicted by Eq. (I-143) is determined. Once the cell-edge pressure corresponding to the critical flux has been found, the saturated cell-edge conditions become known and a homogeneous equilibrium sound speed, a_{HE}, is computed as follows:

$$a_{HE} = \frac{G_{max}}{\rho_{me}} \quad . \tag{I-144}$$

This concludes the calculation of the homogeneous equilibrium sound speed and the corresponding cell-edge conditions for the case of a nonsuperheated vapor at cell center when L / D < 1.5 or the case of only subcooled liquid at cell center. At this point, the logic returns to subroutine CHOKE.

I.2.3. Constants

Several thermodynamic properties, such as the constant-pressure and constant-volume specific heats, are defined as constants in subroutine THERMO. These constants are fully described in Appendix A of this document.

I.2.4. Models as Coded

Subroutines CHOKE and SOUND contain the Fortran coding for the critical flow models. The necessary input to CHOKE includes the following:

AREA	Cell-edge area.
ARATIO	Ratio of cell-edge to donor-cell flow areas.
DADX	(Cell-edge area - cell area) / (0.5 x cell length).
DXC	Donor-cell length.
FAC	Donor-cell flow area.
ALPC	Donor-cell void fraction.
PC	Donor-cell pressure.
PAC	Donor-cell partial pressure of air.
TLC	Donor-cell liquid temperature.
RHOLC	Donor-cell liquid density.
RHOVC	Donor-cell steam / gas-mixture density.
SIGMA	Donor-cell surface tension.
VL	Momentum-solution liquid velocity.
VV	Momentum-solution steam / gas-mixture velocity.
VLO	Old-time liquid velocity.
VVO	Old-time steam / gas-mixture velocity.
VLC	Donor-cell cell-center liquid velocity.
VVC	Donor-cell cell-center steam / gas-mixture velocity.
ICHOKE	Choking indicator: ICHOKE = 0, unchoked flow. ICHOKE = 1, subcooled choked flow. ICHOKE = 2, two-phase choked flow. ICHOKE = 3, single-phase vapor choked flow.

I.2.4.1. Initial Calculations. Upon entry to subroutine CHOKE, several preliminary calculations are performed to prepare for either a subcooled-liquid choking calculation; a two-phase, two-component choking calculation; or a single-phase vapor choking calculation.

The two choked-flow multipliers are set to the user-input values as specified in the INOPTS NAMELIST data or are defaulted to 1.0 if no user-input values are specified.

The cell length-to-hydraulic-diameter ratio, L/D, is checked to determine how subroutine SOUND will calculate the stagnation properties given the cell-center conditions.

For $L/D \geq 1.5$, complete thermal equilibrium is assumed to exist at the cell edge. If the cell-center conditions are not initially in thermal equilibrium, thermal equilibrium conditions are calculated at the cell center assuming a constant-enthalpy process. Once thermal equilibrium has been established at cell center, the equilibrium void fraction is used to determine which choking model to use (subcooled-liquid; two-phase, two-component; or single-phase vapor). Stagnation properties computed in subroutine SOUND to determine the homogeneous equilibrium sound speed and the corresponding cell-edge conditions are calculated using the cell-center thermal equilibrium conditions, rather than any nonequilibrium cell-center conditions that may exist.

For $0.0000011111 \leq L/D < 1.5$, the actual cell-center void fraction is used to determine which choking model is used (either subcooled-liquid; two-phase, two-component; or single-phase vapor). Complete thermal equilibrium is still assumed to exist at the cell edge, but the stagnation conditions computed in subroutine SOUND to calculate the homogeneous equilibrium sound speed and the corresponding cell-edge conditions are calculated using the actual cell-center conditions (which may be either equilibrium or nonequilibrium conditions).

For $L/D < 0.0000011111$, complete nonequilibrium is assumed to exist at the choking plane (cell edge).

In TRAC, the low value of 0.0000011111 for the L/D check means that nonequilibrium equations are not evaluated. In addition, when a noncondensable gas is present in the vapor component, the logic described above for the case when $L/D \geq 1.5$ is followed throughout the choking calculation, regardless of the actual value of L/D.

Next the mixture density, mixture velocity, and slip ratio are calculated from the momentum-solution velocities according to the following:

$$\rho_{mc} = \alpha_c \rho_{gc} + (1.0 - \alpha_c)\, \rho_{\ell c} \quad , \tag{I-145}$$

$$V_m = \frac{\alpha_c \rho_{gc} V_g + (1.0 - \alpha_c)\, \rho_{lc}\, V_l}{\rho_{m_c}} \quad , \tag{I-146}$$

and

$$S = \frac{V_g}{V_l} \quad , \tag{I-147}$$

where α_c is the cell-center void fraction, ρ_{ge} and ρ_{le} are the cell-center phasic densities, and V_g and V_l are the momentum-solution phasic velocities. If a negative slip is calculated, the slip is reset to 1.0, and the calculational sequence proceeds. This should never occur, but in the event that countercurrent flow is sent to CHOKE, a slip of 1.0 will allow CHOKE to run without failing. (Choked flow will not occur in this case anyway.)

I.2.4.2. Determination of Choking Velocities Using the Appropriate Model.
At this point, subroutine CHOKE branches to the appropriate choked-flow model based on the void fraction (either actual or equilibrium as determined by the L/D check described above).

If $\alpha \leq 001$, a subcooled-liquid choking calculation is done.

If $0.01 < \alpha < 0.1$, an interpolation between the subcooled-liquid and the two-phase, two-component choking calculation is performed to determine the choking velocities.

If $0.1 \leq \alpha \leq 0.999$, a two-phase, two-component choking calculation is done.

And if $\alpha > 0.999$, a single-phase vapor choking calculation is performed.

I.2.4.2.1. Subcooled Liquid. If $\alpha \leq 0.01$, a subcooled-liquid calculation is done to determine the choking velocities.

First, subroutine SOUND is called to determine the maximum mass flux and the corresponding cell-edge conditions, as described in Section I.2.2. From this maximum mass flux, the value of the homogeneous equilibrium sound speed to be used in conjunction with the donor-cell conditions to give the correct mass flow is then calculated, such that

$$a_{\mathrm{HE}} = \frac{G_{\max}}{\rho_{mc}} \quad , \tag{I-148}$$

where $G_{\max}$ is the critical mass flux returned by SOUND and ρ_{mc} is the (donor-cell) cell-center mixture density calculated in Eq. (I-145).

Next, a nucleation pressure, which may be lower than the saturation pressure corresponding to the local (donor-cell) liquid temperature, is calculated for the cell edge using the Jones nucleation delay model [Eq. (I-31)]. With the critical temperature, T_c, equal to 647.3 K and Boltzmann's constant, k, equal to 1.380622×10^{-23} J·K^{-1} Eq. (I-31) becomes

$$p_{\text{nuc}} = p_{\text{sat}} - \max \left\{ 0.0,\ 5.691364 \times 10^{-30} \frac{\sigma^{1.5} T_{\text{l}}^{13.76} \left[1 + 13.25 \left(- \frac{1}{1.01325 \times 10^{11}} \frac{\text{D}p}{\text{D}t} \right)^{0.8} \right]^{0.5}}{\left(1 - \frac{\rho_{ge}}{\rho_{\text{l}e}} \right)} - 0.069984 \left(\frac{A_e}{A_c} \right)^2 \rho_{\text{l}} V_{\text{l}}^2 \right\} \quad , \tag{I-149}$$

where p_{sat} is the saturation pressure corresponding to T_l, the donor-cell liquid temperature; σ is the surface tension; ρ_{le} and ρ_{ge} are cell-edge densities; A_e and A_c are cell-edge and cell-center flow areas; and V_{l} is the momentum-solution liquid velocity. The term $\text{D}p/\text{D}t$ is the substantial derivative of pressure and is given by

$$\frac{\text{D}p}{\text{D}t} = \max \left\{ 1.0 \times 10^{-10},\ - \frac{2 |V_{\text{l}}| (p_e - p_c)}{\Delta x} \right\} \quad , \tag{I-150}$$

where V_{l} is again the momentum-solution liquid velocity, p_e is the cell-edge (choke-plane or throat) pressure returned by subroutine SOUND, p_c is the cell-center pressure, and Δx is the cell length.

The code then evaluates Bernoulli's equation to give the following cell-edge velocity:

$$V_{\text{l}e,\text{Bernoulli}} = \left[V_{\text{l}c}^2 + \frac{2 \max \{ 0.0, (p_c - p_{\text{nuc}}) \}}{\rho_{\text{l}e}} \right]^{\frac{1}{2}} \quad , \tag{I-151}$$

where $V_{\text{l}c}$ is the cell-center liquid velocity calculated from Eq. (I-48) as described in Section I.2.2., ρ_{le} is the cell-edge liquid density as evaluated in subroutine SOUND, p_c is the cell-center pressure, and p_{nuc} is the cell-edge nucleation pressure [Eq. (I-149)].

The liquid choking velocity is taken as the maximum of the Bernoulli-predicted velocity and the homogeneous equilibrium sound speed as determined in SOUND. That is,

$$V_{\text{l}e} = \max \left\{ a_{\text{HE}}, V_{\text{l}e,\text{Bernoulli}} \right\} \quad . \tag{I-152}$$

If a sound-speed multiplier was specified through the user-input INOPTS NAMELIST data, this is applied to the liquid choking velocity to give a final predicted value of

$$V_{le}^{p} = \text{CHMLT1} \cdot \max \left\{ a_{\text{HE}},\ V_{le,\text{Bernoulli}} \right\} \quad . \tag{I-153}$$

If the liquid velocity as determined in the momentum solution is less than this maximum choking velocity, the flow is flagged as being unchoked and the calculation is ended. If, however, the liquid velocity determined in the momentum solution is greater than or equal to this maximum choking velocity, then the liquid velocity is reset to be equal to the choking velocity. In addition, a predicted steam/gas-mixture velocity is calculated according to

$$V_{ge}^{p} = V_{le}^{p}\, S \quad , \tag{I-154}$$

where S is the slip ratio [as determined in Eq. (I-147)]. If the predicted steam/gas-mixture choking velocity, V_{ge}^{p}, has changed directions from the momentum-solution steam/gas-mixture velocity, V_g, the steam/gas-mixture choking velocity is reset to zero.

I.2.4.2.2. Two-Phase, Two-Component Fluid. If $0.1 \le \alpha \le 0.999$ a two-phase, two-component choking calculation is done to determine the predicted choking velocities.

Equation (I-43) is extremely difficult to solve analytically. Thus, TRAC obtains the characteristic roots of Eq. (I-43) numerically. This method advantageously maintains generality and facilitates computations under different assumptions.

The solution of Eq. (I-43) requires that p_a, p_v, α, ρ_a, ρ_v, ρ_l, s_a, s_v, and s_l and their derivatives be specified at the cell edge, where the choking criterion is applied. However, these quantities are known only at the cell center. Direct use of the cell-center quantities yields erroneous results caused by the presence of steep gradients near the choking plane. Therefore, an estimate of the thermodynamic state at the cell edge is necessary. To obtain this estimate, subroutine SOUND is called. In addition to determining the thermodynamic state at the cell edge, SOUND also calculates the homogeneous equilibrium sound speed which is used as a first estimate for the largest characteristic root. (When the non-homogeneous effects are not dominant, the desired root is close to the homogeneous equilibrium sound speed.) The procedure used by SOUND to arrive at the cell-edge thermodynamic state and the homogeneous equilibrium sound speed is described in full detail in Section I.2.2.

Because equilibrium is assumed to occur at the cell edge, subroutine THERMO is called to determine saturation properties at the cell edge corresponding to the cell-edge pressure, p_e, estimated in the call to SOUND. The cell-edge void fraction may then be calculated, such that

$$\alpha_e = \frac{\rho_{le} - \rho_{me}}{\rho_{le} - \rho_{ge}}, \tag{I-155}$$

where ρ_{me} is the cell-edge mixture density calculated by subroutine SOUND, and ρ_{le} and ρ_{ge} are the saturated liquid and steam/gas-mixture densities for a cell-edge pressure of p_e.

In addition, entropies and the quantities ρ^*_{le}, ρ^*_{ge}, s^*_{le}, and s^*_{ge} necessary for evaluating the elements of matrix $\underline{\underline{B}}$ (as shown in Fig. I-9.b) are defined at the cell-edge, such that

$$s_{le} = c_{vl} \ln \left(\frac{T_e}{273.15} \right) \quad , \tag{I-156}$$

$$s_{ve} = c_{vl} \ln \left(\frac{T_e}{273.15} \right) + \left(\frac{1}{\rho_{ve}} - \frac{1}{\rho_{le}} \right) \frac{\mathrm{d}T}{\mathrm{d}p_v} \quad , \tag{I-157}$$

$$s_{ae} = c_{pa} \ln \left(\frac{T_e}{273.15} \right) - R_a \ln \left(\frac{\max \left\{ p_{ae},\ 1.0 \times 10^{-5} \right\}}{1.0 \times 10^5} \right) \quad , \tag{I-158}$$

$$s_{ge} = s_{ae} \left(\frac{\rho_{ae}}{\rho_{ge}} \right) + s_{ve} \left(1 - \frac{\rho_{ae}}{\rho_{ge}} \right) \quad , \tag{I-159}$$

and

$$\rho^*_{le} = \left(\frac{\partial \rho_{le}}{\partial p} \right)_T + \left(\frac{\partial \rho_{le}}{\partial T} \right)_p \frac{\mathrm{d}T}{\mathrm{d}p_v} \quad , \tag{I-160}$$

$$\rho^*_{ve} = \left(\frac{\partial \rho_{ve}}{\partial p_v} \right)_T + \left(\frac{\partial \rho_{ve}}{\partial T} \right)_{p_v} \frac{\mathrm{d}T}{\mathrm{d}p_v} \quad , \tag{I-161}$$

$$s^*_{ve} = \frac{1}{T_e} \left[\left(\frac{\partial e_{ve}}{\partial p_v} \right)_T + \left(\frac{\partial e_{ve}}{\partial T} \right)_{p_v} \frac{\mathrm{d}T}{\mathrm{d}p_v} \right]$$

$$- \frac{p_{ve}}{\rho^2_{ve} T_e} \left[\left(\frac{\partial \rho_{ve}}{\partial p_v} \right)_T + \left(\frac{\partial \rho_{ve}}{\partial T} \right)_{p_v} \frac{\mathrm{d}T}{\mathrm{d}p_v} \right] \quad , \tag{I-162}$$

and

$$s^*_{le} = \frac{1}{T_e}\left[\left(\frac{\partial e_{le}}{\partial p}\right)_T + \left(\frac{\partial e_{le}}{\partial T}\right)_p \frac{\mathrm{d}T}{\mathrm{d}p_v}\right]$$

$$- \frac{p_e}{\rho^2_{le} T}\left[\left(\frac{\partial \rho_{le}}{\partial p}\right)_T + \left(\frac{\partial \rho_{le}}{\partial T}\right)_p \frac{\mathrm{d}T}{\mathrm{d}p_v}\right] \quad , \tag{I-163}$$

where T_e is the cell-edge saturation temperature corresponding to the cell-edge partial pressure of steam, p_{ve}; c_{vl} is the liquid constant-volume specific heat (defined in subroutine SETEOS); ρ_{ae}, ρ_{ve}, ρ_{ge}, and ρ_{le} are the cell-edge saturation densities corresponding to the cell-edge pressure, p_e; c_{pa} and R_a are the noncondensable-gas constant-pressure specific heat and the gas constant (both defined in subroutine SETEOS); and p_{ae} is the cell-edge partial pressure of the noncondensable gas as estimated by SOUND.

Next, CHOKE tries to determine the mass flux such that none of the characteristic roots of the governing system of partial differential equations given by Eqs. (I-32) through (I-36) has a positive real part and that the maximum root is zero.

The solution of Eq. (I-43) for a set of λ that includes $\lambda_1 = 0$ requires that

$$\det |\underline{\underline{B}}| = 0 \, . \tag{I-164}$$

Therefore, CHOKE first tries to solve Eq. (I-164).

To set up the elements of matrix $\underline{\underline{B}}$, CHOKE calculates first-guess approximations of the steam/gas-mixture and liquid cell-edge velocities from the homogeneous equilibrium sound speed, a_{HE}, and the cell-center momentum-solution slip value [computed in Eq. (I-147)], such that

$$V_{ge} = \frac{a_{\mathrm{HE}} S \rho_{me}}{\alpha_e \rho_{ge} S + (1-\alpha_e)\rho_{le}} \tag{I-165}$$

and

$$V_{le} = \frac{V_{ge}}{(S + 1.0 \times 10^{-20})} \quad , \tag{I-166}$$

where a_{HE} is the homogeneous equilibrium sound speed by returned subroutine SOUND, S is the slip ratio calculated from the momentum-solution steam / gas-mixture and liquid velocities [as in Eq. (I-147)], α_e is the cell-edge void fraction [computed in Eq. (I-155)], ρ_{me} is the cell-edge total mixture density returned by subroutine SOUND, and ρ_{le} and ρ_{ge} are the saturated cell-edge liquid and steam / gas-mixture densities for the cell-edge pressure p_e.

The virtual mass coefficient in the two phasic momentum equations [Eqs. (I-33) and (I-34)] is assumed to be fixed at a value of 10. Values for the virtual mass coefficient such as 5, 10, and 20 were found to give good mass-flow predictions when compared to data. The value of 10 was arbitrarily chosen because small variations in the virtual mass coefficient in this range (5 to 20) did not significantly affect the calculation.

The determinant of matrix $\underline{\underline{B}}$ may now be evaluated. An iterative procedure is used to vary the mixture velocity around a_{HE} until the rate of change of V_{ge} is less than (or equal to) $0.001a_{\mathrm{HE}}$ per iteration step while satisfying the requirement that the determinant be zero.

Once converged values of V_{ge} and V_{le} have been found using the iteration above, CHOKE sets up the elements in matrix $\underline{\underline{A}}$ and solves for the eigenvalues and eigenvectors of $\underline{\underline{A}}^{-1}\,\underline{\underline{B}}$. This is equivalent to solving Eq. (I-43) if the signs of the eigenvalues are reversed. CHOKE also checks that the absolute value of the root with the largest real part is indeed real and less than (or equal to) $0.01a_{\mathrm{HE}}$.

The predicted values of the choking velocities to be used in conjunction with the donor-cell conditions to give the correct mass-flow rate are now calculated, such that

$$V_{me}^{p} = \frac{\alpha_e \rho_{ge} V_{ge} + (1-\alpha_e)\,\rho_{le} V_{le}}{\rho_{mc}} \quad , \tag{I-167}$$

$$V_{le}^{p} = \mathrm{CHMLT2} \cdot \frac{V_{me}^{p} \rho_{mc}}{\rho_{gc}\alpha_c S + \rho_{lc}(1-\alpha_c)} \quad , \tag{I-168}$$

and

$$V_{ge}^{p} = S V_{le}^{p} \quad , \tag{I-169}$$

where α_e is the cell-edge void fraction calculated in Eq. (I-155); ρ_{ge} and ρ_{le} are the cell-edge saturation densities corresponding to the cell-edge pressure, p_e; ρ_{gc}, ρ_{lc}, and ρ_{mc} are the cell-center steam / gas-mixture, liquid, and total mixture densities; S is the slip ratio calculated from the momentum-solution steam / gas-mixture and liquid velocities as in Eq. (I-147); and CHMLT2 is a user-input choked-flow multiplier.

If the mixture velocity as determined in the momentum solution is less than this predicted mixture velocity, the flow is flagged as being unchoked and the calculation is ended. If, however, the mixture velocity determined in the momentum solution is greater than (or equal to) the predicted mixture choking velocity, then the steam/gas-mixture, liquid, and total mixture velocities are reset to the predicted choking values.

I.2.4.2.3. Interpolation Region Between Subcooled and Two-Phase Models. If $0.01 < \alpha < 0.1$, an interpolation between the subcooled-liquid and the two-phase, two-component choking calculation is performed to determine the predicted choking velocities.

Initially, liquid and steam/gas-mixture choking velocities are calculated using the two-phase, two-component model. In addition, liquid and steam/gas-mixture choking velocities are calculated using the subcooled-liquid choking model. These velocities are combined to produce the predicted liquid and steam/gas-mixture choking velocities using a linear interpolation in alpha, such that,

$$V_{le}^{p} = V_{l,sc} + \left(\frac{\alpha_c - \alpha_{\min}}{\alpha_{\max} - \alpha_{\min}} \right) (V_{l,tp} - V_{l,sc}) \qquad \text{(I-170)}$$

and

$$V_{ge}^{p} = V_{g,sc} + \left(\frac{\alpha_c - \alpha_{\min}}{\alpha_{\max} - \alpha_{\min}} \right) (V_{g,tp} - V_{g,sc}) \quad , \qquad \text{(I-171)}$$

where $V_{l,sc}$ and $V_{g,sc}$ are the liquid and steam/gas-mixture choking velocities calculated using the subcooled-liquid model; $V_{l,tp}$ and $V_{g,tp}$ are the liquid and steam/gas-mixture choking velocities calculated using the two-phase, two-component choking model; α_c is the cell-center void fraction (either actual or equilibrium, depending on the value of L/D); and $\alpha_{\min}$ and $\alpha_{\max}$ are the limits on the void fraction for the interpolation region, currently set to 0.01 and 0.1, respectively.

I.2.4.2.4. Single-Phase Vapor. If $\alpha > 0.999$, a single-phase vapor model is used to determine the choking velocities. Subroutine SOUND is first called to determine cell-edge conditions and the maximum mass flux as described in Section I.2.2. From this maximum mass flux, the value of the homogeneous equilibrium sound speed to be used in conjunction with donor-cell conditions to give correct mass flow is then calculated, such that

$$a_{\mathrm{HE}} = \frac{G_{\max}}{\rho_{mc}} \quad , \qquad \text{(I-172)}$$

where G_{max} is the critical mass flux returned by SOUND and ρ_{me} is the (donor-cell) cell-center mixture density calculated in Eq. (I-145). If a sound-speed multiplier was specified through the user-input INOPTS NAMELIST data, this is applied to the steam / gas-mixture sound speed to give a predicted steam / gas-mixture choking velocity of

$$V_{ge}^{p} = \text{CHMLT2} \cdot a_{\text{HE}} \quad . \tag{I-173}$$

If the momentum-solution steam / gas-mixture velocity, V_g, is less than this predicted steam / gas-mixture choking velocity, the flow is flagged as being unchoked and the calculation is ended. If, however, the steam / gas-mixture velocity as determined in the momentum solution is greater than or equal to the predicted choking velocity, then the steam / gas-mixture velocity is reset to be equal to the predicted steam / gas-mixture choking velocity. In addition, a predicted liquid velocity is calculated according to

$$V_{le}^{p} = \frac{V_{ge}^{p}}{(S + 1.0 \times 10^{-20})} \quad , \tag{I-174}$$

where S is the slip ratio as determined in Eq. (I-147). If the predicted liquid choking velocity at the cell edge, V_{le}^{p}, has changed directions from the momentum-solution liquid velocity, V_l, it is reset to zero.

I.2.4.3. New-Time Choking Velocities. Finally, new-time phasic choking velocities are computed by time-averaging the old-time velocities with the predicted choking velocities just calculated, such that

$$V_l^{n+1} = 0.1\, V_{le}^{p} + 0.9\, V_l^{n} \tag{I-175}$$

and

$$V_g^{n+1} = 0.1\, V_{ge}^{p} + 0.9\, V_g^{n} \quad , \tag{I-176}$$

where V_{le}^{p}, and V_{ge}^{p} are the predicted liquid and steam / gas-mixture choking velocities just calculated, and V_l^{n} and V_g^{n} are the old-time liquid and steam / gas-mixture velocities (either momentum solution or choking). This old-time, new-time method of weighting limits the change in the choking velocity for either phase to only 10% of the actual calculated change and ensures that the choking model lags slightly behind any pressure transients so that the effects of unnatural pressure changes caused by fluid inertia are limited.

This concludes the first pass through the choking model calculation. A second pass is necessary to evaluate the velocity derivatives. This is described in the next section.

I.2.4.4. Second-Pass Velocity m Derivatives. To calculate the derivatives of the liquid and steam/gas-mixture choking velocities with respect to pressure, a second pass through subroutine CHOKE is made with the pressure at cell center equal to 0.99 of the actual cell-center value. A second set of predicted liquid and steam/gas-mixture choking velocities is calculated for this 99% pressure value, using either a subcooled-liquid, a two-phase two-component fluid, or a superheated vapor calculation, exactly as was done in the first pass through subroutine CHOKE. These second-pass predicted choking velocities are then time-averaged to determine new-time choking velocities for the 99% pressure value in a manner similar to that used in the first pass, such that

$$V_{l,2nd}^{n+1} = 0.1V_{le,2nd}^{p} + 0.9V_{l}^{n} \tag{I-177}$$

and

$$V_{g,2nd}^{n+1} = 0.1V_{ge,2nd}^{p} + 0.9V_{g}^{n} \quad , \tag{I-178}$$

where $V_{l,2nd}^{p}$ and $V_{g,2nd}^{p}$ are the second-pass predicted liquid and steam/gas-mixture choking velocities, and V_{l}^{n} and V_{g}^{n} are the old-time liquid and steam/gas-mixture velocities (either momentum-solution or choked).

Once the actual and second-pass new-time liquid and steam/gas-mixture choking velocities have been determined, the derivatives with respect to pressure are calculated as follows:

$$\begin{aligned} \frac{dV_l}{dp} &\approx \frac{\Delta V_l}{\Delta p} \\ &= \frac{\left(V_l^{n+1} - V_{l,2nd}^{n+1}\right)}{(p - 0.99p)} = 100.0\frac{\left(V_l^{n+1} - V_{l,2nd}^{n+1}\right)}{p} \end{aligned} \tag{I-179}$$

and

$$\frac{dV_g}{dp} \approx 100.0\frac{\left(V_g^{n+1} - V_{g,2nd}^{n+1}\right)}{p} \quad , \tag{I-180}$$

where V_{l}^{n+1} and V_{g}^{n+1} are the actual new-time choking velocities, and $V_{l,2nd}^{n+1}$ and $V_{g,2nd}^{n+1}$ are the second-pass, new-time choking velocities for a cell-center pressure of $0.99p$.

With the determination of the new-time choking velocities and their derivatives with respect to pressure, the choking calculation performed in subroutines CHOKE and SOUND is now complete. At this point, the logic returns to the calling subroutine.

I.2.5. Weighting, Magnitude Limits, Rate Limits, and Averaging

This next section describing the averaging technique used to compute cell-center momentum-solution velocities is copied exactly from Section I.2.2.1. It is included here also for completeness.

I.2.5.1. Cell-Center Momentum-Solution Velocities. The velocities obtained from the momentum solution are cell-edge values. However, to evaluate stagnation conditions (in subroutine SOUND), it is necessary to know the phasic velocities at cell center. This transition between cell edge and cell center is accomplished in subroutine VOLV by averaging the mass flux between cell edges, such that

$$V_{gc} = \frac{\frac{1}{2}\left[(\rho_g \alpha)_{e^-} \; V_{g,e^-} A_{e^-} \; + \; (\rho_g \alpha)_{e^+} \; V_{g,e^+} A_{e^+}\right]}{\rho_{gc} \alpha_c A_c} \tag{I-181}$$

and

$$V_{lc} = \frac{\frac{1}{2}\left[(\rho_l (1 - \alpha))_{e^-} \; V_{l,e^-} A_{e^-} \; + \; (\rho_l (1 - \alpha))_{e^+} \; V_{l,e^+} A_{e^+}\right]}{\rho_{lc} (1 - \alpha)_c A_c} \quad , \tag{I-182}$$

where V_{gc} and V_{lc} are the transformed cell-center velocities, ρ_g and ρ_l are the liquid and steam / gas-mixture densities, α is the void fraction, V_l and V_g are the liquid and steam / gas-mixture velocities, and A is the cross-sectional flow area. The subscripts e^- and e^+ refer to upstream cell-edge and downstream cell-edge quantities, while the subscript c refers to cell-center quantities for the particular cell in question. It is assumed that $\rho\alpha$ at the upstream face is equal to the upstream cell product value, whereas $\rho\alpha$ at the downstream face is taken to be equal to the current cell value, because densities and void fractions are normally associated with cell-center rather than cell-edge positions.

This next section describing the weighting technique used to compute new-time choking velocities from predicted and old-time velocities is copied from Section I.2.4.3. It is included here also for completeness.

I.2.5.2. New-Time Choking Velocities. New-time phasic choking velocities are computed by time-averaging the old-time velocities with the predicted choking velocities, such that

$$V_l^{n+1} = 0.1 \; V_{le}^{p} \; + \; 0.9 \; V_l^{n} \tag{I-183}$$

and

$$V_g^{n+1} = 0.1 \; V_{ge}^{p} \; + \; 0.9 \; V_g^{n} \quad , \tag{I-184}$$

where v_{le}^{p} and v_{ge}^{p} are the predicted liquid and steam/gas-mixture choking velocities, and v_{l}^{n} and v_{g}^{n} are the old-time liquid and steam/gas-mixture velocities (either momentum solution or choking). This old-time, new-time method of weighting limits the change in the choking velocity for either phase to only 10% of the actual calculated change and ensures that the choking model lags slightly behind any pressure transients so that the effects of unnatural pressure changes caused by fluid inertia are limited.

I.2.6. Assessment

Two types of assessment are performed on the TRAC-PF1/MOD2 critical flow model: comparing the MOD2 model to other models and comparing calculations using the critical flow model against fine-mesh calculations and test data. Results of the comparisons follow. The results and conclusions presented throughout this section apply to TRAC-M as well.

I.2.6.1. Comparing TRAC-PF1/MOD2 Choked-Flow Model with Other Models.

The primary requirement for an accurate choked-flow model is that it yield results that are close to the homogeneous equilibrium calculations when the flow approaches such a homogeneous limit, because the nonhomogeneous effects are of only secondary importance in most situations. Therefore, the homogeneous equilibrium sound speed calculated by MOD2 should agree with the true sound speed. Figure I-10. compares the MOD2-calculated homogeneous equilibrium sound speed with that obtained from the tables of Hall (Ref. I-9.) for different void fractions at a 560 K saturation temperature. The agreement between the calculations and the tables is excellent.

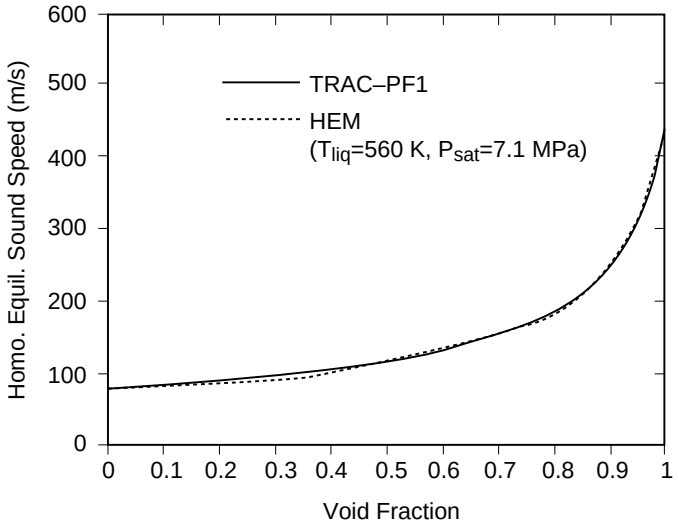

Fig. I-10. Comparison of the two-phase homogeneous equilibrium sound speed.

Figure I-11. compares the MOD2-calculated subcooled critical flow with that from the Burnell model and from the Homogeneous Equilibrium Model (HEM) for stagnation pressures ranging from 7.1 MPa (saturated liquid) to 15.0 MPa (subcooled liquid) at a constant 560 K temperature. The Burnell model is the modified Burnell model from RELAP4/MOD6 (Ref. I-10.) that accounts for nucleation delay by an empirical expression. The HEM mass flux represents a lower limit on the mass flux. As desired, the MOD2 model calculations give results that are similar to those for the Burnell model. The minor discrepancy between the MOD2 choked-flow models and the Burnell models is caused primarily by the difference between the nucleation-delay models.

Figure I-12. compares the MOD2 two-phase critical-flow model calculations with the HEM data at 560 K saturation temperature. Again, the agreement is good. The MOD2-calculated results differ from the HEM data because the nonhomogeneous effects are not accounted for in the HEM. Larger differences between the results obtained from the two models are expected when the upstream phasic velocities differ. (The flow upstream of the break was assumed to be stagnant for this calculation.)

I.2.6.2. Comparing the MOD2 Choked-Flow Model Calculations with the Fine-Mesh Calculations and the Test Data. A true test of the accuracy of a choking model is its ability to predict results similar to those obtained using an extremely fine mesh (natural choking) for geometries with smooth area changes. Therefore, the MOD2 choking calculations are compared with the fine-mesh results and the test data from Tests 4 (Ref. I-11.) and 24 (Ref. I-12.) of the Marviken test facility and the Edwards blowdown experiment (Ref. I-13.).

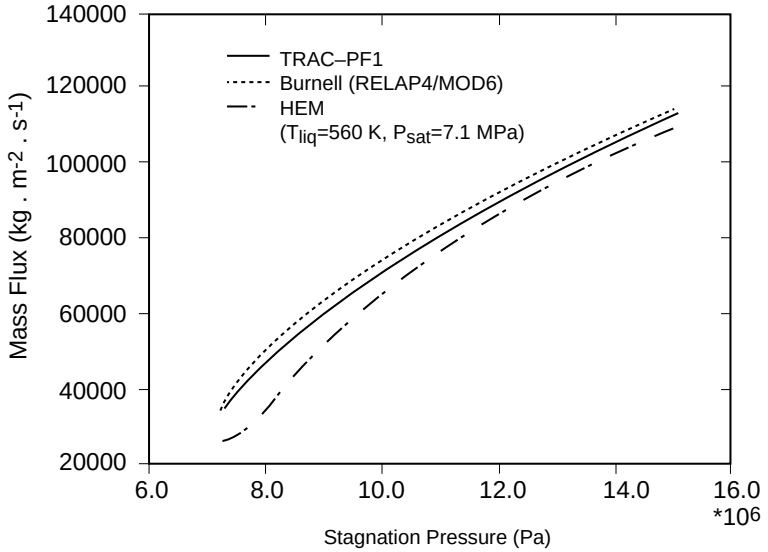

Fig. I-11. Comparison of the subcooled critical mass flux.

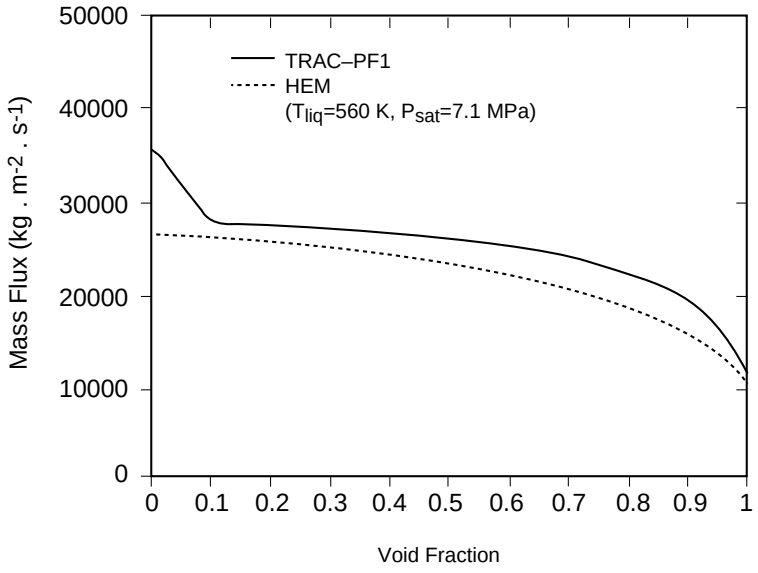

Fig. I-12. Comparison of the two-phase critical mass flux.

I.2.6.2.1. Marviken Test Facility. The Marviken full-scale critical-flow tests assess the ability of computer codes to predict large pressure-vessel blowdowns. The four major components of this facility are a pressure vessel, originally designed to be part of the Marviken nuclear power plant; a discharge pipe; a test nozzle with the minimum flow area in the system; and a rupture-disk assembly. Figure I-13. shows the vessel that still includes part of the core superstructure and the moderator tank plus three gratings installed to eliminate vortex formation. Figure I-14. shows the other components. All elevations in both figures are measured relative to the vessel bottom. Pressure and temperature transducers are located along the vessel and the discharge pipe, as shown in Figs. I-13. and I-14. The signals from the various transducers are processed through a signal-conditioning unit with its channels connected to a pulse-code modulation system.

Before a test is run, the vessel is partially filled with deionized water and heated by removing water from the vessel bottom, passing it through an electric heater, and returning it to the steam dome at the vessel top. This procedure produces a complicated initial temperature distribution in the vessel. A saturated steam dome fills the vessel region above the initial water level. The test is initiated by releasing the rupture disks and is terminated by closing a ball valve in the discharge pipe. We specifically chose Marviken Tests 4 and 24 because Test 4 had the longest nozzle and Test 24 the shortest in the entire test series.

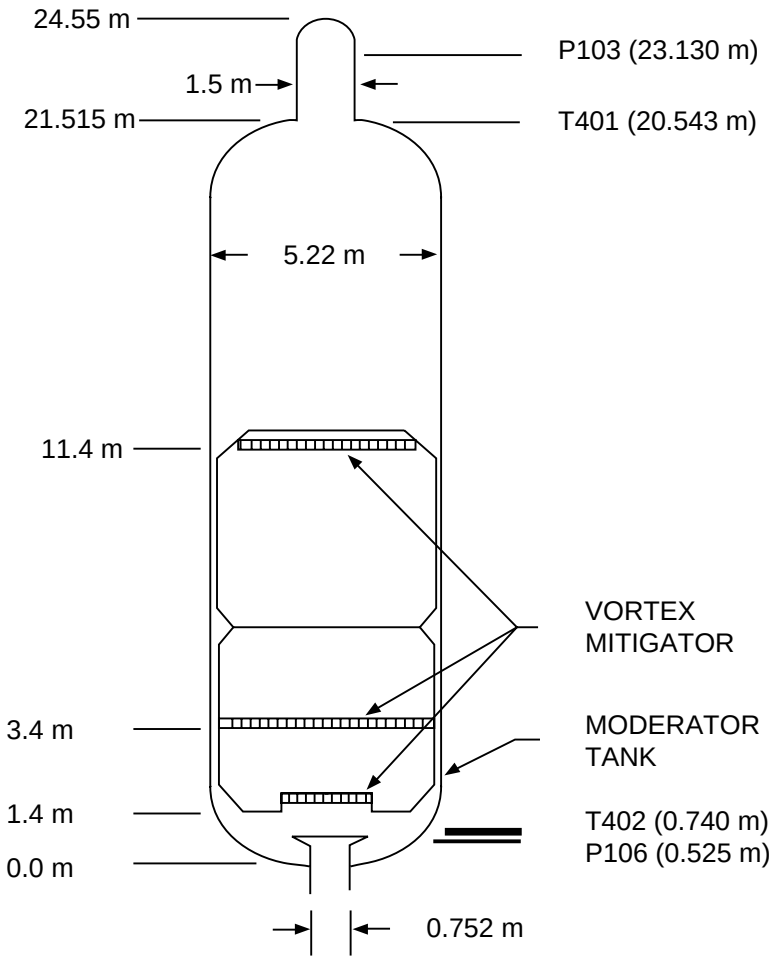

Fig. I-13. Marviken pressure vessel.

The MOD2 model for Marviken Tests 4 and 24 included four components. A zero-velocity FILL component modeled the vessel upper boundary. A PIPE component modeled the vessel above 2.6 m, including the maximum-diameter region plus the top cupola. Another PIPE component modeled the lower part of the vessel, the discharge pipe, the nozzle, and the rupture-disk assembly. A BREAK component provided a pressure boundary condition at the rupture-disk assembly lower boundary. For the fine-noding cases, the nozzles were modeled with 30 cells (15 in the converging section and 15 in the straight portion with a minimum cell length of 0.025 m) for Test 4 and with 12 cells (5 in the converging section and 7 in the straight portion with a minimum cell length of 0.02 m) for Test 24. When using the choked-flow model, the nozzles in both tests were modeled by only two cells, one in the converging section and the other simulating the entire straight section, with the choked-flow model invoked at the downstream edge of the second cell. The default choked-flow multipliers were used in these calculations.

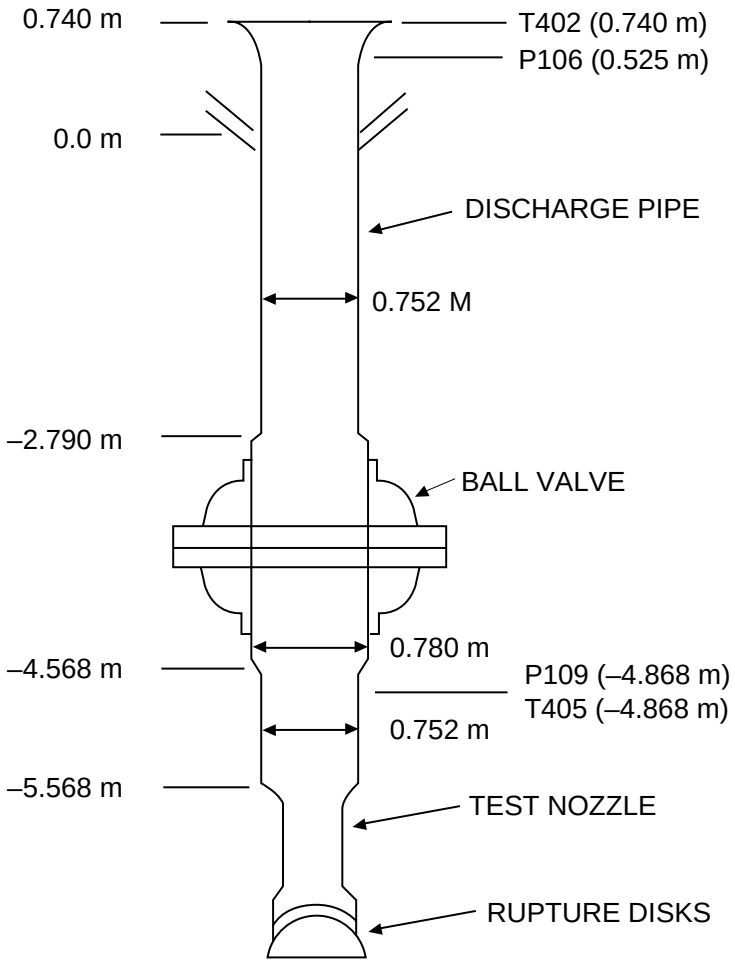

Fig. I-14. Marviken discharge pipe, test nozzle, and rupture-disk assembly.

Figures I-15. and I-16. show the MOD2 mass flows and pressure histories with the choking model and the fine noding compared with the test data. The measured mass flows are derived from velocity (pitot-static) and vessel differential-pressure measurements. The pitot-static data curve is valid throughout the transient, whereas the vessel differential-pressure curve is valid only after ~5 s. The choking calculations give almost identical results to those for the fine-mesh case. Both the choked-flow and the fine-mesh calculations also agree well with the test data except during the subcooled blowdown phase when the mass flow is under-predicted by an average of ~10%. The dip in the measured pressure during the first 3 s of the transient indicates a significantly more pronounced nucleation delay than predicted by the MOD2 model.

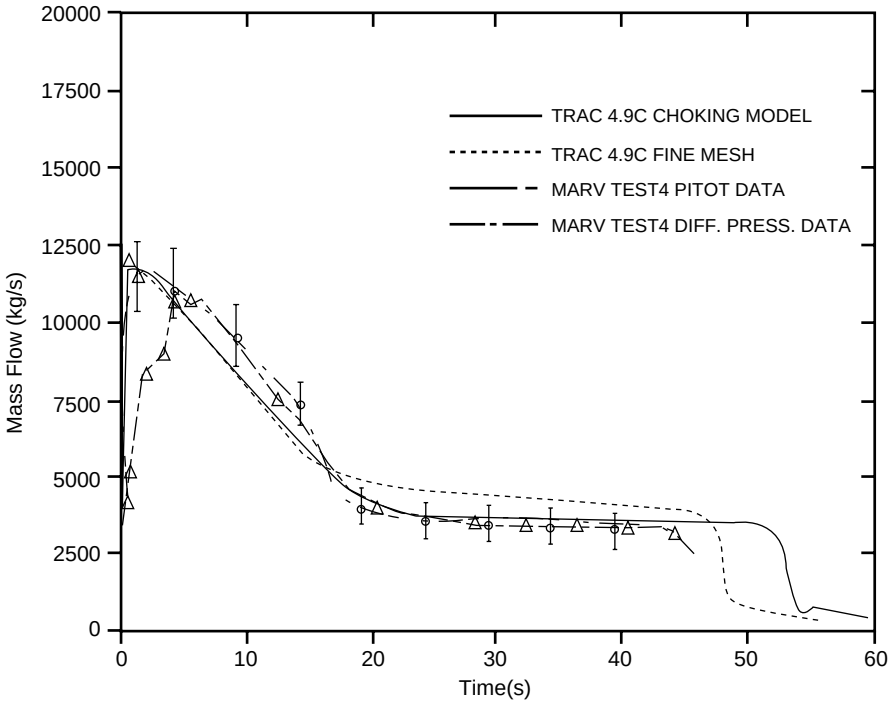

Fig. I-15. Comparison of the nozzle mass flows for Marviken Test 4.

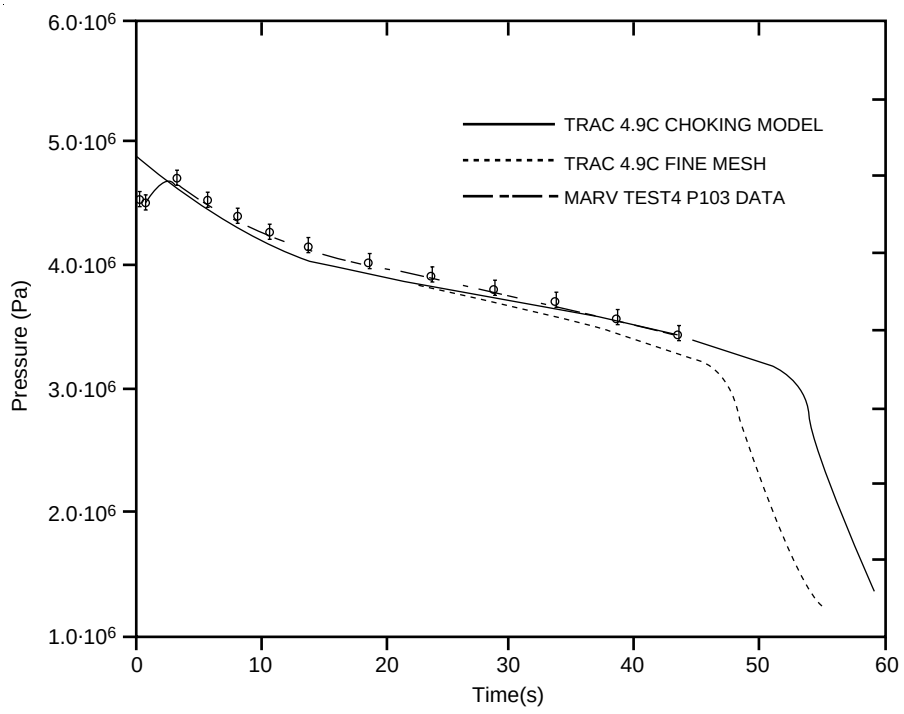

Fig. I-16. Comparison of the system pressure histories for Marviken Test 4.

Figures I-17. and I-18. show the mass flows and pressure histories for Test 24. The agreement between the choking calculation and the results obtained from the fine-mesh case is not as good as for Test 4. This discrepancy is attributed to the predominance of nonequilibrium effects between the phases caused by the short nozzle length. These nonequilibrium effects are not modeled in the MOD2 choking calculation. (The straight sections of the nozzles for Tests 4 and 24, respectively, were 1.5 and 0.166 m long, with L / D ratios of 2.95 and 0.33.)

To investigate the importance of nonequilibrium effects in Test 24, a sensitivity run, with the "frozen" assumption in the characteristic solution (using a seven-equation characteristic model without differential-type mass-transfer terms), will be performed as time permits.

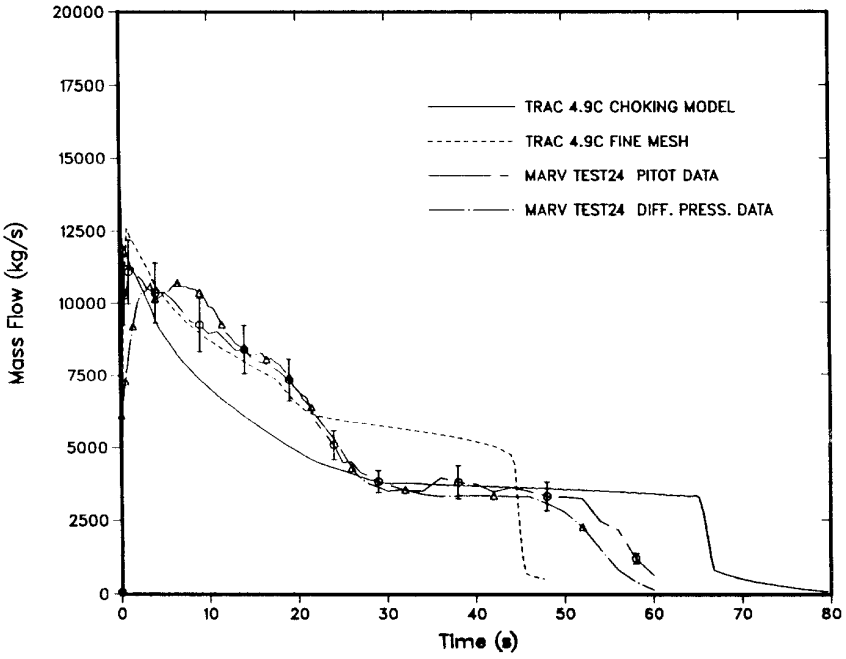

Fig. I-17. Comparison of the nozzle mass flows for Marviken Test 24.

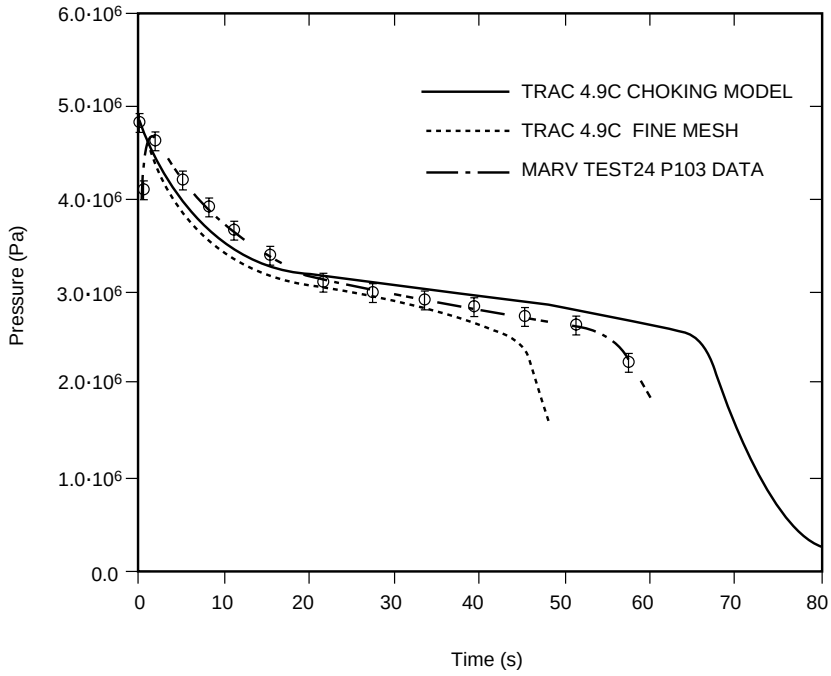

Fig. I-18. Comparison of the system pressure histories for Marviken Test 24.

I.2.6.2.2. Edwards Blowdown Experiment. The Edwards horizontal-pipe blowdown experiment studied depressurization phenomena of initially nonflowing subcooled water. The experimental apparatus consisted of a 4.096-m-long straight steel pipe with a 0.073-m i.d. The apparatus was designed for a maximum 17.24-MPa pressure at temperatures to 616.5 K. The discharge end of the horizontal pipe was sealed with a 0.0127-m-thick glass disk.

The pipe was filled with demineralized water; a hydraulic pump and a control valve regulated the system pressure. The pipe was evacuated by a vacuum pump before it was filled with water. Before the glass disk was ruptured, the pipe was isolated from the supply tank to prevent the discharge of cold water into the pipe during blowdown. Pressure transducers were located at gauge stations GS-1 to GS-7, and a temperature transducer was located at GS-5 (Fig. I-19.). Also provided at GS-5 were two aluminum-alloy disk windows for transient void-fraction measurements, which used an x-ray absorption system. The pipe was insulated and heated electrically. The operating procedure required that degassed water completely fill the pipe. The pipe was pressurized cold to ~25% above the initial depressurization 7-MPa test pressure and checked for leaks. Next, the pressure was reduced to 3.45 MPa and heat was applied gradually for ~1.5 h. During the heating of the water, the system pressure was maintained at ~3.45 MPa above the saturation pressure to prevent liquid flashing. The temperature variation along the pipe was limited by adjusting the voltage control for each heater. Initially the system was brought to an approximately uniform 515 K

temperature[1] and 7-MPa pressure. Because the isolating valve between the pipe and storage tank was closed, the glass disk ruptured, and the data were recorded automatically.

The MOD2 model consisted of a zero-velocity FILL component to simulate the closed end of the pipe, two PIPE components coupled in series, and a BREAK component. Near the discharge end of the pipe, the minimum cell lengths were 0.00509 m for the fine-mesh case and 0.17325 m for the choked-flow model. The choking model was applied at the discharge end, which had the minimum cross-sectional area in the system. We had to estimate this area because fragments of glass remained intact during the experiment. The default choked-flow multipliers were used in these calculations.

Figure I-20. compares the measured and calculated pressure histories near the middle of the pipe (GS-4). The choking and the fine-mesh calculations again agree well, with the choking calculational results closer to the data than the fine-mesh results. Although the discharge mass flow was not measured, the good pressure comparison between the calculations and the test data suggests good mass-flow calculations as well.

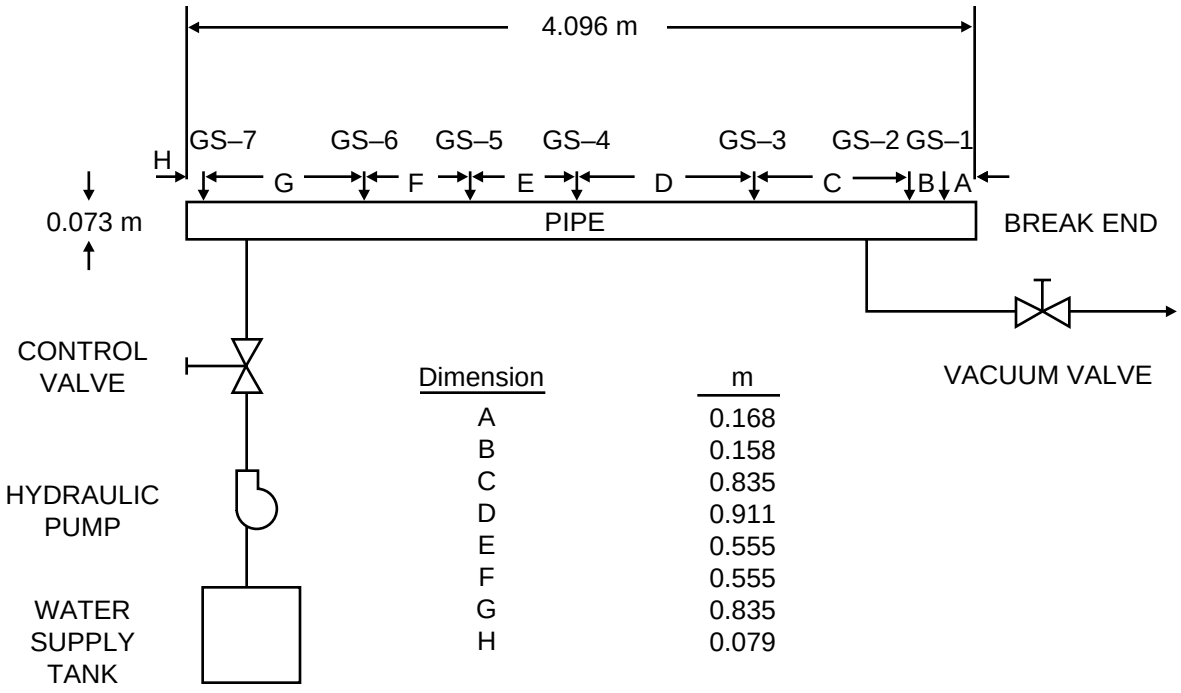

Fig. I-19. The Edwards horizontal-pipe blowdown experiment (adapted from Ref. I-13.).

1. There is some uncertainty in the initial temperature profile. However, we used exactly identical initial conditions in the choking and the fine-mesh calculations to maintain the validity of the comparison between the two calculations.

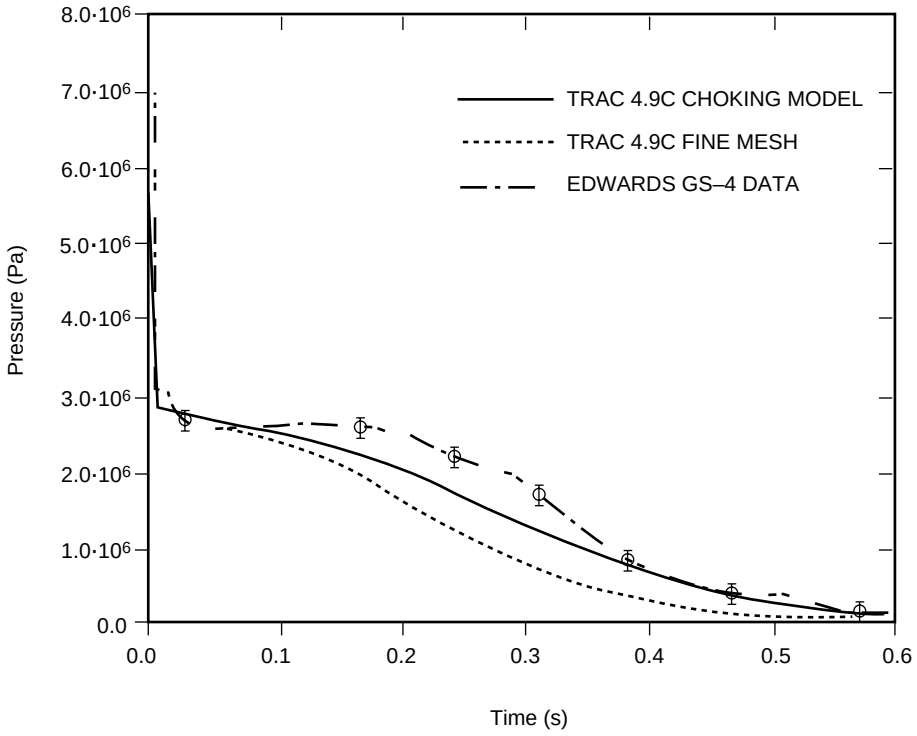

Fig. I-20. Comparison of the system pressure histories for the Edwards blowdown experiment.

I.2.7. Geometry Effects

To account for any geometry effects, the choked-flow model allows the user to input subcooled and two-phase choked-flow multipliers in the INOPTS NAMELIST data. Depending on which choking model is used (either subcooled-liquid, two-phase two-component fluid, or superheated vapor), these multipliers allow the user to adjust the predicted liquid, steam/gas-mixture, or both choking velocities to account for break or nozzle geometry effects. The use of the multipliers is described fully in Section I.2.4. Scaling Considerations

The choking model in TRAC is applicable to large- and small-scale geometries. The favorable results obtained in the Marviken Test 4 and Test 24 comparisons support the large-scale applicability, while the favorable results obtained in the Edwards blowdown test comparison show the model's ability to predict small-scale choking.

I.2.8. Summary and Conclusions

The two-phase, two-component, choked-flow model in TRAC was developed from first principles with a minimal amount of empiricism. The model assumes that thermal equilibrium exists between the phases in the presence or absence of an inert gas. The eigenvalues for the system of coupled differential equations are obtained

numerically. This generality gives the user the freedom to investigate and incorporate differential equations derived under different assumptions. The model yields results similar to those obtained using a fine mesh for components with smooth area changes. However, the quantitative agreement with the fine-mesh calculations is deficient for Marviken Test 24, which has a short nozzle, because the equilibrium assumption may be improper in that case. The results also compare well with other conventional models (the modified Burnell and the HEM). A good mass-flow comparison between the TRAC two-phase model and the HEM was obtained because the upstream fluid was stagnant, which gives minimal nonhomogeneous effects. However, for other two-phase situations, where the upstream liquid and vapor velocities differ significantly from each other, the nonhomogeneous effects may be very important. Comparisons of the TRAC calculations with the data from the separate-effects Marviken tests and the Edwards blowdown experiment also were favorable.

I.3. Countercurrent Flow Limitation (CCFL)

A special model exists in the code that allows the user to invoke characteristic CCFL correlations at specific locations in the 3D VESSEL component or in 1D vertical components. This capability exists in the axial direction in the 3D VESSEL component.

Countercurrent flow and CCFL can occur at any location in the reactor system. For instance, in the case of a reflux-condensation transient associated with a small-break LOCA, countercurrent flow is predicted to exist in the hot leg and in the entrance to the steam-generator inlet plenum. In the VESSEL, CCFL can occur during blowdown as ECC liquid is attempting to fill the downcomer. During reflood, CCFL can occur at the tie plate, where the upflow of steam prevents or limits the fallback of liquid. This is especially important for those systems that employ upper-plenum ECC injection.

Excluding mass transfer, the accurate prediction of the flow rates is dependent primarily on the interfacial drag between the phases (which is itself dependent on the accurate prediction of the flow regime). In a given flow system, CCFL usually occurs at a flow-area restriction. Typically, without the use of the CCFL model, the code predicts the complete turnaround point (zero liquid delivery), but overpredicts the amount of liquid downflow in the region of countercurrent flow. To improve the prediction in the countercurrent region, we added a special CCFL model to the 3D VESSEL and to vertical 1D components.

I.3.1. CCFL in the 3D VESSEL

We designed the CCFL model primarily for use in the tie-plate region of a PWR. The mechanism for countercurrent flow tie-plate geometry is very complex. For instance, in a single-bundle experiment, it has been observed that downflow can exist at the periphery of the plate, whereas upflow may occur in the center region. On the average over time, this behavior can be described by a CCFL (or flooding) correlation. CCFL correlations typically provide a superficial mass flux of liquid downflow versus a superficial mass flux of gas upflow. The correlations are developed from the integral over time of the amount of liquid accumulation below the plate for a given gas-injection

rate. The correlation therefore provides a 1D empirical model of the time-averaged multidimensional countercurrent-flow behavior. These correlations are geometry dependent. For tie plates, the plate thickness, hole diameter (or slot dimensions), number of holes, as well as the type of hardware above and below the tie plate can affect the CCFL characteristics. Rather than try to develop a new mechanistic CCFL model that could predict these complex behaviors in a variety of geometrical configurations, we decided to make use of the vast amount of correlated data already available. Therefore, the TRAC CCFL model provides the user the option to implement a CCFL correlation for the specific geometry available and to apply it at specific locations in the VESSEL. The input is general so that Wallis (Ref. I-14.), Kutateladze (Ref. I-15.), or Bankoff (Ref. I-16.) scaling can be accommodated.

I.3.2. Basis for the Model

The TRAC CCFL model is designed to provide the user with an alternative method for calculating countercurrent flow in geometrically complex reactor hardware. This model allows the user to input the characteristic flooding curve parameters for a specific geometry applied at a particular location in the vessel. Typically, these parameters have been developed from experimental data for the geometry of interest or for hardware of at least similar dimensions. Bankoff (Ref. I-16.) has shown that the data correlate well with the relationship

$$H_g^{1/2} + M_B H_l^{1/2} = C_B \quad , \tag{I-185}$$

where H_g is the dimensionless gas flux, H_l is the dimensionless liquid delivery, C_B is the abscissa intercept, and M_B is the slope.

This relationship is used in the CCFL model because it allows the user to implement either the Wallis scaling (diameter dependence), Kutateladze scaling (surface-tension dependence), or a combination of the two. This is done by defining as follows a variable-length scale in the determination of the dimensionless flux:

$$H_k = j_k \left(\frac{\rho_k}{g w \Delta \rho} \right)^{1/2} , \tag{I-186}$$

$$w = D^{1-E} L^E \quad , \tag{I-187}$$

and

$$L = \left(\frac{\sigma}{g \Delta \rho} \right)^{1/2} , \tag{I-188}$$

where

k refers to the phase (gas or liquid),
j is the superficial velocity,
D is the diameter of the holes
g is the gravitational constant,
σ is the surface tension,
ρ is the density,
$\Delta\rho$ is the difference between the phasic densities, and
E is an interpolation constant between 0 and 1.

Note that for E = 0, the correlation reverts to the Wallis scaling, and for E = 1, reverts to the Kutateladze scaling. For E between 0 and 1, the user can input the scaling proposed by Bankoff. This scaling can be calculated for tie-plate geometry even if no experimental data are available based on the critical wave number, $k_c = 2\pi / t_p$ (Ref. I-16.), so that

$$E = \tanh\ (\eta k_c D) \quad , \tag{I-189}$$

where η is the ratio of the area of the holes to the area of the tie plate and t_p is the thickness of the tie plate. Also, Bankoff developed a correlation for C_B based on the Bond number $L^* = n\pi D(g\Delta\rho/\sigma)^{1/2}$, so that

$$C_B = 1.07 + 4.33 \times 10^{-3} L^* \text{ for } L^* \leq 200 \tag{I-190}$$

and

$$C_B = 1.94 \text{ for } L^* > 200 \, , \tag{I-191}$$

where n is the number of holes.

I.3.3. Input Required

The user supplies the correlation constants M_B, E, and C_B, and the location where the CCFL model is to be applied. Alternatively, the values of C_B and E can be calculated by the code from thermodynamic properties and the input of n, t_p, h, and D.The void fraction in the cell below the interface is used to calculate the vapor flux. The void fraction in the cell above the interface is used to calculate the liquid flux. The surface tension, liquid density, and vapor density in the cell below the interface are used in the CCFL model.

I.3.4. Parametric Range and Scaling Considerations

For the TRAC CCFL model, the user supplies the correlation to be used at a specific location. Thus, the database is dependent on user input because the correlation constants are determined either from experimental data or from estimates based on physical dimensions. If the user provides a correlation that represents data that are similar to the

cell dimensions in geometry and scale, then the code should adequately predict countercurrent flow. Also, CCFL correlations normally scale with pressure because the form of the equations includes the effect of the change in density.

I.4. TEE-Component Offtake Model

The TRAC TEE-component offtake model is designed specifically to handle the case when a small break is made in a large pipe containing horizontal stratified flow (Ref. I-17.). One example of a transient that is particularly well-suited for use with the offtake model is the LOCA, in which a small break occurs in one of the large-diameter horizontal pipes of the reactor inlet or outlet legs. During this transient, horizontal stratified flow may occur, and the flow quality discharged at the break will depend on whether the break is above or below the liquid level. To accurately follow the progression of the transient, it is essential that the offtake flow be predicted correctly.

The TRAC TEE-component offtake model predicts the offtake flow quality that exits the break based on conditions in the main pipe in a manner similar to that developed for use in the RELAP5/MOD2 code (Ref. I-18.). When the entrance plane to the break is submerged, the offtake flow consists mostly of liquid with possibly an entrained gas component. When the entrance plane is above the liquid level, the offtake flow is mostly gas with possibly an entrained liquid component.

The model is implemented as an option that the user may turn on using the INOPTS namelist data flag IOFFTK. When IOFFTK = 1 (default = 0), the user is required to insert an additional line of input for each TEE component within the TRAC input deck specifying the value of the variable IENTRN. This new Card Number 15 requires IENTRN = 1 to implement the offtake model for a particular TEE. Similarly, no offtake model is implemented for any TEE for which IENTRN = 0. To use the model for its intended purpose, the following input guidelines are suggested.

1. The side tube of the TEE is required to be either top, bottom, or centrally located off the main tube.
2. The angle from the low-numbered side of the main tube to the side tube must be 90°. (Variable COST on Card Number 2 in TEE-component input.)
3. The main-tube-junction cell must be horizontal.

If these three conditions are not met by the input deck TEE geometry, the problem currently terminates in the initialization stage with a fatal error concerning inappropriate offtake geometry.

I.4.1. Basis for the Model

Several studies have been performed to investigate the discharge characteristics of a small break located on a horizontal pipe containing stratified flow. In these studies, the offtake was either top, bottom, or centrally oriented from the main tube as shown in Fig. I-21. The following discussion briefly describes each of these three offtake

geometries and the flow correlations developed by Ref. I-18. More detailed descriptions of the original experimental work may be found in Refs. I-19. through I-22.

In each of the three offtake geometries, a critical height at which gas or liquid entrainment begins, h_b, may be calculated using major-phase conditions at the entrance plane such that

$$h_b = \frac{C_1 W_k^{0.4}}{(g\rho_k \Delta\rho)^{0.2}} \quad , \tag{I-192}$$

where C_1 =a constant determined from data, W_k = major-phase mass-flow rate, g = gravitational constant, ρ_k = major-phase density, and $\Delta\rho = \rho_l - \rho_g$ = phasic density difference. For an upward offtake or for a side-oriented offtake with a liquid level *below* the offtake center, the major phase comprises the gas component. For a downward offtake or for a side-oriented offtake with a liquid level *above* the offtake center, the liquid component constitutes the major phase. The values of the constant C_1 recommended for use by Ref. I-18. are summarized in Table I-3. This formulation for h_b can be derived theoretically for each of the three offtake geometries by considering the force exerted on the liquid particles by the accelerating gas flow for liquid entrainment in upward or side-oriented offtakes and by considering surface instability effects for gas entrainment in downward offtakes (Refs. I-19., I-23., and I-24.).

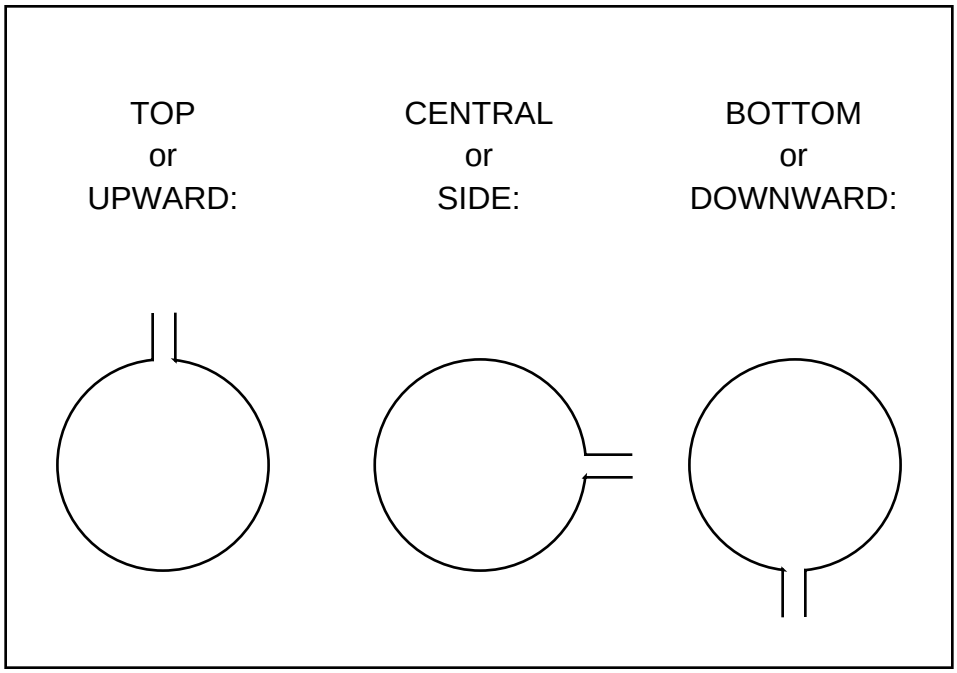

Fig. I-21. Possible offtake geometries.

TABLE I-3.
Critical Height Correlation Constant

Offtake Geometry	Correlation Constant, C_1
Upward	1.67
Downward	1.50
Side (gas entrain.)	0.75
Side (liquid entrain.)	0.69

An actual characteristic height, *h*, measured as the distance from the offtake entrance plane to the liquid level, may be determined for each of the three offtake geometries as shown in Fig. I-22. The nondimensional height ratio, *R*, then may be represented as

$$R = \frac{h}{h_b} \quad , \tag{I-193}$$

where h = actual characteristic height (see Fig. I-22.) and h_b = critical height [as defined by Eq. (I-192)].

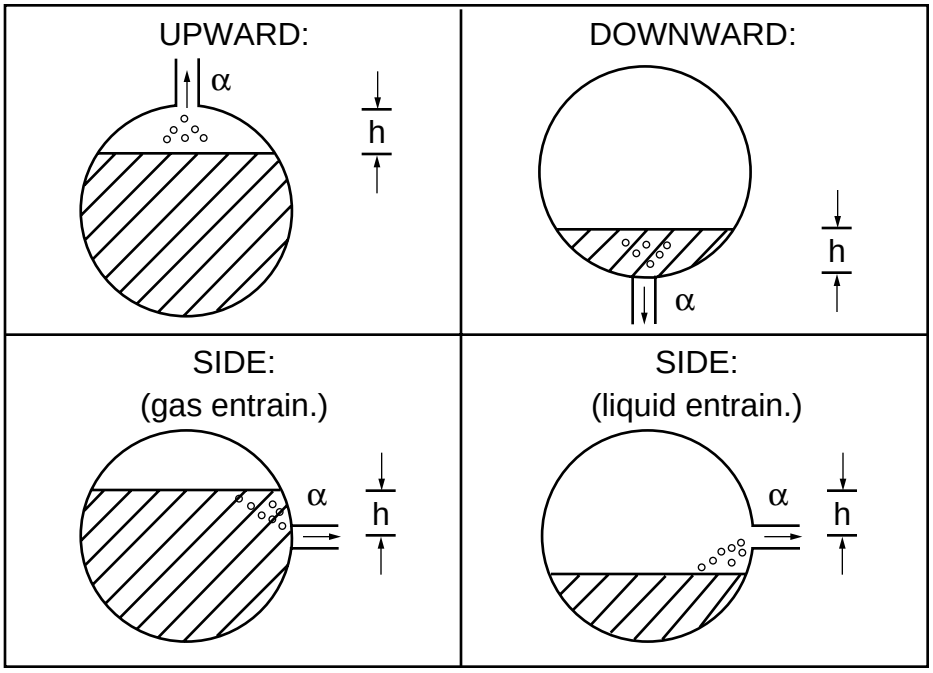

Fig. I-22. Determination of actual characteristic height, *h*.

Reference I-18. recommends the offtake flow quality, which has been correlated as a function of the nondimensional height ratio, R, be calculated for each of the three offtake geometries as follows.

For an upward offtake,

$$x = R^{3.25(1-R)^2} \quad , \tag{I-194}$$

where R = nondimensional height ratio [as defined by Eq. (I-193)].

For a side-oriented offtake,

$$x = x_o^{(1+C_2R)} \left[1 - 0.5R(1+R)\, x_o^{(1-R)}\right]^{0.5} \quad , \tag{I-195}$$

where

$$x_o = \frac{1.15}{1+\sqrt{\frac{\rho_l}{\rho_g}}} \quad , \tag{I-196}$$

R = nondimensional height ratio [as defined by Eq. (I-193)], ρ_l = liquid-phase density at the entrance plane, ρ_g = gas-phase density at the entrance plane, and C_2 = 1.09 for gas entrainment or 1.00 for liquid entrainment.

For a downward offtake,

$$x = x_o^{2.5R} \left[1 - 0.5R\ (1+R) x_o^{(1-R)}\right]^{0.5} \quad , \tag{I-197}$$

where x_o is given by Eq. (I-196), R = nondimensional height ratio [as defined by Eq. (I-193)], ρ_l = liquid-phase density at the entrance plane, and ρ_g = gas-phase density at the entrance plane.

The actual coding for the TRAC offtake model is contained in subroutine OFFTKE and is outlined in Sections I.4.2. and I.4.3.

I.4.2. Assumptions and Preliminary Calculations

The coding for the TEE-component offtake model is contained in subroutine OFFTKE, and the main calculation is described in the next section. However, upon entry into subroutine OFFTKE, several preliminary calculations take place, and these are described here. The offtake void fraction is initialized to be the same as the void fraction of the main-tube-junction cell. In addition, the average flow diameter of the offtake is calculated such that

$$D_{\text{ot}} = \sqrt{\frac{4.0A_j}{\pi}} \quad , \tag{I-198}$$

where A_j = offtake flow area at the entrance plane.

Next, several tests are performed to determine whether to continue the calculation. Subroutine OFFTKE is designed to handle only the case of two-phase, co-current flow out of the main tube break. If these conditions are not met, the offtake calculation ends and the logic returns to the calling subroutine. This is also true if horizontal stratified flow does not exist in the main-tube-junction cell (as indicated by the variable WFHF) or if the average diameter of the offtake is greater than or equal to the main-tube-junction cell average diameter.

However, if co-current, horizontal stratified flow out of the main-tube-junction cell does exist, subroutine OFFTKE continues with its preliminary calculations. The liquid level in the main-tube-junction cell is calculated from the void fraction and average diameter in a call to subroutine LEVEL. In addition, an old-time slip ratio at the offtake entrance plane is calculated as the ratio of old-time gas and liquid velocities such that

$$S = \frac{V_g^n}{V_l^n} \quad , \tag{I-199}$$

where v_g^n = old-time, entrance-plane gas velocity and v_l^n = old-time, entrance-plane liquid velocity. This slip is limited to a minimum value of 1.0×10^{-7} After the preliminary calculations have been performed, the logic splits to handle each of the three possible geometries: upward offtake, side-oriented offtake, or downward offtake.

I.4.3. Model as Coded

The TEE-component offtake model was added into TRAC using subroutine OFFTKE. Based on the offtake geometry and the liquid level conditions in the junction cell of the main tube, subroutine OFFTKE calculates the void fraction that exits out the main tube break. Upon entry into subroutine OFFTKE, several preliminary calculations take place that are detailed in the previous section. Once the preliminary calculations are complete, the logic splits to handle each of the three possible geometries: upward offtake, side-oriented offtake, or downward offtake.

I.4.3.1. Upward Offtake. For the case of the upward offtake, the major-flow component is the gas phase. The actual characteristic height for the upward offtake as shown in Fig. I-22. is approximated as

$$h_{up} = D_1 - h_1 \quad , \tag{I-200}$$

where D_1 = main-tube-junction cell average diameter and h_1 = main-tube-junction cell liquid depth (as defined by a call to subroutine LEVEL).

The major-phase mass-flow rate at the offtake entrance plane is calculated as

$$W_g = \alpha_{ot}^n \rho_g^{n+1} A_j V_g^{n+1} \quad , \tag{I-201}$$

where α_{ot}^{n} = old-time offtake void fraction, ρ_g^{n+1} = new-time donor-cell gas density, A_j = offtake entrance-plane flow area, and v_g^{n+1} = new-time entrance-plane gas velocity.

The critical entrainment height then may be calculated such that

$$h_b = \frac{C_1 W_g^{0.4}}{\left[g\rho_g^{n+1}\left(\rho_l^{n+1} - \rho_g^{n+1}\right)\right]^{0.2}} \quad , \tag{I-202}$$

where C_1 = 1.67 for an upward offtake (as defined by Table I-3.), W_g = major-phase (gas) mass-flow rate [as defined by Eq. (I-201)], g = gravitational constant, ρ_g^{n+1} = new-time donor-cell gas density, and ρ_l^{n+1} = new-time donor-cell liquid density. This critical entrainment height is limited to a minimum value of 1.0×10^{-6}.

The offtake flow quality at the entrance plane is then

$$x = R^{3.25(1-R)^2} \quad , \tag{I-203}$$

where R = nondimensional height ratio of h_{up} [as defined by Eq. (I-200)] to h_b [as defined by Eq. (I-202)], which is limited such that $0.0 \le R \le 1.0$.

Thus, the first prediction of the new-time offtake-model void fraction at the entrance plane is calculated as

$$\alpha_m^{n+1,1} = \frac{x\rho_l^{n+1}}{x\rho_l^{n+1} + (1-x)\rho_g^{n+1}S} \quad , \tag{I-204}$$

where x = offtake entrance-plane flow quality [as defined by Eq. (I-203)], ρ_l^{n+1} = new-time donor-cell liquid density, ρ_g^{n+1} = new-time donor-cell gas density, and S = old-time slip ratio [as defined by Eq. (I-199)]. At this point, this first prediction of the offtake void fraction is sent through several interpolations, averages, and limits to arrive at the final offtake void fraction.

First, if the liquid level in the main-tube-junction cell is above the offtake entrance plane, the offtake void fraction predicted by Eq. (I-204) is modified to ensure that it approaches the value of the void fraction in the main-tube-junction cell as the liquid level reaches the top of the main-tube-junction cell. This interpolation is performed linearly with the main-tube-junction cell liquid depth, h_1, such that

$$\alpha_m^{n+1,2} = f\alpha_m^{n+1,1} + (1-f)\alpha_1^{n+1}, \tag{I-205}$$

where

$$f = \frac{h_1 - D_1}{h_c - D_1}, \tag{I-206}$$

h_1 = main-tube-junction cell liquid depth, D_1 = main-tube-junction cell average diameter, h_c = critical main-tube-junction cell liquid depth at which the liquid level just reaches the offtake entrance plane, $\alpha_m^{n+1,1}$ = first offtake void-fraction prediction [as defined by Eq. (I-204)], and α_1^{n+1} = new-time main-tube-junction cell void fraction.

Next, this offtake void-fraction result is weighted using the horizontal stratified-flow weighting factor to ensure that the offtake void fraction tends toward the main-tube-junction cell void fraction as the flow, moves away from a stratified-flow regime such that

$$\alpha_m^{n+1,3} = \text{WFHF} \cdot \alpha_m^{n+1,2} + (1 - \text{WFHF})\alpha_1^{n+1} \quad , \tag{I-207}$$

where WFHF = horizontal-flow weighting factor, $\alpha_m^{n+1,2}$ = second offtake void-fraction prediction [as defined by Eq. (I-205)], and α_1^{n+1} = new-time main-tube-junction cell void fraction.

Finally, the offtake void-fraction prediction is limited to ensure that the volume of liquid entrained does not exceed the volume that exists in the main-tube-junction cell such that

$$\alpha_{\text{ot}}^{n+1} = \max(\alpha_m^{n+1,3}, \alpha_1^{n+1}), \tag{I-208}$$

where $\alpha_m^{n+1,3}$ = third offtake void-fraction prediction [as defined by Eq. (I-207)] and α_1^{n+1} = new-time main-tube-junction cell void fraction. This concludes the calculative sequence for the case of the upward offtake. At this point, the new-time offtake void fraction, α_{ot}^{n+1}, is returned to the calling subroutine.

I.4.3.2. Side-Oriented Offtake. For the case of the side-oriented offtake, the major-flow component may be either the gas phase or the liquid phase. When the liquid level in the main tube is below the offtake center, the gas phase is the major-flow component and liquid entrainment may occur. However, if the liquid level in the main tube is above the offtake center, the liquid phase becomes the major-flow component and gas entrainment may be possible. The following description first details the case of when the gas phase is the major-flow component and liquid entrainment may occur, and then outlines the case when the liquid phase is the major-flow component and gas entrainment may be possible.

For the case of the side-oriented offtake with a gas major-flow component (the case of possible liquid entrainment), the actual characteristic height as shown in Fig. I-22. is approximated as

$$h_{\text{sd}} = h_1 - 0.5D_1 \quad , \tag{I-209}$$

where h_1 = main-tube-junction cell liquid depth (as defined by a call to subroutine LEVEL) and D_1 = main-tube-junction cell average diameter. Notice that for this offtake configuration, h_{sd} is a negative value, which later causes the nondimensional height ratio, R, to also be negative in value.

The major-phase mass-flow rate at the offtake entrance plane is calculated as

$$W_g = \alpha_{\text{ot}}^n \rho_g^{n+1} A_j V_g^{n+1} \quad , \tag{I-210}$$

where α_{ot}^n = old-time offtake void fraction, ρ_g^{n+1} = new-time donor-cell gas density, A_j = offtake entrance-plane flow area, and V_g^{n+1} = new-time entrance-plane gas velocity.

The critical entrainment height then may be calculated such that

$$h_b = \frac{C_1 W_g^{0.4}}{\left[g \rho_g^{n+1} \left(\rho_{\text{l}}^{n+1} - \rho_g^{n+1} \right) \right]^{0.2}} \quad , \tag{I-211}$$

where C_1 = 0.69 for a side-oriented offtake with a gas major-flow component (as defined by Table I-3.), W_g = major-phase (gas) mass-flow rate [as defined by Eq. (I-210)], g = gravitational constant, ρ_g^{n+1} = new-time donor-cell gas density, and ρ_{l}^{n+1} = new-time donor-cell liquid density. This critical entrainment height is limited to be no less than the larger of 1.0×10^{-6} and 0.5 D_{ot} [see Eq. (I-198)].

The offtake flow quality at the entrance plane is then

$$x = x_o^{(1+C_2 R)} \left[1 - 0.5 R (1+R) x_o^{(1-R)} \right]^{0.5} \quad , \tag{I-212}$$

where

$$x_o = \frac{1.15}{1 + \sqrt{\dfrac{\rho_{\text{l}}^{n+1}}{\rho_g^{n+1}}}} \quad , \tag{I-213}$$

R = nondimensional height ratio of h_{sd} [as defined by Eq. (I-209)] to h_b [as defined by Eq. (I-211)], ρ_{l}^{n+1} = new-time donor-cell liquid density, ρ_g^{n+1} = new-time donor-cell gas density, and C_2 = 1.00 for liquid entrainment.

Thus, the first prediction of the new-time offtake-model void fraction at the entrance plane is calculated as

$$\alpha_m^{n+1,1} = \frac{x \rho_{\text{l}}^{n+1}}{x \rho_{\text{l}}^{n+1} + (1-x)\, \rho_g^{n+1} S} \quad , \tag{I-214}$$

where x = offtake entrance-plane flow quality [as defined by Eq. (I-212)], ρ_{l}^{n+1} = new-time donor-cell liquid density, ρ_g^{n+1} = new-time donor-cell gas density, and S = old-time slip ratio [as defined by Eq. (I-199)]. At this point, this first prediction of the offtake void

fraction is sent through the same interpolations, averages, and limits as was the case for the upward offtake to arrive at the final offtake void fraction.

First, if the liquid level in the main-tube-junction cell is between the bottom and the centerline of the offtake entrance, the offtake void fraction predicted by Eq. (I-214) is modified to ensure that it approaches the value of the void fraction in the main-tube-junction cell as the diameter of the offtake approaches the diameter of the main-tube-junction cell. This interpolation is performed linearly with the main-tube-junction cell liquid depth, h_1 such that

$$\alpha_m^{n+1,2} = f\alpha_m^{n+1,1} + (1-f)\alpha_1^{n+1} \quad , \tag{I-215}$$

where

$$f = \frac{h_c}{h_1} \quad , \tag{I-216}$$

and where h_c = critical main-tube-junction cell liquid depth at which the liquid level just reaches the offtake entrance, h_1 = main-tube-junction cell liquid depth, $\alpha_m^{n+1,1}$ = first offtake void-fraction prediction [as defined by Eq. (I-214)], and α_1^{n+1} = new-time main-tube-junction cell void fraction.

Next, this offtake void-fraction result is weighted using the horizontal stratified-flow weighting factor to ensure that the offtake void fraction tends toward the main-tube-junction cell void fraction as the flow moves away from a stratified-flow regime such that

$$\alpha_m^{n+1,3} = \mathrm{WFHF} \cdot \alpha_m^{n+1,2} + (1-\mathrm{WFHF})\alpha_1^{n+1} \quad , \tag{I-217}$$

where WFHF = horizontal-flow weighting factor, $\alpha_m^{n+1,2}$ = second offtake void-fraction prediction [as defined by Eq. (I-215)], and α_1^{n+1} = new-time main-tube-junction cell void fraction.

Finally, the offtake void-fraction prediction is limited to ensure that the volume of liquid entrained does not exceed the volume that exists in the main-tube-junction cell such that

$$\alpha_{\mathrm{ot}}^{n+1} = \max(\alpha_m^{n+1,3}, \alpha_1^{n+1}) \quad , \tag{I-218}$$

where $\alpha_m^{n+1,3}$ = third offtake void-fraction prediction [as defined by Eq. (I-217)] and α_1^{n+1} = new-time main-tube-junction cell void fraction. This concludes the calculative sequence for the case of the side-oriented offtake with a gas major-flow component. At this point, the new-time offtake void fraction, $\alpha_{\mathrm{ot}}^{n+1}$, is returned to the calling subroutine.

For the case of the side-oriented offtake with a liquid major-flow component (the case of possible gas entrainment), the actual characteristic height as shown in Fig. I-22. is approximated as

$$h_{sd} = h_1 - 0.5D_1 \quad , \tag{I-219}$$

where h_1 = main-tube-junction cell liquid depth (as defined by a call to subroutine LEVEL) and D_1 = main-tube-junction cell average diameter.

The major-phase mass-flow rate at the offtake entrance plane is calculated as

$$W_l = (1-\alpha_{ot}^n)\rho_l^{n+1} A_j V_l^{n+1} \quad , \tag{I-220}$$

where α_{ot}^n = old-time offtake void fraction, ρ_l^{n+1} = new-time donor-cell liquid density, A_j = offtake entrance-plane flow area, and V_l^{n+1} = new-time entrance-plane liquid velocity.

The critical entrainment height then may be calculated such that

$$h_b = \frac{C_1 W_l^{0.4}}{\left[g\rho_l^{n+1}\left(\rho_l^{n+1} - \rho_g^{n+1}\right)\right]^{0.2}} \quad , \tag{I-221}$$

where $C_1 = 0.75$ for a side-oriented offtake with a liquid major-flow component (as defined by Table I-3.), W_l = major-phase (liquid) mass-flow rate [as defined by Eq. (I-220)], g = gravitational constant, ρ_l^{n+1} = new-time donor-cell liquid density, and ρ_g^{n+1} = new-time donor-cell gas density. This critical entrainment height is limited to be no less than the larger of 1.0×10^{-6} and $0.5D_{ot}$ [see Eq. (I-198)].

The offtake flow quality at the entrance plane is then

$$x = x_o^{(1+C_2 R)} \left[1 - 0.5R(1+R)\, x_o^{(1-R)}\right]^{0.5} \tag{I-222}$$

for the range

$$0.0 \;\le\; R \;<\; 0.9 \quad ,$$

where

$$x_o = \frac{1.15}{1 + \sqrt{\frac{\rho_l^{n+1}}{\rho_g^{n+1}}}} \quad , \tag{I-223}$$

R = nondimensional height ratio of h_{sd} [as defined by Eq. (I-219)] to h_b [as defined by Eq. (I-221)], ρ_l^{n+1} = new-time donor-cell liquid density, ρ_g^{n+1} = new-time donor-cell gas density, and C_2 = 1.09 for gas entrainment.

In Eq. (I-222), as R approaches 1, x approaches 0 very rapidly. To avoid an exponential approach toward zero, the term $R(1 + R)$ was replaced with a linear function for the range $0.9 \le R \le 1.0$, resulting in the following formulation for flow quality:

$$x = -10.0 x_o^{(1+C_2 R)} \left[1 - 0.855 x_o^{0.1}\right]^{0.5} (R - 1.0) \qquad \text{(I-224)}$$

for the range

$$0.9 \le R \le 1.0 \quad ,$$

where x_o is defined by Eq. (I-223), C_2 = 1.09 for gas entrainment, and R is again the nondimensional height ratio.

Thus, the first prediction of the new-time offtake-model void fraction at the entrance plane is calculated as

$$\alpha_m^{n+1,1} = \frac{x \rho_l^{n+1}}{x \rho_l^{n+1} + (1 - x)\, \rho_g^{n+1} S} \quad , \qquad \text{(I-225)}$$

where x = offtake entrance-plane flow quality [as defined by Eq. (I-222) or (I-224)], ρ_l^{n+1} = new-time donor-cell liquid density, ρ_g^{n+1} = new-time donor-cell gas density, and S = old-time slip ratio [as defined by Eq. (I-199)]. At this point, this first prediction of the offtake void fraction is sent through the same type interpolations, averages, and limits as was the case for the upward offtake to arrive at the final offtake void fraction.

First, if the liquid level in the main-tube-junction cell is between the centerline and the top of the offtake entrance, the offtake void fraction predicted by Eq. (I-225) is modified to ensure that it approaches the value the of the void fraction in the main-tube-junction cell as the diameter of the offtake approaches the diameter of the main-tube-junction cell. This interpolation is performed linearly with the main-tube-junction cell liquid depth, h_1 such that

$$\alpha_m^{n+1,2} = f \alpha_m^{n+1,1} + (1 - f) \alpha_1^{n+1} \quad , \qquad \text{(I-226)}$$

where

$$f = \frac{D_1 - h_c}{D_1 - h_1} \quad , \qquad \text{(I-227)}$$

D_1 = main-tube-junction cell average diameter, h_c = critical main-tube-junction cell liquid depth at which the liquid level just reaches the offtake entrance, h_1 = main-tube-junction cell liquid depth, $\alpha_m^{n+1,1}$ = first offtake void-fraction prediction [as defined by Eq. (I-225)], and α_1^{n+1} = new-time main-tube-junction cell void fraction.

Next, this offtake void-fraction result is weighted using the horizontal stratified-flow weighting factor to ensure that the offtake void fraction tends toward the main-tube-junction cell void fraction as the flow moves away from a stratified-flow regime such that

$$\alpha_m^{n+1,3} = \text{WFHF} \cdot \alpha_m^{n+1,2} + (1 - \text{WFHF})\, \alpha_1^{n+1} \quad , \tag{I-228}$$

where WFHF = horizontal-flow weighting factor, $\alpha_m^{n+1,2}$ = second offtake void-fraction prediction [as defined by Eq. (I-226)], and α_1^{n+1} = new-time main-tube-junction cell void fraction.

Finally, the offtake void-fraction prediction is limited to ensure that the volume of gas entrained does not exceed the volume that exists in the main-tube-junction cell such that

$$\alpha_{\text{ot}}^{n+1} = \min(\alpha_m^{n+1,3}, \alpha_1^{n+1}) \ , \tag{I-229}$$

where $\alpha_m^{n+1,3}$ = third offtake void-fraction prediction [as defined by Eq. (I-228)] and α_1^{n+1} = new-time main-tube-junction cell void fraction. This concludes the calculative sequence for the case of the side-oriented offtake with a liquid major-flow component. At this point, the new-time offtake void fraction, α_{ot}^{n+1}, is returned to the calling subroutine.

I.4.3.3. Downward Offtake. For the case of the downward offtake, the major-flow component is the liquid phase. The actual characteristic height for the downward offtake as shown in Fig. I-22. is approximated as

$$h_{\text{dn}} = h_1 \quad , \tag{I-230}$$

where h_1 = main-tube-junction cell liquid depth (as defined by a call to subroutine LEVEL).

The major-phase mass-flow rate at the offtake entrance plane is calculated as

$$W_{\text{l}} = (1 - \alpha_{\text{ot}}^n)\rho_{\text{l}}^{n+1} A_j V_{\text{l}}^{n+1} \quad , \tag{I-231}$$

where α_{ot}^n = old-time offtake void fraction, ρ_{l}^{n+1} = new-time donor-cell liquid density, A_j = offtake entrance-plane flow area, and V_{l}^{n+1} = new-time entrance-plane liquid velocity.

The critical entrainment height then may be calculated such that

$$h_b = \frac{C_1 W_l^{0.4}}{\left[g\rho_l^{n+1}\left(\rho_l^{n+1} - \rho_g^{n+1}\right)\right]^{0.2}} \quad , \tag{I-232}$$

where $C_1 = 1.50$ for a downward offtake (as defined by Table I-3.), W_l = major-phase (liquid) mass-flow rate [as defined by Eq. (I-231)], g = gravitational constant, ρ_l^{n+1} = new-time donor-cell liquid density, and ρ_g^{n+1} = new-time donor-cell gas density. This critical entrainment height is limited to a minimum value of 1.0×10^{-6}.

The offtake flow quality at the entrance plane is then

$$x = x_o^{2.5R}\left[1 - 0.5R(1+R)x_o^{(1-R)}\right]^{0.5} \tag{I-233}$$

for the range

$$0.0 \leq R < 0.9 \quad ,$$

where

$$x_o = \frac{1.15}{1 + \sqrt{\frac{\rho_l^{n+1}}{\rho_g^{n+1}}}} \quad , \tag{I-234}$$

R = nondimensional height ratio of h_{dn} [as defined by Eq. (I-230)] to h_b [as defined by Eq. (I-232)], ρ_l^{n+1} = new-time donor-cell liquid density, and ρ_g^{n+1} = new-time donor-cell gas density.

In Eq. (I-233), as R approaches 1, x approaches 0 very rapidly. To avoid an exponential approach toward zero, the term $R(1 + R)$ was replaced with a linear function for the range $0.9 \leq R \leq 1.0$ resulting in the following formulation for flow quality:

$$x = -10.0 x_o^{2.5R}\left[1 - 0.855 x_o^{0.1}\right]^{0.5}(R - 1.0) \tag{I-235}$$

for the range

$$0.9 \leq R \leq 1.0 \quad ,$$

where x_o is defined by Eq. (I-232) and R is again the nondimensional height ratio.

Thus, the first prediction of the new-time model void fraction at the entrance plane is calculated as

$$\alpha_m^{n+1,1} = \frac{x\rho_l^{n+1}}{x\rho_l^{n+1} + (1-x)\,\rho_g^{n+1} S} \quad , \tag{I-236}$$

where x = offtake entrance-plane flow quality [as defined by Eq. (I-233) or (I-235)], ρ_l^{n+1} = new-time donor-cell liquid density, ρ_g^{n+1} = new-time donor-cell gas density, and S = old-time slip ratio [as defined by Eq. (I-199)]. At this point, this first prediction of the offtake void fraction is sent through the same type of interpolations, averages, and limits as was the case for both the upward and side-oriented offtakes to arrive at the final offtake void fraction.

First, if the liquid level in the main-tube-junction cell is below the offtake entrance plane, the offtake void fraction predicted by Eq. (I-236) is modified to ensure that it approaches the value of the void fraction in the main-tube-junction cell as the liquid level reaches the bottom of the main-tube-junction cell. This interpolation is performed linearly with the main-tube-junction cell liquid depth, h_1 such that

$$\alpha_m^{n+1,2} = f\alpha_m^{n+1,1} + (1-f)\,\alpha_1^{n+1} \quad , \tag{I-237}$$

where

$$f = \frac{h_1}{h_c} \ , \tag{I-238}$$

h_1 = main-tube-junction cell liquid depth, h_c = critical main-tube-junction cell liquid depth at which the liquid level reaches the offtake entrance plane, $\alpha_m^{n+1,1}$ = first offtake void-fraction prediction [as defined by Eq. (I-236)], and α_1^{n+1} = new-time main-tube-junction cell void fraction.

Next, this offtake void-fraction result is weighted using the horizontal stratified-flow weighting factor to ensure that the offtake void fraction tends toward the main-tube-junction cell void fraction as the flow moves from a stratified-flow regime such that

$$\alpha_m^{n+1,3} = \mathrm{WFHF} \cdot \alpha_m^{n+1,2} + (1-\mathrm{WFHF})\,\alpha_1^{n-1} \quad , \tag{I-239}$$

where WFHF = horizontal-flow weighting factor, $\alpha_m^{n+1,2}$ = second offtake void-fraction prediction [as defined by Eq. (I-237)], and α_1^{n+1} = new-time main-tube-junction cell void fraction.

Finally, the offtake void-fraction prediction is limited to ensure that the volume of gas entrained does not exceed the volume that exists in the main-tube-junction cell such that

$$\alpha_{\mathrm{ot}}^{n+1} = \min\left(\alpha_m^{n+1,3} \ , \ \alpha_1^{n+1}\right) \quad , \tag{I-240}$$

where $\alpha_m^{n+1,3}$ = third offtake void-fraction prediction [as defined by Eq. (I-239)] and α_1^{n+1} = new-time main-tube-junction cell void fraction. This concludes the calculative sequence for the case of the downward offtake. At this point, the new-time, offtake void fraction, α_{ot}^{n+1}, is returned to the calling subroutine.

I.4.4. Weighting, Magnitude Limits, Rate Limits, and Averaging

For each of the three possible offtake geometries, the solution procedure within subroutine OFFTKE follows the same logic. Once a first prediction of the offtake void fraction is determined, three adjustments are performed to obtain the final offtake void-fraction prediction. The first adjustment is an interpolation based on liquid level to ensure that the predicted offtake void fraction tends toward certain limits as the liquid level approaches certain limits. For example, as the liquid level approaches the top of the main-tube-junction cell, the offtake void fraction for an upward offtake is expected to approach the value of the main-tube-junction cell void fraction. The second adjustment is a simple weighting using the horizontal weighting factor to ensure that the offtake void fraction tends toward the main-tube-junction cell void fraction as the flow moves away from a stratified-flow regime. The final adjustment is a limit to ensure that the volume of liquid or gas being entrained does not exceed the volume of the entrained component that exists in the main-tube-junction cell. Each of these adjustments is performed once the first prediction of the offtake void fraction is obtained, regardless of the offtake geometry. The specific algebraic equations used for these interpolations, weightings, or limits is detailed in the appropriate subsection of the model description in Section I.4.3.

I.4.5. Assessment

Two very simple test cases have been developed to demonstrate how the offtake option works. These tests were chosen because of the existence of “obvious answers” and are meant only to demonstrate that the technique used to implement the offtake model into the TRAC two-step numerics functions properly. Three additional, more detailed assessment calculations are planned for the offtake model using the data from Tests SB-CL-12, SB-CL-15, and SB-CL-16 of the ROSA-IV facility performed by the Japan Atomic Energy Research Institute (JAERI). The three JAERI tests, which involve a 0.5% cold-leg break oriented in each of the three offtake positions, will enable a more rigorous assessment of the offtake model to be performed.

The geometry for both of the two simple analytical problems consists of a horizontal TEE component with a specified mass-flow rate at one end of the main tube and a large drain tank at the other end. The side tube of the TEE forms the offtake and is upwardly oriented for one test and downwardly oriented for the other. A schematic of the input used to model the test case with the upward offtake is shown in Fig. I-23. The mass-flow rate at the inlet FILL was chosen such that a low-velocity, horizontal stratified flow would exist in the TEE main tube. In addition, a mass-flow rate was selected that could maintain a relatively high void fraction in the main-tube-junction cell for the upward offtake and a relatively low void fraction for the downward offtake test case. Pressure boundaries were selected to encourage flow from the main tube into the offtake.

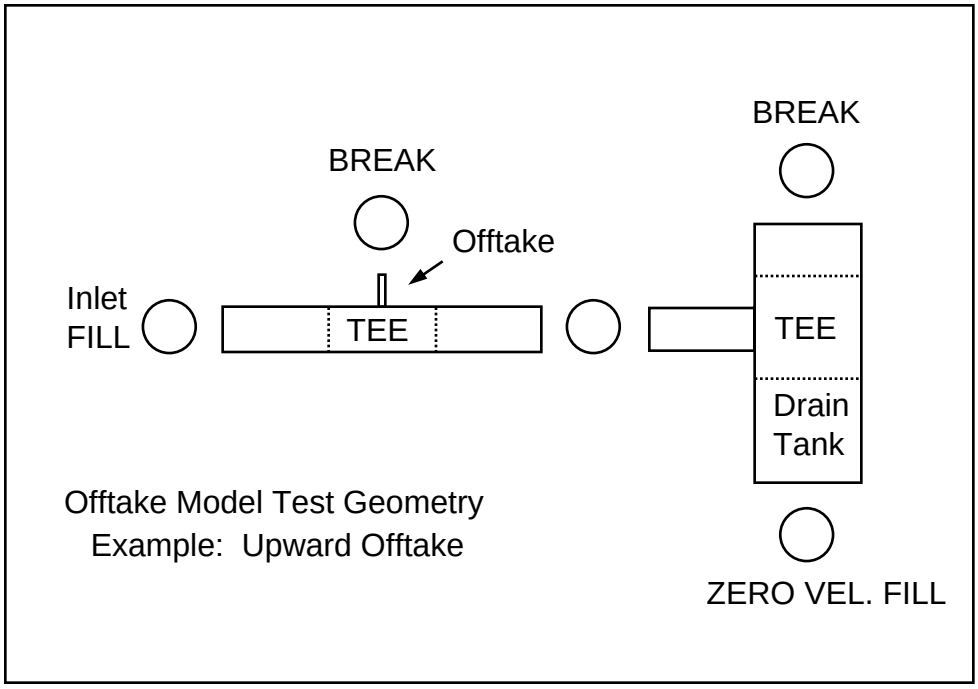

Fig. I-23. Sample input deck schematic.

The results of the upward offtake test case are shown in Figs. I-24. and I-25. Figure I-24. shows the void fractions that TRAC calculates to exist in the main-tube-junction cell and in the offtake cell when the offtake option is not selected. Notice that although the main-tube-junction cell has only a small volume fraction of liquid in it, TRAC shows that the same volume fraction is convected up out of the offtake. For the low-velocity, horizontal stratified flow of this test case, this prediction is not physical. Figure I-25. shows the same example with the offtake option selected. As expected, only the gas exits the offtake for this particular case of low-velocity, high-void, horizontal stratified flow in the main tube.

Similar results are achieved in the downward offtake test case. For low-velocity, low-void flow in the main tube, one expects that only liquid will drain out of a downward offtake. Figure I-26. shows that TRAC does not calculate this result when the offtake option is off. Instead, the flow exiting the offtake is calculated incorrectly as being of nearly the same void fraction as that which exists in the main-tube-junction cell. However, Fig. I-27. shows that if the offtake model is turned on, TRAC is able to predict correctly that only liquid is draining out of the offtake as expected physically.

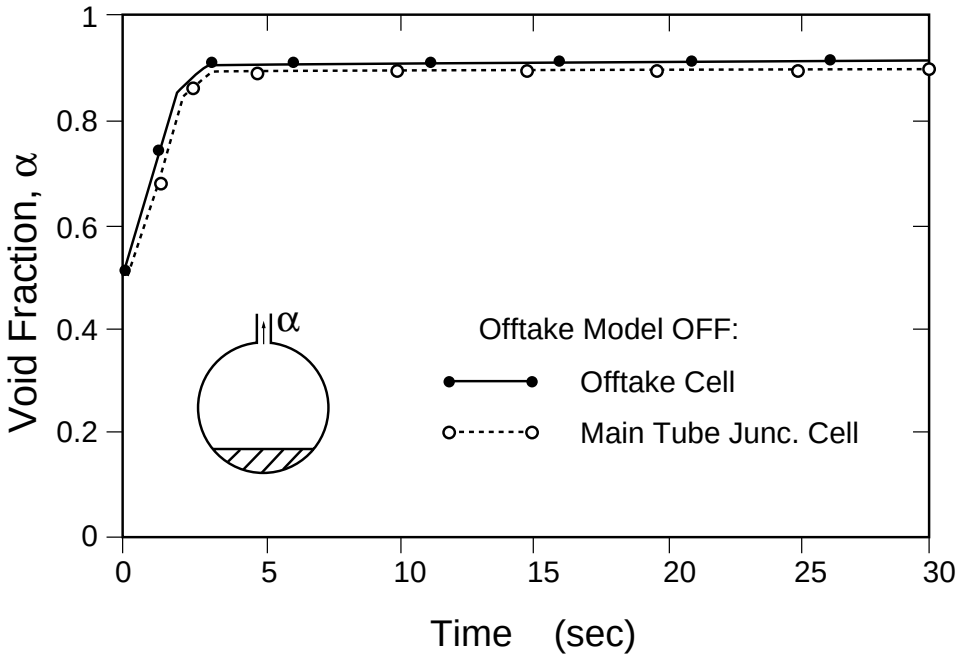

Fig. I-24. Upward offtake test results—no offtake model implemented.

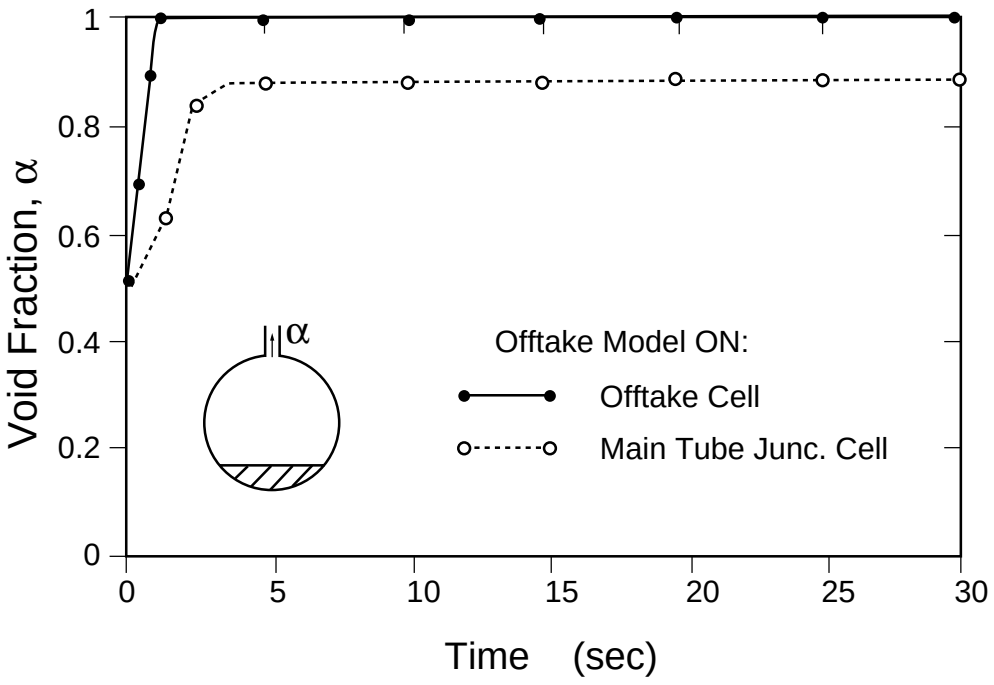

Fig. I-25. Upward offtake test results—offtake model option implemented.

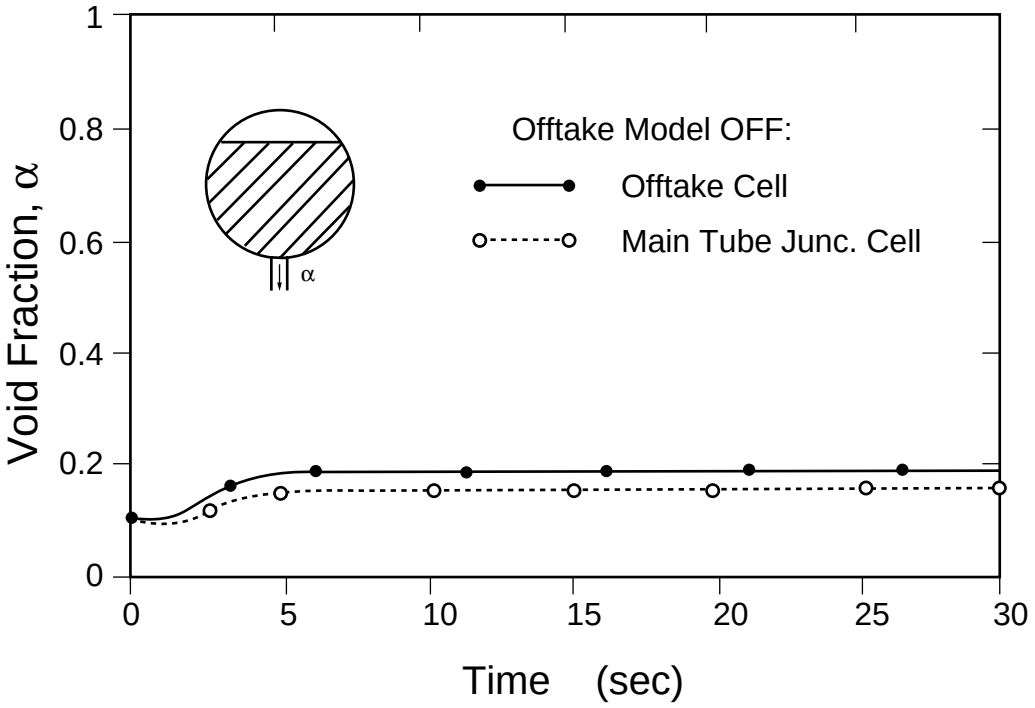

Fig. I-26. Downward offtake test results—no offtake model implemented.

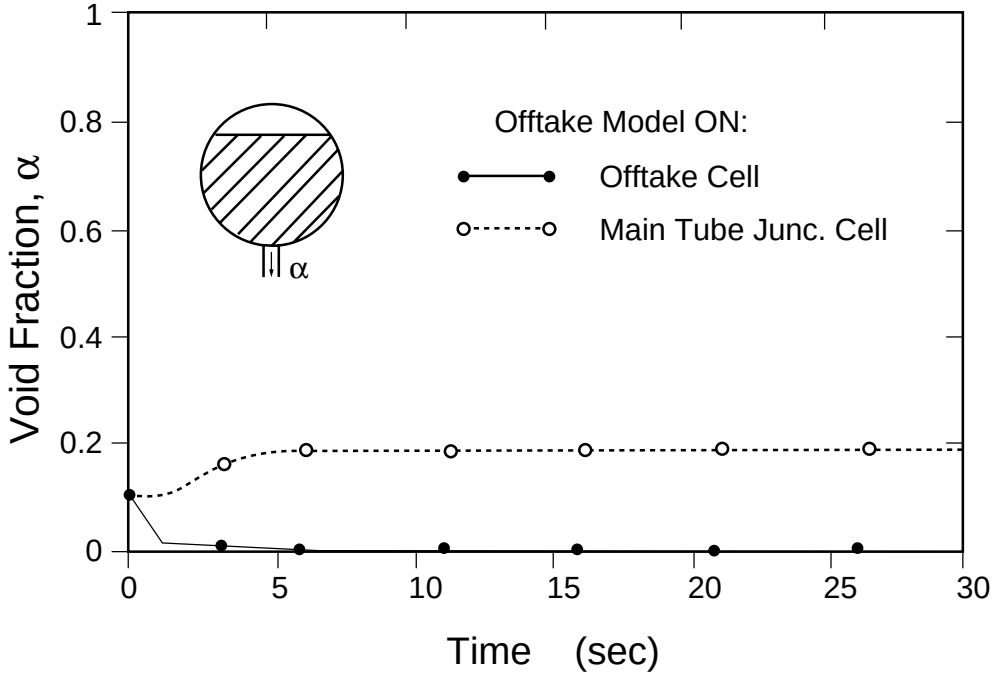

Fig. I-27. Downward offtake test results—offtake model option implemented.

I.4.6. Geometry Effects

In an effort to ensure that the offtake model be used only as was originally intended, the following specific offtake geometry restrictions apply.

1. The side tube of the TEE is required to be either top, bottom, or centrally located off the main tube.
2. The angle from the low-numbered side of the main tube to the side tube must be 90°. (Variable COST on Card Number 2 in TEE-component input.)
3. The main-tube-junction cell must be horizontal.

If these three conditions are not met by the input deck TEE geometry, the problem currently terminates in the initialization stage with a fatal error concerning inappropriate offtake geometry.

I.4.7. Scaling Considerations

The offtake model is most applicable when the transient being modeled includes a small break in a large pipe containing horizontal stratified flow. As the offtake diameter becomes larger and begins to approach the diameter of the main tube, the offtake model will predict an offtake void fraction that tends toward the main-tube-junction cell void fraction.

I.4.8. Summary and Conclusions

The TRAC TEE-component offtake model predicts the flow discharged from a small break in a large pipe containing horizontal stratified flow. The current model is able to accommodate three different offtake geometries: upward offtake, side-oriented offtake, and downward offtake. Using subroutine OFFTKE, TRAC calculates a prediction for the offtake void fraction from flow correlations for the particular offtake geometry being modeled. This first prediction of the offtake void fraction is then sent through one interpolation based on the liquid level, one weighting based on the degree of horizontal stratification, and one limit based on the maximum allowable entrainment volume to arrive at the final offtake void fraction. The technique used to implement the offtake model into the two-step numerics scheme is demonstrated to work effectively by two simple thought problems.

I.5. Reactor-Vessel Vent Valve

Reactor-vessel vent valves, such as those used in Babcock and Wilcox (B & W) plants, are modeled in the VESSEL component with a specific set of input data. The number of vent valves, the vent-valve locations in terms of axial level and azimuthal / radial cell number, and the vent-valve maximum flow areas (i.e., for the valves when fully open) are specified in the VESSEL input. The user then specifies the vent-valve behavior by providing a valve's flow-loss resistance as a function of pressure drop across the valve. As the pressure drop decreases across the vent valve, the valve opening decreases. The flow reduction caused by the partial opening is accounted for by increasing the resistance factor as the vent valve closes. During each time step in a calculation, the

vent-valve resistance factor is determined from the pressure drop across the valve and is used in the radial momentum equations. The inertial effects of the vent valve opening and closing are not modeled in TRAC.

Vent-valve characteristics may be found in B & W final safety analysis reports (FSARs) as well as in other B & W documents. Figure I-28. shows a typical vent-valve resistance curve. The resistance approaches infinity as the pressure drop decreases and the valve openings decrease to zero. The resistance factor at very low pressure drops may be set to a very high value to obtain near-zero flow, or it may be adjusted to reflect an overall leakage flow between the downcomer and upper plenum, such as the leakage flow that occurs between the hot-leg nozzle flange and downcomer.

In the MOD2 code (and TRAC-M), the vent-valve resistance factor input must be of the form

$$\frac{K}{\Delta r_i + \Delta r_{i+1}} = \frac{CFZ}{HD_r} = \text{internally stored value used} , \qquad \text{(I-241)}$$

where K = K-factor loss coefficient, CFZ = default additive-loss coefficient used in MOD2 (and TRAC-M), and Δr_i and Δr_{i+1} = the radial lengths of the fluid cells that connect to the vent valve.

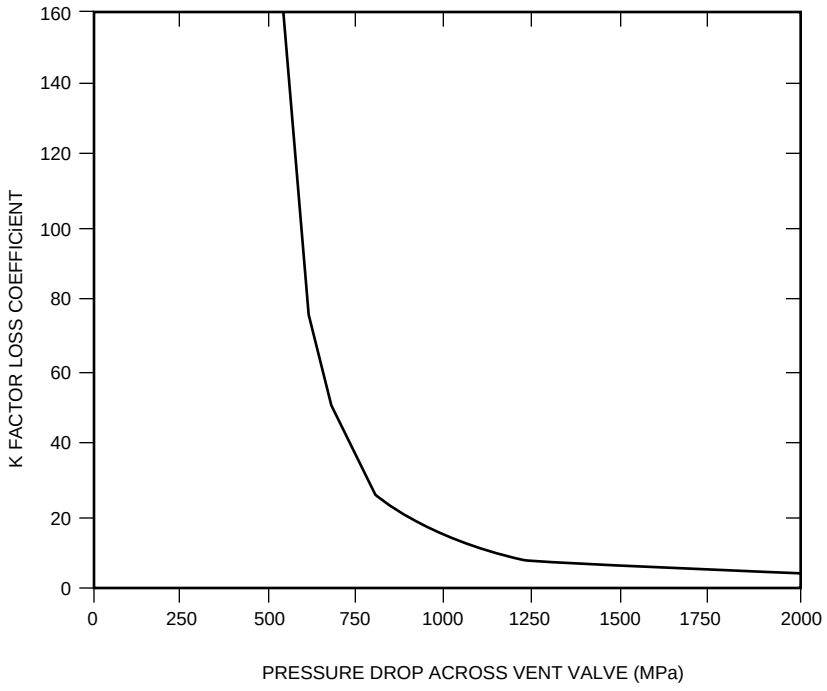

Fig. I-28. Vent-valve resistance vs. pressure drop across the valve.

The namelist variable IKFAC, which is used to change the additive-loss coefficient, does not affect the vent-valve resistance factors because the IKFAC conversion is done before the transient calculations are performed. The vent-valve resistance factors are determined during the transient calculation.

The user specifies the cells that have vent valves by giving the axial level, cell number, and total area of vent valves for each cell with vent valves in the outer radial surface. The user also specifies the vent-valve resistance factor, which can be done in two different ways. In the first option, the user specifies the following for each cell with vent valves: (1) the maximum pressure drop when the vent valve is closed, DPCVN; (2) the minimum pressure drop when the valve is open, DPOVN; (3) the vent-valve resistance when the valve is closed to model leakage, FRCVN (in the input form specified above); and (4) the vent-valve resistance when the valve is open, FRCVO. The code uses FRCVN when the pressure drop is less than DPCVN, uses FRCVO when the pressure drop is greater than DPOVN, and interpolates for pressure drops between DPCVN and DPOVN.

This input option allows only two points to describe the vent-valve resistance characteristics and may not be accurate enough. Therefore, a second option is provided that allows the input of a multiple-point resistance table, which specifies flow-loss resistance versus pressure drop.

For the first option, the two pressure drops and the two resistances are provided for each vent valve. In the second option, a single table is input for all vent valves.

Only one vent valve may be specified in a given VESSEL cell [at the cell's outer radial (or *x*) face]. Actual vent valves at a given cell interface may have to be lumped together.

REFERENCES

I-1. B. S. Massey, *Mechanics of Fluids* (D. Van Nostrand Co., New York, 1968).

I-2. R. C. Blevins, *Applied Fluid Dynamics Handbook* (Krieger Publishing Co., Malabar, Florida, 1992).

I-3. I. E. Idel'Chik, *Handbook of Hydraulic Resistance, Coefficients of Local Resistance and of Friction,* National Technical Information Service Report NTIS AEC-TR-6630 (1960).

I-4. F. M. White, *Fluid Mechanics* (McGraw-Hill Book Co., New York, 1979).

I-5. D. R. Liles, J. W. Spore, T. D. Knight, R. A. Nelson, M. W. Cappiello, K. 0. Pasamehmetohlu, et al., "TRAC-PF1/MOD1, Correlations and Models," Los Alamos National Laboratory report LA-11208-MS (NUREG/CR-5069) (December 1988).

I-6. "RELAP5/MOD1 Code Manual, Volume 1: System Models and Numerical Methods," Idaho National Engineering Laboratory report EGG-2070 Draft, Rev. 1 (NUREG/CR-1826) (March 1981).

I-7. O. C. Jones, Jr., "Flashing Inception in Flowing Liquids," Brookhaven National Laboratory report (BNL-NUREG-51221) (1980).

I-8. V. H. Ransom and J. A. Trapp, "The RELAP5 Choked Flow Model and Application to a Large Scale Flow Test," in *ANS/ASME/NRC International Topical Meeting on Nuclear Reactor Thermal-Hydraulics* (Saratoga Springs, New York, 1980), pp. 799-819.

I-9. Douglas G. Hall and Linda S. Czapary, "Tables of Homogeneous Equilibrium Critical Flow Parameters for Water in SI Units," Idaho National Engineering Laboratory report EGG-2056 (September 1980).

I-10. "RELAP4/MOD6, A Computer Program for Transient Thermal-Hydraulic Analysis of Nuclear Reactors and Related Systems," Idaho National Engineering Laboratory report CDAP-TR-003 (January 1978).

I-11. "Results from Test 4, The Marviken Full-Scale Critical Flow Tests," Joint Reactor Safety Experiments in the Marviken Full Power Station, Sweden, Marviken report MXC204 (September 1979).

I-12. "Results from Test 24, The Marviken Full-Scale Critical Flow Tests," Joint Reactor Safety Experiments in the Marviken Power Station, Sweden, Marviken report MXC224 (September 1979).

I-13. A. R. Edwards and T. P. O'Brien, "Studies of Phenomena Connected with the Depressurization of Water Reactors," *J. Br. Nucl. Energy Soc.* **9**, 125-135 (1970).

I-14. G. B. Wallis, *One Dimensional Two-Phase Flow* (McGraw-Hill, Inc., New York, 1969).

I-15. S. S. Kutateladze, *Izv. Akad. Nauk SSSR, Otd. Tekhn. Nauk* **8**, 529 (1951).

I-16. S. G. Bankoff, R. S. Tankin, M. C. Yuen, and C. L. Hsieh, "Countercurrent Flow of Air/Water and Steam/Water Through a Horizontal Perforated Plate," *Int. J. Heat Mass Transfer* **24** (8), 1381-1395 (1981).

I-17. L. A. Guffee, "TRAC-PF1/MOD2 TEE Component Offtake Model–A Completion Report," Los Alamos National Laboratory unpublished draft report.

I-18. K. H. Ardron and W. M. Bryce, "Assessment of Horizontal Stratification Entrainment Model in RELAP5/MOD2," United Kingdom Atomic Energy Authority, AEE Winfrith draft report AEEW-R 2345 (April 1988).

I-19. C. Smoglie, “Two Phase Flow Through Small Break Branches in a Horizontal Pipe with Stratified Flow,” Kernforschungszentrum Karlsruhe report KfK 3861 (December 1984).

I-20. V. E. Schrock, S. T. Revankar, R. Mannheimer, and C. H. Wang, “Small Break Critical Discharge—The Roles of Vapor and Liquid Entrainment in a Stratified Two-Phase Region Upstream of the Break,” Lawrence Berkeley Laboratory report LBL-22024 (NUREG / CR-4761) (December 1986).

I-21. T. Maciaszek and A. Menponteil, “Experimental Study on Phase Separation in a Tee Junction for Steam-Water Stratified Inlet Flow,” European Two-Phase Flow Group Meeting, Munich, Germany, June 10-13, 1986.

I-22. J. L. Anderson and R. L. Benedetti, “Critical Flow Through Small Pipe Breaks,” Electric Power Research Institute report EPRI NP-4532 (May 1986).

I-23. D. R. L. Harleman, R. L. Morgan, and R. A. Purple, “Selective Withdrawal from a Vertically Stratified Fluid,” International Association for Hydraulic Research, 8th Congress, Montreal, Canada, August 24-29, 1959.

I-24. B. T. Lubin and G. S. Springer, “The Formation of a Dip on the Surface of a Liquid Draining from a Tank,” *J. Fluid Mech.* **29**, 385-390 (1976).

APPENDIX J

SPECIAL COMPONENT MODELS

Some 1D components in TRAC perform functions that cause the 1D fluid equations to be solved in a different way, either changing the equations' normal finite differencing, introducing source terms to the equations, or using complex logic to alter the closure relations to accomplish a specific modeling requirement. The PUMP component produces a momentum source term in the form of an additional Δp on the right-hand side of the momentum equation. The steam/water separator component (SEPD) permits the user to specify the separation efficiency in such locations as the separator at the top of a normal U-tube steam generator. The PLENUM component is a special, single-cell, 1D component that allows the user to connect as many normal 1D components as desired. To accomplish this objective, the PLENUM component interacts with the networking logic in the code and changes the form of the momentum flux terms. The FILL and BREAK components provide boundary conditions to the normal 1D components by allowing the user to specify either flows (FILL) or pressures (BREAK) at the boundary together with the fluid state if an inflow condition exists. The turbine (TURB) component models the removal of energy from the fluid by work performed by turbines. PWR accumulators are modeled by special logic that is built into TRAC's PIPE component, which is triggered by one of two PIPE input options. The PRIZER component models a PWR pressurizer. The VALVE component has a variety of options to adjust the flow area at a user-specified cell face.

Note: Separator (SEPD) and Turbine (TURB) Components. The base code for both TRAC-M/F77 and TRAC-M/F90 had components to model steam/water separators (SEPD) and turbines (TURB). The TRAC-P SEPD component permits the user to specify the separation efficiency in such locations as the separator at the top of a normal U-tube steam generator. The TRAC-P SEPD component received minimal support over the years, and its general use was not, and is not, recommended. (It should be used with caution.) Both TRAC-M/F77, Version 5.5.2, and TRAC-M/F90 (Version 3.0), have a SEPD component that was brought over directly from TRAC-P, and the same caution applies. The separator capability is to be improved in a future TRAC-M/F90 version. In the TURB component, energy is removed from the fluid as a result of work performed by the turbine. The TURB component received minimal support over its years in TRAC-P, and its general use was not, and is not, recommended. (It should be used with caution.) The TRAC-P TURB was brought over directly to TRAC-M. Currently, the TURB component is only available in TRAC-M/F77, and the same caution applies. The TRAC-P TURB has been removed entirely from TRAC-M/F90. An improved turbine-modeling capability is to be included in a future TRAC-M/F90 version. Section J.2. describes the current SEPD component. Section J.6. describes the current TURB component.

NOMENCLATURE

A:	area
A_{norm}:	normalized flow area of valve
AVLVE:	fully open valve flow area
b:	ratio of valve flow area to pipe flow area
C_0, C_1, C_2, C_3:	proportionality constants in Eqs. (J-15) and (J-16)
C_b:	bucket velocity coefficient
C_n:	nozzle velocity coefficient
C_r:	fraction of total reaction energy delivered
d_j:	momentum source cell-edge diameter
D_H:	hydraulic diameter
DPMAX:	pressure offset at which the heaters or sprays achieve their maximum effectiveness
FA:	flow area
FAVLVE:	valve flow-area fraction
FRIC:	additive-loss coefficient
g:	gravitational acceleration constant
h:	normalized pump head (Section J.1.) or specific enthalpy (Section J.6.) or characteristic dimension for valve component (Fig. J-17.)
h_1:	nondimensional head from the single-phase homologous head curves
h_2:	nondimensional head from the fully degraded homologous head curves
H:	pump head or parameter defined by Eq. (J-44)
H_1:	single-phase pump head
H_2:	fully degraded pump head
I:	moment of inertia
K:	form-loss coefficient
$K0$:	fully open valve form-loss coefficient
$K_1 - K_3$:	coefficients of frictional torque
K_{eff}:	effective form-loss coefficient
LMT:	total liquid mass in pressurizer
m:	total number of stages belonging to a turbine
$\dot{m}$:	mass-flow rate
$\dot{m}_{\text{total}}$:	total mass-flow rate
$\dot{m}_{\text{vapor}}$:	vapor mass-flow rate
M:	momentum

$M(\alpha)$: head degradation multiplier (Section J.1.) or momentum (Section J.6.)

n: number of moving blade rows

N: number of cells

$N(\alpha)$: torque degradation multiplier

p: pressure

p_1: pressure at the top of the pressurizer in Eq. (J-37) or pressure in cell 1 in Eq. (J-2)

p_2: pressure in cell 2

p_{set}: pressure from which the system is controlled

P: stage power

P_{enr}: power extracted from energy equation

P_{demand}: generator power demand

P_f: liquid mass weighted fraction of power to be added or subtracted from liquid in each pressurizer cell

$P_{gen,input}$: power input to generator

$P_{gen,output}$: power output by the generator

P_{HEAT}: maximum effective power that can be added to or subtracted from the liquid

P_{ideal}: ideal stage power

P_{in}: total power to be added or subtracted from the liquid

P_{total}: total turbine power

q: normalized volumetric flow

Q: volumetric flow

r: fraction of stage energy transferred

R: valve radius

RFMX: maximum rate of change of the FILL-component parameter

T: torque

T_1: single-phase torque

T_2: fully degraded torque

T_{demand}: torque due to external load

T_f: torque caused by friction and by the bearing and windage

T_{hy}: hydraulic torque

T_{loss}: loss in torque

T_{turb}: turbine torque

TWTOLD: time-step weighting factor for the FILL-component parameter

vol: cell volume

V: velocity

V_a: axial velocity component

$V_B, V_{B'}$: turbine exit velocity

W: blade velocity

x: independent variable

x_t: thermodynamic steam quality

XCO: carryover parameter

XCU: carryunder parameter

XPOS: valve-stem position

y: dependent variable

z: collapsed liquid level

α: void fraction

β: dimensionless hydraulic torque

β_1: dimensionless hydraulic torque from the single-phase homologous torque curves

β_2: dimensionless hydraulic torque from the fully-degraded homologous torque curves

Δp: pressure drop or pressure rise through the pump

Δt: time-step size

Δx or ΔX: cell length

ϕ_{m}: moisture loss

ϕ_{rem}: miscellaneous losses

η_{corr}: correction efficiency

η_{gen}: generator efficiency

η_{nb}: nozzle bucket efficiency

η_{stg}: stage efficiency

θ: inclination angle from vertical or characteristic angle for valve component defined by Eq. (J-45)

ρ: density

ω: pump speed [Eq. (J-1)] or turbine-generator angular speed [Eq. (J-28)] or normalized pump speed [Eq. (J-6)]

ω_s: specific pump speed

Ω: pump-impeller angular velocity

Subscripts

g: gas

l: liquid

liq: liquid

m: two-phase mixture

R: rated

Superscripts

n: current-time value

n + 1: new-time value

J.1. PUMP Component

The PUMP component describes the interaction of the system fluid with a centrifugal pump. The model calculates the pressure differential across the pump and its angular velocity as a function of the fluid-flow rate and the fluid properties. The model can treat any centrifugal pump and allows for the inclusion of two-phase effects.

The pump model is represented by a 1D component with N cells ($N > 1$). The pump momentum is modeled as a source at the interface between cells 1 and 2. This interface will be referred to as the pump interface for the remainder of this discussion. The source is positive for normal operation so that a pressure rise occurs from cell 1 to cell 2. Therefore, it is necessary to construct the cell noding such that the cell number increases in the normal flow direction. This latter requirement is equivalent to requiring the first cell of the component to be in the pump suction and the second cell in the pump discharge for normal operation.

The following considerations were important in creating the PUMP component:

1. compatibility with adjacent components should be maximized,
2. choking at the pump inlet or outlet should be predicted automatically, and
3. the calculated pressure rise across the pump should agree with that measured at steady-state conditions.

The first two criteria precluded the use of a lumped-parameter model. The PUMP component, therefore, combines the PIPE component with pump correlations.

The pump model in TRAC is very similar to that included in RELAP4/MOD5 (Ref. J-1.), although some additional assumptions were made to incorporate the momentum source into the momentum equations. Also, the details of the input for the homologous curves are somewhat different in that the eight curve segments defined in RELAP4/MOD5 are combined into only four segments in TRAC. Reference J-2. (Chapter 9) provides a good discussion of pump operation; Section J.2. of the same reference describes the single-phase homologous curve of a pump. Reference J-3. is a general text on pumps and provides much information about pumps and their operating characteristics. Runstadler (Ref. J-4.) provides an overview of the state of the art in pump modeling in the

mid-1970s, about the time that work began on TRAC and when there was a need for a pump model in the code. Several organizations worked on pump models during the late 1970s and the work continued through the 1980s. Furuya (Ref. J-5.) developed an analytical pump model that yields the two-phase performance characteristics based on single-phase characteristics and the details of the pump geometry.

The similarity factor for pumps that is most often discussed is the specific speed, ω_s, defined in the following equation (Ref. J-3., Eq. 5.9):

$$\omega_s = \frac{\omega Q^{\frac{1}{2}}}{(gH)^{\frac{3}{4}}} \quad , \tag{J-1}$$

where ω is the pump speed, Q is the volumetric flow, g is the acceleration of gravity, and H is the pump head. This specific speed ω_s is dimensionless only if the units of the other parameters are consistent: ω in radians per second ($\mathrm{rad \cdot s^{-1}}$) or revolutions per second (rps), Q in $\mathrm{m^3 \cdot s^{-1}}$ or $\mathrm{ft^3 \cdot s^{-1}}$, H in meters (m) or feet (ft), and g in $\mathrm{m \cdot s^{-2}}$ or $\mathrm{ft \cdot s^{-2}}$. Stepanoff (Ref. J-3., p. 27) points out that ω_s is constant for all similar pumps and ideally does not change with speed for a given pump. However, when it is used as a similarity parameter, ω_s should be calculated at the highest efficiency point of operation. Stepanoff also casts ω_s in another dimensionless form (Ref. J-3., Eq. 5.35), which shows the importance of maintaining certain geometric ratios in similar pumps. This discussion is intended to provide a guide to help the code user determine if a set of homologous curves can be used to describe this pump.

J.1.1. Pump Governing Equations

The pump model is identical to the 1D pipe model except that the momentum equations between cells 1 and 2 are rewritten as

$$\frac{V_g^{n+1} - V_g^n}{\Delta t} = \frac{\left[p_1^{n+1} - p_2^{n+1} + \Delta p^n + \left(\frac{\partial \Delta p}{\partial V} \right)^n \left(V_g^{n+1} - V_g^n \right) \right]}{(\overline{\rho_m})_{3/2}^n \Delta x_{3/2}} - g \cos\theta \tag{J-2}$$

and

$$V_l = V_g \quad , \tag{J-3}$$

where Δp is the pressure rise through the pump evaluated from the pump correlation. Equation (J-2) is implemented in subroutines StbVel1D (FEMOM in TRAC-M/F77) and TFlDS1. The steady-state solution of Eq. (J-2) is

$$\Delta p = p_2 - p_1 + g \cos\theta \quad ,$$

which is the desired result. Friction does not enter explicitly into the pump motion equation because we assume that the friction effects are normally included in the homologous curves defining the pump head. Therefore, additive friction is not allowed between cells 1 and 2 [FRIC(2) = 0.0].

It is necessary to evaluate Δp and its derivative with respect to velocity for a pump cell only once each time step. The source is needed only in routines StbVel1D (FEMOM in TRAC-M/F77) and TF1DS1. This evaluation is performed by subroutine PUMPSR.

J.1.2. Pump Head and Torque from Homologous Curves

The pump correlation curves describe the pump head and torque response as a function of fluid volumetric flow rate and pump speed. Homologous curves (one curve segment represents a family of curves) are used for this description because of their simplicity. These curves describe, in a compact manner, all operating states of the pump obtained by combining positive or negative impeller velocities with positive or negative flow rates.

The following definitions are used in the subsequent development:

H = the pump head = $(\Delta p)/\overline{\rho_m}$,
Q = the pump volumetric flow, and
Ω = the pump impeller angular velocity,

where Δp is the pressure rise across the pump and $\overline{\rho_m}$ is the pump-average mixture density in the cells immediately adjacent to the pump interface. The code user should note that the definition of pump head H above differs from the standard definition by a factor g, the acceleration caused by gravity. To allow one set of curves to be used for a variety of pumps, the following normalized quantities are used

$$h \equiv \frac{H}{H_R} \quad , \tag{J-4}$$

$$q \equiv \frac{Q}{Q_R} \quad , \tag{J-5}$$

and

$$\omega \equiv \frac{\Omega}{\Omega_R} \quad , \tag{J-6}$$

where H_R is the rated head (RHEAD) for the pump, Q_R is the rated volumetric flow (RFLOW), and Ω_R is the rated pump speed (ROMEGA). The pump similarity relations show that

$$\frac{h}{\omega^2} = \mathrm{f}\left(\frac{q}{\omega}\right) \quad . \tag{J-7}$$

For small ω this correlation is not satisfactory and the following combination of variables is used:

$$\frac{h}{q^2} = \mathrm{f}\left(\frac{\omega}{q}\right) \quad . \tag{J-8}$$

Correlation Eq. (J-7) is used in the range $0 \le |q / \omega| \le 1$ and results in two separate curves, one for $\omega > 0$ and one for $\omega < 0$. Correlation Eq. (J-8) is used in the range $0 \le |\omega / q| < 1$ and yields two separate curves, one for $q > 0$ and one for $q < 0$. The four resulting curve segments, as well as the curve-selection logic used in TRAC, are shown in Table J-1.

To account for two-phase effects on pump performance, the pump curves are divided into two separate regimes. Data indicate that two-phase pump performance in the vapor-fraction range of 20-80% is degraded significantly in comparison with its performance at vapor fractions outside of this range. One set of curves describes the pump performance for single-phase fluid (0 or 100% vapor fraction), and another set describes the two-phase, fully degraded performance at some void fraction between 0 and 100%. For single-phase conditions, the curve segments for correlation Eq. (J-7) are input as HSP1 for $\omega > 0$ and HSP4 for $\omega < 0$, and for correlation Eq. (J-8) curve segments are input as HSP2 for $q > 0$ and HSP3 for $q < 0$. The fully degraded version of correlation Eq. (J-7) is input as curve HTP1 for $\omega > 0$ and HTP4 for $\omega < 0$. The fully degraded version of correlation Eq. (J-8) is input as HTP2 for $q > 0$ and HTP3 for $q < 0$.

TABLE J-1.
Definitions of the Four Curve Segments that Describe the Homologous Pump Head Curves [a]

Curve Segment	$\left\|\frac{q}{\omega}\right\|$	w	q	Correlation
1 4	≤ 1 ≤ 1	>0 <0	]	$\left[\frac{h}{\omega^2} = f\left(\frac{q}{\omega}\right)\right]$
2 3	>1 >1		>0 <0]	$\left[\frac{h}{q^2} = f\left(\frac{\omega}{q}\right)\right]$

a. For the special case of both $\omega = 0.0$ and $q = 0.0$, TRAC sets $h = 0.0$

The pump head at any vapor fraction is calculated from the relationship

$$H = H_1 - M(\alpha)(H_1 - H_2), \tag{J-9}$$

where

H	=	the total pump head;
H_1	=	the single-phase pump head = $h_1 H_R$ where h_1 is the nondimensional head from the single-phase homologous head curves;
H_2	=	the fully degraded pump head = $h_2 H_R$, where h_2 is the nondimensional head from the fully degraded homologous head curves;
$M(\alpha)$	=	the head degradation multiplier (input as HDM); and
α	=	the donor-cell void fraction.

To this point, no knowledge of density is required to calculate H from the homologous head curves. The average mixture density in the cells immediately adjacent to the pump interface is always used to convert the total pump head H to Δp, the pressure rise through the pump, by the definition $\Delta p = \rho_m H$.

The development of homologous torque curves parallels the previous development for homologous head curves. The dimensionless hydraulic torque is defined by

$$\beta \equiv \frac{T_{hy}}{T_R} \quad , \tag{J-10}$$

where T_{hy} is the hydraulic torque and T_R is the rated torque (RTORK). The convention used is that a positive T_{hy} works to retard positive pump angular velocity. The dimensionless torque β is correlated as either β / ω or β / q, just as the dimensionless head was correlated. For single-phase conditions, the correlations yield the corresponding four curve segments TSP1, TSP2, TSP3, and TSP4. The fully degraded correlations produce four corresponding curves: TTPI, TTP2, TTP3, and TTP4. The homologous torque curve segments are correlated in the same manner as the head curve segments shown in Table J-1. (replace h with β). For the special case of $\omega = q = 0.0$, the code sets $\beta_1 = \beta_2 = 0.0$.

The single-phase torque T_1 is dependent upon the fluid density and is calculated from

$$T_1 = \beta_1 T_R \left(\frac{\overline{\rho_m}}{\rho_R} \right) \tag{J-11}$$

where β_1 is the dimensionless hydraulic torque from the single-phase homologous torque curves, ρ_m is the pump-average mixture density in the cells immediately adjacent to the pump interface, and $\overline{\rho_m}$ is the rated density (RRHO). The density ratio is needed to correct for the density difference between the pumped fluid and the rated condition. Similarly, the fully degraded torque T_2 is obtained from

$$T_2 = \beta_2 T_R \left(\frac{\overline{\rho_m}}{\rho_R} \right) , \tag{J-12}$$

where β_2 is the dimensionless hydraulic torque from the fully degraded homologous torque curves. For two-phase conditions, the impeller torque is calculated from

$$T = T_1 - N(\alpha)(T_1 - T_2) \quad , \tag{J-13}$$

where T is the total impeller torque and $N(\alpha)$ is the torque degradation multiplier (input as TDM).

In addition to the homologous head and torque curves, the head and torque degradation multipliers defined in Eqs. (J-9) and (J-13) are required. These functions of void fraction are nonzero only in the vapor-fraction range where the pump head and torque are either partially or fully degraded.

J.1.3. Pump Speed

The pump component treats the pump angular velocity as a constant (input) while the motor is energized. After a drive-motor trip, the time rate of change for the pump angular velocity Ω is proportional to the sum of the moments acting on it and is calculated from

$$I \frac{d\Omega}{dt} = -\sum_i T_i = -(T + T_f) \quad , \tag{J-14}$$

where I is the combined impeller, shaft, and motor-assembly moment of inertia (EFFMI); T is the hydraulic torque on the impeller; and T_f is the torque caused by friction and by the bearing and windage. We assume that

$$T_f = C_0 + C_1 \frac{\Omega}{\Omega_R} + C_2 \frac{\Omega|\Omega|}{\Omega_R^2} + C_3 \frac{\Omega^3}{\Omega_R^3} \quad , \tag{J-15}$$

where C_0, C_1, C_2, and C_3 are input constants (TFR0, TFR1, TFR2, and TFR3, respectively). The user may specify a different set of coefficients (TFRL0, TFRL1, TFRL2, and TFRL3) for low pump speed. These coefficients will be applied at speeds below the user-specified value TFRB. As rotational speed approaches zero, the coefficient C_0 linearly approaches zero so that the frictional torque will be vanished at zero speed.

The hydraulic torque T is evaluated using the homologous torque curves and Eq. (J-13). It is a function of the volumetric flow, the upstream void fraction, the average density in the cells immediately adjacent to the pump interface, and the pump angular velocity. For time step (n + 1), Eq. (J-14) is evaluated explicitly,

$$\Omega^{n+1} = \Omega^n - \frac{\Delta t}{I}\left[T(Q,\alpha,\rho_m,\Omega) + C_0 + C_1\frac{\Omega^n}{\Omega_R} + C_2\frac{\Omega^n|\Omega^n|}{\Omega_R^2} + C_3\frac{(\Omega^n)^3}{\Omega_R^3} \right] \quad . \tag{J-16}$$

So that all torque losses go to zero as Ω approaches zero, C_0 is ramped to zero at low pump speed.

J.1.4. Pump Input Options

To invoke the pump model in TRAC, the code user has to specify the following options: pump type (IPMPTY), motor action (IPMPTR), reverse speed option (IRP), degradation option (IPM), and pump curve option (OPTION). The input variables IPMPTR and NPMPTX specify, respectively, the trip number for the pump-trip initiation and the number of pairs of points in the pump-speed table (array SPTBL). If IPMPTR = 0, no pump-trip action occurs, and the pump runs for the entire calculation at the constant speed (OMEGAN) specified in the input.

If the pump motor is energized (trip IPMPTR set OFF), the angular velocity is assumed to be the constant value specified (OMEGAN). If the motor is not energized (trip IPMPTR set ON), the pump speed is allowed to vary.

Two types of pumps are available. For pump type 1 (IPMPTY = 1), the pump-speed variation is specified by the input table. The pump is energized initially at a constant speed specified by input (OMEGAN). Trip IPMPTR may initiate a pump trip, after which the pump speed is taken from a pump-speed table (array SPTBL). The independent variable for the pump-speed table may be elapsed time since trip initiation or any other signal variable. For pump type 1 the torque calculation is not used. Pump type 2 (IPMPTY = 2) is similar to option 1 except that a speed table is not input. Instead, the pump speed is calculated from Eq. (J-16) after a trip has occurred.

If the reverse speed option is specified (IRP = 1), the pump is allowed to rotate in both the forward and reverse directions. If reverse speed is not allowed (IRP = 0), the pump will rotate in the forward direction only. For this case, if negative rotation is calculated (after trip with pump type 2), the speed will be set to zero. If IRP = 0 and a negative pump speed is encountered (i.e., from the speed table), error messages will be printed by subroutines PUMPD, PUMPX, and PUMPSR. (This is a fatal error.)

If the degradation option is turned on (IPM = 1), the degraded pump head and torque are calculated from Eqs. (J-9) and (J-13). If the degradation option is turned off (IPM = 0), only the single-phase head and torque homologous curves are used [equivalent to setting $M(\alpha)$ and $N(\alpha)$ to zero in Eqs. (J-9) and (J-13)].

J.1.5. Pump Homologous Curves

The user may specify pump homologous curves in the input (OPTION = 0) or alternatively may use the built-in pump curves (OPTION = 1 or 2). The first set (OPTION = 1) of built-in pump curves is based on the Semiscale Mod-1 system pump (Refs. J-1. and J-6. through J-8.). The Semiscale pump curves for single-phase homologous head (HSP), fully degraded two-phase homologous head (HTP), head degradation multiplier (HDM), single-phase homologous torque (TSP), and torque degradation multiplier (TDM) are provided in Figs. J-1. through J-5., respectively. The second set (OPTION = 2) of built-in pump curves is based on the Loss-of-Fluid Test (LOFT) system pump (Refs. J-9. through J-11.). The LOFT pump curves for HSP, HTP, HDM, TSP, and TDM are shown in Figs. J-6. through J-10., respectively. For lack of data, the fully degraded two-phase homologous torque curves (TTP) for both Semiscale and LOFT are zero. Where applicable, the curves are numbered corresponding to the conditions provided in Table J-1.

Because these homologous curves are dimensionless, they can describe a variety of pumps by specifying the desired rated density, head, torque, volumetric flow, and angular velocity as input. We recommend that for full-scale PWR analyses, plant-specific pump curves be input; however, if such data are unavailable, the LOFT pump curves (OPTION = 2) generally should be used.

Several restrictions and limitations are present in the current version of the PUMP component. Because there is no pump motor torque versus speed model, the pump speed is assumed to be input if the motor is energized. Pump noding is restricted such that the cell numbers increase in the normal flow direction (NCELLS ≥ 2), the pump momentum source is located between cells 1 and 2 of the pump model, and the additive friction (loss coefficient) between cells 1 and 2 is 0.0 [FRIC (2) = 0.0]. A flow-area change should not be modeled between cells 1 and 2. Finally, the head degradation multiplier $M(\alpha)$ and the torque degradation multiplier $N(\alpha)$ are assumed to apply to all operating states of the pump.

The PUMP component input consists of the same geometric and hydrodynamic data and initial conditions that are required for the PIPE component. In addition, information specific to the PUMP is required. The speed table (SPTBL), as well as the homologous pump curve arrays, must be input in the following order:

$$x(1), y(1), x(2), y(2), \ldots, x(n), y(n) \quad .$$

Here x is the independent variable and y is the dependent variable. Furthermore, the independent variables must increase monotonically on input, that is,

$$x(1) < x(2) < \ldots < x(n-1), x(n) \quad .$$

Linear interpolation is used within the arrays.

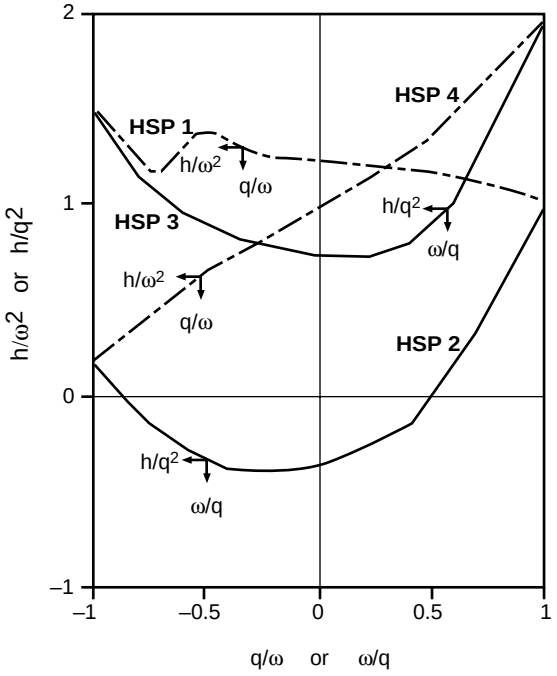

Fig. J-1. Semiscale single-phase homologous head curves.

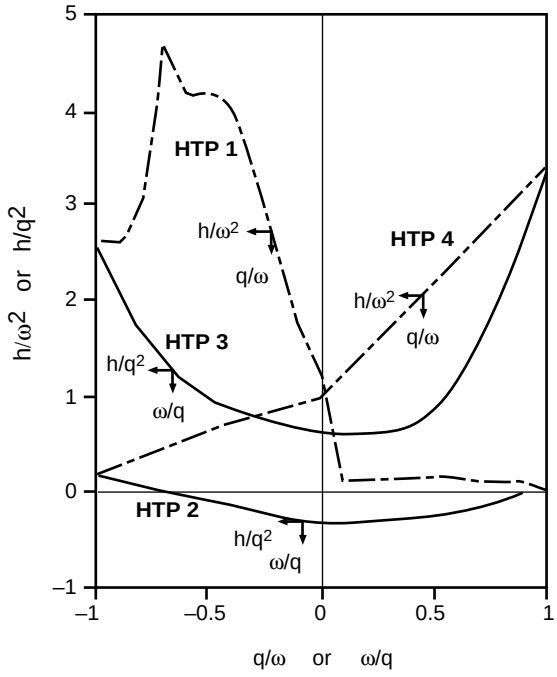

Fig. J-2. Semiscale fully degraded homologous head curves.

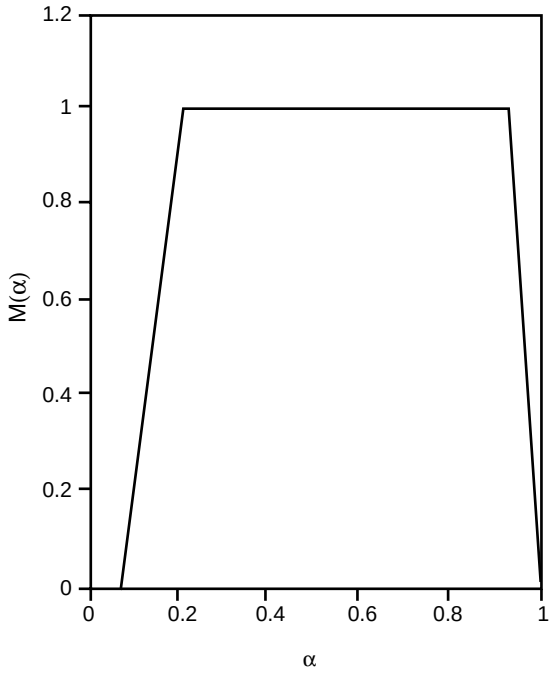

Fig. J-3. Semiscale head degradation multiplier curve.

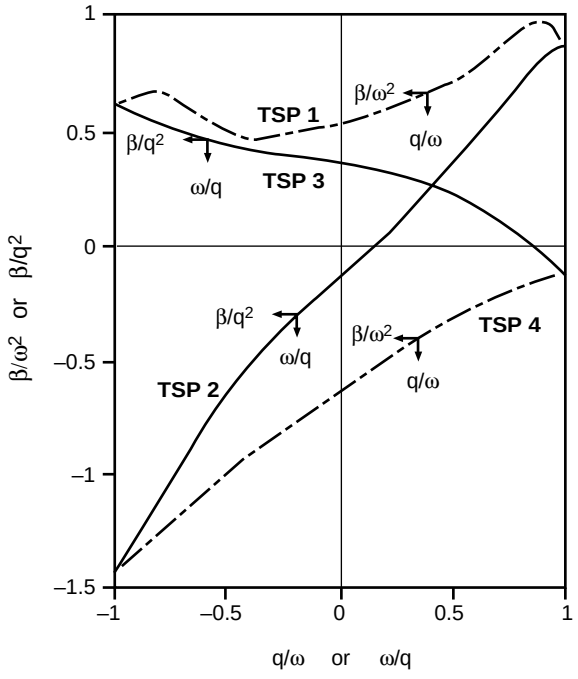

Fig. J-4. Semiscale single-phase homologous torque curves.

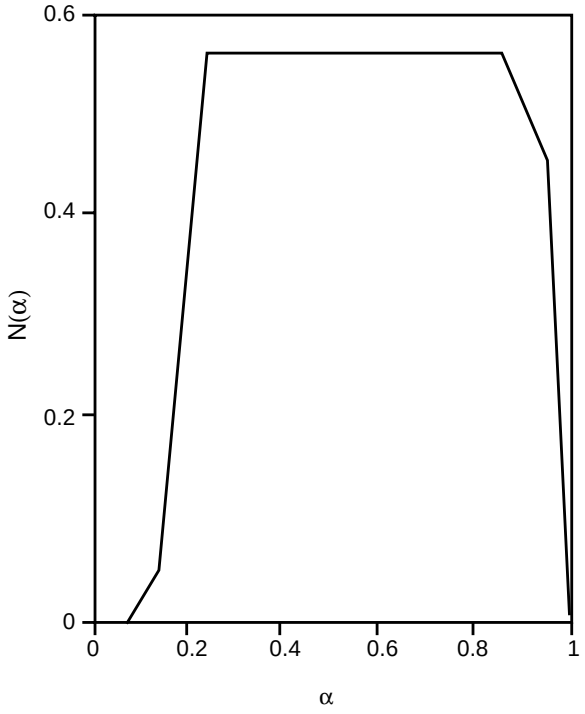

Fig. J-5. Semiscale torque degradation multiplier curve.

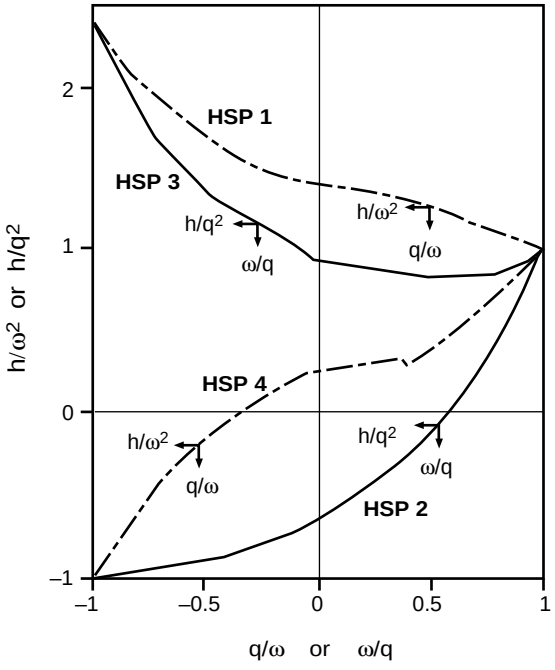

Fig. J-6. LOFT single-phase homologous head curves.

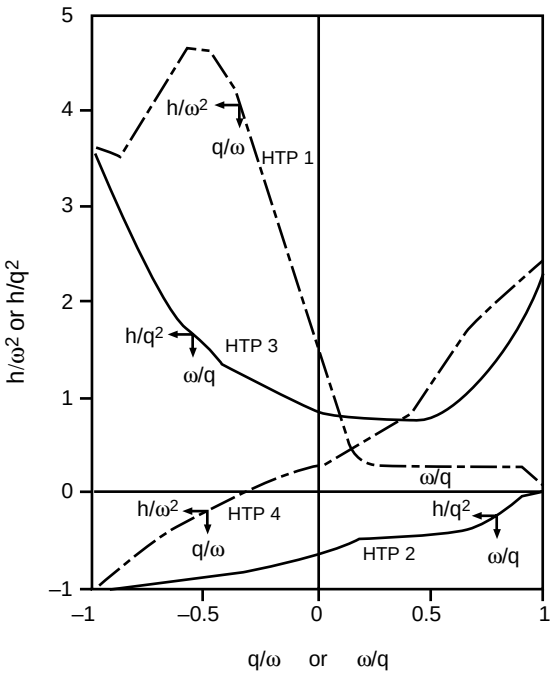

Fig. J-7. LOFT single-phase homologous head curves.

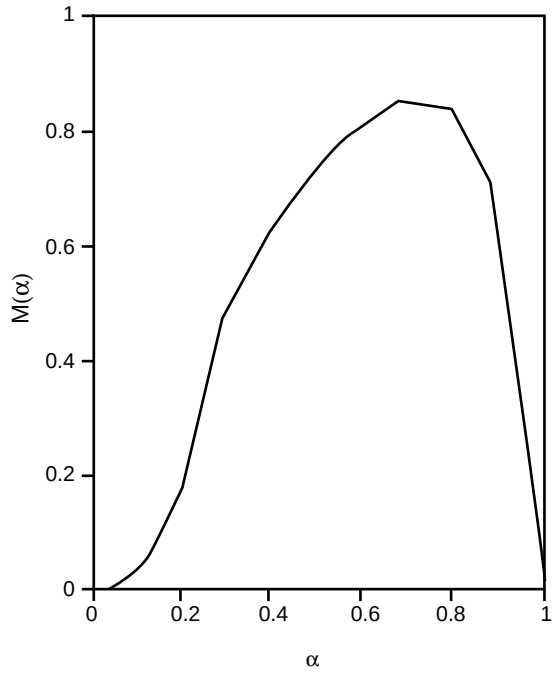

Fig. J-8. LOFT head degradation multiplier curve.

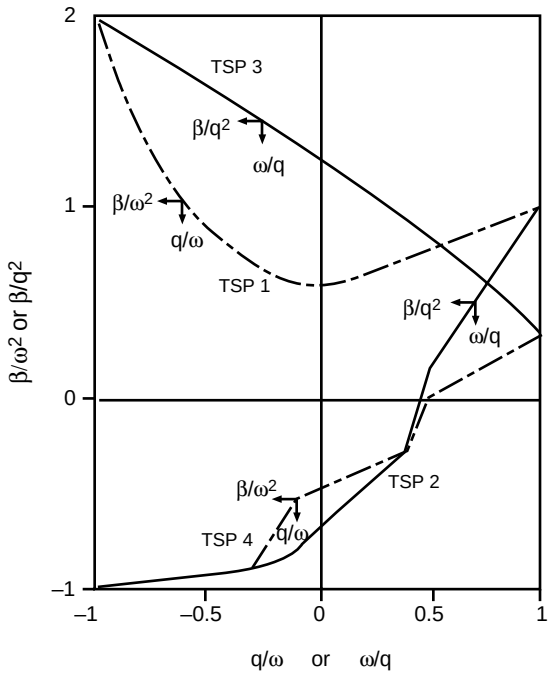

Fig. J-9. LOFT single-phase homologous torque curves.

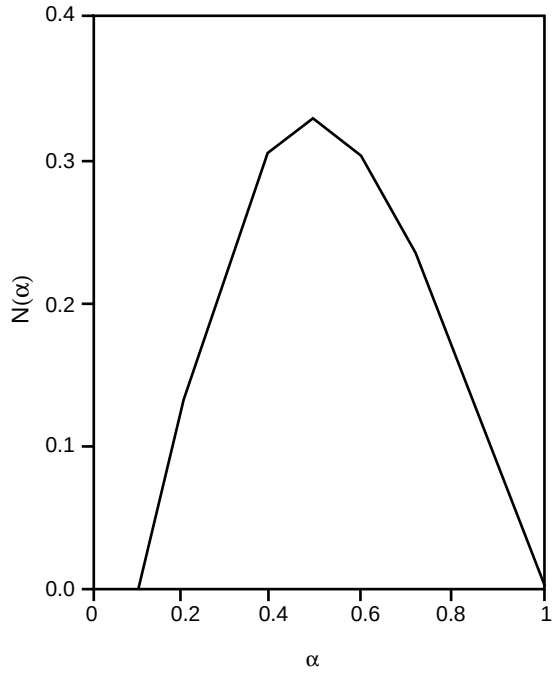

Fig. J-10. LOFT torque degradation multiplier curve.

J.1.6. Pump Conclusions

The pump model included in TRAC has demonstrated a remarkable capability to model reactor pumps under many conditions. Obviously, the quality of the pump simulation is dependent on the quality of the homologous curves used to describe the pump, and we recommend that whenever the data are available, the user input specific curves for the pump under consideration instead of using the built-in curves. An alternative is to use the Tetra Tech model (Ref. J-5.) to generate the fully degraded homologous curves and associated two-phase multiplier curves from the pump geometry and the published single-phase performance curves from the manufacturer. Unless the pump to be modeled is similar to the Semiscale or LOFT pumps, the least desirable option is to select one set of built-in curves.

From a code viewpoint, there is one deficiency regarding the pump model. The assumption of equal phase velocities at the pump interface, although a reasonably good assumption when the pump is operating at a significant rotational speed, breaks down as the pump speed approaches zero. At this point, the homogeneous flow assumption prevents unequal phase velocities and, in particular, prevents countercurrent flow at that one interface. The lack of phase slip can affect the separation of liquid and vapor in the pump suction, and discharge and could result in oscillatory flow to achieve the net effect of countercurrent flow. At the current time, the only solution available to the code user is to replace the PUMP component with an equivalent PIPE component when the pump speed is near zero and the fluid velocities are low.

J.2. Steam/Water Separator Component (SEPD)

Note: **Separator (SEPD) Component.** The base code for both TRAC-M/F77 and TRAC-M/F90 has a component to model steam/water separators (the SEPD component). The TRAC-P SEPD component permits the user to specify the separation efficiency in such locations as the separator at the top of a normal U-tube steam generator. The TRAC-P SEPD component received minimal support over the years, and its general use was not, and is not, recommended. (It should be used with caution.) Both TRAC-M/F77, Version 5.5.2, and TRAC-M/F90 (Version 3.0), have a SEPD component that was brought over directly from TRAC-P, and the same caution applies. The separator capability is to be improved in a future TRAC-M/F90 version. Section J.2. describes the current (obsolete) SEPD component.

In anticipation of specific needs and in acknowledgment of requests from TRAC users, we determined that a component should be added to the code that would separate an incoming two-phase stream into vapor-enriched and liquid-enriched streams. The USNRC requested that we incorporate the separator component used in the TRAC-BWR computer code into TRAC-PF1/MOD1 and TRAC-PF1/MOD2. After examining the method used in the TRAC-BWR, we determined that this was a possible approach to adding a separator component to TRAC-PF1/MOD2, although not necessarily the one that we would otherwise have taken. Our implementation of the SEPD component essentially incorporates a superset of the TEE component, and in the following

discussion we will frequently make use of the terminology of the TEE component, such as “JCELL” and “side leg.”

Several modules of the SEPD component are in essence unchanged from the TRAC-BWR code and, as we did not develop them, we cannot necessarily justify their use. We will therefore limit this discussion to those points at which we know that the version of the SEPD component in TRAC-PF1 / MOD2 differs from the version in TRAC-BWR.

J.2.1. Basis for the Model

The coding for the SEPD component is broken down into three phases: (*i*) determination of the appropriate carryover and carryunder for the current conditions; (*ii*) determination, through quasi-steady-state mass and momentum balances, of the resulting separator exit flows and qualities; and (*iii*) circumvention of the normal solution method to achieve those flows and qualities. The carryover is defined as the ratio of the liquid mass-flow rate to the total mass-flow rate, both evaluated at the exit of the separating JCELL that passes on through the main leg of the component (Fig. J-11.). The carryunder is defined as the ratio of the vapor mass-flow rate to the total mass-flow rate, both evaluated at the exit of the JCELL that passes into the side leg of the SEPD.

References J-12., J-13., and J-14. describe the TRAC-BWR versions of the SEPD component, and Ref. J-15. describes the General Electric (GE) study that forms the basis for the “mechanistic model” described below. Reference J-14., as amended by material in Ref. J-15., provides a general description of the model and of the input for the SEPD component of TRAC.

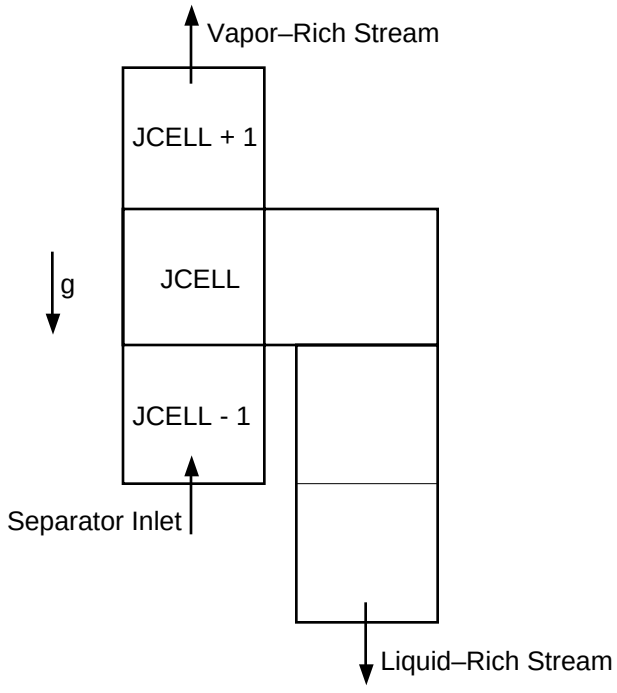

Fig. J-11. Typical separator component nodalization.

We did not perform comparisons with data for our implementation of this existing model. We relied on the correctness of the model development performed by INEEL and GE and did not perform an extensive review of that work. The correlations were not developed at LANL. Refer to Refs. J-10. through J-13.

J.2.2. Assumptions Made in Implementing the Correlation in the Code

Although a detailed discussion of this topic is outside the scope of this document (refer to Refs. J-10. through J-13.), some major points will be discussed so that TRAC users will know under what conditions the use of the SEPD component is recommended and justified.

A primary assumption of the SEPD component as it was implemented in TRAC-BWR and as it is implemented in TRAC-PF1/MOD2 is that the determination of the desired flows and qualities exiting the separating JCELL is based on a quasi-steady-state analysis. As a result, when the flow conditions entering the separator become sufficiently rapidly varying, one should expect the separation calculated by the SEPD component to deviate from reality. Indeed, numerical instabilities could result when conditions are sufficiently far from steady state.

If the "mechanistic" separator is used (the options available to the SEPD component are discussed in Section J.2.4.), it is assumed that the physical separator being modeled is very similar geometrically, if not identical, to a GE BWR steam/water separator. This is a result of the use of a module for this option that was developed at GE specifically for their hardware. The mechanistic option of the SEPD component is not recommended for non GE separators. Other SEPD options are available for arbitrary separator designs for which the user knows the performance data (Ref. J-14., as amended by material in Ref. J-15.).

For any option of the SEPD component, we assume that the separator is oriented vertically (GRAV = +1; Fig. J-11.). This is a relic of the TRAC-BWR ancestry of the SEPD component, and may be relaxed in future versions.

J.2.3. Constants

Aside from the GE-supplied default geometric data (which may be overridden) used for the mechanistic option of the SEPD component (Table J-2.), few constants are used in the model. Subroutine SEPDI uses two constants in its logic to determine whether the SEPD should be activated. These are discussed in Section J.2.4.2. in conjunction with an outline of how that logic operates.

SEPDI also uses a constant factor to determine how much the values of the FRICs can change from one time step to the next. This is discussed in Section J.2.5.

TABLE J-2.
Default Values for the SEPD Component

		IF ISTAGE=0			
		XCO	0.05		
		XCU	0.003		
		IF ISTAGE=2 or 3			
		AI	0.018637		
		AN	0.014411		
		RH	0.0809585		
		THETA	48.0		
		RR1	0.0857208		
	2-Stage SEPD		3-Stage SEPD		
	1st Stage	2nd Stage	1 Stage	2nd Stage	3rd Stage
RWS	0.10794	0.06985	0.10794	0.10794	0.10794
RRS	0.06985	0.06032	0.08572	0.095245	0.0984201
ADS	0.041578	0.0029133	0.009627	0.009627	0.009627
DDS	0.045558	0.0121699	0.025399	0.025399	0.025399
HBS	0.877845	0.16255	1.0699	0.384156	0.384156
HSK	0.2127	0.0	0.45083	0.0	0.0
CKS	10.0	0.5	2.5	1.429	2.563
EFFLD	450.0	95.85	53.44	1.9464	424.96
AA	110.0	20.0	110.0	20.0	20.0
BB	0.5	0.25	0.5	0.25	0.55

J.2.4. Model as Coded

Here we present a summary of the coding used to implement the SEPD component in TRAC. Much of the coding was provided to LANL by INEEL or GE and will not be discussed in detail.

J.2.4.1. Phase 1: Determination of the Appropriate Carryover and Carryunder.

There are currently three options for the SEPD that directly affect the determination of the carryover (*XCO*) and carryunder (*XCU*). These are the conditions TRAC attempts to create at the end of the time step if the SEPD component is functioning. There are several conditions, discussed in Section J.2.4.2. that will cause the SEPD component to cease to separate.

J.2.4.1.1. Ideal Separator. If the user selects the ideal separator, the values of *XCO* and *XCU* are considered constants independent of any current flow conditions in the separator. These constant values are read in at the input stage of the calculation and do not change.

J.2.4.1.2. Mechanistic Separator. By selecting this option, the user instructs TRAC to calculate the target values of *XCO* and *XCU* based on the current conditions in the separator. To do this, TRAC uses the subroutines SSEPOR and SEPDX, provided by GE (Ref. J-15.), that predict the performance of a GE separator given the current flow conditions. The TRAC versions of these routines are identical to those provided by GE and used in TRAC-BWR and will not be discussed here. We again point out that the use of this option to model non-GE separators is not recommended. For separators that differ only slightly from a GE separator, however, the user can input geometric parameters to instruct TRAC as to those differences. The default values of the geometric input are listed in Table J-2.

J.2.4.1.3. User-Prescribed Separator. In many cases, the user knows that the separator being modeled is not ideal, nor is it a standard GE design. In those cases the user-prescribed separator should be used. This option, however, requires that the user know the performance characteristics of the separator. Given a particular set of conditions in the separator, TRAC can then refer to the user-supplied performance curves and determine target values of *XCO* and *XCU*. It is up to the user to correctly characterize the separator performance, and this typically takes the form of

$$XCO = XCO(\dot{m}_{\text{total}}, \text{input quality}) \text{ and}$$

$$XCU = XCU(\dot{m}_{\text{total}}, \text{input quality}) .$$

J.2.4.2. Phase 2: Determination of the Separator Exit Flows and Qualities.

Subroutine SEPDI, written by INEEL, calculates target values of the velocities, the derivatives of the velocities with respect to the pressure, and void fractions exiting the SEPD JCELL that would be necessary to yield the desired values of *XCO* and *XCU*. As discussed in Section J.2.2., a quasi-steady-state assumption is made that may not be strictly true for the rapidly varying conditions of a transient simulation.

If the mechanistic option of the SEPD component is used, the subroutine SEPDI also calculates the FRICs (additive-loss coefficients) required to produce a pressure drop that the GE subroutine SSEPOR determines is appropriate for the current conditions. These FRICs will be used in the next phase of the calculations. If any other option is used, it is up to the user to input the correct FRICs to suit the geometry.

J.2.4.3. Phase 3: Circumvention of the Normal Solution Method to Achieve Those Flows and Qualities.

Subroutine SEPDI, which is called from subroutine SEPD2 (TEE2 in TRAC-M/F77), calculates the target values for *XCO*, *XCU*, convected void fractions, etc., and stores them in the common block SEPCB. This subroutine also calculates values for the velocities and the derivatives of the velocities with respect to the pressure, which are stored in the A array, the main data-storage array. The numerical routines, TF1DS1 and TF1DS, use these values, rather than ones they would otherwise calculate, during the remaining numerical calculations. If the mechanistic option of the SEPD is being used, the FRICs calculated in SEPDI are also used in TF1DS1 and TF1DS.

J.2.5. Weighting, Magnitude Limits, and Averaging

Currently, the only limit placed on the operation of the SEPD is that the FRICs calculated with the mechanistic option may not increase or decrease by more than a factor of 2 from one time step to the next.

J.2.6. Variations in Application of Correlation—Special Cases

Subroutine SEPDI, called from SEPD2 (TEE2 in TRAC-M/F77), begins by deciding whether the SEPD should in fact perform any separation. This is done by examining such things as the direction, magnitude, and quality of the incoming flows. If the quality of the input stream is too low ($\alpha < 0.05$), the component does not attempt to cause a separation. Likewise, if either the vapor or total mass-flow rate of the incoming stream is negative, or if the composition of the incoming stream is essentially all vapor ($1.0 - \dot{m}_{\text{vapor}}/\dot{m}_{\text{total}} < 10^{-6}$) then the SEPD component is deactivated. It becomes reactivated only when these conditions are no longer true.

J.2.7. Assessment

No assessment was performed on the separator model at LANL. Extensive assessment was performed at INEEL and is described in Ref. J-13.

J.2.8. Effects of Applying Correlation Outside of Database

The database for the mechanistic model is made up of GE separators. While we do not know the precise effects of using the mechanistic model for non-GE separators, we caution against the use of this option in these cases. As the SEPD is used, more experience will be gained. It is possible that more definitive statements could be made in the future.

J.2.9. Scaling Considerations

Any discussion of scaling for the SEPD component is dependent on the option invoked for the component. These options were outlined in Sections J.2.4.1.1. through J.2.4.1.3.

The ideal separator is an extremely simple-minded option that would rarely be appropriate, except in situations where nearly constant conditions at the separator were expected to be maintained throughout the simulation. Even then, the numbers input for the values of *XCO* and *XCU* would presumably be based on some experience with the sort of separator being simulated. In such cases then, the effect of scaling is presumed to be taken into account by the user.

The mechanistic option of the SEPD component relies on the model developed by GE that predicts the carryover and carryunder of the separator as a function of the local conditions. This GE model was developed specifically for their hardware design and as a result is most appropriate for full-scale applications.

The user-prescribed separator option requires that the user input performance curves for the SEPD component. It is therefore assumed that the user has appropriate information for the particular separator being modeled, and all effects of scale have been considered by the user.

J.2.10. Summary and Conclusions

The SEPD component of TRAC is an implementation of the model from the TRAC-BWR code, where it is also called the SEPD. As the component was not developed at LANL, we cannot certify the correctness of the method used. The primary development was performed at INEEL and at GE.

The component provides a means for the separation of an incoming two-phase mixture of liquid water and its vapor into one stream that is liquid enriched and one stream that is vapor enriched. Several options are available for determining the performance of the SEPD to enable a close simulation of the physical separator being modeled. The most sophisticated option, known as the mechanistic option, was developed by GE to model the separators that they manufacture. For modeling GE separators, this is the appropriate option. Options also exist to permit the users to input their own performance curves for the separator or to model the separator as one whose performance is independent of current local conditions. In both of these later cases, it is up to the user to provide realistic input.

The models assume that a quasi-steady state exists in the separator, and therefore models will likely break down for sufficiently rapid transients in the SEPD component.

J.3. FILLs

The FILL component replaces the motion equations where it is joined to a 1D component with a boundary condition specifying velocities or mass flows. Since the motion equations are eliminated at that mesh-cell interface, interfacial drag and wall friction terms are not required and nonphysical pressure gradients can develop with no effect on flow because the FILL cell input-specified pressure is used only to evaluate cell properties. Generally a FILL's behavior is well defined by input conditions, but there are peculiarities that must be watched.

The most obvious problem can occur when a user specifies a mass-flow rate from the system into the FILL. In that case, the FILL component determines liquid and vapor velocities into the FILL at the beginning of the time step, based on the old-time macroscopic densities from the adjacent component mesh cell. The end-of-the-step mass-flow rate is determined by the product of these velocities with the new-time macroscopic densities. If the fluid density in the cell adjacent to the FILL changes significantly over the duration of a time step, the actual mass flowing out of the FILL will be different from the expected value.

The user should exercise caution when setting up FILLs with properties that depend on nearby system parameters (especially pressure) through signal-variable (or control block based on signal-variable input) independent-variable evaluated tables. The tables are always evaluated with old-time variables, and situations can occur that are numerically unstable. These instabilities can be controlled by setting TWTOLD to a value greater than zero but less than one. This institutes time-step weighting with the result from the current evaluation of the table multiplied by 1-TWTOLD and added to TWTOLD times the result from the preceding time step. In some cases, controlling the maximum rate of change of the velocity (or mass flow) with the input variable RFMX will also prevent problems from developing. Because of the infinite variety of functional dependencies that can be created with FILL tables, no set guidelines have been developed for the use of TWTOLD and RFMX. Before using them in a large system-model application, a user should carefully test such FILL-table functional forms that have independent or dependent parameters that vary rapidly.

J.4. BREAKs

A BREAK is often considered a pressure boundary condition, but it can affect the flow through more than just the pressure-gradient term in the motion equations. Lack of caution in selecting the fluid void fraction and fluid temperatures and pressure that determine the fluid microscopic densities in the BREAK mesh cell can result in unexpected gravitational pressure heads and a poor prediction of the flow regime used to compute the interfacial drag. When flow is in from a BREAK, the inflow momentum flux has been assumed to be zero in order to provide a numerically stable solution. The TRAC user can account for an inflow momentum flux by input specifying a static rather than dynamic pressure boundary condition (see Section 2.1.7.2.1.). This requires knowing when the transient inflow from the BREAK occurs and then defining the pressure in its static rather than dynamic form. This can be done using control blocks to define the static or dynamic pressure boundary condition based on the flow direction of the BREAK junction velocity.

J.5. PLENUMs

A PLENUM is a simple generalization of 1D flow modeling to a single-cell component with an arbitrary number of junction connections to other 1D components. Having one mesh cell results in complete mixing of fluid from all junction connections as it flows through the PLENUM cell volume. A unique feature of a PLENUM component is that

the junction connections on a side convect momentum across the PLENUM component cell to the junction connections on the other side. There also can be junction connections on other sides that model the PLENUM cell center as having an infinitely large flow area and thus a zero momentum flux to/from the junction. Momentum can be convected across a fluid volume in all three directions with a 3D VESSEL component, but complete mixing as in a PLENUM component will not occur because two or more mesh cells in each direction are required to convect momentum across a VESSEL component between source connections. At the present time, heat structures cannot be coupled to a PLENUM hydro cell because of the different database form of a PLENUM component. The stratified-flow regime is not evaluated in the PLENUM cell. However, stratified flow is evaluated for the interfacial drag term at the PLENUM junctions.

J.6. Turbine (TURB) Component

Note: Turbine (TURB) Component. The base code for both TRAC-M/F77 and TRAC-M/F90 has a component to model turbines (the TURB component). In the TURB component energy is removed from the fluid as a result of work performed by the turbine. The TURB component received minimal support over its years in TRAC-P, and its general use was not, and is not, recommended. (It should be used with caution.) The TRAC-P TURB was brought over directly to TRAC-M. Currently, the TURB component is only available in TRAC-M/F77, and the same caution applies. The TRAC-P TURB has been removed entirely from TRAC-M/F90. An improved turbine modeling capability is to be included in a future TRAC-M/F90 version. Section J.6. describes the current (obsolete) TURB component.

In the turbine, energy is removed from the fluid as a result of work performed by the turbine. The model calculates the momentum and energy losses and the angular velocity as a function of the fluid-flow rate, fluid properties, and the turbine nozzle and blade geometry. These momentum and energy losses are subsequently subtracted from the TRAC momentum and energy equations, respectively.

Each TURB module represents an individual turbine stage. Thus the number of TURB components required in the TRAC model is equal to the total number of individual stages associated with the turbines rather than the number of turbines. However, the code internally recognizes the “family” of stages belonging to a particular turbine, which facilitates turbine-governing and overall turbine-performance calculations that depend on individual stage performances. All the data that are common among the family (i.e., data pertaining to the turbine rather than individual stages, such as the generator efficiency or the generator power demand) are entered under stage 1, and the other stages of the family access these data from stage 1. Modeling an individual stage with a TURB component allows the user complete flexibility for modeling extraction, regeneration, reheating, etc., using the other TRAC components.

In both the impulse and reaction turbines, the thermodynamics of the internal processes is basically the same. In the impulse turbine, the expansion of steam takes place in the nozzles or in fixed blades, and the kinetic energy of steam is converted into mechanical work at the blades. In the reaction turbine, the steam is allowed to expand in moving blades also, thereby transferring the reaction energy into mechanical work. Details of this process are discussed in many standard text books on thermodynamics. Salisbury (Ref. J-16.), in particular, discusses the subject comprehensively. The steam expansion process through a turbine stage is shown in Fig. J-12. Line AB represents isentropic expansion from pressure p_A to pressure p_B. Because of friction and other irreversible losses, the actual state of steam after expansion is B' and not *B*. Thus the steady-state energy equation gives

$$h_A + \frac{V_A^2}{2} = h_B + \frac{V_B^2}{2} = h_{B'} + \frac{V_{B'}^2}{2} + \frac{P}{\dot{m}} \quad , \tag{J-17}$$

where *h* is the fluid enthalpy, *V* is the fluid velocity, $\dot{m}$ is the mass-flow rate, and *P* is the stage work per second. The velocity V_B is the ideal nozzle velocity, such that $P_{\text{ideal}} = \dot{m} V_B^2 / 2,$ and is easily obtained using Eq. (J-17) along an isentrope.

The stage power, *P*, can therefore be calculated as

$$P = \eta_{\text{stg}} P_{\text{ideal}} = \eta_{\text{stg}} \dot{m} \frac{V_B^2}{2} \quad , \tag{J-18}$$

where η_{stg} is the stage efficiency.

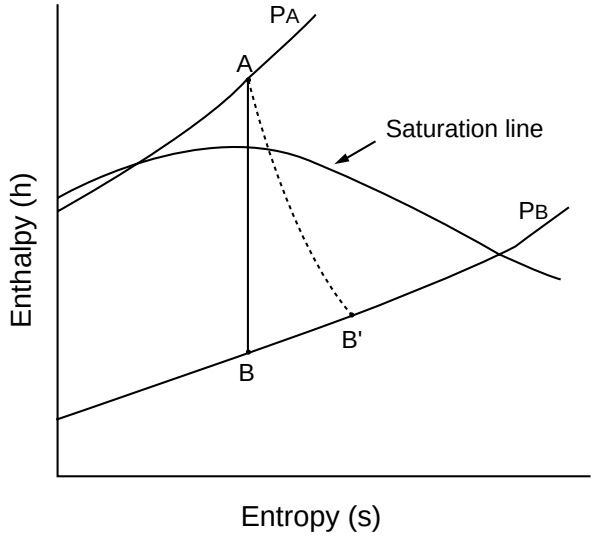

Fig. J-12. Steam expansion through a turbine stage.

The final state B' can be easily computed for a known η_{stg} under steady-state conditions using Eqs. (J-17), (J-18), the continuity equation, and the equation of state. This is the approach followed by Farman and Motloch (Ref. J-17.) in the RETRAN code. However, a preferable approach is to make use of the transient, two-phase TRAC hydrodynamic equations with appropriate sink terms in the momentum and energy equations. The momentum and energy terms corresponding to the turbine power are extracted as shown in a typical noding diagram in Fig. J-13. The energy is always extracted from cell number 2, whereas the momentum is extracted either from the second or the third cell edge depending upon the flow direction. A minimum of three cells are required to model a TURB component. It is clear from Eq. (J-17) that the velocity at the turbine exit would have been V_B had no work been done by the turbine. Owing to the turbine work, the exit velocity is $V_{B'}$ instead of V_B. Thus the momentum loss in the turbine stage is

$$M = \dot{m}(V_B - V_{B'}) = A_j \rho_2 V_j (V_B - V_{B'}) \ , \tag{J-19}$$

where A is the area. The subscript j (j may be 2 or 3, depending on the flow direction) refers to the momentum-sink cell edge. The density ρ_2 is from cell 2. Also, velocity V_B is the same as V_j, the actual cell-edge velocity calculated by the code after it accounts for the momentum loss. Therefore, writing Eq. (J-19) in terms of pressure loss, Δp, gives

$$\Delta p = \rho_2 V_j (V_B - V_j) \quad . \tag{J-20}$$

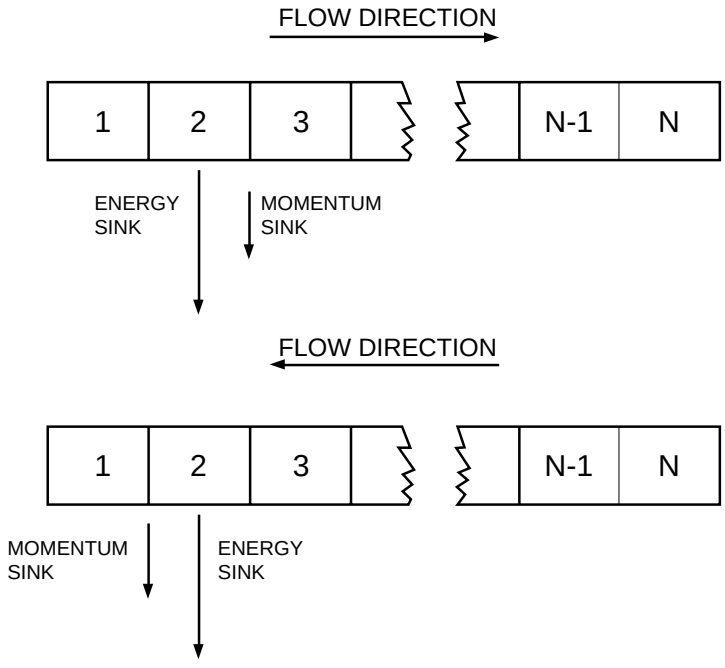

Fig. J-13. Turbine stage noding diagram depicting momentum and energy sink locations.

Experience has shown that translating the above pressure loss into an equivalent FRIC (FRIC is generally an input parameter to accommodate irreversible losses and can be related to an effective form loss K_{eff}) results in much improved code stability than subtracting Δp from the momentum equation directly (with its associated derivative $\partial \Delta p / \partial V_j$, of course). Therefore, writing Δp in terms of the additive-loss coefficient FRIC gives

$$\Delta p = \text{FRIC} \frac{\rho_2 V_j^2 0.5(\Delta X_j + \Delta X_{j-1})}{d_j}$$

$$= \frac{K_{\text{eff}}}{2} \rho_2 V_j^2 \quad ,$$

where d_j is the momentum source cell-edge diameter. Comparison of this equation with Eq. (J-20) leads to

$$\text{FRIC} = \frac{V_B - V_j}{V_j} \frac{d_j}{0.5(\Delta X_j + \Delta X_{j-1})} \quad . \tag{J-21}$$

Because the above value of FRIC is applied at either cell edge 2 or cell edge 3 (depending upon flow direction), the user input additive FRIC values at these cell edges will be overwritten. Therefore FRIC(2) and FRIC(3) should always be input as 0.0.

The energy loss that should be taken out of the total energy equation is given by Eq. (J-18). However, TRAC uses the thermal energy equation, which is obtained after combining the total energy equation with the momentum equation. Some simple algebraic substitutions lead to the following expression for the sink term for the thermal energy equation:

$$P_{\text{enr}} = P - \frac{V_B + V_j}{2} M = P - A_j \frac{V_B + V_j}{2} \Delta p \quad , \tag{J-22}$$

where P_{enr} is the amount to be extracted from the TRAC energy equation. The second term on the right-hand side of Eq. (J-22) appears as a result of combining the momentum equation with the energy equation.

Therefore, Eqs. (J-21) and (J-22) can be used to account for momentum and energy losses as a result of the power produced by a turbine stage provided the stage efficiency is known.

The stage efficiency is given by

$$\eta_{\text{stg}} = \eta_{\text{nb}} - \phi_{\text{m}} - \phi_{\text{rem}} \quad , \tag{J-23}$$

where η_{nb} is the nozzle-bucket efficiency to be obtained from the velocity diagram, ϕ_{m} is the moisture loss, and ϕ_{rem} are the remaining miscellaneous stage losses whose

magnitudes are not easily definable. Term ϕ_{rem} includes nozzle-end loss, windage loss, diaphragm-packing loss, etc. The moisture loss is included as a separate term because it is the most significant loss and its functional formulation is known. These losses are described in detail by Salisbury in Ref. J-16. Salisbury recommends the following expression for the moisture loss:

$$\phi_m = 1.15(1 - x_t) \quad , \tag{J-24}$$

where x is the thermodynamic quality of steam.

The nozzle-bucket efficiency is calculated as

$$\eta_{\text{nb}} = \frac{\text{energy transfer to the blades}}{\text{available energy at the nozzle}} \tag{J-25}$$

$$= \frac{W\dot{m}\sum_{i=1}^{2n} V_{a_i}}{\dot{m}\frac{V_B^2}{2}} = \frac{2W}{V_B^2}\sum_{i=1}^{2n} V_{a_i}$$

where W is the moving blade velocity, V_a is the axial component of velocity relative to the moving blades, and n is the number of rows of moving blades. A vector diagram for two rows of moving blades is presented in Fig. J-14., which can be extended to an arbitrary number of rows by our recursively appending a stationary blade row and a moving blade row in pairs to Fig. J-14. There is no limit on the number of rows allowed in a TURB module. If r is the fraction of stage energy transferred by reaction, the velocity vectors can be written as follows:

$$\begin{aligned}
V_1 &= C_{\text{n}} V_B (1-r)^{1/2} \\
V_2 &= (V_1^2 + W^2 - 2V_1 W \cos\theta_1)^{1/2} \\
V_3 &= \left[(C_{\text{b}} V_2)^2 + r\frac{C_{\text{r}}^2}{2n-1}V_B^2\right]^{1/2} \\
V_4 &= (V_3^2 + W^2 - 2V_3 W \cos\theta_2)^{1/2} \\
V_5 &= \left[(C_{\text{b}} V_4)^2 + r\frac{C_{\text{r}}^2}{2n-1}V_B^2\right] \\
V_6 &= (V_5^2 + W^2 - 2V_5 W \cos\theta_3)^{1/2} \\
V_7 &= \left[(C_{\text{b}} V_6)^2 + r\frac{C_{\text{r}}^2}{2n-1}V_B^2\right]^{1/2} \\
V_{a_1} &= V_1 \cos\theta_1 - W \\
V_{a_2} &= V_3 \cos\theta_2 \\
V_{a_3} &= V_5 \cos\theta_3 - W \\
V_{a_4} &= V_7 \cos\theta_4 \quad ,
\end{aligned} \tag{J-26}$$

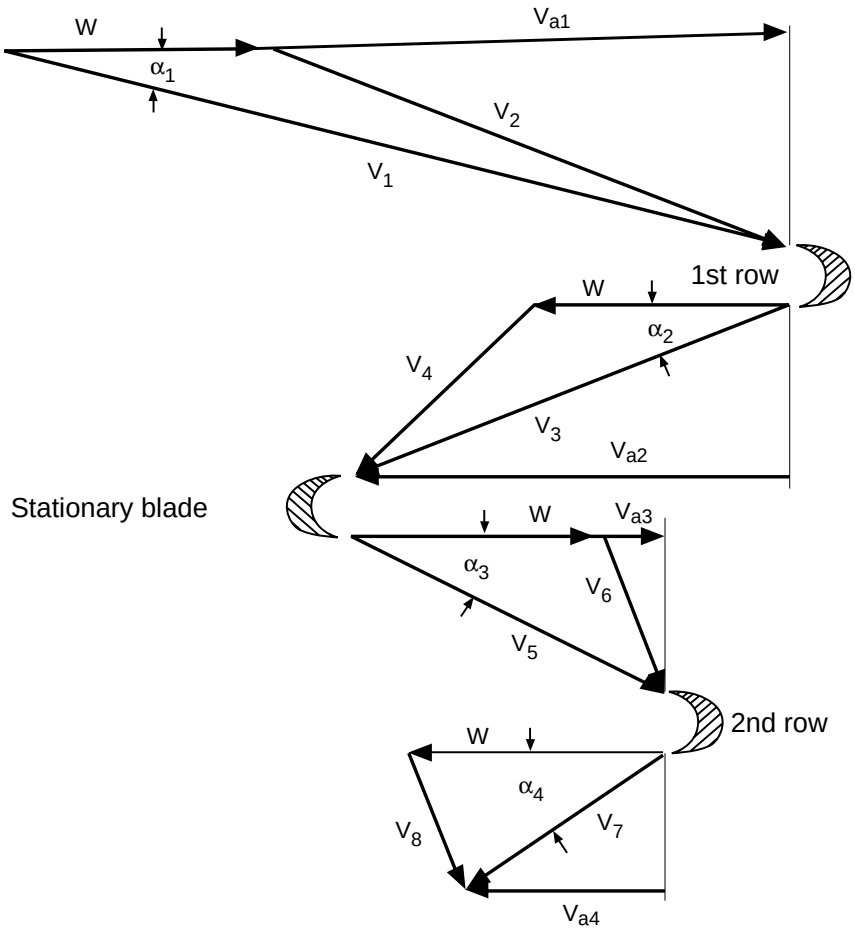

Fig. J-14. Velocity diagram for two rows of moving blades.

where C_n is the nozzle velocity coefficient, C_b is the bucket velocity coefficient, and C_r^2 is the fraction of total reaction energy actually delivered in all rows of blades. It is assumed that equal fractions of reaction energy are delivered in each blade row.

Although the remaining losses, ϕ_{rem}, required in Eq. (J-23) are not easily definable at off-design conditions, their magnitude is generally known at design conditions from the test data. In TRAC, the user is allowed an option of specifying the stage efficiency, η_{stg}, at design conditions. If η_{stg} is input, the code uses Eq. (J-23) to calculate ϕ_{rem} at design conditions. This value of ϕ_{rem} is then assumed constant throughout the transient. If the user does not input η_{stg} at design conditions, ϕ_{rem} is assumed to be zero.

Thus, to summarize, a TURB module performs the following sequence of calculations:

1. With the upstream and downstream pressures and velocities from the previous time step, the ideal nozzle velocity, V_B, is calculated and we assume steam is an ideal gas.
2. With the bucket velocity, *W*, from the previous time step, η_{nb}, is calculated from Eqs. (J-25) and (J-26).
3. The stage efficiency, η_{stg}, is then calculated from Eq. (J-23).
4. Stage power, *P*, is calculated from Eq. (J-18) with $\dot{m}$ from the previous time step.
5. An equivalent FRIC for the momentum equation is calculated from Eq. (J-21) with V_j from the previous time step.
6. The amount to be extracted from the energy equation, P_{enr}, is then calculated from Eq. (J-22).

So far we have discussed how each stage is handled by a TURB module, which represents an individual stage. In general, a turbine has more than one stage, and the governing is accomplished for the turbine as a whole and not for individual stages because only the total load on the turbine is known. Also, the angular speed among the "family" of stages is the same because of direct coupling of the stages. Thus additional calculations that are common among the family of stages are required. These calculations are done after all the stages are processed, and these common data are stored under the first stage of the family.

Total turbine power is calculated as

$$P_{\text{total}} = \sum_{i=1}^{m} P_i \quad , \tag{J-27}$$

where *m* is the total number of stages belonging to a turbine, i.e., the number of stages of the same family. However, the electrical generator power input is less than P_{total} because of the friction at the bearings of the turbine-generator shaft. Therefore, the power input to the generator, $P_{\text{gen,input}}$, is

$$P_{\text{gen,input}} = \sum_{i=1}^{m} P_i - \omega\, T_{\text{f}} \quad , \tag{J-28}$$

where ω is the turbine-generator angular speed and T_{f} is the frictional torque given by

$$T_{\text{f}} = K_1 + K_2\omega + K_3\omega^2 \quad , \tag{J-29}$$

where K_1, K_2, and K_3 are the user-input coefficients. The generator output, $P_{\text{gen,output}}$, is therefore

$$P_{\text{gen,output}} = \eta_{\text{gen}} \left[\sum_{i=1}^{m} P_i - \omega \, T_{\text{f}} \right] \quad , \tag{J-30}$$

where η_{gen} is the generator efficiency, which is treated as constant. At design conditions, this output must be equal to the generator power demand. However, because of uncertainties in stage power calculations, friction torque, and generator efficiency, this equality cannot be satisfied exactly. Thus a correction efficiency, η_{corr}, is defined, such that

$$\eta_{\text{corr}} = \frac{\text{generator power demand at design conditions}}{\left\{ \eta_{\text{gen}} \left[\sum_{i=1}^{m} P_i - \omega \, T_{\text{f}} \right] \right\}_{\text{design conditions}}} \quad .$$

This η_{corr} is calculated during initialization and is used as a constant multiplier during the entire transient. Thus Eq. (J-30) becomes

$$P_{\text{gen,output}} = \eta_{\text{corr}} \eta_{\text{gen}} \left[\sum_{i=1}^{m} P_i - \omega \, T_{\text{f}} \right] \quad . \tag{J-31}$$

At equilibrium conditions, this output should be equal to the generator power demand, P_{demand}, which is input by the user in tabular form. If $P_{\text{gen, output}} > P_{\text{demand}}$ the steam flow through the turbine should be reduced and vice versa. For example, Fig. J-15. shows two typical turbines (a two-stage throttle-governed and a three-stage bypass-governed) without any extractions to illustrate the use of special valve options to control steam flow. As the power demand increases, more steam has to be supplied to the turbine, and in case of a bypass-governed turbine, some additional steam has to be supplied to lower stages. However, as the steam flows through the turbines increase, the amount of steam bypassed must decrease. The turbine bypass valve therefore can be modeled using the appropriate VALVE option. It might, however, be preferable to operate the turbine bypass valve using a controller in order to maintain a constant pressure in the steam generator.

The turbine speed is maintained constant as long as the plant is connected with the external load, i.e., $P_{\text{demand}} \neq 0.0$, to maintain constant grid frequency. To meet this power demand at the desired grid frequency, the steam supply to the turbine is adjusted as discussed above. However, the turbine is allowed to coast down at the receipt of a turbine-trip signal (which is generated by tripping off the generator power demand). The turbine speed in this case is determined by the angular momentum balance

$$I \frac{d\omega}{dt} = T_{\text{turb}} - T_{\text{f}} - T_{\text{loss}} - T_{\text{demand}} \quad , \tag{J-32}$$

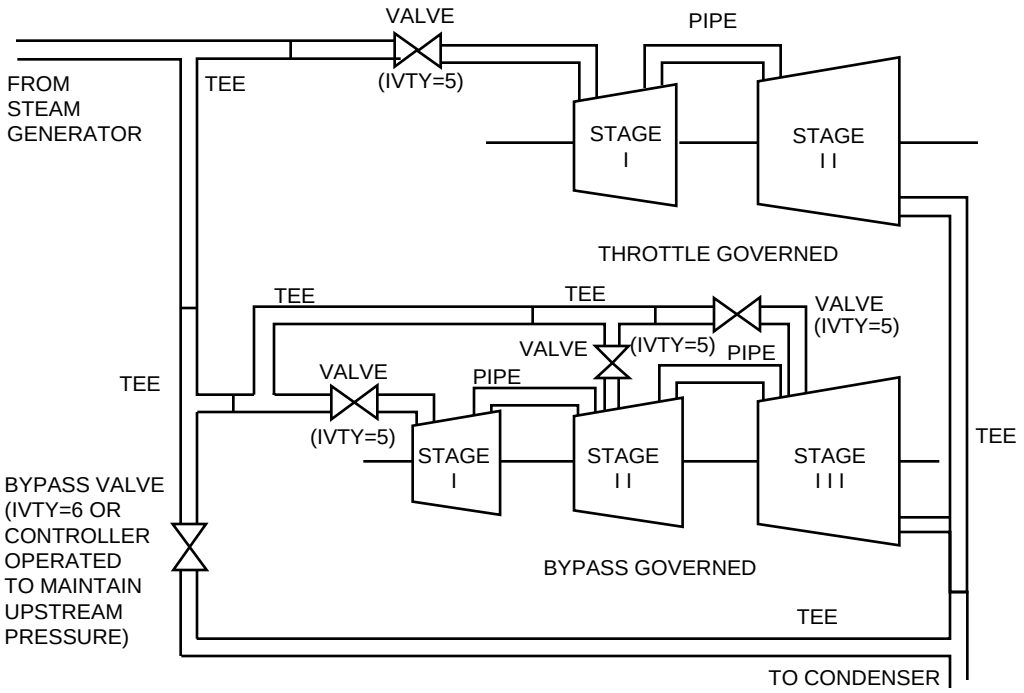

Fig. J-15. A typical noding diagram showing the combined use of turbine and VALVE components.

where I is the turbine-generator assembly moment of inertia, T_{turb} is the total turbine torque output from all stages, T_{loss} is the loss in torque as a result of generator losses, and T_{demand} is the torque due to external load. However, because the turbine is allowed to coast down only when the external load is zero, T_{demand} is 0.0. Also, because the generator is not producing any power, T_{loss} = 0.0. Thus Eq. (J-32) simplifies to

$$I\frac{d\omega}{dt} = \frac{1}{\omega}\sum_{i=1}^{m} P_i - T_{\text{f}} \quad . \tag{J-33}$$

The TURB data are processed in a manner similar to the other 1D components. Subroutine RTURB reads data from the input file, and subroutine RETURB reads data from the restart file. Initialization of any remaining variables not provided by the input or restart files is performed in subroutine ITURB.

For the TURB component, subroutine TURBI calls TRBPOW, which calculates turbine stage efficiency and power. Two additional subroutines, TRBPRE and TRBPST, are called during the prepass and postpass stages, respectively, to perform calculations that are common for a family of different stages related to the same turbine.

J.7. Accumulator Modeling with the PIPE Component

Note: Accumulator Modeling. Early versions of TRAC-P had a specialized ACCUM component to model PWR accumulators. The special ACCUM models were later also included in the PIPE component (which also has built-in wall heat conduction that is not available in the ACCUM). The ACCUM component was removed from TRAC-P before TRAC-M development started.

TRAC provides two user-selected options in the PIPE component for modeling PWR accumulators. The PIPE component with input parameter IACC set to 1 selects the normal PIPE component (IACC = 0), plus an interface sharpener and additional output variables to monitor accumulator behavior. Setting IACC to 2 selects the features of IACC = 1, plus application of a liquid separator model at the bottom of the PIPE. Figure J-16. shows the typical nodalization of an accumulator with respect to gravity, i.e., a vertical stack of cells with cell 1 at the top and cell NCELLS at the bottom (NCELLS is the number of cells in the PIPE component).

The code sets the interfacial drag to zero at each internal interface j ($1 < j <$ NCELLS + 1) in the PIPE component with IACC set to 1 or 2 to enhance the phase separation in the component. Additionally, the IACC = 2 option of the PIPE component will reset the additive friction factor (input array FRIC) at the NCELLS + 1 interface (outlet) as follows to prevent the gas phase from escaping from the component. The manipulation of the FRIC(NCELLS + 1) value begins in the subroutine that reads the input data; subroutine RPIPE sets the FRIC value at the last interface to $-1.123456 \times 10^{+29}$. Subroutine StbVel1D (FEMOM in TRAC-M/F77) interprets this FRIC value as a flag to force the FRIC applied in the liquid momentum equation to zero and the FRIC applied in the gas momentum equation to $+1.123456 \times 10^{+29}$.

The equivalent Darcy loss coefficient $K_{\mathrm{NCELLS+1}}$ in the gas phase corresponding to the FRIC value at the last interface is dependent on the input geometry and is given by

$$K_{\mathrm{NCELLS+1}} = \mathrm{FRIC}_{\mathrm{NCELLS+1}} \frac{\Delta X_{\mathrm{NCELLS}} + \Delta X_{\mathrm{NCELLS+1}}}{D_{\mathrm{H,NCELLS+1}}} \quad , \tag{J-34}$$

where $D_{\mathrm{H,NCELLS+1}}$ is the hydraulic diameter at the last interface, $\Delta X_{\mathrm{NCELLS}}$ is the length of the last cell of the PIPE component, and $\Delta X_{\mathrm{NCELLS+1}}$ is the length of the cell in the adjacent component across the NCELLS + 1 interface. This adjustment, which results in a very high additive loss on the gas phase at the exit of the component together with the zero additive loss on the liquid phase, essentially requires the gas velocity to be zero while the liquid flows subject only to the irreversible pressure drop caused by the interfacial drag.

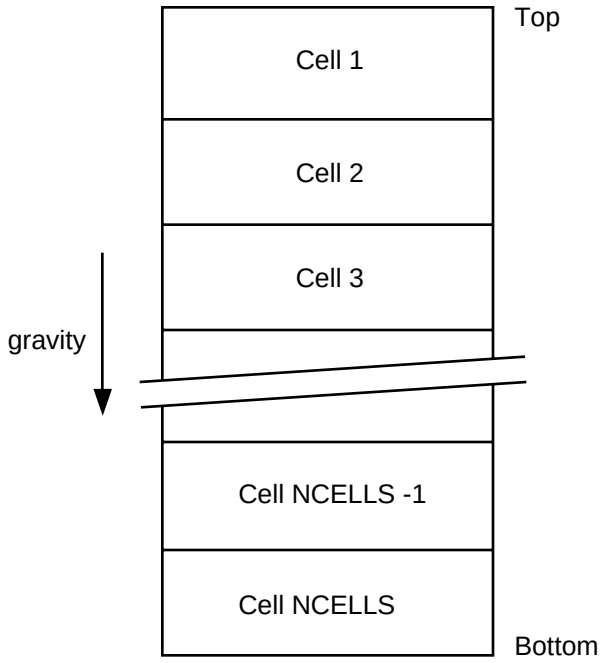

Fig. J-16. Typical component nodalization for the accumulator and pressurizer.

J.8. Pressurizer Component

The code defines the PRIZER component to represent the pressurizer. This component provides a special function during steady-state calculations (input parameter STDYST > 0 on Main-Data Card 4) in that the component simulates a BREAK component to set the system pressure and to permit the system fluid to swell or contract in response to temperature changes without requiring the user to model make-up and let-down systems. Also during the steady-state calculation, the code calculates the effects of the gravity head and thermal nonequilibrium in the fluid in the PRIZER component to prevent small secondary transients at the beginning of the transient calculation.

In addition to these very specialized functions during the steady-state calculations, the PRIZER component provides a representation of pressurizer heaters and sprays by manipulating the energy deposited in or extracted from the liquid in the PRIZER. The code assumes that the PRIZER consists of a vertical stack of cells, with cell 1 at the top and cell NCELLS at the bottom (see Fig. J-16.), and calculates a collapsed liquid level. The total liquid inventory in the PRIZER is

$$\mathrm{vol}_{\mathrm{liq}} = \sum_{i=1}^{\mathrm{NCELLS}} (1-\alpha_i)\mathrm{vol}_i \ , \qquad \text{(J-35)}$$

where vol_i is the volume of cell i and α_i is the associated void fraction. The collapsed liquid level z is

$$z = \sum_{j=1}^{k-1} \Delta X_{\mathrm{NCELLS}+1-j} + \Delta X_{\mathrm{NCELLS}+1-k} \frac{\mathrm{vol}_{\mathrm{liq}} - \sum_{j=1}^{k-1} \mathrm{vol}_{\mathrm{NCELLS}+1-j}}{\mathrm{vol}_{\mathrm{NCELLS}+1-k}} \quad , \tag{J-36}$$

where k is defined such that

$$\mathrm{vol}_{\mathrm{NCELLS}+1-k} > \mathrm{vol}_{\mathrm{liq}} - \sum_{j=1}^{k-1} \mathrm{vol}_{\mathrm{NCELLS}+1-j}$$

and ΔX_i is the length of cell i. Eq. (J-36) represents the standard method used in the code to calculate the collapsed liquid level.

If the collapsed liquid level $z \leq$ ZHTR, an input parameter, no accounting of the heaters or sprays is made. For the case of $z >$ ZHTR, the code calculates the total power P_{in} to be added to or extracted from the liquid as follows:

$$P'_{\mathrm{in}} = P_{\mathrm{HEAT}} \frac{p_{\mathrm{set}} - p_1}{\mathrm{DPMAX}} \quad , \text{ and} \tag{J-37}$$

$$P_{\mathrm{in}} = P'_{\mathrm{in}} \quad \text{if} \quad P'_{\mathrm{in}} < P_{\mathrm{HEAT}} \tag{J-38}$$

$$= P_{\mathrm{HEAT}} \frac{P'_{\mathrm{in}}}{|P_{\mathrm{in}}|} \quad \text{if} \quad P'_{\mathrm{in}} \geq P_{\mathrm{HEAT}} \quad .$$

In the above equations, P_{HEAT} is the user-defined maximum effective power of the heaters and the sprays, p_{set} is the user-input pressure to which the system is controlled, DPMAX is the user-input pressure offset at which the heaters or sprays achieve their maximum effectiveness, and p_1 is the calculated pressure in the first (top) cell of the PRIZER.

The P_{in} is distributed among the cells based on the liquid in each cell by the following algorithm:

$$P_f = P_{\mathrm{in}} \frac{\rho_{\mathrm{liq}} \mathrm{vol}_i (1 - \alpha_i)}{\mathrm{LMT}} \quad , \tag{J-39}$$

where LMT is the total liquid mass in the PRIZER defined by

$$\mathrm{LMT} = \sum_{j=1}^{\mathrm{NCELLS}} \rho_{\mathrm{liq}} \mathrm{vol}_i (1 - \alpha_i) \quad . \tag{J-40}$$

Additionally, for each cell *i*, ρ_l is the microscopic liquid density, α is the void fraction, vol is the cell volume, and P_f is the power deposited in (extracted from) the liquid phase.

It is worth noting that if there is no liquid in the PRIZER, LMT is zero and the code does not perform the calculation to distribute the heat load among the individual cells. For this case, all of the P_f are zero.

The sign of P_{in}, and hence of P_f, indicates whether heat is added or subtracted from the liquid. If the calculated pressure p_1 is above the control pressure p_{set}, the sprays are assumed to be on and heat is removed from the liquid phase. For this case, the model is not mechanistic for four reasons: (1) the reduction in pressure relies on condensation of vapor on the surface of the liquid pool as opposed to the spray itself, (2) removing energy from the liquid results in artificially subcooling the entire liquid pool, (3) there is a net energy extraction from the PRIZER that does not actually occur, and (4) the mass flows associated with the sprays do not occur in the PRIZER.

However, the case when $p_1 < p_{set}$ requires that the heaters be on. This case is reasonably mechanistic in that the heat is added to the liquid. However, the distribution of the energy is not necessarily correct nor does the 1D modeling with a single liquid velocity permit calculating the convective currents within the liquid pool set up by the heat addition. Subroutine PRZR1X performs the calculations described above. When looking at the coding, one should keep in mind that the code keeps a running sum of all of the sources of heat to each cell for each time step.

J.9. Valve

The VALVE module is used to model various types of valves associated with LWRs. The valve action is modeled by controlling the flow area and the form loss at one cell interface of a 1D component. The valve action may not be located at a valve component junction unless that junction is connected to a BREAK.

Two methods are provided for specifying the valve flow area. The flow area *FA* can be computed directly from a flow-area fraction (FAVLVE) according to

$$FA = \text{FAVLVE} \cdot \text{AVLVE} \quad , \tag{J-41}$$

where AVLVE is the input value for the fully open valve flow area. Alternatively, the flow area may be computed from the relative position (XPOS) of the valve stem, which assumes a guillotine-type cut of circular cross section. The relative valve-stem position of XPOS = 1 corresponds to a fully open valve with flow area AVLVE.

Because the hydraulic diameter is used in the wall friction calculation, the fully open valve hydraulic diameter (HVLVE user input) is not changed during a given calculation. HD(ivps) is set equal to HVLVE during initialization and is held constant after the

initialization phase. The form loss for flow through the valve is adjusted according to the valve flow area based on

$$K = K0 + 0.5(1-b) + (1-b)^2 \quad , \tag{J-42}$$

where $K0$ is the fully open valve form loss and b is the ratio of the valve flow area to the pipe flow area.

This formula is recommended in the Crane manual (Ref. J-18.) for gate and ball valves. This formula will overestimate the form loss for partially closed globe and angle valves. For globe and angle valves, $K0$ tends to be large and therefore the total error during opening or closing a globe or angle valve is relatively small. $K0$ is also restricted to be greater than 0.03. $K0$ of zero has been observed to be numerically unstable and the Crane manual indicates that $K0$ should range from $3f$ to $400f$ or (assuming $f = 0.01$) 0.03 to 4.0, depending upon the valve design.

The *FA* fraction or valve-stem position is entered as a constant or a tabular function defined by a table. Use of a table may be trip-initiated according to the control option selected. To increase the flexibility to model various types of valves, two valve tables may be input for trip-controlled valves. The first table is used when the trip set status is $ON_{forward}$ and the second table is used when the trip set status is $ON_{reverse}$. The independent variable for the table is a modeled-system parameter defined by a signal variable or a control block.

Many different types of valves can be modeled because of the flexibility available to choose the independent variable for the valve-action table and to implement table evaluation under trip control. Simple valves that either open or close on a trip may be modeled using an OFF-ON- or ON-OFF-type trip and a table that has relative time (since trip initiation) as the independent variable to obtain the desired rate of opening or closing. Valve leakage can be simulated by restricting the table minimum *FA* fraction or valve-stem position to a value greater than zero. Simple valves can be used to model pipe breaks or the opening of rupture disks.

A simple check valve can be modeled by using a valve table with the appropriate pressure gradient as its independent variable. Alternatively, a check valve can be modeled as a trip-controlled valve with the pressure gradient used as the trip signal and the valve table used to control the rate of valve movement.

A steam-flow control valve [or power-operated relief valve (PORV)J can be modeled using an $ON_{reverse}$-OFF-$ON_{forward}$ trip to control it with the start closing pressure, end closing pressure, end opening pressure, and start opening pressure as the respective trip set points. The rate of opening ($ON_{forward}$ state) can be defined by the first valve table and the rate of closing ($ON_{reverse}$ state) by the second valve table. The rate of opening and closing will be the same only if the first valve table is entered.

A PORV can be modeled by using a table with pressure as the independent variable and a step-like function for the flow-area fraction or valve-stem position. In this case, it is important that the step function not be too steep or the valve flow area may oscillate because of the coupling between the flow through the valve and the pressure variable. A bank of PORVs can be modeled with a single valve component in the same manner by using a multistep function to simulate the multiple pressure set points corresponding to the various valves.

This calculation of flow area assumes a guillotine cut of a circular cross section and is based on standard mensuration formulas. Figure J-17. shows the assumed geometry. When the valve is fully open, the flow area corresponds to the full circle. The stem position is assumed to be normalized such that a zero position is fully closed and a position of 1 is fully open. The calculation of the area and the corresponding hydraulic diameter is normalized similarly.

Subroutine FAXPOS performs the calculation of the normalized flow area. If the relative valve-stem position XPOS is known, the code can calculate the normalized flow area. For a circle with a radius of 1, one can define an H such that

$$\begin{aligned} H &= 1 - h \\ &= \min(1.0, |1.0 - 2 \cdot \mathrm{XPOS}|) \quad , \end{aligned} \tag{J-43}$$

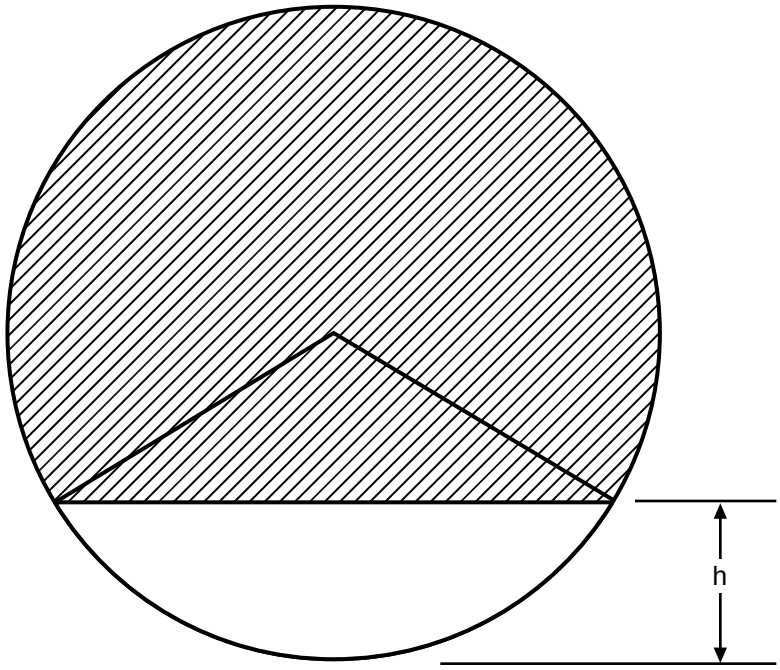

Fig. J-17. Assumed geometry for VALVE flow-area calculation.

where *h* is the dimension shown in Fig. J-17. Then half of the angle subtended by the chord is given by

$$\theta = \cos^{-1} H \quad , \tag{J-44}$$

and the resulting normalized flow area is

$$\begin{aligned} FA &= \frac{1}{\pi}\left(\theta - H\sqrt{1-H^2}\right) \\ &= 3.1830988\times 10^{-1}\left(\theta - H\sqrt{1-H^2}\right) \quad . \end{aligned} \tag{J-45}$$

Because of symmetry, the total normalized flow area is

$$A_{\text{norm}} = FA \quad \text{if} \quad \text{XPOS} \le 0.5 \tag{J-46}$$

$$= 1.0 - FA \quad \text{if} \quad \text{XPOS} > 0.5 \quad . \tag{J-47}$$

For the case in which the VALVE flow area is specified, the code solves Eqs. (J-44) through (J-48) iteratively for the angle θ and then for the stem position XPOS. The procedure is limited to 20 iterations and attempts to converge the solution for θ to less then 1.0×10^{-3}.

Now the angle θ is permitted to vary from 0 to π radians, such that 0 represents a fully closed valve and π a fully open valve. Therefore, the flow area *A* of the VALVE is

$$\begin{aligned} A &= R^2\left[\theta + \sin\theta\cdot\cos\theta\cdot\frac{\text{XPOS}-0.5}{|\text{XPOS}|-0.5}\right] \\ &= 0.25\left[\theta + \sin\theta\cdot\cos\theta\cdot\frac{\text{XPOS}-0.5}{|\text{XPOS}-0.5|}\right] \quad . \end{aligned} \tag{J-48}$$

Subroutine VLVEX applies the user-specified nominal full-open area AVLVE to the normalized value calculated in subroutine FAXPOS to calculate the actual flow area *A*:

$$A = \text{AVLVE}\cdot A_{\text{norm}} \quad . \tag{J-49}$$

REFERENCES

J-1. "RELAP4/MOD5—A Computer Program for Transient Thermal-Hydraulic Analysis of Nuclear Reactors and Related Systems," Vol. 1, Aerojet Nuclear Company report ANCR-NUREG-1335 (September 1976).

J-2. Victor L. Streeter and E. Benjamin Wylie, *Hydraulic Transients* (McGraw-Hill Book Company, New York, 1957).

J-3. A.J. Stepanoff, *Centrifugal and Axial Flow Pumps,* 2nd ed. (John Wiley & Sons, Inc., New York, 1957).

J-4. P. W. Runstadler, "Review and Analysis of State-of-the-Art of Multiphase Pump Technology," Electric Power Research Institute report EPRI/NP-159 (February 1976).

J-5. O. Furuya, "Development of an Analytic Model to Determine Pump Performance Under Two-Phase Flow Conditions," Electric Power Research Institute report EPRI/NP-3519 (May 1984).

J-6. D.J. Olson, "Experiment Data Report for Single- and Two-Phase Steady-State Tests of the 1-1/2-Loop Mod-1 Semiscale System Pump," Aerojet Nuclear Company report ANCR-1150 (May 1974).

J-7. G. G. Loomis, "Intact Loop Pump Performance During the Semiscale MOD-1 Isothermal Test Series," Aerojet Nuclear Company report ANCR-1240 (October 1975).

J-8. D. J. Olson, "Single- and Two-Phase Performance Characteristics of the MOD-1 Semiscale Pump Under Steady-State and Transient Fluid Conditions," Aerojet Nuclear Company report ANCR-1165 (October 1974).

J-9. Douglas L. Reeder, "LOFT System and Test Description (5.5-Ft. Nuclear Core 1 LOCES)," EG&G Idaho, Inc. report TREE-1208 (NUREG/CR-0247) (July 1978).

J-10. U.S. Nuclear Regulatory Commission memo, L. E. Phillips to U.S. Standard Problem Participants, Subject: Additional Information for Prediction of LOFT L2-3 (March 19, 1979).

J-11. EG&G Idaho, Inc, letter, N. C. Kaufman to R. E. Tiller, Subject: Transmittal of Change 1 to NUREG/CR-0247 (Kau-243-80) (October 21, 1980).

J-12. M. M. Giles, "Updated TRAC-BWR Completion Report: Generalized Leak Path and Separator Component Models," EG&G Idaho report SAAMD-83-029 (November 1983).

J-13. W. L. Weaver, "TRAC-BWR Completion report: Implicit Separator/Dryer Model," EG&G Idaho report SE-RST-85-007 (August 1985).

J-14. "TRAC-BD1 Manual: Extensions to TRAC-BD1/MOD1 (Draft)," Idaho National Engineering Laboratory report EGG-2417 (NUREG/CR-4391) (August 1985).

J-15. Y. K. Cheung, V. Parameswaran, and J. C. Shaug, “BWR Refill-Reflood Program, Task 4.7 – Model Development, TRAC-BWR Component Models,” General Electric Company report (NUREG / CR-2574) (April 1983).

J-16. Kenneth Salisbury, *Steam Turbines and Their Cycles* (Robert E. Krieger Publishing Company, Huntington, New York, 1974).

J-17. R. F. Farman and C. G. Motloch, “RETRAN Turbine and Condensing Heat Transfer Models,” in “Proceedings of the First International RETRAN Conference” (Seattle, Washington, September 22-24, 1980), Electric Power Research Institute report EPRI WS-80-150.

J-18. “Flow of Fluids,” Crane Company Technical Paper 409 (May 1942).

APPENDIX K

ADDITIONAL MASS-FIELD CLOSURE

TRAC includes additional modeling capability to track a noncondensable gas in the gas field and a solute in the liquid field. We have incorporated the additional fields fairly simply by assuming that in a given cell, the noncondensable gas moves in a homogeneous mixture with the water vapor and that the solute is homogeneously mixed with the liquid. The advantage of these assumptions is that we need add only two additional mass-conservation equations: one for the noncondensable gas [Eq. (2-15)] and one for the liquid solute [Eq. (2-17)]. The addition of these two fields requires supplemental relationships to provide the necessary constraints and coupling to the rest of the fluid field equations. These relationships are described in Appendix K, Sections K.1. and K.2. The following nomenclature applies to Appendix K.

NOMENCLATURE

A:	flow area
c_p:	specific heat at constant pressure
c_v:	specific heat at constant volume
e:	internal energy
H_{a1} —H_{a3}:	coefficients of polynomial fit for air viscosity
H_{b1} —H_{b3}:	coefficients of polynomial fit for air viscosity
H_{c1} —H_{c3}:	coefficients of polynomial fit for hydrogen viscosity
H_{d1} —H_{d3}:	coefficients of polynomial fit for helium viscosity
k:	thermal conductivity
k_0:	curve fit constant for thermal conductivity
m:	solute concentration
m_{solute}:	solute mass
M:	molecular weight
n:	curve fit exponent for thermal conductivity
P:	pressure
R:	universal gas constant
T:	temperature
V:	velocity
α:	void fraction
Δt:	time-step size
μ:	dynamic viscosity
ρ:	density

Subscripts

a:	refers to noncondensable gas in general
air:	air
g:	gas
helium:	helium
hydrogen:	hydrogen
l:	refer to liquid

K.1. Noncondensable Gas

The inclusion of the noncondensable gas is more complex than that of the liquid solute because of the significant interactions that the noncondensable can have on interfacial and wall condensation. We have assumed that the noncondensable gas is homogeneously mixed with the water vapor so that we need only a single momentum equation for the gas field. Similarly, we assume that the noncondensable gas is in thermal equilibrium with the water vapor so that we need only a single energy equation for the gas field.

We have previously discussed noncondensable-gas effects in Appendices F, G, H, and I as they affect interfacial heat and mass transfer, wall heat transfer, and critical flow. This current discussion describes the correlations required to provide the necessary thermal and transport properties.

Note that TRAC also has an input option controlled by variable IEOS that can turn off phase change. In this case the noncondensable-mass equation is not used, but the user still selects among the noncondensable properties described in this appendix. The IEOS option has not been maintained and its use currently is not recommended.

K.1.1. Code Models

The code treats the noncondensable gas as an ideal gas, and the user can select the gas to be either air, hydrogen, or helium.[1] The current structure of the code permits only a single-species noncondensable gas throughout the complete code calculation. Other than the input option of air, hydrogen, or helium, the code does not permit the user to change the noncondensable gas through input to nitrogen, for example, to model the normal gas blanket in the accumulators of a PWR (for this case, the option to use air is a good approximation for nitrogen).

Equations (2-14) through (2-16) express the mixture relations necessary to describe the noncondensable-gas/water-vapor mixture density, internal energy, and pressure. From thermodynamics, we can define the noncondensable internal energy e_a in terms of the

1. More accurate properties also are available for helium. These optional properties for helium are not discussed here; see Ref. K-12. for complete details. Currently, these properties are only available for light water models (H_2O).

specific heat at constant volume c_v and the gas temperature T_g. The code describes the noncondensable viscosity μ_a with second-order polynomial fits to air, hydrogen, and helium data. The viscosity and specific heat are not strong functions of pressure (Ref. K-1.), and the correlations used for these two quantities do not include a pressure dependence.

The code calculates the thermodynamic and transport properties with the following correlations:

Internal Energy (Ref. K-2., pp. 21-22, Eqs. 1.29-1.32, for air and hydrogen; Ref. K-3., p. 247, for helium)

$$e_a = c_{va} T_g \tag{K-1}$$

and

$$c_{va} = c_{pa} - \frac{R}{M_a} \quad , \tag{K-2}$$

where c_{pa} is the specific heat at constant pressure, R is the universal gas constant, and M_a is the mass of one mole (molecular weight with units of kg) of the noncondensable gas. These two equations yield the following relations:

$$\left.\frac{\partial e_a}{\partial T_g}\right|_{P_a} = c_{va} \tag{K-3}$$

and

$$\left.\frac{\partial e_a}{\partial P_a}\right|_{T_g} = 0.0 \quad . \tag{K-4}$$

Density (Ref. K-1.)

$$\rho_a = \frac{P_a}{R_a T_g} \quad , \tag{K-5}$$

$$\left.\frac{\partial \rho_a}{\partial P_a}\right|_{T_g} = \frac{1}{R_a T_g} \quad , \tag{K-6}$$

and

$$\left.\frac{\partial \rho_a}{\partial T_g}\right|_P = -R_a \rho_a \left.\frac{\partial \rho_a}{\partial P_a}\right|_{T_g} , \tag{K-7}$$

where ρ_a is the noncondensable microscopic density, P_a is the noncondensable partial pressure, and R_a is the noncondensable-gas constant defined as R/M_a.

Viscosity

Air (Ref. K-1.)

For $T_g \leq 502.15$K,

$$\mu_a = H_{a1} + H_{a2}(T_g - 273.15) + H_{a3}(T_g - 273.15)^2 ; \tag{K-8}$$

For $T_g > 502.15$K,

$$\mu_a = H_{b1} + H_{b2}(T_g - 273.15) + H_{b3}(T_g - 273.15)^2 ; \tag{K-9}$$

Hydrogen (Ref. K-1.)

$$\mu_a = H_{c1} + H_{c2} T_g + H_{c3} T_g^{\,2} ; \tag{K-10}$$

Helium (Ref. K-4.)

$$\mu_a = H_{d1} + H_{d2} T_g + H_{d3} T_g^2 ; \tag{K-11}$$

where the Hs are polynomial coefficients to be defined later.

Thermal Conductivity

$$k_a = k_0 T_g^n \quad . \tag{K-12}$$

We use the subroutines THERMO and FPROP for thermodynamic and transport property calculations. SETEOS sets constants used in THERMO. IPROP calls THERMO and FPROP.

K.1.2. Range of Data Over Which Correlations Were Developed and Tested

We use the ideal-gas law for air, hydrogen, and helium density correlations. Because the ideal-gas law accurately predicts gas behavior for low pressure and high temperature, and TRAC usually deals with this range of pressures and temperatures, we consider the ideal-gas correlation to provide an adequate approximation for the gas densities.

Although the specific heat at constant pressure c_p is temperature dependent, we use a constant value for it. This assumption introduces errors that were deemed to be inconsequential to most transients of interest in PWRs. The thermal conductivity k is a strong function of temperature and a weak function of pressure. Consequently, it is computed using an exponential approximation with respect to temperature only. This assumption should introduce inconsequential errors to most transients of interest in PWRs.

The range of data over which the viscosity correlation was probably developed for air and hydrogen was 273.15 K ≤ T ≤ 1073.15 K (Ref. K-3.). TRAC will use this correlation, however, for 273.15 K ≤ T_g ≤ 3000 K and 1.0 Pa ≤ P ≤ 45.0 MPa. The reference cited has no data for air or hydrogen viscosities with temperatures greater than 1073.15 K. However, Holman (Ref. K-1.) has viscosity of air to 2773.15 K and of hydrogen to 1173.15 K; we used these data in the assessment of the correlation. The range of data over which the helium viscosity correlation was developed is 255 K ≤ T_g ≤ 800 K. TRAC uses this correlation for 273.15 K ≤ T_g ≤ 3000 K and 1.0 Pa ≤ P ≤ 45.0 MPa. The reference cited has no data for helium viscosities at temperatures greater than 800 K.

K.1.3. Constants

We have defined in TRAC the following constants for use in Eqs. (K-1) through (K-12):

$$
\begin{aligned}
M_{\text{air}} &= 28.96461\ \text{kg}\cdot\text{mole}^{-1};\\
M_{\text{hydrogen}} &= 2.01594\ \text{kg}\cdot\text{mole}^{-1};\\
M_{\text{helium}} &= 4.00260\ \text{kg}\cdot\text{mole}^{-1};\\
c_{\text{p,air}} &= 1004.832\ \text{J}\cdot(\text{kg}\cdot\text{K})^{-1};\\
c_{p,\text{hydrogen}} &= 14533.2\ \text{J}\cdot(\text{kg}\cdot\text{K})^{-1};\\
c_{p,\text{helium}} &= 5234.0\ \text{J}\cdot(\text{kg}\cdot\text{K})^{-1};\\
H_{a1} &= 1.707623\times10^{-5}\ \text{N}\cdot\text{s}\cdot\text{m}^{-2};\\
H_{a2} &= 5.927\times10^{-8}\ \text{N}\cdot\text{s}\cdot(\text{m}^{2}\cdot\text{K})^{-1};\\
H_{a3} &= -8.14\times10^{-11}\ \text{N}\cdot\text{s}\cdot(\text{m}^{-2}\cdot\text{K}^{-2});\\
H_{b1} &= 1.735\times10^{-5}\ \text{N}\cdot\text{s}\cdot\text{m}^{-2};\\
H_{b2} &= 4.193\times10^{-8}\ \text{N}\cdot\text{s}\cdot(\text{m}^{2}\cdot\text{K})^{-1};\\
H_{b3} &= -1.09\times10^{-11}\ \text{N}\cdot\text{s}\cdot(\text{m}^{-2}\cdot\text{K}^{-2});\\
H_{c1} &= 4.175\times10^{-6}\ \text{N}\cdot\text{s}\cdot\text{m}^{-2};\\
H_{c2} &= 1.588\times10^{-8}\ \text{N}\cdot\text{s}\cdot(\text{m}^{2}\cdot\text{K})^{-1};\\
H_{c3} &= 7.6705\times10^{-13}\ \text{N}\cdot\text{s}\cdot(\text{m}^{-2}\cdot\text{K}^{-2});\\
H_{d1} &= 5.9642\times10^{-6}\ \text{N}\cdot\text{s}\cdot\text{m}^{-2};\\
H_{d2} &= 5.2047\times10^{-8}\ \text{N}\cdot\text{s}\cdot(\text{m}^{2}\cdot\text{K})^{-1};\\
H_{d3} &= -1.5345\times10^{-11}\ \text{N}\cdot\text{s}\cdot(\text{m}^{-2}\cdot\text{K}^{-2});
\end{aligned}
$$

$k_{0,\text{air}} = 2.0910 \times 10^{-4}$ W·(m·K^{n+1})$^{-1}$;

$k_{0,\text{hydrogen}} = 1.6355 \times 10^{-3}$ W·(m·K^{n+1})$^{-1}$;

$k_{0,\text{helium}} = 3.366 \times 10^{-3}$ W·(m·K^{n+1})$^{-1}$;

$n_{\text{air}} = 0.8460$;

$n_{\text{hydrogen}} = 0.8213$;

$n_{\text{helium}} = 0.6680$; and

$R = 6.022169 \times 10^{26} \times 1.380622 \times 10^{-23}$ J·(mole·K)$^{-1}$

$= 8314.339$ J·(mole·K)$^{-1}$.

The code specifies the thermodynamic parameters in the above list in subroutine SETEOS. Function VISCV sets the coefficients for the dynamic viscosity μ_a, as well as for the temperature switch in the expression for air.

K.1.4. Assessment of the Correlation as Applied in TRAC

The equations used for calculating the viscosity of air and hydrogen were obtained by fitting a quadratic polynomial to data from Ref. K-3. with a least-squares method. The error associated with these fits is no greater than 3.34% for air with 502.15 K < $T_g \le$ 1073.15 K, 2.91% for air with 273.15 K $\le T_g \le$ 502.15 K, and 5.23% for hydrogen. Reference K-3. gives values for viscosity only for temperatures up to 1073.15 K, but TRAC uses the polynomial fit for temperatures up to 2973.15 K. Tables K-1. and K-2. compare the results of Eqs. (K-8) and (K-9) with the data in Ref. K-1. The value for viscosity that TRAC calculates is over 25% low for air at 2500.00 K (as compared to data from Ref. K-1.; see Table K-2.). One should keep in mind that other things will happen in the code before the temperature gets this high, so that FPROP will probably never have to calculate viscosity with such a high temperature. Data for the viscosity of hydrogen at values greater than 1073.15 K were not available. The error associated with the viscosity of helium over the range 273.15 K $\le T_g \le$ 1090.15 K is no greater than 5.6%. Data for this assessment were taken from Ref. K-4. Viscosity data for helium at temperatures greater than 1090.15 K were not available.

Figures K-1. through K-10. compare the specific heat at constant volume from TRAC with data at various temperatures and pressures for both air and hydrogen. The data are from Ref. K-4.; we have converted them to specific heat at constant volume through the use of Eq. (K-2). The figures clearly show that the assumed constant specific heat is valid only at low pressures and temperatures; as the temperature or pressure or both increase, the errors associated with the assumption become quite large. Even Eq. (K-2) breaks down as the gas deviates from an ideal gas. We could improve the accuracy of the calculations with a noncondensable gas by representing the specific heats as functions of pressure and temperature. Figures K-11. through K-15. compare the TRAC specific heat at constant volume for helium ($c_{v\text{helium}}$) with data from Ref. K-5. This reference contains no data for helium for temperatures greater than 590 K. The TRAC values for $c_{v\text{helium}}$ vary from the data by approximately 1.2%.

TABLE K-1.
Viscosity Polynomial Assessment for Air
T ≤ 502.15 K

Temperature (K)	Viscosity (Ref. K-1.) ($N \cdot s \cdot m^{-2}$)	Viscosity(TRAC) ($N \cdot s \cdot m^{-2}$)	% Error
273.15	1.70900*E*–05	1.70762*E*–05	–0.0805734
283.15	1.75900*E*–05	1.76608*E*–05	+0.402445
293.15	1.80800*E*–05	1.82291*E*–05	+0.824502
303.15	1.85600*E*–05	1.87811*E*–05	+1.19111
313.15	1.90400*E*–05	1.93168*E*–05	+1.45373
323.15	1.95100*E*–05	1.98362*E*–05	+1.67212
333.15	1.99700*E*–05	2.03394*E*–05	+1.84972
343.15	2.04300*E*–05	2.08263*E*–05	+1.93965
353.15	2.08800*E*–05	2.12969*E*–05	+1.99650
363.15	2.13200*E*–05	2.17512*E*–05	+2.02247
373.15	2.17500*E*–05	2.21892*E*–05	+2.01945
383.15	2.21800*E*–05	2.26110*E*–05	+1.94315
393.15	2.26000*E*–05	2.30165*E*–05	+1.84279
403.15	2.30200*E*–05	2.34057*E*–05	+1.67537
413.15	2.34400*E*–05	2.37786*E*–05	+1.44450
423.15	2.38500*E*–05	2.41352*E*–05	+1.19593
433.15	2.46500*E*–05	2.44756*E*–05	–0.707546
443.15	2.50500*E*–05	2.47997*E*–05	–0.999321
453.15	2.54400*E*–05	2.51075*E*–05	–1.30711
463.15	2.58200*E*–05	2.53990*E*–05	–1.63056
473.15	2.62000*E*–05	2.56742*E*–05	–2.00676
483.15	2.65800*E*–05	2.59332*E*–05	–2.43345
493.15	2.69600*E*–05	2.61759*E*–05	–2.90849

TABLE K-2.
Viscosity Polynomial Assessment for Air
T > 502.15 K

Temperature (K)	Viscosity (Ref. K-1.) ($N \cdot s \cdot m^{-2}$)	Viscosity(TRAC) ($N \cdot s \cdot m^{-2}$)	% Error
503.15	2.73300*E*–05	2.64173*E*–05	–3.33959
513.15	2.77000*E*–05	2.67854*E*–05	–3.30195
550.00	2.84800*E*–05	2.81229*E*–05	–1.25393
600.00	3.01800*E*–05	2.98904*E*–05	–0.959697
650.00	3.17700*E*–05	3.16033*E*–05	–0.524561
700.00	3.33200*E*–05	3.32618*E*–05	–0.174578
750.00	3.48100*E*–05	3.48658*E*–05	+0.160339
800.00	3.62500*E*–05	3.64153*E*–05	+0.455993
850.00	3.76500*E*–05	3.79103*E*–05	+0.691317
900.00	3.89900*E*–05	3.93508*E*–05	+0.925274
950.00	4.02300*E*–05	4.07367*E*–05	+1.25963
1000.00	4.15200*E*–05	4.20682*E*–05	+1.32040
1100.00	4.44000*E*–05	4.45677*E*–05	+0.377699
1200.00	4.69000*E*–05	4.68492*E*–05	–0.108389
1300.00	4.93000*E*–05	4.89126*E*–05	–0.785735
1400.00	5. 17000*E*–05	5.07581*E*–05	–1.82186
1500.00	5.40000*E*–05	5.23856*E*–05	–2.98969
1600.00	5.63000*E*–05	5.37950*E*–05	–4.44932
1700.00	5.85000*E*–05	5.49865*E*–05	–6.00598
1800.00	6.07000*E*–05	5.59600*E*–05	–7.80895
1900.00	6.29000*E*–05	5.67154*E*–05	–9.83238
2000.00	6.50000*E*–05	5.72529*E*–05	–11.9186
2100.00	6.72000*E*–05	5.75724*E*–05	–14.3268
2200.00	6.93000*E*–05	5.76738*E*–05	–16.7766
2300.00	7.14000*E*–05	5.75573*E*–05	–19.3875
2400.00	7.35000*E*–05	5.72228*E*–05	–22.1459
2500.00	7.57000*E*–05	5.66702*E*–05	–25.1384

As mentioned before, the ideal-gas law, used for predicting air, hydrogen, and helium densities, approximates the densities for the gases well (generally less than 5% error for these gases) for high temperatures and low pressures. However, the limits inside THERMO and FPROP allow the pressures to get very high (1.0 Pa ≤ P ≤ 45.0 MPa), and errors may be as high as 20% for air, 26% for hydrogen, and 15% for helium (Figs. K-16. through K-30.) when the pressure reaches its upper limit and the temperature is low (data for these calculations are from Ref. K-6. for the density of air, from Ref. K-7. for the density of hydrogen, and from Ref. K-3. for the density of helium). Reference K-5. has no data for helium for temperatures greater than 590 K.

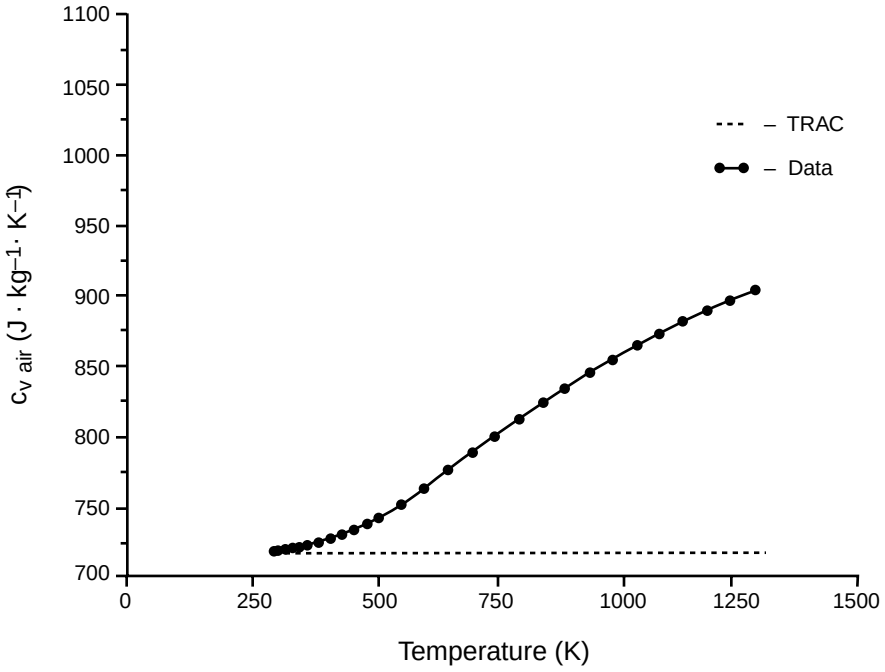

Fig. K-1. Specific heat vs. temperature for air at 100 kPa.

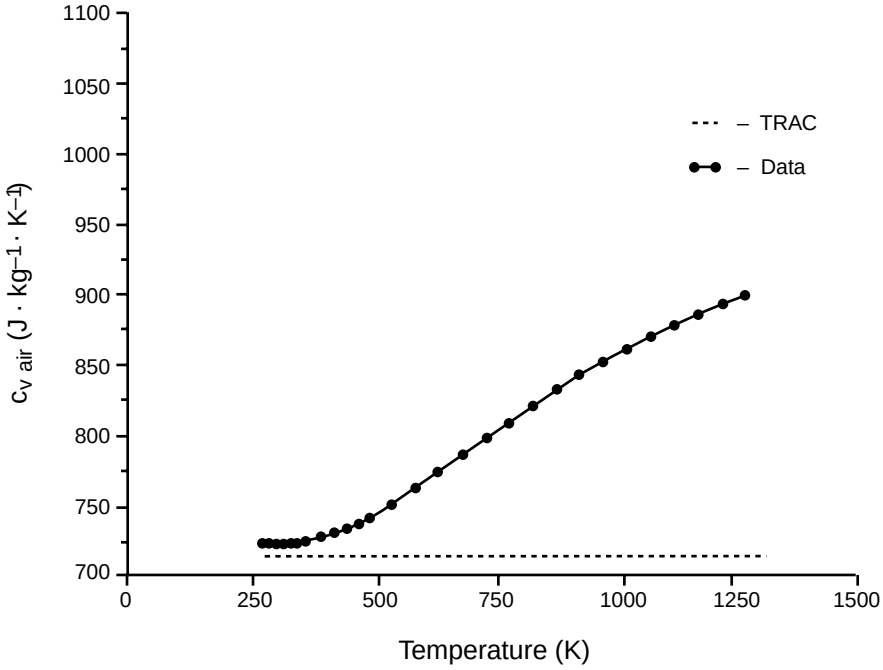

Fig. K-2. Specific heat vs. temperature for air at 400 kPa.

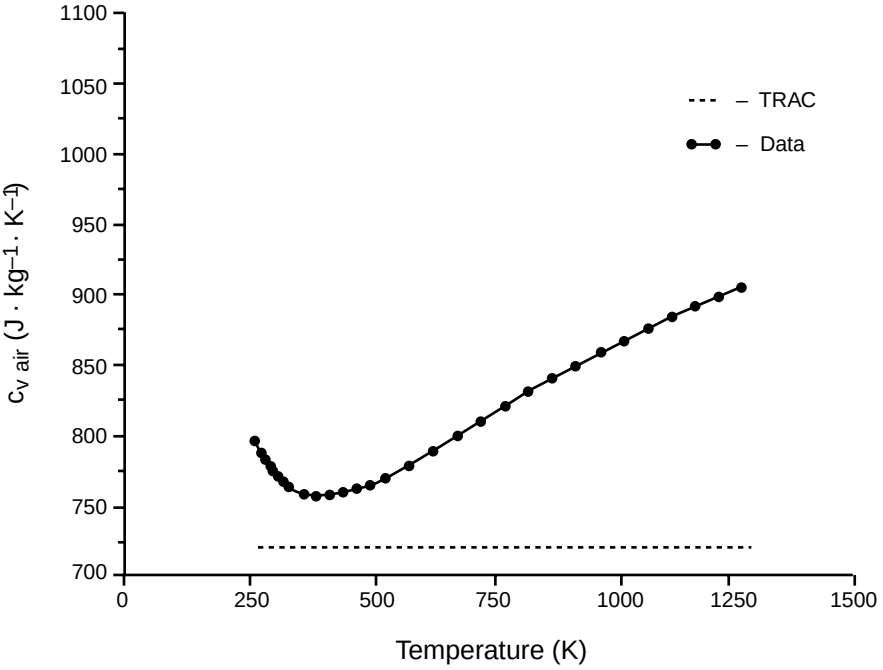

Fig. K-3. Specific heat vs. temperature for air at 4 MPa.

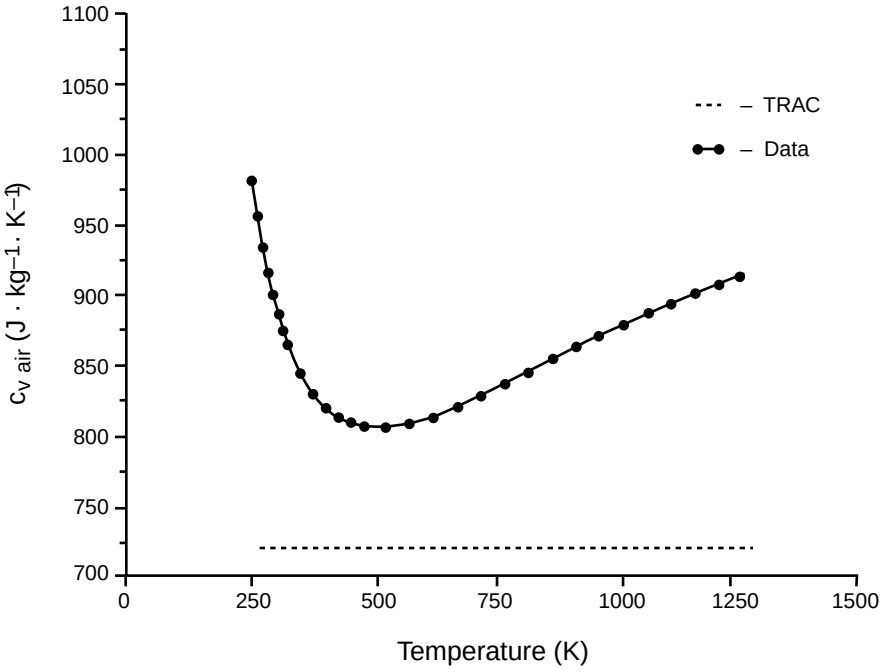

Fig. K-4. Specific heat vs. temperature for air at 15 MPa.

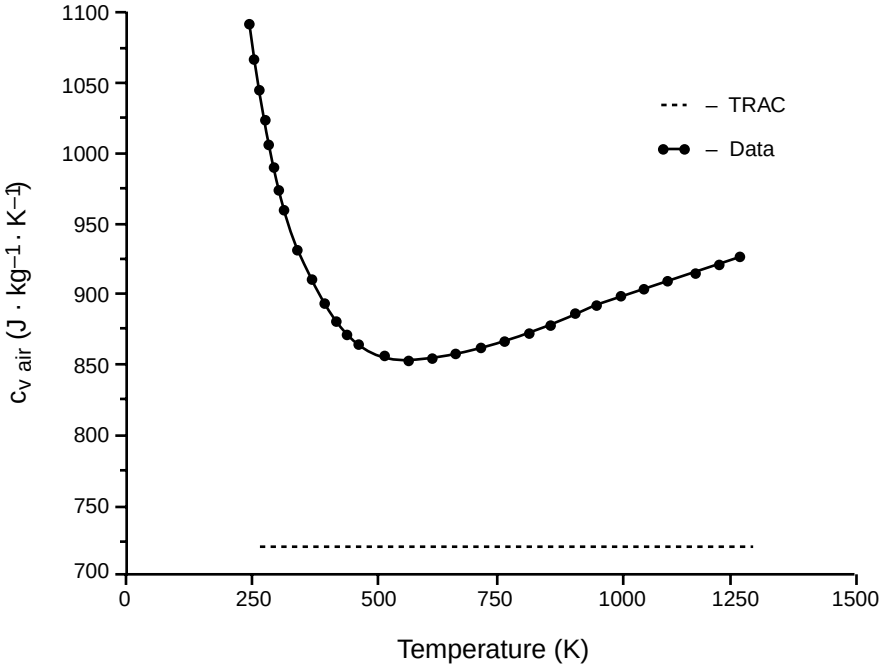

Fig. K-5. Specific heat vs. temperature for air at 40 MPa.

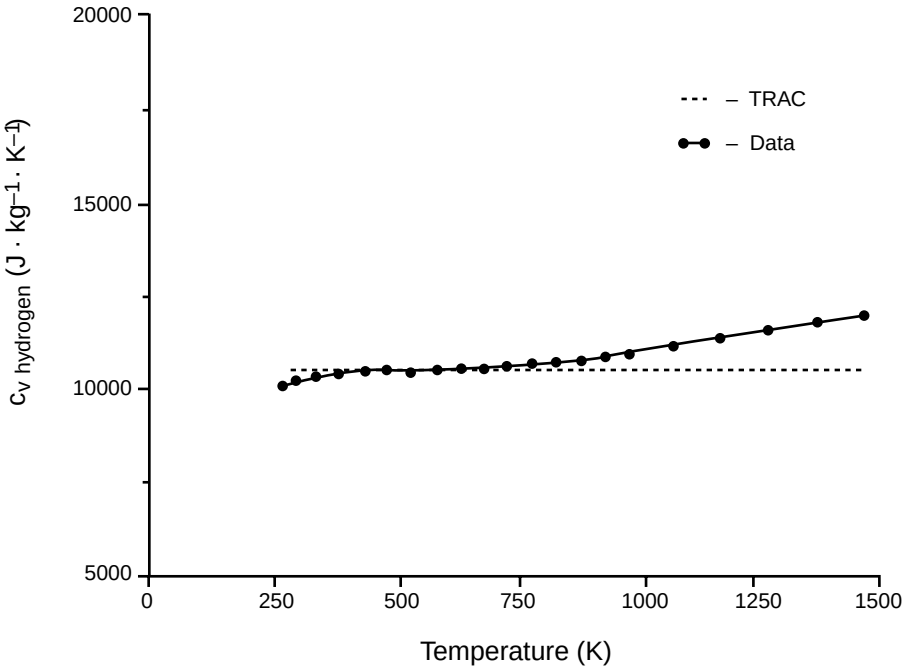

Fig. K-6. Specific heat vs. temperature for hydrogen at 100 kPa.

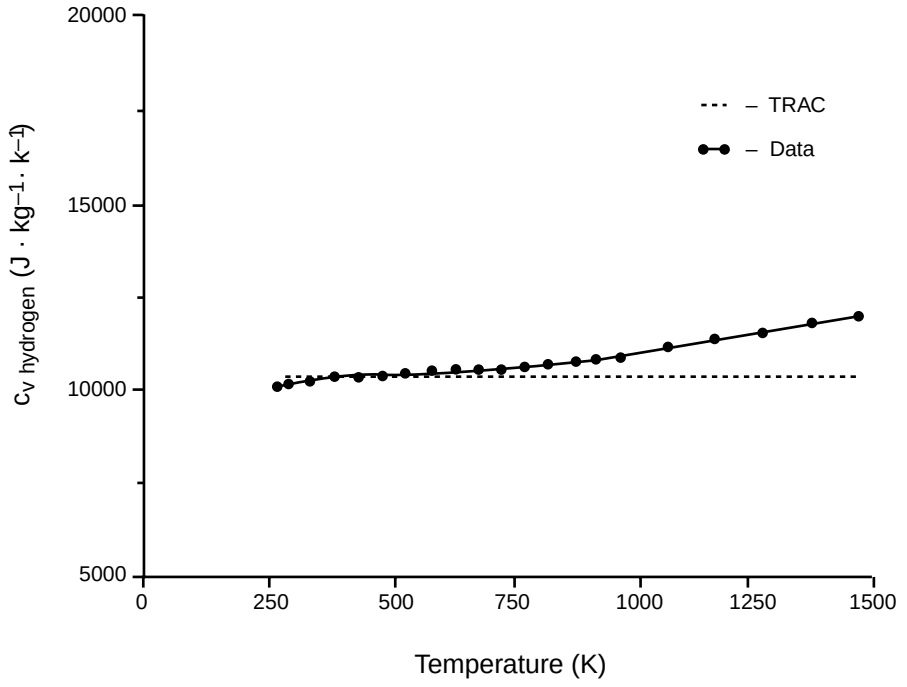

Fig. K-7. Specific heat vs. temperature for hydrogen at 400 kPa.

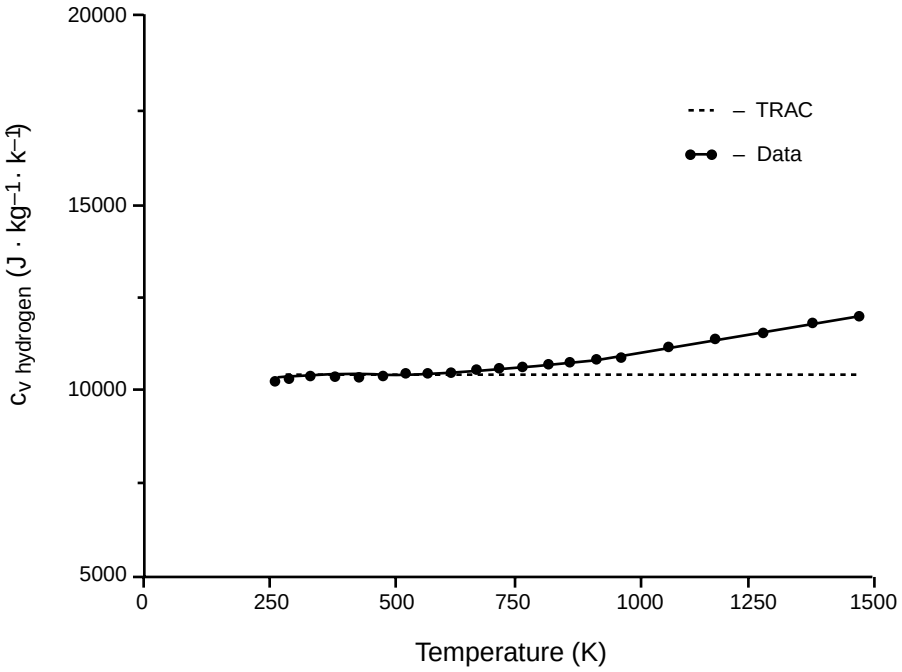

Fig. K-8. Specific heat vs. temperature for hydrogen at 4 MPa.

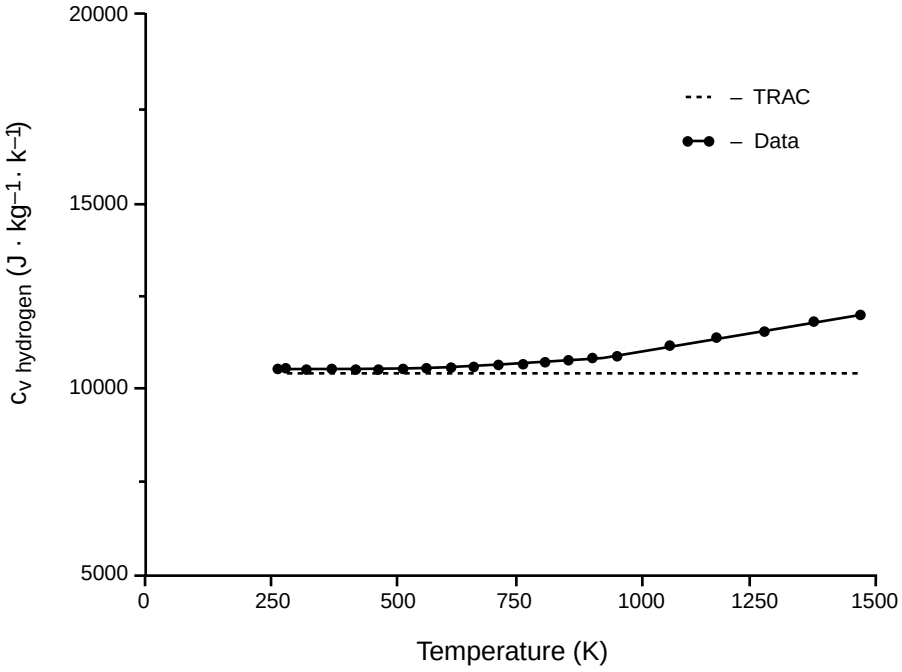

Fig. K-9. Specific heat vs. temperature for hydrogen at 15 MPa.

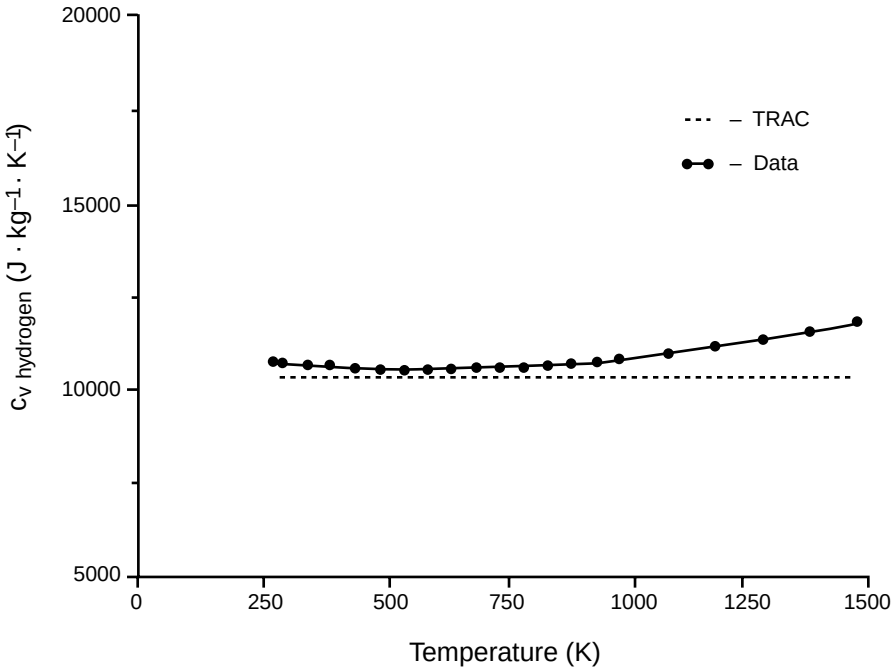

Fig. K-10. Specific heat vs. temperature for hydrogen at 40 MPa.

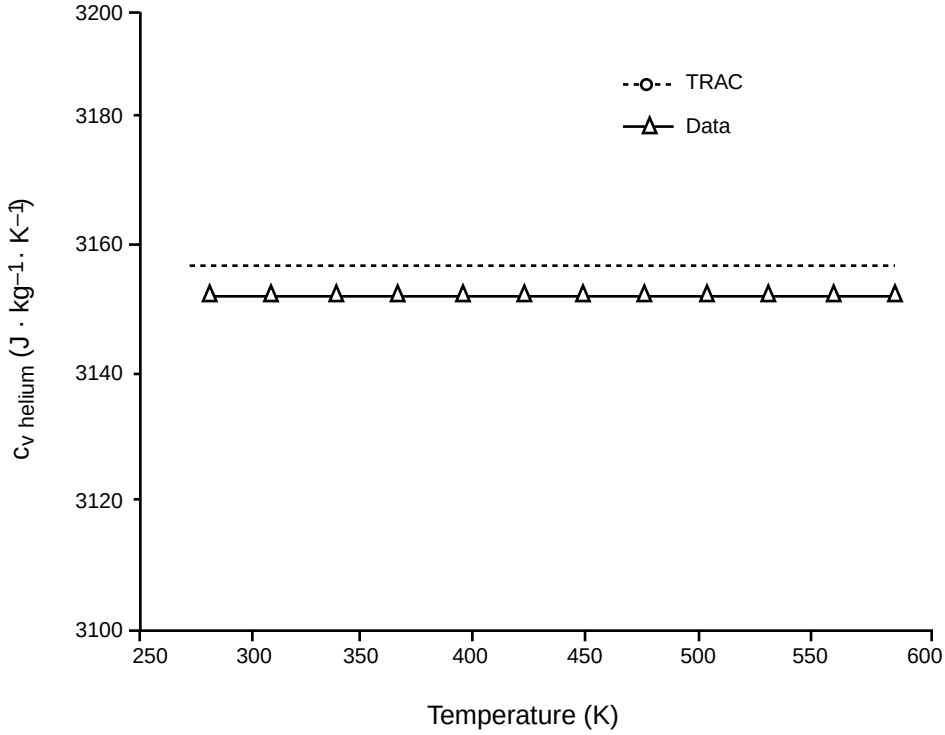

Fig. K-11. Specific heat vs. temperature for helium at 100 kPa.

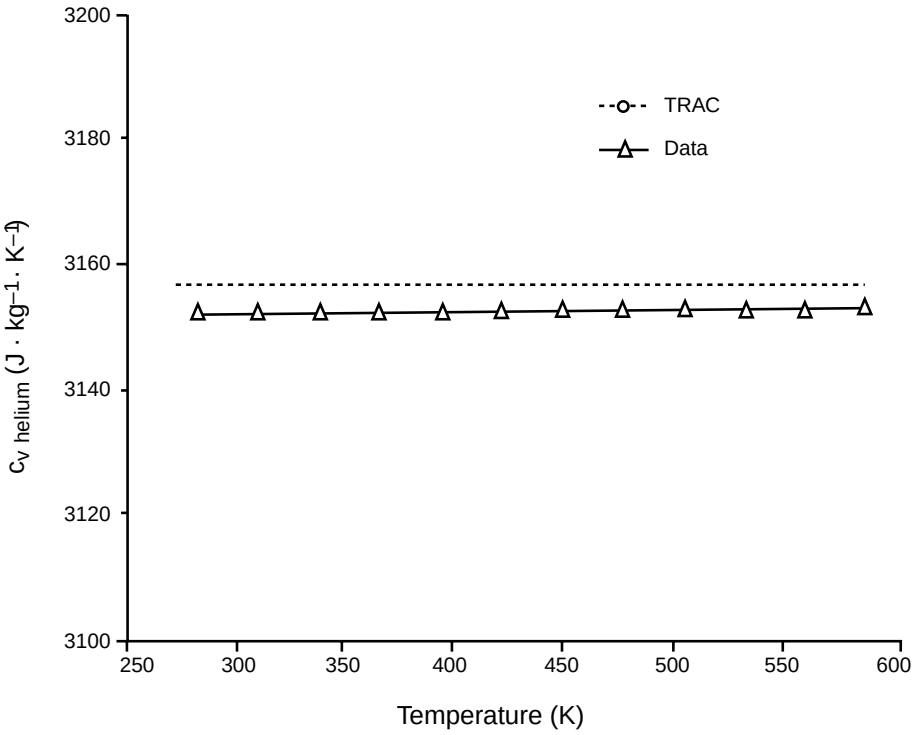

Fig. K-12. Specific heat vs. temperature for helium at 400 kPa.

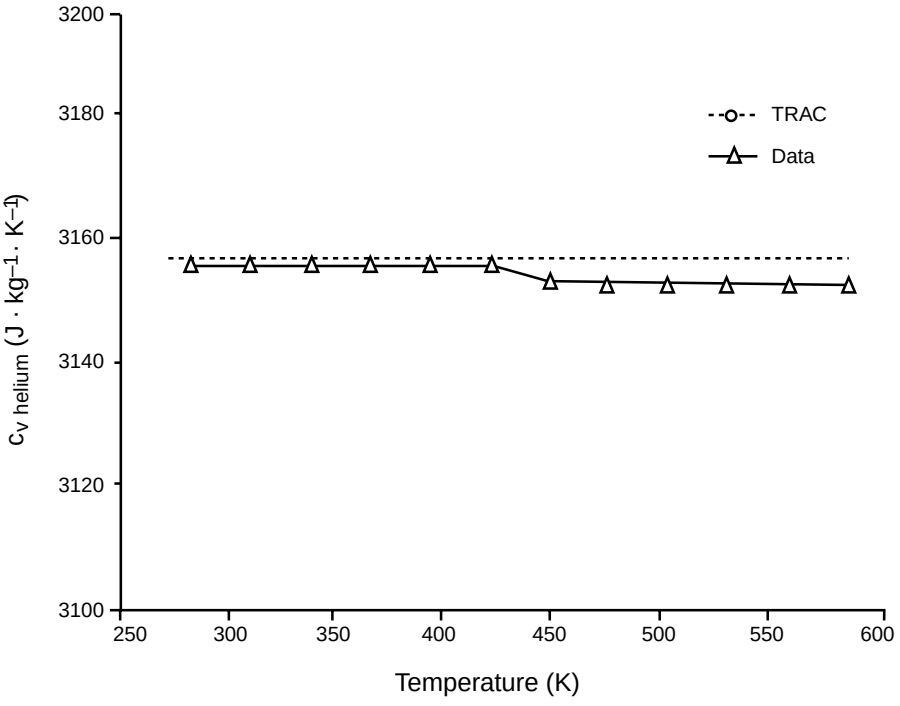

Fig. K-13. Specific heat vs. temperature for helium at 4 MPa.

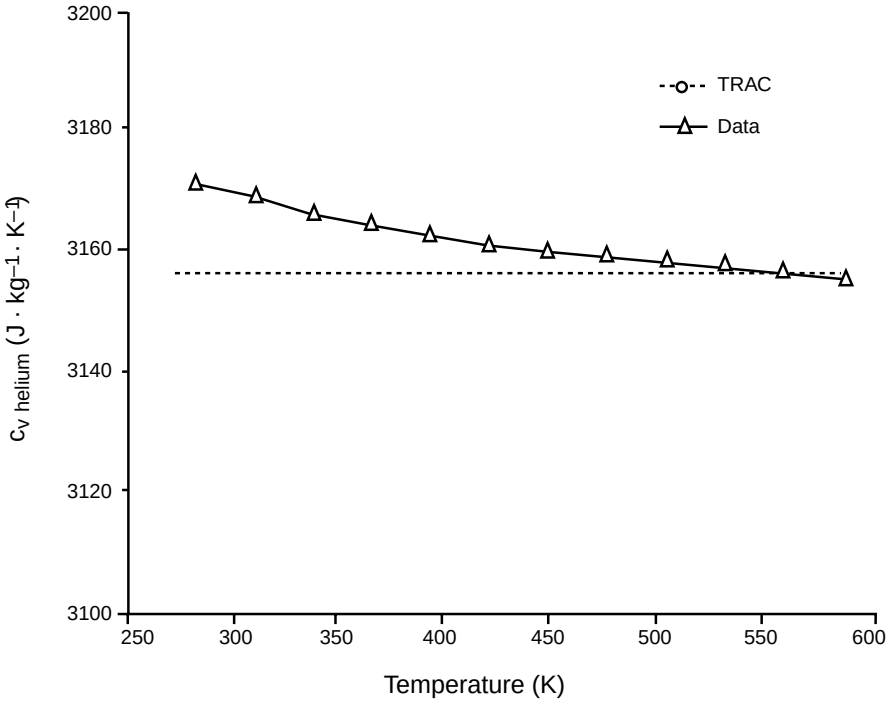

Fig. K-14. Specific heat vs. temperature for helium at 15 MPa.

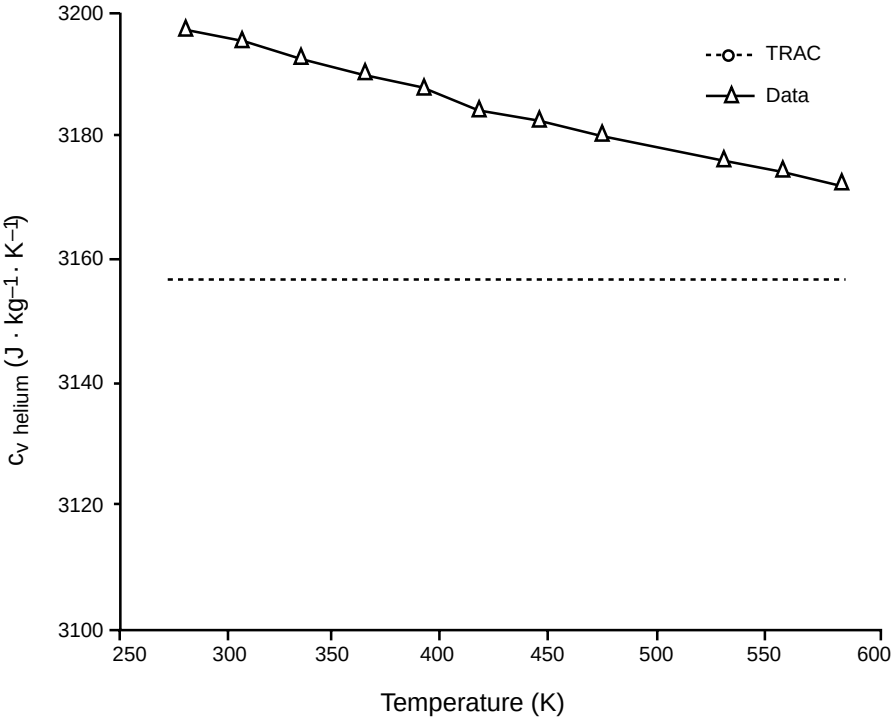

Fig. K-15. Specific heat vs. temperature for helium at 40 MPa.

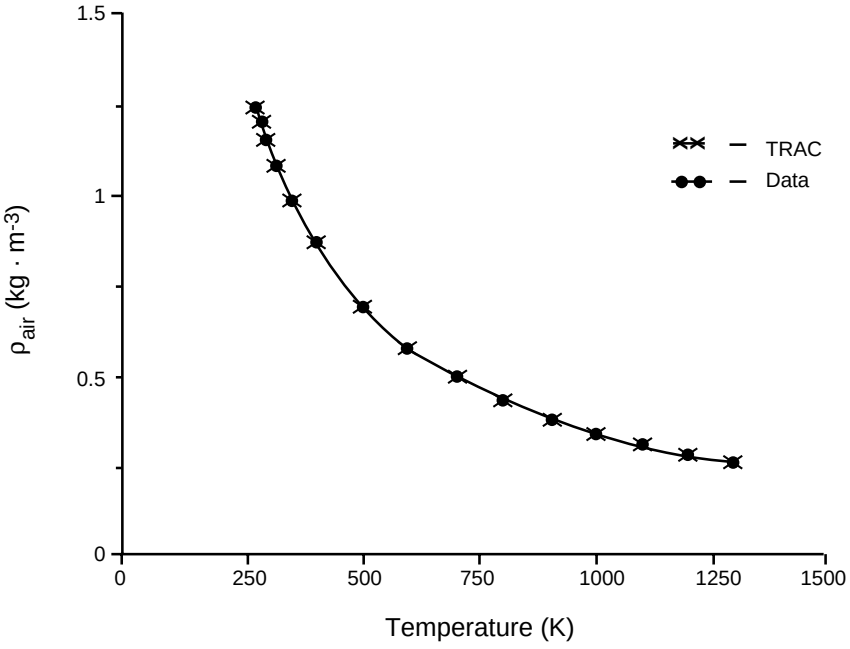

Fig. K-16. Density vs. temperature for air at 100 kPa.

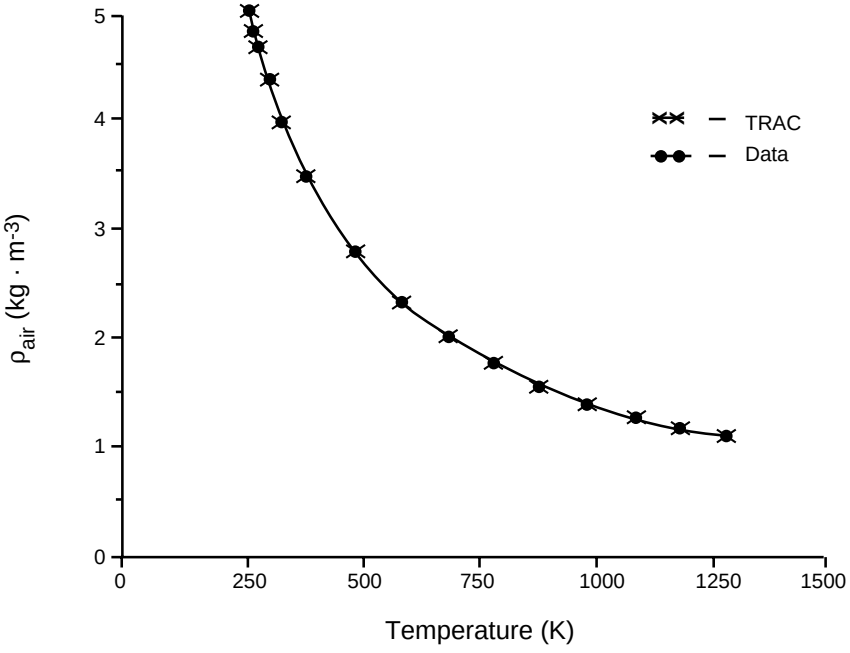

Fig. K-17. Density vs. temperature for air at 400 kPa.

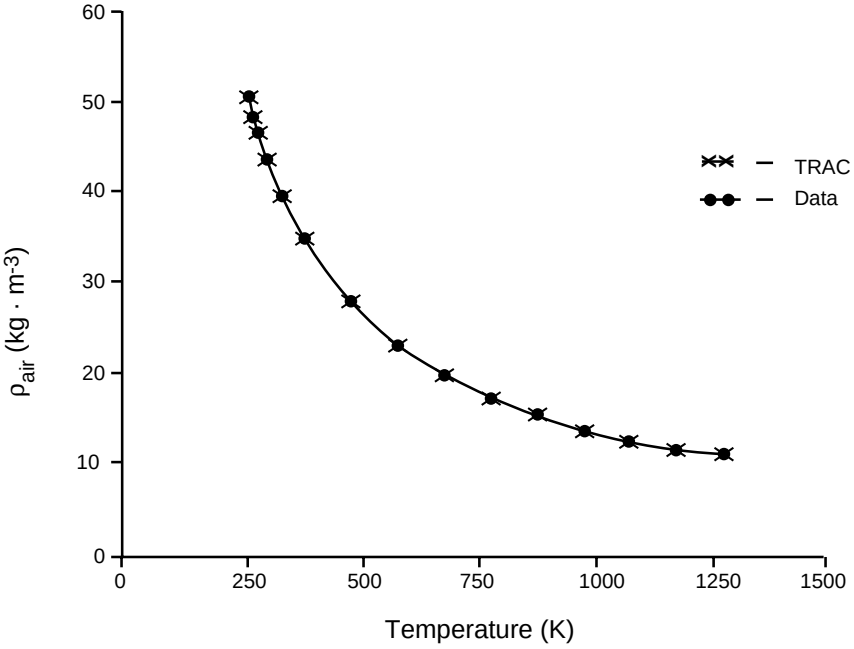

Fig. K-18. Density vs. temperature for air at 4 MPa.

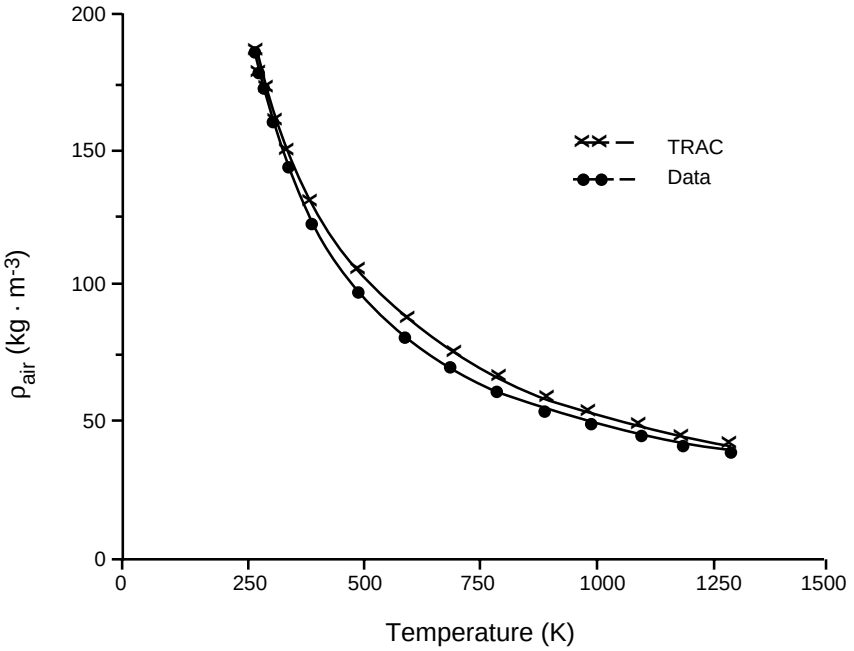

Fig. K-19. Density vs. temperature for air at 15 MPa.

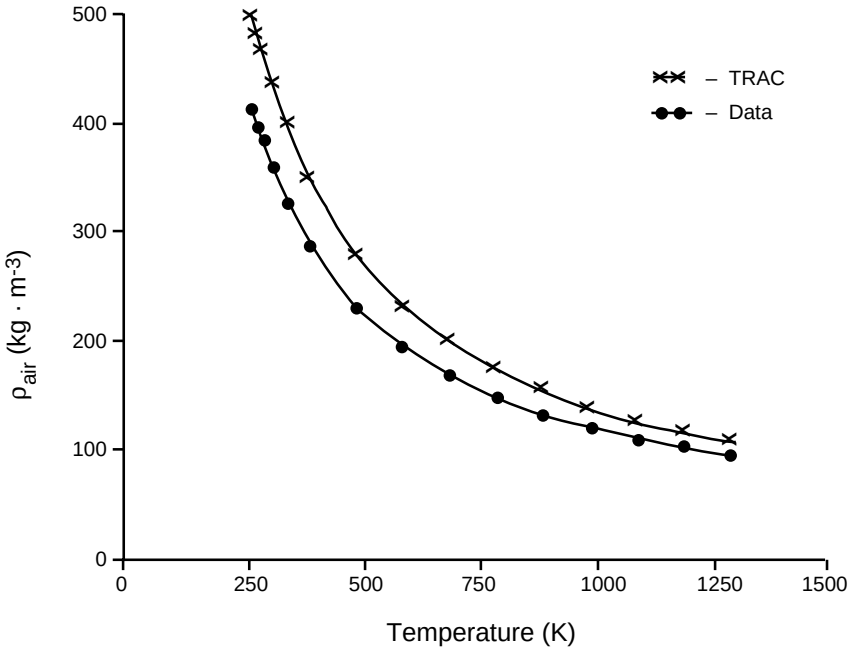

Fig. K-20. Density vs. temperature for air at 40 MPa.

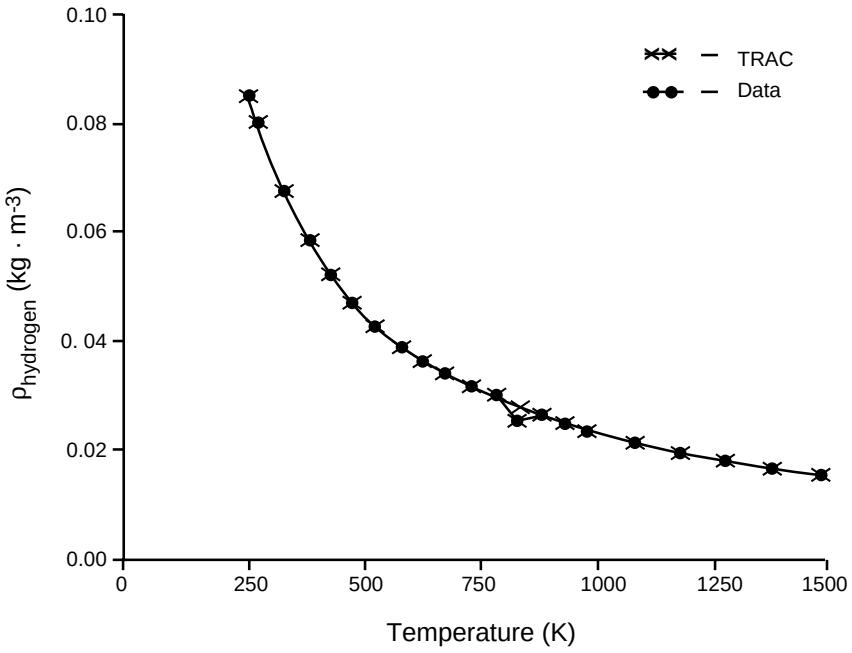

Fig. K-21. Density vs. temperature for hydrogen at 100 kPa.

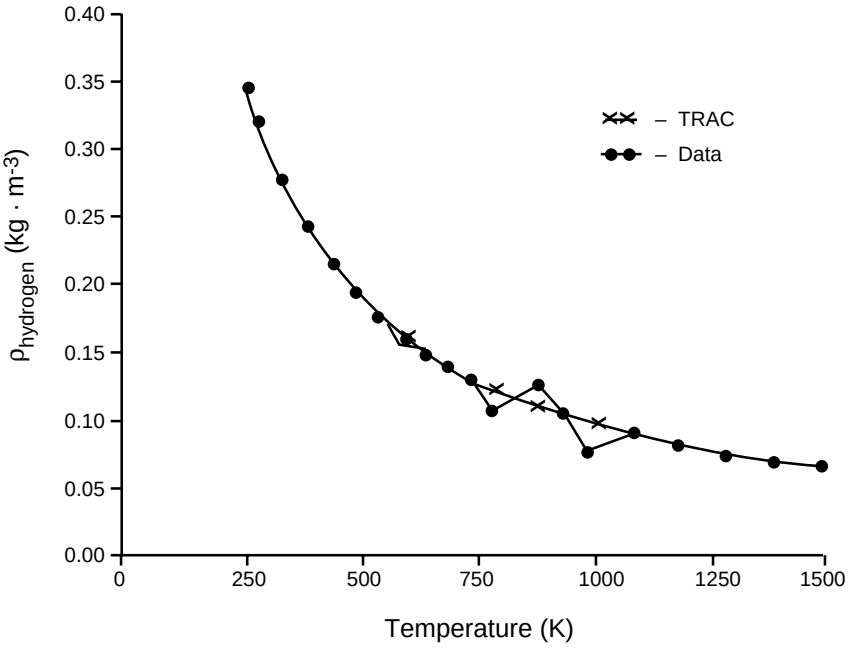

Fig. K-22. Density vs. temperature for hydrogen at 400 kPa.

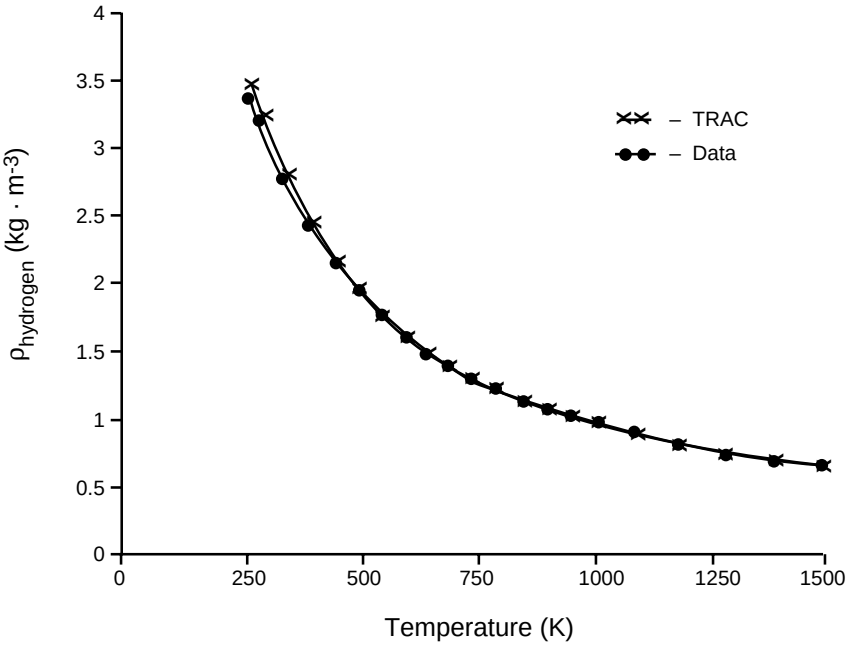

Fig. K-23. Density vs. temperature for hydrogen at 4 MPa.

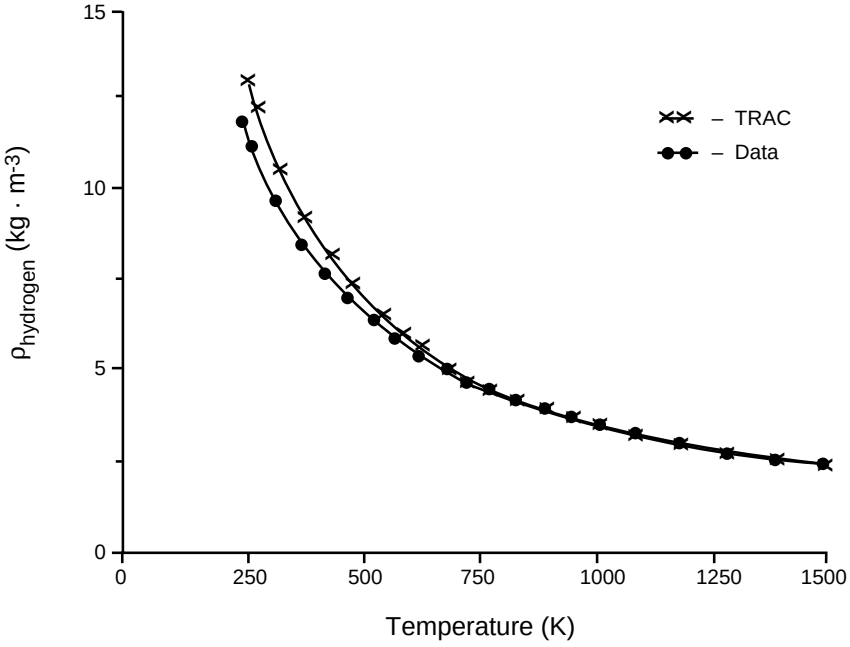

Fig. K-24. Density vs. temperature for hydrogen at 15 MPa.

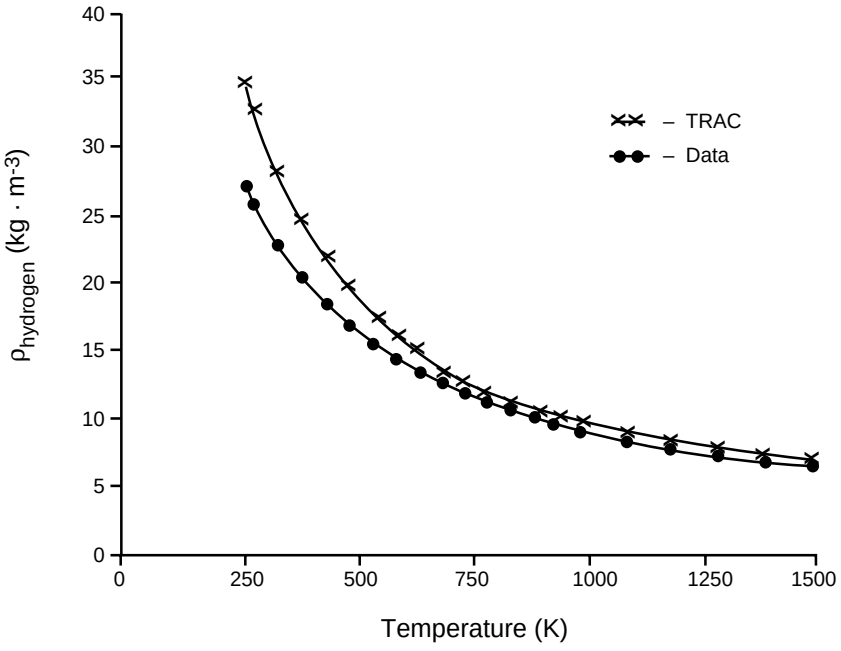

Fig. K-25. Density vs. temperature for hydrogen at 40 MPa.

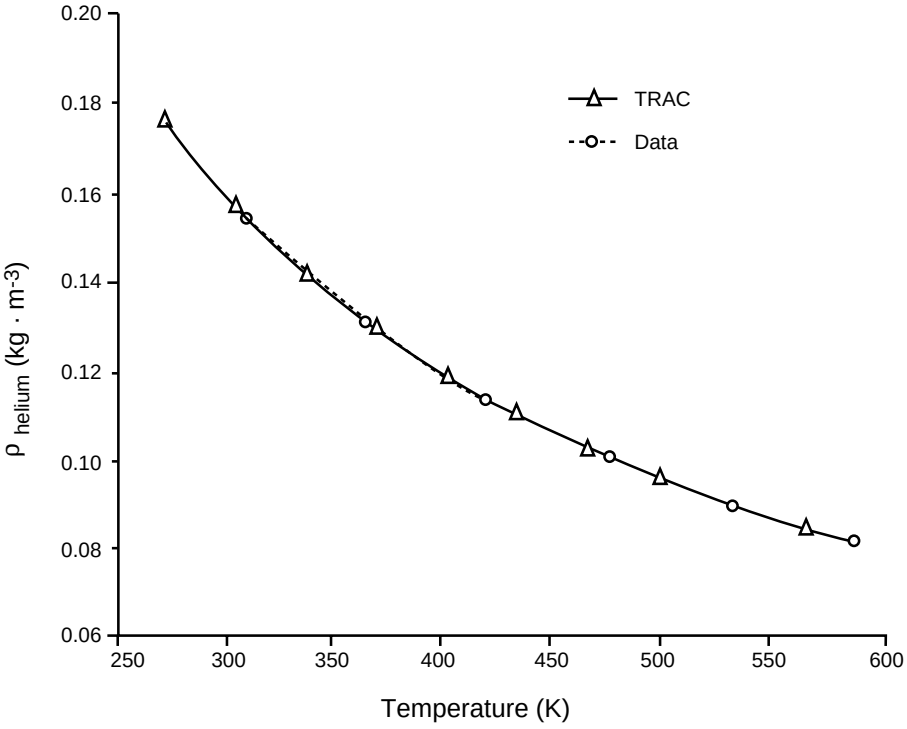

Fig. K-26. Density vs. temperature for helium at 100 kPa.

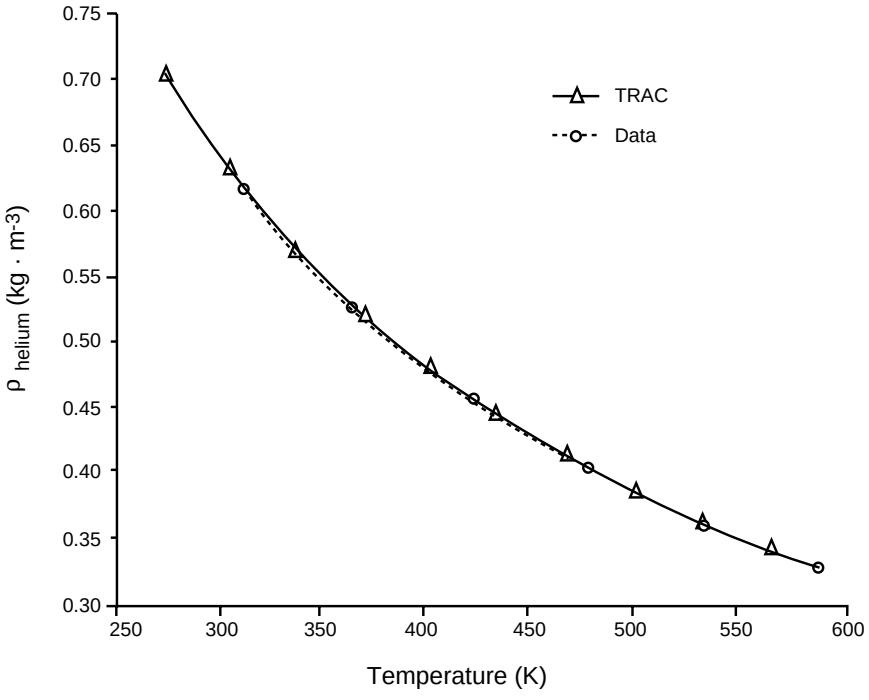

Fig. K-27. Density vs. temperature for helium at 400 kPa.

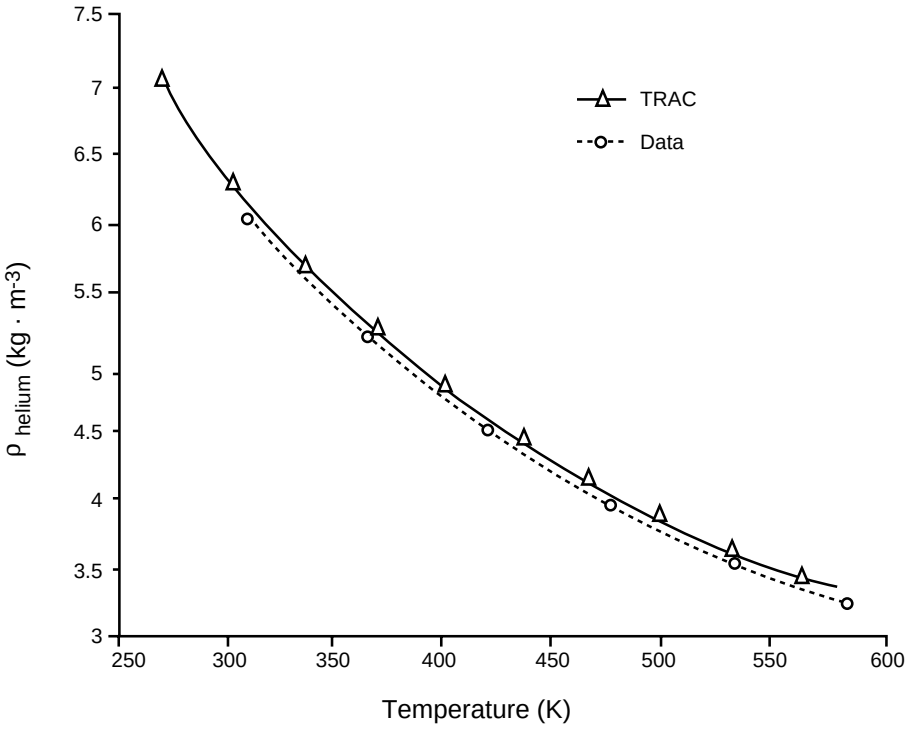

Fig. K-28. Density vs. temperature for helium at 4 MPa.

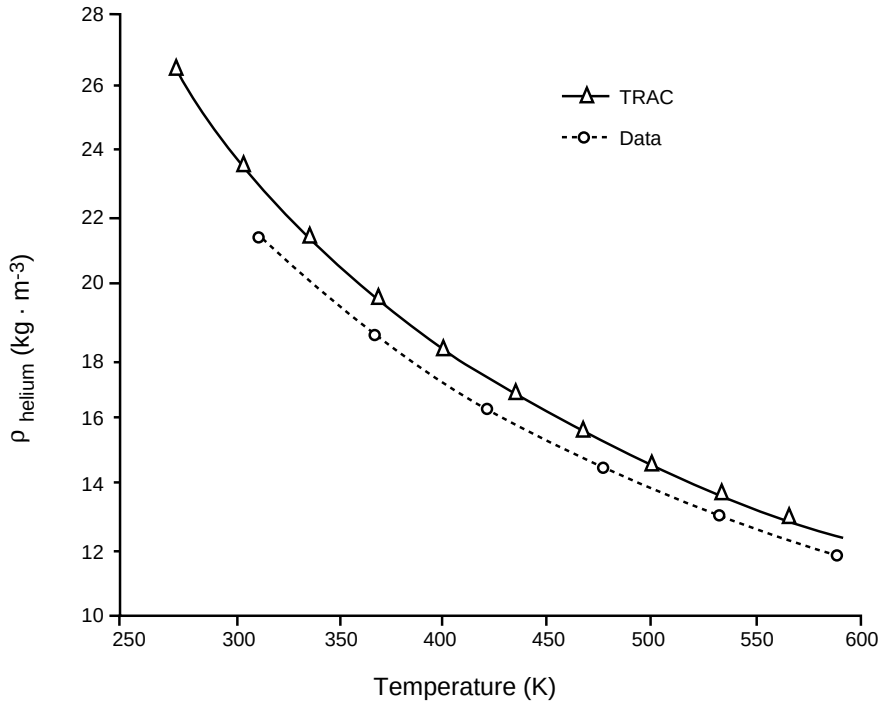

Fig. K-29. Density vs. temperature for helium at 15 Mpa.

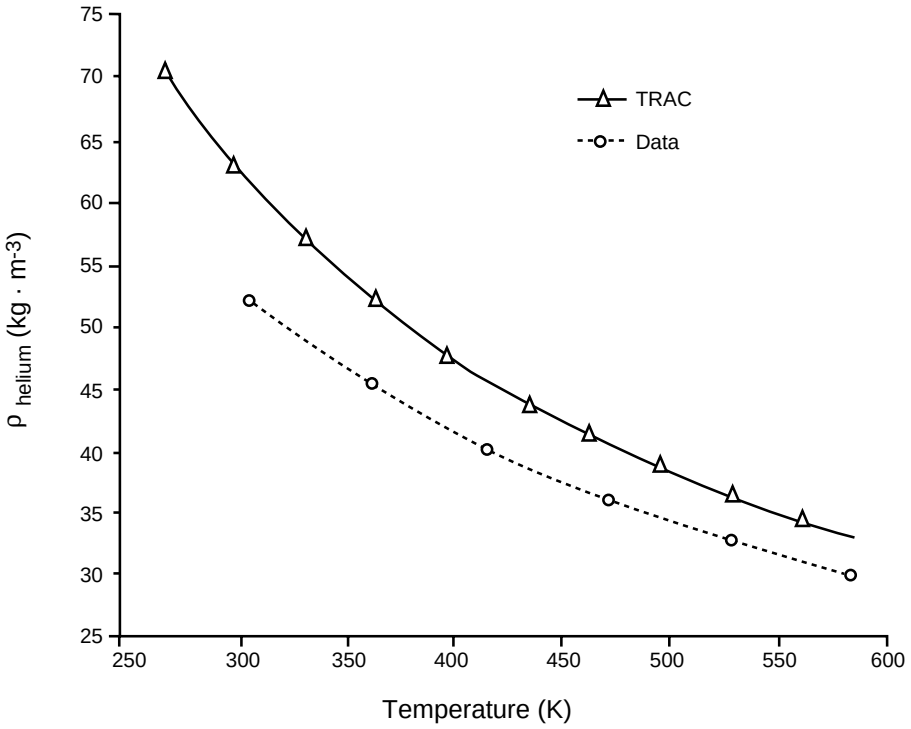

p

Fig. K-30. Density vs. temperature for helium at 40 MPa.

We use an exponential approximation with respect to temperature for the thermal conductivity. For air (Fig. K-31.), the percentage error is no more than 5% for temperatures less than 900 K. Similarly, the error for the hydrogen value at 100 kPa is no higher than 5% for temperatures below 860 K (Figs. K-32. through K-36.). The data for the thermal conductivity of air and hydrogen are taken from Ref. K-4. Data for helium thermal conductivity come from Ref. K-8. The error for helium is less than 5% for temperatures below 850 K (Fig. K-37.). The temperature range of these noncondensable gases of greater than 5% accuracy is suitable for most transients of interest in PWRs.

K.1.5. Conclusions

The code uses a constant for the specific heat of the gases when these values are really temperature dependent. If higher precision were desired, we could incorporate a polynomial fit or tables to specify these values. We feel, however, that a constant approximation for the specific heat yields satisfactory results for most transients of interest.

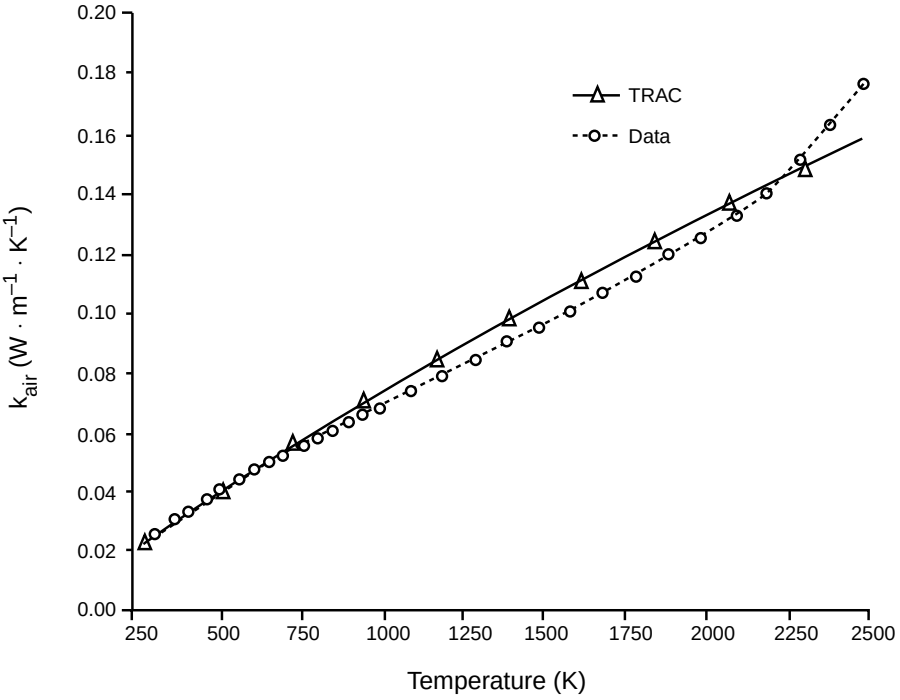

Fig. K-31. Thermal conductivity vs. temperature for air at 100 kPa.

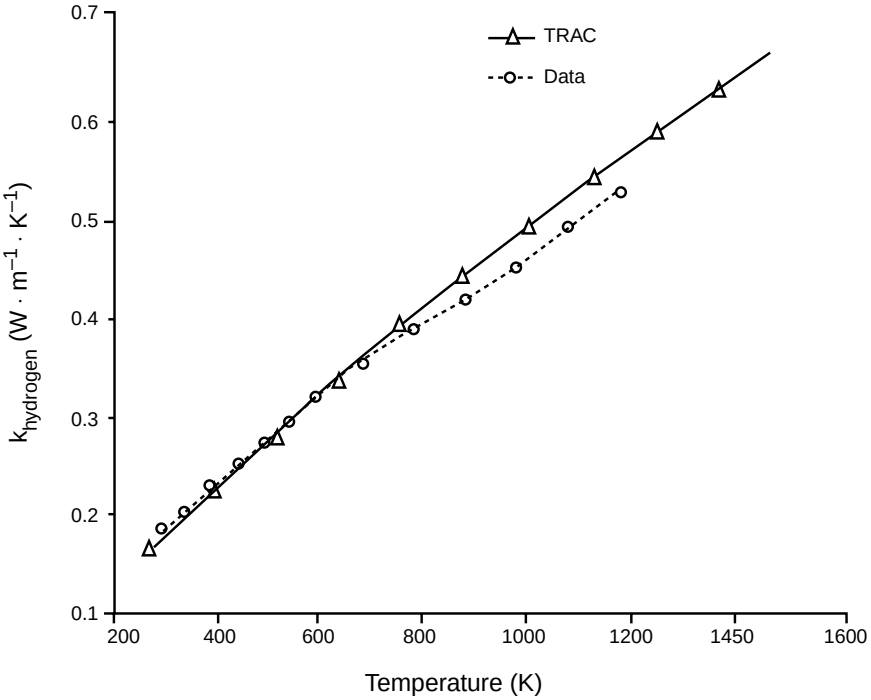

Fig. K-32. Thermal conductivity vs. temperature for hydrogen at 100 kPa.

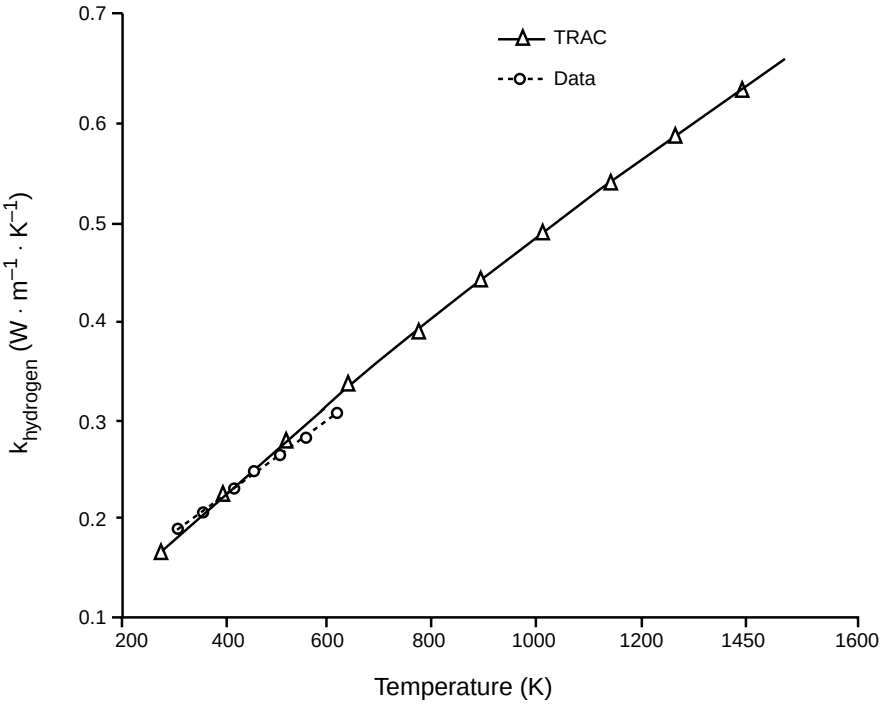

Fig. K-33. Thermal conductivity vs. temperature for hydrogen at 1 MPa.

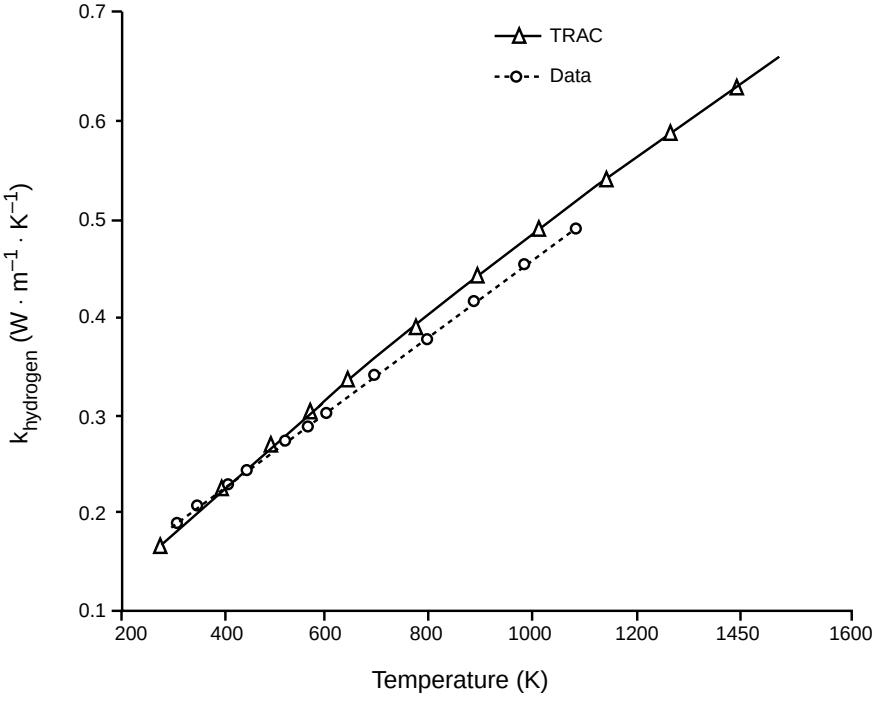

Fig. K-34. Thermal conductivity vs. temperature for hydrogen at 4 MPa.

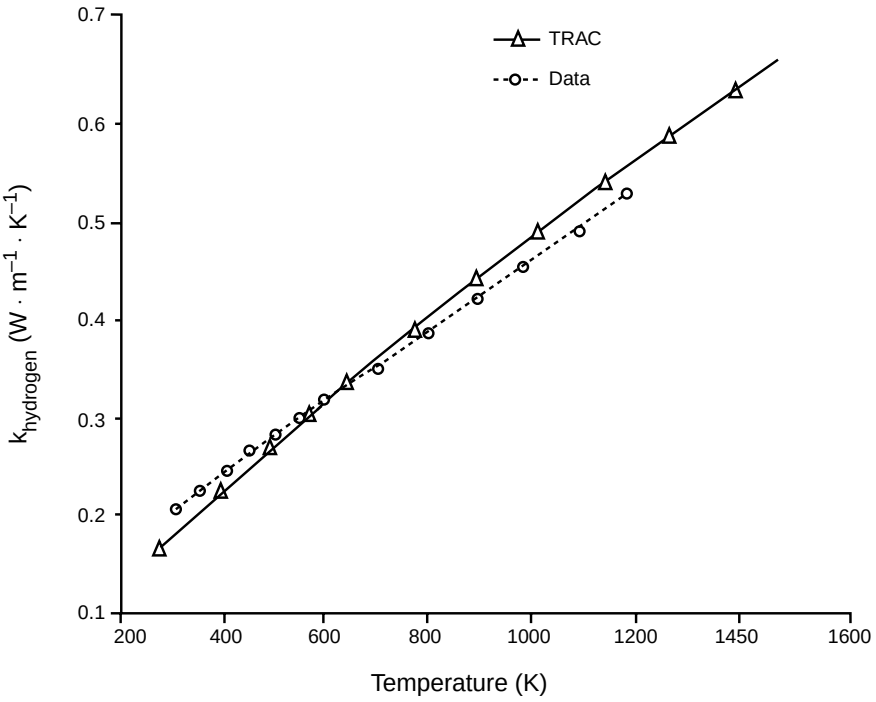

Fig. K-35. Thermal conductivity vs. temperature for hydrogen at 15 MPa.

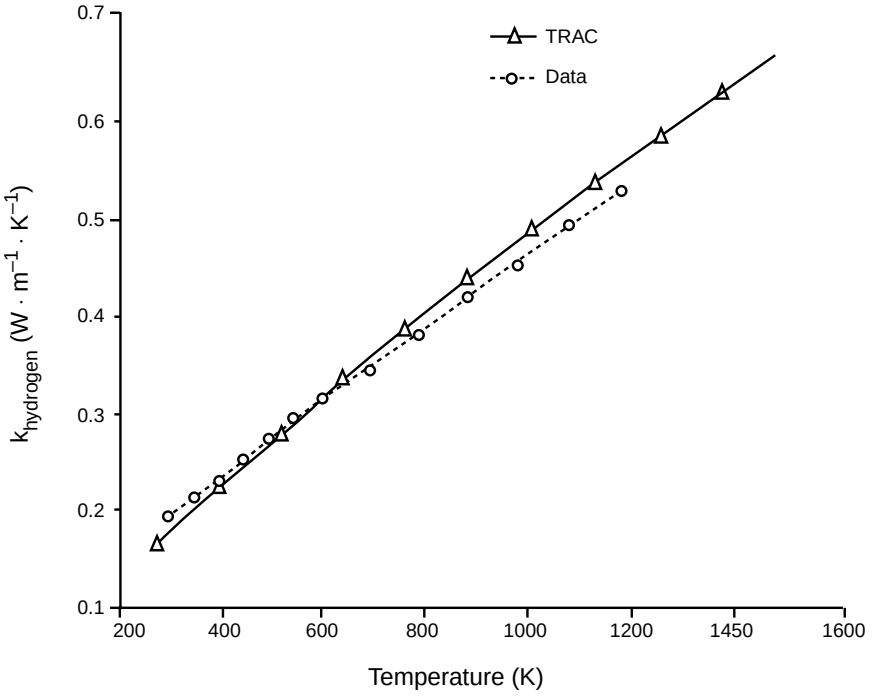

Fig. K-36. Thermal conductivity vs. temperature for hydrogen at 40 MPa.

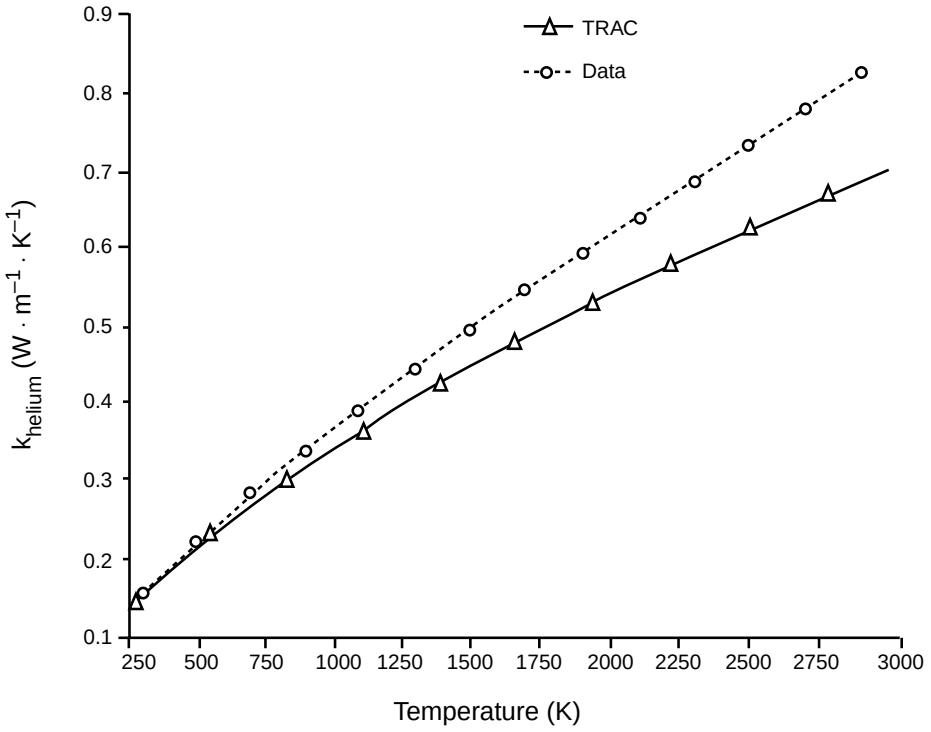

Fig. K-37. Thermal conductivity vs. temperature for helium at constant pressure.

K.2. Liquid Solute

TRAC has an extra mass-continuity equation for tracking a liquid solute (orthoboric acid or a user-defined solute) through all hydro components [see Eqs. (2-17) and (2-42) through (2-44)]. If the liquid solute is orthoboric acid, its concentration in the reactor-core region can be used to determine its neutronic reactivity-feedback effect on the point-reactor kinetics solution for the reactor-core power. The liquid solute has no other effect on the liquid-field processes and properties. The equations solved in TRAC require a correlation for the maximum solubility of the solute material in liquid water.

Because there is no hydraulic feedback effect from the liquid solute on the fluid dynamic solution, the solute mass provides the capability to investigate numerical-diffusion effects and the movement and subsequent distribution of injected coolant.

K.2.1. Model Description

The solubility model for the solute is based on a simple linear correlation between the solute concentration and the liquid temperature. This model is appropriate for dilute solutions of orthoboric acid. The solubility model was developed based on information in Ref. K-9. (p. B-84).

TRAC simulates orthoboric acid with its liquid solute model because of boron's useful design characteristics. Boron has a thermal-neutron-capture cross section of 755 barns that can be used to introduce negative neutronic reactivity to control the reactor-core power. Its reference concentration molality of 0.32 allows appropriate amounts to be dissolved in the liquid-water coolant. Orthoboric acid is also physically and chemically very stable over its range of application (Ref. K-10., p. 218). The default solute in TRAC is orthoboric acid, which can be used in the reactivity-feedback calculation. If the user wishes to use a solute other than orthoboric acid, he can do so by inputting new solubility specifications (see NAMELIST variable ISOLCN and the solubility-parameters card following the NAMELIST-variable input).

TRAC calculates the solute concentration in subroutine BKSSTB for 1D components, in subroutine BKSPLN for the plenum component, and in subroutines FF3D and STBME3 for the 3D vessel component. The evaluation in each of these subroutines has two steps. The first step calculates the solute density and the second step calculates the amount of plated-out solute as well as the final solute concentration in each of the component's mesh cells for the time step.

TRAC calculates the solute density with Eq. (2-17). This equation calculates the solute density directly, with no regard for the solubility of orthoboric acid or for the possible occurrence of plating out. At this point, TRAC assumes infinite solubility of the material already in solution. In doing this calculation for any given mesh cell, TRAC considers each interface with an adjoining mesh cell. The amount of solute mass entering through a mesh-cell interface is defined by

$$m_{\text{solute}} = V_{\text{l}} \cdot \rho_{\text{l}} \cdot m \cdot \Delta t \cdot (1-\alpha) \cdot A \quad , \tag{K-13}$$

where ρ_{l} is the donor-cell liquid density, m is the ratio of donor-cell solute mass to liquid mass, and A is the flow area between the mesh cells.

The convected solute mass is evaluated implicitly by its stabilizer mass equation. In 3D vessel components when NSTAB = 0, the SETS3D stabilizer equations are not evaluated and the convected solute mass is evaluated explicitly by a basic form of its 3D mass equation.

The second set of calculations computes the amount of plated-out solute and obtains the final liquid-solute-concentration ratio. If the cell has voided completely during the time step, all solute in the cell must have either convected out or plated out, and the liquid solute concentration is zero. If the cell has not voided completely (that is, if the cell still contains some liquid coolant), TRAC calls function CONCF, which determines the maximum solubility of orthoboric acid as a function of temperature. This solubility value is known at 303 K and 373 K (Ref. K-9., p. B-84). For temperatures between these two values, TRAC determines the solubility by linear interpolation. For temperatures less than 303 K, TRAC uses the value at 303 K; for temperatures greater than 373 K, TRAC uses the value at 373 K. The maximum possible solute density is the water density times the maximum solubility determined by CONCF. If the new solute density exceeds

this maximum, the code assumes the excess has plated out, and the solute density becomes the maximum value. If the new solute density is less than the maximum, the code assumes that plated-out solute, if it exists in the cell, reenters solution at an infinite rate to the extent that either all the plated-out solute dissolves or the solution becomes saturated. TRAC uses Eqs. (2-43) and (2-44) to calculate the final solute density and the amount plated out. TRAC then finds the new concentration ratio by dividing the new solute density by the coolant density. Plated-out solute remains in the cell until it redissolves.

If a solute other than orthoboric acid is defined, the user must input new maximum and minimum temperatures, as well as solubility values for both temperatures. TRAC calculates the maximum solubility using linear interpolation.

The boron concentration in orthoboric acid is one of four parameters that affect the neutronic reactivity of the reactor core. TRAC calculates their core-region averaged values in subroutine RFDBK. (For a more complete description of reactivity feedback, see Appendix M, Section M.2.5.). When calculating reactivity feedback from boron, TRAC takes into account all forms of boron in the reactor core,

1. dissolved orthoboric acid in the liquid coolant,
2. orthoboric acid plated on core structure,
3. borosilicate glass in burnable-poison pins, and
4. boron oxide in control-rod-cluster pins.

The solubility model for orthoboric acid affects items 1 and 2.

TRAC makes the following assumptions when implementing the solute-tracking feature of the code:

1. The presence of solute in the coolant does not affect any of the liquid properties of the coolant, nor does it affect interfacial or wall heat transfer in any way (this assumption makes the solute concentration a good marker with which the fluid from a particular source can be followed).
2. While the code does allow for plated-out solute, it does not take into account the effects of such solute buildup except through neutronic reactivity feedback when the solute is orthoboric acid. Plated-out solute on structure surfaces could affect wall heat transfer and surface friction (Ref. K-10.).
3. Plating out occurs instantaneously if the concentration exceeds the maximum solubility, such as when liquid coolant boils or flashes. Similarly, the plated-out material dissolves at an infinite rate. No allowance is made for a supersaturated orthoboric solution.
4. The code assumes that the solubility is a function of temperature and is not pressure dependent.

5. The maximum-solubility temperature dependence is assumed to be linear and defined over a limited temperature range.

Reference K-9. (p. B-84) indicates that the maximum solubility of orthoboric acid at 303 K is 6.35 g / 100 cm^3 of water; at 373 K, 27.6 g / 100 cm^3 of water. We interpreted this to mean respective maximum solute concentrations of 0.0635 and 0.276 kg solute / kg water at 303 K and 373 K; this interpretation is consistent with the data in Ref. K-11. (p. 149).

K.2.2. Assessment

TRAC will use the above model to calculate the solubility and concentration of orthoboric acid for temperatures from 273.15 K, the triple-point temperature, to 647.3 K, the critical-point temperature of water. Figure K-38. shows a comparison of the TRAC approximation for solubility with the data from Ref. K-11. (pp. 149-150); the data in Ref. K-10. (p. 221) are similar. The linear approximation for the solubility of boric acid compares well with the data in the temperature range bounded by the two temperatures. On the low end of the temperature scale where we approximate the solubility at 273 K by the solubility at 303, there is a 134% error. Reference K-11. indicates that the solubility is 1 kg / kg water at 444 K, where there is a –72% error associated with the TRAC approximation. The solubility curve based on Ref. K-11. becomes very steep as the temperature approaches 444 K.

If the solubility limits are exceeded, we believe that the typical result would be the creation of a supersaturated solution and / or a suspended precipitate that would not be plated out on the structure surface.

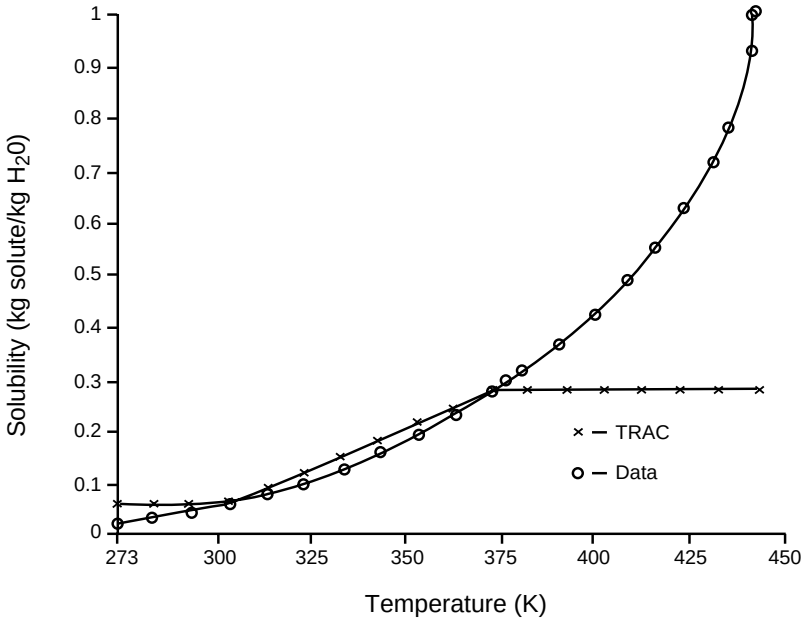

Fig. K-38. Orthoboric-acid solubility vs. liquid temperature.

K.2.3. Summary and Conclusions

We are now aware of data that would permit the construction of a solubility curve in TRAC that is valid over a much wider range of temperatures, although there is still a question of how to treat solubility in the metastable range above 442 K. We believe that such a model should be incorporated. For now, the user can input a linearly dependent maximum-solubility curve fit to data over the temperature range of interest if the default maximum-solubility curve is inappropriate. We do not believe that it is important to incorporate rates into the dissolution/plating processes because most transients in PWRs will not approach the solubility limits.

REFERENCES

K-1. J. P. Holman, *Heat Transfer* (McGraw-Hill Book Co., Inc., New York, 1981).

K-2. Frank M. White, *Fluid Mechanics* (McGraw-Hill Book Co., Inc., New York, 1979).

K-3. Kuzman Raznjevic, *Handbook of Thermodynamic Tables and Charts* (McGraw-Hill Book Co., Inc., New York, 1976).

K-4. J. M. Sicilian and R. P. Harper, *Heavy-Water Properties for the Transient Reactor Analysis Code*, Flow Science, Inc. report FSI-85-Q6-1 (1985).

K-5. *Physical and Thermodynamic Properties of Helium* (Whittaker Controls, Los Angeles, 1957).

K-6. Nissim Marshall, *Gas Encyclopaedia* (Elsevier Scientific Publishing Company, Amsterdam, 1976).

K-7. N. B. Vargaftik, *Tables on the Thermophysical Properties of Liquids and Gases, in Normal and Dissociated States*, 2nd ed. (John Wiley and Sons, New York, 1975).

K-8. *CRC Handbook of Chemistry and Physics*, 63rd ed. (The CRC Press, Inc., Boca Raton, Florida, 1982).

K-9. *CRC Handbook of Chemistry and Physics*, 62nd ed. (The CRC Press, Inc., Boca Raton, Florida, 1981).

K-10. Paul Cohen, *Water Coolant Technology of Power Reactors* (Gordon and Breach Science Publishers, New York, 1969).

K-11. Leopold Gmelin, *Gmelins Handbuch der Anorganischen Chemie*, Supplement to Volume 1, System Number 13 (Boron) (Verlag Chemie, Gmbh., Weinheim/Bergstrasse, 1954).

K-12. E. A. Haytcher and J. C. Lin, “Modification to Helium Properties in the TRAC-PF1/MOD2 Code,” Los Alamos National Laboratory report LA-N7-1 (December 1992).

APPENDIX L

ADDITIONAL FUEL ROD MODELS

The nomenclature applicable to this appendix follows.

NOMENCLATURE

F:	view factor
$h_{contact}$:	heat-transfer coefficient for fuel-cladding interfacial contact
h_{gap}:	gap heat-transfer coefficient
h_{gas}:	heat-transfer coefficient for gap-gas conductance
$h_{radiation}$:	heat-transfer coefficient for fuel-cladding thermal radiation
k_{gas}:	gap-gas thermal conductivity
m'_{Zr}:	mass per unit length of zirconium
q'''_{mw}:	heat source from metal-water reaction
r:	radius
R_c, R_I:	cladding inner radius
R_f:	solid-fuel radius (also total fuel radius)
R^*_f:	fuel radius, including cracked fuel
R_o:	cladding outer radius
$R_{f,new}$:	solid-fuel radius after thermal expansion
$R_{I,new}$:	cladding inner radius after thermal expansion
t:	time
T:	temperature
T_{cI}:	cladding inside temperature
T_{cl}:	fuel centerline temperature
T_{co}:	cladding outside temperature
T_{REF}:	reference temperature (298.0 K)
T_{surf}:	fuel surface temperature
u:	radial displacement
α:	linear thermal-expansion coefficient
Δr_{gap}:	fuel-cladding radial gas gap
Δt:	time step
ΔT:	difference between the actual temperature and T_{REF}
δ:	cracked fuel thickness
δ_0:	initial undeformed radial thickness of the crack fuel

δ_r: factor that includes the mean surface roughness of the fuel and the cladding plus the temperature jump distances

ε: emissivity

ν: Poisson's ratio

ρ: density

ρ_{Zr}: density of zirconium metal

ρ_{ZrO_2}: density of zirconium oxide

σ: Stefan-Boltzmann constant

τ: total oxygen consumed

Subscripts

c: cladding

f: fuel

L.1. Fuel-Cladding Gap Conductance

Subroutine GAPHT calculates the gap heat-transfer coefficient (HTC), h_{gap}, as a function of three components: gap-gas conductance, fuel-cladding interfacial contact, and fuel-cladding thermal radiation. The superposition of these three components gives

$$h_{gap} = h_{gas} + h_{contact} + h_{radiation} , \tag{L-1}$$

where

$$h_{gas} = k_{gas} / (\Delta r_{gap} + \delta_r) , \tag{L-2}$$

$$h_{radiation} = \frac{\sigma F (T_f^4 - T_c^4)}{(T_f - T_c)} , \tag{L-3}$$

and

$$F = \frac{1}{\frac{1}{\varepsilon_f} + \frac{R_f}{R_c}\left(\frac{1}{\varepsilon_c} - 1\right)} . \tag{L-4}$$

where k_{gas} is the gap-gas thermal conductivity, T_f and T_c are the temperatures at the fuel outer surface and cladding inner surface at radii R_f and R_c, respectively, ε_f and ε_c are the corresponding emissivities, and σ is the Stefan-Boltzmann constant. A value of 4.4×10^{-6} m is used for δ_r, which includes the mean surface roughness of the fuel and the cladding plus the temperature jump distances (Refs. L-1 and L-2). The contact

conductance, $h_{contact}$, is zero in the present code. (In the following discussion on thermal expansion, the radii R_f and R_c are called R_f^* and R_I, respectively.)

The fuel-cladding radial gas gap, Δr_{gap}, is found by using the uncoupled, quasi-static approximation (Ref. L-3.). In this approximation the mechanical coupling term in the energy equation and the inertial term in the mechanical force balance are omitted. By neglecting these terms, we assume that the fuel-cladding strains minimally affect the temperature distribution and that displacements are instantaneous. Figure L-1. shows the fuel-cladding gap system modeled in three regions: solid fuel, cracked fuel, and cladding. Gap changes are found by calculating the radial displacement of each region caused by thermal expansion.

The calculations for the deformation of a hollow or solid circular cylindrical body of outer radius b, inner radius a (where $a = 0$ for a solid cylinder), and height h are given in Ref. L-3. for the case where the ratio h/b is large compared to unity. Other assumptions are made that the cylindrical surfaces are free of forces, axial displacement is allowed, and the temperature distribution is a function of the radial distance r only. Because the uncoupled, quasi-static approximation is used, the temperature distributions are assumed to be known from the energy balance. The radial displacement u is given by

$$u(r) = \frac{\alpha}{r(1-\nu)}\left[(1+\nu)\int_a^r \Delta T r \quad dr + \frac{(1-3\nu)r^2 + a^2(1+\nu)}{b^2 - a^2}\int_a^b \Delta T r \; dr\right] \quad , \qquad \text{(L-5)}$$

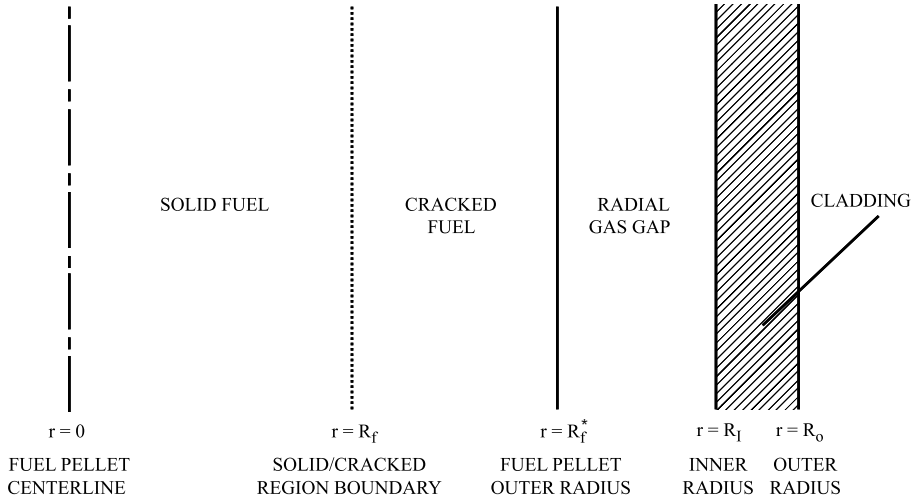

Fig. L-1. Fuel-rod geometry.

where ν is Poisson's ratio, α is the linear thermal-expansion coefficient, and ΔT is $(T - T_{REF})$. For purposes of this calculation, T_{REF} is set to 298.0 K. Equation (L-5) is used to calculate the radial displacement of the cladding inner radius and the solid-fuel radius, $r = R_I$ and $r = R_f$, respectively. If radial symmetry is assumed (so that $\nu = 0$), the results become

$$u(R_I) = \frac{2\alpha_c R_I}{R_o^2 - R_I^2} \int_{R_I}^{R_o} \Delta T_c r \; dr \tag{L-6}$$

and

$$u(R_f) = \frac{2\alpha_f}{R_f} \int_0^{R_f} \Delta T_f r \; dr \; . \tag{L-7}$$

The cladding inner radius and the solid-fuel radius after thermal expansion are

$$R_{I,\,new} = R_I + u(R_I) \tag{L-8}$$

and

$$R_{f,\,new} = R_f + u(R_f) \; . \tag{L-9}$$

The following equation is used for the cracked-fuel thickness,

$$\delta = \delta_o \left[1 + \frac{\alpha_f}{R_f^* - R_f} \int_{R_f}^{R_f^*} \Delta T_f \; dr \right] , \tag{L-10}$$

where δ_o is the initial, undeformed radial thickness of the cracked fuel,

$$\delta_o = R_f^* - R_f \; . \tag{L-11}$$

A parabolic radial temperature distribution is assumed across the fuel pellet,

$$T_f = T_{cl} + (T_{surf} - T_{cl})(r^2 / R_f^{*2}) \; , \tag{L-12}$$

where T_{cl} is the fuel centerline temperature and T_{surf} is the fuel surface temperature. A linear temperature profile is assumed across the cladding,

$$T_c = (T_{co} - T_{cI})(r - R_I)/(R_o - R_I) + T_{cI} \ , \tag{L-13}$$

where T_{co} and T_{cI} are the cladding outside and inside temperatures, respectively.

The radial gap width after thermal expansion is

$$\text{gap width} = R_{I,\,new} - (R_{f,\,new} + \delta) \tag{L-14}$$

or

$$\text{gap width} = (R_I - R_f) + \frac{2\alpha_c R_I}{R_o^2 - R_I^2}\int_{R_I}^{R_o} \Delta T_c r\,dr - \frac{2\alpha_f}{R_f}\int_0^{R_f} \Delta T_f r\,dr$$

$$-\delta_o\left[1 + \frac{\alpha_f}{R_f^* - R_f}\int_{R_f}^{R_f^*} \Delta T_f\,dr\right] . \tag{L-15}$$

Subroutine DELTAR evaluates the fuel-cladding radial spacing.

L.2. Metal-Water Reaction

When Zircaloy reaches a sufficiently high temperature in a steam environment, an exothermic reaction may occur that influences the peak cladding temperatures. This exothermic reaction, called the zirconium-steam reaction, is given by

$$Zr + 2H_2O \rightarrow ZrO_2 + 2H_2 + \text{heat} \ . \tag{L-16}$$

With a sufficient steam supply, the following reaction-rate equation (Refs. L-4. and L-5.) is assumed valid:

$$\tau\frac{d\tau}{dt} = \eta_1 \exp\left(-\frac{\eta_2}{T}\right) , \tag{L-17}$$

where

τ = total oxygen consumed (kg/m^2), η_1 = 16.8 kg^2/m^4s, and η_2 = 2.007 x 10^4 K.

The kinetic parameter τ is converted to an effective zirconium-oxide layer thickness according to

$$1.5(R_o - r) = \tau/(0.26\rho_{ZrO_2}) \ , \tag{L-18}$$

where r = reacting surface radius (m), R_o = cladding outer radius (m), and ρ_{ZrO_2} = density of zirconium oxide (kg/m^3).

Equation (L-18) is based on a reacted-material volume expansion of 50% in the radial direction. This assumption leads to $\rho_{ZrO_2} = 0.90\rho_{Zr}$. Equation (L-18) allows Eq. (L-17) to be rewritten as

$$\tau\frac{d\tau}{dt} = -\eta_3(R_o - r)\frac{dr}{dt} ,$$

where

$$\eta_3 = (0.351\rho_{Zr})^2 .$$

The method outlined in Ref. L-4. is used to calculate the zirconium-oxide penetration depth and associated heat source. The mass per unit length of zirconium (m'_{Zr}) consumed by the reaction in one time step is

$$(m'_{Zr}) = \pi\rho_{Zr}[(r^n)^2 - (r^{n+1})^2] . \qquad \text{(L-19)}$$

Equation (L-17) is used to calculate r^{n+1}, yielding

$$r^{n+1} = R_o - [(R_o - r^n)^2 + 2(\eta_1/\eta_3)\Delta t\exp(-\eta_2/T)]^{1/2} . \qquad \text{(L-20)}$$

If a single-region cladding is assumed, the heat source (q'''_{mw}) added to the conduction equation is

$$q'''_{mw} = 6.45\times10^6 m'_{Zr}[\Delta t(R_o^2 - R_I^2)\pi]^{-1} , \qquad \text{(L-21)}$$

where R_I is the inner cladding radius and 6.45×10^6 J/kg corresponds to the energy released per kilogram of oxidized zirconium.

The metal-water reaction is calculated only at locations that correspond to hydrodynamic-cell boundaries. The effect of the metal-water reaction is included in the intermediate nodes (fine mesh) by linear interpolation of the effect along the length of the cell. The error produced by this method of accounting for the metal-water reaction is small except in a hydrodynamic cell where quenching is occurring. At the bottom of such a cell the rod temperature is low, and the metal-water reaction has no effect. At the top of the cell the metal-water reaction is calculated correctly. When TRAC interpolates in the cell the effect of the metal-water reaction is underestimated. If the rod temperatures exceed 1273 K (the onset of the metal-water reaction), the user should

watch for this situation; if the peak cladding-temperature location is in the same hydrodynamic cell as the quench front, the temperature will be under predicted.

REFERENCES

L-1. L. S. Tong and J. Weisman, *Thermal Analysis of Pressurized Water Reactors*, 2nd ed. (American Nuclear Society, La Grange Park, Illinois, 1979).

L-2. P. E. MacDonald and J. Weisman, "Effect of Pellet Cracking on Light Water Reactor Fuel Temperatures," *Nuclear Technology* 31, 357-366 (1976).

L-3. B. A. Boley and J. H. Weiner, *Theory of Thermal Stresses* (John Wiley and Sons, Inc., New York, 1960).

L-4. J. V. Cathcart, "Quarterly Progress Report on the Zirconium Metal-Water Oxidation Kinetics Program," Oak Ridge National Laboratory report ORNL/NUREG/TM-41 (August 1976).

L-5. "MATPRO–Version 11: A Handbook of Materials Properties for Use in the Analysis of Light Water Reactor Fuel Rod Behavior," Idaho National Engineering Laboratory report TREE-1280 (NUREG/CR-0497) (February 1979).

APPENDIX M

REACTOR-CORE POWER MODEL

The following nomenclature applies to this appendix. On various occasions, mnemonics are used that are equivalent to the code's FORTRAN variables instead of the symbols. These mnemonics are also listed in the nomenclature.

NOMENCLATURE

A_i:	horizontal cross-sectional area of fuel-rod node i
a_1, a_2:	functions of time defined in Eq. (M-27)
a_l, b_l:	linear interpolation parameters for power history defined in Eq. (M-12)
BCR:	control-rod-cluster-pin solute concentration ($kg \cdot m^{-3}$)
BCR0, *BCR1*:	polynomial coefficients for *BCR* defined in Eq. (M-16)
B_m:	core-averaged solute concentration ($kg \cdot m^{-3}$)
BPP:	equivalent burnable-poison-pin solute concentration ($kg \cdot m^{-3}$)
BPP0, *BPP1*:	polynomial coefficients for *BPP* defined in Eq. (M-15)
B_r:	ratio of solute mass to liquid-coolant mass (ppm)
C_i:	power of delayed-neutron precursor concentration in group i (W)
CPOWR:	relative power density of an average rod
D, D^*:	functions of a_1 and a_2 (Eqs. M-30, M-31, M-39, and M-40)
ED_j:	MeV of decay energy per fission per second for decay-heat group j ($MeV \cdot fission^{-1} \cdot s^{-1}$)
E_j:	effective energy fraction of decay-heat group j
H_j:	energy of decay-heat precursor concentration group j ($W \cdot s$)
IDROD:	input array that provides location of supplemental rod
I:	number of delayed-neutron groups or total number of radial nodes in a fuel rod
J:	number of decay-heat groups or total number of average calculational rods in the core
K:	number of input-specified coarse-mesh boundaries axially
k:	neutron multiplication constant
k_{ex}:	excess reactivity expressed in terms of the neutron multiplication constant ($k - 1$)
l:	a constant
m_i:	fuel or coolant mass if x is T_f or T_c in Eq. (M-14); 1 if x is α, B_m or B_r in Eq. (M-14)
m:	arbitrary index

$NZPWTB$: normalized power shape

$NRDX$: number of fuel rods

P: thermal power from fission (W)

P_i: power in mesh cell i

P_1, P_2, P^*_1, P^*_2: polynomial coefficients for P

P_{eff}: effective thermal power

$POWEXP$: neutron flux distribution parameter

P_{tot}: average core power

Q_k: MeV per fission for a given isotope k

$q(t)$: function of time defined in Eq. (M-27)

q''': power density

q'''_{supl}: supplemental rod power-density distribution

R: neutronic reactivity, including both programmed reactivity and feedback reactivity

r: radial

R_1: polynomial coefficient for R

$RDPWR$: relative radial-power density

$RPKF$: power-peaking factors

S: thermal power from an external source of neutrons (W)

S_f: scale factor to normalize the relative-power distributions

T_c: core-averaged coolant temperature

T_f: core-averaged fuel temperature

t: time (s)

V_i: volume of mesh cell i

x: dummy variable

$ZPOWR$: relative power density

$ZPWTB$: the relative axial-power density in a given rod

α: core-averaged gas volume fraction

β: total fraction of delayed neutrons

β_i: fraction of delayed neutrons in group i

Δk: change in reactor multiplication factor

Δt: time-step size

Δz: elevation distance

Λ: effective prompt-neutron lifetime (s)

λ_i: decay constant for delayed-neutron precursors in group i (s^{-1})

λ^H_j: decay constant for decay-heat group j

ρ: density

τ: dummy integration variable

θ: azimuthal

ε: error in estimating P

$\varepsilon_1, \varepsilon_2$: error bounds in estimating P

Subscripts

fdbk: feedback

i: delayed-neutron group or cell number or dummy index for fuel-rod node

j: decay-heat group or dummy index for cell identification

k: dummy isotope index or dummy index for core level

prog: programmed

Superscripts

cor: corrected

est: estimated

$n-1, n, n+1$: old-, current-, and new-time values

M.1. Partitioning of the Core Power into the Heat-Conduction Mesh

The user must supply as a part of the input for the heat-structure components several arrays that enable the code to partition the heat generation into the finite-difference mesh cells that describe the fuel rods (or fuel-rod simulators). These arrays include *RDPWR*, the relative radial-power density at the radial node positions in the rod, Fig. M-1.; *CPOWR*, the relative power density in each (r, θ) mesh cell in the horizontal plane, Fig. M-2.(A); *ZPWTB*, the relative axial-power density in a given rod, Fig. M-3.; and RPKF, the fuel-rod power-peaking factors (relative to the average fuel rod in the horizontal mesh cell) for the additional rods, Fig. M-2.(B). The code assumes that all calculational rods have the same *RDPWR* and *ZPWTB* arrays and that the *CPOWR* and *RPKF* arrays do not vary in the axial direction.

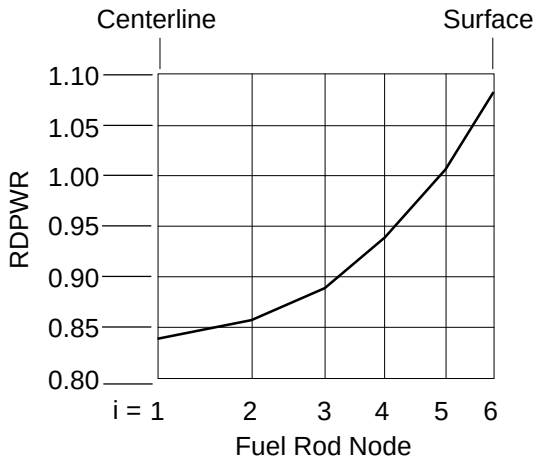

Fig. M-1. Relative radial-power density at radial node positions in the fuel rod.

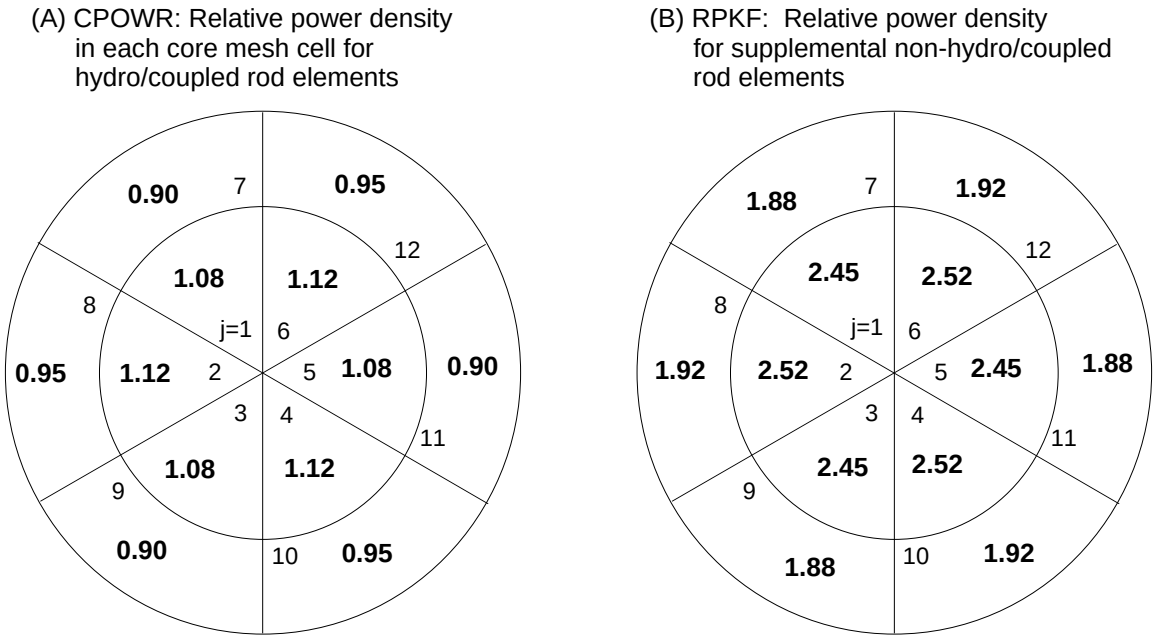

Fig. M-2. Relative power density in each (*r*, *θ*) mesh cell in the horizontal plane.

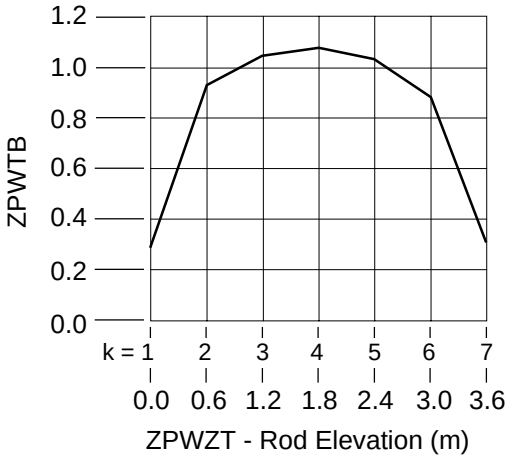

Fig. M-3. Relative axial-power density in a fuel rod.

There are a number of input options available for specifying the axial-power shape as discussed in Section 4.3 of the TRAC-M/F90 User's Manual (Ref. M-5.). The code also permits the user to specify the axial-power shape as a function of an independent variable. This independent variable can be either a signal-variable parameter or a control-block output signal. The purpose of this general definition of the axial-power shape is to permit the code user to vary the axial-power shape during the calculation if desired. An example of this variation is to vary the axial-power shape to account for the changes in power distribution resulting from control-rod insertion, as shown in Fig. M-4.

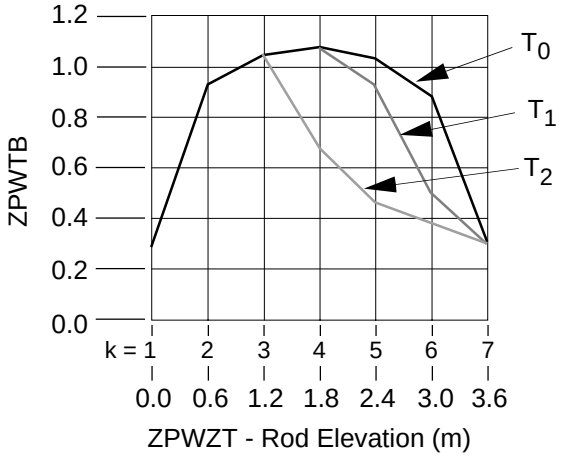

Fig. M-4. Example of multiple entries of axial-power shape to model control-rod insertion as a function of time.

The input-processing subroutine RROD2 normalizes each individual axial-power shape by the following formula:

$$NZPWTB_k = ZPWTB_k \left(\frac{\sum_{i=1}^{K} \Delta z_i}{\sum_{i=1}^{K} ZPWTB_i \Delta z_i} \right) , \qquad \text{(M-1)}$$

where *ZPWTB* is the input power shape and *NZPWTB* is the resulting normalized power shape. The summations are over the axial height of the core and Δz_i is the elevation distance over which the i^{th} shape element applies. (In general, Δz_i is the distance between the centers of adjacent levels; however, at the bottom, it is half the height of the lowest level inside the core; at the top, half the height of the top level in the core.) *ZPOWR*, the relative power density, is determined by interpolation from the *NZPWTB* array.

The code computes the actual solution for the fuel-rod temperatures with a call to subroutine CORE3. Subroutine CORE3 controls the thermal analysis of all calculational rods in the core and calls subroutine FROD for each rod. Subroutine FROD calculates the temperature distribution for an individual rod with a call to subroutine RODHT. The partitioning of the core power is set up initially in subroutine IROD, with partitioning carried out in subroutine RODHT.

The power density q''' in fuel-rod node *i* in cell *j* in core level *k* is

$$q'''_{ijk} = S_f P_{tot} RDPWR_i \; CPOWR_j \; ZPOWR_k , \qquad \text{(M-2)}$$

where P_{tot} is the average core power over the time step, $RDPWR_i$ is the relative power density in fuel node *i*, $CPOWR_j$ is the relative power of the average rod in cell *j*, $ZPOWR_k$ is the relative power density at core elevation *k*, and S_f is the scale factor that normalizes the three input relative-power distributions to a core volume-averaged value of unity. Subroutine CORE3 sets P_{tot} to be

$$P_{tot} = \frac{P^n + P^{n+1}}{2} , \qquad \text{(M-3)}$$

where *P* is the total core power, and the superscripts *n* and *n* + 1 indicate the beginning and end of time step, respectively. The following expression defines the scale factor S_f:

$$S_f = 1 \Big/ \left[\sum_{i=1}^{I} \sum_{j=1}^{J} \sum_{k=1}^{K} (A_i \cdot RDPWR_i \cdot NRDX_j \cdot CPOWR_j \cdot ZPOWR_k \cdot \Delta z_k) \right] , \qquad \text{(M-4)}$$

where A_i is the horizontal cross-sectional area of fuel-rod node *i*, and $NRDX_j$ is the number of fuel rods in cell *j* for which the average fuel-rod condition is to be evaluated.

The summations in Eq. (M-4) are over all nodes in all rods: I is the number of radial nodes in a rod (NODES in the input), J is the number of average calculational rods in the core (from the input, ICRR · NTSX), and K is the number of input-specified coarse-mesh boundaries axially (corresponds to the number of interfaces between levels in the core, ICRU – ICRL + 1).

For the supplemental rod l in cell j (recall that the location of the supplemental rod is specified in input array IDROD), the power density distribution q'''_{supl} is

$$q'''_{supl} = RPFK_j \cdot q'''_{ijk} \text{ provided the value of } IDROD_l = j \ , \qquad \text{(M-5)}$$

where $RPKF_j$ is the specified peaking factor of the supplemental rod relative to the average rod in the same cell.

The input defines all of the necessary parameters in Eqs. (M-2) through (M-5) for partitioning P_{tot} throughout the 2D heat-conduction mesh for each calculational rod in the core. For the most part, the variable names used above correspond to those used in the input description; the exception is A_i, which is calculated from input radial-node radii RADRD.

Because the axial-power shape is normalized in the input-processing subroutines, the factor does not need to be shown explicitly in the expression for S_f. Also, S_f contains the grouping $_i \cdot \Delta \mathbf{z}_k$, which is the volume of the (i, k) mesh cell in the rod; this volume times $NRDX_j$ provides the total volume of actual rods in mesh cell (i, k) with the same power density. Therefore, S_f not only normalizes to the total power throughout the core but also converts the power into a volumetric heat-generation rate for the calculational rod.

M.2. Power Evaluation and Reactor Kinetics

The code determines the core power in subroutine RKIN by either of two methods. In the first method, the user specifies power to be a constant or to be defined by an RPWTB power table supplied through input. The table is a function of a system signal-variable parameter or a control-block output-signal parameter. Values between entries in the table are determined by linear interpolation. Power determination can be trip-controlled by evaluating the power table when the controlling trip is ON and by holding the power constant when the trip is OFF. In the second method, the user determines power from the solution of the point-reactor-kinetics equations. These equations specify the time behavior of the core power level with neutronic reactivity (R) [the sum of programmed reactivity (R_{prog}) and feedback reactivity (R_{fdbk})] as the driving parameter. The user inputs programmed reactivity (defining reactivity effects not accounted for by feedback reactivity, such as fuel reactivity and control-rod movement) with the same forms that define power in the first method (as a constant or by a RPWTB table). Subroutine RFDBK evaluates feedback reactivity based on changes in the core-averaged fuel temperature, coolant temperature, gas volume fraction, and solute concentration.

M.2.1. Point-Reactor Kinetics

The point-reactor-kinetics equations (Refs. M-1. and M-2.) are a coupled set of ($I + 1$) first-order differential equations defining the total fission power P and the delayed-neutron precursor concentrations C_i as a function of time. These equations are given by

$$\frac{dP}{dt} = \frac{R-\beta}{\Lambda}P + \sum_{i=1}^{I} \lambda_i C_i + \frac{S}{\Lambda(1-R)} \tag{M-6}$$

and

$$\frac{dC_i}{dt} = -\lambda_i C_i + \frac{\beta_i P}{\Lambda} \quad \text{for} \quad i = 1, 2, \ldots, I \ , \tag{M-7}$$

where

P = thermal power (W) that results from fission occurring at time t;

t = time (s);

R = neutronic reactivity, (including both programmed reactivity and feedback reactivity) = $(k-1)/k = R_{prog} + R_{fdbk}$;

k = neutron multiplication constant = $1 + \Delta k_{prog} + \Delta k_{fdbk}$;

R_{prog} = programmed reactivity = $\Delta k_{prog}/k$;

R_{fdbk} = feedback reactivity = $\Delta k_{fdbk}/k$;

β = total fraction of delayed neutrons = $\sum_{i=1}^{I} \beta_i$;

β_i = fraction of delayed neutrons in group i;

Λ = effective prompt-neutron lifetime (s);

λ_i = decay constant for the delayed-neutron precursors in group i (s^{-1});

C_i = power of the delayed-neutron precursor concentration in group i (W);

I = number of delayed-neutron groups; and

S = thermal power (W) from an external source of neutrons in the reactor cores that are producing fission.

The TRAC program uses the Kaganove method (Ref. M-3.) outlined in Section M.2.6. to solve these equations.

The code applies the thermal-power solution to the decay-heat equations

$$\frac{dH_j}{dt} = -\lambda_j^H H_j + E_j P \text{ for } j = 1, 2, \ldots, J \ , \tag{M-8}$$

where

P = solution of Eqs. (M-6) and (M-7),
H_j = energy of the decay-heat precursor concentration in group j (W · s),
λ_j^H = decay constant for decay-heat group j,
E_j = effective energy fraction of decay-heat group j, and
J = number of decay-heat groups.

After solving each j^{th} equation represented by Eq. (M-8) for the decay-heat group concentration H_j, the code calculates the total thermal power generated in the reactor-core fuel at time t. The total power comprises nuclear fission, fission-product decay, and external sources as shown by

$$P_{eff} = \left(1 - \sum_{j=1}^{J} E_j\right) P + \sum_{j=1}^{J} \lambda_j^H H_j + S \ . \qquad \text{(M-9)}$$

The code requires the number of delayed-neutron groups, I; the delayed-neutron parameters, λ_i and β_i; the number of decay-heat groups, J; the decay-heat parameters, λ_j^H and E_j; and either the total fission-power history $P(t)$ for $-t \le 0$ or the initial delayed-neutron precursor concentrations $C_i(0)$ and decay-heat concentrations, $H_j(0)$.

M.2.2. Default Data for the Delayed-Neutron Groups

If $I \le 0$ is input (input parameter NDGX), TRAC internally sets I to 6 and defines λ_i and β_i with the values in Table M-1.

TABLE M-1.
Delayed-Neutron Constants

Group i	Decay Constant λ_i (s^{-1})	Neutron Fraction β_i
1	3.87	0.000169
2	1.40	0.000832
3	0.311	0.00264
4	0.115	0.00122
5	0.0317	0.00138
6	0.0127	0.000247

If $I \leq 0$ and no total fission-power history is input, the code assumes that an initial steady-state condition exists to initialize $C_i(0)$ internally. The code sets the time derivative in Eq. (M-7) to zero and calculates the initial values of the C_i from the following:

$$C_i(0) = \frac{\beta_i}{\lambda_i \Lambda} P(0) \text{ for } i = 1, 2, \ldots, I \ , \tag{M-10}$$

where $P(0)$ is the initial power specified through input.

M.2.3. Default Data for the Decay-Heat Groups

If ≤ 0 is input, TRAC internally sets J to 69 and defines λ_j^H and ED_j with the values in Table M-2. These decay-heat parameters were obtained from the 1979 ANS decay-heat standard given in Ref. M-4. If the default decay-heat groups are used or if the user inputs 69 or 71 decay-heat groups, the fraction of fission power due to each of the three isotopes, U^{235}, Pu^{239}, and U^{238}, must be input. In addition, in order to convert the MeVs of decay energy per fission to a fraction of the total fission energy, the MeVs per fission for each of the three isotopes, U^{235}, Pu^{239}, and U^{238}, must be input. D_j in Table M-2. is converted to E_j using the following equation:

$$E_j = ED_j(\lambda_j^H Q_k) \ ,$$

where Q_k is the MeV / fission for isotope k.

If ≤ 0 and no total fission-power history is input, the code assumes that an initial steady-state condition exists to initialize $_j(0)$ internally. The code sets the time derivative in Eq. (M-8) to zero and calculates the initial values of the $_j$ from the following:

$$H_j(0) = \frac{E_j}{\lambda_j^H} P(0) \text{ for } j = 1, 2, \ldots, J \ , \tag{M-11}$$

where $P(0)$ is the initial steady-state power specified through input.

M.2.4. Fission Power History

If the total fission-power history $P(-t)$ is input, TRAC evaluates $C_i(0)$ and $H_j(0)$ from Eqs. (M-7) and (M-8). The $P(-t)$ consists of tabular data pairs (t_l, P_l) for $l = 1, 2, \ldots, L$, where $-t_l + 1 < -t < -t_l$. The code assumes that the total fission power varies linearly between data pairs in the power-history table; that is,

$$P(t) = a_l + b_l t \text{ over the time interval } -t_{l+1} \leq t \leq -t_l \ . \tag{M-12}$$

TABLE M-2.
Decay-Heat Constants

Group	Decay Constant λ_j^H (s^{-1})	MeV of decay energy per fission per second ED_j (MeV/fission-s)
for isotope U ^{235}		
1	22.138	6.5057×10^{-01}
2	0.51587	5.1264×10^{-01}
3	0.19594	2.4384×10^{-01}
4	0.10314	1.3850×10^{-01}
5	0.033656	5.5440×10^{-02}
6	0.011681	2.2225×10^{-02}
7	0.0035870	3.3088×10^{-03}
8	0.0013930	9.3015×10^{-04}
9	0.00062630	8.0943×10^{-04}
10	0.00018906	1.9567×10^{-04}
11	5.4988×10^{-05}	3.2535×10^{-05}
12	2.0958×10^{-05}	7.5595×10^{-06}
13	1.0010×10^{-05}	2.5232×10^{-06}
14	2.5438×10^{-06}	4.9948×10^{-07}
15	6.6361×10^{-07}	1.8531×10^{-07}
16	1.2290×10^{-07}	2.6608×10^{-08}
17	2.7213×10^{-08}	2.2398×10^{-09}
18	4.3714×10^{-09}	8.1641×10^{-12}
19	7.5780×10^{-10}	8.7797×10^{-11}
20	2.4786×10^{-10}	2.5131×10^{-14}
21	2.2384×10^{-13}	3.2176×10^{-16}
22	2.4600×10^{-14}	4.5038×10^{-17}
23	1.5699×10^{-14}	7.4791×10^{-17}
for isotope Pu ^{239}		
24	10.02	2.083×10^{-01}
25	0.6433	3.853×10^{-01}
26	0.2186	2.213×10^{-01}
27	0.1004	9.460×10^{-02}
28	0.03728	3.531×10^{-02}

TABLE M-2. (cont)
Decay-Heat Constants

Group	Decay Constant λ_j^H (s^{-1})	MeV of decay energy per fission per second ED_j (MeV/fission-s)
29	0.01435	2.292×10^{-02}
30	0.004549	3.946×10^{-03}
31	0.001328	1.317×10^{-03}
32	0.0005356	7.052×10^{-04}
33	0.0001730	1.432×10^{-04}
34	4.881×10^{-05}	1.765×10^{-05}
35	2.006×10^{-05}	7.347×10^{-06}
36	8.319×10^{-06}	1.747×10^{-06}
37	2.358×10^{-06}	5.481×10^{-07}
38	6.450×10^{-07}	1.671×10^{-07}
39	1.278×10^{-07}	2.112×10^{-08}
40	2.466×10^{-08}	2.996×10^{-09}
41	9.378×10^{-09}	5.107×10^{-11}
42	7.450×10^{-10}	5.703×10^{-11}
43	2.426×10^{-10}	4.138×10^{-14}
44	2.210×10^{-13}	1.088×10^{-15}
45	2.640×10^{-14}	2.454×10^{-17}
46	1.380×10^{-14}	7.557×10^{-17}
for isotope U^{238}		
47	3.2881	1.2311
48	0.93805	1.1486
49	0.37073	7.0701×10^{-01}
50	0.11118	2.5209×10^{-01}
51	0.036143	7.1870×10^{-02}
52	0.013272	2.8291×10^{-02}
53	0.0050133	6.8382×10^{-03}
54	0.0013655	1.2322×10^{-03}
55	0.00055158	6.8409×10^{-04}
56	0.00017873	1.6975×10^{-04}
57	4.9032×10^{-05}	2.4182×10^{-05}

TABLE M-2. (cont)
Decay-Heat Constants

Group	Decay Constant λ_j^H (s^{-1})	MeV of decay energy per fission per second ED_j (MeV/fission-s)
58	1.7058×10^{-05}	6.6356×10^{-06}
59	7.0465×10^{-06}	1.0075×10^{-06}
60	2.3190×10^{-06}	4.9894×10^{-07}
61	6.4480×10^{-07}	1.6352×10^{-07}
62	1.2649×10^{-07}	2.3355×10^{-08}
63	2.5548×10^{-08}	2.8094×10^{-09}
64	8.4782×10^{-09}	3.6236×10^{-11}
65	7.5130×10^{-10}	6.4577×10^{-11}
66	2.4188×10^{-10}	4.4963×10^{-14}
67	2.2739×10^{-13}	3.6654×10^{-16}
68	9.0536×10^{-14}	5.6293×10^{-17}
69	5.6293×10^{-15}	7.1602×10^{-17}

Substituting Eq. (M-12) into Eq. (M-7) and integrating the resulting equation analytically from $t = -t_L$ [where $C_i(-t_L) = 0$ is assumed] to $t = 0$ gives

$$C_i(0) = \frac{\beta_i}{\lambda_i \Lambda} \sum_{l=1}^{L-1} \left\{ \left(a_l - \frac{b_l}{\lambda_i} \right) (1 - \exp[-\lambda_i (t_{l+1} - t_l)]) + b_l (t_{l+1} \exp[-\lambda_i (t_{l+1} - t_l)] - t_l) \right\} \exp[-\lambda_i t_l] . \quad \text{(M-13)}$$

One obtains a similar expression for $H_j(0)$ by doing the same for Eq. (M-8). The expression for $H_j(0)$ is Eq. (M-13) with replacement of C_i by H_j, λ_i by λ_j^H, β_i by E_j, and Λ by 1. TRAC evaluates these two expressions for $C_i(0)$ and $H_j(0)$ when a fission-power-history table is input.

M.2.5. Reactivity Feedback

Subroutine RFDBK evaluates reactivity feedback. The reactivity-feedback model is based on the assumption that only changes in the core-averaged fuel temperature (T_f), coolant temperature (T_c), gas volume fraction (α), and solute mass (B_m, solute concentration in the coolant volume, or B_r, ratio of solute mass to liquid-coolant mass multiplied by 1×10^6) affect the neutron-multiplication reactivity of the reactor core. The code determines core-averaged values by applying a weighting factor defined as the fuel or coolant density times volume times power to the temperatures and solute ratio and a

weighting factor defined as the volume times power to the gas volume fraction and solute concentration. These factors approximate the product of the local adjoint flux, neutron flux, and volume. The (power)^2 is the neutron flux times the (fission cross section)^2. The neutron flux times the (fission cross section)^2 is approximating the adjoint flux. The adjoint flux is commonly called the importance function as applied in perturbation theory. The (fission cross section)^2 makes the neutron flux perform like the adjoint flux. This weighting-factor product, i.e., adjoint flux times neutron flux times volume, is from perturbation theory where it is used to spatially weight the change in reaction-rate cross sections to estimate their reactivity change. TRAC approximates this weighting-factor product by the product of the affecting-material mass (density times volume) and the fission-power density distribution raised to a user-specified power *POWEXP*.

The averaging process over the reactor core for the general reactivity-feedback parameter x is the following:

$$\bar{x} = \frac{\sum_i x_i \rho_i V_i P_i^{POWEXP}}{\sum_i \rho_i V_i P_i^{POWEXP}} , \qquad \text{(M-14)}$$

where P_i is the power and V_i is the volume of mesh cell i and the assumptions are over all cells in the reactor core. If x is T_f, T_c, or B_r, then ρ_i is the density of the fuel or coolant in cell i; if x is α or B_m, then ρ_i is set to 1.0 for all i.

For *POWEXP* = 1.0, the fission reaction-rate cross-section distribution approximates the adjoint-flux distribution. For *POWEXP* = 2.0, when the fission reaction-rate cross section is spatially constant, the neutron flux approximates the adjoint flux (Galerkin approximation). The appropriate value to use for *POWEXP* will depend on the fuel-loading distribution in the reactor core. Keep in mind, however, that two levels of approximation are being made. First, it is assumed that the affecting-material density times volume times the fission-power density distribution raised to the *POWEXP* power is a good approximation for the perturbation-theory product of the adjoint flux, neutron flux, and volume. Second, it is assumed that the theoretical basis for the use of that weighting factor for reaction-rate cross sections can be applied to the reactivity-feedback parameters that TRAC averages over the reactor core. The TRAC-M/F90 User's Manual (Ref. M-5.) suggests that *POWEXP* be set to 2.0 for the case where the core enrichment is radially constant. A *POWEXP*=1 value may be more appropriate for the case where the radial-power distribution is constant across the reactor core. The user has the option of replacing any of the three spatial shapes (fuel-rod radial, core horizontal plane, and core axial) in the fission-power density distribution with a different shape to weight the spatial averaging of reactivity-feedback parameters over the reactor core. These spatial-shape replacements are specified through input. The axial-power distribution can be input as a function of some user-defined independent variable. For example, if that independent variable is the programmed reactivity of the control rods, the effect of the control rods on the axial-power shape can be accounted for when the control rods are

inserted or withdrawn. An example of this is given in Section 4.3 of the TRAC-M/F90 User's Manual (Ref. M-5.).

The user defines a reactivity coefficient for each of the reactivity-feedback independent-variable parameters, $x = T_f$, T_c, α, and B_m or B_r, by choosing one of the reactivity-coefficient forms in Table M-3. Each reactivity coefficient is defined through input by a table of reactivity-coefficient values that are dependent on all four reactivity-feedback parameters. Each parameter has one or more values specified in defining the table. Defining one value for a parameter corresponds to the reactivity coefficient having no dependence on that reactivity-feedback parameter. Defining two or more values for a parameter gives the reactivity-coefficient dependence on one or more of the reactivity-feedback parameters. Linear interpolation is used to evaluate the reactivity coefficient for values of each parameter between its table values. Multidimensional linear-surface interpolation is performed when the reactivity coefficient is dependent on two or more of the reactivity-feedback parameters. An example of defining input data for the reactivity feedback model is given in Appendix I of the TRAC-M/F90 User's Manual (Ref. M-5.).

Solute in the derivative and solute dependence of a reactivity coefficient is defined in terms of the solute concentration in the coolant channel, B_m, in units of kg/m^3, a macroscopic density, or the solute mass to liquid-coolant mass ratio, B_r, in units of parts solute per million parts liquid coolant (ppm). The solute reactivity coefficient is based on the change in the amount of solute without changing T_c and α when the coefficient is defined as a derivative of B_r. The reactivity-coefficient derivative of B_m is affected by changes in T_c and α. Consequently, having the reactivity coefficient as a derivative of B_r is better if data are available. The solute dependence of a reactivity coefficient is important when the reactivity coefficient is sensitive to a shift in the neutron-energy spectrum. Through the proportionality to the amount of neutron capture in solute, the B_m- or B_r-dependence characterizes this shift. Cross-section/neutronics codes are needed to determine this dependence separate from TRAC.

TABLE M-3.
Reactivity-Coefficient Forms

Form Number	Reactivity-Coefficient Form
0	$\frac{\partial k}{\partial x}$
1	$\frac{1}{k}\frac{\partial k}{\partial x} \cong \frac{\partial R}{\partial x}$
2	$x\frac{\partial k}{\partial x}$
3	$\frac{x}{k}\frac{\partial k}{\partial x} \cong x\frac{\partial R}{\partial x}$

All forms of solute in the reactor core are included in the evaluation of B_m or B_r for solute dependence of the reactivity coefficients. Examples include dissolved boric acid in the liquid coolant, boric acid plated on core structure, borosilicate glass in burnable-poison pins, and boron oxide in control-rod-cluster pins. The first two forms are based on boric-acid convection into the reactor core throughout the modeled system and on plate-out of boric acid in the reactor core as a result of coolant dryout. For the latter two forms, the TRAC user defines the burnable-poison-pin and control-rod-cluster-pin forms through input with what would be their equivalent solute concentrations in the coolant channel. *BBP* or *BCR* define the equivalent concentration in the coolant. A first-order-polynomial function of the core-averaged coolant temperature T_c, the coefficients of which are input parameters, describes the equivalent burnable-poison-pin solute concentration as

$$BPP = BPP0 + BPP1 \cdot T_c \ . \tag{M-15}$$

Whereas the physical amount of solute in the burnable-poison pins is constant during the transient, its effective concentration for neutron capture increases with coolant temperature because of reduced spatial self-shielding of solute to neutrons in those pins. The amount of control-rod-cluster-pin solute in the reactor core depends on the amount of control-rod insertion into the core. Its effective concentration is input as a first-order-polynomial function of programmed reactivity R_{prog} as follows:

$$BCR = BCR0 + BCR1 \cdot R_{prog} \ . \tag{M-16}$$

Both *BPP* and *BCR* in the previous two equations have units of macroscopic solute density ($kg \cdot m^{-3}$) in the coolant-channel volume. Programmed reactivity is assumed to be proportional to the amount of effective solute-mass change caused by control-rod movement in the core. Initially, when the reactor core is at steady-state conditions, *BCR = BCR0*.

Only the dissolved boric acid and that plated on solid structures in the reactor core are included in the evaluation of B_m or B_r for the solute reactivity-coefficient derivative parameter because the amount of solute in burnable-poison pins is constant during the transient that is being evaluated. Control-rod movement changes the amount of solute, but the reactivity change associated with this movement is accounted for in the user-defined programmed reactivity R_{prog}. There is no reactivity feedback from control-rod movement because it is already accounted for in R_{prog}.

After all four reactivity coefficients are evaluated by linear interpolation in their four dimensionally dependent tables, feedback reactivity is evaluated in terms of its change in the neutron multiplication constant over the last time step, $\Delta t^{n-1} = t^n - t^{n-1}$,

$$k^n R^n_{fdbk} = \sum_{j=1}^{n} (\Delta k_{fdbk})^j \tag{M-17}$$

where

$$(\Delta k_{fdbk})^j = \sum_{j=1}^{4} \frac{1}{2}\left[\left(\frac{\partial k}{\partial x_i}\right)^j + \left(\frac{\partial k}{\partial x_i}\right)^{j-1}\right] \times [x_i^j - x_i^{j-1}] \ ,$$

x_1 is T_f, x_2 is T_c, x_3 is α, and x_4 is B_m or B_r. The superscripts n and $n-1$ indicate that the parameter is evaluated at the beginning of the current time step and at the beginning of the previous time step, respectively. There are four reactivity-coefficient-defining forms in Table M-3. Forms 1, 2, and 3 as input are converted to form 0 by TRAC for use in Eq. (M-17). TRAC obtains the value of $(\partial k / \partial x_i)^n$ in Eq. (M-17) by multiplying the reactivity coefficients defined by reactivity-coefficient forms 1, 2, and 3 (Table M-3.) by k^{n-1}, $1 / x_i^n$, and k^{n-1} / x_i^n, respectively. Using k^{n-1} rather than k^n (which is not yet known) to convert reactivity-coefficient forms 1 and 3 to $\partial k / \partial x_i$ is an approximation. The values of $\partial k / \partial x_i$ and x_i at time t^n (the start of the present time step) are evaluated as described above; their values at time t^{n-1} are those saved from their evaluation at the start of the previous time step.

The change in x_i over the last time step (with the other x_i parameters held constant in defining the reactivity coefficient) is defined in the last factor of Eq. (M-17). The term B_m or B_r includes only dissolved boric acid in the liquid coolant and boric acid plated on the core structure. There is no change in the B_r-equivalent solute concentration in burnable-poison pins when T_f, T_c, and α are not considered to vary.

To determine reactivity feedback during the current time step $\Delta t^n = t^{n+1} - t^n$, TRAC would need to know the end-of-time-step values of T_f, T_c, α, B_m or B_r. To evaluate that reactor-core state requires knowing the current core state and the total energy-generation rate, $P_{eff}(t)$, over the time step Δt^n. The neutronic reactivity $R(t)$ defined by the reactivity-feedback contribution, $R_{fdbk}(t)$ must be known to determine the value of $P_{eff}(t)$ from the solution of the point-reactor-kinetics equations. Thus, the evaluation of reactivity feedback during the current time step requires first knowing the time-step solution.

The TRAC code handles this difficulty of needing to know the reactivity feedback in order to evaluate it in time step Δt^n by assuming the Δk feedback-reactivity rate is zero. The Δk programmed-reactivity rate is assumed to be the same as in the previous time step, Δt^{n-1},

$$(\Delta k_{prog}^{\text{est}})^{n+1} = \Delta t^n \left\{ \frac{\Delta k_{prog}^n}{\Delta t^{n-1}} \right\} . \qquad \text{(M-18)}$$

We estimate $(k_{prog})^n$ because the input-defined independent variable needed to evaluate its tabular definition at t^{n+1} is a function of the reactor-core state that is known at time t^n. We have tested a similar approximation for $(\Delta k^{est}_{prog})^n$ in TRAC, but near steady state it caused the sign of $(\Delta k^{est}_{fdbk})^n$ to change each time step. It is better to assume that $(\Delta k^{est}_{fdbk})^n$ is zero than to estimate its value based on its value in the previous time step. Feedback effects for each time step are more tightly coupled to $(\Delta k^{est}_{fdbk})^n$ than to $(\Delta k^{est}_{prog})^n$, which causes the former estimate to be numerically unstable in some situations. Thus, estimates for the neutron-multiplication constant and neutronic reactivity for the reactor state at the end of the present time step are

$$(k^{est})^{n+1} = k^n + (\Delta k^{est}_{prog})^{n+1} \tag{M-19}$$

and

$$(R^{est})^{n+1} = \frac{[(k^{est})^{n+1} - 1]}{(k^{est})^{n+1}} \tag{M-20}$$

After each Δt^{n+1} time-step solution, TRAC compares the actual programmed reactivity with its estimated value. The code corrects any discrepancy by applying

$$(\Delta k^{cor})^n = [(\Delta k_{prog})^n - (\Delta k^{est}_{prog})^n] \cdot \min\left(\frac{\Delta t^{n-1}}{\Delta t^n}, 2\right) \tag{M-21}$$

during the next time step, Δt^n. To prevent a time-step reactivity correction from becoming very large by applying it over a time step $\Delta t^n << \Delta t^{n-1}$, TRAC constrains $(\Delta k^{cor})^n$ in Eq. (M-21) to be no more than twice the Δt^{n-1} time-step value. Including this correction in Δk from the previous time step in the neutron-multiplication constant end-of-time-step estimate at t^{n+1} gives Eq. (M-19) in the modified form,

$$(k^{est})^{n+1} = k^n + (\Delta k^{est}_{prog})^{n+1} + (\Delta k^{cor})^n , \tag{M-22}$$

where

$$k^n = k^{n-1} + (\Delta k_{prog})^n + (\Delta k_{fdbk})^n .$$

In this procedure, we assume that $(\Delta k^{cor})^n$ and $(\Delta k_{fdbk})^{n-1}$ are small enough not to require an iterative evaluation of the present time-step solution and that $(\Delta k^{cor})^n$ is large enough to be included in the next time-step solution rather than be neglected. The code applies a similar estimate and correction procedure to the end-of-time-step power for the case in which the total reactor-core power is specified directly by a table.

M.2.6. Solution of the Point-Reactor Kinetics

The code solves the point-reactor-kinetics equations [Eqs. (M-6) through (M-8)] by the Kaganove method (Ref. M-3.). Its derivation in Ref. M-3. approximates the time dependence of P and $k_{ex} = k - 1 = R/(1-R)$ over each integration time step by second-order polynomials and assumes $\Lambda(t) = l/\left[1+k_{ex}(t)\right]$ where l is a constant. For TRAC, it is more appropriate to approximate the time dependence of P by a second-order polynomial, R by a first-order polynomial, and Λ by a constant because TRAC linearly extrapolates its estimate of $R(t)$ over the fluid-dynamics time step to be evaluated and because the weak time dependence of Λ generally is unknown. These modified assumptions, when applied to the point-reactor-kinetics equations, simplify the form that these equations take when analytically integrated over the neutronics integration time step Δt. The derivation of those analytically integrated equations follows. TRAC then evaluates them for $\Delta t^n / \Delta t$ integration time steps during the Δt^n fluid-dynamics time step.

Currently in TRAC, the neutronics solution is done before the hydraulic and heat-conduction solutions. Otherwise, the linear extrapolation estimates on the previous page would not have to be done if the hydraulic and heat-conduction solutions were done first. The heat-conduction solution would be more implicit if it were done after the neutronics solution. A preferred order would be to do the hydraulics solution first, the neutronics solution next, and then the heat-conduction solution.

We assume that

$$P(t) = P(0) + P_1 t + P_2 t^2 \quad , \tag{M-23}$$

$$R(t) = R(0) + R_1 t \quad , \tag{M-24}$$

and

Λ, λ_i, β_i, λ_j^H, and E_j are constant for $0 \le t \le \Delta t$,

where

$P(0)$, $R(0)$, and $R(1) = [(R^{est})^n - R(0)]/\Delta t^n$ are known values.

Solving Eq. (M-7) for $C_i(t)$ in terms of a functional of the fission power $P(t)$ gives

$$C_i(t) = C_i(0)\exp\left[-\lambda_i t\right] + \frac{\beta_i}{\Lambda}\int_0^t \exp\left[-\lambda_i(t-\tau)\right] P(\tau)d\tau \quad . \tag{M-25}$$

Substituting Eq. (M-25) into Eq. (M-6) and integrating the resulting equation term-by-term gives

$$P(t) = P(0) + \int_0^t \frac{R(\tau)P(\tau)}{\Lambda} d\tau - \sum_{i=1}^{I} \frac{\beta_i}{\Lambda} \int_0^t \exp\,[-\lambda_i (t-\tau)] P(\tau) d\tau$$

$$+ \sum_{i=1}^{I} C_i(0)\,[1 - \exp\,(-\lambda_i t)] + \frac{S}{\Lambda}\left[1 - R(0)t - R_1 \frac{t^2}{2}\right] . \qquad \text{(M-26)}$$

Substituting Eq. (M-23) for $P(\tau)$ and Eq. (M-24) for $R(\tau)$ in Eq. (M-26), evaluating the integrals, and rearranging the resulting equation in terms of the P_1 and P_2 unknowns gives

$$a_1(t)P_1 + a_2(t)P_2 = q(t) , \qquad \text{(M-27)}$$

where

$$a_1(t) = t\Lambda - t^2\left[\frac{1}{2}R(0) + \frac{1}{3}R_1 t\right] + \sum_{i\,=\,1}^{I} \beta_i t^2 I_{i1}(t) ,$$

$$a_2(t) = t^2\Lambda - t^3\left[\frac{1}{3}R(0) + \frac{1}{4}R_1 t\right] + \sum_{i\,=\,1}^{I} \beta_i t^3 I_{i2}(t) ,$$

$$q(t) = S + t\left[R(0) + \frac{1}{2}R_1 t\right][P(0) - S] + \sum_{i\,=\,1}^{I} [\Lambda\lambda_i C_i(0) - \beta_i P(0)]\, t I_{i0}(t) ,$$

and

$$I_{im}(t) = \frac{\int_0^t \exp\,[-\lambda_i (t-\tau)]\tau^m d\tau}{t^{m+1}} , \qquad \text{for } m = 0, 1, 2 .$$

The P_1 and P_2 polynomial coefficients are evaluated by requiring Eq. (M-27) to be satisfied for $t = \Delta t$ (at the end of the integration time step) and $t = \Delta t/2$ (at the midpoint of the integration time step). Solving the two equations

$$a_1(\Delta t)P_1 + a_2(\Delta t)P_2 = q(\Delta t) \qquad \text{(M-28)}$$

and

$$a_1\left(\frac{\Delta t}{2}\right)P_1 + a_2\left(\frac{\Delta t}{2}\right)P_2 = q\left(\frac{\Delta t}{2}\right) \tag{M-29}$$

for P_1 and P_2 gives

$$P_1 = \frac{\left[q(\Delta t)a_2(\frac{\Delta t}{2}) - q(\frac{\Delta t}{2})a_2(\Delta t)\right]}{D} \tag{M-30}$$

and

$$P_2 = \frac{\left[q(\frac{\Delta t}{2})a_1(\Delta t) - q(\Delta t)a_1(\frac{\Delta t}{2})\right]}{D}\ , \tag{M-31}$$

where

$$D = a_1(\Delta t)a_2\left(\frac{\Delta t}{2}\right) - a_1\left(\frac{\Delta t}{2}\right)a_2(\Delta t)\ .$$

The total fission power at the end of the integration time step $t = \Delta t$ from Eq. (M-23) is

$$P(\Delta t)\ =\ P(0) + P_1\Delta t + P_2\Delta t^2\ . \tag{M-32}$$

If we know $P(t)$ for $0 \le t \le \Delta t$, we can evaluate $C_i(\Delta t)$ by substituting Eq. (M-23) into Eq. (M-25) and using

$$\Delta t I_{i0}(\Delta t) = \frac{1 - \exp(-\lambda_i \Delta t)}{\lambda_i}$$

by analytically integrating its definition in Eq. (M-27) as follows:

$$C_i(\Delta t) = C_i(0)[1 - \lambda_i \Delta t I_{i0}(\Delta t)] + \frac{\beta_i}{\Lambda}[P(0)\Delta t I_{i0}(\Delta t)$$

$$+P_1\Delta t^2 I_{i1}(\Delta t) + P_2\Delta t^3 I_{i2}(\Delta t)] \text{ for } i = 1, 2, \ldots, I. \tag{M-33}$$

The code evaluates the decay-heat equations in the same way to give

$$H_j(\Delta t) = H_j(0)[1 - \lambda_j^H \Delta t I_{j0}(\Delta t)] + E_j[P(0)\Delta t I_{j0}(\Delta t)$$

$$+ P_1 \Delta t^2 I_{j1}(\Delta t) + P_2 \Delta t^3 I_{j2}(\Delta t)] \text{ for } j = 1, 2, \ldots, J, \qquad \text{(M-34)}$$

where

$$\Delta t^{m+1} I_{jm}(\Delta t) = \int_0^{\Delta t} \exp\left[-\lambda_j^H (\Delta t - \tau)\right] \tau^m d\tau \ .$$

The code evaluates $\Delta t^{m+1} I_{im}(\Delta t)$ with the following recursion relation:

$$\Delta t^{m+1} I_{im}(\Delta t) = \frac{\Delta t^m - m \Delta t^m I_{im-1}(\Delta t)}{\lambda_i} \ , \qquad \text{for } m = 1, 2 \qquad \text{(M-35)}$$

once

$$\Delta t I_{i0}(\Delta t) \frac{1 - \exp(\lambda_i \Delta t)}{\lambda_i}$$

is first evaluated. For $\lambda_i \Delta t << 1$, Eq. (M-35) results in the loss of several least-significant digits of accuracy with each application of the recursion formula. Thus, for $\lambda_i \Delta t < 1$, TRAC first evaluates $\Delta t^3 I_{i2}(\Delta t)$ using the Maclaurin expansion,

$$\Delta t^{m+1} I_{im}(\Delta t) = \Delta t^{m+1} m! \left[\frac{1}{(m+1)!} - \frac{\lambda_i \Delta t}{(m+2)!} + \frac{(\lambda_i \Delta t)^2}{(m+3)!} - \ \ldots \right] \qquad \text{(M-36)}$$

for $m = 2$, and then evaluates the reciprocal of the Eq. (M-35),

$$\Delta t^m I_{im-1}(\Delta t) = \frac{\Delta t^m - \lambda_i \Delta t^{m+1} I_{im}(\Delta t)}{m} \text{ for } m = 2, 1. \qquad \text{(M-37)}$$

The accuracy of the second-order polynomial approximation for $P(t)$ can be increased by decreasing the integration time-step size Δt. We would like Δt to be as large as possible, however, while we maintain a desired level of accuracy in approximating $P(t)$. To achieve this, the following procedure for automatically adjusting the reactor-kinetics time step in TRAC is used. In the same manner that Eqs. (M-28) and (M-29) were defined, Eq. (M-27) also could be required to be satisfied at $t = \Delta t \ / \ 4$ by

$$a_1\left(\frac{\Delta t}{4}\right)P_1 + a_2\left(\frac{\Delta t}{4}\right)P_2 = q\left(\frac{\Delta t}{4}\right) . \qquad \text{(M-38)}$$

The above equation together with Eq. (M-29), which is evaluated at $t = \Delta t / 2$, are solved over the time range $0 \le t \le \Delta t / 2$ for $P_1 = P_1^*$ and $P_2 = P_2^*$ to give

$$P_1^* = \frac{q\left(\frac{\Delta t}{2}\right)a_2\left(\frac{\Delta t}{4}\right) - q\left(\frac{\Delta t}{4}\right)a_2\left(\frac{\Delta t}{2}\right)}{D^*} \qquad \text{(M-39)}$$

and

$$P_2^* = \frac{q\left(\frac{\Delta t}{4}\right)a_1\left(\frac{\Delta t}{2}\right) - q\left(\frac{\Delta t}{2}\right)a_1\left(\frac{\Delta t}{4}\right)}{D^*} \quad , \qquad \text{(M-40)}$$

where

$$D^* = a_1\left(\frac{\Delta t}{2}\right)a_2\left(\frac{\Delta t}{4}\right) - a_1\left(\frac{\Delta t}{4}\right)a_2\left(\frac{\Delta t}{2}\right) \quad .$$

This solution over half the integration time step provides a more accurate value for $P(t)$ at $t = \Delta t / 2$,

$$P^*\left(\frac{\Delta t}{2}\right) = P(0) + P_1^*\left(\frac{\Delta t}{2}\right) + P_2^*\left(\frac{\Delta t}{2}\right)^2 \quad , \qquad \text{(M-41)}$$

than the solution over the full integration time step at $t = \Delta t / 2$,

$$P\left(\frac{\Delta t}{2}\right) = P(0) + P_1\left(\frac{\Delta t}{2}\right) + P_2\left(\frac{\Delta t}{2}\right)^2 \quad . \qquad \text{(M-42)}$$

The code uses the difference between these two values as a measure of the error in the solution over the full integration time step Δt

$$\varepsilon(\Delta t) = \left| \frac{P\left(\frac{\Delta t}{2}\right) - P^*\left(\frac{\Delta t}{2}\right)}{P^*\left(\frac{\Delta t}{2}\right)} \right| \quad . \qquad \text{(M-43)}$$

It is desirable to increase Δt if the above ε is too small and to decrease Δt if ε is too large. Toward this end, the code defines two error bounds, ε_1 and ε_2 , to provide the desired convergence such that,

1. if $\varepsilon_1 < \varepsilon(\Delta t) < \varepsilon_2$, the code maintains the present value of reactor-kinetics time step Δt;
2. if $\varepsilon_1 < \varepsilon_2 \le \varepsilon(\Delta t)$, the code halves the value of Δt because the error in $P(\Delta t)$ is too large; and
3. if $\varepsilon(\Delta t) \le \varepsilon_1 < \varepsilon_2$, the code doubles the value of Δt because the error in $P(\Delta t)$ is too small.

When Δt is halved, the integration time step is reevaluated. When the third criterion is satisfied, the number of remaining integration time steps to be evaluated over the fluid-dynamics time step must be an even number for the integration time step to be doubled (and the number of remaining integration time steps to be halved). TRAC is programmed to use $\varepsilon_1 = 10^{-6}$ and $\varepsilon_2 = 10^{-4}$. A numerical study showed these values to yield a maximum fractional error less than 10^{-4} and an average fractional error less than 10^{-5} in the fission power solution. The point-reactor-kinetics solution required < 1% of TRAC execution time.

M.3. Conclusions Regarding the Reactor-Core Power Model

The core-power model in TRAC, with all the options and features, has proved to be sufficiently general for describing the core assemblies in most of the reactor-safety-related experiments, particularly ones that are integral in nature, and in reactor plants, provided that the power shape only changes in time in the axial direction. For this to be true, the axial-power shape must be specified as a function of some user-defined independent variable for the axial-power-shape table. The option to specify core power directly with a tabular prescription is generally sufficient for modeling most transients of interest where the power-level behavior is known.

The point-reactor kinetics with reactivity feedback has demonstrated in many cases of the TRAC developmental assessment problem set the ability to describe the transient power response of a reactor core. For example, in the case of anticipated transients without scram, the core-power behavior would not be known because of reactivity-feedback effects, and in this case, reactor kinetics is a necessary capability. In analyzing experiments from the LOFT facility (for example, the L6-1 test simulating a loss-of-steam-load transient) and transients from power plants (for example, the Zion PWR standard test problem), reactor kinetics has demonstrated a good predictive capability. For performing best-estimate analyses of large-break LOCAs, reactor kinetics has demonstrated the ability to predict the shutdown of core power by core voiding before the control-rod scram is effective.

The deficiencies of the core-power model are principally related to the fact that reactor kinetics is based on a point-reactor assumption, and the power distribution is defined by a superposition of fuel-rod-radial, core-axial, and (r, θ)-plane shapes. Axial-shape changes in the power distribution with a known dependence can be simulated, but

fuel-rod-radial and core (r, θ)-plane power-shape changes and power distributions that are not definable by superimposed fuel-rod-radial, core-axial, and (r, θ)-plane shapes cannot be modeled. Reactivity feedback is also based on the point-reactor assumption with little theoretical justification for the procedure used to core average the reactivity-feedback parameters. Asymmetric and localized reactivity-feedback effects and control-rod movements in the reactor core cannot be modeled accurately. However, within these modeling limitations, the core-power model is accurate and efficient in determining the time-dependent behavior of the reactor-core power. To further assess the point-kinetics model requires having good core neutronics data (power shape, reactivity coefficients, etc.) and use of neutronics codes to generate the point-kinetics input data.

REFERENCES

M-1. "Reactor Physics Constants," Argonne National Laboratory report ANL-5800, 2nd ed. (July 1963).

M-2. A. Rodkowsky, Ed., "Naval Reactors Physics Handbook, Vol. 1: Selected Basic Techniques," Library of Congress Number 65-60008 (1964).

M-3. J. J. Kaganove, "Numerical Solution of the One-Group Space-Independent Reactor Kinetics Equations for Neutron Density Given the Excess Reactivity," Argonne National Laboratory report ANL-6132 (1960).

M-4. "American National Standard for Decay Heat Power in Light Water Reactors," American Nuclear Society publication ANSI/ANS-5.1 (1979).

M-5. R. G. Steinke, V. Martinez, N. M. Schnurr, J. W. Spore, and J. V. Valdez, "TRAC-M Fortran 90 (Version 3.0) User's Manual," Los Alamos National Laboratory document LA-UR-00-835 (February 2000).

APPENDIX N

CONTROL PROCEDURE

In this appendix, the description of the control procedure is directly related to the Fortran coding. Consequently, very few equations and symbols are used. The variables are usually described using mnemonics, quite often through a generalized format. Almost all the variables are locally applicable within this appendix with little (if any) reference to other sections. We believe that the description provided for these variables within the text is satisfactory and no additional nomenclature is necessary at the beginning of the section.

This appendix first discusses the general forms of component-action tables and rate-factor tables. Following this discussion are detailed descriptions of TRAC's signal-variable, control-block, trip, and control-parameter evaluation logic. Finally, TRAC's special logic for steady-state evaluation is presented.

N.1. Component-Action Table

Modeling a component's adjustable-hardware action is done by means of a component-action table specified through the component input data. The table defines the component hardware action as a tabular function of an independent variable defined by physical-system parameters. These parameters monitored from the PWR physical-system model are called signal variables in TRAC. They can be applied as the component-action table's independent variable directly or after having been operated on by function operators called control blocks. In this section, the independent variable that is discussed is the independent variable of the component-action table.

Determining a hardware action by evaluating its component-action table is based on a component-action-type option parameter. Its Fortran variable name has the general form IXXXTY where letters XXX are to be replaced by one to three letters characterizing the component action. Those letters for each of the actions in Table N-1. (a replica of Table 2-1.) are shown in the far right column. Through the option parameter, the user specifies if the action is to be held constant, evaluated at all times from the component-action table, or evaluated from the component-action table only when an assigned controlling trip switch is ON and held constant when the trip is OFF. If the component-action table is to be evaluated under trip control, a trip ID number with general-form variable name IXXXTR is specified as part of the component input data. The actual definition of the trip with the ID number label referenced here is specified in the trip input-data section located elsewhere in the input-data file. When IXXXTY defines no trip control for evaluating the component-action table, IXXXTR should be defined by zero or by a blank field on input.

TABLE N-1.
Adjustable Component Hardware
Actions by the Control Procedure

Actions	Components	Variable -Name Letters
Pressure boundary condition and fluid state	BREAK	B
Velocity or mass-flow boundary condition and fluid state	FILL	F
Reactor-core programmed reactivity or power	HEAT STRUCTURE	RPW
Reactor-core axial-power shape	HEAT STRUCTURE	ZPW
Energy deposition in the coolant	PIPE, TEE, TURBINE	POW or PW
Energy generation in the wall	PIPE, PUMP, TEE, VALVE	QP3 or QP
Pump rotational speed	PUMP	PMP or OMG
Turbine power demand	TURBINE	TRB or POP
Valve flow-area fraction or relative stem position	VALVE	V

The independent variable is defined by physical-system parameters in the form of a signal variable or a control-block output variable. The variable to be used is defined by its ID number with the general Fortran variable name IXXXSV. Positive ID numbers define signal variables; negative ID numbers define control-block output variables. Signal variables and control blocks are described in Sections N.3. and N.4.

The number of entry pairs (independent-variable value, component-action value) of tabular input data defining the component-action table is specified by the general Fortran variable name NXXXTB. A plus or minus sign is applied to its value to define the form of the independent variable. When NXXXTB is positive, the independent variable is the IXXXSV parameter. When NXXXTB is negative, the independent variable is the change in the value of the IXXXSV variable during the time the table is evaluated. For this latter form, the initial value of the component action corresponds to the component-action value in the table with an independent-variable value of zero. Internal to TRAC, the change in the IXXXSV variable value is incorporated into the table's abscissa-coordinate values during each time step the table is evaluated by translation of all the abscissa-coordinate (independent-variable) values in the table. As a result, the last interpolated component-action value from the table will correspond to the independent

variable having a value of zero after translation. The user does not need to be concerned with this internal translation of the table's abscissa-coordinate values by TRAC. The only time its effect can be seen by the user is when the component-action table is output on restart. The user only needs to be concerned with initially defining a $NXXXTB < 0$ table with the initial component-action value corresponding to the abscissa-coordinate value of zero.

When a $NXXXTB < 0$ table is to be evaluated under trip control, the change in the IXXXSV variable value over each time step is further multiplied by the value of the controlling trip ON / OFF set status. Fortran variable ISET defines the trip set status. OFF has the value 0, and the two forms of ON, $ON_{forward}$ and $ON_{reverse}$, have values +1 and -1, respectively. Because the component-action table under trip control is only evaluated when the trip is ON, ISET has the value +1 or -1 when the change in the IXXXSV variable value is multiplied by it to evaluate the independent variable. Hence, the trip set-status value affects the direction of interpolated movement in the table. The forward and reverse subscripts for ON correspond to the direction of the interpolated movement action.

The effect the values for IXXXTR, IXXXSV, and NXXXTB has on defining the independent variable are summarized in Table N-2. Evaluation of the component-action table is trip controlled when $IXXXTR \neq 0$. No component-action table is defined (the component action is held constant) when $IXXXSV = 0$ is input. When $NXXXTB < 0$ is input with $IXXXSV \neq 0$, a table is defined, but it has no tabular data. This is a special case where the component action is defined directly by its independent-variable form, that is, a signal variable $(IXXXSV > 0)$ or a control-block output variable $(IXXXSV < 0)$.

TABLE N-2.
Defined Forms of the Component-Action Table's Independent Variable

Component-Action Table's Defining Variables			Component-Action Table's Independent-Variable Form [a]
IXXXTR	**IXXXSV**	**NXXXTB**	
All values	>0	≥0	A
0	>0	<0	DA
≠0	>0	<0	DA*ISET
All values	<0	≥0	B
0	<0	<0	DB
≠	<0	<0	DB*ISET

a. A is a signal variable; B is a control-block output variable.

In the above definition, the direction of interpolation in the component-action table can be trip controlled when $IXXXTR \neq 0$ and $NXXXTB < 0$. The trip set-status value (± 1) is applied to the magnitude of the movement defined by the change in the signal variable or control-block output variable. In most situations, this form is sufficient for modeling the component-action's independent variable. There are a few situations, however, where the user would like further control over the magnitude of the interpolated movement. The user can do this either with a connected series of control-block operators defining the independent variable or by applying a rate factor to the independent-variable forms in Table N-2. Operating on a parameter signal (signal-variable value) with a connected series of control blocks and defining the independent-variable form with the last control-block output variable are extended applications of one of the last three forms in Table N-2. Applying a rate factor to any one of the six forms is a direct adjustment to the rate of interpolated movement when evaluating the component-action table.

N.2. Rate-Factor Table

A rate factor can be applied to the component-action table's independent variable by entering a rate-factor table of tabular data. Specifying a rate-factor table requires that its component-action table be defined ($IXXXSV \neq 0$) and that the user decide to apply a rate factor to the independent-variable form in Table N-2.

Fortran variables NXXXSV and NXXXRF define a rate-factor table in the same way that IXXXSV and NXXXTB, respectively, define the component-action table. In addition to the six independent-variable forms in Table N-2., entering $IXXXTR \neq 0$, NXXXSV = 0, and $NXXXRF \neq 0$ defines the independent-variable form for the rate-factor table to be the difference between the trip-signal value and the trip set-point value that turns the trip OFF. This additional form provides a convenient means for adjusting the rate of interpolated movement in the component-action table. The further the trip signal departs from its desired value, specified by its set-point value that turns the trip OFF, the larger the rate factor and the faster the component action can be adjusted in order to return the trip signal to its desired value. Section N.5., describing how trips are defined, clarifies the explanation for the above form.

When a rate-factor table is defined, the procedure for evaluating the component-action value is as follows. First, TRAC evaluates the rate-factor table's independent-variable value (defined by IXXXTR, NXXXSV, and NXXXRF). The value is then used to linearly interpolate in the rate-factor table (when $NXXXRF \neq 0$) or define directly (when NXXXRF = 0) the rate-factor value. Next, the component-action table's independent-variable value (defined by IXXXTR, IXXXSV, and NXXXTB) is evaluated and multiplied by the rate factor. This product value is used to interpolate linearly in the component-action table (when $NXXXTB \neq 0$) or define directly (when NXXXTB = 0) the component-action value. The component hardware action in the modeled PWR system is then defined with this value. This procedure is evaluated at the beginning of each time step with the current state of the system parameters to evaluate the independent-variable forms for both tables. Not defining a rate-factor table (NXXXSV = 0 and NXXXRF = 0 are

input) reduces the above procedure to evaluating the component-action table's independent-variable value and then using that value to interpolate linearly in the component-action table or define directly the component-action value.

The component-action table and rate-factor table defining variables IXXXTR, IXXXSV, NXXXTB, NXXXSV, and NXXXRF are specified in that order on one input-data card. There is such a card for each type of component action in the component input data unless the IXXXTY option specifies that the component action is to be held constant. Then neither component-action tables nor defining variables are input. There is also a second input-data card defining the component action with the following real-valued general-form variables: XXXIN, XXXOFF, RXXXMX, and XXXSCL. Variable XXXIN defines the initial value for the component action. This value is used when the component action is to be held constant or when the user is evaluating the component action under trip control and the trip is initially OFF. For component actions that are trip controlled, variable XXXOFF defines the component-action value that is used when the trip is OFF after having been ON. Entering XXXOFF = -1×10^{19} defaults TRAC to using the last component-action value evaluated when the trip was ON. Variable RXXXMX defines the maximum rate of change of the component-action value allowed by the user during the simulation. When the component action evaluated from the table varies faster than this maximum rate, the component action is redefined to vary at the maximum rate. Later when the rate of change of the table-evaluated component action falls below the maximum rate, the applied component-action value will be able to catch up to the value determined from the table. Variable XXXSCL is a scale factor to be applied during input to the component-action values in its input table.

The component-action table (with |NXXXTB|*2 values) and its rate-factor table (with |NXXXRF|*2 values) are input in the array data section of the component input. All component-action tables, with two exceptions, have one component-action value for each independent-variable value. Thus, there are two values for each of the |NXXXTB| entry pairs in their tabular data. The two exceptions are the axial-power-shape and the energy-generation-in-the-wall component-action tables. Corresponding to each independent-variable value is an axial-power shape with a relative-power value at each axial interface in the reactor-core model or a QPPP-factor shape with a QPPP-factor value for each mesh cell in the component model.

This section has discussed application of the component-action table in its general form. The XXX letters in all the Fortran variable names defined will need to be replaced by the component action's one to three letters in Table N-1. to give the Fortran variable names. A main point to recognize from this section is that there is one form to the numerical model for applying adjustable control to a component action, even though there are nine different component hardware actions that can be modeled. Understanding the general definition of control variables IXXXTY, IXXXTR, IXXXSV, NXXXTB, NXXXSV, NXXXRF, XXXIN, XXXOFF, RXXXMX, and XXXSCL gives the user the ability to model the dynamics of a myriad of possible control procedures encountered in PWR operation. The next four sections on signal variables, control blocks, trips, and ordered evaluation

of control parameters go into the details of the definition of these tools used to model the control procedure.

N.3. Signal Variables

Signal variables are PWR-modeled system parameters that the TRAC user defines for the control-procedure model to use to determine the adjustment of component hardware actions. Signal variables have their values determined by TRAC at the beginning of each time step and are based on the state of the modeled system. Their values are used in the control procedure to determine the magnitudes of adjustable component hardware actions, which are then applied over the time step. This procedure approximates the magnitudes of the signal variables and component actions as being constant over the time step with step changes at the beginning of each time step. In reality, they vary continuously. Using smaller time steps approximates this more accurately. With the stability-enhanced, two-step, hydrodynamic solution method in TRAC, large time steps are possible. When evaluating with large time steps, control adjustment will be numerically delayed in time by a fraction of a time step. Both the satisfied trip criteria for starting an action and the evaluated dependence that determines the action's magnitude encounter a fractional time-step lag. It is the accumulation of the effects of these time lags that can contribute a significant error when simulating a control procedure that the TRAC user needs to be concerned about.

A unique, positive identification number assigned to Fortran variable name IDSV is defined by the TRAC user for each signal variable. This number serves as the signal-variable label for referencing the use of its value within the control procedure. There are 88 PWR-modeled system parameters that are definable as signal variables. Those signal-variable parameters are listed in Table N-3. Each parameter is defined by a parameter number assigned to Fortran variable name ISVN when a signal variable is defined. Parameter number 0 is problem time defined by Fortran variable names ETIME (beginning-of-time-step problem time), DTO (previous time-step size), or DELT (present time-step size). Parameter numbers 1 through 17 are as yet undefined parameters that the user may program TRAC to determine. Any system parameter can have its value assigned to either of these parameter numbers by programming their value assignment in subroutine SVSET. The remaining system parameters in Table N-3. (except for 55 and 56) are defined for a specific component. Column 2 in Table N-3. shows which component types (1D for the 1D hydro components, 3D for the 3D vessel hydro components, and HS for the heat-structure component) that each signal-variable parameter can be defined for. Parameter numbers 20 through 40 and 65 through 101 require one or two cell / interface or node-cell / node-row numbers ($cell_{\#}$ / $iface_{\#}$ or $ncell_{\#}$ / $nrow_{\#}$) to further delimit the location in the component where the parameter is defined. Parameter numbers 55 and 56 are trip parameters that, when defined as signal variables, can be used for other control purposes.

,

TABLE N-3.
Signal-Variable Parameters

Signal-Variable Parameter No.	Defined For	Parameter Description	Input Location Numbers
0	Global	Problem time (s)	–1 (dto), 0(time), 1(dt)
1–17		Undefined	
18	HS	Reactor power (W, Btu / hr)	Component
19	HS	Reactor-power period (s)	Component
20	1D, 3D	Liquid level (m, ft)	Component, Cell1, Cell2
21	1D, 3D	Cell pressure (Pa, psia)	Component, Cell1, Cell2
22	1D, 3D	Cell gas temperature (K, °F)	Component, $Cell_1$, $Cell_2$
23	1D, 3D	Cell liquid temperature (K, °F)	Component, Cell1, $Cell_2$
24	ID	Slab inner-surface temperature (K, °F)	Component, $Cell_1$, $Cell_2$
25	HS	Slab / rod surface temperature (K, °F)	Component, $Nrow_1$, $Nrow_2$
26	HS	Slab / rod temperature (K, °F)	Component, $Nrow_1$, $Nrow_2$
27	1D, 3D	Cell gas volume fraction	Component, $Cell_1$, $Cell_2$
28	3D	Yθ-face gas mass flow (kg/s, lb_m/hr)	Component, $Iface_1$, $Iface_2$
29	1D, 3D	Z-face gas mass flow (kg / s, lbm / hr)	Component, $Iface_1$, $Iface_2$
30	3D	XR-face gas mass flow (kg/s, lb_m/hr)	Component, $Iface_1$, $Iface_2$
31	3D	Yθ-face liquid mass flow (kg/s, lb_m/hr)	Component, $Iface_1$, $Iface_2$
32	1D, 3D	Z-face liquid mass flow (kg/s, lb_m/hr)	Component, $Iface_1$, $Iface_2$
33	3D	XR-face liquid mass flow (kg/s, lb_m/hr)	Component, $Iface_1$, $Iface_2$
34	3D	Yθ-face gas velocity (m / s, ft / s)	Component, $Iface_1$, $Iface_2$
35	1D, 3D	Z-face gas velocity (m / s, ft / s)	Component, $Iface_1$, $Iface_2$
36	3D	XR-face gas velocity (m / s, ft / s)	Component, $Iface_1$, $Iface_2$
37	3D	Yθ-face liquid velocity (m / s, ft / s)	Component, $Iface_1$, $Iface_2$

TABLE N-3. (cont)
Signal-Variable Parameters

Signal-Variable Parameter No.	Defined For	Parameter Description	Input Location Numbers
38	1D, 3D	Z-face liquid velocity (m / s, ft / s)	Component, $Iface_1$, $Iface_2$
39	3D	XR-face liquid velocity (m / s, ft / s)	Component, $Iface_1$, $Iface_2$
40	1D, 3D	Boron concentration (kg / m^3)	Component, $Cell_1$, $Cell_2$
41	1D	Pump rotational speed (rad / s, rpm)	Component
42	1D	Valve flow-area fraction	Component
43	1D	Valve stem position	Component
44	HS	Neutron multiplication constant $k_{eff} = 1 + \Delta k_{prog} + \Delta_{kfdbk}$	Component
45	HS	Programmed Δk_{prog}	Component
46	HS	Feedback Δk_{fdbk}	Component
47	HS	Fuel-temperature feedback Δk_{Tf}	Component
48	HS	Coolant-temperature feedback Δk_{Tc}	Component
49	HS	Gas-volume-fraction feedback Δk_{α}	Component
50	HS	Solute concentration-ratio feedback Δk_{Bm}	Component
51	HS	Core density·volume·power^{powexp} – averaged fuel temperature (K, °F)	Component
52	HS	Core density·volume·power^{powexp} – averaged coolant temperature (K, °F)	Component
53	HS	Core volume·power^{powexp} – averaged gas volume fraction	Component
54	HS	Core density·volume·power^{powexp} – averaged solute concentration ratio (kg_{sol} / kg_{liq}, $lb_{m\text{-}sol} / lb_{m\text{-}liq}$) or (ppm)	Component
55	Global	Trip-signal value	Trip ID
56	Global	Trip set-status value	Trip ID
57	HS	Prompt-fission power (W, Btu / hr)	Component
58	HS	Decay-heat power (W, Btu / hr)	Component

TABLE N-3. (cont)
Signal-Variable Parameters

Signal-Variable Parameter No.	Defined For	Parameter Description	Input Location Numbers
59	HS	Average slab / rod maximum surface temperature (K, °F)	Component
60	HS	Additional slab / rod maximum surface temperature (K, °F)	Component
61	1D	Pump head (m^2/s^2, lb_f-ft / lb_m)	Component
62	1D	Pump torque (Pa-m^3, lb_f-ft)	Component
63	1D	Pump momentum source (Pa, psia)	Component
64	1D	Valve hydraulic diameter (m, ft)	Component
65	3D	Yθ-face hydraulic diameter (m, ft)	Component, $Iface_1$, $Iface_2$
66	1D, 3D	Z-face hydraulic diameter (m, ft)	Component, $Iface_1$, $Iface_2$
67	3D	XR-face hydraulic diameter (m, ft)	Component, $Iface_1$, $Iface_2$
68	3D	Yθ-face mix. mass flow (kg / s, lb_m / s)	Component, $Iface_1$, $Iface_2$
69	1D, 3D	Z-face mixture mass flow (kg / s, lb_m / s)	Component, $Iface_1$, $Iface_2$
70	3D	XR-face mixture mass flow (kg / s, lb_m / s)	Component, $Iface_1$, $Iface_2$
71	3D	Yθ-face mixture average velocity (m / s, ft / s)	Component, $Iface_1$, $Iface_2$
72	1D, 3D	Z-face mixture average velocity (m / s, ft / s)	Component, $Iface_1$, $Iface_2$
73	3D	XR-face mixture average velocity (m / s, ft / s)	Component, $Iface_1$, $Iface_2$
74	1D, 3D	Cell gas density (kg / m^3, lb_m / ft^3)	Component, $Cell_1$, $Cell_2$
75	1D, 3D	Cell liquid density (kg / m^3, lb_m / ft^3)	Component, $Cell_1$, $Cell_2$
76	1D, 3D	Cell mixture density (kg / m^3, lb_m / ft^3)	Component, $Cell_1$, $Cell_2$
77	1D, 3D	Cell air density (kg / m^3, lb_m / ft^3)	Component, $Cell_1$, $Cell_2$
78	1D, 3D	Cell air mass (kg / m^3, lb_m / ft^3)	Component, $Cell_1$, $Cell_2$

TABLE N-3. (cont)
Signal-Variable Parameters

Signal-Variable Parameter No.	Defined For	Parameter Description	Input Location Numbers
79	1D, 3D	Cell air pressure (Pa, psia)	Component, $Cell_1$, $Cell_2$
80	1D, 3D	Cell air internal energy (W-s / kg, Btu / lb_m)	Component, $Cell_1$, $Cell_2$
81	1D, 3D	Cell gas internal energy (W-s / kg, Btu / lb_m)	Component, $Cell_1$, $Cell_2$
82	1D, 3D	Cell liquid internal energy (W-s / kg, Btu / lb_m)	Component, $Cell_1$, $Cell_2$
83	1D, 3D	Cell saturation temperature based on vapor saturation pressure (K, °F)	Component, $Cell_1$, $Cell_2$
84	1D, 3D	Cell saturation temp. based on total pressure (K, °F)	Component, $Cell_1$, $Cell_2$
85	1D, 3D	Cell gas specific heat (W-s / kg-K, Btu / lbm-°F)	Component, $Cell_1$, $Cell_2$
86	1D, 3D	Cell liquid specific heat (W-s / kg-K, Btu / lbm-°F)	Component, $Cell_1$, $Cell_2$
87	1D, 3D	Cell latent heat of vaporization (W-s / kg, Btu / lb_m)	Component, $Cell_1$, $Cell_2$
88	1D, 3D	Total surface heat loss to the gas (W, Btu / hr)	Component, $NCell_1$, $NCell_2$
89	1D, 3D	Total surface heat loss to the liquid (W, Btu / hr)	Component, $NCell_1$, $NCell_2$
90	1D, 3D	Cell gas / liquid interfacial heat flow (W, Btu / hr)	Component, $Cell_1$, $Cell_2$
91	HS	ROD / SLAB gas HTC (W / m^2-K, Btu / ft^2-°F-hr)	Component, $NCell_1$, $NCell_2$
92	HS	ROD / SLAB liquid HTC (W / m^2-K, Btu / ft^2-°F-hr)	Component, $Ncell_1$, $Ncell_2$
93	1D	Cell SLAB gas HTC (W / m^2-K, Btu / ft^2-°F-hr)	Component, $Cell_1$, $Cell_2$
94	1D	Cell SLAB liquid HTC (W / m^2-K, Btu / ft^2-°F-hr)	Component, $Cell_1$, $Cell_2$
95	1D, 3D	Cell interfacial area x gas HTC (W / K, Btu / hr-°F)	Component, $Cell_1$, $Cell_2$

TABLE N-3. (cont)
Signal-Variable Parameters

Signal-Variable Parameter No.	Defined For	Parameter Description	Input Location Numbers
96	1D, 3D	Cell interfacial area x liquid HTC (W / K, Btu / hr-°F)	Component, $Cell_1$, $Cell_2$
97	3D	Yθ-face interfacial drag C_i (kg / m^4, lb_m / ft^4)	Component, $Iface_1$, $Iface_2$
98	1D, 3D	Z-face interfacial drag C_i (kg / m^4, lb_m / ft^4)	Component, $Iface_1$, $Iface_2$
99	3D	XR-face interfacial drag C_i (kg / m^4, lb_m / ft^4)	Component, $Iface_1$, $Iface_2$
100	1D, 3D	Cell solid-solute concentration (kg / m^3, lb_m / ft^3)	Component, $Cell_1$, $Cell_2$
101	1D, 3D	Cell vapor generation rate (kg / m^3-s, lb_m / ft^3-hr)	Component, $Cell_1$, $Cell_2$
102	1D, HS	Total inner surface heat loss (W, Btu / hr)	Component
103	1D, HS	Total outer surface heat loss (W, Btu / hr)	Component
104	1D, 3D	Cell mixture temperature (K, °F)	Component, $Cell_1$, $Cell_2$

For mesh cells on the secondary side of a TEE component, $Cell_1$ and $Cell_2$ are defined as composites of the total number of mesh cells on the primary side, NCELL1, plus the desired mesh-cell number on the secondary side, N2, i.e.

$Cell_{\#}$ = NCELL1 + N2 where # = 1, 2.

Similarly, for interfaces on the secondary side of a TEE component, $Iface_1$ and $Iface_2$ are defined as composites of the total number of interfaces on the primary side, NCELL1 + 1, plus the desired interface number on the secondary side, N2, i.e.,

$Iface_{\#}$ = NCELL1 + 1 + N2 where # = 1, 2.

For the 3D VESSEL component, $Cell_1$ and $Cell_2$ ($Iface_1$ and $Iface_2$) are defined as composites of 1000 times the relative-cell number in the horizontal X-Y or R-θ plane plus the axial-level number; i.e.,

$Cell_{\#}$ or $Iface_{\#}$ = 1000 · (horizontal-plane relative-cell number)
+ (axial-level number) where # = 1, 2.

When the signal-variable definition spans all cells from $Cell_1$ to $Cell_2$ ($Iface_1$ to $Iface_2$), a 2D array of mesh cells (interfaces) between the minimum and maximum relative-cell numbers and the minimum and maximum axial-level numbers are considered in the VESSEL component.

Note: TRAC-M/F90, post-Version 3.0. Versions of TRAC-M/F90 released after Version 3.0 will require that the signal variable cell number (input variable ICN1) for FILL, BREAK, and PLENUM components be input as 1. This is not a requirement for Version 3.0, TRAC-M/F77, or MOD2.

For heat-structure components, $Ncell_1$ and $Ncell_2$ ($Nrow_1$ and $Nrow_2$) are defined as composites of three location numbers: 1000000 times the node number *i* plus 1000 times the rod/slab number *j* plus the axial node-cell or node-row number *k*; i.e.,

$Ncell_{\#}$ or $Nrow_{\#}$ = 1000000 · i + 1000 · j + k where # = 1, 2.

Hydro node cell *k* lies between heat-transfer node rows *k* and *k* + 1. There are NCRZ node cells and NCRZ + 1 node rows. For signal-variable parameters that are defined on the heat-structure surface, *i* should be 1 for the inner surface or the value of NODES for the outer surface. When *i* is not 1 or NODES for surface-defined parameters, TRAC internally sets *i* = 1 for slabs and *i* = NODES for rods. Signal-variable parameter numbers 88 and 89 define the total surface heat loss to the vapor or liquid from all NRODS rods/slabs so the TRAC user needs to define *j* to be 0 for these two signal-variable parameters. When the heat-structure signal-variable definition spans all node cells (node rows) from $Ncell_1$ to $Ncell_2$ ($Nrow_1$ to $Nrow_2$), a 1D (for the ISVN = 88 and 89 parameters), 2D (for all surface-defined parameters), or 3D array of locations between the minimum and maximum values of *i*, *j*, and *k* are considered in the heat structure.

Using these composite definitions for tee secondary-side mesh cells (interfaces), vessel mesh cells (interfaces), and heat-structure node cells (node rows) enables the TRAC user to define them with a single signal-variable definition form that normally would apply only for single-sided 1D components.

Signal-variable parameter numbers 28 through 39, 65 through 73, and 97 through 99 define mass flow, velocity, hydraulic diameter, and interfacial drag coefficient and have their $Iface_1$ and $Iface_2$ numbers associated with mesh-cell interfaces. A 1D component's mesh-cell interface *i* lies between mesh cells *i*–1 and *i*. For the 3D VESSEL component, the outer-azimuthal, the outer-radial, and the upper-axial interfaces have the number of their mesh cell. If mass flow, velocity, hydraulic diameter, or interfacial drag coefficient are specified on X (or R) or Y (or θ) interfaces for 1D components, their definitions will internally default to the Z-interface definition.

There are six different forms for defining signal-variable parameters when they are location-dependent, that is, when they have |ISVN| parameter numbers 21 through 40 and 65 through 101. The signal variable is the

1. parameter value in mesh cell $|\text{Cell}_1|$ or $|\text{Cell}_2|$ when $\text{Cell}_2 = 0$ or $\text{Cell}_1 = 0$, respectively,
2. maximum value of the parameter in all mesh cells between mesh cells $|\text{Cell}_1|$ and $|\text{Cell}_2|$ when Cell_1 and Cell_2 are both positive,
3. minimum value of the parameter in all mesh cells between mesh cells $|\text{Cell}_1|$ and $|\text{Cell}_2|$ when Cell_1 and Cell_2 are both negative,
4. volume-averaged value of the parameter in all mesh cells between mesh cells $|\text{Cell}_1|$ and $|\text{Cell}_2|$ when Cell_1 and Cell_2 are of opposite signs,
5. difference between the parameter values in mesh cells $|\text{Cell}_1|$ and $|\text{Cell}_2|$ when the ISVN parameter number is prefixed with a minus sign, and
6. difference between the parameter values at the beginning of the present time step and at the beginning of the previous time step in mesh cell $|\text{Cell}_1|$ or $|\text{Cell}_2|$ when $\text{Cell}_2 = 0$ or $\text{Cell}_1 = 0$, respectively, and the ISVN parameter is prefixed with a minus sign.

The fifth and sixth forms can only have parameter numbers -101 through -65 and -40 through -21. The fifth form's signal variable is the parameter value in $|\text{Cell}_1|$ minus the parameter value in $|\text{Cell}_2|$. Mesh-cell numbers are defined by the absolute (positive) values of Cell_1 and Cell_2. Forms 3 and 4 above are the only ones that define $|\text{Cell}_1|$ and $|\text{Cell}_2|$ with negative values. For all six forms, it is the absolute value of Cell_1 and Cell_2 that is used to define the mesh-cell number.

Parameter number 20 is the liquid level between mesh cells $|\text{Cell}_1|$ or $|\text{Cell}_2|$. The liquid level

$$\sum_{i=|\text{Cell}_1|}^{I\pm1} \Delta x_i + f\Delta x_I$$

is the geometric length of collapsed liquid coolant from the bottom interface of mesh cell $|\text{Cell}_1|$, where Δx_i is the length of mesh cell *i*. The collapsed liquid-vapor interface is at a distance $f\Delta x_I$ above the bottom interface of mesh cell *I*. The values of *f* and *I* are defined by requiring that the volume of liquid between mesh cells $|\text{Cell}_1|$ and $|\text{Cell}_2|$ be collapsed to fill the fluid volume of mesh cells $|\text{Cell}_1|$ to $I \pm 1$ (minus when $|\text{Cell}_1| < |\text{Cell}_2|$ and plus when $|\text{Cell}_1| > |\text{Cell}_2|$) and the fraction *f* of the volume of mesh cell *I*; i.e., *f* is defined by

$$\sum_{i=|\mathrm{Cell}_1|}^{|\mathrm{Cell}_2|} (1-\alpha_i)V_i = \sum_{i=|\mathrm{Cell}_1|}^{I\pm1} V_i + fV_I$$

where α_i and V_i are the void fraction and volume of mesh cell i, respectively. This collapsed liquid column can only be evaluated for mesh cells within a component and only for the primary side or secondary side of a TEE component. To combine the liquid heights in several connected components requires defining a liquid water-level signal variable for each component (two signal variables for both sides of a TEE component) and summing them with control blocks using appropriate weighting factors. The cosine of the angle that the component mesh cells are inclined from vertical needs to be multiplied by the liquid water level to give the liquid's vertical height.

N.4. Control Blocks

Control blocks are function operators that operate on input-parameter signals to produce an output-parameter signal. The output signal can then be used as an input parameter to other control blocks. In this way, a control procedure for a component action can be constructed by coupling control-block operators in series and in parallel. PWR-system parameters, defined by signal variables, provide the input-parameter signals for the initial control block(s) and possible subsequent control blocks in a control procedure. The control procedure ends with a final control block whose output-signal value is used to define a component-action table's independent variable of the action directly when the table has no tabular data.

Table N-4. lists the 66 control-block function operations that are available in TRAC. The user selects the desired function operator for a control block and assigns its evaluation for later use in evaluating the control block. The remaining information in the table is the control-block function name and its defined mathematical operation. XOUT is the control-block output value, which can be referenced with the control-block ID number by other control blocks for their input ICB# or by component-action tables for defining their independent variable. The control-block ID number is specified by the user through input with Fortran variable name IDCB and is required to be a negative integer greater than –10 000. Thus, for a control block, defining ICB# with a positive ID number inputs a signal-variable value to the control block; a negative ID number inputs a control-block output-signal value.

In addition to the five possible X#, L#, and C# control-block input parameters in Table N-4., all control blocks require from input a constant gain factor, G, and constant minimum and maximum limit values, XMIN and XMAX, which constrain the output value of XOUT. XMIN and XMAX enable the user to model the nonlinear saturation of a control signal by electronic hardware. The gain factor can be used to model the amplification or attenuation effect on the signal from such hardware. Variables G, XMIN, XMAX, and C# are input with Fortran variable names CBGAIN, CBXMIN, CBXMAX, and CBCON#, respectively.

TABLE N-4.
Control-Block Function Operations

No.	Control-Block Name	Control-Block Mathematical Operational [a]	Block Input [b,c] 1	2	3	Block Const. [c] 1	2
1	Absolute value	XOUT = G*ABS(X1).	X1				
2	Arccosine	XOUT = G*ACOS(X1), XOUT in radians.	X1				
3	Add	XOUT = G*(X1 + X2).	X1	X2			
4	Integerizer	XOUT = G*FLOAT(IFIX(X1)).	X1				
5	Logical “and”	XOUT = G IF((L1.EQ.1.0) .AND.(L2.EQ.1.0)); = 0.0 otherwise.	L1	L2			
6	Arcsine	XOUT = G*ASIN(X1), XOUT in radians.	X1				
7	Arctangent	XOUT = G*ATAN(X1) XOUT in radians.	X1				
8	Arctangent 2	XOUT = G*ATAN(X1,X2), XOUT in radians.	X1	X2			
9	Constant	XOUT = G*C1.				C1	
10	Cosine	XOUT = G*COS(X1), X1 in radians.	X1				
11	Dead band dead zone or dead space	XOUT = G*(X1 – C2) IF(X1.GT.C2); = G*(X1 – C1) IF(X1.LT.C1); OR = 0.0 otherwise	X1			C1	C2
12	Derivative	XOUT = G*(dX1 / dt).	X1	(X2)			
13	Double integrator with XOUT limited	XOUT = G*$\int[\int X1dt + X2]dt$ + XOUT, X1 and (X2) are reset to 0.0 if XOUT is against a limit and the sign of X1 does not change. X2 = 0.0 and XOUT = 0.0 initially. X2 is $\int X1dt$ summed over all previous time. C1 = 0.0 or 1.0 is the polynomial order for approximating the time dependence of X1 and its integral.	X1	(X2)	(X3)	C1	(C2)
14	Divide	XOUT = G*X1 / X2	X1	X2			

TABLE N-4. (cont)
Control-Block Function Operations

No.	Control-Block Name	Control-Block Mathematical Operational [a]	Block Input [b,c] 1	2	3	Block Const. [c] 1	2
15	Logical "exclusive or"	XOUT = G IF(L1 + L2).EQ.1.0); = 0.0 otherwise.	L1	L2			
16	Logical "equivalent"	XOUT = G IF(L1.EQ.L2); = 0.0 otherwise.	L1	L2			
17	Exponential	XOUT = G*EXP(X1).	X1				
18	Logical "flip-flop"	XOUT = G or 0.0, valued flip-flop output that changes state whenever L1 changes state (only if L3 = 1.0).	L1	(L2)	L3		
19	Gate	XOUT = G*X1 IF(L2.EQ.1.0); = 0.0 IF(L2.EQ.0.0).	X1	X2			
20	Greater than or equal to	XOUT = G IF(X1.GE.X2); = 0.0 otherwise.	X1	(X2)			
21	Greater than	XOUT = G IF(X1.GT.X2) = 0.0 otherwise.	X1	X2			
22	Input switch	XOUT = G*X1 IF(L3.EQ.1.0); = G*X2 IF(L3.EQ.0.0).	X1	X2	L3		
23	Integrate	XOUT = G + XOUT, XOUT = 0.0 initially. X1 is not reset to 0.0 when XOUT is against limits. C1 = 0.0 or 1.0 is the polynomial order for approximating the time dependence of X1.	X1			C1	(C2)

TABLE N-4. (cont)
Control-Block Function Operations

No.	Control-Block Name	Control-Block Mathematical Operational [a]	Block [b,c] Input 1	2	3	Block [c] Const. 1	2
24	Integrate with mode control	XOUT = 0.0 IF((L2 + L3).EQ.0.0), reset mode; = XOUT IF((L2 + L3).EQ.1.0), hold mode; or = G* + XOUT IF((L2 + L3).EQ.2.0), integrate mode. C1 = 0.0 or 1.0 is the polynomial order for approximating the time dependence of X1.	X1	L2	L3	C1	(C2)
25	Logical "inclusive or"	XOUT = 0.0 IF((L1 + L2).EQ.0.0); = G otherwise.		L1	L2		
26	First-order lag	XOUT = G*X0 where X0 is the problem time-domain output from the Laplace transform operator 1/(1 + C1*s) operating on X1 in the Laplace transform *s* domain; that is, X0 is the solution of the first-order differential equation C1*dX0/dt + X0 = X1	X1			C1	
27	Logic delay	XOUT = 0.0 IF((L1.EQ.0.0).OR. (TIME.GT.(C1 + C2))); = G IF((L1.EQ.1.0).AND. (TIME.LE.(C1 + C2))), where (C2) is the time when L1 switches from 0.0 to 1.0.	L1	(L2)		C1	(C2)
28	Logic general-purpose counter	XOUT = 0.0 IF(L3.EQ.0.0), reset mode; = G times the number of times L1 has changed state since enabled (when L3 = 1.0), count mode.	L1	(L2)	L3		

TABLE N-4. (cont)
Control-Block Function Operations

No.	Control-Block Name	Control-Block Mathematical Operational [a]	Block [b,c] Input 1	2	3	Block [c] Const. 1	2
29	Logic input switch	XOUT = G*L1 IF(L3.EQ.1.0); = G*L2 IF(L3.EQ.0.0).	L1	L2	L3		
30	Lead-lag transfer function‘	XOUT = G*X0 where X0 is the problem time-domain output from the Laplace transfer operator (1 + C1*s) / (1 = C2*s) operating on X1 in the Laplace transform s domain; that is, X0 is the solution of the first-order differential equation C2*dX0 / dt = X0 = C1*dX1 / dt + X1.	X1	(X2)	(X3)	C1	C2
31	Limited integrator	XOUT = G* X1dt + XOUT, X1 is set to 0.0 if XOUT is again a limit and the sign of X1 does not change; XOUT = 0.0 initially C = 0.0 or 1.0 is the polynomial order for approximating the time dependence of X1.	X1			C1	(C2)
32	Natural logarithm	XOUT = G*ALOG(X1).	X1				
33	Less than or equal to	XOUT = G IF(X1.LE.X2); = 0.0 otherwise	X1	X2			
34	Less than	XOUT = G IF(X1.LT.X2); = 0.0 otherwise	X1	X2			
35	Maximum of two signals	XOUT = G*AMAX1(X1,X2).	X1	X2			
36	Maximum during transient signals	XOUT = G*AMAX1(X1,XOUT).	X1				
37	Minimum of two	XOUT = G*AMIN1(X1,X2).	X1	X2			
38	Minimum during transient	XOUT = G*AMIN1(X1,XOUT).	X1				
39	Multiply	XOUT = G*X1*X2	X1	X2			

TABLE N-4. (cont)
Control-Block Function Operations

No.	Control-Block Name	Control-Block Mathematical Operational [a]	Block Input [b,c] 1	2	3	Block Const. [c] 1	2
40	Logical “not and”	XOUT = 0.0 IF((L1 + L2).EQ.2.0); = G otherwise.	L1	L2			
41	Logical “not equal”	XOUT = G IF(L1.NE.L2); = 0.0 otherwise.	L1	L2			
42	Logical “not inclusive or”	XOUT = G IF((L1 + L2).EQ.0.0); = 0.0 otherwise.	L1	L2			
43	Logical “not” or negation	XOUT = G IF(L1.EQ.0.0); = 0.0 IF(L1.EQ.1.0).	L1				
44	Positive difference	XOUT = G*(X1 – X2) (IF(X1.GT.X2); = 0.0 otherwise.	X1	X2			
45	Quantizer	XOUT = G*FLOAT IF(X1 + 0.5); = 0.0 otherwise.					
46	Ramp	XOUT = G*(TIME-C1) IF(TIME.GT.C1); = 0.0 otherwise.					
47	Random number generator	XOUT = G*RANF where 0.0.LE.RANF.LE.1.0 IF(TIME.GE.C1); = 0.0 otherwise.				C1	
48	Sign function	XOUT = +G*|X1| IF(X2.GE.0.0); = –G*|X1| IF(X2.LT.0.0).	X1	X2			
49	Sine	XOUT = G*SIN(X1), X1 in radians.	X1				
50	Sign inversion	XOUT = –G*X1.	X1				

TABLE N-4. (cont)
Control-Block Function Operations

No.	Control-Block Name	Control-Block Mathematical Operational [a]	Block [b,c] Input 1	2	3	Block [c] Const. 1	2
51	Second-order transfer function	XOUT = G*X0 where X0 is the problem time-domain output from the Laplace transform operator 1/(1 + C1*s + C2*s**2) operating on X1 in the Laplace transform s domain; that is, X0 is the solution of the second-order differential equation C2*d(dX0/dt)/dt + C1*dX/dt + X0 = X1.	X1	(X2)	(X3)	C1	C2
52	Square root	XOUT = G*SQRT(X1).	X1				
53	Step	XOUT = G IF(TIME.GE.C1); = 0.0 otherwise.				C1	
54	Subtract	XOUT = G*(X1 – X2).	X1	X2			
55	Tangent	XOUT = G*TAN(X1) X1 in radians.	X1				
56	Sum constant	XOUT = G*(X1 + C1).	X1			C1	
57	Sum three	XOUT = G*(X1 + X2 + X3).	X1	X2	X3		
58	Variable limiter	XOUT = G*X2 IF(X1.GT.X2), at upper limit; = G*X3 IF(X1.LT.X3), at lower limit; or = G*X1 otherwise between limits.	X1	X2	X3		
59	Weighted summer	XOUT = G*(C1*X1 + C2*X2).	X1	X2		C1	C2
60	Exponentiate	XOUT = G*(X1**X2), where X1 > 0.	X1	X2			
61	Zero-order hold	XOUT = G*X1 IF(L2.EQ.1.0); = XOUT otherwise	X1	L2			

TABLE N-4. (cont)
Control-Block Function Operations

No.	Control-Block Name	Control-Block Mathematical Operational [a]	Block [b,c] Input 1	2	3	Block [c] Const. 1	2
100	Time delay	XOUT = G*X1 where X1 is evaluated at the time the control block is input IF(TIME.LE.C1); = G*X2(TIME–C1) otherwise {X1(TIME–C1) is evaluated at time (TIME–C1)]. The variable is the number of storage table pairs for saving values of X1 over the last C1 seconds. X1 is stored at intervals of approximately C1 / (n – 1) s; the control block will use linear interpolation to obtain the desired value of X1(TIME–C1).	X1	n	(X3)	C1	
101	Function of one independent variable	XOUT = G*f_n(X1). The variable n is the number of function table pairs of values to be input.	X1	n	(X3)	(C1)	

TABLE N-4. (cont)
Control-Block Function Operations

No.	Control-Block Name	Control-Block Mathematical Operational [a]		Block [b,c] Input			Block [c] Const.	
				1	2	3	1	2
102	Function of two or three independent variables	XOUT =	G*f(X1,X2,X3). The variable n is the composite number $10000 * n + 100 * n_2 + n_3$, where n_1 = number of X1 values ($2.LE.n_1.LE.99$), n_2 = number of X2 values ($2.LE.n_2.LE.99$), and n_3 = number of X3 values ($2.LE.n_3.LE.99$), Input zero for X3 and n_3 for tabular function of two independent variables. Input the function table in the following order: the n_1 values of X1, the n_2 values of X2, the n_3 values of X3, and the $n_1*n_2*\max(1,n_3]$ function values.	X1	X2	X3	n	(C2)
200	PI Controller	XOUT =	$A = A_o + \Delta A$ in Fig. N-1., where X1 = ID number of F, X2 = ID number of F_d when F_d is an input parameter rather than a constant value; C1 = F_d constant value; C2 = A_o, the initial XOUT; $G = (\Delta A / \Delta F)_{est}$; XMIN = A_{min}; and XMAX = A_{max}. A third input-data card is required to specify Δt_d and τ. Refer to Fig. N-1. for a schematic diagram of the functional form of this control block	X1	X2		C1	C2

TABLE N-4. (cont)
Control-Block Function Operations

No.	Control-Block Name	Control-Block Mathematical Operational [a]		Block [b,c] Input			Block [c] Const.	
				1	2	3	1	2
201	PIC Controller	XOUT =	$A = A_o + \Delta A$ in Fig. N-2., where X1 - ID number of F; X2=ID number of F_d when F_d is an input parameter rather than a constant value; C1 = F_d constant values; C2 = A_o, the initial XOUT; $G = (\Delta A / \Delta F)_{est}$; XMIN = A_{min}; and XMAX = A_{max}. A third input data card is required to specify Δt_d, τ, and Wt. Refer to Fig. N-2. for a schematic diagram of the functional form of this control block.	X1	X2	(X3)	C1	C1

a. XOUT appearing on the right-hand side of the defining equation indicates its value from the previous evaluation. G is a constant gain factor applied to the XOUT operation result. XOUT appearing on the left-hand side of the defining equation is constrained by constant lower and upper limits XMIN and XMAX in defining the control-block output value.
b. An "X" parameter indicates a continuous variable; an "L" parameter indicates a logical (or discrete) parameter having a value of 0.0 or 1.0 only.
c. Variables enclosed in parentheses are not input variables, but are used internally by the control block for data storage.

Figure N-1. presents the general schematic of a control block. The number of input parameters on the left-hand side ranges from 0 to 3 depending on the control-block operation number. On the other hand, there is only one output parameter from a control block. Its value can vary continuously or stepwise depending on the type of control-block operation. To have the output value 0.0 or 1.0 when it is logical (ICBN = 5, 15, 16, 18, 20, 21, 25, 27, 28, 29, 33, 34, 40, 41, 42, and 43) requires that CBGAIN = 1.0 be input to the control block.

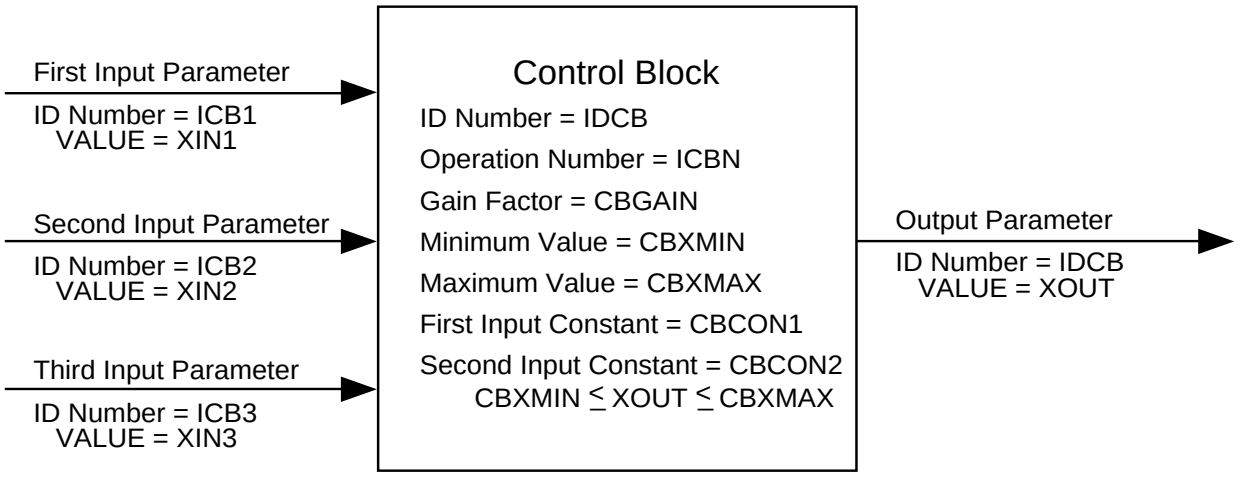

Fig. N-1. Control-block diagram.

TRAC evaluates control blocks by having driver subroutine CBSET call subroutines CONBLK for ICBN = 1 to 61, DELAY for ICBN = 100, LININT for ICBN = 101, and LINT4D for ICBN = 102. Subroutines CONBLK and DELAY are modified forms of subroutines with the same names written by Giles and Milton for the TRAC-BD1 computer program (Ref. N-1.). Their control-block operations ICBN = 56 (defining problem time) and 57 (setting trip status), which are done by signal variable ISVN = 0 and trips in TRAC, have been replaced by operations that sum a constant to an input parameter and sum three input parameters. The rectangular-integration control blocks (ICBN = 13, 23, 24, and 31) have been further generalized to allow the user the option of selecting trapezoidal-rule integration instead.

Before evaluating a control block, the signal variables and control blocks that define its input parameters need to have their values accessed. When evaluating a control procedure with connected control blocks, the connecting arrows define the direction and order for evaluating the control blocks. Time lag produced by forward difference approximating an integrand (compared with evaluating the input parameters first using a backward-difference approximation) has an unstabilizing effect. When the error to be corrected in the signal is increasing, corrective action is numerically delayed by a forward-difference approximated integral controller. Eventually when enough corrective action has been applied to start decreasing the error signal, the forward-difference-approximated integral controller delays the removal of corrective action causing the error signal to overshoot its desired zero value. The inherent weakness of integral controllers to overshoot and produce an oscillatory response that can become unstable (Ref. N-2.) is enhanced by evaluating its integral with a forward-difference approximation. Using a backward-difference approximation has just the opposite effect. Its numerical difference error acts to reduce overshoot by the integral controller. This discussion only applies to the rectangular-integration option (which is zero-order

accurate). When trapezoidal-rule integration (which is first-order accurate) is used, the input parameters must be evaluated first for the control-block algorithm to evaluate correctly.

Consider the very useful proportional-plus-integral (PI) controller shown in Fig. N-2. The proportional-plus-integral-plus-derivative (PID) controller shown in Fig. N-3. is an enhancement of the PI controller that uses the derivative to control the rate of adjustment. Both controllers are control blocks that define a control procedure for a component action. The input PWR-system parameter F and output component action A could be a pressure to control a valve, a mass flow rate to control a pump, a fluid level to control a feedwater pump or valve, or a pressure to control a heater. The purpose of these controllers is to compare the system-parameter value with its desired value and to apply corrective action to return the system parameter to its desired value when it departs. These control blocks could be used to model an actual PI or PID electronic-circuit controller or to adjust a component action to maintain a quoted system-parameter value.

The PI controller shown in Fig. N-2. performs the following operations. In the lower-left corner of the figure, the sum-constant function subtracts from the PWR-system parameter F the desired value F_d to define the ΔF error signal. The next three functions estimate the ΔA change in the component action from its initial value, which should cause ΔF to go to zero as the calculation proceeds. The integrate function integrates ΔF from the initial time to the present. Its integral represents the accumulated error in F. The add function sums its ΔF (proportional) and $\int \Delta F\, dt$ (integral) input signals with appropriate $(\Delta A / \Delta F)_{est}$ and $(\Delta A / \Delta F)_{est} / \Delta t_d$ gain factors to output the PI controller's estimated change in the component action that is required from its initial value. $(\Delta A / \Delta F)_{\text{est}} / \Delta t_d \cdot \int \Delta F\, dt$ corresponds to the ΔA_{PI} value that has accumulated up to the current time; $(\Delta A / \Delta F)_{est} \cdot \Delta F$ corresponds to the desired instantaneous change in ΔA_{PI} at the current time that the PI controller estimates is needed to correct for the ΔF error still remaining. The first-order lag function accounts for the fact that the $(\Delta A / \Delta F)_{est} \cdot \Delta F$ instantaneous change in a component action may not be physically possible or numerically desirable. The maximum rate of change in ΔA is constrained by the CBCON1 time constant, τ, of the first-order lag function. Through the value of τ, the maximum adjustment rate of the hardware can be modeled. When an instantaneous change in ΔA_{PI} over a time step is desired, the first-order lag function evaluates a slower change in ΔA based on the first-order differential equation $\tau * d\Delta A / dt + \Delta A = \Delta A_{\text{PI}}$. The value of ΔA will lag the value of ΔA_{PI} in time by an amount based on the magnitude of τ. Finally, the sum-constant function in the lower-right corner of the figure sums the accumulated ΔA change in the component action since the start of the calculation to the component-action's initial value, A_o. For this controller, its control-block output signal A is applied directly to the component action by defining a component-action table with no entry pairs, NXXXTB = 0.

Proportional + Integral (PI) Controller

$$\Delta A_{PI} = (\Delta A/\Delta F)_{est} \left[\Delta F + (1/\Delta t_d) \int \Delta F dt \right]$$

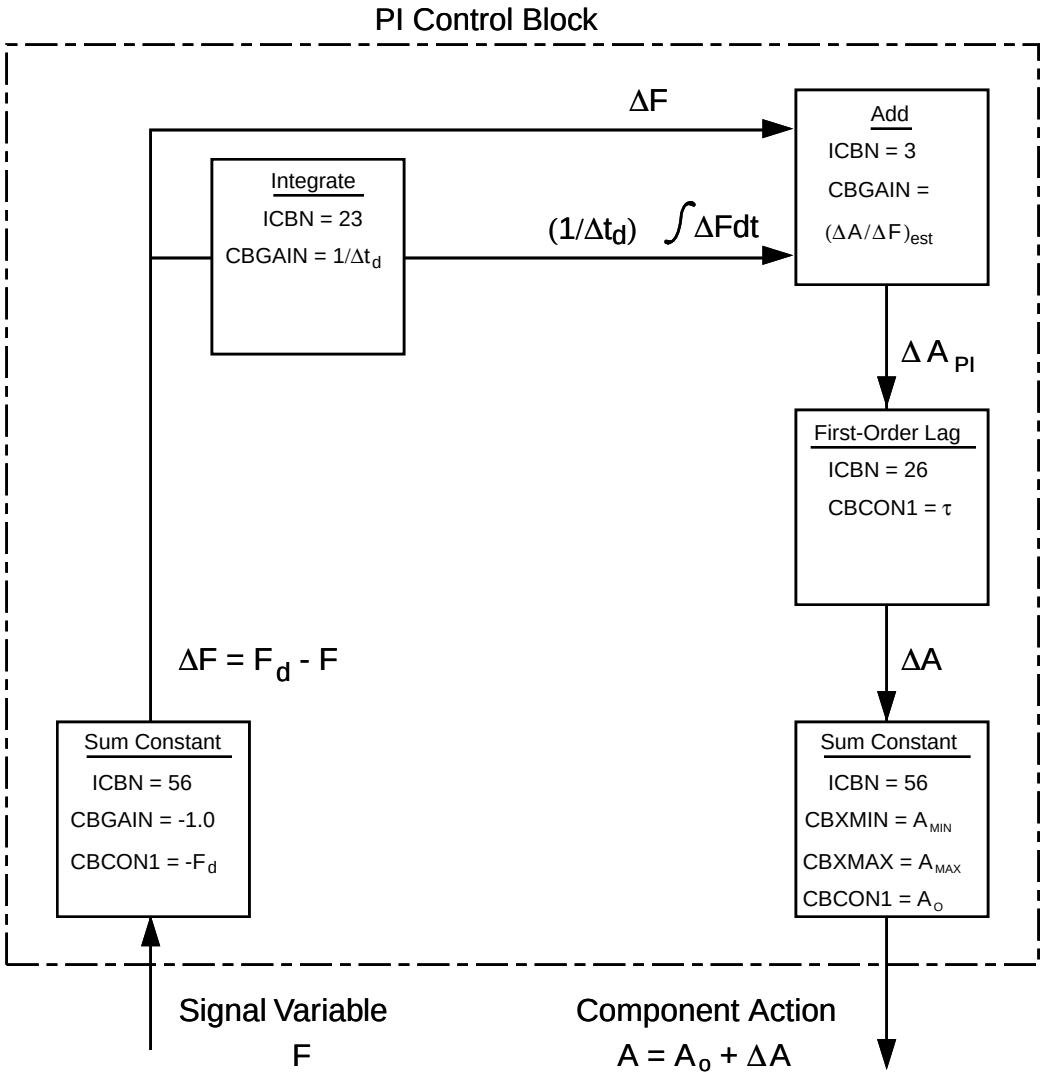

Fig. N-2. Proportional plus integral controller diagram.

Proportional + Integral + Derivative (PID) Controller

$$\Delta A_{PID} = (\Delta A/\Delta F)_{est} \left[\Delta F + (1/\Delta t_d) \int \Delta F dt + \overline{\Delta t_d \ (d\Delta F/dt) + \Delta F} \right]$$

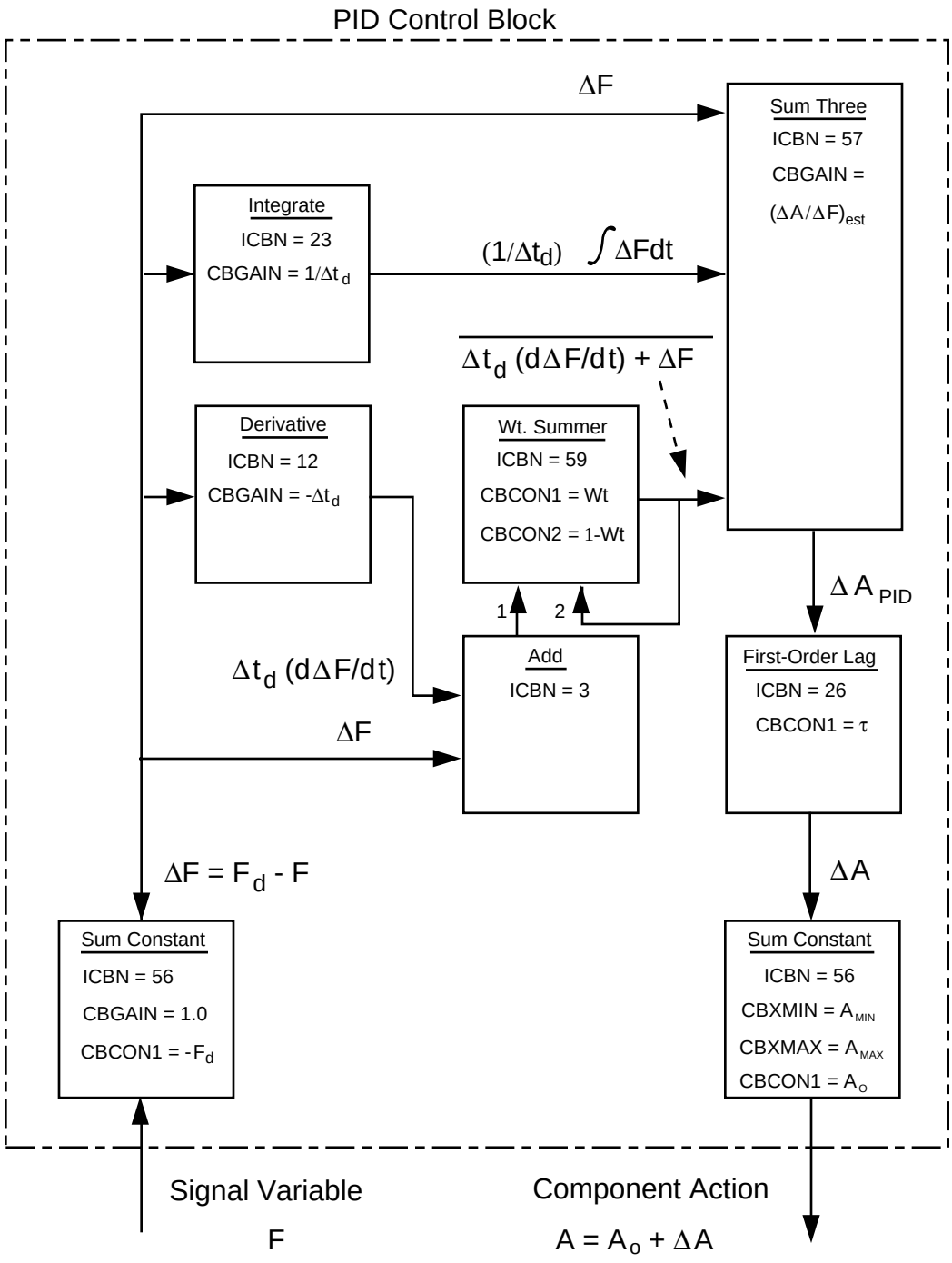

Fig. N-3. Proportional plus integral plus derivative controller diagram.

N.5. Trips

Trips are ON-OFF logical switches for controlling the evaluation of component actions. When the controlling trip for a component action is ON, the component action is evaluated from its component-action table. When the controlling trip is OFF, the component action is not evaluated; it is held constant at its initial value if its trip has never been ON or optionally at its last evaluated value when its trip was ON or at a user-defined input value for when its trip is OFF after being ON. Trips also can be used to implement special time-step data, generate restart-data dumps, and terminate problem execution at the time the trip is set ON.

Determining the ON or OFF set status of a trip is based on the value of its user-defined trip signal. Over the trip-signal value range, the user defines two or four set-point values that delimit two or three subranges labeled with ON or OFF set status. When the value of the trip signal lies within a given subrange, the trip is assigned the set-status label of that subrange. Table N-5. shows 5 of the 10 possible trip-signal-range types that define set status. The ON set status has two forms: $ON_{forward}$ and $ON_{reverse}$. Trip-controlled component action is evaluated for both. They differ only with regard to the sign of the numerical value 1 for the ON set status. The numerical values associated with the three set-status flags in Table N-5. are –1 for $ON_{reverse}$, 0 for OFF, and +1 for $ON_{forward}$.

Input variable ISRT defines the signal-range type for a trip. Table N-5. shows the signal-range types for ISRT = 1, 2, 3, 4, and 5. Assigning a negative sign to these ISRT values and changing $ON_{forward}$ to $ON_{reverse}$ and $ON_{reverse}$ to $ON_{forward}$ defines the other five types. The criteria to decide when the set status of a trip is to be changed are stated in the lower half of Table N-5. The present set status of the trip determines which criterion is to be used. The criteria and signal-range type definitions are based on the requirement that the set-point values satisfy $S_1 < S_2$ for ISRT = ±1 and ±2 and $S_1 < S_2 < S_3 < S_4$ for ISRT = ±3, ±4, and ±5.

For ISRT = ±1 and ±2, there are two set-status subranges. The trip signal needs to be equal to or greater than the S_2 set-point value to change from the left to the right subrange set status. To change from the right to the left subrange set status, the trip signal needs to be equal to or less than S_1. When the trip-signal value lies between S_1 and S_2, the trip has the set status of the left or right subrange from which its signal came.

For ISRT = ±3, ±4, and ±5, there are three set-status subranges. Changing to either of the other two set-status labels is determined in much the same way as for a two-subrange signal-range type. The trip-signal value is compared with S_1 or S_2 to change to left or middle set status and compared with S_3 or S_4 to change to the middle or right set status. The trip-signal value crossing two subranges during a time step will result in the set-status criteria being satisfied twice even though the last criterion being satisfied is the only one edited by TRAC for the time step.

TABLE N-5.
Trip Signal-Range Types

ISRT Signal-Range Type Number	Trip Signal-Range Diagram with Subrange Set Status
1	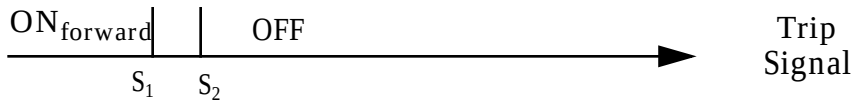
2	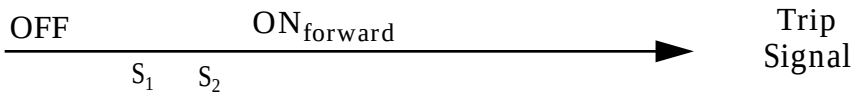
3	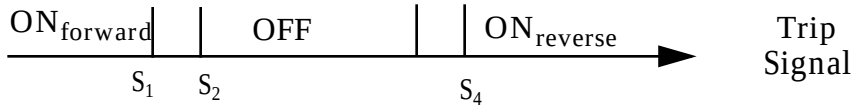
4	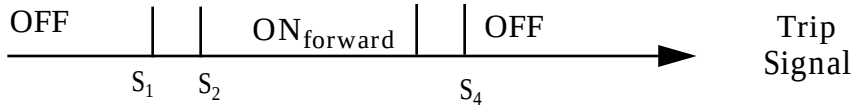
5	

Making ISRT negative changes $ON_{forward}$ to $ON_{reverse}$ and $ON_{reverse}$ to $ON_{forward}$.

ISRT Signal-Range Type Number	Description of How the Trip Set Status is Changed
1	When $ON_{forward}$, trip is set to OFF when the trip signal $\geq S_2$. When OFF, trip is set to $ON_{forward}$ when the trip signal $\leq S_1$.
2	When OFF, trip is set to $ON_{forward}$ when the trip signal $\geq S_2$. When $ON_{forward}$, trip is set to OFF when the trip signal $\leq S_1$.
3	When $ON_{forward}$, trip is set to OFF when the trip signal $\geq S_2$ and $<S_4$. When $ON_{forward}$, trip is set to $ON_{reverse}$ when the trip signal $\geq S_4$. When OFF, the trip is set to $ON_{forward}$ when the trip signal $< S_1$. When OFF, the trip is set to $ON_{reverse}$ when the trip signal $\geq S_4$. When $ON_{reverse}$, trip is set to OFF when trip signal $\leq S_3$ and $> S_1$. When $ON_{reverse}$, trip is set to $ON_{forward}$ when trip signal $\leq S_1$.
4	When $OFF_{(left)}$, trip is set to $ON_{forward}$ when signal $\geq S_2$ and $< S_4$. When $ON_{forward}$, trip is set to OFF when trip signal $\leq S_1$ or $\geq S_4$. When $OFF_{(right)}$, trip is set to $ON_{forward}$ when signal $\leq S_3$ and $> S_1$.
5	When $ON_{forward(left)}$, trip is set to OFF when signal $\geq S_2$ and $< S_4$. When OFF, trip is set to $ON_{forward}$ when trip signal $\leq S_1$ or $\geq S_4$. When $ON_{forward(right)}$, trip is set to OFF when signal $\leq S_3$ and $> S_1$.

Defining a trip-signal range to have more than three set-status subranges can be done by joining two or more trips having the same trip signal and different set-point values. A trip-controlled trip (defined later in this section) is used to join them and to respond as if it were a four or more set-status subrange trip. Whereas trips with three set-status subranges are defined directly by ISRT = ±3, ±4, and ±5, they could be constructed by joining two trips having two set-status subranges with a trip-controlled trip. Three set-status subrange trips have been defined directly, however, because they are a convenient form for regulating a component action under trip control and save the user from having to define three trips to achieve that form.

Signal-range type ISRT = ±3 is the form generally used to regulate a component action under trip control. The trip signal is the controlling parameter, and the component action is to be adjusted so that the trip signal lies within its desired value range from S_1 to S_4. When the trip signal falls below S_1, the left-subrange ON set status has the component action evaluated in a manner that causes the trip-signal value to increase. When the trip signal rises above S_4, the right-subrange ON set status adjusts the component action in the opposite manner to cause the trip-signal value to decrease. For this application, the component-action table needs to have its independent-variable form defined by the change in its IXXXSV variable value so that the ISET set-status value is applied as a factor to the independent variable of Table N-2. This is done by defining the number of entry pairs in the component-action table to be negative, that is, NXXXTB < 0. As described above, the set-point values define the desired value range for the trip signal. The range can be as small or as large as the user feels is appropriate for constraining the trip-signal value based on trip control of the component action.

Each trip-signal set point is defined by a constant value with the possibility of a tabular function being applied to that value as a factor. The user inputs for each set point a constant set-point value to array variable SETP(I), $I = (1,2)$ or $I = (1,4)$ [that satisfies $S_1 < S_2$ or $S_1 < S_2 < S_3 < S_4$, and an ID flag to array variable IFSP(I) to indicate if a tabular-function factor is to be applied to the SETP(I) value. No such factor is applied when IFSP(I) = 0; the set-point value is the constant SETP(I). Entering IFSP(I) ≠ 0 defines the ID number for a set-point factor table of tabular data to be input after the trip and trip-signal defining data. The set-point factor-table independent variable is defined by a signal variable or a control-block output variable. The variable (not the change in the variable value) defines the independent variable of the table. When a set-point factor is to be applied to a set point, its table is linearly interpolated for each time step on the basis of the abscissa-coordinate signal-variable or control-block output-variable value. The input SETP(I) constant value is multiplied by the interpolated function value to determine the set-point value that is used. Set-point factor tables are useful when set points for regulating a component action vary on the basis of some system-parameter dependence. For example, the desired water level in the steam-generator secondary-side downcomer might depend on the reactor power level. A trip with varying water-level set-point values, dependent on the reactor power level, could be used to control the secondary-side feedwater pump or valve.

Associated with each set point is a delay time defined by input array variable DTSP(I), I = (1,2) or I = (1,4). The delay time provides a second criterion that needs to be satisfied before the trip set status is changed. The first criterion requires that the trip-signal value reach or cross the set-point value tested. Once that criterion is met, the second criterion then requires that the delay time of that set-point pass before changing the trip set status. With a delay time, the user is able to model the time necessary for the system hardware or the control-room operator to process the controlling signal and initiate hardware action. Delay time needs to be defined with a non-negative value (negative values are treated as zero). TRAC edits a message when each criterion is satisfied by a trip. For large delay times, it is possible for a number of first-criterion tests to be satisfied before their delay times pass. TRAC can handle up to five such delay-time pending set-status changes stacking up for a trip before the next one is forced to replace the last one in the stack. When it does, a warning message is printed. For a delay-time pending set-status change to stack up, the time its first criterion was met (based on linear interpolation of the trip-signal value to equal the set-point value) plus its delay time must be later than all pending times added earlier to the stack. When that time is equal to or less than one or more pending times in the stack, they are discarded from the stack by this new entry. Through this mechanism, the user can prevent temporary spikes in a trip signal from setting a trip ON and its component action being evaluated. The user does this by defining shorter delay times for the set points that turn a trip OFF than for the set points that turn a trip ON. The difference between these two delay times is the required time interval the trip-signal value needs to stay in the ON subrange to prevent a satisfied OFF criterion that follows from discarding its pending ON set-status change from the stack.

There are three forms for defining the trip signal: a signal parameter, a signal expression, or a trip set-status signal. Two input variables define the trip signal: ITST defines the trip-signal type number and IDSG defines the trip-signal ID number. A signal-parameter trip is defined by ITST = 1 and has a signal-parameter trip signal. That signal parameter is a signal variable with ID number IDSG when IDSG > 0 or a control-block output variable with ID number IDSG when IDSG < 0. A signal-expression trip is defined by ITST = 2 and has a signal-expression trip signal. The trip signal is an arithmetic expression operating on the values of one or more signal variables and control-block output variables. Its definition is input as trip-signal-expression input data with ID number IDSG. The form for that definition is described in the next paragraph. A trip-controlled trip (or trip set-status signal trip) is defined by ITST = 3 and has a trip set-status signal. This signal is the sum or product of the set-status values of two or more other trips. The ID numbers of those trips are input as trip-controlled trip-signal data with ID number IDSG. The set-status values of those trips are to be summed if IDSG > 0 or multiplied if IDSG < 0 to evaluate the trip-controlled trip signal.

Evaluating a signal-expression trip signal involves evaluating an arithmetic expression with 1 to 10 arithmetic subexpressions. Each subexpression has an arithmetic operator and two arguments. The arithmetic operators are addition, subtraction, multiplication, division, exponentiation, maximum value, minimum value, and absolute value. Argument values are defined by signal variables, control-block output variables, input

constants, or an earlier evaluated subexpression in the list of subexpressions. The value of the signal expression is the value of the last subexpression in its list. Through its arithmetic operators, a signal expression allows signal variables from different components of the modeled PWR system to be combined in defining the trip signal. Signal variables that define a subexpression argument can be flagged in the signal-expression definition for reevaluation only at the times the signal-expression trip is set ON. In this way, signal variables evaluated at different times as well as in different components can be combined in defining a trip signal.

The AND or OR logic of blocking or coincidence trips can be implemented with trip-controlled trips. Applying the AND logical operator defines a blocking trip that is ON only if all the trips assigned to it are ON. The trip-controlled trip that has this form multiplies (IDSG < 0) the set-status values of its assigned trips in defining the trip signal and uses an ISRT = 2 signal-range type with $0 < S_1 < S_2 < 1$. It turns out in this case that the trip-controlled trip signal has the same value (0 or 1) as its subrange set-status value. Applying the OR logical operator defines a coincidence trip that is ON only if one or more of the assigned trips are ON. Its corresponding trip-controlled trip adds (IDSG > 0) the set-status values of its assigned trips and uses the same signal-range type and set-point values as above. For a more general coincidence trip, we specify that a number N or more (where $1 \le N \le N_t$) of the N_t assigned trips need to be ON for the coincidence trip to be ON. Within AND or OR logic, this requires logical expressions having logical subexpressions. For example, if $N = 2$ of $N_t = 3$ assigned trips need to be ON for the coincidence trip to be ON, its logical expression would need to have the form: (Trip #1 AND Trip #2) OR (Trip #2 AND Trip #3) OR (Trip #3 AND Trip #1). The form of this logical expression will be different for different values of N or N_t. With trip-controlled trips, the required form is the sum of the set-status values of its assigned trips in all cases. The only difference is in defining the set points according to $(N - 1) < S_1 < S_2 < N$. In this case, the trip-controlled trip-signal value, which is the number of assigned trips that are ON, needs to be greater than S_2 (that is, the value N or greater) to meet the criterion for setting the trip-controlled trip ON.

The three trip-controlled trip examples above barely scratch the surface of the number of ways trip-controlled trips can be used to model AND/OR logical expressions. Switching from an ISRT = 2 to an ISRT = 1 signal-range type applies a NOT logical operator to the logical expression being modeled. Assigning a trip-controlled trip to the definition of another trip-controlled trip signal provides further modeling flexibility. The above discussion assumes that the ON set status of the assigned trips is $ON_{forward}$. Assigning trips with $ON_{reverse}$ set-status subranges to a trip-controlled trip signal provides another dimension for modeling possible logical expressions.

During input, trips are given ID numbers that assign them to

1. control component actions by defining their ID numbers to the general form variables IXXXTR in the component input data,

2. define trip-controlled trip signals with their set-status values, and
3. define signal variables with the trip-signal or set-status value.

Trip ID numbers of magnitude 1 to 9999 are allowed. A negative ID number defines a trip that is to be evaluated during steady-state and transient calculations. A positive ID number trip, on the other hand, is evaluated only during transient calculations. During steady-state calculations, the set-status value specified by input-variable ISET and an initialized trip-signal value of 10^{20} define the positive ID trip constant state. A positive ID trip can be used as a blocking trip during a steady-state or transient calculation when the trip-evaluated set status is the opposite of its input ISET value.

N.6. Control-Parameter Evaluation

Signal variables, control blocks, and trips are assigned ID numbers when input by the user. Their ID numbers provide the means for referencing their values for use in the control procedure. Their ID numbers also define the order in which they are to be evaluated. Within each control-parameter type (signal variables, control blocks, and trips), parameters are evaluated in the order of increasing magnitude of their ID numbers. Thus, control blocks are ordered for evaluation with their ID numbers decreasing in negative value; trips are ordered with their ID numbers increasing in magnitude with either a plus or minus sign. This ordering is done by subroutine ORDER after the control-parameter data are input, and the control-parameter restart data with ID numbers different from those input are added on. For example, a control-block input with ID number -5 would replace a control block with the same ID number from the restart file. Subroutine ORDER would reorder the list of control blocks so that control-block ID = -5 would be placed before control blocks with IDs < -5 and after control blocks with IDs > -5. A trip input with ID number 11 would replace a trip with the same ID from the restart file but not a trip with ID number -11. For the case of two trips having ID numbers with the same magnitude, that is, 11 and -11, subroutine ORDER does not change their relative positions in the trip list. With trip ID = 11 input and trip ID = -11 added on to the trip list from the restart file, trip ID = -11 would follow after trip ID = 11 in the reordered list of trips. Subroutine ORDER is called once at the end of input and restart data processing to reorder the signal-variable, control-block, and trip lists. This saves having to search through ID numbers to determine their evaluation order when the control parameters are evaluated at the beginning of each time step.

Through ID numbers, the order for evaluating control parameters of a given type is defined. The order for evaluating control-parameter types is by default signal variables first, then control blocks, and finally trips. Since signal variables have almost all of their parameters defined by the modeled PWR system, it is appropriate to evaluate them first. The input parameters for control blocks are signal variables and control blocks so that, with proper ordering of control blocks, control blocks are evaluated after signal variables. Trip signals are defined by signal variables, control blocks, and the set status of other trips. With proper ordering of trips, evaluation of trip signals follows the evaluation of signal variables and control blocks.

In general, this approach is able to evaluate control-parameter values at the beginning of the time-step state of the PWR system. There are a few situations, however, where such is not the case. Defining a trip signal or set status to be a signal variable (ISVN = 55 or 56) gives its value at the beginning of the previous time step because signal variables are evaluated before trips. In this case, they should be evaluated after their trips. A control-block procedure with an implicit feedback loop (Fig. N-4., for example) is another exception. To evaluate X with the Add operator control block, ln (X) and thus X need to be known. By evaluating each of the two control blocks once, no matter which is evaluated first, the value of X used to evaluate ln (X) will be one time step behind the value that should be used. Accumulation of such errors over many time steps can cause the value of X to significantly lag its actual value in time. Instability can even result from that lag error. TRAC has not yet been programmed to recognize such implicit-loop structures to implement internally an iterative-loop evaluation able to determine the consistent-solution state.

A multipass control-parameter evaluation procedure has been programmed in TRAC to aid the user in addressing the above two situations. Within each evaluation pass, the user decides which signal variables, control blocks, and trips (in that order) are to be evaluated. Trip signal and set-status signal variables can then be evaluated on a second control-parameter evaluation pass after their defining trips were evaluated on the first pass. The implicit control-block loop can be reevaluated with as many passes as the user decides are needed for convergence. On the last loop evaluation pass, all control blocks whose input parameters are affected by the loop evaluation would then be evaluated. During each of the passes, the user specifies which control parameters, if any, are to be evaluated for each type. Those parameters that are evaluated span a range of ID numbers that the user specifies. All control parameters with ID numbers in that range are evaluated during that pass. An example of such a procedure follows. Assume the following control parameters are to be evaluated:

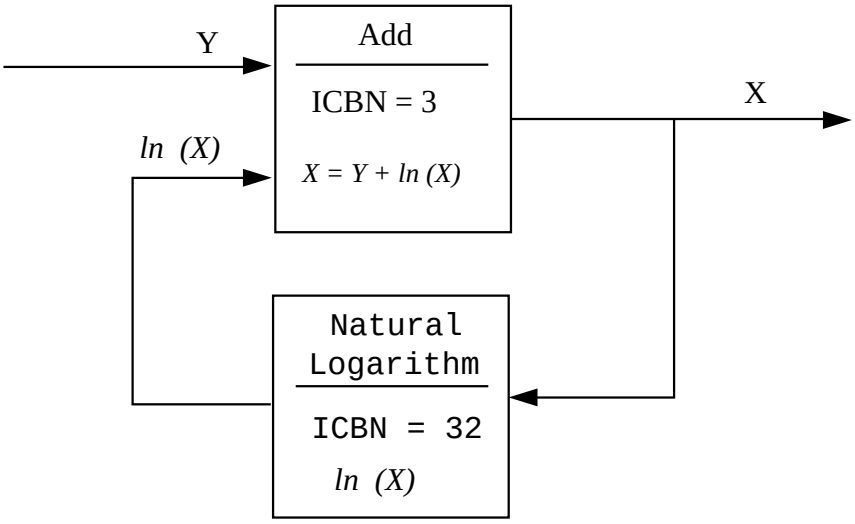

Fig. N-4. Implicit control-block loop example.

1. Signal variables with IDs 3 to 35 define system (component) parameters; signal variables with IDs 39 to 72 define the signal and set status of trips with IDs ±7 to ±18 as well as define other system parameters.
2. Control blocks with IDs -1 to -12 require input parameters from signal variables with IDs 3 to 17 and provide input parameters for control blocks in an implicit loop; control blocks with IDs -13 to -17 are in an implicit loop for which five iterative evaluations are felt to be sufficient to converge on a consistent solution state and control blocks with IDs -18 to -42 require input parameters from the implicit-loop control blocks and from signal variables.
3. Trips with ID ±1 to ±18 require signal variables with IDs 3 to 26 and control blocks with IDs -6 to -10 to define their signals; trips with IDs ±19 to ±30 require signal variables with IDs 18 to 72 and control blocks with IDs -5 to -40 to define their signals.

Evaluating these control parameters could be done with the five evaluation passes shown in Table N-6. After five passes (assuming convergence of the implicit-loop evaluation), all control parameters would have values consistent with each other and the beginning-of-time-step state of the system.

TABLE N-6.
Table ID Numbers of Control Parameters Evaluated During each of Five Control-Parameter Evaluation Passes

Evaluation Pass Number	Signal Variables	Control Blocks	Trips
1	3 to 35	–1 to –17	±1 to ±18
2	39 to 75	–13 to –17	none
3	none	–13 to –17	none
4	none	–13 to –17	none
5	none	–13 to –42	±19 to ±30

N.7. Steady-State Evaluation

The TRAC steady-state evaluation capability provides a time-independent solution that may be of interest in its own right, or as an initial condition for a transient calculation. There are three types of steady-state calculations: generalized, constrained, and static check. A generalized steady-state (GSS) calculation evaluates the time-independent condition of an arbitrarily modeled system with variable system parameters (pump

rotational speed, valve flow area, energy sources, etc.) held constant at their input-specified steady-state values. A constrained steady-state (CSS) calculation is performed like a GSS calculation with the addition of user-selected controllers that adjust specific system parameters to achieve desired steady-state values for specific thermal-hydraulic parameters. A static-check steady-state calculation checks for the presence of unknown or erroneous momentum or energy sources in the modeled system by setting the rotational speed of all pumps and energy sources to zero. All coolant flow in the system should go to zero because of surface friction as the static-check calculation is evaluated.

N.7.1. Generalized Steady State

The same subroutines are called to evaluate the transient and steady-state calculation. For the GSS calculation, however, the following additional procedures are implemented.

1. Pressurizer components are modeled as constant pressure boundary conditions during steady-state calculations. Their coolant mass and energy inventory as well as pressure remain constant regardless of the coolant mass-flow conditions between the pressurizer and its adjoining components.
2. Pump components have their momentum sources averaged over time to prevent oscillations in the solution.
3. The point-reactor kinetics or input-specified power option is not evaluated for the powered heat-structure components. Instead, the nuclear core power during the beginning of the calculation is defined by the product of a constant power-to-flow ratio times the coolant mass flow through the reactor-core region. [The power-to-flow ratio is defined by the difference between liquid-coolant internal energies evaluated by subroutine THERMO, and is based on the input-specified liquid-coolant temperatures in the mesh cells above and below the NCRZ hydro cells coupled to the heat structure. Cells (levels) 1 and NCELLS (NASX) are used when the heat structure is coupled to these cells (levels).] Later in the calculation when the coolant mass flow through the reactor core is approaching its asymptotic value and satisfies the criterion, $((V_{L_i}^{n+1} - V_{L_i}^{n}) / [|V_{L_i}^{n+1}|(t^{n+1} - t^{n})]) \leq \text{EPSPOW} = 0.1$ for mesh cells where $(1 - \alpha_i) > 10^{-4}$ for all mesh cells i along the lower interface of the reactor core, the power is set for the remainder of the calculation at its steady-state power level, RPOWRI. (In addition, $\left|V_{L_i}^{n+1}\right|$ must be $>10^{-4}$ m·s^{-1} for all such cells.) for the non-typical case where $(1-\alpha_i) \leq 10^{-4}$, analogous tests are made for the gas flow. For $0.0001 < \alpha_i < 0.9999$, both the liquid and gas flows must satisfy the flow criteria. These tests are not effective until at least 5 time steps have been completed.

   The user can override this logic with NAMELIST variables IPOWR (an integer switch) and TPOWR (a problem time). The defaults are IPOWR = 0

and TPOWR = 10^{30} seconds. With these defaults, the flow logic described above controls the steady-state reactor power. With IPOWR = 0, the user can choose any time, TPOWR, to activate the steady-state power, RPOWRI; the power will be set to RPOWRI at TPOWRI or that time determined by the flow logic, whichever occurs first. With IPOWR = –1, only TPOWR will determine the time. For both IPOWR = 0 and –1, the power-to-flow-ratio logic is in effect until RPOWRI is set on. Finally, IPOWR = 1 will set RPOWRI on at the start of the steady-state calculation.

4. The time-step sizes for the heat-transfer and fluid-flow calculations are not required to be equal during a steady-state calculation. The user may specify the ratio of these time-step sizes by the time-step data parameter RTWFP. This permits compensation for the difference between the natural time scales of the two processes. Caution should be taken so that the diffusion limit in the rod axial heat conduction is not exceeded because the time-step ratio is too large. Inputting namelist variable NRSLV = 1 and evaluating an implicit axial heat conduction calculation eliminates this concern.

5. During steady-state calculations, trips with positive identification numbers are not evaluated; only trips with negative identification numbers have their set status evaluated each time step. Even though conditions may exist that would cause a change in the set status of positive identification-number trips, their set status remains constant at its input-specified value.

6. Only trip-controlled component actions with the set status of their trip ON are evaluated during a steady-state calculation. All other component actions are held constant at their initial input value even though the input data for the component define a varying component action for the transient calculation.

Steady-state calculations are transient calculations with the above procedures that converge in time to a time-independent solution state of the thermal-hydraulic system. The steady-state calculation ends when the problem time reaches the TEND ending time of the last time-step data set from file TRACIN or when the following convergence criteria, which are tested every ten time steps, are all satisfied:

- for the mesh-cell-centered parameters, where x_1 = coolant pressure, void fraction, liquid temperature, vapor temperature, and air pressure,

$$\max_i \left| \left(x_i^{n+1} - x_i^n \right) / \left[x_i^{n+1} \times \left(t^{n+1} - t^n \right) \right] \right| < \text{EPSS}$$

  for all mesh cells *i* in all hydro components; and

- for the mesh-cell-interface velocities V_{m_i} where m = l for liquid coolant and $m = v$ for vapor coolant,

$$\max_i \left| \left(V_{m_i}^{n+1} - V_{m_i}^{n} \right) / \left[\max\left(1, |V_{m_i}^{n+1}|\right) \times \left(t^{n+1} - t^{n} \right) \right] \right| < \text{EPSS}$$

for all mesh-cell interfaces *i* in all velocity component directions in all hydro components. The value of EPSS is specified by the user through input (word 3 on Main-Data Card 5). The liquid parameters are tested only when $(1-\alpha_i) > \text{MAXFLN} = 10^{-4}$, vapor parameters are tested only when $\alpha_i > \text{MAXFLN}$, and the void fraction is tested only when $\text{MAXFLN} < \alpha_i < (1-\text{MAXFLN})$ and x_i^{n+1} in the denominator is $\text{AMAX1}(\alpha_i, 1-\alpha_i)$ where α_i the void fraction in mesh cell *i*. After every 100 time steps or when a large edit is performed, the maximum value of each convergence criterion and its component mesh-cell location are edited to the terminal and message file.

If the TRAC steady-state calculation reaches the ending time of the last time-step data set and all the parameter convergence criteria have not been met simultaneously, the warning message "steady-state solution not converged" is edited to the terminal, message file, and output file before the calculation ends.

N.7.2. Constrained Steady State

The GSS calculation described in the previous section holds all variable system parameters (pump speed, valve closure, physical dimensions, etc.) constant at their initial input-specified values and solves for the system's time-independent fluid-state solution. This solution generally differs from measured steady-state fluid conditions in an actual system because the input-specified description of the physical system usually is not measured or known precisely and the thermal-hydraulic numerical models and phenomena parameters in TRAC are based on various areas of approximation. All this simulation error gets concentrated in the steady-state fluid solution. The TRAC user may prefer instead to allow the physical-system description to vary from its measured or "best-estimate" values so that some of the steady-state solution's thermal-hydraulic parameters are evaluated to have their measured values. For example, given the measured pump-impeller rotational speed and coolant mass flow, the TRAC user may prefer to allow the impeller speed to vary from its measured speed in order to calculate the measured coolant mass flow through the pump. The TRAC user may prefer to calculate the measured upstream coolant pressure or coolant mass flow through a valve by varying the valve closure state from its measured or best-estimate value. What the TRAC user needs is the ability to constrain selected thermal-hydraulic parameters to their measured or specified values because he believes these values to be accurate and important to the phenomena of interest. This can be done by varying other thermal-hydraulic and physical-system parameters, which are less well known or less important, from their measured or estimated values. By selectively biasing steady-state simulation error to less important system parameters and physical-hardware conditions, the TRAC user can achieve a more accurate steady-state solution and initial condition for analysis of transient system behavior.

A CSS calculation provides the TRAC user with this capability. The user selects and specifies through input proportional plus integral (PI) controllers to adjust specific system parameters in a manner that drives and then constrains selected thermal-hydraulic parameters to desired steady-state values. The TRAC user selects from four types of controllers in Table N-7. that are defined internally in TRAC.

Among those four types are many possible combinations of adjusted and monitored parameters. For each of those combinations are different component types in a modeled system to which they may be applied. Several dozen controllers may be selected for a full-plant model steady-state calculation. For example, a full-plant simulation may have as many as a dozen pumps modeled on the primary and secondary sides of several coolant loops to which the TRAC user may decide to apply a type 1 or 3 controller to each or some portion of these pumps.

The specification of controllers through user-defined input is a simple process. First, the TRAC user chooses the hydro or heat-structure components to which a controller will be applied. In this process, the user selects the adjusted parameter component action that will be varied to constrain the monitored parameter to a desired value. Then, the user defines the desired value of the monitored parameter by the input-specified value for the monitored parameter at its location in the component data. The only other required input for each selected controller is the allowable range over which the adjusted parameter can be varied. This range is defined by a minimum and a maximum value for the adjusted parameter. In this way, the TRAC user constrains the adjusted parameter so that it is not varied outside of an acceptable value range. When the adjusted parameter is constrained to its minimum or maximum value, the controller will no longer be able to constrain the monitored parameter to its desired value.

TABLE N-7.
CSS Calculation Controller Types

Controller Type Number	Adjusted Parameter Allowed to Vary	Monitored Parameter Constrained to Desired Value
1	Pump rotational speed	Coolant mass flow through pump
2	Valve flow area	Valve upstream pressure or coolant mass flow through valve.
3	Pump rotational speed, valve flow area, or fill coolant mass flow	Coolant mass flow through pump, valve, or fill is constrained to equal coolant mass flow at a location elsewhere in modeled system
5	Heat-structure heat-transfer area, thermal conductivity, or coupled hydraulic channel pressure	Single-phase coolant temperature or two-phase gas volume fraction

TRAC uses control-block function 200 to internally define and evaluate the PI controller that is used by each controller type. The only exception is the direct definition of the FILL component's coolant mass flow such that it equals the coolant mass flow monitored elsewhere in the system for a type 3 controller. All PI controller parameters have representative values defined internally in TRAC so that the user does not have to specify appropriate values. The tau (τ) parameter for the first-order lag function of the PI controller is set to 2 s. (For a type 5 controller, tau is constrained to be no less than 5 times the current or previous time-step size.) The Δt_d convergence time constant is set to 4 s for controller types 1 and 2, and to 10 s for controller types 3 and 5. The most sensitive parameter that affects controller adjustment is its gain factor, $(\Delta A / \Delta F)_{est}$. Seven different power-plant models, including some with multiple variations, apply all combinations of controller types on both the primary and secondary sides. These models were tested (Refs. N-3. and N-4.) to determine the applicability of the following gain factors programmed in TRAC:

ROMEGA/(RRHO*RFLOW) for a pump in type 1 and 3 controllers where ROMEGA, RRHO, and RFLOW are pump-characteristic input data,

$-10^5 \le \left[-\max(10^{-2}, 1-f_A) / \max(10^4, \Delta P_{0\ valve}) \le -10^{-7}\right]$ for a valve with monitored upstream pressure in a type 2 controller,

$5\times10^{-4} \le \left[\max(10^{-2}, f_A) / \max(5, \dot{m}_{o\ valve})\right] \le -10^{-2}$ for a valve with monitored coolant mass flow in type 2 and 3 controllers, and

various values for type 5 controllers, which can depend on the adjusted and monitored parameters and the heat-structure wall thickness and nodalization. (Details are given in Ref. N-4.)

Each controller application has a unique value for its optimum gain factor. Fortunately, the integral property of PI controllers makes them robust and stable enough to converge their adjustment with a gain factor that differs by as much as an order of magnitude from its optimum value. The TRAC user can help to provide an appropriate gain factor for valve adjustment by input defining representative conditions for pressure drop or coolant mass flow and valve closure at the valve interface. If the usual input is provided, the valve controller's gain-factor value is constrained by its above definition to an acceptable value.

The adjustment of each controller indirectly feeds back through the thermal-hydraulic solution on the entire system and the other controllers. Direct coupling can occur in one situation, however. A type 2 controller that is adjusting a valve to achieve a desired upstream pressure is directly affected by a type 5 controller that is adjusting the pressure in the same loop. When this interaction occurs, the heat-structure pressure-adjustment factor is applied to the desired pressure upstream of the valve as well as to the pressure of all BREAK components with a fluid-path connection to the heat structure.

N.7.3. Static-Check Steady State

A static-check steady-state calculation checks for the presence of unknown or extraneous momentum and energy sources in the modeled system. TRAC internally turns off the momentum source in all pumps by setting their impeller rotational speed to zero. The energy sources defined for all components also are set to zero. If the gravity vectors that are defined at all mesh-cell interfaces through input are consistent and the modeled system is connected properly, all fluid motion should go to zero eventually and the temperature of all the fluid and structure with heat-transfer paths should equilibrate during the static-check calculation. These results can be used as a positive test to determine that no unknown or extraneous momentum sources exist in the modeled system. The time required for this calculation can be reduced significantly by starting with no fluid motion in the system and with the same fluid and structural temperatures in a mesh cell.

REFERENCES

N-1. M. M. Giles and J. D. Milton, "TRAC-BD1 Control System Model," TRAC-BWR Completion report WR-CD-81-056 (November 1981).

N-2. H. L. Harrison and J. G. Bollinger, *Introduction to Automatic Control*, (International Textbook Company, Scranton, Pennsylvania, 1964), p. 144.

N-3. R. G. Steinke, "Constrained Steady-State Calculation in TRAC-PF1," Los Alamos National Laboratory document LA-UR-89-2123 (July 1989).

N-4. R. G. Steinke, "Constrained Steady-State Type-5 Controller in TRAC-PF1/MOD2," Los Alamos National Laboratory document LA-UR-96-0996 (March 1996).